



KIT SCIENTIFIC REPORTS 7633

Interaction and Transport of Actinides in Natural Clay Rock with Consideration of Humic Substances and Clay Organic Compounds

C. M. Marquardt (Editor)

C. M. Marquardt (Editor)

**Interaction and Transport of Actinides in Natural Clay Rock with
Consideration of Humic Substances and Clay Organic Compounds**

Karlsruhe Institute of Technology
KIT SCIENTIFIC REPORTS 7633

Interaction and Transport of Actinides in Natural Clay Rock with Consideration of Humic Substances and Clay Organic Compounds

by
C. M. Marquardt (Editor)

In collaboration with

Helmholtz-Zentrum Dresden-Rossendorf,
Institut für Ressourcenökologie

Johannes Gutenberg-Universität Mainz,
Institut für Kernchemie

Technische Universität München,
Theoretische Chemie

Universität des Saarlandes,
Institut für Anorganische und Analytische Chemie und Radiochemie

Universität Potsdam,
Institut für Chemie, Physikalische Chemie

Technische Universität Dresden,
Sachgebiet Strahlenschutz und Professur für Radiochemie

Report-Nr. KIT-SR 7633

Impressum

Karlsruher Institut für Technologie (KIT)
KIT Scientific Publishing
Straße am Forum 2
D-76131 Karlsruhe
www.ksp.kit.edu

KIT – Universität des Landes Baden-Württemberg und
nationales Forschungszentrum in der Helmholtz-Gemeinschaft



Diese Veröffentlichung ist im Internet unter folgender Creative Commons-Lizenz
publiziert: <http://creativecommons.org/licenses/by-nc-nd/3.0/de/>

KIT Scientific Publishing 2012
Print on Demand

ISSN 1869-9669

The work described in this report has been financially supported by the German Federal Ministry of Economics and Technology (BMWi). The authors are responsible for the content of their contributions.

BMWi Project No.: 02 E 10156

Partner No. 1: Helmholtz-Zentrum Dresden-Rossendorf, Institut für Ressourcenökologie[§]
K. Schmeide, C. Joseph, S. Sachs, R. Steudtner, B. Raditzky, A. Günther,
G. Bernhard

BMWi Project No.: 02 E 10166

Partner No. 2: Johannes Gutenberg-Universität Mainz, Institut für Kernchemie
S. Amayri, J. Drebert, D.R. Fröhlich, U. Kaplan, J.V. Kratz, T. Reich, N. Stöbener,
N. Trautmann, T. Wunderlich

BMWi Project No.: 02 E 10176

Partner No. 3: Helmholtz-Zentrum Dresden-Rossendorf, Institut für Ressourcenökologie[§],
Forschungsstelle Leipzig[§]
H. Lippold, J. Kulenkampff, M. Gründig, A. Zakhnini

BMWi Project No.: 02 E 10186

Partner No. 4: Technische Universität München, Theoretische Chemie
N. Rösch, S. Krüger, A. Kremleva

BMWi Project No.: 02 E 10196

Partner No. 5: Universität des Saarlandes, Institut für Anorganische und Analytische Chemie
und Radiochemie
R. Kautenburger, Chr. Möser, H.P. Beck

BMWi Project No.: 02 E 10206

Partner No. 6: Karlsruher Institut für Technologie[&], Institut für Nukleare Entsorgung
N. Banik, E. Hartmann, C.M. Marquardt, P. Panak, Th. Schäfer, A. Skerencak

BMWi Project No.: 02 E 10216

Partner No. 7: Universität Potsdam, Institut für Chemie, Physikalische Chemie
K. Brennenstuhl, S. Eidner, K. Jahn, M.U. Kumke, S. Kuke, B. Marmodée,
P.A. Primus, S. Zilm-Gramkow

BMWi Project No.: 02 E 10417

Partner No. 8: Technische Universität Dresden, Sachgebiet Strahlenschutz und Professur
für Radiochemie
M. Acker, A. Barkleit, M. Müller, J. Schott, S. Taut, G. Bernhard

[§] until 2011: Institut für Radiochemie; [§] until 2009: Institut für Interdisziplinäre Isotopenforschung (IIF) Leipzig, [§] { 2009 until 2011 Institut für Radiochemie, Forschungsstelle Leipzig; [&] until 2009: Forschungszentrum Karlsruhe; [@]

Foreword

The present report summarizes the progress and the results obtained within the BMWi¹-financed Joint Research Project “*Interaction and Transport of Actinides in Natural Clay Rock with Consideration of Humic Substances and Clay Organic Compounds*”. The project was conducted in the framework of a program focusing on future research & development studies on the disposal of high-level nuclear waste in deep geological formations in the years 2006 to 2011. The BMWi research program was called "Schwerpunkte zukünftiger FuE-Arbeiten bei der Endlagerung radioaktiver Abfälle (2007-2010)". The work presented here is a continuation of the work within a former BMWi project performed in the years 2003 to 2007 whose results have been published in a Scientific Report of the Forschungszentrum Karlsruhe, Report FZKA-7407 (2008).

Eight partners were involved in this joint research project and they have made their contribution to this report. All project partners are listed on the page before. To make the results of the joint project available for a broader international community and to present them as a unit, it was decided to publish the individual final reports of the project partners as a KIT research report. The final reports are enclosed as PDF files on the CD. The executive summary gives an overview of the covered topics and the obtained results without going into details. Especially, the relationships among the different groups and their studies are pointed out. The results are important contributions for safety assessments of nuclear waste disposal in deep geologic formations.

¹ German Federal Ministry of Economics and Technology (Bundesministerium für Wirtschaft und Technologie)

Content

Executive Summary.....õ õ ç

Content of the CD (q.v. Annex B)

1. *Characterization and quantification of the influence of clay organics on the interaction and diffusion of uranium and americium in the clay*
K. Schmeide, C. Joseph, S. Sachs, R. Steudtner, B. Raditzky, A. Günther, G. Bernhard
Helmholtz-Zentrum Dresden-Rossendorf, Institut für Ressourcenökologie[§]
2. *Migration of actinides in natural clay: interaction of neptunium and plutonium with natural clay*
S. Amayri, J. Drebert, D.R. Fröhlich, U. Kaplan, J.V. Kratz, T. Reich, N. Stöbener, N. Trautmann, T. Wunderlich
Johannes Gutenberg-Universität Mainz, Institut für Kernchemie
3. *Contributions to modelling actinide transport in potential host rock formations: elementary processes and influence of heterogeneous structures*
H. Lippold, J. Kulenkampff, M. Gründig, A. Zakhnini
Helmholtz-Zentrum Dresden-Rossendorf, Institut für Ressourcenökologie[§],
Forschungsstelle Leipzig[§]
4. *Quantum mechanical modeling of actinide complexes: complexation by humic substances and sorption on clay minerals*
N. Rösch, S. Krüger, A. Kremleva
Technische Universität München, Theoretische Chemie
5. *Migration of lanthanides and uranium in natural clay formations - from mineral suspensions to compact clays*
R. Kautenburger, Chr. Möser, H.P. Beck
Universität des Saarlandes, Institut für Anorganische und Analytische Chemie und Radiochemie
6. *Influence of clay organic substances on the retardation of actinide ions in the clay barrier*
N. Banik, E. Hartmann, C.M. Marquardt, P. Panak, Th. Schäfer, A. Skerencak
Karlsruher Institut für Technologie[&], Institut für Nukleare Entsorgung
7. *Spectroscopic investigations for an improved process understanding in binary and ternary systems of humic substances – clay – lanthanides: thermodynamic and kinetic parameters*
K. Brennenstuhl, S. Eidner, K. Jahn, M.U. Kumke, S. Kuke, B. Marmodée, P.A. Primus, S. Zilm-Gramkow
Universität Potsdam, Institut für Chemie, Physikalische Chemie
8. *Investigations of temperature dependence of complexation and sorption of trivalent actinides (Am(III)) in the system actinide-NOM-natural clay rock-aquifer*
M. Acker, A. Barkleit, M. Müller, J. Schott, S. Taut, G. Bernhard
Technische Universität Dresden, Sachgebiet Strahlenschutz, Professur für Radiochemie

Executive Summary

1	Introduction.....	1
2	Characteristics of Opalinus clay and pore water	5
3	Natural organic matter / kerogen inventory of natural clay stone	9
4	Complexation reactions of actinides/lanthanides with organic ligands.....	11
4.1	Complexation of trivalent actinides and lanthanides with organic ligands	11
4.2	Complexation of uranium with organic ligands	13
4.3	Complexation of actinides and lanthanides with humic acid and kerogen.....	15
4.4	Spectroscopic investigations for a fundamental process understanding	20
5	Sorption of actinides on natural clay rock.....	23
5.1	Actinides in the system water / clay rock	23
5.2	Sorption of actinides and europium on OPA at elevated temperatures.....	27
5.3	Influence of organic components on actinide and europium sorption on OPA	28
5.4	Miniaturized column experiments	29
5.5	Modeling of the sorption of actinides / lanthanides on OPA	29
6	Diffusion of actinides in OPA.....	31
6.1	Diffusion experiments with HTO, Na, U, Np, Pu, and HA	31
6.2	Extended characterization of actinides on the surface and in solution	33
7	Quantum mechanical modeling of actinide chemistry	37
8	Transport studies by means of PET	41
9	Conclusions and outlook	45
10	Publications resulting from the project	47
Annex A	Structural formula of organic ligands	53
Annex B	Final reports of the project	55

1 Introduction

For the long-term safety assessment of waste repositories detailed knowledge of interactions and transport behavior of long-lived radionuclides within the technical, geo-technical, and geological barrier has a crucial relevance. Hereby, the actinides uranium, neptunium, plutonium, americium, and curium play an important role. In contrast to other countries, Germany has not yet decided in favor of a host rock and hence, a site that is foreseen for final disposal of high-level radioactive waste was not chosen to date. Thus, site specific investigations were not possible concerning a German site in the frame of a national research project. Instead of that, the present project has focused on fundamental investigations to obtain site-independent results that can be applied to a safety analysis of any site. The migration of actinides in a potential host rock formation after their release from the waste container into the aquifer has to be known to assess possible host formations like clay, salt, and granite for their applicability as host rock and to provide the necessary information needed for the required safety case. The aim of the joint project was to elucidate the geochemical behavior of the actinides under anaerobic and reducing conditions in natural clay stone involving the influence of organic components (humic substances and clay organic components).

The influence of the chemical milieu on the mobilization and immobilization of the actinides, including the kinetics of the processes was a key aspect of the investigations. In contrast to salt or other host rock formations, diffusion processes are important for the migration of actinides in clay rock. Therefore, part of the work focused on diffusion experiments to clarify the parameter dependence of diffusion processes. The transport behavior is a function of the clay rock composition and related physical properties, and of various parameters of the aquatic system like pH, Eh, ionic strength, concentration, and charge of the actinides, competing ions, presence of complexing ligands, and content of colloids. For the aquatic chemistry in the aquifer system, organic substances like humic substances play an important role. They determine the migration and retardation behavior of the actinides by their complexing, redox, and colloidal properties. Also the organic components of the natural clay rock – low and high molecular weight compounds - might show similar interactions with actinides.

The present project continues the work of a former joint project dealing with the interaction of actinides and trivalent lanthanides with kaolinite, a model clay system. Furthermore, the impact of humic substances (HS) and natural organic matter (NOM) on the sorption of metal ions was examined. One essential aspect of the previous project was to apply quantum chemical methods (QM) to model the interactions of actinide ions with organic ligands as well as sorption on kaolinite surfaces. On the basis of these results the studies – experimental and QM - were extended in the present project to look on the role of a natural clay rock on the immobilization process of metal ions. This work should clarify, which components of the natural clay are responsible for the sorption as well as for the redox processes.

As a natural clay rock sample, the Bundesanstalt für Geowissenschaften und Rohstoffe (BGR) has provided the partners with several drilling cores of Opalinus clay (OPA) from the Mont Terri project in Switzerland. From this material various samples, powder and cores for sorption and diffusion experiments, have been prepared by the Karlsruher Institute of Technology (KIT). The reground material was distributed to the project partners for the experiments. The OPA has been characterized and extensively studied by several research groups

in Switzerland. This has the advantage that results from our joint project can be compared with the Swiss results.

The basic approach of the present project was to obtain a fundamental process understanding. Along these lines the work can be divided into the following processes that determine the mobilization or immobilization of actinides:

- Complexation: organic ligands like humic substances and clay organic components can bind actinides.
- Redox reactions: redox-sensitive actinides like uranium, neptunium, and plutonium can be reduced by dissolved inorganic and organic compounds or in contact with the surface of clay rock.
- Sorption on clay rock surfaces: actinides/lanthanides can be immobilized by binding on the clay rock surface. The sorption process depends on the physico-chemical conditions of the system like pH value, metal concentration, partial pressure of CO₂, and temperature.
- Diffusion of actinides in a clay rock matrix: experiments of metal ion diffusion through compacted clay columns or small cylindrical OPA cores give insight into the diffusion process and its related parameters.

These four issues were investigated by a pool of different methods, on the one hand non-invasive methods like time-resolved laser fluorescence spectroscopy (TRLFS), UV/Vis/NIR absorption spectroscopy, X-ray absorption spectroscopy (XAS), and positron emission tomography (PET), and on the other hand invasive methods like X-ray photoelectron spectroscopy (XPS), capillary electrophoresis (CE) or liquid-liquid extraction (LLE). Especially with CE and LLE non-fluorescent elements like Np and Pu can be characterized in solutions at trace concentrations when sensitive detection methods are applied like ICP-MS and resonance ionization mass spectroscopy (RIMS).

To support the experimental work on the humate complexation and metal sorption on clay, modeling by quantum chemistry methods was introduced. Modern quantum chemistry methods, e.g., those derived from relativistic density functional theory, were applied to provide accurate geometric, spectroscopic as well as energy data which are directly related to relevant and well-defined species. Thus, these data are useful for interpreting spectroscopic results, especially when geometric models are involved as in the interpretation of EXAFS measurements.

The present scientific report summarizes the work of the joint project "Interaction and Transport of Actinides in Natural Clay Rock with Consideration of Humic Substances and Clay Organic Compounds". The individual projects presented here were supported by the Federal Ministry of Economics and Technology (BMWi) in the frame of a program focusing on future research & development studies on disposal of radioactive waste in deep geological formations. The project started in 2006 and ended in 2011. The interested reader can get more detailed information from the individual final reports of the partners that can be found as an-

nexes on the CD attached. Most of the important results were also published in journals. A list of these publications is provided at the end of this report (Chapter 10).

2 Characteristics of Opalinus clay and pore water

The work of the joint research project was based upon the interaction of natural Opalinus clay (OPA) and its components with the actinide ions of uranium, neptunium, plutonium, americium, and curium. The OPA used in this work originates from the Mont Terri underground facility in Switzerland. The samples provided from the Bundesanstalt für Geowissenschaften und Rohstoffe (BGR) are drilling cores from the bore holes BHE-24 and -25, BLT-11 to -14 and BDR-2. The OPA is foreseen as host rock formation for high radioactive waste in Switzerland. Therefore, much work has been performed on the characterization of this type of clay by Swiss research groups. Nevertheless, the delivered OPA batches from BGR have also been characterized by this joint project regarding their elemental composition, mineralogy, cation exchange capacity, specific surface area, and carbon content. Herewith, it should be ensured that the used material possesses the same mean properties as the material used by the Swiss research groups. At the Karlsruher Institut für Technologie (KIT-INE) powder samples and small clay cores were prepared for the joint project at aerobic and anaerobic conditions. The following powder samples were characterized: aerobic powder samples from the drilling core BHE-24/1 (PAE-BHE-24/1); anaerobic powder samples from the drilling core BLT-11/1 (PAN-BLT-11/1) and BDR-2 (PAN-BDR-2). The key properties are summarized and compared with data from Swiss investigations in *Table 2-1*, *Table 2-2*, and *Table 2-3*.

From these investigations it is obvious that the OPA material used within this joint project has very similar characteristics as the material described in the literature. Therefore, results obtained in our research program can be compared with results from the Swiss investigations.

Beside the OPA and for comparison reasons, other clay materials have been used in the project. The characteristics of these materials are not discussed here, but can be gleaned in the individual final reports. The following clay materials were used: clay samples from the bore hole EST104 in the natural Callovo-Oxfordian clay rock (COx) in the underground facility Bure in France², bentonite from Milos, Texas-montmorillonite (STx-1), synthetic beidellite, synthetic Ca/Ba-montmorillonite, the clay mineral illite du Puy, as well as calcite as a clay rock component.

² 1) Andra Dossier 2005 – Référentiel du site de Meus/Haute Marne, C.R.P.ADS.04.0022; Andra: Paris, France (2005). B) Gaucher, E.C.; Blanc, P.; Bardot, F.; Braibant, G.; Buschaert, S.; Crouzet, C.; Gautier, A.; Girard, J.P.; Jacquot, E.; Lassin, A.; Negrel, G.; Tournassat, C.; Vinsot, A.; Altmann, S. : Modelling the porewater chemistry of the Callovian-Oxfordian formation at a regional scale. *Comptes Rendus Geoscience*, 338(12-13), 917-930 (2006).

Table 2-1: Specifications of the OPA used in the experiments compared with data from Nagra (Switzerland).

Parameters	PAE-BHE-24/1 ($< 500 \mu\text{m}$)	PAN-BLT-11/1 ($< 200 \mu\text{m}$)	PAN-BDR-2	Nagra ³
Specific surface, (N ₂ -BET, m ² /g)	41.3	38.8	31.3	24-37
Cation exchange capacity (meq/100 g)	10.3	12.9	10.8	11.1-16.0
Total carbon TC (wt.%)	2.49	1.87	2.54	-
Total organic carbon TOC (wt.%)	1.09	0.96	0.63	0.8

Table 2-2: Mineralogy of the OPA sample BHE-24/1 in comparison to data from literature: averaged data of OPA from Mont Terri without carbonate-rich sandy facies (all data in wt.% \pm standard deviation (1σ)).

Mineral	BHE-24/1	Mont Terri ⁴	Mont Terri ³
Kaolinite	22.5 \pm 1.3	15 - 37	22 \pm 2
Kaolinite-serpentine	13.8 \pm 2.7	-	-
Illite	26.5 \pm 1.3	15 - 30	32 \pm 6
Illite/smectite mixed layers	-	5 - 20	11 \pm 2
Chlorite	< 5.0	3 - 18	10 \pm 2
Quartz	21.9 \pm 1.1	10 - 32	14 \pm 4
Calcite	13.1 \pm 0.7	4 - 22	13 \pm 8
Dolomite/ankerite	nd*	0 - 1	nd*
Siderite	nd*	0 - 6	3 \pm 1.8
Feldspar	< 4.0	0 - 8	2 \pm 1.6
Pyrite	1.5 \pm 0.1	0 - 3	1.1 \pm 0.5
Total organic carbon	0.6 \pm 0.3	0.4 - 1.2	0.8 \pm 0.5

³ Nagra: Projekt Opalinuston – Synthese der geowissenschaftlichen Untersuchungsergebnisse, Entsorgungsnachweis für abgebrannte Brennelemente, verglaste hochaktive sowie langlebige mittelaktive Abfälle. Technical Report NTB 02-03, NAGRA Nationale Genossenschaft für die Lagerung radioaktiver Abfälle, Wetztingen/Switzerland (2002).

⁴ Bossart, P. and Thury, M., Mont Terri Rock Laboratory. Project, Programme 1996 to 2007 and Results. Report of the Swiss Geological Survey No. 3, Swiss Geological Survey. Switzerland (2008).

* nd: not detectable

Table 2-3: Characterization of the aerobic handled OPA sample BHE-24/1 and anaerobic handled clay samples BDR-2 and BLT-11/1 by XRF, ICP-MS, and AAS. Errors are omitted for clearness, but they can be found in the individual reports.

Main elements	BHE-24/1 [wt.%]		BDR-2 [wt.%]		BLT-11/1 [wt.%]	Trace elements BHE-24/1 [ppm]	
	JGU	HZDR	JGU	HZDR	HZDR	JGU	
SiO ₂	43.90	39.04	49.31	37.5	36.37	Sc	24
TiO ₂	0.88	0.91	0.93	0.97	0.99	V	151
Al ₂ O ₃	19.19	17.91	18.59	18.02	20.08	Cr	136
Fe ₂ O ₃	6.47	6.53	6.46	6.51	6.04	Co	31
MnO	0.05	0.06	0.06	0.08	0.05	Ni	65
CaO	6.00	5.42	5.65	5.08	3.16	Cu	19
Na ₂ O	0.29	0.59	0.35	0.52	0.54	Zn	124
K ₂ O	3.01	3.47	2.8	3.52	3.61	Ga	24
P ₂ O ₅	0.17	0.21	0.39	0.45	0.25	Rb	128
Cr ₂ O ₃	0.02		0.02			Sr	235
NiO	0.01		0.01			Y	25
MgO	2.35	2.32	2.01	1.96	2.33	Zr	147
SO ₃	nd*		1.12			Nb	19
LOI**	16.78		12.25			Ba	295
						Pb	23
						Th	12
U [ppm]		2.83		2.63	2.93	U	3

* nd.: not detectable, **LOI: loss on ignition, XRF: X-ray fluorescence analysis, AAS: atomic absorption spectroscopy. JGU: University of Mainz, HZDR: Helmholtz-Zentrum Dresden-Rossendorf.

The characterization and application of original OPA pore water was not subject of the project, because the water was not available in sufficient amounts due to practicable and technical reasons⁵. Therefore, for the batch and diffusion experiments synthetic OPA pore water

⁵ The reader is referred for more information about sampling and characterizing of original pore water from the OPA to: 1) Pearson F. J., Arcos D., Bath A., Boisson J. Y., Fernandez A. M., Gäbler H. E., Gaucher E., Gautschi A., Griffault L., Hernan P., and Waber H. N. Geochemistry of water in the Opalinus Clay Formation at the Mont Terri Rock Laboratory. Geol. Ser. 5. 2003. Bern (Schweiz), Bundesamt für Wasser und Geologie, Bern, Schweiz and 2) Bossart P. and Thury M. Mont Terri Rock Laboratory Project, Programme 1996 to 2007 and Results. Swiss Geological Survey (SGS), Rep. Swiss Geol. Surv. 3, Wabern (Switzerland), Swisstopo (2008).

was used. The composition of this water is based on several studies on natural pore water samples originating from OPA within the Mont Terri Project in Switzerland and was recommended from some scientific groups⁶. The synthetic pore water had a pH of 7.6 and an ionic strength of 0.4 M. It consisted mainly of NaCl with minor amounts of CaCl₂, MgCl₂, KCl, SrCl₂, Na₂SO₄, and NaHCO₃. The exact composition of the artificial pore water is given in *Table 2-4*.

Table 2-4: Composition of the synthetic OPA pore water⁶ used in the batch and diffusion experiments.

Salt	Concentration / g L ⁻¹
NaCl	12.38
KCl	0.12
MgCl ₂ ·6H ₂ O	3.48
CaCl ₂ ·2H ₂ O	3.79
SrCl ₂ ·6H ₂ O	0.14
Na ₂ SO ₄	2.00
NaHCO ₃	0.04

⁶ 1) Pearson F. J.: Opalinus Clay experimental water: A1 Type, Version 980318. PSI Internal Report TM-44-98-07, Villigen, Switzerland, Paul Scherrer Institut, PSI (1998). 2) Van Loon L. R., Soler J. M., and Bradbury M. H.: Diffusion of HTO, ³⁶Cl⁻ and ¹²⁵I⁻ in Opalinus Clay samples from Mont Terri - Effect of confining pressure, *Journal of Contaminant Hydrology* 61, 73-83 (2003). 3) AK/HAW: Arbeitskreis hochradioaktiver (HAW) Produkte, Empfehlung des Arbeitskreises HAW Produkte „Referenz-Tonwasser" (2007).

3 Natural organic matter / ? Yfc[Yb]bj YbłcfmicZbUłi fUclay stone

Within the framework of this project the nano- to microscale distribution of natural organic matter (NOM) in the Callovo-Oxfordian clay formation and the Opalinus clay has been characterized. Another activity was focused on the extraction of different hydrophilic and hydrophobic compounds from the natural clay stone samples. With the extracted organic material, actinide complexation studies should be performed later.

Synchrotron based (C-, K-, Ca-, O- and Fe-edge XANES) scanning transmission X-ray microscopy (STXM) and FTIR microspectroscopy were used to identify under high spatial resolution the distribution of clay-organic matter with different functionality using principal component and cluster analysis. The results show that in this old (Jurassic) geological formation, small parts of the organic inventory (1–5%) keeps the structure/functionality and can be mobilized as hydrophilic humic substance type material (humic acid (HA) and fulvic acid (FA)). HA and FA were extracted following the standard International Humic Substance Society (IHSS) isolation procedure. Target spectra analysis shows best correlation for isolated humic acids with organics found in smectite-rich regions, whereas the extractable FA has better spectral similarities with illite mixed layer mineral (MLM) regions.

The major fraction (>95%) of NOM is associated with minerals. In order to understand the importance of NOM on the chemistry of this formation, a protocol was developed allowing extraction and fractionation of organic compounds in the rocks. By this method a large part of the minerals can be removed and almost all (>90%) of the NOM (associated with residual recalcitrant minerals) is suspended in water. The molecular composition of the solvent-soluble, directly extractable part shows the NOM to be thermally immature. The solvent-soluble fractions obtained after acid and alkaline treatments are mostly polar in nature and have a high degree of aliphaticity. C(1s) NEXAFS analysis of water soluble organic fractions indicates an increase in aliphaticity and a decrease in carboxylic and carbonyl groups for consecutive extraction steps.

Based on a protocol established in the petroleum community⁷, the isolation of kerogen has been performed from the OPA whole rock. The motivation of kerogen isolation was to investigate in a further step the complexation behavior of this kerogen with respect to radionuclides (i.e. trivalent actinides; Cm) in batch sorption and spectroscopic studies. This procedure consists of several acid attacks under anoxic atmosphere at 60-70 °C. The crucial point for the separation of organic material is the removal of inorganic impurities – mainly pyrite - that disturbs fundamental spectroscopic complexation studies. The removal of pyrite is realized by an additional chemical leaching procedure. We succeeded to reduce the amount of inorganic mineral phases co-extracted with the kerogen-type material. SEM-EDX measurements showed that the inorganic phases are still present and sum up to a total amount of

⁷ Vandenbroucke, M. and Largeau, C.: Kerogen origin, evolution and structure, *Organic Geochemistry*, 38(5), 719-833 (2007).

18.3 wt.% (Al, Si, Fe, S). This is an improvement to earlier studies⁸, but however, for complexation studies the content of impurities is still too high.

⁸ Deniau, I., Devol-Brown, I., Derenne, S., Behar, F. and Largeau, C.: Comparison of the bulk geochemical features and thermal reactivity of kerogens from Mol (Boom Clay), Bure (Callovo-Oxfordian argillite) and Tournemire (Toarcian shales) underground research laboratories. *Science of The Total Environment*, 389(2-3), 475-485 (2008).

4 Complexation reactions of actinides / lanthanides with organic ligands

As mentioned before, the natural clay rock contains more or less organic components from small molecules like acetate till macromolecular humic acid-like compounds. The exact composition is not known, but formate, acetate, propionate, and lactate have been detected⁹. These low molecular weight anionic ligands constitute the complexing entities of macromolecular clay organics or humic substances. The investigation of the complexation of actinides by low molecular weight ligands can be regarded as the first step to understand the complexation of the much more complex binding mechanism of actinides by macromolecular clay organics or humic substances. In order to investigate the complexation properties not only the meanwhile well-established methods like time-resolved laser fluorescence spectroscopy (TRLFS) and UV-Vis absorption spectroscopy were applied, but also absorption spectroscopy with a long path flow cell (UV-Vis-LPFC), micro titration calorimetry and capillary electrophoresis combined with ICP-MS were adopted. The first application of attenuated total reflection FTIR spectroscopy (ATR-FTIR) yielded new results of the structure of U(VI) carboxylate binding.

The complexation of actinides with ligands acting as model molecules for humic substances was mainly studied, especially molecules that were not considered so far as complexing ligands. Here, the europium complexation with pyromellitic acid can be emphasized. On the other hand, the examinations also focused on the impact of nitrogen, sulfur, and phosphorus containing functional groups on the actinide complexation by carboxylic groups in complex organic ligands.

Due to the fact that elevated temperatures are expected in a repository¹⁰ as a consequence of the heat producing radioactive decay, complexation reactions were examined as a function of temperature.

4.1 Complexation of trivalent actinides and lanthanides with organic ligands

The complexation behavior of Am(III) and Eu(III) with several small organic acids¹¹ was studied by means of UV-Vis measurements with a LPFC¹² and by TRLFS. The stoichiometry of the formed complexes, their stability constants, and thermodynamic data were determined. Several new complexes were identified and thermodynamically characterized, such as the 1:3 Eu(III)-salicylate complex, the 1:1 and 1:2 Am(III)-pyromellitate complexes, and the 1:1

⁹ 1) Courdouan, A., Christl, I., Rabung, Th., Wersin, P., Kretzschmar, R.: Proton and Trivalent Metal Cation Binding by Dissolved Organic Matter in the Opalinus Clay and the Callovo-Oxfordian Formation, *Environ. Sci. Technol.* 42, 5985-5991 (2008). 2) Courdouan, A., Christl, I., Meylan, S., Wersin, P., Kretzschmar, R.: Characterization of dissolved organic matter in anoxic rock extracts and in situ pore water of the opalinus clay, *Appl. Geochem.*, 22, 2926-2939 (2007).

¹⁰ Depending on the storage concept temperatures of about 200 °C are discussed for storage in salt formations and 90 °C for storage in clay rock formations.

¹¹ The ligands were: pyromellitic acid (1,2,4,5-benzene-tetracarboxylic acid), salicylic acid, acetic acid, lactic acid, citric acid, tartaric acid, anthranilic acid, nicotinic acid, picolinic acid, and phthalic acid

¹² LPFC: long path flow cell; FTIR: Fourier transform infrared spectroscopy; DFT: density functional theory.

and 1:2 Am(III)-salicylate complexes. Some complexes were examined by spectrometric methods for the first time in aqueous solution, such as the Am(III) complexes with anthranilic, nicotinic, picolinic, and phthalic acid. In case of molecules with nitrogen containing functional groups, the Am(III) is mainly coordinated by carboxylic groups, however, probably stabilized by nitrogen groups.

Table 4-1: Complex formation constants of Am(III) and Eu(III) as surrogate for trivalent actinides with organic ligands at various temperatures at ionic strength 0.1 M NaClO₄. When intervals for the formation constants are given, the lowest value generally corresponds to the lowest temperature (20/25 °C) and the highest value to the highest temperature (50/65/70 °C). Errors are omitted for clearness but they can be found in the individual reports.

Ligands	T [°C]	Complex formation constant			
		$\log \beta_{11}$	$\log \beta_{12}$	$\log \beta_{13}$	Method
Am(III)					
Acetic acid	25 - 50	2.14 – 2.30			A
Salicylic acid	25	2.56	3.93		A
Lactic acid	25 - 65	2.22 – 2.75			A, B
Pyromellitic acid	20 – 50	5.42 – 5.70	9.74 – 10.80		A, B
Citric acid	25 - 50	6.67 – 7.66	11.80 – 12.36		A
Tartaric acid	25	3.84	6.54		A
Phthalic acid	25	3.99			B, C
Anthranilic acid	25	3.70			B, C
Picolinic acid	25	3.83	7.34		B, C
Eu(III)					
Salicylic acid	25 – 60	1.84 – 1.67	3.56 – 3.70	4.89 – 5.35	B
Lactic acid	25 – 70	2.51 – 2.87	4.45 – 4.78	5.83 – 6.48	B
Pyromellitic acid	25 – 60	4.70 – 5.03			B
Tartaric acid	25	4.17	7.27		A

A: UV-Vis-LPFC: absorption spectroscopy with long path flow cell; B: TRLFS: time resolved laser fluorescence spectroscopy; C: UV-Vis absorption spectroscopy

In general, all studied complexation reactions are endothermic and driven by entropy, expressed in a positive molar standard reaction enthalpy $\Delta_r H_m^\circ$ and molar standard reaction entropy $\Delta_r S_m^\circ$. The consequence is that organic complexes of actinide cations are stabilized in solution at elevated temperatures. The results of these studies are summarized in *Table 4-1*.

The studies on the europium complexation with pyromellitic acid can be pointed out here, because this type of ligand can be regarded as a precursor for humic acid-like compounds.

The pyromellitic acid mimics the structural arrangement of carboxylates in polyphenols and it can form aggregates. This behavior is also typical for humic acids. The pyromellitate complexation is characterized by TRLFS, micro calorimetry, FTIR¹² and DFT¹² calculations. The data indicate that a monomeric and pyromellitic aggregated complex occurs, that chelating and monodentate binding modes are possible and that a 1:1 stoichiometry in both the monomeric and polymeric states prevails.

TUM modeled the complexation of Am(III) with quantum chemical methods (QM). Acetate was used as a model ligand. To inspect the stability of the complexes, the complexation reaction was characterized by the Gibbs free energy of complexation. The coordination number of the Am(III) was varied from 7 to 10 and the Gibbs energies were modeled for a monodentate and a bidentate complex with one acetate molecule. For all coordination numbers bidentate coordination is preferred, as shown by 4 to 17 kJ mol⁻¹ lower endothermic Gibbs free energies. The complexation Gibbs free energies, 49–55 kJ mol⁻¹, for bidentate complexes of various coordination numbers overestimate the experimental results of about 15 kJ mol⁻¹, derived from measured log β values of the project partner TU Dresden as well as earlier experiments¹³. The calculated Gibbs free energy of adding an aqua ligand to the complex with CN = 7 is 5 kJ mol⁻¹ for the bidentate and 12 kJ mol⁻¹ for the monodentate complex. Thus, species with CN = 7 and 8 are energetically nearly degenerate. The addition of a further aqua ligand to reach CN = 9 requires about 20 kJ mol⁻¹; thus a higher coordination is not favorable.

The temperature effect of the actinide complexation with acetate was also studied by QM. For that UO₂²⁺ was used as cation and the results are briefly described in the next section.

4.2 Complexation of uranium with organic ligands

The objective of this work package was to validate existing complexation constants by spectroscopic methods and to measure complexation constants for so far neglected organic ligands. The organic ligands were aliphatic carboxylates, aromatic carboxylates containing nitrogen, aromatic phosphonates, and aromatic sulfonates. These ligands represent a variety of organic ligands in aqueous systems or were chosen as model ligands for humic substances. The complexation reaction with these organic ligands was investigated with hexavalent as well as with tetravalent uranium by TRLFS, UV-Vis spectroscopy, or both.

U(IV)

The complexation of tetravalent uranium (U(IV)) with citric, succinic, mandelic, and glycolic acid was studied by UV-Vis spectroscopy at room temperature. Especially the citric acid shows strong complexation with U(IV) that might enhance the solubility of tetravalent uranium in solution. Due to the strong complexation and the reducing properties of the citric acid, the tetravalent oxidation state of uranium is stabilized. It is assumed that the complex is

¹³ L. R. Morss, N. M. Edelstein, J. Fuger (Eds.). Actinide and Transactinide Elements, 3. ed., Springer, Dordrecht (2006).

formed with the most basic and fully deprotonated ligand cit^{3-} , but also the H_2cit^- is debated. The interaction of U(IV) with succinic, mandelic, and glycolic acid is much weaker than with citric acid. The measured complex formation constants are given in *Table 4-2*.

U(VI)

The complexation of hexavalent uranium (U(VI)) was investigated with citrate, oxalate, lactate, anthranilate, nicotinate, phenylphosphonate, benzenesulfonate and 4-hydroxybenzenesulfonate.

The uranyl citrate complexation was measured at a very low temperature of $-120\text{ }^\circ\text{C}$ by cryo-TRLFS. Measurements at such low temperatures are expected to improve significantly the intensity and resolution of luminescence spectra in consequence of lower quenching effects due to ligands and/or water. Hence, the emission of the complexed species was successfully measured in contrast to room temperature and the complex formation constants were determined directly from the emission spectra. The formation constants obtained are very similar to the constants determined indirectly at room temperature (s. *Table 4-2*).

The complexation of U(VI) with lactate was investigated in the temperature interval between 7 and $65\text{ }^\circ\text{C}$. The complex formation constants for the first and second complex increase with increasing temperature. Hence, the complexation constant is endothermic and entropy-driven; the molar standard reaction enthalpy $\Delta_r H_m^\circ$ and molar standard reaction entropy $\Delta_r S_m^\circ$ are both positive. The U(VI) lactate complexes are much weaker than the complexes with oxalate or citrate.

To elucidate the impact of nitrogen containing functional groups on the metal binding of carboxylic groups, complexation studies of U(VI) with the ligands anthranilic and nicotinic acid were performed. The examinations show that the complexation is dominated by the carboxylic groups – U(VI) is only coordinated by the carboxylic groups – and a significant impact of the nitrogen atomic functional groups was not found. Quantum chemical modeling confirmed that amine and pyridine functional groups are not important for actinyl complexation when carboxylate groups are prevailing. The complex formation constant of the anthranilate is slightly lower than for the nicotinate and this might be explained by electrostatic repulsion between the positive charged amino group and the cation. The pyridine nitrogen might stabilize the cation binding by mesomeric effects.

The effects of acidic phosphorus and sulfur containing functional groups were estimated by complexation studies with U(VI) and phenylphosphonic acid, benzene sulfonic acid, and 4-hydroxybenzenesulfonic acid. The investigation has shown that the complexation strength of aromatic phosphonate groups toward U(VI) is comparable or even higher than that of oxygen functionalities such as carboxylic groups. The formation constant for the phenylphosphonic acid is somewhat higher than for the benzoic acid ($\log \beta_{11} = 3.37 \pm 0.14$). However, the relevance of phosphonate groups of organic substances is small due to their low content in natural organic matter.

For the temperature dependence of actinide complexation, new aspects emerged from QM modeling results. QM modeling shows for the uranyl acetate complexation that mono- and

bidentate complexes at room temperature are energetically almost degenerate, while bidentate complexes become more favorable with increasing temperature. The difference of the complexation Gibbs free energy between mono- and bidentate complexes increases (in absolute terms) from 1 to 5 kJ mol⁻¹ by raising the temperature from room temperature to 90 °C. These computational results suggest that the equilibrium between mono- and bidentate isomers is a function of the temperature. The concentration ratio of bi- and monodentate complexes is estimated to about 2:1 at room temperature and 7:1 at 90 °C. Such a topic has been rarely considered in studies so far, but seems to be rather important for actinide complexation at elevated temperatures.

Table 4-2: Complex formation constants of U(IV) and U(VI) with various organic ligands at 0.1 M NaClO₄ and at room temperature. Only the lactate complexation was studied between 7 and 65 °C.

Ligands	T [°C]	Complex formation constant			Method
		log β _{101 or 11}	log β _{102 or 12}	log β _{202 or 22}	
U(IV)					
Citric acid	25	13.5 ± 0.2	25.1 ± 0.2		A
Mandelic acid	25	4.53 ± 0.09	8.02 ± 0.13		A
Glycolic acid	25	4.71 ± 0.08	8.25 ± 0.15		A
Succinic acid	25	9.0 ± 0.2			A
U(VI)					
Citric acid	-120 25	7.24 ± 0.16 ^a 7.67 ± 0.12 ^b		18.90 ± 0.26 ^a 18.85 ± 0.42 ^b	B, C
Oxalic acid	-120 25	5.88 ± 0.29 ^a 5.92 ± 0.03 ^b	10.26 ± 0.13 ^a 10.30 ± 0.38 ^b		B, C
Lactic acid	7 – 65	2.71 – 3.70	4.40 – 5.64		A, C
Anthranilic acid	25	3.14 ± 0.17			D
Nicotinic acid	25	3.73 ± 0.30	7.46 ± 0.17		C
Phenylphosphonic acid	25	3.61 ± 0.14	6.95 ± 0.22		C
Benzenesulfonic acid	25	2.62 ± 0.07			C
4-Hydroxybenzene sulfonic acid	25	2.67 ± 0.03			C

a: measured at -120 °C; b: measured at 25 °C; A: UV-Vis absorption spectroscopy; B: cryo-TRLFS; C: TRLFS; D: fs-TRLFS (femtosecond TRLFS).

4.3 Complexation of actinides and lanthanides with humic acid and kerogen

In the last decade, many investigations have been performed to elucidate the actinide complexation by humic substances like humic and fulvic acid. Thus, many complexation constants have been determined for binary and ternary humate/fulvate complexes by various

methods. In this project, for the first time, data obtained with cryo time-resolved laser fluorescence spectroscopy (cryo-TRLFS), multiwavenumber infrared spectroscopic data – obtained by attenuated total reflection Fourier transform infrared (ATR-FTIR) spectroscopy – and data from capillary electrophoresis have been applied to deduce complex formation constants of uranyl and europium humates.

U(VI) HA complexes: binary, ternary hydroxo and carbonato humate complexes

These studies have been performed with TRLFS and ATR-FTIR. The mixed uranyl hydroxo humate complex was confirmed and the formation of a ternary uranyl carbonato humate complex of the type $\text{UO}_2(\text{CO}_3)_2\text{HA}(\text{II})^{4-}$ was detected for the first time. The complex formation constant was calculated to be 24.57 ± 0.17 . At pH 8.5 and humic acid concentrations higher than 2 mg L^{-1} , the dominant tricarbonato complex is displaced by the $\text{UO}_2(\text{CO}_3)_2\text{HA}(\text{II})^{4-}$ complex. Hence, humic acids can have a significant impact on the U(VI) speciation, even when strong carbonate complexes occur in solution. The corresponding uranyl carbonato fulvate complex $\text{UO}_2(\text{CO}_3)\text{FA}$, described by Glaus et al.¹⁴, could not be confirmed. In *Table 4-3* the data are summarized.

The influence of temperature on the uranyl humate complexation was measured with TRLFS at 20, 40 and 60 °C. The temperature has a significant impact only at 60 °C, where the formation constant decreases by about 0.35 log units, as seen in *Table 4-3*. However, the formation constants at 20 and 40 °C are significant lower than the result from the ATR-FTIR measurement. Previous studies have delivered a complex formation constant of 6.20 ± 0.56 ¹⁵.

QM contributions to U(VI) humate complexation

In earlier experiments of uranyl complexation with humic acid in the neutral and slightly basic pH range, the ternary mixed uranyl hydroxo humate complex ($\text{UO}_2(\text{OH})\text{HA}(\text{I})$) was proved. However, the experimental results suggest a higher complex formation constant of the mixed complex than the pure uranyl humate complex ($\text{UO}_2\text{HA}(\text{II})$). By quantum chemical calculations (QM) for the model ligand acetate, this result could not be confirmed; the Gibbs free energies of complexation of uranyl monohydroxide with acetate are clearly lower than for uranyl itself; this translates into a lower complexation constant of uranyl monohydroxide. This result can be explained by the lower charge of UO_2OH^+ compared to UO_2^{2+} . This discrepancy demonstrates that at least at neutral to basic pH conditions the complexation of uranyl by humic substances at the microscopic level deserves further exploration. Nevertheless, QM could confirm that the very short distances of about 212 pm found in EXAFS of actinide humate complexes might really be caused by a binding between a metal ion and a hydroxo anion. By QM distances of the U-O_H bond of 212-214 pm were found.

¹⁴ Glaus, M.A., Hummel, W. and van Loon, L.R.: Stability of mixed-ligand complexes of metal-ions with humic substances and low-molecular-weight ligands, *Environ. Sci. Technol.* 29, 2150-2153 (1995).

¹⁵ Pompe, S., Schmeide, K., Bubner, M., Geipel, G., Heise, K.H., Bernhard, G. and Nitsche, H.: Investigation of humic acid complexation behavior with uranyl ions using modified synthetic and natural humic acids, *Radiochim. Acta* 88, 553-558 (2000).

Table 4-3: Conditional complex formation constants for various humate/fulvate complexes in 0.1 M NaClO₄ solutions at room temperature and elevated temperatures.

Humate species	log β	Method
EuHA(III)	6.45 ± 0.29 ^a	A
EuHA-PB(III) ^b	5.5 ± 1.0 ^a	A
UO ₂ HA(II)	6.70 ± 0.25	B
	20 °C	C
	40 °C	C
	60 °C	C
UO ₂ (OH)HA(I)	15.14 ± 0.25	B
	14.89 ± 0.54	C
UO ₂ (CO ₃) ₂ HA(II) ⁴⁻	24.47 ± 0.70	B
	24.57 ± 0.17	D
UO ₂ (CO ₃)FA	n.o.	B
Np(IV)FA	7.3 ± 0.5 ^c	E

a: average value of log β at pH 3, 5, 7, and 10 in 0.01 M NaClO₄; b: Aldrich humic acid with blocked phenolic groups; c: average value of log β at pH 1 and 1.5 in 0.1 M NaCl; n.o.: not observed; A: CE-ICP-MS, capillary electrophoresis coupled to ICP-MS; B: ATR-FTIR, attenuated total reflection Fourier-transform infrared spectroscopy; C: TRLFS, time-resolved laser fluorescence spectroscopy; D: cryo-TRLFS; E: UV-Vis absorption spectroscopy

HA complexes: sulfur functionality

Humic substances show a broad variation of functional groups beside the carboxylic groups e.g. sulfur containing groups. The impact of these sulfur functionalities on the complexation of U(VI) was investigated with synthetic humic acid model substances with varying sulfur content. The obtained results show that the sulfur groups can be involved in U(VI) humate complexation. At sulfur content > 2 wt.%, the loading capacity (LC) as well as the complex formation constant log β increase. The functional entities of thiol groups are suggested to be involved in the complexation. However, the normal content of sulfur in natural humic substances is between 0 and 2 wt.%. Therefore, these functionalities play a minor role in the complexation process in natural aquifer systems. A joint experimental and quantum chemical study showed that also sulfonate groups are not important.

The role of the sulfur functionalities for the Np(V) reduction was also studied. It was clearly shown that the sulfur functionalities contribute to the redox process and can reduce Np(V) to tetravalent Np. However, because of their lower content in natural HA compared to other reducing groups like quinone-like moieties and phenolic groups, sulfur functional groups play a minor role.

Metal-NOM-speciation with CE-ICP-MS

In this work capillary electrophoresis coupled with inductively coupled plasma mass spectrometry (CE-ICP-MS) has been used for studying Eu, Gd, and U interaction with purified Aldrich humic acid (HA). The effect of metal concentration on the HA complexation as well as the competition effect of calcium, magnesium, and aluminum as trivalent metal ion were investigated. Additionally, the impact of phenolic groups on the complexation of Eu(III) by using HA with blocked phenolic groups (HA-PB) was a matter of interest to elucidate the complexation mechanism between trivalent metal ions and HA. A separation of metal ions in HA solution with CE results in three peaks in the electropherograms. This is illustrated for Eu in Figure 4-1 by the red curve.

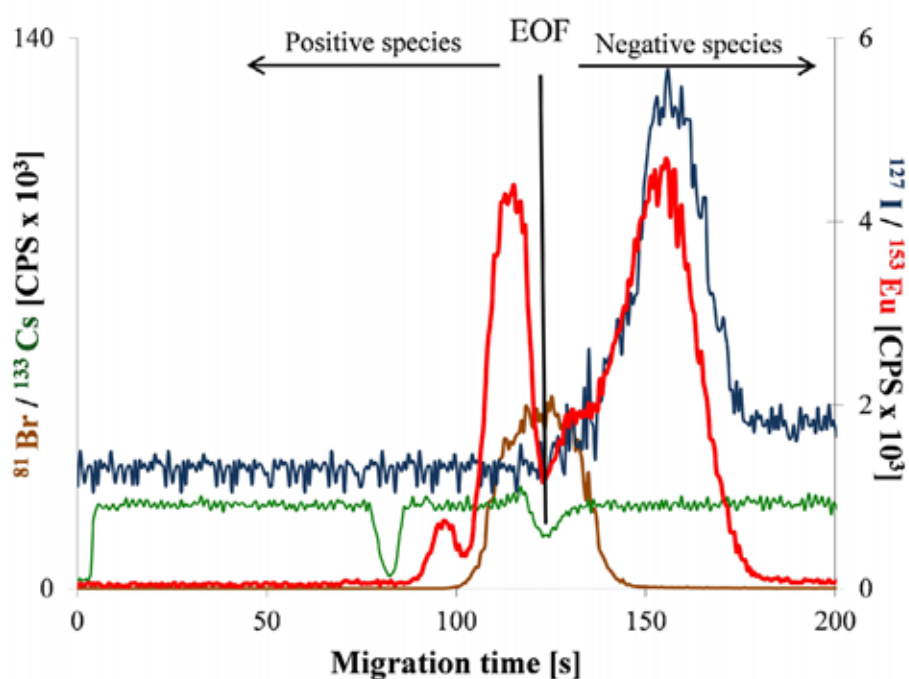


Figure 4-1: CE-ICP-MS electropherogram²⁸ which shows Eu species (^{153}Eu) complexed or uncomplexed with iodinated HA (^{127}I) (details see also text). ^{153}Eu , ^{127}I , ^{81}Br , and ^{133}Cs intensities are plotted as a function of their migration time through the capillary in an electric field (30 kV). The red curve corresponds to the Eu signal, and the blue curve to the iodine signal. 1-bromopropane (^{81}Br) is used as neutral species to monitor the electroosmotic flow of the solution (EOF marker, brown curve). Positive species are found on the left and negative species on the right of the EOF signal. Cs (^{133}Cs) serves as CE electrolyte flow marker (green curve); sample: $3.29 \mu\text{mol L}^{-1}$ Eu, 25 mg L^{-1} AHA, 10 mM NaClO_4 and pH 5.

The first signal at migration time of $93 \pm 1.2 \text{ s}$ represents the uncomplexed, positively charged metal ion before CE-separation. The second signal observed at migration time of $110.4 \pm 2.7 \text{ s}$ represents metal ions complexed on weak binding sites of HA before the CE-separation step. The last signal at migration time of $146.7 \pm 1.0 \text{ s}$ represents metal ions complexed at strong binding sites of HA before CE-separation. The last peak matches quite well with the signal of the ^{127}I corresponding to HA (violet curve in Figure 4-1).

By variation of the metal concentration, adding competing metal ions, and using HA with blocked phenolic groups, differences in the electropherograms were observed. In this way a difference in the humate complexation between Eu(III) and U(VI) could be observed. The humic acid complexes 95% of the Eu(III) cations, and 55% were found on strong binding sites. In case of U(VI) only 26% was complexed by HA, and here, totally on strong sites. It seems that the oxygen atoms in the uranyl structure sterically impede the formation of the weak complexes.

By CE, a differentiation between metal ions that easily dissociate from the humate complex and metal ions strongly bound to humic acid is possible. But the detailed interpretation of the complexation process of these two types of metal bonding is still open. However, all these findings from the CE studies have to be quantified in further investigations to use these results in modeling studies for a safety analysis. Nevertheless, conditional complex formation constants for the EuHA(III) have been calculated (s. *Table 4-3*).

Fulvate complexation of tetravalent Np

A further study of actinide interactions with organic components focused on the complexation of tetravalent Np with fulvic acid (FA). As is generally known the tetravalent Np(IV) hydrolyses already at low pH values forming hydroxo complexes and colloids. Extended XAFS and XPS analysis should clarify whether mixed ternary complexes (Np(OH)_xHA) are existent, or whether a simple binary complex (NpHA(IV)) is formed. The investigations of the Np(IV) fulvate complexation between pH 1 and 3 showed, however, that by means of XAFS and XPS no clear distinction can be made between the ternary and the binary complex. There was no clear correlation between the results of the spectroscopic methods and the pH values, the reaction time, and the nature of the preparation of the Np(IV) fulvate. In some experiments, two Np-O distances were found (~ 2.22 Å and ~ 2.42 Å), in other experiments only one Np-O distance is existent varying between 2.30 and 2.38 Å. It can be concluded from the results that Np is bound to a carboxyl group (monodentate or bidentate) and that oligomers or colloids forming nanoparticles can be excluded. To estimate a complexation constant at pH 1 and 1.5 – conditions with minimized hydrolysis – a pure NpFA(IV) complex is assumed, taking into account the so-called loading capacity (LC) or the degree of deprotonation (α_H) of the fulvic acid. The conditional complex formation constant at ionic strength of 0.1 M NaCl/NaClO₄ was estimated to $\log \beta = 7.0$ or 7.6 at pH 1 and 1.5, respectively. The pH dependence cannot be explained by the present model, but the conditional complexation constant qualitatively matches with literature values of humic complexes of tetravalent actinides as a function of pH.

Kinetic aspects of humate complexation and dissociation of lanthanides

In another work package, the kinetic aspects of metal humate complexation and dissociation, considering also formation and destruction of polynuclear species, were examined. Here, the complexation experiment with Tb(III) and humic acid pre-equilibrated with Al(III) was investigated by using an anion exchange method. As expected, the Al(III) inhibits the Tb(III) complexation and the degree of inhibition depends on the pre-equilibration time of Al(III) with HA. From further findings one can conclude that bound metals do not leave their initial binding sites but the sites themselves become “stronger” with increasing reaction time. That means

that structural changes are induced in the surroundings of the metal, keeping it more and more trapped, for instance due to bridging effects. In this way, the metal becomes less exchangeable for competing metals, and also the access to free binding sites may be increasingly hindered. Spectroscopic studies in the same system confirmed the hindered Tb(III) complexation, but the measurements could not reveal any time dependent effects. One may conclude that stabilizing rearrangements as a basis of the kinetic effect cannot be very significant compared to the initial impact of Al(III) complexation.

Interaction of Cm(III) with kerogen

There is only little known about the interaction between actinides and kerogen, an organic clay component, that can be leached from the solid into the mobile aqueous phase at higher pH values. Such high pH values can occur when groundwater contacts concrete and corrosion of the concrete takes place. Basic research of the interaction of Cm(III) with this polymeric organic component has been started in this project. Complexation experiments of kerogen extracted from natural clay and Cm(III) were performed by TRLFS. The spectroscopic results clearly show a complexation of Cm(III) by the kerogen extract. However, it could not be clarified whether this complexation is caused by the kerogen itself or by inorganic contaminants in the extract such as pyrite (see *Section 3*). It was decided at that time to abdicate on an extensive experimental program, since it was impossible to extract pure kerogen without altering the organic structure. A calculation of a complexation constant for a complex between Cm(III) and kerogen with such impurities would have no meaning and would only lead to false conclusions.

4.4 Spectroscopic investigations for a fundamental process understanding

Luminescence spectroscopy with Eu(III) is an appropriate technique to investigate the complexation properties between metal ions and small or macromolecular organic ligands. This method can be run in the steady-state or time-resolved mode. It has been shown that for spectroscopy under cryogenic conditions – cooling the samples down to $T \sim 5$ K – fluorescence-line-narrowing is achieved. The highly resolved spectra provide detailed information on the complexes with different model ligands. From the excitation of the ${}^5D_0 \leftarrow {}^7F_0$ transition and emission of ${}^5D_0 \rightarrow {}^7F_1$ and ${}^5D_0 \rightarrow {}^7F_2$ transitions spectroscopic information is obtained like the luminescence decay time τ , asymmetry factor r , splitting of the 7F_1 triplet state (ΔE), crystal field strength parameters $N_v(B_{2q})$ and crystal field parameters B_{20} and B_{22} . With these spectroscopic information conclusions can be made concerning the bond between the metal ion and the ligands, including the water molecules coordinated by the metal ion. Only a few

results of complexation studies of Eu(III) and Tb(III) with various ligands¹⁶ are briefly presented here¹⁷.

The luminescence decay time τ of Eu(III) in the complex can be divided into three groups of ligands A, B, and C with decay times of about 420 μs , 750 μs , and >1000 μs . The observed decay times can be explained by the number of water molecules in the first coordination sphere in the complex, steric hindrance, OH-groups of the ligand, and quenching from water molecules in the second coordination sphere.

The asymmetry factor r increases with the molar fraction of the ligands. This can be explained by different charge densities and different symmetries of the complexes because of the specific properties of the ligand as well as mono- and bidentate binding capabilities.

The crystal field strength parameters $N_V(B_{2q})$ for Eu(III) complexes with aromatic carboxylates, aliphatic acids, and methoxybenzoates can be classified into two categories: "loose"¹⁸ and "rigid"¹⁹ complexes with low and high $N_V(B_{2q})$, respectively.

Photo-physical characterization of Eu(III) aquo species at ultra low temperatures (~ 5 K) give a clear evidence of two Eu(III) species: an eight-fold coordinated (minor fraction) and a nine-fold coordinated (major fraction) $\text{Eu}(\text{H}_2\text{O})_n^{3+}$ species. The eight-fold coordinated species shows a longer decay time, has shorter Eu(III)-water distances and a less symmetrical arrangement in comparison with the nine-fold coordinated species. Also the impact of inorganic electrolytes (perchlorate, chloride, sulfate) on the luminescence characteristics of Eu(III) can be studied at $T \sim 5$ K and ionic strengths up to 6 M. Perchlorate and chloride form outer-sphere complexes, whereas sulfate occurs as an inner-sphere complex. The chloride and sulfate ions significantly alter the equilibrium between eight-fold and nine-fold water coordination in different ways. Additionally, the sulfate ions form more than one species. A differentiation, whether monodentate / bidentate sulfate equilibrium or an altered water coordination is responsible for the observation is not clearly possible by these spectral measurements.

Another very interesting point of energy transfer between metal ions and ligands is the ILET, the intra-lanthanide energy transfer. Here, distances between two different lanthanide ions – one energy donor and one energy acceptor – that are bound simultaneously in a complex or on a mineral surface can be measured. Thus, the ILET can be used to deduce information about the distribution of binding sites in a macromolecular complex or of mineral surfaces. With the ILET distances in the range of 5 to 12 Å can be measured that extends the observation range of distances accessible by other methods like EXAFS. ILET was applied to determine the distances between Eu(III) and Nd(III) or Tb(III) and Nd(III) complexed in two differ-

¹⁶ phthalic acid, glycolic acid, 2-hydroxyphenylacetic acid, cyclohexanecarboxylic acid, 2-methoxybenzoic acid, anthranilic acid, 2-hydroxybenzoic acid, 2-hydroxycyclohexanecarboxylic acid, 2-mercaptobenzoic acid, 4-hydroxybenzoic acid, and tropic acid.

¹⁷ More details can be found in Brennenstuhl et al., UPCP final report, annex B Nr. 7.

¹⁸ 4-hydroxybenzoic acid, benzoic acid, 4-methoxy benzoic acid, glycolic acid, 3-hydroxy propionic acid, gallic acid

¹⁹ 2-hydroxybenzoic acid, phthalic acid, 3-methoxy benzoic acid

ent polyacrylic acids (PAA) with mol masses of 1.8 and 450 kg mol⁻¹. The spectroscopic characterization showed that the distances increase from about 0.6 to 1.2 nm with increasing pH from 4 to 8. As for both PAA the lanthanide ions are complexed by functional groups (binding sites) of the polymer chain, the distances of the lanthanide ions reflect the distribution of binding site along this polymer chain.

5 Sorption of actinides on natural clay rock

As discussed before natural clay rock consists of several mineral components. The soluble minerals of clay rock determine the composition of the solution that is in contact with the clay rock. In case of Opalinus clay (OPA) and Callovo-Oxfordian clay (COx) calcite buffers the pH value and determines the calcium and carbonate concentration. These three parameters have a large impact on the sorption of metal ions. Other components of the solution like sulfate, phosphate, chloride, fluoride, and silicate can be neglected, because either they are weak complexing ligands or their concentration is too low in the pore waters. In the project the sorption of europium, thorium, uranium, neptunium, plutonium, and americium on OPA was investigated as a function of pH, ionic strength, and temperature. Also the impact of humic acid and other organic ligands have been investigated. For comparison, other minerals were studied like kaolinite, COx, montmorillonite, illite, bentonite, beidellite, and calcite.

5.1 Actinides in the system water / clay rock

The sorption of actinides and lanthanides generally increases with increasing pH values in the pH range from 3 to ~ 6.5. Trivalent metal ions and hexavalent uranium are sorbed from about 10% up to more than 95%. In the low pH range outer-sphere complexation is the dominant sorption process, as it was proved by spectroscopy for Cm(III) and Sm(III). At pH values greater than pH 6.5, the speciation of the cation governs its sorption properties. As an example: the U(VI) sorption at pH 7.6 is lower than expected from the charge of the aquo ion UO_2^{2+} due to formation of the neutral $\text{Ca}_2\text{UO}_2(\text{CO}_3)_3$ complex. Desorption experiments of Eu(III) and U(VI) showed that the sorbed metal ions are not significantly released into solution at pore water conditions (pH 7.6).

Trivalent actinides / lanthanides:

The sorption of trivalent actinides is nearly constant with 95% of sorbed species at pH values greater than 7. The K_d values are between $\log K_d = 1$ and $3 \text{ m}^3 \text{ kg}^{-1}$ depending on the mineral phases. As shown, the speciation of europium is controlled by the carbonate concentration and the pH value. At pH values of about 8 and in equilibrium with calcite the single-positively charged complex EuCO_3^+ is the prevailing species according to thermodynamic equilibrium modeling. It is supposed that surface species like $\equiv\text{X-OEuCO}_3^-$ and $\equiv\text{X-OEuOHCO}_3$ play a dominant role. Hints from spectroscopic studies confirm this assumption²⁰. The K_d values of the trivalent actinides and lanthanides studied in the present project are summarized in *Table 5-1*.

Hexavalent actinides:

The hexavalent uranium (U(VI)) shows an increasing sorption from 20 to about 95% in the pH range from 3 to 5.5 with a solid to liquid ratio of 4 g L^{-1} . Between pH 5.5 and 7 a maximum plateau of the sorption is reached. From pH 7 to 10 the sorption drops down sharply with a minimum of about 5% sorption. The sharp drop can be explained by the formation of

²⁰ Marques Fernandes, M., Baeyens, B., Bradbury, M.: The influence of carbonate complexation on lanthanide/actinide sorption on montmorillonite, *Radiochimica Acta* 96, 691-697 (2008).

the neutral complex $\text{Ca}_2\text{UO}_2(\text{CO}_3)_3$. This complex is formed because of calcite dissolution from the OPA, providing the calcium and carbonate ions for the formation of such a complex. In studies of pure mineral phases like montmorillonite that does not contain any calcite, such a decrease of the sorption cannot be observed. When raising the pH value up to pH 10 a new complex is formed that shows a lower sorption than the neutral calcium uranyl carbonate complex. This complex is the highly charged uranyl tricarboxylate complex, $\text{UO}_2(\text{CO}_3)_3^{4-}$. This complex becomes the dominant species in solution around pH 10.

At the equilibrium pH of 7.6 between solution and OPA, the K_d value of UO_2^{2+} ($\sim 0.02 \text{ m}^3 \text{ kg}^{-1}$) is rather small compared to the K_d value of Eu(III) , even though the effective charge of the cation is similar (~ 3). The formation of the weakly sorbing $\text{Ca}_2\text{UO}_2(\text{CO}_3)_3$ complex is the reason of the low K_d in contrast to Eu(III) that does not form such a neutral complex but exists as a positively charged EuCO_3^+ complex.

The Pu(VI) sorption is higher than the sorption of U(VI) . The hexavalent Pu is not stable in the OPA system and is reduced to tetravalent Pu(IV) that shows a stronger interaction with the clay. This is expressed in a three orders of magnitude higher K_d value of $13 \text{ m}^3 \text{ kg}^{-1}$ (U(VI) : $0.02 \text{ m}^3 \text{ kg}^{-1}$). In these experiments the formation of Pu(IV) was identified by EXAFS measurements. Furthermore, $\mu\text{-XRD}$ studies confirmed that iron-bearing mineral phase (siderite) is the redox-active mineral phase of OPA that determine the speciation of Pu after uptake on OPA.

Tetravalent actinides:

For the tetravalent plutonium a few sorption experiments have been performed obtaining a K_d value of $83 \pm 34 \text{ m}^3 \text{ kg}^{-1}$. This value possesses a high uncertainty that might be caused by hydrolysis reactions forming colloids or precipitates on the surface of the clay. The process that dominates at the experimental conditions is unclear, because the initial Pu concentration of about $9 \times 10^{-8} \text{ M}$ is near the solubility line. Thus, the K_d value does not properly represent the sorption of an ionic species but rather comprises surface precipitation. However, studies in the literature for the Pu sorption on COx showed lower K_d values of $0.3 - 3.2 \text{ m}^3 \text{ kg}^{-1}$ at Pu concentration of $< 10^{-10} \text{ M}$ ²¹. Here, surface precipitation should not have an impact on the sorption. The results so far obtained pointed out that the chemistry of Pu cannot be clarified.

²¹ Latrille, C., Ly, J. and Herbette, M.: Retention of Sn(IV) and Pu(IV) onto four argillites from the Callovo-Oxfordian level at Bure (France) from eight equilibrated sedimentary waters, *Radiochim. Acta*, 94(8), 421-427 (2006).

Table 5-1: K_d values ($m^3 kg^{-1}$) of the sorption of actinides and lanthanides on OPA in $NaClO_4$ -solution or synthetic pore water (pH 7.6) in air atmosphere, as well as data from PSI/Nagra²² for comparison reasons ($T = 25^\circ C$).

Metal ion	Concentration of metal ion (M)	K_d ($m^3 kg^{-1}$)		
		pH = 7.6	PSI/Nagra	
			pH = 7.2	pH = 7.8
Pu(III) ^a	$1 \cdot 10^{-7}$	159 ± 37^{b2}	22.6 ^a	75.2 ^a
Am(III)	$9 \cdot 10^{-9}$	30 ± 2^{b2}	17.0	63.0
Eu(III)	$1 \cdot 10^{-7}$	50 ± 10^d	59.8	50
	$1.9 \cdot 10^{-6}$	44 ± 1^{e1}		
	$1.9 \cdot 10^{-6}$	1.6 ± 0.1^{e2}		
	$2 \cdot 10^{-9}$	59 ± 1^g		
Th(IV)	$8 \cdot 10^{-9}$	29 ± 16^{b2}	55.4	55.4
Pu(IV)	$9 \cdot 10^{-8}$	83 ± 34^{b2}	-	-
Np(V)	$8 \cdot 10^{-6}$	0.13 ± 0.01^{b1}	-	-
	$10^{-12} - 10^{-8}$	1.45 ± 0.03^{b1}		
Pu(V)	$1 \cdot 10^{-11} - 5 \cdot 10^{-5}$	0.03 ± 0.02^{b2}		
	$3 \cdot 10^{-7}$	0.04 ± 0.01^d	-	-
U(VI)	$3 \cdot 10^{-7}$	0.3 ± 0.2^d		
	$1 \cdot 10^{-7} - 2 \cdot 10^{-4}$	0.03 ± 0.01^{b2}	-	-
	$4.2 \cdot 10^{-7}$	0.15 ± 0.06^{e1}		
	$4.2 \cdot 10^{-7}$	0.024 ± 0.01^{e2}		
Pu(VI)	$1 \cdot 10^{-6}$	0.0222 ± 0.0004^c		
	$1 \cdot 10^{-7}$	13 ± 3^{b2}	-	-

a: The experiments with Pu(III) were performed under argon atmosphere; the values for Pu(III) from PSI were calculated from Am(III) data

b1: JGU: S/L = 2 - 20 g L⁻¹ in saturated calcite solution

b2: JGU experiments with S/L = 2 - 20 g L⁻¹ for Np(V) and 15 g L⁻¹ for U(VI) in synthetic pore water

c: HZDR experiments with S/L = 60 - 300 g L⁻¹ in synthetic pore water

d: KIT-INE experiments with S/L = 10 - 200 g L⁻¹ in synthetic pore water

e1: IAARC experiments with S/L = 4 g L⁻¹ in 0.01 M NaClO₄

e2: IAARC experiments with S/L = 4 g L⁻¹ in synthetic pore water

g: TUD experiments with S/L = 3 g L⁻¹ in synthetic pore water

²² Bradbury, M.H., Baeyens, B.: Far field sorption data bases for performance assessment of a high-level radioactive waste repository in an undisturbed Opalinus Clay host rock. Paul Scherrer Institut, PSI-Bericht 03-08, Villigen, 128 p. (2003).

Pentavalent actinides:

The adsorption of pentavalent Np on OPA was studied in synthetic pore water and aqueous solutions of NaClO₄, NaCl, CaCl₂, and MgCl₂ at an ionic strength of 0.1 and 0.4 M. The Np concentration was varied between 10⁻⁴ and 10⁻¹² M and the pH interval studied was from pH 3 to about 10. The aqueous phase – beside the synthetic pore water - was saturated with calcite to mimic pseudo-natural conditions. The Np(V) sorption increases from pH 3 to higher pH values and has its sorption maximum at about pH 8.3. At greater pH values the sorption decreases due to the formation of negatively charged carbonate complexes. The K_d value depends significantly on the background electrolyte. In synthetic pore water the K_d values are rather small (~ 0.03 m³ kg⁻¹), whereas in NaClO₄ and NaCl they are one order of magnitude higher (~ 0.25 m³ kg⁻¹). With decreasing metal concentration the sorption increases resulting in a concentration independent related K_d value of 1.445 ± 0.033 m³ kg⁻¹ that is one order of magnitude higher than in the higher metal concentration range. The sorption isotherm as a function of Np(V) concentration exhibits a linear part below 10⁻⁸ M with a slope of 1.00 ± 0.01. The data between 10⁻⁸ and 10⁻⁴ M show a slope of 0.69 ± 0.04, reflecting a non-linear sorption behavior of Np(V) on OPA. The decrease in the relative amount of Np sorbed with increasing Np concentration may be explained by different affinities of the sorption sites for Np(V). At higher Np concentrations, the high-affinity sites are already occupied and low-affinity sites are accessed resulting in a weaker sorption of Np(V).

In a parallel study the sorption of Np(V) on OPA and COx in synthetic pore water was monitored over longer time periods under anaerobic conditions and 1% CO₂. The results after 6 weeks contact time are similar to the shorter times with a K_d of ~ 0.04 m³ kg⁻¹. But with longer contact times the amount of neptunium that sorbs on the clay increases from ~ 20% (S/L = 10 g L⁻¹) up to ~ 80%. It is assumed that Np(V) is reduced to Np(IV) with time. However, mainly Np(V) has been found in the system by spectroscopic characterization of similar experiments but at higher Np concentrations necessary for spectroscopy. Thermodynamic equilibrium calculations give hints that Np(IV) can be stable in the system at the measured Eh values. Further investigation must clarify the existence of Np(IV) and the corresponding redox mechanism.

Pentavalent plutonium (Pu(V)) at concentration of 10⁻⁷ M was not stable in synthetic pore water contacted to OPA or COx from the beginning and was reduced to Pu(IV) within the first few weeks. On the surface of the clay tetravalent Pu was detected by XPS and XANES even at high metal concentration of 10⁻⁴ M. The result is consistent with thermodynamic calculations based on the measured Eh values. As expected for a mixture of pentavalent and tetravalent Pu, a higher sorption of about 90% was measured. Sorption experiments at lower Pu(V) concentrations of 10⁻⁹ M yield significantly higher K_d values, which increase within a year by an order of magnitude (log K_d (12 days) = ~ 1.0 (m³ kg⁻¹), log K_d (1 year) = ~ 2.3 (m³ kg⁻¹)). An explanation for this behavior cannot be given, but it clearly shows that the Pu sorption has to be investigated with pure clay minerals to be able to explain, which component is responsible for each single reaction – sorption and reduction – and to elucidate the complex behavior in the natural system.

5.2 Sorption of actinides and europium on OPA at elevated temperatures

The sorption of actinides on OPA was studied in the temperature range from 15 to 80 °C. Generally, the sorption reaction of the actinides is endothermic, i.e., the sorption increases with increasing temperature. The endothermic reaction is also expressed in the positive sorption enthalpy $\Delta_s H$ that was deduced from the van't Hoff plot of the $\ln K_d (R_d)$ values as a function of the inverse temperature in Kelvin. In Table 5-2 all sorption enthalpies with the corresponding entropies are summarized. Discrepancies in the thermodynamic data obtained by experiments performed at different labs, but at the same ionic strength and pH, might be explained by different used S/L ratios. Despite these deviations, for all cations investigated positive entropy is obtained pointing to an entropy-driven sorption reaction.

Table 5-2: Sorption enthalpy and entropy for actinide/lanthanide sorption on OPA in synthetic pore water (SPW) or sodium perchlorate solution. S/L ratios were different in the individual experiments in the range from 2 to 60 g L⁻¹.

System	$\Delta_s H$, kJ mol ⁻¹	$\Delta_s S$, J K ⁻¹ mol ⁻¹
Eu(III), OPA, pH 7.6		
SPW	52 ± 4 ^a	267 ± 12 ^a
SPW	71 ± 2 ^b	259 ± 5 ^b
0.4 M NaClO ₄	21 ± 13 ^a	176 ± 44 ^a
Np(V), OPA, pH 7.6		
SPW	77 ± 16 ^c	210 ± 57 ^c
U(VI), OPA, pH 7.6		
SPW	34 ± 1 ^d	139 ± 3 ^d
SPW	93 ± 3 ^b	273 ± 8 ^b

a: TUD; b: IAARC; c: JGU; d: HZDR

For the observation of increasing sorption with increasing temperature, two explanations can be given: 1. some groups²³ suggest that the negative surface charge on the clay surface becomes more negative with rising temperature. This induces more binding sites for positively charged Eu(III) species, like EuCO_3^+ , which is the dominant Eu(III) species under synthetic OPA pore water conditions at very low Eu(III) concentrations. 2. Other groups²⁴ observed changes in the hydration shell of Cm(III) and Ca(II) cations with rising temperature. These changes might lead to an enforced connection to the clay surface. However, the present studies were only the start-up of more detailed investigations in the future.

²³ 1) Brady, P. V.: Alumina surface chemistry at 25, 40, and 60°C. *Geochim. Cosmochim. Acta* 58, 1213 (1994). 2) Tertre, E., Castet, S., Berger, G., Loubet, M., Giffaut, E.; *Geochim. Cosmochim. Acta* 70, 4579 (2006). 3) Rozalen, M., Brady, P. V., Huertas, F. J. J.; *Colloid Interface Sci.* 333, 474 (2009).

²⁴ 1) Lindqvist-Reis, P., Klenze, R., Schubert, G., Fanghanel, T.: Hydration of Cm^{3+} in aqueous solution from 20 to 200 °C. A time-resolved laser fluorescence spectroscopy study. *Journal of Physical Chemistry B* 109, 3077 (2005). 2) Lim, L. H. V., Prebil, A. B., Ellmerer, A. E., Randolph, B. R., Rode, B. M.: Temperature dependence of structure and dynamics of the hydrated Ca^{2+} ion according to ab initio quantum mechanical charge field and classical molecular dynamics. *Journal of Computational Chemistry* 31, 1195 (2010).

5.3 Influence of organic components on actinide and europium sorption on OPA

Natural clay rock contains more or less organic matter comprising compounds with low molecular weight like formate, acetate, lactate, and high molecular weight compounds like fulvic/humic acid or kerogen. These organic compounds can be released from the clay into an aqueous phase. The impact of these organic compounds on the dissolved radionuclides has necessarily to be assessed. Therefore, several studies have been performed within the scope of this project.

The sorption experiments with U(VI) and OPA²⁵ showed no influence of humic acid on the U(VI) sorption at the equilibrium pH of 7.6, even though more HA is sorbed on the clay with increasing HA concentration. This finding can be explained by the formation of the neutral $\text{Ca}_2\text{UO}_2(\text{CO}_3)_3$ complex, as the main species at pH 7.6. In clay systems without calcite, like the pure kaolinite, this type of complex is not formed and the dissolved humate complexes dominate the U(VI) speciation and suppress uranyl sorption. Looking in more detail on the pH dependence of the HA effect, one can observe that at lower pH values (3 – 5) humic acid significantly enhances the sorption of uranium on the OPA. Surface precipitation of HA saturated with metal ions is the reason of this behavior. At pH 5 to 7.5 the formation of dissolved $\text{UO}_2(\text{OH})\text{HA}(\text{I})$ complexes prevents sorption of U(VI) in presence of HA. Contrary to this observation, the HA has no impact on U(VI) sorption at higher pH values. Here, the carbonate species, including the $\text{Ca}_2\text{UO}_2(\text{CO}_3)_3$, control the sorption mechanism.

In case of Np(V)²⁶ the HA has only a weak impact on the Np(V) sorption and reduces the sorption by about 10% between pH 8 and 9.5. At 10^{-12} M Np(V) concentration the HA effect is less pronounced.

HA significantly affects the sorption of Pu(IV) on OPA in pore water at pH 7.6 and reduces the averaged K_d value from $83.3 \pm 33.7 \text{ m}^3 \text{ kg}^{-1}$ in the absence of HA to $12.7 \pm 8.5 \text{ m}^3 \text{ kg}^{-1}$ in the presence of HA²⁶. The suppression of the sorption is caused mainly due to Pu(IV) humate complexes that show much weaker sorption on the OPA than the metal cation itself or its positively charged inorganic complexes.

For considering the effects of HA in transport models, it must be ascertained that all involved interaction processes (complexation, adsorption) are in a steady local equilibrium under flow conditions, i.e., they must be reversible. So far, it was unclear whether this is actually the case, in particular for adsorption of colloidal humic matter. By means of tracer exchange experiments with radiolabeled humic substances, it became possible to demonstrate that a dynamic equilibrium of adsorption and desorption really exists, even though it was found that humic or fulvic acid cannot be desorbed from clay materials. It also turned out, however, that

²⁵ Schmeide et al., HZDR final report, annex B, Nr. 1, chapter 4

²⁶ Amayri et al., JGU final report, annex B, Nr. 2, chapter 4

the approach with the linear additive model is very often not applicable. It is suggested that mineral-bound and dissolved HA may have different affinities toward metal ions, or that the mineral surface is maybe modified because of the sorption of HA.

Low molecular weight organic compounds like formate, acetate, propionate, lactate, and citrate impede the sorption of U(VI)²⁵ and Eu(III)^{27,28}. The mobilizing effect of the organic ligands on U(VI) increases in the following sequence: formate < lactate ≈ acetate ≤ propionate < tartrate < citrate. The same trend has been obtained with Eu(III) and lactate, tartrate as well as citrate. For instance, in the presence of citrate (1×10^{-2} M), the K_d value for U(VI) amounts to only $0.0011 \pm 0.0003 \text{ m}^3 \text{ kg}^{-1}$, for Eu(III) to $0.417 \pm 0.001 \text{ m}^3 \text{ kg}^{-1}$. A first influence of this organic ligand can be observed at concentrations of more than 10^{-4} M. For Eu(III) the complex formation with citrate and tartrate was confirmed by TRLFS under pore water conditions. Generally, the influence of the organic ligands on the U(VI) and Eu(III) sorption onto OPA correlates with the stability of the respective U(VI) and Eu(III) complexes. For the weaker complexes of formate or lactate, significant impact on the sorption can only be recognized at concentrations that can hardly be found in ground water or after leaching clay rocks. Thus, in the OPA formation the sorption should be the dominant physiochemical process and causes strong retardation of the actinides.

5.4 Miniaturized column experiments

The group of the Universität des Saarlandes has performed preliminary sorption studies by means of miniaturized HPLC columns filled with sand and clay. This dynamic flow through, HPLC-based method allows the rapid determination of sorption coefficients over a range of pH and ionic strength conditions. The experiments were first optimized with iodide (NaI) as “inert tracer” and salicylate (SAL) as a model for an organic complexing ligand and sodium perchlorate as eluent. Good separations could be found in a mixture of 85 wt.% OPA and 15 wt.% sea sand. In first experiments the behavior of europium in the column in absence and presence of salicylate and lactate has been studied at 25 and 60 °C. The questions whether this sort of experiment can be used as a link between batch and diffusion experiment has to be clarified in future discussions.

5.5 Modeling of the sorption of actinides / lanthanides on OPA

For safety assessment a successful modeling of experimental results is mandatory. In the frame of this project, the modeling according to the surface complexation model²⁹ and ion exchange showed clearly, that the clay minerals dominate the sorption of metal ions on the

²⁷ Acker et al., TUD final report, annex B, Nr. 8, chapter 3

²⁸ Kautenburger et al., IAACR final report, annex B, Nr. 5, chapter 3.6

²⁹ Bradbury, M.H., Baeyens, B., Geckeis, H., Rabung, Th.: Sorption of Eu(III)/Cm(III) on Ca-montmorillonite and Na-illite. Part 2: Surface complexation modeling, *Geochimica et Cosmochimica Acta*, Vol. 69, No. 23, 5403–5412 (2005).

OPA. The modeling was quite good, but relevant species – binary and ternary complexes – were so far not considered in the chemical model and this leads to small but in our opinion significant discrepancies between modeling and experimental data. This fact is briefly illustrated for the sorption of europium on OPA³⁰. The calculated speciation of Eu(III) in the presence of OPA is plotted together with the experimental data in *Figure 5-1*.

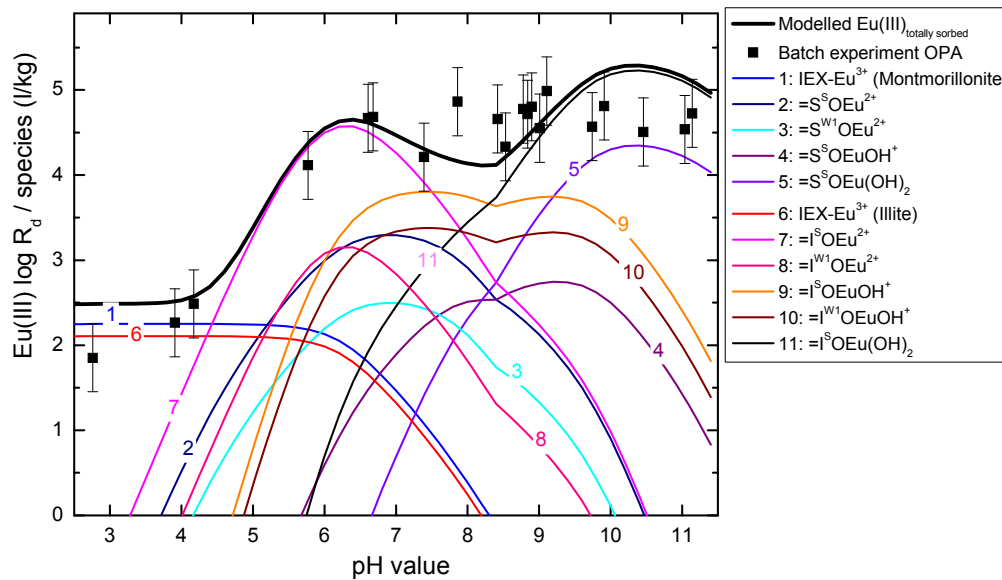


Figure 5-1: Eu(III) sorption on OPA and modeling as a function of pH³⁰. Experimental conditions: $[Eu(III)] = 1 \times 10^{-7} \text{ M}$, $S/L = 2 \text{ g L}^{-1}$, ionic strength = 0.1 M NaClO_4 . (IEX = ion exchange, I = illite, S = smectite, S = strong sites, W1 = weak sites).

In the calculations, the natural clay rocks were simulated by a mixture of illite (36 wt.%), montmorillonite (18 wt.%), and calcite (6 wt.%). Sorption of Eu(III) on the calcite was not considered in the modeling. Calculations took into account sorption to clay minerals and complexation in solution by hydroxide and carbonate ions. Dissolution and precipitation of calcite along the considered pH range was considered and this controls the dissolved calcium and carbonate concentrations. At pH values < 6, Eu(III) speciation is dominated by the free Eu(III) aquo ion and Eu(III) bound by ion-exchange. The difference between model calculations and experimental data shows in terms of the calculated Eu(III) sorption a significant sorption reduction at pH 7 – 9.5. This is due to formation of aqueous $Eu(CO_3)^+$ and $Eu(CO_3)_2^-$ complexes, which were not considered as sorbing species in the model. But they are the dominant species in solution. Nevertheless, other reasons for the divergence of the modeling curve and the experimental data cannot be excluded, like the influence of other mineral phases in natural clay rock on Eu(III) sorption.

³⁰ Banik et al., KIT final report, annex B, Nr. 6, chapter 3.

6 Diffusion of actinides in OPA

6.1 Diffusion experiments with HTO, Na, U, Np, Pu, and HA

The main process responsible for the transport of radionuclides released from a waste container is diffusion. In the present project, the diffusion of HTO, ^{22}Na , $^{233}\text{U(VI)}$, $^{237}\text{Np(V)}$, $^{238, 242}\text{Pu(V)}$ and ^{14}C -labeled HA in OPA was studied under aerobic and anaerobic conditions using OPA core samples. The cores, 2.5 cm in diameter and 1 cm in thickness, were turned parallel to the bedding from the original 10-cm bore cores. From diffusion experiments, the diffusion parameters D_e , D_a , ε , α , and K_d ³¹ were determined. Na^+ , U(VI) , and Np(V) diffusion were investigated in the absence and presence of HA and at 25 and 60 °C, respectively. The diffusion parameters obtained from the experiments are summarized in *Table 6-1*.

In all diffusion experiments the metal ions U, Np, and Pu showed a strong sorption and were never detected by through diffusion experiments. Generally, the apparent diffusion coefficients D_a are much lower for U(VI) and Np(V) compared to Na^+ . Np(V) shows one order of magnitude higher D_a values than U(VI) as expected from its general chemical behavior. In the presence of HA the D_a values of both metal ions are slightly smaller compared to experiments in absence of HA. This metal cation behavior in presence of HA is already known from other studies³². However, the K_d and D_e values from experiments in presence and absence of HA are equal within the uncertainty of the measurement. Differences in the parameters outside the uncertainties can be explained by the application of OPA batches with distinct local porosity of the bore cores or originate from different boreholes with different drilling characteristics, e.g. BAE 25/10, BLT 14.

A temperature effect can also be observed on the diffusion of HTO, Na^+ , Np(V) , and U(VI) . Generally, the D_e values increase with increasing temperature. This effect is more pronounced for the experiment with HTO or Na^+ . In case of U(VI) and Np(V) the change in D_a values is within the range of the uncertainties and thus, can be neglected. But for these two metal ions, the shape of the diffusion curves changes significantly. Both diffusion curves at 60 °C could be best fitted by assuming at least two metal ion species, a fast one and a slower species. By considering the particle size distribution, it was suggested from the U(VI) experiments that the fast species corresponds to an aqueous U(VI) species, whereas the slow species could be a colloidal U(VI) species. In *Table 6-1* these two fractions are denoted by "coll." and "aq.". The D_a factor of the aqueous species is larger than the value for the colloidal species. Hence, the aqueous species is more mobile than the colloids. However, the D_a values of U(VI) and Np(V) are very similar at 60 °C. The trend of the Np(V) K_d values deduced from the diffusion experiment does not match with the K_d values of the batch experiments. K_d^{batch} increases with increasing temperature by about one order of magnitude, whereas the

³¹ D_e : effective diffusion coefficient [m^2/s]; D_a : apparent diffusion coefficient [m^2/s]; ε : diffusion-accessible porosity; α : rock capacity factor; K_d : distribution coefficient.

³² Seida, Y., Terashima, M., Tachi, Y., Iijima, K., Nakazawa, T., Yamada, M. and Yui, M.: Sorption and diffusion of Eu in sedimentary rock in the presence of humic substance, *Radiochim. Acta* 98, 703-709 (2010). Mibus, J. and Sachs, S.: Impact of humic colloids on uranium(VI) migration in clay. Annual Report 2005, FZR-443, Forschungszentrum Rossendorf (2005).

$K_d^{\text{diffusion}}$ remains in the same range. For U(VI) this trend is reversed: K_d^{batch} remains almost constant, whereas $K_d^{\text{diffusion}}$ increases significantly with increasing temperature. However, for a final conclusion more data are necessary to state more precisely the temperature dependence.

Table 6-1: Diffusion parameters of HTO and metal cations in OPA by in-diffusion experiments. For comparison the K_d obtained from sorption studies are listed in the last column. "HA" indicates that the experiment has been performed in the presence of humic acid. For the experiments at 60 °C, two metal ion species were observed for U(VI) denoted by "coll." and "aq" (for explanation see text). Ranges indicated denote diffusion experiments with different OPA cores. Errors are omitted for clearness here, but they can be found in the individual reports.

Tracer, T (°C)		α	D_e ($\times 10^{-11} \text{ m}^2/\text{s}$)	D_a ($\times 10^{-13} \text{ m}^2/\text{s}$)	K_d (Diffusion) m^3/kg	K_d (Sorption) m^3/kg
HTO ^{33,34,35}						
25			0.7 – 2.0	-	-	-
60			3.1 – 4.1	-	-	-
Na ⁺ ³³						
25	- HA	0.44 0.40	1.8 – 2.5 3.1	410 – 570 780	(1.1–1.4)·10 ⁻⁴ 1.1·10 ⁻⁴	- -
60	-	-	3.5	880	1.1·10 ⁻⁴	-
Np(V) ³³						
20	- HA	110 – 243 78	0.7 – 2.3 1.5	2.1 – 2.8 1.9	0.049 – 0.10 0.032	0.034 0.023
60	coll. aq.	69 34	0.2 1.0	0.3 2.9	0.029 0.014	0.157 -
Pu(V) ³⁵		-	1.45 – 1.60	-	-	-
U(VI) ³⁴						
25	- HA	61 48	0.19 0.12	0.31 0.25	0.025 0.02	0.0222 -
60	coll. aq. HA _{coll} HA _{aq.}	605 109 722 120	0.3 0.3 0.22 0.25	0.05 0.28 0.03 0.21	0.25 0.045 0.3 0.05	0.09 - - -

HA behaved different. By using a solution of uranium and HA the HA diffused through the core by a through diffusion experiment.

³³ Amayri et al., JGU final report, annex B, Nr. 2, chapter 4.2

³⁴ Schmeide et al., HZDR final report, annex B, Nr. 1, chapter 5

³⁵ Banik et al., KIT final report, annex B, Nr. 6, chapter 4

From the diffusion experiments with Pu no diffusion parameters could be deduced by the through-diffusion method. The experiments showed that about 20 – 40% of Pu is sorbed on components of the experimental set-up. It was observed that the mobile Pu inventory is dominated by Pu(V). Pu does not show a preferential transport pathway in the clay sample and the Pu is concentrated within the clay core at certain sites. The Pu sorbed on the samples was reduced to Pu(IV). However, further experiments are needed to determine the reducing and subsequently sorbing phase.

6.2 Extended characterization of actinides on the surface and in solution

To elucidate sorption mechanisms of actinides on clay surfaces, a detailed characterization of the species on the surface and in solution is necessary. The type of surface species, the type of coordination on the surface, correlation with elements on the surface belonging to the clay matrix, and speciation in solution contacted with the clay must be determined by sophisticated methods. For that, among others, μ -XRF, μ -XRD, μ -XAS, and normal XAS³⁶ measurements were performed on clay samples loaded with neptunium as well as plutonium. The solutions were characterized by capillary electrophoresis coupled with ICP-MS and RIMS as very sensitive detection methods.

Actinides on the surface of OPA

The elemental distributions of Ca, Fe, Np and Pu in OPA samples prepared after sorption and diffusion experiments were measured by spectroscopy with synchrotron based techniques. Autoradiography was additionally used to characterize the Pu distribution on the OPA surface. From the pattern it is evident that the diffusion of Np and Pu within the OPA is not homogeneous like for HTO. Np and Pu are always concentrated in distinct areas which are distributed differently within the core. This is illustrated for Pu in *Figure 6-1*.

XANES and μ -XANES investigations of these areas showed that Np(V) is partly reduced to Np(IV) under both aerobic and anaerobic conditions. In contrast to Np, a complete reduction of Pu(VI) to Pu(IV) was found on the OPA surface. Furthermore, μ -XRD data confirm that pyrite is one of the redox-active mineral phases for Np and probably siderite for Pu, that determine the speciation of Np and Pu on the surface of OPA. The correlation among the mineral distribution in OPA and the reduced actinides indicates that the reduction of the metal ions occurs on the clay surface. *Figure 6-2* shows as an example the μ -XRF of Fe and Np to demonstrate the correlation between Fe as constituent of OPA and Np sorbed on OPA.

With respect to the assessment of the long-term safety of a nuclear waste repository, even if higher oxidation states of Np and Pu are formed due to oxidative reactions caused by radiolysis near the waste containers, the reduction to the tetravalent oxidation state will immobilize Np and Pu in the clay rock.

³⁶ μ -XRF: micro X-ray fluorescence spectroscopy; μ -XRD: micro X-ray diffraction; μ -XAS: micro X-ray absorption spectroscopy; XAS: X-ray absorption spectroscopy

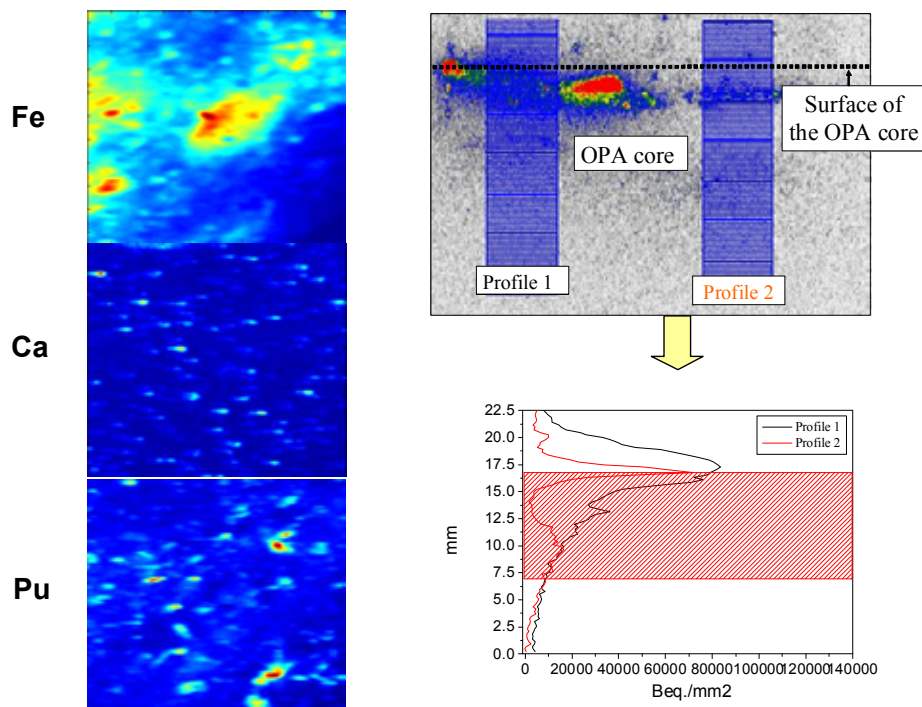


Figure 6-1: On the left: μ -XRF mappings of Fe, Ca, and Pu on OPA prepared by diffusion of $2 \times 10^{-5} \text{ M } ^{242}\text{Pu}$. On the right: Two different diffusion profiles measured after diffusion of ^{238}Pu (10^{-9} M) into OPA with autoradiography. The different colors represent different concentrations. Red indicates the highest and grey the lowest concentration³⁰.

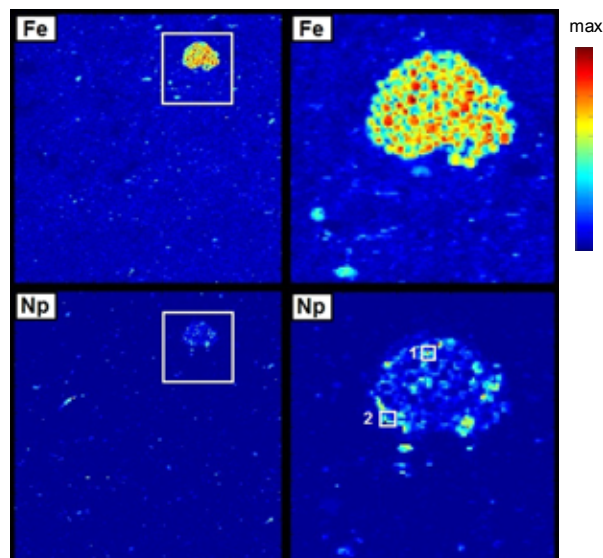


Figure 6-2: Left: μ -XRF mappings ($2 \times 2 \text{ mm}$, step size: $10 \mu\text{m}$) of Fe and Np of an anaerobic sample prepared by sorption of $8 \times 10^{-6} \text{ M } ^{237}\text{Np}$ on OPA thin section. Right: Same element distributions for $500 \times 500 \mu\text{m}$ mappings (step size $1 \mu\text{m}$)²⁶.

Actinides in solution

Capillary electrophoresis (CE), coupled on-line to ICP-MS and off-line to RIMS, has been applied for the characterization of actinides in solutions being in contact with OPA. Due to the strong sorption of the actinides on the clay, only very small concentrations of the non-sorbed metal ions are found in the solution. That was the reason to apply ICP-MS and RIMS as very sensitive detection methods for elements in combination with CE as a separation method for Np and Pu species. The work in the present project was mainly focused on analytical issues. The oxidation states distribution of Np and Pu could be measured down to ultratrace concentration of 10^{-12} M with well prepared solutions. However, the distribution of the Np and Pu oxidation states in solution from the sorption experiments are still in progress and further experiments are needed.

7 Quantum mechanical modeling of actinide chemistry

Parallel to the experimental studies, theoretical work based on quantum chemistry has been implemented in this joint project. Two relevant aspects of actinide environmental chemistry have been treated here: complexation in aqueous solution by inorganic and organic ligands and the interaction of actinide ions and complexes with surfaces of clay minerals. Computational approaches as applied in this project provide insight into these topics on the atomic level. The chemistry of actinides in solution and at clay mineral surfaces was studied commonly to complement pertinent experimental work. Quantum chemical studies, together with spectroscopic experiments, offer the unique opportunity to gain complementary insight at the atomic level and thus are useful for identifying species and developing mechanistic models of actinide chemistry.

Complexes of actinyl ions with small organic ligands have been examined as models of actinyl complexation by functional groups of humic substances. The goal was to characterize how groups beyond carboxyl functions contribute to the ability of humic substances to form complexes with metal ions. In agreement with experimental studies QM showed that sulfonate, amine, and pyridine groups are not important for actinyl complexation in comparison to the prevailing carboxyl groups.

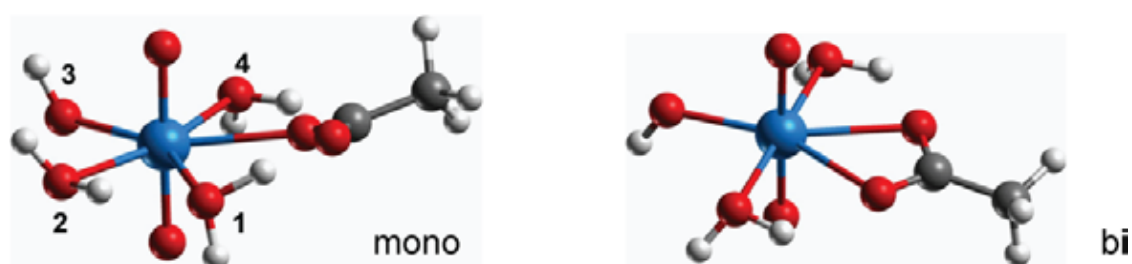


Figure 7-1: Structure of ternary complexes of uranyl with mono- and bidentate coordinated acetate, a *trans*-hydroxo moiety, and aqua ligands. Numbers label the various possible positions of the hydroxide ligand³⁷.

Another important question was the relevance and stability of mixed complexes, complexes with two or more different ligands. The theoretical study of ternary hydroxo-acetate complexes of uranyl(VI) (Figure 7-1) revealed that these complexes should be less stable than binary acetate complexes, as it can be seen from the free Gibbs energies ΔG_{sub} in Table 7-1. This theoretical result is contrary to the interpretation of measured values of complexation constants. Thus, complexation with carboxyl functional groups at neutral to basic conditions in competition with hydrolysis raises still some questions.

³⁷ The possible positions of the hydroxide ligand are discussed in annex D: Rösch et al., TUM Final Report, annex B, Nr. 4, Chapter 4.1.1

Table 7-1: Calculated structure parameters (LDA, distances in pm), symmetric uranyl stretching frequency ν_{sym} (in cm^{-1}) as well as Gibbs free energies ΔG_{sub} of acetate ligand substitution (single-point GGA, in kJ mol^{-1}) of uranyl acetate $[\text{UO}_2(\text{OOCCH}_3)(\text{H}_2\text{O}_n)]^+$ and uranyl trans-hydroxo acetate complexes $[\text{UO}_2(\text{OH})(\text{OOCCH}_3)(\text{H}_2\text{O}_{n-1})]$ with bidentate (bi) and monodentate (mono) coordination ($n = 3, 4$) in aqueous solution.

Ligand ^a		U-O _t	U-O _C	U-C	U-O _W	U-O _H	U-O _{eq}	ν_{sym}	ΔG_{sub}
bi	$[\text{UO}_2]^{2+}$	178.6	237	277	236	–	237	854	-109
	$[\text{UO}_2(\text{OH})]^+$	180.6	244	284	244	212	238	820	-69
mono	$[\text{UO}_2]^{2+}$	178.9	229	340	238	–	236	822	-110
	$[\text{UO}_2(\text{OH})]^+$	180.8	242	341	243	214	237	796	-63

a) U-O_t – uranyl terminal bond, U-O_C – uranium bond to carboxylate, U-C – uranium distance to carboxyl C, U-O_W – uranium bond to aqua ligand, U-O_H – uranium-hydroxide bond, U-O_{eq} – average equatorial U-O bond.

As already mentioned, chemical reactions at elevated temperature are a very important issue in the frame of safety analysis of repositories. For the exemplary case of uranyl complexation with an acetate ligand, QM demonstrated that the weak increase in the complexation constant with increasing temperature can be ascribed to a bidentate isomer. Furthermore, an equilibrium establishes between mono- and bidentate isomers of uranyl acetate and this equilibrium is influenced by temperature. This result also showed that a fundamental understanding of actinide complexation needs to take into account the equilibrium between various isomers of a complex of given composition. However, such a topic has been studied only rarely until now. Preliminary examinations of the reaction mechanism of neptunyl(V) with acetate additionally support this view. Finally the first hydrolysis products of tetravalent actinides of U(IV) and Np(IV) have been modeled by QM providing structural and energetic parameters for these experimentally not easily accessible species. The calculations support that a coordination number of CN = 9 for the aqua ion and the monohydroxide of U(IV) and Np(IV) mainly occur, based on geometry parameters in comparison to experimental findings as well as energy considerations. All results of the QM studies are described in the report of the Technical University of Munich (TUM) (Annex B, Nr. 4)

Quantum chemical modeling of actinide adsorption at mineral surfaces was pioneered by the TUM group and detailed studies of actinyl adsorption on clay mineral surfaces have been carried out in this project. QM was used to answer open questions with respect to actinide adsorption: (i) what is the nature of the adsorbed species, (ii) which surfaces, basal or edge, are more preferred for adsorption, and (iii) what are the main adsorption sites. The project results for basal and edge surfaces of kaolinite confirm the interpretation of adequate EXAFS experiments regarding bidentate adsorption complexes of uranyl(VI). However, a detailed comparison of geometries and energies revealed that monodentate coordination to the surface cannot be excluded. Several adsorption complexes close in energies were found to fit the experimental data, thus various adsorption complexes may coexist on the surface. Besides adsorbed uranyl, uranyl hydroxide was obtained as a sorbed species in the model calculations.

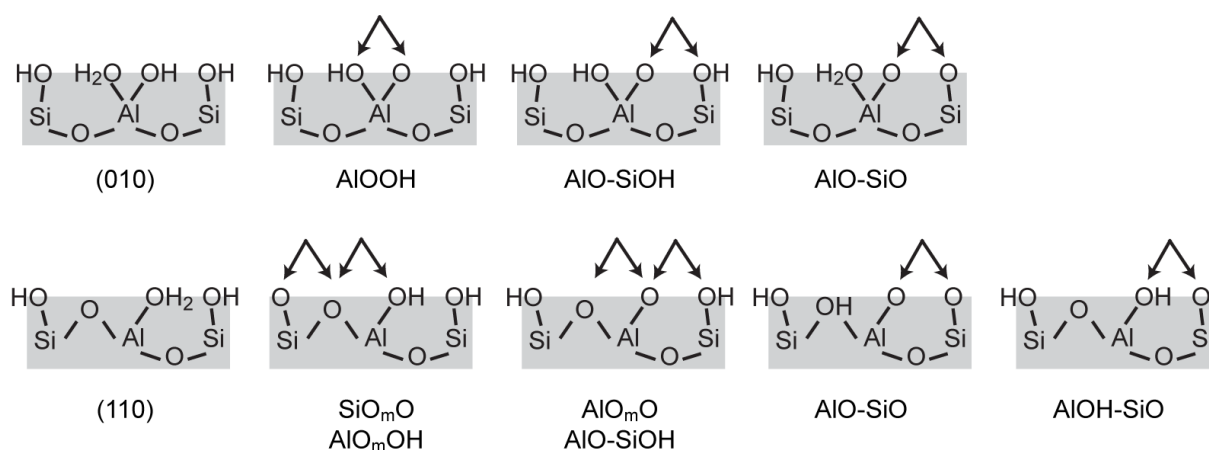


Figure 7-2: Adsorption sites on the (010) and (110) edge surfaces of pyrophyllite considered in quantum chemical modelling studies.

Comparison of structural parameters to experimental data showed that the current interpretation of measured U-O distances to ligands and to the surface should be extended. Shorter U-O bonds have been ascribed to bonds to the surface while longer ones were ascribed to aqua ligands. TUM calculated also rather short bonds of U to hydroxide ligands and relatively long ones, comparable to bonds to aqua ligands, to protonated surface groups. Similar results as for kaolinite were obtained for adsorbed uranyl on edge surfaces of pyrophyllite and a model beidellite. While aluminol sites are preferred for kaolinite and the (110) edge surface of pyrophyllite, a mixed aluminol-silanol site is favorable on the (010) edge surface of pyrophyllite (s. Figure 7-2). Thus, preferred adsorption sites seem to depend on the exposed surface. Another example for a clay surface is the beidellitic substituted pyrophyllite. On this type of surface several adsorption complexes may coexist on the basal surfaces, because rather small differences in adsorption energies were calculated for inner- and outer-sphere complexes of uranyl.

All these examples demonstrate that actinide-clay adsorption systems are rather complex at the atomic level, featuring a variety of surface species which are not easily discriminated. Further computational as well as spectroscopic studies are necessary to develop a mechanistic model at environmental conditions to construct a basis for the interpretation of experimental results. Especially infrared spectroscopy and resonant anomalous X-ray reflectivity techniques will be helpful in this regard, besides quantum chemical studies, to complement available microscopic information.

8 Transport studies by means of PET

Hydrodynamic transport phenomena can contribute to migration of radionuclides in real geological matrices, depending on the geometrical structure of the geotechnical and geological barrier. Positron emission tomography (PET) has been applied to investigate the behavior and pathway distribution of radionuclides in barrier material. By this method transport effects can be characterized. The migration of radionuclides depends on the topology of the material, e.g., geometric distribution and network structure of the transport pathway. The tortuosity is one parameter to describe transport processes and it is beside the porosity and permeability a parameter characterizing porous material. The actual tortuosity effect depends on the nature of the transport processes (advection, molecular diffusion), state variables and driving forces, and presumably, controls chemical reactions within the fluid volume and across the internal surface area, and thus the “effective reaction kinetics”. In tight materials like barrier rocks, transport limitation of chemical interactions plays a decisive role.

PET cameras are sensitive to positron-emitting radionuclides such as ^{18}F or ^{124}I , ^{58}Co , and ^{22}Na . For the work in the frame of this project a preclinical PET scanner was fully customized to geoscientific applications. This GeoPET instrument is one-of-a-kind for the quantitative 4D (3D + time) visualization of transport processes in geological matrices. The GeoPET data can be applied for model validation and parameterization, improvement of process understanding as well as for the direct evaluation of process parameters (e.g., effective transport volume, flow path distribution and heterogeneity). The used ClearPET scanner is a relatively new instrument, utilized for geoscientific applications during the project period. Therefore, the results of the PET studies are provisional to some extent. Nevertheless, advection in homogenized clay samples (kaolinite, OPA powder, synthetic sand-bentonite mixture from the Nagra), in rock cores (Äspö and Grimsel granite) and diffusion in Grimsel bentonite, OPA core, and halite were investigated.

Up to now, all present studies on rock cores with real structures showed strong deviations from homogeneity. In contrast, the samples compacted from suspensions in the laboratory showed a widely homogeneous transport, which could be conveniently fitted with a one-dimensional CXTFIT³⁸ model. However, a homogeneously compacted sand-bentonite sample – denoted as Nagra1 in the report - showed considerable radial variations in the tracer concentration, probably due to the general difficulty of preparing homogeneous large-diameter specimen from moist clay powder. Even an OPA sample compacted from an OPA suspension shows deviations from laterally homogeneous flow, but to a minor extent.

³⁸ CXTFIT: this is a widely used code for estimating transport parameters from tracer experiments.

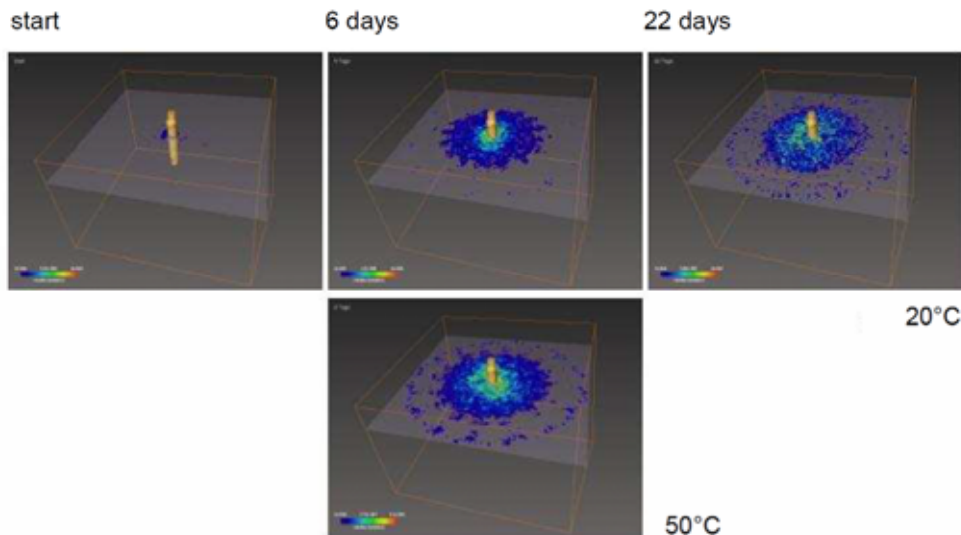


Figure 8-1: Diffusion of $[^{124}\text{I}]^-$ from an axial line source (yellow surface) in Opalinus clay (BLT13/7) at 20 °C (upper row) or 50 °C (lower image)³⁹.

Diffusion experiments have been performed with Grimsel granite from the FEBEX⁴⁰ experiment and $[^{18}\text{F}]\text{KF}$ dissolved in Grimsel ground water. The results of this test were promising in a way as they indicated the feasibility of spatially resolved diffusion experiments. Furthermore, diffusion experiments with two OPA cores were performed. As an example, the diffusion of ^{124}I from an axial line source in OPA is illustrated in *Figure 8-1*. With such investigations the impact of rock structure on transport phenomena could clearly be shown. However, some untypical tracer spreading was observed in OPA, together with a loss of fluid into the sample. This spreading is too fast to be caused by pure molecular diffusion⁴¹. One explanation could be that the OPA was only partial saturated with water, which caused suction into small pores. This was due to damage and alteration of the cores during recovery and storage. Such processes are, however, also relevant to real scenarios; they are likely to occur in excavation damaged zones as well, and therefore deserve further attention.

Such fast spreading did not occur in rock salt (s. *Figure 8-2*), although these samples contained visible fractures. Here, a halite from the Staßfurt line (Saxony-Anhalt, Germany) was charged with ^{124}I -labelled Q-brine.

³⁹ Lippold et al., HZDR-Leipzig, final report, annex B, Nr. 3, chapter 3.5.

⁴⁰ FEBEX: Full-scale Engineered Barriers Experiment in Crystalline Host Rock, FEBEX tunnel in Switzerland

⁴¹ 1) Van Loon, L.R., Baeyens, B., Bradbury, M.H.; *Appl. Geochem.* 20, 2351-2363 (2005). 2) Garcia-Gutierrez, M., Cormenzana, J.L., Missana, T., Mingarro, M., Martin, P.L.; *Phys. Chem. Earth* 31, 523-530 (2006).

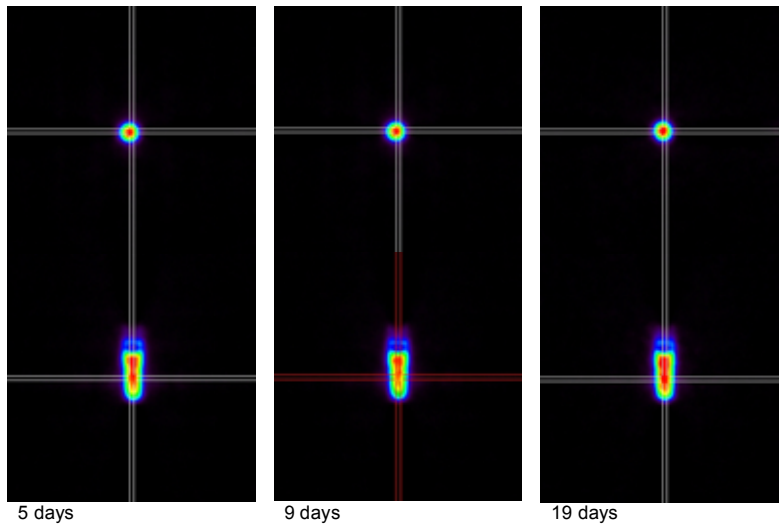


Figure 8-2: Diffusion test with $[^{124}\text{I}]\text{NaI}$ in Q-solution for a halite sample. No movement was observed during 19 days³⁹.

In conclusion, all tracer propagation processes made visible by the PET method turned out to be more complex than expected. Simple models that describe the influence of the bulk material on the basis of 2 or 3 parameters (e.g., porosity, internal surface area) probably overestimate the retention, i.e., they underestimate the transport velocity. Instead, process-dependent parameters must be adopted.

9 Conclusions and outlook

Within this joint project a large number of scientific findings concerning the complexation, sorption and diffusion of actinides and their surrogates were obtained. The results showed that natural clay rock can be a suitable geological barrier for radionuclides released from a waste container. However, a variety of chemical reactions that are not understood well so far can interfere into the efficient retardation of the radionuclides. The database of complexation constants with organic compounds was extended by the addition of aliphatic and aromatic carboxylic acids and it was clarified that sulfur, nitrogen, and phosphorus functionalities of humates play a minor role in the complexation process. Good progress has been achieved in the field of luminescence spectroscopy. Spectroscopic information from the electronic transitions of the metal ion allows getting information of the bond between the metal ion and the ligands, including the water molecules coordinated by the metal ion. By getting more experience in the future, luminescence spectroscopy will be a powerful tool to elucidate reaction mechanisms. A further effective tool is the quantum chemical modeling. Several experimental results could be modeled successfully by quantum chemical methods (QM). Some experimental results were confirmed by QM, like the contribution of non-carboxylic functional groups to HA complexation. Others are in contradiction to QM, like the complexation constant of mixed uranyl hydroxo humates. Thus, QM can help to understand complexation mechanism, e.g., by calculation of relative stability and structural parameters of a species. First experimental work and modeling with QM have been done at elevated temperatures and first trends were obtained for complexation reactions with organics, sorption reactions on clay as well as diffusion in clay.

In the field of sorption reactions with the clay rock OPA, good progress has been made in determining distribution coefficients but also by modeling the results with the surface complexation model. However, these studies point out, that further experiments are necessary with single mineral compounds found in the OPA, like illite, montmorillonite, calcite and iron phases. As shown by the results of this report, combined experimental and computational studies will be a promising route. Concerning diffusion studies the project partners have improved their skills and got rid of some technical difficulties. Some very interesting findings have been obtained with sophisticated spectroscopic methods and QM methods to characterize surface species. But nevertheless, some key questions are still not answered like the redox mechanism on the surface of minerals.

The speciation of Np and Pu on the OPA mineral surface after sorption and diffusion processes was investigated by using different X-ray synchrotron radiation techniques (μ -XRF, μ -XAS, and μ -XRD). The results showed that the highly soluble Np(V) and Pu(VI) were retained by OPA in the reduced and less mobile tetravalent oxidation state of Np and Pu. Np(IV) and Pu(IV) are the most dominant species after sorption and diffusion processes. Furthermore, μ -XRD studies confirmed that iron-bearing mineral phases (pyrite and siderite) are the redox-active mineral phases of OPA which determine the speciation of Np and Pu after uptake on OPA.

The results of this project form a basis for the next step, the more detailed investigations of actinide behavior in the natural clay system at higher ionic strengths and elevated tempera-

tures. For that, a new joint project entitled “Retention of radionuclides relevant for final disposal in natural clay rock and saline systems” has been financially supported by BMWi¹

10 Publications resulting from the project

The following list encompasses the publications resulting from the present joint project. The list is alphabetically indexed by authors.

- Amayri, S.; Jermolajev, A.; Reich, T.; Neptunium(V) sorption on kaolinite, *Radiochim. Acta* 99, 349 (2011).
- Barkleit, A.; Foerstendorf, H.; Heim, K.; Sachs, S.; Bernhard, G.: Complex formation of uranium(VI) with L-phenylalanine and 3-phenylpropionic acid studied by attenuated total reflection Fourier transform infrared spectroscopy. *Appl. Spectr.* 62, 798-802 (2008).
- Barkleit, A.; Geipel, G.; Acker, M.; Taut, S.; Bernhard, G.: First fluorescence spectroscopic investigation of Am(III) complexation with an organic carboxylic ligand, pyromellitic acid. *Spectrochim. Acta A* 549-552, 78, (2011).
- Barkleit, A.; Tsushima, S.; Savchuk, O. et al.: Eu(3+)-mediated polymerization of benzenetetracarboxylic acid studied by spectroscopy, temperature-dependent calorimetry, and density functional theory. *Inorg. Chem.* 5451-5459, 50, (2011).
- Chiu, C.: Density functional studies on uranyl complexation by amino acids. Bachelor thesis, Technische Universität München (2008).
- Fröhlich, D.R.; Amayri, S.; Drebert, J.; Reich, T.: Sorption of Np(V) on Opalinus clay under aerobic/anaerobic conditions. *Radiochim. Acta* 99, 71-77 (2011).
- Fröhlich, D.R.; Amayri, S.; Drebert, J. et al.: Speciation of Np(V) uptake by Opalinus clay using synchrotron microbeam techniques. *Anal. Bioanal. Chem.* 404, 2151-2162 (2012).
- Fröhlich, D.R.; Amayri, S.; Drebert, J.; Reich, T.: Influence of temperature and background electrolyte on the sorption of neptunium(V) on Opalinus Clay. *Appl. Clay Sci.* 69,43-49 (2012).
- Grangeon, S.; Agnès, A.; Lerouge, C. et al.: On nickel occurrence and distribution in a clay-rich formation: Implications for trace elements solubility control. *Geochim. Cosmochim. Acta*, in review (2012).
- Grasset, L. et al.: Sequential extraction and spectroscopic characterisation of organic matter from the Callovo-Oxfordian formation. *Org. Geochem.*, 41(3): 221-233 (2010).
- Gründig, M.; Richter, M.; Seese, A.; Sabri, O.: Tomographic radiotracer studies of the spatial distribution of heterogeneous geochemical transport processes, *Appl. Geochem.* 22, 2334 (2007).
- Günther, A.; Steudtner, R.; Schmeide, K.; Bernhard, G.: Luminescence properties of uranium(VI) citrate and uranium(VI) oxalate species and their application in the determination of complex formation constants. *Radiochim. Acta* 99, 535-541 (2011).
- Hartmann, E.; Baeyens, B.; Bradbury, M. H.; Geckeis, H.; Stumpf, T.: A Spectroscopic Characterization and Quantification of M(III)/Clay Mineral Outer-Sphere Complexes. *Environmental Science & Technology* 42, 7601-7606 (2008).
- Hartmann, E.; Brendebach, B.; Polly, R.; Geckeis, H.; Stumpf, T.: Characterization and quantification of Sm(III)/and Cm(III)/clay mineral outer-sphere species by TRLFS in D₂O and EXAFS studies. *J. Colloid Interface Sci.* 353, 562-568 (2010).
- Hartmann, E.; Geckeis, H.; Rabung, T.; Lutzenkirchen, J.; Fanghanel, T.: Sorption of radionuclides onto natural clay rocks. *Radiochim. Acta* 96, 699-707(2008).

- Joseph, C.; Raditzky, B.; Schmeide, K.; Geipel, G.; Bernhard, G.: Complexation of uranium by sulfur and nitrogen containing model ligands in aqueous solution. In: Uranium, mining and hydrogeology (B.J. Merkel, A. Hasche-Berger, eds.), Springer Verlag, Berlin Heidelberg, p. 539-548 (2008).
- Joseph, C.; Schmeide, K.; Sachs, S. Brendler, V.; Geipel, G.; Bernhard, G.: Sorption of uranium(VI) onto Opalinus Clay in the absence and presence of humic acid in Opalinus Clay pore water. *Chem. Geology* 284, 240-250 (2011).
- Joseph, C.; Stockmann, M.; Schmeide, K.; Sachs, S.; Brendler, V.; Bernhard, G.: Sorption of U(VI) onto Opalinus Clay: Effects of pH and humic acid. *Appl. Geochem.*, submitted (2012).
- Joseph, C.; Van Loon, L.R.; Jakob, A.; Schmeide, K.; Sachs, S.; Bernhard, G.: Effect of temperature and humic acid on the U(VI) diffusion in compacted Opalinus clay. In: The new uranium mining boom. Challenge and lessons learned. (B.J. Merkel, M. Schipek, eds.), Springer Verlag, Berlin Heidelberg, p. 617-626 (2011).
- Joseph, C.; Van Loon, L.R.; Jakob, A.; Steudtner, R.; Schmeide, K.; Sachs, S.; Bernhard, G.: Diffusion of U(VI) in Opalinus clay: Influence of temperature and humic acid. *Geochim. Cosmochim. Acta*, submitted (2012).
- Kautenburger, R.: Influence of metal concentration and the presence of competing cations on lanthanide speciation with humic acid analysed by CE-ICP-MS. *J. Anal. At. Spectrom.* 24, 934 (2009).
- Kautenburger, R.: Endstation Tonstein? *Nachrichten aus der Chemie* 58, 751 (2010).
- Kautenburger, R.: Batch is bad? Leaching of Opalinus clay samples and ICP-MS determination of extracted elements. *J. Anal. At. Spectrom.* 26, 2089 (2011).
- Kautenburger, R.: Geochemische Analytik: Endlager für radioaktiven Müll gesucht. *Analytica PRO* 2012, 59 (2012).
- Kautenburger, R.; Beck, H.P.: Complexation studies with lanthanides and humic acids analysed by ultrafiltration and capillary electrophoresis - inductively coupled plasma mass spectrometry. *J. Chromatogr. A* 1159, 75 (2007).
- Kautenburger, R.; Beck, H.P.: Waste disposal in clay formations: Influence of humic acid on the migration of heavy metal pollutants. *ChemSusChem* 1, 295 (2008).
- Kautenburger, R.; Beck, H.P.: Influence of geochemical parameters on the sorption and desorption behaviour of europium and gadolinium onto kaolinite. *J. Environ. Monit.* 12, 1295 (2010).
- Kautenburger, R.; Möser, C.; Beck, H.P.: Influence of Lanthanide Concentration and the Presence of Competing Metal Ions on Europium and Gadolinium Speciation with Humic Acid Analyzed by CE-ICP-MS. In: Advances in NOM and Humic Substances Research 2008-2010 (Eds: J.A. González-Pérez, F.J. González-Vila & G. Almendros). Proc. IHSS 15 (Vol. 1), 251 (2010).
- Kautenburger, R.; Nowotka, K.; Beck, H.P.: Online analysis of europium and gadolinium species complexed or uncomplexed with humic acid by capillary electrophoresis-inductively coupled plasma mass spectrometry. *Anal. Bioanal. Chem.* 384, 1416 (2006).

- Kautenburger, R.; Nowotka, K.; Beck, H.P.: Iodination of humic acid as ICP-MS marker in speciation studies with lanthanides analyzed by CE-ICP-MS. *Proc. IHSS* 45, 937 (2006).
- Kremleva, A.: Environmental chemistry of uranyl: A relativistic density functional study on complexation with humic substances and sorption at kaolinite. Ph.D. Thesis, Technische Universität München (2009).
- Kremleva, A.; Krüger, S.; Rösch, N.: Density functional model studies of uranyl adsorption on (001) surfaces of kaolinite. *Langmuir* 24, 9515-9524 (2008).
- Kremleva, A., Krüger, S., Rösch, N., Role of Aliphatic and Phenolic Hydroxyl Groups in Uranyl Complexation by Humic Substances. *Inorg. Chim. Acta* 362, 2542–2550 (2009).
- Kremleva, A.; Krüger, S.; Rösch, N.: Quantum chemical modeling of uranyl adsorption on mineral surfaces. *Radiochim. Acta* 98, 635-646 (2010).
- Kremleva, A.; Krüger, S.; Rösch, N.: Uranyl adsorption at (010) edge surfaces of kaolinite. A density functional study. *Geochim. Cosmochim. Acta* 75, 706-718 (2011).
- Kremleva, A.; Zhang, Y.; Shor, A.M.; Krüger, S.; Joseph, C.; Raditzky, B.; Schmeide, K.; Sachs, S.; Bernhard, G.; Rösch, N.: Uranyl(VI) complexation by sulfonate ligands: A relativistic density functional and time-resolved laser-induced fluorescence spectroscopy study. *Eur. J. Inorg. Chem.* 2012, 3636-3644 (2012).
- Křepelová, A.; Brendler, V.; Sachs, S.; Baumann, N.; Bernhard, G.: U(VI)-kaolinite surface complexation in absence and presence of humic acid studied by TRLFS. *Environ. Sci. Technol.* 41, 6142-6147 (2007).
- Křepelová, A.; Reich, T.; Sachs, S.; Drebert, J.; Bernhard, G.: Structural characterization of U(VI) surface complexes on kaolinite in the presence of humic acid using EXAFS spectroscopy. *J. Colloid Interf. Sci.* 319, 40-47 (2008).
- Křepelová, A.; Sachs, S.; Bernhard, G.: Uranium(VI) sorption onto kaolinite in the presence and absence of humic acid. *Radiochim. Acta* 94, 825-833 (2006).
- Křepelová, A.; Sachs, S.; Bernhard, G.: Influence of humic acid on the Am(III) sorption onto kaolinite. *Radiochim. Acta* 99, 253-260 (2011).
- Kulenkampff, J.; Gründig, M.; Richter, M.; Enzmann, F.: Evaluation of positron emission tomography for visualization of migration processes in geomaterials. *Phys. Chem. Earth* 33, 937 (2008).
- Kulenkampff, J.; Wolf, M.; Gründig, M.; Mittmann, H.; Richter, M.: Tomographische Radiotraceruntersuchungen zu Transportprozessen im Salinar und seinem Deckgestein in Staßfurt, *Exkursionsführer und Veröffentlichungen der Deutschen Gesellschaft für Geowissenschaften* 242, 97 (2009).
- Lerouge, C.; Claret, F.; Denecke, M.; Wille, G.; Falkenberg, G.; Ramboz, C.; Beny, C. et al.: Comparative EPMA and μ -XRF methods for mapping micro-scale distribution of iodine in biocarbonates of the Callovian- Oxfordian clayey formation at Bure, Eastern part of the Paris Basin. *Phys. Chem. Earth, Parts A/B/C*, 35(6-8): 271-277 (2010).
- Lippold, H.; Eidner, S.; Lippmann-Pipke, J.: Kinetic effects in the complexation of radionuclides with humic substances in the presence of Fe(III) and Al(III). *Geochim. Cosmochim. Acta* 73(13S), A772 (2009).

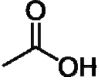
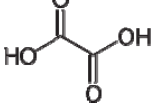
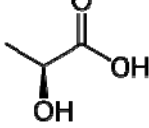
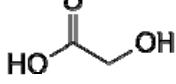
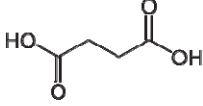
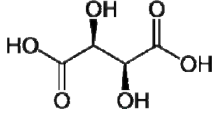
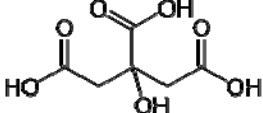
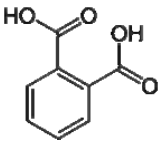
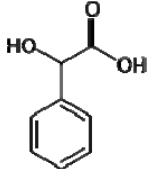
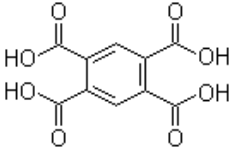
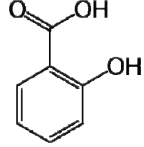
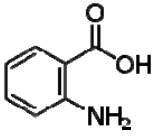
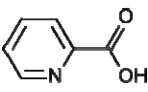
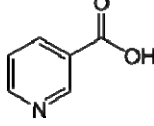
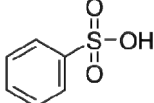
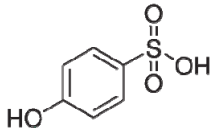
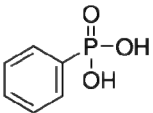
- Lippold, H.; Eidner, S.; Kumke, M.U.; Lippmann-Pipke, J.: Diffusion, degradation or on-site stabilisation – identifying causes of kinetic processes involved in metal-humate complexation. *Appl. Geochem.* 27, 250 (2012).
- Lippold, H.; Lippmann-Pipke, J.: Effect of humic matter on metal adsorption onto clay materials. *Geochim. Cosmochim. Acta* 72(12S), A554 (2008).
- Lippold, H.; Lippmann-Pipke, J.: Effect of humic matter on metal adsorption onto clay materials: Testing the linear additive model. *J. Contam. Hydrol.* 109, 40 (2009).
- Martorell, B.; Kremleva, A.; Krüger, S.; Rösch, N.: Density functional model study of uranyl adsorption on the solvated (001) surface of kaolinite. *J. Phys. Chem. C* 114, 13287–13294 (2010).
- Mibus, J.; Sachs, S.; Nebelung, C.; Bernhard, G.: Migration of uranium(IV)/(VI) in the presence of humic acids in quartz sand: A laboratory column study. *J. Contam. Hydr.* 89, 199-217 (2007).
- Möser, C.: Untersuchungen zum Einfluss geochemischer Parameter auf die Sorption und Desorption von Lanthaniden in Opalinuston im Rahmen der Auswahl eines potentiellen Endlagers. Ph.D.Thesis, Universität des Saarlandes, Saarbrücken (2011).
- Möser, C.; Kautenburger, R.; Beck, H.P.: CE-ICP-MS as speciation technique to analyze the complexation behavior of europium, gadolinium and terbium with humic acid. In: *Advances in NOM and Humic Substances Research 2008-2010* (Eds: J.A. González-Pérez, F.J. González-Vila & G. Almendros). Proc. IHSS 15 (Vol. 3), 139 (2010).
- Möser, C.; Kautenburger, R.; Beck, H.P.: Migration of europium and uranium in Opalinus clay influenced by pH and temperature. *Mineral. Mag.* 75, 1504 (2011).
- Möser, C.; Kautenburger, R.; Beck, H.P.: Complexation of europium and uranium by humic acids analysed by capillary electrophoresis - inductively coupled plasma mass spectrometry. *Electrophoresis* 33, 1482 (2012).
- Müller, M.; Acker, M.; Taut, S.; Bernhard, G.: Complex formation of trivalent americium with salicylic acid at very low concentrations. *J. Radioanal. Nucl. Chem.* 175-180, 286, (2010).
- Nowotka, K.: Untersuchungen zur Migration von Europium und Gadolinium in Kaolinit als Modellmineral für eine Endlagerstätte. Ph.D. Thesis, Universität des Saarlandes (2007).
- Raeder, S.; Hakimi, A.; Stöbener, N.; Trautmann, N.; Wendt, K.: Detection of plutonium isotopes at lowest quantities using in-source resonance ionization mass spectrometry. *Anal. Bioanal. Chem.* 404, 2163-2172 (2012).
- Raeder, S.; Stöbener, N.; Gottwald, T.; Passler, G., Reich, T.; Trautmann, N.; Wendt, K.: Determination of a three-step excitation and ionization scheme for resonance ionization and ultratrace analysis of Np-237. *Spectrochim. Acta B* 66, 242-247 (2011)
- Raditzky, B.; Schmeide, K.; Sachs, S.; Geipel, G.; Bernhard, G.: Interaction of uranium(VI) with nitrogen containing model ligands studied by laser-induced fluorescence spectroscopy. *Polyhedron* 29, 620-626 (2010).
- Ramakrishnan, R.: The DFT+U method in the framework of the parallel density functional code ParaGauss. Ph.D. Thesis, Technische Universität München (2011).
- Ramakrishnan, R.; Matveev, A. V.; Krüger, S.; Rösch, N.: Self-Interaction artifacts on structural features of uranyl monohydroxide from Kohn-Sham calculations. *Theor. Chem. Acc.* 130, 361-369 (2011).

- Ramakrishnan, R.; Matveev, A. V.; Rösch, N.: Effects of the self-Interaction error in Kohn-Sham calculations: A DFT+U case study on penta-aqua uranyl(VI). *Comp. Theor. Chem.* 963, 337-343 (2011).
- Ray, S.R.: A relativistic density functional study of uranyl hydrolysis and complexation by carboxylic acids in aqueous solution, Ph.D. Thesis, Technische Universität München (2009).
- Ray, S.R.; Krüger, S.; Rösch, N.: Uranyl monocarboxylates of aromatic acids: A density functional model study of uranyl humate complexation. *Dalton Trans.* 3590–3598 (2009).
- Ray, S.R.; Krüger, S.; Rösch, N.: Ternary uranyl hydroxo complexes: A computational study of structure, energetics, and stability constants. *Inorg. Chim. Acta* 363, 263-269 (2010).
- Rösch, N.; Krüger, S.: Plane wave density functional model studies of chemistry at surfaces, in: *High Performance Computing in Science and Engineering, Transactions of the Third Joint HLRB and KONWIHR Result and Status Workshop, Garching 2007*, S. Wagner, M. Steinmetz, A. Bode, M. Brehm (eds.), Springer: Berlin, pp. 173-186 (2008).
- Sachs, S.; Bernhard, G.: Sorption of U(VI) onto an artificial humic substance-kaolinite-associate. *Chemosphere* 72, 1441-1447 (2008).
- Sachs, S.; Bernhard, G.: Influence of humic acids on the actinide migration in the environment: suitable humic acid model substances and their application in studies with uranium - a review. *J. Radioanal. Nucl. Chem.* 290, 17-29 (2011).
- Sachs, S.; Bernhard, G.: Humic acid model substances with pronounced redox functionality for the study of environmentally relevant interaction processes of metal ions in the presence of humic acid. *Geoderma* 162, 132-140 (2011).
- Sachs, S.; Brendler, V.; Geipel, G.: Uranium(VI) complexation by humic acid under neutral pH conditions studied by laser-induced fluorescence spectroscopy. *Radiochim. Acta* 95, 103-110 (2007).
- Sachs, S.; Reich, T.; Bernhard, G.: Study of the role of sulfur functionalities in humic acids for uranium(VI) complexation. *Radiochim. Acta* 98, 467-477 (2010).
- Sachs, S.; Schmeide, K.; Bernhard, G.: Interaction of humic acid with actinides: Influence of heteroatomic functional groups other than carboxylic groups. In: *Workshop Peat and Humic Substances. Current research in chemical, physical and biological characterization of peat*. Proceedings Heft 5. University of Applied Sciences Zittau/Görlitz, Zittau, p. 17-20 (2011).
- Schäfer, T.; Denecke, M.A.: Nuclear waste repository research at the micro- to nanoscale. In: *X-Ray Optics and Microanalysis*, M.A. Denecke and C.T. Walker (Editors), Proceedings, AIP Conference Proceedings. Amer. Inst. Physics, Melville, pp. 181-187 (2010).
- Schäfer, T.; Michel, P.; Claret, F.: The application of STXM and μ FTIR to characterize sedimentary organic matter in the Opalinus clay. *J. Phys. Conference Series*, 186: 012095 (2009).
- Schäfer, T.; Michel, P.; Claret, F.; Beetz, T.; Wirick, S.; Jacobsen, C.: Radiation sensitivity of natural organic matter: Clay mineral association effects in the Callovo-Oxfordian argillite. *J. Electron Spectrosc. Relat. Phenom.* 170: 49-56 (2009).
- Schlosser, F.; Moskaleva, L.V.; Kremleva, A.; Krüger, S.; Rösch, N.: Comparative density functional study of the complexes $[\text{UO}_2(\text{CO}_3)_3]^{4-}$ and $[(\text{UO}_2)_3(\text{CO}_3)_6]^{6-}$ in aqueous solution. *Dalton Trans.* 5705-5712 (2010).

- Schmeide, K.; Bernhard, G.: Spectroscopic study of the uranium(IV) complexation by organic model ligands in aqueous solution. In: *Uranium, mining and hydrogeology* (B.J. Merkel, A. Hasche-Berger, eds.), Springer Verlag, Berlin Heidelberg, p. 591-598 (2008).
- Schmeide, K.; Bernhard, G.: Redox stability of neptunium(V) and neptunium(IV) in the presence of humic substances of varying functionality. *Radiochim. Acta* 97, 603-611 (2009).
- Schmeide, K.; Bernhard, G.: Sorption of Np(V) and Np(IV) onto kaolinite: Effects of pH, ionic strength, carbonate and humic acid. *Appl. Geochem.* 25, 1238-1247 (2010).
- Schmeide, K.; Reich, T.; Sachs, S.; Bernhard, G.: Plutonium(III) complexation by humic substances studied by X-ray absorption fine structure spectroscopy. *Inorg. Chim. Acta* 359, 237-242 (2006).
- Schmeide, K.; Sachs, S.; Bernhard, G.: Np(V) reduction by humic acid: Contribution of reduced sulfur functionalities to the redox behavior of humic acid. *Sci. Total Environ.* 419, 116-123 (2012).
- Schott, J.; Acker, M.; Barkleit, A.; Brendler, V.; Taut, S.; Bernhard, G.: The influence of temperature and small organic ligands on the sorption of Eu(III) on Opalinus Clay. *Radiochimica Acta* 1-10, 100, (2012).
- Stedtner, R.; Müller, K.; Schmeide, K.; Sachs, S.; Bernhard, G.: Binary and ternary uranium(VI) humate complexes studied by attenuated total reflection Fourier-transform infrared spectroscopy. *Dalton Trans.* 40, 11920-11925 (2011).
- Stedtner, R.; Sachs, S.; Schmeide, K.; Brendler, V.; Bernhard, G.: Ternary uranium(VI) carbonate humate complex studied by cryo-TRLFS. *Radiochim. Acta* 99, 687-692 (2011).
- Stedtner, R.; Schmeide, K.; Bernhard, G.: Uranium(VI) complexation with lactate and citrate in dependence on temperature (7-65 °C). *Mineralog. Magazine* 75, 1940 (2011).
- Stöbener, N.; Amayri, S.; Gehl, A.K.; Kaplan, U.; Malecha, K.; Reich, T.: Sensitive redox speciation of neptunium with CE-ICP-MS. *Anal. Bioanal. Chem.* 404, 2143-2150 (2012).
- Trautmann, N.; Wendt, K.: Fast chemical separations and laser mass spectrometry – tools for nuclear research. *Radiochim. Acta* 100, 675 (2012).
- Vilas, V.V.; Mathiasch, B.; Huth, J.; Kratz, J.V.; Rubert de la Rosa, S.; Michel, P.; Schäfer, T.: Synthesis and Characterization of the Hybrid Clay-Based Material Montmorillonite–Melanoidin: A Potential Soil Model. *Soil Sci. Soc. Am. J.*, 74(6): 2239-2245 (2010).
- Wolf, M.; Kulenkampff, J.; Enzmann, F.; Gründig, M.; Richter, M.; Lippmann-Pipke, J.; Mittmann, H.: 3D-Visualisierung und Quantifizierung von Fluidströmungen in Salinargestein mittels Positronen-Emissions-Tomographie, *Exkursionsführer und Veröffentlichungen der Deutschen Gesellschaft für Geowissenschaften* 244, 200 (2010).
- Zakharieva, O.; Kremlava, A.; Krüger, S.; Rösch, N.: Uranyl complexation by monodentate nitrogen donor ligands. A relativistic density functional study. *Int. J. Quantum Chem.* 211, 2045-2053 (2011).
- Zhang, Y.: A density functional study of uranyl complexation by sulfur containing humic acids in aqueous solution. Master Thesis, Technische Universität München (2009).

Annex A Structural formula of organic ligands

Structural formula of organic ligands used for complexation studies in the present work

 acetic acid	 oxalic acid	 L-lactic acid	 glycolic acid
 succinic acid	 tartaric acid	 citric acid	
 phthalic acid	 mandelic acid	 pyromellitic acid	 salicylic acid
 anthranilic acid	 picolinic acid	 nicotinic acid	 benzenesulfonic acid
 4-hydroxybenzenesulfonic acid	 phenylphosphonic acid		

Annex B Final reports of the project

Content of the CD

1. *Characterization and quantification of the influence of clay organics on the interaction and diffusion of uranium and americium in the clay*
K. Schmeide, C. Joseph, S. Sachs, R. Steudtner, B. Raditzky, A. Günther, G. Bernhard
Helmholtz-Zentrum Dresden-Rossendorf, Institut für Ressourcenökologie,
2. *Migration of actinides in natural clay: Interaction of neptunium and plutonium with natural clay*
S. Amayri, J. Drebert, D. R. Fröhlich, U. Kaplan, J. V. Kratz, T. Reich, N. Stöbener,
N. Trautmann, T. Wunderlich
Johannes Gutenberg-Universität Mainz, Institut für Kernchemie
3. *Contributions to modelling actinide transport in potential host rock formations: Elementary processes and influence of heterogeneous structures*
H. Lippold, J. Kulenkampff, M. Gründig, A. Zakhnini
Helmholtz-Zentrum Dresden-Rossendorf, Institut für Ressourcenökologie,
Forschungsstelle Leipzig
4. *Quantum Mechanical Modeling of Actinide Complexes: Complexation by Humic Substances and Sorption on Clay Minerals*
N. Rösch, S. Krüger, A. Kremleva
Technische Universität München, Theoretische Chemie
5. *Migration of Lanthanides and Uranium in Natural Clay Formations - From Mineral Suspensions to Compact Clays*
R. Kautenburger, Chr. Möser, H. P. Beck
Universität des Saarlandes, Institut für Anorganische und Analytische Chemie und Radiochemie
6. *Influence of Clay Organic Substances on the retardation of Actinide Ions in the Clay Barrier*
N. Banik, E. Hartmann, C.M. Marquardt, P. Panak, Th. Schäfer, A. Skerencak
Karlsruher Institut für Technologie, Institut für Nukleare Entsorgung
7. *Spectroscopic Investigations for an Improved Process Understanding in Binary and Ternary Systems of Humic Substances – Clay – Lanthanides: Thermodynamic and Kinetic Parameters*
K. Brennenstuhl, S. Eidner, K. Jahn, M.U. Kumke, S. Kuke, B. Marmodée, P.A. Primus,
S. Zilm-Gramkow
Universität Potsdam, Institut für Chemie, Physikalische Chemie
8. *Investigations of temperature dependence of complexation and sorption of trivalent actinides (Am(III)) in the system actinide-NOM-natural clay rock-aquifer*
M. Acker, A. Barkleit, M. Müller, J. Schott, S. Taut, G. Bernhard
Technische Universität Dresden, Sachgebiet Strahlenschutz

**Joint Project: Interaction and transport of actinides
in natural clay rock with consideration of
humic substances and clay organics**

**Characterization and quantification of the influence of
clay organics on the interaction and diffusion of
uranium and americium in the clay**

**Katja Schmeide, Claudia Joseph, Susanne Sachs, Robin Steudtner,
Bianca Raditzky, Alix Günther, Gert Bernhard**

Final Report

BMWi Project No.: 02 E 10156

Das diesem Bericht zugrunde liegende Vorhaben wurde mit Mitteln des Bundesministeriums für Wirtschaft und Technologie unter dem Förderkennzeichen 02 E 10156 gefördert. Die Verantwortung für den Inhalt dieser Veröffentlichung liegt bei den Autoren.

Vorhaben:

VERBUNDPROJEKT: Wechselwirkung und Transport von Actiniden im natürlichen Tongestein unter Berücksichtigung von Huminstoffen und Tonorganika

Charakterisierung und Quantifizierung des Einflusses von Tonorganika auf die Wechselwirkung und die Diffusion von Uran und Americium im Ton

Laufzeit des Vorhabens: 01.07.2006 bis 30.06.2011

Projektleiter: Prof. Dr. G. Bernhard

Institut für Radiochemie, Helmholtz-Zentrum Dresden-Rossendorf

Abstract

The objective of this project was the study of basic interaction processes in the systems actinide - clay organics - aquifer and actinide - natural clay - clay organics - aquifer. Thus, complexation, redox, sorption and diffusion studies were performed.

To evaluate the influence of nitrogen, phosphorus and sulfur containing functional groups of humic acid (HA) on the complexation of actinides in comparison to carboxylic groups, the Am(III) and U(VI) complexation by model ligands was studied by UV-Vis spectroscopy and TRLFS. The results show that Am(III) is mainly coordinated via carboxylic groups, however, probably stabilized by nitrogen groups. The U(VI) complexation is dominated by carboxylic groups, whereas nitrogen and sulfur containing groups play a minor role. Phosphorus containing groups may contribute to the U(VI) complexation by HA, however, due to their low concentration in HA they play only a subordinate role compared to carboxylic groups. Applying synthetic HA with varying sulfur contents (0 to 6.9 wt.%), the role of sulfur functionalities of HA for the U(VI) complexation and Np(V) reduction was studied. The results have shown that sulfur functionalities can be involved in U(VI) humate complexation and act as redox-active sites in HA for the Np(V) reduction. However, due to the low content of sulfur in natural HA, its influence is less pronounced.

In the presence of carbonate, the U(VI) complexation by HA was studied in the alkaline pH range by means of cryo-TRLFS (-120°C) and ATR FT-IR spectroscopy. The formation of the ternary $\text{UO}_2(\text{CO}_3)_2\text{HA}(\text{II})^{4-}$ complex was detected. The complex formation constant was determined with $\log \beta_{0.1\text{M}} = 24.57 \pm 0.17$.

For aqueous U(VI) citrate and oxalate species, luminescence emission properties were determined by cryo-TRLFS and used to determine stability constants. The existing data base could be validated.

The U(VI) complexation by lactate, studied in the temperature range 7 to 65°C, was found to be endothermic and entropy-driven. In contrast, the complex stability constants determined for U(VI) humate complexation at 20 and 40°C are comparable, however, decrease at 60°C.

For aqueous U(IV) citrate, succinate, mandelate and glycolate species stability constants were determined. These ligands, especially citrate, increase solubility and mobility of U(IV) in solution due to complexation.

The U(VI) sorption onto crushed Opalinus Clay (OPA, Mont Terri, Switzerland) was studied in the absence and presence of HA or low molecular weight organic acids, in dependence on temperature and CO₂ presence using OPA pore water as background electrolyte. Distribution coefficients (K_d) were determined for the sorption of U(VI) and HA onto OPA with $(0.0222 \pm 0.0004) \text{ m}^3/\text{kg}$ and $(0.129 \pm 0.006) \text{ m}^3/\text{kg}$, respectively. The U(VI) sorption is not influenced by HA ($\leq 50 \text{ mg/L}$), however, decreased by low molecular weight organic acids ($\geq 1 \times 10^{-5} \text{ M}$), especially by citrate and tartrate. With increasing temperature, the U(VI) sorption increases both in the absence and in the presence of clay organics.

The U(VI) diffusion in compacted OPA is not influenced by HA at 25 and 60°C. Predictions of the U(VI) diffusion show that an increase of the temperature to 60°C does not accelerate the migration of U(VI). With regard to uranium-containing waste, it is concluded that OPA is suitable as host rock for a future nuclear waste repository since OPA has a good retardation potential for U(VI).

Zusammenfassung

Ziel des Projektes war die Untersuchung grundlegender Wechselwirkungsprozesse in den Systemen Actinid - Tonorganika - Aquifer und Actinid - Tongestein - Tonorganika - Aquifer. Dazu wurden Komplexierungs-, Redox-, Sorptions- und Diffusionsstudien durchgeführt.

Um den Einfluss stickstoff-, phosphor- und schwefelhaltiger funktioneller Gruppen von Huminsäuren (HA) auf die Komplexierung von Actiniden im Vergleich zu Carboxylgruppen einzuschätzen, wurde die Am(III)- und U(VI)-Komplexierung mit Modellliganden mittels UV-Vis-Spektroskopie und TRLFS untersucht. Die Ergebnisse zeigen, dass Am(III) hauptsächlich über Carboxylgruppen koordiniert wird, wobei stickstoffhaltige Gruppen wahrscheinlich stabilisierend wirken. Die U(VI)-Komplexierung wird von Carboxylgruppen dominiert, stickstoff- und schwefelhaltige Gruppen spielen eine untergeordnete Rolle. Phosphorhaltige Gruppen können zur U(VI)-Komplexierung durch HA beitragen. Aufgrund ihrer niedrigen Konzentration in HA spielen sie gegenüber Carboxylgruppen jedoch nur eine untergeordnete Rolle. Weiterhin wurde unter Anwendung von synthetischen HA mit variierenden Schwefelgehalten (0 bis 6.9 Gew.%) die Rolle von Schwefelfunktionalitäten der HA für die U(VI)-Komplexierung und Np(V)-Reduktion untersucht. Die Ergebnisse zeigen, dass die HA-Schwefelfunktionalitäten sowohl zur U(VI)-Humat-Komplexierung als auch zur Np(V)-Reduktion durch HA beitragen können. Aufgrund des relativ niedrigen Schwefelgehaltes in natürlichen HA ist dieser Beitrag unter umweltrelevanten Bedingungen jedoch niedrig.

In Gegenwart von Carbonat wurde die U(VI)-Humat-Komplexierung unter alkalischen Bedingungen mittels cryo-TRLFS (-120°C) und ATR FT-IR untersucht. Die Bildung des ternären $\text{UO}_2(\text{CO}_3)_2\text{HA}(\text{II})^{4-}$ Komplexes wurde nachgewiesen. Die Komplexbildungskonstante wurde mit $\log \beta_{0.1\text{M}} = 24.57 \pm 0.17$ bestimmt.

Für U(VI)-Citrat- und Oxalatspezies wurden die Lumineszenzemissionseigenschaften mittels cryo-TRLFS ermittelt und für die Bestimmung von Stabilitätskonstanten genutzt. Literaturwerte konnten so validiert werden.

Die U(VI)-Komplexierung mit Lactat im Temperaturbereich 7 bis 65°C erfolgt endotherm und entropiegetrieben. Dagegen sind die für die U(VI)-Humat-Komplexierung bestimmten Stabilitätskonstanten bei 20 und 40°C vergleichbar, sinken jedoch bei weiterer Temperaturerhöhung auf 60°C.

Die für U(IV)-Citrat-, Succinat-, Mandelat- und Glykolatspezies bestimmten Stabilitätskonstanten zeigen, dass diese Liganden, insbesondere Citrat, die Löslichkeit und somit die Mobilität von U(IV) erhöhen.

Die U(VI)-Sorption an homogenisiertem Opalinustonpulver (OPA, Mont Terri, Schweiz) wurde in Ab- und Anwesenheit von HA oder niedermolekularen organischen Säuren als Funktion der Temperatur und Atmosphäre unter Anwendung von OPA-Porenwasser als Hintergrundelektrolyt untersucht. Verteilungskoeffizienten (K_d) wurden für die U(VI)- und HA-Sorption an OPA mit $(0.0222 \pm 0.0004) \text{ m}^3/\text{kg}$ bzw. $(0.129 \pm 0.006) \text{ m}^3/\text{kg}$ bestimmt. Die U(VI)-Sorption wird durch HA ($\leq 50 \text{ mg/L}$) nicht beeinflusst, jedoch durch niedermolekulare organische Säuren ($\geq 1 \times 10^{-5} \text{ M}$), insbesondere durch Citrat und Tartrat, verringert. Mit steigender Temperatur nimmt die U(VI)-Sorption sowohl in Ab- als auch in Anwesenheit von Tonorganika zu.

Die U(VI)-Diffusion in intakten OPA-Bohrkernen wird durch HA bei 25 und 60°C nicht beeinflusst. Abschätzungen zur U(VI)-Diffusion zeigen, dass eine Temperaturerhöhung auf 60°C die U(VI)-Migration durch OPA nicht beschleunigt. Bezüglich uranhaltiger Abfälle ist OPA als Wirtsgestein für ein nukleares Endlager geeignet, da es ein gutes Rückhaltevermögen gegenüber U(VI) aufweist.

Contents

1	Introduction.....	1
2	Complexation of actinides in different oxidation states with humic substance model ligands and clay organics.....	3
2.1	Am(III) complexation by anthranilic acid, picolinic acid, nicotinic acid and phthalic acid – Determination of complex formation constants by UV-Vis spectroscopy and TRLFS.....	3
2.1.1	Experimental.....	4
2.1.2	Results and discussion.....	5
2.2	U(IV) complexation by citric acid, succinic acid, mandelic acid and glycolic acid – Determination of complex formation constants by UV-Vis spectroscopy...	12
2.2.1	Experimental.....	12
2.2.2	Results and discussion.....	13
2.3	U(VI) complexation by citric acid and oxalic acid – Determination of luminescence properties at -120°C by cryo-TRLFS.....	18
2.3.1	Experimental.....	18
2.3.2	Results and discussion.....	18
2.4	U(VI) complexation by lactic acid – Determination of complex formation constants in dependence on temperature (7 to 65°C) by UV-Vis spectroscopy and TRLFS.....	25
2.4.1	Experimental.....	25
2.4.2	Results and discussion.....	26
2.5	U(VI) complexation by anthranilic acid and nicotinic acid – Determination of complex formation constants by fs-TRLFS and TRLFS.....	30
2.5.1	Experimental.....	30
2.5.2	Results and discussion.....	32
2.6	U(VI) complexation by phenylphosphonic acid – Determination of complex formation constants by TRLFS.....	36
2.6.1	Experimental.....	36
2.6.2	Results and discussion.....	37
2.7	U(VI) complexation by benzenesulfonic acid and 4-hydroxybenzenesulfonic acid – Determination of complex formation constants by TRLFS.....	40
2.7.1	Experimental.....	40
2.7.2	Results and discussion.....	42

3	Complexation and redox reactions of actinides with humic substances.....	45
3.1	Spectroscopic characterization of the ternary U(VI) carbonate humate complex by cryo-TRLFS and ATR FT-IR.....	45
3.1.1	Ternary U(VI) carbonate humate complex studied by cryo-TRLFS.....	46
3.1.1.1	Experimental.....	46
3.1.1.2	Results and discussion.....	46
3.1.2	Binary and ternary U(VI) humate complexes studied by ATR FT-IR.....	50
3.1.2.1	Experimental.....	50
3.1.2.2	Results and discussion.....	50
3.1.3	Conclusion.....	56
3.2	Influence of sulfur functionalities on the interaction behavior of humic acids with actinide ions.....	57
3.2.1	Synthesis and characterization of sulfur containing humic acid model substances.....	59
3.2.1.1	Synthesis.....	59
3.2.1.2	Characterization.....	60
3.2.2	Impact of sulfur functionalities on the U(VI) complexation by humic acids.....	62
3.2.2.1	Experimental.....	63
3.2.2.2	Results and discussion.....	64
3.2.3	Impact of sulfur functionalities on the Np(V) reduction by humic acids.....	70
3.2.3.1	Experimental.....	70
3.2.3.2	Results and discussion.....	70
3.3	U(VI) humate complexation in dependence on temperature (20-60°C).....	74
3.3.1	Experimental.....	74
3.3.2	Results and discussion.....	75
4	Sorption of U(VI) onto Opalinus Clay.....	80
4.1	Characterization of Opalinus Clay.....	81
4.1.1	Leaching of Opalinus Clay with Opalinus Clay pore water.....	85
4.1.1.1	Experimental.....	85
4.1.1.2	Results and discussion.....	85
4.1.2	Leaching of Opalinus Clay in dependence on pH.....	86
4.1.2.1	Experimental.....	86
4.1.2.2	Characterization of the solid.....	88
4.1.2.3	Characterization of the solution.....	89
4.2	Speciation of U(VI) in dependence on background electrolyte.....	90
4.3	The system U(VI) / humic acid / kaolinite in dependence on background electrolyte.....	95
4.3.1	Experimental.....	95

4.3.2	Results and discussion.....	97
4.4	The system U(VI) / humic acid / Opalinus Clay / Opalinus Clay pore water.....	99
4.4.1	Experimental.....	99
4.4.1.1	Sorption experiments.....	100
4.4.1.2	TRLFS measurements.....	102
4.4.2	Results and discussion.....	103
4.4.2.1	Influence of S/L ratio on the U(VI) sorption.....	103
4.4.2.2	Kinetic of the U(VI) and humic acid sorption onto Opalinus Clay.....	104
4.4.2.3	Determination of K_d values for U(VI) and humic acid.....	104
4.4.2.4	Influence of humic acid on the U(VI) sorption onto Opalinus Clay.....	110
4.4.2.5	Influence of CO ₂	111
4.4.2.6	Investigation of the U(VI) speciation by TRLFS under cryogenic conditions....	111
4.5	The system U(VI) / humic acid / Opalinus Clay / 0.1 M NaClO ₄	114
4.5.1	Experimental.....	114
4.5.2	Results and discussion.....	115
4.5.2.1	U(VI) sorption in the absence of humic acid.....	115
4.5.2.2	U(VI) sorption in the presence of humic acid.....	116
4.5.2.3	Humic acid sorption in the presence of U(VI).....	117
4.6	Influence of low molecular weight organic acids on U(VI) sorption onto Opalinus Clay at 25°C.....	119
4.7	Influence of temperature on U(VI) sorption onto Opalinus Clay in the absence and presence of clay organics.....	120
5	Diffusion of U(VI) and humic acid in Opalinus Clay.....	123
5.1	Experimental.....	123
5.2	Data processing.....	126
5.3	Filter diffusion parameters.....	127
5.4	Results and discussion.....	129
5.4.1	HTO diffusion in Opalinus Clay in dependence on temperature.....	129
5.4.2	Aqueous U(VI) and humic acid speciation.....	129
5.4.3	Diffusion of U(VI) and humic acid in Opalinus Clay at 25°C.....	132
5.4.4	Diffusion of U(VI) and humic acid in Opalinus Clay at 60°C.....	135
6	Summary and outlook.....	139
7	References.....	144
8	Acknowledgements.....	157

1 Introduction

A reliable long-term risk assessment for future nuclear waste repository sites requires the identification, characterization and quantification of all migration processes, relevant for potentially released radionuclides, and their underlying chemical and physical processes.

In addition to salt and crystalline rock, argillaceous rock is considered as potential host rock and backfill material for nuclear waste repositories in deep geological formations. The swelling properties of clay minerals, their large surface areas and their high retention efficiency towards safety relevant radionuclides are advantageous and make them ideal barriers against radionuclide migration. In natural clay, organic matter is strongly associated with mineral constituents. Low molecular weight organic acids such as acetic, lactic, propionic and formic acid as well as fulvic and humic acids can be released from the clay under certain conditions. This was shown by extraction experiments (Claret et al., 2003; Glaus et al., 2005; Courdouan et al., 2007, 2008). These clay organics are able to influence the transport of actinides in the environment by forming soluble complexes or stable colloids. Thus, to study basic interaction processes in the systems actinide - clay organics - aquifer as well as actinide - natural clay - clay organics - aquifer, complexation, redox, sorption and diffusion studies have to be performed. Since elevated temperatures of up to 100°C are expected for the disposal of high-level nuclear waste in clay formations (Brasser et al., 2008), these studies should also be performed at elevated temperatures.

The objective of the complexation studies is to determine complex formation constants not known so far or the validation of known complex formation constants by complementary spectroscopic methods to improve the thermodynamic database. Thus, the complexation of Am(III), U(IV) and U(VI) with low molecular weight organic ligands as well as with humic substances will be studied in the present project, partly under variation of the temperature (7 to 65°C), to determine thermodynamic constants. Furthermore, in continuation of the actinide humate complexation studies performed previously, the objective of the present study is to evaluate the influence of nitrogen, phosphorus and sulfur containing functional groups of humic acid on the complexation of actinides in comparison to carboxylic groups. For this, the Am(III) and U(VI) complexation with various model ligands as well as with synthetic humic acids, enriched with sulfur functional groups, will be studied. The sulfur containing synthetic humic acids will also be applied to clarify the role of sulfur functional groups for the Np(V) reduction by humic acid. The specification of those individual processes contributing to the

total complexation and redox activity of humic substances improves the understanding of thermodynamic and kinetic aspects of environmental processes involving humic substances.

The U(VI) humate complexation studies, mainly performed in the acidic pH range or at pH 7 and with exclusion of carbonate so far, should be extended to the alkaline pH range and should be performed in the presence of carbonate. This is to verify or exclude the formation of ternary U(VI) carbonate humate complexes. The information on such a complex is necessary for a reliable geochemical modeling of the mobility of U(VI) under environmentally relevant conditions.

The sorption and diffusion studies within this project will focus on the natural clay 'Opalinus Clay' from the Mont Terri underground laboratory, Switzerland. The U(VI) sorption onto crushed Opalinus Clay will be studied in the absence and presence of humic acid or low molecular weight organic acids and in dependence on temperature (10 to 60°C) using Opalinus Clay pore water as background electrolyte. Furthermore, pH-dependent studies of the U(VI) sorption onto Opalinus Clay will be performed in the absence and presence of humic acid using NaClO₄ as background solution. The U(VI) sorption onto kaolinite will be studied in dependence on ionic strength and composition of the background electrolyte. These sorption studies will lead to a better process understanding. To determine U(VI) migration in Opalinus Clay as well as the influence of humic acid and temperature on the U(VI) migration, the U(VI) diffusion in compacted Opalinus Clay will be studied in the absence and presence of humic acid at 25 and 60°C using synthetic Opalinus Clay pore water. Diffusion and distribution coefficients (D_e and K_d) will be determined for U(VI) and humic acid.

The U(VI) sorption and especially the U(VI) diffusion experiments will contribute to a more realistic description of the migration behavior of U(VI) in the natural clay rock Opalinus Clay since the resulting parameters will be used for modeling the actinide migration through argillaceous rocks in the absence and presence of clay organics in the temperature range up to 60°C. This will lead to an improved risk assessment for potential nuclear waste repositories.

This research project is performed in collaboration with the R&D projects of the Karlsruher Institut für Technologie (Institut für Nukleare Entsorgung), Johannes Gutenberg-Universität Mainz (Institut für Kernchemie), Institut für Interdisziplinäre Isotopenforschung Leipzig (now HZDR, Institut für Radiochemie), Universität des Saarlandes (Institut für Anorganische und Analytische Chemie und Radiochemie), Technische Universität Dresden (Sachgebiet Strahlenschutz), Technische Universität München (Fachgebiet Theoretische Chemie) and Universität Potsdam (Institut für Chemie-Physikalische Chemie) that were funded by Bundesministerium für Wirtschaft und Technologie (BMWi).

2 Complexation of actinides in different oxidation states with humic substance model ligands and clay organics

The complexation of metal ions by humic substances is mainly attributed to carboxylic groups (Kim, 1986; Choppin, 1992; Denecke et al., 1997; Sachs et al., 2005; Schmeide et al., 2003, 2005, 2006) and phenolic OH groups (Pompe et al., 2000b; Sachs and Bernhard, 2005) as their dominant functionalities. In addition to these oxygen containing functional groups, humic substances also contain nitrogen, phosphorus and sulfur containing functionalities.

The objective of this work was to determine the influence of various nitrogen, phosphorus and sulfur containing functional groups on the complexation of actinides in different oxidation states (U(VI) and Am(III)) and to evaluate their contribution in comparison to oxygen containing functional groups. For this, simple organic model ligands that can occur as building blocks for humic substances were used, for instance, anthranilic acid, nicotinic acid, picolinic acid, phenylphosphonic acid, benzenesulfonic acid and 4-hydroxybenzenesulfonic acid (cf. sections 2.1, 2.5, 2.6, 2.7).

A further objective of this work was the determination or validation of complex formation constants to improve the thermodynamic database. Thus, the U(IV) complexation with citric acid, succinic acid, mandelic acid and glycolic acid was studied (cf. section 2.2). The U(VI) complexation with lactic acid was studied in the temperature range 7 to 65°C (cf. section 2.4). Moreover, the up to now unknown luminescence emission properties of U(VI) citrate and oxalate species were determined and applied for the determination of complex formation constants (cf. section 2.3).

2.1 Am(III) complexation by anthranilic acid, picolinic acid, nicotinic acid and phthalic acid – Determination of complex formation constants by UV-Vis spectroscopy and TRLFS

During decomposition of organic matter and the following humification process nitrogen becomes incorporated into HA. The nitrogen content of HA varies between 0.8 and 4.3 wt.% (Stevenson, 1994). The nitrogen functionalities formed are derived from proteinaceous materials (like amino acids or peptides as fragments of proteins), amino sugars and heterocyclic compounds (like pyridines or pyrroles), respectively (Schulten and Schnitzer, 1998; Vairavamurthy and Wang, 2002). Whereas oxygen functionalities are acknowledged as the most important binding partners for actinides, the contribution of these nitrogen

functionalities to the interaction behavior of HA is widely unknown. Only few studies concerning the interaction of HA with certain trace metals such as Co, Ni or Cu (Xia et al., 1997; Croué et al., 2003) have been published, revealing the involvement of amine functionalities in complex formation. Furthermore, in the literature there are references to the complexation of actinides with multidentate N-donor ligands, which play a crucial role for the separation of trivalent actinides from trivalent lanthanides (Guillaumont, 2006; Denecke et al., 2007; Heitzmann et al., 2009). However, concerning the influence of nitrogen containing functionalities on the HA complexation with trivalent actinides, especially Am(III), no results are available so far. To address this lack of knowledge, we studied the complexation of Am(III) with anthranilic acid (AA), nicotinic acid (Nic) and picolinic acid (Pic). For comparison, the complex formation was also studied with phthalic acid (PA) as an example for the interaction of Am(III) with oxygen functionalities. The structures of the ligands are given in Fig. 2.1.

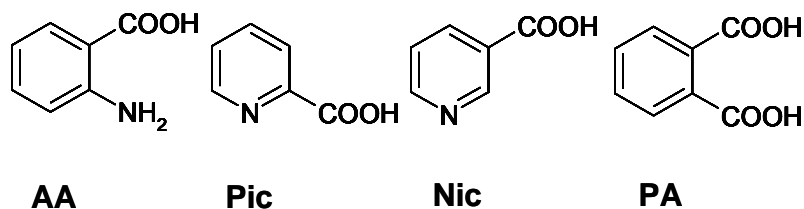


Fig. 2.1. Structures of the model ligands studied.

2.1.1 Experimental

Sample preparation

All experiments were carried out at room temperature ($23 \pm 2^\circ\text{C}$). Solutions were prepared using Milli-Q water (mod. Milli-RO/Milli-Q-System, Millipore, Schwalbach, Germany). The ionic strength was adjusted to 0.1 M by adding 3 M NaClO_4 (p.a., Merck). The measurements were performed at $\text{pH } 3.8 \pm 0.1$ or 6.0 ± 0.1 . The pH adjustments were done with diluted NaOH (high grade, Merck) and HClO_4 (p.a., Merck) solutions. Stock solutions (1×10^{-2} M, pH 3.8 or 6.0) of AA (p.a., Merck), Nic (p.a., Sigma-Aldrich), Pic (99%, Acros Organics) and PA (99%, Sigma-Aldrich) were prepared freshly for each experiment. An Am(III) stock solution was prepared by dissolving AmO_2 in 30% nitric acid with further dilution to a final concentration of 2.2×10^{-4} M. All samples containing Am(III) were prepared in a glove box under nitrogen atmosphere. For spectrophotometric TRLFS titrations, 2.7 mL of a 5×10^{-6} M Am^{3+} solution (pH 3.8 or 6.0, 0.1 M NaClO_4) were titrated with aliquots (38 μL) of the ligand stock solution. Thus, the ligand concentration was varied between 0 and 1×10^{-3} M in 8

titration steps. Static fluorescence measurements were performed at every titration step. The absorption measurements were carried out at a constant metal-to-ligand ratio of 1:200 (Am^{3+} : 5×10^{-6} M, ligand: 1×10^{-3} M) at both pH values. The pH was checked after each titration experiment.

Methods

Absorption spectra were recorded in the wavelength range from 400 to 700 nm using a CARY-5G UV-Vis-NIR spectrometer (Varian). For determination of the Am(III) absorption, the spectra were background corrected and analyzed in the wavelength range from 490 to 530 nm.

The Am(III) luminescence was measured using a pulsed flash-lamp-pumped Nd:YAG-MOPO laser system (Spectra Physics). The excitation wavelength varied from 503 to 508 nm depending on the absorption maxima determined for Am(III) and its complexes with the respective ligands. The luminescence emission was focused into a spectrograph (model 2300i, Acton Research) via fiber optics and recorded using a digital delay generator and an ICCD camera system (Roper Scientific). The gate width of the camera was set to be 500 ns. Am(III) single and time-resolved emission spectra were recorded between 631 and 768 nm, averaging three spectra with 100 laser pulses each. For time-resolved measurements, 60 spectra were recorded at delay times ranging from 30 to 150 ns with a step size of 2 ns.

2.1.2 Results and discussion

Spectroscopic characteristics of Am(III) in aqueous solution

At the pH values studied, Am(III) exhibits a very sensitive absorption band at 503.3 nm in aqueous solution (cf. Fig. 2.2), which is based on the electronic transition from the ${}^7\text{F}_0$ ground state to the first excited state ${}^5\text{L}_6$. This band is strongly influenced by any alteration of the first coordination sphere and therefore, its spectroscopic characteristics provide information on the chemical speciation of the metal ion. Complexation of Am(III) by organic ligands often results in a bathochromic shift of the absorption maximum, as it was described by several authors (Moulin et al., 1987; Morgenstern et al., 2000; Müller et al., 2010).

Excitation of Am(III) solutions at 503 nm yields one unique emission band at about 691 nm (cf. Fig. 2.3), which corresponds to the ${}^5\text{D}_1 \rightarrow {}^7\text{F}_1$ transition. The position of the emission maximum does not differ at the studied pH values, which indicates that only the Am^{3+} aquo ion is predominant up to pH 6. For determination of the luminescence lifetimes, the sum of

the luminescence intensities over the measured wavelength range was fitted by an exponential decay function:

$$I(t) = \sum I \cdot \exp(-t / \tau) \quad (2.1)$$

$I(t)$ is the total luminescence intensity at the time t , I the intensity of the luminescent species at $t = 0$ and τ the corresponding luminescence lifetime. The luminescence decay was mono-exponential and the lifetime for the Am^{3+} aquo ion was determined to be 23.9 ± 0.8 ns, which is in very good agreement with literature data (e.g., Beitz, 1994; Barkleit et al., 2011). The number of associated water molecules in the first coordination sphere of the Am^{3+} aquo ion can be calculated using the following linear relationship given by Kimura and Kato (1998):

$$n \text{ H}_2\text{O} \pm 0.5 = 2.56 \cdot 10^{-7} \cdot \frac{1}{\tau} - 1.43 \quad (2.2)$$

Applying this equation, $n \text{ H}_2\text{O}$ could be calculated to be 9.3 ± 0.5 , which fits other experimental results very well (e.g., 9.6 ± 0.5 published by Barkleit et al. (2011)). The hydration shell water molecules are known to quench fluorescence lifetimes due to the coupling of the fluorophore excited states to the vibrations of the coordinated O-H oscillators (Runde et al., 2000). Hence, with the displacement of inner sphere water molecules against ligand molecules due to complexation, the lifetime of Am(III) should increase, as it was shown by various authors (e.g., Beitz et al., 1994; Kimura and Kato, 1998; Runde et al., 2000; Barkleit et al., 2011).

Interaction of Am(III) with nitrogen containing ligands

The investigated nitrogen containing ligands AA, Pic and Nic generally show similar behavior in aqueous solution. All have comparable dissociation constants (e.g., AA: $\text{p}K_{\text{a}1} = 2.01$ and $\text{p}K_{\text{a}2} = 4.78$ at $I = 0.1$ M and room temperature (Martell et al., 1998)) and occur in three different species in aqueous solution: The fully protonated acid predominates the speciation under very acidic conditions. The zwitterionic species is formed due to dissociation of the carboxylic acid and dominates the speciation at pH 2 - 5. Further increasing pH results in completely deprotonation of the ligand. To investigate the interaction of Am(III) with the zwitterionic and the negatively charged ligand species, the measurements were carried out at pH 3.8 and 6.0.

Fig. 2.2 depicts a summary of the measured absorption spectra of various Am(III) ligand solutions in comparison with an aqueous Am(III) standard solution (5×10^{-6} M) at both studied pH values. Neither with addition of AA nor with addition of Nic to the Am(III) solution a shift of the Am^{3+} (aq.) absorption band was observed at pH 3.8. It seems that Am(III) does not

form a complex with these ligands under the given experimental conditions. At pH 6.0, with addition of AA and Nic the absorption maximum is shifted to higher wavelengths from 503.3 nm to 504.1 nm and 505.4 nm, respectively, indicating a complex formation between Am(III) and the completely dissociated ligands. In contrast to that, with addition of 1×10^{-3} M Pic a bathochromic shift of the absorption maximum to 504.0 nm and a slight decrease of the absorbance is already observable at pH 3.8, indicating a complex formation of Am(III) with the zwitterionic species. This shift is even more pronounced at pH 6.0. A new absorption maximum evolves at 508.1 nm, suggesting the formation of a third Am(III) species with the fully deprotonated Pic.

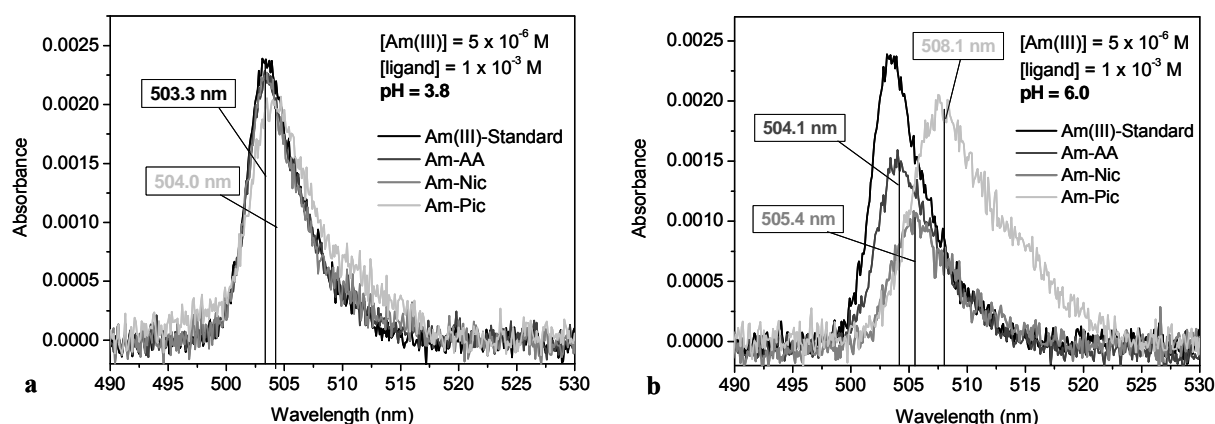


Fig. 2.2. Absorption spectra of Am(III) solutions with nitrogen containing ligands in comparison with an aqueous Am(III) standard solution (5×10^{-6} M) at pH 3.8 (a) and pH 6.0 (b).

The wavelengths of the absorption maxima determined for the Am(III) ligand solutions were used as excitation wavelengths for the TRLFS measurements. Studying the interaction of Am(III) with AA and Nic at pH 3.8, no significant changes of the luminescence intensities as well as of the determined lifetimes were observed with increasing ligand concentration (not shown). Thus, as implied by the UV-Vis measurements, there is no evidence for a complex formation between Am(III) and the zwitterionic species of AA and Nic.

Figure 2.3 depicts the development of the Am(III) emission spectra as a function of Pic concentration. Contrary to the measurements with AA and Nic, in the presence of Pic the spectrum of Am(III) shows an increase in the luminescence intensity with increasing ligand concentration even at pH 3.8, where the ligand should still occur predominantly in its zwitterionic form. The analysis of the time-resolved luminescence spectra results in prolonging lifetimes from 23.9 ± 0.8 ns for the free Am^{3+} aquo ion to an approximately constant value of 27.2 ± 0.1 ns with increasing ligand concentration. Both observations point to a complexation of Am(III) with Pic. According to Eq. (2.2), the lifetime of the determined complex species corresponds to 8.0 ± 0.5 water molecules in the first coordination sphere of

Am(III), implying the replacement of one water molecule by the ligand. This can be interpreted as formation of a 1:1 complex where one Pic molecule displaces one water molecule.

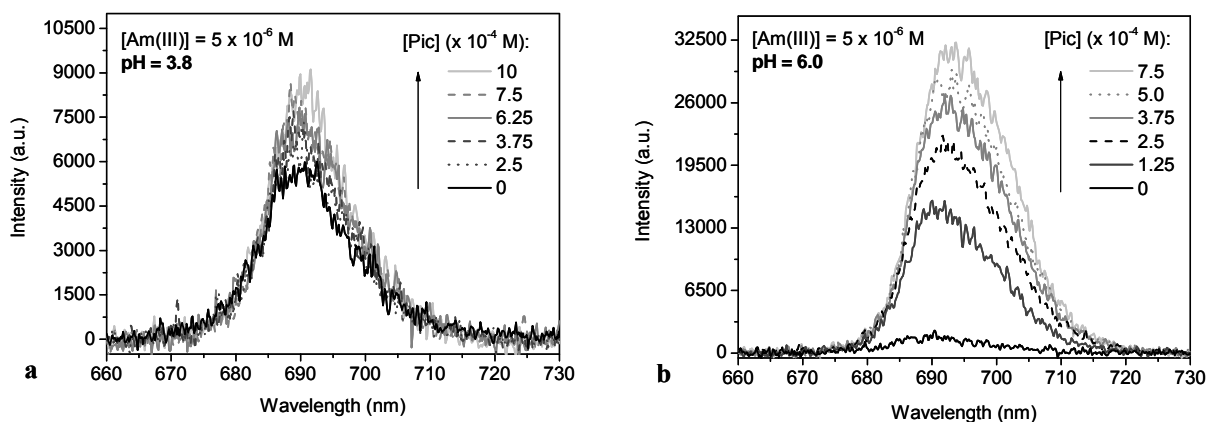
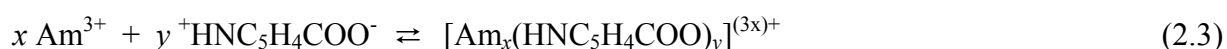


Fig. 2.3. Luminescence emission spectra of 5×10^{-6} M Am(III) at pH 3.8 (a) and pH 6.0 (b) as a function of Pic concentration.

The complex stability constants were calculated via SPECFIT (Binstead et al., 2005), using the following equation for the direct reaction of Am(III) with the zwitterionic Pic species:



The complex formation constant was calculated with $\log \beta_{11} = 3.81 \pm 0.44$ (cf. Table 2.1).

As shown in Fig. 2.3b, the luminescence intensity of Am(III) further increases at pH 6.0. With increasing Pic concentration also a slight shift of the emission maximum from about 691 nm to 694 nm could be observed. In all samples, mono-exponential luminescence decay was determined. The luminescence lifetime increases due to complex formation to 42.0 ± 1.8 ns.

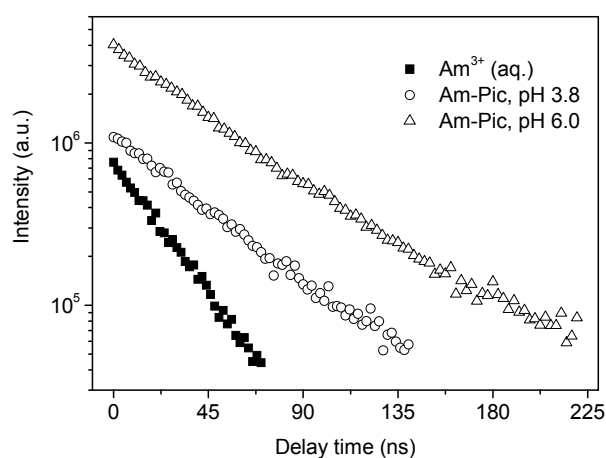


Fig. 2.4. Luminescence decay of Am^{3+} (aq.) in comparison with those measured in the Am(III) picolinate system at pH 3.8 and 6.0.

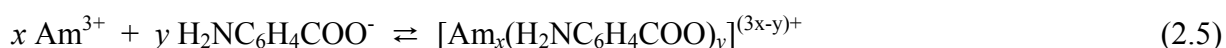
The change of the luminescence decay in dependence on pH is depicted in Fig. 2.4. The lifetime of the determined complex species corresponds to 4.7 ± 0.5 water molecules in the inner coordination sphere of the metal ion, implying the replacement of about 4 water molecules by the ligand, which can be interpreted as formation of 1:1 and 1:2 complexes. The complexation reactions can be expressed as follows:



The averaged formation constants for this reaction were calculated to be $\log \beta_{11} = 3.83 \pm 0.22$ and $\log \beta_{12} = 7.34 \pm 0.04$ (cf. Table 2.1).

As implied by the UV-Vis measurements, a complexation of Am(III) with AA and Nic could also be determined at pH 6.0. Both systems are characterized by an increase in luminescence intensities and lifetimes. Interestingly, in the Am(III) nicotinate system an additional increase of pH up to 7.6 as well as a decrease of the Am(III) concentration in solution during the spectroscopic titration could be determined. The UV-Vis as well as the emission spectra show an increase in the background, indicating the formation of insoluble complex species or colloids. Therefore, the calculation of the complex stability constant was not possible.

For the Am(III) anthranilate complex a luminescence lifetime of 28.6 ± 0.5 ns was determined, corresponding to 7.8 ± 0.5 water molecules in the first coordination sphere. According to that, one water molecule is replaced through ligand exchange, indicating the formation of a 1:1 complex of Am(III) with the fully deprotonated AA:



The complex formation constant was calculated to be $\log \beta_{11} = 3.70 \pm 0.11$ (cf. Table 2.1). Since stability constants for this reaction or for the complexation of Am(III) with other nitrogen containing ligands were not reported in the literature so far, a comparison with other data is not possible.

Interaction of Am(III) with phthalic acid

The aromatic ligand PA offers two carboxylic groups, which are considered to be one of the most dominant functionalities in HA. The dissociation constants of PA reported for an ionic strength of 0.1 M and room temperature are $\text{p}K_{a1} = 2.66$ and $\text{p}K_{a2} = 4.72$ (Martell et al., 2003). Figure 2.5a depicts the absorption spectra of Am(III) phthalate complexes at both investigated pH values. Upon addition of PA the absorption maximum of Am(III) shows a decrease in the absorbance as well as a small bathochromic shift from 503.3 to 503.7 nm and 504.2 nm at pH 3.8 and 6.0, respectively, both indications for complex formation. The small differences in the

spectroscopic characteristics are hints for the formation of only one phthalate complex with Am(III) at both pH values. This assumption is also supported by the TRLFS measurements. At both pH values the analysis of the spectra results in a similar increase of the luminescence intensities with increasing ligand concentration.

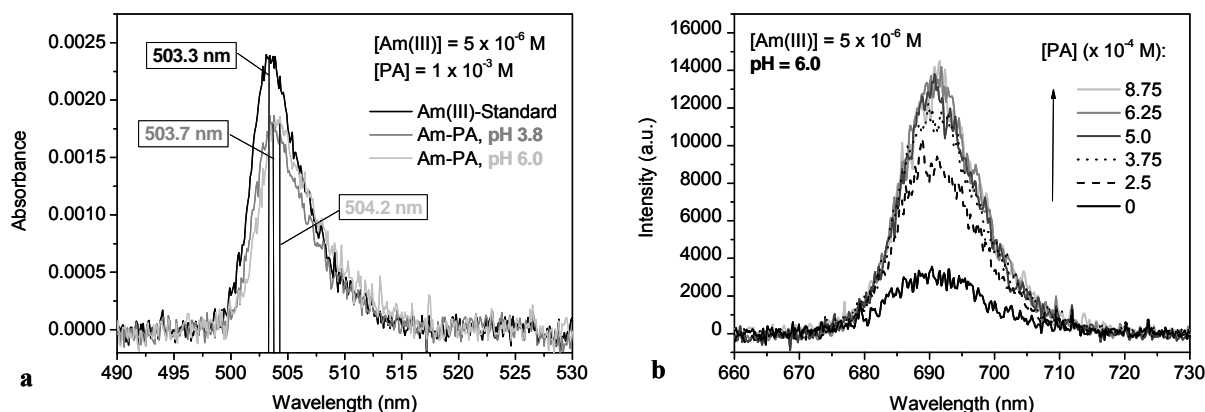


Fig. 2.5. Absorption spectra of Am(III) phthalate solutions (a) and luminescence emission spectra of 5×10^{-6} M Am(III) as a function of PA concentration at pH 6.0 (b).

Figure 2.5b shows the representative emission spectra of Am(III) as a function of the PA concentration at pH 6.0. The position of the peak maxima as well as the luminescence lifetimes determined at pH 3.8 are comparable to those obtained at pH 6.0, indicating the formation of an Am(III) complex with the fully deprotonated ligand. For all measured samples, a mono-exponential luminescence decay was observed. The lifetime of the complex was calculated to be 27.6 ± 1.1 ns, corresponding to 7.8 ± 0.5 water molecules in the inner coordination sphere of the metal ion. According to that, one water molecule is replaced through ligand exchange, indicating the formation of a 1:1 complex of Am(III) with PA. The spectroscopic properties of the Am(III) phthalate complex are listed in Table 2.1.

In analogy to the experiments with the nitrogen containing ligands the complex stability constants were calculated using SPECFIT. The complexation reaction can be expressed as follows:



The averaged formation constant for this reaction was calculated to be $\log \beta_{11} = 3.99 \pm 0.16$. Since the complexation of Am(III) with PA was also studied for the first time, no data are available for comparison. Nevertheless, this value is in agreement with that determined for Eu(III), the analog lanthanide ion ($\log \beta_1 = 3.7 \pm 0.3$ (Jain et al., 2009)). However, in case of Eu(III) also the formation of a 1:2 complex with PA was reported, which was not observed

under the studied experimental conditions in the present work. In comparison with the data of Panak et al. (1995), our complexation constant is slightly higher than the constant determined for the Cm(III) complexation with PA. The authors reported the formation of a 1:1 complex with a stability constant of $\log \beta_{11} = 3.62 \pm 0.02$.

Table 2.1. Summary of the spectroscopic data and determined stability constants $\log \beta$ for the various Am(III) species identified in this study.

Species	pH	M_xL_y	Absorption (nm)	Lifetime (ns)	$n H_2O$	$\log \beta_{0.1 M}$
Am ³⁺	3.8 / 6.0	10	503.3	23.9 ± 0.8	9.3	-
AmAA ²⁺	6.0	11	504.1	28.55 ± 0.5	7.5	3.70 ± 0.11
AmPicH ³⁺	3.8	11	504.0	27.2 ± 0.1	8.0	3.81 ± 0.44
AmPic ²⁺	6.0	11	508.1	42.0 ± 1.8	4.7	3.83 ± 0.22
Am(Pic) ₂ ⁺		12				7.34 ± 0.04
AmNic ²⁺	6.0 – 7.6	11	505.4	27.8 ± 1.2	7.8	-
AmPA ⁺	3.8 / 6.0	11	503.7 / 504.2	27.6 ± 1.1	7.8	3.99 ± 0.16

Conclusion

For the first time, the complexation of Am(III) with the nitrogen containing ligands AA, Nic and Pic as well as with PA was studied in aqueous solution at pH 3.8 and 6.0. All complexes determined for nitrogen containing ligands show comparable complex stabilities (cf. Table 2.1). Only Pic was found to interact with Am(III) at pH 3.8, although it should occur predominantly in its zwitterionic form. It seems very likely that a complexation with zwitterionic ligands is hindered, due to electrostatic repulsion between the protonated nitrogen functionalities and Am³⁺. Based on the present results, it could not be clarified whether the nitrogen is involved in the complexation or not. For example, a chelation of Eu(III) with Pic at pH 6.0 was reported by Park et al. (1999). Barkleit et al. (2011) mentioned that a chelation would cause bi-exponential decay due to the hindrance of the fast ligand-water exchange between the first coordination sphere and the solution. According to that, the mono-exponential decay of all studied complexes supports the assumption that Am(III) is only coordinated via the carboxylic groups. In comparison with the Am(III) complexation by other aromatic ligands containing carboxylic groups, the complex stabilities of the nitrogen containing ligands are somewhat higher than that determined for the Am(III) salicylate ($\log \beta_{11} = 2.56 \pm 0.08$ (Müller et al., 2011)) which has only one carboxylic group. The stability constant determined for Am(III) complexation by pyromellitic acid ($\log \beta_{110} = 5.42 \pm 0.16$ (Barkleit et al., 2011)), which offers three carboxylic groups, is somewhat higher than

those determined for Am(III) complexation by nitrogen containing ligands. Although each of the investigated nitrogen containing ligands offers only one carboxylic group, the stabilities of their determined complexes are comparable to that of the Am(III) phthalate complex, which offers two carboxylic groups. This indicates a stabilization of the Am(III) complexes with nitrogen containing ligands.

Transferring these results to the HA system, the Am(III) complexation by HA should be more influenced by nitrogen containing functional groups than U(VI), due to the softer character of Am(III) according to Pearson's theory (Pearson, 1963). However, the obtained results allow the conclusion that these functionalities play only a subordinate role compared to oxygen functionalities in HA.

2.2 U(IV) complexation by citric acid, succinic acid, mandelic acid and glycolic acid – Determination of complex formation constants by UV-Vis spectroscopy

Both the speciation and the mobility of actinides in aquatic systems strongly depend on their oxidation state due to the different precipitation, complexation, sorption and colloid formation behavior of the various oxidation states (e.g., Choppin, 2006). Under reducing conditions as prevalent in deep underground nuclear waste repositories as well as in the depth of flooded uranium mines, actinide species occur in lower oxidation states. For instance, in contrast to U(VI) which is mobile, U(IV) is much less mobile due to the low solubility of U(IV) hydrous oxide ($\text{UO}_2 \cdot x\text{H}_2\text{O}(\text{am})$) (Neck and Kim, 2001; Opel et al., 2007). However, in the presence of inorganic or organic ligands U(IV) may become mobile due to formation of soluble complexes. Thus, the speciation of U(IV) in aqueous solution has to be studied to predict its migration behavior in natural environments. In this work, citric acid, succinic acid as well as mandelic acid and glycolic acid were chosen as model ligands to study the U(IV) complexation. These ligands stand for a variety of organic ligands in aqueous systems. This study is described in more detail in (Schmeide and Bernhard, 2008).

2.2.1 Experimental

Sample preparation

Sample solutions were prepared in an inert gas glove box (N_2 atmosphere) using CO_2 -free solutions. The U(IV) concentration was kept constant at 1×10^{-3} M or 5×10^{-4} M, the ligand concentration was varied between 0 and 0.2 M. The concentration of hydrogen ions (1.0, 0.5,

0.1 M) was adjusted by adding aliquots of 5 M HClO₄ simultaneously taking into consideration the [H⁺] stemming from the U(IV) stock solution. The ionic strength was 1.0 M (H,Na)ClO₄. The amount of U(VI) in the samples was ≤ 1.5% of the total U as determined by fluorescence spectroscopy.

Spectroscopic measurements

The UV-Vis absorption spectra were recorded with a high-resolution dual beam UV-Vis-NIR spectrophotometer (CARY-5G, Varian). The measurements were performed using a 1-cm quartz glass cuvette (Hellma) in the spectral range from 800 to 300 nm with a speed of 60 nm/min at room temperature (22 ± 1°C). The cuvette was always filled and sealed in the inert gas box. Each spectrum was analyzed in two regions of wavelength: 446 to 524 nm and 570 to 727 nm.

Calculations

Stability constants were determined using the factor analysis program SPECFIT (Binstead et al., 2005). For this, the acidity constants of citric acid (pK_{a1} = 5.31, pK_{a2} = 4.17, pK_{a3} = 2.84 at I = 0.5 M NaClO₄) (Hummel et al., 2005), succinic acid (pK_{a1} = 5.12, pK_{a2} = 3.93 at I = 0.5 M), mandelic acid (pK_a = 3.18 at I = 1.0 M) and glycolic acid (pK_a = 3.61 at I = 1.0 M) (Martell et al., 1998) as well as the formation constants of U(IV) hydrolysis species (Guillaumont et al., 2003) were applied. Ionic strength corrections were conducted applying the Specific Ion Interaction Theory (SIT) (Guillaumont et al., 2003).

2.2.2 Results and discussion

U(IV) complexation with citric acid

The complexation of U(IV) with citric acid has been investigated in dependence on hydrogen ion concentration (0.1, 0.5, 1.0 M). From the pK_a values reported for citric acid (cf. paragraph Calculations) follows, that the citric acid is completely protonated in the pH range applied in this work. That means, citric acid does not contribute to the ionic strength under these pH conditions. Thus, the ionic strength of the sample solutions is mainly determined by [H⁺].

Exemplary, Fig. 2.6 shows the evolution of the U(IV) spectrum in the two wavelength ranges analyzed for increasing citric acid concentrations (0 to 0.2 M) at an acidity of [H⁺] = 0.5 M. In the wavelength range 570 to 727 nm, the solvated U⁴⁺ shows absorption maxima at 649.1 nm and 671.7 nm in the absence of citric acid. With increasing citric acid concentration the intensity of the peak at 649 nm decreases and simultaneously, the peak is shifted to longer

wavelengths. At U(IV):citric acid ratios higher than 1:20 the intensity of this peak increases again. In the wavelength range 446 to 524 nm, the intensity of the peak at 495 nm decreases with increasing citric acid concentration. The intensity of the shoulder at 486 nm increases when the U(IV):citric acid ratio is higher than 1:20. These changes of the U(IV) spectrum can be attributed to the complexation of U(IV) by citric acid.

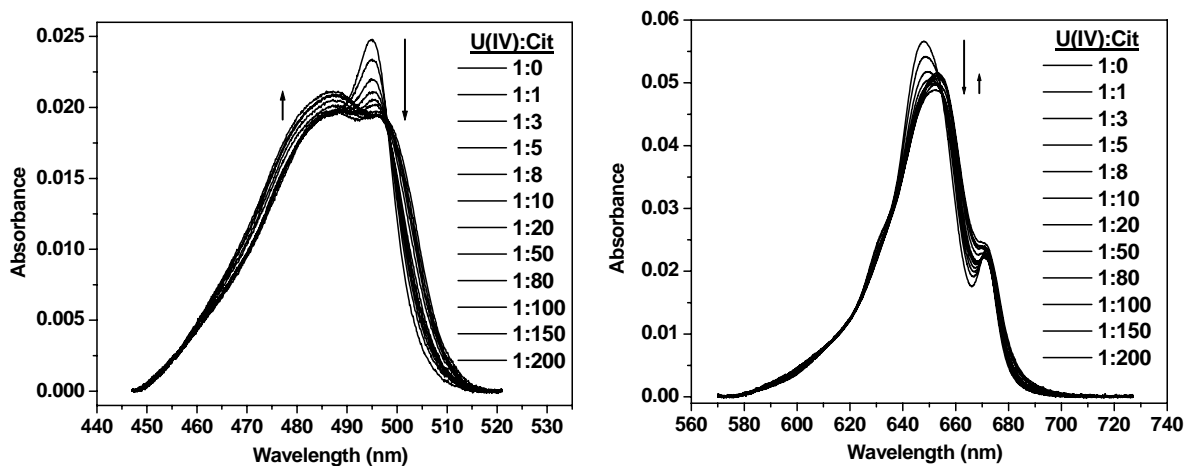


Fig. 2.6. Two wavelength ranges of the UV-Vis spectra for 1×10^{-3} M U(IV) as a function of the citric acid (Cit) concentration at $[H^+] = 0.5$ M and $I = 0.5$ M.

The experimental data were analyzed considering the most basic form of the citrate anion Cit^{3-} . The U(IV) citrate complexation reaction can be expressed as:



For the calculation of the stability constants, 8 datasets were analyzed (4 series of experiments ($[H^+] = 1$ M, 0.5 M, 0.1 M (2x)) with 2 wavelength ranges each). Thereby, the formation of 1:1 and 1:2 complexes was detected in the citrate media. Within the experimental uncertainty, no significant effect of the acidity and ionic strength of the sample solutions on the stability constants has been observed. The mean values of the stability constants were determined with $\log \beta_{101} = 13.5 \pm 0.2$ und $\log \beta_{102} = 25.1 \pm 0.2$. Due to the strong complexation of U(IV) by citric acid, the U(IV) hydrolysis is prevented. The stability of An(IV) citrate complexes against hydrolysis is already described in the literature (e.g., Durbin et al., 1998; Suzuki et al., 2006). Furthermore, U(IV) is stabilized against oxidation due to complexation. The stability of U(IV) against oxidation can further be explained by the reducing properties of citric acid (Bonin et al., 2007; Sevostyanova, 1982).

The $\log \beta$ values determined for 1:1 and 1:2 complexes in this work are higher than the values reported by Nebel and Urban (1966) with 11.5 and 19.5 and also slightly higher than the values reported by Bonin et al. (2008) with 12.8 and 24.1.

From Table 2.2 follows that the $\log \beta$ values obtained for U(IV) complexation by citric acid fit well in the series of $\log \beta$ values determined for the complexation of further tetravalent actinides (Th(IV), Np(IV), Pu(IV)) by citric acid.

Table 2.2. Stability constants for the system An(IV) citrate.

	Th(IV)	U(IV)	Np(IV)	Pu(IV)
$\log \beta_{101}$	11.6 ($I = 0.1$ M) ^a	11.5 ($I = 0.5$ M) ^b	13.6 ($I = 0.6$ M) ^d	15.3 ($I = 0.5$ M) ^e
	13.0 ($I = 0.5$ M) ^b	12.8 ($I = 0.8$ M) ^c		17.6 ($I = 0.15$ M) ^f
	12.5 ($I = 0.3$ M) ^c	13.5 \pm 0.2 ^g		13.8 ($I = 1.0$ M) ^c
$\log \beta_{102}$	21.1 ($I = 0.1$ M) ^a	19.5 ($I = 0.5$ M) ^b	25.3 ($I = 0.4$ M) ^d	30.2 ($I = 0.5$ M) ^e
	21.0 ($I = 0.5$ M) ^b	24.1 ($I = 0.8$ M) ^c		25.0 ($I = 0.15$ M) ^f
	22.9 ($I = 0.3$ M) ^c	25.1 \pm 0.2 ^g		26.6 ($I = 1.0$ M) ^c

^a (Raymond et al., 1987), ^b (Nebel and Urban, 1966), ^c (Bonin et al., 2008), ^d (Bonin et al., 2007), ^e (Nebel, 1966), ^f (Yule, 1991), ^g (this work: $I = 0.11$ to 1.0 M).

In the literature, most of the studies assume that An(IV) is complexed by the most basic form of the citrate anion (Cit^{3-}) (Nebel, 1966; Nebel and Urban, 1966; Raymond et al., 1987; Bonin et al., 2007; Bonin et al., 2008). However, recent structural studies on uranyl complexes with citric and citramalic acid (Felmy et al., 2006; Thuéry, 2007; Thuéry, 2008) suggest that citrate is bound to the cation both by its carboxylate site to the central carbon atom and by its hydroxyl group in alpha position (chelate formation), i.e. with the acid-base form H_2Cit^- . This option also has to be taken into account.

U(IV) complexation with succinic acid, mandelic acid and glycolic acid

The complexation of U(IV) with succinic and mandelic acid has been investigated at an acidity of $[\text{H}^+] = 0.1$ and 0.5 M and an ionic strength of 0.5 and 1.0 M, respectively. From the pK_a values reported for these ligands (cf. paragraph Calculations) follows, that the ligands are completely protonated under the experimental conditions applied in this work.

Figures 2.7 to 2.9 show the evolution of the U(IV) spectrum in the two wavelength ranges analyzed for increasing ligand concentrations (0 to 0.2 M). The U(IV) complexation reaction can be expressed as:



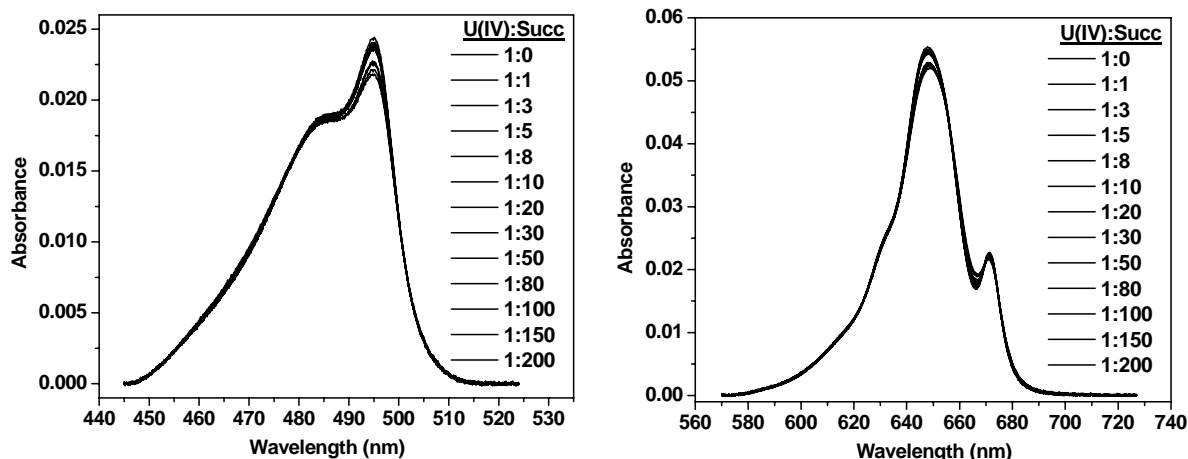


Fig. 2.7. Two wavelength ranges of the UV-Vis spectra for 1×10^{-3} M U(IV) as a function of the succinic acid (Succ) concentration at $[H^+] = 0.5$ M and $I = 0.5$ M.

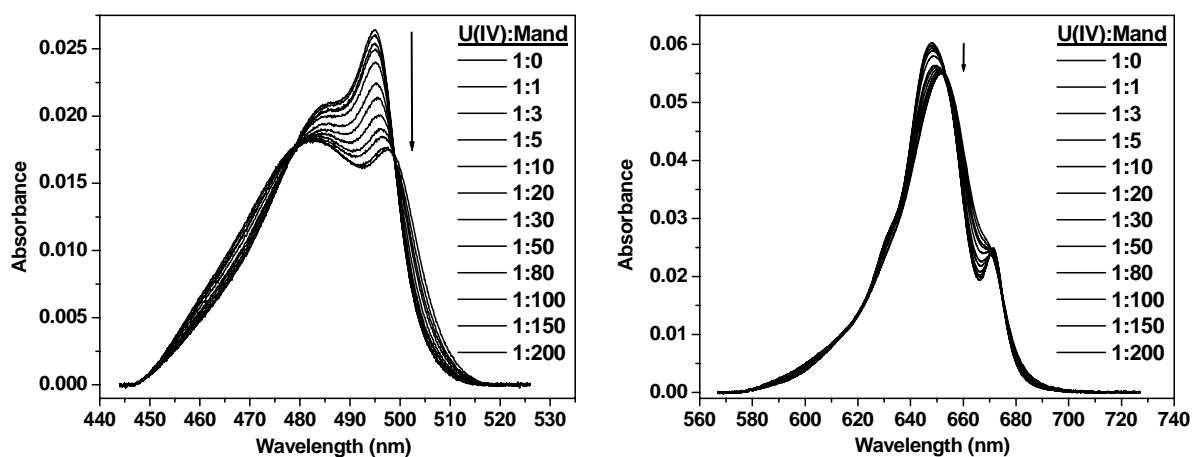


Fig. 2.8. Two wavelength ranges of the UV-Vis spectra for 1×10^{-3} M U(IV) as a function of the mandelic acid (Mand) concentration at $[H^+] = 0.5$ M and $I = 1.0$ M.

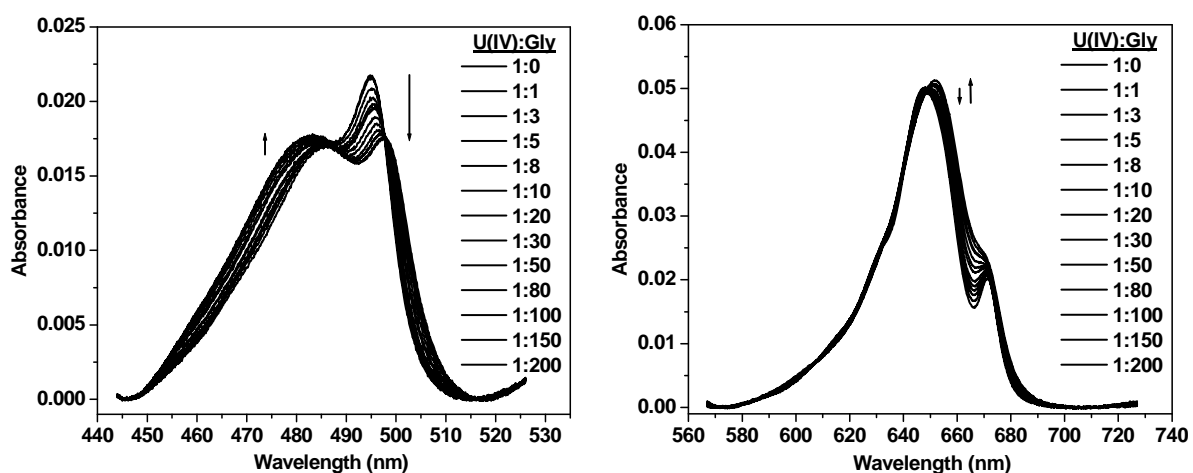


Fig. 2.9. Two wavelength ranges of the UV-Vis spectra for 1×10^{-3} M U(IV) as a function of the glycolic acid (Gly) concentration at $[H^+] = 0.1$ M and $I = 1.0$ M.

Especially, the spectra obtained for the U(IV) succinate system (cf. Fig. 2.7) show that the changes of the peak intensity and position are much weaker pronounced than in case of the U(IV) citrate system. For the U(IV) complexation by succinic acid, the formation of 1:1 complexes of the type $M_xH_yL_z$ was detected with $\log \beta_{101} = 9.0 \pm 0.2$ ($I = 0.5$ M). This value is lower than the stability constant determined with $\log K = 9.78$ ($I = 0.5$ M) by means of solubility experiments by (Merkusheva et al., 1970).

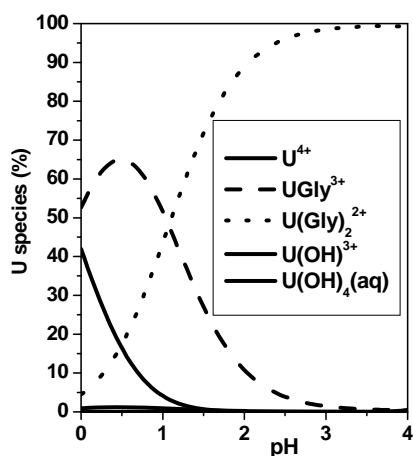


Fig. 2.10. U(IV) speciation in the presence of glycolic acid ($[U(IV)] = 5 \times 10^{-4}$ M, $[Gly] = 0.1$ M, $I = 1.0$ M).

In contrast to succinic acid, the formation of 1:1 and 1:2 complexes in solution was detected in the mandelate and glycolate media. The stability constants for 1:1 and 1:2 U(IV) ligand complexes of the type $M_xH_yL_z$ were determined with $\log \beta_{101} = 4.53 \pm 0.09$ and $\log \beta_{102} = 8.02 \pm 0.13$ for mandelate and with $\log \beta_{101} = 4.71 \pm 0.08$ and $\log \beta_{102} = 8.25 \pm 0.15$ for glycolate. The U(IV) speciation, calculated for the glycolic acid system (Fig. 2.10), exemplifies that the U(IV) hydrolysis is impeded due to the strong complexation of U(IV) by the ligand.

Conclusion

The stability constants for 1:1 and 1:2 U(IV) citrate complexes were determined with $\log \beta_{101} = 13.5 \pm 0.2$ and $\log \beta_{102} = 25.1 \pm 0.2$. This shows a strong interaction between U(IV) and citric acid. That means, the uranium speciation in citrate containing waters is strongly influenced by the U(IV) citrate complex. The comparison of the stability constants determined for the U(IV) complexation with various ligands shows that the interaction of U(IV) with succinate, mandelate and glycolate is much weaker than the interaction of U(IV) with citrate. Due to complexation with organic ligands the solubility and the mobility of U(IV) in aquatic systems is increased.

2.3 U(VI) complexation by citric acid and oxalic acid – Determination of luminescence properties at -120°C by cryo-TRLFS

Citric acid and oxalic acid are known to form strong complexes with U(VI) in aqueous solution in the acidic to alkaline pH range. The objective of the present study was to determine the up to now unknown luminescence emission properties of the U(VI) citrate and U(VI) oxalate species formed in the pH range from 2 to 4 and to apply these luminescence properties for the determination of complex formation constants. For this, time-resolved laser-induced fluorescence spectroscopy (TRLFS) at room temperature and TRLFS coupled with a cryogenic temperature technique (-120°C, cryo-TRLFS) were applied. The results of this study are published in-depth by Günther et al. (2011).

2.3.1 Experimental

The preparation of the sample solutions for the TRLFS measurements at 25°C ([U(VI)] = 5×10^{-5} M, [ligand] = 0 to 5×10^{-4} M, $I = 0.1$ or 0.5 M, pH 2 to 4) and at -120°C ([U(VI)] = 5×10^{-5} M, [ligand] = 0 to 5×10^{-3} M, $I = 0.1$, pH 3.5) as well as the TRLFS measurements are described in detail in (Günther et al., 2011).

2.3.2 Results and discussion

TRLFS measurements at room temperature (25°C)

Figure 2.11a shows the luminescence emission spectra of U(VI) as a function of the total citric acid concentration at pH 3.5 as an example. It was found that the luminescence intensity decreases with increasing ligand concentration. The U(VI) luminescence signals of the complex solutions do not shift in comparison to the luminescence emission bands of the reference solution without citric acid. Each time-resolved spectrum shows a mono-exponential luminescence decay (not shown). That means, that the formed U(VI) citrate species do not show luminescence at room temperature and only the luminescence properties of the uncomplexed U(VI) cation are visible in the spectra. The averaged luminescence lifetimes of the U(VI) cation are $\tau = 1561 \pm 163$ ns ($I = 0.1$ M) and $\tau = 1712 \pm 190$ ns ($I = 0.5$ M). Dynamic quenching due to citric acid or due to complex species at a $[U]_0:[cit]_0$ ratio higher than 1:1 can not be excluded.

Similar results were obtained for TRLFS measurements of U(VI) oxalate at pH 2 to 4. Exemplary, the luminescence spectra of this system obtained at pH 3 are shown in Fig. 2.11b.

With increasing ligand concentration the luminescence intensity decreases without shift of the emission bands. Generally, the exponential luminescence decay is of first order. We observed only a decrease of the luminescence of the uncomplexed U(VI) ion. The averaged lifetimes of the UO_2^{2+} cation up to $[\text{U}]_0:[\text{ox}]_0$ ratios of 1:3 ($I = 0.1 \text{ M}$) and 1:2 ($I = 0.5 \text{ M}$) are determined with $\tau = 1343 \pm 66 \text{ ns}$ ($I = 0.1 \text{ M}$) and $\tau = 1299 \pm 46 \text{ ns}$ ($I = 0.5 \text{ M}$), respectively. The lifetimes seem to be quite short for UO_2^{2+} , however, reference solutions without ligand measured under the same experimental conditions showed data in the same range. At $[\text{U}]_0:[\text{ox}]_0$ ratios in the solution higher than 1:3 ($I = 0.1 \text{ M}$) or higher than 1:2 ($I = 0.5 \text{ M}$) we did not observe an exponential luminescence decay with a continuous decrease of the luminescence intensity during measuring time of $20 \mu\text{s}$. A small increase of the luminescence intensity was detected in the first 400 ns of the time-resolved measurements. Then, the luminescence intensity decreased mono-exponentially. Here, it seems that the system is not photo stable. A decomplexation of U(VI) oxalates might be possible.

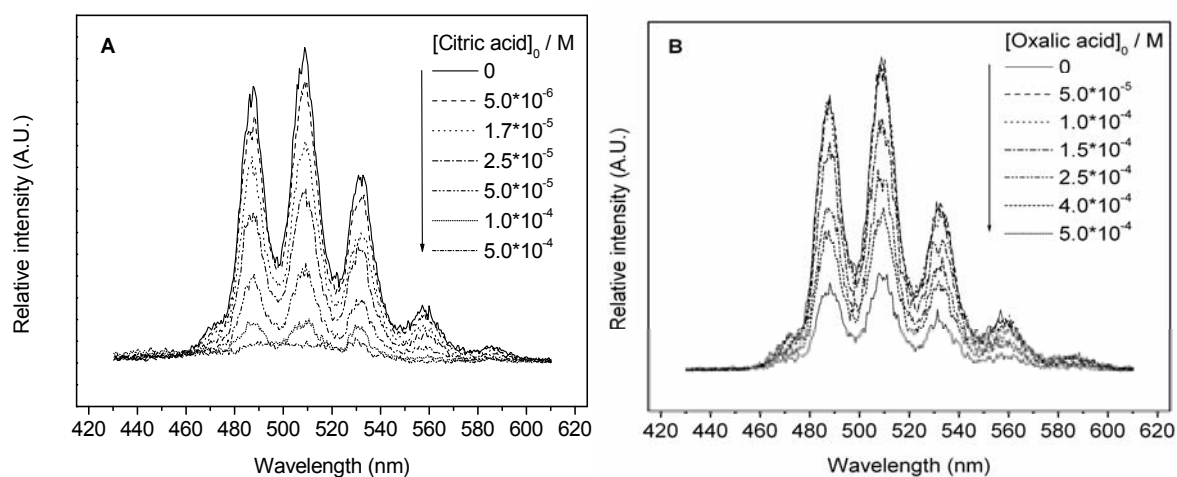


Fig 2.11. Luminescence emission spectra of U(VI) as a function of the ligand concentration measured at room temperature (25°C), $[\text{U(VI)}]_0 = 5 \times 10^{-5} \text{ M}$, $I = 0.1 \text{ M}$: (a) – citric acid at pH 3.5, (b) – oxalic acid at pH 3.

TRLFS measurements at cryogenic temperature (-120°C)

The aim of the TRLFS measurements of the U(VI) ligand complex solutions at cryogenic temperature conditions was to study whether U(VI) complex species can be detected directly at low temperature. Measurements at -120°C are expected to improve significantly the intensity and resolution of luminescence spectra in consequence of lower quenching effects due to ligands and/or water.

The measurements at cryogenic temperature of a series of complex solutions containing constant U(VI) concentration and increasing ligand concentrations at constant pH showed at

first a small decrease and after that, a significant increase of the luminescence intensity (not shown here).

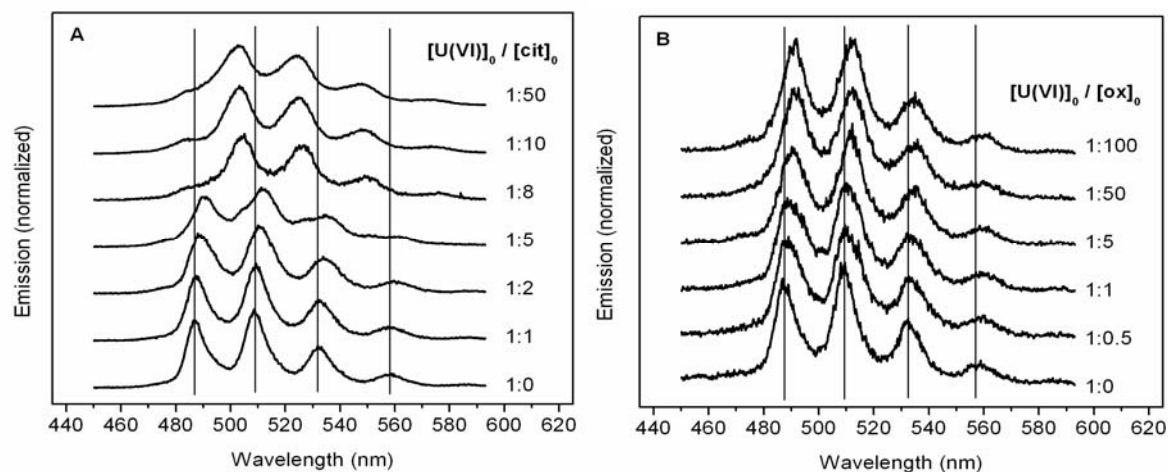


Fig. 2.12. Luminescence emission spectra of U(VI) as a function of the ligand concentration measured at cryogenic temperature (-120°C), $[\text{U(VI)}]_0 = 5 \times 10^{-5} \text{ M}$, $I = 0.1 \text{ M}$, pH 3.5: (a) – citric acid, (b) – oxalic acid.

In contrast to the TRLFS measurements at room temperature, it can be seen that the U(VI) luminescence signals shift significantly to higher wavelengths at a $[\text{U}]_0:[\text{cit}]_0$ ratio of 1:2 and higher. This is shown in Fig. 2.12a, where the normalized luminescence emission spectra of U(VI) as a function of the total citric acid concentration measured at -120°C are compiled. For the U(VI) oxalic acid system we found comparable results with the exception, that the shift of the luminescence signals with increasing ligand concentration is less pronounced compared to the shifts due to the complexation of U(VI) by citric acid under the given experimental conditions (Fig. 2.12b). These results clearly show, that at cryogenic temperature (-120°C) the determination of emission properties of U(VI) citrate and U(VI) oxalate species is possible.

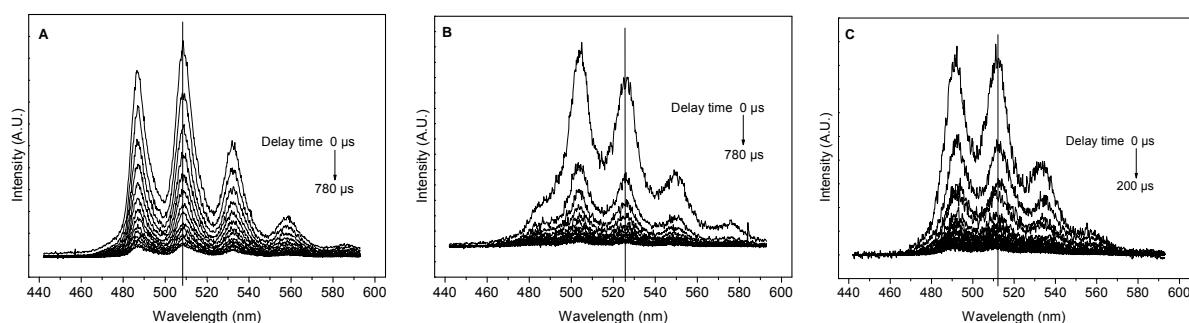


Fig. 2.13. Time-resolved luminescence emission spectra measured at cryogenic temperature (-120°C), $[\text{U(VI)}]_0 = 5 \times 10^{-5} \text{ M}$, $I = 0.1 \text{ M}$, pH 3.5: (a) – without ligand, (b) – with $4 \times 10^{-4} \text{ M}$ citric acid, (c) – with $5 \times 10^{-3} \text{ M}$ oxalic acid (not all spectra of the measurements are shown here).

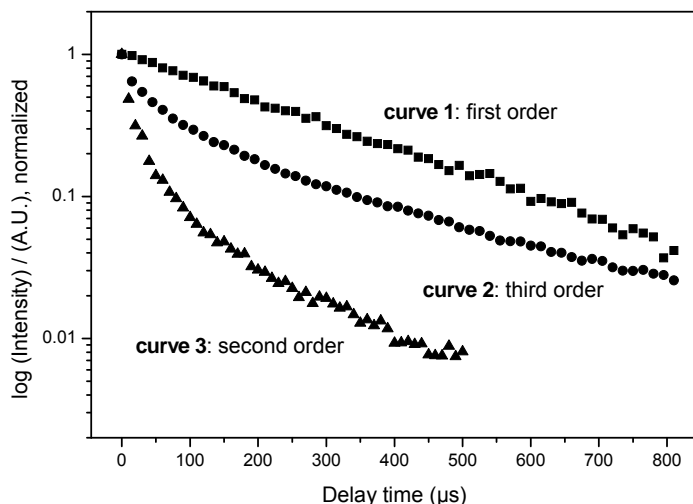


Fig. 2.14. Exponential luminescence decay of U(VI) measured at cryogenic temperature (-120°C), $[\text{U(VI)}]_0 = 5 \times 10^{-5} \text{ M}$, $I = 0.1 \text{ M}$, $\text{pH } 3.5$, curve 1 – without ligand, curve 2 – with $4 \times 10^{-4} \text{ M}$ citric acid and curve 3 – with $5 \times 10^{-3} \text{ M}$ oxalic acid.

Figures 2.13a-c show three examples for time-resolved measurements at -120°C : spectra of U(VI) solution in absence of ligands (Fig. 2.13a) in comparison to spectra of U(VI) solutions in the presence of citric acid (Fig. 2.13b) or oxalic acid (Fig. 2.13c). Their corresponding luminescence decay curves are shown in Fig. 2.14. Time-resolved spectra of the U(VI) citric acid system show a three-exponential luminescence decay at a $[\text{U}]_0:[\text{cit}]_0$ ratio of 1:2 and higher (example: curve 2 in Fig. 2.14). Thus, three U(VI) species are the main components in these complex solutions. The averaged luminescence lifetimes are $\tau_1 = 286 \pm 29 \mu\text{s}$ for the uncomplexed U(VI) cation, $\tau_2 = 79 \pm 15 \mu\text{s}$ and $\tau_3 = 10 \pm 3 \mu\text{s}$ for two different complex species. The luminescence lifetime of the uncomplexed U(VI) cation at cryogenic temperature is much higher than that at room temperature. The reason for this is the decrease of the dynamic quenching effect by water because the water molecules take stable grid places in the ice crystal after shock freezing of the samples. Comparable results were obtained by Wang et al., 2004. By analysis of the exponential luminescence decay obtained for U(VI) oxalic acid samples maximal three different lifetimes were obtained, too. For the uncomplexed U(VI) cation $\tau_1 = 261 \pm 13 \mu\text{s}$ was determined. The lifetimes $\tau_2 = 9 \pm 3 \mu\text{s}$ and $\tau_3 = 102 \pm 7 \mu\text{s}$ were assigned to the U(VI) oxalate species. Exemplary, curve 3 in Fig. 2.14 shows a bi-exponential decay of the U(VI) luminescence in oxalate solution at the high $[\text{U}]_0:[\text{ox}]_0$ ratio of 1:100. That means, at this concentration ratio only the two U(VI) oxalate species but no uncomplexed U(VI) occur.

Complex formation constants and luminescence properties of the single species

The complex formation constants for the different U(VI) citrate and U(VI) oxalate species, formed according to Eq. (2.9) or Eq. (2.10), determined with SPECFIT are summarized in Table 2.3.

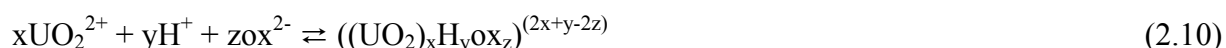
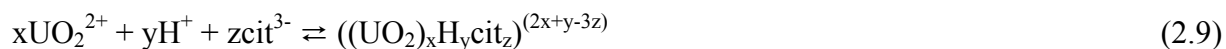


Table 2.3. Complex formation constants of U(VI) citrate and U(VI) oxalate species calculated with SPECFIT and selected literature data.

Species	xyz	log β_{xyz}	Ionic medium	Method / references
UO ₂ cit ⁻	101	7.67 ± 0.12	0.1 M NaClO ₄	TRLFS ^a / this work
		7.24 ± 0.16	0.1 M NaClO ₄	TRLFS ^b / this work
		7.51 ± 0.11	0.5 M NaClO ₄	TRLFS ^a / this work
		7.40 ± 0.21	0.1 M KNO ₃	Potentiometry ^c
(UO ₂) ₂ (cit) ₂ ²⁻	202	18.85 ± 0.42	0.1 M NaClO ₄	TRLFS ^a / this work
		18.90 ± 0.26	0.1 M NaClO ₄	TRLFS ^b / this work
		18.75 ± 0.34	0.5 M NaClO ₄	TRLFS ^a / this work
		18.87 ± 0.06	0.1 M KNO ₃	Potentiometry ^c
UO ₂ ox	101	5.92 ± 0.03	0.1 M NaClO ₄	TRLFS ^a / this work
		5.88 ± 0.29	0.1 M NaClO ₄	TRLFS ^b / this work
		5.63 ± 0.06	0.5 M NaClO ₄	TRLFS ^a / this work
		6.36 ± 0.07	0.1 M NaClO ₄ / 20°C	Spectrophotometry ^c
UO ₂ (ox) ₂ ²⁻	102	10.30 ± 0.38	0.1 M NaClO ₄	TRLFS ^a / this work
		10.26 ± 0.13	0.1 M NaClO ₄	TRLFS ^b / this work
		10.79 ± 0.37	0.5 M NaClO ₄	TRLFS ^a / this work
		10.59 ± 0.07	0.1 M NaClO ₄ / 20°C	Spectrophotometry ^c

^a Spectra measured at room temperature (25°C)

^b Spectra measured at cryogenic temperature (-120°C)

^c Rajan and Martell, 1965

The results show that the first U(VI) citrate species formed in the low pH range is of type ML. The second U(VI) citrate complex is binuclear of type M₂L₂. The carboxylic groups of citric acid in these complexes are completely deprotonated. These stoichiometric compositions of the U(VI) citrate species were obtained by analysis of all TRLF spectra measured at room temperature (analyzing the decrease of the luminescence intensity of the uncomplexed U(VI) ion) as well as measured at cryogenic temperature (analyzing the emissions of the complex species in addition) using factor analysis program SPECFIT.

The results obtained for the U(VI) oxalate system after the same fit procedure of the corresponding TRLFS data show that in addition to the 1:1 U(VI) oxalate species of type ML, a 1:2 species of type ML₂ is formed. The complex formation constants determined for the citrate and oxalate system by means of TRLFS at room temperature and cryogenic temperature are in good agreement with complex formation constants determined at $I = 0.5$ M NaClO₄ by concurrently performed UV-Vis spectroscopic measurements at room temperature: $\log \beta(\text{UO}_2\text{cit}^-) = 7.51 \pm 0.05$, $\log \beta((\text{UO}_2)_2(\text{cit})_2^{2-}) = 18.89 \pm 0.04$, $\log \beta(\text{UO}_2\text{ox}) = 6.34 \pm 0.35$, $\log \beta(\text{UO}_2(\text{ox})_2^{2-}) = 10.40 \pm 0.13$. Accepted formation constants for U(VI) citrate species in NaClO₄ solution as background electrolyte and at $I = 0.1$ M or $I = 0.5$ M were not found in the literature and corresponding data bases. Thus, the formation constants obtained by evaluating luminescence emission data are comparable with data obtained by potentiometry for the corresponding complex species formed in KNO₃ (Table 2.3). In the case of the U(VI) oxalate system the complex formation constants are in good agreement with literature data, which were determined applying spectrophotometry under almost identical experimental conditions (Table 2.3).

In addition to the determination of the stoichiometry (x,y,z) of the U(VI) complexes and the corresponding stability constants we divided the mixed emission spectra into single component spectra with the data analysis program SPECFIT. The results of the mathematical deconvolution of the mixed TRLF spectra (measured at -120°C) for the U(VI) citrate and oxalate system are shown in Figs. 2.15a,b. The spectroscopic data are given in Table 2.4.

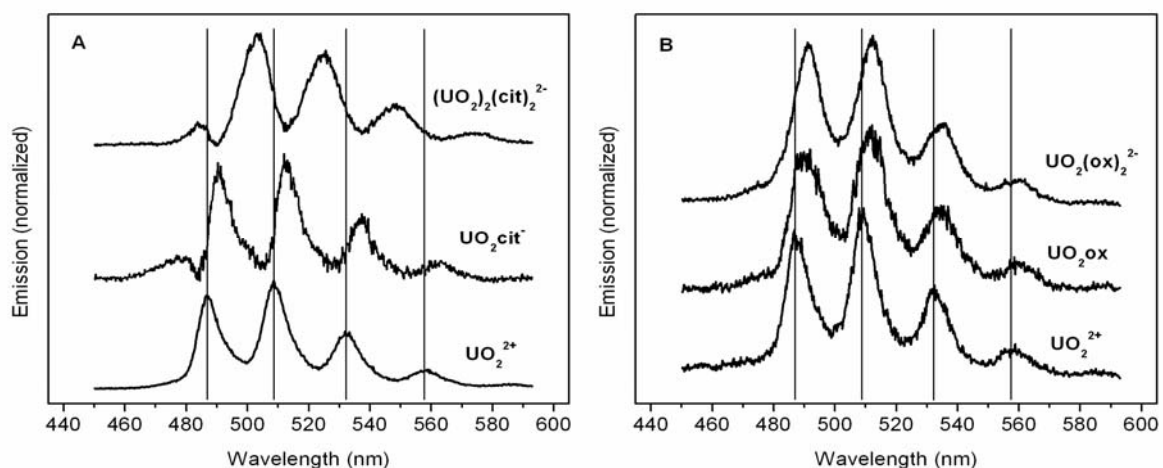


Fig. 2.15. TRLF - single component spectra of the different U(VI) citrate species (a) and U(VI) oxalate species (b) in comparison to the spectrum of UO_2^{2+} as result of the peak deconvolution by SPECFIT.

Table 2.4. Luminescence properties of U(VI) citrate and U(VI) oxalate species in comparison to the U(VI) cation at -120°C.

System	Species	Luminescence emission bands (nm)					
U(VI)/cit	UO ₂ ²⁺	472.8	487.9	509.1	532.1	557.6	585.1
	UO ₂ cit ⁻	475.3	491.8	513.5	537.0	561.9	
	(UO ₂) ₂ (cit) ₂ ²⁻	483.6	502.7	524.5	548.1	574.0	
U(VI)/ox	UO ₂ ²⁺	473.3	488.1	509.4	532.6	557.7	585.1
	UO ₂ ox	472.9	490.8	511.6	534.1	559.5	587.1
	UO ₂ (ox) ₂ ²⁻	472.6	491.0	512.2	534.8	559.9	

The main emission bands of the 1:1 and 2:2 U(VI) citrate complexes show a bathochromic shift of up to 14-16 nm compared to the emission bands of the uncomplexed U(VI) ion. In contrast, the shift of the emission bands of both U(VI) oxalate species to the emission bands of the uncomplexed U(VI) ion is less pronounced (about 3 nm). The pronounced shift in the spectra at [U]₀:[cit]₀ ratios from 1:5 to 1:8 can not be explained, since the calculated U(VI) species distributions (17.8% UO₂²⁺; 40.0% 1:1 complex; 42.2% 2:2 complex for the first case and 11.0% UO₂²⁺; 42.2% 1:1 complex, 46.8% 2:2 complex for the second case) are not so different.

The calculated U(VI) citrate species distribution applying complex formation constants determined in this work shows that both U(VI) citrate species are formed concurrently at pH 3.5 in the same ratio. Therefore, it is very difficult to assign surely the luminescence lifetimes obtained at -120° C (cf. section TRLFS measurements at cryogenic temperature (-120°C)) to the individual U(VI) citrate complex species, because the absolute intensities of the species are not known. According to the calculated species distribution at different U(VI) to oxalic acid concentration ratios in the samples using obtained complex formation constants by SPECFIT (at first the formation of the 1:1 complex at low oxalic acid concentrations and later additionally the formation of the 1:2 U(VI) oxalate species at higher oxalic acid concentrations) the short lifetime τ_2 is assigned to the 1:1 complex species and the longer lifetime τ_3 to the 1:2 U(VI) oxalate complex.

Conclusion

For the first time, luminescence properties and stability constants were determined for aqueous U(VI) citrate and oxalate species in the acidic pH range by laser-induced fluorescence spectroscopy at -120°C. This is a great improvement toward TRLFS

measurements at room temperature, where emission signals of the complex species are not detectable.

2.4 U(VI) complexation by lactic acid – Determination of complex formation constants in dependence on temperature (7 to 65°C) by UV-Vis spectroscopy and TRLFS

After disposal in nuclear waste repositories the chemical and migration behavior of actinides depends on many factors, e.g., pH value and redox potential of the solution, concentration of complex partners and temperature. It is estimated that maximum temperatures in the near field of a repository could reach 100°C (Brasser et al., 2008) in dependence on the waste forms (Rao et al., 2002) and the host rock (Warwick et al., 1997). Thus, for long-term safety assessment, knowledge of the interaction of actinides such as uranium with inorganic and organic ligands at elevated temperatures is required. The majority of the complexation studies are conducted at ambient conditions (18 - 25°C) and data are published in (Guillaumont et al., 2003; Hummel et al., 2005). Thermodynamic data on the hydrolysis of U(VI) and the complexation of U(VI) by some carboxylates at elevated temperatures are summarized by Rao (2007). In the present work, the U(VI) complexation by lactic acid (pH 3.0) was studied in the temperature range from 7 to 65°C. For this, UV-Vis absorption spectroscopy and TRLFS were applied. The results of this study will be published in (Steudtner et al., 2012, in preparation).

2.4.1 Experimental

The complexation experiments were performed at a fixed U(VI) concentration of 5×10^{-4} M (UV-Vis) or 5×10^{-5} M (TRLFS). The lactate concentration was varied between 0 and 0.1 M (UV-Vis) or 0 and 0.01 M (TRLFS). These measurements were carried out at an ionic strength of 0.1 M (NaClO₄) at pH 3 and at variable temperatures (7, 25, 45, 65°C). The pH value was adjusted with HClO₄ or NaOH. The UV-Vis measurements were performed using a CARY-5G UV-Vis-NIR Spectrometer (Varian). The spectra were recorded between 375 and 500 nm. The luminescence of U(VI) was measured after excitation with laser pulses at 266 nm (Minilite laser system, Continuum) and an averaged pulse energy of 250 μJ. The emitted fluorescence light was detected using a spectrograph (iHR 550, HORIBA Jobin Yvon) and an ICCD camera (HORIBA Jobin Yvon). The TRLFS spectra were recorded from 450.0 to 649.9 nm by accumulating 50 laser pulses using a gate time of 20 μs.

2.4.2 Results and discussion

UV-Vis measurements

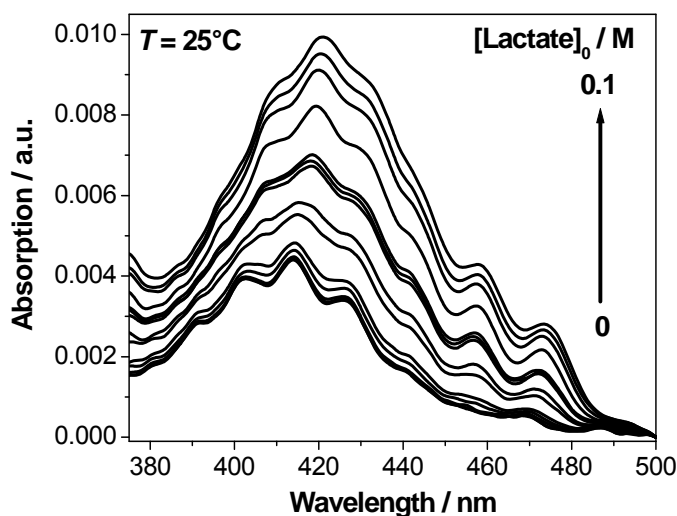


Fig. 2.16. Absorption spectra of U(VI) solutions as a function of the lactate concentration ($[U(VI)] = 5 \times 10^{-4}$ M, $I = 0.1$ M, pH 3, 25°C).

Exemplary for the UV-Vis spectrophotometric titrations of U(VI) solutions as a function of the lactate concentration in the temperature range from 7 to 65°C , the absorption spectra obtained at 25°C are shown in Fig. 2.16. At each temperature, an increase of the absorbance and a red shift of 10 nm of the absorption maxima, in comparison to the bands of the free U(VI) ion, indicate the formation of U(VI) lactate species. The absorption spectra were evaluated using the factor analysis program SPECFIT (Binstead et al., 2005). Single component spectra of three species (free UO_2^{2+} and two complex species) could be extracted and complex formation constants for the 1:1 and the 1:2 complex were determined. The U(VI) band positions of the various U(VI) lactate species are compiled in Table 2.5.

Table 2.5. Main absorption bands of the U(VI) species in the U(VI) lactate system.

U(VI) species	Band positions / nm						
UO_2^{2+}	391.3	402.4	414.4	426.6	439.4	453.6	468.6
UO_2Lac^+	396.1	408.2	419.4	431.4	443.4	457.4	472.9
$\text{UO}_2(\text{Lac})_2$	400.0	412.5	423.3	435.3	447.6	461.7	476.6

For the free UO_2^{2+} ion, an absorption maximum at 414.4 nm was detected. The 1:1 and the 1:2 complex exhibit an absorption maximum at 419.4 and 423.3 nm, respectively. No significant changes of the molar absorption coefficient of the U(VI) species were observed

when the temperature of U(VI) lactate solutions was increased from 7 to 65°C. The complex formation reaction of U(VI) with lactate can be written as follows:



The complex formation constants, determined for the 1:1 and 1:2 complexes, increase by 3.9 and 17.4 times, respectively, when the temperature is increased from 7 to 65°C (cf. Table 2.6). The complex formation constants, determined by Starý and Balek (1962) in 0.1 M NaClO₄ solution at 20°C by extraction can be included very good in the temperature-dependent study. This verifies the determined complex formation constants.

Table 2.6. Summary of complex stability constants ($\log \beta$) of the U(VI) lactate complexes ($I = 0.1 \text{ M (NaClO}_4\text{)}$) in comparison to literature data.

Complex	T / °C	UV-Vis	TRLFS	Extraction
		$\log \beta_{11}$	$\log \beta_{11}$	$\log \beta_{11}$
UO ₂ Lac ⁺	7	2.75 ± 0.09	2.71 ± 0.08	---
	20	---	---	2.81 ± 0.06
	25	2.94 ± 0.08	3.18 ± 0.08	---
	45	3.19 ± 0.15	3.29 ± 0.21	---
	65	3.34 ± 0.07	3.70 ± 0.13	---
		$\log \beta_{12}$	$\log \beta_{12}$	$\log \beta_{12}$
UO ₂ (Lac) ₂	7	4.40 ± 0.27	---	---
	20	---	---	4.56 ± 0.10
	25	4.85 ± 0.19	---	---
	45	5.55 ± 0.20	---	---
	65	5.64 ± 0.20	---	---
Reference		this work	this work	(Starý and Balek, 1962)

TRLFS measurements

Exemplary for all temperatures, Fig. 2.17 shows the luminescence spectra of U(VI) as a function of the lactate concentration measured at 25°C. The U(VI) luminescence spectra are characterized by six emission bands (at 470.7, 488.0, 509.3, 532.6, 557.9 and 585.1 nm) that were consistent with the typical band positions of the free UO₂²⁺ ion observed by Billard et al. (2003). At all temperatures studied, we observed a decrease of the U(VI) luminescence intensity with increasing ligand concentration but no shift of the U(VI) emission bands. This

is characteristic for static luminescence quenching due to complex formation by forming a non-fluorescent U(VI) lactate species. The fluorescence decay of the free UO_2^{2+} ion can be described by a mono-exponential decay function and the calculated lifetimes are summarized in Table 2.7.

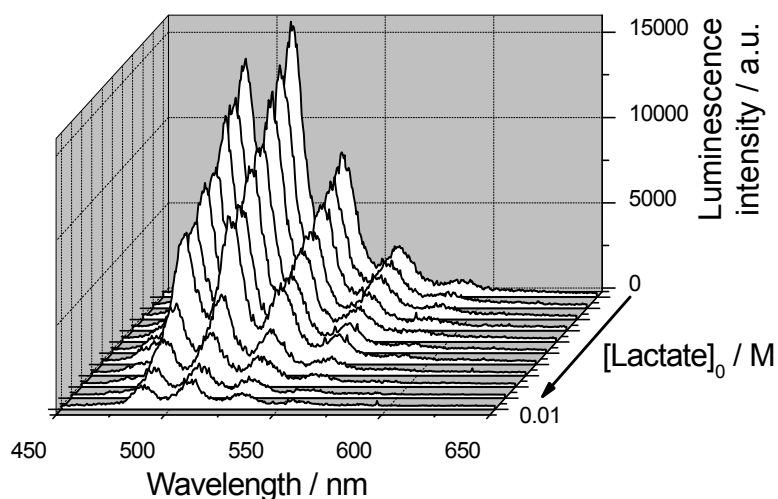


Fig. 2.17. Luminescence spectra of U(VI) solutions as a function of the lactate concentration ($[\text{U(VI)}] = 5 \times 10^{-5} \text{ M}$, $I = 0.1 \text{ M}$, pH 3, 25°C).

Table 2.7. Temperature-dependence of fluorescence lifetimes (τ) of the free UO_2^{2+} ion as function of the lactate concentration ($[\text{U(VI)}] = 5 \times 10^{-5} \text{ M}$, $I = 0.1 \text{ M}$, pH 3).

$T / ^\circ\text{C}$	7	25	45	65
Lactate / M	$\tau / \mu\text{s}$	$\tau / \mu\text{s}$	$\tau / \mu\text{s}$	$\tau / \mu\text{s}$
0	5.27	1.32	0.36	0.12
1×10^{-5}	5.08	1.26	0.36	0.13
1×10^{-4}	5.00	1.28	0.36	0.14
5×10^{-4}	4.67	1.23	0.34	0.09
1×10^{-3}	4.30	1.13	0.35	0.12
5×10^{-3}	1.99	0.77	0.28	0.08
1×10^{-2}	1.53	0.57	0.22	0.06

The lifetime of the free UO_2^{2+} ion decreases with increasing ligand concentration caused by an additional dynamic quenching process. The determined lifetimes can be used to calculate the luminescence intensities if no dynamic quenching occurs (Stern and Volmer, 1919; Glorius et al., 2008). The corrected luminescence intensities were then used to calculate the concentration of the non-complexed U(VI) in every sample. In contrast to the UV-Vis

measurements, only the complex formation constant for the complex reaction given in Eq. (2.11) could be calculated from the luminescence spectra.

The results of the UV-Vis and TRLFS measurements show an increase of the complex formation constants with increasing temperature from 7 to 65°C (cf. Table 2.6). Similar effects of the temperature were previously observed for a few reactions of U(VI) with other carboxylates (Rao, 2007).

The enthalpy (ΔH) and entropy (ΔS) of the complexation were determined graphically from the temperature-dependent stability constants by using the van't Hoff equation in a modified linear form. The plot of the natural logarithm of the equilibrium constant versus the reciprocal temperature gives a straight line.

$$\ln \beta = -\frac{\Delta H}{RT} + \frac{\Delta S}{R} \quad (2.13)$$

The slope is equal to minus the enthalpy divided by the universal gas constant ($R = 8.314 \text{ J}\cdot\text{K}^{-1}\cdot\text{mol}^{-1}$) and the intercept is equal to the entropy divided by R . When the complex stability constants (Table 2.6) are introduced into the van't Hoff plot, the slope is negative (cf. Fig. 2.18). A negative slope represents an endothermic reaction. Energy is used for formation of the U(VI) lactate complexes from the reactants. ΔH and ΔS values of $18.7 \pm 1.8 \text{ kJ}\cdot\text{mol}^{-1}$ and $119.2 \pm 6.1 \text{ J}\cdot\text{mol}^{-1}\cdot\text{K}^{-1}$ for the UO_2Lac^+ complex and of $40.8 \pm 7.0 \text{ kJ}\cdot\text{mol}^{-1}$ and $230.4 \pm 22.5 \text{ J}\cdot\text{mol}^{-1}\cdot\text{K}^{-1}$ for the $\text{UO}_2(\text{Lac})_2$ complex are calculated. A positive entropy change indicates a spontaneous reaction between U(VI) and lactate. It can be concluded that the complexation of U(VI) with lactate is endothermic (ΔH pos.) and entropy-driven (ΔS pos.). Similar thermodynamics has been observed for the complexation of U(VI) with other carboxylates such as acetate and malonate (Rao, 2007).

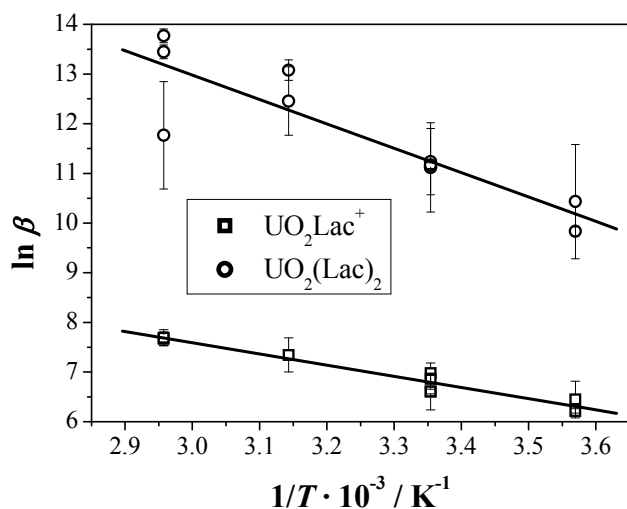


Fig. 2.18. van't Hoff plot of the obtained U(VI) lactate complex stability constants.

Conclusion

Thermodynamic parameters were determined for the U(VI) lactate system by absorption and fluorescence spectroscopy. The complex stability constants of the U(VI) lactate complexes (UO_2Lac^+ , $\text{UO}_2(\text{Lac})_2$) increase with increasing temperature (7 – 65°C). The complexation of U(VI) with lactate is endothermic (ΔH pos.) and entropy-driven (ΔS pos.). Since the U(VI) lactate complexes are weaker than the U(VI) citrate and oxalate complexes (cf. section 2.3), the influence of lactate on the speciation of U(VI) and thus, on the migration behavior of U(VI) in a nuclear waste repository is lower compared to the influence of citric or oxalic acid.

2.5 U(VI) complexation by anthranilic acid and nicotinic acid – Determination of complex formation constants by fs-TRLFS and TRLFS

Analog to the Am(III) complexation study (cf. section 2.1), the complexation of U(VI) with nitrogen containing organic model ligands was investigated in order to simulate humic substance functionalities. Representing simple aromatic structural units of HA molecules, anthranilic acid (AA) and nicotinic acid (Nic) were selected (cf. Fig. 2.19). Since AA exhibits unique fluorescence emission after excitation, the U(VI) complexation by AA was studied using a femtosecond-pulsed laser system (fs-TRLFS). Since Nic shows no distinct fluorescence emission or analyzable spectra under the studied conditions, the U(VI) complexation by Nic was studied applying a conventional TRLFS system. The results of this study are published in-depth by Raditzky et al. (2010).

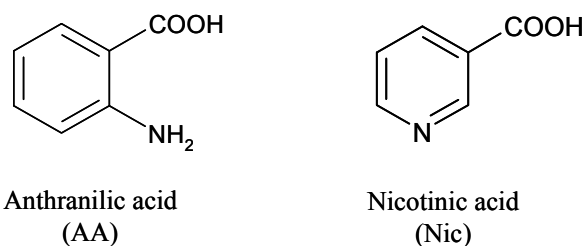


Fig. 2.19. Structures of the nitrogen containing model ligands AA and Nic.

2.5.1 Experimental

Sample preparation

Anthranilic acid (p.a., Merck) and nicotinic acid (p.a., Sigma-Aldrich) stock solutions were prepared freshly for each experiment. The complex solutions were prepared from stock

solutions of the ligand (1×10^{-3} M) and $\text{UO}_2(\text{ClO}_4)_2$ (5×10^{-3} M in 0.02 M HClO_4). The ionic strength was kept constant in all measurements at 0.1 M by adding aliquots of an NaClO_4 stock solution. All experiments were carried out at $23 \pm 2^\circ\text{C}$. Solutions were prepared using Milli-Q water (mod. Milli-RO/Milli-Q-System, Millipore, Schwalbach, Germany) and necessary pH adjustments were done with diluted NaOH and HClO_4 solutions. Table 2.8 summarizes the composition of all solutions studied.

Table 2.8. Composition of the studied solutions.

Ligand	Used system	c_{metal} (M)	c_{ligand} (M)	pH
AA	fs-TRLFS	$0 - 3 \times 10^{-4}$	1×10^{-5}	1.5 – 4.5
Nic	Minilite	5×10^{-5}	$0 - 8 \times 10^{-4}$	2.5 – 4.5

TRLFS measurements

fs-TRLFS system

A Nd:YVO₄ laser (Spectra Physics) was used as pump source for the Ti:Sapphire oscillator. After amplification, third harmonic generation was used to provide femtosecond pulses with an excitation wavelength of 266 nm. The emitted fluorescence was focused into a spectrograph (Acton Research) and collected by an intensified CCD camera (Picostar HR, La Vision Inc.). The delay generator allows time delays between 0 and 100 ns in various steps from ps up to ns. The time-resolved spectra were recorded from 348 to 551 nm at delay times ranging from 0 to 30 ns in 0.1 ns increments. The gate width for the fluorescence detection was set to 2 ns.

TRLFS system

The U(VI) luminescence in solution was measured using a Nd:YAG laser system (Continuum Minilite II, Continuum Electro Optics Inc.) with an excitation wavelength of 266 nm. The trigger input of the detection system was coupled directly to the trigger output of the laser. The luminescence emission was focused into a spectrograph (iHR 550, HORIBA Jobin Yvon) via fiber optics and detected using an ICCD camera system and a built-in delay generator (HORIBA Jobin Yvon). The TRLFS spectra were measured from 371 to 674 nm at a gate time of 2 μs by averaging 100 laser pulses. For the time-resolved measurements 101 spectra were recorded during a delay time of 10000 ns with a step size of 100 ns. The first time step started between 40 and 80 ns after the excitation pulse.

2.5.2 Results and discussion

Interaction of U(VI) with anthranilic acid

Like other amino acids, AA is an amphoteric compound. It occurs in three different species in aqueous solution: the completely protonated acid (AAH₂), the zwitterionic species (AAH^{+/-}) and the completely deprotonated anthranilate (AA⁻). The pK_a values of AA at an ionic strength of 0.1 M and room temperature are pK_{a1} = 2.01 and pK_{a2} = 4.78 (Martell et al., 1998). Figure 2.20a shows the fluorescence emission spectra of AA as a function of the U(VI) concentration at pH 3.5.

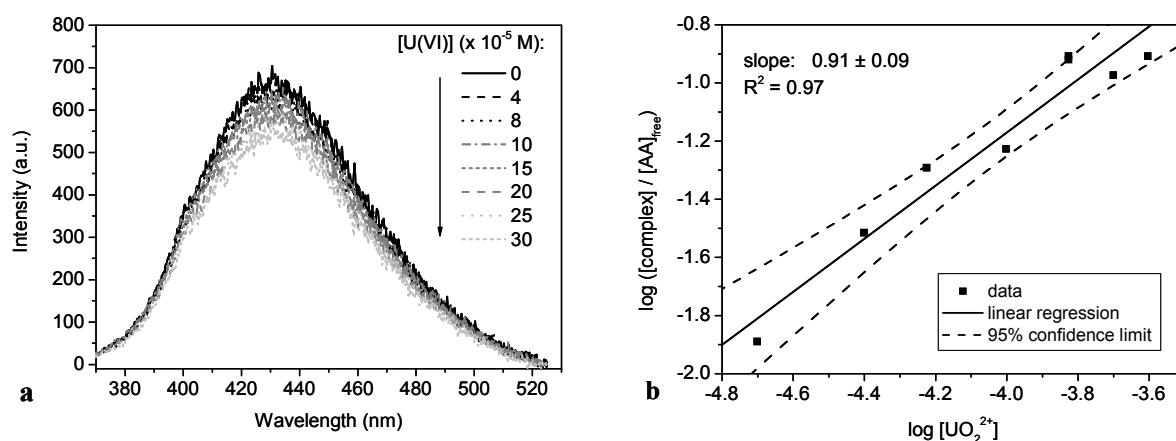


Fig. 2.20. (a) Fluorescence emission spectra of 1×10^{-5} M AA as a function of the U(VI) concentration and (b) slope analysis of the complex formation of U(VI) with AA at pH 3.5.

With addition of the metal ion the fluorescence intensity of AA decreases with increasing U(VI) concentration. The observed decrease is typical for static fluorescence quenching processes due to complex formation, thereby reducing the concentration of non-complexed AA. No shift of the main emission band was observed, implying that the formed complex does not show any fluorescence in the considered wavelength range. The obtained fluorescence lifetimes are in good agreement with those determined for the ligand species without U(VI) (Raditzky et al., 2010). For all experiments no changes in the lifetimes were observed, which verifies the assumption of static quenching and exclude the occurrence of dynamic quenching effects. For all measurements at pH < 2, a complexation of AA with U(VI) could not be detected.

For the experiments at pH values above 2, the following equation for the direct reaction of U(VI) with the zwitterionic AAH^{+/-} species was obtained:



Assuming that the measured luminescence intensity is proportional to the concentration of the free prevailing AA species in equilibrium, the stoichiometry can be graphically determined via validation plot, using a modified logarithmic form of the mass action law:

$$\log \frac{[(\text{UO}_2)_x (\text{H}_3\text{NC}_6\text{H}_4\text{COO})_y]^{(2x)+}}{[{}^+\text{H}_3\text{NC}_6\text{H}_4\text{COO}^-]^y} = x \log [\text{UO}_2^{2+}] + \log \beta_{xy} \quad (2.15)$$

An example for the slope analysis at pH 3.5 is given in Fig. 2.20b. A slope near 1 was determined, suggesting the formation of a predominant 1:1 complex. The spectra analysis program SPECFIT (Binstead et al., 2005) was used to validate the determined stoichiometry and to calculate the stability constant of the complex. The averaged formation constant for this reaction was calculated to be $\log \beta_{11} = 3.14 \pm 0.17$ (cf. Table 2.9). This is comparable to literature data ($\log \beta_{11} = 2.95 \pm 0.01$), although this value was determined in a 20% mixture of ethanol and water (Mahmoud et al., 1996). The formation of a 1:2 complex or a chelate was not detectable under the given experimental conditions (low concentrations, fixed ligand concentration). To estimate whether or not the $-\text{NH}_3^+$ functionality dissociates during the complex formation, the stability constants derived from the slope analysis were plotted as a function of $\log [\text{H}^+]$, as described in (Geipel et al., 2004). From the slope of this plot the number of protons released due to complex formation can be obtained. Taking into account that AA is not completely deprotonated in the pH range from 2.5 to 4.5, only one proton can possibly be released. A slope of about -0.1 was derived, leading to the conclusion that the proton of the protonated amino group is not released during the complexation. Therefore, it is very probable that the amino group does not participate in complex formation at the investigated pH range and that the U(VI) ion is only coordinated via the carboxylic group. This is in agreement with literature data. Alcock et al. (1996a) examined the AA complex with U(VI) using crystal structure analysis discovering that the amino group does not participate in chelating U(VI).

Interaction of U(VI) with nicotinic acid

Like AA, Nic exists as zwitterionic species (${}^+\text{HNC}_5\text{H}_4\text{COO}^-$) in aqueous solution. The dissociation constants as well as the species distribution of Nic are comparable to those of AA. The luminescence spectra of U(VI) as a function of the Nic concentration at pH 2.5 are given in Fig. 2.21a. In all samples a mono-exponential luminescence decay was observed indicating the presence of the free U(VI) ion with a lifetime of about $1.29 \pm 0.10 \mu\text{s}$. With increasing Nic concentration a strong decrease of the U(VI) luminescence intensity was observed. No shifts of the main emission bands were detected. Therefore, it is concluded that

the formed complex does not show any luminescence in the considered wavelength range and time scale.

The complex formation of Nic with U(VI) was determined in the whole examined pH range from 2.5 to 4.5. In analogy to the experiments with AA a slope analysis was performed. The validation plot for the complexation of U(VI) with Nic at pH 2.5 is shown in Fig. 2.21b. Unlike AA, the slope was calculated to be 1.32 ± 0.10 , suggesting the additional formation of 1:2 complexes at higher ligand concentrations.

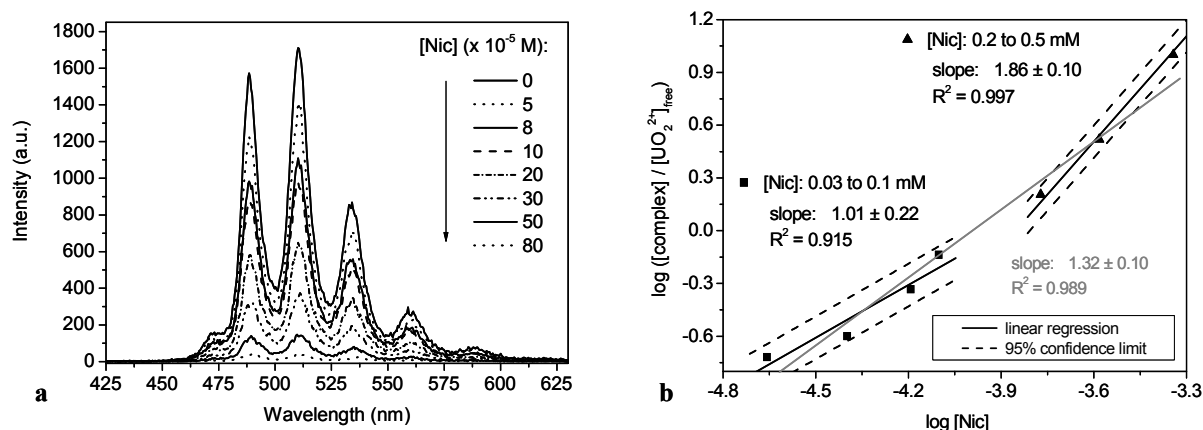


Fig. 2.21. (a) Luminescence spectra of 5×10^{-5} M U(VI) as a function of Nic concentration and (b) slope analysis of the complex formation of U(VI) with Nic at pH 2.5.

To verify this, the plotted data points were split into two sections with different ligand concentration ranges (section 1: [Nic]: 3×10^{-5} M to 1×10^{-4} M, section 2: [Nic]: 2×10^{-4} M to 5×10^{-4} M) and the slope of each section was calculated separately. The results show that a 1:2 complex is formed at ligand concentrations above 1×10^{-4} M. According to the measurements with AA, we suggest that the $-\text{NH}^+$ functionality of Nic does not dissociate during the complex formation, resulting in the following equation for the direct reaction of U(VI) with the zwitterionic Nic species:



The averaged formation constants for this reaction were calculated to be $\log \beta_{11} = 3.73 \pm 0.30$ and $\log \beta_{12} = 7.46 \pm 0.17$ (cf. Table 2.9). These values are in good agreement with constants determined for the complexation of U(VI) with picolinic acid, which is an isomer of Nic. The formation constants for $[(\text{UO}_2)_x(\text{Pic})_y]^{2x-y}$ were found to be $\log \beta_{11} = 3.75$ and $\log \beta_{12} = 7.48$ (Budantseva et al., 2006). It was concluded that the binding of U(VI) takes place via the carboxylic group of the ligand. The formation of a chelate is not possible at the considered pH and concentration range. This is in agreement with literature data. For the U(VI) nicotinate

complex Alcock et al. (1996b) described a structure where U(VI) is located in an inversion centre of two ligand molecules and is only coordinated by oxygen atoms. It is interesting that the formation constant of the U(VI) anthranilate complex is slightly lower than that of the nicotinate system. It seems that the amino group causes an electrostatic repulsion between $-\text{NH}_3^+$ and UO_2^{2+} , while this repulsion is understated in the Nic molecule in consequence of the *meta* position of $-\text{NH}^+$. In addition to that, the pyridine nitrogen seems to stabilize the U(VI) complexation due to electronic and mesomeric effects.

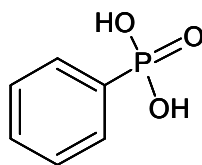
Table 2.9. Summary of complex stability constants for the U(VI) ligand species ($I = 0.1 \text{ M}$).

Ligand	pH	$\log \beta_{11}$	$\log \beta_{12}$
Anthranilic acid	1.5	-	
	2.5	3.20 ± 0.20	
	3.5	3.03 ± 0.20	
	4.5	3.21 ± 0.20	
averaged $\log \beta$		3.14 ± 0.17	
Nicotinic acid	2.5	3.75 ± 0.12	7.35 ± 0.34
	3.5	3.90 ± 0.15	7.48 ± 0.24
	4.5	3.54 ± 0.18	7.54 ± 0.11
	averaged $\log \beta$	3.73 ± 0.30	7.46 ± 0.17

Transferring these results to the HA system, the present investigation has shown that oxygen containing functional groups dominate the U(VI) complexation in the investigated pH range. It is known from literature that deprotonation reactions of organic ligands can be forced in the presence of metal ions. The possibility of dissociation and chelate formation even at low pH is reported, e.g., it was shown that phenolic OH groups contribute to the interaction between U(VI) and HA already at pH 4 (Pompe et al., 2000b). Accordingly in the case of Nic and AA, it is also possible that the acidity of the nitrogen functional groups could be influenced when coordinated to U(VI). This study showed that this is not the case for both investigated ligands. However, it can not be excluded that deprotonated amino groups may contribute to the U(VI) complexation at pH values above 4.5, e.g. due to hydrogen bonding. In future, this has to be studied in more detail to answer this question.

2.6 U(VI) complexation by phenylphosphonic acid – Determination of complex formation constants by TRLFS

Phosphorus has been known to be present in the humic fractions of natural organic matter (Stevenson, 1994), although in small and widely varying amounts (e.g., 0.12 - 1.42 wt.% in soil HA (Makarov, 1997)). The identity and stability of phosphorus associated with humic substances is not fully understood. However, from ^{31}P -NMR spectroscopy it was concluded that the organic phosphorus detected in HA is probably derived from phosphonic acids, phospholipids or phosphoric mono- and diesters (Makarov, 2005; He et al., 2006). The aim of the work was to investigate the potential influence of phosphorus containing functionalities on the U(VI) complexation in comparison to oxygen functionalities, using phenylphosphonic acid (cf. Fig. 2.22) as a simple organic model ligand for aromatic phosphonate functionalities in HA. The U(VI) complexation was examined using time-resolved laser-induced fluorescence spectroscopy (TRLFS).



Phenylphosphonic acid
(PPA)

Fig. 2.22. Structure of the phosphorus containing model ligand PPA.

2.6.1 Experimental

Sample preparation

Phenylphosphonic acid (99%) was purchased from Acros Organics. The complex solutions were made from stock solutions of the ligand (1×10^{-3} M), which were prepared freshly for each experiment, and $\text{UO}_2(\text{ClO}_4)_2$ (5×10^{-3} M in 0.02 M HClO_4). The TRLFS experiments were performed at a total U(VI) concentration of 5×10^{-5} M by varying the ligand concentration from 0 to 5×10^{-4} M. To minimize the formation of hydrolytic species of U(VI), the complex formation experiments were performed in the pH range 1.5 to 4.0. Solutions were prepared using Milli-Q water (mod. Milli-RO/Milli-Q-System, Millipore, Schwalbach, Germany). The ionic strength was adjusted to 0.1 M by adding 0.5 M NaClO_4 (p.a., Merck). The pH was adjusted using diluted NaOH (high grade, Merck) and HClO_4 (p.a., Merck) solutions.

TRLFS measurements

The spectra were recorded at room temperature using a Nd:YAG laser system (Continuum Minilite II, Continuum Electro Optics Inc.). The excitation wavelength was 266 nm with pulse energies between 0.2 and 0.5 mJ. The U(VI) luminescence emission was focused into a spectrograph (iHR 550, HORIBA Jobin Yvon GmbH) via fiber optics and detected using an ICCD camera system and a built-in delay generator (HORIBA Jobin Yvon). All settings of the camera and spectrograph as well as the collection and storage of the measured data were controlled by the software LabSpec 5.21.12 (HORIBA Jobin Yvon). The TRLFS spectra were measured from 371 to 674 nm at a gate time of 2 μ s by averaging 100 laser pulses. For the time-resolved measurements 101 spectra were recorded during a delay time of 10000 ns with a step size of 100 ns.

2.6.2 Results and discussion

Figure 2.23a shows the luminescence emission spectra of U(VI) as a function of the PPA concentration at pH 2.

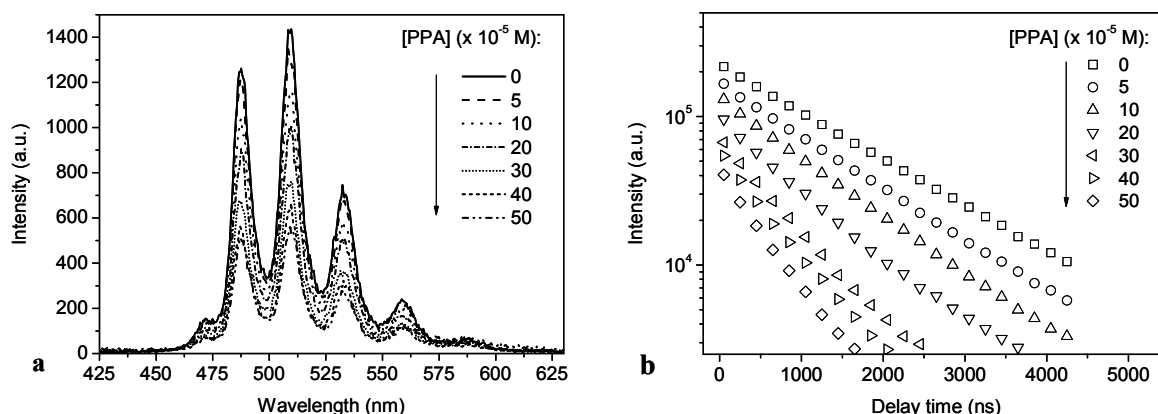


Fig. 2.23. (a) Emission spectra of 5×10^{-5} M U(VI) as a function of PPA concentration and (b) luminescence decay of U(VI) as a function of the ligand concentration at pH 2.

The spectra show a strong decrease of the U(VI) luminescence intensity with increasing ligand concentration at all pH values studied. No shift of the main emission bands was observed, implying that the formed complex does not show any luminescence emission in the considered wavelength range. The observed decrease is typical for static fluorescence quenching processes due to complex formation, thereby reducing the concentration of non-complexed metal ion. A mono-exponential luminescence decay was observed in all samples between pH 1.5 and 3.0. In the absence of the ligand, a luminescence lifetime of about 1.39 ± 0.11 μ s was determined, which can be attributed to the free UO_2^{2+} ion. Only for the samples at

pH 4.0 it was possible to determine a bi-exponential luminescence decay, due to the formation of U(VI) hydroxo species. However, with increasing ligand concentration the lifetime of the free UO_2^{2+} ion decreases to $0.55 \pm 0.05 \mu\text{s}$ (cf. Fig. 2.23b), indicating additional dynamic quenching processes caused by the free ligand.

The determined lifetimes were used to correct the measured U(VI) intensities for the dynamic quenching part, using the $I_0/I = \tau_0/\tau$ relation deduced from the Stern-Volmer equation:

$$\frac{I_0}{I} = \frac{\tau_0}{\tau} = 1 + K_{SV} \cdot [Q] \quad (2.17)$$

where I_0 and τ_0 represent the U(VI) intensity and lifetime, respectively, without dynamic quench, whereas I and τ are the measured intensity and lifetime, respectively, when the quenching substance Q (in this case the free PPA) is added. The corrected luminescence intensities were then used to calculate all necessary concentrations (e.g., the concentration of the uncomplexed UO_2^{2+}). To estimate the complexation constant, the intensity ratio $((I_0/I)-1)$ was plotted against the concentration of the uncomplexed ligand. The slope represents the stability constant K_{SV} . Figure 2.24a shows the Stern-Volmer plot for the complex formation of U(VI) with PPA at pH 2.0.

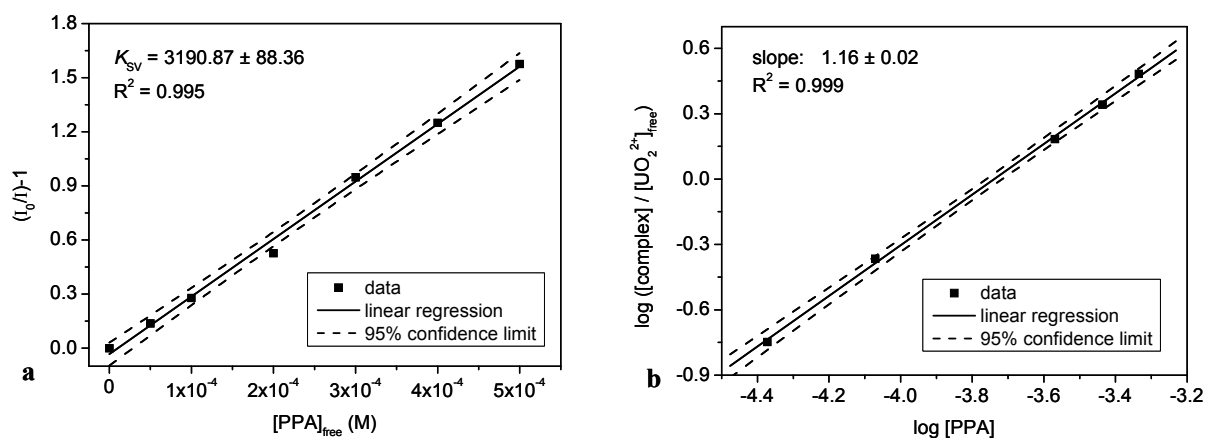


Fig. 2.24. (a) Stern-Volmer plot and (b) slope analysis of the complex formation of U(VI) with PPA at pH 2.

The $\text{p}K_a$ values of PPA at an ionic strength of 0.1 M and room temperature are $\text{p}K_{a1} = 1.7$ and $\text{p}K_{a2} = 7.0$ (Martell et al., 1998). Thus, the complex formation between pH 1.5 and 4.0 can be written as:



The averaged formation constant for this reaction was calculated to be $\log K_{II} = 3.49 \pm 0.08$ (Stern-Volmer plot) (cf. Table 2.10).

Assuming that the corrected luminescence intensity is proportional to the concentration of the free UO_2^{2+} ion in equilibrium, the stoichiometry of the complex can be graphically determined via slope analysis, using a modified logarithmic form of the mass action law:

$$\log \frac{[(\text{UO}_2)_x(\text{C}_6\text{H}_5\text{PO}_3\text{H})_y]^{(2x-y)+}}{[\text{UO}_2^{2+}]^x} = y \log [\text{C}_6\text{H}_5\text{PO}_3\text{H}] + \log K_{xy} \quad (2.19)$$

An example for the slope analysis at pH 2 is given in Fig. 2.24b. A slope > 1 was calculated, suggesting the formation of 1:1 and 1:2 complexes. The spectra analysis program SPECFIT (Binstead et al., 2005) was used to validate the graphically determined stoichiometry and to calculate the stability constants of the complexes. The averaged formation constants are listed in Table 2.10. In comparison with aliphatic phosphorus containing ligands, the stability constants for the U(VI) phenylphosphonate system are somewhat smaller than those determined for the complexation of U(VI) with e.g., phosphoethanolamine $\log \beta_{11} = 4.5 \pm 0.1$ (Koban and Bernhard, 2007). This suggests a destabilization of the U(VI) phenylphosphonate system due to structural or steric reasons.

Table 2.10. Summary of the complex stability constants of the U(VI) ligand species ($I = 0.1 \text{ M}$).

Complex	$\text{M}_x\text{L}_y^{\text{a}}$	$\log K_{xy}^{\text{b}}$ (SV-plot)	$\log K_{xy}^{\text{b,c}}$ (slope analysis)	$\log \beta_{xy}^{\text{b}}$ (SPECFIT)
$\text{UO}_2\text{C}_6\text{H}_5\text{PO}_3\text{H}^+$	11	3.49 ± 0.08	3.50 ± 0.12	3.61 ± 0.14
$\text{UO}_2(\text{C}_6\text{H}_5\text{PO}_3\text{H})_2$	12			6.95 ± 0.22

^a M... metal; L...ligand

^b \pm t-distribution for 95% confidence interval

^c fixed slope ($n = 1$)

The present investigation has shown that the complexation strength of aromatic phosphonate groups toward U(VI) is comparable or even higher than that of oxygen functionalities such as carboxylic groups. The obtained formation constants are for example higher than those determined for the U(VI) complex formation with benzoic acid (e.g., $\log \beta_{11} = 3.37 \pm 0.14$ (Glorius et al., 2007)). Transferring these results to the HA system, the phosphorus containing functional groups may contribute to the U(VI) complexation by HA, however, due to the low concentrations of phosphorus in HA these functionalities play only a subordinate role compared to oxygen functionalities, especially carboxylic groups.

2.7 U(VI) complexation by benzenesulfonic acid and 4-hydroxybenzenesulfonic acid – Determination of complex formation constants by TRLFS

The sulfur content of HA varies between 0 and 2 wt.% (Stevenson, 1982). Regarding to their oxidation states, reduced sulfur (e.g. thiols, sulfides) or oxidized sulfur groups (e.g. sulfonates, sulfates) could be found (Solomon et al., 2003). Complexation studies of HA with zinc (Xia et al., 1997) and mercury (Skylberg et al., 2006) showed that reduced sulfur groups (probable thiols) are favored to coordinate the metal ions. See also literature compiled in section 3.2.

The aim of this work was to determine the influence of sulfur containing functional groups on the U(VI) complexation and to evaluate their contribution in comparison to oxygen containing functional groups. For this, simple organic model ligands that can occur as building blocks for HA are used in the first instance with the objective to transfer the results to HA. As model ligands benzenesulfonic acid (BSA) and 4-hydroxybenzenesulfonic acid (HBSA) were applied. Their structures are given in Fig. 2.25. These model ligands represent an intermediate state since the oxidation state of sulfur is between the most reduced form (thiol) and the most oxidized form (ester-SO₄-S). However, also sulfonate groups are present in HA. The U(VI) complexation was examined using time-resolved laser-induced fluorescence spectroscopy (TRLFS).

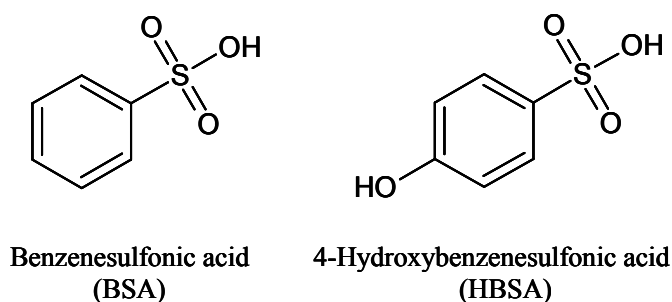


Fig. 2.25. Structures of the sulfur containing model ligands BSA and HBSA.

2.7.1 Experimental

Sample preparation

A U(VI) stock solution (5×10^{-3} M UO₂(ClO₄)₂ in 0.05 M HClO₄) was used for all experiments. Aqueous ligand stock solutions (0.2 M) of BSA (sodium salt, 97%, Sigma-Aldrich, St. Louis, Missouri, USA) and HBSA (sodium salt, dihydrate, 99%, Acros Organics, Geel, Belgium) were prepared freshly for the experiments. The TRLFS measurements were

performed at a constant U(VI) concentration of 1.08×10^{-4} M. The ligand concentration was varied between 0 and 5×10^{-3} M. The ionic strength was kept constant at 0.1 M by adding aliquots of a 0.2 M NaClO₄ stock solution (NaClO₄·H₂O, *p.a.*, Merck, Darmstadt, Germany). All solutions were prepared with distilled water. The pH was adjusted to pH 2.4 ± 0.05 with HClO₄ (*p.a.*, Merck) to minimize the formation of hydrolytic U(VI) species.

TRLFS measurements

All experiments were performed at room temperature ($21 \pm 2^\circ\text{C}$) under ambient atmosphere ($p\text{CO}_2 = 10^{-3.5}$ atm). TRLFS laser pulses at 410 nm with an average pulse energy of 0.6 mJ (Nd:YAG-MOPO laser system, mod. GCR 230 (20 Hz), Spectra Physics, Mountain View, USA) were used for excitation of the U(VI) luminescence. The sample solution was rinsed through a flow-through cuvette (Hellma, Müllheim, Germany) with a speed of 1 ml/min using a peristaltic pump (mod. Reglo Digital, Ismatec, IDEX Health & Science GmbH, Wertheim, Germany) to remove possibly formed photodegradation products. The emitted luminescence light was detected in a right angle setup by an Acton Research 300i spectrograph (Acton Research corporation, Acton MA, USA). The spectra were recorded in time-resolved mode using an ICCD camera (1024 pixels; mod. PI-MAX 3, Roper Scientific GmbH, Ottobrunn, Germany). The time difference between the trigger of the laser system and the start of the camera was adjusted by a delay generator DG 540 (Stanford Research Instruments, Sunnyvale, USA). The spectra were recorded in the wavelength range from 467 to 601 nm by accumulating 100 laser pulses using a camera gate time of 5 μs . For the time-resolved measurements the delay times were varied from 30 to 10,030 ns after application of the laser pulse using a step size of 100 ns. All settings of the camera and the spectrograph were computer controlled with the program WinSpec/32, version 2.5.19.6, Roper Scientific 2003. The measured time-resolved spectra were analyzed using the program OriginPro 7.5G (OriginLab Corporation, USA) in order to determine the fluorescence lifetimes. The time dependency of the luminescence signal was analyzed by fitting the sum of the luminescence intensities over the measured wavelength range by an exponential decay function:

$$I(t) = \sum I \cdot e^{-\frac{t}{\tau}} \quad (2.20)$$

where $I(t)$ is the total luminescence intensity at the time t , I the luminescence intensity of the luminescent compound (in this case U(VI)) at $t = 0$ and τ the corresponding lifetime.

2.7.2 Results and discussion

Figure 2.26 shows the luminescence spectra of the U(VI) sample solutions as a function of the ligand concentration for BSA (a) and HBSA (b) at pH 2.4. Both ligands cause a strong decrease of the U(VI) luminescence intensity with increasing ligand concentration. No shift of the luminescence peaks is observed. Both observations are typical for this so-called static luminescence quenching. With this effect, all processes of luminescence decrease caused by the formation of non-luminescent complexes, thereby reducing the concentration of the non-complexed luminescent compound, are described.

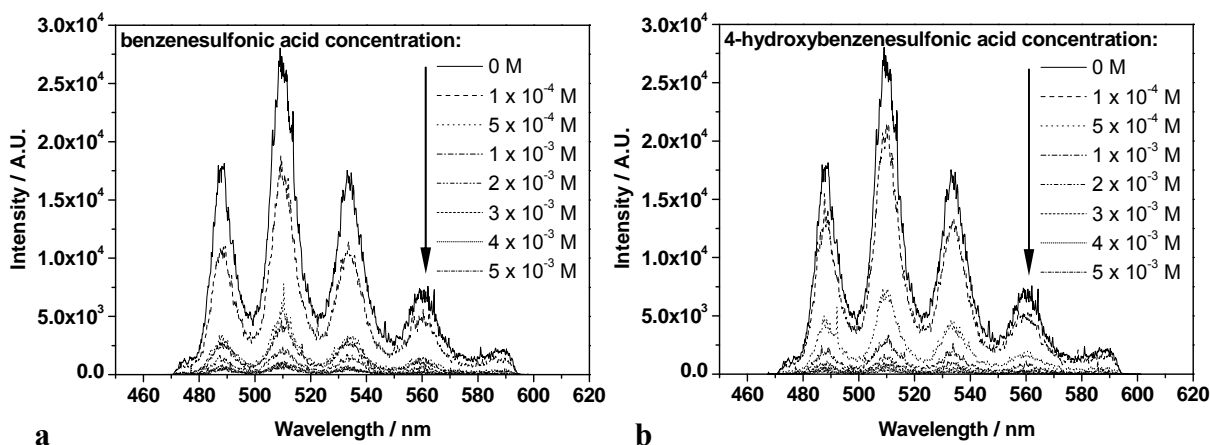


Fig. 2.26. Luminescence spectra of U(VI) (1.08×10^{-4} M) with benzenesulfonic acid (a) and 4-hydroxybenzenesulfonic acid (b) at pH 2.4 as a function of the ligand concentration.

The luminescence decay is mono-exponential in all samples. In the absence of the ligand, the luminescence lifetime, which can be attributed to the non-complexed U(VI) ion, amounts to 1830 ± 20 ns, which is in agreement with literature values (Moll et al., 2003; Günther et al., 2007). However, the lifetime decreases with increasing ligand concentration (Fig. 2.27) for BSA from 1450 ± 20 ns to 110 ± 3 ns and for HBSA from 1320 ± 10 ns to 70 ± 2 ns. This indicates an additional dynamic luminescence quenching, caused by the free ligand. For determination of the stability constant the U(VI) luminescence signal has to be corrected for the dynamic quenching part. For this, the Stern-Volmer equation (2.21) is used.

$$\frac{I_0}{I} = \frac{\tau_0}{\tau} = 1 + K_{sv} \cdot [Q] \quad (2.21)$$

I_0/I is the ratio of the U(VI) luminescence intensity without dynamic quench (I_0) to the measured intensity (I). For determination of I_0 the ratio of the respective luminescence lifetimes of U(VI) without quencher (τ_0) and with quencher (τ) is used. K_{SV} presents the Stern-Volmer constant, Q is the quenching substance (in this case the free organic ligand). This correction method is well established and described in more detail in the literature (e.g., Geipel et al., 2004).

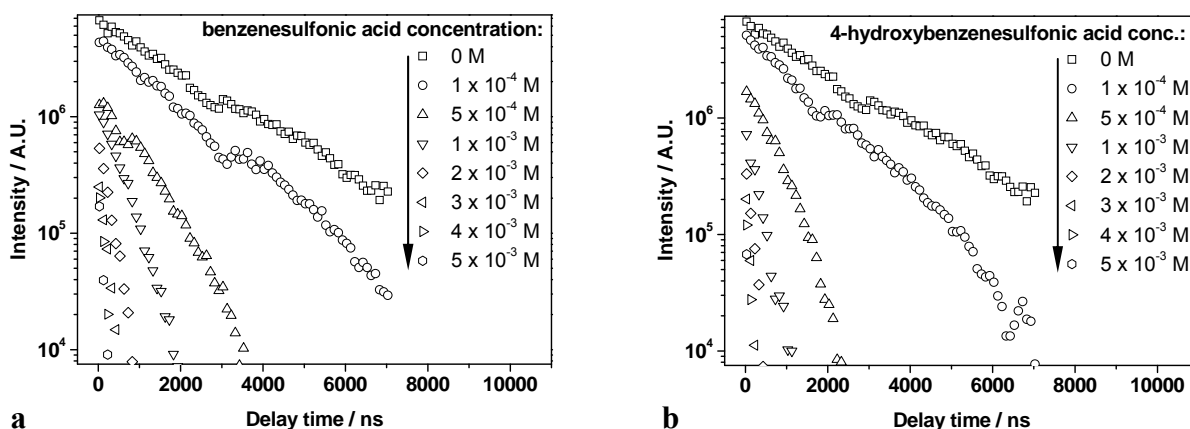


Fig. 2.27. Luminescence decay of U(VI) as a function of the ligand concentration (dynamic quenching).

In order to determine the complex stability constants, knowledge of the ligands pK_a values is necessary. In the case of BSA, the pK_a values reported in the literature for the sulfonate group vary in a wide range from -6.56 ± 0.06 (Cerfontain et al., 1975) to 2.554 (Dean, 1999). As shown by Joseph et al. (2008) using potentiometric titration the pK_a has to be significantly smaller than 0. Dong et al. (2009) assumed pK_a values for the sulfonate group of BSA and HBSA with -2.7 and -2, respectively. Thus, under the experimental conditions applied in this study, the sulfonate group at both ligands can be regarded as deprotonated. The pK_a of the hydroxyl group in HBSA is 8.56 ± 0.05 (Joseph et al., 2008), and therefore, it occurs in its protonated form. Thus, only the deprotonated sulfonate group has to be considered in a complex formation reaction (2.22).



Based on this reaction the following logarithmic form of the mass action law was obtained:

$$\log \frac{[\text{UO}_2\text{L}_n^{(2-n)+}]}{[\text{UO}_2^{2+}]} = n \cdot \log [\text{L}^-] + \log K \quad (2.23)$$

With the assumption that the corrected luminescence intensity I_0 is proportional to the concentration of the free U(VI) ion in equilibrium, the complex stoichiometry and the complex stability constant can be graphically determined via validation plot (Fig. 2.28). The slope (n) of this plot represents the stoichiometry of the formed complex, the intersection with the y-axis at $\log [L^-] = 0$ is equal to the equilibrium constant $\log K$.

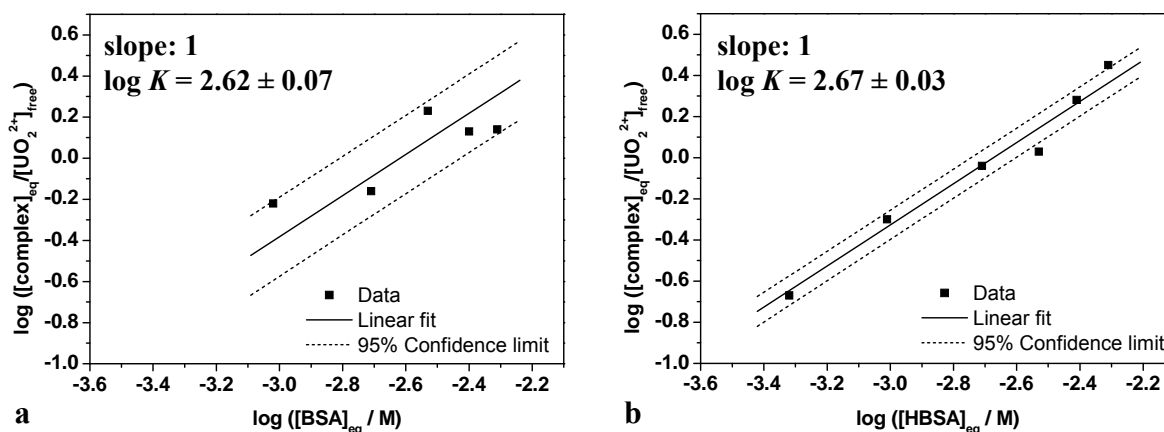


Fig. 2.28. Validation plot of the complexation of U(VI) with benzenesulfonic acid (a) and 4-hydroxybenzenesulfonic acid (b) at pH 2.4.

For both complex systems a slope close to 1 was calculated indicating the formation of a predominant 1:1 complex.

For low BSA concentrations (1×10^{-4} and 5×10^{-4} M), stability constants out of the confidence limit (95%) were calculated. Thus, they were not considered in the validation plot ($[\text{BSA}] = 1 \times 10^{-3}$ to 5×10^{-3} M). For the complexation of U(VI) by BSA, a 1:1 complex with a stability constant of $\log K = 2.62 \pm 0.07$ was determined. Joseph et al. (2008) did not observe a static quench in their TRLFS measurements, because the BSA concentrations used for their experiments were too low ($[\text{BSA}] = 1 \times 10^{-4}$ to 8×10^{-4} M). Thus, they concluded that there was no complexation of U(VI) by BSA.

For HBSA, the lowest ligand concentration of 1×10^{-4} M showed no static quench after dynamic quench correction. Thus, it was not considered in the validation plot (Fig. 2.28b). The stability constant for the formation of a 1:1 complex was determined to be $\log K = 2.67 \pm 0.03$. This value corroborates the stability constant of $\log K_{110} = 2.76 \pm 0.15$ determined by Joseph et al. (2008) using TRLFS with ultrafast pulses (fs-TRLFS).

The experimental results show that the sulfonate group of both ligands interacts with U(VI) with the same strength independent of the presence of an additional p-hydroxyl group at the aromatic compound.

However, compared to the interaction of U(VI) with oxygen functionalities of HA (Pompe et al., 2000b) the constants determined for the interaction of U(VI) with sulfonate groups are three orders of magnitude lower. Thus, complexation of U(VI) by oxygen functionalities will be preferred compared to sulfonate groups. This is in agreement with the results of Sachs and Bernhard (2010), discussed in section 3.2.2.

3 Complexation and redox reactions of actinides with humic substances

3.1 Spectroscopic characterization of the ternary U(VI) carbonate humate complex by cryo-TRLFS and ATR FT-IR

Knowledge of the actinide speciation in natural systems is of great importance for understanding of their transport behavior. The migration of actinides such as uranium in the environment is affected by complexation, sorption and redox processes, their solubility, as well as their ability to form colloids (Silva and Nitsche, 1995; Kim, 2006). The complexation of U(VI) with various inorganic and organic ligands and the consequences for the chemical speciation of U(VI) under environmentally relevant conditions has been studied thoroughly and data are summarized e.g. in (Guillaumont et al., 2003; Hummel et al., 2005). Besides low molecular weight organic ligands, humic substances (fulvic acids (FA) and humic acids (HA)), polyelectrolytic organic macromolecules, which occur in soils, sediments and waters, can influence the interaction behavior of actinides in the environment due to their complexing, sorption and redox properties and their ability for colloid formation (Kim, 1986; Choppin, 1992; Silva and Nitsche, 1995).

Under environmentally relevant conditions, actinide ions, such as UO_2^{2+} , can be complexed by HA. In previous studies, the formation of a binary ($\text{UO}_2\text{HA}(\text{II})$ (Czerwinski et al., 1994; Pompe et al., 1998; Montavon et al., 2000)) and a ternary ($\text{UO}_2(\text{OH})\text{HA}(\text{I})$ (Zeh et al., 1997; Sachs et al., 2007a; Pashalidis and Buckau, 2007)) complex of U(VI) with HA was described based on the metal ion charge neutralization model (CNM, (Kim and Czerwinski, 1996)). Complex stability constants determined for the $\text{UO}_2\text{HA}(\text{II})$ complex range from $\log \beta = 5.83 \pm 0.09$ (Montavon et al., 2000) to 6.33 ± 0.15 (Czerwinski et al., 1994) ($I = 0.1 \text{ M}$). For the ternary $\text{UO}_2(\text{OH})\text{HA}(\text{I})$ complex, complex stability constants were determined with 14.7 ± 0.5 (Zeh et al., 1997), 14.89 ± 0.54 (Sachs et al., 2007a) and 15.3 (Pashalidis and Buckau, 2007). Beside the binary humate complex, the ternary humate

complex can dominate the U(VI) speciation under weak acidic and near-neutral pH conditions in the presence of HA under carbonate-free conditions (Sachs et al., 2007a). However, in the presence of carbonate, the formation of ternary U(VI) carbonato humate complexes is assumed in the literature (Glaus et al., 1995) comparable to ternary Eu(III), Am(III) and Cm(III) carbonato humate (Dierckx et al., 1994; Panak et al., 1996) as also discussed in (McCarthy et al., 1998) and (Reiller, 2005). Furthermore, the potential formation of ternary actinide carbonato humate complexes was already discussed in sorption studies (Křepelová et al., 2006; Schmeide and Bernhard, 2010). Information on such complexes is necessary for a reliable description of the mobility of actinides under environmentally relevant conditions. Hence, the objective of this study was the direct spectroscopic identification and characterization of aqueous U(VI) humate complexes as function of pH and carbonate concentration by time-resolved laser-induced fluorescence spectroscopy at low temperature (cryo-TRLFS) and by attenuated total reflection Fourier-transform infrared (ATR FT-IR) spectroscopy. The results of the study are published in-depth by Steudtner et al. (2011a, 2011b).

3.1.1 Ternary U(VI) carbonato humate complex studied by cryo-TRLFS

3.1.1.1 Experimental

Complexation experiments were performed at a fixed U(VI) concentration of 1×10^{-5} M. The HA concentration was varied between 0 and 100 mg/L. The measurements were carried out at an ionic strength of 0.1 M. The pH values of the solutions were adjusted to pH 8.5 using diluted HClO₄ and NaOH solutions. For further experimental details see Steudtner et al. (2011a).

3.1.1.2 Results and discussion

Binary UO₂²⁺-CO₃²⁻ system

The binary UO₂²⁺-CO₃²⁻ system is used for evaluation of the measurement system at low temperature. The measured emission spectra of the HA-free samples in both series are characterized by five emission bands and the fluorescence decay can be described by a mono-exponential decay function (Table 3.1). The obtained fluorescence lifetimes and the positions of the emission bands are in very good agreement with literature data (Wang et al., 2004; Steudtner et al., 2010) for UO₂(CO₃)₃⁴⁻ (Table 3.1), since the UO₂(CO₃)₃⁴⁻ complex dominates the U(VI) speciation at pH 8.5 in the absence of HA.

Table 3.1. Band positions and fluorescence lifetime of the HA-free samples in comparison to literature data of $\text{UO}_2(\text{CO}_3)_3^{4-}$.

	Fluorescence emission (nm)					τ (μs)	T (K)	Reference
Series 1	480.7	499.9	520.3	542.5	566.6	834.1 ± 8.9	153	this work
Series 2	480.2	499.3	519.9	543.4	565.4	820.4 ± 11.8	153	this work
$\text{UO}_2(\text{CO}_3)_3^{4-}$	480.8	500.1	520.9	543.1	566.8	829.3 ± 13.5	153	(Steudtner et al., 2010)
$\text{UO}_2(\text{CO}_3)_3^{4-}$	479.6	499.2	519.9	542.4	565.5	883.6	6	(Wang et al., 2004)

Series 1: Ternary UO_2^{2+} -HA- CO_3^{2-} system – constant [U]

Figure 3.1 shows the luminescence spectra of U(VI) as a function of the HA concentration. A decrease of the U(VI) luminescence intensity is observed with increasing HA concentration. No shift in the peak maxima of the fluorescence emission bands is detected. At low temperature ($T = 153$ K) fluorescence quenching effects are suppressed (Wang et al., 2008; Wimmer et al., 2009). Thus, the decrease in the U(VI) luminescence intensity points to a complexation between $\text{UO}_2(\text{CO}_3)_3^{4-}$ and HA forming a non-fluorescent U(VI) carbonato humate species. Also the binary $\text{UO}_2\text{HA}(\text{II})$ complex (Pompe et al., 2000b) and the ternary $\text{UO}_2(\text{OH})\text{HA}(\text{I})$ complex (Sachs et al., 2007a) do not show individual fluorescence signals.

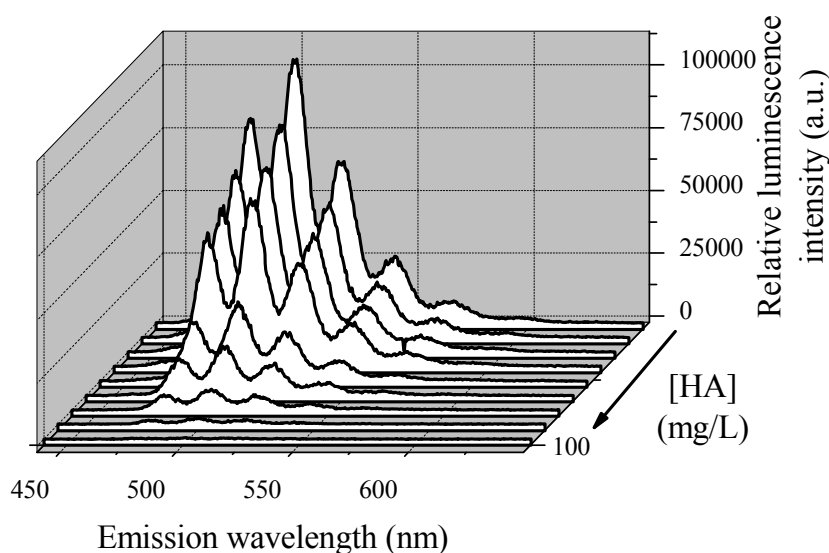


Fig. 3.1. U(VI) luminescence spectra ($t = t_0$) as a function of the HA concentration at pH 8.5 ($[\text{U}(\text{VI})]_{\text{tot}} = 1 \times 10^{-5}$ M, $[\text{HA}]_{\text{tot}} = 0 - 100$ mg/L, $I = 0.1$ M (NaClO_4), $T = 153$ K, $p\text{CO}_2 = 10^{-3.5}$ atm).

Based on the measured fluorescence spectra, the complex stability constant of the U(VI) carbonato humate complex is calculated applying the complexation models mentioned above. The obtained complex stability constants are summarized in Table 3.2. Within the experimental uncertainties, the $\log K$ values agree very well. By slope analysis (Fig. 3.2) a slope of 1.12 ± 0.11 is obtained. This value verifies the assumed ligand exchange reaction for the complex formation.

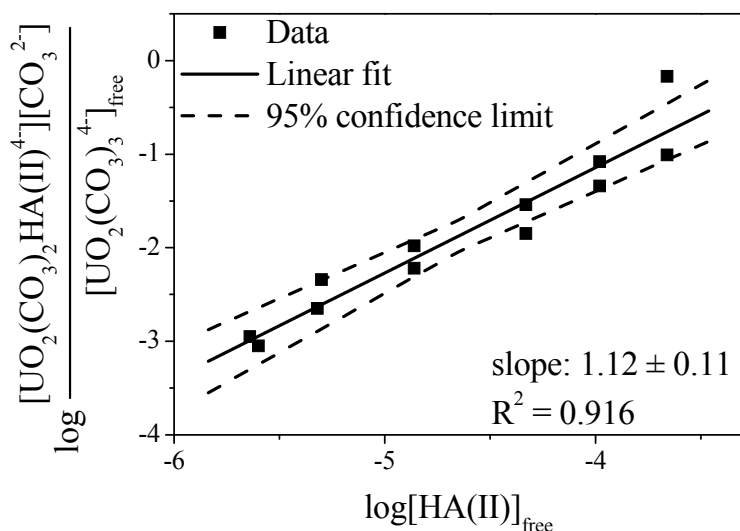


Fig. 3.2. Slope analysis for the complexation of U(VI) with HA at pH 8.5 ($[\text{U}(\text{VI})]_{\text{tot}} = 1 \times 10^{-5}$ M, $[\text{HA}]_{\text{tot}} = 0 - 100$ mg/L, $I = 0.1$ M (NaClO_4), $T = 153$ K, $p\text{CO}_2 = 10^{-3.5}$ atm).

Series 2: Ternary UO_2^{2+} -HA- CO_3^{2-} system – constant [HA]

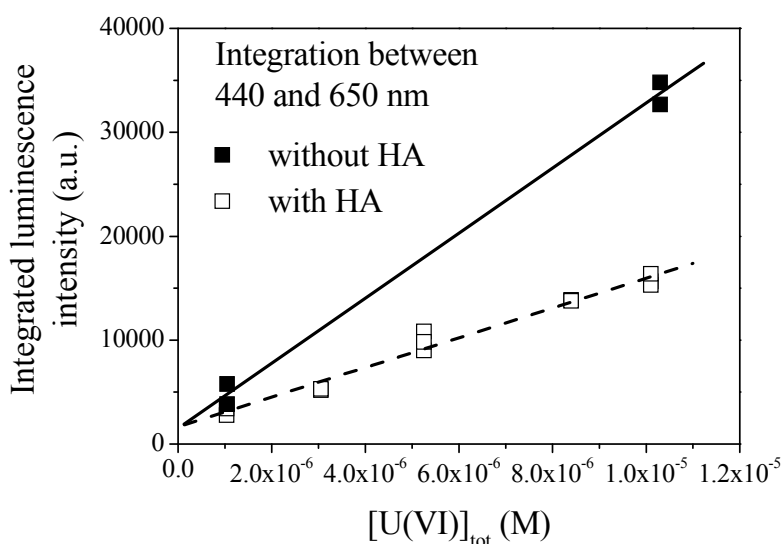


Fig. 3.3. Integrated luminescence intensity of U(VI) as a function of the U(VI) concentration in the absence and presence of HA at pH 8.5. ($[\text{U}(\text{VI})]_{\text{tot}} = 1 \times 10^{-6} - 1 \times 10^{-5}$ M, $[\text{HA}]_{\text{tot}} = 2$ mg/L, $I = 0.1$ M (NaClO_4), $T = 153$ K, $p\text{CO}_2 = 10^{-3.5}$ atm).

In agreement to series 1, the U(VI) luminescence spectra of series 2 obtained in the absence and presence of HA exhibit the luminescence characteristics of the $\text{UO}_2(\text{CO}_3)_3^{4-}$ complex. The fluorescence lifetime and the position of the emission bands are in very good agreement with series 1 and literature data, cf. Table 3.1.

The integrated luminescence intensity of U(VI) as a function of the U(VI) concentration in the absence and presence of HA is depicted in Fig. 3.3. With increasing U(VI) concentration the U(VI) luminescence intensity increases linearly in the absence and presence of HA. The U(VI) luminescence intensity determined for the U(VI)-HA system is lower than that determined for the HA-free system. This can be attributed to a static fluorescence quenching process due to the complex formation. For all experiments no shift of the main emission bands and no changes in the fluorescence lifetimes are observed, which verifies the assumption of static fluorescence quenching and excludes the occurrence of dynamic quenching effects. The formed U(VI) carbonato humate complex does not show any fluorescence in the considered wavelength range, which corresponds to the results of series 1. The complex stability constants determined for the $\text{UO}_2(\text{CO}_3)_2\text{HA}(\text{II})^{4-}$ complex by mathematical analysis and by the multivariate data analysis program SPECFIT amount to $\log K = 2.97 \pm 0.26$ and $\log K = 2.56 \pm 0.41$ ($\log \beta_{\text{SPECFIT}} = 24.30 \pm 0.41$), respectively. The results agree very well with the data obtained from series 1 (Table 3.2).

Table 3.2. Complex stability constants obtained for the formation of $\text{UO}_2(\text{CO}_3)_2\text{HA}(\text{II})^{4-}$ ($I = 0.1 \text{ M (NaClO}_4)$).

$\text{UO}_2(\text{CO}_3)_3^{4-} + \text{HA}(\text{II}) \rightleftharpoons \text{UO}_2(\text{CO}_3)_2\text{HA}(\text{II})^{4-} + \text{CO}_3^{2-}$		$\log K$
Series 1 – constant [U]	mathematical analysis	2.98 ± 0.17
	SPECFIT	2.82 ± 0.09
Series 2 – constant [HA]	mathematical analysis	2.97 ± 0.26
	SPECFIT	2.56 ± 0.41
Mean		2.83 ± 0.17

The complex stability constants for the $\text{UO}_2(\text{CO}_3)_2\text{HA}(\text{II})^{4-}$ complex, compiled in Table 3.2, range from $\log K = 2.56 \pm 0.41$ to $\log K = 2.98 \pm 0.17$. The average formation constant is calculated with $\log K = 2.83 \pm 0.17$ for an ionic strength of 0.1 M. The brutto stability

constant for the reaction of the single components determined by SPECFIT amounts to $\log \beta_{\text{SPECFIT}} = 24.57 \pm 0.17$ ($\text{UO}_2^{2+} + 2\text{CO}_3^{2-} + \text{HA(II)} \rightleftharpoons \text{UO}_2(\text{CO}_3)_2\text{HA(II)}^{4-}$).

3.1.2 Binary and ternary U(VI) humate complexes studied by ATR FT-IR

3.1.2.1 Experimental

Complexation experiments were performed at a fixed U(VI) concentration of 1×10^{-3} M. The HA concentration was kept constant at 1 g/L. The measurements were carried out at an ionic strength of 0.1 M. The pH values of the solutions were titrated between pH 10 and 2 using diluted HClO_4 and NaOH solutions. For further experimental details see Steudtner et al. (2011b).

3.1.2.2 Results and discussion

U(VI) speciation in the presence of humic acid

For U(VI) speciation calculations in the presence of HA, the geochemical speciation code EQ3/6 (Wolery, 1992) modified for HA calculation (Sachs et al., 2004) was used applying the currently accepted thermodynamic data for U(VI) compiled in (Guillaumont et al., 2003), as well as complex stability constants and loading capacities (LC) for $\text{UO}_2\text{HA(II)}$ (Montavon et al., 2000; Pompe et al., 2000a, 2000b) and $\text{UO}_2(\text{OH})\text{HA(I)}$ (Sachs et al., 2007a). The LC represents the mole fraction of complexing sites of a HA accessible for metal ion complexation under the given experimental conditions (Kim and Czerwinski, 1996). The pH-dependency of the LC was calculated from the literature data by linear regression resulting in Eq. (3.1).

$$\text{LC} = -0.555 + 0.186 \cdot \text{pH} \quad (3.1)$$

The pH-dependent U(VI) speciation in the presence of HA is shown in Fig. 3.4 for experimental conditions applied in this study. The speciation pattern shows the free UO_2^{2+} ion as the predominant species below pH 3.0. Upon increasing pH from 3.0 to 4.0, the fraction of UO_2^{2+} decreases with the start of complexation of U(VI) by HA. Under the considered conditions, the binary $\text{UO}_2\text{HA(II)}$ complex and the ternary $\text{UO}_2(\text{OH})\text{HA(I)}$ complex dominate the U(VI) speciation in the pH range between 3.5 and 7.5 with maxima at pH 4.2 and 6.5, respectively. Above pH 7.5, the U(VI) speciation is dominated by the U(VI) carbonate species $(\text{UO}_2)_2\text{CO}_3(\text{OH})_3^-$ and $\text{UO}_2(\text{CO}_3)_3^{4-}$. UO_2Cl^+ and $\text{UO}_2(\text{CO}_3)_2^{2-}$ contribute less than 5% to the U(VI) speciation under the chosen conditions (Fig. 3.4). It should be noted that the

OECD/NEA Chemical Thermodynamics Database (Guillaumont et al., 2003) predicts further U(VI) species, e.g. chloro, oligomeric hydroxo and carbonate complexes, which are not shown in Fig. 3.4 for clarity since their contribution is less than 1%.

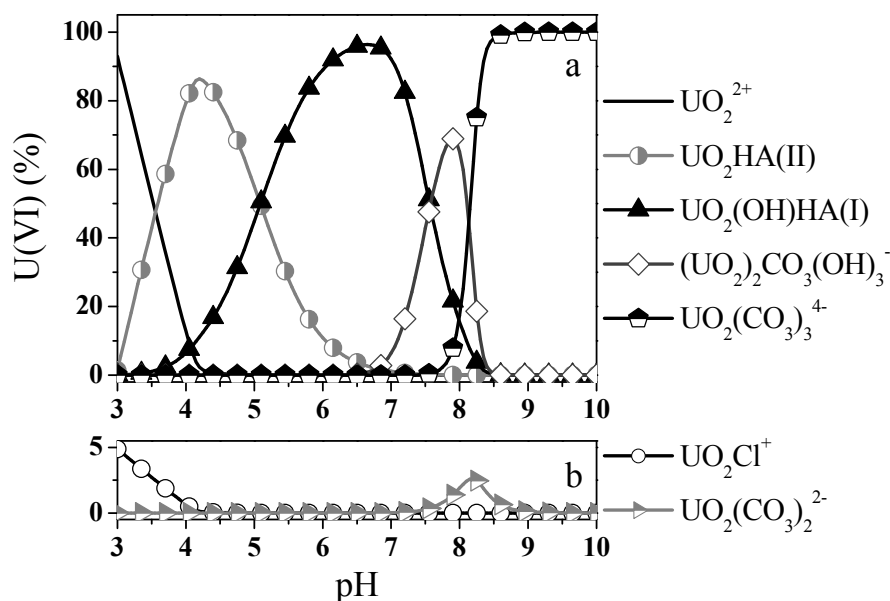


Fig. 3.4. Speciation of U(VI) in the presence of HA ($[\text{U(VI)}] = 1 \text{ mM}$, $[\text{HA}]_{\text{tot}} = 1 \text{ g/L}$, $I = 0.1 \text{ M}$ (NaCl), $p\text{CO}_2 = 10^{-3.5} \text{ atm}$). U(VI) species below 1% are not plotted.

FT-IR spectroscopy of U(VI) humate solutions as a function of pH value

ATR FT-IR spectroscopy can be applied for the identification of molecular species in aqueous solution. Previous investigations have shown the sensitivity of the UO_2 asymmetric stretching mode (ν_3) to changes in the coordination environment (Lefevre et al., 2008; Müller et al., 2008; Müller et al., 2009). Complexation of UO_2^{2+} weakens the O=U=O bonds, increases bond lengths and causes shifts to lower frequencies of $\nu_3(\text{UO}_2)$. The extent of these shifts is related to the stability of the U(VI) ligand interaction. This sensitivity allows the use of this mode as a marker for specific molecular information on coordination of UO_2^{2+} in aqueous solution. Further molecular information on complexation reactions can also be obtained from the vibrational modes of the inorganic or organic ligand. For instance, the carbonate ion can be coordinated in a mono or a bidentate configuration with metal ions, resulting in a reduction of the symmetry of the free carbonate ion with D_{3h} to C_{2v} . Then, the band of the IR active $\nu_3(\text{CO}_3^{2-})$ is split into an asymmetric and a symmetric band. From the magnitude of splitting, coordination can be elucidated, e.g. for a bidentate coordination a higher splitting is observed than for monodentate coordination (Jolivet et al., 1980).

The results of the spectrophotometric titrations of aqueous solutions of 1 mM U(VI) and 1 g/L HA at two different carbonate concentrations are depicted in Fig. 3.5. The titrations were

performed starting from pH 10 down to an acidic pH level. The spectra shown in Fig. 3.5 were obtained from solutions prepared under ambient atmosphere ($p\text{CO}_2 = 10^{-3.5}$ atm). In comparison, Fig. 3.5 represents the data derived from solutions prepared under N_2 atmosphere. Since the ATR FT-IR measurements were performed at ambient atmosphere, carbonate could not be completely excluded. These solutions contain a significantly reduced amount of carbonate ($p\text{CO}_2 = 10^{-5.5}$ atm). The IR data exhibit different spectral features as a function of pH. The band in the range from 970 to 870 cm^{-1} is assigned to the antisymmetric stretching vibrational mode (ν_3) of the UO_2^{2+} unit (Quiles and Burneau, 2000). A comparison of both series shows very similar results at acidic pH values (< 6). In contrast, the U(VI) complexation behavior strongly differs at higher pH values (> 6), where carbonate influences the speciation.

At ambient atmosphere, the IR spectra obtained in the pH range from 9.2 to 7.4 show absorption of $\nu_3(\text{UO}_2)$ at 895 cm^{-1} and two strong bands at 1503 and 1386 cm^{-1} (Fig. 3.5). These bands are assigned to the asymmetric and symmetric stretching vibrations of bidentate complexed carbonate, respectively (Bargar et al., 2000). The spectra obtained in the pH range from 9.2 to 7.4 are contradictory to the recently accepted thermodynamic data shown in Fig. 3.4. The U(VI) speciation show the predominance of the $\text{UO}_2(\text{CO}_3)_3^{4-}$ complex only at $\text{pH} > 8.5$. However, the spectra are dominated by carbonate complexed U(VI) up to $\text{pH} 7.4$. In addition, a smaller blue shift of $\nu_3(\text{UO}_2)$ compared to the $\text{UO}_2(\text{CO}_3)_3^{4-}$ model spectrum (Müller et al., 2008) is detected. The spectral data at high pH (Fig. 3.5) provide an indication for a change of the U(VI) carbonate speciation in the presence of HA possibly due to the formation of a ternary U(VI) carbonate humate complex and can not clearly be resolved at this state of knowledge.

Upon decreasing pH to 6.8, the U(VI) speciation changes which becomes obvious from the hypsochromic shift of $\nu_3(\text{UO}_2)$ to 914 cm^{-1} and from the decreasing intensity of the carbonate modes. In addition, further bands at 1523 and 1460 cm^{-1} are observed in the spectrum at pH 6.8, which are in agreement with bands previously reported as intrinsic optical absorption properties of aqueous U(VI) species containing hydroxyl groups (Müller et al., 2009). From comparison of the spectrum at pH 6.8 with the spectrum obtained at pH 7.2 in the titration series with the strongly reduced carbonate concentration (cf. Fig. 3.5) it might be conceivable that very similar complexes with absorption of $\nu_3(\text{UO}_2)$ at about 912 cm^{-1} are formed. The thermodynamic data predict a formation of the $\text{UO}_2(\text{OH})\text{HA}(\text{I})$ complex for those near neutral pH conditions (cf. Fig. 3.4).

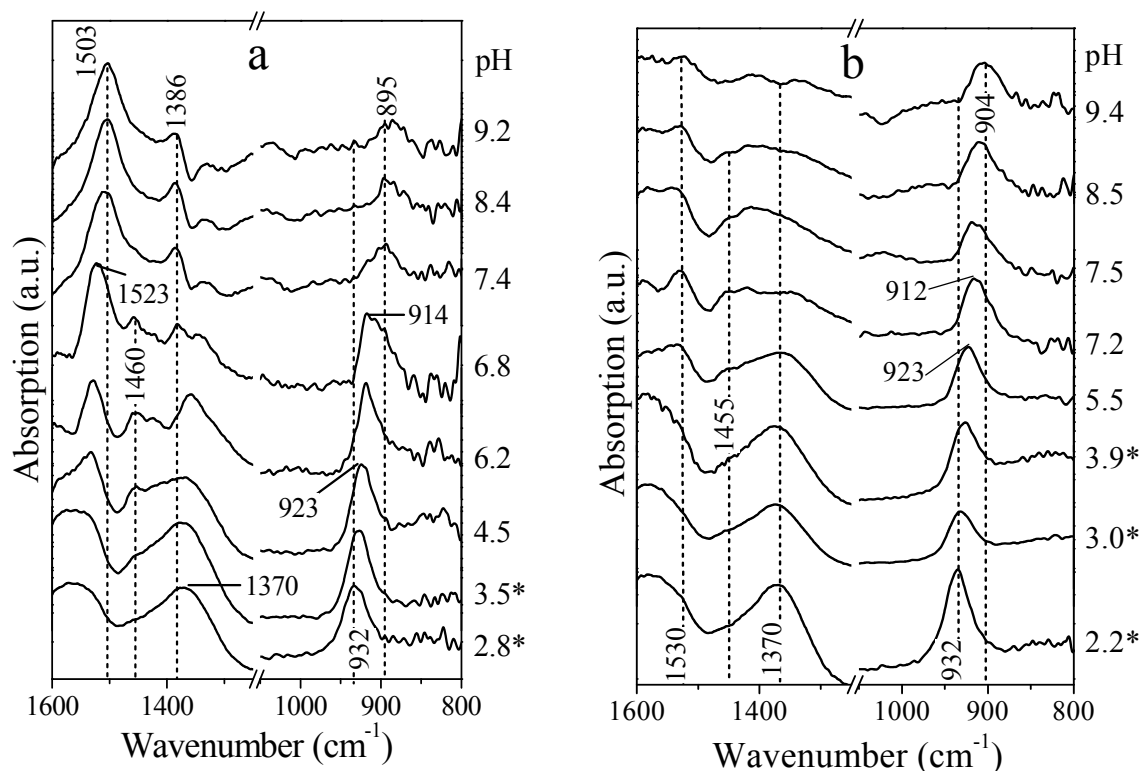


Fig. 3.5. Infrared spectra of U(VI) humate solutions as function of carbonate content and pH value ($[U(VI)] = 1 \text{ mM}$, $[HA]_{\text{tot}} = 1 \text{ g/L}$, $I = 0.1 \text{ M}$ (NaCl)): at ambient atmosphere ($p\text{CO}_2 = 10^{-3.5} \text{ atm}$) (a) and at reduced carbonate concentration ($p\text{CO}_2 = 10^{-5.5} \text{ atm}$) (b). *Between pH 2.2 and 3.9 suspended precipitates were measured.

Since no differences between both titration systems could be detected upon further decreasing the pH level below 6.0, a combined discussion of the results can be provided. An increasing acidity of the solutions results in further changes in the U(VI) speciation. The $\nu_3(\text{UO}_2)$ band indicates the transfer from one U(VI) species with absorption at about 914 cm^{-1} to another with absorption maximum at about 923 cm^{-1} between pH 4.5 and 5.5. This species can be attributed to the binary humate complex $\text{UO}_2\text{HA(II)}$ which is supported by the thermodynamic data (cf. Fig. 3.4).

A brown precipitate was formed in the solution at a very acidic pH level ($\text{pH} < 4.0$). At pH 1.1 the solid species was separated from the solution by centrifugation. The spectrum of the supernatant exhibited one band with absorption maximum of $\nu_3(\text{UO}_2)$ at 961 cm^{-1} which is assigned to the fully hydrated UO_2^{2+} cation (Müller et al., 2008; Quiles and Burneau, 2000). In the spectra of the suspended precipitate obtained between pH 2.2 and 3.9, one single peak with a maximum at 932 cm^{-1} was observed. This absorption band is in very good agreement with data published by Schmeide et al. (2003). In this work a solid U(VI) humate species was precipitated at pH 2. Its characterization by infrared spectroscopy showed one band centered

at 934 cm⁻¹. In the present work the presence of precipitates in the U(VI) humate solutions at pH higher than 4.0 was ruled out by application of PCS and ultracentrifugation.

$$[HA(II)] = LC \times \frac{PEC \times HA}{z} \quad (\text{Kim and Czerwinski, 1996}) \quad (3.2)$$

[HA(II)] ...concentration of HA in mol/L

LC ...loading capacity calculated based on Eq. (3.1)

PEC ...proton exchange capacity ((4.60×10⁻³ eq/g) (Pompe et al., 2000a))

HA ...concentration of HA in g/L

z ...charge of complexing metal ion

Determination of complex formation constants for the U(VI) humate system

For the first time, multiwavenumber infrared spectroscopic data are applied for the calculation of complex stability constants. The quantitative analysis was carried out applying the data analysis program SPECFIT (Gampp et al., 1985; Binstead et al., 2005). The signal of the antisymmetric (ν_3) stretching vibration of the UO₂²⁺ unit between 870 and 1000 cm⁻¹ was used for analysis. As initial data the U(VI) concentration (ICP-MS), total inorganic carbon content (TIC), the HA concentration (based on Eq. (3.2) (Kim and Czerwinski, 1996)), the pK values of carbonate and the stability constants (log $\beta_{0.1M}$) of the relevant U(VI) hydroxide complexes (UO₂OH⁺, (UO₂)₂(OH)₂²⁺, (UO₂)₃(OH)₅⁺, (UO₂)₄(OH)₇⁺), carbonate complexes (UO₂CO_{3(aq)}, UO₂(CO₃)₂²⁻, UO₂(CO₃)₃⁴⁻) and of the mixed hydroxo carbonate complex ((UO₂)₂CO₃(OH)₃⁻), taken from Guillaumont et al. (2003), were imported into the program. From the variations in the infrared spectra as a function of pH, stability constants for the U(VI) humate complexation were calculated using the following procedure.

Based on relevant complexation studies of HA with actinides and lanthanides, possible U(VI) humate species of the type M_xHA_y or M_xL_zHA_y with L representing OH⁻ or CO₃²⁻ were introduced in the data analysis program. SPECFIT performs a global analysis of the equilibrium system with singular value decomposition and non-linear regression modeling by the Levenberg–Marquardt method. The analysis of the present data was conducted for different species compositions of the formed complexes. The best modulation represents a minimum of the residual spectra of the imported data in combination with a realistic model for the complexation reaction. Four different species could be detected in the U(VI) humate systems under the experimental conditions applied in this study. For each aqueous complex the stability constant and the single component spectrum were successfully extracted. The results of the SPECFIT analyses are summarized in Table 3.3.

Table 3.3. Calculated complex formation constants and band maxima of the antisymmetric stretching vibration of U(VI) humate complexes in comparison to literature data.

#	U(VI) humate species	[U(VI)]	$\log \beta_{0.1 \text{ M}}$	$\nu_3(\text{UO}_2)$ (cm^{-1})	Reference
(1)	$\text{UO}_2\text{HA(II)}^*$	1 mM	---	932	(Steudtner et al., 2011b)
		0.1 M	---	934	(Schmeide et al., 2003)
(2)	$\text{UO}_2^{2+} + \text{HA(II)} \rightleftharpoons \text{UO}_2\text{HA(II)}$	1 mM	6.70 ± 0.25	925	(Steudtner et al., 2011b)
		0.5 mM	6.20 ± 0.56	---	(Pompe et al., 2000b)
(3)	$\text{UO}_2^{2+} + \text{OH}^- + \text{HA(I)} \rightleftharpoons \text{UO}_2(\text{OH})\text{HA(I)}$	1 mM	15.14 ± 0.25	913	(Steudtner et al., 2011b)
		< 0.01 mM	14.89 ± 0.54	---	(Sachs et al., 2007a)
		solid	15.3	---	(Pashalidis and Buckau, 2007)
(4)	$\text{UO}_2^{2+} + 2 \text{CO}_3^{2-} + \text{HA(II)} \rightleftharpoons \text{UO}_2(\text{CO}_3)_2\text{HA(II)}^{4-}$	1 mM	24.47 ± 0.70	895	(Steudtner et al., 2011b)
		< 0.01 mM	24.57 ± 0.17	---	(Steudtner et al., 2011a)
(5)	$\text{UO}_2\text{FA} + \text{CO}_3^{2-} \rightleftharpoons \text{UO}_2\text{FACO}_3$	n/a	$5.0 (I=0.3 \text{ M})$	---	(Glaus et al., 1995)

*solid

The formation constants $\log \beta$ for aqueous $\text{UO}_2\text{HA(II)}$ and $\text{UO}_2(\text{OH})\text{HA(I)}$ at an ionic strength of 0.1 M were calculated to be 6.70 ± 0.25 and 15.14 ± 0.25 , respectively. These values are in very good agreement with data determined by Pompe et al. (2000b) and Sachs et al. (2007a) by means of TRLFS and by Pashalidis and Buckau (2007) by solubility measurements. The complex formation constant determined for the aqueous complex $\text{UO}_2(\text{CO}_3)_2\text{HA(II)}^{4-}$ with $\log \beta_{0.1 \text{ M}} = 24.47 \pm 0.70$ is in very good agreement with the value obtained from cryo-TRLFS measurements as reported by Steudtner et al. (2011a). Thus, the formation of a mixed U(VI) carbonato fulvate (UO_2FACO_3) complex which was only described by Glaus et al. (1995), can not be confirmed in our studies, neither by ATR FT-IR nor by cryo-TRLFS. In contrast, we identified a reaction between one UO_2^{2+} ion, two carbonate ions and one humate unit according to Eq. 4 in Table 3.3, thus, forming the ternary $\text{UO}_2(\text{CO}_3)_2\text{HA(II)}^{4-}$ complex. A comparable mixed complexation reaction with humate and carbonate as a second ligand was already described for Eu(III) by Dierckx et al. (1994), who detected the formation of a ternary $\text{Eu}(\text{CO}_3)_2\text{HA(I)}$ complex in solution.

The normalized single component spectra of the different complexes formed in the U(VI) humate carbonate system, derived by mathematical deconvolution of the mixed infrared spectra are presented in Fig. 3.6. It should be noted, that the bands of $\nu_3(\text{UO}_2)$ are rather broad and at this state of knowledge a contribution of further species to the FT-IR signal can not be

ruled out completely. Generally, a reduced absorption can be derived for the ternary complexes compared to the binary complexes from the obtained data.

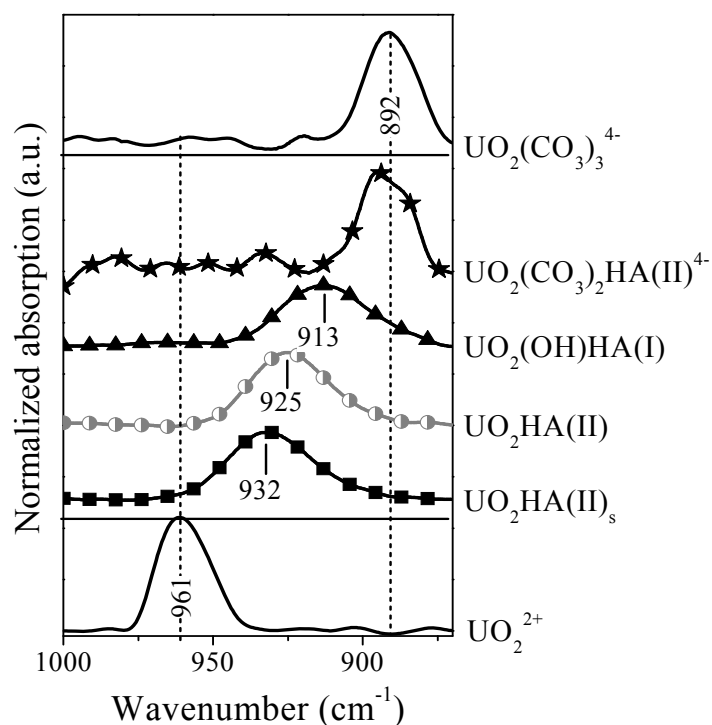
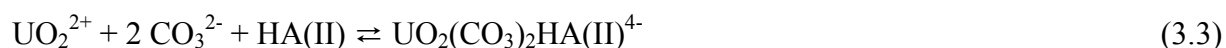


Fig. 3.6. Normalized single component IR spectra of different U(VI) species resulting from peak deconvolution with SPECFIT ([U(VI)] = 1 mM, [HA]_{tot} = 1 g/L, I = 0.1 M (NaCl)). The model spectra of UO₂²⁺ and UO₂(CO₃)₃⁴⁻ are taken from (Müller et al., 2008).

3.1.3 Conclusion

For the first time, the complexation between U(VI) and HA in the presence of carbonate was studied applying cryo-TRLFS and ATR FT-IR spectroscopy. In both studies, the formation of the ternary U(VI) carbonato humate complex UO₂(CO₃)₂HA(II)⁴⁻ was observed and the complex formation reaction of U(VI) carbonato humate complex can be written in general as:



The complex stability constant for the UO₂(CO₃)₂HA(II)⁴⁻ complex is calculated with $\log \beta_{0.1 \text{ M}} = 24.57 \pm 0.17$. The result of the slope analysis with a slope of 1.12 ± 0.11 verifies the postulated ligand exchange reaction. In addition, IR spectroscopy was used to validate the complex formation constant of the ternary U(VI) carbonato humate complex. From the variations in the IR spectra as a function of pH, stability constants for the U(VI) humate complexation were calculated. The obtained complex stability constant of $\log \beta_{0.1 \text{ M}} = 24.47 \pm 0.70$ for the UO₂(CO₃)₂HA(II)⁴⁻ complex validated the constant measured

by cryo-TRLFS. In addition, the formation constants $\log \beta$ for aqueous $\text{UO}_2\text{HA}(\text{II})$ and $\text{UO}_2(\text{OH})\text{HA}(\text{I})$ at an ionic strength of 0.1 M were calculated with 6.70 ± 0.25 and 15.14 ± 0.25 , respectively. These values are in very good agreement with data determined by TRLFS (Pompe et al., 2000b; Sachs et al., 2007a) and by solubility measurements (Pashalidis and Buckau, 2007).

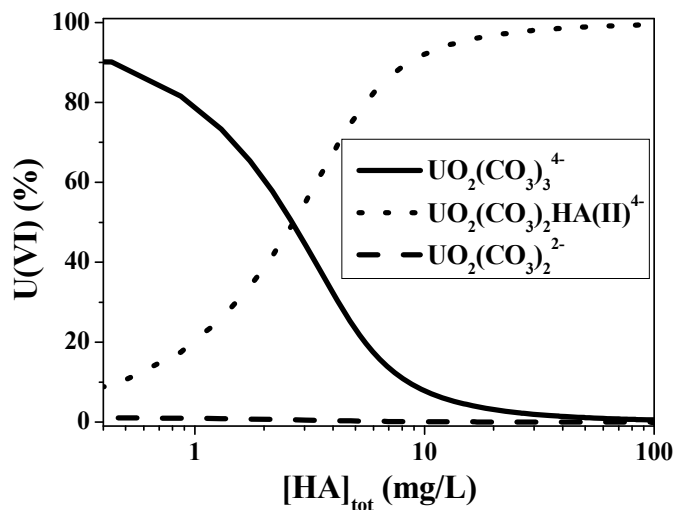


Fig. 3.7. Revised U(VI) species distribution at pH 8.5 in the presence of CO_2 and HA as a function of the HA concentration ($[\text{U}(\text{VI})]_{\text{tot}} = 1 \times 10^{-5}$ M, $I = 0.1$ M (NaClO_4), $p\text{CO}_2 = 10^{-3.5}$ atm).

Using the complex formation constant determined for the ternary U(VI) carbonato humate complex, the species distribution of U(VI) was recalculated for the experimental conditions applied in this study. The revised U(VI) speciation in the presence of CO_2 and HA is shown in Fig. 3.7. Up to an environmentally relevant HA concentration of 2 mg/L (Gaffney et al., 1996) the U(VI) species distribution is dominated by the $\text{UO}_2(\text{CO}_3)_3^{4-}$ complex. Above 2 mg/L the $\text{UO}_2(\text{CO}_3)_2\text{HA}(\text{II})^{4-}$ complex becomes increasingly important. It can be concluded that in the presence of HA the formation of the ternary U(VI) carbonato humate complex can significantly influence the U(VI) speciation under environmental conditions. This result is similar with previous studies with regard to the formation of ternary lanthanide or actinide carbonato humate complexes (Dierckx et al., 1994; Panak et al., 1996).

3.2 Influence of sulfur functionalities on the interaction behavior of humic acids with actinide ions

Humic substances (humic and fulvic acids) exhibit different amounts of sulfur depending on their origin. For instance, soil and aquatic humic substances are characterized by 0.1-3.6 and

0.5-1.43 wt.% sulfur, respectively (Xia et al., 1998). For humic acids (HA), sulfur contents ranging from, e.g., 0 to 2 wt.% were reported (Stevenson, 1982). Sulfur occurs in humic substances in multiple oxidation states in form of oxidized (sulfonates, ester-bonded sulfates, sulfonic acids, sulfones, sulfoxides) and reduced (thiols, sulfides, di- and polysulfides, thiophenes) organic sulfur functionalities (e.g., Vairavamurthy et al., 1997; Xia et al., 1998; Olivella et al., 2002). These functionalities occur in different proportions caused by the different sources of humic substances but also by the method used for isolation of the humic material (e.g., Xia et al., 1998; Hutchison et al., 2001).

Although the complexation behavior of HA is mainly attributed to carboxylic and phenolic OH groups, sulfur containing ligands which are less abundant in HA can complex metal ions. They play a role in complexing trace metals, e.g., Cd, Co, Ni, Pb, and Hg (Xia et al., 1998), which are classified as soft acids or borderline metals by Pearson's theory (Pearson, 1963). Extended X-ray absorption fine structure spectroscopic studies of the binding environment of Zn(II) (Xia et al., 1997) and Hg(II) (Xia et al., 1999; Hesterberg et al., 2001) complexed with humic substances reveal the involvement of reduced sulfur functionalities such as thiols, disulfides, polysulfides, and disulfanes in the complexation. Although actinide ions like UO_2^{2+} are classified as hard acids according to Pearson's theory, there is a possibility that their complexation behavior toward organic ligands is influenced by sulfur functionalities, such as thiols, classified as soft bases. There are references which document the role of thiol groups for the stabilization of U(VI) cysteine complexes (Raghavan and Santappa, 1970) and the involvement of thiol groups in the complexation of U(VI) with thiosalicylic acid (Raghavan and Santappa, 1970 and 1973). The stabilization of U(VI) cysteine complexes by thiol groups can further be deduced from Günther et al. (2007), who studied the complexation of U(VI) with L-cysteine in comparison to glycine.

In contrast, the redox activity of humic substances has been primarily ascribed to the reversible hydroquinone/quinone redox couple with semiquinone-type free radicals as significant electron donor/acceptor intermediate species (e.g., Lovley et al., 1996; Scott et al., 1998; Cory and McKnight, 2005; Aeschbacher et al., 2011). Furthermore, it is ascribed to the oxidation of phenolic OH groups to phenoxy radicals (e.g., Helburn and MacCarthy, 1994; Rocha et al., 2003; Schmeide and Bernhard, 2009; Sachs and Bernhard, 2011a) with their subsequent reactions, such as coupling reactions and tautomerizations (Musso, 1967), leading to a regeneration of phenolic OH groups. In addition, reduced forms of organically bound sulfur present in natural organic matter have been proposed as potential redox-active groups (Szulczewski et al., 2001; Fimmen et al., 2007; Ratasuk and Nanny, 2007). By means of

XANES spectroscopy, it could be shown that a thiol/disulfide redox couple is involved in the Cr(VI) reduction by humic substances in chromium-contaminated soils analog to the Cr(VI) reduction by simple thiol containing compounds such as cysteine and glutathione (Szulczewski et al., 2001). Thus, it is to check whether or not sulfur functional groups in humic substances act as redox-active functional units also toward actinides such as Np(V). In the present project, the role of sulfur functionalities of HA for the U(VI) complexation and Np(V) reduction in aqueous solution was studied. For that synthetic HA model substances with varying sulfur contents were synthesized based on the melanoidin concept (e.g., Sachs and Bernhard, 2011b). The studies performed and their results, which are described in the following sections, are published in-depth by Sachs et al. (2010) and Schmeide et al. (2012a).

3.2.1 Synthesis and characterization of sulfur containing humic acid model substances

3.2.1.1 Synthesis

Sulfur containing HA model substances with varying amounts of sulfur (type M1-S) were synthesized according to HA type M1 (Pompe et al., 1996) using D(+)-xylose (>99%, Fluka, Taufkirchen, Germany), glycine (99%, Aldrich, Steinheim, Germany), L-phenylalanine (for biochemistry, Merck), and L-cysteine (for biochemistry, Merck) as precursors. In order to ensure constant molar amino acid concentrations in the reaction mixtures, the glycine concentration in the reaction mixtures was decreased for the same amount as the L-cysteine concentration was increased. Table 3.4 summarizes the composition of the reaction mixtures for the syntheses of HA type M1-S with varying amounts of sulfur. For comparison, sulfur free synthetic HA type M1 was synthesized under identical conditions in the absence of L-cysteine. The synthesis procedure is described in detail in (Sachs et al., 2010).

Table 3.4. Reaction mixtures for the synthesis of HA type M1 and M1-S (Sachs et al., 2010).

	M1 (He4/07-A1)	M1-S-1 (He4/07-A2)	M1-S-2 (He3/08-A3)	M1-S-3 (He2/09-A4)
D(+)-xylose (g)	3.4	3.4	3.4	3.4
L-phenylalanine (g)	1.0	1.0	1.0	1.0
Glycine (g)	0.500	0.340	0.156	0
L-cysteine (g)	0	0.250	0.550	0.807
H ₂ O (mL)	8	8	8	8

3.2.1.2 Characterization

Elemental composition and functional group contents

Table 3.5 summarizes the results of the elemental analysis as well as of the determination of functional groups (Sachs et al., 2010; Schmeide et al., 2012a). The synthetic products exhibit an elemental composition close to that of natural HA. Due to the use of increasing amounts of cysteine for the synthesis, the sulfur content of the HA is increased from 0 to 6.9 wt.%.

The synthetic products exhibit low proton exchange capacities (PEC) and carboxylic group contents. However, HA with low amounts of functional groups are also found in nature. With increasing initial cysteine concentration in the starting materials and thus, with increasing sulfur content of the HA, PEC and carboxylic group content are increased. The phenolic/acidic OH group content of all synthetic HA is nearly the same. HA type M1 shows an apparent dissociation constant (pK_{app}) comparable to natural HA. With increasing sulfur content of the HA from 0 to 3.9 wt.%, the pK_{app} values are decreased, indicating an increase in the acidic strength of the materials. Under consideration of the experimental error, a further increase of the sulfur content to 6.9 wt.% does not affect pK_{app} .

Table 3.5. Characterization of synthetic HA type M1 and M1-S (Sachs et al., 2010; Schmeide et al., 2012a).

HA	Elemental composition				
	C (wt.%)	H (wt.%)	N (wt.%)	S (wt.%)	O (wt.%)
M1	59.8 ± 0.1	5.4 ± 0.1	5.2 ± 0.1	0	29.5 ± 0.2
M1-S-1	61.3 ± 0.1	5.4 ± 0.1	4.9 ± 0.1	1.9 ± 0.1	26.6 ± 0.1
M1-S-2	59.2 ± 0.3	5.2 ± 0.1	4.6 ± 0.1	3.9 ± 0.1	27.1 ± 0.3
M1-S-3	60.1 ± 0.1	5.5 ± 0.1	4.7 ± 0.1	6.9 ± 0.1	22.7 ± 0.1
Natural HA ^a	50 - 60	4 - 6	2 - 6	0 - 2	30 - 35
HA	Functional groups				
	COOH (meq/g)	Phenol./acidic OH (meq/g)	PEC (meq/g)	pK_{app}	
M1	1.18 ± 0.20	1.82 ± 0.01	1.56 ± 0.13	4.30 ± 0.23	
M1-S-1	1.49 ± 0.02	2.35 ± 0.02	1.63 ± 0.16	4.12 ± 0.17	
M1-S-2	1.64 ± 0.06	1.86 ± 0.02	1.90 ± 0.17	3.58 ± 0.28	
M1-S-3	1.70 ± 0.14	1.88 ± 0.01	1.96 ± 0.23	3.76 ± 0.13	
Natural HA	1.5 - 5.7 ^b	2.1 - 5.7 ^b		3.35 - 4.85 ^c	

^a Stevenson, 1982. ^b Stevenson, 1994. ^c Kurková, 2004.

Independent of the sulfur content, all synthetic products exhibit comparable FTIR spectra (not shown) indicating similar overall structures (Sachs et al., 2010). The HA show FTIR absorption bands that are comparable to those of natural HA (Stevenson, 1994).

Identification of sulfur species

The sulfur speciation in synthetic HA type M1-S was studied by X-ray photoelectron spectroscopy (XPS) at the Institut für Kernchemie, Johannes Gutenberg-Universität Mainz. XPS spectra of synthetic HA were measured in comparison to those of L-cysteine and purified natural HA from Aldrich (AHA; S = 3.8 ± 0.1 wt.%; Sachs et al., 2004) as described in detail in (Sachs et al., 2010). The dry sample powders were pressed into indium foil without further treatment. Spectra were recorded with the UNI-SPECS ESCA System (Specs GmbH, Berlin, Germany) with a PHOIBOS 100 energy analyzer. The spectra were excited by non-monochromatic Mg K_{α} radiation (1253.6 eV). The pass energy (E_p) of the analyzer was 13 or 50 eV, depending on the desired signal-to-noise ratio and spectral resolution. The resolution measured as the full width at half-maximum of the Ag $3d_{5/2}$ line was 1.0 eV ($E_p = 13$ eV) or 2.3 eV ($E_p = 50$ eV). The vacuum during the measurements was 2×10^{-8} mbar. The electrostatic charging of the sample surface was corrected by setting the C 1s binding energy of aliphatic carbon equal to 285.0 eV. The data evaluation is described in Sachs et al. (2010). Errors of the determined binding energies and relative line intensities were ± 0.1 eV and $\pm 5\%$, respectively.

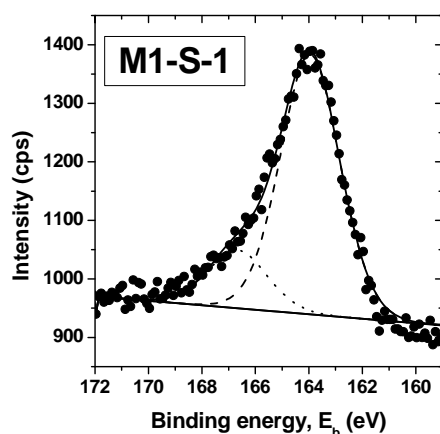


Fig. 3.8. XPS spectrum of the S $2p$ lines of HA model substance M1-S-1 measured with $E_p = 50$ eV (● Experiment, --- Fit; Sachs et al., 2010).

Figure 3.8 shows a XPS spectrum of the S $2p$ lines of HA M1-S-1. The XPS spectrum of HA M1-S-2 (not shown) is similar (Sachs et al., 2010). The theoretical fit of the spectra resulted in two peaks indicating the occurrence of at least two different types of sulfur species. In

contrast to that, HA M1-S-3 shows one S 2*p* line. The spectrum of AHA points also to the occurrence of two different sulfur species comparable to HA M1-S-1 and M1-S-2. Table 3.6 summarizes the binding energies (E_b) of the S 2*p* lines as well as the percentage of the individual sulfur components on the total sulfur content of the HA.

Table 3.6. Binding energies (E_b) of S 2*p* XPS lines and percentage of the individual sulfur species on the total sulfur content (Sachs et al., 2010).

Sample	E_b (eV)	% of S_{total}	E_b (eV)	% of S_{total}	E_b (eV)	% of S_{total}
L-cysteine	163.8	100				
AHA	164.5	70-80			168.3	20-30
M1-S-1	164.0	82	166.7	18		
M1-S-2	163.9	90-95	166.8	5-10		
M1-S-3	163.9	100				

All studied HA as well as cysteine show a S 2*p* line at about 164.0 eV. In addition to that, HA M1-S-1 and M1-S-2 show a signal at about 166.8 eV, whereas the second sulfur line of AHA is found at 168.3 eV. Based on literature data for sulfur containing organic model compounds (Lindberg et al., 1970), the signals can be attributed to reduced and oxidized sulfur species. The S 2*p* line at 164.0 eV corresponds to thiols, dialkylsulfides and/or disulfides, which can not easily be distinguished. The peak centered at about 166.8 eV is ascribed to sulfoxides. The signal at 168.3 eV in the spectrum of AHA results from contributions of higher oxidized sulfur species like sulfones and/or sulfonates. Comparable sulfur species were already found for natural humic substances by XPS (Urban et al., 1999) and XANES (e.g., Xia et al., 1998; Prietzel et al., 2007). Table 3.6 shows, the amount of reduced sulfur groups of the synthetic products increases from about 82% in M1-S-1 to 100% in M1-S-3. In HA M1-S-3 no oxidized sulfur species are detectable. From quantitative analysis of the XPS spectra it can be concluded that reduced sulfur functionalities dominate the sulfur speciation in all studied HA. Comparable high fractions of reduced sulfur functionalities were already described for natural HA extracted from soils (Hutchison et al., 2001).

3.2.2 Impact of sulfur functionalities on the U(VI) complexation by humic acids

The U(VI) complexation of sulfur containing HA model substances M1-S was studied in comparison to that of sulfur free HA M1 applying two independent spectroscopic methods, time-resolved laser-induced fluorescence spectroscopy (TRLFS) and TRLFS with femtosecond laser pulses (fs-TRLFS). The influence of sulfur containing functional groups of

HA on the U(VI) complexation was estimated and compared to that of oxygen containing functional groups (Sachs et al., 2010).

3.2.2.1 Experimental

Sample preparation

Complexation experiments were performed in air ($p\text{CO}_2 = 10^{-3.5}$ atm) at room temperature. U(VI) humate solutions were prepared from stock solutions of HA (0.2 g/L) and $\text{UO}_2(\text{ClO}_4)_2$ (1×10^{-4} M U(VI), 0.1 M HClO_4). The sample preparation is described in (Sachs et al., 2010). Table 3.7 summarizes the composition of the studied samples. For TRLFS measurements, HA-free U(VI) solutions were used for calibration of the U(VI) luminescence signal as a function of the U(VI) concentration.

Table 3.7. U(VI) humate solutions studied by TRLFS and fs-TRLFS ($\text{pH} = 3.80 \pm 0.02$; $I = 0.1$ M NaClO_4 ; $p\text{CO}_2 = 10^{-3.5}$ atm; Sachs et al., 2010).

HA	Method	U ($\mu\text{mol/L}$)	HA (mg/L)
M1	TRLFS	0.63-5.50	10
	fs-TRLFS	0.78-10.9	10
M1-S-1	TRLFS	0.82-9.66	10
	fs-TRLFS	0.81-13.0	10
M1-S-2	TRLFS	0.93-10.4	10
	fs-TRLFS	0.78-15.2	10
M1-S-3	TRLFS	1.00-15.5	10
	fs-TRLFS	0.98-27.4	10

Spectroscopic measurements

The U(VI) luminescence as function of the U(VI) concentration was measured by TRLFS using a Nd:YAG laser system (Continuum Minilite II, Continuum Electro Optics Inc., Santa Clara, USA) pulsed with a repetition rate of 10 Hz. The excitation wavelength was 266 nm, the pulse energies about 300 μJ . The luminescence emission was focused into a spectrograph (iHR 550, HORIBA Jobin Yvon GmbH, Munich, Germany) and detected using an intensified camera system with 1024 useable pixels and a built-in delay generator (HORIBA Jobin Yvon). TRLFS spectra were measured by averaging 200 laser pulses in the wavelength range between 371 and 674 nm with a gate width of 2 μs at delay times of 150 or 175 ns.

The fs-TRLFS measurements for determination of the HA fluorescence as a function of the U(VI) concentration were performed with a femtosecond laser pulse based TRLFS system. The system is described in (Geipel et al., 2004). A Nd:YVO₄ laser (Spectra Physics, Mountain

View, USA) with a repetition rate of 1 kHz was used as pump source for a Ti:Sapphire oscillator. After amplification, third harmonic generation was applied to provide femtosecond pulses with an excitation wavelength of 266 nm and pulse energies between 0.09 and 0.11 μJ . The fluorescence signal was focused into a spectrograph (Acton Research, 300i, Acton, USA) and collected by an ICCD camera system with 1376 useable pixels (Picostar HR, LaVision Inc., Göttingen, Germany). Time-resolved fluorescence spectra were collected at delay times between 0 and 30 ns after application of the laser pulse, with time steps of 0.1 or 0.2 ns applying a delay generator. Spectra were measured with a gate width of 2 ns in the wavelength range between 327 and 533 nm (Sachs et al., 2010).

3.2.2.2 Results and discussion

Results of TRLFS measurements

Figure 3.9a shows selected U(VI) luminescence spectra as function of the U(VI) concentration at constant HA concentration.

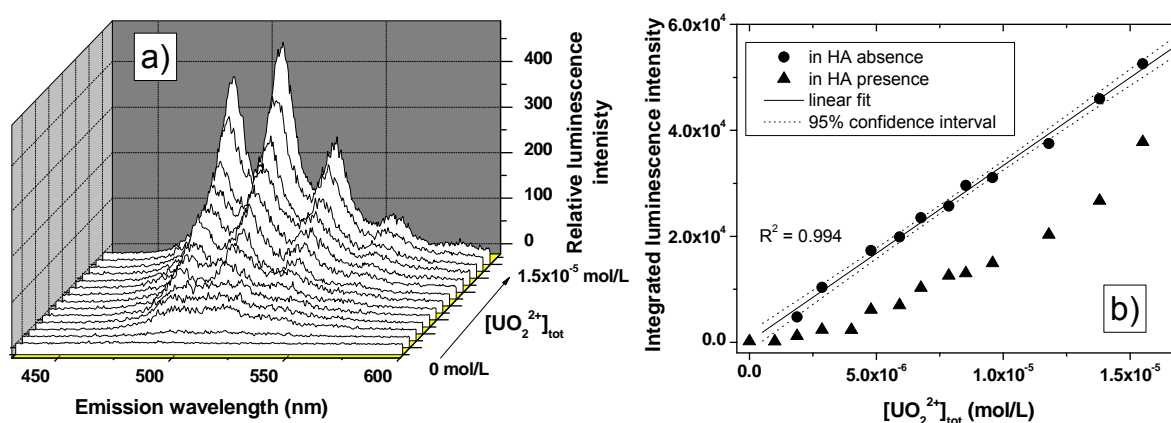


Fig. 3.9. (a) U(VI) luminescence in the presence of HA M1-S-3 as a function of the U(VI) concentration. (b) Integrated luminescence intensities of U(VI) (430-600 nm) in the absence and presence of HA M1-S-3 (delay time $t = 175$ ns; $[\text{UO}_2^{2+}]_{\text{tot}} = 0\text{-}15.5$ $\mu\text{mol/L}$; $[\text{HA}] = 0$ or 10 mg/L; $I = 0.1$ M NaClO_4 ; $\text{pH} = 3.80 \pm 0.02$; $p\text{CO}_2 = 10^{-3.5}$ atm; Sachs et al., 2010).

The U(VI) luminescence intensity is increased with increasing U(VI) concentration in the presence of constant HA concentrations. The obtained U(VI) luminescence spectra represent the sum of the luminescence of the free UO_2^{2+} ion and of the first hydrolytic uranyl species (UO_2OH^+). No emission signals of HA or U(VI) humate complexes were detected. The luminescence spectra were deconvoluted using single spectra of UO_2^{2+} and UO_2OH^+ to isolate the contribution of the free UO_2^{2+} ion to the overall luminescence signal. The spectrum of UO_2OH^+ was included in the peak deconvolution because of the strong fluorescence yield of

UO_2OH^+ in comparison to UO_2^{2+} . However, the concentration of UO_2OH^+ (<2%) present in the experiments was neglected in the further data evaluation. In the absence of HA, the U(VI) speciation in solution is dominated by the UO_2^{2+} ion which occurs to >98% under the applied experimental conditions.

A static quenching of the luminescence of the free UO_2^{2+} ion was observed for the complexation of UO_2^{2+} with HA. After peak deconvolution, the UO_2^{2+} luminescence intensities for each sample, with and without HA, were integrated between 430 and 600 nm (Fig. 3.9b). The results of the solutions without HA were used to determine the free UO_2^{2+} concentration when U(VI) humate is present.

The TRLFS data were evaluated based on the metal ion charge neutralization model (CNM; Kim and Czerwinski, 1996). According to this model, the UO_2^{2+} ion binds two proton exchanging sites of the HA molecule (Eq. (3.4)).



HA(II) represents the HA ligand and $UO_2HA(II)$ is the U(VI) humate complex. The complex stability constant K is formulated by

$$K = \frac{[UO_2HA(II)]}{[UO_2^{2+}]_{free} \cdot [HA(II)]_{free}} \quad (3.5)$$

$[UO_2HA(II)]$ is the U(VI) humate complex concentration, $[UO_2^{2+}]_{free}$ the free UO_2^{2+} concentration and $[HA(II)]_{free}$ the free HA ligand concentration. CNM introduces the loading capacity (LC; Eq. (3.6)) which corresponds to the maximal available mole fraction of HA binding sites under the applied experimental conditions.

$$LC = \frac{[UO_2HA(II)]_{max}}{[HA(II)]_{tot}} \quad (3.6)$$

$[UO_2HA(II)]_{max}$ is the maximal UO_2^{2+} concentration permissible for complexation with functional sites of a given HA and $[HA(II)]_{tot}$ the total molar HA concentration (Eq. (3.7)).

$$[HA(II)]_{tot} = \frac{[HA] \cdot PEC}{2} \quad (3.7)$$

In Eq. (3.7) $[HA]$ stands for the weight concentration of HA in g/L, PEC for the proton exchange capacity of HA in eq/g, and 2 for the nominal charge of the complexing UO_2^{2+} ion. Applying this model, the metal ion complexation by HA is described independently of the experimental conditions and the origin of the HA. Comparable complexation constants are obtained for the complexation of a metal ion with different HA. Differences in the

complexation behavior of HA under the same experimental conditions are reflected in different LC values. If sulfur containing functional groups influence the U(VI) complexation by HA, various LC values should result for HA with different sulfur contents.

Complexation constants $\log K$ and LC values that were determined from the TRLFS measurements as described in (Sachs et al., 2010) are summarized in Table 3.8. Under consideration of the standard deviations, the complexation constants for all HA are similar. The LC values of HA M1 and M1-S-1 with 0 and 1.9 wt.% sulfur, respectively, are comparable. However, with further increasing sulfur content of the HA up to 6.9 wt.%, a significant increase of the LC values up to 44% was determined by TRLFS. This increase of the LC values points to an increase of the mole fraction of maximal available U(VI) binding sites of HA with sulfur contents >2 wt.%.

Table 3.8. Complexation data for the complexation of U(VI) with HA type M1-S in comparison to sulfur free HA M1 (pH = 3.80 ± 0.02 ; $I = 0.1$ M NaClO₄; $p\text{CO}_2 = 10^{-3.5}$ atm; Sachs et al., 2010).

	TRLFS		fs-TRLFS		
	LC (%) ^a	$\log K$	C_L ($\mu\text{mol/L}$) ^b	$C_{L,\text{norm.}}$ (%) ^c	$\log K$
M1	28.8 ± 4.8	5.98 ± 0.18	2.21 ± 1.29	28 ± 17	5.65 ± 0.11
M1-S-1	27.3 ± 1.4	6.15 ± 0.09	2.25 ± 1.59	28 ± 20	5.56 ± 0.11
M1-S-2	38.6 ± 3.0	6.19 ± 0.22	3.60 ± 0.68	38 ± 7	6.13 ± 0.11
M1-S-3	44.2 ± 2.1	6.38 ± 0.25	4.78 ± 1.47	49 ± 15	5.68 ± 0.09

^a LC: Loading capacity of HA (Kim and Czerwinski, 1996).

^b C_L : Total concentration of HA ligand sites (Ryan and Weber, 1982).

^c $C_{L,\text{norm.}}$: Total concentration of HA ligand sites normalized to the total HA concentration $[\text{HA(II)}]_{\text{tot}}$ as defined by Kim and Czerwinski (1996).

Results of fs-TRLFS measurements

Time-resolved fluorescence spectra of the HA were measured with constant HA concentration as a function of the U(VI) concentration. The spectra at the fluorescence maximum at $t = 0$ ns relative to the laser pulse were used for data evaluation. Selected spectra for HA type M1-S-3 are shown in Fig. 3.10a. The spectra were integrated between 410 and 500 nm and the resulting fluorescence intensities were normalized to 100%. Figure 3.10b depicts the normalized fluorescence intensities of HA M1-S-3 as a function of the total U(VI) concentration. With increasing U(VI) concentration a decrease of the HA fluorescence is observed. This static fluorescence quenching process proceeds non-linear as already reported

by Acker (2003). After saturation of the HA binding sites with U(VI), the HA shows a residual fluorescence.

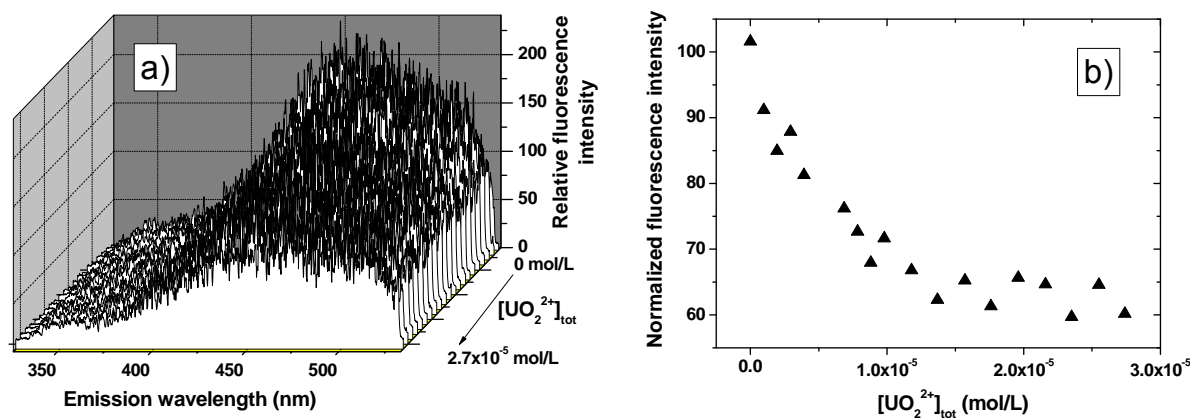


Fig. 3.10. (a) Fluorescence spectra of HA M1-S-3 as a function of the U(VI) concentration. (b) Integrated fluorescence intensities of HA M1-S-3 (410-500 nm; delay time $t = 0$ ns; $[\text{UO}_2^{2+}]_{\text{tot}} = 0\text{-}27.4$ $\mu\text{mol/L}$; $[\text{HA}] = 10$ mg/L; $I = 0.1$ M NaClO₄; pH = 3.80 ± 0.02 ; $p\text{CO}_2 = 10^{-3.5}$ atm; Sachs et al., 2010).

An evaluation of the fs-TRLFS data based on CNM is not possible as already described in (Sachs et al., 2007a). Ryan and Weber (1982) developed a model for evaluation of non-linear fluorescence quenching data. Assuming the formation of a 1:1 complex between a humic substance as ligand and a metal ion, this model provides a correlation between the measured fluorescence intensities, the complex concentration ($[\text{ML}]$) and the total concentration of ligand (C_L) present in solution (Eq. (3.8)).

$$\frac{[\text{ML}]}{C_L} = \frac{I_L - I_M}{I_L - I_{ML}} \quad (3.8)$$

I_L represents the fluorescence of the free ligand at start of the fluorescence titration, I_M the measured fluorescence intensity at a certain metal ion concentration and I_{ML} the residual fluorescence intensity when the available ligand is completely bound. I_{ML} is a limiting value at the endpoint of the fluorescence titration below which the fluorescence intensity does not decrease due to further addition of metal ions.

Including mass balances for metal ion and ligand as well as the conditional stability constant of an assumed 1:1 complex, Eq. (3.9) is obtained according to (Ryan and Weber, 1982):

$$I_M = \frac{(I_{ML} - I_L)}{(2 \cdot K \cdot C_L)} \cdot [(K \cdot C_L + K \cdot C_M + 1) - \sqrt{(K \cdot C_L + K \cdot C_M + 1)^2 - 4 \cdot K^2 \cdot C_L \cdot C_M}] + I_L \quad (3.9)$$

Normalizing the fluorescence intensity data on a relative scale, I_L is equal to 100. Using the measured fluorescence intensities as a function of the added metal ion concentration (C_M), the total ligand concentration (C_L) available for complexation under the applied experimental conditions and the conditional stability constant (K) can be obtained solving Eq. (3.9) by non-linear regression (Ryan and Weber, 1982). The fitting procedure is described in (Sachs et al., 2010).

Considering the formation of a 1:1 complex between UO_2^{2+} and HA as given in Eq. (3.4), C_L represents the HA ligand concentration ($[HA(II)]$) available for complexation of UO_2^{2+} under the applied experimental conditions. Relating this value to the total HA concentration ($[HA(II)]_{tot}$; Eq. (3.7)), a value is obtained ($C_{L, norm.}$) which corresponds to LC.

Table 3.8 summarizes the complexation constants ($\log K$) and the total ligand concentrations (C_L) for the complexation of U(VI) with HA M1(-S). Under consideration of the standard deviations, all HA show similar $\log K$ values. Although the total ligand concentrations (C_L) are characterized by high standard deviations, it becomes obvious that these are increased from 2.2 $\mu\text{mol/L}$ (M1) to 4.8 $\mu\text{mol/L}$ (M1-S-3). This might partly be caused by the increase of the PEC values and the carboxylic group contents of the HA (cf. Table 3.5) resulting in a higher number of potentially available binding sites. However, by normalizing C_L to $[HA(II)]_{tot}$, the increase in PEC is taken into account. Comparing the $C_{L, norm.}$ for all HA it becomes evident that the total ligand concentrations of HA M1-S-2 and M1-S-3 are significantly higher than those of HA M1 and M1-S-1. This points again to an increase of the available number of HA binding sites for U(VI) complexation with increasing sulfur content.

Comparison of the complexation data

The U(VI) complexation constants measured by TRLFS and fs-TRLFS, respectively, are comparable for the individual HA. The $\log K$ values deduced from fs-TRLFS are slightly lower than those from TRLFS. This can be attributed to technical measurement reasons of both laser systems as discussed by Acker (2003), causing experimental uncertainties in the determination of the luminescence of the free UO_2^{2+} ion and the fluorescence of the HA.

Despite of the high uncertainties of C_L , LC and $C_{L, norm.}$ values obtained from TRLFS and fs-TRLFS measurements, respectively, agree well. This allows the conclusion that under the applied conditions the number of HA binding sites available for complexation of U(VI) is increased with increasing HA sulfur content beginning from sulfur contents >2 wt.%. Taking the XPS data into account, it can be specified that the increase of the number of U(VI) binding sites can be ascribed to an increasing amount of reduced sulfur functionalities,

probably thiol groups. The increase of LC and $C_{L,norm.}$ correlates also with the increasing acidity of the HA reflected in decreasing pK_{app} values. The steady rise of the fraction of HA binding sites for U(VI) points to a contribution of reduced sulfur functionalities to the complexation in the acidic pH range. Thiol groups, which can be assumed as the dominating sulfur species in the studied HA, are normally protonated in the acidic pH range (e.g., -SH in cysteine: $pK_a = 8.33$; Bräse et al., 2007). In our former study (Pompe et al., 2000b), the influence of HA phenolic OH groups, which are characterized by similar acidities as thiol groups, on the U(VI) complexation at pH 4 was investigated. Already at pH 4, where phenolic OH groups are assumed to be protonated, U(VI) LC values of HA were found to be decreased after blocking of phenolic OH groups. This decrease was ascribed to a contribution of intermolecular hydrogen bonds between phenolic OH groups and axial oxygen atoms of the UO_2^{2+} ions to the complexation. A contribution of phenolic OH groups acting as ligands after proton release due to mesomeric substituent effects was also not excluded. Such effects could also impact the acidity of thiol groups resulting in their involvement in the U(VI) complexation. The formation of hydrogen bonds between thiol groups and axial oxygen atoms of the UO_2^{2+} unit and/or stabilizing electronic effects between free electrons of sulfur atoms and the UO_2^{2+} ion may contribute to the complexation or the stabilization between U(VI) and HA. Nevertheless, other processes that can influence the fraction of HA binding sites should also be taken into account. Steric hindrances within the HA, which might be overcome in the presence of increasing sulfur contents, could influence the complexation behavior of the sulfur free HA. Moreover, an inhibitory effect of L-cysteine on the melanoidin formation, that was discussed in (Kwak and Lim, 2004; Sachs et al. 2010), could influence the molecular size/mass of the HA with possible consequences for the complexation properties. The hypothesis that thiol groups are involved in the interaction between HA and U(VI) is supported by the literature (Raghavan and Santappa, 1970 and 1973; Günther et al., 2007).

Natural HA predominantly show sulfur contents between 0 and 2 wt.% (Stevenson, 1982). To estimate the role of sulfur functionalities for the U(VI) complexation by HA with environmentally relevant sulfur contents in comparison to oxygen functionalities, the complexation behavior of HA M1 and M1-S-1 with 0 and 1.9 wt.% sulfur, respectively, has to be considered (Table 3.8). For these HA no differences in the complexation constants ($\log K$) and also in the fraction of ligand sites (LC, C_L) were observed. From that it can be concluded that for environmentally relevant sulfur concentrations in HA and under acidic conditions, reduced sulfur functionalities play only a subordinate role for the U(VI) complexation compared to oxygen containing functional groups, especially carboxylic groups. However,

with increasing sulfur content the complexation behavior toward U(VI) may change. Furthermore, the role of sulfur functionalities for the U(VI) complexation may change with increasing pH value (Sachs et al., 2010).

3.2.3 Impact of sulfur functionalities on the Np(V) reduction by humic acids

The role of sulfur functional groups of HA for their reduction capability toward Np(V) was studied for the first time. For this, the Np(V) reduction capability of HA model substances M1-S was studied as a function of pH (pH 5.0, 7.0 and 9.0) under anaerobic conditions and compared to that of the respective sulfur free synthetic HA type M1.

3.2.3.1 Experimental

Sample preparation

The samples were prepared in a glove box (N₂ atmosphere) according the procedure described by Schmeide et al. (2012a). The final Np and HA concentrations were 5×10⁻⁶ M and 100 mg/L, respectively. The ionic strength of the solutions was 0.1 M (NaClO₄). The pH values of the samples (pH 5.0, 7.0, 9.0) were adjusted with NaOH (p.a., Merck) or HClO₄ (p.a., Merck) solutions, no buffers were added. During the experiments, the pH of the solutions was checked and readjusted repeatedly. All samples were stored in 50 mL centrifuge tubes (Cellstar, Greiner Bio-One, Kremsmünsterand, Austria) at room temperature. The tubes were wrapped in aluminum foil to exclude light-induced degradation processes of the organic material. The experiments were conducted over an 11-month period. The Np concentration in solution was determined by liquid scintillation counting (LSC, Winspectral α/β, Wallac 1414, Perkin Elmer, Rodgau, Germany) using α-β discrimination. For this, 600 μL aliquots were mixed with 15 mL of a Ultima Gold scintillation cocktail (Perkin Elmer).

Methods for Np redox speciation

For monitoring the concentrations of Np(V) and Np(IV) in solution over time, samples were taken after different time intervals and characterized by solvent extraction, ultrafiltration, and *E_h* measurements as described by Schmeide et al. (2012a).

3.2.3.2 Results and discussion

Exemplary, the results of the Np(V) reduction experiments at pH 5.0 and 7.0 are shown in Fig. 3.11 as Np(V) fraction of total Np versus equilibration time.

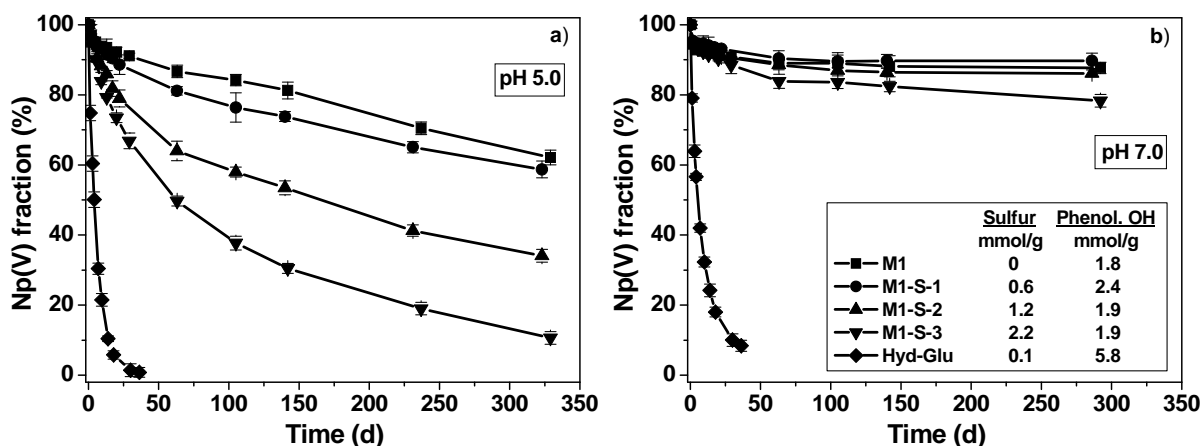


Fig. 3.11. Time-dependence of the Np(V) reduction by HA type M1(-S) at pH 5.0 (a) and pH 7.0 (b). For comparison, the Np(V) reduction by HA type Hyd-Glu (Schmeide and Bernhard, 2009) is shown. The legend holds for both figures. ($[\text{Np}]_{\text{tot}} = 5 \times 10^{-6} \text{ M}$; $[\text{HA}] = 100 \text{ mg/L}$; $I = 0.1 \text{ M}$ (NaClO_4), N_2 ; Schmeide et al., 2012a).

At pH 5.0, the ability to reduce Np(V) increases in the sequence $\text{M1} < \text{M1-S-1} < \text{M1-S-2} < \text{M1-S-3}$ (Fig. 3.11a). Since the phenolic/acidic OH group content is nearly the same for these HA, the increasing Np(V) reduction can be correlated to the increasing sulfur contents of the HA (0 to 6.9 wt.% which correspond to molar sulfur concentrations of 0 to 2.2 mmol/g, cf. inset Fig. 3.11b). Reduced organic sulfur species, such as thiols, dialkylsulfides and/or disulfides, were determined as the dominating sulfur functionalities in these HA by XPS (Sachs et al., 2010). Their percentage of the total sulfur content is generally high and moreover, increases from M1-S-1 (82%) via M1-S-2 (90-95%) to M1-S-3 (100%). Szulczewski et al. (2001) showed by XANES spectroscopy that thiols are oxidized to disulfides during Cr(VI) reduction by HA. Ratasuk and Nanny (2007) identified thiols and disulfides as the main redox moieties of humic substances at pH 6.5 by means of cyclic oxidation and reduction reactions. Thus, for the Np(V) reduction by sulfur containing HA it is concluded that, in addition to hydroquinone-like moieties and non-quinoid phenols, the reduced sulfur functional groups contribute to the reduction capability of HA.

In contrast to the results obtained at pH 5.0, the differences in the reduction behavior of the HA type M1(-S) with different sulfur contents are much smaller at pH 7.0 (cf. Fig. 3.11b). Merely for M1-S-3, with the highest content of reduced sulfur species, a slightly stronger Np(V) reduction is observed. Generally, however, rate and extent of Np(V) reduction at pH 7.0 is low. The curves obtained at pH 9.0 (not shown) run parallel to those obtained at pH 7.0, however, the Np(V) fraction in solution is about 10% lower compared to pH 7.0. Again M1-S-3 induces a slightly stronger Np(V) reduction compared to the other humic acids, however, overall the effect of increasing sulfur contents is small.

The redox potentials, determined in the Np/HA sample solutions at pH 5.0, decrease from 294 ± 10 mV (Np/M1) via 279 ± 8 mV (Np/M1-S-1) and 205 ± 4 mV (Np/M1-S-2) to 188 ± 2 mV (Np/M1-S-3). The trend of decreasing redox potentials in Np/HA sample solution with increasing content of reduced sulfur functional groups of HA correlates with increasing Np(V) reduction from M1 to M1-S-3. In (Schmeide et al., 2012a) the redox potentials measured in the sample solutions are discussed in detail in the context of the E_h -pH diagram for neptunium and are compared to the pH-dependency of the redox potential generally observed for HA as well as to the redox potentials given in the literature for the tripeptide glutathione and for the macromolecular protein thioredoxin, which both can serve as model substances to illustrate redox potentials of thiols.

Furthermore, to illustrate the pH-dependency of the redox reactions and especially to explain the stronger effect of reduced sulfur functional groups of HA on Np(V) at pH 5.0 compared to that at pH 7.0 or 9.0, all potential electron-transfer reactions for the Np(V) reduction by sulfur functional groups of HA are given and discussed in (Schmeide et al., 2012a).

In the following the reduction behavior of the HA enriched with sulfur functional groups (M1-S) will be compared to that of a HA enriched with phenolic OH groups. For this, the Np(V) reduction by HA type Hyd-Glu, studied at pH 5.0 and 7.0 under identical experimental conditions (Schmeide and Bernhard, 2009), is shown in Fig. 3.11. Hyd-Glu is a synthetic HA model substance that was synthesized by oxidation of hydroquinone in the presence of glutamic acid in alkaline solution (Sachs and Bernhard, 2011a). Elemental composition and carboxylic group content of Hyd-Glu are comparable to those of natural HA. However, its phenolic/acidic OH group content (5.8 ± 0.2 meq/g) is in the range of the upper value given for natural HA (2.1-5.7 meq/g (Stevenson, 1994)) and higher than the phenolic/acidic OH group content of HA type M1-S (cf. Table 3.5).

As can be seen in Fig. 3.11, both rate and extent of Np(V) reduction was higher in the case of Hyd-Glu which can be attributed to its enhanced phenolic/acidic OH group content. At pH 5.0, quantitative reduction of Np(V) ($\geq 99\%$ Np(IV)) was achieved by Hyd-Glu within 36 d whereas only about 37% Np(V) were reduced by M1-S-3 within this time. For the Np(V) reduction by Hyd-Glu two kinetics are observed, whereby the fast one predominates. Also for the Np(V) reduction by sulfur containing HA type M1-S two kinetics can be observed. After a fast Np(V) reduction in the initial phase, further Np(V) reduction proceeded with a slow kinetics. Even after the long experimental period of about 11 months Np(V) was only partially reduced to Np(IV) and equilibrium has not been reached. If reduced-sulfur structures other than thiol groups in HA occur essentially as intra-molecular bridges as reported by

Vairavamurthy et al. (1997), then steric hindrances within the HA colloids may be responsible for this effect to some extent. The results show that phenolic OH groups contribute stronger and faster to the total Np(V) reducing capacity of HA than sulfur functional groups. This effect becomes stronger with increasing pH value.

Thus, in contrast to HA type Hyd-Glu which was shown to be suitable to stabilize the reduced states of redox-sensitive actinides such as Np in redox and sorption studies (Schmeide and Bernhard, 2009 and 2010) due to its high reducing capacity, HA type M1-S are suitable primarily for mechanistic studies of redox and complexation processes.

The ultrafiltration results verified the results of solvent extraction (cf. Schmeide et al., 2012a). A fundamental parameter of humic substances is their reducing capacity (RC) which represents the electron equivalents per mass unit humic substance transferred by a humic substance to an added oxidant. The Np(V) reducing capacities at pH 5.0, calculated from the Np(IV) concentration in the sample solutions after 11 months, increase in the sequence M1 (0.019 meq/g HA) < M1-S-1 (0.022 meq/g HA) < M1-S-2 (0.034 meq/g HA) < M1-S-3 (0.045 meq/g HA). These Np(V) reducing capacities correlate linearly with the content of sulfur functional groups of the HA according to Eq. (3.10).

$$\text{RC (meq/g HA)} = 0.0175 + 0.0125 \cdot [\text{S}_{\text{total}}] \text{ (mmol/g HA)}; R^2 = 0.97 \quad (3.10)$$

The results obtained in the present work have shown that in addition to quinone-like moieties and non-quinoid phenols (Schmeide and Bernhard, 2009) that dominate the redox behavior of humic substances, sulfur functional groups act as further redox-active sites in humic substances toward actinides. However, the impact of the individual reducing moieties is pH-dependent. While reduced sulfur functional groups contribute to the Np(V) reduction preferentially at slightly acidic pH, phenolic OH groups play a role preferentially in the alkaline pH range. In natural humic substances the content of sulfur functional groups is low compared to other redox-active functional units (quinoid moieties and phenolic OH groups). Moreover, the ratio of reduced to total (reduced and oxidized) sulfur functional groups is lower in most natural humic substances. Thus, in nature the extent of the contribution of sulfur functional groups to the overall redox and complexation capacity of humic substances is expected to be less pronounced.

For the interaction of metal ions with humic substances it can be concluded that, although certain functional groups dominate, there is an overlapping of different reduction and complexation paths.

3.3 U(VI) humate complexation in dependence on temperature (20-60°C)

The storage of heat producing radioactive waste will result in a significant temperature increase in the surrounding host rock. Temperature distributions for different conditions have been calculated, e.g., within the Opalinus Clay temperatures may reach a maximum of ~75°C in the vicinity of nuclear spent fuel canisters (Johnson et al., 2002). Thermal evolution is an important aspect in the long-term safety assessment of nuclear waste repositories since the temperature can affect many processes which influence the migration behavior of actinides.

The formation of metal humate complexes has been the focus of many studies, however, only few studies regarding temperature effects have been published so far. Marquardt et al. (1996) investigated the Np(V) complexation with HA at temperatures from 21 to 60°C. Samadfam et al. (1996) studied the complexation thermodynamics of Sr(II) with Aldrich HA in the temperature range between 10 and 40°C. The Ni(II) humate equilibrium reaction was investigated up to 80°C by Warwick et al. (1997). Interestingly, all groups noted a decrease in binding with increasing temperature.

The aim of this work was to determine the temperature-dependence of the U(VI) humate complexation in aqueous solution. To determine the HA proton exchange capacity (PEC) in dependence on temperature, potentiometric titrations of HA were performed between 20 and 80°C. The U(VI) complexation was studied at 20, 40 and 60°C using time-resolved laser-induced fluorescence spectroscopy (TRLFS).

3.3.1 Experimental

Purified commercially available natural HA from Aldrich (AHA, batch A2/98) was used for all measurements. The purification process is described in detail elsewhere (Sachs et al., 2004). Solutions were prepared using Milli-Q water (mod. Milli-RO/Milli-Q-System, Millipore, Schwalbach, Germany). The ionic strength was kept constant at 0.1 M (NaClO₄).

Potentiometric titration

All solutions were prepared with carbonate free deionized water under N₂ atmosphere in a glove box. A HA stock solution was prepared by dissolving 10 mg AHA in 1 mL 0.1 M NaOH (high grade, Merck). This solution was diluted with 0.1 M NaClO₄ obtaining a total volume of 50 mL. To determine the excess volume of NaOH, which was not used to deprotonate the HA, an aliquot of the AHA stock solution was titrated against 0.1 M HClO₄

(p.a., Merck). The titrations were carried out in a temperature-controlled glass vessel ($T = 20-80 \pm 0.1^\circ\text{C}$) under nitrogen atmosphere with the automatic titration system GP Titrino 736 (Methrom, software TiNet 2.50). The pH values were measured with a Schott Blue Line 11pH electrode, which was calibrated at the designated temperature for each experimental run with WTW DIN buffer solutions.

Preparation of U(VI) humate solutions

The samples were prepared from stock solutions of AHA (0.2 g/L), which were prepared freshly for each experiment and $\text{UO}_2(\text{ClO}_4)_2$ (5×10^{-4} M in 5×10^{-3} M HClO_4). The TRLFS studies were performed at constant HA (5 mg/L) and varying U(VI) (1.7×10^{-6} to 1.7×10^{-5} M) concentration. All samples were tempered in a water filled thermostat at 20, 40 or 60°C until the solutions reached the designated temperature ($\pm 1^\circ\text{C}$). The pH values were then adjusted to 3.79 ± 0.02 with diluted NaOH and HClO_4 solutions. Reference samples of U(VI) without AHA were prepared under the same experimental conditions to determine the relative luminescence intensity as a function of the UO_2^{2+} concentration. The total U concentration in each sample was checked by ICP-MS analysis. To verify the AHA concentration, the amount of total organic carbon (TOC) was determined in the humate solutions.

TRLFS measurements

The U(VI) luminescence in solution was measured using a Nd:YAG laser system (Continuum Minilite II, Continuum Electro Optics Inc.). The fourth harmonic oscillation of the Nd:YAG (266 nm) with pulse energies between 0.2-0.5 mJ was used to excite U(VI). The emission signal was focused into a spectrograph (iHR 550, HORIBA Jobin Yvon) via fiber optics and detected using an ICCD camera system and a built-in delay generator (HORIBA Jobin Yvon). Aliquots of the tempered solutions were filled in a quartz cuvette and stored in a thermostatic cuvette holder (Quantum Northwest). To minimize temperature deviations, the samples were tempered at least 15 minutes prior to the measurements. The U(VI) luminescence spectra were recorded 175 ns after the excitation pulse to exclude the detection of occurring AHA fluorescence. The spectra were collected in the wavelength range between 371 and 674 nm at a gate time of 2 μs by averaging 100 laser pulses.

3.3.2 Results and discussion

As a precondition for the complexation studies, the proton exchange capacity (PEC) of AHA was determined in dependence on temperature applying potentiometric titration. As it is

depicted in Fig. 3.12, all PEC values between 20 and 60°C amount to about 4.45 ± 0.04 meq/g and do not show significant differences. Starting at 70°C, the PEC decreases with further increasing temperature to 3.77 ± 0.13 meq/g at 80°C. This indicates a change in the HA structure, presumably due to the irreversible loss of water, as it was described by Kolokassidou et al. (2007) for $T > 70^\circ\text{C}$. Thus, a different complexation behavior of AHA toward U(VI) can be expected at higher temperatures.

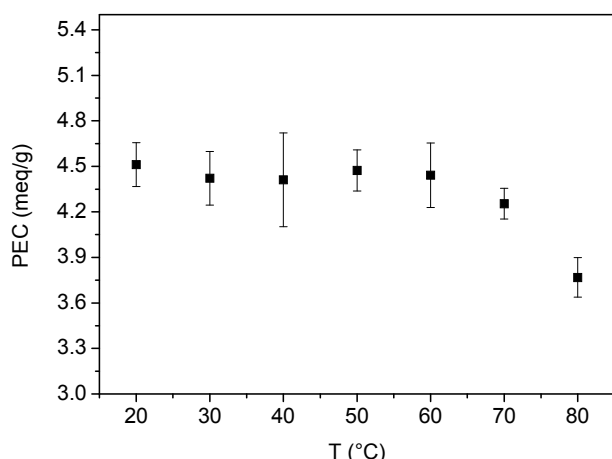


Fig. 3.12. Proton exchange capacity (PEC) of AHA in dependence on temperature.

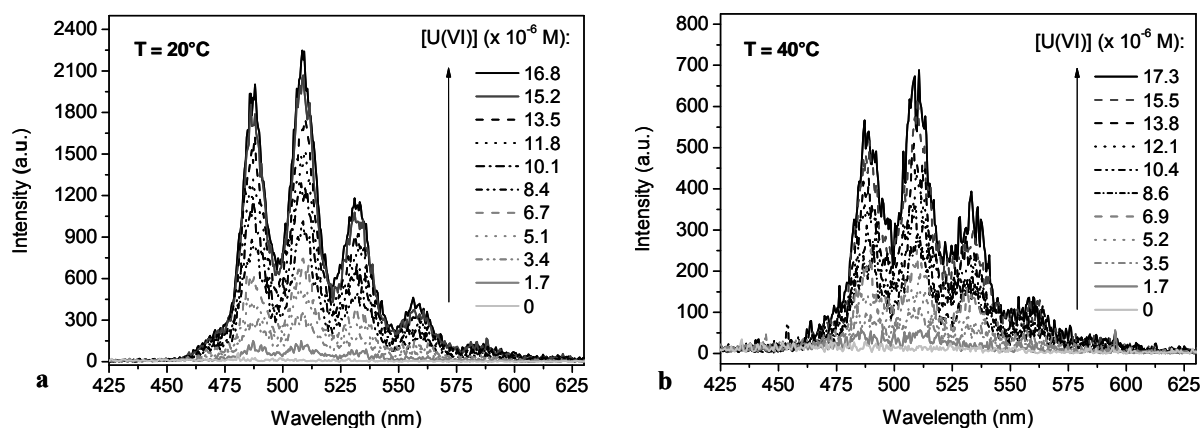


Fig. 3.13. Luminescence emission spectra of U(VI) humate solutions as a function of U(VI) concentration at 20°C (a) and 40°C (b).

Generally, the luminescence intensity of U(VI) as well as the lifetime decrease with increasing temperature. Simultaneously, the signal-to-noise ratio decreases. Therefore, it was not possible to measure the U(VI) luminescence adequately at temperatures above 60°C at the studied experimental conditions. Figure 3.13 shows the baseline-corrected emission spectra of the U(VI) humate solutions at 20 and 40°C. The measured luminescence is a sum of the spectra of the free UO_2^{2+} ion and the first hydrolytic species UO_2OH^+ , which occurs in the

studied solutions (pH 3.8) with about 2%. Therefore, all spectra were deconvoluted by a non-linear least-square method according to Pompe et al. (1998) to calculate the luminescence contribution of the free uranyl ion to the sum spectra.

Figure 3.14a shows the emission spectra for the U(VI) humate solutions at 40°C after peak deconvolution. The determined UO_2^{2+} luminescence intensities of the U(VI) humate solutions as well as the reference solutions were integrated in the wavelength range between 430 and 600 nm. The results are shown in Fig. 3.14b. A strong decrease of the U(VI) luminescence intensities of the humate containing solutions compared to those without HA was observed, due to the complex formation between AHA and U(VI).

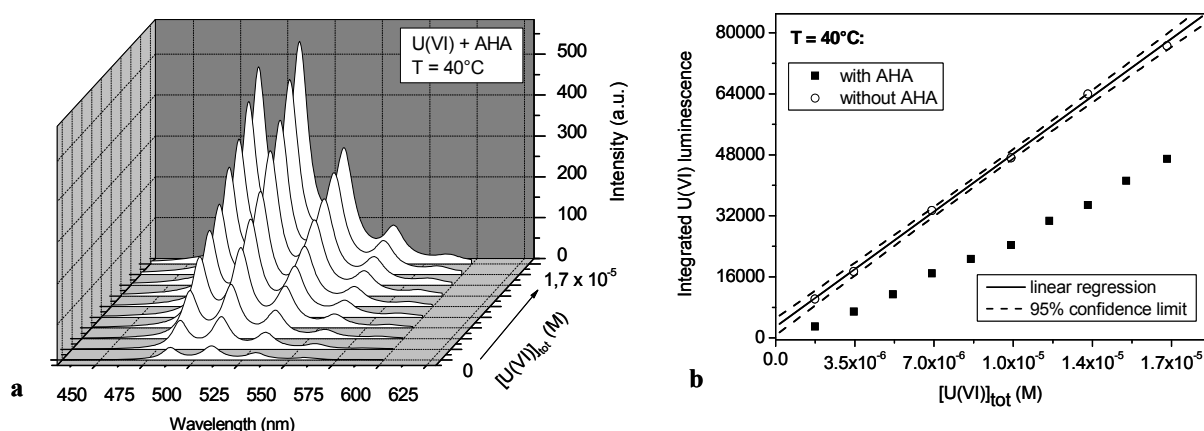


Fig. 3.14. Deconvoluted emission spectra of U(VI) humate solutions (a) and integrated luminescence intensities of the investigated solutions with and without AHA (b), plotted as a function of the U(VI) concentration at 40°C.

The experimental data were evaluated using the charge neutralization model by Kim and Czerwinski (1996). According to this model, the complexation reaction can be written as:



It is assumed that UO_2^{2+} binds two complexing sites of the HA molecule. Because not all complexing sites of HA are available for the complexation, the loading capacity (LC) was introduced by this model:

$$\beta = \frac{[\text{UO}_2\text{HA(II)}]}{[\text{UO}_2^{2+}]_{\text{free}} \cdot ([\text{HA(II)}]_{\text{tot}} \cdot \text{LC} - [\text{UO}_2\text{HA(II)})} \quad (3.12)$$

The LC was determined graphically by linear regression of the experimental data after rearranging Eq. (3.12):

$$[\text{UO}_2^{2+}]_{\text{free}} = \text{LC} \cdot \frac{[\text{UO}_2^{2+}]_{\text{free}} \cdot [\text{HA(II)}]_{\text{tot}}}{[\text{UO}_2\text{HA(II)}]} - \frac{1}{\beta} \quad (3.13)$$

$$[\text{HA(II)}]_{\text{tot}} = \frac{[\text{HA}] \cdot \text{PEC}}{z} \quad (3.14)$$

$[\text{HA(II)}]_{\text{tot}}$ was calculated according to Eq. (3.14) using the PEC values previously determined for each temperature. The graphic determination of LC is shown in Fig. 3.15 for the studies at 40°C. Applying LC, the complex stability constants were calculated for each experimental point, according to Eq. (3.12). The calculated stability constants as well as the LC values for 20, 40 and 60°C are summarized in Table 3.9.

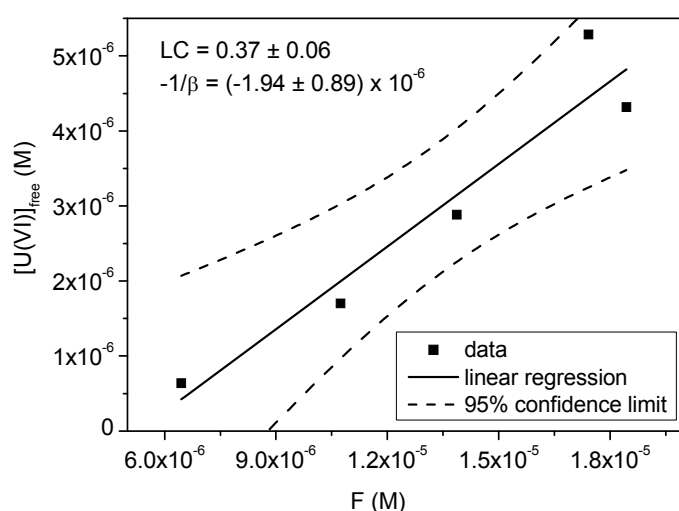


Fig. 3.15. Graphic determination of the loading capacity (LC) for the U(VI) complexation with AHA at 40°C.

Table 3.9. Summary of the determined complexation constants and loading capacities for the U(VI) complexation with AHA in dependence on temperature.

T (°C)	PEC (meq/g)	LC (%)	log $\beta_{0.1 \text{ M}}$
20	4.51 ± 0.15	34.9 ± 2.8	5.73 ± 0.07
40	4.41 ± 0.31	38.1 ± 2.0	5.75 ± 0.13
60	4.44 ± 0.21	16.9 ± 3.9	5.38 ± 0.21

As implied by the determined PEC values, the LC as well as the complex stability constants determined at 20 and 40°C are comparable. The log β of about 5.7 is in good agreement with literature data (e.g., log β = 5.88 ± 0.22 (Pompe et al., 1998) and log β = 6.20 ± 0.56 (Pompe et al., 2000b)). At 60°C, the LC value decreases significantly to 17%, which is an indication that fewer AHA complexing sites are available for U(VI) at increased temperature. The

complexation constant is also decreased to $\log \beta = 5.38 \pm 0.21$, which seems to be a typical behavior for HA and was already reported for other systems in literature.

Marquardt et al. (1996) found a decrease in the relative contribution of Np(V) humate from 38 to 13% with increasing temperature. Also Samadfam et al. (1996) and Warwick et al. (1997) demonstrated that the humate binding decreases with increasing temperature. Furthermore, Warwick et al. (1997) mentioned the appearance of coagulation of HA at 60 and 80°C. Although we could not verify this for 60°C, it might be possible that coagulation or precipitation of the AHA is increased at higher temperatures.

Kolokassidou et al. (2007), who studied the thermal stability of HA from Gorleben groundwaters, observed a reversible water release due to thermal treatment of HA at 60°C. Above 70°C, this process becomes irreversible, maybe due to the release of chemisorbed water molecules and water molecules produced by condensation or decarboxylation. They also determined the formation of more condensed polyaromatic structures above 70°C, which could be an explanation for the decreasing complexation tendency of HA.

In conclusion, the U(VI) humate binding is reduced at elevated temperatures, as it was also found for several other metals. Therefore, the formation of potentially mobile metal humate species may be limited in the vicinity of heat generating nuclear waste.

4 Sorption of U(VI) onto Opalinus Clay

To determine the retardation ability of the clay host rock toward radionuclides, knowledge about the geochemical interaction processes between radionuclides and the host rock such as sorption or diffusion is necessary. In this chapter the results of the sorption studies for U(VI) and argillaceous rock are presented. In an argillaceous rock nuclear waste repository the radioactive decay of the actinides and their fission products will result in elevated temperatures of up to 100°C close to the waste containers (Brasser et al., 2008). Thus, in addition, temperature-dependent U(VI) sorption experiments were performed.

In the past, many clay sorption studies focused on the interaction of actinides with pure clay minerals such as kaolinite (Redden et al., 1998; Thompson et al., 1998; Kornilovich et al., 2000; Křepelová et al., 2006; Sachs and Bernhard, 2008; Schmeide and Bernhard, 2010). Since pure clay minerals have a definite composition, the possible interaction processes are easier to elucidate and to model. Inert background electrolytes such as sodium chloride (Redden et al., 1998; Kornilovich et al., 2000) or sodium perchlorate (Kowal-Fouchard et al., 2004; Bradbury and Baeyens, 2006; Křepelová et al., 2006; Sachs and Bernhard, 2008; Schmeide and Bernhard, 2010) were used for the experiments. Thus, an influence of competing complexing ions had not to be considered.

In this work, sorption studies were extended from pure clay minerals and inert background electrolytes to complex natural systems. In natural environments, complex salt solutions, the so-called pore waters of argillaceous rock, occur as background electrolytes of the clay. Pore water contains ions which can act as competing reactants in sorption studies. As a representative for natural clay, Opalinus Clay (OPA) from Mont Terri, Switzerland, which is discussed as possible host rock for nuclear waste disposal sites, was investigated.

In natural clay, organic matter is strongly associated with mineral constituents. Humic substances, such as fulvic and humic acids (HA) as well as low molecular weight organic acids, can be released from the clay under certain conditions. This was shown by extraction experiments (Claret et al., 2003; Glaus et al., 2005; Courdouan et al., 2007, 2008). Because of the variety of functional groups, humic substances show a pronounced ability for complex formation. Furthermore, they are known for their inherent redox properties (Schmeide and Bernhard, 2009) and for their ability to form stable colloids (Artinger et al., 2002). Due to this, they can influence the transport of actinides in the environment.

In the present study, the U(VI) sorption onto OPA was investigated in the absence and presence of HA or low molecular weight organic acids, in dependence on temperature and

CO₂ presence. In all experiments, OPA pore water (Pearson, 1998) was used as background electrolyte. In addition, the U(VI) sorption onto OPA was investigated in dependence on pH using 0.1 M NaClO₄ as background electrolyte. The results were compared to the experiments of Křepelová et al. (2006), who investigated the U(VI) sorption onto kaolinite.

The obtained sorption results provide a contribution to the thermodynamic sorption database used for modeling of geochemical interaction processes of actinide ions and possible host rocks of a nuclear waste repository.

4.1 Characterization of Opalinus Clay

For the studies OPA from the Mont Terri Rock Laboratory, Switzerland, was used. There, OPA occurs with a maximum overburden of about 300 m and a thickness of about 150 m (Pearson et al., 2003). Bore cores were taken by the Federal Institute for Geosciences and Natural Resources (BGR) using air as drilling medium (Bossart and Thury, 2008) in September 2003.

Table 4.1. Mineralogy of OPA shaly facies (average of nine samples) (Pearson et al., 2003).

Mineral	wt. %
Clay minerals	58-76
• Illite	16-40
• Illite/smectite ML	5-20
• Chlorite	4-20
• Kaolinite	15-33
Quartz	6-24
Calcite	5-28
Siderite	1-4
Albite	0.6-2.2
K-feldspar	1-3.1
Dolomite/ankerite	0.2-2
Pyrite	0.6-2
Organic carbon	< 0.1-1.5

Generally, the OPA formation is subdivided into five lithological sub-units with ‘sandy’, ‘shaly’, and ‘calcareous-sandy’ facies (Pearson et al., 2003). In the present study, sorption experiments with U(VI) were carried out with two OPA batches. Batch BHE-24/1 and batch BLT-11/01 were used for sorption experiments under aerobic and anaerobic conditions,

respectively. Both batches can be assigned to the shaly fraction of OPA. Table 4.1 presents the mineralogy of OPA for shaly facies as average of nine samples (Pearson et al., 2003).

Both OPA batches were characterized before starting the sorption experiments. The determined properties are summarized in Table 4.2.

Table 4.2. Main characteristics of OPA batches BHE-24/1 and BLT-11/01.

Batch	BHE-24/1	BLT-11/01
Grain size	< 500 μm	< 200 μm
N₂-BET ^a	(41.3 \pm 0.5) m ² /g	(38.8 \pm 0.3) m ² /g
TOC ^b	(1.09 \pm 0.06) wt. %	(0.96 \pm 0.02) wt. %
TC ^b	(2.49 \pm 0.02) wt. %	(1.87 \pm 0.01) wt. %
CEC ^c	(10.26 \pm 0.52) meq/100 g	(12.89 \pm 0.14) meq/100 g
Main components / wt. % ^d		
SiO₂	39.04 \pm 3.90	36.37 \pm 3.64
Al₂O₃	17.91 \pm 1.79	20.08 \pm 2.01
Fe₂O₃	6.53 \pm 0.65	6.04 \pm 0.60
CaO	5.42 \pm 0.11	3.16 \pm 0.06
K₂O	3.47 \pm 0.35	3.61 \pm 0.36
MgO	2.32 \pm 0.05	2.33 \pm 0.05
U content ^d	(2.83 \pm 0.28) ppm	(2.93 \pm 0.29) ppm

^a Determined by using a surface area and pore size analyzer (mod. Coulter SA 3100, Beckman Coulter, Fullerton, USA). ^b TOC ... total organic carbon; TC ... total carbon; determined by a multi N/C 2100 analyzer (Analytik Jena, Jena, Germany). ^c The cation exchange capacity (CEC) was determined by the compulsive exchange method (Sumner and Miller, 1996). ^d Determined by inductively coupled plasma-mass spectrometry (ICP-MS; mod. ELAN 9000, Perkin Elmer, Boston, USA; Error: \pm 10%) and atomic absorption spectroscopy (AAS; mod. AAS-4100, Perkin Elmer; Error: \pm 2%) after digestion of the OPA sample with HNO₃ (*p.a.*, Merck, Darmstadt, Germany; distilled by sub-boiling), HCl (*suprapur*, Merck) and HF (*suprapur*, Merck) in a microwave oven (mod. multiwave, Anton Paar, Perkin Elmer) (only compounds > 1 wt.% are shown).

The Fourier transform infrared (FTIR) spectra (FTIR spectrometer Spectrum 2000 GX, Perkin Elmer; KBr method) of the batches BHE-24/1 and BLT-11/01 are shown in Fig. 4.1a. The comparison of the spectra shows negligible differences between the batches. In Fig. 4.1b the IR spectra of some mineral components of OPA are compared to the IR spectrum of OPA. From all mineral spectra shown, spectral contributions can be found in the OPA spectrum.

The OPA batches were characterized additionally by X-ray diffraction (XRD). Powder XRD data were collected for both batches of OPA on a Bruker AXS D8 diffractometer (Bruker AXS GmbH, Karlsruhe, Germany) in θ - θ geometry with curved PG-secondary monochromator using CuK α radiation. The scan mode was 'locked-coupled' (Bragg-Brentano geometry). Data were collected from 7 to 70 $^{\circ}2\theta$ using a step size of 0.05 $^{\circ}2\theta$ and a step time of 21-54 s. The data were analyzed by phase evaluation using the EVA code (Bruker AXS).

The corresponding diffractograms and mineral patterns are shown in Fig. 4.2. Due to the mineralogical heterogeneity of OPA it was not possible to quantify the different mineral contributions by XRD. However, for the minerals shown in Fig. 4.2, XRD patterns were found in the diffractogram of OPA.

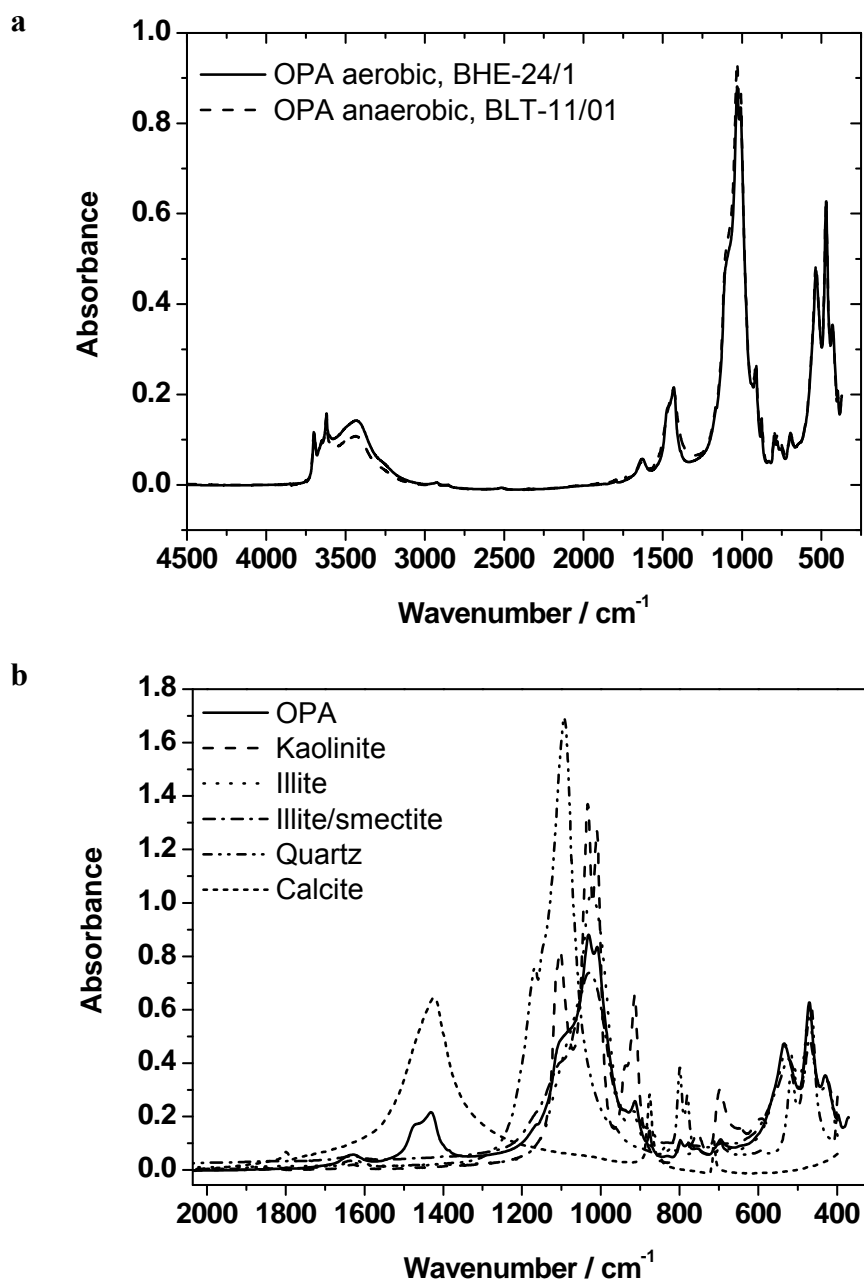


Fig. 4.1. (a) FTIR spectra of OPA batches. (b) FTIR spectra of some mineral components of OPA compared to FTIR spectra of OPA batch BHE-24/1.

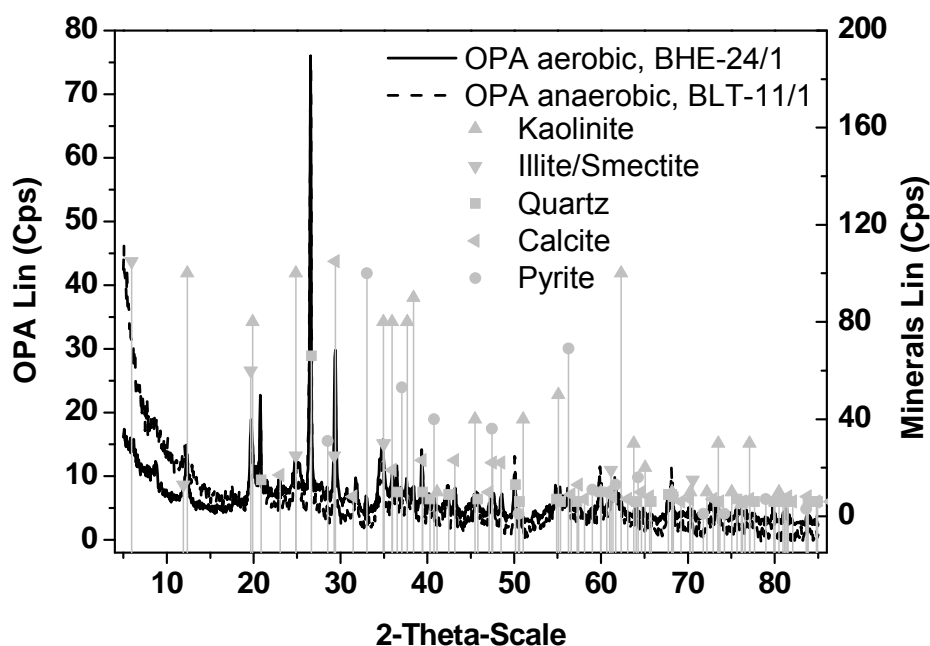


Fig. 4.2. X-ray diffractogram of the OPA batches BHE-24/1 and BLT-11/01 and patterns of different minerals contained in OPA.

The so-called OPA pore water was synthesized in this study according to the model of Pearson (1998) (pH 7.6; cf. Table 4.3) in Milli-Q water (18 M Ω ; mod. Milli-RO/Milli-Q-System, Millipore, Schwalbach, Germany). For this composition the true ionic strength (I_t) of 0.36 M is calculated using the speciation code EQ3/6 (Wolery, 1992) (cf. Table 4.3).

Table 4.3. Composition of OPA pore water: modeled by Pearson (1998) (pore water_{theor}), prepared for the experiments (pore water_{exp}) and ions leached out from OPA during 7 d contact time with OPA pore water (Δ leached_{7d}) (Δ leached_{7d} = difference between pore water_{exp} and pore water_{exp7d}).

Element/Ion	Pore water _{theor} / mol/L	Pore water _{exp} / mol/L	Δ leached _{7d} / mol/L
Na ^a	2.4×10^{-1}	n.a. ^e	n.a. ^e
K ^a	1.6×10^{-3}	$(2.3 \pm 0.2) \times 10^{-3}$	$-(0.1 \pm 0.5) \times 10^{-3}$
Mg ^b	1.7×10^{-2}	$(1.6 \pm 0.03) \times 10^{-2}$	$(0.03 \pm 0.06) \times 10^{-2}$
Ca ^b	2.6×10^{-2}	$(2.5 \pm 0.05) \times 10^{-2}$	$(0.2 \pm 0.1) \times 10^{-2}$
Sr ^a	5.1×10^{-4}	$(4.9 \pm 0.5) \times 10^{-4}$	$(0.1 \pm 1.0) \times 10^{-4}$
Al ^a	-	b.d. ^f	$(1.6 \pm 0.2) \times 10^{-7}$
Si ^a	-	b.d. ^f	$(7.7 \pm 0.8) \times 10^{-5}$
U ^a	-	b.d. ^f	$(5.3 \pm 0.5) \times 10^{-9}$
Cl ^c	3.0×10^{-1}	$(2.9 \pm 0.3) \times 10^{-1}$	$-(0.06 \pm 0.57) \times 10^{-1}$
SO ₄ ²⁻ ^c	1.4×10^{-2}	$(1.4 \pm 0.04) \times 10^{-2}$	$(0.11 \pm 0.09) \times 10^{-2}$
CO ₃ ²⁻ /HCO ₃ ^{-d}	4.8×10^{-4}	$(4.0 \pm 0.1) \times 10^{-4}$	$(3.4 \pm 0.3) \times 10^{-4}$
I_t	0.36	0.37	-

^a ICP-MS (Error: $\pm 10\%$).

^b AAS (Error: $\pm 2\%$).

^c IC (Error: ± 3 -10%).

^d TC – TOC (Error: $\pm 3\%$).

^e n.a.: not analyzed.

^f b.d.: below detection limit.

4.1.1 Leaching of Opalinus Clay with Opalinus Clay pore water

This experiment was carried out with batch BHE-24/1 after investigation of the U(VI) sorption onto OPA in OPA pore water in dependence on solid-to-liquid ratio (S/L) (section 4.4.2.1). Using the optimal S/L ratio, a leaching experiment was conducted in order to determine the ions released from the clay into the pore water in dependence on time.

4.1.1.1 Experimental

2 g OPA was weighed into a 500 mL polypropylene (PP) bottle. Subsequently, 500 mL of pore water were added. The pore water was prepared in a perfluoroalkoxy bottle, because glass bottles may release ions also present in the clay. The clay suspension was continuously shaken using an overhead shaker modified for the use of high volume bottles (mod. REAX 20, Heidolph Instruments, Schwabach, Germany). In the beginning of the experiment, samples were taken every day; after 8 d three times a week; after 34 d only once a week. After 90 d the experiment was stopped. The pH value was readjusted before each sampling. For sampling, the bottle was removed from the shaker and placed on a magnetic stirrer (mod. Big Squid, IKA, Staufen, Germany). Then, a well-mixed aliquot of the suspension of 10 mL was taken. The samples were centrifuged for phase separation (30 min, 4000 rpm; mod. Megafuge 1.0, Heraeus Sepatech, Osterode/Harz, Germany). After centrifugation, the supernatants were filtered (450 nm, polyethersulfone, vwr international, Darmstadt, Germany). Prior to filtering, the filters were rinsed with 1 mL sample solution. Filtrates were analyzed for K, Sr, Ba, Al, Si, Fe and U by ICP-MS, for Mg and Ca by AAS, and for F⁻, Cl⁻, SO₄²⁻ and PO₄³⁻ by ion chromatography (IC; mod. IC separation center 733, Metrohm, Herisau, Switzerland). The total inorganic carbon (TIC) content was measured using the multi N/C 2100 analyzer as difference of TC and TOC. During the investigations the concentrations of Fe, F⁻ and PO₄³⁻ were always below the detection limit of ICP-MS and IC.

After the leaching experiment, X-ray diffraction (XRD) experiments were performed to investigate a possible alteration of the clay mineral structure and formation of secondary mineral phases. For that, the solid was separated from the aqueous phase and lyophilized. Powder XRD data were collected for the leached out OPA.

4.1.1.2 Results and discussion

The leaching experiment showed that the concentrations of ions in the filtrates were in equilibrium after 7 d. Thus, this time was chosen as optimal pre-equilibration time for the

sorption experiments.

The initial ion composition of pore water in the experiment (pore water_{exp}) and the ions leached out during 7 d contact time of OPA with pore water (Δ leached_{7d}) are shown in Table 4.3.

It can be seen that the leaching of the alkaline and earth alkaline metal ions (except for calcium) can be neglected since the experimental errors of the concentrations measured after 7 d are larger than the values themselves.

Obviously, aluminum and silicon ions are leached out due to dissolution processes of clay minerals and quartz in OPA. Sulfate and carbonate ions are also released. They originate from pyrite oxidation and different carbonate minerals in the clay. The increase of the calcium and carbonate concentration in solution indicates the dissolution of the calcite fraction of OPA.

On the basis of the composition of pore water_{exp} and under consideration of the concentrations of the leached out ions calcium, aluminum, silicon, sulfate and carbonate an I_t of 0.34 M was calculated for the pore water used in our experiments.

After the leaching experiment, the remaining OPA was studied by XRD. Compared to the diffractogram of untreated OPA (cf. Fig. 4.2) additional patterns were detected in the resulting diffractogram of the leached out clay (not shown). These could be attributed to NaCl, which is the main salt component in pore water. Further changes in the diffractogram of the leached out OPA sample were not observed. Thus, it can be concluded, that the mineral structure of OPA is not changed due to contact with pore water. This verifies that pore water indeed is close to equilibrium with OPA.

4.1.2 Leaching of Opalinus Clay in dependence on pH

4.1.2.1 Experimental

Suspensions of OPA (batch BHE-24/1) in 0.1 M NaClO₄ were prepared as a function of pH to determine the amount of U(VI) and competing ions leached out of OPA.

The experiments were performed under ambient atmosphere ($p\text{CO}_2 = 10^{-3.5}$ atm) at room temperature. 40 mg OPA were weighed into 15 mL polypropylene (PP) centrifuge tubes (mod. Cellstar, Greiner Bio-One GmbH, Frickenhausen, Germany). Subsequently, 5 mL 0.1 M NaClO₄ were added and pH values were adjusted between pH 3 and 10. For pre-equilibration, the samples were continuously shaken on a horizontal shaker (mod. Promax 2020, Heidolph Instruments, Schwabach, Germany) and the pH values were periodically checked and readjusted. After one week of pH adjustment (4-5 times), the volume was filled

up to 10 mL with 0.1 M NaClO₄, thus, an S/L of 4 g/L was reached. After that, only small amounts of HClO₄ and NaOH had to be added for pH readjustment until the pH values were stable (usually after three weeks). Thus, the effect of pH adjustment on the S/L ratio was negligible.

At the end, the final pH values of the samples were determined and the samples were centrifuged and the supernatants were filtered as described in section 4.1.1.1.

The filtrates of the blank suspensions were analyzed for Na, K, Sr, Al, Si, P, Fe, and U by ICP-MS, for Mg and Ca by atomic absorption spectroscopy (AAS) (mod. AAS-4100, Perkin Elmer), and for F⁻, Cl⁻ and SO₄²⁻ by ion chromatography (IC; mod. IC separation center 733, Metrohm, Herisau, Switzerland). The total inorganic carbon content was measured as difference of the total carbon and the total organic carbon determined using the multi N/C 2100 analyzer. During the investigations the concentration of P was always below the detection limit of ICP-MS. Additionally, the filtrates of the blank suspensions were investigated for colloids and for the size of the colloidal particles with a BI-90 photon correlation spectroscope (Brookhaven Instruments, USA). A detailed description of the instruments and the procedure is given in (Dreissig et al., 2011).

X-ray diffraction measurements

X-ray diffraction (XRD) experiments were performed to investigate a possible alteration of the clay mineral structure and formation of secondary mineral phases due to change of the pH value. 2 g OPA were weighed into three 500 mL PP bottles each. Subsequently, 500 mL 0.1 M NaClO₄ were added in each bottle to reach an S/L ratio of 4 g/L. The pH values were adjusted to pH 4, 7 and 10, respectively. The suspensions were continuously shaken using an overhead shaker modified for the use of high volume bottles (mod. REAX 20, Heidolph Instruments). The pH values were periodically checked and readjusted. After 90 d the experiment was stopped. Each solid was separated from the aqueous phase and lyophilized. Powder XRD data were collected for the leached out OPA.

Mössbauer spectroscopy

The OPA samples used for XRD measurements were also studied by Mössbauer spectroscopy to clarify the oxidation state of the iron mineral phases in OPA. ⁵⁷Fe Mössbauer spectra were recorded at room temperature in transmission mode using standard instrumental configuration by WissEl (Starnberg, Germany). The ⁵⁷Co in the rhodium matrix was used as Mössbauer source. A quantitative analysis of the spectra was made using the NORMOS program package of R.A. Brand (Brand, 1987).

Zeta potential measurements

Due to the high carbonate content of OPA, a determination of its point of zero charge (pzc) by potentiometric titration was not feasible. To get information about the clay charge, zeta potential measurements of OPA suspensions were performed with laser Doppler velocimetry using a Zetasizer Nano ZS (Malvern Instruments, Malvern, U.K.) with disposable capillary cells. Suspensions of OPA in 0.1 M NaClO₄ (S/L = 0.1 g/L) were prepared in the pH range from pH 2.5 to 7.5 as described in section 4.5.1. The zeta potential measurements were repeated tenfold. The temperature was maintained at 25 ± 0.1°C. Agglomerated colloids were re-suspended as flocks by ultrasound before measurement.

4.1.2.2 Characterization of the solid

The zeta potential of OPA suspensions decreased with increasing pH from pH 2.5 to 7.5. In this pH range, it remained always negative, which implies that the charge of the OPA particles is negative throughout the studied pH range.

Exemplary for the studied pH range, OPA samples, that were leached at pH 4, 7 and 10 for 90 d, were studied by XRD. Compared to the diffractogram of untreated OPA (Fig. 4.2), additional patterns were detected in the resulting diffractograms (not shown). These were attributed to the background electrolyte NaClO₄. As expected for pH 4 and 7, the calcite pattern in the respective diffractograms of the leached out samples did not appear due to acid addition. Further changes in the diffractograms were not observed. Secondary mineral phases could not be detected.

The samples used for XRD were investigated also by Mössbauer spectroscopy. The ratios of Fe(II)/Fe(III) in untreated aerobic OPA and pH-equilibrated OPA samples are shown in Table 4.4. The OPA is stored under aerobic conditions. Thus, about 45% of Fe occur as Fe(III). Due to contact with water a further oxidation takes place. This effect can be observed for the whole pH range studied. Thus, it can be assumed, that during the pH-dependent sorption experiments about 50% of iron is present as Fe(II) in the OPA samples.

Table 4.4. Results of Mössbauer spectroscopy.

Sample	Fe(II) / %	Fe(III) / %
Untreated OPA	55.1 ± 2.0	44.9 ± 1.2
pH 4	47.5 ± 2.8	52.5 ± 2.0
pH 7	49.5 ± 2.1	50.5 ± 1.5
pH 10	48.2 ± 4.4	51.8 ± 3.2

4.1.2.3 Characterization of the solution

Filtrates of OPA suspensions with pH values between pH 3 and 10 were analyzed for clay leached out ions. The filtrates were checked also for the presence of colloids by photon correlation spectroscopy. In all samples, colloids were not detected.

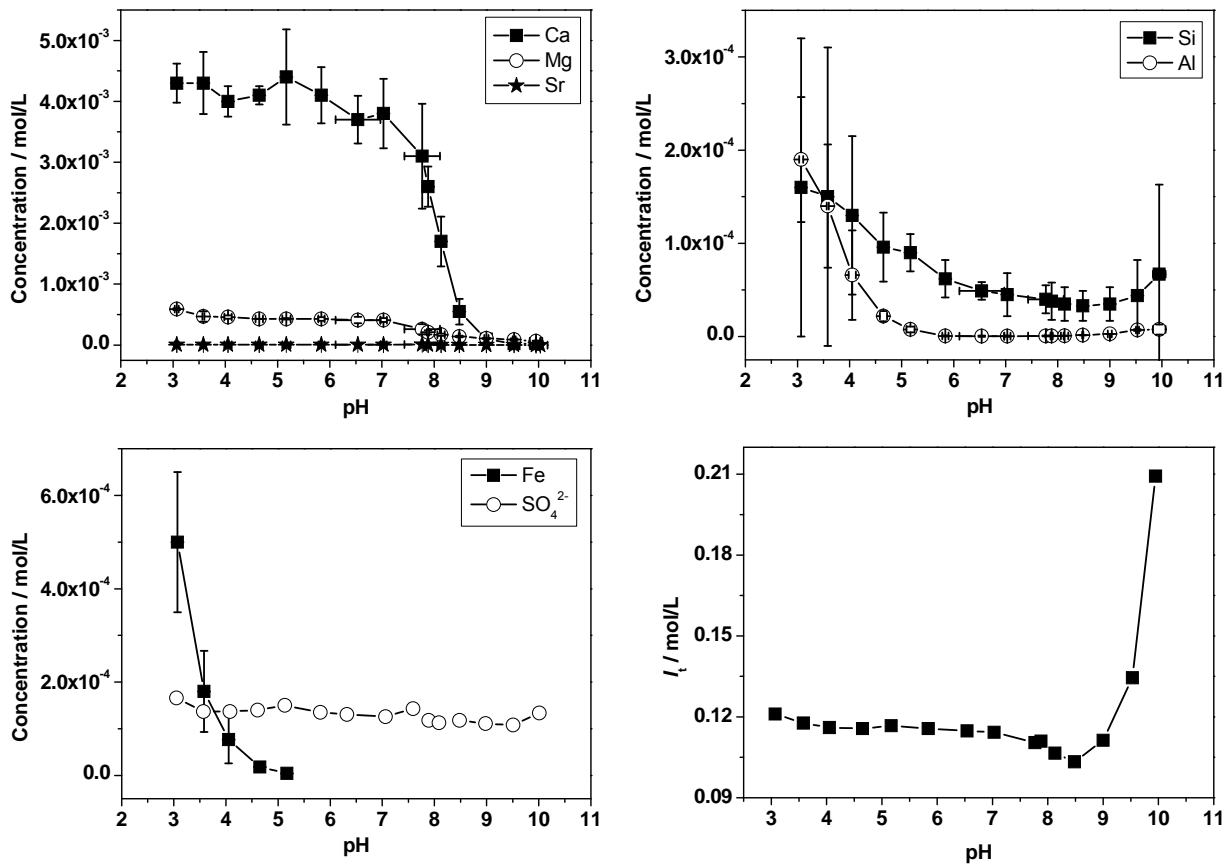


Fig. 4.3. Concentrations of Ca, Mg, Sr, Si, Al, Fe and SO_4^{2-} in the filtrates of OPA suspensions with 0.1 M NaClO_4 (S/L = 4 g/L) and the resulting true ionic strength (I_t) under consideration of the competing ions as a function of pH.

In Fig. 4.3, the concentrations of OPA leached out ions are shown for Ca, Mg, Sr, Si, Al, Fe and SO_4^{2-} as a function of pH. The comparison of the leached out alkaline earth elements shows that at pH 3 the calcium concentration is about seven times higher than the magnesium concentration. Strontium is only present in trace concentrations. The influence of pH on the clay mineral and quartz fractions of OPA is illustrated by the aluminum and silicon concentrations in solution. Only at $\text{pH} \leq 5$, iron is measured in solution. Its contribution originates from the pyrite, siderite and chlorite fractions of OPA, which are dissolved under these conditions. Due to oxidation of pyrite, sulfate is formed (Pearson et al., 2003). The observed behavior of minerals dissolution is in agreement with their geochemistry.

The pH-dependent concentrations of competing ions in solution lead to a pH-dependent ionic strength (cf. Fig. 4.3). The resulting true ionic strength (I_t) was calculated under consideration of the composition of the background electrolyte including the competing ions K, Mg, Ca, Sr, Al, Si, Fe, F⁻, Cl⁻, SO₄²⁻ and CO₃²⁻ using the speciation code EQ3/6 (Wolery, 1992). In the pH range from pH 3 to 9, I_t amounts to 0.11 M in average. Above pH 9, I_t increases to 0.21 M at pH 10, which is due to carbonate dissolution. Under natural conditions the S/L ratio of clay rock and water is much larger resulting in a higher ionic strength in the background electrolyte, the so-called pore water. For OPA the composition of its pore water was modeled by Pearson (Pearson, 1998). Its I_t amounts to 0.36 M at pH 7.6 (Joseph et al., 2011). That means, under environmentally relevant conditions the ionic strength is two to three times larger than those observed in these experiments.

4.2 Speciation of U(VI) in dependence on background electrolyte

The U(VI) speciation was calculated using the speciation code EQ3/6 (Wolery, 1992) and the thermodynamic data for U(VI) compiled in (Guillaumont et al., 2003), including data for the Ca₂UO₂(CO₃)₃(aq) complex (Bernhard et al., 2001). In the presence of HA, the U(VI) speciation was calculated using a modified EQ3/6 code (Sachs et al., 2004) with integrated metal ion charge neutralization model (CNM; (Kim and Czerwinski, 1996)) for description of the U(VI) humate complexation. The calculations were performed using literature data for the binary complex UO₂HA(II) (Montavon et al., 2000; Pompe et al., 2000a, 2000b), the ternary complex UO₂(OH)HA(I) (Sachs et al., 2007a) and the carbonate humate complex UO₂(CO₃)₂HA(II)⁴⁺ (Steudtner et al., 2011a, 2011b).

For speciation calculations the pH-dependence of the HA loading capacity (LC) (Kim and Czerwinski, 1996) must be known. LC depends on the cation which is complexed. Due to the fact that in this study several competing ions are present in solution which can be complexed by HA an average pH-dependent LC equation was used for speciation calculations. Literature data show, that various divalent cations (e.g., calcium, strontium, lead, copper, cadmium, zinc) exhibit a similar complexation with HA (Paulenová et al., 2000; Mansel et al., 2003; Beck et al., 2004). In addition, the LC values determined for U(VI) HA complexation were considered (Pompe et al., 1998, 2000b; Montavon et al., 2000; Sachs et al., 2007a). The pH-dependence of LC was obtained by linear regression (Eq. (4.1)) and used for speciation calculations:

$$LC = 0.1633 \cdot \text{pH} - 0.4134 \quad (4.1)$$

In Fig. 4.4, the speciation of U(VI) (1×10^{-6} M) in dependence on the background electrolyte (0.1 M NaClO₄, 0.39 M NaCl, OPA pore water) is presented in the absence and presence of 50 mg/L HA, respectively.

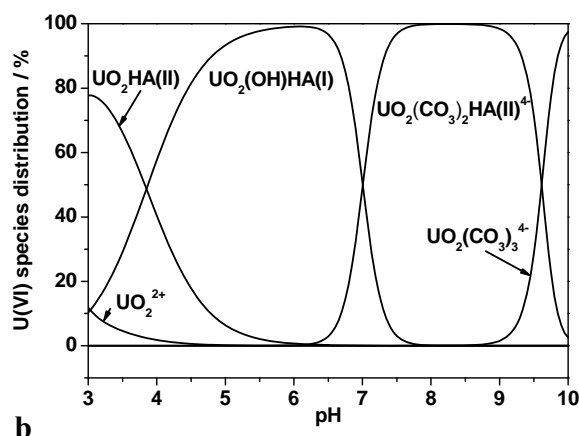
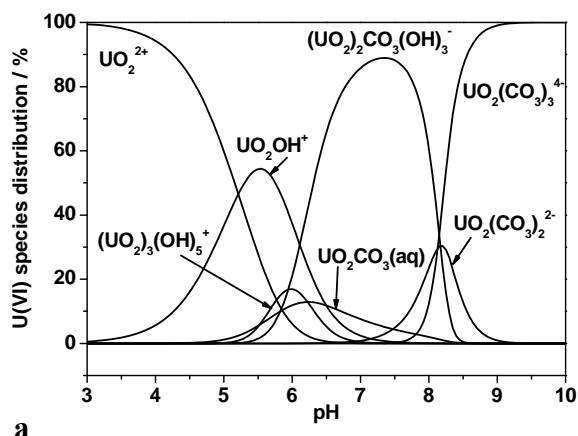
Due to the fact that most of the sorption experiments were performed at pH 7.6, the pH of the OPA pore water, the first part of the following discussion is focused on pH 7.6.

In 0.1 M NaClO₄ (Fig. 4.4a,b), the U(VI) speciation is dominated by $(\text{UO}_2)_2\text{CO}_3(\text{OH})_3^-$ (87%). In the presence of HA, the carbonato humate complex $\text{UO}_2(\text{CO}_3)_2\text{HA}(\text{II})^{4-}$ determines the U(VI) speciation to almost 100%. If 0.39 M NaCl is used as background electrolyte (Fig. 4.4c,d), the U(VI) speciation changes to $\text{UO}_2(\text{CO}_3)_3^{4-}$ (59%), $(\text{UO}_2)_2\text{CO}_3(\text{OH})_3^-$ (26%) and $\text{UO}_2(\text{CO}_3)_2^{2-}$ (13%). In the presence of HA, the U(VI) speciation is still dominated by $\text{UO}_2(\text{CO}_3)_2\text{HA}(\text{II})^{4-}$.

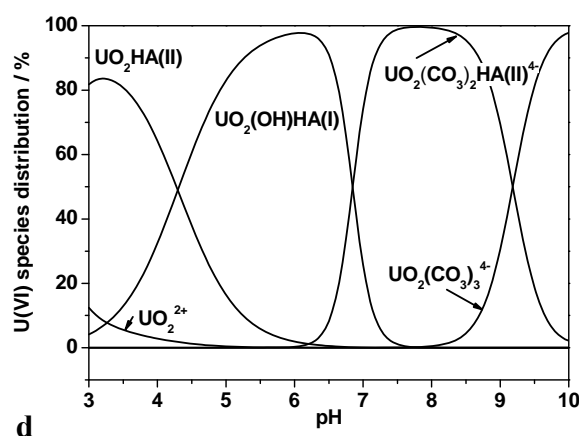
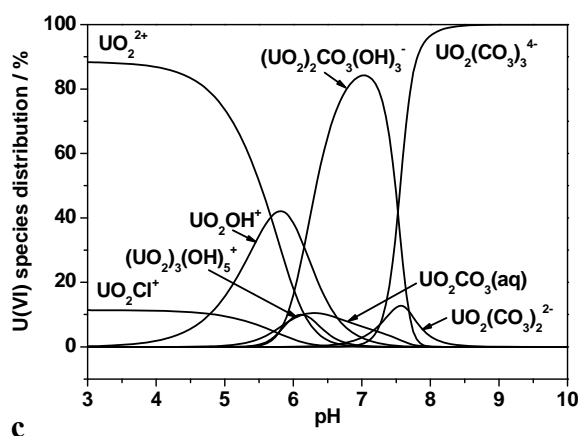
Figures 4.4e,f show the speciation of U(VI) in the absence and presence of HA (50 mg/L) in pore water as a function of pH. It should be noted that the OPA pore water composition is only valid for pH 7.6. As the concentrations of all ions are a function of pH, Figs. 4.4e,f gives an exact picture only for pH 7.6. The changing carbonate concentrations and the dissolution of calcite as a function of pH, however, have been considered.

In pore water at pH 7.6, the U(VI) speciation is dominated by $\text{Ca}_2\text{UO}_2(\text{CO}_3)_3(\text{aq})$ (Bernhard et al., 2001) (Fig. 4.4e), indicating a significant influence of calcium and carbonate ions present due to dissolution of calcite. Further charged alkaline earth carbonato complexes with U(VI) are reported in the literature, such as $\text{CaUO}_2(\text{CO}_3)_3^{2-}$, $\text{SrUO}_2(\text{CO}_3)_3^{2-}$ and $\text{MgUO}_2(\text{CO}_3)_3^{2-}$ (Dong and Brooks, 2006). Their presence was considered here, too, but was modeled to be negligible at pH 7.6 and thus, not considered in further discussions. The U(VI) speciation in the presence of HA is shown in Fig. 4.4f. Also in the presence of 50 mg HA/L the $\text{Ca}_2\text{UO}_2(\text{CO}_3)_3(\text{aq})$ complex is the dominating species at pH 7.6. That means the presence of HA has no effect on the speciation of U(VI) in pore water.

0.1 M NaClO₄



0.39 M NaCl



OPA pore water

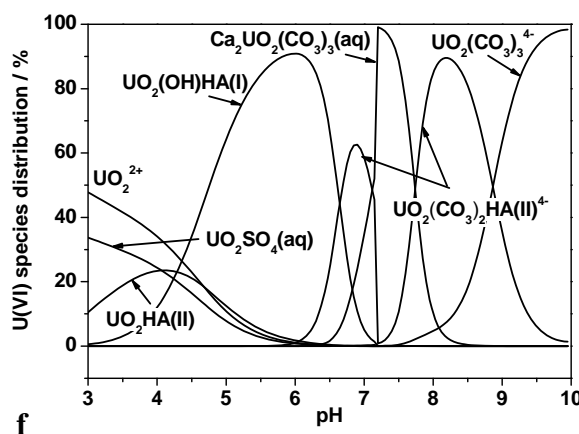
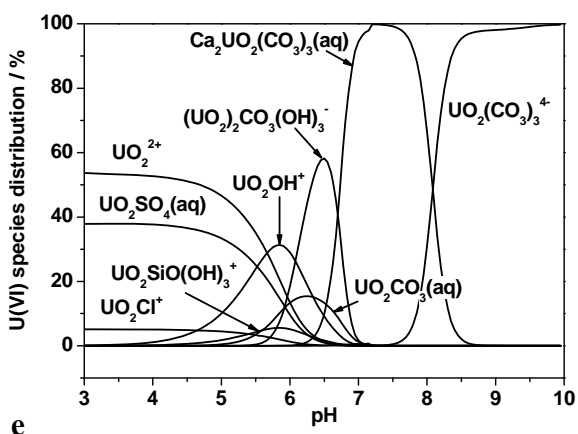


Fig. 4.4. Speciation of U(VI) in 0.1 M NaClO₄ (a, b), 0.39 M NaCl (c, d) and OPA pore water (e, f) in the absence (a, c, e) and presence (b, d, f) of HA ([U(VI)] = 1 × 10⁻⁶ M; [HA] = 50 mg/L; pCO₂ = 10^{-3.5} atm). Only species > 5% are shown.

Because of the large effect of calcium on the U(VI) speciation, its influence on the HA speciation was also studied. The results from the speciation modeling show, that at pH 7.6 the

calcium humate complex, CaHA(II) , clearly dominates the HA speciation with about 69% (not shown). It can be concluded that HA binding sites are nearly saturated with calcium ions in pore water. Due to the presence of the neutral $\text{Ca}_2\text{UO}_2(\text{CO}_3)_3(\text{aq})$ complex in solution an interaction of U(VI) with HA can be excluded. That means that the HA speciation in OPA pore water is not affected by the presence of U(VI).

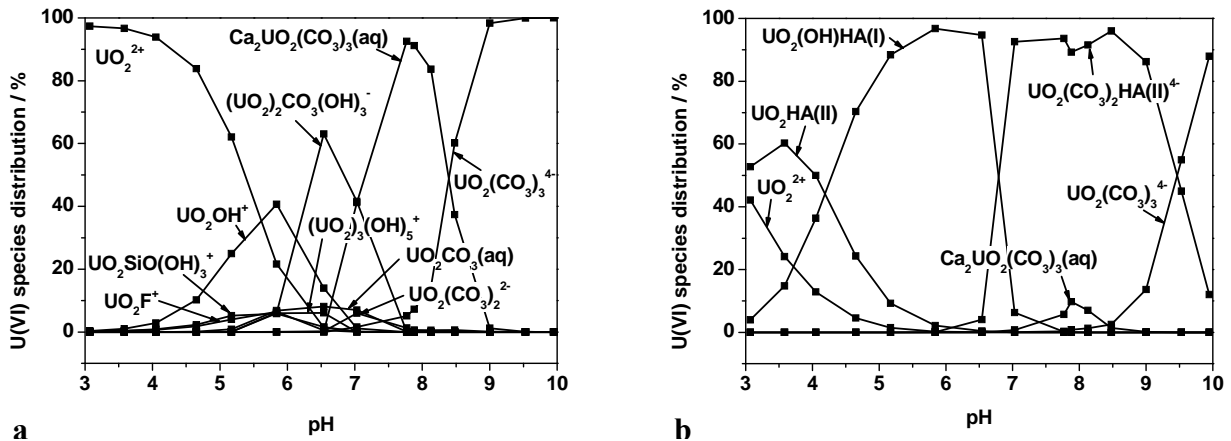


Fig. 4.5. Speciation of U(VI) in 0.1 M NaClO_4 in the (a) absence and (b) presence of 50 mg/L HA under consideration of the ions leached out from OPA ($[\text{U(VI)}] = 1 \times 10^{-6} \text{ M}$; $[\text{HA}] = 50 \text{ mg/L}$; $p\text{CO}_2 = 10^{-3.5} \text{ atm}$). Only species $> 5\%$ are shown.

In connection with the OPA leaching experiments in dependence on pH discussed in section 4.1.2, in Fig. 4.5, the U(VI) speciation in the absence and presence of HA is shown as a function of pH. Since the concentration of ions leached out from OPA was determined at specific pH values (cf. section 4.1.2.3), the U(VI) speciation was calculated only for these pH values (shown as points in Fig. 4.5). The lines were drawn for visual reasons. In the absence of HA at $\text{pH} > 6$, the uranyl carbonato species $(\text{UO}_2)_2\text{CO}_3(\text{OH})_3^-$, $\text{Ca}_2\text{UO}_2(\text{CO}_3)_3(\text{aq})$ and $\text{UO}_2(\text{CO}_3)_3^{4-}$ are dominant due to the presence of carbonate in solution. The presence of $\text{Ca}_2\text{UO}_2(\text{CO}_3)_3(\text{aq})$ demonstrates the large influence of the competing ion calcium on the U(VI) speciation. Further charged alkaline earth carbonato complexes with U(VI) are reported in the literature, such as $\text{CaUO}_2(\text{CO}_3)_3^{2-}$, $\text{SrUO}_2(\text{CO}_3)_3^{2-}$ and $\text{MgUO}_2(\text{CO}_3)_3^{2-}$ (Dong and Brooks, 2006), that theoretically can be present in the investigated sample solutions. However, they are modeled to be negligible in the investigated pH range and thus, not considered in further discussions.

The presence of HA affects the U(VI) speciation significantly (Fig. 4.5b). At low pH values ($\sim \text{pH} 3$), $\text{UO}_2\text{HA(II)}$ dominates the speciation. Uranyl hydroxo humate, $\text{UO}_2(\text{OH})\text{HA(I)}$, is the prevailing species in solution in the pH range from pH 4.5 to 7. Due to the presence of carbonate in solution at $\text{pH} > 6$, the uranyl carbonato humate complex $\text{UO}_2(\text{CO}_3)_2\text{HA(II)}^{4-}$ is

formed. $\text{UO}_2(\text{CO}_3)_2\text{HA}(\text{II})^{4-}$ prevents significantly the formation of $\text{Ca}_2\text{UO}_2(\text{CO}_3)_3(\text{aq})$ which is formed only in a very small amount in the pH range from pH 7 to 9.

The HA speciation, depicted in Fig. 4.6, shows that in the whole pH range the U(VI) humate complexes formed play only a subordinate role in comparison to the humate complexes formed with the OPA leached out calcium. $\text{CaHA}(\text{II})$ dominates the HA speciation in the pH range from pH 3 to about 8.5.

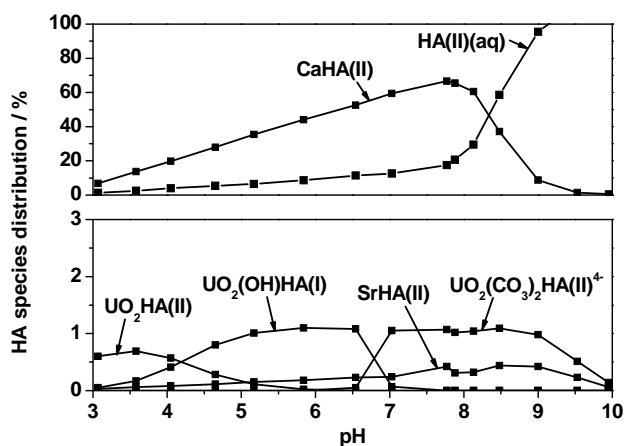


Fig. 4.6. Speciation of HA in 0.1 M NaClO_4 in the presence of U(VI) under consideration of the ions leached out from OPA ($[\text{U}(\text{VI})] = 1 \times 10^{-6} \text{ M}$; $[\text{HA}] = 50 \text{ mg/L}$; $p\text{CO}_2 = 10^{-3.5} \text{ atm}$).

Certain amounts of magnesium, aluminum and iron are also contained in solution, however, complexation data for humate complexes with these ions based on CNM are not available in the literature. Few studies determined conditional stability constants for such complexes (Pandey et al., 2000; Tipping et al., 2002; Lippold et al., 2005). However, for speciation calculations, pH- and ionic strength-independent complex formation constants and respective pH-dependent LC values are required. Especially for iron and aluminum different hydrolyzed species can be expected in solution in dependence on pH. Thus, different humate complexes can be expected analog to U(VI). Although there are only few complexation data available, it is known, that the interaction of aluminum with HA is stronger than that of calcium or magnesium (Beck et al., 2004), however, much weaker than that of iron (Lippold et al., 2007). Iron is a strongly competing ion concerning the complexation of HA with UO_2^{2+} (Teterin et al., 2001). Tochiyama et al. (2004) demonstrated that Fe(III) forms stronger complexes with HA than Fe(II). The oxidation state of the dissolved iron in the investigated system is not known. However, several redox processes can take place. On one hand, atmospheric oxygen can oxidize the mineralogically bound Fe(II) in OPA. On the other hand, HA has reducing properties (Reiller, 2005; Schmeide and Bernhard, 2009; Sachs and Bernhard, 2011a) and potentially could reduce Fe(III) present in solution. However, since the experiments were

performed under aerobic conditions, it is assumed, that Fe(III) is the dominating oxidation state in solution.

At low pH values, HA precipitates to a certain extent due to protonation of the HA carboxylic groups. In the presence of metal ions this effect is increased due to additional screening of the HA negative charge by these ions. Thus, one can expect that at pH 3, where increased concentrations of aluminum and iron are present in solution, no aquatic but rather solid complexes of HA with aluminum and iron are formed.

Based on this discussion a sequence of the present competing ions and U(VI) concerning their interaction strength with HA can be assumed as follows: $\text{Fe(III)} > \text{Al(III)} \geq \text{U(VI)} > \text{Sr(II)} > \text{Ca(II)} > \text{Mg(II)}$. However, since the calcium concentration in solution is about two orders of magnitude higher than the concentrations of the other ions (cf. Fig. 4.3) the HA speciation will still be dominated by CaHA(II) over a wide pH range, also after addition of the missing complexation data of various magnesium, aluminum and iron humate complexes to the EQ3/6 data base. The higher complexation constants of the Fe(III), Al(III), U(VI) and Sr(II) HA complexes can not compensate their low concentrations as shown by SrHA(II) and the various U(VI) humate complexes (cf. Fig. 4.6).

4.3 The system U(VI) / humic acid / kaolinite in dependence on background electrolyte

In order to determine the influence of the applied background electrolyte on the U(VI) and HA sorption onto kaolinite, batch sorption experiments were carried out using 0.1 M NaClO₄, 0.39 M NaCl and OPA pore water. The U(VI) sorption was investigated in the absence and presence of HA and the HA sorption was examined in the absence and presence of U(VI). The results were interpreted using the U(VI) speciation calculations shown in section 4.2.

4.3.1 Experimental

A ²³³U(VI) stock solution was used for all experiments. For that, a solution of ²³³UO₂(NO₃)₂ (Eckert & Ziegler, Valencia, CA, USA) was dried up. After adding the threefold molar quantity of 0.01 M NaHCO₃ (*p.a.*, Merck, Darmstadt, Germany) to form ²³³UO₂(CO₃)₃⁴⁻ as precursor, a surplus of 0.1 M HCl (*p.a.*, Merck) was added and ²³³UO₂Cl₂ was formed. The specific activity of the ²³³U(VI) stock solution, determined with liquid scintillation counting (LSC; mod. TriCarb 3100 TR, Perkin Elmer, Freiburg, Germany) using Ultima Gold (Perkin Elmer) as scintillation cocktail, amounts to 11.93 kBq/mL (1.44×10^{-4} M ²³³UO₂Cl₂).

For the studies with HA, synthetic HA type M42 was applied both as ^{14}C -labeled synthetic HA (batch M180A, 23.08 MBq/g) and non-labeled HA (batch M145) (Pompe et al., 1998; Sachs et al., 2004). HA type M42 represents a HA like melanoidin from xylose and glutamic acid. It shows an elemental composition and functional group content (proton exchange capacity: (3.34 ± 0.18) meq/g (^{14}C -M42) and (3.51 ± 0.07) meq/g (M42)) comparable to those of most natural HA. Consequently, its sorption and metal ion complexation behavior is also comparable to that of natural HA (e.g. (Pompe et al., 1998; Schmeide et al., 2003, 2006; Křepelová et al., 2006)). A HA stock solution of 5 g/L was prepared by mixing 5 mg of ^{14}C -M42 with 45 mg M42, adding 1880 μL of 0.1 M NaOH and filling up the volume to 10 mL with Milli-Q water (18 M Ω ; mod. Milli-RO/Milli-Q-System, Millipore, Schwalbach, Germany).

Solutions of 0.1 M NaClO_4 and 0.39 M NaCl were prepared by dissolution of $\text{NaClO}_4 \cdot \text{H}_2\text{O}$ (*p.a.*, Merck) or NaCl (*p.a.*, Merck), respectively, in Milli-Q water. A solution of OPA pore water was prepared as described in section 4.1.

For pH adjustment, diluted HClO_4 (*p.a.*, Merck), HCl and NaOH (*p.a.*, Roth, Karlsruhe, Germany) solutions were used. For studies with NaClO_4 and NaCl, a calculated amount of 1 M NaHCO_3 (*p.a.*, Merck) was added to accelerate equilibration with atmospheric CO_2 . The pH values were measured using a laboratory pH meter (mod. inoLab pH 720, WTW, Weilheim, Germany) with SenTix[®] Mic pH microelectrodes (WTW), calibrated using standard buffers (WTW) at pH 7 and 9.

Batch sorption experiments were performed under ambient atmosphere ($p\text{CO}_2 = 10^{-3.5}$ atm) at room temperature. 40 mg kaolinite (KGa-1b, described in (Křepelová et al., 2006; Sachs et al., 2007b)) were weighed into 15 mL polypropylene (PP) centrifuge tubes (mod. Cellstar, Greiner Bio-One GmbH, Frickenhausen, Germany). Subsequently, 10 mL of the background electrolyte (0.1 M NaClO_4 , 0.39 M NaCl, OPA pore water) were added and the pH value was adjusted to pH 7.6. Thus, an S/L ratio of 4 g/L was used. All sorption samples were prepared in triplicate. For pre-equilibration, the samples were continuously shaken on a horizontal shaker (mod. Promax 2020, Heidolph Instruments, Schwabach, Germany) and the pH values were periodically checked and readjusted for 13 d.

After pre-equilibration, 70 μL of a $^{233}\text{U(VI)}$ stock solution were added to the kaolinite suspensions to obtain a final $^{233}\text{U(VI)}$ concentration of 1×10^{-6} M. For the investigation of the U(VI) sorption onto kaolinite in the presence of HA, additionally 20 or 100 μL HA stock solution were added subsequently. The final concentration of HA in solution amounted to 10 or 50 mg/L. After U(VI) and HA addition, the pH values were readjusted immediately. For

equilibration, the samples were shaken on a horizontal shaker for 3 d, whereby the pH was readjusted each day. After 3 d, the final pH values of the samples were determined and the samples were centrifuged and the supernatants were filtered as described in section 4.1.1.1. For comparison, additional kaolinite samples with HA in the absence of $^{233}\text{U(VI)}$ were prepared. The filtrates were analyzed simultaneously for the final U(VI) and HA concentration by LSC. For LSC, 1 mL of the filtrate was mixed with 15 mL Ultima Gold (Perkin Elmer) as scintillation cocktail.

In addition, blank suspensions of kaolinite in the three different background electrolytes were prepared and processed under the same conditions to determine the amount of U(VI) leached out of kaolinite.

Finally, the U(VI) or HA sorption onto vial walls was determined. For this, 7 mL 1 M HNO_3 (U(VI) sorption) or 1 M NaOH (HA sorption) were added to the emptied vials and the vials were shaken for 3 d. The solutions were analyzed by LSC for U(VI) and HA, respectively.

The amount of U/HA adsorbed on the mineral surface was calculated as the difference between the initial U(VI)/HA concentration and U(VI)/HA remaining in solution after the sorption experiment. The values were corrected by the wall sorption and the U(VI) concentration in the blank samples.

4.3.2 Results and discussion

In Table 4.5, the results of the U(VI) sorption experiments with kaolinite are shown.

Table 4.5. U(VI) sorbed onto kaolinite in dependence on background electrolyte (S/L = 4 g/L, pH 7.6).

Background electrolyte	0.01 M NaClO_4 ^a	0.1 M NaClO_4	0.39 M NaCl	0.36 M OPA pore water
$[\text{U(VI)}] = 1 \times 10^{-6}$ M	~ 98%	(88.4 ± 1.1)%	(85.1 ± 1.5)%	(42.4 ± 4.2)%
$[\text{U(VI)}] = 1 \times 10^{-6}$ M + $[\text{HA}] = 10$ mg/L	~ 90%	(87.2 ± 1.7)%	(85.4 ± 2.2)%	(36.0 ± 1.9)%
$[\text{U(VI)}] = 1 \times 10^{-6}$ M + $[\text{HA}] = 50$ mg/L	~ 65%	(38.8 ± 4.6)%	(53.1 ± 1.4)%	(30.7 ± 2.8)%

^a At pH 7.5 (Křepelová et al., 2006).

With increasing ionic strength of the inert background electrolyte the U(VI) sorption onto kaolinite decreases only slightly. This effect was diminished (10 mg HA/L) and even inverted (50 mg HA/L) in the presence of HA. This decrease of U(VI) sorption in the absence of HA is

due to the rising presence of $\text{UO}_2(\text{CO}_3)_3^{4-}$ in U(VI) speciation at an ionic strength of 0.39 M at pH 7.6. This U(VI) species sorbs only weakly onto kaolinite compared to $(\text{UO}_2)_2\text{CO}_3(\text{OH})_3^-$ dominating the U(VI) speciation at ionic strength of 0.1 M. In addition, the samples of the 0.39 M experiments showed an end pH of 7.5, where the U(VI) speciation is composed of $\text{UO}_2(\text{CO}_3)_3^{4-}$ (36%), $(\text{UO}_2)_2\text{CO}_3(\text{OH})_3^-$ (48%) and $\text{UO}_2(\text{CO}_3)_2^{2-}$ (12%). Thus, the U(VI) sorption decreases only slightly. The U(VI) speciation in the presence of 50 mg HA/L does not give an explanation for the increase of U(VI) sorption with increasing ionic strength. In both systems $\text{UO}_2(\text{CO}_3)_2\text{HA}(\text{II})^{4-}$ is the dominating species at pH 7.6. This U(VI) species sorbs to some extent onto kaolinite. With increasing ionic strength changes in the macromolecular configuration of HA occur. More and more negative charges of the HA molecules are screened by the ions in solution. Thus, HA folds itself to a coil. In this configuration more HA can sorb onto the clay surface compared to the more open HA form at low ionic strength.

If the complex background electrolyte OPA pore water is used in the sorption experiments, the amount of sorbed U(VI) decreases further. This is due to the formation of the neutral aquatic $\text{Ca}_2\text{UO}_2(\text{CO}_3)_3$ complex, which seems to sorb only weakly onto the clay possibly due to its neutral character.

The presence of 10 mg HA/L has in all investigated systems no significant effect on U(VI) sorption. However, at higher HA concentrations of 50 mg HA/L the U(VI) sorption decreases significantly in all investigated systems. This is due to the formation of the U(VI) humate complex, $\text{UO}_2(\text{CO}_3)_2\text{HA}(\text{II})^{4-}$, which leads to the mobilization of U(VI).

Table 4.6. HA sorbed onto kaolinite in dependence on background electrolyte (S/L = 4 g/L, pH 7.6).

Background electrolyte	0.01 M NaClO ₄ ^a	0.1 M NaClO ₄	0.39 M NaCl	0.36 M OPA pore water
[HA] = 10 mg/L	~ 23%	(72.1 ± 4.2)%	(74.0 ± 5.7)%	(68.9 ± 5.4)%
[HA] = 50 mg/L	~ 10%	(17.2 ± 1.6)%	(28.3 ± 1.5)%	(33.8 ± 1.5)%
[HA] = 10 mg/L + [U(VI)] = 1 × 10 ⁻⁶ M	~ 50%	(72.4 ± 3.5)%	(74.3 ± 6.0)%	(74.5 ± 4.8)%
[HA] = 50 mg/L + [U(VI)] = 1 × 10 ⁻⁶ M	-	(19.7 ± 1.2)%	(30.6 ± 1.5)%	(37.6 ± 1.4)%

^a At pH 7.5 (Křepelová et al., 2006).

The HA sorption onto kaolinite in the absence and presence of U(VI) is given in Table 4.6. The increase of the ionic strength from 0.01 M to 0.1 M leads to an increase in HA sorption. As discussed, with increasing ionic strength more ions are present in solution which screen

the negatively charged functional groups of the HA molecules. Thus, less repulsing effects from negatively charged clay surface appear and HA sorption onto the clay mineral increases. However, an additional increase of the ionic strength to 0.39 M has no significant effect on HA sorption. Also the change to the complex background electrolyte, OPA pore water, has a negligible effect on HA sorption.

In all investigated systems the percentage of HA sorption decreases with increasing HA concentration. However, this effect is reduced with increasing ionic strength.

Unless for 0.01 M NaClO₄, in all other investigated systems U(VI) does not have an influence on HA sorption at both investigated HA concentrations.

4.4 The system U(VI) / humic acid / Opalinus Clay / Opalinus Clay pore water

In the present study, the U(VI) sorption onto OPA in the absence and presence of HA was investigated by means of batch sorption experiments. The ternary system U(VI) / HA / OPA is investigated using synthetic OPA pore water (Pearson, 1998) as background electrolyte. Due to the fact that the influence of competing ions, originating from the pore water, on this system is studied, it should be rather described as a quaternary system. The pore water consists of ions originating from mineral leaching processes such as calcium, strontium, sulfate and carbonate. These ions can control the speciation of U(VI) and HA by forming soluble or insoluble species or occupying important binding sites. In this study the discussion of the pore water effects on the speciation (cf. section 4.2) is coupled with sorption and spectroscopic experiments to verify the speciation results. The outcome of this study is published in (Joseph et al., 2011).

4.4.1 Experimental

In this study, OPA (batch BHE-24/1) and HA (M42, batch M180A) were used for the experiments as described in the sections 4.1 and 4.3.1, respectively, with the exception that HA was solved in OPA pore water. OPA pore water was applied as background electrolyte in all experiments (cf. section 4.1). In all experiments the pH was controlled and, if necessary, adjusted to $\text{pH } 7.6 \pm 0.05$ using diluted HCl and NaOH. Due to the small amounts of added HCl and NaOH an effect on the S/L ratio was negligible. The pH value was measured using a laboratory pH meter (mod. inoLab pH 720, WTW, Weilheim, Germany) with SenTix[®] Mic pH microelectrodes (WTW), calibrated using standard buffers (WTW) at pH 7 and 9.

A U(VI) stock solution (5×10^{-4} M $^{238}\text{UO}_2(\text{ClO}_4)_2$ in 0.005 M HClO_4) was used for all experiments. In addition, ^{233}U was used as tracer. For that, a solution of $^{233}\text{UO}_2(\text{NO}_3)_2$ was applied, which was transformed into a $^{233}\text{UO}_2(\text{ClO}_4)_2$ solution by drying up and adding the threefold molar quantity of 0.01 M NaHCO_3 to form $^{233}\text{UO}_2(\text{CO}_3)_3^{4-}$ as precursor. After that, a surplus of 0.1 M HClO_4 was added and $^{233}\text{UO}_2(\text{ClO}_4)_2$ was formed. The specific activity of the ^{233}U stock solution was determined with LSC using Ultima Gold (Perkin Elmer) as scintillation cocktail. It amounts to 8.4 kBq/mL ($[\text{}^{233}\text{U}] = 1.02 \times 10^{-4}$ M).

At first, sorption experiments with the binary systems U(VI) / OPA and HA / OPA were performed. U(VI) sorption studies onto OPA were carried out to find the optimal solid-to-liquid ratio (S/L ratio) for the experiments, to avoid experimental conditions, where the U(VI) sorption is extremely high or low. After that, kinetic sorption studies with U(VI) or HA and OPA were performed to evaluate the time required to obtain sorption equilibrium. Distribution coefficients, K_d , for the sorption of U(VI) and HA onto OPA in pore water were determined by investigating the sorption isotherms for U(VI) and HA. Finally, the system U(VI) / HA / OPA was investigated. The experiments are discussed with increasing complexity in the order U(VI) or HA / OPA / pore water and U(VI) / HA / OPA / pore water. The experimental conditions of all experiments carried out are compiled in Table 4.7. The studies were performed under ambient atmosphere ($p\text{CO}_2 = 10^{-3.5}$ atm) at room temperature. With the exception of the system U(VI) / HA / OPA, which was investigated both under aerobic and anaerobic conditions.

Table 4.7. Experimental conditions of experiments.

Experiment	Solute	[U(VI)] / mol/L	[HA] / mg/L	S/L / g/L
S/L ratio dependence	U(VI)	1×10^{-6}	-	0.5 - 300
Kinetic sorption studies	U(VI) or HA	1×10^{-6}	10	60
U(VI) sorption isotherm	U(VI)	$1 \times 10^{-8} - 1 \times 10^{-4}$	-	60
		$1 \times 10^{-8} - 5 \times 10^{-7}$	-	4
HA sorption isotherm	HA	-	10 - 320	60
U(VI) and HA sorption	U(VI) and HA	1×10^{-6}	10, 50	60

4.4.1.1 Sorption experiments

According to the S/L ratio (cf. Table 4.7), a respective amount of clay was weighed into 15 mL PP centrifuge tubes (mod. Cellstar, Greiner Bio-One GmbH, Frickenhausen, Germany). Subsequently, 10 mL pore water were added and the pH value was adjusted. For pre-equilibration, the samples were continuously shaken on a horizontal shaker (mod. Promax 2020, Heidolph Instruments) for 7 d and the pH values were periodically readjusted.

After pre-equilibration, aliquots of a U(VI) or HA stock solution were added to the suspensions to obtain the U(VI) and HA concentrations compiled in Table 4.7. The pH values were readjusted immediately. The samples were shaken on the horizontal shaker to equilibrate for 3 d (U(VI) sorption) or 1 d (HA sorption). After that, the final pH values of the samples were determined. The samples were centrifuged and the supernatants were filtered as described in section 4.1.1.1. The filtrates were analyzed for the final U(VI) and HA concentration by ICP-MS and LSC, respectively. For LSC, 1 mL of the filtrate was mixed with 15 mL Ultima Gold. In addition, blank suspensions of OPA in pore water were prepared and processed under the same conditions to determine the amount of U(VI) leached out of OPA.

Finally, the U(VI) or HA sorption onto vial walls was investigated. 7 mL 1 M HNO₃ (U(VI) sorption) or 1 M NaOH (HA sorption) were added and the vials were shaken for 3 d. The solutions were analyzed by ICP-MS or LSC for U(VI) and HA, respectively.

The amount of U/HA adsorbed on the mineral surface was calculated as the difference between the initial U(VI)/HA concentration and U(VI)/HA remaining in solution after the sorption experiment. The values were corrected by the wall sorption and the U(VI) concentration in blanks.

Every sorption experiment was carried out as described in this section. Any deviations from this procedure are explained in the respective sections.

S/L ratio dependence

Due to the fact that these experiments were carried out before the leaching experiment (cf. section 4.1.1), a pre-equilibration and contact time of 3 d each was used according to previous U(VI) sorption studies performed with kaolinite in NaClO₄ (Křepelová et al., 2006). These experiments were performed in duplicate.

Kinetic sorption experiments

For this, 12 g OPA were weighed into 250 mL bottles and 200 mL pore water were added. Aliquots of a U(VI) or HA stock solution were added and the suspensions were stirred with a magnetic stirrer. After different contact times aliquots of the suspensions were taken.

U(VI) and HA sorption isotherms

For the U(VI) sorption isotherm ²³³U was used. The U(VI) sorption isotherm was measured as a function of the U(VI) concentration and of the S/L ratio whereas the HA sorption isotherm

was only measured as a function of HA concentration. The $^{233}\text{U(VI)}$ and HA concentration in the filtrates was determined by LSC. All experiments were performed in duplicate.

Influence of HA on the U(VI) sorption

After pre-equilibration, HA was added instantly after addition of $^{233}\text{U(VI)}$. For comparison, additional OPA samples with $^{233}\text{U(VI)}$ in the absence of HA and with HA in the absence of $^{233}\text{U(VI)}$ were prepared. The further handling of the samples was analog to section 4.4.1.1 except that the filtrates were analyzed simultaneously for the final U(VI) and HA concentration by LSC. All sorption experiments were performed in triplicate.

Because of the presence of Fe(II) minerals in OPA, the filtrates were analyzed with respect to a possible reduction of U(VI) to U(IV). The redox speciation of U after the sorption experiments was determined by solvent extraction using thenoyltrifluoroacetone (TTA; p.a., Fluka/Sigma-Aldrich, Steinheim, Germany) according to Bertrand and Choppin (1982). For TTA extractions, 2 mL of the filtrates were acidified to pH 0.5 using degassed HCl (37%). After that, 2 mL of freshly prepared 0.5 M TTA solution in degassed xylene (p.a., Fluka) were added and the samples were shaken vigorously for 10 min. The samples were then centrifuged for phase separation (10 min, 4000 rpm). Under these conditions, U(IV) species are extracted by TTA into the organic phase whereas U(VI) remains in the aqueous phase. The resulting U(VI) concentrations in the aqueous phases were analyzed by LSC.

4.4.1.2 TRLFS measurements

To identify the U(VI) species in the pore water in the absence and presence of HA, TRLFS measurements were performed under cryogenic conditions at 153 K. TRLFS measurements at room temperature are not suitable, since the U(VI) concentration is too low. In addition, as reported by Bernhard et al. (2001) and Wang et al. (2004) the uranyl carbonato species ($(\text{UO}_2)_2(\text{OH})_3\text{CO}_3^-$, $\text{UO}_2\text{CO}_3(\text{aq})$, $\text{UO}_2(\text{CO}_3)_2^{2-}$, $\text{UO}_2(\text{CO}_3)_3^{4-}$), possibly present in solution, show no luminescence properties at room temperature.

Since pore water contains a large amount of chloride, which acts as strong luminescence quencher, special pore water was prepared for this experiment substituting all chloride by perchlorate. Speciation calculations confirmed that these small changes of the background electrolyte do not affect the speciation of U(VI) in solution at pH 7.6. Applying this, sorption experiments were performed analog to those described in 4.4.1.1 in the section *Influence of HA on the U(VI) sorption*. The filtrates after sorption experiments were studied in comparison to U(VI) added pore water samples by means of TRLFS.

For the measurements, aliquots of pore water and filtrates were filled into plastic cuvettes (mod. BI-SCP, Brookhaven Instruments, Holtsville, NY, USA), placed immediately in a freezer at 255 K and stored for 1 d. For TRLFS measurements, the frozen samples were transferred as ice cubes from the plastic cuvettes into a specifically designed sample holder. The sample holder has one hole to insert the ice cube and windows for laser irradiation. After transfer, the samples were cooled to 153 K via a cryogenic cooling system (mod. TG-KKK, KGW-Isotherm, Karlsruhe, Germany).

TRLFS laser pulses at 410 nm with an average pulse energy of 4 mJ (Nd:YAG-MOPO laser system, mod. GCR 230 (20 Hz), Spectra Physics, Mountain View, USA) were used for excitation of the U(VI) luminescence. The emitted luminescence light was detected in a right angle setup by a Jobin Yvon 270M spectrograph (Jobin Yvon GmbH, Munich, Germany). The resulting spectra were measured in time-resolved mode using an ICCD camera (512 pixel; mod. Spectrum One, Horiba-Jobin Yvon). The time difference between the trigger of the laser system and the start of the camera was adjusted by a delay generator DG 540 (Stanford Research Instruments, Sunnyvale, USA). The spectra were recorded in the wavelength range from 454 to 604 nm by accumulating 20 to 100 laser pulses using a gate time of the camera of 500 μ s. Delay times varied from 50 ns to 4 ms after application of the laser pulse in 10 μ s increments.

4.4.2 Results and discussion

4.4.2.1 Influence of S/L ratio on the U(VI) sorption

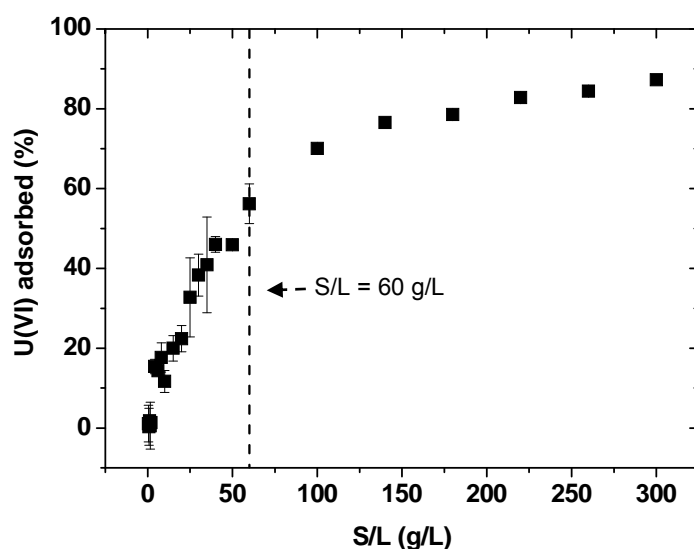


Fig. 4.7. U(VI) adsorbed onto OPA as a function of S/L ratio ($[U(VI)] = 1 \times 10^{-6}$ M; OPA pore water).

The U(VI) sorption onto OPA as a function of the S/L ratio is shown in Fig. 4.7. An S/L ratio of 60 g/L was chosen for the following sorption studies. Under these conditions, about 50% U(VI) is adsorbed onto OPA, an adequate amount for interpretation of the sorption results.

4.4.2.2 Kinetic of the U(VI) and humic acid sorption onto Opalinus Clay

The U(VI) and HA sorption onto OPA as a function of time is shown in Fig. 4.8. It becomes evident that HA reaches sorption equilibrium very fast (within 1 h) with an average amount of adsorbed HA of $(91.2 \pm 0.1)\%$. Thus, 1 d was considered to be sufficient to achieve the sorption equilibrium between HA and OPA during the sorption experiments. For U(VI) a much slower sorption kinetic was observed. The U(VI) sorption equilibrium is reached within 24 h with an average sorption of $(55.0 \pm 0.2)\%$. After that, the amount of sorbed U(VI) remains roughly stable for the investigated time of 247 h. Based on these results, an equilibration time of 3 d was chosen for the sorption experiments with U(VI).

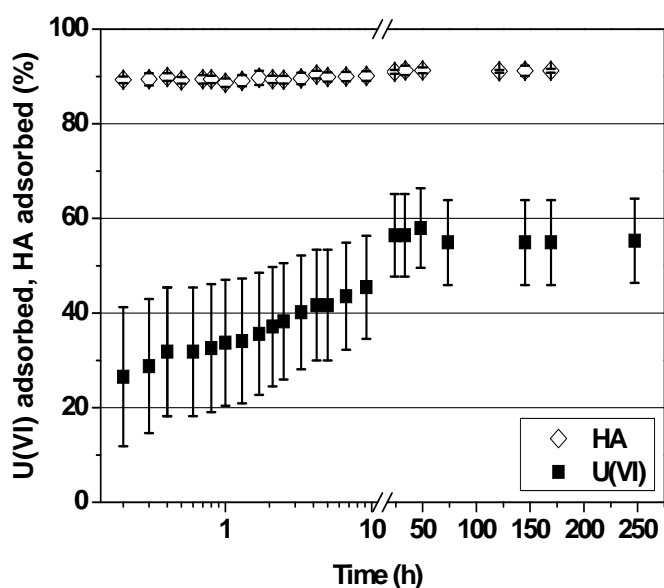


Fig. 4.8. U(VI) and HA sorbed onto OPA as a function of time ($[U(VI)] = 1 \times 10^{-6}$ M; $[HA] = 10$ mg/L; S/L = 60 g/L; OPA pore water).

4.4.2.3 Determination of K_d values for U(VI) and humic acid

The U(VI) and HA sorption results obtained by varying the U(VI) or HA concentration at constant S/L ratio are depicted in Fig. 4.9 and 4.10. The data were fitted using the Freundlich isotherm (Freundlich, 1906). The Freundlich isotherm is described by Eq. (4.2):

$$a_{eq} = c_{eq}^{n_F} \cdot k_F \quad (4.2)$$

where a_{eq} (mg/g or Bq/g) is the amount of U(VI) or HA adsorbed on the solid phase, c_{eq} (mg/L or Bq/L) is the equilibrium concentration of U(VI) or HA in solution, k_F (m^3/kg) and n_F are the Freundlich coefficients.

The distribution coefficient K_d (m^3/kg) is defined as follows:

$$K_d = \frac{a_{eq}}{c_{eq}} \quad (4.3)$$

The K_d values for the U(VI) and HA sorption onto OPA were calculated using the logarithmic form of Eq. (4.2). Setting $n_F = 1$, k_F is equal to K_d .

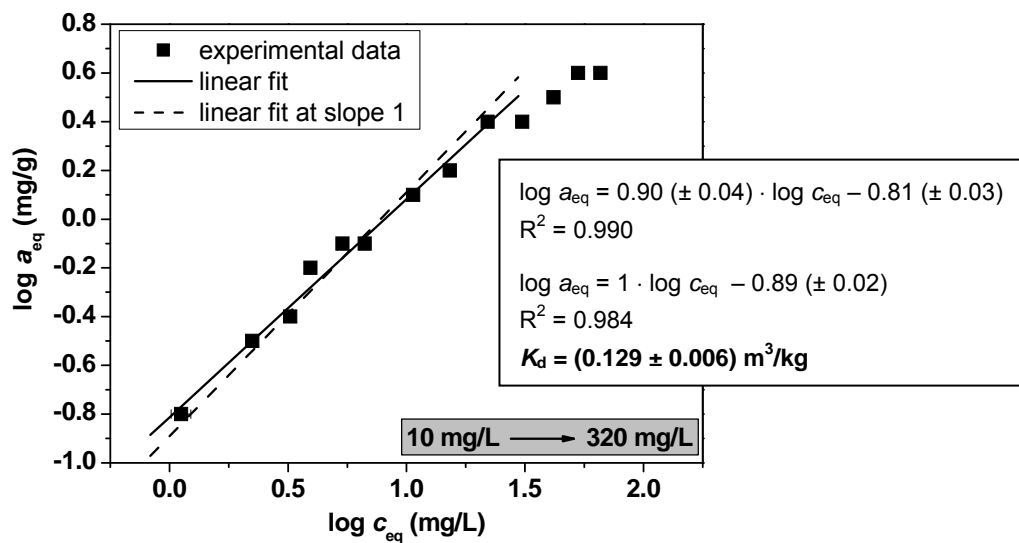


Fig. 4.9. Freundlich isotherm of the HA sorption onto OPA with varying HA concentration ([HA] = 10 – 320 mg/L; S/L = 60 g/L; OPA pore water); a_{eq} : amount of HA sorbed onto OPA, c_{eq} : equilibrium concentration of HA in solution, K_d : distribution coefficient.

The Freundlich sorption isotherm for the HA sorption onto OPA in pore water is shown in Fig. 4.9. With initial HA concentrations between 10 and 160 mg/L the amount of adsorbed HA increases linearly. At higher initial HA concentrations (> 160 mg/L) the slope of the adsorbed amount of HA slightly decreases indicating the achievement of a saturation of binding sites for HA sorption. Since the Freundlich isotherm definition excludes the saturation range, the K_d value of adsorbed HA onto OPA was determined for the range 10 - 160 mg HA/L. The K_d value amounts to $(0.129 \pm 0.006) m^3/kg$.

In pore water, calcium humate is the dominant HA species in solution (cf. section 4.2). Previously, the influence of calcium ions on the HA sorption onto various clay minerals, such as kaolinite (Saada et al., 2003) and montmorillonite (Sutton and Sposito, 2006; Majzik and Tombacz, 2007), was investigated. An increased HA sorption was observed, when calcium

ions were present in solution (Saada et al., 2003). Sutton and Sposito (2006) simulated the HA sorption onto Ca-montmorillonite. They observed differences in the sorption behavior when Ca-saturated HA was used instead of pure HA. The protonated HA existing under acidic conditions interacted mainly with the clay mineral by hydrogen bonds. The Ca-saturated HA preferred to adsorb via cation bridges. But also a few water bridges and indirect hydrogen bonds mediated by water molecules were formed. For the present study, because of the heterogeneity of OPA, it can not be estimated which mineral phase of OPA acts as the main adsorbent for CaHA(II). However, it can be assumed, that also cation bridges originating mainly from calcium may play an important role in the sorption process.

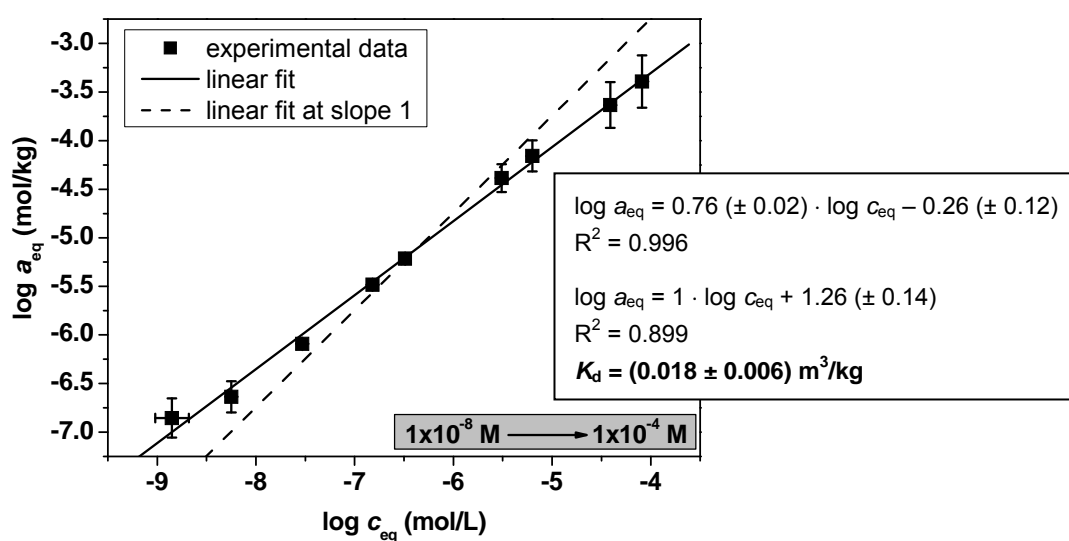


Fig. 4.10. Freundlich isotherm of the U(VI) sorption onto OPA with varying U(VI) concentration ($[U(VI)] = 1 \times 10^{-8} - 1 \times 10^{-4} \text{ M}$; $S/L = 60 \text{ g/L}$; OPA pore water); a_{eq} : amount of U(VI) sorbed onto OPA, c_{eq} : equilibrium concentration of U(VI) in solution, K_d : distribution coefficient.

In Fig. 4.10 the sorption isotherm for the U(VI) sorption onto OPA is presented. Using the Freundlich equation and a fixed slope of 1, a K_d value of $(0.018 \pm 0.006) \text{ m}^3/\text{kg}$ was determined. Experiments with an S/L ratio of 4 g/L were also performed (not shown). There, a K_d value of $(0.065 \pm 0.025) \text{ m}^3/\text{kg}$ was determined using U(VI) concentrations of $1 \times 10^{-8} - 5 \times 10^{-7} \text{ M}$. Amayri et al. (2008) determined for the U(VI) sorption onto OPA a K_d value of $(0.03 \pm 0.01) \text{ m}^3/\text{kg}$ using an S/L ratio of 15 g/L and U(VI) concentrations of $1 \times 10^{-8} - 1 \times 10^{-4} \text{ M}$. They determined a Freundlich coefficient of $n_F = 1.21$, pointing to a non-linear sorption. For the U(VI) sorption onto OPA presented in this study, also a non-linear sorption behavior was observed, but in contrast to Amayri et al. (2008), n_F values of 0.76 ($S/L = 60 \text{ g/L}$) and 0.64 ($S/L = 4 \text{ g/L}$) were determined. Thus, two different interaction behaviors for the U(VI) sorption onto OPA were observed, which can be attributed to the

chosen U(VI) concentrations and S/L ratios during the experiments, which is discussed in detail next.

To extrapolate from laboratory experiments to real field conditions, it is necessary to assume that the K_d values are independent of S/L ratios. Comparing the results presented here and in the study of Amayri et al. (2008), it is obvious, that the determined K_d values depend on the S/L ratio used in the experiments. Phillippi et al. (2007) investigated the phenomenon of K_d -S/L ratio dependence in detail by modeling the sorption in the system U(VI) / carbonate / Fe(III)-coated sand. They observed that the U(VI) sorption in the absence of carbonate and also the carbonate sorption in the absence of U(VI) were independent of the S/L ratio. In the ternary system, however, a dependence on the S/L ratio was observed. The described effect was also observed by Zheng et al. (2003), who investigated the U(VI) sorption onto two soils containing different amounts of calcium carbonate. With increasing U(VI) concentration the U(VI) sorption decreased. They concluded, that this behavior was an artifact due to calcite dissolution. They proposed that high S/L ratios should be used for determining K_d values in calcareous soils. Then, the complete calcite dissolution can be avoided and the calcite saturation of the solution is maintained. To verify this assumption for our results, an additional Freundlich sorption isotherm was calculated using the data of the U(VI) sorption onto OPA as a function of S/L ratio (cf. Fig. 4.7). The results are depicted as K_d vs. S/L ratio in Fig. 4.11.

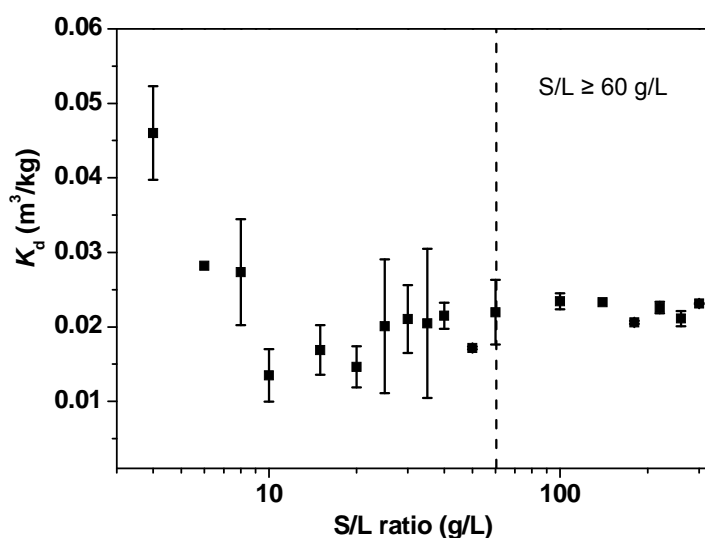


Fig. 4.11. Distribution coefficient (K_d) of the U(VI) sorption onto OPA as a function of S/L ratio ([U(VI)] = 1×10^{-6} M; S/L = 4 – 300 g/L; OPA pore water).

From the results given in Fig. 4.11 it can be concluded that for an initial U(VI) concentration of 1×10^{-6} M, an S/L ratio-independent K_d can only be obtained for S/L ratios ≥ 60 g/L. For

these S/L ratios the respective Freundlich isotherm shows the highest linearity of all discussed isotherms in this study ($n_F = 0.997$; not shown). The resulting K_d value amounts to $(0.0222 \pm 0.0004) \text{ m}^3/\text{kg}$. Thus, this K_d value is representative for the investigated system U(VI) / OPA / pore water. Since this K_d value is independent of S/L for $S/L \geq 60 \text{ g/L}$, it can be used to predict the sorption behavior of U(VI) onto OPA, which has relevance for performance assessment of OPA as a host rock for a nuclear waste repository.

The obtained K_d value of $(0.0222 \pm 0.0004) \text{ m}^3/\text{kg}$ indicates a weak sorption affinity of U(VI) toward OPA, obviously due to the predominant formation of the $\text{Ca}_2\text{UO}_2(\text{CO}_3)_3(\text{aq})$ complex in solution.

Wu et al. (2009) determined a K_d value of $(0.025 \pm 0.005) \text{ m}^3/\text{kg}$ for Np(V) sorption onto OPA by batch sorption experiments. This is very close to the respective U(VI) value determined in the present work, implying similar sorption affinities for U(VI) and Np(V) toward OPA. This is in contrast to results obtained for U(VI) and Np(V) sorption onto pure clay minerals, e.g. kaolinite (Křepelová et al., 2006; Schmeide and Bernhard, 2010), where at pH 7.5 98% of U(VI), but only 24.5% of Np(V) are sorbed. This difference can be attributed to the absence of $\text{Ca}_2\text{UO}_2(\text{CO}_3)_3(\text{aq})$ in those systems. Only little is known about the interaction of this complex with other minerals. Fox et al. (2006) investigated the U(VI) sorption onto ferrihydrite and quartz in the presence of different calcium concentrations in solution. Under conditions where the $\text{Ca}_2\text{UO}_2(\text{CO}_3)_3(\text{aq})$ species predominates the U(VI) speciation, a decreasing U(VI) sorption onto both minerals was observed with increasing calcium concentration. Meleshyn et al. (2009) studied the influence of this complex on the U(VI) sorption onto Ca- and Na-bentonites using NaNO_3 or $\text{Ca}(\text{NO}_3)_2$ as background electrolytes. Under near-neutral pH conditions, $\text{Ca}_2\text{UO}_2(\text{CO}_3)_3(\text{aq})$ dominates the U(VI) speciation in $\text{Ca}(\text{NO}_3)_2$, whereas $(\text{UO}_2)_2\text{CO}_3(\text{OH})_3^-$ is the predominant species in NaNO_3 . In $\text{Ca}(\text{NO}_3)_2$ a lower U(VI) sorption was observed than in NaNO_3 . Using NaNO_3 as background electrolyte, the U(VI) sorption onto Ca-bentonite was lower compared to the U(VI) sorption onto Na-bentonite. This was also attributed to the formation of $\text{Ca}_2\text{UO}_2(\text{CO}_3)_3(\text{aq})$ due to leaching of calcium ions.

The low U(VI) sorption affinity toward OPA can not exclusively be attributed to the formed $\text{Ca}_2\text{UO}_2(\text{CO}_3)_3(\text{aq})$ complex. Bradbury and Baeyens (Personal communication, 2010) investigated U(VI) sorption onto Na-illite as principal sorbing mineral phase in OPA rock ((23 ± 2) wt.%). The experimental data were described by a two site protolysis non-electrostatic surface complexation and cation exchange sorption model. The modeling results were used to predict sorption isotherms measured onto OPA, whereby Bradbury and Baeyens

(Personal communication, 2010) observed an overestimation of the U(VI) sorption isotherm. After addition of the complexation constant of the so-called “non-sorbing U(VI) species” $\text{Ca}_2\text{UO}_2(\text{CO}_3)_3(\text{aq})$ to the model, the resulting model underestimated the experimental data. It was concluded that illite is not a suitable model to predict the sorption behavior of U(VI) onto OPA. Other U(VI) species-sorbing mineral phases have to be present in OPA. Hartmann et al. (2008) studied the U(VI) sorption onto OPA from Benken, Switzerland, in 0.1 M NaClO_4 by batch and spectroscopic experiments as a function of pH. A significant decrease of the U(VI) sorption at pH 6.5-9.0 was observed. To reproduce the experimental data, model calculations were performed. They demonstrated that calculated and experimental data show a divergence, which was reduced when $\text{Ca}_2\text{UO}_2(\text{CO}_3)_3(\text{aq})$ was included as non-sorbing species in calculations. They concluded that this complex prevents U(VI) sorption onto OPA significantly. But finally, they ascertained still a difference between calculations and experiments and assumed that $\text{Ca}_2\text{UO}_2(\text{CO}_3)_3(\text{aq})$ adsorbs to some extent to the minerals surface. This assumption is confirmed in the present study. The U(VI) sorption onto the clay mineral kaolinite in pore water ($S/L = 4 \text{ g/L}$) was studied under identical experimental conditions such as described in this section (cf. section 4.3 and (Joseph et al., 2009)). The results showed that the specifically sorbed amount of U(VI) toward kaolinite is higher ($(2.2 \pm 0.2) \mu\text{g/m}^2$) than onto OPA ($(0.045 \pm 0.003) \mu\text{g/m}^2$). Based on these results, it can be concluded, that also kaolinite as a main fraction in OPA ((15-33) wt.%) is not a sufficient model for description of the available binding sites. Zheng et al. (2003) investigated the U(VI) sorption in natural geologic settings, in detail onto two soils (pH 5 and pH 8) containing different concentrations of calcium carbonate. They showed that at high calcium carbonate concentrations (pH 8) the U(VI) sorption onto the soil was lower, which was attributed to the increased formation of $\text{Ca}_2\text{UO}_2(\text{CO}_3)_3(\text{aq})$. They modeled their results using two different surface complexation models, a ferrihydrite model and a ferrihydrite and clay model. With the first model the sorption data at pH 8 were fitted very well, supporting ferrihydrite as main adsorbent fraction in the soil. With the second model nearly identical results were obtained. Zheng et al. (2003) concluded that under these conditions U(VI) sorption onto clay minerals is relatively weak compared to U(VI) sorption onto ferrihydrite. OPA contains about 2-6 wt.% iron containing mineral phases, namely pyrite and siderite. Whether these phases are the main adsorbent phases for $\text{Ca}_2\text{UO}_2(\text{CO}_3)_3(\text{aq})$ in OPA is unknown up to now.

4.4.2.4 Influence of humic acid on the U(VI) sorption onto Opalinus Clay

OPA contains about 1 wt.% organic carbon (cf. Table 4.1). It is known that only a small portion of the TOC (about 0.15 wt.%) consists of humic material (Pearson et al., 2003), that means a fraction of 1.5×10^{-3} wt.% of OPA. In the present experiments, a HA concentration of 50 mg HA/L in maximum is used. Under consideration that HA type M42 contains (56.1 ± 0.3)% carbon (Sachs et al., 2004), at an S/L ratio of 60 g clay/L a TOC of 0.05 wt.% results. That means the experiments are performed in 30-fold excess. The results of the U(VI) sorption onto OPA in the absence and presence of HA are summarized in Table 4.8.

Table 4.8. U(VI) and HA sorption onto OPA under ambient atmosphere ($p\text{CO}_2 = 10^{-3.5}$ atm) or inert gas conditions (N_2 -box) (S/L = 60 g/L; OPA pore water).

	U(VI) adsorbed / $\mu\text{g}/\text{m}^2$		HA adsorbed / $\mu\text{g}/\text{m}^2$	
	$p\text{CO}_2 = 10^{-3.5}$ atm	N_2 -box	$p\text{CO}_2 = 10^{-3.5}$ atm	N_2 -box
[U(VI)] = 1×10^{-6} M	0.045 ± 0.003	0.046 ± 0.002	-	-
[U(VI)] = 1×10^{-6} M + [HA] = 10 mg/L	0.044 ± 0.003	0.047 ± 0.001	3.5 ± 0.2	3.9 ± 0.1
[U(VI)] = 1×10^{-6} M + [HA] = 50 mg/L	0.045 ± 0.002	0.049 ± 0.002	17.6 ± 0.6	19.5 ± 0.4
[HA] = 10 mg/L	-	-	3.5 ± 0.3	3.9 ± 0.1
[HA] = 50 mg/L	-	-	17.6 ± 0.5	19.3 ± 0.4

Table 4.8 shows, that under ambient conditions the U(VI) sorption is not influenced by HA. These results are in agreement with the U(VI) speciation results, where the presence of HA has no effect on the U(VI) speciation at pH 7.6 (cf. Fig. 4.4). In contrast to this, Křepelová et al. (2006) showed that the presence of HA decreased the U(VI) sorption onto kaolinite at pH 7.5 in 0.1 M NaClO_4 . This effect was increased with increasing HA concentration and was attributed to the formation of dissolved U(VI) humate complexes. However, in the presence of calcium ions the formation of U(VI) humate complexes is inhibited, as verified by the present data.

Table 4.8 presents the HA sorption onto OPA. With increasing HA concentration the adsorbed amount of HA onto OPA increases. At both HA concentrations used, no influence of U(VI) on the HA sorption can be observed. This corresponds to the HA speciation results and can be attributed to the neutral character of the $\text{Ca}_2\text{UO}_2(\text{CO}_3)_3(\text{aq})$ complex. Kornilovich et al. (2000) and Křepelová et al. (2008) proposed for the sorption of metal ions onto clay

minerals in the presence of humic acid, that the metal ion can be located between the solid phase and the humic acid. In the quaternary system U(VI) / HA / OPA / pore water studied here it is assumed that the place of the metal ion is occupied by calcium, but not by U(VI). U(VI) and HA do not affect each other in the sorption process.

Finally, it was tested by means of solvent extraction, whether the added U(VI) is reduced to U(IV) in the systems U(VI) / OPA / pore water or U(VI) / HA / OPA / pore water. U(IV) could not be detected in the extracts. Thus, a reduction of U(VI) by OPA or by HA can be excluded under the studied conditions.

4.4.2.5 Influence of CO₂

In addition to the sorption experiments performed under ambient conditions, the U(VI) sorption onto OPA was investigated under inert gas atmosphere. The results are also shown in Table 4.8. Due to the fact that in both experiments different OPA batches were used, the respective BET values of the OPA batches were incorporated in the data analysis. Thus, the sorbed U(VI) and HA amounts are presented in $\mu\text{g}/\text{m}^2$ OPA.

Because OPA pore water was used as background electrolyte, the U(VI) and HA speciation is independent of the surrounding atmosphere. Under inert gas conditions the same U(VI) and HA speciations are present in solution like under ambient conditions. That means, the $\text{Ca}_2\text{UO}_2(\text{CO}_3)_3(\text{aq})$ complex still dominates the U(VI) speciation and CaHA(II) is still the determining species of the HA speciation. As expected, the amounts of sorbed U(VI) and HA onto OPA obtained under inert gas conditions agree well with the results obtained under ambient atmosphere. Small differences can be attributed to the different OPA batches applied in the respective sorption experiments.

The conclusion is, that CO₂ from the surrounding gas atmosphere has no significant influence on the U(VI) and HA sorption in the OPA / OPA pore water system.

The reduction of U(VI) to U(IV) by the systems OPA / OPA pore water and HA / OPA / OPA pore water was investigated by solvent extraction. U(IV) was not detected in the extracts. However, a potential formation of an insoluble U(IV) species on the clay surface can not be completely excluded. For this, the surface has to be investigated closer, for example, by extended X-ray absorption fine structure (EXAFS) spectroscopy.

4.4.2.6 Investigation of the U(VI) speciation by TRLFs under cryogenic conditions

To identify the U(VI) species present in solution, TRLFs measurements were performed at 153 K. The results are shown in Table 4.9.

Table 4.9. Luminescence properties of the measured U(VI) species ($\lambda_{\text{ex}} = 410 \text{ nm}$).

Sample	Main luminescence emission bands / nm
<i>Pore water (chloride free)</i>	
[U(VI)] = $1 \times 10^{-6} \text{ M}$	485.0, 501.6, 522.8, 545.4, 571.3
<i>Filtered supernatant after sorption</i>	
[U(VI)] = $1 \times 10^{-6} \text{ M}$	485.1, 502.1, 523.2, 545.2, 571.1
[U(VI)] = $1 \times 10^{-6} \text{ M}$ + [HA] = 10 mg/L	485.4, 501.9, 522.9, 545.6, 571.9
[U(VI)] = $1 \times 10^{-6} \text{ M}$ + [HA] = 50 mg/L	485.8, 502.6, 523.9, 546.6, 569.5

^a Error: $\pm 0.3 \text{ nm}$.

The main luminescence emission bands of the U(VI) species present in chloride free pore water and in the filtrates of the respective sorption samples in the absence and presence of HA are very similar. This indicates that the same U(VI) species is present in all solutions. Except for the first emission band, the measured peak positions are almost identical to those published by Wang et al. (2004) and Bernhard and Geipel (2007) for $\text{Ca}_2\text{UO}_2(\text{CO}_3)_3(\text{aq})$. At low temperatures as shown in (Bernhard and Geipel, 2007), the main luminescence emission bands of $\text{UO}_2(\text{CO}_3)_3^{4-}$ are shifted to lower wavelengths in average by about 3.5 nm compared to the $\text{Ca}_2\text{UO}_2(\text{CO}_3)_3(\text{aq})$. For measurements at cryogenic temperatures, Wang et al. (2004) showed the main luminescence emission bands of different uranyl carbonato species. These bands differ from the corresponding bands of the free uranyl ion by a blueshift of several nanometers (average values: $\text{Ca}_2\text{UO}_2(\text{CO}_3)_3(\text{aq})$: 15 nm; $\text{UO}_2\text{CO}_3(\text{aq})$: 19 nm; $\text{UO}_2(\text{CO}_3)_3^{4-}$: 19 nm; $\text{UO}_2(\text{CO}_3)_2^{2-}$: 21 nm; $(\text{UO}_2)_2(\text{OH})_3\text{CO}_3^-$: 23 nm). The shift of the luminescence emission bands compared to the free uranyl ion (not shown) measured in the present study in average amounts to 15 nm and can be assigned to the blueshift obtained for $\text{Ca}_2\text{UO}_2(\text{CO}_3)_3(\text{aq})$. Thus, the presence of other uranyl carbonato species can be excluded since then the shift has to be at least $\geq 4 \text{ nm}$ higher than the measured shift.

For $\text{Ca}_2\text{UO}_2(\text{CO}_3)_3(\text{aq})$ a luminescence lifetime of about 1 ms is reported (Wang et al., 2004; Bernhard and Geipel, 2007). The lifetimes of the U(VI) species in pore water and in the filtrates of the sorption samples in the absence and presence of HA approximate also 1 ms, which additionally indicates the occurrence of $\text{Ca}_2\text{UO}_2(\text{CO}_3)_3(\text{aq})$. That means the calculated U(VI) speciation given in section 4.2 is confirmed by TRLFS measurements.

In conclusion, U(VI) sorption onto OPA in synthetic OPA pore water as background electrolyte was studied by batch sorption experiments. It was demonstrated that U(VI)

sorption onto OPA is very weak. A K_d value of $(0.0222 \pm 0.0004) \text{ m}^3/\text{kg}$ was determined, which was shown to be independent of S/L ratios $\geq 60 \text{ g/L}$. Thus, this K_d value can be used to predict U(VI) sorption at real field conditions. The K_d value determined for U(VI) is close to that obtained for the Np(V) sorption onto OPA ($(0.025 \pm 0.005) \text{ m}^3/\text{kg}$; (Wu et al., 2009)). This points out that both actinides have nearly the same sorption affinity toward OPA in the OPA / pore water system.

Due to dissolution of calcite in OPA, calcium ions are present in the pore water and form the aquatic $\text{Ca}_2\text{UO}_2(\text{CO}_3)_3$ complex with U(VI). This complex predominates U(VI) speciation under pore water conditions. HA was added to the system to investigate the influence of organic matter on the U(VI) sorption onto OPA. $\text{Ca}_2\text{UO}_2(\text{CO}_3)_3(\text{aq})$ predominates also the U(VI) species distribution in the presence of HA. Consequently, the U(VI) sorption onto OPA is not influenced by HA. The dominant presence of the $\text{Ca}_2\text{UO}_2(\text{CO}_3)_3(\text{aq})$ complex in solution in the absence and presence of HA was verified by TRLFS measurements.

With regard to the sorption capability of complex clay formations, it is not sufficient to investigate the sorption and retention properties of pure clay minerals such as kaolinite or illite toward actinides. As shown for the U(VI) sorption onto OPA from Mont Terri, Switzerland, calcite is one of the most important mineral phases in this heterogeneous multicomponent system, since it determines the pore water composition, which in turn affects the U(VI) speciation and therefore, also the U(VI) sorption. That means not only the complexity of the natural clay formation but also the resulting pore water chemistry is of great importance for performance assessment studies.

The speciation of HA in this system is also influenced by the presence of dissolved calcium ions. The cations saturate the binding sites of HA almost completely.

Concerning a nuclear waste repository, where OPA is intended to be used as geological barrier, the following can be concluded. If U(VI) as part of the nuclear waste is released into clay formation in a worst case scenario, it will be complexed by Ca^{2+} and CO_3^{2-} ions leached out from OPA, whereby $\text{Ca}_2\text{UO}_2(\text{CO}_3)_3(\text{aq})$ is formed. Due to the weak sorption affinity of this complex toward OPA, this can contribute to an enhanced mobility of U(VI) in the host rock. Organic matter such as HA shows no significant influence on the U(VI) sorption behavior.

Further studies were performed to approach further real field conditions by studying the diffusion of U(VI) in intact OPA rock cores (cf. section 5).

4.5 The system U(VI) / humic acid / Opalinus Clay / 0.1 M NaClO₄

In this section, the U(VI) sorption onto OPA in the absence and presence of HA was investigated by means of batch sorption experiments to study the influence of pH and competing ions on the ternary system U(VI) / HA / OPA. To identify the competing ions in solution, leaching studies were performed and the results were integrated in U(VI) and HA speciation calculations to assess their influence on speciation. The outcome of these studies will be published in (Joseph et al., 2012a, in preparation).

4.5.1 Experimental

A U(VI) stock solution (5×10^{-4} M UO₂(ClO₄)₂ in 0.005 M HClO₄) was used for all experiments.

For the studies with HA, synthetic HA type M42 was applied both as ¹⁴C-labeled synthetic HA (batch R2/06A, 8.9 ± 0.6 MBq/g) and non-labeled HA (batch M145) (Pompe et al., 1998; Sachs et al., 2004). HA type M42 represents a HA like melanoidin from xylose and glutamic acid. Its elemental composition and functional group content (proton exchange capacity: (3.61 ± 0.30) meq/g (¹⁴C-M42) and (3.51 ± 0.07) meq/g (M42)) is comparable to those of most natural HA. Thus, its sorption and metal ion complexation behavior is also comparable to that of natural HA (e.g. (Pompe et al., 1998; Křepelová et al., 2006; Schmeide et al., 2006)). A HA stock solution of 5 g/L was prepared by mixing 16 mg of ¹⁴C-M42 with 34 mg M42, adding 1940 μL of 0.1 M NaOH and filling up the volume to 10 mL with Milli-Q water. A solution of 0.1 M NaClO₄ was prepared by dissolution of NaClO₄·H₂O in Milli-Q water.

For pH adjustment diluted HClO₄ and NaOH solutions were used. For studies at pH values > 7, a calculated amount of 1 M NaHCO₃ was added to accelerate equilibration with atmospheric CO₂. The pH values were measured using a laboratory pH meter with SenTix[®] Mic pH microelectrodes, calibrated using standard buffers at pH 1, 4, 7 and 9.

Batch sorption experiments were performed under ambient atmosphere ($p\text{CO}_2 = 10^{-3.5}$ atm) at room temperature. The samples were prepared as described in section 4.1.2.1.

After pre-equilibration, 20 μL of a U(VI) stock solution were added to the OPA suspensions to obtain a final U(VI) concentration of 1×10^{-6} M. For the investigation of the U(VI) sorption onto OPA in the presence of HA, additionally 100 μL HA stock solution were added 1 h before addition of U(VI) for saturation of HA with clay leached out competing ions. The final concentration of HA in solution amounted to 50 mg/L. After U(VI) and HA addition, the pH values were readjusted immediately. For equilibration, the samples were shaken on a

horizontal shaker for 3 d, whereby the pH was readjusted each day. After 3 d, the final pH values of the samples were determined and the samples were centrifuged and the supernatants were filtrated as described in 4.1.1.1. The filtrates were analyzed for the final U(VI) and HA concentration by ICP-MS and LSC, respectively. For LSC, 1 mL of the filtrate was mixed with 15 mL Ultima Gold as scintillation cocktail. Prior to the measurements of the U(VI) concentrations in the samples containing HA, HA was removed by digestion in a microwave oven (mod. Multiwave, Anton Paar, Graz, Austria) with HNO₃ (*p.a.*, Merck; distilled by sub-boiling) in order to avoid any disturbing effects of HA during ICP-MS measurements.

In addition, blank solutions of U(VI) and HA in 0.1 M NaClO₄ without clay were prepared as a function of pH to determine the amount of precipitated HA. These samples were processed under the same conditions.

Finally, the U(VI) or HA sorption onto vial walls was determined. For this, 7 mL 1 M HNO₃ (U(VI)) or 1 M NaOH (HA) were added to the emptied vials and the vials were shaken for 3 d. The solutions were analyzed by ICP-MS and LSC for U(VI) and HA, respectively.

The amount of U/HA adsorbed on the mineral surface was calculated as the difference between the initial U(VI)/HA concentration and U(VI)/HA remaining in solution after the sorption experiment. The values were corrected by the wall sorption and the U(VI) concentration in the blank samples (cf. section 4.1.2.1).

4.5.2 Results and discussion

4.5.2.1 U(VI) sorption in the absence of humic acid

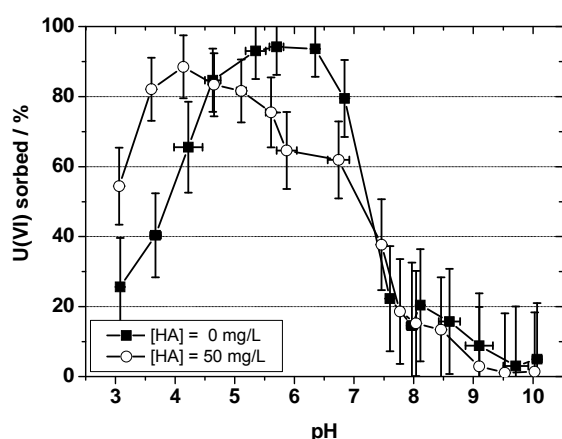


Fig. 4.12. U(VI) sorption onto OPA in the absence and presence of HA as a function of pH ($[U(VI)] = 1 \times 10^{-6}$ M; $[HA] = 0$ or 50 mg/L; $I = I_t$ (cf. Fig. 4.3); $pCO_2 = 10^{-3.5}$ atm). Uncertainties were calculated following the law of error propagation.

The U(VI) sorption onto OPA as a function of pH is shown in Fig. 4.12. In the absence of HA, the U(VI) sorption increases from about 20% at pH 3 to about 95% at pH 5.5. The comparison with the respective U(VI) speciation in Fig. 4.5a shows, that the strongest U(VI) sorption occurs when UO_2OH^+ and $(\text{UO}_2)_2\text{CO}_3(\text{OH})_3^-$ are the dominating U(VI) species in solution. Above pH 7, a strong decrease of the U(VI) sorption is observed. This is due to formation of $\text{Ca}_2\text{UO}_2(\text{CO}_3)_3(\text{aq})$, which is known to sorb only weakly onto OPA (Joseph et al., 2011). In the pH range from pH 7.5 to 10, the U(VI) sorption decreases further to about 5% at pH 10. Here, the weakly sorbing $\text{UO}_2(\text{CO}_3)_3^{4-}$ complex becomes the dominant species in solution.

Compared to the U(VI) sorption onto kaolinite (Křepelová et al., 2006), the U(VI) sorption curve is shifted to lower pH values in case of OPA, which points to the fact that OPA has a lower pzc than kaolinite. For the basal aluminol sites of kaolinite (KGa-1) pzc values between 3.9-6.0 (e.g., Brady et al., 1996; Redden et al., 1998) are reported. Thus, it can be concluded, that pzc of OPA has to be smaller than 6.0 at least. That means, at pH values > 8.5 , where the surface of OPA is predominantly negatively charged, the weak sorption of $\text{UO}_2(\text{CO}_3)_3^{4-}$ can be interpreted by electrostatic repulsion effects. However, in the pH range, where the neutral $\text{Ca}_2\text{UO}_2(\text{CO}_3)_3(\text{aq})$ complex is the dominant species in solution, a low but compared with $\text{UO}_2(\text{CO}_3)_3^{4-}$ higher U(VI) sorption can be observed. One reason can be that the neutral complex is less electrostatically repulsed than the negatively charged species, since the calcium ion possibly screens the negatively charged surface by charge neutralization.

4.5.2.2 U(VI) sorption in the presence of humic acid

The presence of HA influences the U(VI) sorption onto OPA significantly (Fig. 4.12). Between pH 3 and 4.5, the U(VI) sorption is increased in comparison to the U(VI) sorption in the absence of HA. This is due to precipitation of HA, which is caused by charge neutralization of their carboxylic groups by protons as well as by cations present in solution due to clay leaching or even by U(VI) added to the solution. Furthermore, a subsequent U(VI) sorption onto precipitated HA could be also possible. Both processes lead to an overestimation of the U(VI) sorption onto OPA. However, it can be concluded that HA, sorbed onto OPA or precipitated, offers additional binding sites for U(VI). Such influence of HA was already described in the literature for the U(VI) sorption on kaolinite (Křepelová et al., 2006; Sachs and Bernhard, 2008), cypris clay (Beneš et al., 1998), phyllite (Schmeide et al., 2000) and bentonite (Ren et al., 2010).

Between pH 4.5 and 7.5, the U(VI) sorption is decreased in comparison to the U(VI) sorption in the HA free system. This is due to the formation of the aquatic $\text{UO}_2(\text{OH})\text{HA}(\text{I})$ complex. Thus, the presence of HA leads to a mobilization of U(VI) in the near-neutral pH range which was also observed for kaolinite (Křepelová et al., 2006; Sachs and Bernhard, 2008).

In the pH range from pH 7.5 to 8, HA seems to have no effect on the U(VI) sorption onto OPA. This can be attributed to the presence of $\text{Ca}_2\text{UO}_2(\text{CO}_3)_3(\text{aq})$ in solution and to the saturation of HA binding sites with calcium as already shown by Joseph et al. (2011) for the system U(VI) / HA / OPA / OPA pore water (pH 7.6, $I_t = 0.34$) where the U(VI) sorption onto OPA was also not influenced by HA. The present study shows that also at a lower ionic strength an influence of HA on the U(VI) sorption can not be observed. However, at lower pH values, where an even higher concentration of calcium is present in solution, HA interacts with U(VI) (cf. Fig. 4.5). That means, the absence of a HA interaction with U(VI) in the pH range from 7.5 to 8 can be exclusively ascribed to the presence of the neutral $\text{Ca}_2\text{UO}_2(\text{CO}_3)_3(\text{aq})$ complex in solution and not to the saturation of HA binding sites by calcium or other competing ions.

At pH values > 8 , no difference in U(VI) sorption can be observed compared to the U(VI) sorption in the absence of HA. This is in contrast to the U(VI) sorption on kaolinite (Sachs and Bernhard, 2008), cypris clay (Beneš et al., 1998) and phyllite (Schmeide et al., 2000), where an additional mobilization of U(VI) was observed. However, it is in agreement with the observations made for the U(VI) sorption onto muscovite (Schmeide et al., 2000).

4.5.2.3 Humic acid sorption in the presence of U(VI)

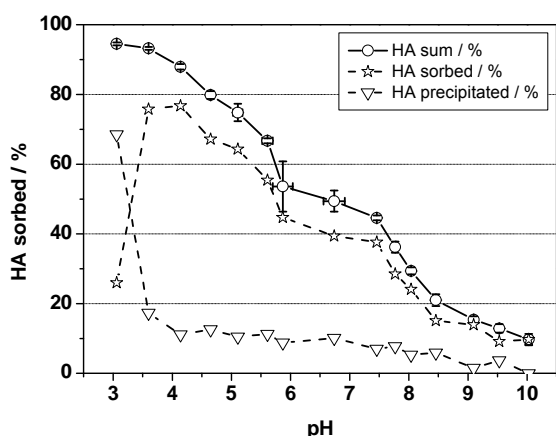


Fig. 4.13. HA sorption onto OPA in the presence of U(VI) as a function of pH ($[\text{HA}] = 50 \text{ mg/L}$; $[\text{U(VI)}] = 1 \times 10^{-6} \text{ M}$; $I = I_t$ (cf. Fig. 4.3); $p\text{CO}_2 = 10^{-3.5} \text{ atm}$). Uncertainties were calculated following the law of error propagation.

To support the discussion in section 4.5.2.2, the HA sorption onto OPA in the presence of U(VI) was investigated. The results are shown in Fig. 4.13. The amount of precipitated HA was determined by pH-dependent HA+U(VI) blank solutions. The amount of HA sorbed was calculated as the difference of HA sum and HA precipitated.

Due to deprotonation of HA functional groups with increasing pH, HA becomes more negatively charged. Furthermore, the OPA surface charge is more negative with increasing pH. Thus, due to electrostatic repulsion effects, the HA sorption decreases with pH. Such sorption behavior is typical for HA and was already described for several systems (Schmeide et al., 2000; Křepelová et al., 2006; Sachs and Bernhard, 2008; Niu et al., 2009). The high amount of sorbed HA of nearly 95% at pH 3 points rather to a precipitation than a sorption, because the carboxylic groups of the HA are protonated as well as complexed by several metal ions present in solution. As shown by Fig. 4. both HA sorption and precipitation occurs. The HA sorption onto OPA in 0.1 M NaClO₄ as a function of pH was already investigated by Lippold and Lippmann-Pipke (2009) and compared to the HA sorption onto illite and montmorillonite (S/L = 5 g/L, [HA] = 5 mg/L, pH 3-6). They observed the lowest sorption for OPA, which was explained with the presence of non-argillaceous constituents in OPA. Here, a tenfold higher HA concentration was used. However, the huge influence of non-argillaceous OPA constituents could be confirmed. As shown in section 4.1.2, calcium from the calcite mineral fraction is dissolved and complexed by HA. CaHA(II) dominates over a wide pH range the HA speciation.

In conclusion, U(VI) sorption onto OPA in 0.1 M NaClO₄ as background electrolyte was studied by batch sorption experiments as a function of pH and in the absence and presence of HA under consideration of the OPA leached out ions. The study showed, that the U(VI) speciation is affected by the dissolved competing ions. Predominantly calcium ions, which are formed by calcite dissolution, influence the U(VI) speciation between pH 7 and 8.5. The Ca₂UO₂(CO₃)₃(aq) complex predominates the U(VI) speciation in solution. With appearance of this complex, which sorbs only in a low amount onto OPA (Joseph et al., 2011), the U(VI) sorption decreases strongly between pH 7 and 7.5.

The presence of HA influences the U(VI) sorption significantly. In the acidic pH range, an increase of the U(VI) sorption is observed. Under near-neutral conditions the U(VI) sorption is decreased due to mobilization of U(VI) by HA. At pH > 7, the negatively charged UO₂(CO₃)₂HA(II)⁴⁻ complex determines the U(VI) speciation. This complex competes with the Ca₂UO₂(CO₃)₃(aq) complex.

The competing ions leached out from OPA influence also the HA speciation. Over a wide pH range, the CaHA(II) complex is the dominating HA species in solution.

Concerning the application of OPA as host rock for a nuclear waste repository it can be concluded, that not the clay minerals but the calcite fraction plays the most important role due to its huge influence on U(VI) and HA speciation. Due to the formation of $\text{Ca}_2\text{UO}_2(\text{CO}_3)_3(\text{aq})$, U(VI) is mobilized and due to the high salt content in solution, HA forms complexes with several ions which decreases its ability to complex actinides. OPA has the strongest retardation effect on U(VI) in the pH range 5-7. To approach natural conditions, the observations made at $\text{pH} > 7$ are interesting. Here, the biggest part of U(VI) ($\geq 80\%$) is mobile and HA has no significant influence on the U(VI) / OPA interaction. That means, if U(VI) is released into the near field of a nuclear waste repository it is not stopped by the clay. However, further investigations concerning the migration behavior of U(VI) through OPA are needed. Also concerning the interaction of U(VI) with OPA there are still open questions. Especially the U(VI) species sorbed on OPA at pH 7.5 have to be determined closer. It is to clarify if U(VI) sorbs as a ternary uranyl carbonate surface species and onto which mineral fraction of OPA U(VI) is sorbed primarily.

4.6 Influence of low molecular weight organic acids on U(VI) sorption onto Opalinus Clay at 25°C

In natural clay, organic matter is strongly associated with mineral constituents. Besides humic substances, such as fulvic and humic acids, also low molecular weight organic acids, such as acetate, lactate, propionate and formate, can be released from the clay under certain conditions. This was shown by extraction experiments (Claret et al., 2003; Glaus et al., 2005; Courdouan et al., 2007, 2008). Thus, we studied the influence of formate, lactate, acetate, propionate, tartrate and citrate on the sorption of U(VI) onto OPA (Schmeide et al., 2012b, in preparation).

Applying a similar experimental procedure as described in section 4.4, the U(VI) sorption onto OPA (BHE-24/1) was studied under the following conditions: $[\text{}^{233}\text{U(VI)}] = 1 \times 10^{-6}$ M, [ligand] = 0 to 1×10^{-2} M, S/L = 60 g/L, OPA pore water, $p\text{CO}_2 = 10^{-3.5}$ atm, $T = 25^\circ\text{C}$. The OPA suspensions were pre-equilibrated for 7 d. After that, aliquots of U(VI) and ligand stock solutions were added simultaneously. The sorption time was 7 d. The samples were analyzed by LSC.

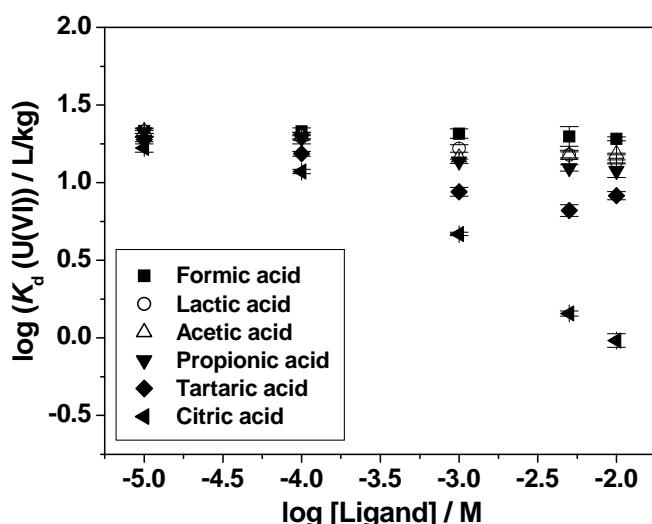


Fig. 4.14. Influence of low molecular weight organic acids on the U(VI) sorption onto OPA at 25°C.

Figure 4.14 shows the influence of the various model ligands on the U(VI) sorption onto OPA. The results show that the low U(VI) sorption onto OPA in the absence of ligands ($K_d = (0.0222 \pm 0.0004) \text{ m}^3/\text{kg}$, Joseph et al., 2011) further decreases with increasing concentration of low molecular weight organic acids (1×10^{-5} to 1×10^{-2} M) due to complex formation in aqueous solution. The mobilizing effect of the organic ligands on U(VI) increases in the following sequence: formate < lactate \approx acetate \leq propionate < tartrate < citrate (cf. Fig. 4.14). For instance, in the presence of citrate (1×10^{-2} M), which has been identified as important ligand in radioactive waste problems, the K_d value for U(VI) amounts to only $(0.0011 \pm 0.0003) \text{ m}^3/\text{kg}$. The influence of the organic ligands on the U(VI) sorption onto OPA correlates with the stability of the respective U(VI) complexes. In contrast, humic acid ($\leq 50 \text{ mg/L}$) does not change U(VI) sorption (cf. Joseph et al., 2011). Also in the presence of the low molecular weight organic acids, a reduction of U(VI) to U(IV) was not detected.

4.7 Influence of temperature on U(VI) sorption onto Opalinus Clay in the absence and presence of clay organics

Since elevated temperatures are expected for the disposal of high-level nuclear waste in clay formations, the influence of temperature on the U(VI) sorption onto OPA was studied in the temperature range from 10 to 60°C both in the absence of ligands and in the presence of lactic acid or citric acid (Schmeide et al., 2012b, in preparation).

Applying a similar experimental procedure as described in section 4.4, the U(VI) sorption onto OPA (BHE-24/1) was studied under the following conditions: $[^{233}\text{U(VI)}] = 1 \times 10^{-6} \text{ M}$,

[lactic or citric acid] = 0 to 1×10^{-2} M, S/L = 60 g/L, OPA pore water, $p\text{CO}_2 = 10^{-3.5}$ atm, $T = 10 - 60^\circ\text{C}$. The OPA suspensions were pre-equilibrated for 7 d. After that, aliquots of U(VI) and ligand stock solutions were added simultaneously. The sorption time was 7 d. The samples were analyzed by LSC.

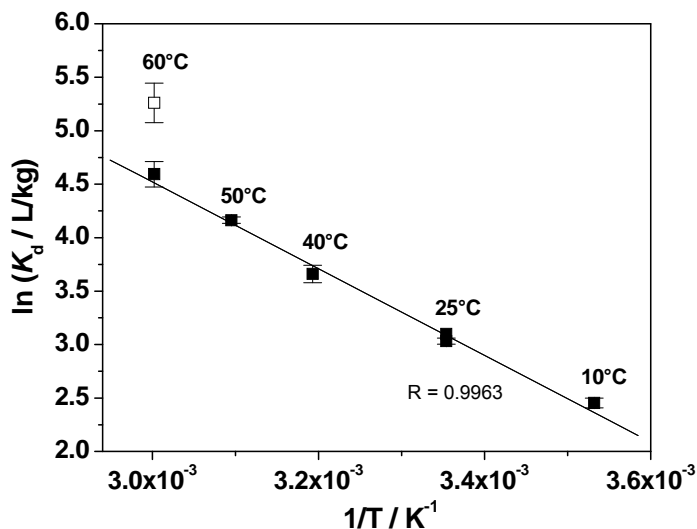


Fig. 4.15. Influence of temperature on the U(VI) sorption onto OPA in the absence of ligands.

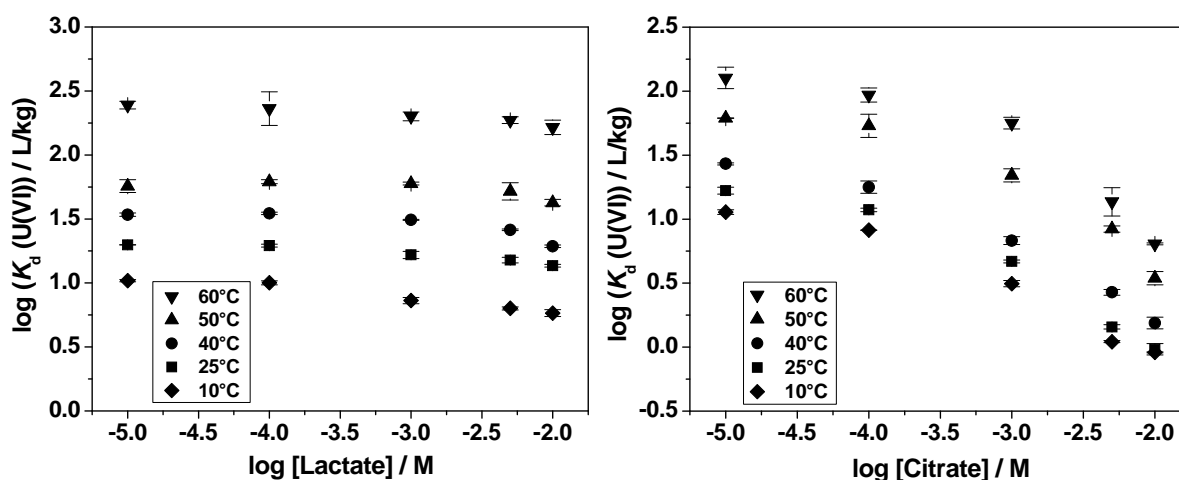


Fig. 4.16. Influence of temperature on the U(VI) sorption onto OPA in the presence of lactic acid and citric acid.

Figure 4.15 shows that the U(VI) sorption increases with increasing temperature in the absence of organic ligands (up to one order of magnitude in the temperature range 10-60°C). For U(VI), an apparent endothermic sorption enthalpy was determined with 34 ± 1 kJ/mol. The entropy amounts to $\Delta S = 139 \pm 3$ J·mol⁻¹·K⁻¹. An increased sorption with increasing temperature was also observed for the sorption of Ni²⁺ and Ln³⁺ onto montmorillonite (Tertre et al., 2005) as well as for the sorption of Eu³⁺ and NpO₂⁺ onto OPA (Schott et al., 2012;

Fröhlich et al., 2012, submitted). Furthermore, an increased interaction of U(VI) with OPA at 60°C was also detected by diffusion experiments (cf. section 5.4.4).

Figure 4.16 shows that the stronger U(VI) sorption onto OPA with increasing temperature is maintained also in the presence of lactate and citrate, when present in the concentration range from 1×10^{-5} to 1×10^{-2} M.

For interpretation of the sorption results, the U(VI) speciation in aqueous solution has to be known. The temperature-dependent studies of the U(VI) complexation with lactate (pH 3.0, $T = 7 - 65^\circ\text{C}$) or citrate (pH 1-10, $T = 10 - 60^\circ\text{C}$) (cf. section 2.4 and (Steudtner et al., 2011c)) have shown that the complex formation constants increase with increasing temperature (about one order of magnitude in the studied temperature range). The complex formation between U(VI) and lactate as well as citrate was found to be endothermic and entropy-driven. The U(VI) citrate complexes are stronger than the U(VI) lactate complexes. Consequently, citric acid has to be taken into account for safety assessment for nuclear waste repositories.

Also in the presence of HA, the U(VI) sorption onto OPA increases (not shown), however, as was observed at 25°C, HA (50 mg/L) does not change U(VI) sorption up to 50°C.

5 Diffusion of U(VI) and humic acid in Opalinus Clay

For safety assessment, a profound knowledge of the migration behavior of radionuclides in natural clay formations such as OPA, which is governed by molecular diffusion processes, is required, also at elevated temperatures. So far, the diffusion studies in the case of OPA are mainly focused on experiments at room temperature with tracers such as tritiated water (HTO), $^{36}\text{Cl}^-$, $^{125}\text{I}^-$ (Van Loon et al., 2003) or $^{134}\text{Cs}^+$ (Jakob et al., 2009). However, only few studies are known, which are focusing on the diffusion properties of actinides in OPA. For instance, Wu et al. (2009) investigated the diffusion and sorption of Np(V) in/onto OPA and Bauer et al. (2006) the Pu diffusion in OPA. Actinides diffusion studies in natural clays at elevated temperatures can not be found in the literature. The first diffusion studies at elevated temperatures focused on conservative tracers and mainly on simple clay minerals. For instance, González-Sánchez et al. (2008) investigated the HTO diffusion through compacted clay minerals, namely illite, montmorillonite, and kaolinite, at different temperatures and ionic strengths. Natural clay was investigated at higher temperatures by Van Loon et al. (2005), who determined the activation energies of the self-diffusion of HTO, $^{22}\text{Na}^+$ and $^{36}\text{Cl}^-$ in OPA.

As discussed in section 4, HA are able to influence the migration behavior of metal ions. This was shown for the diffusion of U(VI) in quartz sand (Mibus et al., 2007b) and in compacted kaolinite (Sachs et al., 2007b) and for the diffusion of Eu(III) in sedimentary rock (Seida et al., 2010).

In the present work, the diffusion of HTO, $^{233}\text{U(VI)}$ and ^{14}C -labeled HA in OPA is studied at 25 and 60°C under anaerobic conditions using OPA core samples. From HTO diffusion experiments, values for the transport porosity (ϵ) of the respective clay samples are determined. The U(VI) diffusion is investigated in the absence and presence of HA. The speciation of U(VI) at elevated temperatures is unknown so far.

The obtained parameters contribute to the thermodynamic database used for modeling of geochemical migration processes of actinide ions through argillaceous rocks discussed as possible host rocks for a nuclear waste repository.

The outcome of this study will be published in (Joseph et al., 2012b, in preparation).

5.1 Experimental

Pristine OPA samples from the Mont Terri Rock Laboratory in Switzerland were used for diffusion experiments. The bore cores were taken by the Federal Institute for Geosciences and

Natural Resources (BGR) using air as drilling medium (Bossart and Thury, 2008). The bore core BLT-14 was taken at a depth of 0.25-0.5 m. The preparation of the OPA bore core samples (thickness: 11 mm, diameter: 25.5 mm) was performed at the Karlsruher Institut für Technologie, Institut für Nukleare Entsorgung (KIT-INE). The sample BLT-14 can be assigned to the sandy fraction of OPA. Table 5.1 presents the mineralogy of OPA sandy facies determined by Pearson et al. (2003).

Table 5.1. Mineralogy of OPA sandy facies (average of four samples). (Pearson et al., 2003).

Mineral	wt.%
Clay minerals	45-70
• Illite	15-35
• Illite/smectite ML	5-20
• Chlorite	4.4-15
• Kaolinite	13-35
Quartz	16-32
Calcite	7-17
Siderite	1.1-3
Albite	0.8-2.2
K-feldspar	2.5-5
Dolomite/ankerite	0.3-2
Pyrite	0.7-3.2
Organic carbon	0.2-0.5

According to Pearson (1998) synthetic OPA pore water (pH 7.6; cf. Table 4.3) was prepared in Milli-Q water and used as background electrolyte in all diffusion experiments. To avoid bacterial growth during the experiment, 1×10^{-3} mol/L NaN_3 (*purified*, Merck, Darmstadt, Germany) was added to the pore water.

A $^{233}\text{U(VI)}$ stock solution was used for all experiments and prepared as described in section 4.3.1. The specific activity of the $^{233}\text{U(VI)}$ stock solution determined with LSC using Ultima Gold as scintillation cocktail amounts to 15.2 kBq/mL (1.8×10^{-4} M $^{233}\text{UO}_2\text{Cl}_2$).

For the studies with HA, a synthetic ^{14}C -labeled HA type M42 was applied (batch M180A, 23.08 MBq/g, proton exchange capacity: 3.34 ± 0.18 meq/g) (Pompe et al., 1998; Sachs et al., 2004). A HA stock solution of 5 g/L was prepared by dissolving 50 mg of ^{14}C -M42 with 1890 μL of 0.1 M NaOH and filling up the volume to 10 mL with pore water.

The details of the diffusion cells applied in the experiments were described by Van Loon et al. (2003). Four identical diffusion cells were used for the experiments; two cells were conditioned at 25°C and two cells at 60°C, respectively. Each OPA bore core sample was placed in the cells between two stainless steel filter plates (316L, pore diameter: 0.01 mm,

thickness: 1.55 mm, porosity: 0.3, density: 5000 kg/m³; MOTT industrial division, Farmington, USA).

The confining pressure on each sample was 5 MPa. The experimental set-up used for the diffusion experiments at 25°C was described previously (Van Loon et al., 2003). The experiments were performed under anaerobic conditions (N₂, 0% CO₂). Each diffusion cell was coupled with a peristaltic pump (mod. Ecoline, Ismatec, IDEX Health & Science, Glattbrugg, Switzerland) and a source and receiving reservoir filled with 200 mL and 20 mL synthetic OPA pore water, respectively. The solutions were circulating through the end plates of the cells in order to saturate the samples. The saturation time amounted to three weeks. Subsequently, the solutions were replaced by fresh ones, whereby the source reservoir contained the tracer and thereby tracer diffusion was started.

For the diffusion experiments at 60°C, the experimental set-up was changed slightly (Fig. 5.1). The diffusion cells were placed in a temperature controlled laboratory sand-bath (mod. ST-72, Harry Gestigkeit GmbH, Düsseldorf, Germany) and the reservoirs were stirred and heated on top of a magnetic stirrer with integrated heating function (mod. MR 3002, Heidolph, Schwabach, Germany).

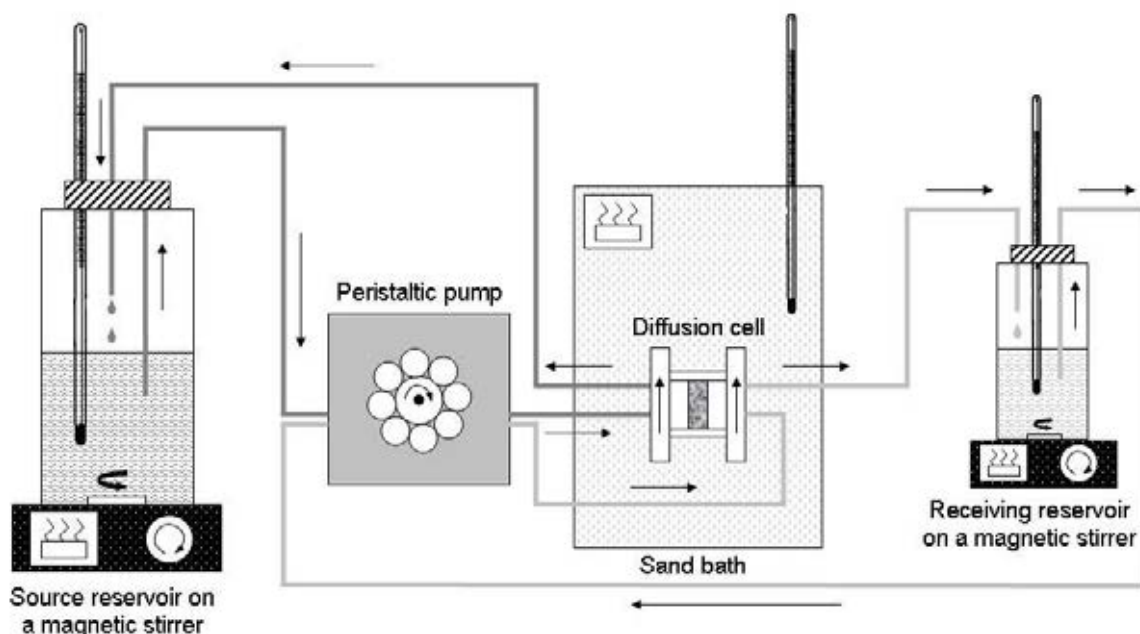


Fig. 5.1. Experimental set-up for the diffusion experiment at 60°C (based on Van Loon et al., 2003).

At first, with all four diffusion cells – two cells at 25°C, two cells at 60°C – HTO through- and out-diffusion experiments were performed as described by Van Loon et al. (2003) in order to determine values for the porosity (ϵ) of the clay samples ($[HTO]_0 = 1000 \text{ Bq/mL}$). After that, the ²³³U(VI) in-diffusion in the absence and presence of ¹⁴C-HA was studied.

Using two diffusion cells, the $^{233}\text{U(VI)}$ diffusion at 25°C (cell 1) and 60°C (cell 3) was investigated. The simultaneous diffusion of $^{233}\text{U(VI)}$ and $^{14}\text{C-HA}$ was studied (cell 2 (25°C) and cell 4 (60°C)) under exclusion of light to minimize possible light-induced HA degradation processes ($[^{233}\text{U(VI)}] = 1 \times 10^{-6} \text{ mol/L}$, $[^{14}\text{C-HA}] = 10 \text{ mg/L}$). During the duration of the experiment the pH in the concentration reservoirs was not readjusted.

After three months, the diffusion experiments were stopped and the clay samples were removed from the cells. Using the abrasive peeling technique (Van Loon and Eikenberg, 2005), U(VI) and HA diffusion profiles were determined. The peeled layers were extracted for $^{233}\text{U(VI)}$ content by 1 M HNO_3 (Roth, Karlsruhe, Germany) and for $^{14}\text{C-HA}$ content by 1 M NaOH (Merck, Darmstadt, Germany). The tracer concentrations in the extracts were determined by LSC.

The solutions of the source reservoirs traced with $^{233}\text{U(VI)}$ and $^{14}\text{C-HA}$ were analyzed for Na, K, Sr, Ba, Al, Si, P, Mn, Fe and U by ICP-MS, for Mg and Ca by AAS, and for SO_4^{2-} and Cl^- by IC. The total inorganic carbon content was measured using the multi N/C 2100 analyzer as difference of the total carbon and the total organic carbon. During the diffusion experiments the concentrations of Fe and P were always below the detection limit of ICP-MS. The pH value and the redox potential (BlueLine 31 Rx redox electrode; Schott, Mainz, Germany) of the source reservoir solutions for the $^{233}\text{U(VI)}$ and $^{14}\text{C-HA}$ diffusion experiments were measured only at the end of the experiment to decrease the impact of impurities and the loss of CO_2 into the surrounding N_2 atmosphere during the experiment.

Because of the presence of Fe(II) minerals in OPA, the solutions in the source reservoirs were analyzed with respect to a possible reduction of U(VI) to U(IV) by solvent extraction using thenoyltrifluoroacetone according to Bertrand and Choppin (1982) (cf. section 4.4.1.1).

Furthermore, the size distribution of $^{233}\text{U(VI)}$ and $^{14}\text{C-HA}$ in the solutions of the source and receiving reservoirs was determined by ultrafiltration at the start and end of diffusion experiments. Ultrafiltration centrifugal devices with molecular weight cutoffs of 1 to 1000 kD (MicrosepTM, Pall Corporation, Port Washington, NY, USA) were applied.

5.2 Data processing

For the migration of the used radionuclides through the OPA bore core samples molecular diffusion was assumed. The theoretical background of such a diffusion process has been described previously (Van Loon et al., 2003; Van Loon and Soler, 2004). For determination of the diffusion parameters a one-dimensional model composed of source reservoir, filter, OPA bore core sample, filter and receiving reservoir was applied as described in (Jakob et al.,

2009). The OPA sample and the filters were considered as homogeneous with a single value for the transport porosity.

The diffusive flux J [mol/(m²·s)] of a solute is given by Fick's first law:

$$J = -D_e \cdot \frac{\partial C}{\partial x}, \quad (5.1)$$

where the effective diffusion coefficient D_e [m²/s] is multiplied by minus concentration gradient. C [mol/m³] means the tracer concentration in the mobile phase and x [m] denotes the spatial coordinate. The change of concentration with time, t [s], is expressed by Fick's second law:

$$\frac{\partial C}{\partial t} = D_a \cdot \frac{\partial^2 C}{\partial x^2}. \quad (5.2)$$

D_a [m²/s] represents the apparent diffusion coefficient. In the evaluation of the experiments, the concentration values were decay corrected.

Both diffusion coefficients are linked by the rock capacity factor α [-] according to:

$$D_a = \frac{D_e}{\alpha}. \quad (5.3)$$

The rock capacity factor α is defined as:

$$\alpha = \varepsilon + \rho \cdot K_d \quad (5.4)$$

where ε [-] is the diffusion-accessible porosity, ρ [kg/m³] the dry bulk density and K_d [m³/kg] the sorption distribution coefficient. For non-sorbing tracers such as HTO with $K_d = 0$ it is assumed, that α is equal to ε . The parameter D_e represents a measure for the solute flux through the clay. D_a accounts additionally for the tracer interaction with the clay.

For HTO, D_e and α were determined by modeling the through-diffusion flux of HTO taking into account the time history of the HTO concentration in the receiving reservoir. For ²³³U(VI) and ¹⁴C-HA, the values for the diffusion parameters (D_e , α , ε , K_d) were determined by fitting the experimental tracer distribution profiles in the clay.

All experimental results were evaluated using the commercial software COMSOL Multiphysics 3.5a (2008).

5.3 Filter diffusion parameters

For fitting the clay diffusion parameters, the diffusion characteristics of the adjacent stainless steel filter plates for HTO, U(VI) and HA have to be included in the model, because they can

influence the retardation and migration of the tracer. In case of HTO, the filter K_d value was assumed to be 0. The corresponding filter D_e value, D_f , was taken from (Glaus et al., 2008) and amounts to $2.3 \times 10^{-10} \text{ m}^2/\text{s}$ at 25°C .

The temperature dependence of molecular diffusion can be described by the Arrhenius equation (Eisenberg and Kauzmann, 1969). With a known D_e value at a defined temperature (T_1), D_e at temperature T_2 can be calculated as follows:

$$D_e^{T_2} = D_e^{T_1} \cdot e^{\frac{E_a}{R} \left(\frac{1}{T_1} - \frac{1}{T_2} \right)} \quad (5.5)$$

where E_a is the activation energy [kJ/mol] and R is the gas constant, $8.3144621 \text{ J/mol/K}$. Using the E_a value of bulk water ($E_a = 18 \text{ kJ/mol}$) (Van Loon and Soler, 2004), D_f of HTO at 60°C was determined to be $4.93 \times 10^{-10} \text{ m}^2/\text{s}$.

In contradiction to HTO, for $^{233}\text{U(VI)}$ and $^{14}\text{C-HA}$ an interaction of the tracers with the filters can be assumed. The respective filter K_d values were obtained by sorption (25°C) and extraction experiments (60°C). For the sorption experiments, fresh filter plates were contacted with solutions of $1 \times 10^{-6} \text{ mol/L } ^{233}\text{U(VI)}$ or $10 \text{ mg/L } ^{14}\text{C-HA}$ in OPA pore water. After 2, 5 and 7 d, aliquots of the sample solutions were analyzed by LSC. The sorption of $^{233}\text{U(VI)}$ and $^{14}\text{C-HA}$ onto the filter plates was in equilibrium almost after 2 d. K_d values were determined with $7 \times 10^{-5} \text{ m}^3/\text{kg}$ and $1 \times 10^{-4} \text{ m}^3/\text{kg}$ for $^{233}\text{U(VI)}$ and $^{14}\text{C-HA}$, respectively. At 60°C , a sorption equilibrium of $^{233}\text{U(VI)}$ and $^{14}\text{C-HA}$ onto fresh filter plates was not reached within 28 d. Thus, after finishing the clay diffusion experiment, $^{233}\text{U(VI)}$ and $^{14}\text{C-HA}$ were extracted from the filter plates used in diffusion cells 3 and 4 with 1 M HNO_3 and 2 M NaOH , respectively. After 5 d shaking, the extracts were analyzed by LSC. The resulting K_d values amount to $K_d(^{233}\text{U(VI)}) = 5 \times 10^{-3} \text{ m}^3/\text{kg}$ and $K_d(^{14}\text{C-HA}) = 3.4 \times 10^{-3} \text{ m}^3/\text{kg}$.

Values for D_f of U(VI) and HA were taken from literature. If the diffusion coefficient of a certain species in bulk water, D_w [m^2/s], is known, D_f can be estimated by $D_f = D_w/10$ (Glaus et al., 2008). At 25°C , D_f of $\text{Ca}_2\text{UO}_2(\text{CO}_3)_3(\text{aq})$, the dominating U(VI) species in OPA pore water (Joseph et al., 2011), was assumed to be $4.6 \times 10^{-11} \text{ m}^2/\text{s}$ based on the corresponding D_w from (Kerisit and Liu, 2010). During fitting routine this value had to be decreased slightly to $3.5 \times 10^{-11} \text{ m}^2/\text{s}$. For D_w of HA at 25°C different values were published depending on origin and molecular size of HA (Morris et al., 1999; Mibus et al., 2007a). In this study, published D_w values for calcium humate complexes (Nebbioso and Piccolo, 2009) were applied and D_f was averaged to $1.3 \times 10^{-11} \text{ m}^2/\text{s}$. Using Eq. (5.5), the applied D_f values at 60°C were $D_f(\text{U(VI)}) = 7.65 \times 10^{-11} \text{ m}^2/\text{s}$ and $D_f(\text{HA}) = 2.84 \times 10^{-11} \text{ m}^2/\text{s}$.

5.4 Results and discussion

5.4.1 HTO diffusion in Opalinus Clay in dependence on temperature

The results obtained for HTO diffusion through OPA are summarized in Table 5.2. For both temperatures, 25 and 60°C, the values are in good agreement with literature data given by Van Loon and Soler (2004) for shaly facies OPA samples. The small differences observed can be explained by the sandy facies OPA samples applied in the current experiments. The ε values obtained by HTO diffusion experiments were incorporated in the $^{233}\text{U(VI)}$ and $^{14}\text{C-HA}$ diffusion model.

Table 5.2. Diffusion parameters of HTO in OPA determined by through-diffusion experiments at 25 and 60°C.

	25°C		60°C	
	Cell 1	Cell 2	Cell 3	Cell 4
C_0 [Bq/mL]	999 ± 8	1027 ± 4	1021 ± 4	1022 ± 11
V_0 [$\times 10^{-6}$ m ³] ^a	201.62	202.48	200.57	201.22
D_e [$\times 10^{-11}$ m ² /s]	1.60 ± 0.09	1.31 ± 0.09	3.93 ± 0.07	4.10 ± 0.10
ε [-]	0.24 ± 0.02	0.20 ± 0.02	0.23 ± 0.07	0.26 ± 0.06
C_0 [Bq/mL] ^b	1217 ± 83		~ 1200 ± 90	
D_e [$\times 10^{-11}$ m ² /s] ^b	1.21 ± 0.08		3.67 ± 0.22 / 3.93 ± 0.24	
ε [-] ^a	0.09 ± 0.02		0.12 ± 0.01 / 0.19 ± 0.02	

^a Initial volume of the source reservoir.

^b Values from Van Loon and Soler (2004) measured at 23°C (5 MPa) and at 65°C (3 MPa).

5.4.2 Aqueous U(VI) and humic acid speciation

To interpret the diffusion results, information about the aqueous U(VI) and HA species present in solution is needed. In section 4.2 is shown, that the $\text{Ca}_2\text{UO}_2(\text{CO}_3)_3(\text{aq})$ complex dominates the U(VI) speciation in OPA pore water at room temperature to nearly 100%. The presence of HA has no influence on this speciation. At the beginning of the diffusion experiment (25°C), the same U(VI) species predominates in solutions of the source reservoirs. The diffusion experiments were carried out for three months. After that, the U(VI) speciation was recalculated on the basis of the ion concentrations of Na, K, Sr, Al, Si, Ca, Mg, Ba, Mn, Cl^- , SO_4^{2-} , and CO_3^{2-} , the concentrations of $^{233}\text{U(VI)}$ and $^{14}\text{C-HA}$, the pH and the redox potential (E_h) in the source reservoir solutions. The results are summarized in Table 5.3.

Table 5.3. Characterization of the source reservoir solutions at 25 and 60°C at the end of the $^{233}\text{U(VI)}$ and $^{14}\text{C-HA}$ diffusion experiments as well as U(VI) speciation in the reservoirs calculated for these conditions.

	25°C		60°C	
	Cell 1	Cell 2	Cell 3	Cell 4
$C(^{233}\text{U(VI)})$ [mol/L]	1.05×10^{-6}	9.30×10^{-7}	5.96×10^{-7}	5.00×10^{-7}
$C(^{14}\text{C-HA})$ [mg/L]	-	8.9	-	7.0
pH	8.75	8.60	7.92	7.66
E_h [mV]	300	240	140	30
T [°C]	23.3	23.3	61.5	59.2
U(VI) speciation (aqueous species accounting for 99% or more)				
- $\text{Ca}_2\text{UO}_2(\text{CO}_3)_3(\text{aq})$	98.88%	98.14%	n.k.	n.k.
- $\text{UO}_2(\text{CO}_3)_3^{4-}$	0.84%	0.86%	n.k.	n.k.
- $\text{UO}_2(\text{CO}_3)_2\text{HA(II)}^{4-}$	-	0.71%	-	n.k.

n.k. ... not known

At 25°C, at the end of the diffusion experiments, in all reservoir solutions the $\text{Ca}_2\text{UO}_2(\text{CO}_3)_3(\text{aq})$ is still the dominating species, also in the presence of HA as shown for cell 2.

At 60°C, the present U(VI) species in OPA pore water are not known. Experiments still have to be performed to investigate the system closer.

The oxidation state of uranium in the source reservoir solutions was investigated by solvent extraction. No U(IV) was detectable in the reservoir solutions at 25°C and at 60°C.

In Fig. 5.2, the particle size distributions of $^{14}\text{C-HA}$ colloids in the presence of $^{233}\text{U(VI)}$ in the source reservoir solutions of cells 2 and 4 at start and at end of the experiments are shown.

At 25°C, before the diffusion experiment was started, the HA colloids present in source reservoir solution showed a wide size distribution, whereby HA colloids > 100 kD were clearly predominating. Furthermore, Fig. 5.2a shows, that no interaction occurred between $^{14}\text{C-HA}$ and $^{233}\text{U(VI)}$. In contrast to HA, $^{233}\text{U(VI)}$ passed all particle size filters without any significant hindrance. Thus, it was present in the filtrates to almost 100% related to the $^{233}\text{U(VI)}$ concentration of the unfiltered solution. Within three months (Fig. 5.2b), HA degradation processes occurred to some extent. The fraction of HA colloids < 100 kD was slightly increased. However, still no significant interaction between $^{14}\text{C-HA}$ and $^{233}\text{U(VI)}$ was observable even after 87 days.

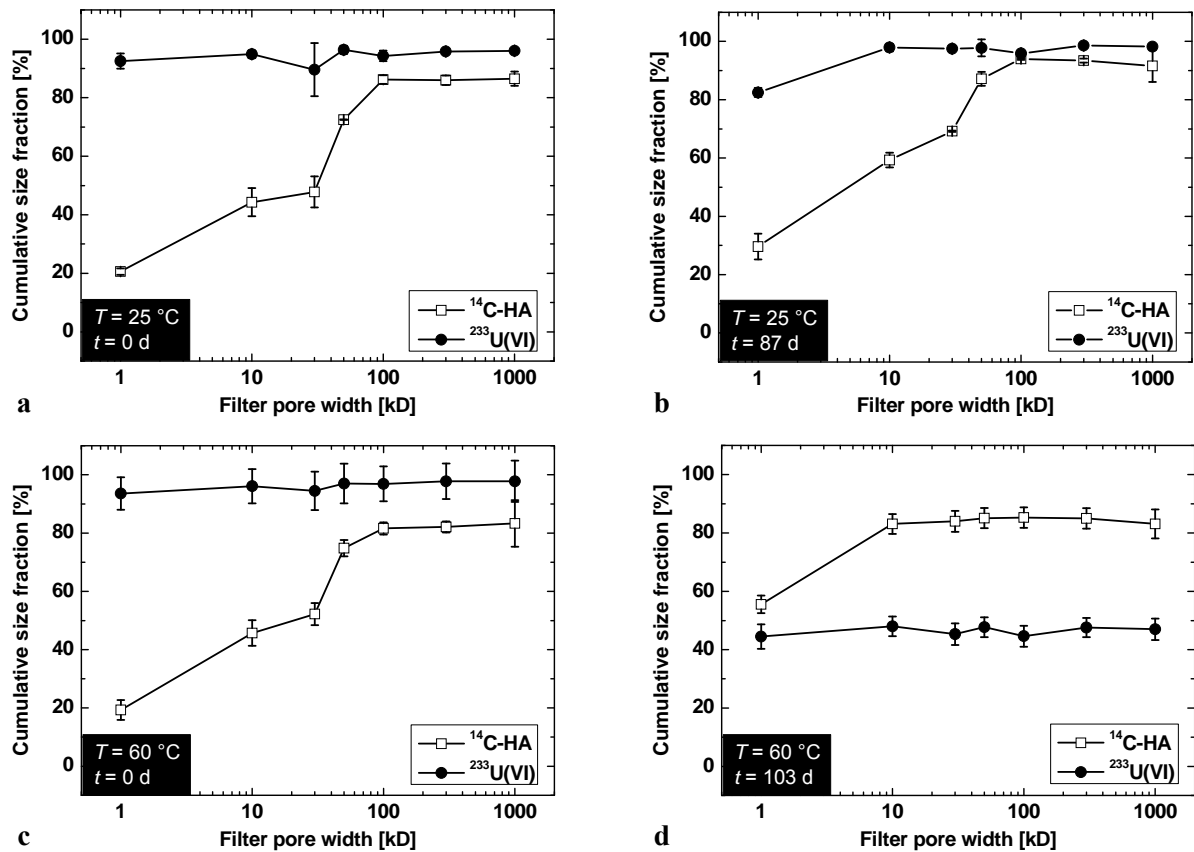


Fig. 5.2. Particle size distribution of $^{14}\text{C-HA}$ colloids in the presence of $^{233}\text{U(VI)}$ in the solutions of the source reservoirs at 25°C (cell 2; a + b) and 60°C (cell 4; c + d) at the beginning (a + c) and end (b + d) of the diffusion experiments.

At 60°C , the particle size distribution of $^{14}\text{C-HA}$ and $^{233}\text{U(VI)}$ at the beginning of the experiment (Fig. 5.2c) was similar to that at 25°C (Fig. 5.2a). However, the particle size distribution obtained after three months shows that the HA degradation at 60°C is stronger than that at 25°C , since the fractions of HA colloids < 100 kD are increased (Fig. 5.2d). An interaction between $^{14}\text{C-HA}$ and $^{233}\text{U(VI)}$, which would be depicted by a similar particle size distribution, can not clearly be detected. However, at 60°C , about 50% of $^{233}\text{U(VI)}$ was found to be retained on the various particle size filters (Fig. 5.2d). These U(VI) particles must have a size > 1000 kD. These results are an indication toward a change of the U(VI) speciation at 60°C . Presumably, U(VI) forms colloids in OPA pore water at 60°C . These are not able to pass the applied particle size filters. Otherwise, with a fraction of about 50% also aqueous U(VI) species were present in solution, which passed the filters.

Also the receiving reservoir solutions of cell 2 and cell 4 were analyzed regularly for their particle size distribution. No $^{233}\text{U(VI)}$ was detectable in these reservoirs. However, at the end of the diffusion experiment at 25°C diffused HA colloids (< 1 kD) were detected in the receiving reservoir of cell 2. At 60°C , already after one week, the solution in the receiving

reservoir of cell 4 turned yellow, which is an indication of the presence of HA. About 25 d after starting the diffusion experiment, small HA colloids (< 1 kD) could clearly be detected in the receiving reservoir solution. A further characterization of the diffused molecules was not performed due to their very low concentration. However, since the color of the solution changed, it can be excluded, that the detected diffused ^{14}C is CO_3^{2-} , which is a potential degradation product of HA. A filtration effect of the clay was observed also by Sachs et al. (2007b) for the HA diffusion through compacted kaolinite.

5.4.3 Diffusion of U(VI) and humic acid in Opalinus Clay at 25°C

The experiments were conducted for three months. Within this time span no $^{233}\text{U(VI)}$ could be detected in the receiving reservoirs of cell 1 and 2. However, as discussed in section 5.4.2, diffused HA colloids were found.

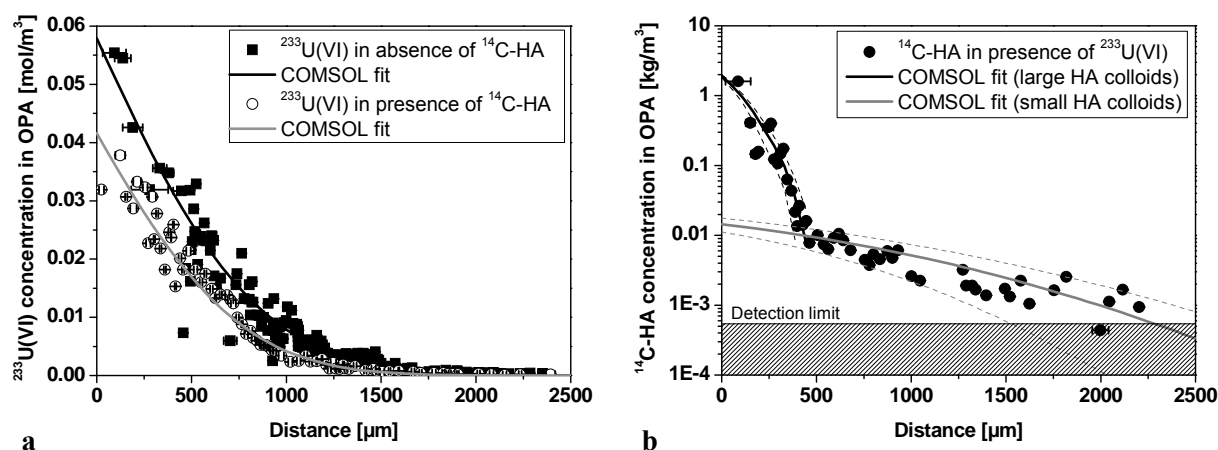


Fig. 5.3. Concentration profiles of $^{233}\text{U(VI)}$ in the absence (filled symbols) and presence (open symbols) of $^{14}\text{C-HA}$ (a) and of $^{14}\text{C-HA}$ in the presence of $^{233}\text{U(VI)}$ (b) in OPA at 25°C.

In Fig. 5.3a the $^{233}\text{U(VI)}$ diffusion profiles determined in the absence and presence of HA are shown. The comparison of the two data sets leads to the conclusion that in the presence of HA $^{233}\text{U(VI)}$ penetrates less the clay than in the absence of HA. Such a reduced metal ion diffusion in the presence of HA was already described by Seida et al. (2010) for the Eu(III) diffusion in sedimentary rock and by Mibus and Sachs (2006) for the U(VI) diffusion in compacted kaolinite.

Based on the $^{233}\text{U(VI)}$ distribution profiles in the samples both transport parameters, D_e and K_d , can be adjusted individually. Their values are summarized in Table 5.4. The K_d value for U(VI) determined by the present diffusion studies agrees well with the K_d value determined previously by means of sorption experiments using crushed OPA material (cf. section 4, Joseph et al., 2011). In contrast, Wu et al. (2009) determined for the Np(V) / OPA system a

larger K_d value by means of diffusion experiments ($K_d = 0.1 \pm 0.01 \text{ m}^3/\text{kg}$) than by batch sorption measurements ($K_d = 0.025 \pm 0.005 \text{ m}^3/\text{kg}$). The authors concluded that during the diffusion experiment Np(V) was partially reduced to Np(IV). Since in the present study the K_d values determined for the U(VI) / OPA system by batch sorption and diffusion experiments are comparable, a reduction of U(VI) to U(IV) can be excluded. This was also verified by solvent extraction experiments (cf. section 5.4.2).

Table 5.4. Compilation of further data of the experiments and of the best-fit parameter values. The data are based on the $^{233}\text{U(VI)}$ and $^{14}\text{C-HA}$ diffusion profiles and concentration data in the source and receiving reservoir at 25°C.

	U(VI) in the absence of HA (cell 1)		U(VI) in the presence of HA (cell 2)	
	$^{233}\text{U(VI)}$	$^{233}\text{U(VI)}$	HA	
			large colloids	small colloids
$C_0(^{233}\text{U(VI)})$ [mol/L]	1.07×10^{-6}	9.98×10^{-7}		
$C_0(^{14}\text{C-HA})$ [mg/L]	-		10.1	3 ^a
V_0 [$\times 10^{-6} \text{ m}^3$]	202.18		167.71	
t [d]	89		87	
ρ [kg/m^3]	2424		2392	
ε [-] ^b	0.24 ± 0.02		0.20 ± 0.02	
α [-]	61 ± 7	48 ± 7	309 ± 45	5 ± 1.2
D_e [$\times 10^{-12} \text{ m}^2/\text{s}$]	1.9 ± 0.4	1.2 ± 0.3	0.65 ± 0.25	0.4 ± 0.25
D_a [$\times 10^{-14} \text{ m}^2/\text{s}$]	3.1 ± 0.3	2.5 ± 0.3	0.21 ± 0.05	8 ± 3
K_d [m^3/kg]	0.025 ± 0.003	0.020 ± 0.003	0.129 ± 0.018	0.002 ± 0.0005
K_d [m^3/kg] ^c	0.0222 ± 0.0004		0.129 ± 0.006	

^a Based on C_0 and the fact, that about 30% of HA colloids are $< 1 \text{ kD}$ (cf. Fig. 5.2b).

^b Determined by HTO through-diffusion.

^c Determined by sorption experiments (cf. section 4, Joseph et al., 2011).

In comparison to Np(V) (Wu et al., 2009), the K_d of U(VI) determined by diffusion is one order of magnitude smaller, which implicates a weaker interaction of U(VI) with OPA compared to that of Np(V) – or of Np(IV) after reduction – with OPA. This is in contrast to the findings of Křepelová et al. (2006) and Schmeide and Bernhard (2010), who investigated the U(VI) and Np(V) sorption onto kaolinite, respectively. At pH 8, the K_d value of U(VI) was about one order of magnitude higher than the K_d of Np(V) ($C_0(\text{An}) = 1 \times 10^{-5} \text{ M}$, $I = 0.01 \text{ M NaClO}_4$, $p\text{CO}_2 = 10^{-3.5} \text{ atm}$). The reason for these results was the absence of non-argillaceous components in the investigated system. In the present study, these components

determine the U(VI) speciation (calcite) and Np oxidation state (pyrite) and lead to the reverse result.

The D_e value for the Np(V) diffusion in OPA amounts to $(6.9 \pm 1.1) \times 10^{-12} \text{ m}^2/\text{s}$ (Wu et al., 2009). The D_e of U(VI) shown in Table 5.4 is smaller. That means, if the same concentration gradient in diffusion experiments with Np(V) and U(VI) is applied, U(VI) would diffuse with a smaller flux through OPA than Np(V). However, the comparison of the D_a values, where the interaction of the actinides with OPA is considered additionally, shows, that the Np(V) diffusion in OPA is with a value of $D_a = (2.8 \pm 0.4) \times 10^{-14} \text{ m}^2/\text{s}$ in the same range as that for U(VI). This leads to the conclusion, that the migration of both actinides through OPA is similar.

A comparison of the K_d as well as D_e values determined for U(VI) in the absence and presence of HA shows that the diffusion of U(VI) might be slightly hindered in the presence of HA molecules. However, based on the experimental uncertainties, it is concluded that HA does not have a significant effect on U(VI) diffusion through compacted water-saturated OPA. The system U(VI) / HA / OPA was also investigated by means of batch sorption experiments (cf. section 4.4, Joseph et al., 2011). There, also no influence of HA on the U(VI) interaction with OPA was observed. This result is confirmed by the diffusion experiments with intact OPA bore core samples.

In Fig. 5.3b, the diffusion profile measured for HA in OPA at 25°C is shown. The profile is indicative for the presence of two size fractions of HA colloids, which are assigned to 1) a high molecular size HA colloid fraction (large HA colloids) and 2) a low molecular size HA colloid fraction (small HA colloids). Within three months, the larger colloids diffused only about 500 µm into the OPA bore core due to restriction in the available pore space and due to strong sorption onto the OPA surface. However, the smaller HA colloid fraction showed a weaker sorption affinity toward OPA and diffused through the entire OPA sample and therefore, could be detected in the receiving reservoir. For both HA size fractions, the values for the diffusion parameters are presented in Table 5.4.

In comparison to the HA diffusion through compacted kaolinite ($D_a = 2.2 \times 10^{-12} \text{ m}^2/\text{s}$, pH 7, $\rho = 1670 \text{ kg/m}^3$; (Sachs et al., 2007b)), the HA diffusion through OPA is much slower, which is due to the higher bulk dry density of OPA providing less pore space for diffusion. Joseph et al. (2011) determined the K_d value of HA with OPA by batch sorption experiments (cf. section 4.4.2.3 and Table 5.4). This result is in very good agreement with the K_d value fitted for the large HA colloid fraction in the present diffusion experiment.

5.4.4 Diffusion of U(VI) and humic acid in Opalinus Clay at 60°C

Similar to the experiments at 25°C, also at 60°C no $^{233}\text{U(VI)}$ (cell 3 and 4), however, diffused small HA colloids (cell 4) were detected in the receiving reservoirs.

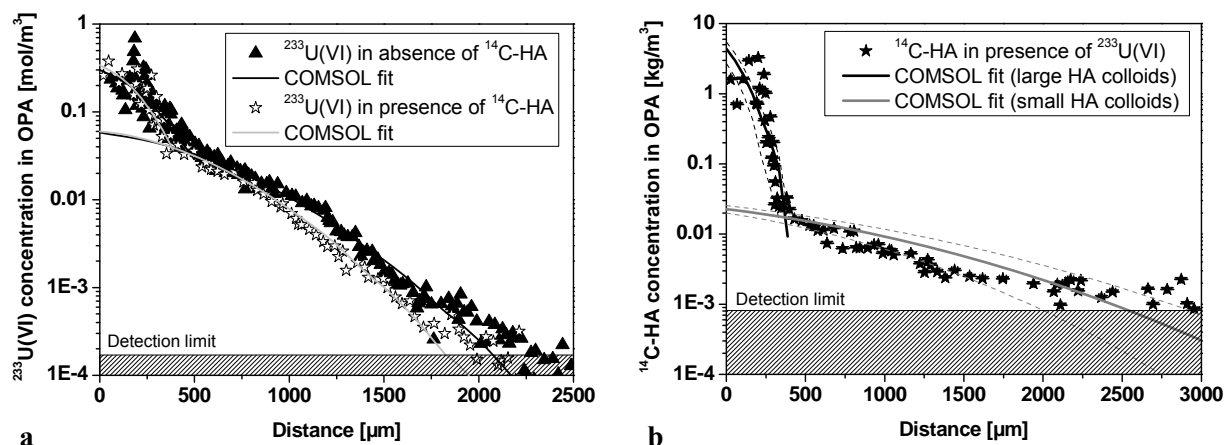


Fig. 5.4. Concentration profiles of $^{233}\text{U(VI)}$ in the absence (filled symbols) and presence (open symbols) of $^{14}\text{C-HA}$ (a) and of $^{14}\text{C-HA}$ in the presence of $^{233}\text{U(VI)}$ (b) in OPA at 60°C.

Fitting the $^{233}\text{U(VI)}$ diffusion profiles, it became obvious that at least two different U(VI) species are involved in the diffusion process (Fig. 5.4a). Taking into account the particle size distribution, these two species were attributed to a diffusing colloidal and aqueous U(VI) species, respectively. The colloidal U(VI) species was restricted in its migration and diffused only about 500 μm into the OPA sample. The aqueous U(VI) species was more mobile (about sixfold D_a of the colloidal species; cf. Table 5.5) and could be detected at a diffusion distance of about 2.5 mm.

In comparison to the $^{233}\text{U(VI)}$ diffusion at 25°C, the interaction of $^{233}\text{U(VI)}$ with OPA is stronger at 60°C for both U(VI) species. The fitted K_d value for the colloidal U(VI) species is one order of magnitude larger than that at 25°C. Several studies investigated the interaction of metal ions with mineral surfaces in dependence on temperature. For instance, an increased sorption at elevated temperatures was observed for Ni^{2+} and Ln^{3+} onto montmorillonite (Tertre et al., 2005) and for Eu^{3+} onto OPA (Schott et al., 2012, accepted). In the case of actinides, Fröhlich et al. (2012, submitted) described such a behavior for the Np(V) sorption onto OPA and Schmeide et al. (2012b, in preparation) for the U(VI) sorption onto OPA (cf. section 4.7).

Table 5.5. Compilation of further data of the experiments and of the best-fit parameter values. The data are based on the $^{233}\text{U(VI)}$ and $^{14}\text{C-HA}$ diffusion profiles and concentration data in the source and receiving reservoir at 60°C .

	U(VI) in the absence of HA (cell 3)		U(VI) in the presence of HA (cell 4)			
	$^{233}\text{U(VI)}$		$^{233}\text{U(VI)}$		HA	
	colloidal	aqueous	colloidal	aqueous	large colloids	small colloids
$C_0(^{233}\text{U(VI)})$ [mol/L]	1.00×10^{-6}		9.94×10^{-7}			
$C_0(^{14}\text{C-HA})$ [mg/L]	-				9.91	5.95^a
V_0 [$\times 10^{-6} \text{ m}^3$]	202.02		221.67			
t [d]	102		103			
ρ [kg/m^3]	2421		2404			
ε [-]	0.23 ± 0.07^b		0.26 ± 0.06^b			
α [-]	605 ± 122	109 ± 12	722 ± 120	120 ± 12	962 ± 481	3.9 ± 0.5
D_e [$\times 10^{-12} \text{ m}^2/\text{s}$]	3 ± 1	3 ± 0.5	2.2 ± 0.8	2.5 ± 0.5	1.2 ± 0.8	0.35 ± 0.15
D_a [$\times 10^{-14} \text{ m}^2/\text{s}$]	0.50 ± 0.07	2.8 ± 0.2	0.30 ± 0.07	2.1 ± 0.2	0.12 ± 0.02	9 ± 2
K_d [m^3/kg]	0.25 ± 0.05	0.045 ± 0.005	0.3 ± 0.05	0.05 ± 0.005	0.4 ± 0.2	0.0015 ± 0.0002

^a Based on C_0 and the fact, that about 60% of HA colloids are < 1 kD (cf. Fig. 5.2d).

^b Determined by HTO through-diffusion.

With increasing temperature also D_e increases. Using Eq. (5.5), concerning the U(VI) diffusion in OPA for the activation energy E_a a value of about 10 kJ/mol was estimated. Such a value seems low when compared to an E_a value for HTO of 21.1 ± 1.6 kJ/mol, for Na^+ of 21.0 ± 3.5 kJ/mol and for Cl^- of 19.4 ± 1.5 kJ/mol (Van Loon et al., 2005). This result shows that the migration of U(VI) in OPA is less influenced by temperature than the diffusion of HTO, Na^+ or Cl^- . However, the calculated activation energy is based on two temperatures and therefore only a preliminary result. More temperature-dependent measurements have to be performed to verify this value. In the future, the knowledge of the verified E_a for U(VI) in OPA would enable the calculation of D_e values at other temperatures.

The D_a values for the U(VI) diffusion in OPA at 25°C and 60°C (aqueous U(VI) species) are, considering their uncertainties, almost equal to each other. This leads to the conclusion, that the migration of U(VI) through OPA is similar at both investigated temperatures. The breakthrough of U(VI) through OPA at 25°C and at 60°C will be nearly at the same time. Based on the averaged values of the diffusion parameters at 25°C and 60°C modeling calculations were performed. In Fig. 5.5, the calculated concentration of $^{233}\text{U(VI)}$ in the receiving reservoir as a function of time is presented. The results show, that at 25°C and 60°C and using 11 mm thick OPA samples about 9 and 14.5 years, respectively, would be needed

for U(VI) breakthrough.

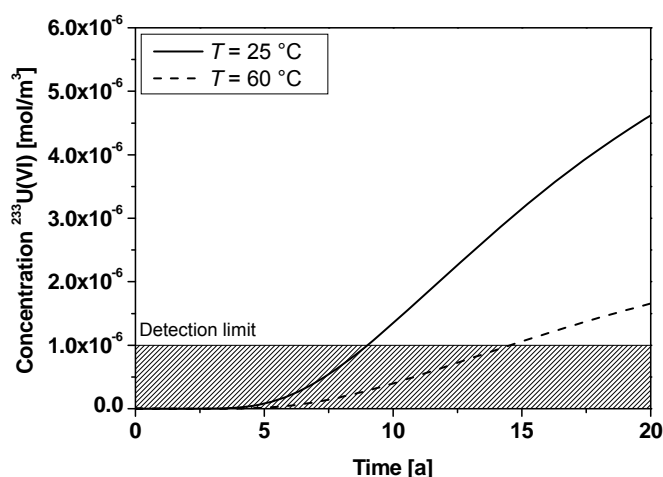


Fig. 5.5. Calculated $^{233}\text{U(VI)}$ concentration in the receiving reservoir as a function of time for a temperature of 25°C and 60°C, respectively.

In Fig. 5.4a, the $^{233}\text{U(VI)}$ diffusion profiles at 60°C in the absence and presence of HA are shown. The differences between both profiles are smaller compared to the analog profiles obtained at 25°C. This points to the fact that also at 60°C, HA has a negligible effect on the $^{233}\text{U(VI)}$ diffusion through OPA. Indeed, the corresponding diffusion parameter values support such a conclusion (Table 5.5).

The comparison of the U(VI) diffusion parameters in the absence and presence of HA of both U(VI) species shows, that their K_d values are slightly increased and their D_e values are slightly decreased in the presence of HA. However, within experimental uncertainties, no significant influence of HA on U(VI) diffusion at 60°C can be observed. That means, independent of temperature, HA has no significant influence on U(VI) migration through OPA. It should be mentioned, that small diffusing HA colloids have only a very minor potential for complexing and transporting U(VI).

In Fig. 5.4b, the HA diffusion through OPA at 60°C is presented. The profile is very similar to that depicted in Fig. 5.3b and shows again the presence of at least two diffusing HA size fractions. In contrast to the profile at 25°C, at 60°C the data of the large HA colloid fraction scatter over a much wider range close to the OPA boundary downstream making the fitting procedure more difficult. Presumably, this scatter results from the HA degradation process (cf. Fig. 5.2), which is taking place during the diffusion experiment and is increased at elevated temperature. The different present and formed HA degradation species show different sorption and diffusion properties resulting in a more complex HA diffusion profile in OPA. However, in this case, the interpretation of the HA profile was limited to two HA size fractions only.

However, the obtained K_d values indicate a little stronger interaction of the large HA colloid fraction with OPA at 60°C than at 25°C. For the small HA colloid fraction such an influence of temperature on K_d was not detected. Due to large uncertainties, also no effect of temperature on D_e for both HA fractions could be detected. However, the earlier detection of HA in the receiving reservoir at 60°C in comparison to the experimental findings at 25°C points to a higher D_e value for HA diffusion (small HA colloids) at 60°C.

In conclusion, diffusion experiments with $^{233}\text{U(VI)}$ in pristine samples of consolidated OPA were carried out under anaerobic conditions. The influence of both HA and elevated temperature on the $^{233}\text{U(VI)}$ diffusion was investigated.

Speciation calculations showed, that $\text{Ca}_2\text{UO}_2(\text{CO}_3)_3(\text{aq})$ is the dominating U(VI) species in the source reservoir solution and thus, the main diffusing U(VI) species at 25°C during the whole diffusion experiment. At 60°C, particle size distribution measurements pointed to the presence of at least one colloidal and one aqueous U(VI) species in solution. For HA, a wide particle size distribution was measured, whereby a degradation process occurred which became stronger at higher temperature.

By fitting the diffusion profiles best-fit parameter values for K_d and D_e were determined. At 25°C, K_d values were obtained for U(VI) ($K_d = 0.025 \pm 0.003 \text{ m}^3/\text{kg}$) and HA (large HA colloids; $K_d = 0.129 \pm 0.018 \text{ m}^3/\text{kg}$) which are in good agreement with K_d values from batch sorption experiments using crushed OPA material (cf. section 4.4.2.3, Joseph et al., 2011).

In agreement with the speciation studies, at 60°C diffusion profiles of two U(VI) species were observed, which were attributed to a colloidal and an aqueous U(VI) species. The colloidal U(VI) species showed a stronger interaction with OPA. Hence, this species diffused only about 500 μm in OPA. Compared to the colloidal U(VI) species, the aqueous U(VI) species showed a weaker interaction with OPA and it penetrated deeper into the clay. However, compared to U(VI) at 25°C, both U(VI) species showed higher K_d and D_e values. Based on D_e at 25°C and 60°C, for an activation energy E_a a preliminary value of about 10 kJ/mol was determined for diffusion of U(VI) in OPA. In addition, almost equivalent D_a values were determined for the U(VI) diffusion at 25°C and 60°C (aqueous U(VI) species) through OPA. The breakthrough of U(VI) through OPA would thus be independent of temperature and occurs nearly at the same time.

All diffusion experiments showed, that the effect of HA on $^{233}\text{U(VI)}$ diffusion is negligible and independent of temperature.

The diffusion results for HA at 25°C and 60°C showed that two distinct HA size fractions – a large- and a small-sized colloid fraction – were diffusing through the OPA samples. Within

three months the high molecular size HA colloids diffused only about 500 μm into the clay, whereas the low molecular size HA colloids diffused through the entire OPA samples and were consequently detected in the receiving reservoir. These findings demonstrate the filtration effect of the compacted clay. For the large HA colloid fraction an increased K_d value was determined at 60°C compared to that at 25°C.

Regarding the suitability of OPA as host rock for a future nuclear waste repository, it can be concluded, that OPA has indeed a good retardation potential for U(VI). In this study, it could be shown, that the U(VI) diffusion behavior through OPA is comparable to that of the Np(V)/Np(IV) system. Calculations for 25°C and 60°C at a sample thickness of 11 mm show that it would need about 9 and 14.5 years, respectively, for U(VI) breakthrough. Thereby, humic substances being ubiquitous in soils and sediments and which show good complexation abilities for cations, have only a minor influence on U(VI) migration through OPA even at elevated temperatures.

6 Summary and outlook

The objective of this project was the study of basic interaction processes in the systems actinide - clay organics - aquifer and actinide - natural clay - clay organics - aquifer. Thus, the studies performed can be divided into complexation, redox, sorption and diffusion studies.

The complexation of Am(III), U(IV) and U(VI) with a variety of ligands in aqueous systems was studied by means of various spectroscopic techniques, such as UV-Vis absorption spectroscopy, attenuated total reflection Fourier-transform infrared (ATR FT-IR) spectroscopy as well as time-resolved laser-induced fluorescence spectroscopy (TRLFS). The TRLFS measurements were performed both in the temperature range between 7 and 65°C and at cryogenic temperature (-120°C, cryo-TRLFS). Furthermore, TRLFS with femtosecond laser pulses (fs-TRLFS) was applied.

One objective of the complexation studies was the identification of further humic acid functional groups that contribute to the actinide complexation beside the oxygen containing functional groups that are generally acknowledged as the main complexing sites of humic substances. For this, simple organic model ligands that can occur as humic acid building blocks (e.g., anthranilic, nicotinic, picolinic, phenylphosphonic, benzenesulfonic and 4-hydroxybenzenesulfonic acid as well as phthalic acid for comparison) were applied to study

the influence of nitrogen, phosphorus and sulfur containing functional groups on the complexation of actinides in different oxidation states (Am(III) and U(VI)). The complexation of Am(III) with anthranilic, nicotinic, picolinic and phthalic acid in aqueous solution was studied for the first time. The results show that Am(III) is mainly coordinated via carboxylic groups, however, probably stabilized by nitrogen groups. The studies of the U(VI) complexation with the nitrogen and sulfur containing ligands show that the U(VI) complexation is dominated by carboxylic groups. The complexation strength of aromatic phosphonate groups toward U(VI) is comparable or even higher than that of carboxylic groups. Thus, the phosphorus containing functional groups may contribute to the U(VI) complexation by humic acid, however, due to the low phosphorus concentration in humic acid also this functionality plays only a subordinate role compared to carboxylic groups. The humate complexation of Am(III) should be more influenced by nitrogen containing functional groups than that of U(VI).

These model investigations on actinide complexation by various functional groups were extended by studying the role of sulfur functionalities of humic acid for the U(VI) complexation applying synthetic humic acid model substances with varying sulfur contents (0 to 6.9 wt.%). These were synthesized based on the melanoidin concept. The results have shown that sulfur functionalities can be involved in U(VI) humate complexation, however, at environmentally relevant sulfur concentrations in humic acid (0-2 wt.%), reduced sulfur functionalities play only a subordinate role for the U(VI) complexation compared to carboxylic groups.

A further objective of the complexation studies was the determination of complex formation constants not known so far or their validation by complementary spectroscopic methods to improve the thermodynamic database. Thus, the U(IV) complexation with citric, succinic, mandelic and glycolic acid was studied at room temperature. Especially the interaction between U(IV) and citric acid was found to be very strong ($\log \beta_{101} = 13.5 \pm 0.2$ and $\log \beta_{102} = 25.1 \pm 0.2$). However, also the other ligands are able to increase the solubility and thus, the mobility of U(IV) in aquatic systems due to complex formation. The U(VI) complexation with lactic acid was studied in the temperature range 7 to 65°C. Thermodynamic parameters of the U(VI) lactate system were determined by absorption and fluorescence spectroscopy. The complex stability constants of the U(VI) lactate complexes (UO_2Lac^+ , $\text{UO}_2(\text{Lac})_2$) were found to increase with increasing temperature. The complexation of U(VI) with lactate is endothermic (ΔH pos.) and entropy-driven (ΔS pos.). In contrast, the

complex stability constants determined for the U(VI) humate complexation at 20 and 40°C are comparable, however, decrease at 60°C.

For the first time, luminescence emission properties and complex formation constants were determined for aqueous U(VI) citrate and oxalate species in the acidic pH range by cryo-TRLFS (-120°C). The stability constants determined for these species at cryogenic temperature are in good agreement with those determined by TRLFS measurements at room temperature and moreover, validate the existing data base. Generally, the U(VI) citrate and oxalate complexes are stronger than the U(VI) lactate complexes. Thus, their influence on the U(VI) migration should be stronger than that of lactate.

For the first time, the U(VI) complexation by humic acid was studied in the presence of carbonate applying cryo-TRLFS and ATR FT-IR spectroscopy. The formation of a ternary U(VI) carbonato humate complex of the type $\text{UO}_2(\text{CO}_3)_2\text{HA}(\text{II})^{4-}$ was detected. The complex formation constant was determined with $\log \beta_{0.1 \text{ M}} = 24.57 \pm 0.17$. Speciation calculations for the alkaline pH range show that at humic acid concentrations $> 2 \text{ mg/L}$, the U(VI) speciation changes from predominantly $\text{UO}_2(\text{CO}_3)_3^{4-}$ to predominantly $\text{UO}_2(\text{CO}_3)_2\text{HA}(\text{II})^{4-}$. It can be concluded that under environmentally relevant conditions in the presence of humic acid the formation of the ternary U(VI) carbonato humate complex can significantly influence the U(VI) speciation.

The role of humic acid sulfur functionalities for the Np(V) reduction in aqueous solution was studied applying synthetic humic acid model substances with varying sulfur contents (0 to 6.9 wt.%). The results have shown that in addition to quinone-like moieties and non-quinoid phenols that dominate the redox behavior of humic substances, sulfur functional groups act as further redox-active sites in humic substances toward Np. However, in nature the extent of the contribution of sulfur functional groups to the overall redox capacity of humic substances is expected to be less pronounced since the content of sulfur functionalities in natural humic substances is low compared to other redox-active functional units. Moreover, the ratio of reduced to total sulfur functional groups is lower in most natural humic substances.

The sorption and diffusion studies within this project focused on the natural clay ‘Opalinus Clay’ from the Mont Terri underground laboratory, Switzerland. The U(VI) sorption onto crushed Opalinus Clay was investigated in the absence and presence of humic acid or low

molecular weight organic acids, in dependence on temperature. Thereby, Opalinus Clay pore water was used as background electrolyte. The results show that the U(VI) sorption onto Opalinus Clay is low and not influenced by humic acid (≤ 50 mg/L). This can be attributed to the dissolution of calcite, a mineral constituent of the clay. The resulting calcium ions in the pore water influence both the U(VI) speciation and the speciation of humic acid. Thus, the U(VI) speciation in pore water is dominated by the neutral $\text{Ca}_2\text{UO}_2(\text{CO}_3)_3(\text{aq})$ complex both in the absence and presence of humic acid. The humic acid speciation is predominated by the $\text{CaHA}(\text{II})$ complex. Distribution coefficients, K_d , for the sorption of U(VI) and humic acid onto Opalinus Clay were determined with $(0.0222 \pm 0.0004) \text{ m}^3/\text{kg}$ and $(0.129 \pm 0.006) \text{ m}^3/\text{kg}$, respectively. These values were confirmed by diffusion experiments using compacted Opalinus Clay.

In contrast to humic acid, low molecular weight organic acids ($\geq 1 \times 10^{-5}$ M) are able to decrease U(VI) sorption due to complex formation in solution. The mobilizing effect of the organic ligands on U(VI) increases in the following sequence: formate < lactate \approx acetate \leq propionate < tartrate < citrate. The influence of the organic ligands on the U(VI) sorption onto Opalinus Clay correlates with the stability of the respective U(VI) complexes.

In the absence of organic ligands, the U(VI) sorption onto Opalinus Clay increases with increasing temperature. For U(VI), an apparent endothermic sorption enthalpy was determined with 34 ± 1 kJ/mol. The stronger U(VI) sorption onto Opalinus Clay with increasing temperature is maintained also in the presence of lactate and citrate, when present in the concentration range from 1×10^{-5} to 1×10^{-2} M.

The studies of the U(VI) sorption onto Opalinus Clay performed in Opalinus Clay pore water as well as the pH-dependent studies in 0.1 M NaClO_4 lead to a better process understanding. Furthermore, the obtained sorption results contribute to the thermodynamic sorption database used for modeling the geochemical interaction processes of actinide ions and potential host rocks for nuclear waste repositories.

The U(VI) diffusion in compacted Opalinus Clay was studied in the absence and presence of humic acid at 25 and 60°C under anaerobic conditions using synthetic Opalinus Clay pore water. The objective was to determine U(VI) migration in Opalinus Clay as well as the influence of humic acid and temperature on U(VI) migration. The diffusion and distribution coefficients (D_e and K_d) determined for U(VI) and humic acid at 25 and 60°C show that humic acid has no significant influence on the U(VI) diffusion. The diffusion profiles obtained for humic acid in Opalinus Clay at 25 and 60°C show the contributions of at least

two different humic acid particle size fractions (< 1 kD and 10-100 kD). The smaller humic acid fraction diffused through the whole Opalinus Clay samples at both temperatures within three months whereas the larger humic acid fraction diffused only about 500 µm into the clay. This shows a filtration effect of the compacted clay and also the different sorption affinity of the humic acid size fractions toward Opalinus Clay. At 60°C, the diffusion profiles of two U(VI) species were observed, which were attributed to a colloidal and an aquatic U(VI) species. The colloidal U(VI) species and the large humic acid colloid fraction showed a stronger interaction with the clay at 60°C. In addition, the D_e value of the aquatic U(VI) species increased with increasing temperature. Altogether, predictions of the U(VI) diffusion show that an increase of the temperature to 60°C does not accelerate the migration of U(VI) through Opalinus Clay. With regard to uranium-containing waste, it can be concluded that Opalinus Clay is suitable as host rock for a future nuclear waste repository since Opalinus Clay has a good retardation potential for U(VI).

The U(VI) sorption and especially the U(VI) diffusion experiments contribute to a more realistic description of the migration behavior of U(VI) in the natural clay rock Opalinus Clay since the obtained parameters can be used for modeling the actinide migration through argillaceous rocks in the absence and presence of clay organics in the temperature range up to 60°C. This leads to an improved risk assessment for potential nuclear waste repositories.

Building on the complexation, sorption and diffusion studies performed so far, future studies should focus on the geochemical behavior of radionuclides and especially actinides in solutions with higher ionic strength as relevant for potential nuclear waste repositories in clay formations in the north of Germany as well as in salt rock. Thus, the complexation of actinides with relevant clay organics has to be studied at higher salinities and partly at higher temperatures. Furthermore, actinide sorption and diffusion on/in natural clay rock (Opalinus Clay) and clay minerals (e.g., illite, montmorillonite) have to be investigated in the absence and presence of clay organics at higher salinities and exemplarily also at higher temperatures. With regard to sorption and migration, beside quantitative parameters also the speciation of the formed surface complexes has to be determined by means of spectroscopic methods. In addition, the influence of higher salinities on the retention capacity of potential container corrosion products (secondary iron (hydro)oxides such as magnetite or green rust) for actinides has to be quantified.

7 References

- Acker, M. (2003) Zeitaufgelöste laserinduzierte Fluoreszenzspektroskopie mit ultrakurzen Anregungspulsen und ihre Anwendung zur Untersuchung der Fluoreszenzeigenschaften von gelösten Huminstoffen, Protocatechusäure und deren U(VI)komplexen, PhD Thesis, TU Dresden, Dresden.
- Aeschbacher, M., Vergari, D., Schwarzenbach, R.P. and Sander, M. (2011) Electrochemical analysis of proton and electron transfer equilibria of the reducible moieties in humic acids. *Environ. Sci. Technol.* **45**, 8385-8394.
- Alcock, N.W., Kemp, T.J., Roe, S.M. and Leciejewicz, J. (1996a) The roles of N- and O-coordination in the crystal and molecular structures of uranyl complexes with anthranilic and pyrazinic acids. *Inorg. Chim. Acta* **248**, 241-246.
- Alcock, N.W., Errington, W., Kemp, T.J. and Leciejewicz, J. (1996b) Diaquadioxobis(pyridine-3-carboxylato)-uranium(VI). *Acta Cryst. C* **52**, 615-617.
- Amayri, S., Buda, R.A., Fröhlich, D., Heinrich, J., Klimach, T., Kratz, J.V., Reich, T., Trautmann, N. and Wunderlich, T. (2008) Sorption of actinides (Th, U, Np, Pu, Am) on Opalinus Clay in synthetic porewater. NRC 7, Budapest, Hungary.
- Artinger, R., Rabung, T., Kim, J.I., Sachs, S., Schmeide, K., Heise, K.H., Bernhard, G. and Nitsche, H. (2002) Humic colloid-borne migration of uranium in sand columns. *J. Contam. Hydrol.* **58**, 1-12.
- Bargar, J.R., Reitmeyer, R., Lenhart, J.J. and Davis, J.A. (2000) Characterization of U(VI)-carbonato ternary complexes on hematite: EXAFS and electrophoretic mobility measurements. *Geochim. Cosmochim. Acta* **64**, 2737-2749.
- Bauer, A., Fiehn, B., Marquardt, C.M., Klein, M., Römer, J., Schäfer, T., Görtzen, A. and Kienzler, B. (2006) Results on the Pu Diffusion in the Opalinus Clay. 6th EC FP - FUNMIG IP, Stockholm, Schweden.
- Beck, H.P., Wagner, H., Gottfreund, T. and Zeitz, M. (2004) Investigations of the behaviour of the heavy elements Cu, Zn, Cd, and Pb in the ternary system metal - humic acid - sand. In: *Wissenschaftliche Berichte, FZK-6999*, C.M. Marquardt (Ed.), Forschungszentrum Karlsruhe, Karlsruhe, pp. 155-156.
- Beneš, P., Kratzer, K., Vlčková, Š. and Šebestová, E. (1998) Adsorption of uranium on clay and the effect of humic substances. *Radiochim. Acta* **82**, 367-373.
- Bernhard, G., Geipel, G., Reich, T., Brendler, V., Amayri, S. and Nitsche, H. (2001) Uranyl(VI) carbonate complex formation: Validation of the $\text{Ca}_2\text{UO}_2(\text{CO}_3)_3(\text{aq.})$ species. *Radiochim. Acta* **89**, 511-518.
- Bernhard, G. and Geipel, G. (2007) Bestimmung der Bindungsform des Urans in Mineralwässern. *Vom Wasser* **105**, 7-10.
- Bertrand, P.A. and Choppin, G.R. (1982) Separation of actinides in different oxidation-states by solvent-extraction. *Radiochim. Acta* **31**, 135-137.
- Billard, I., Ansoborlo, E., Apperson, K., Arpigny, S., Azenha, M.E., Birch, D., Bros, P., Burrows, H.D., Choppin, G., Couston, L., Dubois, V., Fanghänel, T., Geipel, G., Hubert, S., Kim, J.I., Kimura, T., Klenze, R., Kronenberg, A., Kumke, M., Lagarde, G., Lamarque, G., Lis, S., Madic, C., Meinrath, G., Moulin, C., Nagaishi, R., Parker, D., Plancque, G., Scherbaum, F., Simoni, E., Sinkov, S. and Viallesoubranne, C. (2003) Aqueous solutions of uranium(VI) as studied by time-resolved emission spectroscopy: A round-robin test. *Appl. Spectrosc.* **57**, 1027-1038.
- Binstead, R.A., Zuberbühler, A.D. and Jung, B. (2005) SPECFIT - Global Analysis System. Version 3.0.37, Spectrum Software Associates, Marlborough.
- Bonin, L., Den Auwer, Ch., Ansoborlo, E., Cote, G. and Moisy, P. (2007) Study of Np speciation in citrate medium. *Radiochim. Acta* **95**, 371-379.

- Bonin, L., Cote, G. and Moisy, Ph. (2008) Speciation of An(IV) (Pu, Np, U and Th) in citrate media. *Radiochim. Acta* **96**, 145-152.
- Bossart, P. and Thury, M. (2008) Mont Terri Rock Laboratory. Project, Programme 1996 to 2007 and Results. Reports of the Swiss Geological Survey No. 3, Swiss Geological Survey.
- Bradbury, M.H. and Baeyens, B. (2006) Modelling sorption data for the actinides Am(III), Np(V) and Pa(V) on montmorillonite. *Radiochim. Acta* **94**, 619-625.
- Brady, P.V., Cygan, R.T. and Nagy, K.L. (1996) Molecular controls on kaolinite surface charge. *J. Colloid Interface Sci.* **183**, 356-364.
- Brand, R.A. (1987) Improving the validity of hyperfine fields distributions from magnetic-alloys. 1. Unpolarized source *Nucl. Instrum. Methods Phys. Res., Sect. B* **28**, 398-416.
- Brasser, T., Droste, J., Müller-Lyda, I., Neles, J.M., Sailer, M., Schmidt, G. and Steinhoff, M. (2008) Endlagerung wärmeentwickelnder radioaktiver Abfälle in Deutschland. GRS - 247, Öko-Institut and Gesellschaft für Anlagen- und Reaktorsicherheit (GRS).
- Bräse, S., Bülle, J. and Hüttermann, A. (2007) Organische und bioorganische Chemie. Das Basiswissen für Master- und Diplomprüfungen, Wiley-VCH, Weinheim.
- Budantseva, N.A., Andreev, G.B., Fedoseev, A.M., Antipin, M.Y. and Krupa, J.-C. (2006) Interaction of neptunium(V) with picolinic, nicotinic and isonicotinic acids. *Radiochim. Acta* **94**, 69-74.
- Cerfontain, H., Koeberg-Telder, A. and Kruk, C. (1975) Solutes in Sulfuric-Acid. 7. Ionization of benzenesulfonic acid; determination of pK_{BH} by ^{13}C NMR. *Tetrahedron Lett.* **42**, 3639-3642.
- Choppin, G.R. (1992) The role of natural organics in radionuclide migration in natural aquifer systems. *Radiochim. Acta* **58**, 113-120.
- Choppin, G.R. (2006) Actinide speciation in aquatic systems. *Marine Chem.* **99**, 83-92.
- Claret, F., Schäfer, T., Bauer, A. and Buckau, G. (2003) Generation of humic and fulvic acid from Callovo-Oxfordian Clay under high alkaline conditions. *Sci. Total Environ.* **317**, 189-200.
- COMSOL (2008) Multiphysics 3.5a. Finite-element software package. <http://www.comsol.com>.
- Cory, R.M. and McKnight, D.M. (2005) Fluorescence spectroscopy reveals ubiquitous presence of oxidized and reduced quinones in dissolved organic matter. *Environ. Sci. Technol.* **39**, 8142-8149.
- Courdouan, A., Christl, I., Meylan, S., Wersin, P. and Kretzschmar, R. (2007) Characterization of dissolved organic matter in anoxic rock extracts and in situ pore water of the Opalinus Clay. *Appl. Geochem.* **22**, 2926-2939.
- Courdouan, A., Christl, I., Rabung, T., Wersin, P. and Kretzschmar, R. (2008) Proton and trivalent metal cation binding by dissolved organic matter in the Opalinus Clay and the Callovo-Oxfordian formation. *Environ. Sci. Technol.* **42**, 5985-5991.
- Croué, J.P., Benedetti, M.F., Violleau, D. and Leenheer, J.A. (2003) Characterization and copper binding of humic and nonhumic organic matter isolated from the south platte river: Evidence for the presence of nitrogenous binding site. *Environ. Sci. Technol.* **37**, 328-336.
- Czerwinski, K.R., Buckau, G., Scherbaum, F. and Kim, J.I. (1994) Complexation of the uranyl ion with aquatic humic acid. *Radiochim. Acta* **65**, 111-119.
- Dean, J.A. (1999). *Lange's handbook of chemistry*. McGraw-Hill, Inc., New York.
- Denecke, M.A., Pompe, S., Reich, T., Moll, H., Bubner, M., Heise, K.H., Nicolai, R. and Nitsche, H. (1997) Measurements of the structural parameters for the interaction of uranium(VI) with natural and synthetic humic acids using EXAFS. *Radiochim. Acta* **79**, 151-159.
- Denecke, M.A., Panak, P.J., Burdet, F., Weigl, M., Geist, A., KlENZE, R., Mazzanti, M. and Gompper K. (2007) A comparative spectroscopic study of U(III)/Am(III) and Ln(III) complexed with N-donor ligands. *C. R. Chimie* **10**, 872-882.

- Dierckx, A., Maes, A. and Vancluysen, J. (1994) Mixed complex-formation of Eu^{3+} with humic acid and a competing ligand. *Radiochim. Acta* **66**, 149-156.
- Dodge, C.J. and Francis, A.J. (1997) Biotransformation of binary and ternary citric acid complexes of iron and uranium. *Environ. Sci. Technol.* **31**, 3062-3067.
- Dong, H.T., Du, H.B., Wickramasinghe, S.R. and Qian, X.H. (2009) The Effects of Chemical Substitution and Polymerization on the pK_a Values of Sulfonic Acids. *J. Phys. Chem. B* **113**, 14094-14101.
- Dong, W.M. and Brooks, S.C. (2006) Determination of the formation constants of ternary complexes of uranyl and carbonate with alkaline earth metals (Mg^{2+} , Ca^{2+} , Sr^{2+} , and Ba^{2+}) using anion exchange method. *Environ. Sci. Technol.* **40**, 4689-4695.
- Dreissig, I., Weiss, S., Hennig, C., Bernhard, G. and Zänker, H. (2011) Formation of uranium(IV)-silica colloids at near-neutral pH. *Geochim. Cosmochim. Acta* **75**, 352-367.
- Durbin, P.W., Kullgren, B., Xu, J. and Raymond, K.N. (1998) Development of decorporation agents for the actinides. *Rad. Protec. Dos.* **79**, 433-443.
- Eisenberg, D. and Kauzmann, W. (1969). *The structure and properties of water*. Oxford University Press, Ely House, London.
- Felmy, A.R., Cho, H., Dixon, D.A., Xia, Y., Hess, N.J. and Wang, Z. (2006) The aqueous complexation of thorium with citrate under neutral to basic conditions. *Radiochim. Acta* **94**, 205-212.
- Fimmen, R.L., Cory, R.M., Chin, Y.-P., Trouts, T.D. and McKnight, D.M. (2007) Probing the oxidation-reduction properties of terrestrially and microbially derived dissolved organic matter. *Geochim. Cosmochim. Acta* **71**, 3003-3015.
- Fox, P.M., Davis, J.A. and Zachara, J.M. (2006) The effect of calcium on aqueous uranium(VI) speciation and adsorption to ferrihydrite and quartz. *Geochim. Cosmochim. Acta* **70**, 1379-1387.
- Freundlich, H. (1906) Concerning adsorption in solutions. *Z. Phys. Chem. Stoechiom. Verwandtschafts.* **57**, 385-470.
- Fröhlich, D.R., Amayri, S., Drebert, J. and Reich, T. (2012, submitted) Influence of temperature and background electrolyte on the sorption of neptunium(V) on Opalinus Clay. *Appl. Clay Sci.*
- Gaffney, J.S., Marley, N.A. and Clark, S.B. (1996) *Humic and fulvic acids - Isolation, structure and environmental role*, American Chemical Society.
- Gampp, H., Maeder, M., Meyer, C.J. and Zuberbühler, A.D. (1985) Calculation of equilibrium-constants from multiwavelength spectroscopic data. 2. SPECFIT - 2 user-friendly programs in basic and standard fortran-77. *Talanta* **32**, 257-264.
- Geipel, G., Acker, M., Vulpius, D., Bernhard, G., Nitsche, H. and Fanghänel, Th. (2004) An ultrafast time-resolved fluorescence spectroscopy system for metal ion complexation studies with organic ligands. *Spectrochim. Acta Part A* **60**, 417-424.
- Glaus, M.A., Hummel, W. and van Loon, L.R. (1995) Stability of mixed-ligand complexes of metal-ions with humic substances and low-molecular-weight ligands. *Environ. Sci. Technol.* **29**, 2150-2153.
- Glaus, M.A., Baeyens, B., Lauber, M., Rabung, T. and Van Loon, L.R. (2005) Influence of water-extractable organic matter from Opalinus Clay on the sorption and speciation of Ni(II), Eu(III) and Th(IV). *Appl. Geochem.* **20**, 443-451.
- Glaus, M.A., Rossé, R., Van Loon, L.R. and Yaroshchuk, A.E. (2008) Tracer diffusion in sintered stainless steel filters: measurement of effective diffusion coefficients and implications for diffusion studies with compacted clays. *Clay Clay Min.* **56**, 677-685.

- Glorius, M., Moll, H. and Bernhard, G. (2007) Complexation of uranium(VI) with aromatic acids in aqueous solution – a comparison of hydroxamic acids and benzoic acid. *Radiochim. Acta* **95**, 151-157.
- Glorius, M., Moll, H., Geipel, G. and Bernhard, G. (2008) Complexation of uranium(VI) with aromatic acids such as hydroxamic and benzoic acid investigated by TRLFS. *J. Radioanal. Nucl. Chem.* **277**, 371-377.
- González-Sánchez, F., Van Loon, L.R., Gimmi, T., Jakob, A., Glaus, M.A. and Diamond, L.W. (2008) Self-diffusion of water and its dependence on temperature and ionic strength in highly compacted montmorillonite, illite and kaolinite. *Appl. Geochem.* **23**, 3840-3851.
- Guillaumont, D. (2006) Actinide(III) and lanthanide(III) complexes with nitrogen ligands: Counterions and ligand substituent effects on the metal-ligand bond. *Theochem - J. Molec. Struct.* **771**, 105-110.
- Guillaumont, R., Fanghänel, Th., Fuger, J., Grenthe, I., Neck, V., Palmer, D.A. and Rand, M.H. (2003) Update on the Chemical Thermodynamics of Uranium, Neptunium, Plutonium, Americium and Technetium. *Chemical Thermodynamics Vol. 5.* (OECD Nuclear Energy Agency, ed.) Elsevier, Amsterdam.
- Günther, A., Geipel, G. and Bernhard, G. (2007) Complex formation of uranium(VI) with the amino acids L-glycine and L-cysteine: A fluorescence emission and UV-Vis absorption study. *Polyhedron* **26**, 59-65.
- Günther, A., Steudtner, R., Schmeide, K. and Bernhard, G. (2011) Luminescence properties of uranium(VI) citrate and uranium(VI) oxalate species and their application in the determination of complex formation constants. *Radiochim. Acta* **99**, 535-541.
- Hartmann, E., Geckeis, H., Rabung, T., Lützenkirchen, J. and Fanghänel, T. (2008) Sorption of radionuclides onto natural clay rocks. *Radiochim. Acta* **96**, 699-707.
- He, Z., Ohno, T., Cade-Menun, B.J., Erich, M.S. and Honeycutt, C.W. (2006) Spectral and chemical characterization of phosphates associated with humic substances. *Soil Sci. Soc. Am. J.* **70**, 1741-1751.
- Heitzmann, M., Bravard, F., Gateau, C., Boubals, N., Berthon, C., Pécaut, J., Charbonnel, M.-C. and Delangle, P. (2009) Comparison of two tetrapodal N,O ligands: Impact of the softness of the heterocyclic N-donors pyridine and pyrazine on the selectivity for Am(III) over Eu(III). *Inorg. Chem.* **48**, 246-256.
- Helburn, R.S. and MacCarthy, P. (1994) Determination of some redox properties of humic acid by alkaline ferricyanide titration. *Anal. Chim. Acta* **295**, 263-272.
- Hesterberg, D., Chou, J.W., Hutchison, K.J. and Sayers, D.E. (2001) Bonding of Hg(II) to reduced organic sulfur in humic acid as affected by S/Hg ratio. *Environ. Sci. Technol.* **35**, 2741-2745.
- Hummel, W., Anderegg, G., Rao, L., Puigdomènech, I. and Tochiyama, O. (2005) Chemical Thermodynamics of Compounds and Complexes of U, Np, Pu, Am, Tc, Se, Ni and Zr with Selected Organic Ligands. *Chemical Thermodynamics Vol. 9.* (OECD Nuclear Energy Agency, ed.) Elsevier, Amsterdam.
- Hutchison, K.J., Hesterberg, D. and Chou, J.W. (2001) Stability of reduced organic sulfur in humic acid as affected by aeration and pH. *Soil Sci. Soc. Am. J.* **65**, 704-709.
- Jain, A., Yadav, K., Mohopatra, M., Godbole, S.V. and Tomar, B.S. (2009) Spectroscopic investigation on europium complexation with humic acid and its model compounds. *Spectrochim. Acta Part A* **72**, 1122-1126.
- Jakob, A., Pflingsten, W. and Van Loon, L. (2009) Effects of sorption competition on caesium diffusion through compacted argillaceous rock. *Geochim. Cosmochim. Acta* **73**, 2441-2456.

- Johnson, L.H., Niemeyer, M., Klubertanz, G., Siegel, P. and Gribi, P. (2002) Calculations of the temperature evolution of a repository for spent fuel, vitrified high-level waste and intermediate level waste in Opalinus Clay. Technical Report 01-04, Nagra, Wettingen.
- Jolivet, J.P., Thomas, Y., Tavel, B. and Lorenzelli, V. (1980) Vibrational study of coordinated CO_3^{2-} ions. *J. Mol. Struct.* **60**, 93-98.
- Joseph, C., Raditzky, B., Schmeide, K., Geipel, G. and Bernhard, G. (2008) Complexation of Uranium by Sulfur and Nitrogen Containing Model Ligands in Aqueous Solution. In: *Uranium Mining and Hydrogeology*, B. J. Merkel and A. Hasche-Berger (Eds.), Springer, Berlin, pp. 539-548.
- Joseph, C., Schmeide, K., Sachs, S. and Bernhard, G. (2009) Uranium(VI) and humic acid sorption onto kaolinite and Opalinus Clay. Annual Report 2008, FZD-511, Forschungszentrum Dresden-Rossendorf, Institute of Radiochemistry, 47.
- Joseph, C., Schmeide, K., Sachs, S., Brendler, V., Geipel, G. and Bernhard, G. (2011) Sorption of uranium(VI) onto Opalinus Clay in the absence and presence of humic acid in Opalinus Clay pore water. *Chem. Geol.* **284**, 240-250.
- Joseph, C., Schmeide, K., Sachs, S., Stockmann, M., Brendler, V. and Bernhard, G. (2012a, in preparation) Sorption of U(VI) onto Opalinus Clay: Effects of pH and humic acid. *Appl. Geochem.*
- Joseph, C., Van Loon, L.R., Jakob, A., Schmeide, K., Sachs, S. and Bernhard, G. (2012b, in preparation) Diffusion of U(VI) in Opalinus Clay: Influence of temperature and humic acid. *Geochim. Cosmochim. Acta.*
- Kerisit, S. and Liu, C.X. (2010) Molecular simulation of the diffusion of uranyl carbonate species in aqueous solution. *Geochim. Cosmochim. Acta* **74**, 4937-4952.
- Kim, J.I. (1986) Chemical behaviour of transuranic elements in natural aquatic systems, *Handbook on the Physics and Chemistry of the Actinides*, Elsevier.
- Kim, J.I. and Czerwinski, K.R. (1996) Complexation of metal ions with humic acid: Metal ion charge neutralization model. *Radiochim. Acta* **73**, 5-10.
- Kim, J.I. (2006) Significance of actinide chemistry for the long-term safety of waste disposal. *Nucl. Eng. Technol.* **38**, 459-482.
- Koban, A. and Bernhard, G. (2007) Uranium(VI) complexes with phospholipid model compounds – a laser spectroscopic study. *J. Inorg. Biochem.* **101**, 750-757.
- Kolokassidou, C., Pashalidis, I., Costa, C.N., Efstathiou, A.M. and Buckau, G. (2007). Thermal stability of solid and aqueous solutions of humic acid. *Thermochim. Acta* **454**, 78-83.
- Kornilovich, B., Pshinko, G., Spasenova, L. and Kovalchuk, I. (2000) Influence of humic substances on the sorption interactions between lanthanide and actinide ions and clay minerals. *Adsorpt. Sci. Technol.* **18**, 873-880.
- Kowal-Fouchard, A., Drot, R., Simoni, E. and Ehrhardt, J.J. (2004) Use of spectroscopic techniques for uranium(VI)/montmorillonite interaction modeling. *Environ. Sci. Technol.* **38**, 1399-1407.
- Křepelová, A., Sachs, S. and Bernhard, G. (2006) Uranium(VI) sorption onto kaolinite in the presence and absence of humic acid. *Radiochim. Acta* **94**, 825-833.
- Křepelová, A., Reich, T., Sachs, S., Drebert, J. and Bernhard, G. (2008) Structural characterization of U(VI) surface complexes on kaolinite in the presence of humic acid using EXAFS spectroscopy. *J. Colloid Interface Sci.* **319**, 40-47.
- Kurková, M., Klika, Z., Kliková, C. and Havel, J. (2004) Humic acids from oxidized coals. I. Elemental composition, titration curves, heavy metals in HA samples, nuclear magnetic resonance spectra of HAs and infrared spectroscopy. *Chemosphere* **54**, 1237-1245.
- Kwak, E.-J. and Lim, S.-I. (2004) The effect of sugar, amino acid, metal ion, and NaCl on model Maillard reaction under pH control. *Amino Acids* **27**, 85-90.

- Lefevre, G., Kneppers, J. and Fedoroff, M. (2008) Sorption of uranyl ions on titanium oxide studied by ATR-IR spectroscopy. *J. Colloid Interface Sci.* **327**, 15-20.
- Lindberg, B.J., Hamrin, K., Johansson, G., Gelius, U., Fahlmann, A., Nordling, C. and Siegbahn, K. (1970) Molecular spectroscopy by means of ESCA. II. Sulfur compounds. Correlation of electron binding with structure. *Phys. Scripta* **1**, 286-298.
- Lippold, H., Mansel, A. and Kupsch, H. (2005) Influence of trivalent electrolytes on the humic colloid-borne transport of contaminant metals: competition and flocculation effects. *J. Contam. Hydrol.* **76**, 337-352.
- Lippold, H., Evans, N.D.M., Warwick, P. and Kupsch, H. (2007) Competitive effect of iron(III) on metal complexation by humic substances: Characterisation of ageing processes. *Chemosphere* **67**, 1050-1056.
- Lippold, H. and Lippmann-Pipke, J. (2009) Effect of humic matter on metal adsorption onto clay materials: Testing the linear additive model. *J. Contam. Hydrol.* **109**, 40-48.
- Lovley, D.R., Coates, J.D., Blunt-Harries, E.L., Phillips, E.J.P. and Woodward, J.C. (1996) Humic substances as electron acceptors for microbial respiration. *Nature* **382**, 445-448.
- Mahmoud, M.R., Ibrahim, S.A., Hassan, A.M.A. and Ahmed, I.T. (1996) Ternary complexes of N-(2-acetamido)iminodiacetic acid and some aromatic acids. Isolation and stability constants in solution. *Transition Met. Chem.* **21**, 1-4.
- Majzik, A. and Tombacz, E. (2007) Interaction between humic acid and montmorillonite in the presence of calcium ions I. Interfacial and aqueous phase equilibria: Adsorption and complexation. *Org. Geochem.* **38**, 1319-1329.
- Makarov, M.I. (1997) Phosphorus compounds of soil humic acids. *Eurasian Soil Sci.* **30**, 395-402.
- Makarov, M.I. (2005) Phosphorus-containing components of soil organic matter: P-31 NMR spectroscopic study (a review). *Eurasian Soil Sci.* **38**, 153-164.
- Mansel, A., Crustewitz, C. and Kupsch, H. (2003) Geochemische Untersuchungen zur Retention von reaktiven Kohlenstoffverbindungen für toxische Schwermetalle. Abschlussbericht, Universität Leipzig, Institut für Interdisziplinäre Isotopenforschung.
- Marquardt, C., Herrmann, G. and Trautmann, N. (1996) Complexation of neptunium(V) with humic acids at very low metal concentrations. *Radiochim. Acta* **73**, 119-125.
- Martell, A.E., Smith, R.M. and Motekaitis, R.J. (1998) NIST Critically Selected Stability Constants of Metal Complexes Database, Version 5.0.
- Martell, A.E., Smith, R.M. and Motekaitis, R.J. (2003) NIST Critically Selected Stability Constants of Metal Complexes Database, Version 7.0.
- McCarthy, J.F., Czerwinski, K.R., Sanford, W.E., Jardine, P.M. and Marsh, J.D. (1998) Mobilization of transuranic radionuclides from disposal trenches by natural organic matter. *J. Contam. Hydrol.* **30**, 49-77.
- Meleshyn, A., Azeroual, M., Reeck, T., Houben, G., Riebe, B. and Bunnenberg, C. (2009) Influence of (Calcium-)Uranyl-Carbonate Complexation on U(VI) Sorption on Ca- and Na-Bentonites. *Environ. Sci. Technol.* **43**, 4896-4901.
- Merkusheva, S.A., Kumok, V.N. and Skorik, N.A. (1970) *Radiokhim.* **12**, 175-178.
- Mibus, J. and Sachs, S. (2006) Impact of humic colloids on uranium(VI) migration in clay. Annual Report 2005, FZR-443, Forschungszentrum Rossendorf, 60.
- Mibus, J., Müller, C., Sachs, S. and Kuchler, R. (2007a) Determination of diffusion coefficients of humic acid in bulk water. Annual Report 2006, FZD-459, Forschungszentrum Dresden-Rossendorf, 63.

- Mibus, J., Sachs, S., Pffingsten, W., Nebelung, C. and Bernhard, G. (2007b) Migration of uranium(IV)/(VI) in the presence of humic acids in quartz sand: A laboratory column study. *J. Contam. Hydrol.* **89**, 199-217.
- Moll, H., Geipel, G., Reich, T., Bernhard, G., Fanghänel, T. and Grenthe, I. (2003) Uranyl(VI) complexes with alpha-substituted carboxylic acids in aqueous solution. *Radiochim. Acta* **91**, 11-20.
- Montavon, G., Mansel, A., Seibert, A., Keller, H., Kratz, J.V. and Trautmann, N. (2000) Complexation studies of UO_2^{2+} with humic acid at low metal ion concentrations by indirect speciation methods. *Radiochim. Acta* **88**, 17-24.
- Morgenstern, M., Klenze, R. and Kim, J.I. (2000) The formation of mixed-hydroxo complexes of Cm(III) and Am(III) with humic acid in the neutral pH range. *Radiochim. Acta* **88**, 7-16.
- Morris, K.F., Cutak, B.J., Dixon, A.M. and Larive, C.K. (1999) Analysis of diffusion coefficient distributions in humic and fulvic acids by means of diffusion ordered NMR spectroscopy. *Anal. Chem.* **71**, 5315-5321.
- Moulin, V., Robouch, P., Vitorge, P. and Allard, B. (1987) Spectrophotometric study of the interaction between americium(III) and humic materials. *Inorg. Chim. Acta* **140**, 303-306.
- Musso, H. (1967) Phenol coupling. In: Taylor, W.I., Battersby, A.R., editors. *Oxidative coupling of phenols*. New York, Marcel Dekker, p. 1-94.
- Müller, K., Brendler, V. and Foerstendorf, H. (2008) Aqueous uranium(VI) hydrolysis species characterized by attenuated total reflection fourier-transform infrared spectroscopy. *Inorg. Chem.* **47**, 10127-10134.
- Müller, K., Foerstendorf, H., Tsushima, S., Brendler, V. and Bernhard, G. (2009) Direct spectroscopic characterization of aqueous actinyl(VI) species: A comparative study of Np and U. *J. Phys. Chem. A* **113**, 6626-6632.
- Müller, M., Acker, M., Taut, S. and Bernhard, G. (2010) Complex formation of trivalent americium with salicylic acid at very low concentrations. *J. Radioanal. Nucl. Chem.* **286**, 175-180.
- Nebbioso, A. and Piccolo, A. (2009) Molecular rigidity and diffusivity of Al^{3+} and Ca^{2+} humates as revealed by NMR spectroscopy. *Environ. Sci. Technol.* **43**, 2417-2424.
- Nebel, D. (1966) Spektralphotometrische Untersuchung des Gleichgewichtes Pu^{IV} -Citrat in wässriger Lösung. *Z. Phys. Chem.* **232**, 161-175.
- Nebel, D. and Urban, G. (1966) Potentiometrische Untersuchungen zur Komplexbildung von Ce^{III} , Ce^{IV} , Th^{IV} , U^{IV} und Citrat in wässriger Lösung. *Z. Phys. Chem.* **233**, 73-84.
- Neck, V. and Kim, J.I. (2001) Solubility and hydrolysis of tetravalent actinides. *Radiochim. Acta* **89**, 1-16.
- Niu, Z.W., Fan, Q.H., Wang, W.H., Xu, J.Z., Chen, L. and Wu, W.S. (2009) Effect of pH, ionic strength and humic acid on the sorption of uranium(VI) to attapulgite. *Appl. Radiat. Isot.* **67**, 1582-1590.
- Olivella, M.A., del Rio, J.C., Palacios, J., Vairavamurthy, M.A. and de las Heras, F.X.C. (2002) Characterization of humic acid from leonardite coal: an integrated study of Py-GC-MS, XPS and XANES techniques. *J. Anal. Appl. Pyrol.* **63**, 59-68.
- Opel, K., Weiß, S., Hübener, S., Zänker, H. and Bernhard, G. (2007) Study of the solubility of amorphous and crystalline uranium dioxide by combined spectroscopic methods. *Radiochim. Acta* **95**, 143-149.
- Panak, P., Klenze, R., Kim, J.I. and Wimmer, H. (1995) A study of intramolecular energy transfer in Cm(III) complexes with aromatic ligands by time-resolved laser fluorescence spectroscopy. *J. Alloys Compd.* **225**, 261-266.

- Panak, P., Klenze, R. and Kim, J.I. (1996) A study of ternary complexes of Cm(III) with humic acid and hydroxide or carbonate in neutral pH range by time-resolved laser fluorescence spectroscopy. *Radiochim. Acta* **74**, 141-146.
- Pandey, A.K., Pandey, S.D. and Misra, V. (2000) Stability constants of metal-humic acid complexes and its role in environmental detoxification. *Ecotoxicol. Environ. Safety* **47**, 195-200.
- Park, Y.J., Lee, B.H., Kim, W.H. and Do, Y. (1999) Investigation of Coordinational Properties of Europium(III) Complexes with Picolinic Acid Using Eu(III) Excitation Spectroscopy. *J. Colloid Interface Sci.* **209**, 268-270.
- Pashalidis, I. and Buckau, G. (2007) U(VI) mono-hydroxo humate complexation. *J. Radioanal. Nucl. Chem.* **273**, 315-322.
- Paulenová, A., Rajec, P., Žemberyová, M., Sasköiová, G. and Višacký, V. (2000) Strontium and calcium complexation by humic acid. *J. Radioanal. Nucl. Chem.* **246**, 623-628.
- Pearson, F.J. (1998) Opalinus Clay experimental water: A1Type, Version 980318. PSI Internal report TM-44-98-07, Paul Scherrer Institut.
- Pearson, F.J., Arcos, D., Bath, A., Boisson, J.Y., Fernández, A.M., Gäbler, H.E., Gaucher, E., Gautschi, A., Griffault, L., Hernán, P. and Waber, H.N. (2003) Mont Terri Project - Geochemistry of Water in the Opalinus Clay Formation at the Mont Terri Rock Laboratory. Reports of the Federal Office for Water and Geology, Geology Series No. 5, Federal Office for Water and Geology.
- Pearson, G.R. (1963) Hard and soft acids and bases. *J. Am. Chem. Soc.* **85**, 3533-3539.
- Phillippi, J.M., Loganathan, V.A., McIndoe, M.J., Barnett, M.O., Clement, T.P. and Roden, E.E. (2007) Theoretical solid/solution ratio effects on adsorption and transport: Uranium(VI) and carbonate. *Soil Sci. Soc. Am. J.* **71**, 329-335.
- Pompe, S., Bubner, M., Denecke, M.A., Reich, T., Brachmann, A., Geipel, G., Nicolai, R., Heise, K.H. and Nitsche, H. (1996) A comparison of natural humic acids with synthetic humic acid model substances: characterization and interaction with uranium(VI). *Radiochim. Acta* **74**, 135-140.
- Pompe, S., Brachmann, A., Bubner, M., Geipel, G., Heise, K.H., Bernhard, G. and Nitsche, H. (1998) Determination and comparison of uranyl complexation constants with natural and model humic acids. *Radiochim. Acta* **82**, 89-95.
- Pompe, S., Bubner, M., Schmeide, K., Heise, K.H., Bernhard, G. and Nitsche, H. (2000a) Influence of humic acids on the migration behavior of radioactive and non-radioactive substances under conditions close to nature. Synthesis, radiometric determination of functional groups, complexation. *Wissenschaftlich-Technische Berichte, FZR-290*, Forschungszentrum Rossendorf.
- Pompe, S., Schmeide, K., Bubner, M., Geipel, G., Heise, K.H., Bernhard, G. and Nitsche, H. (2000b) Investigation of humic acid complexation behavior with uranyl ions using modified synthetic and natural humic acids. *Radiochim. Acta* **88**, 553-558.
- Prietzl, J., Thieme, J., Salomé, M. and Knicker, H. (2007) Sulfur K-edge XANES spectroscopy reveals differences in sulfur speciation of bulk soils, humic acid, fulvic acid, and particle size separates. *Soil Biol. Biochem.* **39**, 877-890.
- Quiles, F. and Burneau, A. (2000) Infrared and Raman spectra of uranyl(VI) oxo-hydroxo complexes in acid aqueous solutions: a chemometric study. *Vib. Spectrosc.* **23**, 231-241.
- Raditzky, B., Schmeide, K., Sachs, S., Geipel G. and Bernhard, G. (2010) Interaction of uranium(VI) with nitrogen containing model ligands studied by laser-induced fluorescence spectroscopy. *Polyhedron* **29**, 620-626.
- Raghavan, A. and Santappa, M. (1970) Complexes of uranyl ion with some amino and mercapto acids. *Curr. Sci.* **13**, 302-303.

- Raghavan, A. and Santappa, M. (1973) Complexes of uranyl ion with amino and mercapto acids. *J. Inorg. Nucl. Chem.* **35**, 3363-3365.
- Rajan, K.S. and Martell, A.E. (1965) Equilibrium studies of uranyl complexes. III. Interaction of uranyl ion with citric acid. *Inorg. Chem.* **4**, 462-469.
- Rao, L.F., Jiang, J., Zanonato, P.L., Di Bernardo, P., Bismondo, A. and Garnov, A.Y. (2002) Complexation of uranium(VI) with malonate at variable temperatures. *Radiochim. Acta* **90**, 581-588.
- Rao, L.F. (2007) Thermodynamics of actinide complexation in solution at elevated temperatures: Application of variable-temperature titration calorimetry. *Chem. Soc. Rev.* **36**, 881-892.
- Ratasuk, N. and Nanny, M.A. (2007) Characterization and quantification of reversible redox sites in humic substances. *Environ. Sci. Technol.* **41**, 7844-7850.
- Raymond, D.P., Duffield, J.R. and Williams, D.R. (1987) Complexation of plutonium and thorium in aqueous environments. *Inorg. Chim. Acta* **140**, 309-313.
- Redden, G.D., Jinhe, L. and Leckie, J. (1998) Adsorption of U(VI) and Citric Acid on Goethite, Gibbsite, and Kaolinite. Comparing Results for Binary and Ternary Systems. In: *Adsorption of Metals by Geomedia. Variables, Mechanisms and Model Applications* Academic Press, San Diego, pp. 291.
- Reiller, P. (2005) Prognosticating the humic complexation for redox sensitive actinides through analogy, using the charge neutralisation model. *Radiochim. Acta* **93**, 43-55.
- Ren, X.M., Wang, S.W., Yang, S.T. and Li, J.X. (2010) Influence of contact time, pH, soil humic/fulvic acids, ionic strength and temperature on sorption of U(VI) onto MX-80 bentonite. *J. Radioanal. Nucl. Chem.* **283**, 253-259.
- Rocha, J.C., Sargentini, E., Zara, L.F., Rosa, A.H., Santos, A. and Burba, P. (2003) Reduction of mercury(II) by tropical river humic substances (Rio Negro) - Part II. Influence of structural features (molecular size, aromaticity, phenolic groups, organically bound sulfur). *Talanta* **61**, 699-707.
- Ryan, D.K. and Weber, J.H. (1982) Fluorescence quenching titration for determination of complexing capacities and stability constants of fulvic acid. *Anal. Chem.* **54**, 986-990.
- Saada, A., Gaboriau, H., Cornu, S., Bardot, F., Villieras, F. and Croue, J.P. (2003) Adsorption of humic acid onto a kaolinitic clay studied by high-resolution argon adsorption volumetry. *Clay Miner.* **38**, 433-443.
- Sachs, S., Schmeide, K., Brendler, V., Křepelová, A., Mibus, J., Geipel, G., Heise, K.H. and Bernhard, G. (2004) Investigation of the Complexation and the Migration of Actinides and Non-radioactive Substances with Humic Acids under Geogenic Conditions: Complexation of Humic Acids with Actinides in the Oxidation State IV Th, U, Np. *Wissenschaftlich-Technische Berichte, FZR-399*, Forschungszentrum Rossendorf.
- Sachs, S. and Bernhard, G. (2005) NIR spectroscopic study of the complexation of neptunium(V) with humic acids: Influence of phenolic OH groups on the complex formation. *Radiochim. Acta* **93**, 141-145.
- Sachs, S., Schmeide, K., Reich, T., Brendler, V., Heise, K.H. and Bernhard, G. (2005) EXAFS study on the neptunium(V) complexation by various humic acids under neutral pH conditions. *Radiochim. Acta* **93**, 17-25.
- Sachs, S., Brendler, V. and Geipel, G. (2007a) Uranium(VI) complexation by humic acid under neutral pH conditions studied by laser-induced fluorescence spectroscopy. *Radiochim. Acta* **95**, 103-110.
- Sachs, S., Křepelová, A., Schmeide, K., Koban, A., Günther, A., Mibus, J., Brendler, V., Geipel, G. and Bernhard, G. (2007b) Joint Project: Migration of actinides in the system clay, humic substance, aquifer - Migration behavior of actinides (uranium, neptunium) in clays:

- Characterization and quantification of the influence of humic substances. *Wissenschaftlich-Technische Berichte, FZD-460, Forschungszentrum Dresden-Rossendorf.*
- Sachs, S. and Bernhard, G. (2008) Sorption of U(VI) onto an artificial humic substance-kaolinite-associate. *Chemosphere* **72**, 1441-1447.
- Sachs, S., Reich, T. and Bernhard, G. (2010) Study of the role of sulfur functionalities in humic acids for uranium(VI) complexation. *Radiochim. Acta* **98**, 467-477.
- Sachs, S. and Bernhard, G. (2011a) Humic acid model substances with pronounced redox functionality for the study of environmentally relevant interaction processes of metal ions in the presence of humic acid. *Geoderma* **162**, 132-140.
- Sachs, S. and Bernhard, G. (2011b) Influence of humic acids on the actinide migration in the environment: suitable humic acid model substances and their application in studies with uranium-a review. *J. Radioanal. Nucl. Chem.* **290**, 17-29.
- Samadfam, M., Niitsu, Y., Sato, S. and Ohashi, H. (1996) Complexation thermodynamics of Sr(II) and humic acid. *Radiochim. Acta* **73**, 211-216.
- Schmeide, K., Pompe, S., Bubner, M., Heise, K.H., Bernhard, G. and Nitsche, H. (2000) Uranium(VI) sorption onto phyllite and selected minerals in the presence of humic acid. *Radiochim. Acta* **88**, 723-728.
- Schmeide, K., Sachs, S., Bubner, M., Reich, T., Heise, K.H. and Bernhard, G. (2003) Interaction of uranium(VI) with various modified and unmodified natural and synthetic humic substances studied by EXAFS and FTIR spectroscopy. *Inorg. Chim. Acta* **351**, 133-140.
- Schmeide, K., Reich, T., Sachs, S., Brendler, V., Heise, K.H. and Bernhard, G. (2005) Neptunium(IV) complexation by humic substances studied by X-ray absorption fine structure spectroscopy. *Radiochim. Acta* **93**, 187-196.
- Schmeide, K., Reich, T., Sachs, S. and Bernhard, G. (2006) Plutonium(III) complexation by humic substances studied by X-ray absorption fine structure spectroscopy. *Inorg. Chim. Acta* **359**, 237-242.
- Schmeide, K. and Bernhard, G. (2008) Spectroscopic study of the uranium(IV) complexation by organic model ligands in aqueous solution. In: *Uranium, Mining and Hydrogeology* (B.J. Merkel, A. Hasche-Berger, eds.), Springer Verlag, Berlin Heidelberg, 591-598.
- Schmeide, K. and Bernhard, G. (2009) Redox stability of neptunium(V) and neptunium(IV) in the presence of humic substances of varying functionality. *Radiochim. Acta* **97**, 603-611.
- Schmeide, K. and Bernhard, G. (2010) Sorption of Np(V) and Np(IV) onto kaolinite: Effects of pH, ionic strength, carbonate and humic acid. *Appl. Geochem.* **25**, 1238-1247.
- Schmeide, K., Sachs, S. and Bernhard, G. (2012a) Np(V) reduction by humic acid: Contribution of reduced sulfur functionalities to the redox behavior of humic acid. *Sci. Total Environ.* **419**, 116-123.
- Schmeide, K., Joseph, C. and Bernhard, G. (2012b, in preparation) Influence of organic ligands and temperature on U(VI) sorption onto Opalinus Clay.
- Schott, J., Acker, M., Barkleit, A., Brendler, V., Taut, S. and Bernhard, G. (2012, in press) The influence of temperature and small organic ligands on the sorption of Eu(III) on Opalinus Clay. *Radiochim. Acta*, DOI: 10.1524/ract.2012.1921.
- Schulten, H.R. and Schnitzer, M. (1998) The chemistry of soil organic nitrogen: a review. *Biol. Fertil. Soil* **26**, 1-15.
- Scott, D.T., McKnight, D.M., Blunt-Harris, E.L., Koselar, S.E. and Lovley, D.R. (1998) Quinone moieties act as electron acceptors in the reduction of humic substances by humics-reducing microorganisms. *Environ. Sci. Technol.* **32**, 2984-2989.

- Seida, Y., Terashima, M., Tachi, Y., Iijima, K., Nakazawa, T., Yamada, M. and Yui, M. (2010) Sorption and diffusion of Eu in sedimentary rock in the presence of humic substance. *Radiochim. Acta* **98**, 703-709.
- Sevostyanova, E.P. (1983) Stability of Np(IV), Np(V), and Np(VI) in citric acid solutions. *Soviet Radiochem.* **25**, 321-326.
- Shanbhag, P.M. and Choppin, G.R. (1981) Binding of Uranyl by Humic-Acid. *J. Inorg. Nucl. Chem.* **43**, 3369-3372.
- Silva, R.J. and Nitsche, H. (1995) Actinide environmental chemistry. *Radiochim. Acta* **70**, 377-396.
- Skylberg, U., Bloom, P.R., Qian, J., Lin, C.M. and Bleam, W.F. (2006) Complexation of mercury(II) in soil organic matter: EXAFS evidence for linear two-coordination with reduced sulfur groups. *Environ. Sci. Technol.* **40**, 4174-4180.
- Solomon, D., Lehmann, J. and Martinez, C.E. (2003) Sulfur K-edge XANES spectroscopy as a tool for understanding sulfur dynamics in soil organic matter. *Soil Sci. Soc. Am. J.* **67**, 1721-1731.
- Starý, J. and Balek, V. (1962) Untersuchung der Uran(VI)-Komplexe mit alpha-Hydroxysäuren durch Extraktionsmethode. *Coll. Czech. Chem. Comm.* **27**, 809-815.
- Stern, O. and Volmer, M. (1919) The fading time of fluorescence. *Physik. Zeitschr.* **20**, 183-188.
- Stedtner, R., Arnold, T., Geipel, G. and Bernhard, G. (2010) Fluorescence spectroscopic study on complexation of uranium(VI) by glucose - a comparison of room and low temperature measurements. *J. Radioanal. Nucl. Chem.* **284**, 421-429.
- Stedtner, R., Sachs, S., Schmeide, K., Brendler, V. and Bernhard, G. (2011a) Ternary uranium(VI) carbonate humate complex studied by cryo-TRLFS. *Radiochim. Acta* **99**, 687-692.
- Stedtner, R., Müller, K., Schmeide, K., Sachs, S. and Bernhard, G. (2011b) Binary and ternary uranium(VI) humate complexes studied by attenuated total reflection Fourier-transform infrared spectroscopy. *Dalton Trans.* **40**, 11920-11925.
- Stedtner, R., Schmeide, K. and Bernhard, G. (2011c) Uranium(VI) complexation with lactate and citrate in dependence on temperature (7-65°C). *Mineralog. Magazine* **75**, 1940.
- Stedtner, R., Schmeide, K. and Bernhard, G. (2012, in preparation) Complexation of U(VI) with lactate between 7 and 65°C. *J. Alloys Comp.*
- Stevenson, F.J. (1982). *Humus Chemistry*. 1st ed., John Wiley and Sons, New York.
- Stevenson, F.J. (1994) *Humus Chemistry. Genesis, Composition, Reactions*. 2nd ed., John Wiley and Sons, New York.
- Sumner, M.E. and Miller, W.P. (1996) Cation exchange capacity and exchange coefficients. In: *Methods of Soil Analysis. Part 3: Chemical Methods*, D. L. Sparks, A. L. Page, P. A. Helmke, R. H. Loeppert, P. N. Soltanpour, M. A. Tabatabai, C. T. Johnston and M. E. Sumner (Eds.), Soil Science Society of America Inc., USA, pp. 1201.
- Sutton, R. and Sposito, G. (2006) Molecular simulation of humic substance-Ca-montmorillonite complexes. *Geochim. Cosmochim. Acta* **70**, 3566-3581.
- Suzuki, Y., Nankawa, T., Yoshida, T., Ozaki, T., Ohnuki, T., Francis, A.J., Tsushima, S., Enokida, Y. and Yamamoto, I. (2006) Reduction behavior of uranium in the presence of citric acid. *Radiochim. Acta* **94**, 579-583.
- Szulczewski, M.D., Helmke, P.A. and Bleam, W. (2001) XANES spectroscopy studies of Cr(VI) reduction by thiols in organosulfur compounds and humic substances. *Environ. Sci. Technol.* **35**, 1134-1141.
- Tertre, E., Berger, G., Castet, S., Loubet, M. and Giffaut, E. (2005) Experimental sorption of Ni²⁺, Cs⁺ and Ln³⁺ onto a montmorillonite up to 150°C. *Geochim. Cosmochim. Acta* **69**, 4937-4948.

- Teterin, Y.A., Nefedov, V.I., Nikitin, A.S., Teterin, A.Y., Ivanov, K.E., Maslakov, K.I., Utkin, I.O., Bubner, M., Reich, T., Pompe, S., Heise, K.H. and Nitsche, H. (2001) Interaction of UO_2^{2+} and Fe^{3+} ions with natural humic acid. *Russ. J. Inorg. Chem.* **46**, 886-891.
- Thompson, H.A., Parks, G.A. and Jr. Brown, G.E. (1998) Structure and composition of uranium(VI) complexes at the kaolinite-water interface. In: Adsorption of metals by geomedia. Variables, mechanisms and model applications, E. A. Jenne (Ed.), Academic Press, San Diego, pp. 349-370.
- Thuéry, P. (2007) Uranyl ion complexation by citric and citramalic acids in the presence of diamines. *Inorg. Chem.* **46**, 2307-2315.
- Thuéry, P. (2008) Novel two-dimensional uranyl-organic assemblages in the citrate and D(-)-citramalate families. *Cryst. Eng. Comm.* **10**, 79-85.
- Tipping, E., Rey-Castro, C., Bryan, S.E. and Hamilton-Taylor, J. (2002) Al(III) and Fe(III) binding by humic substances in freshwaters, and implications for trace metal speciation. *Geochim. Cosmochim. Acta* **66**, 3211-3224.
- Tochiyama, O., Niibori, Y., Tanaka, K., Kubota, T., Yoshino, H., Kirishima, A. and Setiawan, B. (2004) Modeling of the complex formation of metal ions with humic acids. *Radiochim. Acta* **92**, 559-565.
- Urban, N.R., Ernst, K. and Bernasconi, S. (1999) Addition of sulfur to organic matter during early diagenesis of lake sediments. *Geochim. Cosmochim. Acta* **63**, 837-853.
- Vairavamurthy, M.A., Maletic, D., Wang, S., Manowitz, B., Eglinton, T. and Lyons, T. (1997) Characterization of sulfur-containing functional groups in sedimentary humic substances by X-ray absorption near-edge structure spectroscopy. *Energ. Fuel* **11**, 546-553.
- Vairavamurthy, A. and Wang, S. (2002) Organic nitrogen in geomacromolecules: Insights on speciation and transformation with K-edge XANES spectroscopy. *Environ. Sci. Technol.* **36**, 3050-3056.
- Van Loon, L.R., Soler, J.M. and Bradbury, M.H. (2003) Diffusion of HTO, $^{36}\text{Cl}^-$ and $^{125}\text{I}^-$ in Opalinus Clay samples from Mont Terri - Effect of confining pressure. *J. Contam. Hydrol.* **61**, 73-83.
- Van Loon, L.R. and Soler, J.M. (2004) Diffusion of HTO, $^{36}\text{Cl}^-$, $^{125}\text{I}^-$, and $^{22}\text{Na}^+$ in Opalinus Clay: Effect of Confining Pressure, Sample Orientation, Sample Depth and Temperature. PSI-Bericht Nr. 04-03, Paul Scherrer Institut.
- Van Loon, L.R. and Eikenberg, J. (2005) A high-resolution abrasive method for determining diffusion profiles of sorbing radionuclides in dense argillaceous rocks. *Appl. Radiat. Isot.* **63**, 11-21.
- Van Loon, L.R., Muller, W. and Iijima, K. (2005) Activation energies of the self-diffusion of HTO, $^{22}\text{Na}^+$ and $^{36}\text{Cl}^-$ in a highly compacted argillaceous rock (Opalinus Clay). *Appl. Geochem.* **20**, 961-972.
- Wang, Z.M., van de Burgt, L.J. and Choppin, G.R. (1999) Spectroscopic study of lanthanide(III) complexes with carboxylic acids. *Inorg. Chim. Acta* **293**, 167-177.
- Wang, Z.M., Zachara, J.M., Yantasee, W., Gassman, P.L., Liu, C.X. and Joly, A.G. (2004) Cryogenic laser induced fluorescence characterization of U(VI) in Hanford vadose zone pore waters. *Environ. Sci. Technol.* **38**, 5591-5597.
- Wang, Z., Zachara, J.M., Liu, C., Gassman, P.L., Felmy, A.R. and Clark, S.B. (2008) A cryogenic fluorescence spectroscopic study of uranyl carbonate, phosphate and oxyhydroxide minerals. *Radiochim. Acta* **96**, 591-598.
- Warwick, P., Hall, A., Zhu, J., Dimmock, P.W., Robbins, R., Carlsen, L. and Lassen, P. (1997) Effect of temperature on the nickel humic acid equilibrium reaction. *Chemosphere* **35**, 2471-2477.
- Wimmer, C., Arnold, T. and Großmann, K. (2009) Untersuchungen zur Fluoreszenz von Lactat bei Raumtemperatur und tiefen Temperaturen. *CIT* **81**, 501-504.

- Wolery, T.J. (1992). EQ3/6, A Software Package for the Geochemical Modeling of Aqueous Systems, UCRL-MA-110662 Part I, Lawrence Livermore National Laboratory.
- Wu, T., Amayri, S., Drebert, J., Van Loon, L.R. and Reich, T. (2009) Neptunium(V) sorption and diffusion in Opalinus Clay. *Environ. Sci. Technol.* **43**, 6567-6571.
- Xia, K., Bleam, W. and Helmke, P.A. (1997) Studies of the nature of binding sites of first row transition elements bound to aquatic and soil humic substances using X-ray absorption spectroscopy. *Geochim. Cosmochim. Acta* **61**, 2223-2235.
- Xia, K., Weesner, F., Bleam, W.F., Bloom, P.R., Skyllberg, U.L. and Helmke, P.A. (1998) XANES studies of oxidation states of sulfur in aquatic and soil humic substances. *Soil Sci. Soc. Am. J.* **62**, 1240-1246.
- Xia, K., Skyllberg, U.L., Bleam, W.F., Bloom, P.R., Nater, E.A. and Helmke, P.A. (1999) X-ray absorption spectroscopic evidence for the complexation of Hg(II) by reduced sulfur in soil humic substances. *Environ. Sci. Technol.* **33**, 257-261.
- Yule, L. (1991) A comparison of the binding of plutonium and iron to transferrin and citrate. Thesis, University of Wales.
- Zeh, P., Czerwinski, K.R. and Kim, J.I. (1997) Speciation of uranium in Gorleben groundwaters. *Radiochim. Acta* **76**, 37-44.
- Zheng, Z.P., Tokunaga, T.K. and Wan, J.M. (2003) Influence of calcium carbonate on U(VI) sorption to soils. *Environ. Sci. Technol.* **37**, 5603-5608.

8 Acknowledgements

The authors would like to thank S. Heller and J. Seibt for HA synthesis, characterization and sample preparation as well as S. Gürtler, A. Ritter, Ch. Müller, J. Seibt and A. Schliephake for their help in performing the experiments.

Furthermore, we thank H. Görner for elemental analyses, U. Schaefer, A. Ritter and C. Eckardt for ICP-MS analyses, ion chromatography and BET determination, C. Nebelung for the help during LSC measurements, S. Weiß for zeta potential and photon correlation spectroscopic measurements, A. Scholz for XRD measurements and Dr. H. Reuther for Mössbauer spectroscopy.

We also thank Dr. K. Müller and K. Heim for FTIR and ATR FTIR measurements and for their help in spectra interpretation, Dr. G. Geipel for support during TRLFS measurements and for discussion of laser spectroscopic results, M. Eilzer for technical support during TRLFS measurements as well as Dr. V. Brendler for speciation calculations and helpful discussions and Dr. A. Barkleit for helpful discussions concerning f-element spectroscopy.

We thank Prof. Dr. T. Reich and J. Drebert (Johannes Gutenberg-Universität Mainz, Institut für Kernchemie) for XPS measurements and data evaluation.

Dr. L.R. Van Loon and Dr. A. Jakob (Paul Scherrer Institut, Laboratory for Waste Management) is especially thanked for their immense support concerning diffusion experiments and COMSOL modeling.

Furthermore, we thank the Bundesanstalt für Geowissenschaften und Rohstoffe (BGR) and the Karlsruher Institut für Technologie, Institut für Nukleare Entsorgung (KIT-INE) (especially Dr. C.M. Marquardt) for providing and preparing ground and homogenized OPA as well as intact OPA bore core samples.

The authors are grateful for providing of ^{243}Am from the transplutonium element production facilities at Oak Ridge National Laboratory within a collaboration between the Forschungszentrum Dresden-Rossendorf and Prof. Dr. H. Nitsche from the Lawrence Berkeley National Laboratory, supported by the U.S. Department of Energy, Office of Basic Energy Sciences.

Finally, we would like to thank all other colleagues who contributed to the success of the project.

**Migration of actinides in natural clay: Interaction of neptunium and plutonium with
natural clay**

S. Amayri, J. Drebert, D. R. Fröhlich, U. Kaplan
J. V. Kratz, T. Reich, N. Stöbener, N. Trautmann, T. Wunderlich

Institut für Kernchemie, Universität Mainz

Final Report

Support Contract Number
02 E 10166

Institut für Kernchemie
Johannes Gutenberg-Universität Mainz
Fritz-Straßmann-Weg 2
55128 Mainz
Germany

Content

Abstract	4
1 Introduction	5
2 Materials and methods	7
2.1 Materials.....	7
2.2 Analytical techniques	10
3 Experimental	13
3.1 Sorption (batch experiments)	13
3.2 Diffusion.....	15
3.3 Speciation	18
3.3.1 XAS, μ -XAS, μ -XRF, and μ -XRD	18
3.3.2 CE-ICP-MS	20
3.3.3 CE-RIMS.....	20
4 Results and discussion.....	21
4.1 Batch experiments	21
4.1.1 Batch experiments with Np(V)	21
4.1.2 Sorption isotherms.....	21
4.1.3 Influence of pH and pCO ₂	24
4.1.4 Influence of humic acid (HA)	29
4.1.5 Influence of temperature	31
4.1.6 Influence of ionic strength and background electrolyte	35
4.1.7 Sorption isotherms of Th, U, Np, Pu, and Am in OPA pore water	37
4.2 Diffusion experiments	40
4.3 Speciation experiments	48
4.3.1 XAS, μ -XAS, μ -XRF, and μ -XRD	48
4.3.2 CE-ICP-MS	75
4.3.3 CE-RIMS.....	82
5 Summary	89
6 References	91
7 Acknowledgment	98

Abstract

The objective of this project was to investigate the transport and retardation processes of the actinides, mainly neptunium (Np) and plutonium (Pu), from a repository of spent nuclear fuels in an accidental scenario. The interaction of Np and Pu in their relevant oxidation states with natural Opalinus Clay (OPA) from Mont Terri, Switzerland has been studied in detail. Furthermore, experiments with thorium (Th), uranium (U), and americium (Am) were performed for comparison.

The sorption of NpO_2^+ , UO_2^{2+} , Pu^{3+} , Am^{3+} , Pu^{4+} , and Th^{4+} on OPA in pore water at pH 7.6 was investigated in batch experiments and distribution coefficients were determined. The results showed that the tri- and tetravalent actinides are strongly sorbed on OPA with K_d values higher than those of the hexa- and pentavalent actinides, which are weakly sorbed.

The sorption of Np(V) on OPA was studied as a function of pH, aerobic/anaerobic conditions, partial pressure of CO_2 , presence/absence of humic acid (HA), background electrolyte, ionic strength, and temperature. The results showed a strong influence of these parameters on Np(V) sorption.

Diffusion parameters for Np(V) were determined for the first time from diffusion experiments with intact OPA bore cores as a function of temperature and presence/absence of humic acid using OPA pore water as mobile phase.

The speciation of Np and Pu on the OPA mineral surface after sorption and diffusion processes was investigated by using different X-ray synchrotron radiation techniques (X-ray absorption spectroscopy (XAS), micro XAS (μ -XAS), micro X-ray fluorescence spectroscopy (μ -XRF), and micro X-ray diffraction (μ -XRD)). The results showed that Np(IV) and Pu(IV) are the most dominant species after sorption and diffusion processes. Furthermore, μ -XRD studies confirmed that iron-bearing mineral phases (pyrite and siderite) are the redox-active mineral phases of OPA which determine the speciation of Np and Pu after uptake on OPA.

CE-RIMS and CE-ICP-MS were successfully applied to detect the Np and Pu species at ultratrace concentrations close to environmental conditions.

The results of this study will be used as input parameters for performance assessment of a future repository for high-level nuclear waste to improve the thermodynamic databases for the uptake of actinides by clay rocks.

1 Introduction

The presence of plutonium (Pu) and minor actinides such as neptunium (Np) in nuclear waste is a major concern for the long-term safety of nuclear waste repositories because of their possible migration from the repository to the environment. The toxicity of the actinide elements and the long half-lives of their isotopes are the primary causes for concern [1].

Argillaceous rocks such as Opalinus Clay (OPA) are under consideration in several European countries, for example in Germany, Switzerland, France, and Belgium as potential host rock and as backfill material for a high-level nuclear waste repository [2 - 5].

The mobility of Np, Pu, and other actinides in aquifers is among several processes controlled by the diffusion in materials as well as the sorption on the surfaces. In the clay formations diffusion is considered to be the main transport mechanism for radionuclides released from a repository [6, 7]. For these reasons, a quantitative knowledge of radionuclide diffusion and sorption onto clay minerals is desirable. To predict the radionuclide mobility in the environment, it is also necessary to have fundamental knowledge about their interaction with rock pore water. Because high-level nuclear waste will significantly heat up the near field of the repository, it is also important to study the radionuclide migration at elevated temperatures.

In general, the lighter actinides have a wide variety of oxidation states from III-VII. Np can exist in aqueous solution in the oxidation states III - VII. The pentavalent cation, NpO_2^+ , dominates the aqueous speciation under a wide range of environmental conditions and has a low tendency for hydrolysis, precipitation, and sorption on natural minerals [8 - 10].

Pu exhibits a complicated redox chemistry, where four oxidation states (III - VI) can coexist in natural waters [11, 12]. The lower oxidation states III and IV are the most interesting species with respect to their migration in the environment. Pu^{3+} and Pu^{4+} are stabilized by acidic conditions and prevail as solids with low solubility, which leads to high sorption on mineral surfaces. Over a wide Eh/pH range Pu(IV) is predominant and due the possible formation of colloids, PuO_2 is considered to be one of the most important solids for Pu risk assessment [13].

Hydrolysis, solubility, colloid formation, complexation with inorganic (i.e., dissolved inorganic carbon in OPA pore water) or organic ligands (i.e., HA), and sorption on mineral surfaces are chemical processes that govern the migration behavior of actinides (especially Np and Pu) in the environment. Up to now the migration process of Np and Pu in the environment is not completely understood. Therefore, their chemical species in aqueous

systems determined by redox-reaction and complexation during uptake on clay mineral surfaces have to be considered.

In the framework of this project, “Interaction and transport of actinides in natural clay rocks, under consideration of humic substances and clay organic matter”, OPA from the Mont Terri Rock Laboratory, Switzerland, and the corresponding pore water (pH = 7.6, I = 0.4 [14]) have been selected as references to study the sorption of Np and Pu on natural clay. OPA is rather complex with respect to its mineralogical composition. It consists of 66 ± 11 wt% clay minerals (kaolinite, illite, illite/smectite mixed layers, and chlorite), 14 ± 4 wt% quartz, 13 ± 8 wt% calcite, 3 ± 1.8 wt% siderite, 1.1 ± 0.5 wt% pyrite, and 0.8 ± 0.5 wt% organic carbon [3]. Organic compounds, which can be released from OPA under certain conditions, such as fulvic and humic acids, can interact with the actinides released from the nuclear waste in an incident scenario and significantly affect the sorption and migration behavior of them due to their complexation and redox properties and their ability to form stable colloids.

In this project the basic interaction processes of NpO_2^+ , Pu^{3+} , Pu^{4+} , Pu^{6+} , and analogous actinides (i.e., UO_2^{2+} , Am^{3+} , Th^{4+}) in aqueous solutions with OPA were studied. The influence of HA on the sorption of Np and Pu onto OPA was also investigated.

Batch and diffusion experiments were completed by synchrotron based X-ray absorption spectroscopy to determine the structural parameters of Np and Pu sorbed on OPA.

Very sensitive methods such CE-ICP-MS or CE-RIMS were further developed and applied to study the behavior of Np and Pu under environmental conditions enabling the speciation of Np and Pu oxidation states in solution at ultratrace concentrations. CE-RIMS delivers a detection limit for Pu which is better by 2 to 3 orders of magnitude than the one obtained with the previously developed CE-ICP-MS (0.5 ppb for Pu).

2 Materials and methods

2.1 Materials

Opalinus Clay (OPA): In this work, various OPA batches from the Mont Terri Rock Laboratory, Switzerland, were used. Aerobic and anaerobic OPA samples, i.e., powders, thin sections or cylinders were prepared from OPA bore cores. An overview of the different OPA batches and their applications are summarized in Tab. 1.

Table 1: OPA (from Mont Terri) batches and their applications.

OPA bore core	Depth / m	Preparation	Type	Experiment
BHE 24/1	3.30 - 3.56	aerobic	powder	batch / XAS
BDR 2	7.31 - 7.60	anaerobic	powder	batch / XAS
BAE 25/10	6.27 - 6.45	aerobic	thin section, bore core	μ -XAS, diffusion
BHE 24/2	3.56 - 3.89	anaerobic	powder	batch / XAS
BLT 14	2.12 - 2.52	aerobic	bore core	batch / diffusion

Aerobic and anaerobic OPA powders were prepared in air and under Ar atmosphere from OPA bore cores (BHE 24/1) and (BDR 2 or BHE 24/2), respectively. The specific surface area of the aerobic powder measured by N₂ BET equals 41.3 ± 0.5 m²/g, the cation exchange capacity is equal to 10 ± 4 (meq/kg) [15]. The mineral composition and the content of the trace elements of the used aerobic OPA were measured by X-ray fluorescence analysis and published by Fröhlich et al. [16]. More information about the main physicochemical characteristics of Mont Terri OPA such as composition, microstructure, surface area, surface charge, etc. can also be found in [3]. All OPA powders and cylinders were prepared at the Karlsruhe Institute of Technology - Institute for Nuclear Waste Disposal (KIT-INE).

OPA pore water: The synthetic OPA pore water had a pH of 7.6 and an ionic strength of 0.4 M. It consisted mainly of NaCl with minor amounts of CaCl₂, MgCl₂, KCl, SrCl₂, Na₂SO₄, and NaHCO₃ [14]. The exact composition of the artificial pore water used in the batch and diffusion experiments is given in Tab. 2.

Table 2: Composition of the synthetic OPA pore water [14] used in the batch and diffusion experiments.

Salt	Concentration / g/L
NaCl	12.38
KCl	0.12
MgCl ₂ ·6H ₂ O	3.48
CaCl ₂ ·2H ₂ O	3.79
SrCl ₂ ·6H ₂ O	0.14
Na ₂ SO ₄	2.00
NaHCO ₃	0.04

Humic acids (HA): To study the influence of HA on the sorption and diffusion experiments, the synthetic HA type M42 (batch M145) [17] was used. Synthetic HA M42 has an elemental composition similar to natural HA. The carboxyl group content and proton exchange capacity (PEC) of M42 are 3.51 ± 0.07 meq/g and 3.76 ± 0.09 meq/g, respectively. Phenolic/acidic OH groups content is 2.0 ± 0.2 meq/g. The unmarked M42 HA (batch 145) was used in XAS investigations. Sorption and diffusion experiments were performed using ¹⁴C-labeled ([¹⁴C] M42 batch R2/06). ¹⁴C M42 has a specific activity of 5.8 ± 0.6 MBq/g, a proton exchange capacity of 3.11 ± 0.39 meq/g, and a carboxylic acid content of 2.90 ± 0.06 meq/g [18]. The humic acids M42 were provided by Helmholtz-Zentrum Dresden-Rossendorf - Institute of Radiochemistry.

Chemicals: All chemicals were at least analytical grade. Ultrapure deionized water (resistivity 18 MΩ, Synergy™ Millipore water system, Millipore GmbH, Schwalbach, Germany) was used to prepare the solutions. Experiments under anaerobic conditions (absence of CO₂) were carried out in an argon glove box (Unilab, MBraun, Garching, Germany) with < 10 ppm O₂ using boiled Millipore water for preparing all solutions. All background electrolytes (i.e., OPA pore water, 0.1 M NaClO₄, CaCl₂) and solutions (i.e., NaOH and HClO₄) were prepared by dissolution of the related p.a. chemicals from different commercial sources (Merck, Fluka, Alfa Aesar, Roth and Sigma-Aldrich) in Millipore water.

Stock solutions:

Humic acid: Stock solutions of M42 with 2 g/L were prepared for sorption and speciation experiments by weighting of 10 mg of HA, adding 0.4 mL of 0.1 M NaOH, and filling up with saturated CaCO₃ or OPA pore water to 5 mL.

Calcite solutions: For sorption experiments with Np under different partial pressures of CO₂ (ambient pCO₂ = 10^{-3.5} and pCO₂ = 10^{-2.3} atm), solutions saturated with respect to CaCO₃ (Merck, Germany) at different pH were prepared under aerobic conditions and in a glove box (Unilab, MBraun, Garching, Germany) filled with a gas mixture of 99.5% Ar and 0.5% CO₂ (Westfalen AG, Germany). In a first step, the pH of aliquots of Millipore water was adjusted by adding appropriate amounts of HClO₄ and NaOH. To the samples of pH > 8.5 under aerobic and pH > 7.5 under anaerobic conditions, specified amounts of NaHCO₃ and Na₂CO₃ calculated with MINTEQ V.2.52 [19] were added to accelerate the equilibration adjustment with the surrounding atmosphere. Then, CaCO₃ was added to all solutions until saturation was reached to ensure calcite equilibrium. All solutions were stirred in open polyethylene (PE) tubes up to two weeks until equilibrium indicated by a constant pH was reached. The tubes were sealed and stored until utilization. In the batch experiments, only the supernatant solution after centrifugation for 10 min at 4.030 g (3K30, Sigma, Germany) was used.

Thorium: A 5×10^{-6} M ²³²Th stock solution was obtained from solid Th(NO₃)₄·5H₂O (p.a., Merck) which was dissolved in 0.1 M HCl to avoid any precipitation of Th by hydrolysis. ²²⁸Th (T_{1/2} = 1.912 a) was added as tracer (2.5×10^{-11} M) to the solution.

Uranium: The ²³⁸U stock solution was obtained by dissolving solid UO₂(NO₃)₂·6H₂O (p.a., Merck) in 0.1 M HNO₃. The concentration of the stock solution was 1.0×10^{-1} M.

Neptunium: The procedures for preparing the stock solutions of ²³⁷Np(V) and ²³⁹Np(V) were the same as described in detail elsewhere [16]. The oxidation state of ²³⁷Np stock solution was verified by UV-vis absorption spectroscopy with the characteristic absorption band of Np(V) at 980.4 nm. The concentrations of ²³⁷Np and ²³⁹Np were determined by γ -ray spectroscopy. The resulting stock solutions had a pH value of about 1.5 and a concentration of 1×10^{-2} M ²³⁷Np(V) and 8×10^{-9} M ²³⁹Np(V). For the sorption experiments, the pH of the Np stock solutions was adjusted to 3 - 4 using 5 M NaOH.

Plutonium: For the experiments carried out with ^{239}Pu , a $3 \times 10^{-3} \text{ M } ^{239}\text{Pu}$ stock solution in 9 M HCl was used. The Pu solution was evaporated to dryness and the residue was dissolved in 10 M HCl (with some drops of conc. HNO_3 to oxidize to Pu(VI)). The ^{239}Pu solution was purified from its decay products including ^{241}Am using anion exchange chromatography at 55 °C (150 mm \times 4 mm glass column filled with Dowex AG 1-X8 from Bio-Rad Laboratories, Hercules, USA). After a washing step with 8 M HCl, Pu was eluted with 0.5 M HCl. The eluate was evaporated to dryness, fumed three times with 1 M HClO_4 , and dissolved in 1 M HClO_4 . A well characterized $^{239}\text{Pu(VI)}$ stock solution (1.8 mL) was obtained with this purification procedure. The trivalent, tetravalent, and pentavalent oxidation states of Pu were obtained from the purified Pu(VI) stock solution by potentiostatic electrolysis. The oxidation state purity was verified by UV-vis spectroscopy at the characteristic absorption bands at 600 nm for Pu(III), 470 nm for Pu(IV), 568 nm for Pu(V), and 830 nm for Pu(VI) [20, 21].

The concentration of the ^{239}Pu stock solutions was determined by liquid scintillation counting (LSC). The resulting stock solutions had a concentration of $6 \times 10^{-4} \text{ M Pu(III)}$, $6 \times 10^{-4} \text{ M Pu(IV)}$, $5 \times 10^{-4} \text{ M Pu(V)}$, and $3 \times 10^{-3} \text{ M Pu(VI)}$. The same purification procedure was applied to obtain $1 \times 10^{-3} \text{ M } ^{242}\text{Pu(VI)}$ stock solution, which was used for the preparation of OPA thin sections and diffusion samples for $\mu\text{-XAS}$, -XRF , and -XRD investigations.

Americium: A $2.5 \times 10^{-5} \text{ M}$ stock solution of ^{241}Am in 0.005 M HCl was prepared by diluting a concentrated ^{241}Am solution ($5 \times 10^{-3} \text{ M}$ in 1 M HCl) with Millipore water. The purity of the resulting ^{241}Am stock solution was checked by α - and γ -ray spectroscopy.

2.2 Analytical techniques

α -spectroscopy: The concentrations of ^{239}Pu , ^{242}Pu , and ^{237}Np in solutions were determined by α -spectroscopy. A silicon surface barrier detector (ORTEC, USA) with an active area of 450 mm² and a detector resolution of < 25 keV at 5.5 MeV was used. The detector efficiency was about 14%. It was controlled regularly by measuring a standard ^{241}Am source. Special sample preparation was required. Therefore, a small volume \sim (10 - 20) μL of the sample was deposited on a titanium or tantalum foil and evaporated to dryness. Counting times up to 24 h were chosen.

γ -ray spectroscopy: Concentrations and purity of ^{237}Np , ^{239}Np , ^{241}Am , and ^{22}Na solutions were determined by γ -ray spectroscopy using the γ -lines at 29.4 and 86.5 keV for ^{237}Np , 103.4

and 106.1 keV for ^{239}Np , 59.5 keV for ^{241}Am , and 1274.5 keV for ^{22}Na . All measurements were accomplished on a spectroscopic system consisting of a HPGe (GMX-13180-S, EG and G ORTEC, USA) coaxial γ -ray detector, Canberra Inspector 2000 (model IN2K, Canberra Industries, Inc., USA) analyzer, and a PC equipped with Genie 2000 gamma acquisition and analysis software (V. 3.0, Apr 05, 2004; Canberra Industries, Inc., USA). The mixed radionuclide γ -ray standard reference solution QCY48 (Solution number: R6/50/38, Amersham, AET Technology QSA GmbH, Germany) was used for calibration of the spectroscopic system. All samples were counted until an error level of about 3% was achieved at a confidence level of 2σ . In the case of ^{237}Np , the results were also confirmed by liquid scintillation counting

UV-vis spectroscopy: The purity of the oxidation states of ^{237}Np and ^{239}Pu was verified by UV-vis absorption spectroscopy using a high-resolution UV-vis spectrometer (Cary 50 Bio, Varian, USA (for Np) and Tidas 100, J&M Analytik AG, Germany (for Pu)). The samples were measured in 1.5 mL polymethylmethacrylat semi-microcuvettes (Brand GmbH, Wertheim, Germany).

Liquid scintillation counting (LSC): $^{232}\text{Th}/^{228}\text{Th}$, ^{237}Np , ^{239}Pu concentrations were determined using LSC (home built scintillation counter) by measuring 1 mL sample in 10 mL scintillation cocktail Ultima Gold™ AB (for sorption experiments) or Ultima GOLD XR (for diffusion experiments) (PerkinElmer LAS GmbH, Rodgau-Jügesheim, Germany). The samples were counted until a 2σ error of 2% was attained. The activities of HTO and $^{22}\text{Na}^+$ were measured using a Beckman LS6800 liquid scintillation counter (Beckman Coulter, USA).

Inductively coupled plasma - mass spectrometry (ICP-MS): ^{238}U and ^{232}Th concentrations in the samples were determined by ICP-MS measurements using an Agilent 7500ce unit (Agilent Technologies, Waldbronn, Germany).

Capillary electrophoresis (CE): CE was coupled online to ICP-MS to separate the different oxidation states of Pu and Np in various solutions. The coupling of the homemade CE to the ICP-MS was performed as described in [22, 23]. Standard LSC vials (20 mL), or for small sample volumes, 300 μL PE vials were used for the buffer and sample solutions. For hydrodynamic sample injection, 60 – 100 mbar was applied for 4 – 10 s. A fused-silica

capillary with an inner diameter of 50 μm (PolyMicro Technologies, Phoenix, AZ) and 60 – 80 cm length was used. Before use, the capillary was purged for 5 min at 1 bar with 0.1 M HCl, 0.1 M NaOH, and for 10 min at 1 bar with Milli-Q deionized water and the electrolyte solution (1 M acetic acid at $\text{pH} \approx 2.4$). Using a MiraMist CE nebulizer (Burgener Research Inc., Mississauga, Canada), a detection limit of 0.5 ppb for Pu [23] and Np has been obtained.

Resonance ionization mass spectrometry (RIMS): For the speciation of Pu and Np at ultratrace level, an experimental setup of offline coupling CE and RIMS was developed and optimized [23 - 26]. The RIMS setup consisted of a high repetition rate solid-state laser system (three titanium-sapphire lasers pumped by a pulsed Nd:YAG laser (Clark-MXR ORC-1000 or DM-60, Photonics Industries, Bohemia, NY, USA)) and a reflectron time-of-flight (TOF) mass spectrometer. The high selectivity and sensitivity of the CE-RIMS allowed the determination of the oxidation as well as the isotope ratios of Pu at ultratrace level, e.g., under environmental conditions. The limit of detection of RIMS is about 10^6 atoms for Pu [24, 25] and about 10^7 atoms for Np [26]. Compared to CE-ICP-MS this method should yield an improvement in the detection of at least two orders of magnitude.

pH and Eh measurements: The pH of solutions was measured using a pH meter inoLab or Cond pH 720 (WTW GmbH, Weilheim, Germany) equipped with a pH electrode (blue line 16 pH, Schott, Mainz, Germany) and a temperature sensor (TFK 150, WTW, Weilheim, Germany). The pH meters were calibrated with certified commercial (DIN) buffers (pH 4.01, 6.87, and 9.18 from Schott, Mainz, Germany). The redox electrode (blue line 31 RX, reference system: Ag/AgCl, Schott, Germany) was used for Eh measurements. It was checked with a standard solution of known redox potential (240 mV, HI 7021 ORP solution, HANNA instruments, USA).

Liquid-liquid extraction: Chemical extraction was applied in combination with LSC to determine the redox behavior of Np in aqueous solutions after sorption experiments. As extracting agents, a solution of 0.5 M di(2-ethylhexyl) phosphoric acid (HDEHP) (Merck) diluted in toluene was used. A 0.5 mL portion of the supernatant was shaken together with 2 mL 1 M HCl and 2.5 mL 0.5 M HDEHP (in toluene) solutions for 5 min. The phases were separated by centrifugation at 4.030 g and 2 mL of each phase were analysed by γ -ray spectroscopy (Np(V) in H_2O , and Np(IV) in organic solution). The oxidation state of Np

sorbed on OPA was investigated analogously by shaking the dried clay powder with 2.5 mL 1 M HCl and 2.5 mL of HDEHP solution for 5 minutes.

3 Experimental

3.1 Sorption (batch experiments)

The sorption behavior of the actinides Th, U, Np, Pu, and Am on OPA (Mont Terri) was investigated by batch experiments. The effects of different parameters such as pH, solid-to-liquid ratio (S/L), nuclide concentration, aerobic/anaerobic conditions, partial pressure of CO₂ (p(CO₂), background electrolyte, ionic strength, temperature, and presence/absence HA were investigated. An overview of the performed batch experiments is presented in Tab. 3.

Table 3: Overview of the performed batch experiments.

Actinide	Investigated parameters
Th(IV)	pH, S/L ratio, background electrolyte
U(IV)	concentration
Np(V)	pH, S/L ratio, concentration, aerobic/anaerobic cond., p(CO ₂), background electrolyte, ionic strength, temperature, presence/absence HA
Pu(III)	S/L ratio
Pu(IV)	pH, S/L ratio, background electrolyte
Pu(VI)	pH, S/L ratio, background electrolyte, temperature, , presence/absence HA
Am(III)	S/L ratio

In most batch experiments, suspensions of well characterized aerobic and anaerobic dry powders of OPA (typically 2 - 20 g/L for amount isotherms, 15 g/L for concentration isotherms and other experiments) were prepared in synthetic pore water at pH 7.6, 0.1 M NaClO₄ or saturated CaCO₃ solution (only for experiments with Np(V)) in closed 10 mL polycarbonate (Np batch experiments) or 50 mL polyallomer (Pu batch experiments) centrifuge tubes (Beckman Coulter, USA) at room temperature under aerobic and anaerobic conditions. Experiments under anaerobic conditions were performed in the absence of CO₂ in

a glove box (Unilab, MBraun, Garching, Germany) filled with high purity Ar gas (> 99.99%) in order to avoid oxidation processes, i.e. Pu(III) to Pu(IV).

Some Np(V) sorption experiments were also done under anaerobic conditions at high partial pressure of CO₂ (10^{-2.3} atm). The samples were sealed and preconditioned by shaking in an end-over-end rotator (SB 3, Stuart Scientific, UK) for 72 h. After that aliquots of the stock nuclide solution of ²³²Th/²²⁸Th (²²⁸Th was added as a tracer), ²³⁸U, ²³⁷Np/²³⁹Np (²³⁹Np was used as tracer in the concentration isotherm experiment, and in pH dependence experiments at 7 × 10⁻¹² M concentration), ²³⁹Pu, and ²⁴¹Am were added individually to the samples and the pH was adjusted immediately with HClO₄ and NaOH solutions of different concentrations to the desired value (Δ pH = ± 0.05). The total concentrations of actinides were about 8 × 10⁻⁹ M ²³²Th(IV), 2 × 10⁻⁴ - 1 × 10⁻⁷ M ²³⁸U(VI), 5 × 10⁻⁵ - 1 × 10⁻¹¹ M ²³⁷Np(V)/²³⁹Np (for concentration isotherm), 8 × 10⁻⁶ M ²³⁷Np(V) (for amount isotherm, and other experiments), 7 × 10⁻¹² M ²³⁹Np(V), 1 × 10⁻⁷ M ²³⁹Pu(III), 9 × 10⁻⁸ M ²³⁹Pu(IV), 1 × 10⁻⁷ M ²³⁹Pu(VI) and 9 × 10⁻⁹ M ²⁴¹Am. The concentration of 8 × 10⁻⁶ M Np in 0.1 M NaClO₄ is below the solubility of any solid phase, e.g., NaNpO₂CO₃(s) [27]. Then, the samples were shaken for at least 60 h. During this time, the pH of the solutions was checked twice and was readjusted if necessary. Afterwards the solid and liquid phases were separated by centrifugation at 108.800 g for one hour in a centrifuge Avanti J-30I (Beckman Coulter, USA). The actinides uptake was determined by γ-ray spectroscopy, LSC or ICP-MS of the supernatants.

Temperature dependent investigations up to 80 °C were carried out using the same procedure, except that the samples were placed on a heatable multipoint magnetic stirrer (IKA RT 10 power IKAMAG, IKA, Staufen, Germany) equipped with a massive aluminum block with boreholes for the samples. The block was heated to the desired temperature with a fluctuation of less than ± 3 °C. The samples were stirred with stirring bars of 5 mm length (VWR, Germany). Blank samples were run along with all batch experiments. The loss of Np and Pu to the walls of the centrifuge tubes was found to be negligible (≈ 1 - 2% of the initial Np conc. and max. 5% of the Pu conc.). The oxidation state of Np after the sorption experiments under anaerobic conditions was checked via liquid-liquid extraction using HDEHP (Merck, Germany) as extracting agent.

For the LSC measurements of ²²⁸Th, the supernatants were stored for more than 3 months until the decay products of ²²⁸Th were in equilibrium.

During the sorption experiments with Np and Pu, the Eh under aerobic conditions was approximately equal to + 350 ± 25 mV (SHE). In the case of anaerobic conditions, the Eh was equal to - 60 ± 25 mV and - 120 ± 25 mV (SHE) for Np and Pu(III), respectively.

The percentage of the actinide sorbed was calculated by using the following equation:

$$\text{Sorption\%} = \left(1 - \frac{[\text{An}]_{\text{eq}}}{[\text{An}]_0}\right) \times 100\% \quad (1)$$

A convenient representation of sorption data is the sorption coefficient, K_d , which is defined by the following equations:

$$K_d = \frac{V}{m} \times \left(\frac{[\text{An}]_0 - [\text{An}]_{\text{eq}}}{[\text{An}]_{\text{eq}}}\right) \quad (2)$$

or

$$K = \frac{x}{[\text{An}]_{\text{eq}}^n} \quad (3)$$

where $[\text{An}]_{\text{eq}}$ and $[\text{An}]_0$ (mol/L) are the equilibrium and initial concentrations of the sorbate in solution, respectively; V is the volume of experimental solution in m^3 ; x (mol) is the amount of sorbate; m is the mass of sorbent (kg), and n is a constant. For $n = 1$, K equals the distribution coefficient K_d (m^3/kg).

3.2 Diffusion

For the diffusion experiments, a cylinder of about 25 mm diameter and 11 mm height was cut out from the aerobic OPA bore cores (BAE 25/10 or BLT 14). The orientation of the cylinder in the diffusion cell was so that the direction of transport (diffusion) was perpendicular to the bedding. The density of the intact and dry OPA samples was between 2402 und 2429 kg/m^3 . All diffusion experiments were carried out in artificial pore water ($\text{pH} = 7.6$) as mobile phase under aerobic conditions in presence/absence of HA (M42) at room temperature (20 ± 2 °C) [28] and 60 ± 2 °C. For the diffusion experiments, 0.003 M NaN_3 was added to the pore water to avoid bacterial growth. The diffusion setup and the experimental procedures were the same as those used for the through-diffusion experiments by Van Loon et al. [29]. A schematic drawing and a photograph of the experimental setup of the diffusion experiment are shown in Fig. 1. The set up comprises a diffusion cell (stainless steel, RM-Stahlhandel GmbH, Flörsheim am Main, Germany), an 8-channel peristaltic pump (Ismatec, Ecoline VC-MS/CA8-6, IDEX Health & Science GmbH, Wertheim-Mondfeld, Germany), a 250 mL container and a 25 mL container (Schott Duran, Mainz, Germany). The OPA sample was sandwiched between two stainless steel filter plates (stainless steel: 316 L, pore diameter: 10 μm , diameter: 25.4 mm, thickness: 1.57 mm, Ligacon AG, Switzerland) and mounted in a

diffusion cell. The large container was filled with 210 mL artificial OPA pore water and the small one with 20 mL. The sample was saturated by circulating the OPA pore water solutions against both ends of the sample for at least 5 weeks. Subsequently, the solutions were replaced by fresh ones and the solution in the large container was spiked with the desired tracer. The radiotracers studied in this work were: HTO, $^{22}\text{Na}^+$, $^{237}\text{Np(V)}$, $^{237}\text{Np(V)}$ -HA M42, and $^{242}\text{Pu(VI)}$ (used only for spectroscopic investigations).

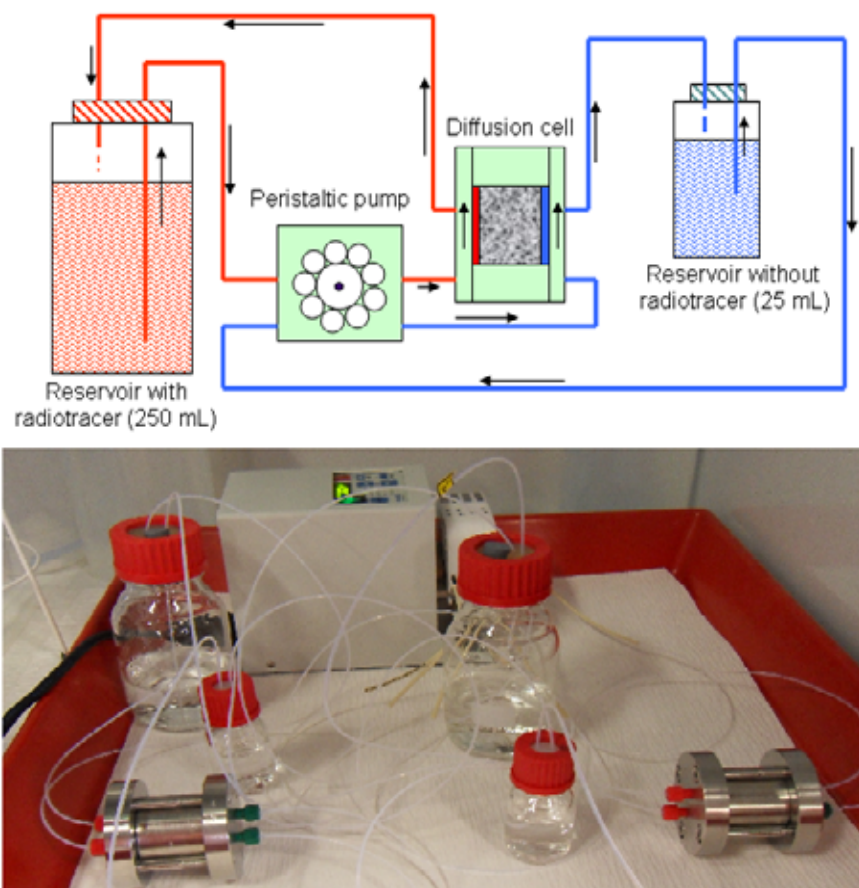


Figure 1: Schematic drawing (adapted from [29]) and a photograph of the experimental setup of the diffusion experiment.

Table 4: Overview of the tracers used and their activities.

Cell Nr.	OPA	ρ (kg/m ³)	Temp. (°C)	[HTO] (MBq/L)	[²² Na] (MBq/L)	[²³⁷ Np(V)] (MBq/L)	[HA] (MBq/L)
1 [28]	BAE 25/10	2420	20	1.23	1.00	0.05	-
2	BLT 14	2412	20	1.30	5.10	0.05	-
3	BLT 14	2429	20	1.30	5.10	0.05	0.06
4	BLT 14	2402	60	1.30	5.10	0.05	-

After the completion of HTO or ²²Na⁺ through-diffusion experiments, the solutions in both containers were replaced by artificial pore water without tracer and out-diffusion was started. At given time intervals, the activity in the solutions was measured, and the solutions were replaced by fresh ones. The activities of HTO and ²²Na⁺ in the samples were measured by LSC. This procedure was repeated until all the activity in the OPA sample had diffused out. Once this had been achieved, a new radiotracer, in particular ²³⁷Np, ²³⁷Np-HA (M42), and ²⁴²Pu(VI) was added to the large container and diffusion of the new tracer was started. In case of experiments with HA, HA was added simultaneously with Np to the reservoir. The high-concentration reservoir was filled with 210 mL of artificial pore water and spiked with 50×10^6 Bq/m³ Np (see Tab. 4). The diffusion time was in all cases up to 35 days. During this time, the Eh in the high-concentration reservoir was controlled (SHE \approx + 350 mV) and no significant changes were observed. In order to check the evolution of the concentration of ²³⁷Np(V) as a function of diffusion time in the high concentration reservoir, 0.5 mL of solution were withdrawn regularly from this reservoir and measured by γ -ray spectroscopy. After this time, the high concentration reservoir was exchanged by a smaller one (20 mL) containing artificial pore water with $1 - 5 \times 10^9$ Bq/m³ ²²Na⁺ and the same concentration of ²³⁷Np(V) as in the replaced high-concentration reservoir. The diffusion experiment was terminated about one day after adding ²²Na⁺ to the reservoir. The OPA sample was then removed from the diffusion cell and mounted on a sample holder for abrasive peeling with P220 abrasive paper (MATADOR Silicon Carbide Paper, waterproof P220 Article-No. 971 C, Starck GmbH & Co. KG, Germany). The abrasive peeling technique has been described elsewhere [30]. The activities of ²³⁷Np and ²²Na in the peeled OPA layers were measured by γ -ray spectroscopy.

For diffusion experiments at 60 °C, the diffusion cell was heated in an incubator (INE-200 heating incubator, Memmert GmbH, Germany) with a temperature fluctuation of less than ± 2 °C. The experimental data processing of through-, out-, and in-diffusion experiments of

HTO, ^{22}Na , and ^{237}Np was performed with a home made computer code and has been described in detail elsewhere [7, 28].

3.3 Speciation

3.3.1 XAS, μ -XAS, μ -XRF, and μ -XRD

For synchrotron based X-ray absorption spectroscopy (XAS) measurements, the sorption samples were centrifuged after a contact time of at least 60 h and the solid and liquid phases were separated by centrifugation at 108,000 g for 1 h. Np wet paste samples were prepared under air and Ar atmosphere. The samples were put in Perspex sample holders with Kapton windows. For measurements of Np and Pu at about 15 K, the solid residues were dried for 3 days either under aerobic or Ar atmosphere. Then all powders were grinded and loaded into special PE XAS sample holders (SH-01c) and heat sealed. Anaerobic XAS samples were prepared in a glove box (Ar box > 99.99%). The transport of anaerobic samples was performed in an anaerobic transport container (Anaerobic jar, Schuett-biotec GmbH, Göttingen, Germany), which was purged with argon, or in a special dewar filled with liquid nitrogen (Voyageur 12, AIR LIQUIDE Deutschland GmbH, Germany), where the samples were shock frozen until measurement.

Both Np and Pu L_{III} -edge absorption spectra (Np: 17630 eV, Pu: 18070 eV) were collected in fluorescence mode at the Rossendorf beamline ROBL [31] at the European Synchrotron Radiation Facility (ESRF) in France using a 13-element Ge solid-state detector. A Si(111) double-crystal monochromator was used for tuning the energy of the incident X-ray beam. Yttrium foil was used for calibrating the X-ray energy. The EXAFS analysis was performed with the software packages Athena [32] and EXAFSPAK [33]. Backscattering phase and amplitude functions required for data fitting were calculated with FEFF 8.20 [34] using crystal structures of $(\text{UO}_2)_2\text{SiO}_4 \cdot 2\text{H}_2\text{O}$ [35], $\text{K}_3\text{NpO}_2(\text{CO}_3)_2 \cdot 0,5 \text{H}_2\text{O}$ [36], NpO_2 [37], $\text{Eu}_{1,3}\text{Fe}_{0,7}\text{O}_{6,3}\text{Ti}_{2,0}$ [38]. For modeling possible interactions of Np or Pu with Si, Fe, etc., U or Eu were replaced in the crystal structures by Np or Pu. The shift in threshold energy, ΔE_0 , was allowed to vary as a global parameter in the fits.

μ -XAS, μ -XRF, and μ -XRD measurements were performed at the MicroXAS beamline at the Swiss Light Source, Paul Scherrer Institut (PSI), Switzerland [39]. For these investigations, several OPA samples were prepared by contacting with $^{237}\text{Np}(\text{V})$ or $^{242}\text{Pu}(\text{VI})$ solutions (at about pH = 7.6). Three kinds of samples were prepared: (i) Np or Pu solutions were deposited directly by pipetting on the OPA thin sections. The solution was given time to evaporate

completely before the procedure was repeated until the whole amount of solution was placed on the thin section, (ii) Np or Pu was sorbed on OPA thin sections using a sorption cell (homemade) with a contact time of at least three days, (iii) small pieces of OPA were taken from an in-diffusion experiment with Np(V) or Pu(VI), which lasted for more than one month. Np and Pu loadings in all OPA thin sections were between 96 and 1389 ng/mm². Thin sections were prepared on glass slides from OPA batches (BAE 25/10 for aerobic samples and BLT 14 for anaerobic and diffusion samples). The preparation of these samples was performed at the Max-Planck-Institut für Chemie in Mainz. The thickness of the clay was approximately 20 to 30 μm, the contacted area was always smaller than 1 cm².

μ-XRF and μ-XAS measurements of all samples were performed using a Kirkpatrick-Baez mirror microfocusing system and a double-crystal monochromator with three different crystal pairs (Si (111), Si (311) and Ge (111)). In this experiment, a pair of Si(111) crystals was used. The ring current during the measurement was about 400 mA. X-ray fluorescence was measured using a Ketek single-element Si-detector. μ-XRF mappings of elements of interest (i.e. Ca, Fe, Sr, As, Np, Pu) were collected at an excitation energy above the Np or Pu L_{III}-edge. Overview maps were taken at a step size of 20 - 10 μm, fine mappings were performed in 5 - 1 μm steps. All measurements were done with a beam size (h × w) of ≈ 1 - 2 × 2 - 4 μm². A Zr foil (17998 eV) was used for energy calibration. As Np has a similar fluorescence energy (E(L_α) = 13950 eV) compared to Sr (E(K_α) = 14160 eV), which is present at amounts of ≈ 235 ppm in OPA [16], potential hot spots of Np were remapped at an excitation energy of 17550 eV to exclude Sr interferences. XRF maps were analyzed using a PSI intern MATLAB code. Np and Pu hot spots were studied by Np or Pu L_{III}-edge μ-XANES in fluorescence mode. Deadtime corrections for the measured XANES spectra were performed using an in-house java applet code. Background and energy correction of the spectra were performed with the software package Athena [32].

The XANES spectra were analyzed using a software package for ITFA [40] and reference spectra of Np(IV) and Np(V). ITFA allows to determine the relative amount of different Np oxidation states in the sample from XANES spectrum.

The μ-XRD measurements were performed using the above mentioned beam size and a Pilatus 100K detector. Experimental parameters such as sample-detector distance, detector plane orientation, etc., were refined by measuring different reference powders or foils (i.e., Al₂O₃, SiO₂, Si-Zr). The analysis of the diffraction patterns was performed with the program Area Diffraction Machine [41].

Element maps of two thin sections were obtained with the Jeol JXA 8200 electron microprobe of the Max-Planck-Institut für Chemie, Mainz, Germany, which is equipped with one energy dispersive (EDX) and five wave length dispersive detectors (WDX). An acceleration voltage of 15 kV, a beam current of 30 nA, and a dwell time of 0.2 s were used. In order to get an overview, the entire sample was mapped with a beam diameter of 15 μm and a step size of 20 μm . Mg, Al, Ca, Si, and Fe were measured with WDX spectrometers, Ti with an EDX spectrometer and, in addition, the BSE (back-scattered electrons) image was recorded.

Areas of particular interest were mapped with a beam diameter of 2 μm and step sizes of 2.5 or 1.5 μm . Al, Na, Ca, Si, and Fe were measured with WDX spectrometers, Ti, Mg, K with an EDS spectrometer and, in addition, the BSE image was recorded.

3.3.2 CE-ICP-MS

The redox behavior of individual Pu oxidation states (i.e. Pu(III) and Pu(IV)) in OPA pore water (pH = 7.6), HNO₃ (pH = 0.9), and NaClO₄ (pH = 7.6) was investigated under aerobic and anaerobic conditions using CE-ICP-MS. In all experiments Pu(III) and Pu(IV) were freshly prepared from a Pu(VI) stock solution by potentiostatic electrolysis and checked by UV-vis spectroscopy. Then, a defined amount of Pu(III) or Pu(IV) from the stock solution was added to the corresponding solutions. The pH/Eh values were measured directly after addition and checked again after 5 - 7 days. The Pu concentration in all samples was about 30 - 50 ppb or $\sim 1 - 2 \times 10^{-7}$ mol/L. The speciation of Pu was analyzed by CE-ICP-MS after 60 min, 80 min, and 7 days.

3.3.3 CE-RIMS

The principle of the off-line coupling CE to ICP-MS is based on collecting fractions of the different oxidation states of Pu eluted from the capillary at different retention times. From each fraction, a separate filament is prepared and studied by RIMS on its Pu content. In a first validation of the method, it was possible to determine successfully the oxidation state composition of a known Pu mixture (6×10^9 atoms) [42]. In this work, the development and optimization of CE coupled to RIMS for the speciation of Pu at ultratrace level was performed and successfully applied to sorption samples from batch experiments of Pu(III) and Pu(IV) on OPA. The memory effect of Pu(IV) sorbed on the capillary inner surface was also shown by this method. The Pu detection limit by CE-RIMS was about 10^6 atoms [23]. For the detection of ultratrace

amounts of Np by RIMS, extensive spectroscopic investigations have been carried out. Five excitation/ionization schemes involving autoionizing states for efficient and selective resonant excitation and ionization were identified, which can be used for RIMS measurements of Np. An overall efficiency of 0.3% was determined with a synthetic sample of a known number of ^{237}Np atoms [26].

4 Results and discussion

4.1 Batch experiments

4.1.1 Batch experiments with Np(V) [16]

The sorption behavior of Np(V) on OPA was investigated in batch experiments by varying different parameter such as pH (6 - 10), Np(V) concentration (10^{-12} - 10^{-4} M), solid to-liquid ratio ($S/L = 2 - 20$ g/L), partial pressure of CO_2 ($10^{-3.5}$ and $10^{-2.3}$ atm), temperature (20 - 80 °C) in the absence and presence of HA under aerobic and anaerobic conditions in saturated calcite solution and using synthetic OPA pore water (pH 7.6, $I = 0.4$ M), NaClO_4 , NaCl , CaCl_2 , and MgCl_2 as background electrolytes. All batch experiments were carried out with well characterized aerobic (BHE 24/1) and anaerobic (BDR 2) dry powders of OPA (see also Tab. 1).

4.1.2 Sorption isotherms

The sorption isotherms were measured with saturated calcite solutions as background electrolyte to avoid partial dissolution of the calcite contained in OPA. Following the procedure described above (Sect. 3.1), two sorption isotherms under aerobic conditions using aerobic OPA powder (BHE 24/1) were measured at pH 8.2 by varying the S/L ratio between 2 - 20 g/L (at $[\text{Np(V)}] = 8 \times 10^{-6}$ M) and the Np(V) concentration between 10^{-12} and 10^{-4} M using ^{237}Np and ^{239}Np as tracer (at S/L ratio = 15 g/L), respectively. At picomolar concentration, only ^{239}Np was used. The percentage of sorbed Np(V) and the distribution coefficient (K_d) were calculated by using eqs. 1 and 2. Table 5 shows the distribution coefficient K_d (m^3/kg) for the sorption of 8×10^{-6} M Np(V) on aerobic OPA in saturated calcite at pH 8.2 under aerobic conditions as a function of the S/L ratio.

Table 5: K_d values for the sorption of 8×10^{-6} M Np(V) on OPA (BHE 24/1) as a function of the S/L ratio at pH = 8.2 under calcite saturation and aerobic conditions.

S/L / g/L	K_d / m ³ /kg
2	0.141 ± 0.029
4	0.120 ± 0.017
6	0.135 ± 0.012
8	0.120 ± 0.011
10	0.123 ± 0.008
15	0.120 ± 0.008
20	0.123 ± 0.008

As shown in Tab. 5, the K_d is not influenced by the S/L ratio under these experimental conditions; the mean value of K_d equals 0.126 ± 0.013 m³/kg. A constant K_d for this Np(V) concentration and range of S/L ratio was reported also for the sorption of Np(V) on other minerals [43, 44].

In the second batch series, the sorption of Np on OPA was measured at pH 8.2 under aerobic conditions by varying the Np(V) concentration between 10^{-12} and 10^{-4} M and using ²³⁹Np as tracer. The S/L ratio of this series was 15 g/L corresponding to $\approx 65\%$ sorption. The result is shown in Fig. 2, where the data of Tab. 5 are included as well.

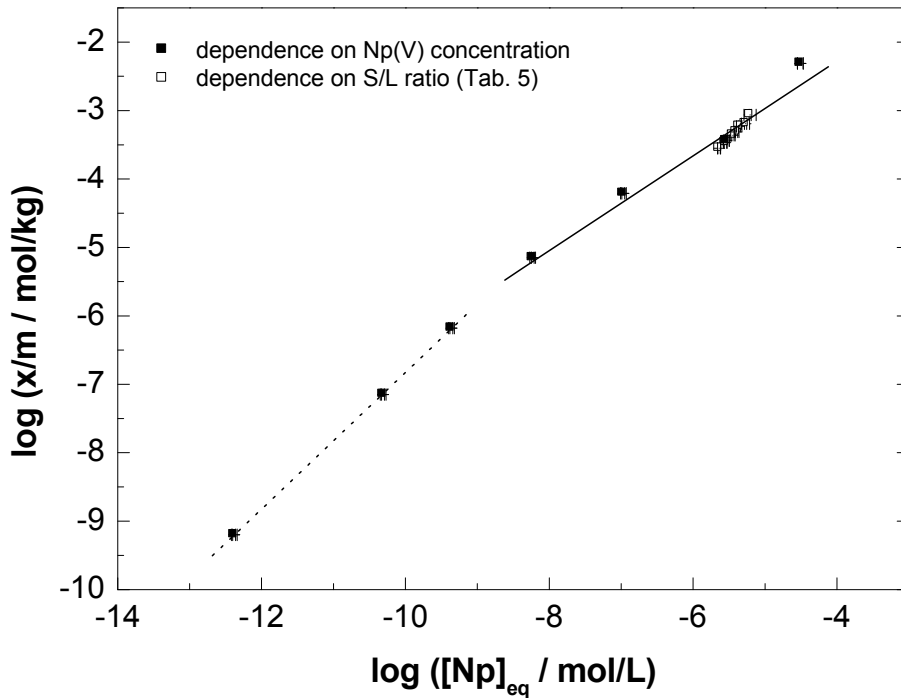


Figure 2: Sorption of Np(V) on OPA (BHE 24/1) as a function of Np(V) concentration and S/L ratio at pH = 8.2 under calcite saturation and aerobic conditions. For all points the error bars (calculated from the 1σ error of the measured activity) are smaller than the symbols (smaller than 0.1 log units).

The sorption isotherm (Fig. 2) can be described by the Freundlich type formalism given by eq. 3 [45]. The isotherm in Fig. 2 can be divided into two parts. The linear part below 10^{-8} M provides a slope of 1.00 ± 0.01 (dotted line). In this concentration range, sorption remains constant with a related K_d value of 1.445 ± 0.033 m³/kg. The data between 10^{-8} and 10^{-4} mol/L show a slope of 0.69 ± 0.04 (solid line), reflecting a non-linear sorption behavior of Np(V) on OPA. The decrease in the relative amount of Np sorbed with increasing Np concentration may be explained by different affinities of the sorption sites for Np(V) due to different sorption characteristics of the various minerals contained in OPA. Apparently enough sorption sites with a high affinity are available at concentrations below 10^{-9} M Np(V) and the system is far away from site saturation. At higher Np concentrations, the high affinity sites are already occupied and low-affinity sites are accessed resulting in a weaker sorption of Np(V).

A similar isotherm measurement at a lower pH of 7.6 in synthetic OPA pore water did not show such a behavior [46]. In this case, sorption of 10^{-5} - 10^{-11} M Np(V) on OPA was lower by up to two orders of magnitude. On one hand, lower sorption can be explained by the lower pH value as Np(V) sorption decreases with decreasing pH (see next Sect.). On the other hand, the Ca^{2+} concentration in OPA pore water (see Tab. 2) exceeds the corresponding concentration in saturated calcite solution at pH = 8.2 by two orders of magnitude (as calculated with Visual MINTEQ V. 2.52 [19]). The ionic strength of pore water is ≈ 0.4 M compared to < 0.01 M in saturated calcite solution. Probably, the deviations in pH, electrolyte composition, and ionic strength are the reasons for the different sorption behaviors.

4.1.3 Influence of pH and pCO_2

Neptunium

For sorption experiments at different pH (pH 6 - 10) and pCO_2 ($10^{-3.5}$ and $10^{-2.3}$ atm), saturated calcite solutions as background electrolyte were used. Batch experiments were performed under aerobic conditions (aerobic OPA powder (BHE 24/1)) and anaerobic conditions (anaerobic OPA powder (BDR 2), Ar glove box, $\text{pCO}_2 = 10^{-2.3}$ atm) using a S/L ratio of 15 g/L. Fig. 3 shows the sorption of Np(V) on OPA at initial concentrations of 7×10^{-12} and 8×10^{-6} M under aerobic and anaerobic conditions. At both concentrations under aerobic conditions, the sorption edge occurs between pH 7.0 - 7.5. In the absence of oxygen under a higher partial pressure of CO_2 ($10^{-2.3}$ atm), which has been estimated for the OPA host rock formation [47], the sorption edge and sorption maximum are shifted to lower pH due to higher carbonate concentrations resulting from the increased pCO_2 , which has a significant influence on Np(V) speciation (see Fig. 4). The sorption maximum under aerobic conditions is between pH 8 - 9. In the case of the micromolar Np(V) concentration, maximum sorption is reached at pH 8.9 with 66% Np(V) sorbed. The curve with picomolar Np concentration exhibits maximum sorption at pH 8.3 with 95% Np(V) sorbed. In both cases, sorption decreases at pH > 9.5 due to the complexation of Np with carbonate in aqueous solution (see Fig. 4). The K_d for a Np(V) equilibrium concentration of 3×10^{-13} M at pH 8.3 amounts to $1.343 \pm 0.105 \text{ m}^3/\text{kg}$ and exceeds the corresponding value for $[\text{Np}]_{\text{eq}} = 3 \times 10^{-6}$ M ($K_d = 0.110 \pm 0.008 \text{ m}^3/\text{kg}$) by one order of magnitude.

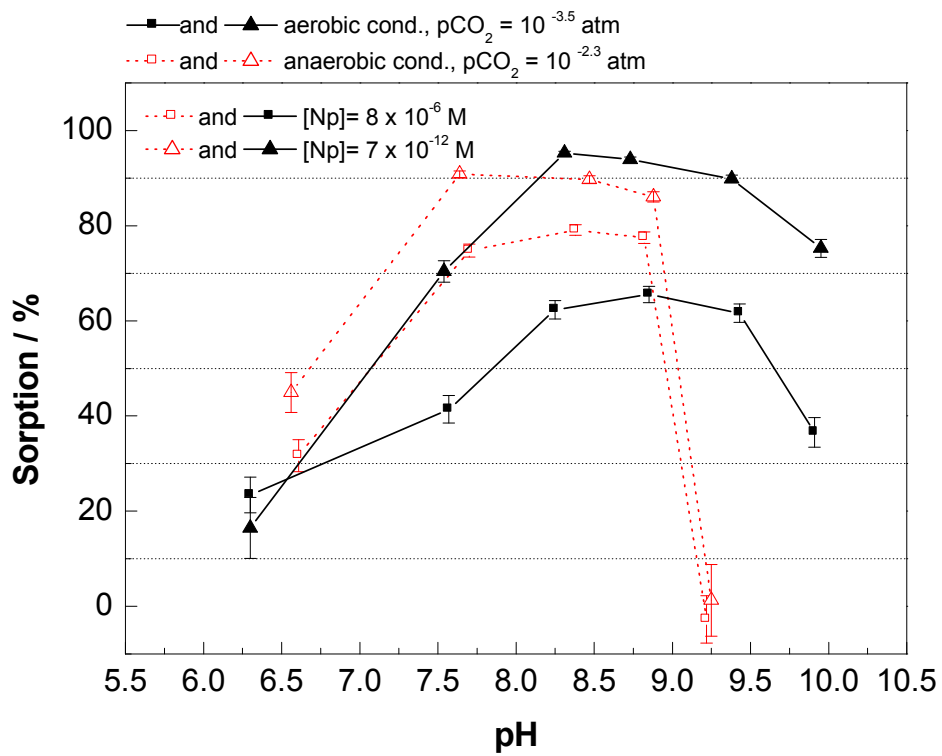


Figure 3: Sorption of 8×10^{-6} and 7×10^{-12} M Np(V) on 15 g/L OPA as a function of pH in saturated calcite solution under aerobic and anaerobic ($p_{\text{CO}_2} 10^{-2.3}$ atm) conditions.

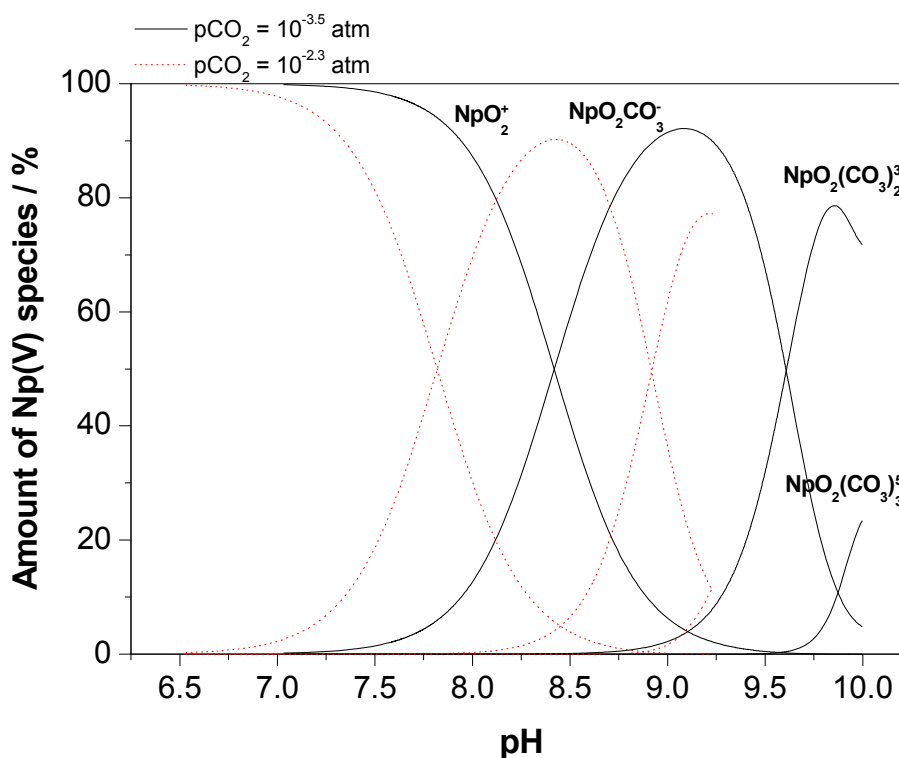


Figure 4: Np(V) speciation in aqueous solution under calcite saturation condition as a function of pH for 8×10^{-6} M Np(V) and $p\text{CO}_2$ equal to $10^{-3.5}$ atm (solid lines) and $10^{-2.3}$ atm (dotted lines); species present at a level less than 1% are not shown. The distribution of Np(V) complexes was calculated with the geochemical equilibrium speciation software Visual MINTEQ V. 2.52 [19]. The thermodynamic data contained in the database of MINTEQ are those given in [10] and the NIST (National Institute of Standards and Technology, USA) database 46.6.

Under anaerobic conditions, the percentage of Np(V) sorbed is almost constant between pH 7.5 - 9 with maximum sorption occurring at pH 8.4 for 8×10^{-6} M Np(V) (80% sorbed) and pH 7.6 – 8.6 for 7×10^{-12} M Np(V) (90% sorbed), respectively. There is no sorption of Np(V) at pH > 9.25 at both Np concentrations due to the formation of negatively charged Np-carbonate species, which are predicted from speciation calculations (see Fig. 4). The maximum K_d value at micromolar Np(V) concentration ($0.252 \text{ m}^3/\text{kg}$ at pH 8.4, Fig. 5) exceeds the corresponding value under aerobic conditions by a factor of 2. At lower Np concentration, the highest K_d of $0.660 \text{ m}^3/\text{kg}$ occurs at pH 7.6. The stronger sorption of 8×10^{-6} M Np(V) in the absence of oxygen was found to be caused by a partial reduction of

Np(V) to Np(IV) as determined by liquid-liquid extraction using HDEHP as extracting agent. This result is supported by Eh measurements in the near neutral pH range, indicating a lower redox potential of ≈ 100 mV under anaerobic conditions compared to ≈ 400 mV (SHE) under aerobic conditions. The decrease in the redox potential might be caused by the dissolution of iron(II) containing minerals (pyrite and siderite), which make up 4.1% of OPA. Due to the lower solubility of Np(IV) compared to Np(V) [10], a precipitation of Np(IV) in this pH range can not be excluded. It has also to be taken into account that aerobic and anaerobic OPA samples are from different bore cores. Therefore, differences in the sorption behavior may be related to minor differences in the mineralogy and specific surface areas of the two OPA samples.

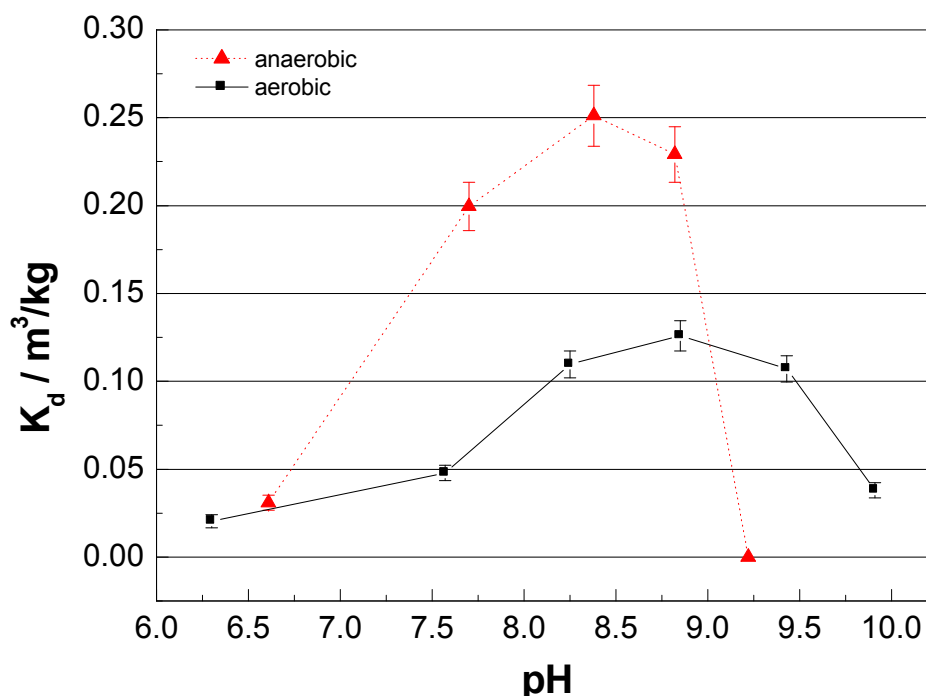


Figure 5: Sorption of 8×10^{-6} M Np(V) on 15 g/L OPA as a function of pH under aerobic and anaerobic ($p_{\text{CO}_2} 10^{-2.3}$ atm) conditions in saturated calcite solution.

Plutonium

The sorption of Pu(IV) and Pu(VI) on OPA (BHE 24/1) has been studied by batch experiments as a function of pH in 0.1 M NaClO₄ solution. A similar experiment was conducted with Th(IV) as an oxidation state analogue. Experiments were performed with a S/L ratio of 1 g/L (Pu(IV) and Th(IV)), and 2 g/L (Pu(VI)) in the pH range 1 - 8 with

concentrations of 4×10^{-7} M for Pu(IV) and Th(IV) and 1×10^{-7} M for Pu(VI). The obtained results are shown in Fig. 6. The sorption of Pu(IV) and Pu(VI) as well as of Th(IV) on OPA is strongly influenced by the pH. The sorption increases with increasing pH up to pH 4 (for Pu(IV) and Th(IV)) and to pH 6 (for Pu(VI)). For Pu(IV) and Th(IV), a similar sorption behavior was found as a function of pH. The sorption edges of Pu(IV) and Th(IV) are both at about pH 1.5 with maximum sorption of 99% between pH 4 and 8. The sorption edge of Pu(VI) is shifted to a higher pH value (pH = 2.5) with maximum sorption of 99% between pH 6 and 8. In case of Pu(VI) a partial reduction to Pu(IV) can not be excluded. Due to the strong sorption of Pu(IV) and Pu(VI) on OPA in the natural pH range (7 – 9), this would lead to an enhanced immobilization and retardation of the aqueous plutonium. A similar behavior was found for Pu(IV) and Th(IV) sorption on kaolinite [48].

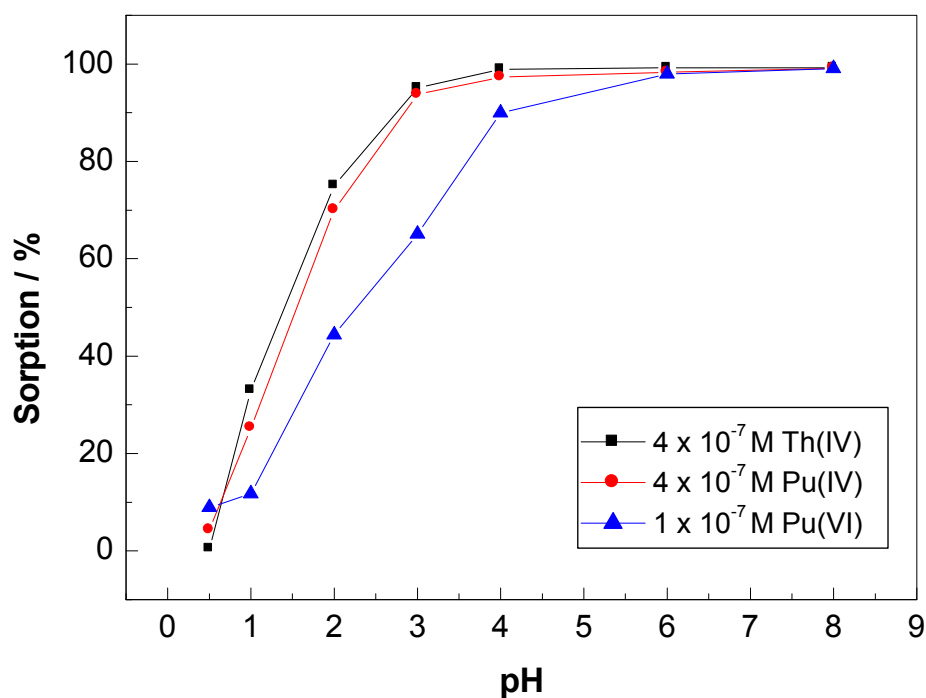


Figure 6: Sorption of Pu(IV), Pu(VI), and Th(IV) on OPA in 0.1 M NaClO₄ as a function of pH at S/L ratio of 1 g/L for Pu(IV) and Th(IV)), and 2 g/L for Pu(VI) under aerobic conditions.

4.1.4 Influence of humic acid (HA)

Neptunium

^{14}C labelled synthetic HA (M42) [18] was used at a concentration of 10 mg/L to study the influence of HA on the sorption of Np(V) onto OPA as a function of pH under the same experimental conditions as in the Chapter 4.1.3. The preparation of the samples was carried out analogously to the other batch experiments. HA was added instantly after addition of $^{237}\text{Np(V)}$ or $^{239}\text{Np(V)}$.

Figures 7 and 8 show the sorption of 7×10^{-12} M and 8×10^{-6} M Np(V) on OPA under aerobic and anaerobic ($p_{\text{CO}_2} 10^{-2.3}$ atm) conditions in the presence of HA, respectively. For comparison, data for Np uptake in the absence of HA are also shown.

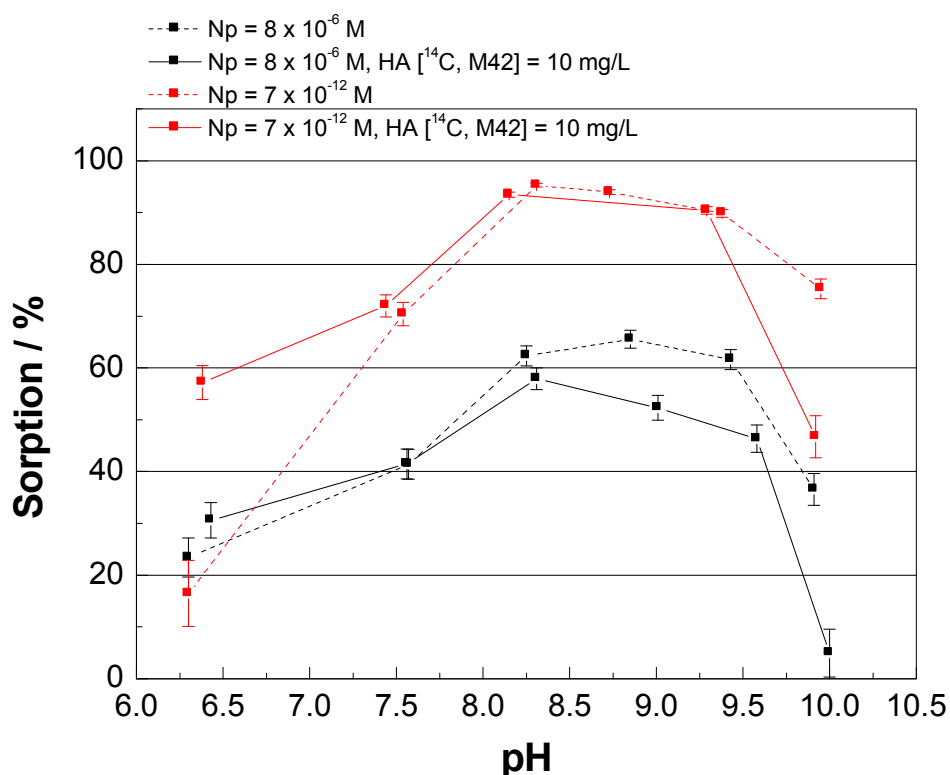


Figure 7: Sorption of 8×10^{-6} M and 7×10^{-12} M Np(V) on 15 g/L OPA in the presence/absence of HA as a function of pH under aerobic conditions in saturated calcite solution.

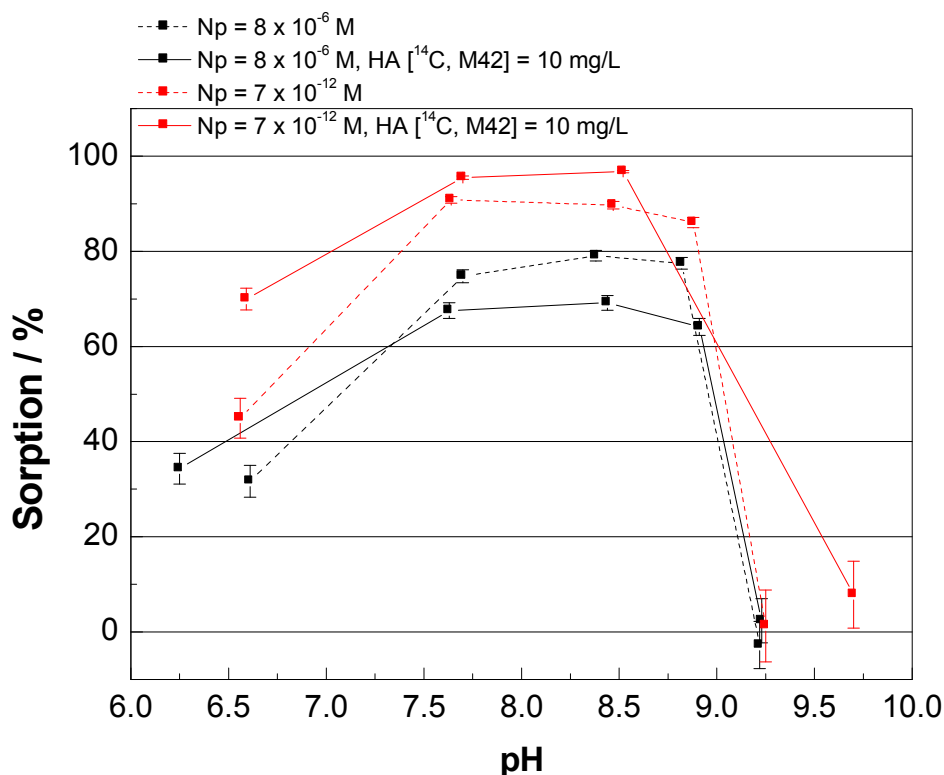


Figure 8: Sorption of 8×10^{-6} and 7×10^{-12} M Np(V) on 15 g/L OPA in the presence/absence of HA as a function of pH under anaerobic conditions ($p_{\text{CO}_2} 10^{-2.3}$ atm) in saturated calcite solution.

At 8×10^{-6} M Np(V) and $p(\text{CO}_2) = 10^{-3.5}$ atm, the presence of HA reduces slightly the amount of Np sorbed on OPA in the pH range of 8 – 10, probably due to formation of Np humate or ternary Np humate-carbonate complexes [27, 49]. This effect of HA is less pronounced at 7×10^{-12} M Np(V).

Plutonium

The Pu(IV) sorption onto OPA (BHE 24/1) was also investigated in the presence and absence of HA under aerobic conditions in OPA pore water (pH = 7.6). Analogous to Np batch experiments with HA, ^{14}C (M42) was used at a concentration of 10 mg/L. Pu(IV) sorption isotherms were measured as a function of the S/L ratio between 2 - 20 g/L at constant Pu(IV) concentration of 1×10^{-7} M. After preconditioning the batch samples, aliquots of ^{239}Pu (IV) and HA stock solution were added and mixed at same time with the suspensions. After 62 h contact time, the solid and liquid phases were separated by centrifugation. Then aliquots of

the suspensions were taken and analyzed by LSC. The influence of HA on the sorption of Pu(IV) on OPA is shown in Tab. 6.

Table 6: K_d values for the sorption of Pu(IV) on OPA in absence / presence (10 mg/L) of HA under aerobic conditions as a function of S/L ratio in OPA pore water at pH = 7.6.

S / L / g/L	$K_d / m^3/kg$	
	With HA	Without HA
2	4.64 ± 0.35	70.50 ± 4.88
4	6.49 ± 0.47	122.46 ± 8.64
6	8.88 ± 0.63	125.71 ± 9.00
8	10.94 ± 0.78	40.56 ± 2.84
10	13.07 ± 0.93	97.48 ± 6.99
15	30.18 ± 2.14	78.69 ± 5.52
20	14.56 ± 1.03	47.97 ± 3.38

HA significantly affects the sorption of Pu(IV) on OPA in pore water at pH 7.6 and reduces the averaged K_d value from $83.3 \pm 33.7 m^3/kg$ in the absence of HA to $12.7 \pm 8.5 m^3/kg$ in the presence of HA. This effect is probably due to the formation of Pu humate complexes, since tetravalent actinides form strong complexes with HA [49]. Pu(IV) is significantly mobilized in the presence of HA under these experimental conditions. Our results are in good agreement with sorption data reported for Pu(III/IV) on kaolinite in the presence of HA compared to the HA-free system [48, 50].

4.1.5 Influence of temperature [51, 52]

Neptunium

The German concept for nuclear waste disposal proceeds on the assumption that the temperature at the contact surface of the containers with the host mineral will stay below 100 °C [53]. This increase in temperature might change the physical properties of the host rock formation and influence the sorption and migration of the radionuclides. Therefore, the effect of temperature has to be taken into account. Until now, the effect of temperature on radionuclide sorption, especially on clay minerals has not been investigated in much extent and only few studies have been reported on Np and Pu sorption up to 80 °C [54, 55]. More information is available for the sorption of non-radioactive heavy metals or lanthanides (Ni^{2+} ,

Cs⁺, Cd²⁺, Co²⁺, and Eu³⁺) onto several clay minerals such as smectite, montmorillonite, and kaolinite [56 - 59]. Therefore, the sorption of micromolar Np(V) on OPA (BHE 24/1) at temperatures up to 80 °C in synthetic OPA pore water (pH = 7.6, I = 0.4) under aerobic conditions was studied and the results were compared with our data at room temperature [28]. Figure 9 shows the percentage of Np(V) sorbed on OPA in dependence of S/L ratio and temperature compared to the results at 20 °C [28].

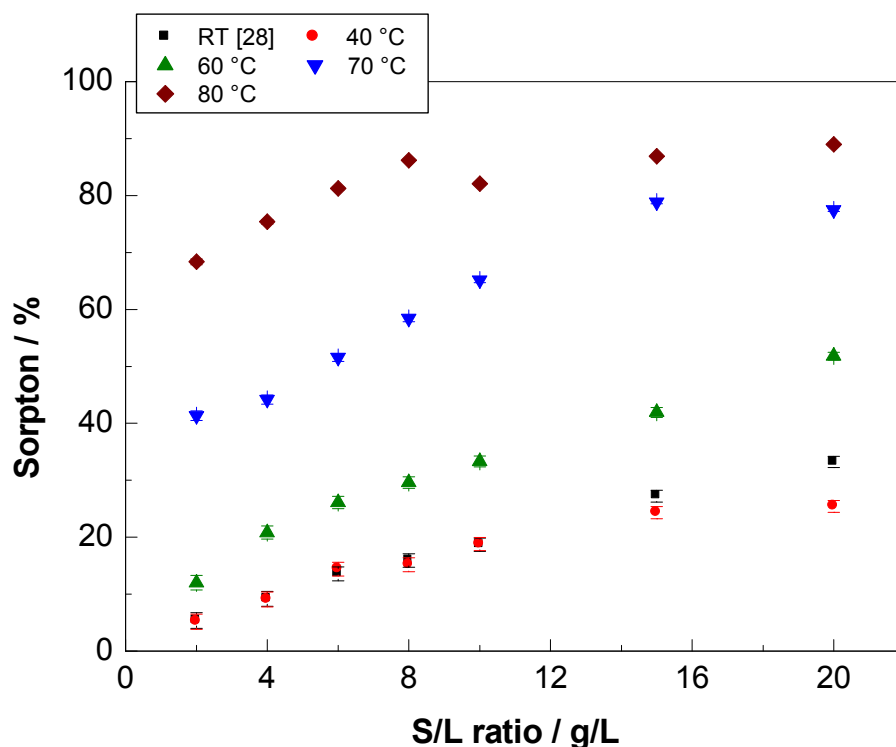


Figure 9: Sorption of 8×10^{-6} M Np(V) on OPA (BHE 24/1) as a function of S/L ratio and temperature in OPA pore water under aerobic conditions.

The sorption of Np does not change as temperature is raised from room temperature to 40 °C. Between 40 and 80 °C, sorption increases continuously with increasing temperature. At 80 °C an average K_d value of 0.678 ± 0.254 m³/kg is reached which exceeds the corresponding value at room temperature by a factor > 27. The average K_d values for different temperatures are summarized in Tab. 7.

Table 7: Averaged K_d values for the sorption of Np(V) on OPA (S/L = 2 - 20 g/L) in OPA pore water in dependence of temperature under aerobic conditions.

Temperature / °C	pH	[Np] ₀ / mol/L	K_d / m ³ /kg
20 ^[28]	7.6	8×10^{-6}	0.025 ± 0.005
40	7.6	1×10^{-5}	0.023 ± 0.004
60	7.5	8×10^{-6}	0.056 ± 0.005
70	7.5	1×10^{-5}	0.235 ± 0.072
80	7.5	8×10^{-6}	0.678 ± 0.254
preconditioned at 60 °C sorption at 20 °C	7.5	8×10^{-6}	0.028 ± 0.009

To exclude the possibility that a change of the surface structure of OPA due to higher temperature causes the observed increase in Np(V) sorption, one batch series was performed in which the preconditioning of OPA was carried out at 60 °C. After cooling of the suspension to room temperature, the K_d values were determined as described before. As can be seen from Tab. 7, the preconditioning of the clay suspension at elevated temperature had no effect on the neptunium sorption on OPA. Within experimental uncertainties, the K_d values are identical. Higher sorption at elevated temperature might be caused by an increase of the negative charge on the clay surface as it was reported for other clay minerals, e.g., kaolinite [60]. For rutile it was also reported that the point of zero net proton charge (pH_{znpc}) is shifted by 0.7 units to lower pH values as temperature increases from 25 to 100 °C; for pH values above the pH_{znpc} , the negative surface charge also increased with increasing temperature [61]. During the experiment, we observed that the heating of the clay suspension was followed by a decrease in pH (at 80 °C with 20 g/L OPA the pH decreased from 7.6 to 7.0). This effect is possibly the result of a stronger deprotonation of the surface and therefore supports the assumption of an increase in the negative surface charge.

Our results indicate that Np(V) sorption on OPA is an endothermic reaction. This trend is in good agreement with studies of Runde et al. [55], who investigated Np(V) sorption on hematite, montmorillonite, and silica. For all minerals, neptunium sorption increased when temperature was raised up to 80 °C.

By using the Van't Hoff equation (4), the apparent sorption enthalpy of Np(V) on OPA can be calculated:

$$\log(K_d) = \frac{\Delta_r S^{App}}{2.3R} - \frac{\Delta_r H^{App}}{2.3R} \times \frac{1}{T}, \quad (4)$$

where $\Delta_r H^{\text{App}}$ is the apparent reaction enthalpy in kJ/mol, $\Delta_r S^{\text{App}}$ the apparent entropy in J/K mol, T the absolute temperature in Kelvin and R the universal gas constant. By performing an Arrhenius plot ($\log(K_d)$ vs. $1/T$) between 40 and 80 °C as shown in Fig. 10, an apparent sorption enthalpy of 77.3 ± 15.8 kJ/mol was derived for the sorption of Np(V) on OPA. This value lies in the same order of magnitude as those reported for the sorption of Ni^{2+} (33 ± 10 kJ/mol) and Eu^{3+} (39 ± 10 kJ/mol) on montmorillonite at $\text{pH} = 7.0 \pm 0.5$ [57, 58] or Co^{2+} (27 - 42 kJ/mol) and Cd^{2+} (26 - 40 kJ/mol) on kaolinite at $\text{pH} 7.0$ and 7.5 , respectively [59].

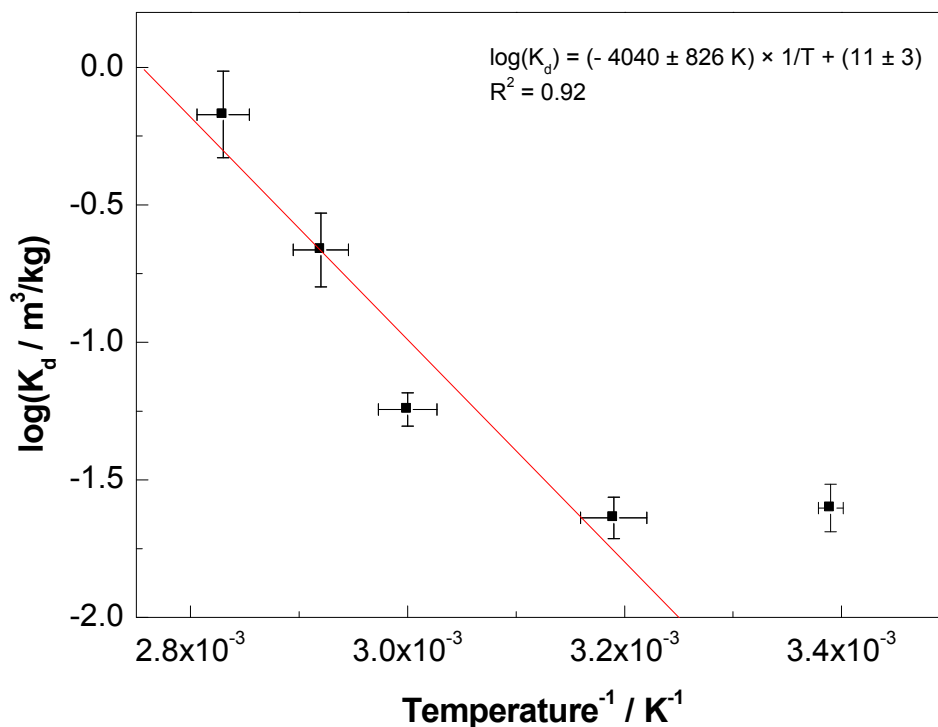


Figure 10: Arrhenius plot for the sorption of Np(V) on OPA in OPA pore water at $\text{pH} = 7.6$ under aerobic conditions using the average K_d values shown in Table 7.

Plutonium

Analogous to Np, the influence of temperature on the sorption of Pu(VI) on OPA (BHE 24/1) was investigated. Sorption isotherms at room temperature (20 °C) and 60 °C were carried out with a Pu(VI) concentration of about 1×10^{-7} M as a function of S/L ratio (2 - 20 g/L) under aerobic conditions using OPA pore water ($\text{pH} = 7.6$) as a background electrolyte. Table 8 presents the obtained K_d values at both temperatures as a function of the S/L ratio. The

sorption of Pu(VI) increases with increasing temperature. The K_d value at 60 °C is about 6 times higher than at 20 °C ($12.5 \pm 3.3 \text{ m}^3/\text{kg}$). This result is in good agreement with the data for Np(V) sorption on OPA and indicates that Pu(VI) sorption on OPA is an endothermic reaction, which would have a positive implication for the nuclear waste disposal in OPA.

Table 8: K_d values for the sorption of Pu(VI) on OPA at room temperature (20 °C) and 60 °C under aerobic conditions as a function of S/L ratio in OPA pore water at pH 7.6.

S/L / g/L	$K_d / \text{m}^3/\text{kg}$	
	20 °C	60 °C
2	11.28 ± 0.87	94.20 ± 6.81
4	7.83 ± 0.60	96.02 ± 6.92
6	10.62 ± 0.79	96.98 ± 4.93
8	11.26 ± 0.85	65.09 ± 4.70
10	13.26 ± 0.97	60.48 ± 4.21
15	15.69 ± 1.21	52.73 ± 3.78
20	17.7 ± 0.87	72.95 ± 4.96

A partial reduction of Pu(VI) to Pu(IV) under these experimental conditions can not be excluded.

4.1.6 Influence of ionic strength and background electrolyte [51, 52]

Since pore water consists of several constituents (mainly NaCl, CaCl₂, and MgCl₂), the influence of ionic strength at both 0.1 M and 0.4 M NaClO₄, NaCl, MgCl₂, and CaCl₂ electrolytes on the sorption of 8×10^{-6} M Np(V) onto OPA was studied in individual batch experiments at room temperature and pH 7.6.

Figure 11 shows the $\log(K_d)$ values for different background electrolytes as a function of S/L ratio. In all cases, Np(V) sorption does not depend on the amount of OPA, which is in good agreement with results mentioned above [16] and studies reported elsewhere [43].

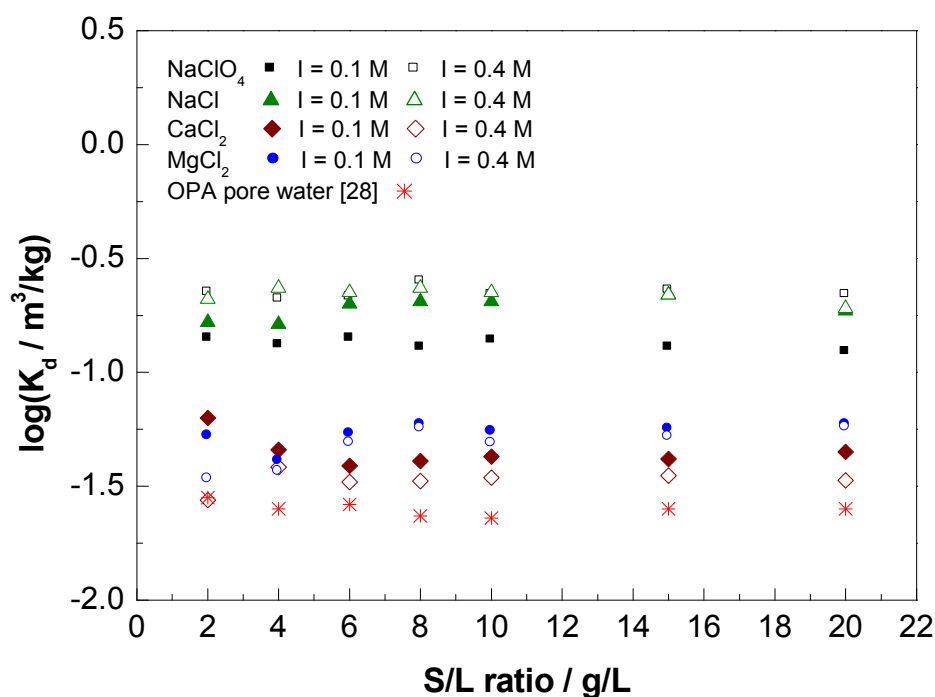


Figure 11: Log K_d values of the sorption of $\sim 8 \times 10^{-6}$ M Np(V) on OPA as a function of S/L ratio and background electrolyte at pH ≈ 7.6 under aerobic conditions at room temperature. For clarity error bars (typically between 0.1 and 0.4 log units) are omitted.

In Fig. 11, two groups of $\log(K_d)$ can be distinguished. Background electrolytes containing Na^+ gave $\log(K_d)$ values above - 1.0, while electrolyte solutions with divalent cations have $\log(K_d)$ values around - 1.5. The values reported for synthetic OPA pore water [28] lie in the same range as for the CaCl_2 and MgCl_2 electrolytes, independent from ionic strength (0.1 or 0.4 M). Small differences in K_d might be explained by the slightly different pH values. The average K_d values and the corresponding standard deviations (1σ) are presented in Tab. 9. Furthermore, in NaClO_4 solution, a weak, but pronounced dependence of Np(V) sorption on ionic strength was noticed. The K_d for sorption of Np(V) in NaClO_4 solution increased by a factor of two from $0.133 \pm 0.009 \text{ m}^3/\text{kg}$ to $0.231 \pm 0.013 \text{ m}^3/\text{kg}$ with increasing ionic strength from 0.1 to 0.4 M. In case of kaolinite, the sorption of Np(V) increased by $\sim 10\%$ in the near neutral pH range when the ionic strength increased from 0.01 to 0.1 M NaClO_4 [43, 49].

Table 9: Averaged K_d values for the sorption of Np(V) on OPA (S/L = 2 - 20 g/L) as a function of different background electrolytes and ionic strength under aerobic conditions at room temperature.

Electrolyte	Ionic strength / M	$K_d / m^3/kg$	pH	$[Np]_0 / mol/L$
NaClO ₄	0.1	0.133 ± 0.009	7.8	1×10^{-5}
	0.4	0.231 ± 0.013	7.7	1×10^{-5}
NaCl	0.1	0.214 ± 0.012	7.8	9×10^{-6}
	0.4	0.224 ± 0.017	7.8	9×10^{-6}
CaCl ₂	0.1	0.045 ± 0.008	7.4	8×10^{-6}
	0.4	0.034 ± 0.003	7.2	8×10^{-6}
MgCl ₂	0.1	0.054 ± 0.006	7.8	9×10^{-6}
	0.4	0.037 ± 0.008	7.7	9×10^{-6}
Synthetic OPA pore water ^[28]	0.4	0.025 ± 0.005	7.6	8×10^{-6}

From speciation calculations using Visual MINTEQ V. 2.52 [19], differences in neptunium speciation in investigated background electrolytes at different ionic strength can be excluded as reason for these different K_d values.

4.1.7 Sorption isotherms of Th, U, Np, Pu, and Am in OPA pore water

The migration behavior of actinides in OPA pore water at environmentally-relevant conditions is essential for repository safeguarding, especially because only few sorption studies concerning the actinide sorption on OPA have been published [28, 15].

In this work, the distribution coefficients (K_d values) were determined by batch experiments for Th(IV), U(VI), Np(V), Pu(III, IV, VI), and Am(III)) on OPA (BHE 241) using pore water (pH = 7.6) as background electrolyte under aerobic conditions (except for Pu(III) under Ar atmosphere) as a function of S/L ratio (2 - 20 g/L) and actinide concentration (only U(VI) and Np(V), see Fig. 12) at constant S/L of 15 g/L. Batch experiments were performed as described in Sect. 3.1. Results from batch sorption experiments (sorption isotherms) are expressed through the K_d values. When $n = 1$ in eq. 3, $K = (x/m) / [An]_{eq}^n = K_d$, which is the slope of the isotherm at the origin. In case of the Freundlich isotherm [45], the constants K and n can be determined from a linear fit of eq. (5) to the experimental data.

$$\log \frac{x}{m} = \log K + n \log [An]_{eq} \quad (5)$$

The intercept of the line then equals $\log K_d$ and the slope is n .

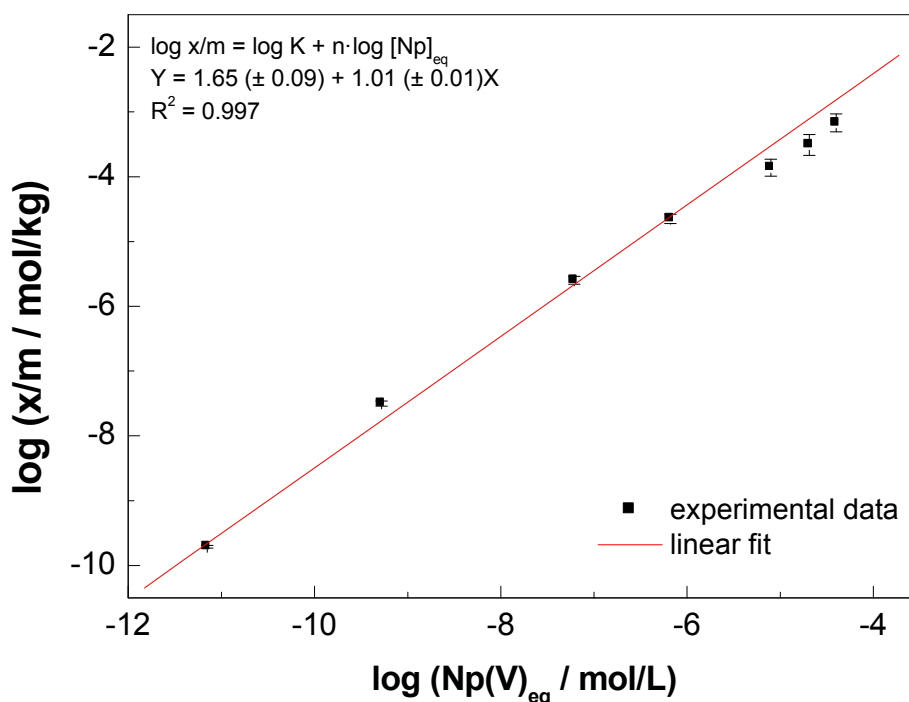


Figure 12: Freundlich isotherm of Np(V) sorption on OPA as a function of Np(V) concentration at S/L ratio 15 g/L in OPA pore water (pH = 7.6) under aerobic conditions.

The slope of the fit line is $n = 1.01 (\pm 0.01)$, the intercept is $\log K_d = 1.65 (\pm 0.09)$ and the related K_d value is equal to $0.04 \pm 0.01 \text{ m}^3/\text{kg}$. The obtained K_d value agrees well with the previously determined K_d value ($0.025 \pm 0.005 \text{ m}^3/\text{kg}$) for Np sorption in dependence of S/L (2 - 20 g/L) [28].

In the same way, the sorption of U(VI) on OPA in pore water was investigated by varying the U(VI) concentration between 1.6×10^{-4} - 1.3×10^{-7} M at constant S/L ratio of 15 g/L under aerobic conditions. The results show a linear sorption behavior (Freundlich isotherm) resulting in a K_d value of $0.05 \pm 0.01 \text{ m}^3/\text{kg}$. By using eq. 2, an average K_d value of $0.03 \pm 0.01 \text{ m}^3/\text{kg}$ was determined, which agrees well with data from Joseph et al. [15] ($K_d = 0.02 \pm 0.01 \text{ m}^3/\text{kg}$). Since experimental K_d values for Pu sorption on OPA are missing and estimated K_d values were derived from chemical analogous (Th(IV) and Am(III) [62]), we measured the K_d values of Pu(III, IV, VI) and its analogous Th(IV), Am(III) as well as for Np(V) and U(VI) for the first time under identical experimental conditions in pore water at pH 7.6.

Figure 13 shows the sorption isotherms of Th, Np, Pu, and Am in pore water at pH 7.6 by variation of the S/L ratio between 2 - 20 g/L.

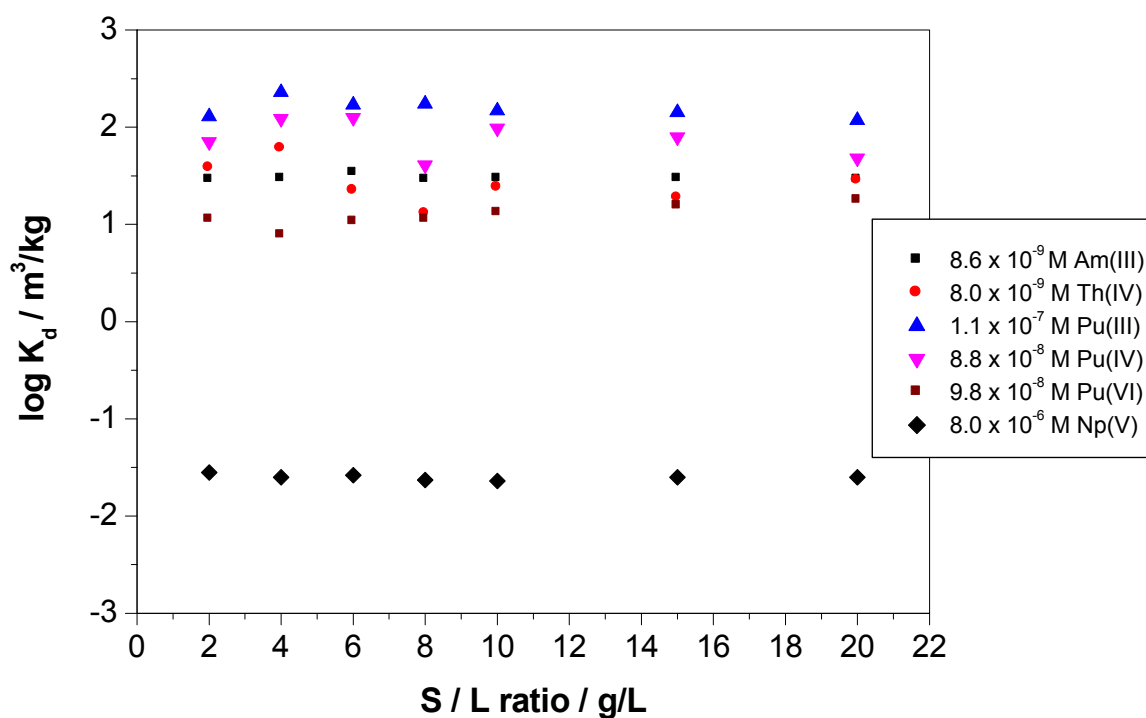


Figure 13: Log K_d values for the sorption of Th(IV), Pu(III, IV, VI), Np(V) and Am(III) on OPA in pore water (pH = 7.6) as function of S/L ratio (2 - 20 g/L) (uncertainty in log K_d values is $< \pm 0.4$ log units).

Linear sorption behavior under these experimental conditions was observed in all cases. The sorption data of Np(V), Pu(III), Am(III) can also be fitted by using the Freundlich isotherm (not shown). The average K_d values of all studied actinides obtained from sorption isotherms in comparison to published data [62] are summarized in Tab. 10.

Table 10: Averaged K_d values for the sorption of actinides on OPA in OPA pore water (pH = 7.6).

Actinide	S/L ratio g/L	[actinide] mol/L	$K_d / m^3/kg$		
			This work pH = 7.8	Ref. [62]	
				pH = 7.2	pH = 7.6
Am(III)	2 - 20	8.6×10^{-9}	29.8 ± 1.8	17.0	63.0
Pu(III)	2 - 20	1.1×10^{-7}	158.7 ± 37.1	22.6	75.2
Th(IV)	2 - 20	8.0×10^{-9}	29.0 ± 15.6	55.4	55.4
Pu(IV)	2 - 20	8.8×10^{-8}	83.3 ± 33.7	-	-
Np(V)	2 - 20	8.0×10^{-6}	0.03 ± 0.01	-	-
	15	5.0×10^{-5} - 1.0×10^{-11}			
U(VI)	15	1.6×10^{-4} -	0.03 ± 0.01	-	-
		1.3×10^{-7}			
Pu(VI)	2 - 20	9.8×10^{-8}	12.5 ± 3.3	-	-

As can be seen from Tab. 10, the measured K_d values depend on the oxidation state of the actinide element. K_d values for the tri- and tetravalent actinides are in the range of 30 - 159 m^3/kg , indicating strong sorption on OPA in pore water at pH 7.6. The measured K_d values for Th(IV), Pu(III/IV) and Am(III) are in the same order of magnitude with the corresponding K_d values from literature [62]. The K_d value of Pu(VI) is lower than those for Th(IV), Pu(III, IV), and Am(III), but it is about three orders of magnitude higher than the K_d values of U(VI) and Np(V). This is probably due to a partial reduction of Pu(VI) to Pu(IV) during the batch experiments, which causes the higher sorption on OPA (confirmed by EXAFS). U(VI) and Np(V) are weakly sorbed on OPA with K_d values of $0.03 \pm 0.01 m^3/kg$. As a conclusion, tri- and tetravalent actinides will be immobilized in the host rock OPA in comparison to penta- and hexavalent actinides, which will be more mobile.

4.2 Diffusion experiments

Because OPA has a very low hydraulic conductivity, diffusion is considered to be the main process responsible for the transport of radionuclides released from a repository [7]. Due to little diffusion data available for actinides, the main objective of our investigation was to study the diffusion of Np(V) as a function of temperature in the presence/absence of HA by

using OPA pore water (pH = 7.6) as a mobile phase to determine diffusion parameters needed for transport modeling.

The distribution coefficient K_d , as one of the most important parameters to evaluate the migration behavior of radionuclides in argillaceous rocks, can be also obtained by diffusion experiments [7, 28]. Diffusion experiments may be a more representative method to simulate the migration behavior of radionuclides transported from the nuclear repository into the environment, but they take a longer time and are more complicated to perform compared to batch experiments. During diffusion experiments, it is also difficult to change and control physicochemical parameters such as pH, Eh, etc. of the contact solutions. Due to many problems in diffusion experiments, only few studies showed a good agreement between K_d values obtained by batch experiments and diffusion measurements [63 - 69]. One of the goals was to compare K_d values from batch experiments on suspended material with the values derived from in-diffusion experiments. To make this comparison as close as possible, several chemical parameter were identical during both the batch and diffusion experiments, i.e., Np(V) concentration (8×10^{-6} M), pore water (pH = 7.6), HA (M42) concentration 10 mg/L, and aerobic conditions. The experimental setup for the diffusion experiments is shown in Fig. 1 and an overview of the used tracers and their concentrations can be found in Tab. 4 (see Sect. 3.2). The experimental data processing of through-, out-, and in-diffusion experiments has been described in [7, 28]. A computer code based on Mathematica 6.0 has been developed for modeling through-, out-, and in-diffusion experiments. It was used to determine the diffusion coefficients (D_e) and the rock capacity factors (α) for tritiated water (HTO), $^{22}\text{Na}^+$, Np, and the distribution coefficient (K_d) of $^{22}\text{Na}^+$ and Np in OPA. Since HTO can be considered as a nonsorbing tracer, i.e., $K_d = 0$, α is equal to porosity (ε). Making the assumption that the pore space determined for HTO is accessible for $^{22}\text{Na}^+$ [7], the K_d value for $^{22}\text{Na}^+$ can be calculated by eq. 6. ε is obtained from the through diffusion experiment with HTO.

$$\alpha = \varepsilon + \rho \cdot K_d \quad (6)$$

where ε is the diffusion-accessible porosity; ρ (kg/m^3) is the bulk dry density.

The values for D_e and α for HTO and $^{22}\text{Na}^+$ were obtained by fitting the results of experimental data of both transient and steady-state phases to the analytical solution of accumulated activity. The quality of the parameters D_e and α was tested by using them as input parameters in the equation of flux (eq. 7).

$$J(L, t) = \frac{1}{S} \cdot \frac{\partial A}{\partial t}, \quad (7)$$

where $J(L, t)$ is the flux at the low-concentration boundary ($x = L$) at diffusion time t , A (Bq/m³) is the radionuclide activity in solution, t (s) is the diffusion time, and S (m²) is the cross section area of the sample.

Figure 14 shows as an example the flux and the accumulated activity of cell 1 (Tab. 4) as a function of diffusion time obtained by through-diffusion of HTO and ²²Na. As can be seen, the flux increases with diffusion time at the transient phase and becomes constant at the steady phase. In the transient phase, the flux depends on diffusion time, D_e , ε , and α , while in the steady state the flux depends only on D_e . The accumulated activity increases with time, becoming a linear function of time at the steady phase.

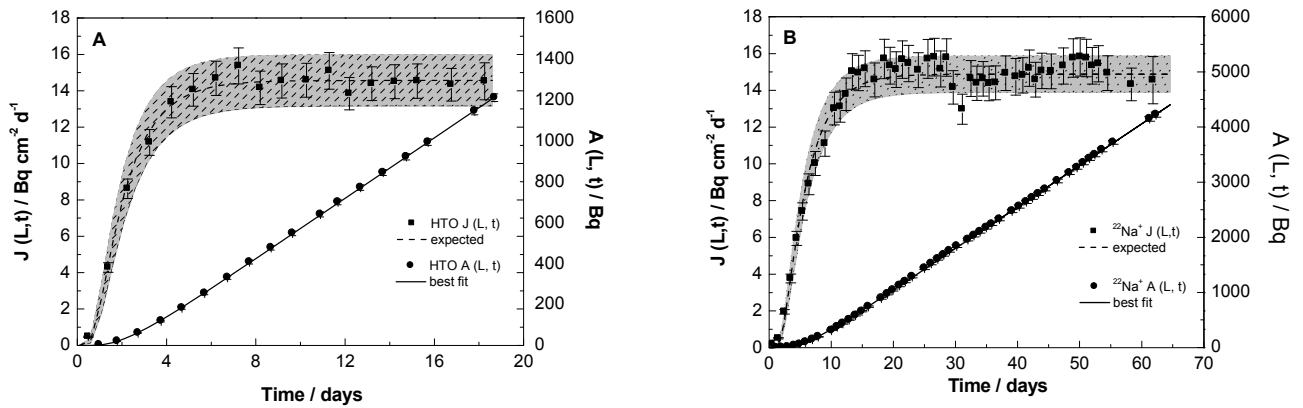


Figure 14: Through-diffusion curves of cell 1 for HTO (A) and ²²Na⁺ (B) with flux ($J(L, t)$) and accumulated activity (A_{cum}) as a function of diffusion time through OPA in pore water at aerobic condition (The shaded area represents the uncertainty of the calculated curve).

As can be seen from Fig. 14, the experimental data of flux J for both HTO and ²²Na⁺ as a function of diffusion time are in good agreement with the calculated data. The non-sorbing tracer HTO reached steady state after about 6 days, while the weak sorbing cation ²²Na⁺ took longer time (about 15 days) to reach it. Moreover, the diffusion parameters of HTO and ²²Na⁺ were determined also by out-diffusion experiments and similar values for D_e and α were obtained. In case of ²²Na⁺, the diffusion parameters D_e and K_d were also obtained by in-diffusion experiments after diffusion of Np and were in excellent agreement with those obtained by the through-diffusion technique, indicating that both methods can be used to study the diffusion behavior of radionuclides in the clay. The obtained diffusion parameters (D_e , ε , α , and K_d) for HTO and ²²Na⁺ are summarized in Tab. 11.

Table 11: Diffusion parameters (D_e) for HTO and (D_e and D_a) for $^{22}\text{Na}^+$ in OPA by through- and in-diffusion experiments, respectively.

Cell	Temp. (°C)	HTO		$^{22}\text{Na}^+$			
		ε	D_e ($\times 10^{-11} \text{ m}^2/\text{s}$)	α	D_e ($\times 10^{-11} \text{ m}^2/\text{s}$)	D_a ($\times 10^{-11} \text{ m}^2/\text{s}$)	K_d ($\times 10^{-3} \text{ m}^3/\text{kg}$)
1	20 ± 2	0.15 ± 0.01	1.50 ± 0.10	0.50 ± 0.02^a 0.44 ± 0.03^b	1.9 ± 0.1^a 1.8 ± 0.2^b	3.8 ± 0.2^a 4.1 ± 0.4^b	0.15 ± 0.03^a 0.14 ± 0.01^b
2	20 ± 2	0.20 ± 0.01	1.97 ± 0.14	0.44 ± 0.01	2.5 ± 0.4^a	5.7 ± 0.9^a	0.10 ± 0.01^a
3 ^c	20 ± 2	0.14 ± 0.01	1.73 ± 0.12	0.40 ± 0.01	3.1 ± 0.7^a	7.8 ± 1.8^a	0.11 ± 0.01^a
4	60 ± 2	0.19 ± 0.01	3.13 ± 0.22	0.40 ± 0.01	3.5 ± 0.7^a	8.8 ± 1.8^a	0.11 ± 0.01^a
[29]	23 ± 2	0.09 ± 0.02	1.48 ± 0.07	0.44 ± 0.01			
[63]	23 ± 2			0.33 ± 0.03	1.6 ± 0.1^a	4.8 ± 0.3^a	0.10 ± 0.02^a

^a Values measured in through-diffusion experiments, ^b values measured in in-diffusion experiments, and ^c presence of HA

As shown in Tab. 11, all samples have a similar porosity, which is representative for OPA from Mont Terri [29]. The D_e values of HTO for cells 1 to 3 are in the same range as values from the literature [29]. The obtained D_e of cell 4 at 60 °C is higher by a factor of about 1.5 than for those at room temperature. From the literature, it is known that the diffusion of HTO increases with increasing temperature. Our D_e value at 60 °C agrees well with the corresponding experimental data from Van Loon et al. [7] (55 °C: $2.95 \pm 0.22 \times 10^{-11} \text{ m}^2/\text{s}$; 65 °C: $3.63 \pm 0.35 \times 10^{-11} \text{ m}^2/\text{s}$). In the case of $^{22}\text{Na}^+$ similar diffusion parameters were obtained in all experiments. The K_d values were constant within the experimental errors. The obtained D_e or D_a values (apparent diffusion coefficient $D_a = D_e / \alpha$) are for all cells comparable (within experimental error). The presence of HA (cell 3) and an increase in temperature up to 60 °C (cell 4) had no significant effect on the diffusion of $^{22}\text{Na}^+$ in OPA.

In all diffusion experiments, stainless steel filter plates were used to confine the clay in the diffusion cell. The filters have retarding and sorption effects which can be important at the clay boundary. Since the amount of Np(V) sorbed on the filter plates was very low, the sorption effect is negligible and only the retardation effect of the filter was taken into account by introducing the diffusion coefficient (D_f) of Np(V) in the filter. The parameter D_f (m^2/s) can be estimated by $D_f = (D_w/10)$ [70], where D_w (m^2/s) is the diffusion coefficient of Np(V) in water (OPA pore water). Using the capillary method [71], D_w values of $^{237}\text{Np(V)}$ in OPA pore water in presence/absence of HA and at elevated temperature (60 °C) were determined to be $6.0 \pm 1.0 \times 10^{-10} \text{ m}^2/\text{s}$ in absence of HA, $7.0 \pm 1.0 \times 10^{-10} \text{ m}^2/\text{s}$ in presence of HA, and

$2.8 \pm 0.5 \times 10^{-9} \text{ m}^2/\text{s}$ at $60 \text{ }^\circ\text{C}$. These values were used for correcting the retardation effect of the filter plates in the in-diffusion experiment with Np(V).

The in-diffusion experiments with $^{237}\text{Np(V)}$ were started after the through- and out-diffusion studies of HTO had been completed (for cell 1 after HTO and $^{22}\text{Na}^+$ through- and out-diffusion). The Np(V) concentration in all diffusion experiments was $8 \times 10^{-6} \text{ M}$, the HA (M42) concentration was 10 mg/L , and the diffusion time was about 35 days. Figure 15 shows the concentration profile of $^{237}\text{Np(V)}$ and $^{22}\text{Na}^+$ in OPA of cell 1. The diffusion distance for $^{237}\text{Np(V)}$ and $^{22}\text{Na}^+$ were less than 1 mm in 35 days and 17 h, respectively.

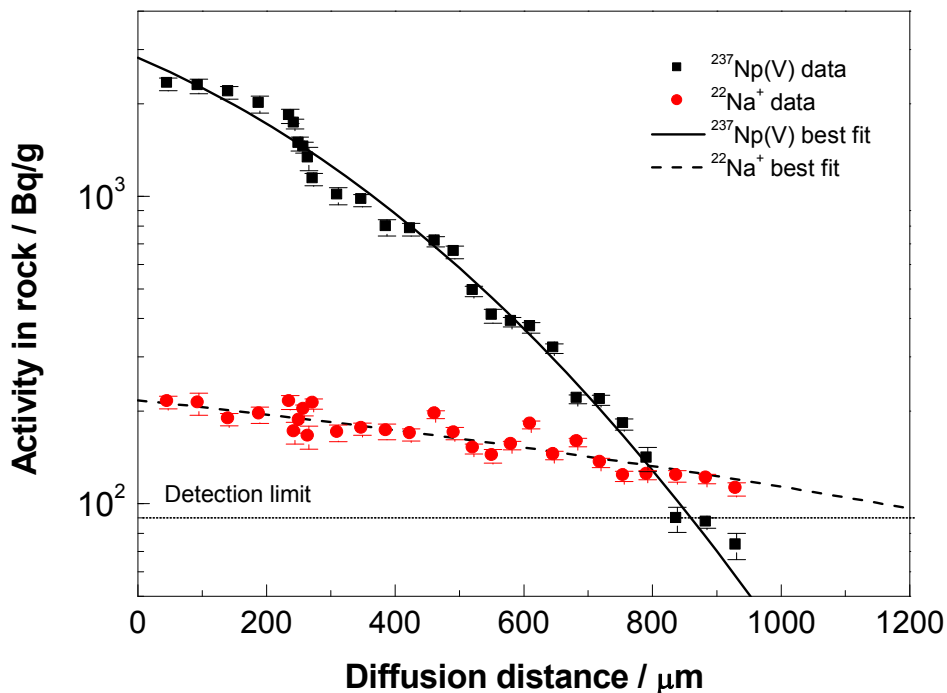


Figure 15: Diffusion profile of $8 \times 10^{-6} \text{ M } ^{237}\text{Np(V)}$ and $2 \times 10^{-10} \text{ M } ^{22}\text{Na}^+$ in OPA of cell 1 in OPA pore water under aerobic conditions.

The values for D_e and α were obtained by modeling the obtained data using our developed Mathematica code. The distribution ratio K_d was deduced by eq. 6, where ε was obtained from the through-diffusion experiment with HTO. In case of Np(V), α is mainly impacted by K_d due to the strong sorption of Np(V) on OPA. The quality of the parameters D_e and α is tested by using them as input parameters for the calculation of the radionuclide concentration in the high-concentration reservoir. Figure 16 shows for example the activity of $^{237}\text{Np(V)}$ in the source reservoir of cell 1 as a function of diffusion time.

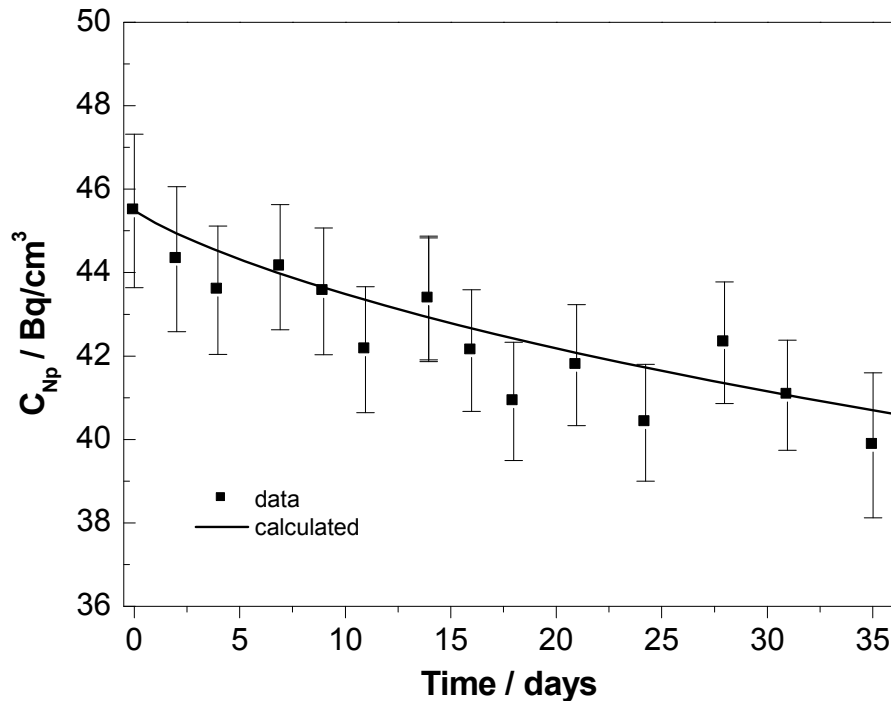


Figure 16: Concentration of $^{237}\text{Np(V)}$ in the source reservoir of cell 1 during in-diffusion.

As can be seen from Fig. 16, the calculated data for the Np(V) concentration in the high-concentration reservoir are in fairly good agreement with the experimental data. While Np(V) diffusion at room temperature (cells 1 and 2) could be fitted very well by the same evaluation procedure as described above, it was not possible to describe the data obtained at 60 °C well by the same model (black line in Fig. 17). It seems that the curve at 60 °C consists of two parts, one with slow diffusion at the beginning and a part of faster diffusion at distances > 500 μm . Using two fit curves (red lines) the experimental data can be better described. One possible explanation of this effect would be a change of Np speciation during diffusion in OPA. A temperature gradient within the clay can be excluded from the experimental conditions. Nevertheless, both fits result in K_d values that are at least five times smaller compared to the results of our batch experiments at 60 °C (see Tab. 13). To understand and explain this effect, further diffusion experiments are required.

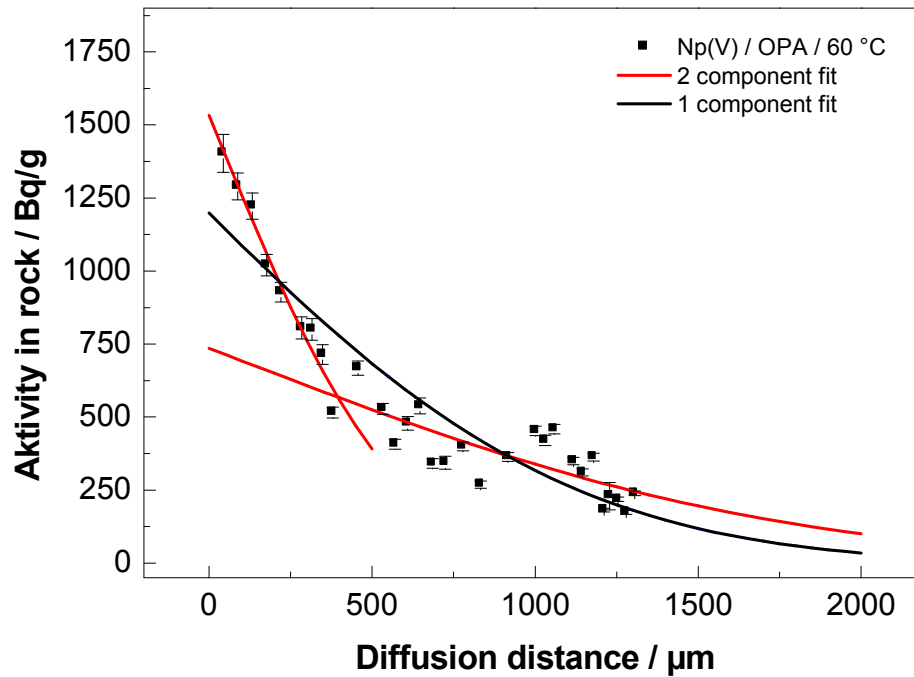


Figure 17: Diffusion profile of $8 \times 10^{-6} \text{ M } ^{237}\text{Np(V)}$ in OPA at $60 \text{ }^\circ\text{C}$ in OPA pore water under aerobic conditions (cell 4).

The obtained diffusion parameters for all in-diffusion experiments with Np(V) in absence (cell 1 and 2)/presence of HA (cell 3) at room temperature and at $60 \text{ }^\circ\text{C}$ (cell 4) are summarized in Tab. 12.

Table 12: Diffusion parameters for $8 \times 10^{-6} \text{ M } ^{237}\text{Np(V)}$ in OPA by in-diffusion experiments of cells 1 - 4.

Cell	Np(V)			
	α	$D_e / (\times 10^{-11} \text{ m}^2/\text{s})$	$D_a / (\times 10^{-13} \text{ m}^2/\text{s})$	$K_d / \text{m}^3/\text{kg}$
1 ^[28]	243 ± 4	0.7 ± 0.1	2.8 ± 0.1	0.10 ± 0.01
2	110 ± 3	2.3 ± 0.2	2.1 ± 0.2	0.049 ± 0.003
3 ^c	78 ± 2	1.5 ± 0.1	1.9 ± 0.1	0.032 ± 0.002
4	48 ± 2^a	1.0 ± 0.1^a	2.1 ± 0.2^a	0.019 ± 0.001^a
	69 ± 2^b	0.2 ± 0.02^b	0.30 ± 0.03^b	0.029 ± 0.002^b
	34 ± 2^b	1.0 ± 0.07^b	2.9 ± 0.2^b	0.014 ± 0.001^b

^a Values obtained from 1 component fit, ^b values obtained from 2 component fit, and ^c presence of HA

As can be seen from Tab. 12, the K_d and D_a values obtained for Np diffusion in the presence of HA (cell 3) are slightly decreased compared to experiments in the absence of HA (cells 1 and 2). However, the α value in case of cell 3 is by about 30% lower. D_a values for cells 2 - 4 are similar within experimental errors (considering only the values obtained from 1 component fit for cell 4 at 60 °C). In contrast to batch experiments, the K_d values obtained from diffusion experiment decreased with increasing temperature. This trend was also shown by in-diffusion studies in compacted montmorillonite [72]. The difference between cell 1 and 2 in the obtained diffusion parameters, which are both performed only with Np(V), can be explained by the usage of two different OPA batches (cell 1: BAE 25/10, cell 2: BLT 14) and the lower porosity of OPA in the cell 1.

The K_d value of $0.10 \pm 0.01 \text{ m}^3/\text{kg}$ obtained by the in-diffusion experiment of cell 1 in intact OPA is four times the value of $0.025 \pm 0.005 \text{ m}^3/\text{kg}$ obtained by batch experiments using OPA suspensions. A possible reason for this difference could be that two different OPA batches BHE 24/1 and BAE 25/10 were used in batch and diffusion experiments, respectively. In addition, a small part of Np(V) could be reduced to Np(IV) after diffusion into the intact clay (see Sect. 4.3).

To better compare the diffusion results of cells 2 - 4, three new batch experiments with the same OPA batch (BLT 14) were performed. Therefore, one cylinder of OPA batch BLT 14 was pulverized and sieved to a particle size of less than 150 μm . This powder was used for batch experiments with $8 \times 10^{-6} \text{ M}$ Np(V) under aerobic conditions in OPA pore water (pH = 7.6) at room temperature, 60 °C, and in the presence of HA (M42). In the sorption experiments, the S/L ratio was varied between 2 and 20 g/L. The results of the batch experiments performed at room temperature, 60 °C, and in the presence of HA (M42) in comparison to the diffusion results are shown in Tab. 13.

Table 13: Averaged K_d values for the sorption of $8 \times 10^{-6} \text{ M}$ Np(V) on OPA (BLT 14, S/L ratio of 2 - 20 g/L) in OPA pore water as a function of temperature and HA under aerobic conditions in comparison to diffusion results.

Cell	Averaged $K_d / \text{m}^3/\text{kg}$	
	Batch exp.	Diffusion exp.
2	0.034 ± 0.010	0.049 ± 0.003
3	0.023 ± 0.002	0.032 ± 0.002
4	0.157 ± 0.052	0.019 ± 0.001

As shown from Tab. 13, slightly lower K_d values were obtained for cell 2 and 3 in the case of batch experiments in comparison to the related diffusion experiments. In contrast to diffusion experiment, the K_d value for the OPA suspension increased significantly with increasing temperature (endothermic process). HA causes a slight mobilization of Np(V), which, however lies in the range of experimental error. Therefore, it can be concluded that the interaction mechanisms between Np(V) and OPA during sorption and diffusion are significantly different, pointing out that the processes that determine the endothermic behavior in batch experiments are almost not relevant in diffusion experiments. With respect to the safety assessment of a nuclear waste repository, the usage of sorption data would lead to an overestimation of Np(V) uptake by OPA at 60 °C, while room temperature data seem to be sufficient for conservative estimates.

4.3 Speciation experiments

4.3.1 XAS, μ -XAS, μ -XRF, and μ -XRD

The uptake mechanism of Np and Pu by OPA as a function of different chemical parameters such as pH, metal concentration, S/L ratio, background electrolyte, and presence/absence of HA was studied by micro-spectroscopic investigations using synchrotron based X-ray techniques such as μ -XAS, μ -XRF, and μ -XRD. These methods have been used to determine the speciation of Np and Pu on OPA after sorption and diffusion processes. The spatially resolved investigations were complemented by EXAFS measurements of wet and dried powder samples from batch experiments to determine the structural parameters of the near neighbour environment of sorbed Np or Pu on the OPA surface. In the literature, there is no information regarding XAS, μ -XAS, μ -XRF, and μ -XRD studies of Np or Pu sorption on OPA. Until now, only few speciation studies of Np and Pu sorption on natural clays were performed. Duff et al. studied Pu sorption on tuff by μ -XRF and μ -XANES [73, 74].

XAS measurements of Np

The sorption of Np(V) on OPA has been investigated as a function of pH in the absence/presence of HA (M42) or dissolved FeCl₂ in different background electrolytes such as 0.1 M NaClO₄ (pH 8.5), OPA pore water (pH = 7.6), and saturated calcite solution (pH = 8.5) under aerobic and anaerobic conditions. Samples were prepared with a total ²³⁷Np(V) concentration of 8×10^{-6} M, S/L ratio of 15 g/L, 10 mg/L HA (M42), 1×10^{-3} M FeCl₂. The Np L_{III}-edge

(17630 eV) EXAFS data were collected in fluorescence mode at room and low temperatures (about 15 K) at the Rossendorf beamline ROBL [31] at ESRF using a 13-element Ge solid state detector. Table 14 shows an overview of the measured XAFS samples.

Table 14: Details of the Np samples measured by XAS.

Sample	OPA / (CO ₂ /Ar) ^a	pH	Electrolyte	OPA batch	HA	Np loading ppm	State ^c	Temp.	Transport
1	aerobic/CO ₂	8.5	sat. CaCO ₃ solution	BHE 24/1	-	91	WP	RT	under air
2	anaerobic/CO ₂ ^b	8.5	sat. CaCO ₃ solution	BDR 2	-	109	WP	RT	
3	aerobic/CO ₂	8.5	0.1 M NaClO ₄	BHE 24/1	-	108	WP	RT	
4	anaerobic/Ar	8.5	0.1 M NaClO ₄	BDR 2	-	121	WP	RT	
5	aerobic/Ar	8.5	0.1 M NaClO ₄	BHE 24/1	-	110	WP	RT	
6	anaerobic/Ar	7.6	pore water	BDR 2	-	52	WP	RT	
7	aerobic/CO ₂	8.5	sat. CaCO ₃ solution	BHE 24/1	yes	93	WP	RT	anaerobic jar filled with Ar
8	anaerobic/Ar	8.5	sat. CaCO ₃ solution	BHE 24/2	yes	94	WP	RT	
9	anaerobic/Ar	8.5	sat. CaCO ₃ solution	BHE 24/2	-	105	P	15 K	
10	anaerobic/Ar	7.6	pore water	BHE 24/2	-	43	P	15 K	
11	anaerobic/Ar	8.5	0.1 M NaClO ₄ + 10 ⁻³ M FeCl ₂	BHE 24/2	-	267	P	15 K	Voyageur 12 filled with LN ₂
12	anaerobic/Ar	8.5	0.1 M NaClO ₄	BHE 24/2	-	151	P	15 K	
13	anaerobic/Ar	8.5	sat. CaCO ₃ solution	BHE 24/2	-	101	P	15 K	
14	anaerobic/Ar	7.6	pore water	BHE 24/2	-	57	P	15 K	

^a CO₂: pCO₂ = 10^{-3.5} atm, ^b CO₂: pCO₂ = 10^{-2.3} atm, ^c WP: wet paste, P: powder, RT: room temperature

Figure 18 shows the raw Np L_{III}-edge k³-weighted EXAFS data, the fit with the best theoretical model, and the corresponding Fourier transform magnitudes (FT) of samples 1 - 6. All FTs are uncorrected for scattering phase shifts (R + Δ), causing peaks to appear at shorter distances.

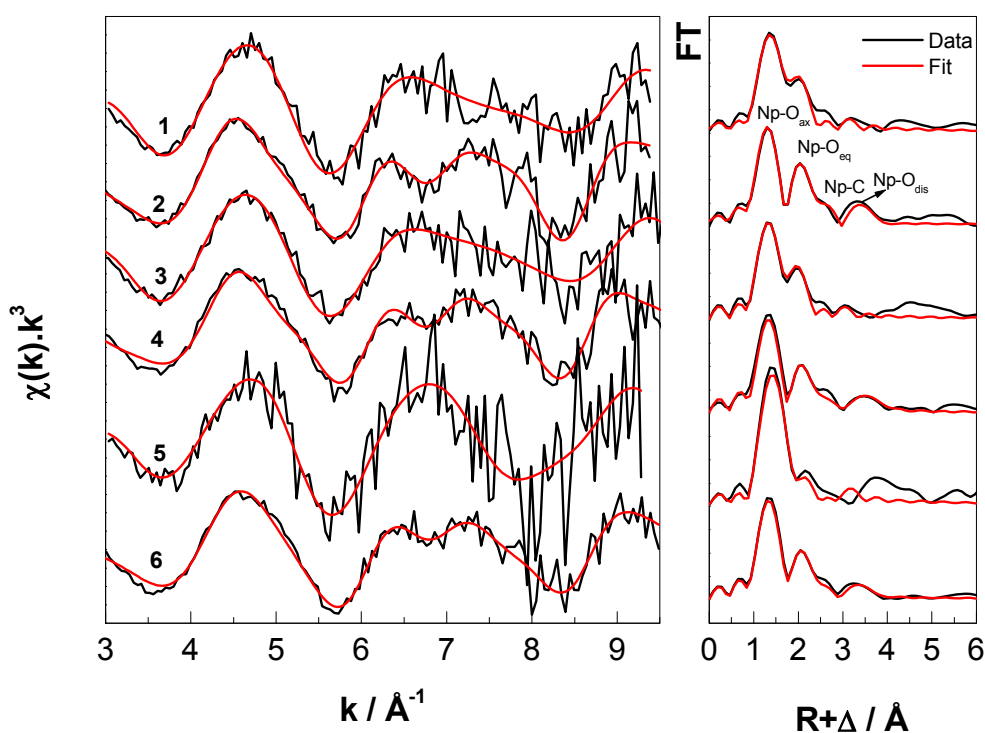


Figure 18: Np L_{III}-edge k^3 -weighted EXAFS spectra (left) and the corresponding Fourier transform magnitudes (right) of samples 1 - 6.

As can be seen from Fig. 18, samples 2, 4, and 6 of anaerobic OPA prepared under anaerobic conditions in different background electrolytes show similar EXAFS spectra and have different EXAFS pattern compared to samples 1, 3, 5 of aerobic OPA. They show a double oscillation structure between k 6 - 8 \AA^{-1} , which is a characteristic for carbonate species. The Fourier transform spectra of samples 2, 4, and 6 show four coordination shells at 1.83 \AA , 2.52 \AA , 2.98 \AA , and 4.25 \AA , which are related to Np-O_{ax} axial, Np-O_{eq} equatorial, Np-C, and Np-O_{dis} distal (distal oxygen atom of the CO₃²⁻ group), respectively. In the samples 1, 3, 5 only two coordination shells were observed (Np-O_{ax} and Np-O_{eq}). Table 15 summarizes the structural parameters derived from the EXAFS fits. The average Np-O_{eq} bond distance of samples 1, 3 and 5 is somewhat shorter than in the Np(V) aquo ion [75]. This could indicate inner-sphere sorption of a Np(V) at the OPA surface. The neptunium coordination shells and bond distances of samples 2, 4, and 6 are consistent with the formation of a Np(V) carbonate species at the OPA surface [76], which is also in good agreement with our previous result for Np(V) sorption on kaolinite [77].

In all samples, the obtained distances of both Np-O_{ax} and Np-O_{eq} indicate that the pentavalent oxidation state of Np was dominant. The reduction of Np(V) to Np(IV) under anaerobic conditions could not be confirmed (possible oxidation during transportation).

Table 15: EXAFS structural parameters for the Np samples 1 – 6 in Tab. 14.

Sample	2x O _{ax}	5x O _{eq}	C ^d		O _{dis}		$\Delta E_0 /$ eV	red. error
	R / Å	R / Å	N	R / Å	N	R / Å		
1	1.85	2.46					- 8.1	0.64
2	1.83	2.52	2.4	2.98	2.4	4.25	- 8.9	0.51
3	1.83	2.45					- 10.3	0.87
4	1.85	2.54	2.5	3.00	2.5	4.26	- 6.6	0.38
5	1.86	2.41					- 9.2	3.60
6	1.85	2.51	1.9	3.00	1.9	4.24	- 9.5	0.33
NpO ₂ (H ₂ O) ₄ ⁺ [75]	1.82	2.49						
NpO ₂ (CO ₃) ₃ ⁵⁻ [76]	1.86	2.53	2.7	2.98	3.0	4.22		

During fit the coordination numbers for O_{ax}, and O_{eq} were held constant and the coordination numbers for C and O_{dis}, were linked together and adjusted as one parameter. The average value of the Debye-Waller factors σ^2 for O_{ax}, O_{eq}, and O_{dis} were 0.0026 Å², 0.011 Å², and 0.008 Å², respectively. Debye-Waller factor σ^2 for C was held constant at 0.003 Å².

Using an iterative transformation factor analysis (ITFA) method [40], the oxidation state of Np in the measured XANES spectra was checked and the amount of Np(IV) to Np(V) in each spectrum was determined and compared to reference spectra of Np(IV) and Np(V) taken from [75]. In case of a mixture of Np(IV) and Np(V), the percentage of both oxidation states was taken into account in the fitting of the related EXAFS spectra. The amount of Np(IV) in samples 1 - 6 was less than 14% (due to data quality the error can be estimated to about $\pm 10\%$) and therefore, the reduction of Np(V) to Np(IV) was not considered. Samples 7 - 10 were transported in an anaerobic transport container filled with Ar gas. Samples 11 – 14 were shock frozen and transported in a liquid nitrogen dewar. By using these two transport options, the reduction of Np(V) to Np(IV) in most of the samples (7 - 12) was clearly observed as can be seen in Tab. 16.

Table 16: Amount of Np(IV) and Np(V) in EXAFS samples 7 - 14 determined using ITFA [40].

Sample	Np(IV) / %^a	Np(V) / %^a
7	25	75
8	38	62
9	47	53
10	49	51
11	64	36
12	18	82
13	11	89
14	9	91

^a Error value from ITFA is about 10%

As shown in Tab. 16, the reduction of Np(V) to Np(IV) was most significant in samples 8 - 11 under anaerobic conditions, independent of the background electrolyte or presence of HA. In the presence of solvated FeCl₂ (sample 11), the maximum amount of Np(IV) was reached (64%). EXAFS spectra of samples 7 - 10 together with the best fit to the data and their corresponding Fourier transform magnitudes are shown in Fig. 19.

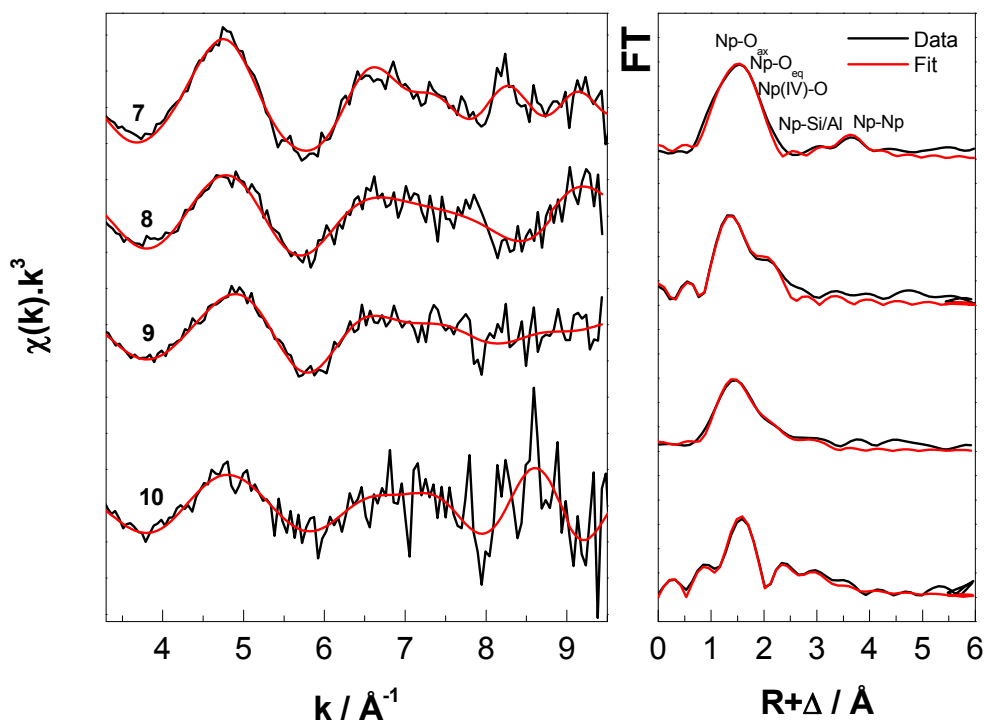


Figure 19: Np L_{III} -edge k^3 -weighted EXAFS spectra (left) and the corresponding Fourier transform magnitudes (right) of samples 7-10.

Samples 7 and 8, which were prepared in presence of HA under aerobic and anaerobic conditions, respectively, show similar EXAFS pattern with minor differences. In both cases, the structural parameters derived from the EXAFS fits show three coordination shells Np-O_{ax}, Np-O_{eq}, and Np(IV)-O at distances about 1.80 Å, 2.45 Å, 2.27 Å, respectively. One additional peak at about 3.84 Å was observed in sample 7 (above the noise level), which can be assigned to Np-Np interaction. The Np(IV)-O distance at about 2.27 Å is in good agreement with the characteristic distance of Np(IV) [78]. Similar Np-O distances as for samples 7 and 8 were found for sample 9 with an additional Np-Si/Al coordination shell at distances of 3.19 Å. The obtained Np-O and Np-Al/Si distances for sample 10 were at 1.78 Å (Np-O_{ax}), 2.60 Å (Np-O_{eq}), 2.32 Å (Np(IV)-O), and 3.28 Å/3.55 Å (Np-Al/Si). EXAFS spectra of samples 11 - 14 are presented in Fig. 20 together with the corresponding Fourier transform magnitudes.

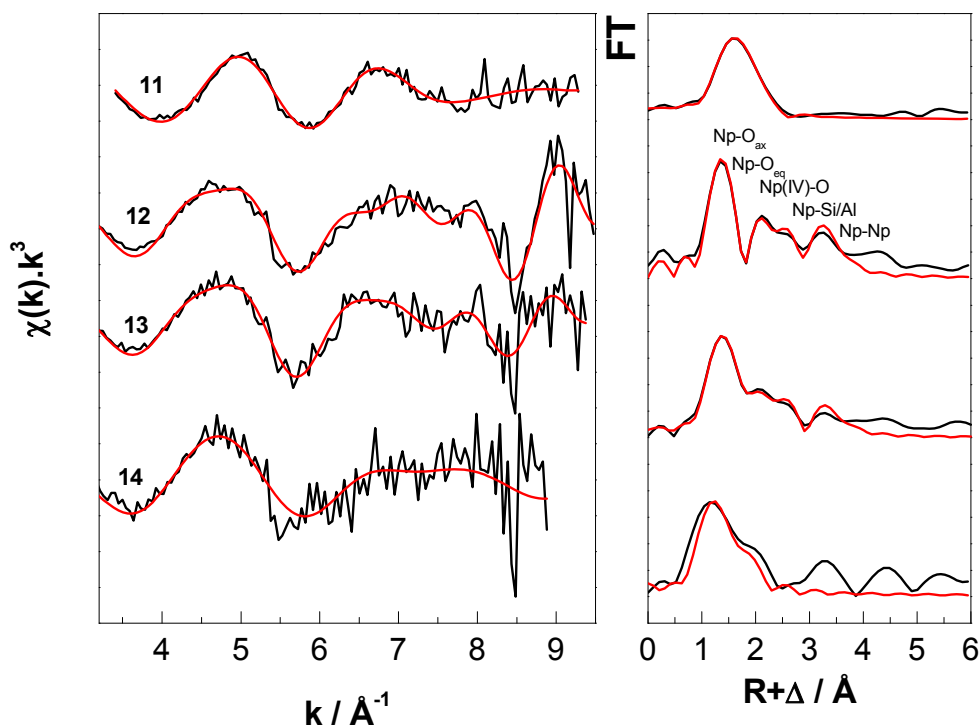


Figure 20: Np L_{III} -edge k^3 -weighted EXAFS spectra (left) and the corresponding Fourier transform magnitudes (right) of samples 11 - 14.

Unfortunately, all four EXAFS spectra show a poor signal-to-noise ratio compared to the previous samples. These spectra were collected using 6-bunch mode (max. current 80 mA), where previous samples were collected using 7/8 multi-bunch operation mode (max. current 200 mA). Due to the addition of solvated FeCl_2 in sample 11, the reduction of Np was confirmed with 64% of Np(IV) (see Tab. 16). Three Np-O coordination shells at 1.85 Å, 2.41 Å, 2.21 Å were obtained from the EXAFS measurements of sample 11. Similar distances were obtained for samples 12 and 13 with an additional Np-Np coordination shell at about 3.55 Å. In samples 11 - 13 a Np-Al/Si interaction at about 3.14 Å was also observed. However, this Np-Np coordination shell did not improve the reduced error of the fit significantly. According to the lower beam intensity and lower Np loading (57 ppm) of sample 14, it was only possible to analyze the Np-O_{ax} and Np-O_{eq} coordination shells of this sample. Finally, from all EXAFS results, we can conclude that under both aerobic and anaerobic conditions a partial reduction of Np(V) to Np(IV) occurred, clearly pronounced under anaerobic conditions as well as in the presence of solvated FeCl_2 . HA and background electrolyte had not influence on the Np speciation on OPA. Formation of Np carbonate

species at the OPA surface was detected under anaerobic conditions, probably due to the increase of CO₂ partial pressure. Formation of Np polynuclear species was detected in some anaerobic samples, in which Np(IV) was detected.

μ-XAS, μ-XRF, and μ-XRD measurements of Np(V)

By EXAFS measurements on bulk samples, it was possible to determine the structural parameters of Np sorbed on OPA as a function of several chemical parameters. However, these EXAFS investigations provide only an average over all Np species present in the sample. Microscopic techniques may allow a more selective approach for the speciation. Using μ-XAS and μ-XRF analysis one can attain information on elemental correlations and the distribution of contaminant. Therefore, these techniques are well suited to study heterogeneous materials such as OPA. By using μ-XRD it is also possible to identify crystalline mineral phases within a complex mixture on a micro scale. In this study, the uptake of Np by OPA was investigated by a combination of these synchrotron based methods. As already mentioned, all investigations were performed at the MicroXAS beamline at SLS. The elemental distributions of Np and other elements (e.g., Fe, Ca) of this heterogeneous natural sorbent were determined by μ-XRF mapping. The distribution of mineral phases near Np enrichments (hot spots) was investigated using μ-XRD. Np hot spots located on the samples were analyzed by μ-XANES to determine its oxidation state after uptake or diffusion processes. An overview of all Np samples measured at SLS is shown in Tab. 17.

Table 17: Details of the Np samples measured at SLS.

Sample	Preparation	Activity Bq	Np loading ng/mm²
1	deposition of 8×10^{-6} M ²³⁷ Np(V) on OPA thin section under aerobic conditions	107	96
2		823	792
3		2379	1389
4		118	69
5	sorption of 8×10^{-6} M ²³⁷ Np(V) on OPA under anaerobic conditions	11	22
6	diffusion of 8×10^{-6} M Np(V) in an intact OPA bore core under aerobic condition	86	-

The Np loading in all samples was between 96 ng/mm² and 1389 ng/mm². For the diffusion sample it was not possible to determine the Np concentration on the surface due to the shape of this massive piece of clay. The focus will primarily be put on samples 1, 3, and 6 as representatives for other measured samples.

Figure 21 shows a $\approx 500 \times 500 \mu\text{m}$ mapping of sample 1 measured by μ -XRF and electron microprobe. The Fe mapping was measured by both methods with good statistics and therefore chosen to align both measurements. Slight differences in the signal intensity can probably be a result of topographic differences on the sample due to swelling of the clay when contacted with Np solution. As can be seen from Fig. 21, Fe and Np are distributed heterogeneously on the thin section and several spots of Fe and Np enrichments are present. The interference between Np (L_{α}) and Sr (K_{α}) was considered, since Sr is present in OPA with a concentration of up to 235 ppm [16]. For verification of Np, the Np- L_{III} edge absorption spectrum of the interested spot was measured below 17550 eV and at an energy of 17630 eV. Due to the high-energy used by μ -XRF analysis, it was not possible to measure the lighter elements such as Al and Si contained in OPA simultaneously with Np and Fe. Furthermore, it was also not possible to perform any μ -XRD measurements on the areas of interest to get further information about the mineralogical environment of Np due to high impurities in the standard glass object slides used for the preparation of sample 1. Therefore, only electron microprobe analysis was done in sample 1 to determine the distributions of Al, Si, Ca, Na, and Ti (see Fig. 21). While Al and Si are present on the whole sample as it can be expected, based on the mineral composition of OPA, the mappings of Ca and Fe show certain hot spots, probably calcite and siderite/pyrite, respectively. The Fe distribution determined by both μ -XRF and microprobe analysis fit very well and were used to identify the areas measured by μ -XRF.

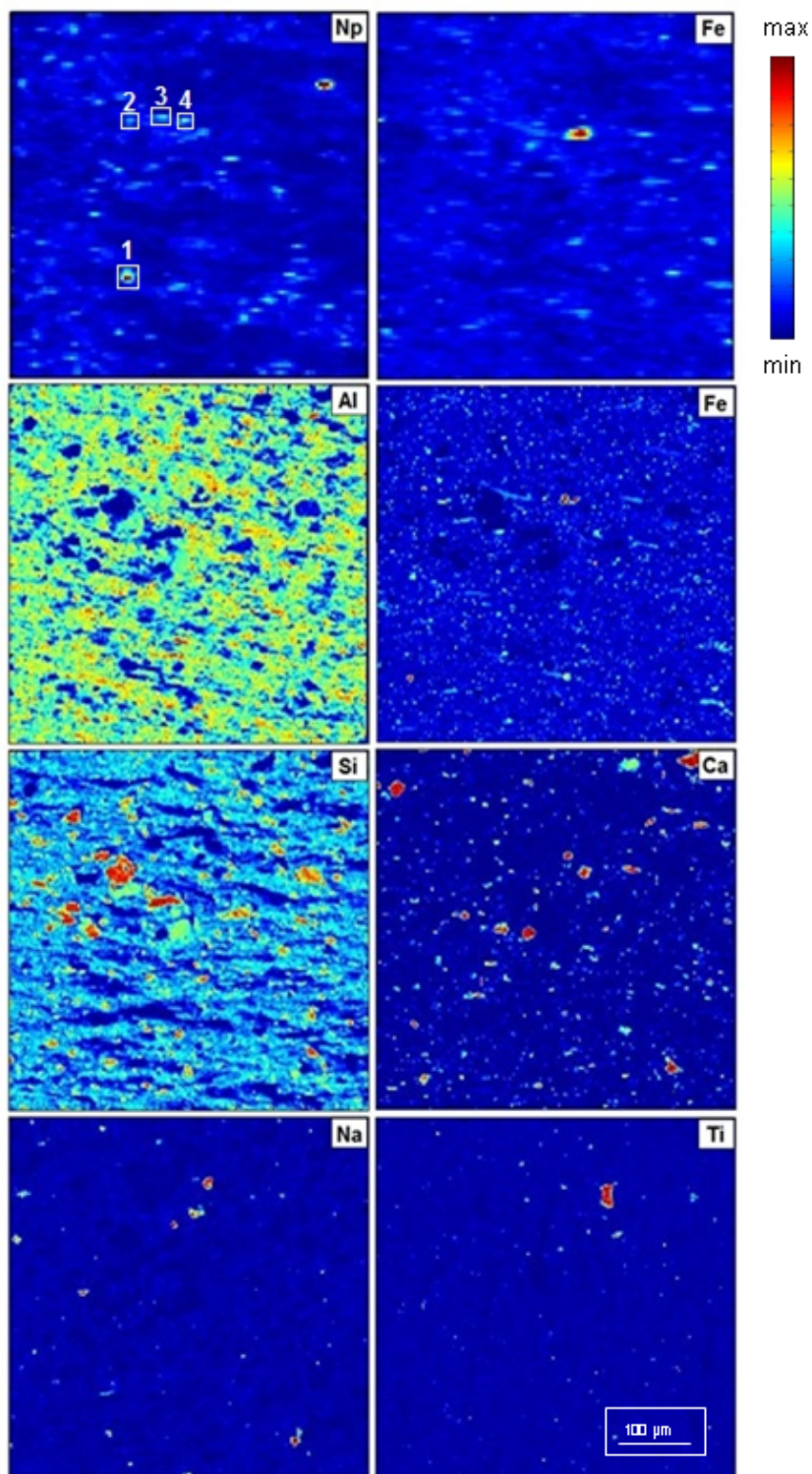


Figure 21: μ -XRF mappings ($\approx 500 \times 500 \mu\text{m}$, step size: $5 \mu\text{m}$) of Fe and Np (two upper mappings) compared to electron microprobe measurements (step size: $2.5 \mu\text{m}$) of Al, Fe, Si, Ca, Na, and Ti. XANES spectra were recorded at spots 1 – 4 (Fig. 22).

Four Np hot spots on sample 1, whose positions are marked in Fig. 21, were selected and measured by μ -XANES (see Fig 22). Using ITFA [40] normalized XANES spectra were compared to reference spectra of Np(IV) and Np(V) [75] and their amounts were determined.

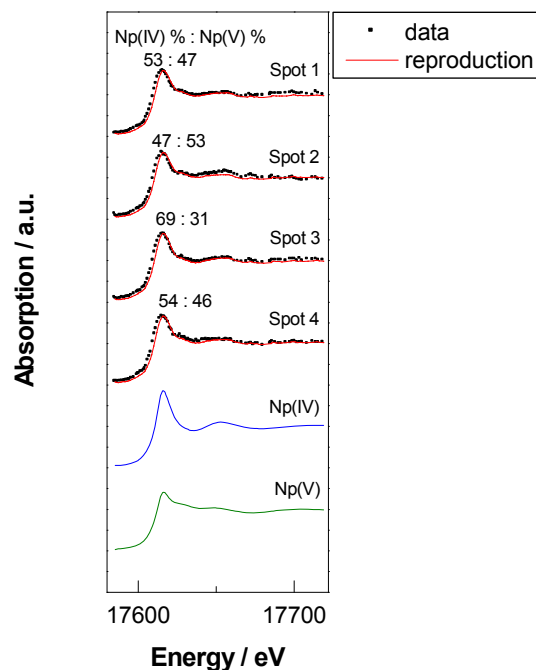


Figure 22: Normalized Np L_{III} -edge XANES spectra measured on spots 1 - 4 marked in Fig. 21 together with the reproductions from IFTA using reference spectra of Np(IV) and Np(V).

A mixture of Np(IV) and Np(V) was found in all XANES spectra. The amount of Np(IV) was determined by IFTA and was between 47% and 69%, although the experiment was carried out under aerobic condition. Np(V) has been partly reduced to Np(IV), probably by iron(II) bearing minerals contained in OPA. μ -XRF measurements (Fig. 21) do not show a clear correlation between Np and other measured elements. This correlation was also not confirmed by scatter plots (not shown) using the program XY-MAP display [79]. The fact that spots of Np(IV) are not located directly on Fe hot spots may be explained by the short contact time between Np and Fe during sample preparation. At high Np concentration as in sample 3 (10 times more than in sample 1), it was also not possible to see any correlations between the measured elements. Np was distributed homogeneously on the whole sample surface. Additionally, Np(V) was the dominating species on OPA. In both samples the precipitation of Np on the OPA thin sections during evaporation cannot be excluded. To prevent any Np precipitation during sample preparation, a thin section (sample 5) was prepared using a sorption cell under anaerobic conditions. High purity quartz glass object slides (Heraeus Holding GmbH, Hanau, Germany) were used to eliminate any impurities and allow us to perform μ -XRD investigations. Unfortunately, under aerobic conditions the sorption of Np on

OPA thin section was very low and it was not possible to measure this sample. For sample 5, which was prepared under anaerobic condition, the Np loading was sufficient (22 ng/mm^2) for the measurements and several Np hot spots were detected (see Fig. 23). As can be seen in the upper right corner of the Np and Fe mappings in Fig. 23, a clear correlation between Np and Fe can be found. Two points from this mapping were selected to study the speciation of Np.

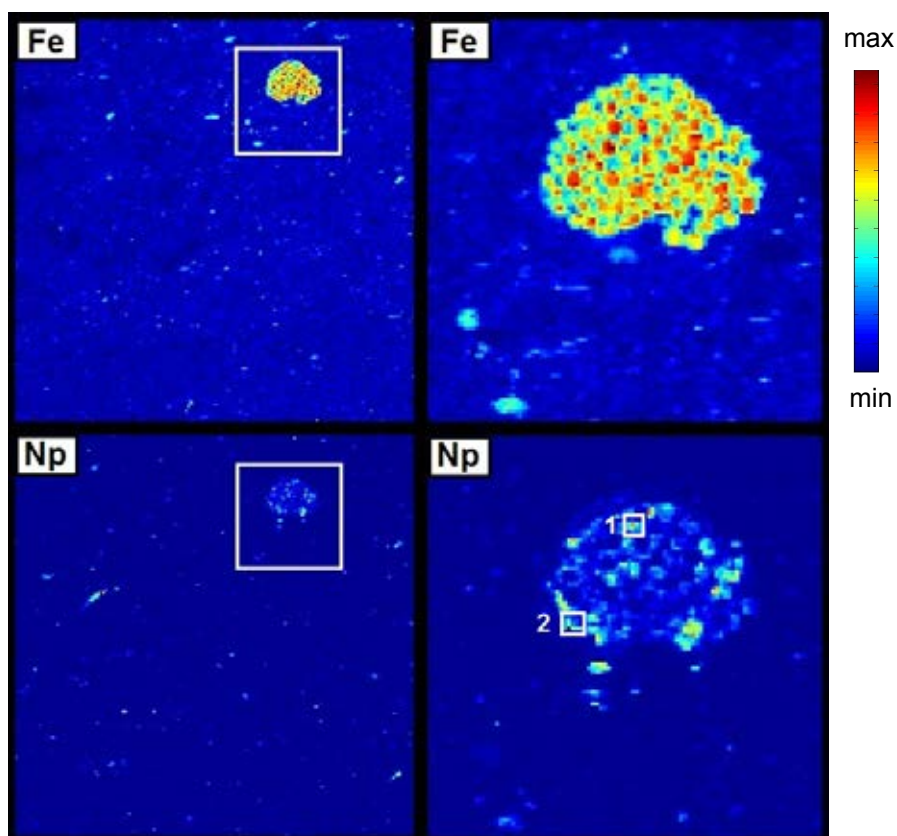


Figure 23: Left: μ -XRF mappings ($2 \times 2 \text{ mm}$, step size: $10 \mu\text{m}$) of Fe and Np of an anaerobic sample prepared by sorption of $8 \times 10^{-6} \text{ M } ^{237}\text{Np}$ on OPA thin section. Right: Same element distributions for $500 \times 500 \mu\text{m}$ mappings (step size $1 \mu\text{m}$). XANES spectra were recorded at spots 1 and 2 (Fig. 24).

Figure 24 show the normalized XANES spectra of spots 1 and 2 of sample 5 with the percentages of Np(IV) and Np(V) determined by ITFA.

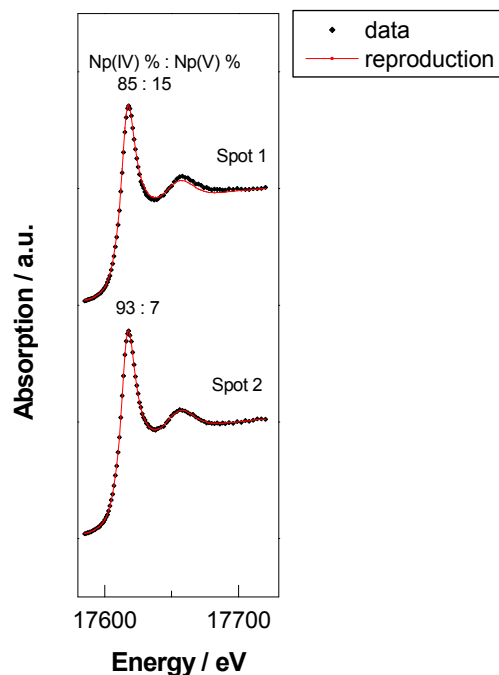


Figure 24: Normalized Np L_{III} -edge XANES spectra measured on spots 1 and 2 marked in Fig. 23 together with the reproductions from IFTA using reference spectra of Np(IV) and Np(V).

The measured XANES spectra of spots 1 and 2 of sample 5 show a similar near-edge structure, which is different from the spectra of spots 1 - 4 in sample 1 prepared under aerobic condition (see Fig. 22). The spectra of sample 1 show a broader adsorption peak and the characteristic Np(V) shoulder. Sample 5, which was prepared under anaerobic condition, shows an almost quantitative reduction of Np(V) to Np(IV) ($\text{Np(IV)} \geq 85\%$). The μ -XRF distribution mappings show clearly that Np reduction has occurred near the iron bearing mineral contained in OPA. To determine which iron mineral is responsible for this reduction, μ -XRD measurements were performed at spots 1 and 2. The collected XRD images (Fig. 25) at each point were analyzed using the program Area Diffraction Machine [41] and compared to the diffraction patterns of different iron bearing minerals. As can be seen from Fig 25, the collected diffraction images of spots 1 and 2 agree well with XRD pattern of pyrite (circles), which is present to about 1 - 3% in OPA [3]. Pyrite appears to be one of the redox-active mineral phases in OPA, which determine the Np speciation after the sorption process.

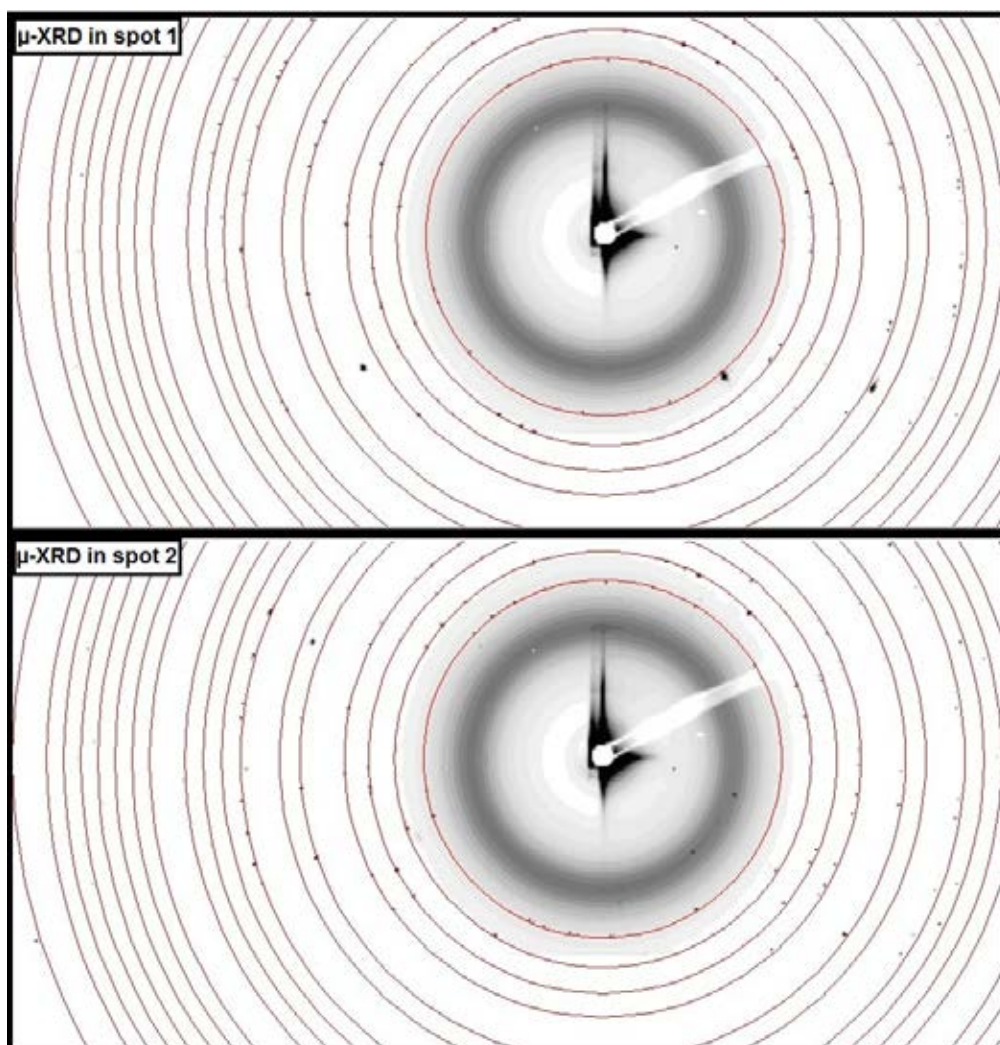


Figure 25: μ -XRD images ($20 \times 20 \mu\text{m}$, step size: $1 \mu\text{m}$, $E = 17700 \text{ eV}$) of spots 1 and 2 presented in the μ -XRF mapping of sample 5 (Fig. 23). μ -XRD patterns of pyrite are shown as circles.

To investigate the Np speciation on OPA after diffusion, sample 6 was prepared from an intact OPA bore core that was contacted with $8 \times 10^{-6} \text{ M } ^{237}\text{Np}$ in OPA pore water ($\text{pH} = 7.6$) for more than one month. Figure 26 show the element distributions of Ca, Fe, and Np on this sample.

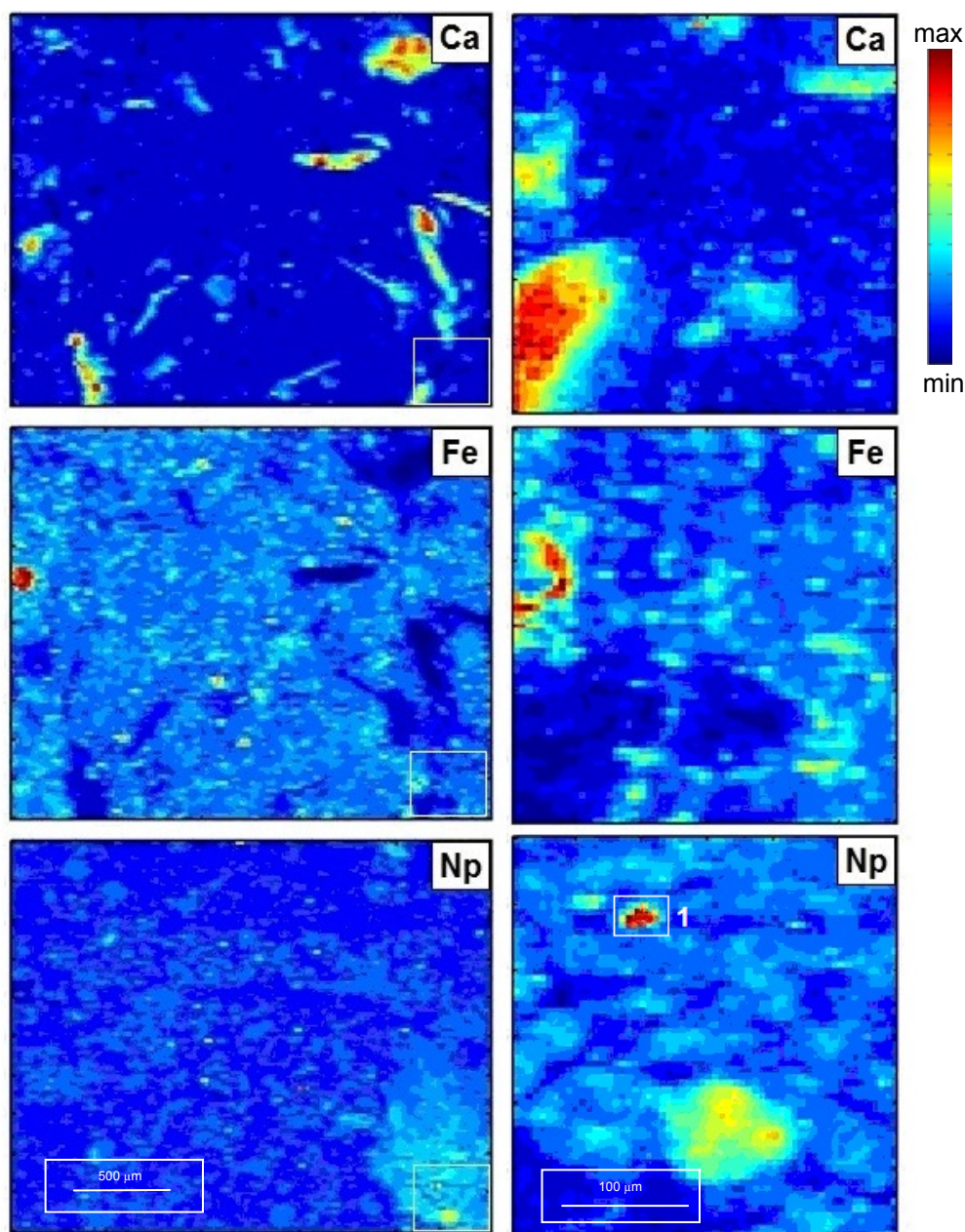


Figure 26: Left: μ -XRF mappings (2.0×2.5 mm, step size: $20 \mu\text{m}$) of Ca, Fe, and Np of an aerobic sample prepared from in an intact OPA bore core after diffusion of $8 \times 10^{-6} \text{ M } ^{237}\text{Np}$ for one month. Right: Same element distributions for $300 \times 300 \mu\text{m}$ mapping (step size $5 \mu\text{m}$). A XANES spectrum was recorded at spot 1 (Fig. 28).

Due to lower Np loading in the diffusion sample and the sample was not strongly shielded as in the case of the other samples, higher Ca concentrations with several Ca hot spots were observed. Iron was homogeneously distributed in the sample with very high concentration (10^5 counts, perhaps from the stainless steel filter used in diffusion experiment) and only few hot spots were detected. In case of Np, areas with slightly elevated Np concentrations can be

found on the lower right region of the mapping (see Fig. 26). Using XY Display program [79], tri-color (red-blue-green) mappings of Ca, Fe, and Np in the diffusion sample are presented in Fig. 27.

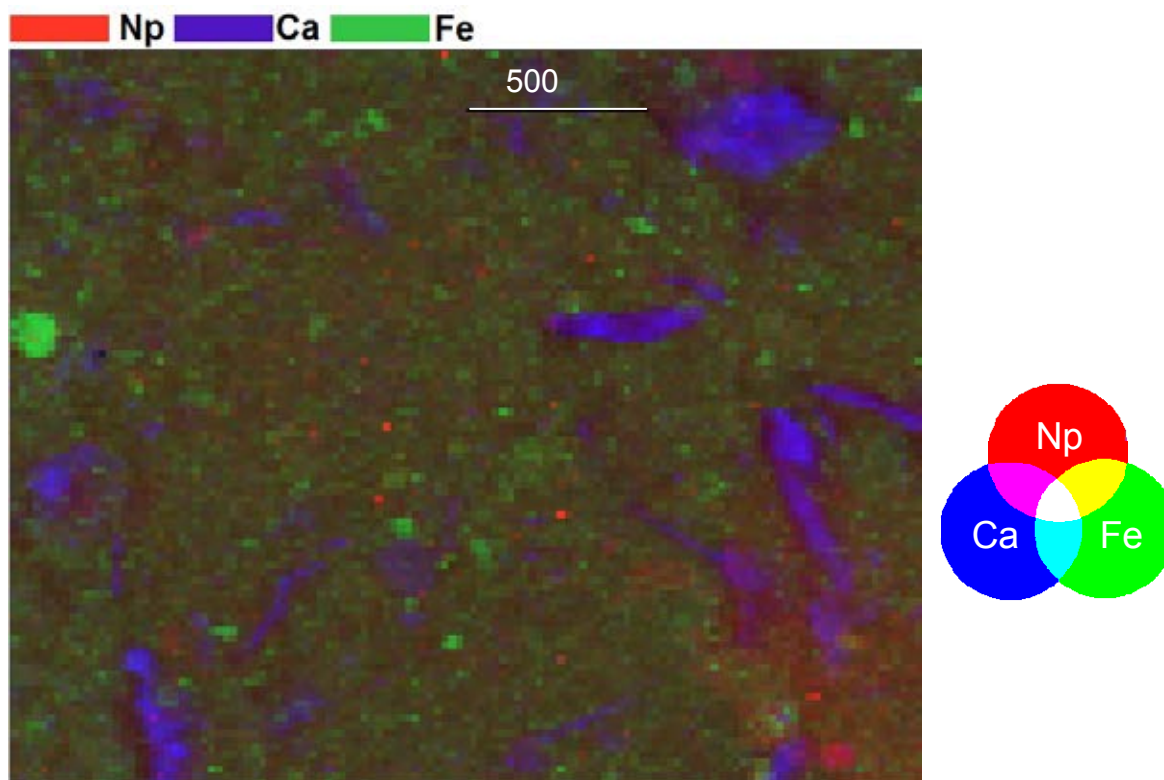


Figure 27: Tri-color mapping of the distributions of Ca, Fe, and Np in the diffusion sample from μ -XRF mapping in Fig. 26 (left).

This tri-color μ -XRF mapping indicates that Ca, Fe, and Np are distributed heterogeneously throughout the sample. The pure green, blue, and red colours of the Fe-, Ca- and Np-rich areas indicate that these elements are segregated. Ca and Fe hot spots are not associated with Np show up as numerous areas in blue and green colors. The correlation between Np, Fe, and Ca was also not confirmed by a scatter plot.

μ -XANES measurement on the Np hot spot selected in Fig. 26 (right) showed that Np(IV) is the dominating species (Fig. 28) with an amount of 82% as determined by ITFA.

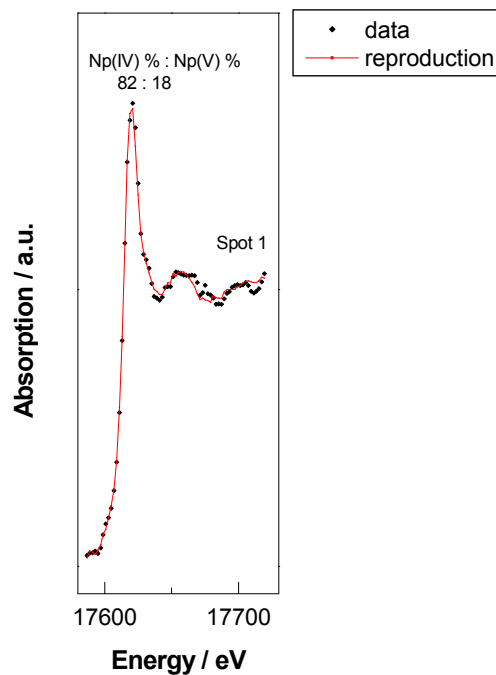


Figure 28: Normalized Np L_{III} -edge XANES spectrum measured on spot 1 marked in Fig. 26 together with the reproduction from IFTA using reference spectra of Np(IV) and Np(V).

Because the diffusion sample was a thick one (not a thin section), it was not possible to perform μ -XRD measurements at the Np hot spot.

As conclusion, from spectroscopic investigations with synchrotron based techniques, it was possible to determine the elemental distributions of Ca, Fe, and Np in OPA samples prepared from sorption and diffusion experiments by using μ -XRF analysis. μ -XANES investigations on Np hot spots of thin sections and diffusion samples showed that Np(V) is partly reduced to Np(IV) under both aerobic and anaerobic conditions. The reduction was more pronounced under anaerobic condition and in diffusion experiments. These results are in good agreement with our previous diffusion [28] and sorption [16] investigations. Furthermore, μ -XRD data confirm that pyrite is one of the redox-active mineral phases of OPA determining the speciation of Np after uptake on OPA. This indicates that the reduction process takes place on the OPA surface and not in solution. With respect to the assessment of the long-term safety of a nuclear waste repository, even if Np(V) is formed in the near field of the storage containers, the reduction to Np(IV) by OPA will immobilize Np and thus prevent its transport to the far field, showing OPA as a suitable host rock.

XAS measurements of Pu

The sorption of Pu on OPA has been investigated by XAS as a function of pH, Pu oxidation state (III, IV, V, and VI) in the absence and presence of HA (M42), Na₂CO₃/NaHCO₃, dissolved FeCl₂, in different background electrolytes such as 0.1 M NaClO₄ (pH = 8.5), OPA pore water (pH = 7.6) under aerobic and anaerobic conditions. Samples were prepared with a total ²³⁹Pu concentration of 1 - 2 × 10⁻⁵ M, S/L ratio of 6 g/L, 10 mg/L HA (M42), 5 × 10⁻³ M FeCl₂, and 2.1 M Na₂CO₃/1 M NaHCO₃ solution. Pu L_{III}-edge (18070 eV) XAS data were collected in fluorescence mode at low temperature (about 15 K) at the Rossendorf beamline ROBL [31] at the ESRF using a 13-element Ge solid state detector. Details of the measured XAS samples can be found in Tab. 18.

Table 18: Details of the Pu samples measured by XAS.

Sample	Pu oxid. state	OPA / (CO ₂ ^a /Ar) ^a	pH	Electrolyte	OPA batch	HA	Pu loading ppm	State ^b	Transport
1	VI	aerobic/CO ₂	7.6	pore water	BHE 24/1	-	375	P	under air
2	IV	aerobic/CO ₂	7.6	pore water	BHE 24/1	-	375	P	under air
3	IV	anaerobic/Ar	7.6	pore water	BHE 24/2	-	370	P	under air
4	III	anaerobic/Ar	7.6	pore water	BHE 24/2	-	370	P	anaerobic jar filled with Ar
5	IV	anaerobic/Ar	7.6	0.1 M NaClO ₄	BHE 24/2	-	372	P	
6	III	anaerobic/Ar	7.6	0.1 M NaClO ₄	BHE 24/2	-	372	P	
7	V	anaerobic/Ar	7.7	pore water	BHE 24/2	-	436	P	Voyageur 12 filled with LN ₂
8	V	anaerobic/Ar	7.8	pore water	BHE 24/2	yes	436	P	
9	VI	aerobic/CO ₂	7.7	pore water	BHE 24/1	yes	733	P	anaerobic jar filled with Ar
10	VI	aerobic/CO ₂	8.5	pore water + Na ₂ CO ₃ /NaHCO ₃	BHE 24/1	-	732	P	
11	VI	anaerobic/Ar	7.5	pore water + FeCl ₂	BHE 24/2	-	733	P	
12	VI	aerobic/Ar	7.8	pore water	BHE 24/1	-	733	P	
13	IV	aerobic/CO ₂	7.7	pore water	BHE 24/1	yes	404	P	
14	IV	anaerobic/Ar	7.7	pore water	BHE 24/2	-	405	P	Voyageur 12 filled with LN ₂
15	IV	anaerobic/Ar	7.7	pore water	BHE 24/2	yes	404	P	
16	III	anaerobic/Ar	7.7	pore water	BHE 24/2	yes	435	P	
17	III	anaerobic/Ar	7.5	pore water + FeCl ₂	BHE 24/2	-	436	P	

^a CO₂: pCO₂ = 10^{-3.5} atm, ^b P: powder

XANES measurements were performed to determine the oxidation state of Pu in the sorption samples as can be seen for example in Fig. 29. The XANES spectra of samples 1 - 8 have similar shape and showed that the Pu L_{III}-edge in all spectra occurs at 18068 ± 1 eV, which agrees well with the Pu L_{III}-edge energy of the Pu(IV) aquo ion [80, 81]. The so called “-yl” shoulder, which is used to distinguish Pu(V) and Pu(VI) from other oxidation states (III and IV), can not be seen in the measured XANES spectra. The same XANES spectra (not shown) were obtained also for the other samples (9 - 17). The oxidation state of Pu in the measured XANES spectra was analyzed by ITFA. The amount of Pu(IV) was about 99% in all samples. It follows from this XANES investigation, that Pu(IV) is the dominant oxidation state in all samples (except the samples prepared with dissolved iron(II) chloride), independent on the initial Pu oxidation state (III, IV, V, and VI), the background electrolyte used, the presence/absence of HA, and the aerobic/anaerobic conditions during sample preparation. The presence of HA did not stabilize Pu(III) and the addition of dissolved iron(II) chloride did not completely reduce Pu to Pu(III).

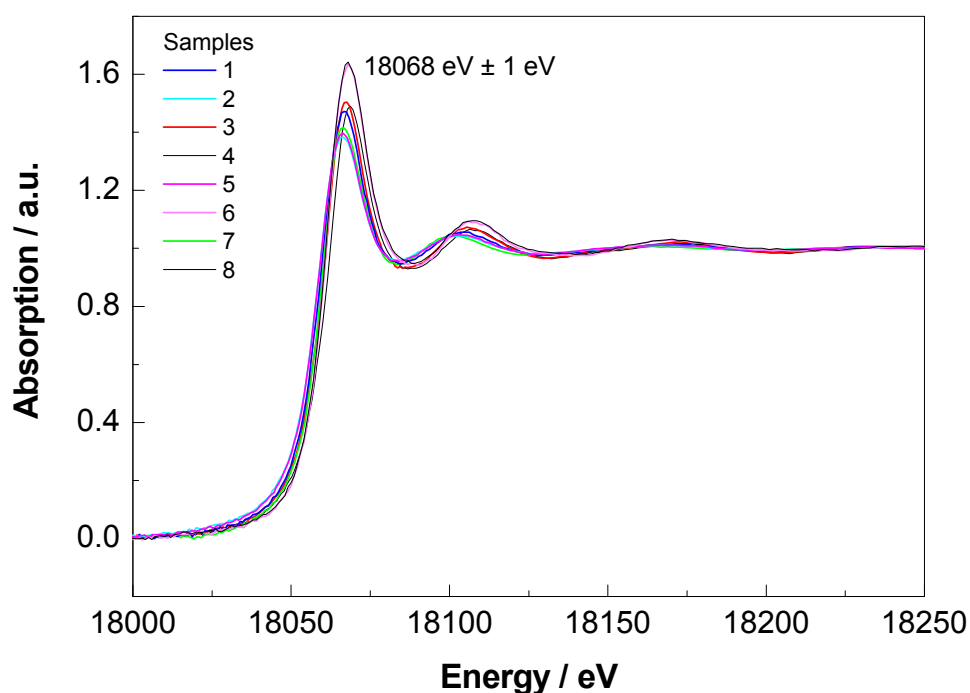


Figure 29: Pu L_{III}-edge XANES spectra of samples 1 - 8.

Figure 30 shows the raw Pu L_{III}-edge EXAFS data, the fit with the best theoretical model, and the corresponding Fourier transform magnitudes of samples 1 and 2 prepared under aerobic condition.

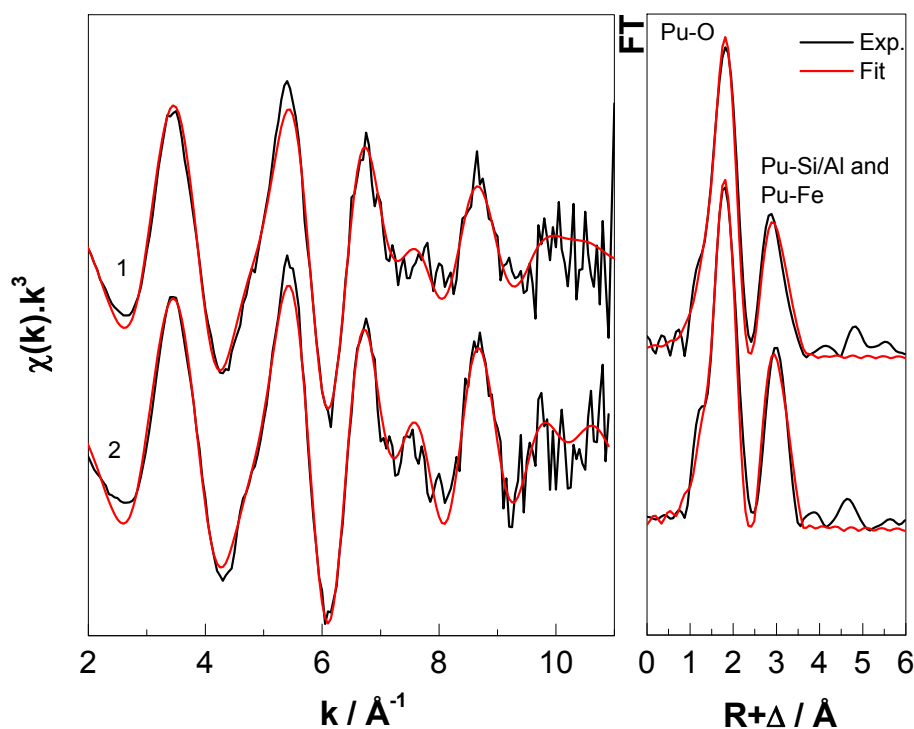


Figure 30: Pu L_{III} -edge k^3 -weighted EXAFS spectra (left) and the corresponding Fourier transform magnitudes (right) of samples 1 and 2 prepared under aerobic condition.

As can be seen from Fig. 30, the EXAFS spectra of samples 1 and 2 prepared under aerobic conditions show a similar EXAFS structure. The Fourier transform spectra show two main peaks. The first peak at 2.34 Å (corrected for phase shift) is related to the Pu-O coordination shell. The second peak can be modelled by two coordination shells, i.e., Pu-Al/Si and Pu-Fe at 3.13 Å and 3.46 Å, respectively.

EXAFS spectra of samples 3 - 6 prepared under anaerobic condition in different background electrolytes (OPA pore water and 0.1 M NaClO_4) are presented in Fig. 31. As can be seen, samples 3 - 6 have identical EXAFS patterns, which differ from the EXAFS spectra of samples 1 and 2 prepared under aerobic conditions. In the Fourier transform spectra of samples 3 - 6 only two coordination shells Pu-O and Pu-Si/Al can be found at about 2.34 Å and 3.14 Å, respectively. Comparing EXAFS spectra of sample 3 and 4 prepared in OPA pore water with samples 5 and 6 prepared in 0.1 M NaClO_4 , no influence of the background electrolyte can be observed. Aerobic samples have a characteristic EXAFS pattern between k 6 and 9 Å^{-1} . In their Fourier transform spectra the amplitude of the second peak was significantly higher compared to other samples prepared under anaerobic conditions.

According to the EXAFS results the speciation of Pu by uptake on OPA is depending on the OPA batch, whether it has been prepared under aerobic or anaerobic conditions. In this context the redox-active iron-bearing mineral phase (pyrite or siderite) seems to play an important role by reduction of Pu(VI) under aerobic conditions.

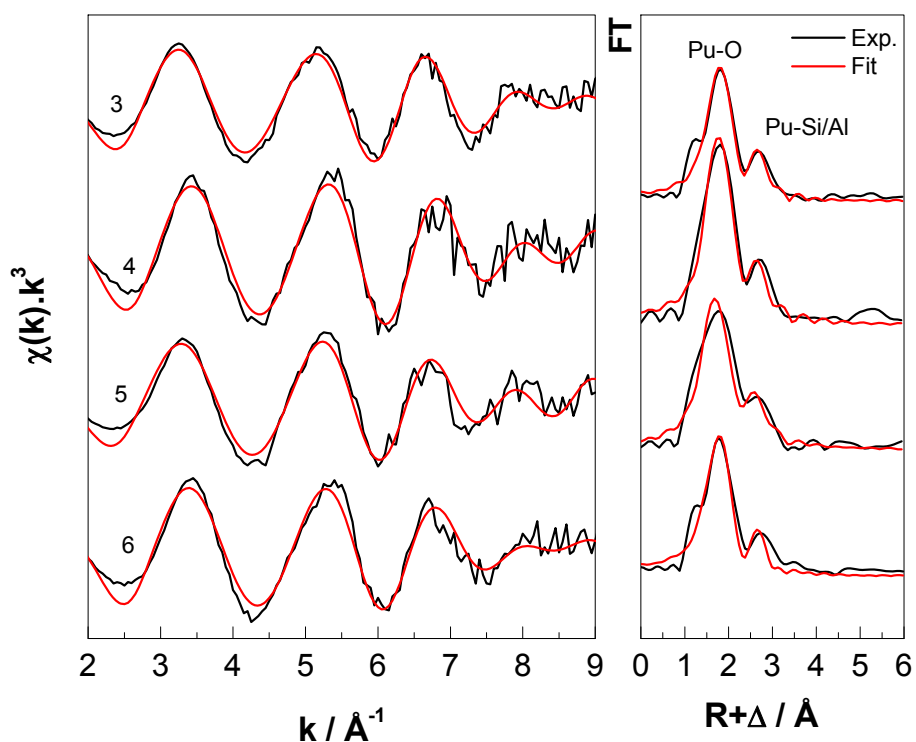


Figure 31: Pu L_{III}-edge k^3 -weighted EXAFS spectra (left) and the corresponding Fourier transform magnitudes (right) of samples 3 - 6 prepared under anaerobic condition.

No influence of HA was observed on the sorption of Pu on OPA. Figure 32 shows as an example the EXAFS spectra of samples 7 and 8 for Pu(V) sorption on OPA in the absence and presence of HA, respectively. EXAFS spectra of both samples are very similar. Three coordination shells, i.e., Pu-O, Pu-Si/Al, and Pu-Pu, were observed in the Fourier transform spectra at about 2.29 Å, 3.19 Å, and 3.78 Å, respectively. The additional Pu-Pu coordination shell was observed only in these two samples because a small amount of Pu(IV) colloids remained in the Pu(V) stock solution after potentiostatic electrolysis from the initial Pu(VI) solution.

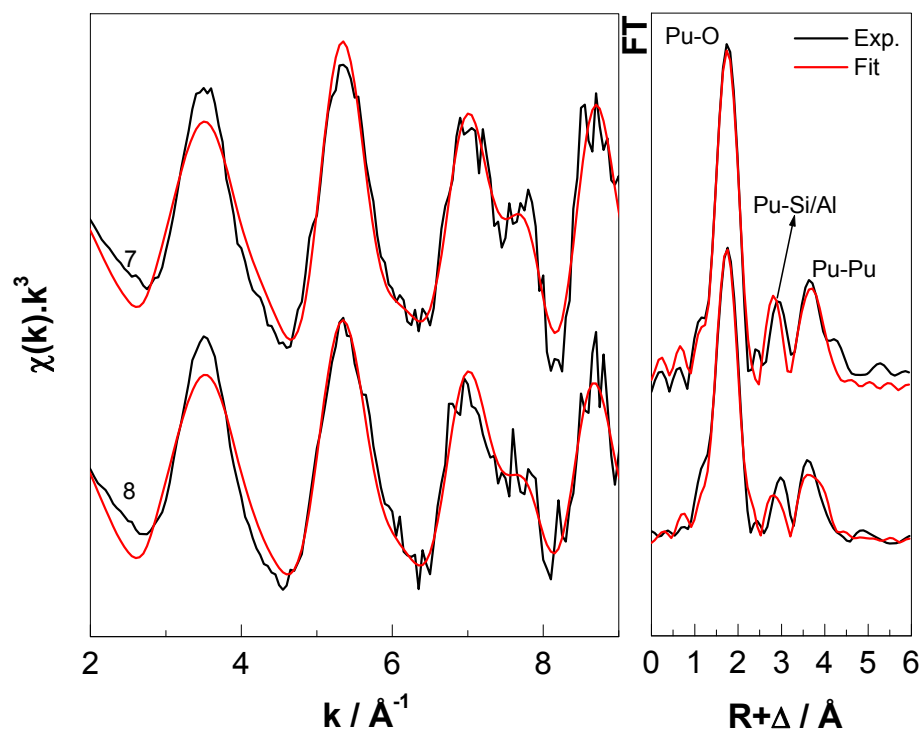


Figure 32: Pu L_{III} -edge k^3 -weighted EXAFS spectra (left) and the corresponding Fourier transform magnitudes (right) of samples 7 - 8 prepared under anaerobic condition in absence and presence of HA, respectively.

The obtained structural parameters derived from EXAFS fits of samples 1 - 8 are summarized in Tab. 19.

Table 19: EXAFS structural parameters for the Pu samples 1 – 8 in Tab. 18.

Sample	Pu-O			2x Pu-Si/Al ^a		2x Pu-Fe ^a		Pu-Pu			$\Delta E_0 /$ eV	red. error
	N	R / Å	$\sigma^2 / \text{Å}^2$	R / Å	$\sigma^2 / \text{Å}^2$	R / Å	$\sigma^2 / \text{Å}^2$	N	R / Å	$\sigma^2 / \text{Å}^2$		
1	8.8	2.34	0.013	3.13	0.004	3.46	0.006				- 9.5	0.21
2	8.6	2.34	0.012	3.13	0.004	3.46	0.005				- 10.2	0.22
3	8.4	2.40	0.021	3.17	0.008						- 12.4	0.12
4	9.9	2.34	0.020	3.14	0.007						- 11.2	0.36
5	11.1	2.34	0.026	3.14	0.007						- 13.7	0.11
6	9.5	2.36	0.022	3.15	0.007						- 11.5	0.14
7	9.5	2.29	0.011	3.21	0.010			5.9	3.77	0.009	- 3.0	0.29
8	9.5	2.30	0.012	3.18	0.02			4.0	3.78	0.007	- 2.5	0.29
Pu(IV)(aq) ^[82]	7.8	2.39	0.007									
Pu(OH) ₄ (am.) ^[82]	4.6	2.32	0.011					2.2	3.85	0.006		

^a The coordination numbers for Si/Al and Fe were held constant during the fit, $\Delta R = \pm 0.02 \text{ Å}$, $\Delta \sigma^2 = \pm 0.001 \text{ Å}^2$

The Pu-O distance in all samples was about 2.34 Å and agrees with that of Pu(OH)₄(am) [82]. A shorter Pu-O distance was found in samples 7 and 8 compared to [82], perhaps due to precipitation of Pu(IV) colloids. The obtained Pu-Pu distance in samples 7 and 8 is shorter than determined by Dardenne et al. for Pu(OH)₄(am.). The detection of Pu-Al/Si interactions in all samples is indicative of inner-sphere sorption of Pu(IV) on the clay minerals present in OPA. The XANES results confirm also that Pu(IV) is the dominant oxidation state after interaction of Pu(III/IV/V/VI) with OPA. Our EXAFS results are in good agreement with a previous EXAFS study on the sorption of Pu(III) and Pu(IV) onto kaolinite [77].

μ-XAS, μ-XRF, and μ-XRD measurements of Pu(VI)

The speciation of ²⁴²Pu(VI) on OPA after sorption and diffusion processes has been investigated by μ-XAS, μ-XRF, and μ-XRD measurements. Fluorescence mappings of Pu, Ca, Fe, Mn, and Sr on OPA were collected. Spots of high local Pu concentration were analyzed by μ-XANES and μ-XRD to determine the oxidation state of Pu and the distribution of mineral phases near Pu enrichments. Analogous to Np, experiments with a similar set of samples were prepared. Details of the Pu samples prepared is shown in Tab. 20.

Table 20: Details of the Pu samples measured at SLS.

Sample	Preparation (under aerobic conditions)	Activity Bq	Pu loading ng/mm²
1	deposition of 2×10^{-5} M ²⁴² Pu(VI) on OPA thin section	750	96
2	sorption of 2×10^{-5} M ²⁴² Pu(VI) on OPA thin section	917	311
3	diffusion of 2×10^{-5} M ²⁴² Pu(VI) in an intact OPA bore core	400	7

As shown in Tab. 20, the Pu loading in the samples was between 7 ng/mm² and 311 ng/mm². In the following the focus will be put on samples 2 and 3. Figure 33 shows as an example the collected μ-XRF mappings for Pu, Ca, and Fe of sample 2.

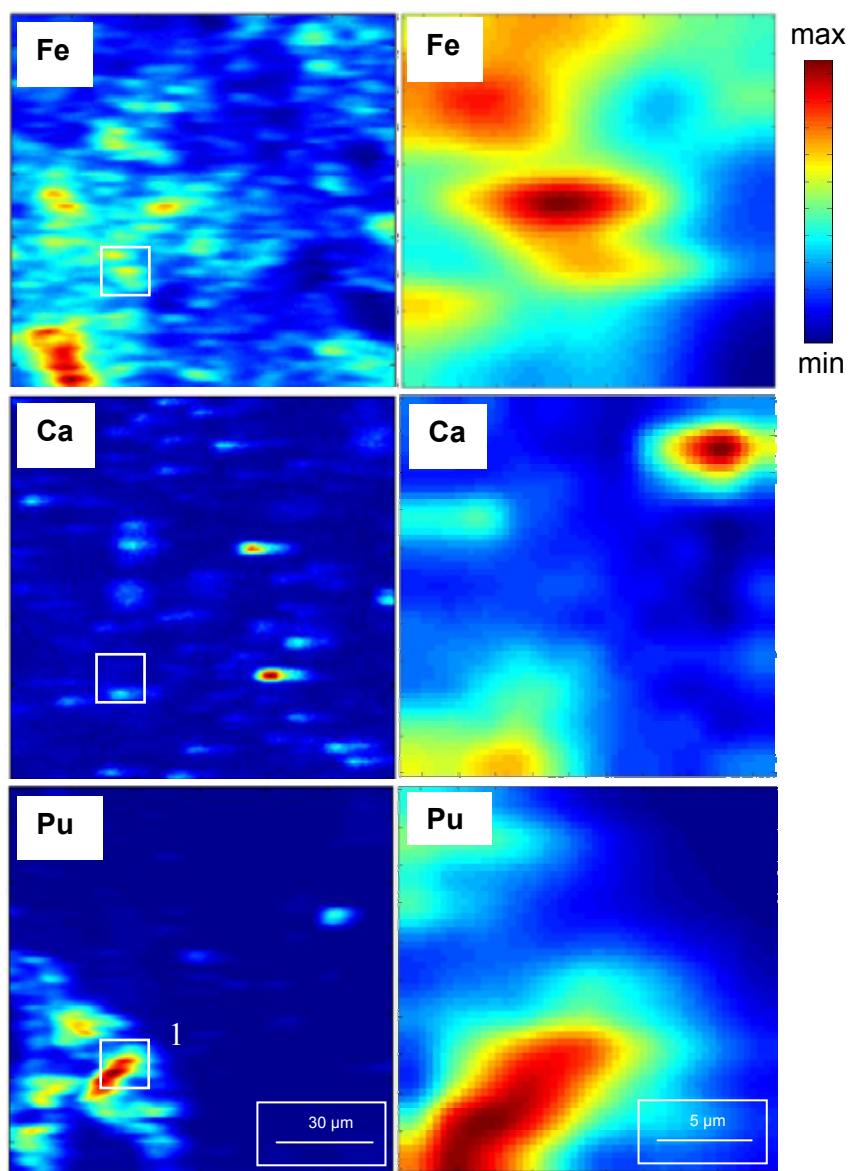


Figure 33: Left: μ -XRF mappings ($120 \times 120 \mu\text{m}$, step size: $10 \mu\text{m}$) of Fe, Ca, and Pu of sample 2 prepared by sorption of $2 \times 10^{-5} \text{ M } ^{242}\text{Pu}$ on OPA thin section. Right: Same element distributions for $20 \times 20 \mu\text{m}$ mapping (step size $2 \mu\text{m}$). A XANES spectrum was recorded at spot 1 (Fig. 35).

As can be seen from Fig. 33, fluorescence mappings with good signal intensity were collected for the sample 2. The elements Fe, Ca, and Pu are distributed heterogeneously on the thin section and several hot pots can be observed. In some areas, as can be seen by the presence of purple pixels in the left corner of tri-color mapping (Fig. 34), Pu is associated with Fe.

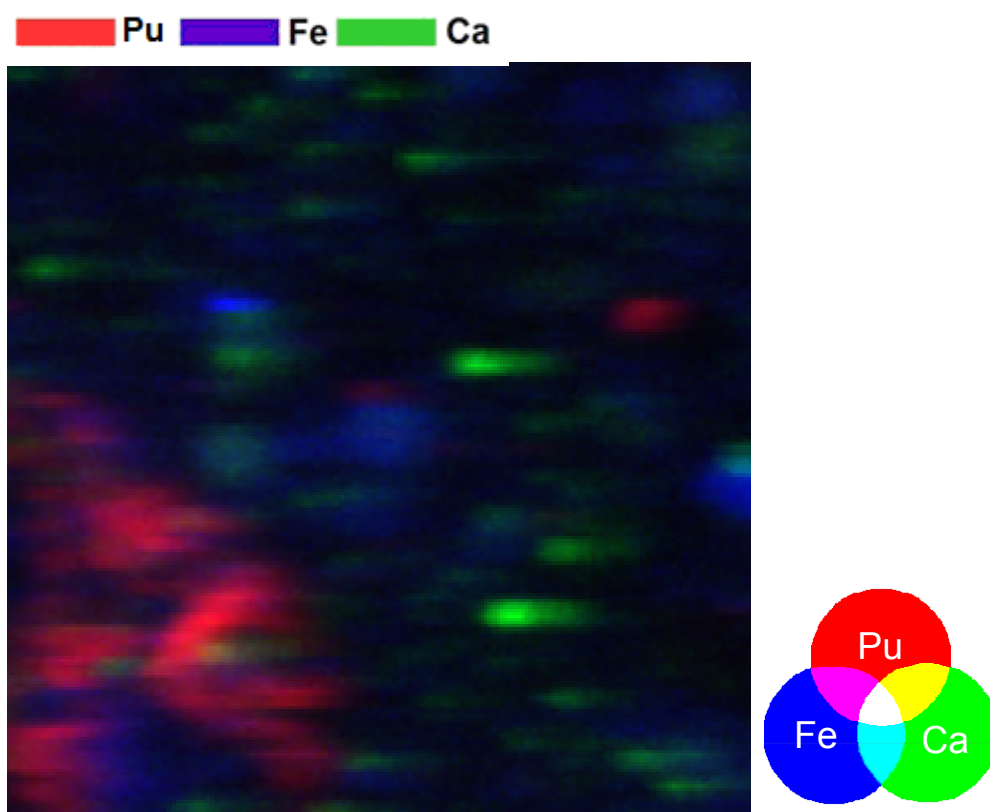


Figure 34: Tri-color mapping of the distributions of Ca, Fe, and Pu in the sorption sample from μ -XRF mapping (left) in Fig. 33.

To determine the oxidation state of Pu and the mineral phases near the Pu hot spot in sample 2 after sorption on OPA thin section, μ -XANES and μ -XRD measurements were performed on the Pu hot spot marked in Fig. 33. The normalized XANES spectrum and μ -XRD images are shown in Figs. 35 and 36, respectively. Using ITFA the amount of Pu(IV) in the XANES spectrum was determined to be 97% in the hot spot.

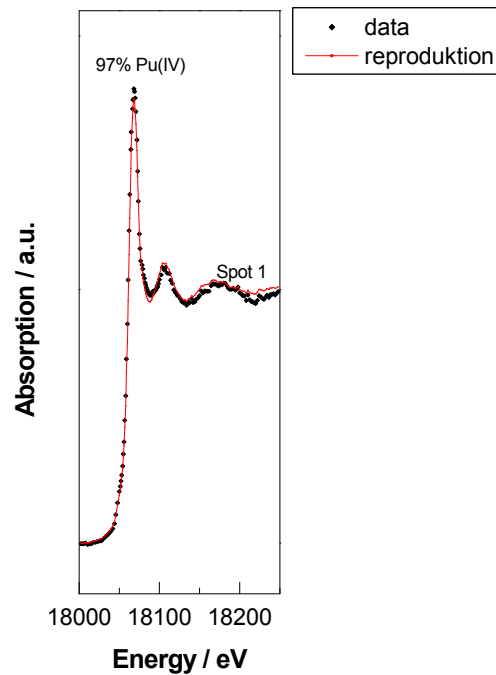


Figure 35: Normalized Pu L_{III}-edge XANES spectrum measured on spot 1 marked in Fig. 33 together with reproduction from IFTA.

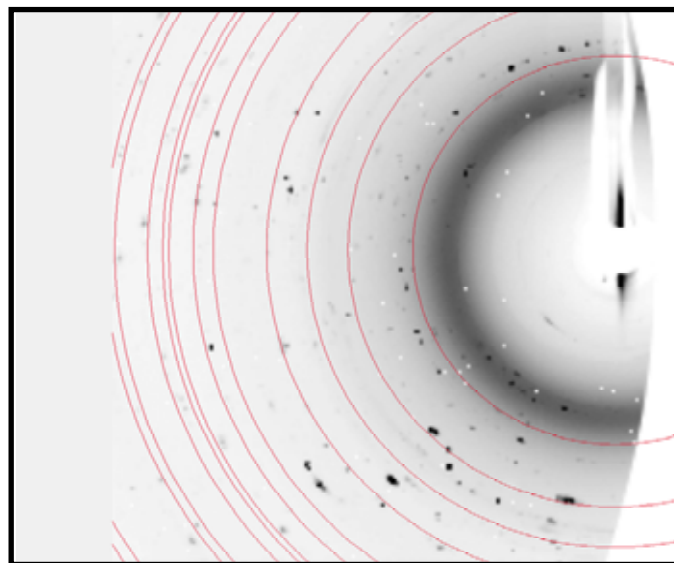


Figure 36: μ -XRD images ($20 \times 20 \mu\text{m}$, step size: $2 \mu\text{m}$, $E = 18070 \text{ eV}$) of the Pu hot spot presented in the μ -XRF mapping of sample 2 (Fig. 33). μ -XRD patterns of siderite are shown as red circles.

As can be seen in Fig. 36, the collected XRD images near Pu hot spot 1 indicate that Pu potentially localizes on siderite mineral phases contained to about 3% in OPA [3]. Most of all other crystalline/micro crystalline phases (black points) are related to silicate mineral phases,

especially kaolinite (points in the circles close to the center). This preliminary result showed that siderite is one of the redox-active mineral phases in OPA, which determine the Pu speciation after sorption process.

For the diffusion sample with very low Pu loading (7 ng/mm^2), it was also possible to perform μ -XRF and μ -XANES measurements. Figure 37 shows the distributions of Ca, Fe, and Pu on this sample. As can be seen, several Pu and Fe hot spots can be found. Ca is heterogeneously distributed on the OPA thin section. Also in this sample, as in the sorption sample, there are some areas in which Pu was associated with Fe. The μ -XANES spectrum of the Pu hot spot showed that Pu(IV) is the dominating oxidation state after diffusion into OPA (Fig. 38). Due to the thickness of the diffusion sample, it was not possible to carry out any μ -XRD measurements.

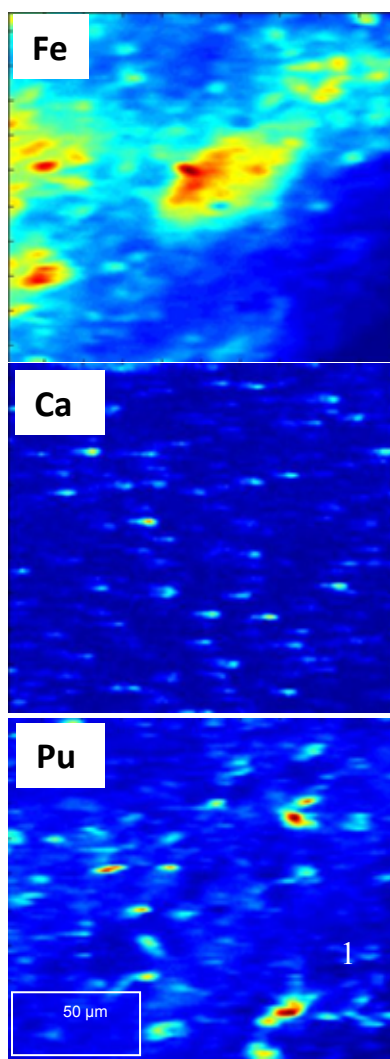


Figure 37: μ -XRF mappings ($200 \times 200 \mu\text{m}$, step size: $2 \mu\text{m}$) of Fe, Ca, and Pu of sample 3 prepared by diffusion of $2 \times 10^{-5} \text{ M } ^{242}\text{Pu}$ on OPA. A XANES spectrum was recorded at spot 1 (Fig. 38).

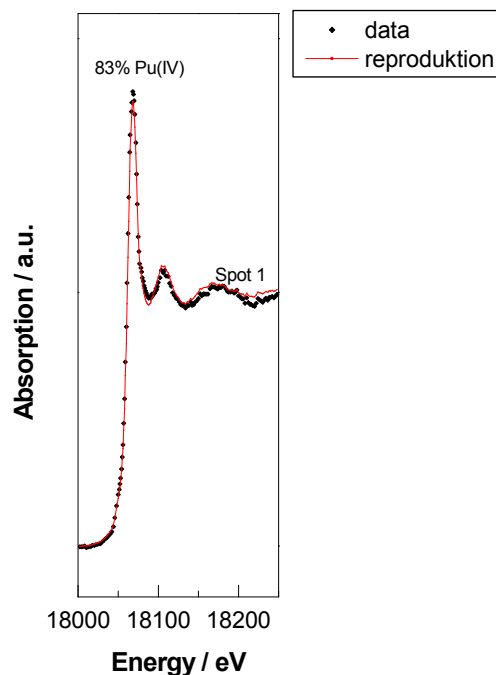


Figure 38: Normalized Pu L_{III} -edge XANES spectrum measured on spot 1 marked in Fig. 37 together with reproduction from IFTA.

In conclusion, it was possible to determine the elemental distributions of Ca, Fe, and Pu in OPA samples after sorption and diffusion experiments by μ -XRF. Bulk-XAS and μ -XANES measurements showed a complete reduction of Pu(VI) to Pu(IV) in all samples prepared under both aerobic and anaerobic conditions. These results are in good agreement with our previous results of Pu uptake on kaolinite [77]. Furthermore, preliminary analysis of the μ -XRD patterns indicates that siderite is one of the redox-active mineral phases of OPA, which determines the speciation on Pu after uptake on OPA. The obtained results indicate that OPA is a suitable host rock for high level nuclear waste disposal.

4.3.2 CE-ICP-MS

Redox speciation of Np(IV) and Np(V)

A highly sensitive CE-ICP-MS method was developed for the speciation of Np(IV) and Np(V) in solution. The separation of the two species was performed using the homemade capillary electrophoresis described in Sect. 2.2.

A stock solution containing 3.1×10^{-5} M Np(IV) and 9.2×10^{-6} M Np(V) was prepared by partial reduction of Np(V) with hydroxylammonium chloride. The content of Np(IV) and Np(V) was checked by liquid-liquid-extraction of Np(IV) with HDEHP in toluene and subsequent measurement of the activity in the organic and aqueous phases by liquid scintillation counting (LSC).

Good separation of Np(IV) from Np(V) was possible with the described CE-setup using a solution of 1 M acetic acid with pH 2.3 as background electrolyte and a voltage of 25 kV (Fig. 39). During separation, an external pressure of 30 mbar was applied to prevent clogging of the capillary.

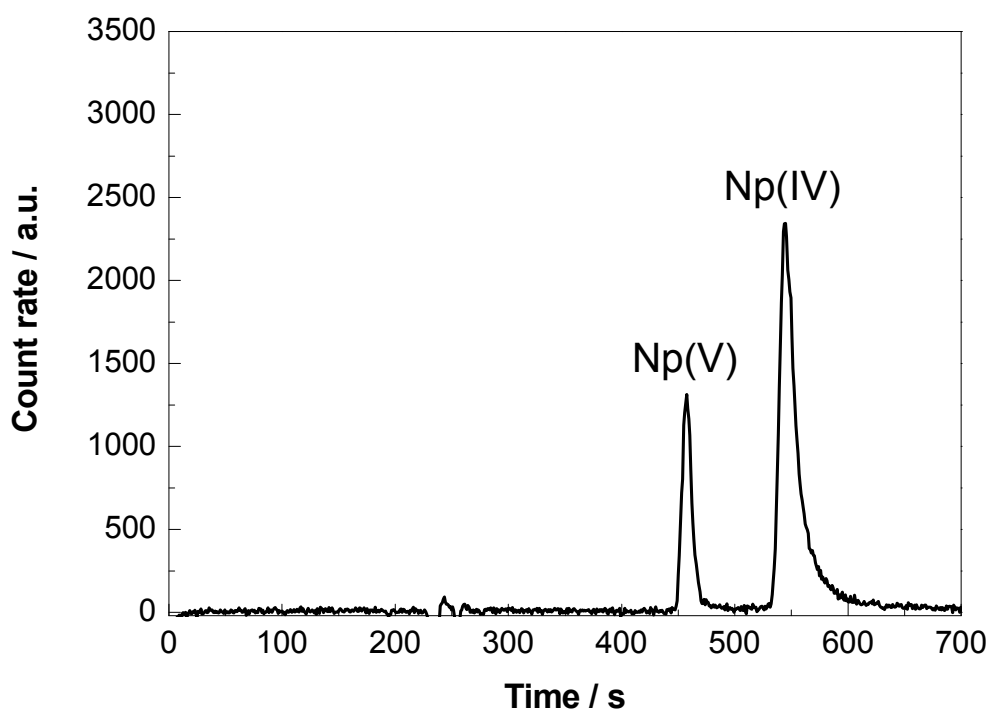


Figure 39: Electropherogram of a mixture of 3.1×10^{-8} M Np(IV) and 9.2×10^{-9} M Np(V).

A dilution series was prepared by dilution of the stock solution. After the measurement of this series, the peak areas for Np(IV) and Np(V) were calculated and plotted versus the respective concentrations (Fig. 40). As expected, a linear increase of the peak areas with the concentration was observed in both cases. Therefore, it can be concluded that there is no significant loss of Np(IV) in the given concentration range due to sorption or oxidation during the CE separation with the chosen parameters.

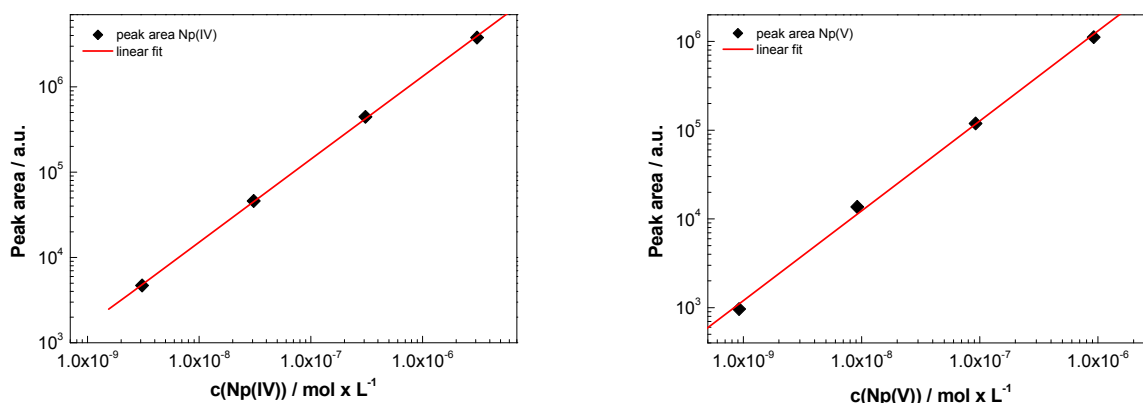


Figure 40: Results from dilution series for Np(V) and Np(IV) obtained with CE-ICP-MS.

Redox behavior of Pu(III) and Pu(IV) under aerobic condition [23]

The redox behavior of different Pu oxidation states in OPA pore water and related solutions was studied under aerobic and anaerobic conditions using on-line coupling CE-ICP-MS. Several experimental parameters and setups were tested to optimize the separation performance [23]. It was found that the sample medium has a significant influence on the separation efficiency. Experiments with 50 ppb $^{239}\text{Pu(VI)}$ in different mixtures of 0.2 M HNO_3 and 1 M CH_3COOH showed a better separation and a lower detection limit when the sample was prepared in a medium that had a similar composition as the electrolyte used in the capillary (1 M CH_3COOH). The speciation of Pu in a mixture of 1:4 ($\text{HNO}_3/\text{CH}_3\text{COOH}$) was $1.6 \pm 0.1\%$ Pu(III), $59.3 \pm 3.0\%$ Pu(IV), $33.5 \pm 1.7\%$ Pu(V), and $5.6 \pm 0.3\%$ Pu(VI).

Kinetic measurements of 50 ppb Pu(III) in 1 M CH_3COOH at pH 1.8 showed that Pu(III) is stable up to 40 minutes, i.e., during the typical measuring time for CE-ICP-MS. After a longer time Pu(III) is oxidized to Pu(IV) and Pu(VI).

The redox stability of Pu(III) and Pu(IV) in OPA pore water (pH = 7.6, I = 0.4 M), and for comparison in 0.2 M HNO_3 (pH = 0.9) and 0.4 M NaClO_4 (pH = 7.6) was investigated by CE-ICP-MS under aerobic conditions. Freshly prepared stock solutions of Pu(III) and Pu(IV) were added individually to the different solutions. After a contact time of 5 days, aliquots were taken and analyzed by CE-ICP-MS to determine the speciation of Pu in solution. The pH/Eh values were measured directly after Pu addition and checked again after 5 days. Figures 41 and 42 show the electropherograms of 50 ppb Pu(III) and Pu(IV), respectively, in the investigated solutions after a contact time of 5 days.

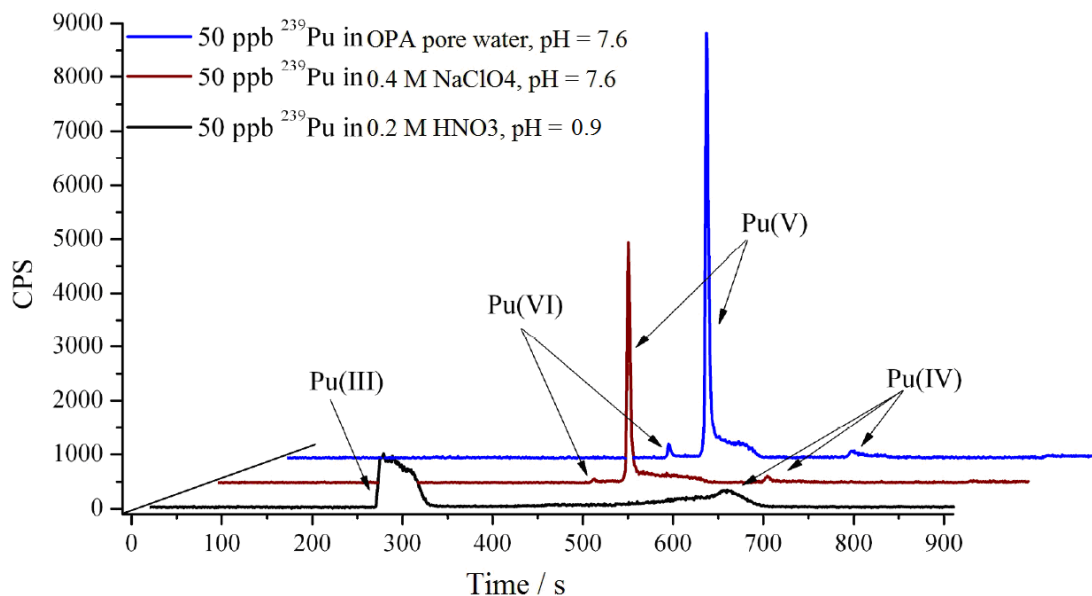


Figure 41: Electropherogram of 50 ppb $^{239}\text{Pu}(\text{III})$ in different solutions after a contact time of 5 days under aerobic conditions.

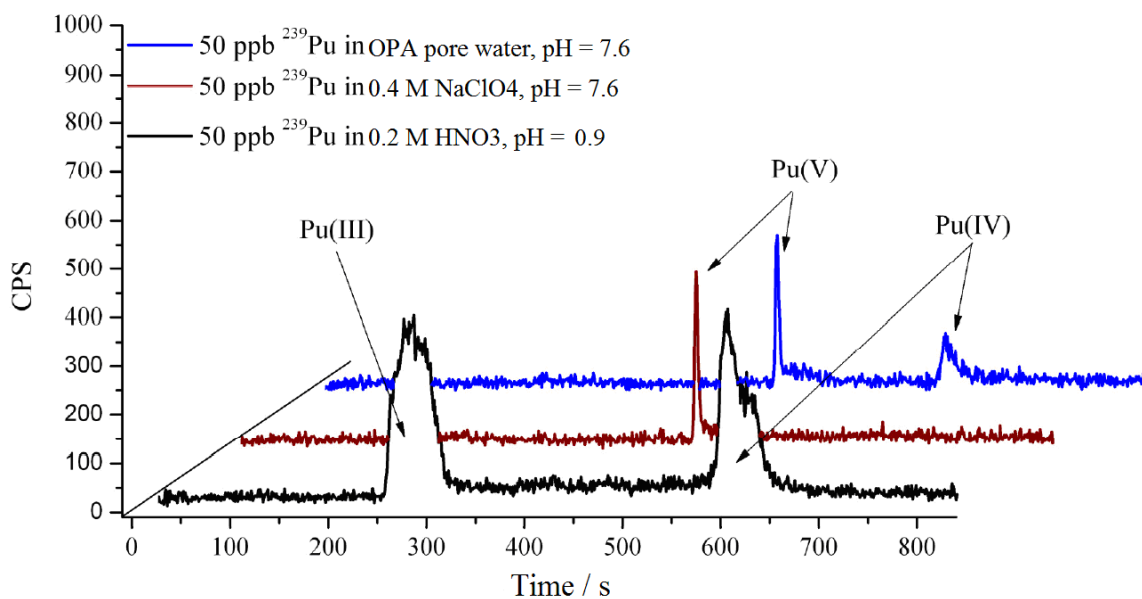


Figure 42: Electropherogram of 50 ppb $^{239}\text{Pu}(\text{IV})$ in different solutions after a contact time of 5 days under aerobic conditions.

As can be seen from Figs. 41 and 42, higher signal intensities were obtained in all Pu(III) solutions compared to Pu(IV). This can be explained by the strong tendency of Pu(IV) to sorb on tube walls. In case of Pu(III) the obtained signals in both 0.4 M NaClO₄ and OPA pore water are more intensive and better resolved compared to 0.2 M HNO₃. The distribution of Pu

species (Tabs. 21 and 22) in each sample was obtained from the peak areas in the measured electropherograms.

Table 21: Pu species and Eh values of 50 ppb Pu(III) in 0.2 M HNO₃ (pH = 0.9), 0.4 M NaClO₄ (pH = 7.6), and OPA pore water (pH = 7.6) solutions after a contact time of 5 days under aerobic conditions.

Solution	SHE Eh/mV	Species / %			
		Pu(III)	Pu(IV)	Pu(V)	Pu(VI)
0.2 M HNO ₃	792 ± 50	45 ± 3	55 ± 3	0	0
0.4 M NaClO ₄	602 ± 50	0	9 ± 1	88 ± 5	3 ± 1
OPA pore water	520 ± 50	0	8 ± 1	89 ± 5	3 ± 1

Table 22: Pu species and Eh values of 50 ppb Pu(IV) in 0.2 M HNO₃ (pH = 0.9), 0.4 M NaClO₄ (pH = 7.6), and OPA pore water (pH = 7.6) solutions after a contact time of 5 days under aerobic conditions.

Solution	SHE Eh/mV	Species / %			
		Pu(III)	Pu(IV)	Pu(V)	Pu(VI)
0.2 M HNO ₃	800 ± 50	57 ± 3	43 ± 2	0	0
0.4 M NaClO ₄	600 ± 50	0	0	100 ± 5	0
OPA pore water	500 ± 50	0	51 ± 3	49 ± 3	0

As can be seen from Tab. 21, at pH 7.6 the majority of Pu(III) was oxidized to Pu(V) in both NaClO₄ and OPA pore water solutions. Table 22 shows that Pu(V) is the dominant species in 0.4 M NaClO₄ solution at pH 7.6, while in OPA pore water both Pu(IV) and Pu(V) are present with about 50%. The measured Eh values of Pu(III) and Pu(IV) in all solutions agree well with data from Takeno et. al. [83].

Redox behavior of Pu(III) and Pu(IV) under anaerobic conditions [23]

To investigate the redox behavior of Pu close to environmental conditions, the redox stability of Pu(III) and Pu(IV) was studied under anaerobic conditions (Ar atmosphere). Aliquots from Pu(III) or Pu(IV) stock solutions were added to 0.2 M HNO₃ (pH = 0.9), 0.4 M NaClO₄ (pH = 7.6), or OPA pore water (pH = 7.6, I = 0.4 M). The Pu(III) and Pu(IV) concentrations were 30 ppb in all samples. Eh and pH values were measured immediately after addition of Pu as well

as after 5 days. The speciation of Pu was analyzed by CE-ICP-MS after 60 min, 80 min, and 5 days. Furthermore, the redox stability of a mixture of Pu(III) and Pu(IV) (each 50 ppm) was also investigated under same experimental conditions by CE-ICP-MS after a contact time of 5 days.

Figure 43 shows the distribution of the different Pu species in OPA pore water as a function of time after addition of 30 ppb Pu(III) under anaerobic conditions.

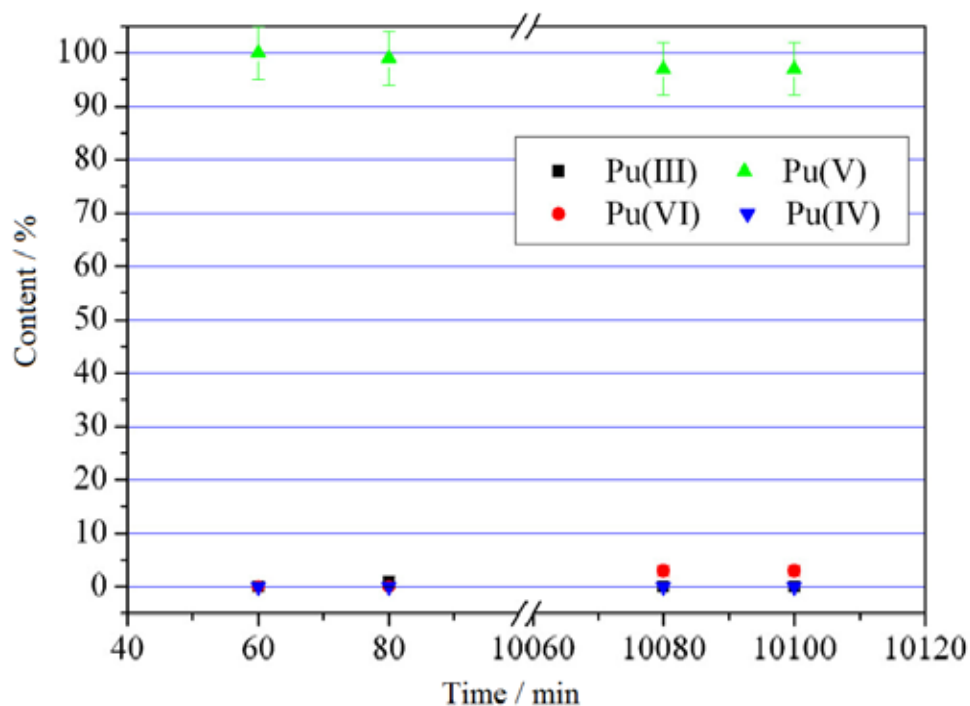


Figure 43: Pu species as a function of time after addition of 30 ppb Pu(III) to OPA pore water (pH = 7.6) under anaerobic conditions.

Figure 44 shows the distribution of the Pu species as a function of time after addition of 30 ppb Pu(IV) to OPA pore water under anaerobic conditions.

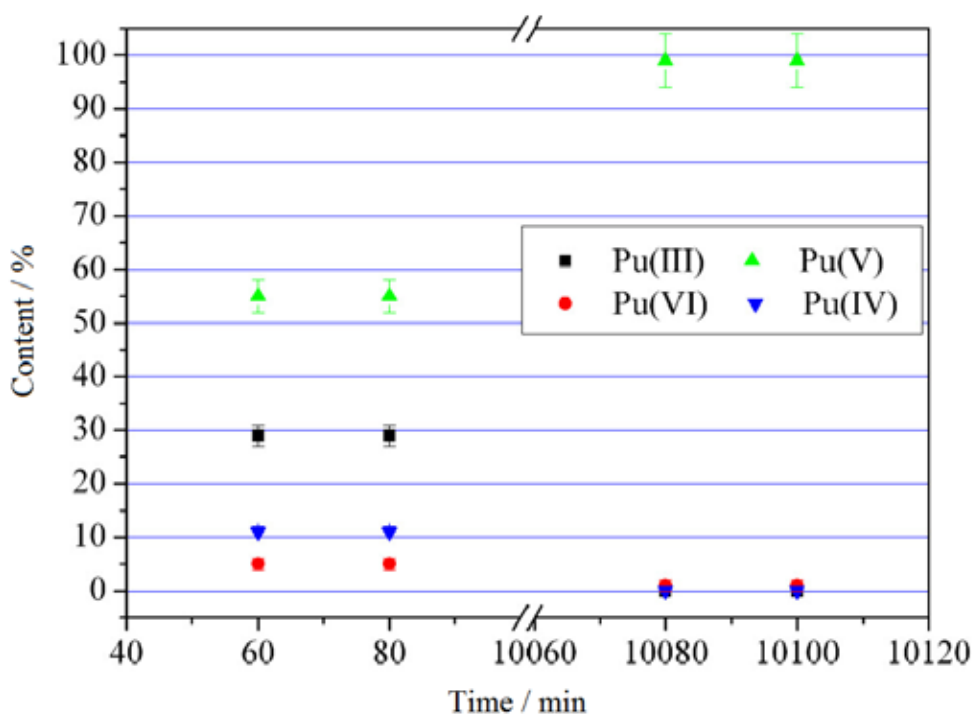


Figure 44: Pu species as a function of time after addition of 30 ppb Pu(IV) to OPA pore water (pH = 7.6) under anaerobic conditions.

As can be seen from Figs. 43 and 44, under anaerobic conditions Pu(V) is the dominating species in OPA pore water after a contact time of 7 days independent of the initial Pu oxidation state. The oxidation of Pu(III) to Pu(V) in OPA pore water under anaerobic conditions was completed within the first hour. The Pu species after addition of 30 ppb Pu(III) or Pu(IV) to 0.2 M HNO₃ (pH = 0.9), 0.4 M NaClO₄ (pH = 7.6), and OPA pore water (pH = 7.6) after a contact time of 7 days under anaerobic conditions are presented in Tabs. 23 and 24.

Table 23: Pu species and Eh values of 30 ppb Pu(III) in 0.2 M HNO₃ (pH = 0.9), 0.4 M NaClO₄ (pH = 7.6), and OPA pore water (pH = 7.6) after a contact time of 7 days under anaerobic conditions.

Solution	SHE Eh / mV (after 5 days)	Species / %			
		Pu(III)	Pu(IV)	Pu(V)	Pu(VI)
0.2 M HNO ₃	647 ± 50	75 ± 4	4 ± 1	10 ± 1	11 ± 1
0.4 M NaClO ₄	297 ± 50	0	0	32 ± 2	68 ± 4
OPA pore water	334 ± 50	0	0	97 ± 5	3 ± 1

Table 24: Pu species and Eh values of 30 ppb Pu(IV) in 0.2 M HNO₃ (pH = 0.9), 0.4 M NaClO₄ (pH = 7.6), and OPA pore water (pH = 7.6) after a contact time of 7 days under anaerobic conditions.

Solution	SHE Eh / mV (after 5 days)	Species / %			
		Pu(III)	Pu(IV)	Pu(V)	Pu(VI)
0.2 M HNO ₃	611 ± 50	99 ± 5	0	1 ± 1	0
0.4 M NaClO ₄	469 ± 50	0	0	78 ± 4	22 ± 2
OPA pore water	376 ± 50	0	0	99 ± 5	1 ± 1

As can be seen, Pu(V) is the dominating species in OPA pore water under anaerobic conditions. In 0.4 M NaClO₄ solutions at pH 7.6 a mixture of Pu(V) and Pu(VI) was found. In case of 30 ppb Pu(III) in 0.2 M HNO₃, all Pu oxidation states were presented in solutions after 7 days. The analogous experiment with 30 ppb Pu(IV) in HNO₃, only Pu(III) was detected after 7 days. Under anaerobic conditions, the measured Eh values in pore water solutions (for both Pu(III) and Pu(IV) experiments) were lower than for 0.4 M NaClO₄ (pH 7.6), 0.2 M HNO₃ and related Eh values under aerobic conditions.

4.3.3 CE-RIMS

Another aim of this work was to improve the sensitivity of speciation methods for Np and Pu. For the detection and speciation of Np and Pu at ultratrace level, offline coupling of CE and RIMS has been successfully applied. Pu samples for RIMS measurements were collected off-line with the CE technique and filaments were prepared by electrodeposition and measured [23, 26]. Furthermore, RIMS was applied for first time to detect smallest amount of ²³⁷Np and to determine the oxidation states of Pu in supernatant after Pu sorption on OPA.

RIMS measurements on ²³⁷Np

The detection and speciation of Np at an ultratrace level require highly sensitive and selective methods. While the short-lived isotope ²³⁹Np can be detected by means of γ -ray spectrometry, only very few sensitive and selective methods exist for the detection ²³⁷Np. Due to its long half-life, radiometric methods are not sensitive enough, while most mass spectrometric methods are limited by isobaric interferences.

Therefore, we have developed a RIMS method for the detection of ^{237}Np . In RIMS, sample atoms are evaporated from a heated filament and ionized by laser radiation of three different wavelengths. The laser ions are separated by a time-of-flight (TOF) mass spectrometer and finally detected by multi channel plate (MCP) detectors. The wavelengths of the laser radiation match three subsequent optical transitions of Np and are chosen to excite the atom into an autoionizing state (AI) in the last step. Since the involved optical transitions are unique to Np, this kind of ionization shows an outstanding selectivity for the element.

The samples for RIMS are prepared by electrodeposition of Np from a 20% solution of $(\text{NH}_4)_2\text{SO}_4$ onto a Ta foil at a voltage of 14 V. After electrodeposition, the foil is covered by sputtering with a $\sim 1 \mu\text{m}$ layer of Ti, which serves as a reducing agent.

The laser setup consists of three tunable titanium-sapphire lasers (Ti:sa) with output powers of up to 3 W at a repetition rate of 10 kHz. The Ti:sa lasers are jointly pumped by a frequency doubled Nd:YAG laser (DM-60, Photonics Industries, Bohemia, NY, USA). Since the Ti:sa lasers in use can only generate radiation between 11500 and 14000 cm^{-1} , the light of one laser has to be frequency doubled by a β -barium borate crystal (BBO) to reach the ionization potential of Np at 50535 cm^{-1} with a three-step excitation scheme.

Because only few energy levels of Np suitable for a three step excitation/ionization scheme with Ti:sa lasers were known, resonance ionization spectroscopy (RIS) was applied to identify such levels. The setup used for RIS is similar to one used for RIMS and also consists of three Ti:sa lasers. A graphite furnace loaded with $\sim 1 \mu\text{g}$ Np was used as an atomic beam source in these experiments. Compared to the setup described above, this leads to a much higher ionization efficiency, but makes background suppression for thermally emitted ions impossible.

In order to identify possible second excitation states (SES), frequency doubled light from a Ti:sa laser was used to excite Np atoms into different first excitation states (FES) between 24798 and 26264 cm^{-1} taken from literature [84]. A second Ti:sa was scanned across its tuning range to populate SES. The light from a third Ti:sa was introduced for nonresonant ionization of the Np atoms from the SES. In a separate experiment, two Ti:sa lasers were used to populate several SES identified previously, while the third laser was scanned in order to excite AI levels. Our experiments led to the identification of numerous previously unknown high-lying energy levels and AI states of Np [26]. Up to now, the most efficient ionization could be obtained with the excitation scheme shown in Fig. 45. Applying this scheme, an overall efficiency for the detection of ^{237}Np of 2×10^{-6} could be demonstrated, which corresponds to a limit of detection of 1×10^7 atoms (4 fg).

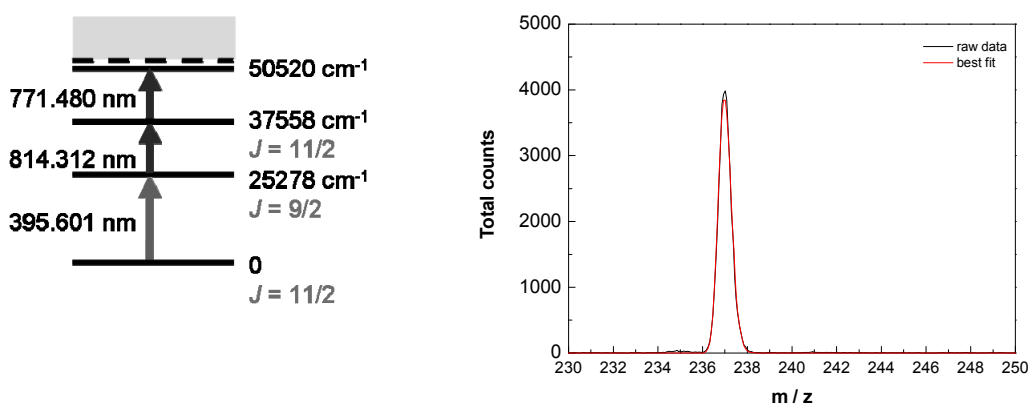


Figure 45: Scheme for resonant excitation and ionization of ^{237}Np and mass spectrum obtained with 4×10^{11} atoms ^{237}Np yielding a detection efficiency of 2×10^{-6} .

RIMS measurements on ^{239}Pu

As already mentioned, CE-RIMS was carried out for the first time with real samples from batch experiments for the determination of the K_d values of Pu(III) and Pu(IV) sorbed on OPA. At first, the coupling of CE to RIMS was tested by determining the speciation in samples which contained only Pu(III) or Pu(IV) at different concentrations of 0.05 ppt, 5.0 ppt, and 500 ppt. The samples were prepared by mixing defined aliquots from freshly prepared stock solutions of Pu(III) and Pu(IV) to 1 M CH_3COOH solution. The related fractions were separated by CE and the Pu content in each fraction was determined by RIMS. The results are shown in Tab. 25.

Table 25: RIMS results of Pu(III) and Pu(IV) samples at different concentrations.

Conc. / ppt	0.05	5	500
Pu(III) fraction	2.77×10^6	2.04×10^9	4.39×10^8
Pu(IV) fraction	1.88×10^7	1.88×10^9	1.91×10^9
$\Sigma_{\text{theo. atoms}}$	10^7	10^9	10^{11}

As can be seen from Tab. 25, in case of the low concentrations (0.05 and 5 ppt) the number of atoms found in the Pu(III) and Pu(IV) fractions are rather close to the theoretically expected value of Pu atoms. However, for the higher concentration (500 ppt) the obtained values are too low, maybe due to sorption effects on the wall of the capillary. The values given in Tab. 25 for 0.05 ppt Pu are close to the detection limit of this method.

RIMS application for real Pu/OPA batch samples

As shown before in Sect. 4.1, about 99% of initial Pu was removed from solution and sorbed on OPA in a short time and only 1% of Pu remained in the solution. At this very low Pu concentration, it is not possible to perform speciation studies by using conventional methods. Using CE-RIMS speciation investigation at ultratrace concentrations was possible. CE-RIMS was therefore applied for the first time to real samples from batch experiments of Pu(III) and Pu(IV) sorbed on OPA under anaerobic conditions in OPA pore water at pH 7.6. For each oxidation state, 2 samples with S/L ratios of 1.0 g/L (sample 1) and 10.0 g/L (sample 2) were chosen. After separation of the solid and liquid phases, aliquots from supernatants were taken and the Pu species were separated by CE. After preparing the filaments, RIMS analyses were carried out.

For each sample, four filaments were prepared with the fractions 1 to 4 of "Pu(III)", "Pu(V)/Pu(VI)", "Pu(IV)", and the "Pu-background/not separated species", respectively.

As an example, Figs. 46 a – d show the mass spectra of fractions 1 – 4 of the sample 1 (S/L = 1.0 g/L), where Pu(III) was added for the batch experiments.

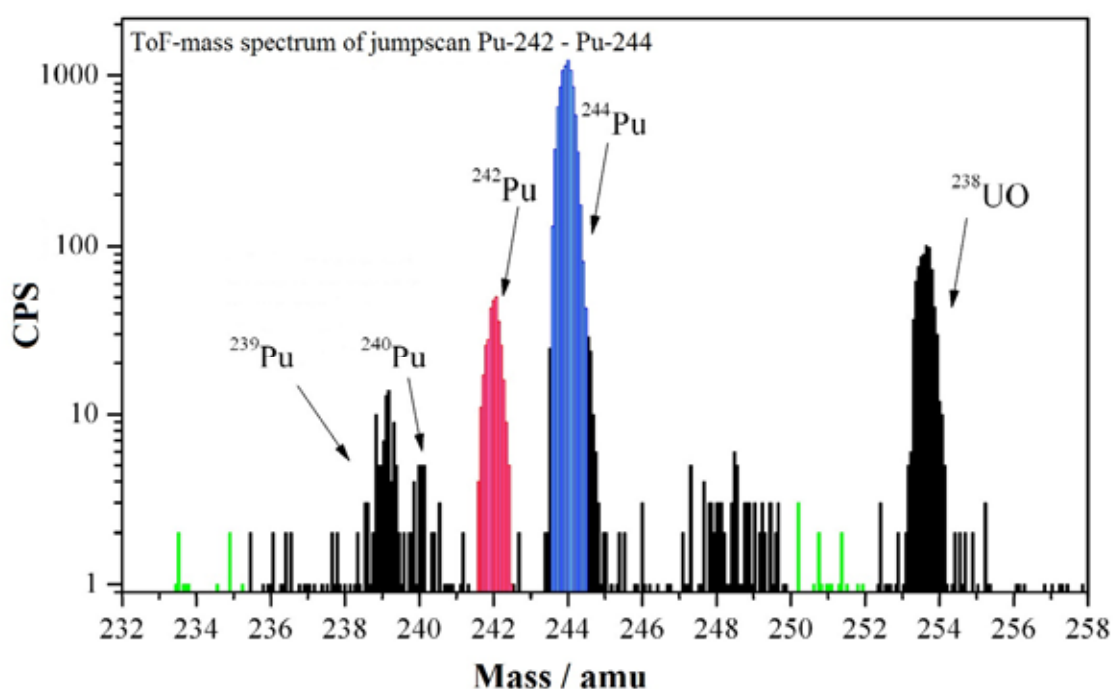


Figure 46a: CE-RIMS spectrum of fraction 1 (Pu(III)) of the sample 1.

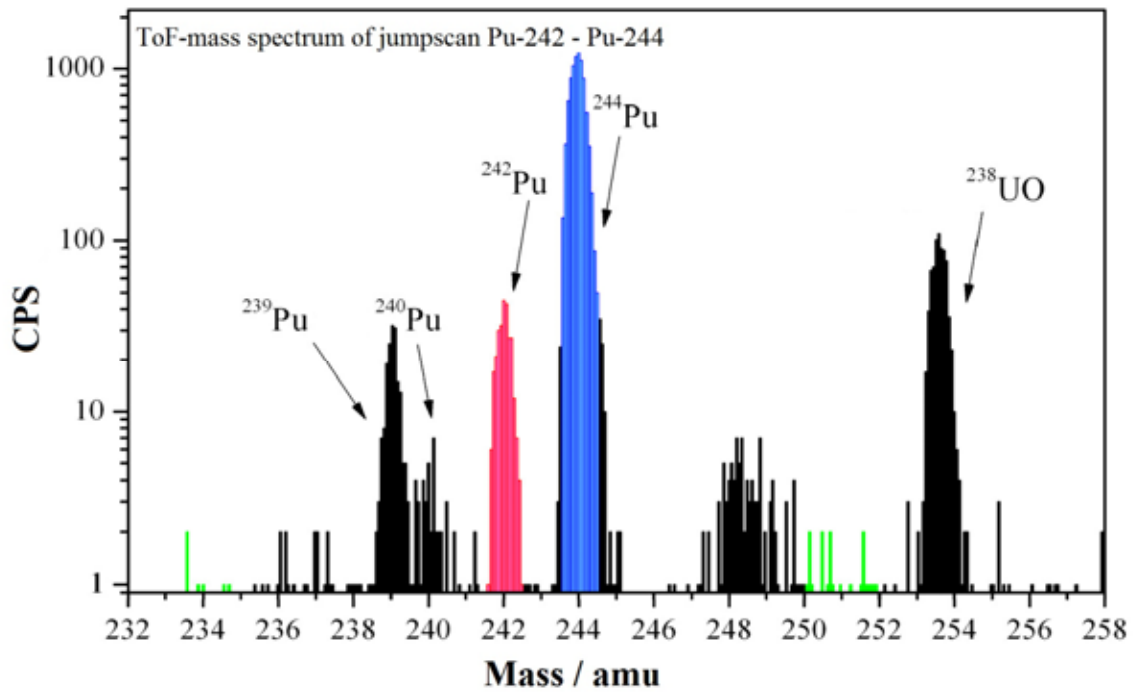


Figure 46b: CE-RIMS spectrum of fraction 2 (Pu(V)/Pu(VI)) of sample 1.

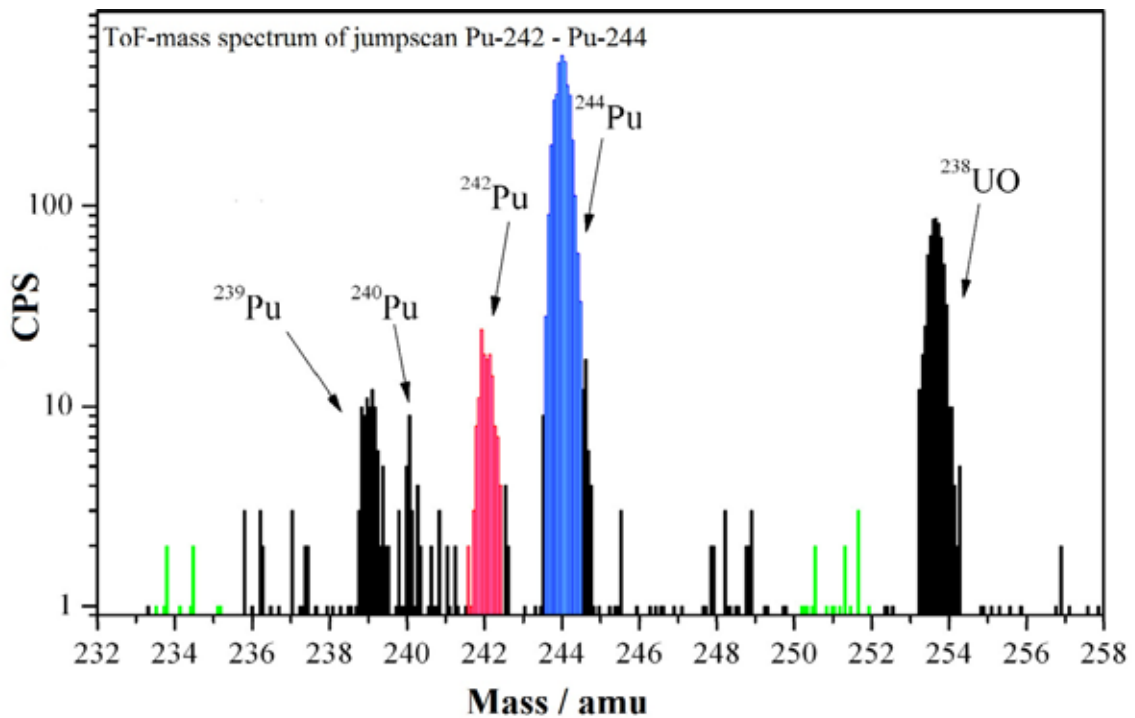


Figure 46c: CE-RIMS spectrum of fraction 3 (Pu(IV)) of sample 1.

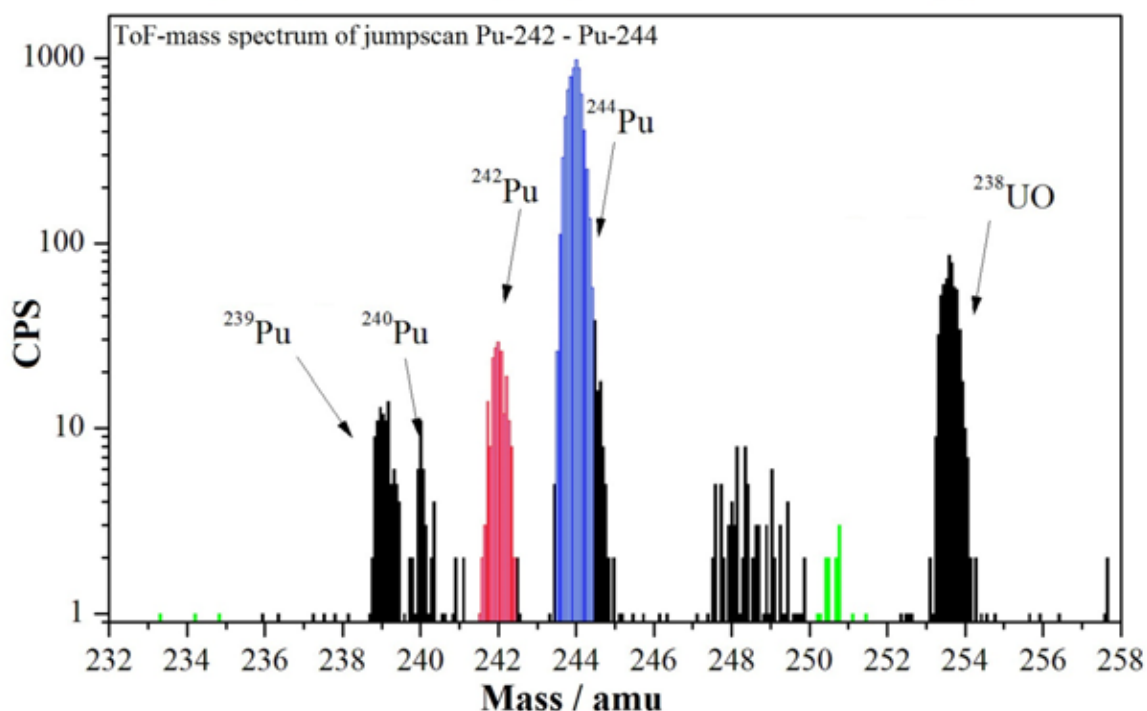


Figure 46d: CE-RIMS spectrum of fraction 4 (Pu-background/not separated species) of sample 1.

As can be seen from Figs. 46 a – d, well resolved mass spectra of the isotopes ^{239}Pu , ^{240}Pu , ^{242}Pu (as analysis isotope), ^{244}Pu (as tracer isotope), and the molecular ion ^{238}UO (as impurity in the sample) were obtained. A fluctuation in the amount of $^{239}\text{Pu}/^{240}\text{Pu}$ can be seen in the spectra. This is an indicator of a contamination in the samples. The ^{238}UO content remains relatively constant.

The determined atomic numbers of ^{242}Pu were converted in content percentage, based on the total amount of ^{242}Pu atoms in each of the four filaments of the samples 1 and 2. The distribution of Pu species in the samples obtained from CE-RIMS analysis is given in Tab. 26.

Table 26: Species composition in sample 1 and 2 obtained from CE-RIMS analysis.

Sample	²⁴² Pu atoms			
	Pu(III)%	Pu(V/VI)%	Pu(IV)%	Background%
	Pu(III) batch experiment			
1	28.3 ± 4.8	23.8 ± 4.4	26.5 ± 7.0	21.3 ± 4.8
2	40.8 ± 11.9	22.2 ± 7.1	37.0 ± 14.8	- ^a
Pu(IV) batch experiment				
1	25.9 ± 3.4	30.2 ± 3.6	16.6 ± 3.1	27.3 ± 4.5
2	95.1 ± 6.7	2.8 ± 0.4	1.2 ± 0.3	1.0 ± 0.2

^a not analyzed filament

As can be seen from Tab. 26, after sorption of Pu on OPA from a Pu(III) solution, the pore water supernatant contained a mixture of Pu(III), Pu(V)/Pu(VI) and Pu(IV). In conclusion, the conditions (pH, Eh, ionic composition) in the pore water were oxidizing for Pu(III). A reducing effect due to the anaerobic environment and the OPA could not be observed. Analogous to the results of Pu(III), the supernatant after Pu(IV) uptake contained a mixture of Pu(III), Pu (V)/(VI), and Pu(IV).

As a conclusion, a mixture of different Pu oxidation states in supernatant solutions was obtained independent of the initial Pu oxidation state added to the suspensions. RIMS was successfully applied to real samples. It was possible to detect and determine the Pu species at ultratrace concentrations close to environmental conditions.

5 Summary

The objective of this project was to investigate the main transport and retardation processes of the actinides, mainly neptunium (Np) and plutonium (Pu), for a repository of spent nuclear fuels in an accidental scenario. The aim of this study was to deliver input parameters for the performance assessment of a future repository. The results should improve the thermodynamic databases for the immobilization of actinides by clay rocks and allow an assessment of argillaceous rocks as potential host for nuclear waste disposal.

The interaction of Np and Pu in their relevant oxidation states with natural Opalinus Clay (OPA) and the influence of humic acid (HA, M42) have been studied in detail. Furthermore, batch experiments with thorium (Th), uranium (U), and americium (Am) were performed for comparison.

The sorption of Np(V) on OPA was studied in batch experiments as a function of various parameters. The results showed that Np(V) uptake is strongly influenced by pH, aerobic/anaerobic conditions, partial pressure of CO₂, background electrolyte, ionic strength, and temperature. Stronger sorption was found under anaerobic conditions due to partial reduction of Np(V) to Np(IV). Under aerobic condition, the sorption decreases significantly at pH > 9 due to carbonate complexation in aqueous solution. The use of NaClO₄ as a background electrolyte leads to an overestimation of Np(V) sorption on OPA compared to OPA pore water. It was also confirmed that Np(V) sorption on OPA is an endothermic reaction. The influence of HA on the sorption of Np(V) and Pu(IV) on OPA was investigated as a function of pH, partial pressure of CO₂ for Np, and solid-to-liquid ratio for Pu(IV). The mobilizing effect of HA on the sorption of Np on OPA (pH > 7.5) was more pronounced at higher Np(V) concentration. In case of Pu(IV), HA affects the sorption on OPA in pore water at pH 7.6 and reduces the K_d value by about one order of magnitude.

Diffusion experiments of Np(V) with intact OPA bore cores were performed as a function of temperature and presence/absence of HA (M42) by using OPA pore water (pH = 7.6) as mobile phase. From these experiments the diffusion parameters were determined for the first time.

The sorption of NpO₂⁺, UO₂²⁺, PuO₂²⁺, Pu³⁺, Am³⁺, Pu⁴⁺, and Th⁴⁺ on OPA was investigated in batch experiments and distribution coefficients were determined. It was shown that the sorption of all actinides in OPA pore water (pH = 7.6) was proportional to the solid-to-liquid ratio of OPA. The K_d value depends on the oxidation state of actinide element. The tri- and tetravalent actinides are stronger sorbed on OPA with higher K_d values compared with hexa- and pentavalent actinides (U and Np), which are weakly sorbed.

Batch and diffusion experiments were combined with microscopic X-ray synchrotron radiation techniques (X-ray absorption spectroscopy (XAS), micro XAS (μ -XAS), micro X-ray fluorescence spectroscopy (μ -XRF), and micro X-ray diffraction (μ -XRD)) to identify the sorbed Np and Pu species on the surface of OPA. XAS measurements on bulk samples of Np(V) sorbed on OPA under anaerobic conditions show that Np(V) carbonate complexes are formed on the OPA surface. Under anaerobic conditions, inner-sphere sorption of a mixture of Np(V) and Np(IV) was observed. In the case of Pu, it was confirmed that Pu(IV) is the dominating oxidation state, independent of the initial Pu oxidation state, background electrolyte, presence/absence of HA, and aerobic/anaerobic conditions. Inner-sphere sorption of Pu(IV) on OPA was also observed. Additionally, it was shown that the type of OPA (aerobic or anaerobic) has a significant influence on the speciation of Pu on OPA.

From μ -XRF measurements, the spatial distributions of Fe, Ca, Mn, and sorbed Np or Pu on OPA thin sections were determined. μ -XANES (micro X-ray absorption near-edge structure) measurements of Np and Pu hot spots showed a reduction of Np(V) to Np(IV) and of Pu(VI) to Pu(IV) in both sorption and diffusion samples. This result agrees well with EXAFS results on bulk samples. Furthermore, μ -XRD measurements performed around Np or Pu hot spots showed that pyrite and siderite are the redox-active mineral phases in OPA.

The redox behavior of Pu under environmental conditions at trace level concentrations was studied using CE-ICP-MS (capillary electrophoresis coupled to inductively coupled plasma mass spectrometry) and CE-RIMS (capillary electrophoresis coupled to resonance ionization mass spectrometry). With the CE-ICP-MS method the limit of detection for all four oxidation states of Pu in solution could be reduced down to 0.5 ppb.

6 References

- [1] Gomper, K.: Zur Abtrennung langlebiger Radionuklide. In Radioaktivität und Kernenergie, Hoffmann, J.; Kuczera, B., Eds. Forschungszentrum Karlsruhe, pp. 153 - 167 (2001).
- [2] Hoth, P., Wirth, H., Reinhold, K., Bräuer, V., Krull, P., Feldrappe, H.: Endlagerung radioaktiver Abfälle in tiefen geologischen Formationen Deutschlands – Untersuchung und Bewertung von Tongesteinsformationen. Bundesanstalt für Geowissenschaften und Rohstoffe BGR, Hannover/Germany (2007).
- [3] NAGRA: Projekt Opalinuston – Synthese der geowissenschaftlichen Untersuchungsergebnisse, Entsorgungsnachweis für abgebrannte Brennelemente, verglaste hochaktive sowie langlebige mittelaktive Abfälle. Technical Report NTB 02-03, NAGRA Nationale Genossenschaft für die Lagerung radioaktiver Abfälle, Wettingen/Switzerland (2002).
- [4] OECD: Safety of geological disposal of high-level and long-lived radioactive waste in France – An international peer review of the “Dossier 2005 Argile” concerning disposal in the Callovo-Oxfordian formation. NEA No. 6178, OECD (2006).
- [5] Honty, M., De Craen, M.: Mineralogy of the Boom Clay in the Essen-1 borehole. External report SCK-CEN-ER-87; SCK-CEN Belgian Nuclear Research Centre, Mol/Belgium (2009).
- [6] Gautschi, A.: Hydrogeology of a fractured shale (Opalinus Clay): Implications for deep geological disposal of radioactive wastes. *Hydrogeol. J.* **9**, 97 - 107 (2001).
- [7] Van Loon, L. R., Soler, J. M.: Diffusion of HTO, $^{36}\text{Cl}^-$, $^{125}\text{I}^-$ and $^{22}\text{Na}^+$ in Opalinus Clay: Effect of confining pressure, sample orientation, sample depth and temperature. PSI technical report 04-03, Paul Scherrer Institut, Villigen/Switzerland (2004).
- [8] Lieser, K. H., Mühlenweg, U.: Neptunium in the hydrosphere and in the geosphere. *Radiochim. Acta* **43**, 27 - 35 (1988).
- [9] Thompson, R. C.: Neptunium: the neglected actinide. A review of the biological and environmental literature. *Radiat. Res.* **90**, 1 - 32 (1982).
- [10] Kaszuba, J. P., Runde, W. H.: The aqueous geochemistry of neptunium: dynamic control of soluble concentrations with applications to nuclear waste disposal. *Environ. Sci. Technol.* **33**, 4427 - 4433 (1999).
- [11] Choppin, G. R.: Humics and radionuclide migration, *Radiochimica Acta* **44/45**, 23 - 28 (1988).
- [12] Clark, D.: The chemical complexities of plutonium. *Los Alamos Sci.* **26**, 364 - 381 (2000).

- [13] Clark, D. L., Hecker, S. S., Jarvinen, G. D., Neu, M. P.: Plutonium. In: *The Chemistry of the Actinide and Transactinide Elements*. 3rd Ed. (Morss, L. R., Edelstein, N. M., Fuger, J., Katz, J. J., eds.) Springer, Dordrecht, The Netherlands, Chapt. 7, pp. 813 - 1264 (2006).
- [14] Pearson, F. J.: Opalinus Clay experimental water: A1 type, Version 980318, PSI internal report TM-44-98-07. Paul Scherrer Institut, Villigen/Switzerland (1998).
- [15] Joseph, C., Schmeide, K., Sachs, S., Brendler, V., Geipel, G., Bernhard, G.: Sorption of uranium(VI) onto Opalinus Clay in the absence and presence of humic acid in Opalinus Clay pore water. *Chem. Geol.* **284**, 240 - 250 (2011).
- [16] Fröhlich, D. R., Amayri, S., Drebert, J., Reich, T.: Sorption of neptunium(V) on Opalinus Clay under aerobic/anaerobic conditions. *Radiochim. Acta* **99**, 71 - 77 (2011).
- [17] Sachs, S., Schmeide, K., Brendler, V., Křepelová, A., Mibus, J., Geipel, G., Heise K. H., Bernhard, G.: Investigation of the complexation and the migration of actinides and non-radioactive substances with humic acids under geogenic conditions. Complexation of humic acids with actinides in the oxidation state IV Th, U, Np. Report FZR-399, Forschungszentrum Rossendorf, Dresden, Germany (2004).
- [18] Sachs, S.: Kurzcharakterisierung der synthetischen Huminsäure Typ [14C]M42 (Chargen R2/06 und R2/06A) im Vergleich zur synthetischen Huminsäure Typ M42 (Charge M145), Forschungszentrum Dresden-Rossendorf, personal communication (2006).
- [19] Gustafsson, J. P.: Geochemical equilibrium speciation model Visual MINTEQ V. 2.52. KTH, Department of Land and Water Resources Engineering, Stockholm/Sweden (2007), <http://www.lwr.kth.se/English/OurSoftware/vminteq>.
- [20] Cohen, D.: Electrochemical studies of plutonium ions in perchloric acid solution. *J. Inorg. Nucl. Chem.* **18**, 207 - 210 (1961).
- [21] Cohen, D.: The absorption spectra of plutonium ions in perchloric acid solutions. *J. Inorg. Nucl. Chem.* **18**, 211 - 218 (1961).
- [22] Kuczewski, B., Marquardt, C. M., Seibert, A., Geckeis, H., Kratz, J. V., Trautmann, N.: Separation of plutonium and neptunium species by capillary electrophoresis-inductively coupled plasma-mass spectrometry and application to natural groundwater samples. *J. Anal. Chem.* **75**, 6769 - 6774 (2003).
- [23] Wunderlich, T.: Anwendung der CE-ICP-MS und RIMS sowie Entwicklung und Anwendung der CE-RIMS auf Umweltproben. Johannes Gutenberg-Universität Mainz, PhD Thesis 2009.
- [24] Grüning, C., Huber, G., Klopp, P., Kratz, J. V., Kunz, P., Passler, G., Trautmann, N., Waldek, A., Wendt, K.: Resonance ionization mass spectrometry for ultratrace analysis of plutonium with a new solid state laser system, *Int. J. Mass Spectrom.* **235**, 171 - 178 (2004).

- [25] Wendt, K., Trautmann, N.: Recent developments in isotope ratio measurements by resonance ionization mass spectrometry. *Int. J. Mass Spectrom.* **242**, 161 - 168 (2005).
- [26] Raeder, S., Stöbener, N., Gottwald, T., Passler, G., Reich, T., Trautmann, T., Wendt, K.: Determination of a three-step excitation and ionization scheme for resonance ionization and ultratrace analysis of Np-237. *Spectrochim. Acta* **B66**, 242 - 247 (2011).
- [27] Neck, V., Runde, W., Kim, J. I., Kanellakopoulos, B.: Solid-liquid equilibrium reactions of neptunium(V) in carbonate solution at different ionic-strength. *Radiochim. Acta* **65**, 29 - 37 (1994).
- [28] Wu, T., Amayri, S., Drebert, J., Van Loon, L. R., Reich, T.: Neptunium(V) sorption and diffusion in Opalinus Clay. *Environ. Sci. Technol.* **43**, 6567 - 6571 (2009).
- [29] Van Loon, L. R., Soler, J. M., Bradbury, M. H.: Diffusion of HTO, $^{36}\text{Cl}^-$ and $^{125}\text{I}^-$ in Opalinus Clay samples from Mont Terri: Effect of confining pressure. *J. Contam. Hydrol.* **61**, 73 - 83 (2003).
- [30] Van Loon, L. R., Eikenberg, J.: A high-resolution abrasive method for determining diffusion profiles of sorbing radionuclides in dense argillaceous rocks. *Appl. Radiat. Isot.* **63**, 11 - 21 (2005).
- [31] Matz, W., Schell, N., Bernhard, G., Prokert, F., Reich, T., Claußner, J., Oehme, W., Schlenk, R., Dienel, S., Funke, H., Eichhorn, F., Betzl, M., Pröhl, D., Strauch, U., Hüttig, G., Krug, H., Neumann, W., Brendler, V., Reichel, P., Denecke, M. A., Nitsche, H.: ROBL-a CRG beamline for radiochemistry and materials research at the ESRF. *J. Synchrotron Rad.* **6**, 1076 - 1085 (1999).
- [32] Ravel, B., Newville, M.: ATHENA, ARTEMIS, HEPHAESTUS: Data analysis for X-ray absorption spectroscopy using IFEFFIT. *J. Synchrotron Rad.* **12**, 537 - 541 (2005).
- [33] George, G. N., Pickering, I. J.: EXAFSPAK: A suite of computer programs for analysis of X-ray absorption spectra. Stanford Synchrotron Radiation Laboratory, Stanford, CA, USA (2000).
- [34] Ankudinov, A. L., Bouldin, C. E., Rehr, J. J., Sims, J., Hung, H.: Parallel calculation of electron multiple scattering using Lanczos algorithms. *Phys. Rev. B* **65**, 104107/1-11 (2002).
- [35] Demartin, F., Gramaccioli, C. M., Pilati, T.: The importance of accurate crystal structure determination of uranium minerals. II. Soddyite $(\text{UO}_2)_2(\text{SiO}_4)\cdot 2\text{H}_2\text{O}$. *Acta Cryst.* **C48**, 1 - 4 (1992).
- [36] Volkov, Y. F., Visyashcheva, G. I., Tomilin, S. V., Kapshukov, I. I., Rykov, A. G.: Study of the carbonate compounds of pentavalent actinides with alkali metal cations. *Radiokhim.* **23**, 243 - 247 (1981).

- [37] Benedict, U., Dabos, S., Dufour, C., Spirlet, J. C., Pagès, M.: Neptunium compounds under high pressure. *J. Less-Common Met.* **121**, 461 - 468 (1986).
- [38] Chtoun E. H., Hanebali L., Garnier P.: Analyse par diffraction des rayons x, méthode de Rietveld, de la structure des solutions solides $(1-x)A_2Ti_2O_7 - xFe_2TiO_5$ A= Eu, Y. *Annales de Chimie* **26(3)**, 27 - 32 (2001).
- [39] Borca, C. N., Grolimund, D., Willimann, M., Meyer, B., Jefimovs, K., Vila-Comamala, J., David, C.: The microXAS beamline at the Swiss Light source: towards nano-scale imaging. *J. Phys.* **186**, 012003, 1 - 3 (2009).
- [40] Roßberg, A., Reich, T., Bernhard, G.: Complexation of uranium(VI) with protocatechuic acid - application of iterative transformation factor analysis to EXAFS spectroscopy. *Anal. Bioanal. Chem.* **376**, 631 - 638 (2003).
- [41] Lande, J., Webb, S.: The Area Diffraction Machine. Stanford Synchrotron Radiation Laboratory, Stanford/USA (2007).
<http://www.areadiffractionmachine.googlecode.com>
- [42] Bürger, S., Banik, N. L., Buda, R. A., Kratz, J. V., Kuczewski, B., Trautmann, N.: Speciation of the oxidation states of plutonium in aqueous solutions by UV-vis spectroscopy, CE-ICP-MS, and CE-RIMS. *Radiochim. Acta* **95**, 433 - 438 (2007).
- [43] Amayri, S., Jermolajev A., Reich, T.: Neptunium(V) sorption on kaolinite. *Radiochim. Acta* **99**, 349 - 357 (2011).
- [44] Wu, T., Amayri, S., Reich, T.: Neptunium(V) sorption onto gibbsite. *Radiochim. Acta* **97**, 99 - 103 (2009).
- [45] Langmuir, D.: *Aqueous Environmental Geochemistry*. Prentice Hall, Upper Saddle River, pp. 353 - 364 (1997).
- [46] Amayri, S., Drebert, J., Fröhlich, D. R., Kaplan, U., Reich, T.: Distribution coefficients for the sorption of actinides (Th, U, Np, Pu, Am) on Opalinus Clay in synthetic pore water (in preparation 2011).
- [47] Pearson, F. J., Arcos, D., Bath, A., Boissin, J.-Y., Fernández, A. M., Gäbler, H.-E., Gaucher, E., Gautschi, A., Griffault, L., Hern´an, P., Waber, H. N.: Mont Terri Project - Geochemistry of water in the Opalinus Clay formation at the Mont Terri Rock Laboratory. Reports of the Federal Office for Water and Geology, Geology Series, No. 5, Bern (2003).
- [48] Banik, N. L., Buda, R. A., Bürger, S., Kratz, J. V., Trautmann, N.: Sorption of tetravalent plutonium and humic substances onto kaolinite. *Radiochim. Acta* **95**, 569 - 575 (2007).
- [49] Schmeide, K., Bernhard, G.: Sorption of Np(V) and Np(IV) onto kaolinite: Effects of pH, ionic strength, carbonate and humic acid. *Appl. Geochem.* **25**, 1238 - 1247 (2010).

- [50] Buda, R. A., Banik, N. L., Kratz, J. V., Trautmann, N.: Studies of the ternary systems humic substances - kaolinite - Pu(III) and Pu(IV). *Radiochim. Acta* **96**, 657 - 665 (2008).
- [51] Fröhlich, D. R.: Speziation von Neptunium bei der Migration in Tongestein. Johannes Gutenberg-Universität Mainz, PhD Thesis 2011.
- [52] Fröhlich, D.R., Amayri, S., Drebert, J., Reich, T.: Influence of temperature and background electrolyte on the sorption of neptunium(V) on Opalinus Clay. *Appl. Clay Sci.* (submitted 2011).
- [53] Brassler, T., Droste, J., Müller-Lyda, I., Neles, J., Sailer, M., Schmidt, G., Steinhoff, M.: Endlagerung wärmeentwickelnder radioaktiver Abfälle in Deutschland. GRS - 247, GRS Gesellschaft für Anlagen- und Reaktorsicherheit mbH (2008).
- [54] Lu, N., Reimus, P. W., Parker, G. R., Conca, J. L., Triay, I. R.: Sorption kinetics and impact of temperature, ionic strength and colloid concentration on the adsorption of plutonium-239 by inorganic colloids. *Radiochim. Acta* **91**, 713 -720 (2003).
- [55] Runde, W., Conradson, S. D., Efurud, D. W., Lu, N., Van Pelt, C. E., Tait, C. D.: Solubility and sorption of redox-sensitive radionuclides (Np, Pu) in J-13 water from Yucca Mountain site: comparison between experiment and theory. *Appl. Geochem.* **17**, 837 - 853 (2002).
- [56] Bauer, A., Rabung, T., Claret, F., Schäfer, T., Buckau, G., Fanghänel, T.: Influence of temperature on sorption of europium onto smectite: The role of organic contaminants. *Appl. Clay Sci.* **30**, 1 - 10 (2005).
- [57] Tertre, E., Berger, G., Castet, S., Loubet, M., Giffaut, E.: Experimental sorption of Ni^{2+} , Cs^{+} and Ln^{3+} onto montmorillonite up to 150 °C. *Geochim. Cosmochim. Acta* **69**, 4937 - 4948 (2005).
- [58] Tertre, E., Berger, G., Simoni, E., Castet, S., Giffaut, E., Loubet, M., Catalette, H.: Europium retention onto clay minerals from 25 to 150 °C: Experimental measurements, spectroscopic features and sorption modelling. *Geochim. Cosmochim. Acta* **70**, 4563 - 4578 (2006).
- [59] Angove, M. J., Johnson, B. B., Wells, J. D.: The influence of temperature on the adsorption of cadmium(II) and cobalt(II) on kaolinite. *J. Col. Inter. Sci.* **204**, 93 - 103 (1998).
- [60] Ward D. B., Brady P. V.: Effect of Al and organic acids on the surface chemistry of kaolinite. *Clays Clay Miner.* **46**, 453 - 465 (1998).
- [61] Machesky, M. L., Wesolowski, D. J., Palmer, D. A., Ichiro-Hayashi, K.: Potentiometric titrations of rutile suspensions to 250°C. *J. Col. Inter. Sci.* **200**, 298 - 309 (1998).

- [62] Bradbury, M. H. and Baeyens, B.: Far field sorption data bases for performance assessment of a high-level radioactive waste repository in an undisturbed Opalinus Clay host rock. PSI report 03-08, Paul Scherrer Institut, Villigen / Switzerland (2003).
- [63] Van Loon, L. R., Baeyens, B., Bradbury, M. H.: Diffusion and retention of sodium and strontium in Opalinus Clay: Comparison of sorption data from diffusion and batch sorption measurements, and geochemical calculations. *Appl. Geochem.* **20**, 2351 - 2363 (2005).
- [64] Wang, X. K., Chen, Y. X., Wu, Y. C.: Diffusion of Eu(III) in compacted bentonite - effect of pH, solution concentration and humic acid. *Appl. Radiat. Isot.* **60**, 963 - 969 (2004).
- [65] Wang, X. K., Chen, C. L., Zhou, X., Tan, X. L., Hu, W. P.: Diffusion and sorption of U(VI) in compacted bentonite studied by a capillary method. *Radiochim. Acta* **93**, 273 - 278 (2005).
- [66] Tachi, Y., Shibutani, T., Sato, H., Yui, M.: Sorption and diffusion behavior of selenium in tuff. *J. Contam. Hydrol.* **35**, 77 - 89 (1998).
- [67] Tachi, Y., Shibutani, T., Sato, H., Yui, M.: Experimental and modeling studies on sorption and diffusion of radium in bentonite. *J. Contam. Hydrol.* **47**, 171 - 186 (2001).
- [68] Mukai, S., Kataoka, S.: Diffusion of some radionuclides in compacted Ca-bentonite under reducing condition. *Radiochim. Acta* **82**, 179 - 182 (1998).
- [69] Bradbury, M. H., Baeyens, B. A.: Comparison of apparent diffusion coefficients measured in compacted kunigel V1 bentonite with those calculated from batch sorption measurements and D_e (HTO) data: A case study for Cs(I), Ni(II), Sm(III), Am(III), Zr(IV) and Np(V). PSI technical report Nr. 03-02, Paul Scherrer Institut, Villigen / Switzerland (2003).
- [70] Glaus, M. A., Rosse', R., Van Loon, L. R., Yaroshchuk, A. E.: Tracer diffusion in sintered stainless steel filters: Measurement of effective diffusion coefficients and implications for diffusion studies with compacted clays. *Clays Clay Miner.* **56**, 677 - 685 (2008).
- [71] Wang, J. H.: Self-diffusion and structure of liquid water. I. Measurement of self-diffusion of liquid water with deuterium as tracer. *J. Am. Chem. Soc.* **73**, 510 - 513 (1951).
- [72] Kozai, N., Inada, K., Kozaki, T., Sato, S., Ohashi, H., Banba, T.: Apparent diffusion coefficients and chemical species of neptunium(V) in compacted Namontmorillonite. *J. Contam. Hydrol.* **47**, 149 - 158, (2001).
- [73] Duff, M. C., Newville, M., Hunter, D. B., Bertsch, P. M., Sutton, S. R., Triay, I. R., Vaniman, D. T., Eng, P., Rivers, M. L.: Micro-XAS studies with sorbed plutonium on tuff. *J. Synchrotron Rad.* **6**, 350 - 352 (1999).

- [74] Duff, M. C., Hunter, D. B., Triay, I. R., Bertsch, P. M., Kitten, J., Vaniman, D. T.: Comparison of two micro-analytical methods for detecting the spatial distribution of sorbed Pu on geological materials. *J. Contam. Hydrol.* **47**, 211 - 218 (2001).
- [75] Reich, T., Bernhard, G., Geipel, G., Funke, H., Hennig, C., Rossberg, A., Matz, W., Schell, N., Nitsche, H.: The Rossendorf Beam Line ROBL - a dedicated experimental station for XAFS measurements of actinides and other radionuclides. *Radiochim. Acta* **88**, 633 - 637 (2000).
- [76] Clark, D. L., Conradson, S. D., Ekberg, S. A., Hess, N. J., Neu, M. P., Palmer, P. D., Runde, W. H., Tait, C. D.: EXAFS studies of pentavalent neptunium carbonate complexes. Structural elucidation of the principal constituents of neptunium in groundwater environments. *J. Am. Chem. Soc.* **118**, 2089 - 2090 (1996).
- [77] Reich, T., Reich, T. Y., Amayri, S., Drebert, J., Banik, N. L., Buda, R. A., Kratz, J. V., Trautmann, N.: Application of XAFS spectroscopy to actinide environmental science. *AIP Conf. Proc. (X-Ray Absorption Fine Structure (XAFS13))* **882**, 179 - 83, (2007).
- [78] Moyes, L. N., Jones, M. J., Reed, W. A., Livens, F. R., Charnock, J. M., Mosselmans, J. F. W., Hennig, C., Vaughan, D. J., Patrick, R. A. D.: An X-ray absorption spectroscopy study of neptunium(V) reactions with mackinawite (FeS). *Environ. Sci. Technol.* **36**, 179 - 183 (2002).
- [79] Marcus, M., XY display with mask.exe. ALS Advanced Light Source, LBNL Lawrence Berkeley National Laboratory, Berkeley/USA, <http://xraysweb.lbl.gov/uxas/Beamline/Software/Documentation/Documentation.htm>, (2007).
- [80] Conradson, S. D., Clark, D. L., Neu, M. P., Runde, W. H., Tait, C. D.: Characterizing the plutonium aquo ions by XAFS spectroscopy. *Los Alamos Sci.* **26**, 418 - 421 (2000).
- [81] Conradson, S. D., Al Mahamid, I., Clark, D. L., Hess, N. J., Hudson, E. A., Neu, M. P., Palmer, P. D., Runde, W. H., Tait, C. D.: Oxidation state determination of plutonium aquo ions using X-ray absorption spectroscopy. *Polyhedron* **7**, 599 - 602 (1998).
- [82] Dardenne, K., Seibert, A., Denecke, M. A., Marquardt, Ch. M.: Plutonium(III,IV,VI) speciation in Gorleben groundwater using XAFS. *Radiochim. Acta* **97**, 91 - 97 (2009).
- [83] Takeno N.: Atlas of Eh-pH diagrams intercomparison of thermodynamic databases; Geological survey of Japan open file report No. 419; National institute of advanced industrial science and technology research center for deep geological environments (2005).
- [84] Blaise, J., and Wyart, J.-F.: Selected constants, energy levels and atomic spectra, Vol. 20, tables internationales de constantes, Université P. et M. Curie, Paris, (1992).

7 Acknowledgment

This work was financed by the Federal Ministry of Economics and Technology (BMWi) under contract No. 02E10166 and Actinet-I3 under contract No. 232631. We acknowledge the ESRF and SLS for provision of synchrotron beam time and thank A. Roßberg, A. Scheinost, C. Henning, and D. Banerjee from the Helmholtz-Zentrum Dresden-Rossendorf (HZDR) for the experimental support during the XAS measurements at ROBL. For support during the μ -XAS experiments we thank D. Grolimund and C. Borca from Paul Scherrer Institute (PSI). Further we thank N. Beiser and N. Groschopf from the Institute of Geosciences, Johannes Gutenberg-Universität Mainz for XRF analysis and Dr. Ch. Marquardt from the Institute for Nuclear Waste Disposal, Karlsruher Institut für Technologie (KIT), for providing the OPA samples. M. Biegler, J. Huth, and J. Krause from the Max-Planck-Institut für Chemie in Mainz are acknowledged for preparation and microprobe measurements of the OPA thin sections.

Daniel Fröhlich and Nils Stöbener were financially supported by the DFG Interdisciplinary Research Training Group Program 826 “Trace Analysis of Elemental Species: Development of Methods and Applications”.

We would like to thank all colleagues who contributed to the success of this work.

Contributions to modelling actinide transport in potential host rock formations: Elementary processes and influence of heterogeneous structures

Holger Lippold, Johannes Kulenkampff, Marion Gründig, Abdelhamid Zakhnini

Helmholtz-Zentrum Dresden-Rossendorf (HZDR)
Institut für Radiochemie
Forschungsstelle Leipzig*
Permoserstr. 15, 04318 Leipzig

ABSCHLUSSBERICHT

Vorhabensbezeichnung:

„Beiträge zur Modellierung des Actinidentransports in potentiellen Wirtsgesteinsformationen – Teilthema 1: Mobilitätsbestimmende Elementarprozesse des huminstoffgebundenen Transports, Teilthema 2: Einfluss der heterogenen Struktur auf den Lösungs- und Kolloidtransport“

Förderkennzeichen: 02E10176
Berichtszeitraum: 01.07.2006 bis 30.06.2011
Projektleiter: Dr. H. Lippold

Teilprojekt im Rahmen des Verbundvorhabens

„Wechselwirkung und Transport von Actiniden im natürlichen Tongestein unter Berücksichtigung von Huminstoffen und Tonorganika“

Leipzig, Dezember 2011

* bis Dezember 2009: Institut für Interdisziplinäre Isotopenforschung (IIF)

Das diesem Bericht zugrunde liegende Vorhaben wurde mit Mitteln des Bundesministeriums für Wirtschaft und Technologie unter dem Förderkennzeichen 02E10176 gefördert. Die Verantwortung für den Inhalt dieser Veröffentlichung liegt bei den Autoren.

Kurzfassung

Die wesentliche Zielsetzung des Gesamtvorhabens bestand in der Bereitstellung von Bewertungsgrundlagen zur Abschätzung des Einflusses natürlicher organischer Komplexbildner auf die Mobilität von Actiniden in Tongestein als möglicher Endlagerformation. Ein Schwerpunkt lag auf der Hinterfragung der Gültigkeit vereinfachender Prozessvorstellungen bei der Modellierung huminstoffgebundener Transportvorgänge. Durch Nutzung des analytischen Potentials von Radiotracerverfahren und spektroskopischen Sondenmethoden wurden die maßgeblichen Wechselwirkungsprozesse innerhalb des ternären Systems Metall / Huminstoff / Tongestein eingehend untersucht. Fragen der Verknüpfung von Elementarprozessen waren dabei ebenso zu betrachten wie die Reversibilität von Adsorptionsvorgängen und kinetische Effekte in der Metall-Huminstoff-Komplexbildung.

Umfangreiche Adsorptionsstudien mit Opalinuston und anderen Tonmaterialien haben gezeigt, dass sowohl Huminstoffe als auch niedermolekulare Tonorganika einer Desorption von Metallen bei pH-Wert-Abnahme prinzipiell entgegenwirken. Dies kann auf die pH-Abhängigkeiten der Wechselwirkungen in den binären Randsystemen zurückgeführt werden, lässt sich jedoch nicht quantitativ anhand der zugehörigen Verteilungskoeffizienten beschreiben. Entsprechende Annahmen zur linearen Additivität von Einzelprozessen in Transportmodellen müssen daher grundsätzlich für das jeweilige System verifiziert werden.

Der dynamische Charakter der Adsorption von Huminstoffen konnte in Traceraustausch-Studien erstmals direkt nachgewiesen werden, obwohl Desorptionsversuche zunächst nicht auf einen reversiblen Prozess hindeuteten. Der Austausch im Sättigungszustand erfordert allerdings wesentlich mehr Zeit als die Einstellung des Adsorptionsgleichgewichts. Die Adsorptionskinetik ist somit kein zuverlässiges Kriterium, um die Bedingungen für ein ständiges Gleichgewicht in Fließsystemen abzuschätzen.

Abweichend von gleichgewichtsthermodynamischen Modellansätzen ist die Huminstoffkomplexbildung mehrwertiger Metalle durch Stabilisierungsprozesse über längere Zeiträume gekennzeichnet, in deren Ergebnis sich auch Konkurrenzeffekte verstärken. Diese Phänomene müssen in Experiment und Modell berücksichtigt werden. Das notwendige Verständnis der zugrunde liegenden Vorgänge auf molekularer Ebene konnte wesentlich verbessert werden.

Gleichrangig mit chemischen Wechselwirkungen auf molekularer Skala müssen die Transporteigenschaften des realen Barrierematerials untersucht werden, da diese den tatsächlichen Retardationseffekt der Wechselwirkung determinieren. Da auf jeder Größenskala transportbestimmende Strukturen vorhanden sind, bestimmen deren Skalierungseigenschaften zugleich die Übertragung von der molekularen auf die makroskopische Skala.

So wurden im Rahmen eines weiteren Aufgabenpaketes Transportstudien an möglichen Barrierematerialien (Tonen und Kristallingestein) durchgeführt. Hierzu wurde die GeoPET-Methode eingesetzt, die eine äußerst selektive und extrem empfindliche Konzentrationsbestimmung für radiomarkierte chemische Spezies in Raum und Zeit mit geeigneter Auflösung ermöglicht. Durch die Beschaffung eines

hochauflösenden PET-Scannern konnten die experimentellen Bedingungen gegenüber dem bisher genutzten Human-PET-Scanner und einer Eigenentwicklung optimiert werden. Es zeigte sich aber, dass die deutlich höhere Auflösung und Empfindlichkeit einen höheren Aufwand bei der Korrektur von materialbedingten Abbildungsfehlern erfordert.

Mit Hilfe des GeoPET-Verfahrens konnte die Ausbreitung konservativer Tracer durch Advektion in geklüftetem Kristallingestein und in gering kompaktierten Tonen quantitativ abgebildet werden. Der gemessene räumlich-zeitliche Verlauf der Tracerausbreitung zeigt vergleichbare Eigenschaften wie Transportsimulationen am selben Material, wenn ausreichend genaue Strukturinformationen vorliegen. In allen anderen Fällen weisen deutliche Abweichungen zwischen Modell und Beobachtung auf die besondere Bedeutung der Berücksichtigung heterogener Materialstrukturen hin.

Für die Beobachtung rein diffusiver Stoffausbreitung in Bohrkernen wurde ein Verfahren entwickelt, das geeignet ist, Anisotropie und präferentielle Wegsamkeiten nachzuweisen. Dabei stellte sich heraus, dass sich der Ausbreitungsprozess in realen, druckentlasteten Tonbohrkernen aufgrund der Teilsättigung deutlich komplizierter darstellt als reine molekulare Diffusion. Derartige Bedingungen sind in-situ relevant und in Auflockerungszonen ebenfalls zu erwarten.

Das Projekt war Bestandteil des Verbundvorhabens „Wechselwirkung und Transport von Actiniden im natürlichen Tongestein unter Berücksichtigung von Huminstoffen und Tonorganika“ (Förderkennzeichen 02E10156, 02E10166, 02E10176, 02E10186, 02E10196, 02E10206, 02E10216) unter Beteiligung folgender Einrichtungen:

- Helmholtz-Zentrum Dresden-Rossendorf (HZDR), Institut für Radiochemie
- Johannes-Gutenberg-Universität Mainz, Institut für Kernchemie
- Karlsruher Institut für Technologie (KIT), Institut für Nukleare Entsorgung
- Universität des Saarlandes, Institut für Anorganische und Analytische Chemie und Radiochemie
- Universität Potsdam, Institut für Chemie – Physikalische Chemie
- Technische Universität München, Fachgebiet Theoretische Chemie

Die Abschlussberichte zu den einzelnen Projekten werden im Rahmen eines zusammenfassenden Gesamtberichtes durch KIT veröffentlicht.

Abstract

As a main objective of the project, a basis was to be provided which allows an evaluation of the influence of natural organic complexants on the mobility of actinides in clay rock as a possible geological host formation for a final repository. A major focus was placed on the critical assessment of the applicability of simplifying assumptions for modelling humic-bound transport. Taking advantage of the analytical potential of radiotracer techniques and spectroscopic probe methods, relevant interactions within the ternary system metal / humic substance / clay were investigated in detail. The question of linking elementary processes was considered, as was the reversibility of adsorption as well as kinetic effects in metal-humic complexation.

Extensive adsorption studies with Opalinus clay and other clay materials have shown that metal desorption on acidification is generally counteracted by humic substances as well as low-molecular-weight clay organics. This can be explained by the pH dependences of the interactions in the constituent binary subsystems, but it cannot be quantitatively described by means of the corresponding partition coefficients. Thus, the assumption of linear additivity for single processes in transport models must be verified for every individual system under consideration.

By means of tracer exchange studies, the dynamic character of adsorption of humic matter was directly proven for the first time, although desorption experiments did not indicate a reversible process. The exchange at surface saturation requires, however, much more time than attaining the overall adsorption equilibrium. Thus, adsorption kinetics is not a reliable criterion for assessing the conditions of a steady equilibrium in flow systems.

Deviating from modelling approaches on the basis of equilibrium thermodynamics, complexation of higher-valent metals with humic substances is characterised by long-term stabilisation processes, leading to an increase in competition effects as well. These phenomena need to be considered in experiment and model. The necessary understanding of the underlying processes on a molecular scale was significantly improved.

Transport properties of the real barrier material are equally relevant as are chemical interactions on the molecular scale because the actual retarding effect of these interactions is determined by the transport behaviour. A hierarchy of transport-determining structures is present over a large scale. Therefore, the transfer function from the molecular scale to the macroscale is governed by the scaling characteristics of these structures.

For this reason, we conducted transport studies with possible barrier materials (clays and crystalline rocks). We applied the GeoPET method, benefiting from its exceeding selectivity and extreme sensitivity for concentrations of radiolabelled chemical species, providing time-dependent tomographic images of the tracer concentration at due spatial resolution. The acquisition of a high-resolution PET scanner greatly improved the experimental conditions compared to the human-medical PET scanner and the in-house developed scanner applied before. It turned out, however, that the significant improvement in resolution and sensitivity required higher expenses for proper corrections of image artifacts induced by material properties.

By means of the GeoPET method, the propagation of conservative tracers by advection in jointed crystalline rocks and low-compacted clays was mapped quantitatively. The measured spatio-temporal evolution of the tracer concentration shows features comparable to transport simulations on the same material, provided that structural information is available at a sufficient precision. In all other cases, significant deviations between model and observation demonstrate the particular importance of a consideration of heterogeneous material structures.

Another method was developed for the observation of diffusive spreading of substances in drill cores, capable of establishing anisotropy and preferential transport pathways. These measurements revealed a more complex propagation process than pure molecular diffusion in real and decompressed clay cores, which is related to their partial saturation. Such conditions are relevant in-situ, and they are expected to be present in excavation-damaged zones as well.

The project was part of the joint project "Interaction and transport of actinides in natural clay rock considering humic substances and clay organic matter" (reference numbers 02E10156, 02E10166, 02E10176, 02E10186, 02E10196, 02E10206, 02E10216) of the following institutions:

- Helmholtz-Zentrum Dresden-Rossendorf (HZDR), Institut für Radiochemie
- Johannes-Gutenberg-Universität Mainz, Institut für Kernchemie
- Karlsruher Institut für Technologie (KIT), Institut für Nukleare Entsorgung
- Universität des Saarlandes, Institut für Anorganische und Analytische Chemie und Radiochemie
- Universität Potsdam, Institut für Chemie – Physikalische Chemie
- Technische Universität München, Fachgebiet Theoretische Chemie

The final reports of the individual projects will be published within the framework of a comprising report by KIT.

Table of contents

1. Introduction	7
2. Experimental	10
2.1. Materials	10
2.1.1. Humic materials	10
2.1.2. Radiochemicals	10
2.1.3. Clay materials	11
2.2. Methods	13
2.2.1. General remarks, analytical equipment	13
2.2.2. Quantitative determination of metal-humate complexation	13
2.2.3. Studies on adsorption / desorption	14
2.2.4. Laser fluorescence spectroscopy	15
2.2.5. Positron emission tomography (PET)	15
3. Results and discussion	23
3.1. Co-adsorption of Tb(III) and humic acid onto clay materials as a function of pH	23
3.1.1. Tb(III) adsorption in the absence and presence of humic acid	23
3.1.2. Adsorption of humic acid and humate complexation of Tb(III)	24
3.1.3. Modelling co-adsorption of Tb(III) and humic acid by means of a combined K_d approach (linear additive model)	25
3.2. Adsorption of Tb(III) onto clay materials in the presence of propionate and lactate	29
3.3. Radiotracer studies on the dynamics of adsorption equilibria for the system Tb(III) / humic acid / kaolinite	32
3.4. Elucidating time-dependent changes in the competition effect of Al(III) on Tb(III)-humate complexation	38
3.4.1. Evidence of stabilisation processes	38
3.4.2. Spectroscopic probing	40
3.5. Transport studies by means of positron emission tomography	45
3.5.1. Advection in homogenised clay samples	45
3.5.2. Advection in rock cores	51
3.5.3. Diffusion	55
4. Conclusions and outlook	66
5. References	69

List of abbreviations

CPU	central processing unit
DOC	dissolved organic carbon
EIT	electrical impedance tomography
FA	fulvic acid
FEM	finite element method
FWHM	full width at half maximum
HA	humic acid
HS	humic substance
LOR	line of response
LuYAP	cerium-doped lutetium yttrium aluminium perovskite
LYSO	cerium-doped lutetium yttrium orthosilicate
MRT	magnetic resonance tomography
MWCO	molecular weight cut-off
NIST	National Institute of Standards and Technology
OPA	Opalinus clay
OSEM	ordered subsets expectation maximisation
PE	polyethylene
PET	positron emission tomography
STIR	software for tomographic image reconstruction
VSG	visualisation science group
X- μ CT	X-ray computed microtomography

List of symbols

c	concentration
c	velocity of light
D	solid / liquid distribution ratio (mol / mol)
E	energy
I	intensity
K_d	solid / liquid distribution coefficient (mL / g)
m_e	rest mass of an electron
$t_{1/2}$	half-life
x	distance
β	stability constant
λ	wavelength
μ	linear attenuation coefficient
θ	scattering angle

1. Introduction

Predictive models on the migration of radionuclides in the event of release from underground disposal facilities are an important component of risk assessment studies in the selection process for a repository site. Because of their high radio- and chemotoxicity in conjunction with very long half-lives, actinides are in the focus of long-term safety analyses. In addition to the adsorption behaviour of the metal species, their interaction with colloidal components of the aqueous phase has been recognised to be of primary relevance. The capability of clays to adsorb cationic contaminants is outstanding, and it provides a barrier function as long as the net positive charge is not eliminated by negatively charged ligands. Besides formation of hydroxo / carbonate species at high pH values, interaction with aquatic humic substances as main constituents of colloidal DOC (dissolved organic carbon) can be decisive for the mobility of actinides or other contaminant metals [1-6]. Similarly, complex formation with organic components of natural clay is a potential mechanism to subvert the geochemical barrier.

It must be noted, however, that both mobilising and retarding effects are possible. Solid-liquid distribution of metals in the presence of humic substances is determined by the interaction of three elementary processes: (i) metal adsorption (ii) metal-humic complexation and (iii) adsorption of the humic substance. Extensive studies are undertaken to collect equilibrium data for these interactions, which are controlled by acid-base equilibria, redox processes and electrolyte composition. Since the dependencies are different for each interaction process, it is impractical to collect conditional data on metal adsorption for ternary systems (metal / humic substance / solid phase). In order to describe the influence of humic substances in transport models, data collected for binary systems need to be linked in an appropriate manner. As a major topic of this project, a combined K_d approach (linear additive model [7, 8]) was tested for suitability in reconstructing ternary systems on the basis of data determined for the binary subsystems. This conception has been incorporated in advanced transport codes where humic carriers are considered (for a literature review, see [9]). In its simplicity, it is, however, not unanimously accepted.

The adsorption studies presented in this report are focused on clay rock as a potential host formation for a final repository. According to an agreement within the joint project "Interaction and transport of actinides in natural clay rock considering humic substances and clay organic matter", natural clay material from the Opalinus clay formation (Mont Terri, Switzerland) was used as a reference sample. In addition, the clay minerals montmorillonite, illite and kaolinite were applied as adsorbent materials. The pH-dependence of metal adsorption was investigated in the absence and presence of humic acid as well as of propionic acid and lactic acid as representatives of low-molecular-weight organic matter occurring in natural clay rock.

The applicability of equilibrium approaches such as the linear additive model is affected by so-called kinetic effects. Complexation of higher-valent metals with humic substances has been found to be accompanied by slow processes leading to an increase in complex inertness [10-15]. In order to consider such phenomena in transport systems, a kinetically controlled availability model (KICAM) was developed [16, 17] and implemented in a coupled chemical transport code based on equilibrium and rate constants (K1-D) [18, 19]. In this model, a rapid complexation step is followed by a slow step, in which the metal changes from a fast-dissociating state to

a slowly-dissociating state. However, the chemical background of the different binding modes could not be elucidated so far. In this project, systematic studies were conducted to shed more light on the underlying processes, using laser fluorescence spectroscopy as a powerful technique to detect structural alterations on a molecular scale [20]. These investigations were focused on time-dependent phenomena in the competitive complexation with Al(III) as an important higher-valent electrolyte constituent in terrestrial waters.

In simple models on reactive solute transport, it is presumed that all involved interaction processes are in a steady local equilibrium under flow conditions. More sophisticated models also consider slow kinetics, but in any case, a dynamic exchange must be possible, i.e., the processes must be reversible. As regards adsorption of humic matter, it is unclear whether this requirement is actually met for these colloidal substances. In column experiments with geological materials, recoveries were found to be considerably lower than 100%. Besides filtration effects, irreversible adsorption may be a reason. As yet, the dynamics of adsorption equilibria has never been investigated for these substances. Tracer exchange experiments are uniquely suited for this purpose. By means of a homemade technique for ^{14}C -labelling of humic substances, it became possible to examine the reversibility of this process for the first time.

In addition to the possibility of distinction, an important advantage of radiotracers is the very low detection limit. Partitioning of actinides in DOC-containing systems has been found to be concentration-dependent [21] and therefore must be investigated at adequate concentration levels in order to generate reliable data. Conventional analytical methods are too insensitive for this purpose. Radioactive tracers provide analytical access to very dilute systems, in accordance with scenarios to be considered in the far-field of a nuclear waste repository. Besides ^{14}C -labelled humic and fulvic acids, [^{160}Tb]terbium(III) was used in this project, suitable as a short-lived tracer analogue of trivalent actinides such as Am(III), Cm(III) or Pu(III).

Another benefit of radiotracers is that they can be quantitatively localised in solid matrices. Migration of radionuclides fundamentally depends on the transport properties of the host rocks – including structural parameters from the nanoscale up to the field scale – and on interactions of dissolved or particle-bound radionuclides with the solid matrix. Since these structural influences are only present in the intact material, transport parameters of the real barrier material with its original structure need to be investigated to the same extent as geochemical interactions in suspensions. Experiments with compacted columns of ground material mainly reflect the effect of the reduced volume fraction of the fluid.

Transport properties of porous media have always been in the focus of petrophysics as well as chemical and reservoir engineering [22-24]. The porosity effect, which can be studied to some extent with compacted homogeneous material, is strongly modified by tortuosity effects, which reflect the topology, i.e., geometry distributions and network structure of the transport paths. The actual tortuosity effect depends on the nature of the processes (advection, molecular diffusion), state variables and driving forces, and thus is an effective, process-dependent tensor quantity. Presumably, it controls chemical reactions within the fluid volume and across the internal surface area, and thus the “effective reaction kinetics”. In tight materials like barrier rocks, transport limitation of chemical interactions plays a decisive role.

We apply positron emission tomography (PET) to investigate the behaviour and pathway distribution of radionuclides in order to reveal these transport effects in barrier material [25-27]. With the method of GeoPET, we benefit from the quantitative and spatially resolved detectability of radiotracers in solid matrices. The method has been adapted from applications in nuclear medicine. PET cameras are sensitive to positron-emitting radionuclides such as ^{18}F or ^{124}I . ^{18}F is the most frequently applied medical PET nuclide. Its half-life ($t_{1/2}$) of 110 min is, however, rather short. For geosciences, we also apply longer-lived nuclides, e.g., ^{58}Co ($t_{1/2} = 70.8$ d) or ^{22}Na ($t_{1/2} = 2.6$ y), which enables long-term diffusion experiments using other labelling methods, albeit at the expense of a higher noise level because these nuclides are non-pure positron emitters.

We fully customised a preclinical PET scanner to geoscientific applications. This GeoPET instrument is one-of-a-kind for the quantitative 4D (3D + time) visualisation of transport processes in geological matrices. Due to the higher density of geological material compared to body tissue, well-engineered correction procedures had to be developed and have been successfully implemented in the software. In this way, the physical limit of the spatial resolution (1.3 mm) has been finally reached. Compared to other solute visualisation techniques such as electrical impedance tomography (EIT) or nuclear magnetic resonance tomography (MRT), PET is about 10^{10} times more sensitive. Moreover, it is selective towards radiolabelled chemical species. This makes it an ideal method for the quantitative observation of labelled compounds in time and space. These data can be applied for model validation and parameterisation, improvement of process understanding as well as for the direct evaluation of process parameters (e.g., effective transport volume, flow path distribution and heterogeneity).

2. Experimental

2.1. Materials

2.1.1. Humic materials

Humic acid (HA) from Sigma-Aldrich (Germany), herein referred to as Aldrich HA, was purified by repeated precipitation and redissolution with 0.1 M HCl and 0.1 M NaOH / 0.01 M NaF, respectively, followed by dialysis and lyophilisation. An aquatic fulvic acid (FA) was isolated from surface water collected on the raised bog "Kleiner Kranichsee" (near Carlsfeld, Germany). Purification was carried out according to the recommendations of the International Humic Substances Society [28] (adsorption onto DAX-8 resin at pH 2, rinsing with 0.1 M HCl, elution with 0.1 M NaOH, evaporation, salt removal by cation exchange and dialysis, lyophilisation). Basic properties of the humic materials are specified in Table 1. Elemental analyses were performed with a Vario EL III (Elementar, Germany), acidities were determined by means of an automatic titrator TitroLine alpha (Schott, Germany) as described in Ref. [29].

Table 1. Elemental compositions, total acidities and contents of functional groups of humic materials used in the project.

		Aldrich HA	Bog water FA
C	(wt.-%)	50.5	49.2
H	(wt.-%)	4.8	4.4
N	(wt.-%)	3.8	4.5
Total acidity	(meq g ⁻¹)	6.0	8.1
Carboxylic groups	(meq g ⁻¹)	5.2	5.5
Phenolic hydroxyl groups*	(meq g ⁻¹)	0.8	2.6

* Taken as difference between total acidity and COOH content.

2.1.2. Radiochemicals

[¹⁶⁰Tb]Tb(III) ($t_{1/2} = 72.3$ d) was produced by neutron activation of natural Tb(III) (1 mg mL⁻¹, as nitrate) at the TRIGA Mark II reactor of the University of Mainz. 40 h of irradiation at a neutron flux of 7×10^{11} n cm⁻² s⁻¹ yielded a specific activity of 2 MBq mg⁻¹. After transformation into a perchlorate system by evaporating with concentrated HClO₄, a stock solution in 0.1 M NaClO₄ was prepared. [¹²⁴I]NaI ($t_{1/2} = 4.1$ d) was purchased from Eckert & Ziegler (Germany), [⁵⁸Co]CoCl₂ ($t_{1/2} = 70.8$ d) from Polatom (Poland). N.c.a. [¹⁸F]KF ($t_{1/2} = 1.8$ h) was kindly provided by the University of Leipzig, clinic and polyclinic for Nuclear Medicine. [⁸⁶Y]YCl₃ ($t_{1/2} = 14.7$ h) was produced by HZDR. [1-¹⁴C]propionate and [1-¹⁴C]L-lactate (specific activity: 2 GBq mmol⁻¹) were supplied as sodium salts by American Labelled Chemicals Inc. (US).

¹⁴C-labelled humic substances were prepared by an azo-coupling reaction [30]. The reaction scheme is shown in Fig. 1. For preparing the reactive benzenediazonium ion, ~ 6 MBq [¹⁴C]aniline hydrochloride (Biotrend, Germany) were added to 400 µL of a

solution of 0.1 M NaNO₂ in 1 M HCl, placed in an ice bath. 50 μL of this mixture were then given to 1000 μL of a solution of 0.5 g L⁻¹ of humic or fulvic acid in borate buffer (also cooled to 0°C), together with 80 μL of 0.1 M NaOH to maintain the pH value in a range between 8 and 9. This mixture was allowed to react in the ice bath for 30 min.

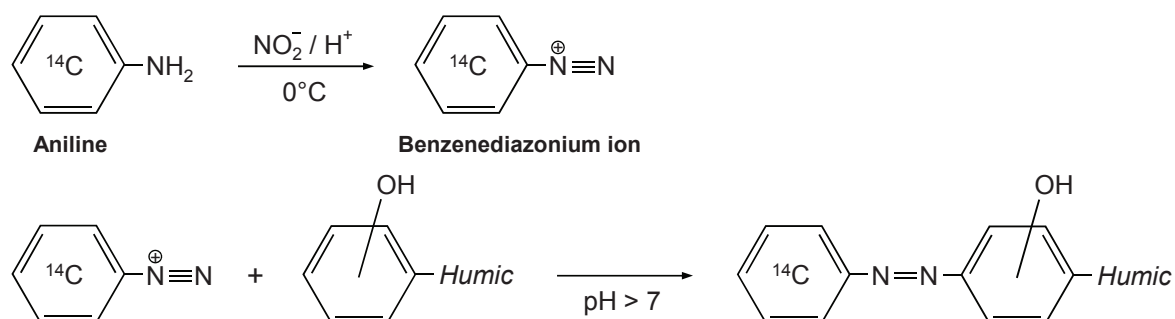


Figure 1. Reaction scheme for labelling humic acid with ¹⁴C by azo coupling with [¹⁴C]aniline.

For PET studies, humic acid was labelled with ¹²⁴I by the Iodogen method [31]. Halogenation is achieved by electrophilic substitution at activated positions within aromatic structures of humic molecules after oxidation of [¹²⁴I]⁻ by Iodogen (1,3,4,6-tetrachloro-3a,6a-diphenylglycouril). The heterogeneous reaction was performed in glass vials with 150 μg Iodogen coating (added in 200 μL chloroform). A solution of [¹²⁴I]NaI (~ 100 MBq) and HA in borate buffer (pH 8) was prepared, and portions of 500 μL were dispensed into several vials containing Iodogen, followed by permanent shaking for 10 min.

For separating from non-reacted radioactive material, humic acid was precipitated by acidification to pH < 1 with concentrated HClO₄. After centrifugation (20 min at 5000 rpm), the supernatant was removed with a pipette, and the precipitate was redissolved in 10⁻² M NaOH. This procedure was repeated (8-10 times) until the activity in the supernatant was negligible. Finally, the precipitate was dissolved in 0.1 M NaClO₄ / 10⁻³ M NaOH. Fulvic acid (which cannot be precipitated) was purified by ultrafiltration, using Microsep centrifuge filters (Pall, US) with a MWCO of 1 kDa. The retentate was rinsed ~ 10 times with 1 mL 0.1 M NaClO₄ until the activity in the filtrate was negligible (60 min centrifugation at 7000 rpm for each filtration step). Specific activities were about 1 MBq mg⁻¹ and 500 MBq mg⁻¹ for ¹⁴C- and ¹²⁴I-labelled humic material, respectively.

2.1.3. Clay materials

Opalinus clay samples (BHE-24/1) from the Mont Terri rock laboratory (Switzerland) were provided the German Federal Institute for Geosciences and Natural Resources (BGR). The clay minerals kaolinite (KGa-1b), illite (IMt-1) and Na-montmorillonite (SWy-2) were standard materials obtained from the Source Clays Repository of the Clay Minerals Society of America. Some characteristics are given in Table 2. All samples except for kaolinite were ground. Illite was suspended in water to remove coarse particles.

Table 2. Characteristics of the clay materials used in the project.

	Kaolinite KGa-1b	Illite IMt-1	Montmorill. SWy-2	OPA clay BHE-24/1
BET surface area (m ² g ⁻¹)	14 [32]	39 [35]	29 [37]	41 [39]
Cation exch. capacity (meq g ⁻¹)	0.03 [33]	0.08 [35]	0.87 [37]	0.10 [39]
Point of zero charge (pH)	5.5 [34]	3.5 [36]	4.2 [38]	n.a.

n.a.: not applicable.

2.2. Methods

2.2.1. General remarks, analytical equipment

All experiments were conducted under ambient conditions (atmospheric CO₂ pressure, room temperature where not otherwise stated). Water was purified with an SG Ultra Clear system. Adjustment of pH values was accomplished by adding diluted HClO₄ or NaOH, using a Sentix 41 combination electrode (WTW, Germany) for measurement. Usage of buffer systems was avoided. All batch experiments were performed with 0.1 M NaClO₄ as a background electrolyte, using PE vials.

A 1480 Wallac WIZARD 3" gamma counter (Perkin Elmer, US) was used for measurements of ¹⁶⁰Tb activities. All samples of a test series were made up to equal volumes to ensure a uniform measuring geometry. ¹⁴C determinations were carried out with a Tri-Carb 3110 TR Liquid Scintillation Analyser (Perkin Elmer, US). Aliquots of 1 mL were mixed with 10 mL Ultima Gold scintillation cocktail (Perkin Elmer, US). The results were corrected for colour quenching caused by humic material.

UV-Vis spectrometry was conducted by means of a Lambda 45 spectrophotometer (Perkin Elmer, US). Elemental analyses by ICP-OES were performed by means of a Spectroflame P/M instrument (Spectro, Germany).

2.2.2. Quantitative determination of metal-humate complexation

Anion exchange method. Following a study by Hiraide et al. [40], the anion exchange resin Sephadex DEAE A-25 (Sigma-Aldrich) was used as a separating agent. Prior to use, it was washed with methanol, rinsed with 0.1 M NaClO₄ and kept therein after pH adjustment. Metal / HA systems were prepared with pH-adjusted stock solutions. For separating the humic-bound metal fraction from the free metal fraction, the exchange resin was added as a slurry of ~ 300 mg to 4 mL solutions. Humic material, including bound metals, is quantitatively adsorbed. After shaking for 1 min and sedimentation, an aliquot of the supernatant was taken, and the decrease in metal concentration relative to the initial concentration was measured. Corrected for the water content of the slurry, this depletion is equal to the concentration of humic-bound metal. For time-dependent studies on the competition effect of Al(III), solutions of Al(III) and HA were mixed and left to stand in the dark for different periods of time (up to 6 months) before Tb(III) was introduced to the system. The exchange resin was then added after a reaction time of 2 - 5 min. Preliminary stopped-flow experiments based on fluorescence quenching had proven that the process of Tb(III)-humate complexation is accomplished within few seconds (Fig. 2).

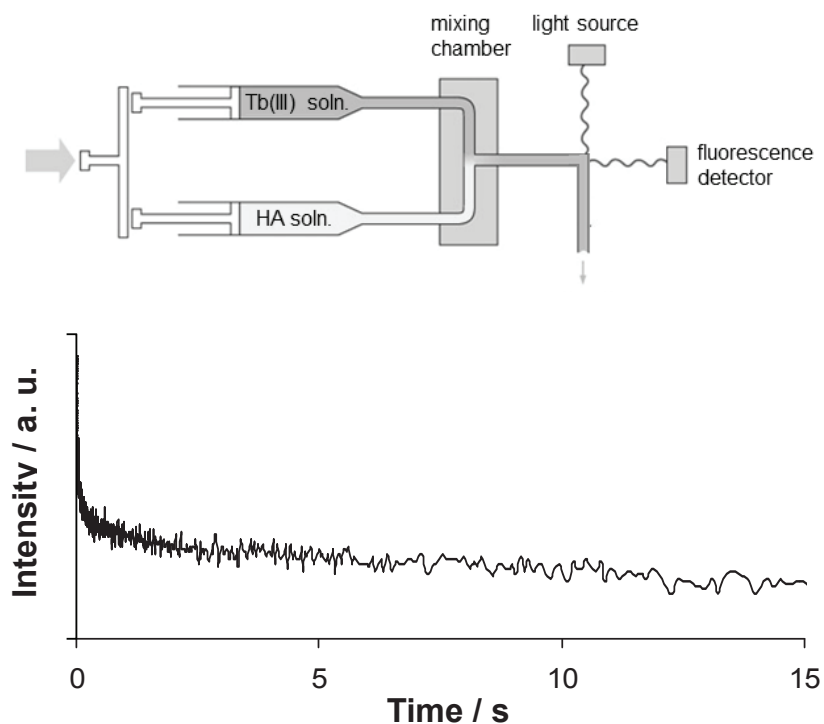


Figure 2. Stopped-flow experiments for monitoring the process of Tb(III)-humate complexation as a function of time, based on the quenching of fluorescence light emitted by HA (5 mg L⁻¹ HA, 10 μM Tb, 0.1 M NaClO₄, pH 4.0, λ_{exc} = 325 nm, 380 nm < λ_{em} < 580 nm).

Cation exchange method. Humic-bound Tb fractions were also determined on the basis of a metal exchange equilibrium between HA and a cation exchange resin, Bio-Rad AG 50W-X2. Humic acid is not adsorbed in this case. In order to avoid changes in pH, the cation exchanger was converted into its Na⁺ form by treating with 1 M NaOH. For equilibration, 10 mL of pH-adjusted solutions of Tb(III) or Tb(III) / HA in 0.1 M NaClO₄ were shaken with 10 mg of exchange resin. After 48 h, an aliquot was taken for analysis. The concentration of humic-bound metal c_M^{HA} was calculated from the relationship

$$c_M^{HA} = c_M^{total} \left(1 - \frac{D}{D_0} \right) \quad (1)$$

with D and D_0 denoting the solid-liquid distribution ratios of the metal (moles adsorbed / moles in solution) in the presence and absence of HA, respectively [41].

2.2.3. Studies on adsorption / desorption

For pre-conditioning to a series of pH values, stock suspensions of montmorillonite, illite or Opalinus clay in 0.1 M NaClO₄ were prepared and weighed. Dispersing was facilitated by sonication. The pH was then adjusted by adding HClO₄ or NaOH until the buffering capacities of the solids were exhausted (20 - 30 readjustments within a period of several weeks). When the pH values were stable, another weighing was

carried out, and an appropriate amount of solution was removed to attain a final solid-liquid ratio of 5 g L^{-1} , allowing for the volumes of Tb(III) / HA / propionate / lactate solutions to be added. The pH of kaolinite suspensions (used in the studies described in Section 3.3.) was left unchanged at 4.7. While stirring, the suspensions were then dispensed into 5 mL centrifuge tubes (PP), and the solutes were introduced (small amounts of near-neutral solutions), giving a total volume of 4 mL. After rotating end-over-end at 10 rpm for different time periods, the systems were centrifuged at 7000 rpm for 5 min, an aliquot of the supernatant was sampled, and the depletion was determined. In desorption studies, 3 mL of the supernatant were replaced by 3 mL of 0.1 M NaClO_4 solution, and the diluted systems were again rotated for different time periods. After centrifugation, aliquots were analysed for changes in concentration. Wall adsorption was found to be negligible for all solutes. Details on tracer exchange experiments are given in Section 3.3.

2.2.4. Laser fluorescence spectroscopy

Spectroscopic probing studies on possible structural backgrounds of kinetic effects in metal-humate complexation were carried out in cooperation with the university of Potsdam. Steady-state fluorescence spectra were recorded by means of a FluoroMax-3P spectrofluorometer (Jobin Yvon, US). For time-resolved laser-induced fluorescence spectroscopy (TRLFS), a pulsed Nd-YAG laser (Spectra-Physics, US) was used in combination with an optical parametric oscillator (GWU Lasertechnik, Germany). The fluorescence emission was detected by an iCCD camera coupled to a spectrograph (Andor Technology, UK). To record a full fluorescence decay of Tb(III) as a spectroscopic probe, 120 spectra (in the range of $450 \text{ nm} < \lambda_{\text{em}} < 700 \text{ nm}$) were acquired in steps of $15 \mu\text{s}$ (100 accumulations each in $50 \mu\text{s}$ time slots) with an initial delay of $1 \mu\text{s}$ to exclude any contribution of HA fluorescence. Decay curves were obtained by integrating the intensities within the range of the principal spectral band (${}^5\text{D}_4 \rightarrow {}^7\text{F}_5$ transition, $533 \text{ nm} < \lambda_{\text{em}} < 562 \text{ nm}$). Emission spectra for Eu(III) as a probe were recorded with an initial delay of $10 \mu\text{s}$ in a decay time frame of 5 ms (10^4 accumulations). The fluorescence intensities were corrected for drifts in the laser light intensity and in the spectral background. Further details are given in the results chapter. Test series with Al(III) / HA systems of different ages were prepared as described in Section 2.2.2. Acquisition of spectra was started 2 min after addition of Tb(III) or Eu(III).

2.2.5. Positron emission tomography (PET)

Principle. The localisation of positron-emitting radionuclides is based on the coincident detection of annihilation photons that are emitted pairwise in antiparallel direction when a positron hits an electron after deceleration to the thermal state. With an annular arrangement of scintillation detectors, the source of radiation can be assigned to the connecting line. As this line of response (LOR) is randomly oriented for every annihilation event, the radionuclide can be exactly localised at the intersection point of a multitude of LORs. From the frequency of detected coincidences, the radiotracer activity in a volume element (voxel) can be quantitatively determined.

This rather simple principle of quantitative image generation is complicated by a number of additional physical effects which – in the case of biomedical PET applications – are regarded as second-order corrections. These are more significant in the case of dense material, and interactions between matter and radiation have to be considered in more detail. The effects are:

- (i) slowing down of the positrons to the thermal state; the slow-down length decreases with increasing material density (cross section) [42],
- (ii) absorption of single annihilation photons according to Lambert-Beer's law

$$I(x) = I_0 \exp(-\mu x) \quad (2)$$

where I is the intensity, x is the distance, and μ is the linear attenuation coefficient, which can be derived from the mass absorption coefficients [43],

- (iii) scattering of photons, predominantly by Compton scattering, which causes an energy loss of photons of the initial energy E_0 to E_f

$$E_f = \frac{E_0}{1 + \alpha_E (1 - \cos\theta)} \quad (3)$$

with

$$\alpha_E = \frac{E_0}{m_e c^2} \quad (4)$$

where θ is the scattering angle, m_e is the rest mass of an electron, and c is the velocity of light. In usual PET applications, small angle scattering with angles $< 30^\circ$ is prevailing. This could be confirmed with our own Monte Carlo simulations for dense material as well [44].

Equipment. In the application period for this project, a human-medical PET scanner at the clinic and polyclinic of Nuclear Medicine of the University of Leipzig and an inhouse-developed PET scanner with a higher resolution, yet lower efficiency, were applied, predominantly for testing the feasibility of PET studies on transport processes in geomaterials. Successful demonstrational experiments enabled the acquisition of a commercial high-resolution PET scanner “ClearPET” (Raytest, Germany), which was not expected at the time of application and which allowed us to expand our transport studies considerably.

ClearPET [45-47], which was actually designed for 3D radiotracer studies with small animals, consists of 20 detector modules, each with 256 double-layered scintillation crystals on 4 position-dependent photomultiplier tubes. In a first phase, until June 2008, only 8 cassettes were installed, entailing a lower efficiency and a lower signal-to-noise ratio. The crystals are LYSO-LuYAP-phoswich combinations, size $2 \times 2 \times 10$ mm. This allows directional filtering of the incident photons and thus precise localisation of the decay events. The complete gantry of about 2 m in diameter is rotating around the specimen, both increasing the spatial covering of detector positions and equalising differences in the detection probability of the individual channels. The diameter of the field of view is adjustable between 70 mm and

144 mm, with a maximum length of 110 mm. The activity range is in the order of 30 dB, with a maximum activity around 100 MBq. The sensitivity of the scanner is better than 10 kBq per voxel, only limited by the detection probability and the natural background radiation. The currently achievable spatial resolution of about 1 mm is due to the free path of the emitted positrons before annihilation. One disadvantage of the modular construction of the scanner is an inhomogeneous sensitivity distribution within the field of view, which is caused by the gaps between the individual detector crystals. All events (“singles”) are recorded on 5 CPUs in parallel as partial listmode files. These are later combined by coincidence sorting, with simultaneous random detection, to yield listmode files of all coincident and random events. These files of “prompts” and “randoms”, with sizes of 1-10 GBytes, are archived as raw data.

Software. The tomographic reconstruction scheme is based on the open-source STIR library (version 1.4) [48, 49], complemented by some proprietary software. The final reconstruction product is a time series of data sets (interfile format) of quantitative tracer concentrations in 3D with voxel dimensions of $1.15 \times 1.15 \times 1.15 \text{ mm}^3$. The STIR image reconstruction operates in the space of projections, i.e., the bin-wise presentation of the LORs as a function of segment (inclination of the projection plane), view (azimuth of the LOR), axial coordinate and tangential coordinate. The original reconstruction consists of 7 steps:

- (1) binning (computing bin-wise projections from the listmode files of prompts and randoms)
- (2) random correction (bin-wise subtraction)
- (3) deadtime correction (correction of the scanner response curve)
- (4) absorption correction by means of a transmission scan
- (5) scatter correction by subtracting a nonlinear fit of the counts outside the field of view (resp. radiation source) to a Gauss function
- (6) iterative image reconstruction and normalisation with the STIR OSEM algorithm
- (7) image calibration (application of the scanner efficiency factor)

Most of these steps had to be adapted to the conditions of geological specimens with their considerably higher mass attenuation coefficient and scatter fractions compared to tissue. These adaptations refer to the following details:

To (2): It was found in the course of the experiments that the random correction was deficient in the presence of high background radiation, which is caused by background gradients due to scattered radiation from sources within or outside the field of view. This is due to the weakly occupied projection arrays, which is a common characteristic of 3D-PET projection data. The algorithm of random detection by delayed coincidence sorting is prone to bin-wise prompt-random missing of proximate bins. Thus, in the presence of high background radiation, a high amount of bins with negative values was found when the original random correction was applied. These negative bins were not considered subsequently. This effect produced image artifacts and quantification errors. It was repaired by some spatial balancing of the negative bins over the nearest neighbors, applying the R-package “SPATSTAT” (open-source software for spatial statistics) [50].

To (4): It was not possible to apply transmission scans with line sources that were positioned outside the field of view because the strong attenuation of the material caused low count rates on the opposite sides, which were hardly above the

background. However, because the specimens have simple geometries and a well-defined composition, the attenuation image could be constructed with the help of mass attenuation coefficients from the NIST XCOM (photon cross sections database) [51]. The correction factor for each bin is calculated from the line integral over the attenuation coefficient distribution for each LOR, which is the projection of the attenuation image. It must be noticed that this correction is crucial for providing consistent input data for the reconstruction and thus has to be applied to the projections.

To (5): The scatter correction, based on an extrapolation of weakly occupied points of the projection outside the field of view into it, turned out to increase the noise level, rather than to improve image quality. Therefore, we skipped the scatter correction so far. However, scatter causes significant blurring and image artifacts. We could characterise and quantify the extent and origin of scatter by Monte Carlo simulations of a number of PET experiments with fixed radiation sources using the software OpenGATE [52]. The simulations show that scatter fractions of up to 70% have to be considered, mainly depending on the density of the material. Both the new version of STIR (2.1) and the Monte Carlo simulations provide potential correction methods which will be applied in future.

To (6): The OSEM algorithm appears to be sensitive to obscure coincidences, which may be due to erroneous corrections or scatter [53]. These obscure coincidences produce ring artifacts, which are related to the inhomogeneous sensitivity distribution, and they produce radial artifacts. Both effects can be distinguished in most tomograms. Such reconstruction artifacts could be eliminated or at least reduced by “physics-based” inversion algorithms. Prospectively, such algorithms could be developed by combining a physical model of the observed process (i.e., partial differential equations) with the Monte Carlo forward simulation of the PET measurements. However, this approach is hampered by the lack of computing resources up to now.

The inhomogeneous sensitivity distribution is another issue of the reconstruction procedure (normalisation). The sensitivity is determined by measuring a homogeneous source of radiation, filling the complete field of view (Fig. 3). The gaps between the detector blocks produce gaps in the projections and strong local variations near these gaps. The STIR OSMAPOS algorithm shows a marked influence of the normalisation on the final image, which is probably a deficiency of this algorithm. Therefore, other reconstruction algorithms and procedures for the normalisation will be tested and applied in future.

To (7): The normalisation, together with the errors of its measurements and image artifacts, enter into the image calibration. Thus, we usually skipped the original calibration procedure and applied image-derived calibrations, either based on the known total activity or on known point sources within the field of view.

The image files are in the Interfile format, an old-established image format for medical tomograms, consisting of a header file in text format and a binary file. The rudimentary information in these files was extended, and all corrections were applied to the binary data, including the radioactive decay correction.

Most manipulations of the images were conducted with the free statistical software environment “R” [54]. Image smoothing algorithms based on R-packages were added, such as mean and median filtering in the space domain and smoothing splines in the time domain. Also, fitting algorithms for parameter estimation were applied, such as “CXTFIT” [55]. Finally, the tomograms were converted to the format of the software “Avizo fire” (VSG) for 3D-t visualisation and image analysis. First steps were done to utilise the data sets for the calibration of calculations by the finite element method (FEM). Parameters were even directly derived by optimising the FEM parameterisation.

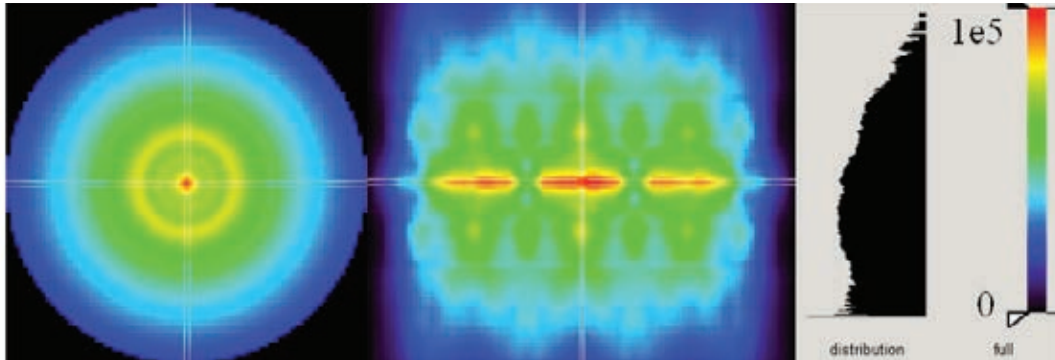


Figure 3. Normalisation image of ClearPET (backprojection image of a homogeneous activity distribution throughout the complete field of view).

Samples and their preparation. Homogeneous artificial clay samples as well as drill cores from intact crystalline and mud rocks have been investigated. The artificial samples were prepared from suspensions of kaolinite (Kao) and Opalinus clay (OPA1) in water and synthetic Opalinus clay pore water, respectively. These samples were compacted in a compression apparatus (Pero, Germany), shown in Fig. 4.

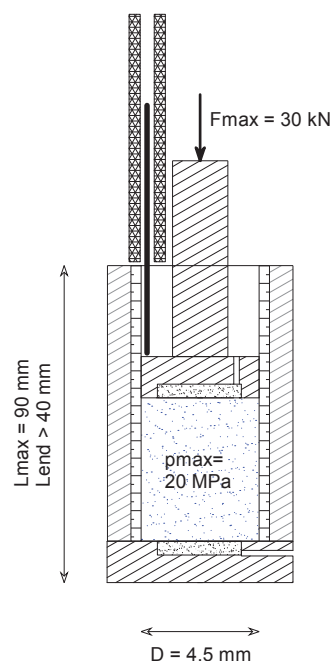


Figure 4. Schematic view of the compaction apparatus.

A highly viscous paste, prepared with the adequate pore water, was filled into a sample container (diameter 5 cm) with end plates of porous metal. Then, the sample was compacted at constant pressure on the mobile end plate, allowing drainage through the end plates. The compaction, recorded with a length transducer, was terminated after pore pressure equilibration (primary compaction), which is indicated by a significant decrease of the compaction rate when the secondary phase of structural particle rearrangement is reached after some days (depending on the material) (Fig. 5).

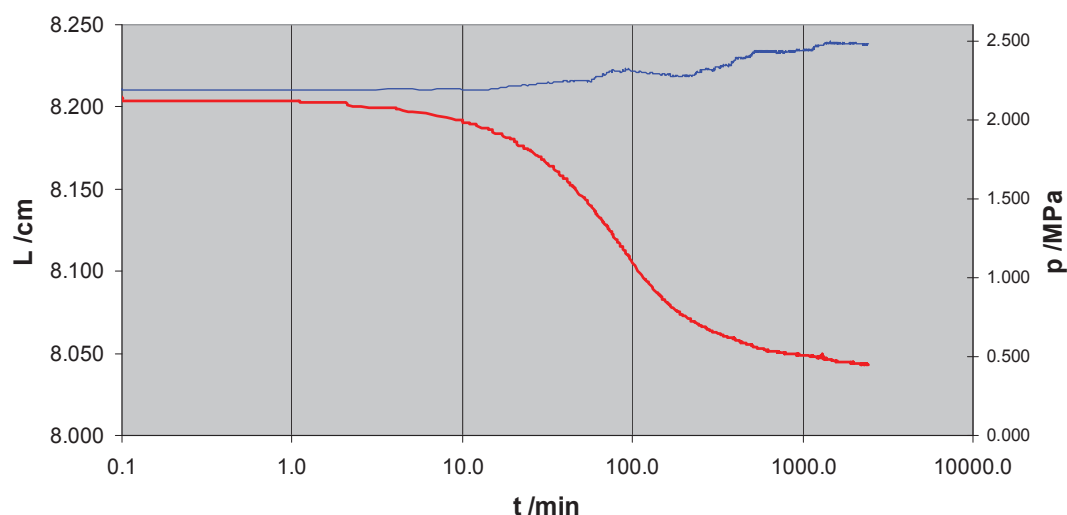


Figure 5. Compaction curve of the kaolinite sample (red: extension, blue: pressure).

The compacted sample was then transferred into a flow-through cell with end plates of sintered glass. The experimental conditions are shown in Table 3. The final porosities depend on a variety of conditions like particle size and added fluid volume.

Table 3. Experimental conditions for the preparation of compacted clay samples.

	Kao	OPA1
Material	kaolinite paste	Opalinus clay powder
Fluid	water	synthetic OPA pore water with 0.01 M KI
Pressure (MPa)	2.5	0.5
Compaction time (h)	120	50
Final porosity	0.63	0.41

Intact drill cores of consolidated material were cast into resin. The end plates with the fluid ports were made of plastic and were attached to the samples with a minimum gap (~ 0.1 mm) in order to reduce the dead volume. Otherwise, the radiation originating from the tracer accumulation in the dead volume would deteriorate the image quality. It could be shown that the shape of the tracer pulse is already smoothed strongly by passing the input volume.

Advection experiments. For advection-dispersion experiments, a tracer pulse was pumped through the sample (Fig. 6). Flow rate, driving pressure and tracer volume were chosen according to the properties of the sample. Before and after tracer

injection, the sample was conditioned with carrier solution in order to impede selective sorption of the tracer. During injection, repeated PET scans of the sample were recorded with a frame rate and duration according to the propagation time of the labelled compound and to the decay time of the radionuclide.

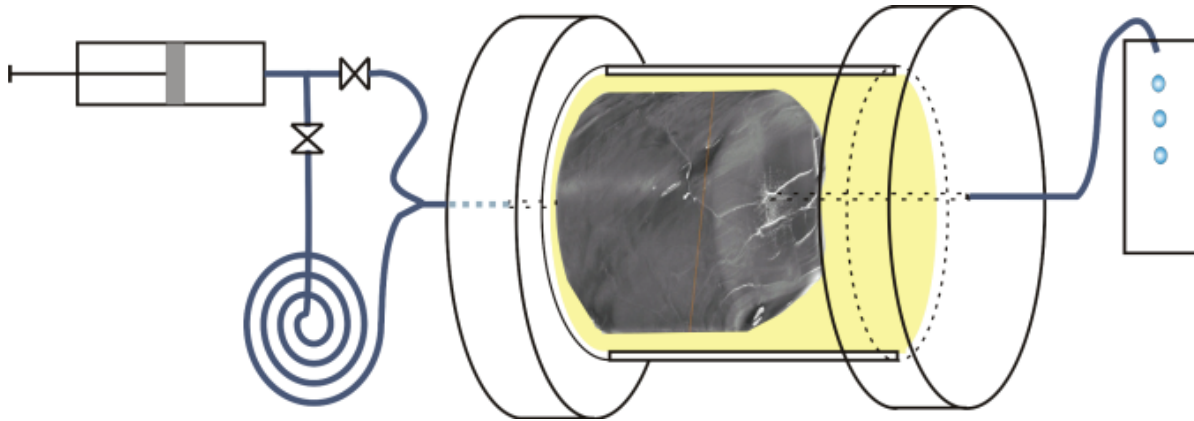


Figure 6. Typical setup of an advection experiment. In a first stage, the sample is preconditioned by injecting carrier solution. Then, the compound (labelled with an appropriate radionuclide) is injected, followed again by carrier solution.

Diffusion experiments. Diffusion experiments were conducted by introducing tracer solutions to an axial central blind hole (diameter 5 mm) in the sample which was completely cast into resin. The tracer-filled hole was closed with a screw. Then, repeated scans were taken over periods of up to 3 weeks with ^{124}I as a tracer. Prospectively, diffusion times of about 1 year will be feasible using ^{58}Co , or even 5 years using ^{22}Na .

It has to be noticed that unconventional PET nuclides like ^{124}I or ^{58}Co emit strong γ -radiation in the spectral range near 511 keV. The impact of these interferences has been studied, together with the scattering characteristics, by Monte Carlo simulations of all nuclear physical effects that are present, using the OpenGATE code (Fig. 7). First results from these simulations, which also served to quantify the strong effects of Compton scattering, show a significant decrease in the signal-to-noise ratio of the images compared to ^{18}F [44]. The results of the simulations will be applied in error estimations and in determinations of detection limits.

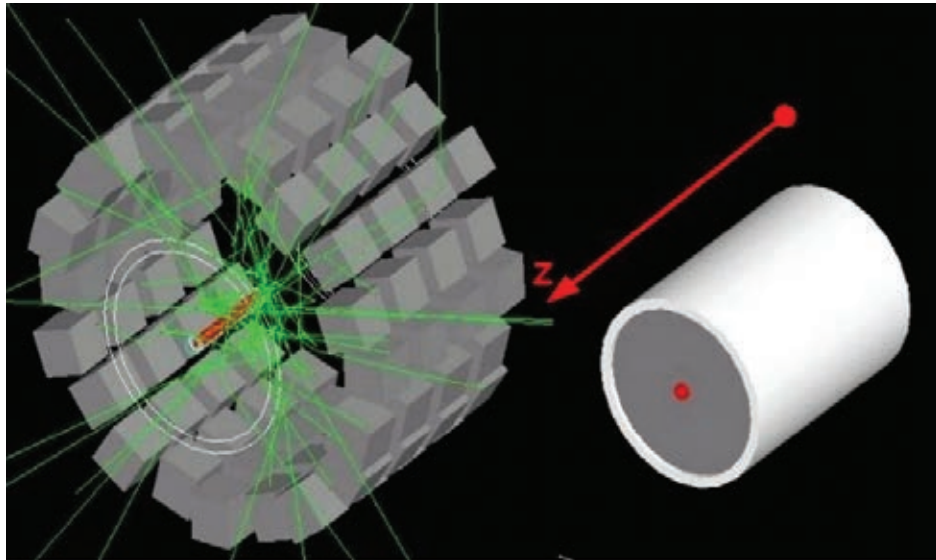


Figure 7. Definition of scanner configuration (left) and phantom (i.e., a model of source and sample, right), together with exemplary ray paths of the emitted photons (green lines) as simulated with OpenGATE. The locations of the detected events are stored in a listmode file, together with their history (e.g., origin, number of scatter events, scatter angle, energy loss).

3. Results and discussion

3.1. Co-adsorption of Tb(III) and humic acid onto clay materials as a function of pH

3.1.1. Tb(III) adsorption in the absence and presence of humic acid

In Figs. 8a - 8c, adsorption of Tb(III) onto illite, montmorillonite and Opalinus clay in the absence and presence of Aldrich humic acid is shown as a function of pH. The initial concentrations of Tb(III) and HA were fixed at 10^{-7} M and 5 g L^{-1} , respectively. The data are represented as solid-liquid distribution coefficients K_d . With increasing pH (limited to values of up to 6.4 due to the onset of Tb hydroxide precipitation), $\log K_d$ values increase from about 2 to 4 for illite and Opalinus clay, and from 3 to 4 for montmorillonite. Metal adsorption is promoted on raising the pH since more binding sites are provided by deprotonation of surface hydroxyl groups. At the highest pH, adsorption amounts to nearly 99%.

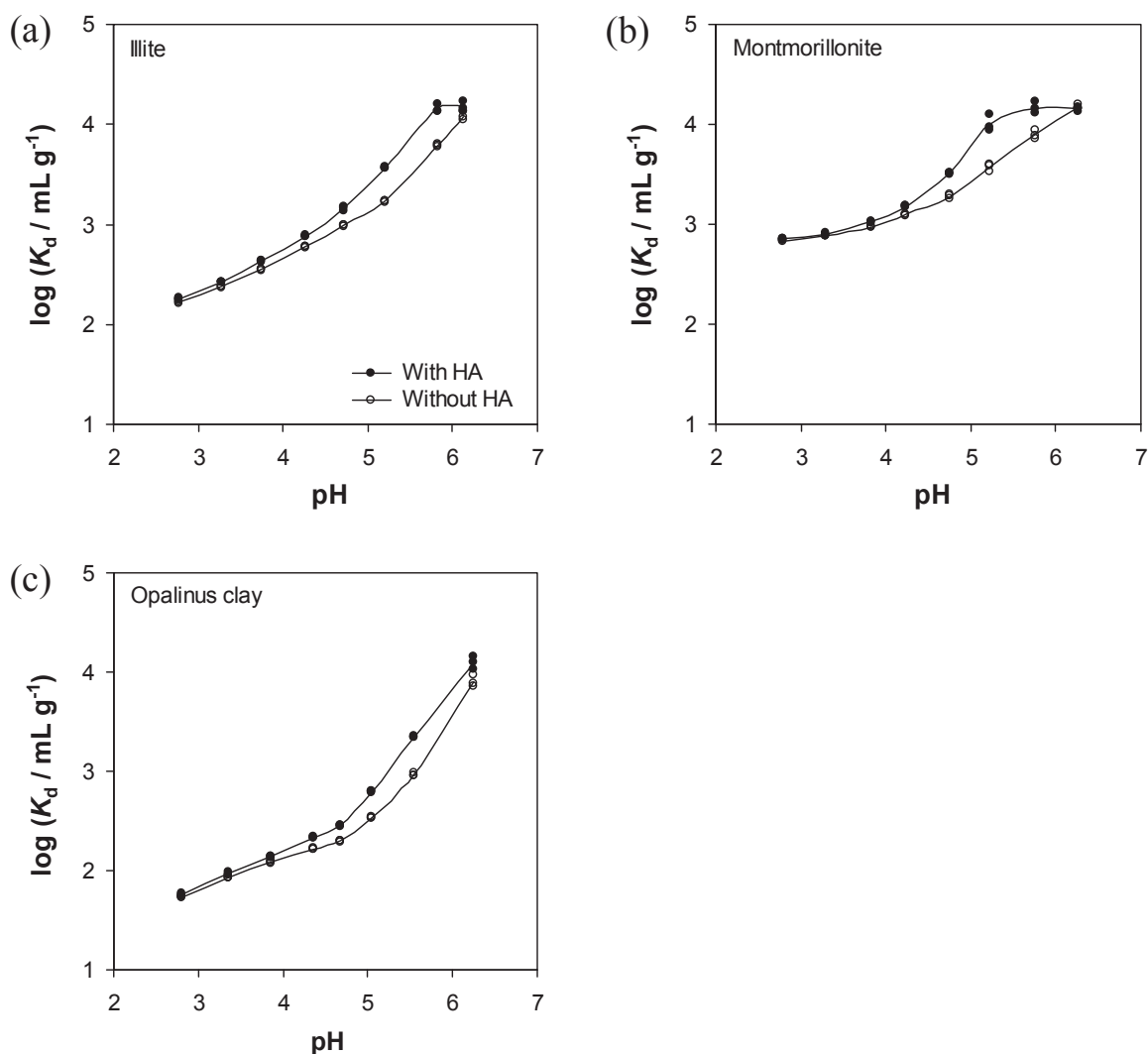


Figure 8. Adsorption of Tb(III) (10^{-7} M) onto clay materials (5 g L^{-1}) in 0.1 M NaClO_4 , in the absence and presence of humic acid (5 mg L^{-1}), as a function of pH.

For all clay materials under study, adsorption is increased in the presence of humic acid throughout the pH range investigated. Obviously, binding is mediated by HA in that additional Tb is co-adsorbed as a humate complex. An important conclusion that may be drawn is that desorption of metals from clay barriers, occurring in consequence of acidification processes, will be counteracted in the presence of humic matter, i.e., the situation will not deteriorate by humic-bound transport.

3.1.2. Adsorption of humic acid and humate complexation of Tb(III)

Fig. 9a shows the adsorption behaviour of humic acid on the clay materials. Adsorbed amounts are lowest for Opalinus clay, which also applies to the adsorption of Tb (Fig. 8c). This is explained by the content of non-argillaceous constituents such as quartz, calcite and pyrite. Generally, adsorption of HA increases on acidification since the electrostatic repulsion by negative charges on both HA and solid surface is reduced by protonation of acidic centres. The occurrence of a maximum in the case of illite is probably due to mineral dissolution.

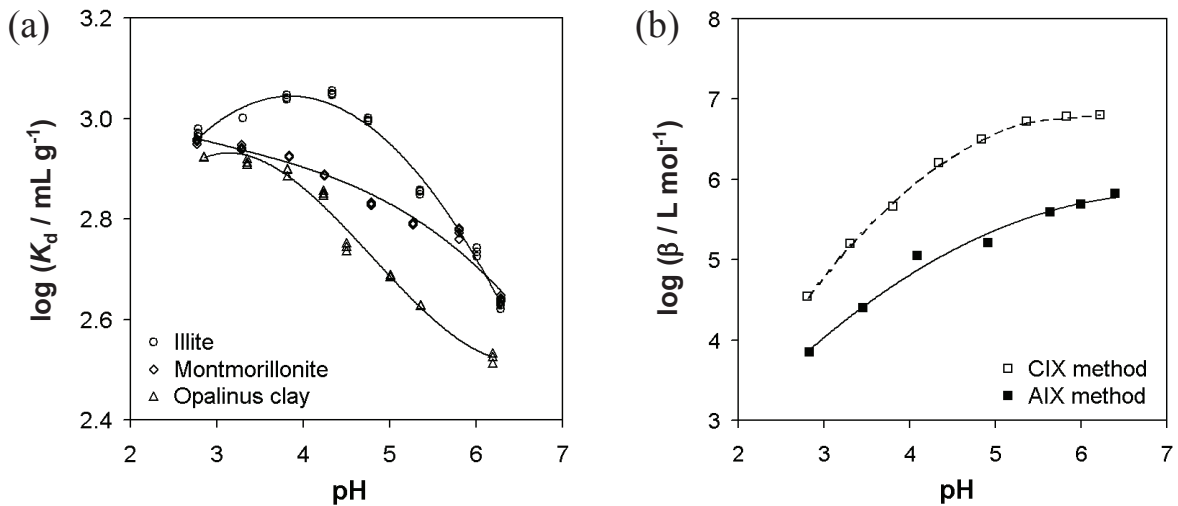


Figure 9. Adsorption of humic acid onto clay materials (a) and complexation of Tb(III) with humic acid (b) in 0.1 M NaClO₄ as a function of pH (CIX: cation exchange, AIX: anion exchange, concentrations as indicated in Fig. 8).

The pH dependence of Tb-humate complexation is shown in Fig. 9b. These data are given as conditional stability constants β , calculated according to Eq. (5) for a hypothetical 1:1 stoichiometry.

$$\beta = \frac{c_M^{\text{HA}}}{c_M c_L} \quad (5)$$

In this equation, c_L is the equilibrium concentration of free ligands, here simplistically defined by Eq. (6), where c_{HA} is the concentration of humic acid, and PEC is its proton exchange capacity per unit mass. The value of 5.6 meq g⁻¹ was taken from Ref. [56].

$$c_L = c_{HA}PEC - c_M^{HA} \quad (6)$$

The results from cation exchange experiments differ considerably from those obtained with the anion exchange method. This may be due to the fact that binding of HA to the anion exchange resin is a competitive reaction in respect of metal binding since the humic ligands are involved in the fixation. Thus, part of the bound metal fraction might be displaced in the separation process, which would explain the lower $\log \beta$ values. Errors in the cation exchange data may arise from adsorption of HA to the inner walls of the PE vials or even to the resin, but this has been checked.

From both data sets in Fig. 9b, it is visible that complexation is suppressed with decreasing pH because the ligands are blocked by protonation. Accordingly, the influence of humic acid on the adsorption of Tb(III) onto the clay materials diminishes at low pH, reflected by the convergence of the curves in Figs. 8a - 8c. Towards alkaline pH, a convergence is observed as well. Most likely, this can be explained by the decrease in adsorption of HA. Since Tb-humate complexation takes place in the aqueous phase to an increasing extent, the humic acid loses its mediating function in respect of Tb adsorption, and a competitive situation arises instead.

3.1.3. Modelling co-adsorption of Tb(III) and humic acid by means of a combined K_d approach (linear additive model)

With the apparent interrelations described above, it should be possible to predict the pH-dependent effect of HA quantitatively on the basis of the data for Tb adsorption in the absence of HA, Tb-humate complexation and HA adsorption. According to the linear additive model [7, 8], these processes are considered as a system of interdependent equilibria. For simplicity, they are all represented by K_d values in the following equations, where Γ is the adsorbed amount per unit mass of solid, and c is the equilibrium concentration. The indices S and M-HA stand for solid phase and metal-humate complex, respectively.

$$K_d^{M/S} = \frac{\Gamma_M}{c_M} \quad (7)$$

$$K_d^{M/HA} = \frac{\Gamma_M^{HA}}{c_M} = \frac{c_M^{HA}}{c_M c_{HA}} \quad (8)$$

$$K_d^{HA/S} = \frac{\Gamma_{HA}}{c_{HA}} = \frac{\Gamma_{M-HA}}{c_{M-HA}} \quad (9)$$

Combining Eqs. (7) - (9) yields Eq. (10) for co-adsorption of metal and metal-humate complex:

$$K_d^{(M + M-HA)/S} = \frac{K_d^{M/S} + K_d^{HA/S} K_d^{M/HA} c_{HA}}{1 + K_d^{M/HA} c_{HA}} \quad (10)$$

To reconstruct the pH dependence of Tb adsorption in the presence of HA, the experimentally determined values of $K_d^{M/HA}$, $K_d^{HA/S}$ and c_{HA} as a function of pH were fitted by polynomials, and $K_d^{(M+M-HA)/S}$ was calculated for the measured $K_d^{M/S}$ / pH data using values obtained by interpolation. The results are shown in Figs. 10a - 10c.

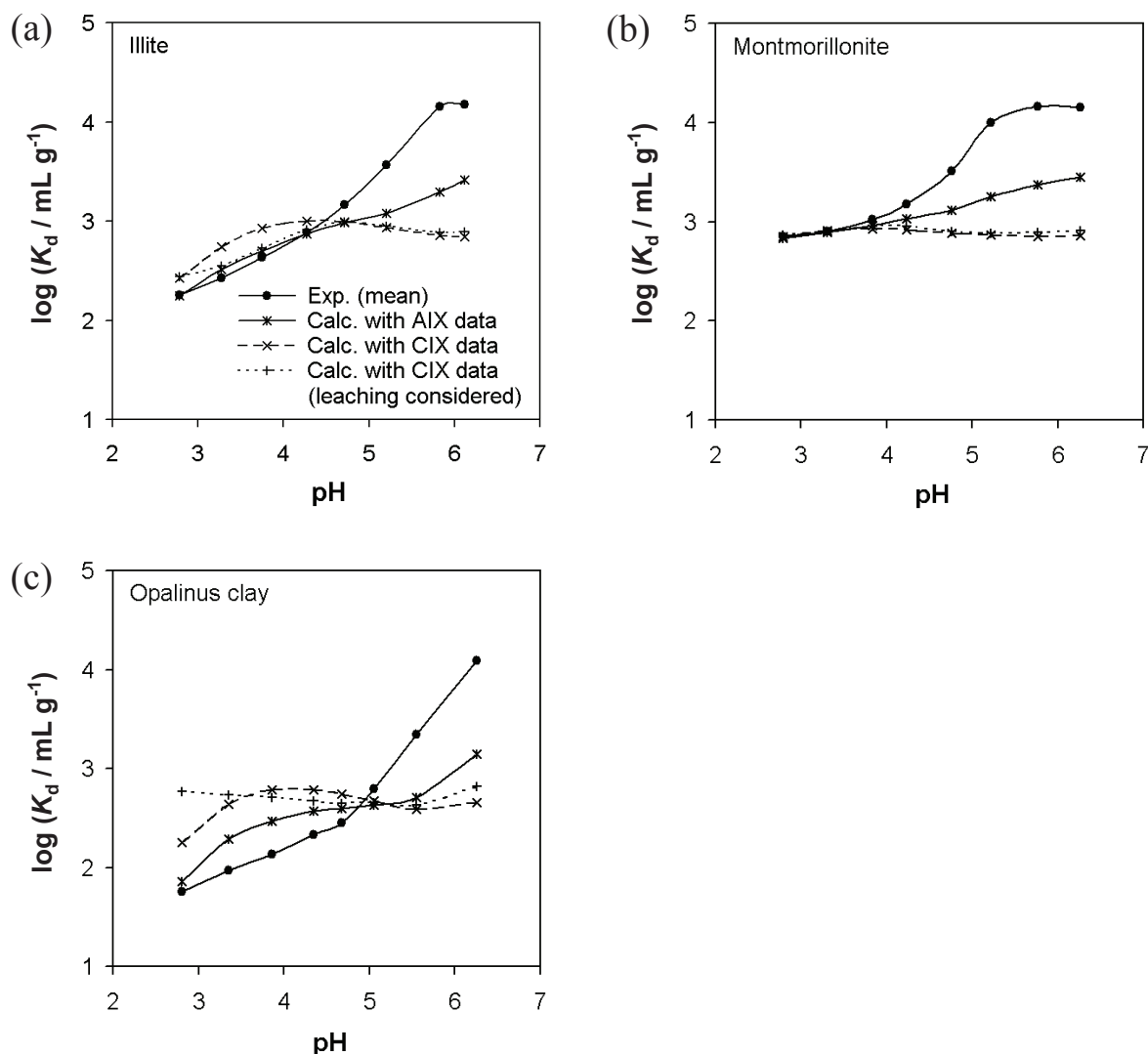


Figure 10. Adsorption of Tb(III) in ternary systems. Experimental data (solid dots) and calculated data based on the linear additive model.

Clearly, the linear additive model fails to reproduce the measured data, which applies to all clay materials investigated. Regarding experimental errors as a possible reason, the largest uncertainty is ascribed to the data for metal-humate complexation. Expectedly, there is a striking difference between the calculated results based on data from anion and cation exchange experiments, respectively, but neither of them approximates the experimental values. Leaching of metals from the clay materials by mineral dissolution could be a major source of error since, in the ternary systems, binding of Tb(III) to HA may be influenced by competitive effects, which are not accounted for if complexation data are determined for perchlorate

solutions only. Significant quantities of Ca, Mg, Al and Fe were detected in the supernatants of the adsorption systems. The highest concentrations were found for Opalinus Clay (Fig. 11).

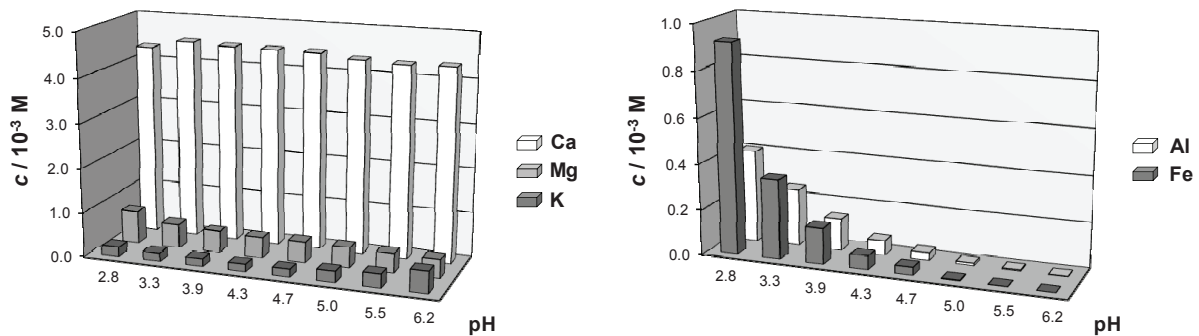


Figure 11. Metal concentrations in the supernatant solutions of the adsorption systems with Opalinus clay.

In particular, Ca is released due to calcite dissolution. Surprisingly, Ca concentrations were found to be independent of the pH. The expected increase on acidification was only observed for the trivalent metals Al and Fe. To investigate the competitive influence of all these metals, complexation studies were also conducted with the supernatant solutions, using the cation exchange method. In fact, Tb binding was found to be markedly reduced (data not shown). However, the implications on the model calculations turned out to be minor (see Fig. 10).

Erroneous data are also possible for HA adsorption. Radiolabelling of humic substances must not only meet the criterion of stability but also of non-selectivity to ensure that the detected tracers are representative of the humic molecules as a whole. Although this has been proven (cf. results in Section 3.3.), an element of uncertainty remains. However, enforcing the agreement between experimental and calculated values by adjusting HA adsorption as a fit parameter yields unrealistic trends beyond any reasonable limits of error.

Therefore, we conclude that the discrepancy is not attributable to experimental inaccuracies but to the conception of the model itself, specifically to the supposition that the individual processes are independent of each other. For instance, in Eq. (9), it is assumed that the adsorption of the M–HA complex is not different from the adsorption of HA. This cannot apply unrestrictedly since metal binding is comparable to protonation, and the influence of protonation on HA adsorption is evident from the pH dependence shown in Fig. 9a. In order to get an idea of the area of validity of Eq. (9), we investigated HA adsorption on montmorillonite as a function of metal concentration, using aluminium as an example of trivalent metals. As can be seen in Fig. 12, adsorption is increased on metal addition, but the effect is insignificant at concentrations below 10^{-5} M. Thus, it can be excluded that HA adsorption is affected by the presence of only 10^{-7} M Tb.

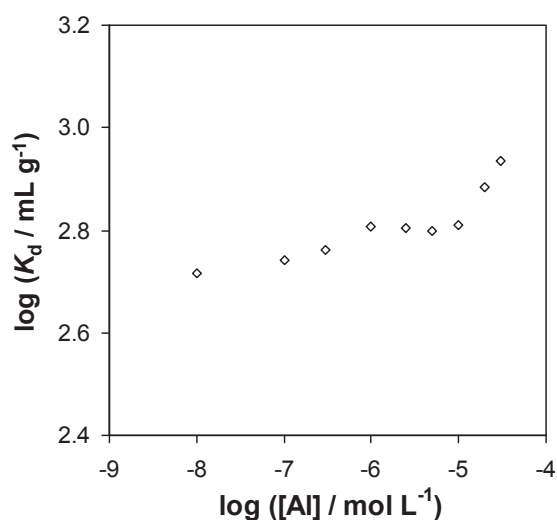


Figure 12. Adsorption of humic acid (5 mg L^{-1}) onto montmorillonite (5 g L^{-1}) in 0.1 M NaClO_4 (pH 6.0) in the presence of Al(III).

On the other side, direct adsorption of M will be impeded with increasing adsorption of M–HA. However, in consideration of the fact that the sorption capacity of humic material exceeds that of a mineral surface by orders of magnitude, a blocking effect should not be of major relevance to the performance of the model.

Another implicit assumption is that the stability of the M–HA complex in solution is equal to its stability in the adsorbed state. This is probably the weakest point of the model. First, it must be taken into consideration that complexation is potentially counteracted by adsorption, as may be inferred from the comparison between cation and anion exchange data in Fig. 9b. Furthermore, adsorption of humic substances, as multicomponent systems, is accompanied with some fractionation [57-59], and it has been reported that the capability of metal binding is not evenly distributed over molecular weight fractions [60-62]. If, for instance, fractions with high metal loads are preferably adsorbed, metal adsorption will be underestimated by the model as it operates with an averaged metal load, determined for the humic substance as a whole. For illite and montmorillonite, Tb adsorption is largely underestimated. For Opalinus clay, however, there is both underestimation and overestimation depending on the pH value, possibly as a consequence of the complexity of this material. A combined action of contrary effects is certainly conceivable.

3.2. Adsorption of Tb(III) onto clay materials in the presence of propionate and lactate

Propionic and lactic acid, besides formic and acetic acid, are the main components of low-molecular-weight organic matter present in natural clay rock. DOC quantities of 10 mg L^{-1} and 57 mg L^{-1} have been found in the pore waters of Opalinus clay and Callovo-Oxfordian clay, respectively [63]. In weakly acidic solutions, propionic and lactic acid are largely dissociated ($pK_a = 4.87$ and 3.86 , respectively). In this work package, we investigated the influence of these organic anions on Tb(III) adsorption onto the clay materials used in the studies with humic acid (Section 3.1.), covering the same range of pH values. In first experiments with Opalinus clay at constant pH, concentrations of propionate and lactate were varied in order to find the minimum amounts that cause a distinct effect (Fig. 13).

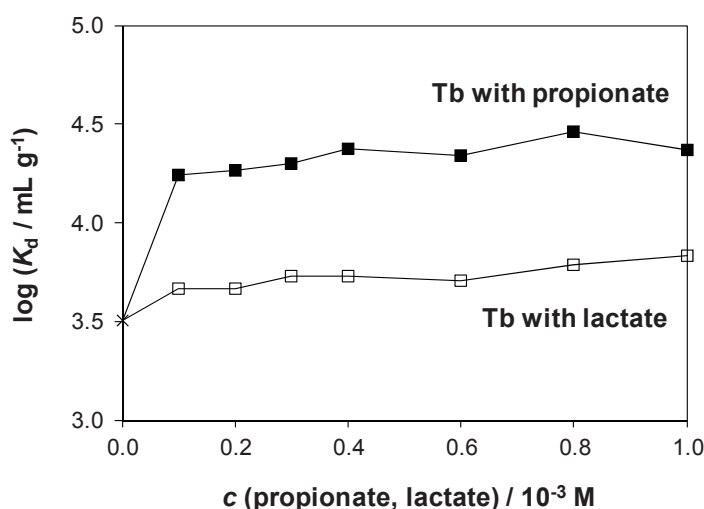


Figure 13. Adsorption of Tb(III) (10^{-7} M) onto Opalinus clay (1 g L^{-1}) in the presence of Na L-lactate or Na propionate, as a function of the concentration (0.1 M NaClO_4 , pH 6.0).

Obviously, the presence of propionate and lactate causes an increase in Tb(III) adsorption. This result is surprising, considering the fact that both the solid surface and the organic compounds are negatively charged. Given that both anions act as ligands that form complexes with Tb(III) – otherwise they would not cause any effect – only a decrease in adsorption is conceivable since the positive net charge of the metal would be reduced by all means.

Adsorption studies at variable pH values, using defined clay minerals in addition, should give more information that allows an interpretation of the unexpected behaviour. The concentrations of lactate and propionate were fixed at $2 \times 10^{-4} \text{ M}$ ($\sim 20 \text{ mg L}^{-1}$, corresponding to the DOC concentration found for Opalinus clay pore water). The results are shown in Fig. 14.

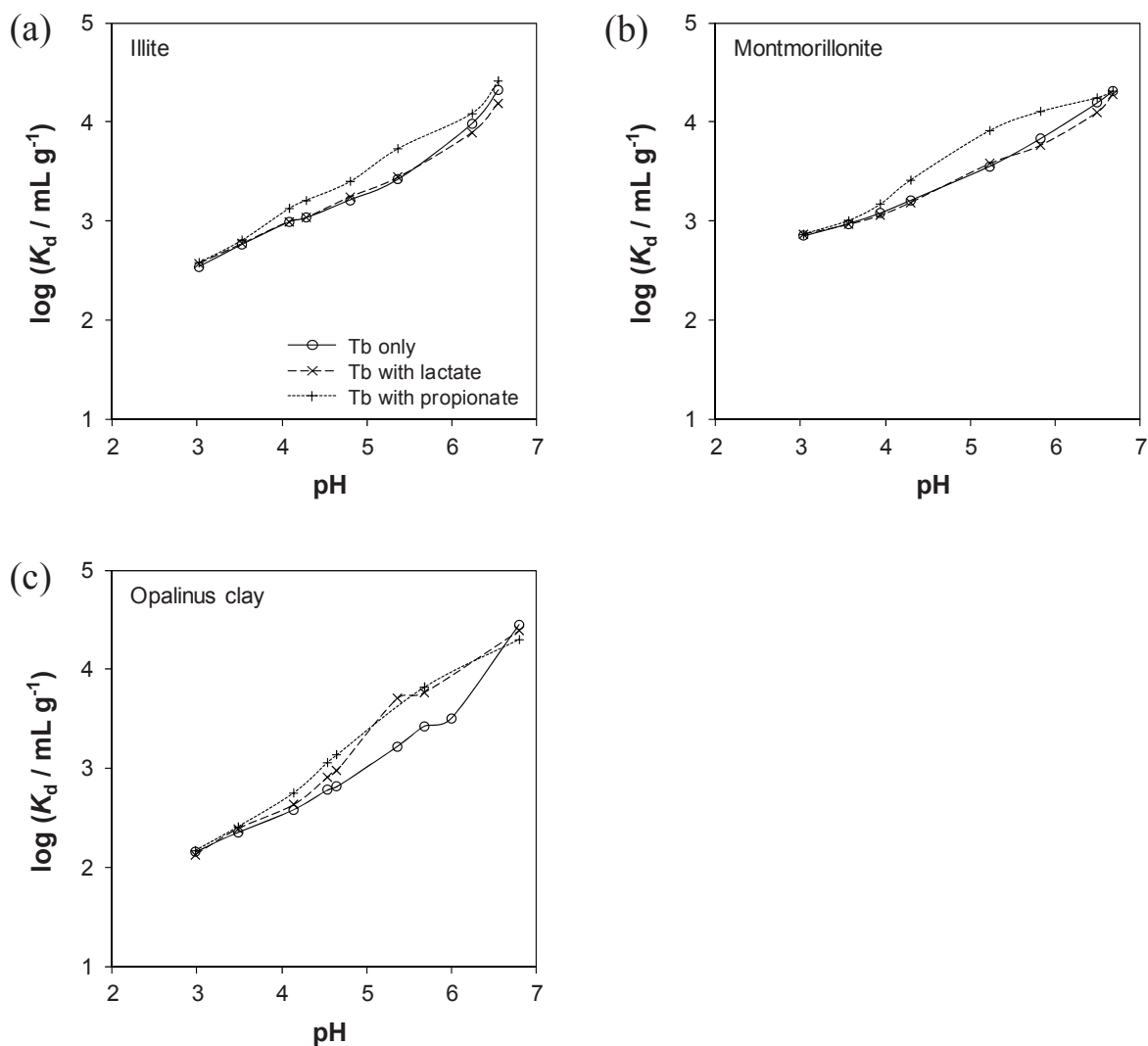


Figure 14. Adsorption of Tb(III) (10^{-7} M) onto clay materials (1 g L^{-1}) in 0.1 M NaClO_4 , in the absence and presence of Na L-lactate or Na propionate (2×10^{-4} M), as a function of pH.

For Opalinus clay, the increase in Tb(III) adsorption in the presence of both organic compounds was also found for more acidic solutions. The influence diminishes at low pH, which may be due to the increasing protonation of the acids. Similar results were obtained for illite and montmorillonite as far as the effect of propionate is concerned. In contrast, the effect of lactate was found to be negligible. Only in near-neutral solutions, a very minor decrease in Tb(III) adsorption occurs. It may be concluded that also the presence of low-molecular-weight organic matter, similarly to humic matter, does not cause an additional mobilisation of metals that are desorbed from clay rock in case of pH drops.

The reason of the observed immobilising effects is, however, far from obvious. By means of ^{14}C -labelled compounds, also adsorption of lactate and propionate onto the clay materials was examined. Only for Opalinus clay, adsorbed amounts were significant (Fig. 15). This may be due to the high degree of mineral dissolution (see Fig. 11). For Opalinus clay, amounts of released metals were found to be

considerably higher than for illite and montmorillonite. Presumably, the organic anions form complexes with these metals and may be adsorbed as such. It is thus possible that mixed complexes with Tb(III) are formed, which are stronger adsorbed than Tb(III) as an aqueous species. This may also apply to the other clay materials, even though no adsorption was found for the organic compounds in the absence of Tb(III).

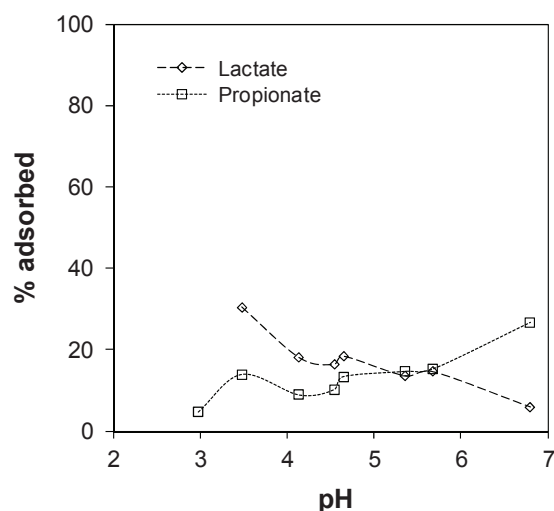


Figure 15. Adsorption of Na L-lactate and Na propionate (2×10^{-4} M) onto Opalinus clay (1 g L^{-1}) in 0.1 M NaClO_4 as a function of pH.

A contrary explanation is conceivable as well, namely, that the competition effect of released metals with respect to Tb(III) adsorption is reduced by the complexation process, given that the organic complexes are less adsorbed than the free metals. However, both these interpretations cannot be corroborated quantitatively and are thus merely speculative at this stage. Further studies are certainly necessary. Nonetheless, these findings show that the high electrolyte contents in pore waters must be explicitly considered when investigating the influence of clay organics.

3.3. Radiotracer studies on the dynamics of adsorption equilibria for the system Tb(III) / humic acid / kaolinite

These basic investigations were performed with kaolinite KGa-1b as a well-defined clay material of high purity. In addition to Aldrich humic acid, a fulvic acid isolated from bog water was used as an organic component. First, the kinetics of adsorption was examined for both humic substances. The results are shown in Fig. 16. For the humic acid, it takes about 2 days until the adsorption equilibrium is attained, which is very long compared to adsorption of metals for example. For the fulvic acid, the final state is already reached after few hours, probably due to the lower average molecular weight of this material.

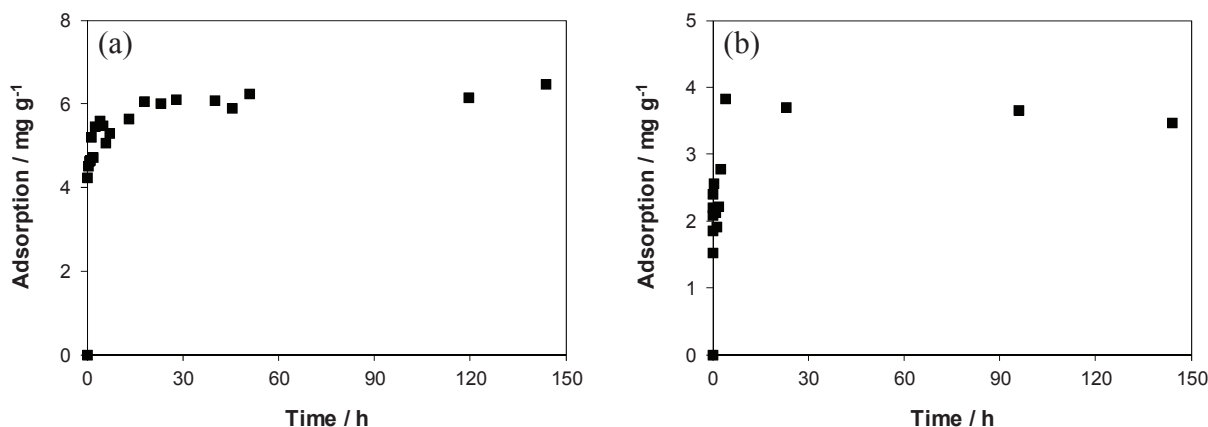


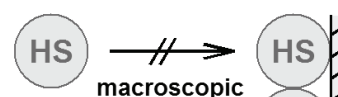
Figure 16. Adsorption of humic acid (a) and fulvic acid (b) onto kaolinite as a function of time (150 mg L⁻¹ HA or FA, 5 g L⁻¹ kaolinite, 0.1 M NaClO₄, pH 4.7, analysis: UV-Vis spectrometry – extinction at 400 nm).

The character of this equilibrium state is, however, an open question. As outlined in the introduction, low recoveries are obtained in flow-through experiments with packed columns. This may indicate that adsorption of humic substances is in part irreversible. Filtration effects, considered as a second possible reason, are unlikely to occur in column fillings with coarse particles (grain sizes in the mm range).

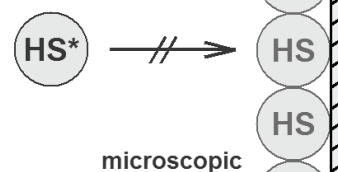
In this project, direct investigations on the reversibility of adsorption of humic materials were realised for the first time, taking advantage of the radiolabelling principle. In this way, it is possible to “look into” the dynamics of adsorption equilibria. The experimental approach is illustrated in Fig. 17. The state of surface saturation is visible from the fact that an increase in concentration no longer results in an increase in adsorption; the adsorption isotherm reaches a plateau. In this situation, a radiolabelled tracer is added to the system. If it is not adsorbed, the equilibrium is a static one. Adsorption is then a “sticking”, i.e., the interaction process is irreversible. If, however, a decrease in the concentration of the tracer is detected, an exchange must take place since free binding sites are not available. In this case, it can be concluded that there is a dynamic equilibrium of adsorption and desorption, i.e., the interaction process is reversible, and there is a permanent movement onto the surface and back into the solution.

Surface saturation:

no further adsorption when increasing the concentration

**Static equilibrium, irreversible adsorption:**

labelled tracer HS* is not adsorbed

**Dynamic equilibrium, reversible adsorption:**

labelled tracer HS* is adsorbed



Figure 17. Principle of tracer exchange experiments on the reversibility of adsorption of humic substances (HS).

For these studies, kaolinite suspensions were prepared as described in Section 2.2.3. The experimental conditions were not limited to the state of surface saturation. Instead, a series of systems was prepared for a range of HS concentrations (4 mg L^{-1} - 180 mg L^{-1}) to cover the whole adsorption isotherm, using non-labelled humic substances. The systems were completed by adding a small amount of ^{14}C -labelled humic material as a radiotracer. The concentration of the tracer solution was 0.1 mg L^{-1} , and the added volume of $20 \mu\text{L}$ was negligible compared to the total volume of 4 mL . Thus, the composition of the systems was not significantly changed by introducing the tracer.

Two different procedures were applied: In 1-step experiments, the radiotracer was added together with the non-labelled substance. In 2-step experiments, the tracer was not introduced right from the beginning. First, the system was allowed to equilibrate, containing the non-labelled substance only. An equilibration time of 48 h (end-over-end rotation) was chosen according to the adsorption kinetics shown in Fig. 16a. Subsequently, the tracer was added, and the system was again rotated for 48 h.

A prerequisite of this experimental concept is that the radiolabelled humic molecules are representative of the humic material as a whole, i.e., the labelling reaction must not be selective towards any fractions with specific properties, and the chemical modifications must be minor enough to avoid changes in the behaviour. In Fig. 18, adsorption isotherms for humic acid, obtained by using different analytical methods, are compared. The depletions in the adsorption experiment were determined (i) by means of UV-Vis spectrometry and (ii) by analysis of the ^{14}C -labelled tracer (1-step experiment). In the latter case, the measured decrease in the concentration of the tracer is scaled up to the decrease in the total concentration of humic acid. Here, the UV-Vis data were also needed to correct the measured count rates for colour quenching by HA. For this purpose, the decrease in the count rate at a constant tracer concentration was determined for aqueous solutions as a function of HA concentration. Obviously, both data sets are in good agreement. So it may be concluded that the humic material is well represented by the labelled portion.

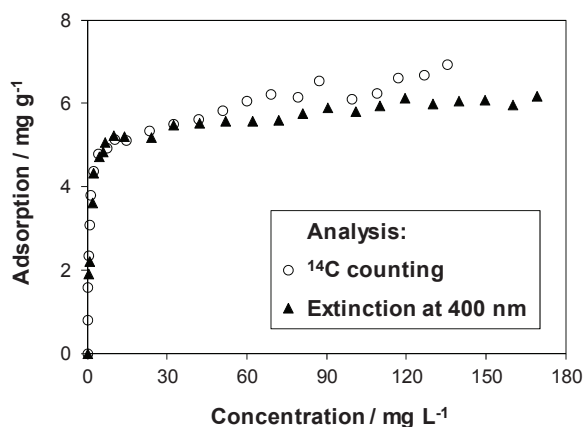


Figure 18. Isotherm of adsorption of humic acid onto kaolinite, based on radiotracer analysis and UV-Vis spectrometric analysis, respectively (5 g L^{-1} kaolinite, 0.1 M NaClO_4 , pH 4.7).

In order to test the experimental strategy, a first study was performed with ^{160}Tb]Tb(III), presuming that adsorption is reversible in this case. Fig. 19a shows the results of 1-step and 2-step experiments, conducted according to the procedure described above even though equilibration times of 48 h were not necessary for the metal. The “normal” adsorption isotherm, obtained in the 1-step experiment (open circles), reaches its plateau value at equilibrium concentrations higher than $\sim 60 \text{ mg L}^{-1}$. If the radiotracer is subsequently introduced into these systems, it will certainly be confronted with saturated surfaces. However, the 2-step experiments (full circles) show that adsorption is not blocked at all. Instead, exactly the same adsorption isotherm is obtained. This result is very instructive as it clearly indicates a permanent exchange process between the adsorbed state and the dissolved state, i.e., the radiotracer is involved in a dynamic equilibrium of adsorption and desorption.

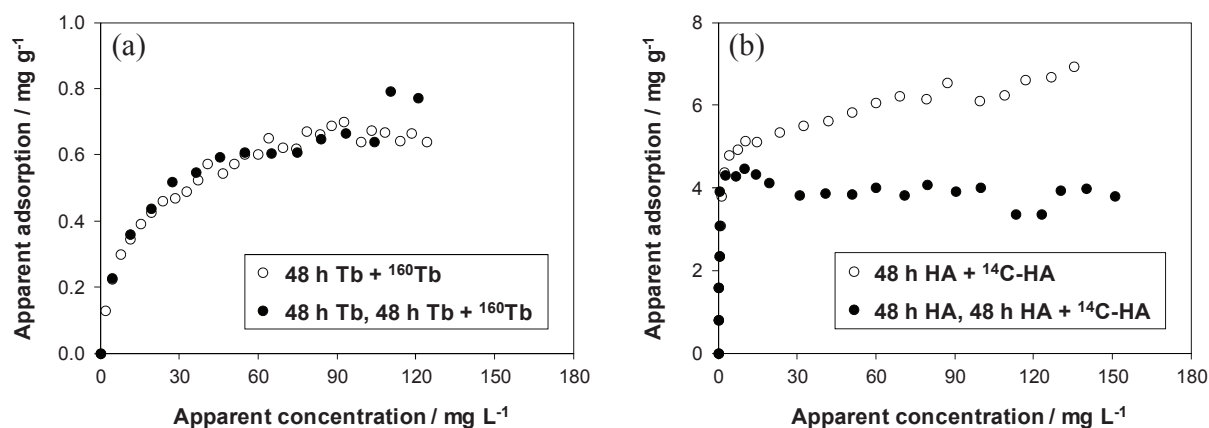


Figure 19. Isotherms of adsorption of Tb(III) (a) and humic acid (b) onto kaolinite in 0.1 M NaClO_4 , obtained with ^{160}Tb and ^{14}C -labelled HA as radiotracers, which were added in small amounts together with the non-radioactive substances (open circles) or after equilibration (full circles). Suspension concentrations for systems with Tb(III) and HA were 25 g L^{-1} and 5 g L^{-1} , resulting in pH values of 4.4 and 4.7, respectively. More details are given in the text.

Fig. 19b shows the results of analogous experiments with humic acid. Evidently, the adsorption isotherms obtained in 1-step and 2-step procedures are not identical. In the latter case, the adsorption plateau is lowered by about one third. However, it is not shifted to zero, which is the most remarkable finding. Consequently, an exchange must take place for humic molecules as well, even though they are extremely large compared to metal ions. It appears that adsorption of humic matter is in fact reversible. There is a dynamic equilibrium, which is, however, not quantitatively represented by the radiotracer. For this reason, the term “apparent” is used in the axis titles.

In view of the intermediate plateau level, it seemed likely that different results would be obtained if the time for exchange was varied. This supposition was confirmed, as can be seen from Fig. 20. If the second equilibration period is reduced to 6 h, the apparent adsorption plateau is situated considerably lower. It is remarkable that a maximum occurs at low concentrations. The following decrease reflects the approach to the state surface saturation. The hindrance of tracer adsorption is in fact limited to the plateau region of the isotherm. In another experiment, the tracer was given 168 h (one week) for exchange. In this case, the plateau level was found to be higher compared to the results for 48 h. If the time is increased to 672 h (4 weeks), further progress of the tracer can be observed.

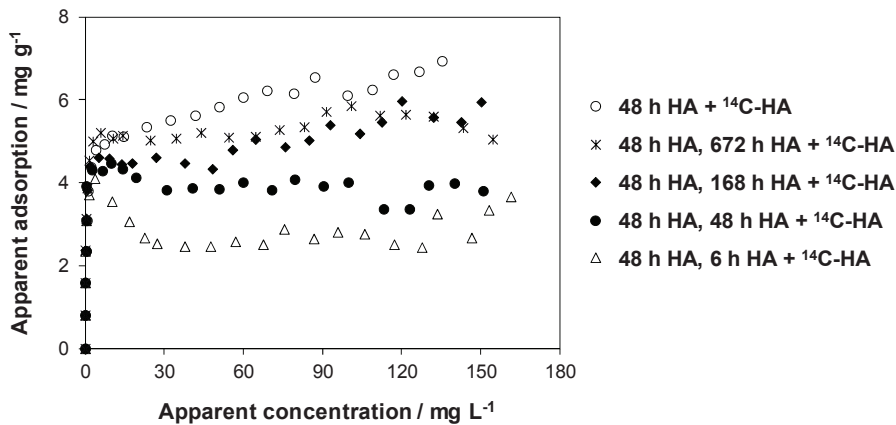


Figure 20. Apparent adsorption isotherms obtained in tracer exchange experiments at different times of exchange (experimental details as in Fig. 18).

In Fig. 21a, the averaged data of all apparent adsorption plateaus are plotted as a function of the time of exchange. Analogous experiments were performed with the fulvic acid. The results obtained (Fig. 21b) turned out to be similar. For both materials, the tracer exchange at surface saturation requires much more time than attaining the overall adsorption equilibrium (cf. Fig. 16). This is surprising since both processes, in principle, are governed by the same dynamics.

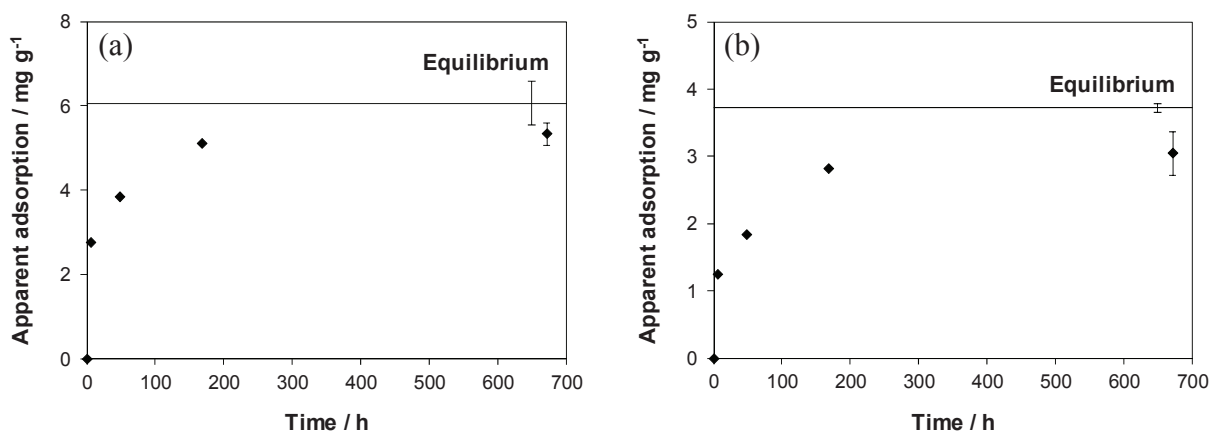


Figure 21. Mean plateau values of apparent adsorption isotherms obtained in tracer exchange experiments with humic acid (a) and fulvic acid (b) at different times of exchange (experimental details as in Fig. 18). The solid lines indicate the mean plateau values of the isotherms obtained for total adsorption (instantaneous tracer addition).

It appeared to be probable that the slow kinetics of exchange might be related to the desorption process as a rate-limiting step. To test this assumption, desorption experiments were performed, covering a time frame of 4 weeks as in the tracer exchange studies. The experimental layout is based on the adsorption isotherm (Figs. 22a and 23a for HA and FA, respectively). Starting from a total concentration of 40 mg L⁻¹ HA or FA, a certain equilibrium concentration is attained. After centrifugation, 3 out of 4 mL of the supernatant were replaced by “fresh” 0.1 M NaClO₄ solution. With this dilution, the total concentration is reduced accordingly, and the new equilibrium state can be assigned by means of the adsorption isotherm. The corresponding shifts in adsorption and concentration are shown as grey arrows. Thus, desorption is to be expected. As the increase in concentration is, however, rather small, demands on the analytical precision are high. For the fulvic acid, results obtained by UV-Vis spectrometry were not satisfactory, mainly due to background values caused by dissolution of clay components. Using ¹⁴C-labelled FA proved to be indispensable.

The concentrations of HA and FA in the supernatant as a function of time (after dilution) are shown in Figs. 22b and 23b, respectively. For the humic acid, no change in concentration was detected over the entire time span. For the fulvic acid, a minor decrease was observed. Apparently, there is a delayed adsorption process in spite of the dilution step. This is surprising, the more so as no comparable trend was observed in the adsorption kinetics (Fig. 16b). The essential outcome of these experiments is, however, that the expected desorption process does not take place for both humic materials.

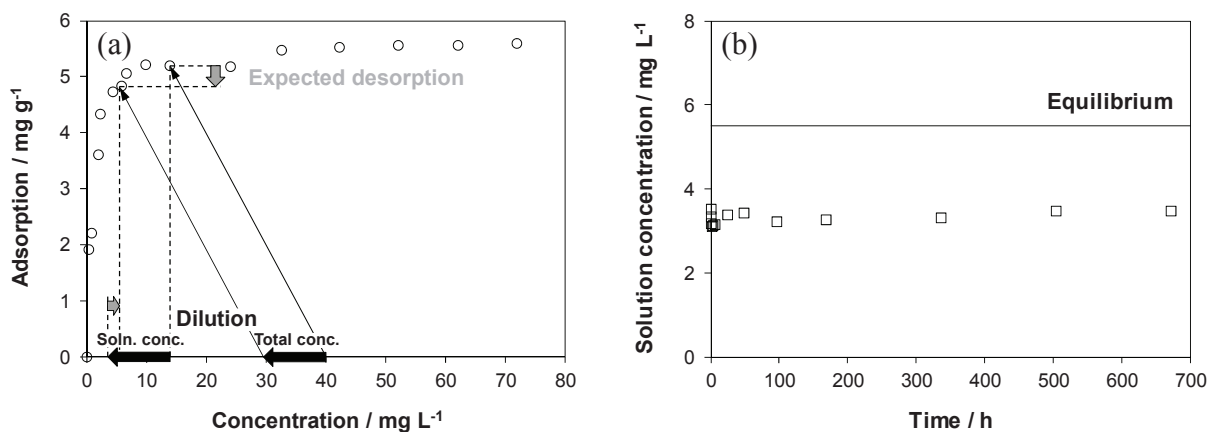


Figure 22. Desorption experiments with humic acid. Expected desorption after dilution, based on the adsorption isotherm (a), and measured solution concentrations after dilution as a function of time (b) (5 g L^{-1} kaolinite, 0.1 M NaClO_4 , pH 4.7, analysis: UV-Vis spectrometry – extinction at 254 nm).

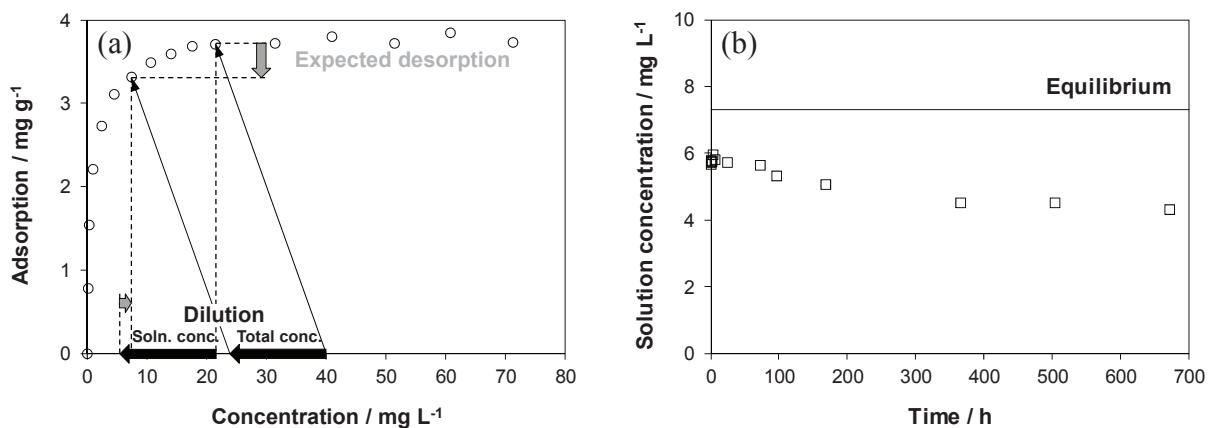


Figure 23. Desorption experiments with fulvic acid (^{14}C -labelled). Expected desorption after dilution, based on the adsorption isotherm (a), and measured solution concentrations after dilution as a function of time (b) (5 g L^{-1} kaolinite, 0.1 M NaClO_4 , pH 4.7, analysis: ^{14}C counting).

These results are problematic in view of reactive transport modelling since reversibility of adsorption is presumed in general (see literature review in [9]). On the other hand, the absence of any desorption is contradictory to our findings obtained from the tracer exchange experiments described above. If desorption is impossible, there should not be any exchange as well. Possibly, the competition exerted by the ^{14}C -labelled tracer is a stronger driving force than a concentration gradient. The discrepancy is still in need of full clarification.

3.4. Elucidating time-dependent changes in the competition effect of Al(III) on Tb(III)-humate complexation

3.4.1. Evidence of stabilisation processes

The results of time-dependent complexation studies, obtained by using the anion exchange method, are shown in Fig. 24. Al(III) / HA systems had been pre-equilibrated over a time period of up to 6 days before Tb(III) was added. The dotted line in Fig. 24a shows the percentage of Tb(III) bound to HA in the absence of Al(III). The competition effect of Al(III) is reflected in the distance of the data points from this line.

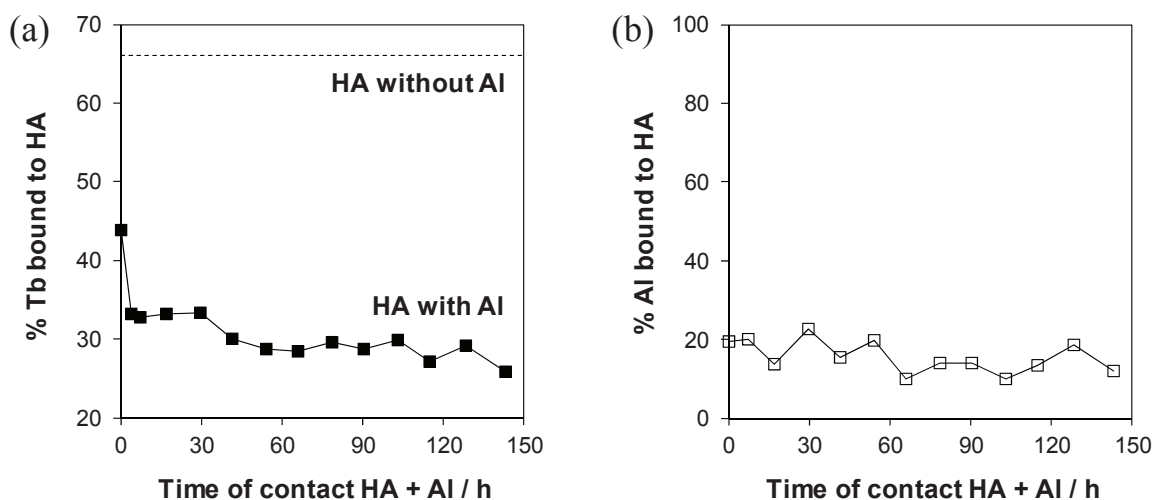


Figure 24. Complexation of Tb(III) with HA after pre-equilibration of HA and Al(III) (a) and complexation of Al(III) with HA (b) as a function of contact time, determined by the anion exchange method (10^{-7} M [^{160}Tb]Tb, 10^{-5} M Al, 5 mg L^{-1} HA, 0.1 M NaClO_4 , pH 4.0).

About one third of originally bound Tb(III) is instantaneously excluded from complexation, and interestingly, there is a further significant decrease within a period of 2 days. No corresponding changes in the stability of Al(III)-humate complexes were detectable, i.e., the amount of bound Al(III) was constant during the time of observation (Fig. 24b). Consequently, the increase in competition must be based on qualitative changes. A parallel series of experiments was prepared to cover a range of ageing times of up to 6 months since in the previous project, trends in the competition effect of Fe(III) were found on this time scale [64, 65]. However, no further changes in the humic-bound fractions of Tb(III) were observed in the Al(III) system.

To elucidate the background of the time-dependent effect, our first attention was given to possible shifts in the pH value of Al(III) / HA systems. For Fe(III), we found that the time-dependent increase in competition was accompanied by a concomitant increase in pH. Since reversal of Fe(III) hydrolysis is the only proton-consuming process possible in this system, we concluded that the polynuclear hydrolysis species are metastable when bound to HA. They are only slowly degraded, and the

increase in the counteractive effect is thus explained by the delayed occupation of binding sites [64].

Also the aqueous chemistry of Al(III) is characterised by the formation of polynuclear species. Depending on the concentration, the tridecamer $[AlO_4Al_{12}(OH)_{24}(H_2O)_{12}]^{7+}$ ("Al₁₃") can dominate the speciation in weakly acidic solutions [66]. For Al(III) / HA systems, however, the time-dependent development of the pH value turned out to be completely different (Table 4). A decrease occurred straight away, and no further change was observed over a period of 4 weeks.

Table 4. Time-dependent changes in pH for metal / HA systems (5×10^{-5} M Fe(III) or Al(III), 20 mg L^{-1} HA).

Time	Fe(III) / HA	Al(III) / HA
0 min	pH 5.0	pH 5.0
5 min	pH 5.1	pH 4.6
28 days	pH 5.3	pH 4.6

Such a pH drop is the normal effect to be expected when metal ions are bound to acidic groups of humic substances since protons are released in exchange for the metal. Two different conclusions may be drawn: (a) Polynuclear Al(III) species remain stable when interacting with HA, or (b) the polycations are destructed immediately, consuming fewer protons than are released from the humic ligands. Anyway, the observed time dependence in the competition effect cannot be explained by a metastability of polynuclear species in this case.

Interestingly, this time frame corresponds to kinetic effects in respect of complex dissociation reported in the literature [10-12]. Based on these findings, a "diffusion theory" has been established. According to this hypothesis, complexation proceeds in two steps (Fig. 25a): Subsequent to a fast equilibration with weak binding sites on the colloid surface, there is a slow in-diffusion process to stronger sites which are not directly accessible.

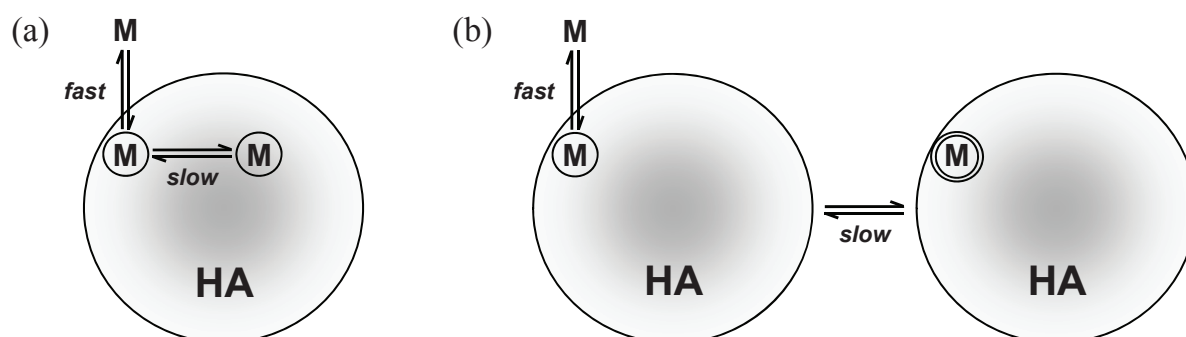


Figure 25. Intra-molecular "diffusion" (a) and on-site stabilisation (b) as possible explanations for an increase in complex inertness with time of contact.

This interpretation is now widely accepted as it provides a plausible explanation for an increasing hindrance of complex dissociation. However, in consideration of the fact that similar time dependence was found for the competition effect on complex formation, the theory must be called into question since both phenomena probably reflect one and the same process. If we assume that Al(III) migrates from outer sites to inner sites during the time span concerned, the access for Tb(III) should be facilitated with time because the initial sites of Al(III) are vacated; but on the contrary, binding of Tb(III) is impeded with time. Consequently, in-diffusion cannot serve as an explanation for our results, and because of the temporal accordance, it may be inferred that this assumption is also inapplicable to the dissociation studies described in the literature.

Instead, our findings give rise to the conclusion that bound metals do not leave their initial binding sites but the sites themselves get “stronger”, as schematically illustrated in Fig. 25b. We suppose that structural changes are induced in the surroundings of the metal, keeping it more and more trapped, for instance due to bridging effects. In this way, the metal becomes less exchangeable for competing metals, and also the access to free binding sites may be increasingly hindered.

3.4.2. Spectroscopic probing

With the objective of providing evidence of structural alterations, we employed time-resolved laser-induced fluorescence spectroscopy (TRLFS) as a powerful technique for probing rearrangement processes on a molecular scale. Figure 26a shows the fluorescence decay of Tb(III), which is indirectly excited by the humic acid.

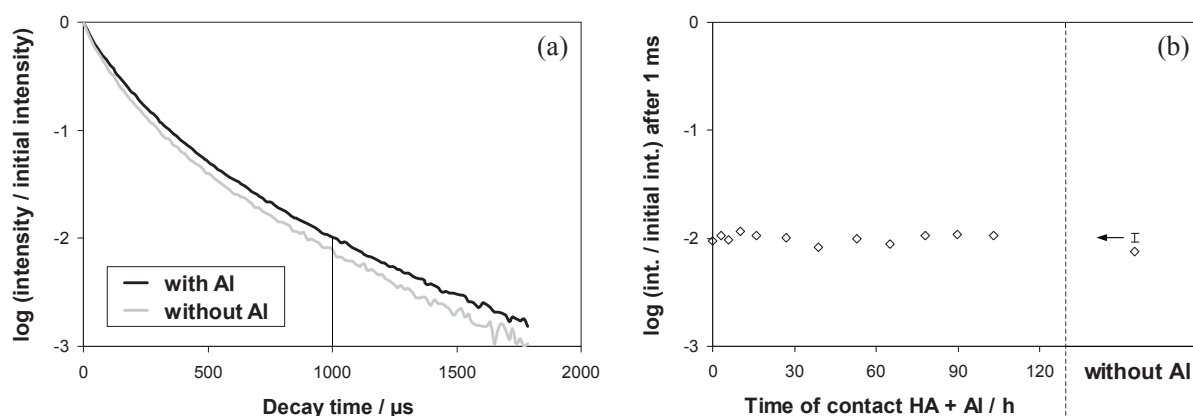


Figure 26. Fluorescence decay of Tb(III) in contact with HA in the absence and presence of Al(III) (a); decay value after 1 ms as a function of contact time (b) (10^{-5} M Tb, 2×10^{-5} M Al, 10 mg L^{-1} HA, 0.1 M NaClO_4 , pH 4.0, $\lambda_{\text{exc}} = 325.0 \text{ nm}$). The error bar indicates the standard deviation around the mean value of the time-dependent data series. The decay curve for the system with Al consists of the averaged data of all curves obtained for different contact times.

Generally, the fluorescence lifetime of the metal depends on the presence of opportunities for energy transfer, e.g., to water or other ligands, but also back to the humic molecule. This energy back transfer depends on the molecular structure in the microenvironment of Tb(III). Consequently, the fluorescence decay may be sensitive to possible changes induced by complexation with Al(III). In fact, it can be seen that the fluorescence lifetime is significantly influenced by the presence of Al(III).

In Fig. 26b, relative intensities after a decay time of 1 ms are plotted for Al(III) / HA systems that had been allowed to stand for different time periods before Tb(III) was added. On the right-hand side, the value for the system without Al(III) is shown together with the range of variation for the time-dependent data series. The time frame was chosen according to the observed increase in the competition effect. However, no corresponding trend can be found in the intensity values. The reflected structural changes occur immediately and thus cannot be the background of the stabilisation process in question.

The impact of Al(III) complexation is also visible in the fluorescence emission spectrum of the humic acid (Fig. 27a). The fluorescence is quenched in the range of higher wavelengths, i.e., the fluorophores with the largest π -systems are most influenced. Also these spectra do not show any dependence on the ageing time of Al(III) / HA systems, shown for the fluorescence intensity at 500 nm in Fig. 27b.

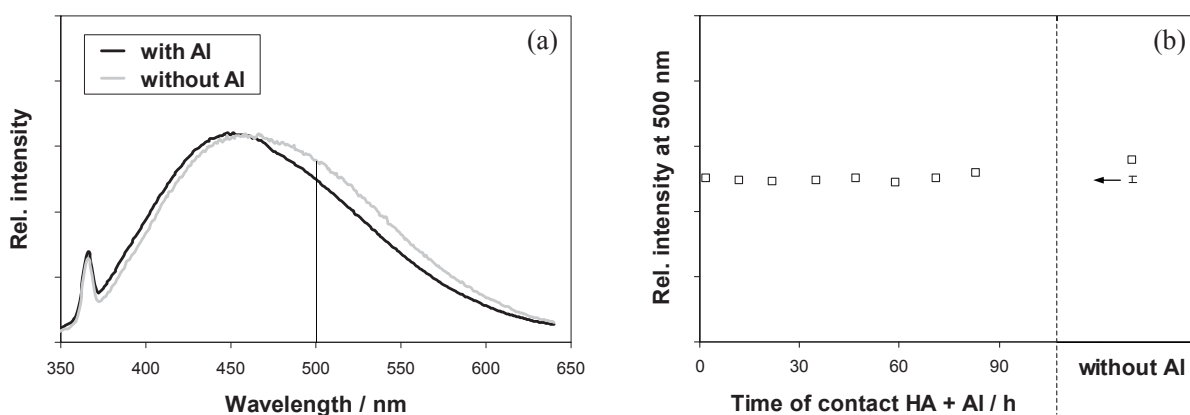


Figure 27. Fluorescence spectrum of humic acid in the absence and presence of Al(III) (a); intensity at 500 nm as a function of contact time (b) (2×10^{-5} M Al, 10 mg L^{-1} HA, 0.1 M NaClO_4 , pH 4.0, $\lambda_{\text{exc}} = 325.0 \text{ nm}$). Averaged data were used analogously to Fig. 26.

Further attempts to find indications of rearrangement processes on a longer time scale were undertaken with Eu(III) as a probe metal, which can provide more detailed information than Tb(III). Figure 28 shows fluorescence emission spectra of Eu(III), recorded by TRLFS with an initial delay of $10 \mu\text{s}$ to skip the fast decaying fluorescence of humic acid (cf. Fig. 27a). The two main spectral bands around 592 nm and 615 nm are assigned to the $^5\text{D}_0 \rightarrow ^7\text{F}_1$ and $^5\text{D}_0 \rightarrow ^7\text{F}_2$ transitions, respectively. At an excitation wavelength (λ_{exc}) of 361.7 nm, Eu(III) is directly excited (black spectrum). In the presence of humic acid, the fluorescence is enhanced by an

energy transfer from the humic ligands, i.e., there is an indirect excitation in addition (grey spectrum).

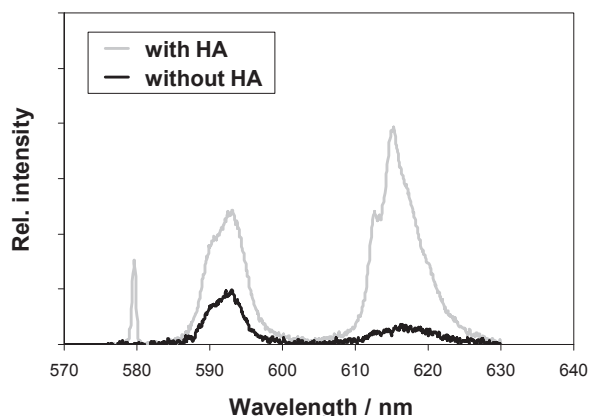


Figure 28. Fluorescence spectrum of Eu(III) in the absence and presence of HA (10^{-5} M Eu, 10 mg L^{-1} HA, 0.1 M NaClO_4 , pH 4.0, $\lambda_{\text{exc}} = 361.7 \text{ nm}$).

If the excitation wavelength is only slightly lowered to 356.0 nm, the direct excitation mode no longer exists, and Eu(III) is only indirectly excited by humic acid (Fig. 29a). When comparing the peak ratios, one can recognise that the grey spectrum in Fig. 28 is a composite of the grey spectrum in Fig. 29a and the black spectrum in Fig. 28. In a more quantitative analysis by a fitting procedure, the composite spectrum obtained via direct and indirect excitation can be separated into two constituent spectra resulting only from direct and only from indirect excitation, respectively. In this way, the Eu(III)-humate complex can be distinguished from non-bound Eu(III), and the humic-bound fraction can be directly derived from the relative contributions of the constituent spectra. In addition to this quantitative information, the spectrum is also sensitive to possible qualitative changes in the microenvironment of humic-bound Eu(III).

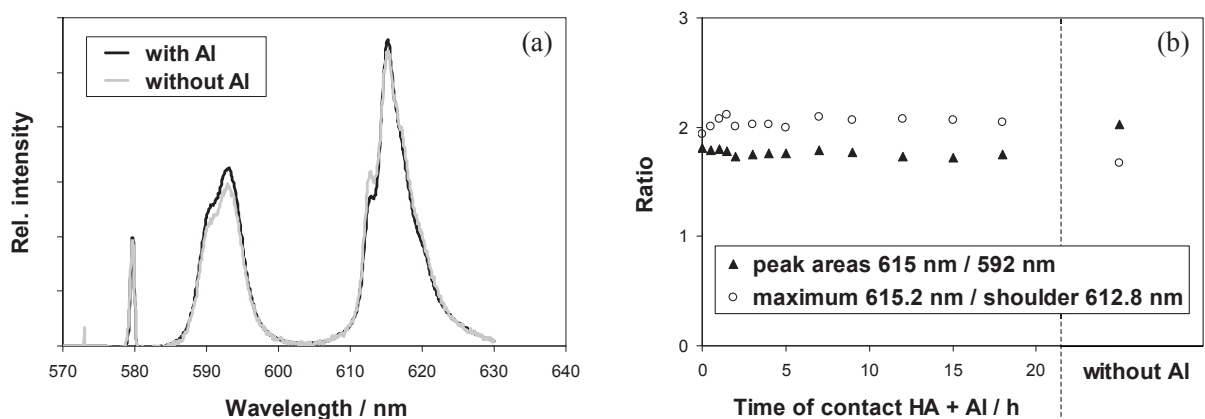


Figure 29. Fluorescence spectrum of Eu(III) in contact with HA in the absence and presence of Al(III) (a); intensity ratios as a function of contact time (b) (10^{-5} M Eu, 2×10^{-5} M Al, 10 mg L^{-1} HA, 0.1 M NaClO_4 , pH 4.0, $\lambda_{\text{exc}} = 356.0 \text{ nm}$). The spectrum for the system with Al consists of the averaged data of all spectra obtained for different contact times.

As can be seen in Fig. 29a, the intensity ratios within the spectrum are indeed slightly altered in the presence of Al(III). The integral intensity (area) of the band around 592 nm is increased with respect to the band around 615 nm, and the maximum intensity of the sub-band (shoulder) at 612.8 nm is decreased with respect to the band maximum at 615.2 nm. Since only humic-bound Eu(III) is “visible” at an excitation wavelength of 356.0 nm, these changes are not attributable to the partial displacement of Eu(III) by Al(III). Obviously, there are structural rearrangements. In Fig. 29b, the specified spectral features are plotted for systems where Al(III) and HA had been in contact for different time periods before Eu(III) was introduced. Again, it turned out that the changes occurred at once, and there was no indication of a time-dependent trend corresponding to the competition effect.

Such a time-dependent series of spectra was also recorded at an excitation wavelength of 361.7 nm where Eu(III) is excited both directly and indirectly. Together with the spectrum for Eu(III) in the absence of HA and the time-dependent spectra for indirect excitation ($\lambda_{\text{exc}} = 356.0$ nm), these data allowed us to calculate the respective proportions of humic-bound Eu(III) as described above. They are shown in Fig. 30. The competition effect of Al(III) is clearly visible. However, a time dependence is not discernible from these data.

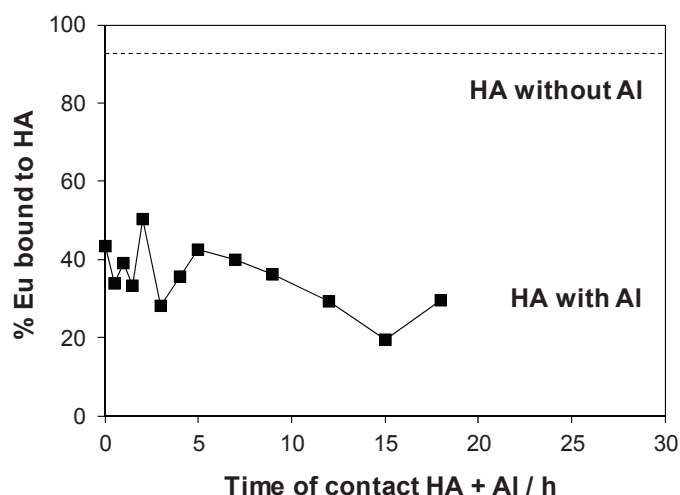


Figure 30. Complexation of Eu(III) with HA after pre-equilibration of HA and Al(III), determined by analysis of Eu(III) fluorescence spectra at $\lambda_{\text{exc}} = 356.0$ nm and $\lambda_{\text{exc}} = 361.7$ nm (concentrations as specified in Fig. 29).

At first sight, this result is surprising since it seems to contradict the findings for Tb(III) shown in Fig. 24a. It must be noted, however, that the concentration of Eu(III) is higher by two orders of magnitude. A concentration of at least 10^{-5} M is necessary to obtain sufficient fluorescence intensity. This is half of the concentration of Al(III), which was proven to induce instantaneous structural rearrangements. Thus, it is not unlikely that the subsequent addition of Eu(III) has similar implications. If the time dependence in the competition effect, observed for 10^{-7} M Tb(III), is caused by comparatively minor changes, these are probably outweighed by the complexation of the probe metal, and consequently, the kinetic effect simply does not occur. Possibly, this reasoning may also be applied to the TRLFS studies with Tb(III) where the same probe concentration was used, i.e., the probe metal could not “see” time-dependent

changes because they were eliminated by the probe itself. In addition, however, the fluorescence spectra of Al(III) / HA systems, recorded in the absence of probe metals, did not show any time-dependent trend (Fig. 27). One may conclude that stabilising rearrangements as a basis of the kinetic effect cannot be very massive compared to the initial impact of Al(III) complexation.

3.5. Transport studies by means of positron emission tomography

3.5.1. Advection in homogenised clay samples

Kaolinite test sample. A first continuous injection test was conducted with the sample Kao, which is a compacted sample prepared with a kaolinite-sand suspension. The fluid contained 0.01 M [^{124}I]KI with an activity of 66 MBq, the flow rate was set to 0.005 mL min $^{-1}$, and the pressure was 0.4 MPa. 40 images were recorded during the experimental period of one week. A selection of these images is shown in Fig. 31. The partial assembly of the scanner with only 8 cassettes caused noisy images. However, the tracer propagation is clearly discernible as a homogeneous dispersive advection.

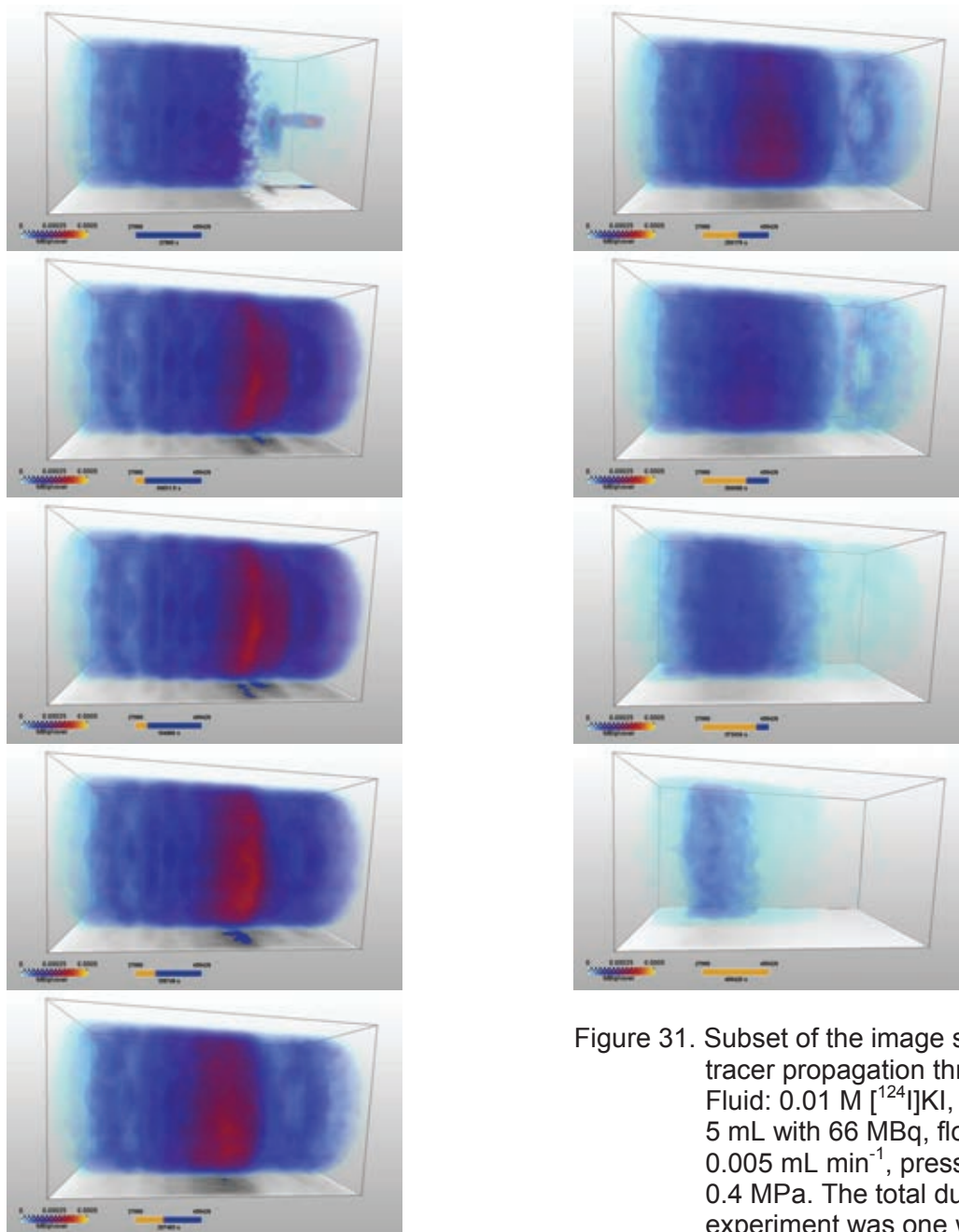


Figure 31. Subset of the image sequence of tracer propagation through Kao. Fluid: 0.01 M [^{124}I]KI, tracer pulse: 5 mL with 66 MBq, flow rate: 0.005 mL min $^{-1}$, pressure: 0.4 MPa. The total duration of the experiment was one week.

The tracer propagation was considered as 1D-dispersive advection and was analysed accordingly using CXTFIT (Figs. 32 and 33). The fit was based on the sum-activity of selected slices because the fitting algorithm is limited to a relatively small number of data points (about 150). The fit results indicated a velocity of 0.47 mm h^{-1} and a dispersivity of $1.1 \times 10^{-9} \text{ m}^2 \text{ s}^{-1}$.

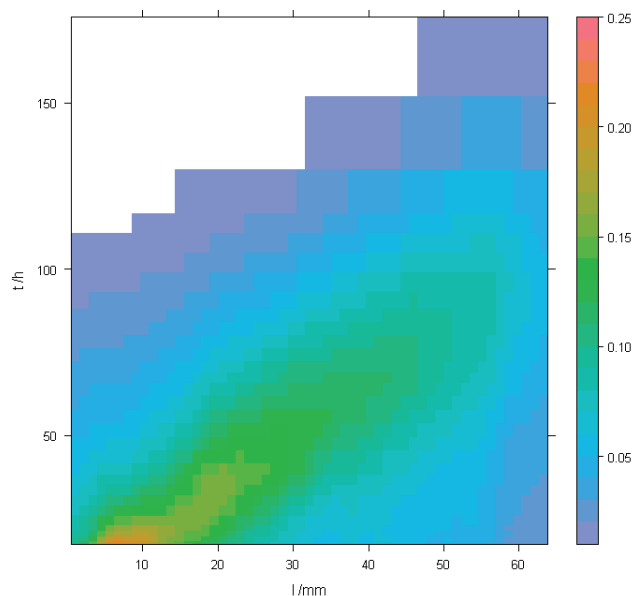


Figure 32. Sum of activity over each slice versus axial location and propagation time.

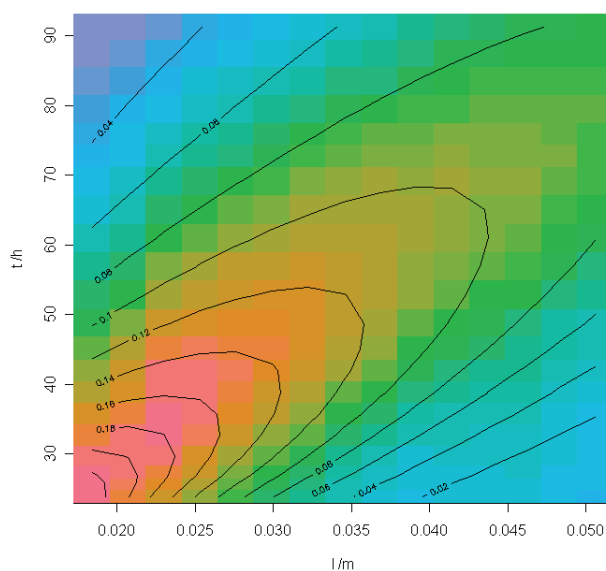


Figure 33. CXTFIT best-fit curves in the region unaffected by boundary effects.

Opalinus clay test sample. The sample OPA1 was made by compaction of a suspension of Opalinus clay powder in synthetic OPA pore water, which was also used as injection fluid together with 0.01 M KI as a carrier. Again, ^{124}I was applied as a tracer, injected as a pulse of 4 mL. The flow rate was 0.02 mL min^{-1} , and the

pressure was 0.3 MPa. 26 images were recorded during 50 hours (selection in Fig. 34). The images were considerably clearer than in the study with Kao because the scanner had been extended from 8 to 20 cassettes. However, significant image artifacts were still caused by initial technical deficiencies. The images generally show dispersive plug flow with minor lateral inequalities, but without preferential flow paths.

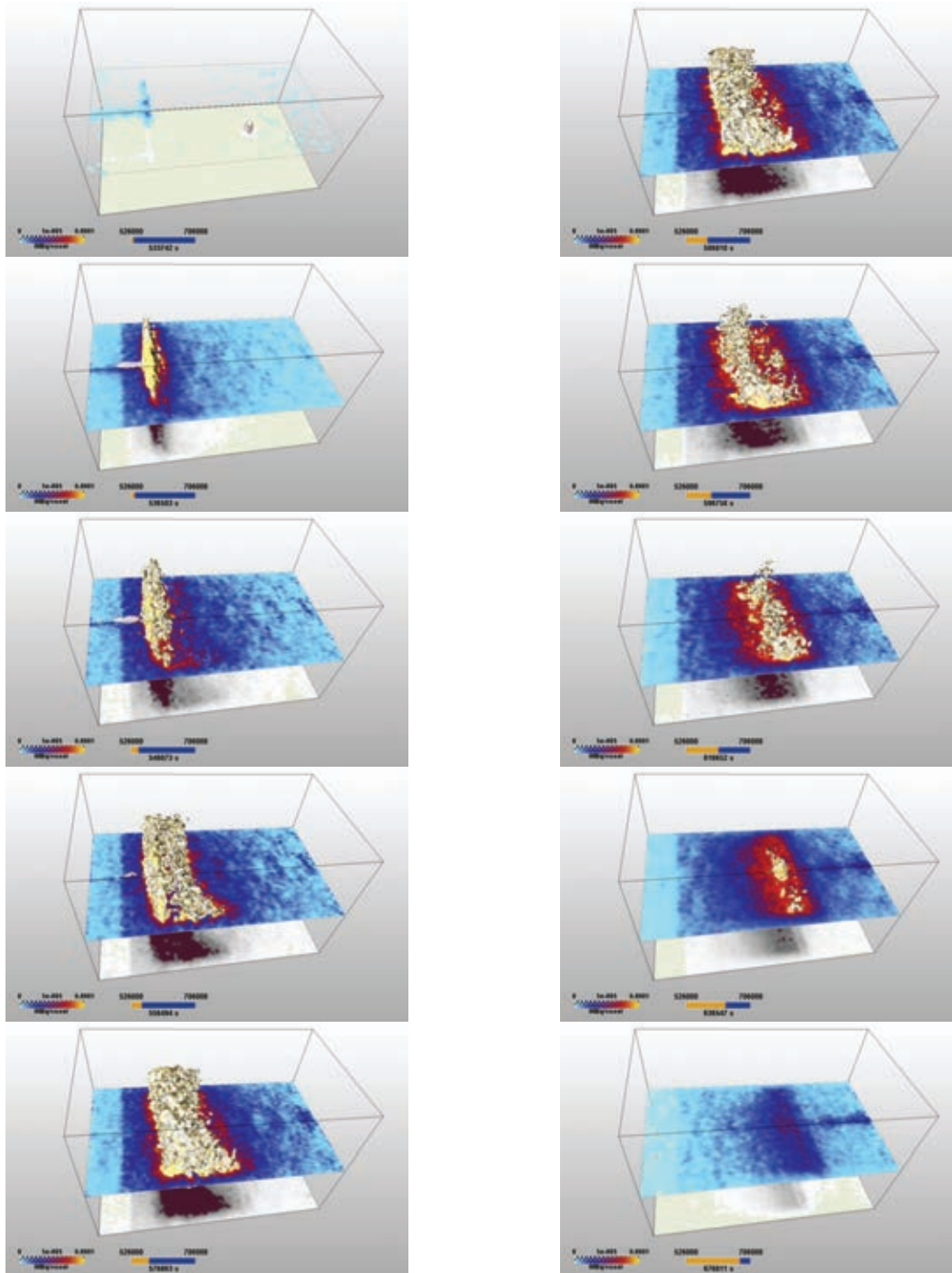


Figure 34. Conservative injection test with $[^{124}\text{I}]\text{KI}$ and OPA1 (projection at the bottom, central slice colour-coded, isosurface of distribution of maximum activity).

Smoothing splines with respect to time were applied to all 215000 points of the image. The maximum of the smoothing curve was identified as a convenient measure of the arrival time. This maximum value can be interpreted as transport efficiency of the individual spatial points. Low values of this maximum imply no significant contribution of this voxel to the transport process. Thus, a 3D-data set of the pathway efficiency (maximum value of activity) and of the arrival times (which can be interpreted as velocity distribution) could be derived (Fig. 35).

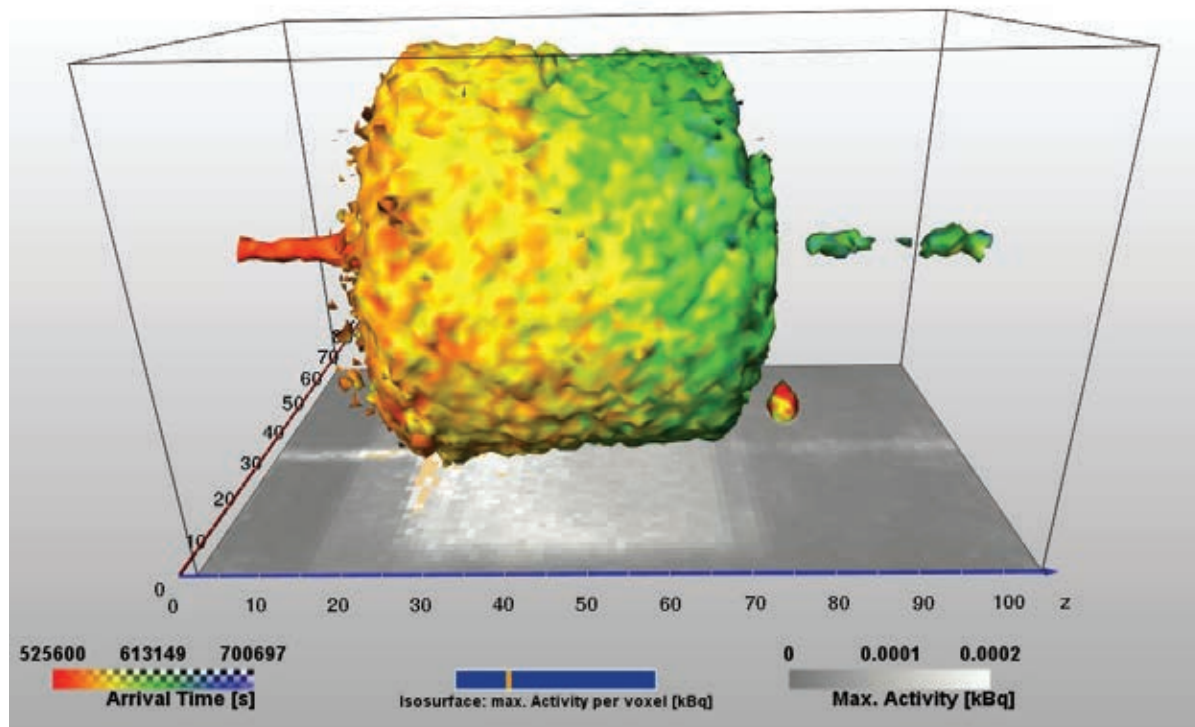


Figure 35. Travel time (colour-coded) and pathway efficiency (projection on the horizontal plane) for OPA1 (conservative tracer test), showing slight lateral differences.

A second study on OPA1 was conducted with Aldrich humic acid (50 mg L^{-1}), labelled with ^{124}I by the Iodogen method. It was injected into the sample without prior conditioning with HA solution. The sample contained the carrier solution from the preceding experiment (OPA water with 0.01 M KI). The flow rate was 0.01 mL min^{-1} , the pressure was 0.3 MPa . 32 images were taken during 10 days of injection (Figs. 36 and 37). During the whole period, the most part of detected ^{124}I remained immobile in the sample near the injection end plate, while a small portion travelled with a velocity corresponding to the preceding experiment. This fraction was identified as free iodide, probably a residue of the labelling procedure.

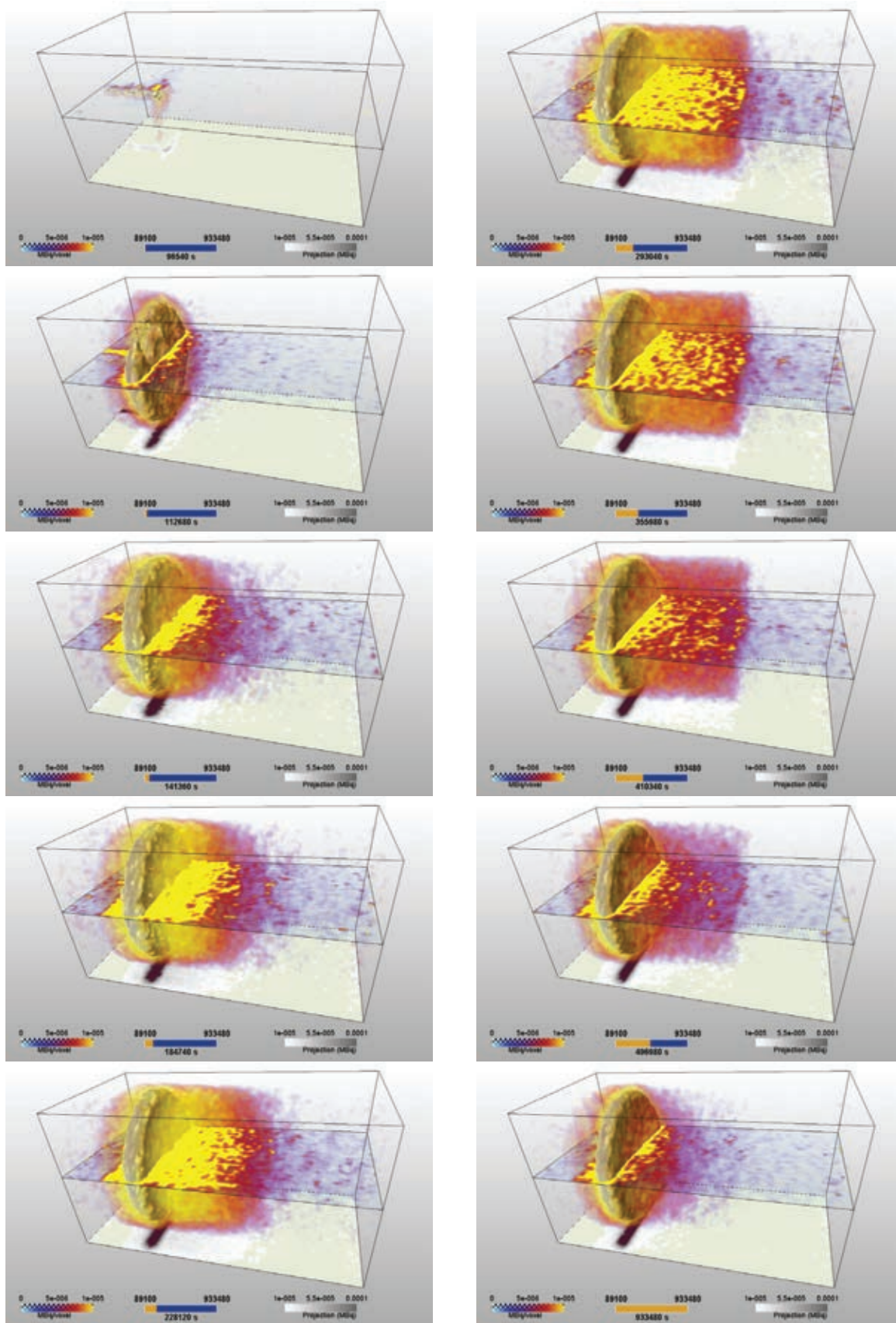


Figure 36. Flow test with ^{124}I -labelled HA and OPA1 (projection at the bottom, central slice colour-coded, isosurface of distribution of maximum activity).

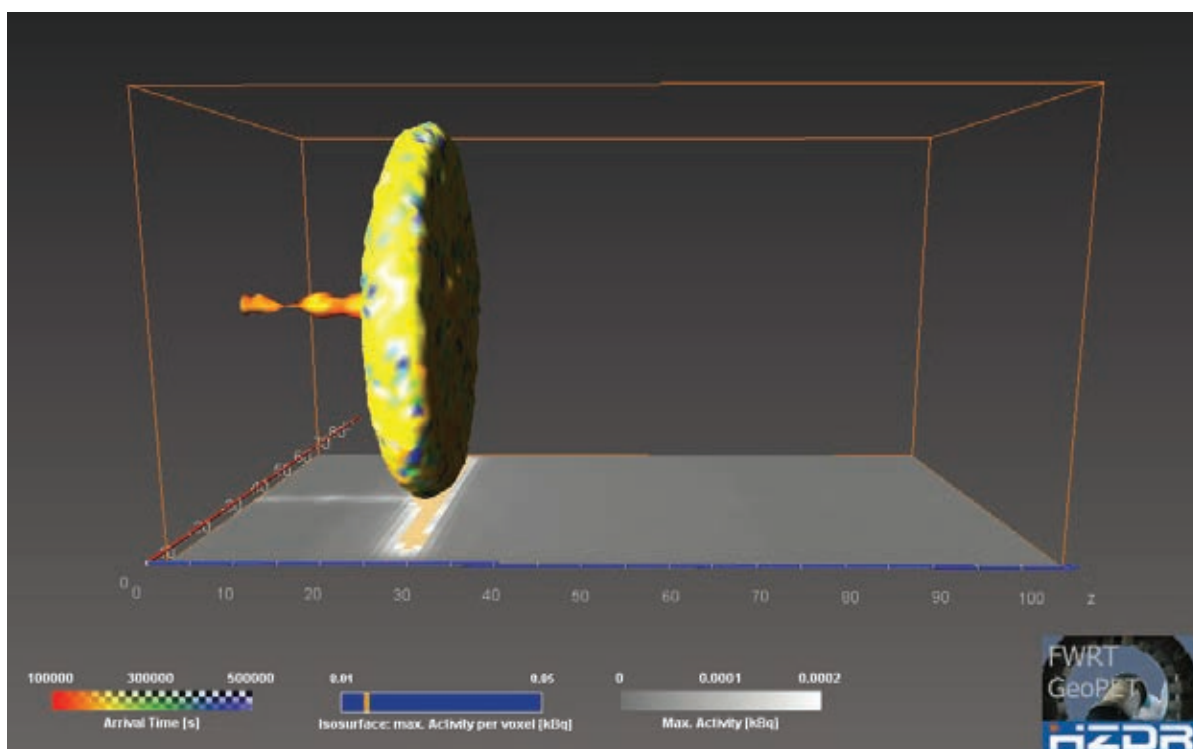


Figure 37. Travel time (colour-coded) and pathway efficiency (projection on the horizontal plane) for OPA1 (flow test with ^{124}I -labelled HA), showing immobility of the tracer at the inlet.

Synthetic sand-bentonite column Nagra1. Nagra1 is a compacted 80/20-sand-bentonite sample with an initial water content of 10%. The density after compaction was 1.5 g cm^{-3} (max. porosity ~ 0.65 , considering saturated conditions after compaction). After conditioning with 40 mL synthetic Grimsel formation water (“Grimsel water”) [67] at a flow rate of $0.001 \text{ mL min}^{-1}$, 100 mL of Grimsel water with ^{58}Co cobalt hexacyano complex (0.5 MBq mL^{-1}) were injected at the same flow rate. The first arrival of the tracer occurred after injection of 27 mL. The maximum specific activity of 0.07 MBq mL^{-1} was reached after injection of 60 mL. In spite of diffuse and noisy PET images (Fig. 38), probably due to the noise generated by the additional γ -activity of the non-ideal PET nuclide ^{58}Co , it can be seen that the tracer distribution is very inhomogeneous. During the whole period, the evolution of the tracer distribution was uneven and patchy, with a strong increase in activity from the axis to the cylinder surface and a steady gradient from the inlet to the outlet until termination of the injection period.

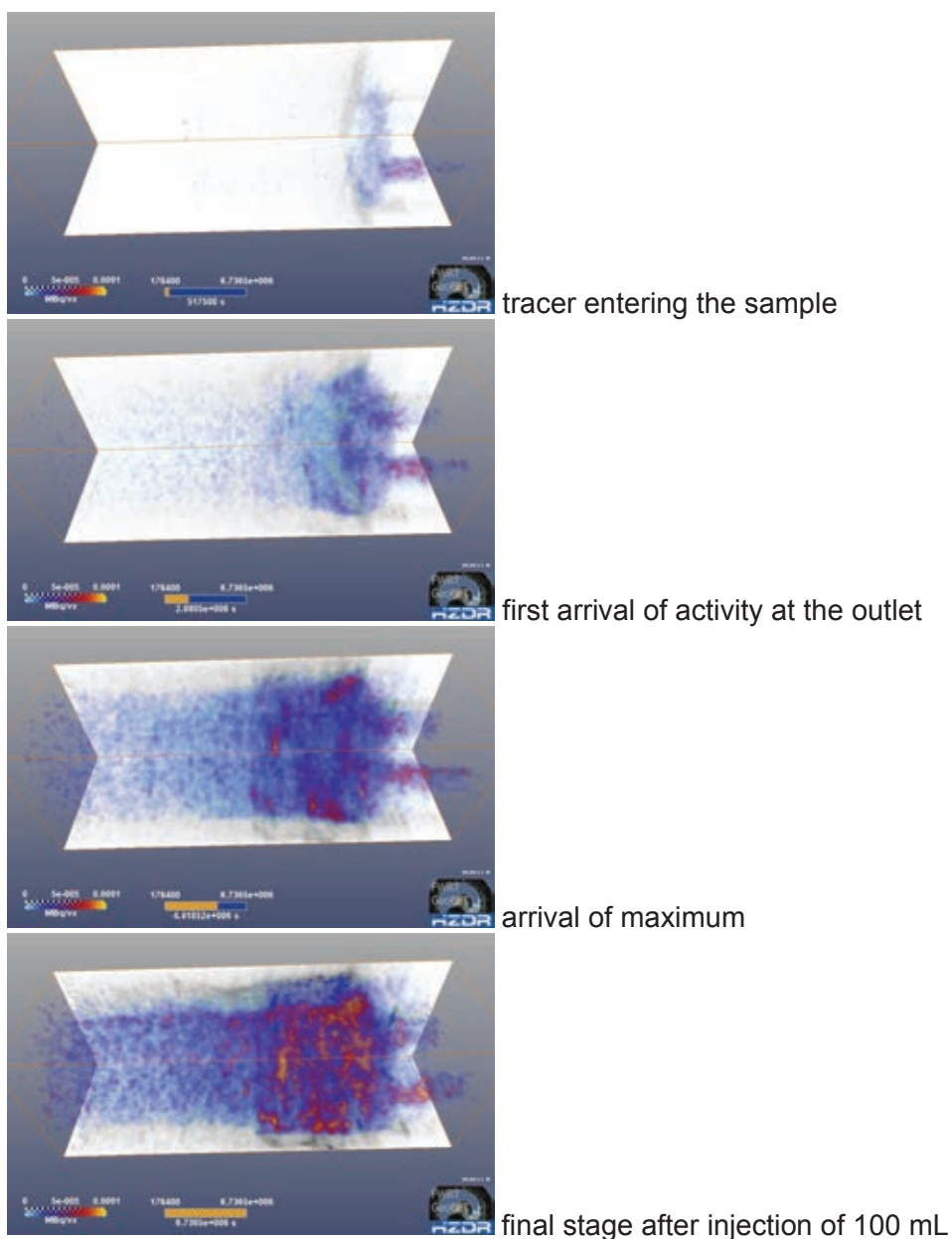


Figure 38. Transport of [^{58}Co]cobalt hexacyano complex as a conservative tracer in a sand-bentonite column. The images show a patchy and non-uniform tracer distribution.

3.5.2. Advection in rock cores

Åspö granite. X-ray computed microtomography (X- μCT) and PET measurements were conducted with a granitic core from the hard rock laboratory Åspö (Fig. 39). Conservative tracers (F^- , I^-), marked with the positron-emitting radionuclides ^{18}F and ^{124}I , and Aldrich humic acid, labelled by complexation with ^{86}Y , were used as radiotracers to observe transport processes of both dissolved components and colloids in the crystalline matrix along a longitudinal fracture. Flow rates ranged from 0.1 to 0.001 mL min^{-1} . The volume of the tracer pulse was always 5 mL.

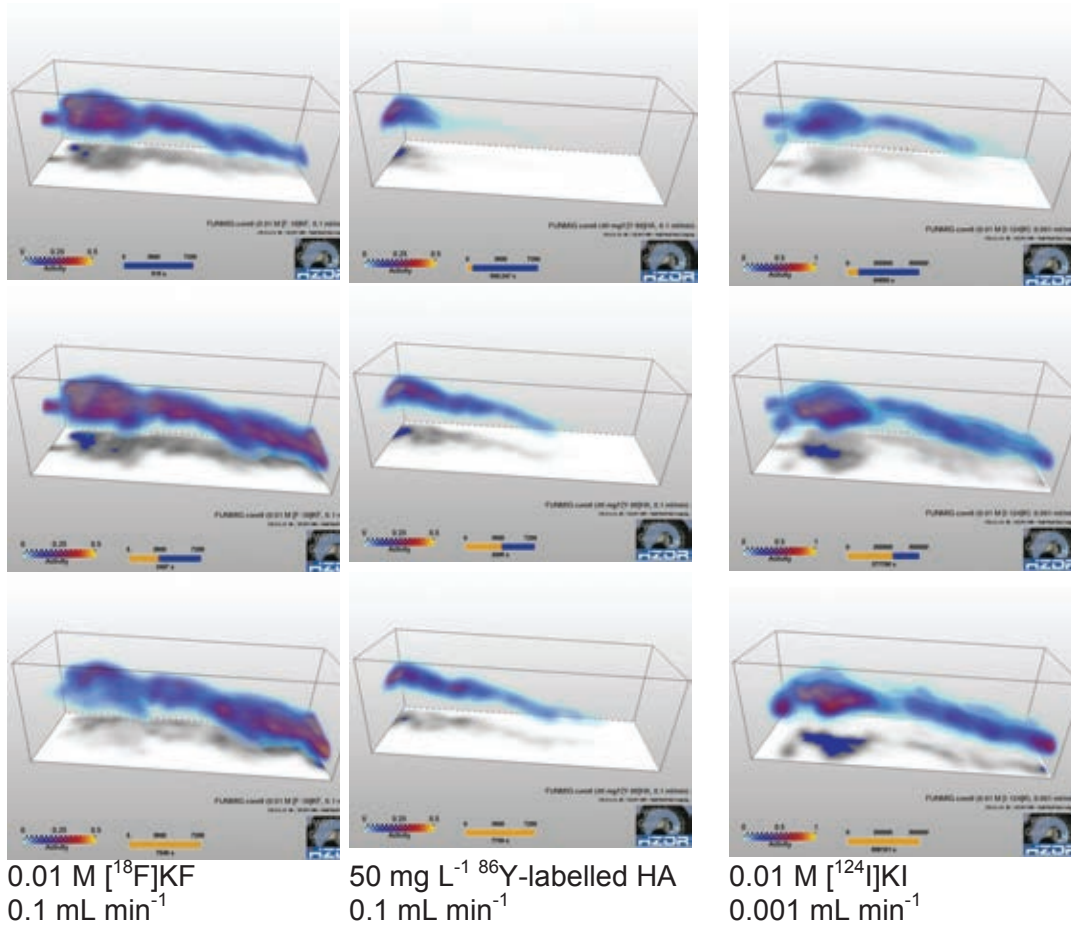


Figure 39. Transport of fluoride, HA and iodide in the granite core Äspö8. The images were taken for comparable injection volumes. The injection flow rate for iodide was considerably slower than those for the other tracers.

These experiments were performed with a medical PET scanner ECAT Exact HR+ (Siemens, Germany) at the clinic and polyclinic for Nuclear Medicine, University of Leipzig. The spatial resolution of this scanner is ~ 5 mm, which is far beyond the aperture of the fracture. Nevertheless, the characteristics of the transport processes are significant: In all cases, the flow path is strongly localised, with some zones of stronger “accumulation” of activity. Probably, these are zones with lower flow velocity, where the specific activity (per volume) attains higher values than in zones with short times of residence. The measurements with fluoride and with HA were conducted at the same flow rate. The transport of the HA is more localised to one tortuous line and is strongly delayed compared to fluoride. The pulse did not arrive at the outlet during the experiment. The activity distribution of iodide, which was injected at a much lower flow rate, is similar to the activity distribution of fluoride for a comparable injected volume. However, the transport path of iodide appears to be more localised and less diffuse than that of fluoride. This effect is not related to imaging issues since additional gamma lines of ¹²⁴I should cause more noise and thus more diffuse images. Obviously, the higher kinetic energy due to the higher flow rate causes a stronger dispersion effect within the fracture.

The general behaviour – localised flow paths and local tracer accumulations – was reproduced by Lattice-Boltzmann simulations based on the segmented image of the

fracture (Fig. 40). These simulations were conducted at the University of Mainz, Institute of Geosciences.

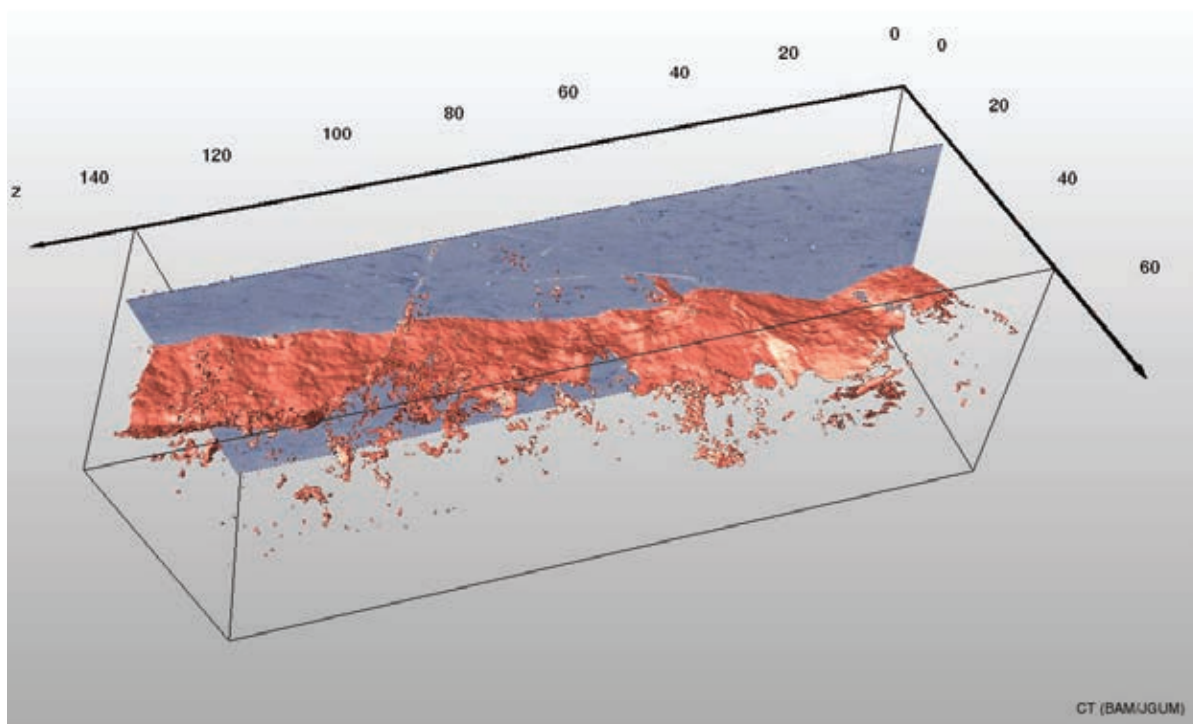
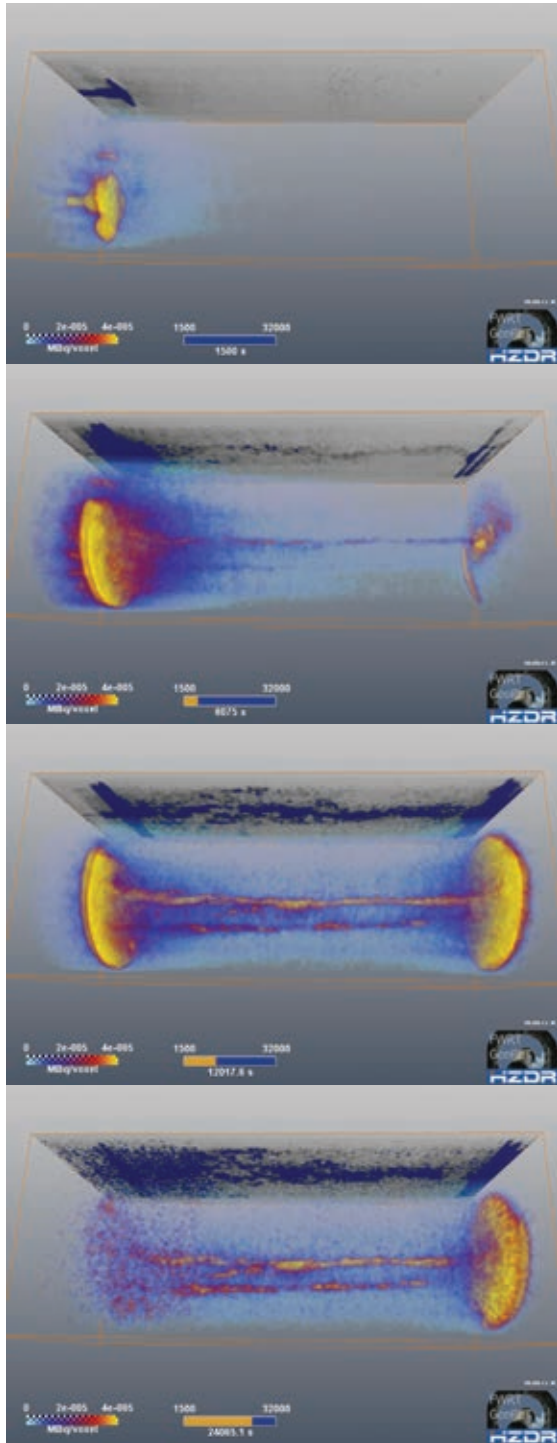


Figure 40. Projection of the X- μ CT image (produced by BAM, Berlin, processed by the Institute of Geosciences, University of Mainz), with the segmented fracture.

Grimsel granite Nagra2. A granite core from a fracture zone of the Grimsel test site was provided by Nagra (Switzerland) for flow experiments with PET monitoring. The test procedure was similar to the experiments with the Äspö sample, but now conducted with the higher-resolving ClearPET in our laboratories, which allowed a considerably longer observation period. 24 images have been recorded during the injection of 0.001 M [^{18}F]KF in synthetic Grimsel water over 12 hours at a flow rate of 0.1 mL min $^{-1}$ (Fig. 41).



25 min, $V = 1.5$ mL

100 min, $V = 9$ mL (5 mL tracer solution and 4 mL carrier solution)
 first appearance of the tracer at the outlet
 after 120 min

200 min, $V = 17$ mL

400 min, $V = 34$ mL
 maximum activity at the outlet after ~ 450 min

Figure 41. PET monitoring of the flow in the axially fractured Grimsel granite core Nagra2, flow rate 0.1 mL min^{-1} , Grimsel water with ^{18}F , tracer pulse length 5 mL.

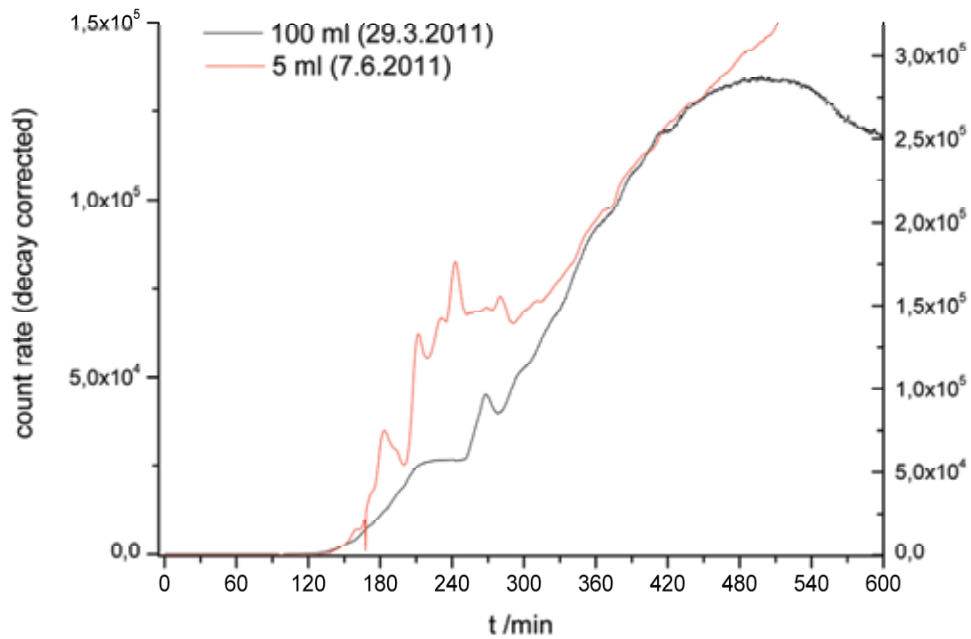


Figure 42. Break-through curves for the sample Nagra2 for two different tracer pulse lengths (red: 5 mL, black: 100 mL). Decay-corrected count rate measured by means of the flow-through counter “GABI” (Raytest, Germany).

With ClearPET, the resolution is close to the order of the maximum fracture aperture of 0.5 mm - 3 mm. However, two distinct pathways, passed with different velocities, are clearly discernable. The fast central pathway was quickly passed within ~ 20 min. Therefore, the temporal variations during the break-through were not resolved. For technical reasons, the inlet into the sample is equipped with a sintered glass filter plate (pore size $1 \mu\text{m}$), which causes accumulation of the tracer in this zone and temporal smoothing of the input pulse. This is the reason for much longer apparent residence times observed in the break-through curves recorded at the outlet (Fig. 42).

The tracer at inlet and outlet causes background gradients of scattered radiation which appear as activity clouds near the end planes. A scatter correction of the PET data would considerably reduce this effect. An appropriate method for high scatter fractions is in development, but not yet applicable. In the zones with low background, the benefit of the higher resolution compared to the medical scanner is obvious. Features of the tortuous flow path are now observable.

3.5.3. Diffusion

Grimsel granite Febex1. This Grimsel granite core originates from the FEBEX experiment (FUN05-001, 5.18m). An axial blind hole was drilled into a section of the core, which appeared to be intact. The end plane was sealed, leaving a port connecting the hole to a fluid injection pump. All other surfaces of the sample were open to atmosphere. In a first step, the borehole was filled with 0.01 M $[^{18}\text{F}]\text{KF}$. Carrier solution was then injected at a flow rate of 0.02 mL min^{-1} . 15 PET images were recorded during the experiment. These measurements were carried out with the partially equipped ClearPET scanner, yielding lower image quality.

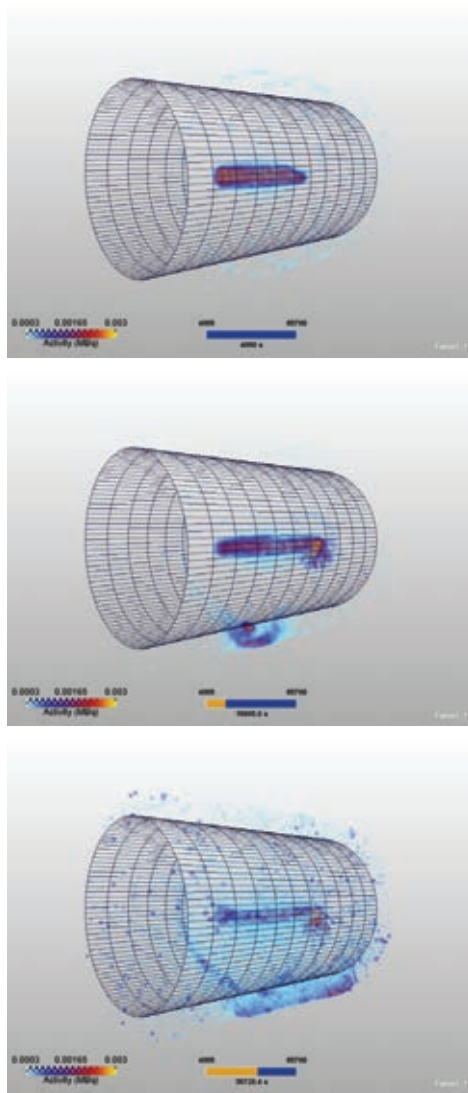


Figure 43. PET images taken during injection of [^{18}F]KF solution into Grimsel granite, sample Febex1. The tracer was filled into an axial blind hole, followed by injection of carrier solution.

The images (Fig. 43) are noisy, which is caused by the limited number of detectors. However, the central source was initially clearly visible. No effect of the injection was observable at the beginning, apart from the decrease in activity in the borehole due to dilution. After about 2 hours, the images showed activity appearing as a ring on the shell of the cylinder. Later on, seepage of fluid through a fracture became obvious. This effect – clearly visible source and sink, but no detectable activity between – was frequently observed in following experiments. It is due to the fact that activity below the local background radiation cannot be detected. This local background depends on the general background, but also on the fraction of scattered radiation and thus on the experimental conditions.

Another experiment was conducted with ^{124}I in synthetic Grimsel water. The “labelled fluid” was filled into the blind hole. Then, the sample was left to stand for 20 days without external driving pressure, wrapped in aluminum foil.

This test (Fig. 44) showed diffusional spreading of the tracer into the sample. Here, no direct loss through the fracture was observed. The tracer gradually “vanishes” under the background level. This level is rather high because the partially equipped scanner was applied. Furthermore, ^{124}I emits additional gamma radiation in the sensitive energy range. Nonetheless, these results were promising in that they indicated the feasibility of spatially resolved diffusion experiments. Applying the fully extended scanner and higher specific activity (reduction of the borehole volume) would certainly yield improved images.

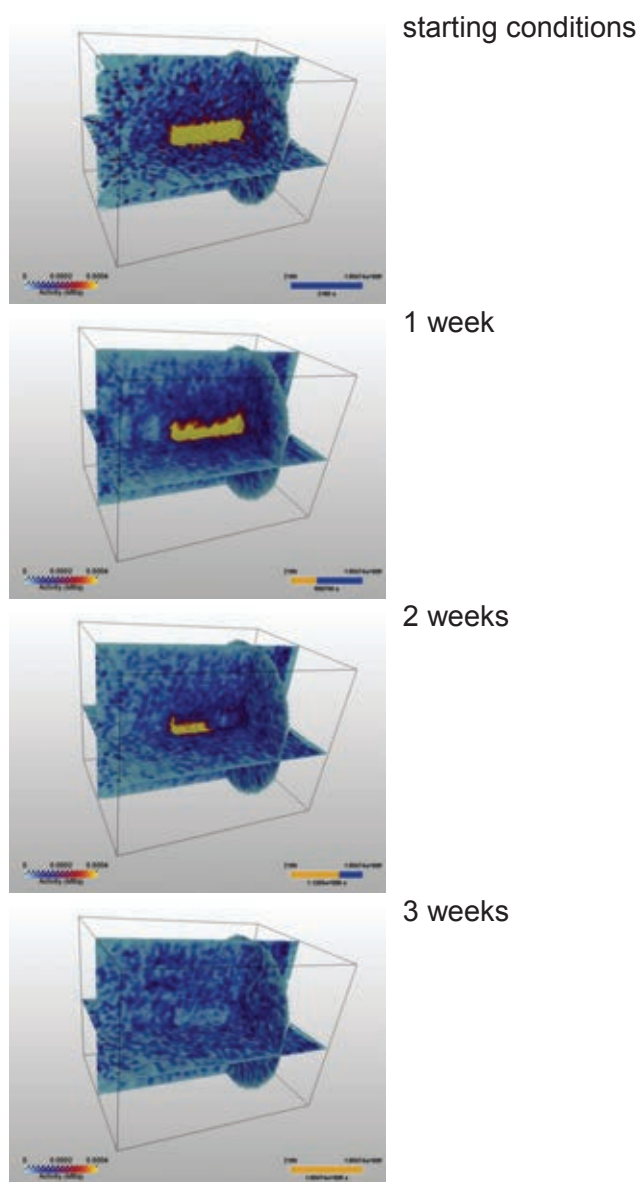


Figure 44. Diffusion of 0.001 M ^{124}I NaI in the fractured Grimsel granite core Febex1, starting from an axial blind hole.

Opalinus clay core OPA2. This sample is an intact clay core. It was completely cast into resin, leaving a central circular gap (thickness 0.1 mm, diameter 50 mm) for fluid injection. Synthetic Opalinus clay pore water with ^{124}I as a tracer was injected at a flow rate of $0.006 \text{ mL min}^{-1}$. 1 mL of “labelled fluid” ($0.001 \text{ M } [^{124}\text{I}]\text{NaI}$ in synthetic pore water, 75 MBq) were injected, followed by 20 mL of carrier solution. The pressure was steadily increasing up to 1 MPa, but no fluid appeared at the outlet. 24 images were recorded during this injection phase (Fig. 45).

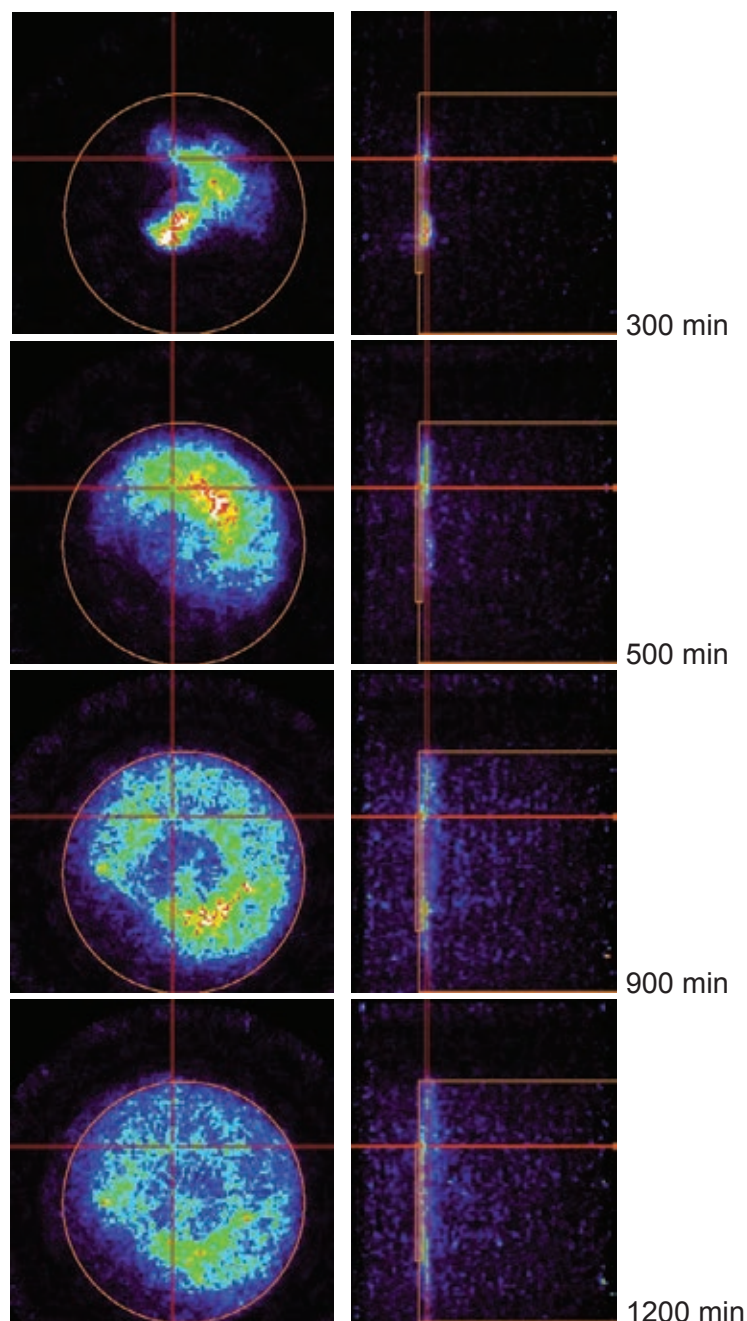


Figure 44. PET images of the OPA2 sample taken during injection of $[^{124}\text{I}]\text{I}^-$ in pore water. Left: radial slice, right: vertical slice at the position of the red lines, orange: geometry of the sample and the injection zone (without decay correction).

The images in Fig. 45 show that the tracer migrates from the injection gap into the slit between resin and rock material. The image after 300 min represents the termination of the tracer pulse. After that, the carrier solution flushes the injection gap, while the tracer migrates through distinct zones into the sample.

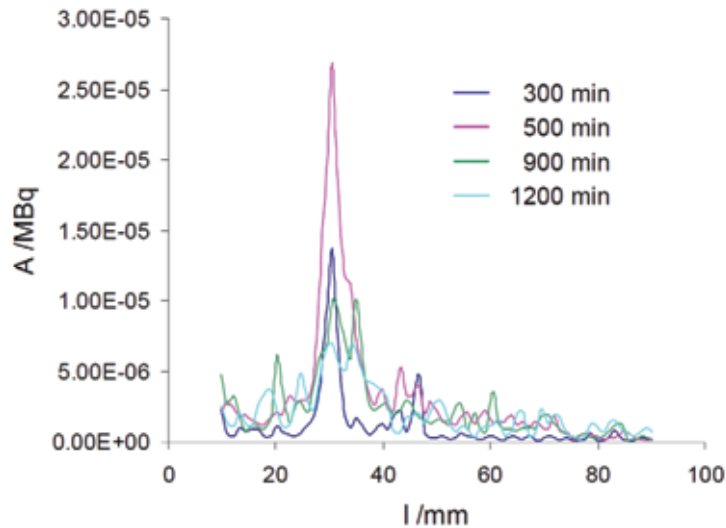


Figure 46. Activity profile along the paraxial line in Fig. 45 (without decay correction).

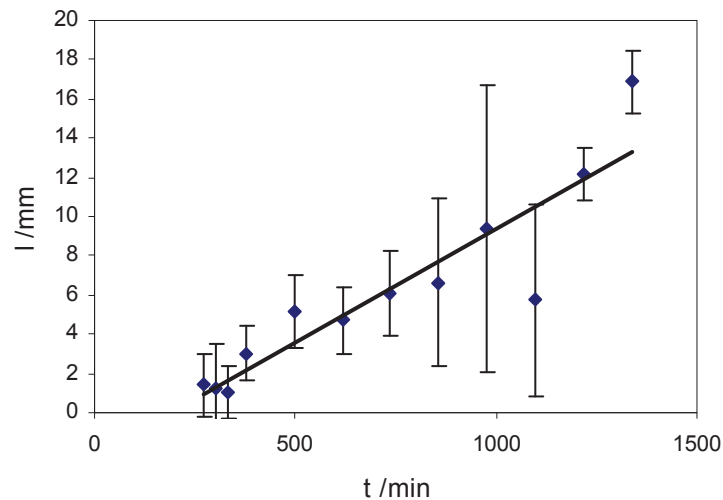


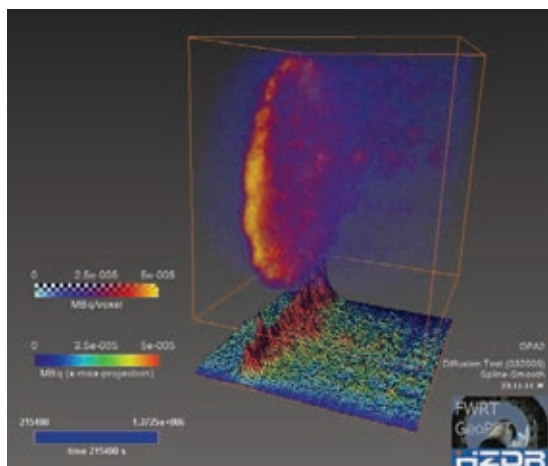
Figure 47. Spatial FWHM of the peak zone (20 mm - 45 mm) in Fig. 46.

Fig. 46 shows one paraxial profile of a zone with high activity. The left side of the peak is determined by the end plate, and the right flank is slowly moving into the material. A Gauss fit to the peaks for each time step yields the spatial FWHM (Fig. 47), from which we determined a local velocity of $(0.72 \pm 0.08) \text{ mm h}^{-1}$.

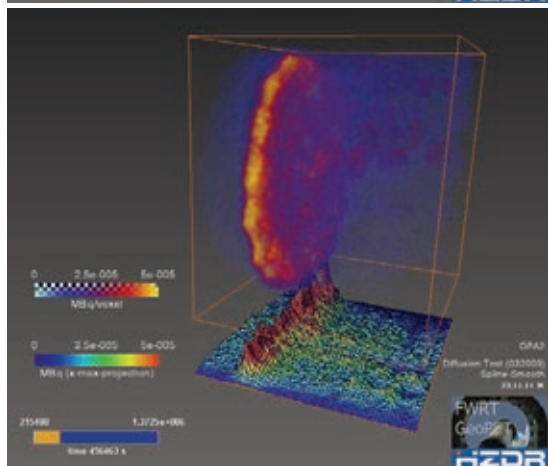
Here, we have to consider irregular conditions because the increasing pressure shows that either the sample contained air which was increasingly compressed, or reactions between pore water and rock material occurred and caused clogging of pathways.

Principally, this method allows deriving local velocities and their distribution on the millimeter scale in media with extremely low permeability, where (within reasonable time frames) the tracer enters only into a thin layer in the millimeter range. This example thus demonstrates that ultra-low fluid permeabilities together with the velocity distribution can be determined from time-dependent PET observations as a non-destructive method.

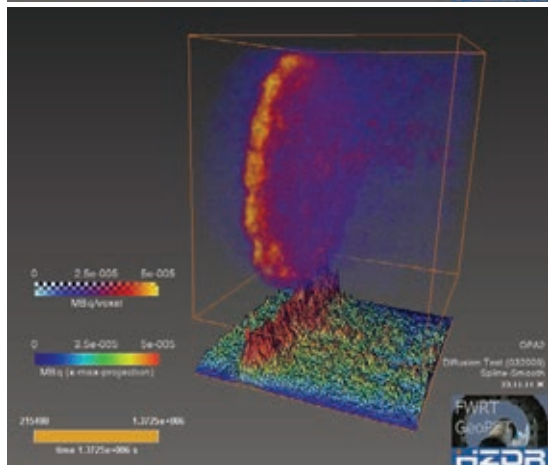
After reaching the threshold pressure of 1 MPa, the pump was stopped, and the evolution of the tracer distribution – driven by diffusion only – was recorded during the decay period of the tracer over 14 days (Fig. 48).



start of diffusion after 2.5 d



5.3 d



15.8 d

Figure 48. Diffusion of $[^{124}\text{I}]^-$ in OPA2 after the injection period (see Fig. 46).

No significant changes in the point-wise tracer distribution were observable during this diffusion period of 2 weeks. Nevertheless, the slice-wise integral (projection at the bottom of the images in Fig. 48) was slightly broadening with time. The total progress of the “diffusion front” was in the order of 1 mm in 14 days (0.07 mm d^{-1}), i.e., below the resolution of the PET scanner. Obviously, longer observation periods are required in Opalinus clay in order to derive parameters.

Opalinus clay cores BLT13/7. Samples were prepared from an Opalinus clay core (drill hole BLT13/7). The core samples (diameter 10 cm) had been shrink-wrapped after drilling and then stored. They were cut into 8 cm long sections. Immediately after cutting, the samples were impregnated with epoxy and then completely cast in epoxy resin. An axial blind drill hole (diameter 5 mm, depth 50 mm, volume 1 mL) was drilled into the samples and then charged with synthetic Opalinus clay pore water. The bore was provided with a closing screw.

It was found that the fluid was rapidly sucked into the sample bulk volume. Over a period of 3 months, about 30 mL of solution had to be added until the fluid level apparently stabilised. After this resaturation period, the holes were cleaned and filled with $0.001 \text{ M } [^{124}\text{I}]\text{KI}$ in synthetic Opalinus clay pore water. The samples were stored at 20°C or 50°C , and about 10 PET images were taken until the activity of the tracer decayed below the detection threshold (Figs. 49 and 50). This threshold depends on the specific activity and thus on the tracer distribution.

After 10 days, the tracer in the samples stored at 50°C had spread over the complete sample and fell below the detection threshold (Fig. 50). The tracer distribution in the samples stored at 20°C did not reach this uniform distribution before decay below the threshold.

In principle, the evolution of the tracer distribution could be fitted to the 2D-circular solution of the diffusion equation in order to derive a diffusion coefficient for I^- . However, we clearly observe 3D-anisotropy. Therefore, the assumptions of this equation are not valid. Instead, a 3D-FEM analysis is currently being conducted with the COMSOL Multiphysics optimisation module, aiming at the derivation of an apparent diffusion tensor [68].

Fig. 49 shows that the fluid was again lost into the bulk volume during the tracer test. Obviously, the spreading is by far too fast to be caused by molecular diffusion, and the loss of water indicates that suction causes advective transport.

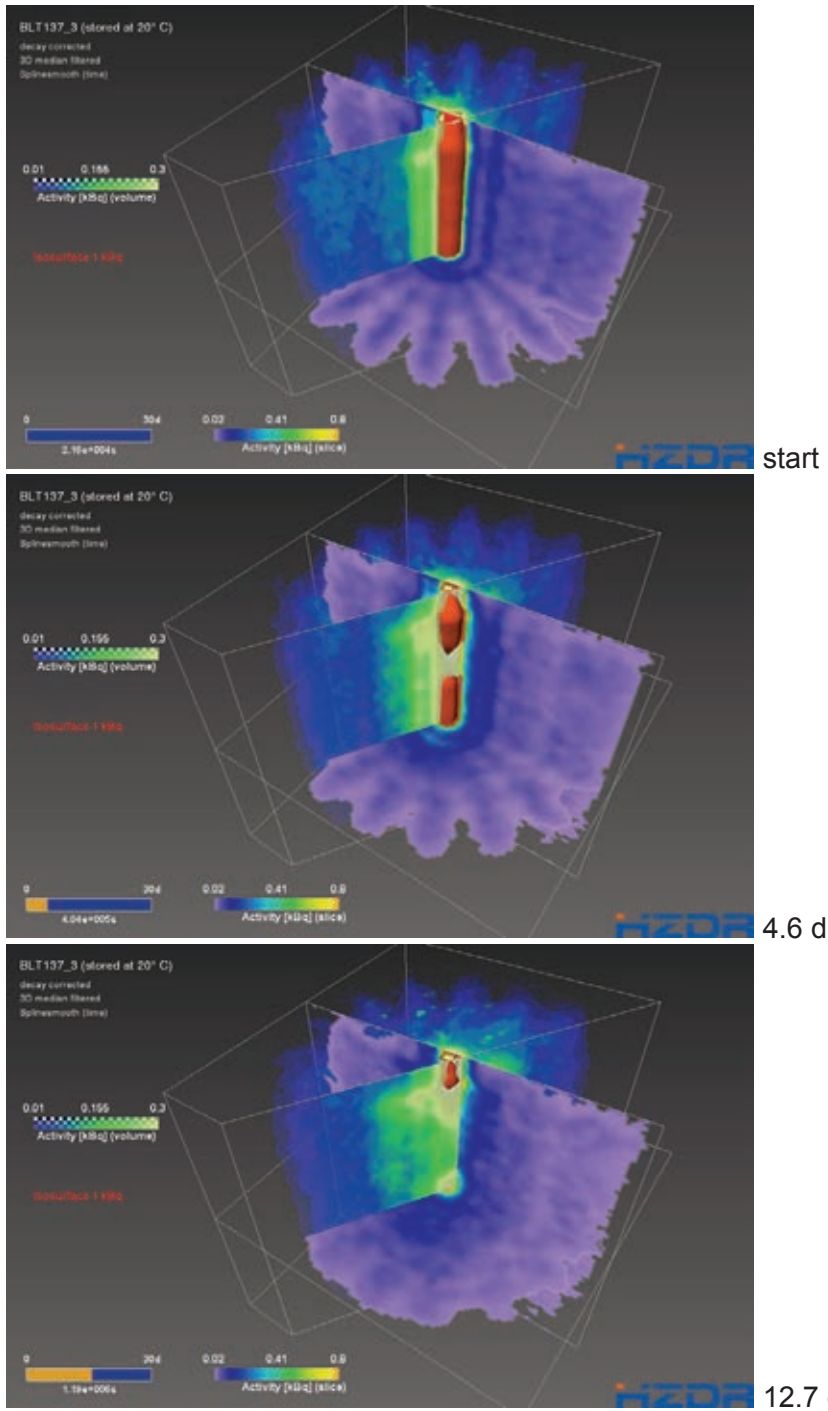


Figure 49. Diffusion of $[^{124}\text{I}]^-$ from an axial line source in Opalinus clay (BLT13/7) at 20°C. The red isosurface marks the maximum of the tracer distribution, where labelled fluid is present. The reduced activity at the center is caused by the formation of an air bubble, and after 20 days, the drill hole was nearly dry.

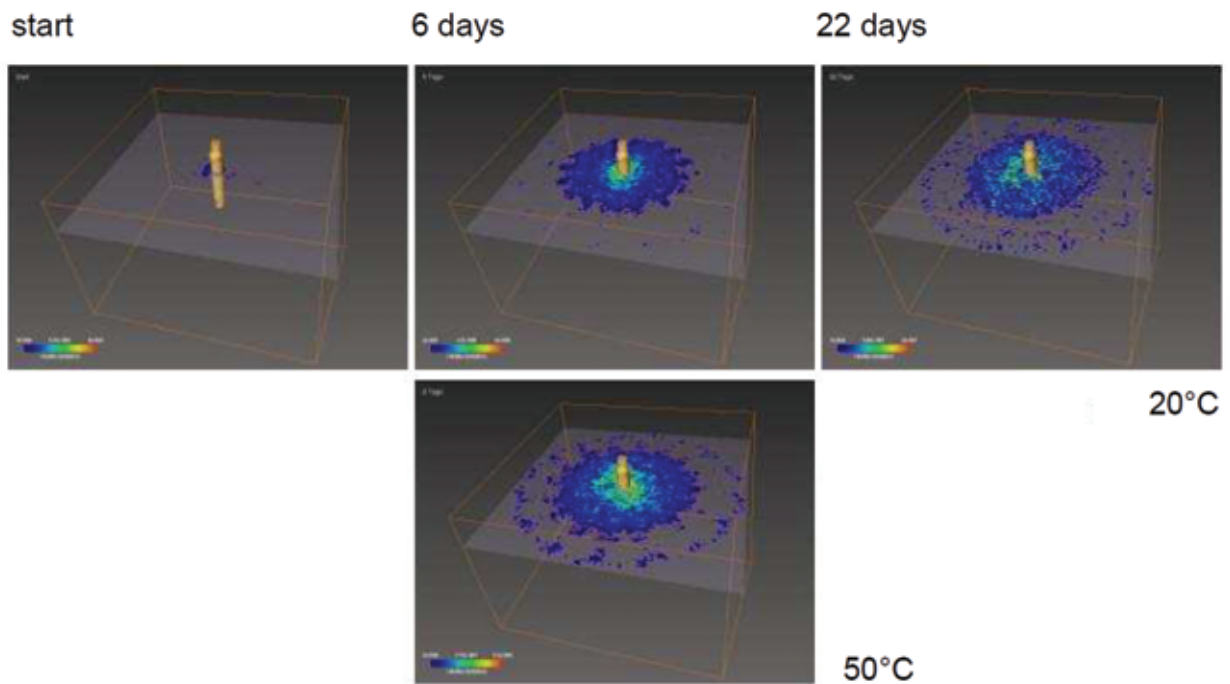


Figure 50. Diffusion in Opalinus clay (BLT13/7) from an axial line source (yellow surface). The samples were stored at 20°C (upper row) or 50°C (lower image).

The most meaningful zone for evaluating the diffusion process is far away from the source and therefore always near the noise level. This noise level is caused to a large extent by scattered events, which also produce blurring with similar characteristics like tracer diffusion. In order to identify these scatter characteristics, and – if possible – to filter or correct scattered events, we conducted Monte Carlo simulations with OpenGATE (see Fig. 7). The scatter fraction was determined with these simulations to be as high as 75%. Simulation results in comparison with measured images are shown in Fig. 51. It is obvious that the deceptive cloud of apparent activity around the source, as well as star-shaped and circular artifacts, are produced by scattered events, which are projected by the STIR OSMAPSL algorithm into low-sensitivity zones near the source of scatter. It is possible, and currently under progress, to develop a scatter correction algorithm that is based on OpenGATE simulations of the experimental conditions.

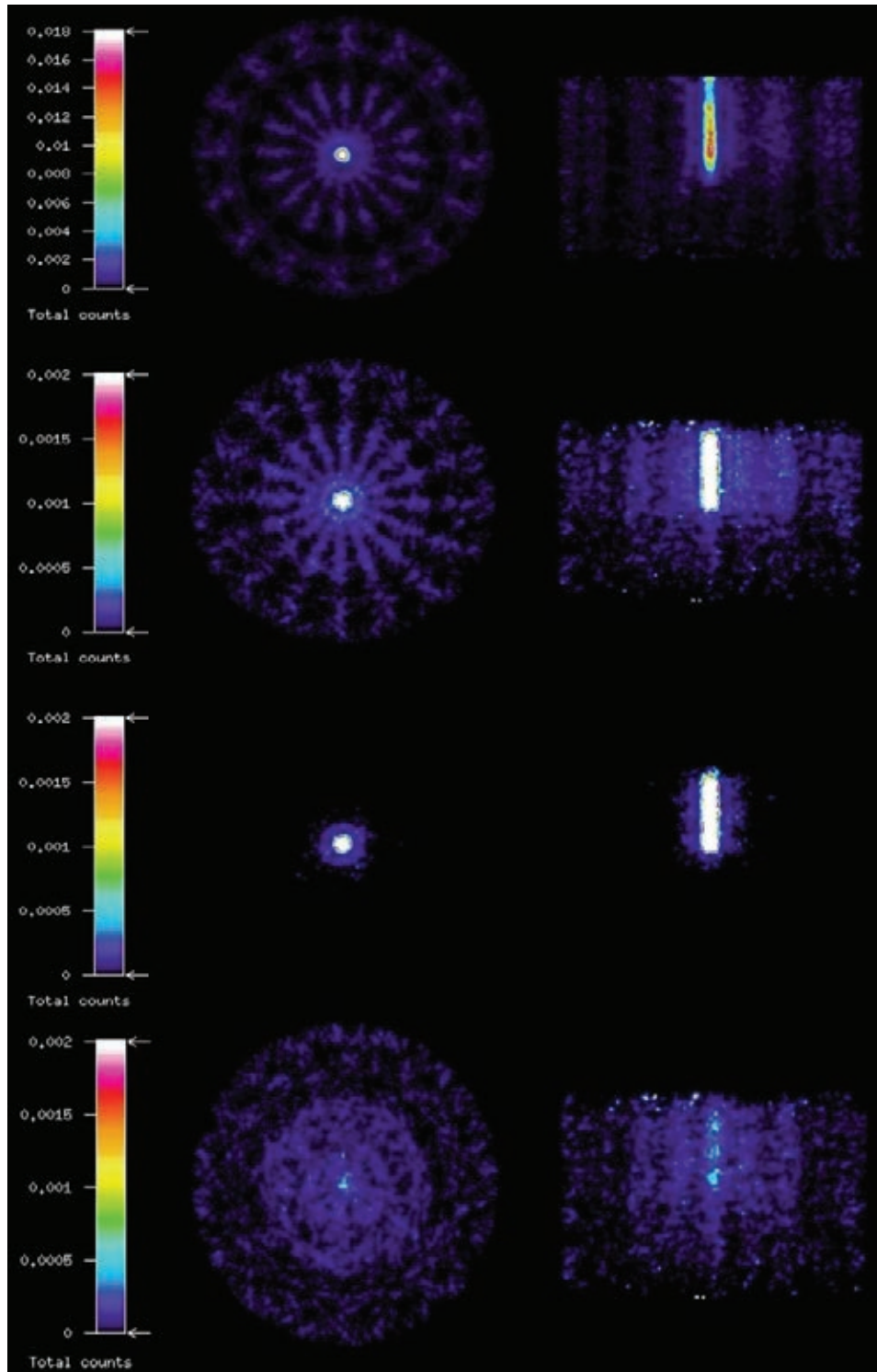


Figure 51. Reconstructions of measured and simulated results for the initial conditions (line source in Opalinus clay) of the experiment with BLT13/7 (see Fig. 48). Left: transaxial (x-y) views, right: vertical (x-z) cross sections. Images in the topmost row represent the measured image. Images in the second row are based on all coincidences (true and scattered) from the respective simulation. The images in the third row represent the reconstruction of the simulated true coincidences without scattered events. The bottom row of images represents the reconstruction based only on the simulated scattered coincidences.

Halite test samples. Two halite test samples (half-cylinders, diameter 10 cm, thickness 5 cm) from the Staßfurt region (Saxony-Anhalt, Germany) were furnished with radial blind holes (diameter 5 mm, depth 3 cm). One sample was charged with synthetic Q-solution, according to the formation fluid, the other one with 50% diluted Q-solution, according to the water in the hanging wall of the salt formation (Buntsandstein). The solutions have been “labelled” with ^{124}I . The holes were closed, and the samples were scanned for 19 days (Fig. 52). During this period, no changes could be observed in the images.

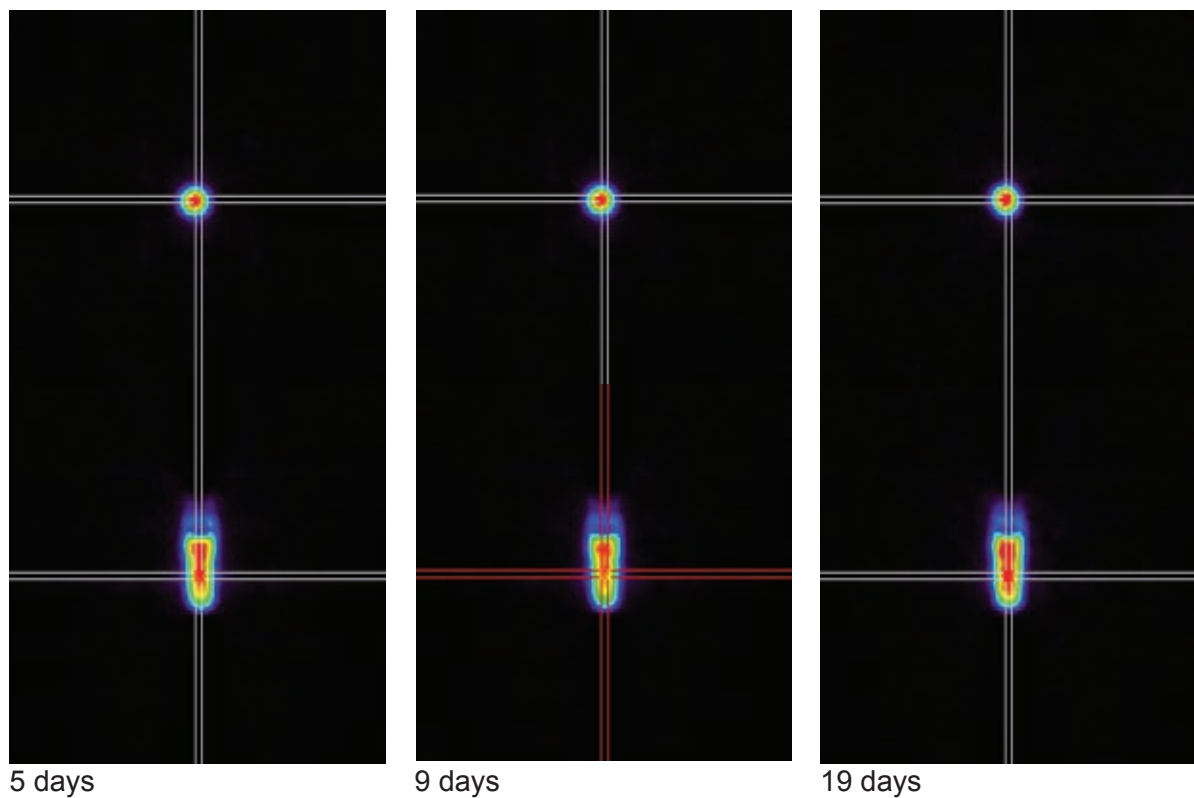


Figure 52. Diffusion test with ^{124}I NaI in Q-solution for a halite sample. No movement was to be observed during 19 days.

4. Conclusions and outlook

In terms of sorption properties, clay barriers are known to be superior to other possible host formations for a final repository. In the event of pH drops, however, release of contaminant metals is to be expected. Humic-bound transport would deteriorate the situation, but the investigations within this project have shown that metal adsorption onto clay materials is increased by the presence of humic matter throughout the acidic pH range. Surprisingly, similar results were also obtained for propionic acid and lactic acid as representatives of low-molecular-weight organic matter, which is most abundant in natural clay material. It appears that a mobilisation of metals in consequence of acidification is generally counteracted by organic complexants in clay systems.

Although the general trends of the effect of humic acid can be explained by the pH dependences of metal-humate complexation and humic acid adsorption, quantitative estimates by means of the linear additive model did not reproduce the experimental data. Most likely, this may be ascribed to selectivities in complexation and adsorption within the polydisperse system of humic molecules. Studies with fractionated humic material might be helpful to substantiate this reasoning. Identifying the criteria for the applicability of the linear additive model is of fundamental importance since this approach is implicit in most conceptual models that consider humic-bound transport. The assumption must be verified for every individual system under consideration.

As another prerequisite for transport modelling, adsorption of humic matter must be reversible because a dynamic process is assumed. In this respect, our studies led to different results. On the one hand, it was found that humic and fulvic acids cannot be desorbed from kaolinite on dilution. By tracer exchange experiments with ^{14}C -labelled materials, however, it could be demonstrated for the first time that a dynamic equilibrium exists, albeit the exchange process takes much more time than the adsorption process at the bare surface (more than one month compared to several hours for fulvic acid). Consequently, in order to assess whether a steady equilibrium can be maintained in flow systems, the kinetics of adsorption is certainly not a valid criterion.

Furthermore, kinetic effects must be considered that lead to an increasing inertness of metal-humic complexes. These stabilisation processes also affect competitive reactions. In complexation studies with purified humic substances, equilibration times must be long enough to cover these phenomena, which occur on different time scales. A fundamental understanding of the molecular processes involved is indispensable. This project significantly contributed to gaining more insight in this respect. The wide-spread notion that humic-bound metals undergo an in-diffusion process, moving from weak peripheral sites to strong internal sites, turned out to be inapplicable. A delayed degradation of polynuclear species in touch with humic colloids does not occur in general. An on-site stabilisation is most probable, even though spectroscopic evidence was only obtained for instantaneous structural rearrangements induced by bound metals. Subsequent changes on the time scale of the kinetic effect can only be minor. Nonetheless, in view of these ageing processes, the reversibility of metal-humate complexation needs to be examined in more detail. Tracer exchange studies, performed in a similar way as was done with the adsorption systems, appear to be a promising approach.

The ClearPET scanner is a relatively new instrument, utilised for geoscientific applications during the project period. Therefore, the results of the PET studies are provisional to some extent. Significant improvements of the images are expected from enhanced and new reconstruction codes. Error analysis will be possible with the establishment of MC simulations.

Nevertheless, the impact of rock structure on transport phenomena could be clearly shown. Up to now, all our studies on rock cores with real structure showed strong deviations from homogeneity. In contrast, the samples compacted from suspensions showed a widely homogeneous transport, which could be conveniently fitted with a one-dimensional CXTFIT model. However, the homogeneously compacted sample Nagra1 (sand-bentonite) shows considerable radial variations in the tracer concentration, probably due to the general difficulty of preparing homogeneous large-diameter specimen from moist clay powder. Even the sample OPA1 shows deviations from laterally homogeneous flow, but to a minor extent.

Therefore, our working hypothesis is that homogeneous transport is an idealised notion, which may be convenient for simplified models, but which is rarely realised. One of the aims of studies on heterogeneous transport is the transformation of parameters determined in batch experiments to the conditions of real, consolidated material. In most cases, effective parameters for volume and active surface area have to be anticipated, which reflect the heterogeneous response of the medium to the process, and which can be considerably smaller than the total quantities. Such effective parameters can be derived from usual break-through curves. However, only methods for spatially resolved process observation give insight into the causes of reduced efficiencies in the pore space.

We observed some untypical tracer spreading in Opalinus clay, together with a loss of fluid into the sample. This spreading is too fast to be caused by pure molecular diffusion [69, 70]. We had to suppose that the sample was only partially saturated with water, which caused suction into small pores. This was due to damage and alteration of the cores during recovery and storage. Similar effects have been reported in Refs. [71-73]. Such processes are, however, also relevant to real scenarios; they are likely to occur in excavation damaged zones as well, and therefore deserve further attention.

Such fast spreading did not occur in rock salt, although these samples contained visible fractures. In the recently finished project 02C1536, it could be shown that two different styles of propagation of conservative tracers occur in salt rocks. If the distribution in the medium is finely dispersed, we often observe disappearance of the tracer between inlet and outlet as the activity falls below the detection threshold, or we find an effuse, not necessarily homogeneous tracer cloud. However, in some cases, the tracer concentration over larger ranges may be derived as integral value. This propagation style presumably occurs in dense, fine-pored material. In fractured matrices, soils and macroporous material, we frequently observed strongly localised transport pathways. Here, we were able to align PET experiments with X- μ CT-based Lattice-Boltzmann simulations. We found accordance in the major structure, but additional transport pathways were visible in the PET image which could not be segmented in the X- μ CT image.

Strong localisation was also present in crystalline rocks that were investigated in the framework of this project. The fractured samples showed distinct flow paths on the fracture plane, not a diffuse cloud that filled the complete fracture volume. Thus, the effective transport volume is limited to these restricted pathways. Consequently, retarding interactions of contaminants will be limited to this reduced internal surface area. In spite of this zoning, humic acid as a potential carrier was strongly retarded in the granite core from Äspö.

In summary, all tracer propagation processes that we made visible by the PET method turned out to be more complex than anticipated. Simple models that describe the influence of the bulk material on the basis of 2 or 3 parameters (e.g., porosity, internal surface area) probably overestimate the retention, i.e., they underestimate the transport velocity. Instead, process-dependent parameters must be adopted.

5. References

- [1] Lieser, K.H., Ament, A., Hill, R., Singh, R.N., Stingl, U., Thybusch, B., *Radiochim. Acta* 49 (1990) 83-100.
- [2] Dearlove, J.P.L., Longworth, G., Ivanovich, M., Kim, J.I., Delakowitz, B., Zeh, P., *Radiochim. Acta* 52/53 (1991) 83-89.
- [3] Kim, J.I., Zeh, P., Delakowitz, B., *Radiochim. Acta* 58/59 (1992) 147-154.
- [4] Choppin, G.R., *Radiochim. Acta* 58/59 (1992) 113-120.
- [5] Liu, J., Lippold, H., Wang, J., Lippmann-Pipke, J., Chen, Y.H., *Chemosphere* 82 (2011) 866-871.
- [6] Liu, J., Wang, J., Chen, Y.H., Lippold, H., Lippmann-Pipke, J., *J. Environ. Sci.-China* 22 (2010) 1695-1702.
- [7] Zachara, J.M., Resch, C.T., Smith, S.C., *Geochim. Cosmochim. Acta* 58 (1994) 553-566.
- [8] Samadfam, M., Sato, S., Ohashi, H., *Radiochim. Acta* 82 (1998) 361-365.
- [9] Lippold, H., Lippmann-Pipke, J., *J. Contam. Hydrol.* 109 (2009) 40-48.
- [10] Cacheris, W.P., Choppin, G.R., *Radiochim. Acta* 42 (1987) 185-190.
- [11] Choppin, G.R., Clark, S.B., *Mar. Chem.* 36 (1991) 27-38.
- [12] Rao, L., Choppin, G.R., Clark, S.B., *Radiochim. Acta* 66/67 (1994) 141-147.
- [13] King, S.J., Warwick, P., Hall, A., Bryan, N.D., *Phys. Chem. Chem. Phys.* 3 (2001) 2080-2085.
- [14] Geckeis, H., Rabung, T., Ngo Manh, T., Kim, J.I., Beck, H.P., *Environ. Sci. Technol.* 36 (2002) 2946-2952.
- [15] Artinger, R., Kienzler, B., Schüßler, W., Kim, J.I., *J. Contam. Hydrol.* 35 (1998) 261-275.
- [16] Schüßler, W., Artinger, R., Kienzler, B., Kim, J.I., *Environ. Sci. Technol.* 34 (2000) 2608-2611.
- [17] Schüßler, W., Artinger, R., Kim, J.I., Bryan, N.D., Griffin, D., *J. Contam. Hydrol.* 47 (2001) 311-322.
- [18] Warwick, P.W., Hall, A., Pashley, V., Bryan, N.D., Griffin, D., *J. Contam. Hydrol.* 42 (2000) 19-34.
- [19] Bryan, N.D., Barlow, J., Warwick, P., Stephens, S., Higgs, J.J., Griffin, D., *J. Environ. Monit.* 7 (2005) 196-202.
- [20] Lippold, H., Eidner, S., Kumke, M.U., Lippmann-Pipke, J., *Appl. Geochem.* 27 (2012) 250-256.
- [21] Seibert, A., Mansel, A., Marquardt, C.M., Keller, H., Kratz, J.V., Trautmann, N., *Radiochim. Acta* 89 (2001) 505-510.
- [22] Wyllie, M.R.J., Rose, D., *Trans. AIME* 189 (1950) 105-118.
- [23] Lorenz, P.B., *Nature* 189 (1961) 386-387.
- [24] Shen, L., Chen, Z., *Chem. Eng. Sci.* 62 (2007) 3748-3755.
- [25] Richter, M., Gründig, M., Zieger, K., Seese, A., Sabri, O., *Radiochim. Acta* 93 (2005) 643-651.
- [26] Gründig, M., Richter, M., Seese, A., Sabri, O., *Appl. Geochem.* 22 (2007) 2334-2343.
- [27] Kulenkampff, J., Gründig, M., Richter, M., Enzmann, F., *Phys. Chem. Earth* 33 (2008) 937-942.
- [28] Aiken, G.R., in: Aiken, G.R., MacKnight, D.M., Wershaw, R.L., MacCarthy, P. (Eds.), "Humic substances in soil, sediment and water: geochemistry and isolation", Wiley-Interscience, New York 1985, pp. 363-385.
- [29] Stevenson, F.J., "Humus Chemistry. Genesis, Composition, Reactions", John Wiley and Sons, New York 1994.
- [30] Mansel, A., Kupsch, H., *Appl. Radiat. Isot.* 65 (2007) 793-797.
- [31] Fraker, P.J., Speck, J.C., *Biochem. Biophys. Res. Commun.* 80 (1978) 849-857.
- [32] Lund, T.J., Koretsky, C.M., Landry, C.J., Schaller, M.S., Das, S., *Geochem. Trans.* 9 (2008) 9.
- [33] Borden, D., Giese, R.F., *Clays Clay Min.* 49 (2001) 444-445.
- [34] Huertas, J.F., Chou, L., Wollast, R., *Geochim. Cosmochim. Acta* 62 (1998) 417-431.

- [35] Vejsada, J., Hradil, D., Řanda, Z., Jelínek, E., Štulík, K., *Appl. Clay Sci.* 30 (2005) 53-66.
- [36] Gonçalves, M.A., Figueiras, J., in: *Actas do VIII Congresso de Geoquímica dos Países de Língua Portuguesa, Aveiro (Portugal) 2005*, pp. 513-518.
- [37] Moronta, A., Ferrer, V., Quero, J., Arteaga, G., Choren, E., *Appl. Catal. A-Gen.* 230 (2002) 127-135.
- [38] Fan, M., Boonfueng, T., Xu, Y., Axe, L., Tyson, T.A., *J. Colloid Interface Sci.* 281 (2005) 39-48.
- [39] Summarising Report "Wechselwirkung und Transport von Actiniden im natürlichen Tongestein unter Berücksichtigung von Huminstoffen und Tonorganika", BMWi, 2012, in preparation.
- [40] Hiraide, M., Tillekeratne, S.P., Otsuka, K., Mizuike, A., *Anal. Chim. Acta* 172 (1985) 215-221.
- [41] Schubert, J., *J. Phys. Colloid. Chem.* 52 (1948) 340-350.
- [42] Levin, C.S., Hoffmann, E.J., *Phys. Med. Biol.* 44 (1999) 781-799.
- [43] Zaidi, H., Hasegawa, B., *J. Nuc. Med.* 44 (2003) 291-315.
- [44] Zakhnini, A., Kulenkampff, J., Sauerzapf, S., Pietrzyk, U., Lippmann-Pipke, J., *Comput. Geosci.* (2012), in preparation.
- [45] Auffray, E., Bruyndonckx, P., Devroede, O., Fedorov, A., Heinrichs, U., Korjik, M., Krieguer, M., Kuntner, C., Lartizien, C., Lecoq, P., Leonard, S., Morel, C., Mosset, J.B., Pedrini, C., Petrosyan, A.G., Pietrzyk, U., Rey, M., Saladino, S., Sappey-Marinié, D., Simon, L., Streun, M., Tavernier, S., Vieira, J.M., Ziemons, K., *Nucl. Inst. Meth. A* 527 (2004) 171-174.
- [46] Ziemons, K., Auffray, E., Barbier, R., Brandenburg, G., Bruyndonckx, P., Choi, Y., Christ, D., Costes, N., Declais, Y., Devroede, O., Dujardin, C., Fedorov, A., Heinrichs, U., Korjik, M., Krieguer, M., Kuntner, C., Largeton, G., Lartizien, C., Larue, H., Lecoq, P., Leonard, S., Marteau, J., Morel, C., Mosset, J.B., Parl, C., Pedrini, C., Petrosyan, A.G., Pietrzyk, U., Rey, M., Saladino, S., Sappey-Marinié, D., Simon, L., Streun, M., Tavernier, S., Vieira, J.M., *Nucl. Inst. Meth. A* 537 (2005) 307-311.
- [47] Sempere Roldan, P., Chereul, E., Dietzel, O., Magnier, L., Pautrot, C., Rbah, L., Sappey-Marinié, D., Wagner, A., Zimmer, L., Janier, M., Tarazona, V., Dietzel, G., *Nucl. Inst. Meth. A* 571 (2007) 498-501.
- [48] Thielemans, K., Mustafovic, S., Tsoumpas, C., IEEE Nuclear Science Symposium Conference Record, 2007, pp. 2174-2176.
- [49] Thielemans, K., <http://stir.sourceforge.net>.
- [50] Baddeley, A., Turner, R., *J. Stat. Softw.* 12 (2005) 1-42.
- [51] Berger, M.J., Hubbell, J.H., Seltzer, S.M., Chang, J., Coursey, J.S., Sukumar, R., Zucker, D.S., Olsen, K., <http://physics.nist.gov/xcom>.
- [52] Jan, S., Santin, G., Strul, D., Staelens, S., Assie, K., Autret, D., Avner, S., Barbier, R., Bardies, M., Bloomfield, P.M., Brasse, D., Breton, V., Bruyndonckx, P., Buvat, I., Chatziioannou, A.F., Choi, Y., Chung, Y.H., Comtat, C., Donnarieix, D., Ferrer, L., Glick, S.J., Groiselle, C.J., Guez, D., Honore, P.F., Kerhoas-Cavata, S., Kirov, A.S., Kohli, V., Koole, M., Krieguer, M., van der Laan, D.J., Lamare, F., Largeton, G., Lartizien, C., Lazaro, D., Maas, M.C., Maigne, L., Mayet, F., Melot, F., Merheb, C., Pennacchio, E., Perez, J., Pietrzyk, U., Rannou, F.R., Rey, M., Schaart, D.R., Schmidlein, C.R., Simon, L., Song, T.Y., Vieira, J.M., Visvikis, D., Van de Walle, R., Wieers, E., Morel, C., *Phys. Med. Biol.* 49 (2004) 4543-4561.
- [53] Weber, S., Morel, C., Simon, L., Krieguer, M., Rey, M., Gundlich, B., Khodaverdi, M., *Nucl. Inst. Meth. A* 569 (2006) 381-385.
- [54] <http://www.r-project.org>.
- [55] Toride, N., Leij, F.J., van Genuchten, M.T., Research Report 137, US Salinity Laboratory, USDA, ARS, 1999.
- [56] Paulenová, A., Rajec, P., Kandrác, J., Sasköiová, G., Tothová, E., Bartoš, P., Švec, V., Góra, R., *J. Radioanal. Nucl. Ch.* 246 (2000) 617-622.
- [57] Zhou, Q., Maurice, P.A., Cabaniss, S.E., *Geochim. Cosmochim. Acta* 65 (2001) 803-812.

- [58] Hur, J., Schlautman, M.A., *J. Colloid Interface Sci.* 264 (2003) 313-321.
- [59] Reiller, P., Amekraz, B., Moulin, C., *Environ. Sci. Technol.* 40 (2006) 2235-2241.
- [60] Lakshman, S., Mills, R., Patterson, H., Cronan, C., *Anal. Chim. Acta* 282 (1993) 101-108.
- [61] Tanaka, T., Nagao, S., Sakamoto, Y., Ohnuki, T., Ni, S., Senoo, M., *J. Nucl. Sci. Technol.* 34 (1997) 829-834.
- [62] Christl, I., Kretzschmar, R., *Geochim. Cosmochim. Acta* 65 (2001) 3435-3442.
- [63] Courdouan, A., Christl, I., Rabung, T., Wersin, P., Kretzschmar, R., *Environ. Sci. Technol.* 42 (2008) 5985-5991.
- [64] Lippold, H., Evans, N.D.M., Warwick, P., Kupsch, H., *Chemosphere* 67 (2007) 1050-1056.
- [65] Marquardt, C.M. (Ed.), "Migration of actinides in the system clay, humic substances, aquifer", *Wiss. Berichte FZKA 7407*, Karlsruhe 2008.
- [66] Akitt, J.W., Greenwood, N.N., Khandelwal, B.L., Lester, G.D., *J. Chem. Soc., Dalton Trans.* (1972) 604-610.
- [67] Hoehn, E., Eikenberg, J., Fierz, T., Drost, W., Reichlmayr, E., *J. Contam. Hydrol.* 34 (1998) 85-106.
- [68] Schikora, J., Diploma Thesis, Dresden Technical University, 2012, in preparation.
- [69] Van Loon, L.R., Baeyens, B., Bradbury, M.H., *Appl. Geochem.* 20 (2005) 2351-2363.
- [70] Garcia-Gutierrez, M., Cormenzana, J.L., Missana, T., Mingarro, M., Martin, P.L., *Phys. Chem. Earth* 31 (2006) 523-530.
- [71] Arson, C., Gatmiri, B., *Phys. Chem. Earth* 33 (2008) S407-S415.
- [72] Savoye, S., Page, J., Puente, C., Imbert, C., Coelho, D., *Environ. Sci. Technol.* 44 (2010) 3698-3704.
- [73] Jougnot, D., Revil, A., Lu, N., Wayllace, A., *Water Resour. Res.* 46 W08514 (2010) 1-17.

**Quantum Mechanical Modeling of Actinide Complexes:
Complexation by Humic Substances
and Sorption on Clay Minerals**

**Abschlussbericht für das Teilprojekt
„Quantenmechanische Modellierung von Aktinoidenkomplexen: Komplexierung
durch Huminstoffe und Sorption an Tonmineralen“**

**im Rahmen des Verbundprojektes
„Wechselwirkung und Transport von Actiniden im natürlichen Tongestein unter
Berücksichtigung von Huminstoffen und Tonorganika“**

Förderkennzeichen 02E10186

Projektlaufzeit Juli 2006 bis Juni 2011

**Notker Rösch, Sven Krüger, Alena Kremleva
Department Chemie, Technische Universität München
85747 Garching**

Contents

1 Introduction	3
2 Tasks of the Project and Prerequisites	5
3 Development of the State of the Art.....	9
4 Results	11
4.1 Actinide complexation in aqueous solution	11
4.1.1 Hydrolysis and ternary complexes	11
Uranyl monohydroxide.....	11
Uranyl hydroxo acetate.....	14
Diacetate complexes	16
4.1.2 Complexation by non-carboxylic groups	18
Complexation by sulfur containing groups	18
Complexation by nitrogen containing groups	21
4.1.3 Carboxylate complexation: Effect of temperature and mechanism	23
Temperature dependency of uranyl acetate complexation	23
Neptunyl acetate complexation	26
4.1.4 An(IV) complexes	28
4.1.5 Am(III) complexes	31
Am(III) aqua ion.....	31
Am(III) acetate	31
4.2 Adsorption of actinides on clay minerals	32
4.2.1 Clay mineral surfaces and surface models	32
4.2.2 Adsorption on kaolinite	35
Adsorption of uranyl(VI) on basal surfaces	35
Adsorption of complexes on the basal Al(o) (001) surface of kaolinite	39
Adsorption of neptunyl(V) on basal surfaces.....	41
Adsorption of uranyl(VI) on edge surfaces	43
4.2.3 Adsorption on 2:1 clay minerals.....	45
Structure of 2:1 clay minerals: pyrophyllite and beidellite	45
Adsorption of uranyl(VI) on basal surfaces of beidellite	47
Adsorption of uranyl(VI) on edge surfaces of pyrophyllite	49
Adsorption of uranyl(VI) on edge surfaces of beidellite.....	52
4.3 Methodic topics	54
5 Summary	55
6 Publications Resulting from this Project.....	57
7 References	58

Das diesem Bericht zugrundeliegende Vorhaben wurde mit Mitteln des Bundesministeriums für Wirtschaft und Technologie unter dem Förderkennzeichen 02E10186 gefördert. Die Verantwortung für den Inhalt der Veröffentlichung liegt bei den Autoren.

1 Introduction

Migration of actinides is a central topic in the safety analysis of long-term storage of highly radioactive waste. The modeling for predicting the speciation, chemical interactions, and the distribution of actinides in the environment is an important instrument of nuclear waste management as well as of remediation of contaminated sites of uranium mining and former nuclear weapon production. Various chemical and physical processes involving actinides have to be known in some detail as basis of such modeling.

Distribution and transport of actinide elements in the environment are determined by solubility, the versatile aqueous complexation chemistry [1-3], colloid formation and a large variety of solid phases [4,5]. In addition to the chemistry proper of the actinides, under natural conditions one has to take into account also the interaction of aqueous species with other colloids, soils, minerals, and natural organic matter [6,7]. Sorption and colloid formation strongly affect the chemical state as well as the transport behavior of actinide ions. The aquatic chemistry of the more common oxidation states of the early actinides is now fairly well understood [1,3,8]. Much less is known regarding colloid formation, sorption at mineral surfaces, especially for clay minerals, and the interaction with natural organic matter. The latter two topics have been the focus of research of the consortium “Wechselwirkung und Transport von Actiniden im natürlichen Tongestein unter Berücksichtigung von Huminstoffen und Tonorganika”. Quantum chemical modeling of actinide chemistry as the central topic of this project has been applied for the first time to the adsorption of actinide ions on clay minerals. Studies of the complexation of actinide ions with organic molecules, which also serve as model functional groups of humic substances, have been extended. These main topics were complemented by the characterization of less well studied actinide species and oxidation states. As a unifying concept, this project complements the experimental studies of the consortium regarding the common goal of improving our knowledge of actinide chemistry at the atomic level, to reach a mechanistic understanding of the essential processes of actinide environmental chemistry.

Two forms of natural organic matter are of concern in this project. On the one hand, humic substances [9], ubiquitous in the geosphere, originate essentially from the degradation of biological materials and are the major organic component of soils, but they also are present in surface and ground waters [9]. The soluble fraction of humic substances, fulvic and humic acids, are composed of very variable organic molecules of varying size and content of functional groups, depending on their origin [9]. They complexate metal ions and are redox active and in this way affect the speciation and the distribution of metals ions in the environment [6,7,9]. Carboxyl groups are considered to be most important for metal, hence also actinide complexation [10-15]. In the previous project it was shown in experimental and computational studies that also alcoholic and phenolic groups contribute to the complexation [16-18]. The possible role of other functional groups is largely unknown.

Experimental efforts to identify and characterize actinide humate complexes mainly rely on extended X-ray absorption fine structure spectroscopy (EXAFS) [19,20] for the determination of average structural parameters. Fourier transform infrared spectroscopy (FT-IR) [21] yields vibrational properties, and time resolved laser fluorescence (TRLFS) studies [22,23] are able to characterize the complexation behavior. Computational studies are useful as they provide information complementary to spectroscopic results [24-26]. For this purpose small organic molecules are used as models of pertinent functional groups of humic substances. This approach has also been chosen in various experimental studies [27-29], allowing a direct comparison of results. The study of actinide complexation by small organic acids is also relevant to the examination of the role of the second form of natural organic matter examined in this project, clay organic matter. To a considerable fraction, the organic content of clays is composed of small carboxylic acids, larger acidic organic molecules similar to fulvic acids, and kerogen [30,31]. Complexation of actinides with these species as well as the interaction of this organic content with clay minerals modifies the adsorption chemistry of actinides [32-36].

Actinide adsorption on minerals has widely been studied experimentally, applying batch and column experiments as well as spectroscopic methods [37-39]. Macroscopic experiments show that the adsorption depends on the charge of the actinide ion, yielding adsorption at lower pH for higher charged species. Adsorption is further affected by the presence of organic matter or other metal ions [32-36,40]. Spectroscopic methods like EXAFS, TRLFS, and vibrational spectroscopy allow a microscopic view on adsorbed actinide species. Inner- and outer-sphere complexes as well as mono- and polynuclear adsorbates have been identified; all these complexes may even coexist [41,42]. Preferred mineral surface orientations and their structures in contact with aqueous solution are known only in a few cases. Therefore, a microscopic picture of actinide adsorption at mineral surfaces is currently a topic of intense research as such knowledge is a prerequisite for a thorough thermodynamic modeling. In this project we contributed the first systematic studies of actinide adsorption on clay minerals by density functional calculations of periodic slab models [43].

In experimental investigations on the aqueous chemistry and the sorption of actinides one typically has to treat complex natural systems with a set of species present. Hence, special efforts, e.g., variation of pH, concentrations, ionic strength etc. or chemical manipulations, are required to characterize individual species in these complex systems. Quantum chemical studies provide a complementary view on well defined isolated model species and thus useful references, especially for spectroscopic studies. As exemplified in this report, valuable accurate information on structural and vibrational properties can be obtained in this way, complementing the interpretation of experiments. The calculation of

thermodynamic properties of species in solution and at surfaces presents a more challenging task, but also here important qualitative results have been obtained.

2 Tasks of the Project and Prerequisites

This project was devoted to various topics of actinide environmental chemistry as relevant to safety issues of deep geological storage of radioactive waste. A central theme was the interaction of actinide ions with solvated surfaces of clay minerals, a topic pioneered by the work of this project. In addition, complexation of actinide ions with organic and inorganic ligands in aqueous solution was studied. Here organic ligands represent species of low molecular weight, that are present as natural organic matter in clay formations, and they serve as models of functional groups of humic substances. This project also contributed to the understanding of the hydrolysis of common actinide ions and included some evaluation and development of computational methods related to modeling of solvation.

Surfaces of clay minerals have been modeled as periodic slabs, separated by an appropriate amount of space, more than 1 nm wide, to avoid artificial interactions of neighboring slab instances. In this way, three-dimensional periodicity of the model is achieved, allowing application of established methods for calculating the electronic structure of solids. The electronic structure is calculated at the density functional theory (DFT) level. In this project the projector-augmented-wave (PAW) method as implemented in the program VASP (Vienna ab initio simulation package) [44-49] was used throughout. In this method one-electron wave functions are represented by plane waves augmented by local atomic contributions (at the relativistic level if required) [50]; this approach allows an accurate treatment of heavy elements like actinides. Exchange-correlation potentials of the local density approximation (LDA) and the generalized-gradient approximation (GGA) type [51] have been applied. While LDA in general yields accurate geometries, it overestimates binding energies, especially for weak interactions like hydrogen bonds [51,52]. GGA tends to overestimate bond lengths of heavy-element compounds, but provides considerably improved binding energies [51,52]. Thus, some geometry optimizations were carried out with the LDA functional (as suggested by Perdew and Zunger [53]), while energies and optimizations involving relatively weakly bound water molecules were determined at the GGA level, using the functional suggested by Perdew and Wang (PW91) [54]. Solvation effects on mineral surfaces and adsorption complexes were described by adding the first solvation shell to adsorbates and, in the same spirit, about a water monolayer to the surface. Although this approach of modeling of adsorption systems is well established in other fields, it was applied for the first time by us for the adsorption of actinide species on mineral surfaces [55].

The second major topic of the project was the characterization of complexes of actinides in aqueous solution. Complexation of actinyl ions by various organic ligands was examined as continuation and extension of the central topic of the previous project, the

modeling of actinyl complexation by humic substances and other natural organic matter. New aspects were the complexation by several functional groups, by N- and S-containing groups, as well as the study of ternary complexes as models of species at about neutral pH conditions. In the later phase of the project, this theme was extended to the mechanism and the temperature dependence of complexation by carboxylic groups. Small organic compounds were used as models of functional groups of humic substances. This approach to the complicated chemistry of humic substances had been applied already in earlier experimental [27-29] and computational [56-58] studies. Besides uranyl(VI) as the prototypical actinyl ion, also An(IV) and Am(III) species were examined as examples of less studied actinide species. As most of the other topics mentioned, the latter task was also inspired by the work of partners in the research consortium.

Electronic structure calculations on actinide complexes in solution were also carried out by means of DFT methods. The accurate relativistic density functional Douglas-Kroll-Hess method [59,60] was employed in its scalar-relativistic form, as implemented in the parallel high-performance software PARAGAUSS [61] which is developed by our group. For geometry optimizations mainly the VWN LDA functional [62] was used, while energies were calculated with the GGA functional according to Becke and Perdew (BP) [63,64], fully selfconsistently or in single point fashion employing LDA geometries. Short-range chemical interactions with the aqueous solvent were modeled by explicitly treating aqua ligands [56,57]. In addition, a polarizable continuum model (PCM) [65] was used to account for long-range (electrostatic) solvation effects.

The work of the present project was divided into three parts:

A Complexes in aqueous solution

- **Ternary carboxylate complexes**

At environmental pH conditions, hydrolysis and carbonate complexation of actinide ions determine the speciation. Thus, the corresponding complexes and not only the aqua ions of actinides have to be regarded as the educts of complexation reactions with other ligands and also ternary complexes including aqua, hydroxide or carbonate ligands may be formed. In this task, hydroxo and carbonato complexes of actinyl ions were modeled as reference. Ternary complexes with carboxylates as common functional groups of humic substances were also examined.

- **Dicarboxylates**

Dicarboxylate complexes of actinyl ions are well known from experiment, but had not yet been studied computationally. Compared to monocarboxylates these complexes are more complicated with regard to possible combinations of coordination numbers and ligand binding modes. As models for the actinide complexation by humic substances, these complexes can be regarded either as an actinide ion coordinated by (two) small

humic substance molecules or as adducts of a large flexible humic substance species where two carboxylate groups are involved in the binding. Thus, this task was also intended to contribute to resolving open issues of actinide complexation by humates.

- **Alternative functional groups of humic substances**

In the preceding project our computational studies, together with experiments of the project partner Helmholtz-Zentrum Dresden-Rossendorf, had shown that phenolic or even aliphatic OH groups of humic substances contribute to complexation [57]. This work was to be extended by combined experimental and computational studies on nitrogen- and sulfur-containing groups for the exemplary case of uranyl(VI). The goal was to help understand modifications in the complexation behavior of humic substances of varying chemical composition.

- **Temperature dependence and reaction mechanism of carboxylate complexation**

The complexation of actinyl ions by simple organic ligands, e.g., acetate, had already been explored in the preceding project. This task was to be extended to more involved topics, such as the mechanism of complexation in aqueous solution and the temperature dependence of corresponding thermodynamic parameters.

- **An(IV) complexes**

Due to their large formal charge, An(IV) ions represent a challenge for quantum chemical modeling of the corresponding complexes in an aqueous solution. In this task a combined modeling and method development effort was to be undertaken to make An(IV) species accessible to accurate computational treatment. Starting with aqua ions, hydrolysis complexes were treated, ultimately aiming at more complex species. Also experimentally, the oxidation state (IV) of U and Np is less well characterized compared to the more common oxidation states and the results of this task were intended to help augmenting such knowledge.

- **Complexation of Am(III)**

Experimental as well as computational studies on americium are rare. In this task, the Am(III) aqua ion as well as Am(III) complexes with organic ligands were to be explored in collaboration with the project partner TU Dresden, to contribute to the understanding of the aqueous chemistry of this most stable oxidation state of Am.

B Surfaces of clay minerals and adsorbed complexes

- **Clay mineral surfaces**

As a prerequisite of adsorption studies, basal and edge surfaces of clay minerals were characterized with respect to their termination, functional groups, and interaction with aqueous solution. Kaolinite, pyrophyllite, and substituted pyrophyllite as a model of clay minerals with charged layers were examined.

- **Adsorption of actinyl on kaolinite**

Adsorption of actinyl ions on kaolinite were studied as an exemplary system of actinide adsorption on the surfaces of clay minerals, complementing parallel experimental work of the project partners. Inner- and outer-sphere adsorption complexes were compared; various adsorption sites of different protonation state were studied for inner-sphere adsorption. Geometric and energetic results were compared to experimental findings for kaolinite and other clay and related minerals.

- **Adsorption of actinyl complexes**

Near neutral pH conditions, not only solvated actinyl ions but also various hydroxide or carbonate complexes may interact with clay mineral surfaces, hence were to be characterized as adsorbates, for the exemplary case of uranyl. The results of this task are useful for differentiating various surface species in experiment.

- **Adsorption of actinyl at 2:1 clay minerals**

As examples of the common 2:1 clay minerals, neutral pyrophyllite and a substituted model mineral with charged layers, similar to beidellite, were studied as substrates for actinyl adsorption. Here the focus was on the edge surfaces as the basal siloxane terminated surfaces are less reactive. Results were compared to those for kaolinite to provide first insight into the variability of actinide adsorption on various clay mineral surfaces.

C Method development

PCM as well as QM/MM and dynamical approaches to model solvation were explored in this task to evaluate their potential for the project.

A technical prerequisite for the large number of demanding calculations carried out in this project was the application of efficient high-performance software for computers with parallel architecture. Complexes in solution were described with the parallel density functional package PARAGAUSS [61], developed in our group and available on a local Linux cluster as well as at the high-performance facilities of Leibniz-Rechenzentrum München. Periodic slab model calculations as models of mineral surfaces have been treated using the PAW approach as implemented in the parallel density functional software VASP which also was used on local as well as central high-performance facilities. The Linux cluster of the group, used for carrying out the work of the project, currently comprises about 160 cores. This local resource was essential for the timely delivery and the overall success of the project. Six dedicated two-processor two-core nodes as well as a stronger four-processor two-core node had been granted which had been put into operation shortly after the start of the project.

3 Development of the State of the Art

Quantum chemical modeling of the chemistry of actinides under environmental conditions is a rather difficult task as several challenges have to be met [25,26,43,66]. The electronic structure of the actinides requires a relativistic treatment including accurate consideration of electron correlation as these elements are very heavy and the three valence shells 5f, 6d, and 7s are involved in bonding. For environmental actinide chemistry modeling the interaction with water as ubiquitous solvent and the surfaces of minerals in contact with an aqueous phase represent yet another challenge.

The electronic structure of solvated complexes is commonly described with a density functional approach, using either gradient-corrected or hybrid exchange-correlation functionals [66]. Wave function based correlated methods of similar quality like Møller-Plesset perturbation theory [25,67] are also used whereas accurate approaches, e.g., complete active space or coupled cluster methods, are rarely applied and only to smaller complexes in view of their computational demand [68]. Relativistic effects are most easily accounted for by replacing core electrons with an effective core potential [69-71] which allows a nonrelativistic treatment of the valence electronic structure. Direct relativistic all-electron methods, like the Douglas-Kroll-Hess approach [59,60] used in this work or the ZORA (zeroth-order regular approximation) approach [72-74], are computationally more demanding, hence less frequently applied to actinide species in solution. Scalar relativistic as well as spin-orbit interaction including variants of these methods are available [60]. Spin-orbit interaction is especially important for the calculation of electronic spectra [74,75] and accurate thermodynamic properties [76] as well as for oxidation and reduction reactions [66]. On the other hand, it had been demonstrated that spin-orbit effects on geometries and reaction energies of species with only a few f electrons are small [77-79].

Two approaches are available to treat solvation effects on actinide complexes in solution, embedding of the complex in a polarizable continuum model (PCM) [80,81] of bulk water or an explicit molecular treatment of the aqueous solvation environment. The latter method requires a dynamical approach in combination with periodic boundary conditions [82]. When applying the PCM method explicit inclusion of the first solvation shell into the quantum mechanically treated part of the system is mandatory and has been established as standard procedure [25,73,83]. Especially for charged complexes also the chemical interaction with the second solvation shell may be important [84-86], e.g. due to charge transfer, not covered in the PCM approach. Parameters of PCM models have to be chosen carefully to achieve reliable results [84,86,87]. An explicit dynamical treatment of solvation of actinide complexes with a Car-Parinello molecular dynamics approach [88] was presented for some uranyl(VI) complexes and their reactions [82,89] as well as for the solvated Cm(III) ion [90]. As these calculations are quite demanding, they are typically restricted to periodic boxes that include 50–100 water molecules, representing 0.5–1 M

solutions. Thus, in dynamical simulations of more complex and larger systems, empirical force fields are typically applied instead of quantum mechanics [82,91]. An appealing but methodologically intricate intermediate approach is represented by a coupled quantum mechanical and molecular mechanical (QM/MM) model [90,92] where a complex and its immediate solvation environment are treated quantum mechanically, embedded in a larger amount of water molecules that are treated at the force field level. The challenge of this approach, which has already been applied to various types of chemical systems [93-95], is a consistent coupling between the QM and MM parts, especially for water as a solvent. Moreover, due to the dynamics of the aqueous solution a clear separation of the QM and MM parts is not given [96] and has to be introduced as an approximation. Also, the choice of the size of both regions matters. For $[\text{UO}_2\text{F}_4(\text{H}_2\text{O})_n]^{2-}$ it was shown that the experimentally determined five-fold coordination of uranyl could be reproduced only with an explicit QM model of the first solvation shell of 11 aqua molecules [97].

Thus far most computational studies on actinide complexes in solution still address uranium [25,26,66] which is the most commonly studied actinide. In the last years also other actinides have been treated (see Section 4.1.4-6). The computational approaches mentioned above are also applicable to various oxidation states of the early actinides up to Cm. Some noteworthy examples are mentioned in the following. The hydrolysis of Pa(V) has been studied with a dynamical density functional approach showing a variety of oxo and hydroxo complexes to be stable in aqueous solution [98]. In a study of Th(IV) hydrolysis, dimeric complexes have been shown to be stable, in agreement with experimental evidence [99]. Structure calculations on Np(VII) hydroxo and carbonato complexes supported the experimental identification of the Np(VII) tetraoxo dihydroxo species in basic solutions in the presence of carbonate [100]. Pu(IV) and Pu(VI) nitrate and chloro complexes were characterized with GGA density functional calculations [101], achieving good agreement with experiment. The expected similarity of oxidation state (VI) complexes to Np and U congeners was confirmed computationally [101]. The Cm(III) aqua ion was modeled dynamically with quantum mechanical and QM/MM approaches [90]. The coordination number of Cm was determined as 8 with the expected square anti-prismatic structure of the first solvation shell. The calculated structure agreed with results of EXAFS experiments [90].

Quantum chemical modeling of actinide adsorption at mineral surfaces is an emerging field that developed essentially during the time of this project [43,102]. The first studies of this type were published in 2006 [103,104], one by our group. In most studies, periodic slab models combined with a plane-wave approach were used to represent the mineral surfaces [105-108], but also (finite) cluster models were applied [110-113]. These latter models have the advantage to admit a straightforward treatment of charged systems, facilitating the calculation of adsorption energies, at the price of unphysical boundary conditions. In almost

all studies density functional theory was chosen for calculating electronic structures, with the exception of a cluster study on Cm adsorption on corundum where also the MP2 approach was applied to account for correlation [112]. As for complexes in solution, the most frequently studied actinide adsorbate is uranyl(VI). Adsorption of uranyl on corundum [103,113], gibbsite [108,111], kaolinite [43,105-107], titanium dioxide [104], goethite [110], and hematite [114] has been examined so far. In agreement with experimental hints at neutral and higher pH, preferentially bidentate inner-sphere uranyl complexes were modeled. On the other hand, adsorption of hydrolysis species and surface precipitation as well as adsorption of uranyl complexes with various ligands can occur. Here only three studies are available which treated uranyl hydroxide [107,113] and uranyl dimer complexes [111] as adsorbates. The only other actinides for which adsorption on mineral surfaces has been studied quantum mechanically are Np(V) [115] and Cm(III) [112].

An important aspect when modeling actinide adsorption on mineral surfaces is the treatment of solvation. In early studies only the first solvation shell of the actinide ion was taken into account. As the structure and properties of mineral surfaces are modified due to solvation [107,116,117], an explicit (molecular) description of the solvent is necessary. Thus, as a simple solvation model, some studies added a few water molecules to the model [108,109], up to about a monolayer [106,107,110,112] above the mineral surfaces. This approach excludes long-range solvation effects. As a large number of explicit water molecules leads to a potential energy surface of the model system with many close lying minima, a dynamic treatment is necessary when this more realistic solvation treatment is carried out in periodic slab surface models. This computationally rather costly approach has already been chosen for the examination of solvated mineral surfaces [116,118], but has not yet been applied to actinide adsorption on them. The authors plan such studies in the subsequent project.

4 Results

In this section we review the main results of the project; we will follow the project plan. First we present computational results for various actinide complexes in aqueous solution. Then we describe studies on the surfaces of clay minerals and actinyl adsorption thereon. A section on pertinent method development completes this report. Where publications are already available, the presentation will be more concise. Publications resulting from this project are included among the references and also listed in Section 6.

4.1 Actinide complexation in aqueous solution

4.1.1 Hydrolysis and ternary complexes

Uranyl monohydroxide

Uranyl monohydroxide has been studied as this hydrolysis species of U(VI) is one of the less characterized hydrolysis species of uranyl [119]; it is of importance as a reference

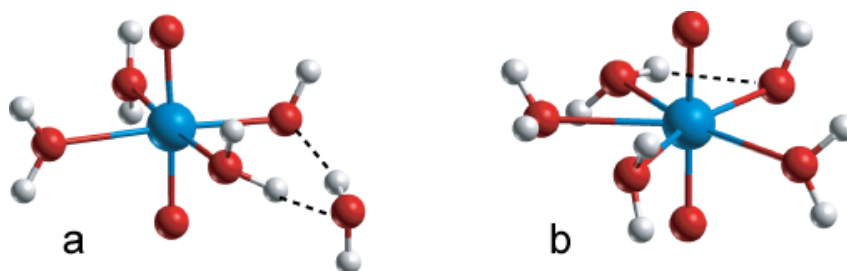


Figure 1. Structure of solvated uranyl monohydroxide $[\text{UO}_2\text{OH}(\text{H}_2\text{O})_4]^+$. (a) Isomer 1, coordination number four. (b) Isomer 2, coordination number five

species for ternary uranyl hydroxo complexes in solution and at mineral surfaces (see below). Uranyl monohydroxide is the simplest hydrolysis product of uranyl(VI) in aqueous solution. Few data are available for $[\text{UO}_2\text{OH}]^+$ although uranyl hydrolysis has been extensively studied [120]. Experimentally this species is not easily accessible as it appears as a major species only at low uranium concentrations and in a narrow pH interval above pH 3 [121]. At larger uranium concentrations and higher pH values, mononuclear complexes with more than a single hydroxide ligand or polynuclear hydrolysis species dominate [122-124]. Earlier computational studies characterized $[\text{UO}_2\text{OH}]^+$ as a five coordinate species in aqueous solution [125-130]. Most computational studies produced a bent geometry for the OH ligand (relative to the U-O direction). Computational results in the literature for the Gibbs free energy of hydrolysis ranged from -1.3 kJ mol^{-1} [130] to 55 kJ mol^{-1} [125].

In our model calculations, $[\text{UO}_2\text{OH}]^+$ species were generated by deprotonation of $[\text{UO}_2(\text{H}_2\text{O})_5]^{2+}$ at various positions, assuming the typical five-coordination of uranyl. Subsequent geometry optimization for complexes in solution then lead to 7 structural isomers of the model complex $[\text{UO}_2\text{OH}(\text{H}_2\text{O})_4]^+$. These isomers differ in the structure of the hydrogen bonds between aqua and hydroxide ligands. For the isomer labeled as 1, an aqua ligand moved to a position in the second solvation shell. Thus, this isomer corresponds to a four-coordinate species. The relative stability of all these isomers was characterized by abstraction of an aqua ligand, thus referring to $[\text{UO}_2\text{OH}(\text{H}_2\text{O})_3]^+$ as a common reference species. Reaction energies as well as Gibbs free energies (Table 1) show that the four-coordinate isomer 1 is by $7\text{--}15 \text{ kJ mol}^{-1}$ more stable than the five-coordinate structures. Interestingly, this result is independent of the density functional approach applied, as it was qualitatively confirmed by calculations at the LDA level of theory and by two GGA variants. The geometries of all calculated isomers of uranyl monohydroxide are rather similar (Table 1). Five-coordinated species feature an uranyl bond of 180 pm, a bond to the hydroxide ligand $\text{U-O}_\text{H} = 210\text{--}212 \text{ pm}$, and an average equatorial bond length $\text{U-O}_{\text{eq}} = 237\text{--}239 \text{ pm}$ which was also obtained for various other five-coordinated uranyl(VI) complexes [56-58]. Four-coordinated species show a slightly shorter uranyl bond, $179\text{--}180 \text{ pm}$, and, in line with the lower coordination, a lower value of U-O_{eq} , 230 pm. While the

Table 1. Calculated structural parameters of various isomers (VWN, distances in pm), symmetric uranyl stretching frequency ν_s (in cm^{-1}), and Gibbs free energy of aqua ligand abstraction (BP including standard state corrections, in kJ mol^{-1}) of uranyl aqua and uranyl monohydroxide complexes $[\text{UO}_2(\text{H}_2\text{O})_n(\text{OH})]^+$ with $n = 3-4$ in aqueous solution.^a

Complex	isomer	CN	U-O _t ^b	U-O _H	<U-O _w >	U-O _{eq}	ν_s	ΔG_{abs}
$[\text{UO}_2(\text{H}_2\text{O})_5]^{2+}$		5	177.7	–	237	237	869	
$[\text{UO}_2(\text{H}_2\text{O})_3(\text{OH})]^+$		4	179.8	209	236	230		
$[\text{UO}_2(\text{H}_2\text{O})_4(\text{OH})]^+$	1	4	179.3	217	234	230	841	11
	2	5	180.2	212	244	237	830	2
	3	5	180.3	211	244	238	827	1
	4	5	180.3	212	244	237	– ^c	–4
	5	5	180.2	210	245	238	831	2
	6	5	180.3	210	245	237	829	4
	7	5	180.0	210	246	239	834	–1
Exp.								
$[\text{UO}_2]^{2+}$ ^d			177(12)		241	241	870 ^d	
$[\text{UO}_2\text{OH}]^+$							849 ^e	

(a) Coordination number CN of uranyl, U-O_t – uranyl bond, U-O_H – uranyl-hydroxide bond, <U-O_w> – average uranyl-water bond, U-O_{eq} – average equatorial uranyl-ligand bond. (b) Average values. (c) A numerically reliable result could not be achieved. (d) Ref.[132] (e) Ref. [131].

bond to the hydroxide ligand of the four-coordinate complex $[\text{UO}_2\text{OH}(\text{H}_2\text{O})_4]^+$ is longer, 217 pm, than in the other isomers, the species $[\text{UO}_2\text{OH}(\text{H}_2\text{O})_3]^+$ with U-O_H = 209 pm exhibits a value close to those calculated for five-coordinate uranyl monohydroxide, 210–212 pm (Table 1). The relatively long U-O_H bond of four-coordinate $[\text{UO}_2\text{OH}(\text{H}_2\text{O})_4]^+$ can be traced back to a rather short hydrogen bond between the aqua ligand in the second shell and the OH group (Fig. 1). This result has to be regarded as a special feature of this model; a similar U-O_H bond as shown by all other isomers is expected when the full coordination of the OH ligand by a second shell of water molecules is taken into account in all species.

For uranyl monohydroxide an estimate of the symmetric vibrational frequency of the uranyl unit of 849 cm^{-1} is available [131]. Our calculated results of 841 cm^{-1} for four-coordinated and about 830 cm^{-1} for various five-coordinated uranyl monohydroxide isomers (Table 1) are in favour of the four-coordinated species, in line with the energy considerations (see above). The calculated symmetric vibrational frequency of uranyl of 869 cm^{-1} , in good agreement with the experimental value, 870 cm^{-1} [132], lends further support to our model calculations.

The Gibbs free energy of hydrolysis of the four-coordinated uranyl monohydroxide species is calculated at 23 kJ mol^{-1} (GGA), including standard state corrections. When the

five-coordinated isomers are taken into account via a weighted average according to the Boltzmann distribution, this value is increased by 1 kJ mol⁻¹ only. Our computational result agrees reasonably well with the experimental value, 30±1 kJ mol⁻¹ [121,133,134], as well as with results of a density functional Car-Parinello molecular dynamic simulation which yielded 34 kJ mol⁻¹ for the BLYP GGA, and 21 kJ mol⁻¹ for the BP GGA functional [127].

Uranyl monohydroxide served also as an exemplary species to probe effects of self-interaction artefacts in LDA and GGA variants of the Kohn-Sham DF method [135]. The DFT+U approach offers an empirical (partial) correction of such artefacts (see Section 4.3). Strong effects of self-interaction have been identified for the species [UO₂OH]⁺ in the gas phase. Compared to self-interaction free coupled cluster calculations at the CCSD(T) level, U-O_t is overestimated by 1 pm with the LDA approach, U-O_H is underestimated by 2 pm, and the U-O_H-H angle is calculated to be linear (180°) instead of 148° [135]. As we showed earlier for uranyl [136], self-interaction weakens the uranyl bond. Due to bond competition, the U-O_H bond is underestimated. Our analysis demonstrated the rather strong overestimation of the U-O_H-H angle to be an indirect effect of artificial uranyl bending and a spurious π -interaction between the OH ligand and the uranyl moiety [135]. These artifacts are essentially corrected with the LDA+U approach, applying a parameter U = 2 eV. Similar effects as for the LDA approach were obtained in GGA calculations [135]. For the modeling of actinide complexes in solution, inspection of the self-interaction effects on fully coordinated complexes is more relevant. As an exemplary case we carried out an analogous calculation on an isomer of [UO₂OH(H₂O)₄]⁺ in the gas phase [135]. While the direct effects of the weakening of the uranyl bond by 1 pm and the underestimation of the U-O_H bond by 2 pm are also present in this case, the indirect effect on the U-O_H-H angle is strongly damped. For the aqua complex of uranyl monohydroxide this angle is overestimated in a GGA calculations by only 8°. Thus, we conclude that one has to take into account a slight weakening of actinyl bonds and a corresponding underestimation of ligand bond lengths by about 2 pm when comparing conventional LDA and GGA calculations to experiment.

Uranyl hydroxo acetate

The complexation of actinides at environmental pH conditions competes with hydrolysis. Especially for actinides in higher oxidation states like uranyl(VI), which features a rich variety of hydrolysis products, also ternary complexes have been described [137], e.g., with aqua, hydroxide, and carbonate ligands. Therefore, ternary complexes with hydroxide ligands have also been suggested for the complexation with humic substances [21,138-140]. Interestingly, complexation constants for uranyl monohydroxide by humate have been reported to be similar or slightly higher than for uranyl ions by humate [21,138-140]. Similar results have been obtained for Am(III) and Cm(III) [141,142]. As the complexation chemistry of uranyl(VI) in the range of approximately neutral pH is of particular relevance for safety issues of deep geological repositories for radioactive waste, we undertook a study

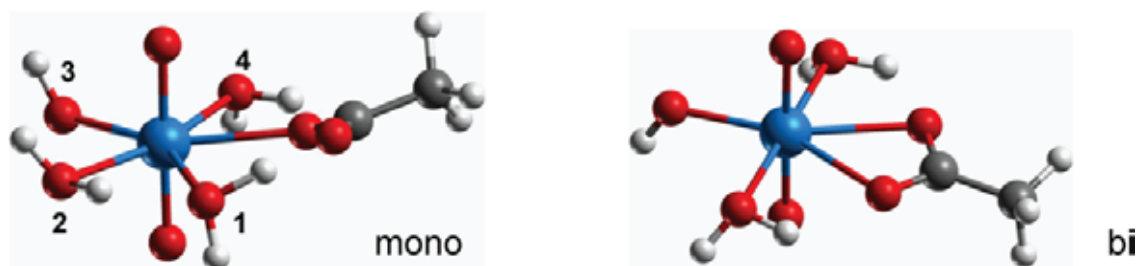


Figure 2. Structure of ternary complexes of uranyl with mono- and bidentate coordinated acetate, a trans-hydroxo moiety, and aqua ligands. Numbers label the various possible positions of the hydroxide ligand.

of ternary uranyl acetate complexes in aqueous solution [143]. These results may also serve as models of carboxylic functional groups of humic substances. Until now structural and vibrational properties of such complexes are only poorly known; therefore, this work provides hints for a direct spectroscopic identification of the corresponding complexes.

Mono- and bidentate acetate coordination of acetate to uranyl monohydroxide at various relative positions of the ligands in the first coordination shell of uranyl have been modeled (Fig. 2). For the monodentate acetate coordination four isomers result, while the local symmetry of the bidentate acetate species reduces the variety of relative ligand positions to two, with the OH ligand in cis or trans position relative the acetate (Fig. 2).

In Table 2, geometric as well as vibrational and energetic characteristics of ternary uranyl hydroxo acetate complexes are compared to their binary uranyl acetate congeners for the more stable trans isomers. Cis isomers of uranyl hydroxo acetate exhibit similar characteristics, but are slightly less stable, as expected due to repulsion of the anionic ligands [143]. As a result of bonding competition, the hydroxide ligand in these ternary complexes induces marked structural changes compared to the binary acetate complexes. The uranyl bond elongates by 2 pm. In line with this weakening of the uranyl bond, the symmetric uranyl stretching frequency is red shifted by about 30 cm^{-1} (Table 2), a value which is rather similar to our result for uranyl monohydroxide (see above). A somewhat smaller red shift was observed in a recent attenuated total reflection (ATR) FT-IR experiment for the asymmetric uranyl vibration in ternary uranyl hydroxo humat complexes compared to uranyl humate [138], by 12 cm^{-1} for uranyl humate solution and about 20 cm^{-1} for uranyl humate solid. U-O bonds to the acetate ligand increase by 7 pm and 13 pm for mono- and bidentate ligand coordination, respectively. In consequence, also the U-C distance to the carbon atom of the acetate ligand increases in case of bidentate coordination, but not for monodentate species where the carboxyl C-O bond decreases. Also the bonds of the aqua ligands to uranyl are elongated, by 7–8 pm (Table 2). In line with earlier findings for other uranyl complexes [56,58], all these changes have no effect on the average equatorial distance U-O_{eq} , which for binary and ternary complexes is calculated in the typical range of 236–238 pm for five-coordinate uranyl(VI) complexes. Once again these

Table 2. Calculated structure parameters^a (LDA, distances in pm), symmetric uranyl stretching frequency ν_{sym} (in cm^{-1}) as well as Gibbs free energies ΔG_{sub} of ligand substitution (single-point GGA, in kJ mol^{-1}) of uranyl acetate $[\text{UO}_2(\text{OOCCH}_3)(\text{H}_2\text{O}_n)]^+$ and uranyl trans-hydroxo acetate complexes $[\text{UO}_2(\text{OH})(\text{OOCCH}_3)(\text{H}_2\text{O}_{n-1})]$ with bidentate (bi) and monodentate (mono) coordination ($n = 3, 4$) in aqueous solution.

Ligand		U-O _t	U-O _C	U-C	U-O _W	U-O _H	U-O _{eq}	ν_{sym}	ΔG_{sub}
bi	$[\text{UO}_2]^{2+}$	178.6	237	277	236	–	237	854	-109
	$[\text{UO}_2(\text{OH})]^+$	180.6	244	284	244	212	238	820	-69
mono	$[\text{UO}_2]^{2+}$	178.9	229	340	238	–	236	822	-110
	$[\text{UO}_2(\text{OH})]^+$	180.8	242	341	243	214	237	796	-63

(a) U-O_t – uranyl bond U-O_t, U-O_C – uranium bond to carboxylate, U-C – uranium distance to carboxyl C, U-O_W – uranyl bond to aqua ligand, U-O_H – uranyl-hydroxide bond, U-O_{eq} – average equatorial uranyl-ligand bond.

examples show that the geometric parameter U-O_{eq}, which is commonly determined in EXAFS studies, is not sensitive to the coordination modes or types of ligands. The only key characteristic geometric feature of uranyl hydroxo acetate complexes is the rather short bond of the hydroxide ligand U-O_H, 212–214 pm, which may be used as fingerprint in experimental structure analysis.

The Gibbs free energies of complexation of uranyl monohydroxide with acetate (Table 2) are clearly lower than for uranyl itself; this translates into a lower complexation constant of uranyl monohydroxide. This result can be rationalized by the lower charge of $[\text{UO}_2\text{OH}]^+$ compared to $[\text{UO}_2]^{2+}$. This finding is qualitatively at variance with experimental results for uranyl hydroxo humate species (see above) although the experimentally determined red shift of the uranyl asymmetric vibrational frequency also points to a change in ligand bonding to uranyl comparable with our results. All these results demonstrate that at least at neutral to basic pH conditions the complexation of uranyl by humic substances at the microscopic level deserves further exploration.

Diacetate complexes

Uranyl diacetate species are present in solutions of uranyl and acetate at weakly acidic pH [144] and may serve also as models of uranium complexed by more than one carboxyl group of humic substances. Two acetate ligands were coordinated to uranyl ion in bidentate/bidentate, bidentate/monodentate, and monodentate/monodentate fashion (Fig. 3) and the first coordination shell was filled up with aqua ligands to reach the common coordination numbers CN = 5 and 6. The 1:1 complexes of acetate with uranyl show very similar Gibbs free energies of complexation for bidentate and monodentate coordinations with the bidentate coordination slightly preferred (Table 3). The various 1:2 uranyl acetate complexes are very close in energies too. Monodentate/monodentate and bidentate/monodentate coordinations are essentially degenerate, while bidentate/bidentate coordination is about 10 kJ mol^{-1} less favorable (Table 3). The calculated structural

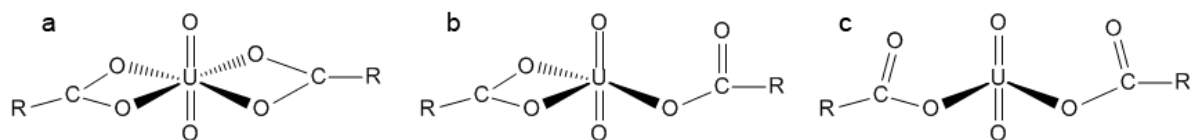


Figure 3. Coordination modes of biacetate complexes $[\text{UO}_2(\text{OOCCH}_3)_2]^0$: (a) bidentate-bidentate, (b) bidentate-monodentate, (c) monodentate-monodentate.

parameters are rather similar for all three diacetate complexes. The U-O_t bond is 179–180 pm and marginally shorter values are calculated for twofold bidentate ligand coordination as for the monoacetate complex (Table 3). The average U-O_C bond to the acetate ligands amounts to 237–241 pm for all three types of coordination, which is slightly longer than for bidentate monoacetate. An average equatorial distances U-O_{eq} of 236–238 pm is obtained for all five-coordinate species. This geometric parameter depends essentially only on the coordination number (see above) [56,58], as is demonstrated for the six-coordinate bidentate/bidentate diacetate complex with $\text{U-O}_{\text{eq}} = 242$ pm. The only structural parameter characteristic for the coordination mode is the U-C distance to the carboxyl group. Its average elongates from about 280 pm for bidentate coordinated complexes to about 330 pm for monodentate species for 1:1 as well as 1:2 complexes (Table 3).

An EXAFS study on uranyl acetate complexation suggests the prevalence of 1:2 complexes at pH 2 to 3.2 [144] and interprets a slight increase in U-O_{eq} with time as a change of the coordination mode from mono- to bidentate. The resolved U-O_t bond of about 179 pm is in good agreement with our calculational results. U-O_{eq} of 242–245 pm is longer

Table 3. Calculated structure parameters^a (LDA, distances in pm) and Gibbs free energies ΔG_{sub} of ligand substitution (GGA, in kJ mol^{-1}) of uranyl mono- and diacetate $[\text{UO}_2(\text{OOCCH}_3)_m(\text{H}_2\text{O}_n)]^0$, $m = 1$ and 2, with monodentate (mono) and bidentate coordination of ligands in aqueous solution. Experimental results for uranyl diacetate are given for comparison.

Coord.	Ac^-	CN	U-O_t	U-O_C	U-C	U-O_{eq}	ΔG_{sub}
bi	1	5	178.7	237	277	237	-108
mono	1	5	179.0	228	333	236	-107
bi/bi	2	5	179.2	237	277	238	-175
	2	6	179.8	241	280	242	
bi/mono	2	5	179.7	237	305	236	-185
mono/mono	2	5	179.9	238	336	236	-186
EXAFS ^b							
pH 1.8, 3 months			179(2)		294(2.2)	245(4.4)	
pH 1.8			179(2)		292(2.3)	242(4.6)	
pH 3.2			178(2)		292(1.9)	245(3.8)	

(a) Ac^- – number of acetate ligands, CN – coordination number of uranyl, U-O_t – uranyl bond, U-O_C – uranium bond to carboxylate, U-C – uranium distance to carboxyl C, U-O_{eq} – average equatorial uranyl-ligand bond. (b) Ref. 144

than our calculated values for five-coordinate complexes (Table 3) but fits to $U-O_{eq}$ of the bidentate/bidentate diacetate complex with $CN = 6$ of 242 pm (Table 3). Thus, comparison of EXAFS and calculated results suggests a prevailing coordination of 6, at variance with the lower measured coordination numbers. Also the increase of $U-O_{eq}$ with time may be due to an increase of the average coordination number. The measured U-C distance of $292-294 \pm 3$ pm, together with a coordination number of ~ 2 , confirming the presence of diacetate complexes, lies between the values calculated for purely mono- or bidentate coordinated diacetate complexes. Thus, a mixture of mono- and bidentate coordinated ligands should be present, in agreement with calculated Gibbs free energies of complexation (see above).

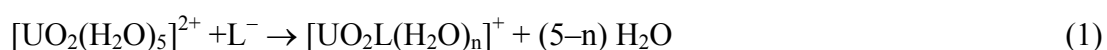
4.1.2 Complexation by non-carboxylic groups

To complement ongoing experimental efforts of the project partner Helmholtz-Zentrum Dresden-Rossendorf in characterizing the role and importance of other than carboxylic functional groups in actinide complexation by humic substances, we studied uranyl complexation as an exemplary case with small organic species which exhibit S- and N-related heterogroups as models of analogous functional groups of humic substances.

Complexation by sulfur containing groups

The complexation of uranyl(VI) by a single sulfonate or thiolate ligand was examined as a model of the corresponding functional groups of humic substances [145]. Humic substances typically show a sulfur content of less than 1.5 % [9]. Yet, at environmentally relevant low actinide concentrations, a contribution of such functional groups can be excluded only by demonstrating that their propensity for complexation is less favorable than that of other functional groups. This computational modelling was related to experimental TRLFS studies at Helmholtz-Zentrum Dresden Rossendorf on the complexation by benzenesulfonic acid (BSA) and 4-hydroxybenzenesulfonic acid (HBSA) [145] as well as complexation by sulfur enriched humic acids [146] which mainly feature sulfur in high oxidation state as thiolate groups. An interesting finding of earlier TRLFS studies was that HBSA complexates uranyl while for BSA no complexation could be detected [147]. This little surprising finding motivated our study together with an experimental reinvestigation of these systems under strictly comparable conditions.

Uranyl complexes in aqueous solution with BSA, HBSA, and also methylsulfonate as ligands have been optimized, assuming five-fold coordination. For comparison also methanethiolate was included in this study. Table 4 collects pertinent geometric parameters of all complexes treated and Gibbs free energies of the model complexation reaction



Mono-, bi-, and tridentate coordination of the sulfonate group to uranyl was examined. While optimizations lead to stable structures with mono- and bidentate coordination (Fig. 4), no energetic minimum could be found for tridentate coordination. The uranyl bond length as

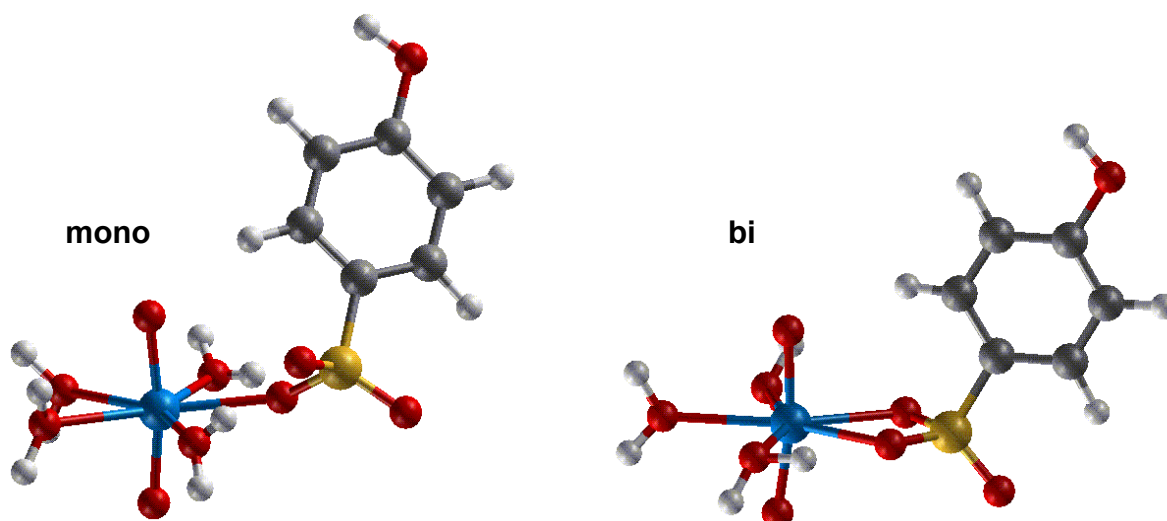


Figure 4. Mono- and bidentate uranyl complexes $[\text{UO}_2(\text{C}_6\text{H}_4\text{OH})\text{SO}_3(\text{H}_2\text{O})_n]^+$ with an HBSA ligand in aqueous solution.

well as the average equatorial U-O distance U-O_{eq} , the structure parameters commonly determined in EXAFS investigations, are very similar for all three sulfonates and vary only marginally with the coordination mode (Table 4). For monodentate coordination, U-O_t is elongated by less than 0.5 pm and U-O_{eq} is 1–2 pm shorter than for bidentate coordination. These results indicate a slightly stronger uranyl-ligand interaction for monodentate coordination. The weak variation of the distance U-O_{eq} between mono- and bidentate complexes is in line with earlier findings for carboxylates which showed that the value of U-O_{eq} mainly reflects the coordination number, but not the coordination mode [56,148]. The trend of the uranyl-sulfonate bond, tentatively interpreted as stronger for monodentate complexes, is corroborated by the distances U-O_s from uranyl to the sulfonate oxygen centers. For monodentate complexes a short bond of ~ 230 pm was calculated, while for bidentate coordination two bonds of ~ 240 pm were determined. Another clear geometric differentiation of the coordination modes is provided by the U-S distances which amount to ~ 310 pm for bidentate coordination, but to ~ 360 pm for monodentate species. This geometric feature of uranyl monosulfonate complexes is best suited for a potential differentiation of the coordination mode by EXAFS measurements. With regard to the complexation behaviour of BSA and HBSA, note that the geometric parameters of BSA and HBSA complexes are more similar to each other than to the corresponding methylsulfonate complex.

Comparison of sulfonate complexes to uranyl methanethiolate reveals notable differences in the structure. The uranyl bond $\text{U-O}_t = 179$ pm is up to 1 pm longer than for the sulfonate complexes, pointing towards stronger bonding of the ligand. The bond $\text{U-S} = 267$ pm is clearly much shorter than the U-S values of sulfonate complexes. Averaging jointly over the equatorial distances U-O and U-S yields a value of 247 pm, considerably larger than the value U-O_{eq} of ~ 237 pm calculated for five-coordinate uranyl sulfonate or

Table 4. Calculated distances^a (pm) of mono- and bidentate uranyl(VI) sulfonate $[\text{UO}_2\text{L}(\text{H}_2\text{O})_n]^+$, $\text{L} = \text{RSO}_3^-$, and thiolate, $\text{L} = \text{RS}^-$, with $n = 4$ for monodentate and $n = 3$ for bidentate complexes. Results for the complexes with the acetate ligand, $\text{L} = [\text{CH}_3\text{COO}]^-$, are given for comparison. Gibbs free energies ΔG_{sub} (single-point BP, kJ mol^{-1}) including standard state corrections are estimated according Eq. (1).

Ligand	coord. mode	R	U-O _t	U-O _{S/C}	U-S/C	U-O _{eq}	ΔG_{sub}
RSO_3^-	mono	CH_3	178.7	229	354	237	-35
		C_6H_5	178.7	232	362	236	-27
		$\text{C}_6\text{H}_4\text{OH}$	178.7	231	361	236	-26
	bi	CH_3	178.3	240, 242	306	238	-32
		C_6H_5	178.4	240, 243	308	238	-26
		$\text{C}_6\text{H}_4\text{OH}$	178.6	240, 242	307	238	-23
RS^-		CH_3	179.3	–	267	247	-75
RCOO^-	mono	CH_3	178.9	229	340	236	-105
	bi	CH_3	178.6	237, 237	277	237	-108

(a) U-O_t – average terminal uranyl bond, U-O_{S/C} – bond to oxygen centers of the sulfur-containing or carboxylic ligand L, U-S/C – distances to the S/C center of L, U-O_{eq} – average equatorial U-O/S bond.

acetate complexes (Table 4). Thus, this quantity is a simple geometric feature for identifying thiolate complexes by means of EXAFS.

Gibbs free energies of sulfonate complexation calculated according to the model equation (1) yield only small differences, of up to 3 kJ mol^{-1} , between complexes with BSA and HBSA ligands. Thus, one expects that both acids show a very similar complexation behaviour for uranyl, as confirmed by very recent TRIFS experiments of the project partner Helmholtz-Zentrum Dresden-Rossendorf. In these spectroscopic measurements, the complexation constant of uranyl complexation with BSA and HBSA were determined at 2.62 and 2.67, respectively [145]. Interestingly, these values are rather close to the complexation constants measured for uranyl monoacetate, 2.5–2.9 [149-151]. This similarity is at variance with the calculated Gibbs free energies of complexation: -20 kJ mol^{-1} to -35 kJ mol^{-1} for sulfonate complexation, but more exothermic, -105 kJ mol^{-1} for mono-, and -108 kJ mol^{-1} for bidentate coordination of acetate. Recall that complexation constants of organic acids have been shown to correlate with the corresponding pK_a values [152].

The higher pK_a value of acetic acid, 4.76, is reflected by our calculated results, but not by the experimental complexation constants for acetate and sulfonate ligands which feature pK_a values below zero [153]. Thus, the measured unexpectedly high complexation constants of sulfonates, at variance with general trends [152] and our computational results, represent an open problem, to be examined in more detail. Note that an earlier finding of a rather high

Table 5. Gibbs free energies ΔG_{sub} (single-point BP) of ligand substitution for complexes $[\text{UO}_2(\text{H}_2\text{O})_4\text{L}_\text{N}]^{2+}$, $\text{L}_\text{N} = \text{NH}_2\text{Me}$, NMe_3 , and NC_5H_5 , in solution, optimized without constraints. Results for complexes with neutral ligands $\text{L} = \text{CH}_3\text{OH}$, $\text{C}_6\text{H}_5\text{OH}$, and CH_3COOH , as well as the anionic ligand CH_3COO^- are given for comparison. Free energies $\Delta G_{\text{sub}}^{\text{H}}$ of complexation with protonated ligands $\text{L}_\text{N}\text{H}^+$ or neutral ligands LH . All energies in kJ mol^{-1} .

		ΔG_{sub}	$\Delta G_{\text{sub}}^{\text{H}}$
L_N	NH_2CH_3	-9	120
	$\text{N}(\text{CH}_3)_3$	39	158
	NC_5H_5	13	111
L	CH_3OH	8	28
	$\text{C}_6\text{H}_5\text{OH}$	57	57
	CH_3COOH	20	33
	CH_3COO^- mono	-109	
	CH_3COO^- bi	-110	

complexation constant, at variance with the correlation with pK_a , had been rationalized by the coexistence of inner- and outer-sphere complexes [152].

Complexation by nitrogen containing groups

Just as sulfur, nitrogen is also a smaller component, reaching up to ~4 %, in the elemental composition of humic substances [9]. Nitrogen appears in various functional groups, e.g., in amines and amides, as well as in amino, imino, and heterocyclic moieties. While multidentate nitrogen donor ligands are common in separation chemistry [154,155], such complexating units are not to be expected in humic substances. Thus, we examined amines, pyridine, and amino acids [156,157] as models of more probable N-donor functional groups of humic substances. Especially amino acid groups may be of interest as they allow chelate complexation of metal ions.

Structural parameters for uranyl complexes with methylamine, trimethylamine, and pyridine, like the uranyl bond and bonds to aqua ligands, are similar to monocarboxylate complexes [156]. U-N bonds of ~248 pm are a characteristic feature, as they are longer than U-O bonds of carboxyl complexes (229 pm monodentate, 237 pm bidentate, see above). This relationship reflects the larger size of the N atom compared to O. Consequently, the average equatorial U-O/N distance, which is often measured by EXAFS, elongates by 2 pm [156] compared to uranyl monoacetate.

Table 5 compares Gibbs free energies ΔG_{sub} of complexation with neutral N-donor ligands or with their conjugate cationic acids ($\Delta G_{\text{sub}}^{\text{H}}$) according to the reaction

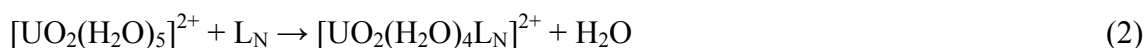


Table 6. Geometry parameters^a (in pm) and Gibbs free energies ΔG_{sub} (single-point BP, in kJ mol^{-1}) of ligand substitution for complexes $[\text{UO}_2\text{L}(\text{H}_2\text{O})_3]^{0,+}$ of uranyl with the α -amino-isobutyric acid anion AIB and the neutral acid AIBH. For comparison also results for the carboxylates with acetate, benzoate, salicylate, and glycolate and given. Bidentate (bi) and chelate coordination of the ligand are compared.

Coord.	Ligand	U-O _t	U-O _C	U-N/O	U-C	U-O _W	U-O _{eq}	ΔG_{sub}
bi.	acetate	179	237		277	237	237	-110
	benzoate	179	237		277	236	237	-98
	salicylate	178	237		277	237	237	-61
	glycolate	178	239		277	235	237	-78
	AIB cis	179	237		276	239	238	-82
	AIB trans	179	237		276	237	237	-88
	AIBH	178	241		277	235	237	-59
chelate	salicylate	179	218	246	341	240	237	-49
	glycolate	179	223	244	326	238	236	-82
	AIB	179	226	248	325	237	238	-118

(a) U-O_t – average uranyl bond, U-O_C – uranium bond to carboxylate, U-N/O – uranium bond to N or O centers of chelating ligands, U-C – uranium distance to carboxyl C, U-O_W – uranyl bond to aqua ligand, U-O_{eq} – average equatorial uranyl-ligand bond.

to results for methanol, phenol, and acetic acid. Neutral amines and pyridine show low complexation energies, comparable to those calculated for neutral OH functional groups. While methylamine complexates slightly stronger than an aqua ligand, $G_{\text{sub}} = -9 \text{ kJ mol}^{-1}$, trimethylamine yields an endothermic complexation energy of 39 kJ mol^{-1} due to its larger steric demand. As neutral amine or pyridine groups are present at about neutral or higher pH, no sizeable contribution to actinide complexation in humic substances is expected because at these conditions the prevailing carboxyl groups are deprotonated. Also at low pH, where these groups acquire their cationic acid form, alcoholic, phenolic and neutral carboxyl groups form more favorable complexation sites, as is demonstrated by the much higher endothermic $\Delta G_{\text{sub}}^{\text{H}}$ values calculated for the N-donor ligands (Table 5) [156].

The complexation of uranyl by amino acids was studied in exploratory fashion on the examples glycine, alanine, and α -amino-isobutyric acid (AIB) [157]. The latter model ligand was treated in more detail as a corresponding EXAFS study is available [27]. Bidentate and chelate coordination of the amino acid group may be invoked as favorable coordination modes of the ligand. For bidentate coordination U-O bonds to the carboxyl group and to aqua ligands in general are rather similar (Table 6). Neutral AIB is an exception where the average U-O_C distance to the carboxyl group, 241 pm, is by 6 pm longer than the bonds to aqua ligands. Also, the geometric features of isomers (cis and trans orientation of the N lone pair with respect to the carboxyl group) of bidentate coordinated AIB and other carboxylic

acids are very similar (Table 6). Chelate complexes are easily distinguishable geometrically from their bidentate congeners. The single bond U-O_C is by more than 10 pm shorter and the bonds to the amine group or the hydroxyl ligand in case of carboxylic acids, 244–248 pm, are longer than typical U-O_C distances of bidentate complexes, 237–241 pm (Table 6). A marked difference between bidentate and chelate coordination, useful for identification by means of EXAFS, is the U-C distance. It is calculated to ~277 pm for bidentate coordination of AIB and to 325 pm for the corresponding chelate complexes. Similar results were obtained for salicylate and glycolate complexes (Table 6).

Comparison of energy parameters for bidentate and chelate complexes of uranyl with the three exemplary amino acids shows that for the neutral form of the acids bidentate complexation is preferred by about 45 kJ mol⁻¹, while the anionic form of the ligand is more stable in chelate complexes, by 20–30 kJ mol⁻¹. Thus bidentate coordination is expected at acidic pH, while chelate complexes should appear in the basic regime, in agreement with experimental results [27]. Chelate complexes of carboxylic acids show a free energy of complexation that is lower or comparable to bidentate complexes, but the uranyl AIB chelate complex shows the highest endothermic complexation energy among all examples studied (Table 6). Thus, at lower to neutral pH where amino acids are protonated, carboxyl groups are preferred for uranyl complexation. On the other hand, at basic pH conditions, amino acid moieties offer more favorable sites for complexation via the formation of chelate complexes. Taking into account the low nitrogen content of humic substances, only a slight increase of the complexing ability is thus expected, due to amino acid groups, at high pH conditions.

4.1.3 Carboxylate complexation: Effect of temperature and mechanism

Temperature dependency of uranyl acetate complexation

The majority of actinide complexation studies were carried out at room temperature. Only few data are available at elevated temperatures [28,158] that are of interest when modelling chemical processes for safety issues of deep geological storage sites where temperatures of 100°C and above have to be considered in the near field.

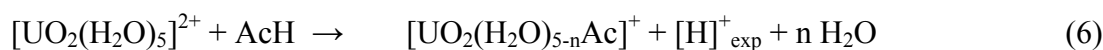
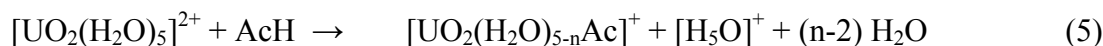
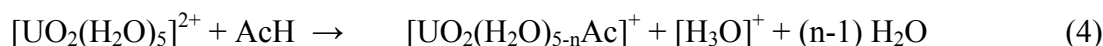
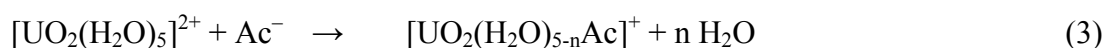
The hydrolysis of uranyl(VI) was studied experimentally in the temperature range from 10 to 94 °C [159-161]. In that temperature interval hydrolysis of uranyl proceeds as formation of [UO₂OH]⁺, [(UO₂)₂(OH)₂]²⁺, and [(UO₂)₃(OH)₅]⁺ in acidic solutions, and all three hydrolysis constants increase with temperature, but to a different degree [161]. Therefore, the speciation of U(VI) varies with temperature T.

Several experimental studies examined the complexation of uranyl with carboxylates at elevated temperature [28,162-164]. Titration calorimetry was used to determine the enthalpy of complexation from 10 to 85 °C. The complexation of uranyl with acetate, malonate, oxydiacetate, and thiodiacetate is always endothermic and driven by entropy. The

enthalpy and entropy of complexation both become more positive at higher T. The complexes are stabilized at higher T as the increase of the entropy term $T\Delta S$ exceeds the enthalpy change. Similar thermodynamic trends have been observed for the complexation of carboxylates with other actinide and lanthanide cations, including Th(IV) [165], Nd(III) [166], and Sm(III) [162].

To inspect the microscopic origins of these findings, we examined uranyl acetate complexes at 25, 50, 75, and 90 °C. Monodentate and bidentate 1:1 and 1:2 uranyl complexes with acetate were optimized in the gas phase and in solution, applying the BP functional. Thermodynamic corrections of the energy values, to determine enthalpy and entropy terms, were first calculated from a normal mode analysis in the gas phase. The temperature dependence of solvation effects was modelled via the temperature variation of the dielectric constant $\epsilon(\text{H}_2\text{O})$ of water [167,168] and the cavitation energy [169]. The values $\epsilon(\text{H}_2\text{O}) = 78.4, 69.9, 61.5,$ and 56.3 at $25\text{ °C}, 50\text{ °C}, 75\text{ °C},$ and 90 °C as derived from [167] were used. The Gibbs free energy ΔG_{aq} of complexation reactions in solution was estimated by invoking a thermodynamic cycle that involves the Gibbs free energy ΔG_{gas} in the gas phase, adding for each species its Gibbs free energy ΔG_{sol} of solvation. Reaction free energies were adjusted to the standard concentration of 1 M for solutes ($\Delta G_{\text{st}}(T) = 7.91, 8.57, 9.23,$ and 9.63 kJ mol^{-1} for $T = 25\text{ °C}, 50\text{ °C}, 75\text{ °C},$ and $90\text{ °C},$ respectively) and to the standard concentration of water, 55.34 M ($\Delta G_{\text{st}}(T) = 17.85, 19.34, 20.83,$ and 21.73 kJ mol^{-1} at $T = 25, 50, 75,$ and $90\text{ °C},$ respectively) for each solvated water molecule.

To examine the effect of temperature on the uranyl complexation by acetate we studied the model reactions



for monodentate ($n = 1$) and bidentate ($n = 2$) ligand coordination.

Equation (3) models the standard equation of metal complex formation, but has the disadvantage of including cations as well as anions. As inaccuracies of a PCM method are particularly pronounced for charged species and commonly larger for anions [170,171], it is computationally favourable to use Eqs. (4–6) because they comprise only cations and thus tend to afford a more favourable error compensation. From Gibbs free energies, determined according to Eqs. (4–6), corresponding values of Eq. (3) can be derived with the Gibbs free energy of deprotonation of acetic acid. Here the experimental value of the pK_a of acetic acid at normal conditions (4.59 ± 0.01), which increases with temperature to 4.72 at 70 °C, can be used [28]. In Eq. (4) the solvated proton is modelled as H_3O^+ , in Eq. (5) as Zundel ion, while

Table 7. Thermodynamic parameters of uranyl(VI) monoacetate complexation with mono- and bidentate coordination for various temperatures as calculated from Eq. (3) in the gas phase (g) and in solution (s) at the GGA level as well as with standard state corrections (st).

	$\Delta E(s)$	$\Delta H_{st}(g)$	$-\Delta(ST)(g)$	$\Delta G_{st}(s)$	$\log \beta$
mono					
25	-125.3	-117.2	10.2	-107.0	18.8
50	-127.1	-118.2	11.1	-107.1	17.4
75	-129.3	-119.6	12.0	-107.6	16.2
90	-130.9	-120.7	12.5	-108.2	15.6
bi					
25	-90.6	-70.1	-38.1	-108.2	19.0
50	-91.6	-68.9	-41.3	-110.1	17.9
75	-93.0	-67.9	-44.4	-112.4	16.9
90	-94.0	-67.6	-46.3	-113.9	16.4

in Eq. (6) the value of 1105 kJ mol^{-1} is used for the solvation energy of the proton as obtained in a systematic ion cluster-pair study [172] (in agreement with experimental data).

Table 7 provides the Gibbs free energies estimated according to Eq. (3) for 1:1 uranyl mono- and bidentate complexes with acetate. The experimental value ΔG of the 1:1 complex formation was measured at -15 kJ mol^{-1} at room temperature [28]; it decreases slightly with increasing temperature. At $70 \text{ }^\circ\text{C}$, ΔG amounts to -20 kJ mol^{-1} [28]. As a result, the corresponding complexation constant increases from 2.61 ± 0.03 to 3.01 ± 0.05 when T increases from $25 \text{ }^\circ\text{C}$ to $70 \text{ }^\circ\text{C}$ [28]. An U-C contact of 290 pm and coordination number 1.3 was resolved at pH 2.84 , confirming the presence of inner-sphere 1:1 uranyl complexes with acetate [28].

The calculated data from Eq. (3) do not fit the experiment (Table 7). The free energy change of the reaction, about -110 kJ mol^{-1} at $25 \text{ }^\circ\text{C}$, considerably overestimates (in absolute terms) the experiment, resulting in too large a complexation constant of ~ 19 (Table 7). This failure in reproducing the free energy of complexation mainly is to be attributed to shortcomings of the solvation model mentioned above [170,171]. Much better results were obtained for the trend with increasing temperature. The monodentate complex is marginally less stable than the bidentate one and that difference becomes larger with T, rendering bidentate coordination increasingly more favourable. Going from $25 \text{ }^\circ\text{C}$ to $75 \text{ }^\circ\text{C}$, ΔG decreases by 1 kJ mol^{-1} for monodentate complexes and 4 kJ mol^{-1} for bidentate complexes. The latter value agrees very well with the experimental results, a change by 5 kJ mol^{-1} at $70 \text{ }^\circ\text{C}$ [28].

Bidentate and monodentate complexes show opposite signs of the gas phase entropy contribution to the Gibbs free energy. The entropy term $-T\Delta S$ stabilizes the bidentate complex by $\sim 40 \text{ kJ mol}^{-1}$, but slightly destabilizes the monodentate complex by $\sim 10 \text{ kJ mol}^{-1}$ (Table 7). This effect can be rationalized by the fact that bidentate coordination implies the

Table 8. Temperature dependence of the Gibbs free energy ΔG (GGA) of uranyl(VI) complexation by an acetate ligand according to model reactions Eqs. (3–6) for mono- and bidentate coordination. Given are values at 25 °C and their change $\Delta^2 G$ upon temperature increase to 90 °C as well as the difference $\Delta(\text{bi-mono})$ of $\Delta^2 G$ values of mono and bidentate complexes in solution (s) including standard state corrections (st).

	Eq.	3	4	5	6
$\Delta G_{\text{st}}(\text{s}, 25)$	mono	-107	-3	-57	-36
	bi	-108	-4	-58	-37
$\Delta^2 G_{\text{st}}(\text{s}, 90)$	mono	-1	-7	-5	-7
	bi	-6	-12	-9	-12
	$\Delta(\text{bi-mono})$	-5	-5	-5	-5

release of one more aqua ligand from the first coordination shell of the uranyl aqua complex than for complexes with monodentate coordination, which lowers the reaction entropy. Experimental results show complexation with acetate to be entropy driven [28]. According to our calculations, this holds only for the bidentate complex.

Using Eqs. (4–6) more realistic Gibbs free energies were calculated for the complexation of uranyl with acetate (Table 8). Eq. (4) yields a marginally exothermic reaction in best agreement with experiment. Modelling the solvated proton as $[\text{H}_5\text{O}_2]^+$ species again overestimates the Gibbs free energy, leading to a reaction energy of about -60 kJ mol^{-1} , while invoking the experimental solvation energy of a proton provides an intermediate value of the reaction Gibbs free energy, about -40 kJ mol^{-1} . These examples demonstrate that the solvation energy of a proton is an essential quantity for determining reliable computational values for the free energy of complexation by an acid.

Independent of the absolute values calculated, our results show that mono- and bidentate complexes at room temperature are energetically almost degenerate (Table 8) while bidentate complexes become more favourable with increasing temperature. The difference of the complexation Gibbs free energy between mono- and bidentate complexes increases (in absolute terms) from 1 kJ mol^{-1} to 5 kJ mol^{-1} when the temperature is raised from room temperature to 90 °C. This trend is independent of the model equation used, as these equations differ only by the representation of the solvated proton. These computational results suggest that the concentration ratio of bi- and monodentate complexes increases from about 2:1 at room temperature to 7:1 at 90 °C. As the bidentate conformer of uranyl monoacetate shows the stronger temperature effect and dominates at elevated temperatures, we ascribe the temperature dependence of uranyl acetate complexation to the bidentate coordinated species.

Neptunyl acetate complexation

Neptunyl(V) acetate has been chosen as an exemplary case for the detailed examination of a complexation reaction as the monoacetate complex is neutral. Thus, solvation effects are small and this facilitates the modeling. Table 9 lists the geometric parameters of neptunyl

Table 9. Geometry parameters^a (in pm) of the five-coordinated Np(V) aquo ion and the monoacetate complex [NpO₂Ac] with mono- and bidentate coordination of the acetate ligand in comparison to experimental results.

		Np-O _t	Np-O _C	Np-C	Np-O _{eq}
NpO ₂ ⁺	calc.	183			254
	exp.	182-185			246-252
[NpO ₂ Ac]	calc. mono	184	249	347	253
	bi	184	252	290	253
	exp. pH = 0.6	183			251(4.5)
	2.7	184		291(0.7)	251(4.5)
	3.7	184		290(1.9)	251(5.2)

(a) Np-O_t – average neptunyl bond, Np-O_C – neptunium bond to carboxylate, Np-C – neptunium distance to carboxyl C, Np-O_{eq} – average equatorial neptunyl-ligand bond.

aqua and monoacetate complexes. Coordination number 5 was assumed in these models as is typical for neptunyl(V) complexes [29,173-175]. The neptunyl bond length Np-O_t of 183 pm as well as the average bond length of aqua ligands Np-O_{eq}, 254 pm, agree with available experimental data (Table 9). Acetate may coordinate to neptunyl in mono- or bidentate fashion. Employing a GGA functional, we calculated the bidentate five-coordinate complex to be ~15 kJ mol⁻¹ more stable than the monodentate complex. As result of acetate coordination, the neptunyl bond increases by 1 pm (Table 9). Np-O_C bonds to the acetate ligand are only slightly shorter than bonds to aqua ligands. These bonds are 249 pm for monodentate and 252 pm for bidentate coordination, while the average bonds to aqua ligands are 254 pm in either case. From these results a value of 253 pm for Np-O_{eq} is calculated, independent of the coordination mode (Table 9). These results are in rather good agreement with a recent EXAFS study of neptunyl acetate complexes in aqueous solution [176] by the project partner Helmholtz-Zentrum Dresden-Rossendorf. In that study Np-O_t was measured at 184 pm and Np-O_{eq} at 251 pm. Interestingly, both quantities do not change with increasing pH. A measured Np-C distance of about 290 pm also agrees very well with our calculations (Table 9), confirming a bidentate coordination of the acetate ligand. These experimental results support our more general result that average equatorial actinyl-oxygen distances, here Np-O_{eq}, depend mainly on the coordination number, but not on the type or number of ligands (Table 9).

In addition to optimizing stable structures we traced the reaction of solvated neptunyl(V) with an acetate ligand starting from a five-coordinate outer-sphere complex, employing a restricted geometry optimization (Fig. 5). We used the decreasing distance Np-C as a reaction coordinate. For the outer-sphere complex a Np-C distance of 498 pm was calculated. With decreasing Np-C distance, at about 400 pm, a barrier is reached on the way to monodentate coordination of the ligand. In the course of that reaction an aqua ligand is

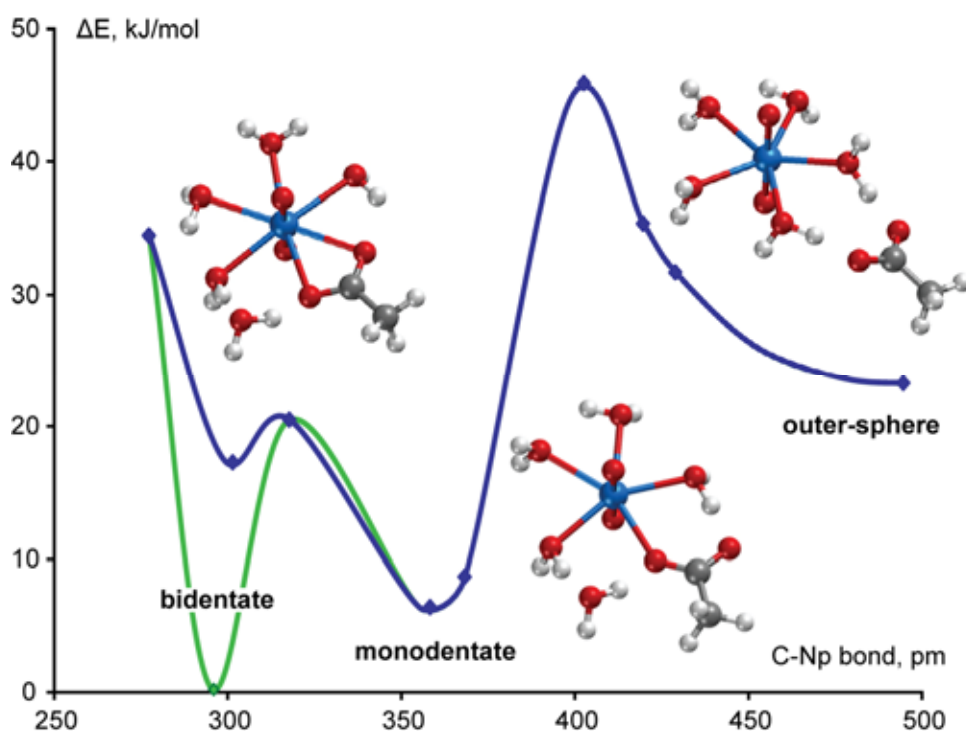


Figure 5. Complexation of neptunyl(V) by acetate. Reaction pathway from outer-sphere to inner-sphere mono- and bidentate complexes as a function of the distance Np-C. For bidentate complexation, six- (blue) and five-coordinate species (green) were optimized.

expelled from the first solvation shell, leading to a five-coordinate monodentate species. Further decrease of Np-C results in bidentate coordination of the acetate ligand, at Np-C = 298 pm, with the overall coordination number 6 of neptunyl. This species is energetically by $\sim 10 \text{ kJ mol}^{-1}$ less stable than the monodentate complex (Fig. 5). Removal of a second aqua ligand from the first coordination shell leads to a five-coordinate bidentate species, which is slightly more stable than the monodentate complex. From these results one may tentatively conclude that mono- and bidentate neptunyl monoacetate complexes are in a fast dynamic equilibrium while the outer-sphere complex, higher in energy by about 25 kJ mol^{-1} , is separated by a higher barrier of about 40 kJ mol^{-1} . Thus, although not noticed in the EXAFS results (Table 9) [176], monodentate complexes should contribute to the speciation of neptunyl(V) at low pH.

4.1.4 An(IV) complexes

Aqua ions and monohydroxides of uranium and neptunium in the oxidation state IV have been studied at the GGA level of DFT in aqueous solution as exemplary complexes of this less well explored oxidation state. The large charge of the complexes poses an additional challenge in computational studies because long-range solvation effects are important (see Section 4.3). Previous computational studies addressed uranium and neptunium(IV) aqua complexes, but their structure optimizations were limited to systems in the gas phase and by

Table 10. Calculated structure parameters^a (GGA, distances in pm) of U(IV) and Np(IV) aqua complexes and monohydroxides as well as reaction energies (in kJ mol⁻¹) of adding an aqua ligand for coordination numbers CN = 8–10. All models for systems in aqueous solution.

CN	8	9	10	8	9
	An-O _W			ΔE	
U ⁴⁺	239	242	247	-64	-25
[UOH] ³⁺	247	250	255	-38	-17
Δ	8	8	8		
Np ⁴⁺	238	241	246	-36	-25
[NpOH] ³⁺	245	248	253	-33	-23
Δ	7	7	7		
	An-O _H				
[UOH] ³⁺	204	206	207		
[NpOH] ³⁺	205	205	208		

(a) CN – coordination number of actinide ion, An-O_W – average actinide bond to aqua ligands, An-O_H – bond between actinide ion and OH ligand.

symmetry constraints [177]. To the best of our knowledge, our calculations on the monohydroxides were the first such studies.

The aqua ions of An(IV) were modeled for coordination number CN = 8–10. With increasing CN, the average An-O distance was calculated to increase (Table 10), from 239 pm for CN = 8 to 247 pm for CN = 10 for U⁴⁺. For neptunium, these bond lengths are by 1 pm shorter, in line with the smaller radius of the Np⁴⁺ ion. These results compare fairly well to EXAFS measurements of these quantities, 240–244 pm for uranium [178-182] and 237-240 pm for neptunium [29,174,183]. Thus, the tentatively best agreement with experiment is achieved for CN = 9 for uranium and CN = 8 for neptunium. The experimental studies suggest CN = 9–11 for uranium [178-182] as well as for neptunium [29,174,183]. Also our calculated energies of water addition to [An(H₂O)_n]⁴⁺ favor complexes with higher coordination. Addition of an aqua ligand was calculated endothermic, by 64 kJ mol⁻¹ for uranium and 36 kJ mol⁻¹ for neptunium, for CN = 8. For CN = 9 this reaction energy decreases for both complexes to 25 kJ mol⁻¹. Taking into account that entropy corrections will favor lower coordination numbers as an additional aqua ligand is brought to the first coordination sphere, CN = 9 seems plausible for both aqua ions. For neptunium, CN = 8 in addition might be present as a minority species (Table 10). Longer An-O bonds were calculated with the hybrid B3LYP functional for complexes in the gas phase, ranging from 245 pm for CN = 8 to 255 pm for CN = 10 for uranium and being again slightly shorter for neptunium [177]. The typical contraction of bonds to aqua ligands due to long-range

Table 11. Calculated structure parameters (GGA, distances in pm) and Gibbs free energies (in kJ mol^{-1}) of addition of an aqua ligand of the Am(III) aqua ion for coordination 7–10.

CN	Am-O		ΔG
	VWN	BP	BP ^a
7	236		4
8	239	247	22
9	243	249	30
10	248		
Exp. ^b	247-249		

(a) BP single point at VWN geometries (b) Refs. [184-186].

solvation effects will bring these results in close agreement to ours. In that study results on energies were shown to favor CN = 9 for uranium and CN = 8–9 for neptunium [177].

Hydrolysis of an aqua ligand to yield the monohydroxide $[\text{AnOH}(\text{H}_2\text{O})_n]^{3+}$ leads to an elongation of the bonds to aqua ligands, by 8 pm for uranium and 7 pm for neptunium, irrespective of the coordination number (Table 10). This finding, together with the observation that during the structure optimization none of the aqua ligands moved to a position in the second solvation shell, shows that up to CN = 10 steric repulsion is of minor importance for the structure of these complexes. For larger numbers of hydroxide ligands a corresponding lowering of coordination number due to increasing bonding competition between weakly bound aqua ligands and strong bound hydroxide ligands was demonstrated for Th(IV) in a quantum chemical study [99]. An-O_H bonds of the monohydroxide were calculated between 204 and 208 pm for CN = 8–10, showing a slight increase with increasing coordination number (Table 10). Interestingly, the tendency to slightly longer bonds for uranium compared to neptunium is broken for CN = 8 (Table 10). Energies of adding an aqua ligand are always lower for the monohydroxides compared to the aqua complexes of the same coordination number. This finding can be rationalized by bond competition between the hydroxide and the aqua ligands and the stronger metal-ligand bond of the latter. The exothermic reaction energies of adding an aqua ligand, 38 kJ mol^{-1} for CN = 8 and 17 kJ mol^{-1} for CN = 9 for uranium, 33 kJ mol^{-1} for CN = 8 and 23 kJ mol^{-1} for CN = 9 for neptunium, again suggest CN = 9 to be preferred when entropy effects are considered. More detailed thermodynamic calculations are in progress.

In summary, our calculations support CN = 9 for the aqua ion and the monohydroxide of U(IV) and Np(IV), based on geometry parameters in comparison to experimental findings as well energy considerations. Early hydrolysis of U(IV) and Np(IV) is geometrically characterized by the appearance of a short An-O bond of ~205 pm to the hydroxide ligand and an increase of the distance to the first hydration shell, by 7–8 pm.

Table 12. Calculated structure parameters (LDA, distances in pm) and Gibbs free energies (single point BP, Eq. (7), in kJ mol⁻¹) of complexation of Am(III) monoacetate with coordination numbers of the Am(III) ion of 7-10.

CN	mono				bi			
	Am-O _C	Am-O	Am-C	ΔG	Am-O _C	Am-O	Am-C	ΔG
7	238	239	341	55	238	240	277	51
8	241	242	340	62	241	243	279	52
9	243	245	334	66	243	245	282	49
10	244	249	343	68	245	249	283	55

(a) Am-O_C – americium bond to carboxylate, Am-O – average americium bond to all ligands, Am-C – americium distance to carboxyl C.

4.1.5 Am(III) complexes

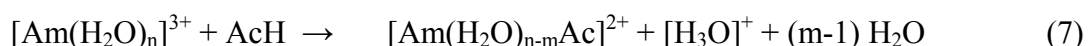
Am(III) aqua ion

As a prerequisite for the examination of Am(III) complexes we modeled the aqua ion. EXAFS experiments gave an average Am-O distance of ~248 pm [184-186] and coordination numbers of 10±0.3 [184], 8.4±1 [185], and 7.4±1[186]. Our calculated results (Table 11) yield the energy of adding an aqua ligand at only 4 kJ mol⁻¹ for coordination 7; the values for coordination numbers 8 and 9 are somewhat higher, 22 and 30 kJ mol⁻¹, respectively. Thus, coordination 7 and 8 are essentially degenerate, in agreement with the suggestion of a coordination of about 8 by more recent EXAFS results [185, 186]. While for lower coordination numbers VWN optimizations lead to shorter Am-O distances of 236-243 pm, BP results of 247 pm for CN = 8 and 249 pm for CN = 9 agree very well with experiment [184-186].

Am(III) acetate

Am(III) complexation with organic ligands was studied in detail for the standard model ligand acetate. Mono- and bidentate coordination of acetate were examined, varying the coordination number of Am³⁺ from 7 to 10. For all these complexes, as earlier for the aqua ion, we obtained the expected septet electronic configuration in our scalar-relativistic calculations. Table 12 collects the geometric characteristics of these complexes. As expected, the bond lengths Am-O_C from Am to the acetate ligand increase with increasing coordination number CN, from 238 pm for CN = 7 to about 245 pm for CN = 10, reflecting the increasing bond competition with aqua ligands. This competing effect also shows up in the average Am-O bond to all ligands, which increases from about 240 pm to 250 pm when CN is raised from 7 to 10. As for other carboxylate complexes (see above) [56,143,148], Am-O is independent of the coordination mode and thus may be used as fingerprint of the coordination number in EXAFS measurements. The coordination mode is best identified by the Am-C distance, about 340 pm for monodentate and 280 pm for bidentate complexes (Table 12). To inspect the stability of the complexes, the complexation reaction was

characterized by the Gibbs free energy of complexation with acetic acid (Table 12), which is directly relevant at low pH:



Here n is the coordination number, 7–10, and $m = 1$ for monodentate and 2 for bidentate acetate coordination. As shown by the endothermic Gibbs free energies, for all coordination numbers bidentate coordination is preferred. This preference ranges from 4 kJ mol⁻¹ to 17 kJ mol⁻¹. The complexation Gibbs free energies, 50–55 kJ mol⁻¹, for bidentate complexes of various coordination numbers overestimate the experimental results of about 15 kJ mol⁻¹, derived from measured log β values of the project partner TU Dresden as well as earlier experiments [187]. The calculated Gibbs free energy of adding an aqua ligand to the complex with CN = 7 is 5 kJ mol⁻¹ for the bidentate and 12 kJ mol⁻¹ for the monodentate complex. Thus, species with CN = 7 and 8 are energetically nearly degenerate. Addition of a further aqua ligand to reach CN = 9 requires about 20 kJ mol⁻¹; thus a higher coordination is not favorable.

4.2 Adsorption of actinides on clay minerals

Adsorption on the surfaces of clay minerals is an important retardation mechanism, governing the distribution of actinides in the environment. A detailed understanding of this process is of timely interest for the risk assessment of possible deep geological repositories [188,189]. Despite a large amount of experimental studies on the adsorption of actinides at clay minerals [190-199], there are still many open questions, e.g., (i) what is the nature of the adsorbed species; (ii) which surfaces, basal or edge, are more preferred for adsorption; (iii) what are the main adsorption sites, etc. Computational approaches as applied in this project provide insight into these topics on the atomic level, hence are able to complement experimental investigations.

4.2.1 Clay mineral surfaces and surface models

Clay minerals are hydrous aluminum phyllosilicates, built of interconnected sheets of Si tetrahedra and Al octahedra to form layered structures. We studied 1:1 and 2:1 clay minerals. The 1:1 clay mineral kaolinite consists of one tetrahedral Si sheet bound to an octahedral Al sheet [200]. 2:1 clay minerals consist of an octahedral sheet sandwiched between two tetrahedral sheets. The simplest 2:1 clay mineral without substitutions is pyrophyllite [201]. Families of other clay minerals can formally be derived from these two prototypes by substitutions, which create permanently charged layers that are neutralized by interlayer counterions. As example, we modeled beidellite which exhibits substitutions of Si⁴⁺ by Al³⁺ in the tetrahedral sheet.

In general, clay minerals feature an ideal (001) cleavage plane, the so-called basal plane. The (001) surface of kaolinite can be terminated by Al octahedra – Al(o), or Si tetrahedra – Si(t), see Fig. 6. The (001) planes of 2:1 phyllosilicates are siloxane surfaces,

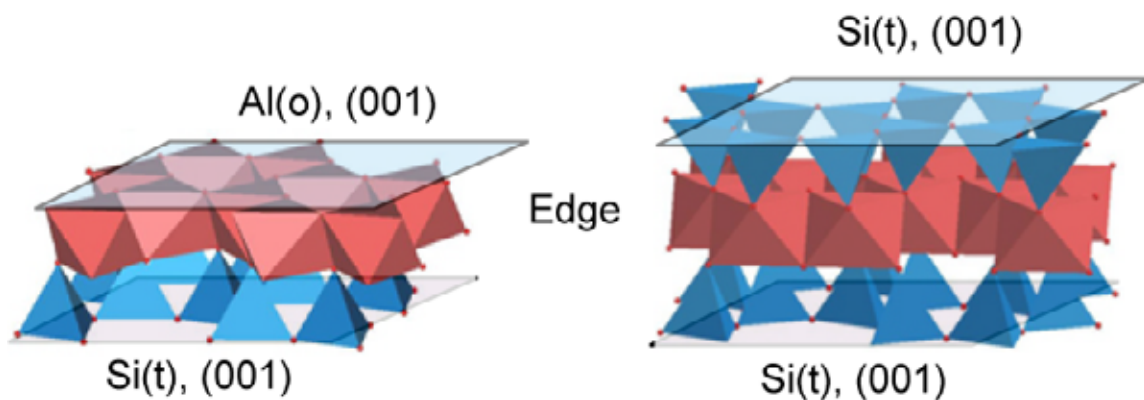


Figure 6. Structures of basal and edge surfaces of kaolinite and pyrophyllite.

formed by Si(t) planes. We modeled the surfaces of clay minerals by invoking the periodic supercell approach. Potential artifacts due to translational symmetry are avoided by rather large unit cells that contain up to a few hundreds of atoms.

To study adsorption on the basal surfaces of kaolinite we used (2×1) and (2×2) unit cells that comprised only a single two-sheet layer [105]. Adsorption of uranyl on bare surfaces was modeled using both the local density approximation (LDA) and the generalized gradient approximation (GGA). To account for surface solvation 20 water molecules, covering a (2×2) unit cell (surface area: 1.82 nm^2) of the (001) kaolinite surface by about a monolayer, were introduced into the quantum chemical model. As LDA is known to overestimate weak interactions, all models with surface solvation were optimized at the GGA level to improve the description of hydrogen bonds.

Fig. 7a shows an optimized kaolinite one-layer model. Two thirds of the OH groups, “uOH”, on the optimized (001) Al(o) kaolinite surface are in “upright” orientation, perpendicular to the (001) plane. The remaining OH groups, “lOH”, are oriented parallel to the (001) plane [105]. Fig. 7b presents a top view of the Al(o) (001) surface of kaolinite, featuring both uOH and lOH moieties. The Si(t) surface is rather rigid; it hardly undergoes any relaxation compared to the bulk structure. Surface solvation of the Al(o) (001) surface of kaolinite did not change the ratio between upright and lying OH groups. The hydroxide groups formed hydrogen bonds with water molecules, of types $\text{uOH} \cdots \text{OH}_2$ and $\text{lOH} \cdots \text{H}_2\text{O}$. These H bonds stabilized both types of surface OH groups. The Si(t) (001) surface of kaolinite was shown to be hydrophobic as the 20 water molecules tend to form a water cluster far above the surface, forming only two H bonds with surface oxygen centers [202].

The basal (001) surface of charged 2:1 clay minerals of beidellitic type was modeled by a (2×2) unit cell (area: 1.82 nm^2) that contained two structural substitutions of Si^{4+} centers by Al^{3+} cations. The charge was neutralized by two Na^+ counterions, each solvated by five water molecules, and adsorbed as outer-sphere complexes on the siloxane surface. Surface solvation in this case was represented by 16 additional water molecules.

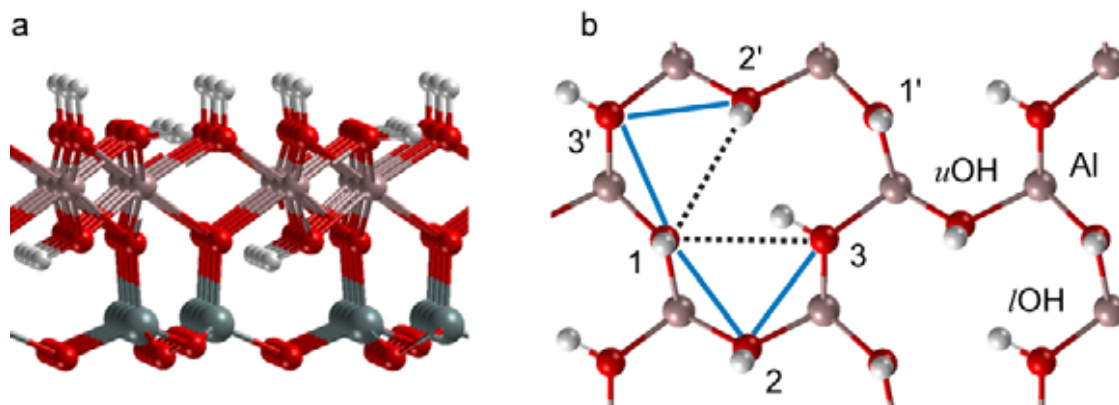


Figure 7. (a) Side view of a single-layer model of kaolinite where atomic “sublayers” are indicated. (b) Top view of the Al(o) basal (001) surface of kaolinite. uOH – upright surface OH group, lOH – lying surface OH group. Symmetry inequivalent surface oxygen centers are numbered for convenience. Corresponding equivalent centers are labeled by a prime. Solid blue lines – short-bridge sites, dashed lines – long-bridge sites.

Besides basal planes, clay mineral particles exhibit edge surfaces (Fig. 6) which are assumed to be more reactive [203]. They are terminated by unsaturated oxygen centers which can exchange protons with the solution and in this way generate a pH-dependent surface charge. The exact atomic structures of edge surfaces are not known. Various empirical models exist to predict favorable edge planes and their atomic structures. The most popular among them is the crystal growth theory of Hartmann and Perdok [204-206]. For dioctahedral 2:1 clay minerals it predicts six edge surfaces: (010), (100), (± 110), and (± 130).

For the kaolinite, we studied the (010) surface as an exemplary edge surface [107]. The terminations of edge surfaces can be constructed by (formally) cutting the crystal parallel to the surface of interest, breaking the weakest bonds, and preserving the stoichiometry of Si and Al ions. Using this strategy, we identified four possible terminations for the (010) kaolinite surface. Two of these terminations, S0 and S1, were selected for further studies as more favorable based on an empirical bond strength model [207] and considerations regarding the dissolution of kaolinite [107]. Both terminations of the (010) kaolinite surface were modeled with (2×2) unit cells of $\sim 1.5 \text{ nm}^2$ surface area. Although of different surface structure, they comprise similar surface groups, SiOH, AlOH, AlOH₂. The construction of the terminations and the protonation schemes have been discussed in detail [107]. Protons of silanol groups move to neighboring aluminol groups, forming SiO⁻ and two AlOH₂ groups [107]. Surface solvation was approximated by 22 adsorbed water molecules. Although smaller in area than the (001) surface of kaolinite, the (010) surface is rougher; therefore, more water molecules were used to cover it. The main effect of solvation of the edge surfaces is a rearrangement of protons on the surface [107].

Pyrophyllite is the only mineral for which the atomic structures of different edge

terminations have been computationally characterized at the atomic scale [208,209]. We chose the (010) and (110) edge surfaces of pyrophyllite for examining uranyl adsorption [210]. Pyrophyllite edge surfaces models were modeled with (2×1) unit cells of ~1.1 nm² surface area, covered by 15 water molecules to approximate solvation. In contrast to kaolinite, solvation does not lead to rearrangement of protons. Thus, bare and solvated edge surfaces of pyrophyllite exhibit the same surface groups. Compared to kaolinite, edge surfaces of pyrophyllite are more complex. Besides aluminol and silanol surface groups they also offer mixed sites AlOSi with oxygen centers bound to aluminum and silicon. In our studies of uranyl adsorption on edge surfaces of substituted pyrophyllite, modeling the mineral beidellite, we applied a monoclinic unit cell which is common to various charged 2:1 clay minerals. As for pyrophyllite edge surfaces, a (2×1) unit cell and 15 water molecules to approximate surface solvation were used. The same types of surface groups are present as on edge surfaces of pyrophyllite.

Solvation of surfaces and complexes adsorbed on them was directly introduced into the quantum chemical models by explicit water molecules. As an approximation when calculating the energetics, we assumed that long-range solvation effects are comparable for the surfaces with and without adsorbates. For the molecular species appearing in formal adsorption reactions, like H₂O, H₃O⁺, [UO₂(H₂O)₅]²⁺ (see below), solvation energies including long-range effects were estimated using the COSMO solvation model as implemented in the program ParaGauss [65].

4.2.2 Adsorption on kaolinite

Three topics will be addressed in this section. First, results on uranyl adsorption on basal planes of kaolinite are described [105] together with surface solvation effects [106]. As the Si(t) basal surface of kaolinite was shown to be less reactive regarding uranyl adsorption [105] than the Al(o) surface, the following section on neptunyl NpO₂⁺ adsorption contains only models of adsorption complexes on the hydroxylated Al(o) surface. Finally, computational results for uranyl adsorption on edge surfaces of kaolinite including surface solvation effects [107] are discussed.

Adsorption of uranyl(VI) on basal surfaces

The two principal types of species postulated for metal adsorption at mineral surfaces are inner-sphere and outer-sphere complexes. The adsorption of uranyl on the bare Al(o) and Si(t) (001) basal surfaces of kaolinite was studied in detail by comparing mono- and bidentate short- and long-bridge inner-sphere as well as outer-sphere complexes [106,105]. The short-bridge bidentate sites are formed by surface O centers bound to the same Al atom (Fig. 7b, solid lines), while the long-bridge sites are two O centers bound to different Al atoms (dashed lines). Uranyl was shown to adsorb at long-bridge sites only when both surface AlO groups of the site are deprotonated [106]. The uranyl complex adsorbed at a long-bridge AlO-AlOH site converged to a complex at the nearest short-bridge AlOOH site

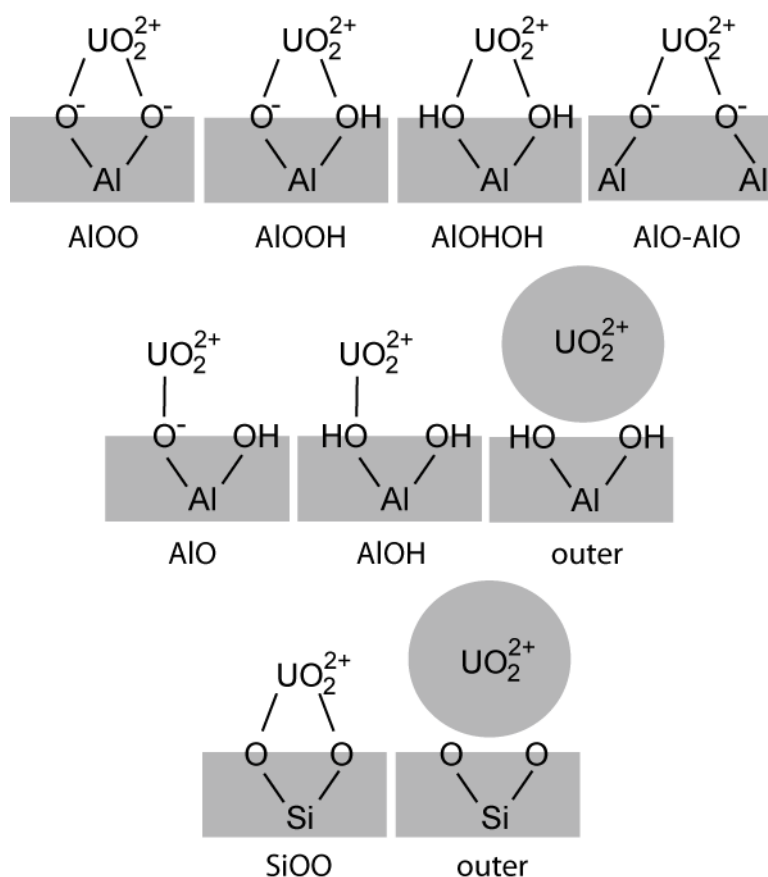


Figure 8. Schematic representation of the model adsorption complexes studied for the basal Al(o) and Si(t) surfaces of kaolinite: bidentate short-bridge (AlOO, AlOOH, AlOHOH, SiOO) and long-bridge (AlO-AlO) inner-sphere complexes, monodentate inner-sphere (AlO, AlOH) and outer-sphere complexes.

[106]. This result suggests that sites available for uranyl adsorption are pH dependent, as the long-bridge site is occupied only when deprotonated. Adsorption at different pairs of surface groups (uu, ul) was also examined [105,106], but turned out to be similar for chemically similar sites (AlOO, AlOOH, etc.).

Fig. 8 schematically presents all adsorption complexes modeled. The Al(o) surface implies more adsorption sites due to its hydroxylation and deprotonation of surface OH groups at higher pH. The Si(t) surface is commonly assumed to be less reactive as it exhibits only coordinatively saturated oxygen centers. The adsorption complexes shown in Fig. 8 imply charged unit cells. The program VASP provides accurate compensating corrections for charged unit cells only for cubic lattices. Therefore, models with the neutral unit cell had to be created by invoking surface defects. For modeling uranyl adsorption on a Si(t) surface, two protons were removed at the opposite side [Al(o)] of the slab model to compensate the charge of the adsorbed uranyl ion. When modeling uranyl adsorption at an Al(o) surface, two silanol defects per (2×2) unit cell were introduced at the opposite side [Si(t)] which may be deprotonated when necessary for charge compensation. For the details see Ref. 105.

Table 13. Calculated structural parameters^a (in pm) of various models of adsorption complexes of uranyl on the bare basal Al(o) (001) surface of kaolinite. Experimental results are provided for comparison.

Site	U-O _t	U-O _{surf}	U-O _w	U-O _{eq}	U-Al
LDA					
AlOO	185	208/223	251/253/253	237	308
AlOOH	184	210/260	247/248/248	243	327
GGA					
AlOO	187	213/219	263/266/266	245	311
AlO-AlO	187	218/229/260	266/271	249	330/340
AlOOH	186	213/264	257/260/262	251	332
outer-sph		U-O _w			
Model 1	184	242/250/256/265/281		253	
Model 2	184	238/249/257/263/279		257	
Exp.					
Ref. 211	180	228(×2), 248(×3)		240	330
Ref. 212	180			236-240	310/330

(a) U-O_t – uranyl bond, U-O_{surf} – U bonds to the surface O, U-O_w – uranyl bonds to aqua ligands, U-O_{eq} – average equatorial uranyl-ligand bond, U-Al – distance to surface Al center.

Comparison of exemplary adsorption complexes on the bare Si(t) surface with the corresponding species at the Al(o) surface revealed that the Si(t) surface is energetically less favorable for uranyl adsorption, in agreement with common expectations [105]. Complexes with monodentate coordination of uranyl on the bare Al(o) surface were calculated to be of similar stability as the bidentate adsorption complexes [105]. The adsorption complex at the long bridge AlO-AlO site exhibits a third contact to a neighboring AlOH group [106]. However, as monodentate complexes feature longer U-Al contacts than bidentate complexes at sites of the same degree of deprotonation, comparison of U-Al distances with EXAFS results [197,211,212] suggests bidentate species to be present [105]. Among various bidentate inner-sphere complexes on the bare Al(o) surface of kaolinite those at deprotonated short-bridge sites of the types AlOO and AlOOH and at the long-bridge AlO-AlO sites agree reasonably well with EXAFS results (Table 13) with the exception of the too long uranyl bond. These complexes also exhibit the shortest values for U-Al distances (AlOO: 308 pm, AlOOH: 327 pm) and average distances U-O_{eq} of uranium to equatorially coordinated O atoms (AlOO: 237 pm, AlOOH: 243 pm) [105]. The results just mentioned were obtained at the LDA level. When comparing calculated GGA results to experiment, one should take into account that GGA functionals tend to overestimate geometric parameters [106]. At the GGA level, the following results were obtained: U-Al at AlOO – 311 pm, AlO-AlO – 330/340 pm, and AlOOH – 332 pm; U-O_{eq} at AlOO – 245 pm, AlO-AlO – 249 pm, AlOOH – 251 pm (Table 13). Suitably adjusted calculated results (for details

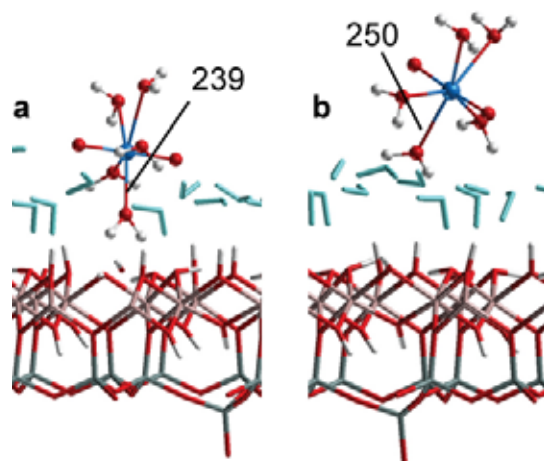


Figure 9. Outer-sphere adsorption complexes of uranyl at the (001) Al(o) surface of kaolinite including surface solvation: (a) uranyl in contact with the surface via an aqua ligand of the first solvation shell; (b) first solvation shell of uranyl not in contact with the surface.

see Refs. 106 and 107) are in line with experimental results obtained for pH values close to the pH of neutral charge of kaolinite ($\text{pH}_{\text{ZPC}} = 5.5$) and above where deprotonated sites are to be expected. In addition, deprotonation of surface hydroxide groups will be facilitated in the field of adsorbed uranyl cations. Thus, adsorption at deprotonated sites is also possible for pH below pH_{ZPC} .

Surface solvation modeled by a monolayer coverage of water molecules only slightly affects inner-sphere bidentate adsorption complexes. Compared to the adsorption complexes on the bare Al(o) surface, U-Al distances were elongated by 3–4 pm; the average equatorial U-O_{eq} distances decreased by 2 pm on average and uranyl U-O_t bonds were only slightly elongated, by 1–2 pm [106]. Thus, surface solvation does not seem to play a decisive role for a qualitatively correct modeling of uranyl adsorption on basal crystal planes of kaolinite.

Although outer-sphere adsorption on the bare Al(o) kaolinite surface was not found to be preferred, some interesting trends were observed which can be extended to other clay minerals. A model of an outer-sphere complex has been set up where the solvated uranyl ion is in direct contact with the support via one of the aqua ligands of its first coordination sphere. This model exhibits one shorter U-O_w distance, 242 pm (at the GGA level), to an aqua ligand adjacent to the surface; see Model 1 in Table 13. The other U-O_w bonds are in the range of 250–280 pm [43]. One of these aqua ligands is attracted by the surface, resulting in a rather long U-O_w contact of 280 pm. Therefore, we also explored the effect of an additional water molecule at that location on the surface (Model 2 in Table 13). Yet, a very similar outer-sphere complex with one short U-O_w contact to the aqua ligand directed to the surface and one rather long U-O_w bond (279 pm) was obtained. Thus, outer-sphere complexes at the bare Al(o) surface exhibit a “splitting” of the first coordination shell. This finding is at variance with the common expectation based on experimental findings that

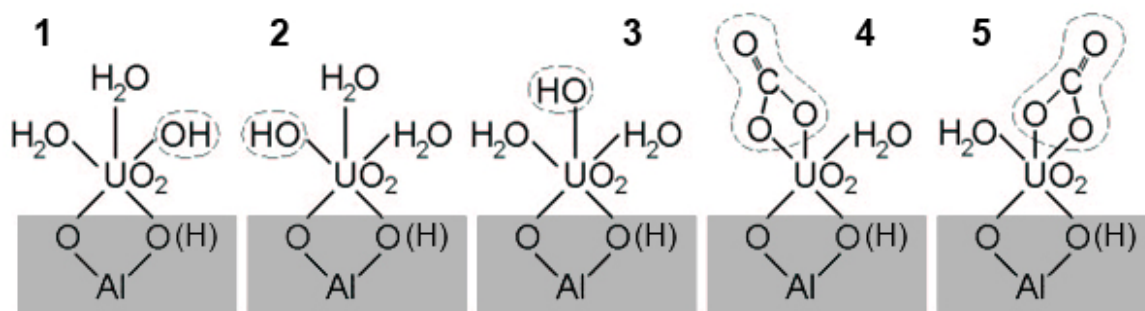


Figure 10. Schematic representation of adsorption complexes of $[\text{UO}_2\text{OH}]^+$ and $[\text{UO}_2\text{CO}_3]^0$ on the basal Al(o) (001) surface of kaolinite.

outer-sphere complexes should show structural characteristics (very) similar to those of a solvated uranyl ion [195]. Similar results also hold at the Si(t) surface.

From these results one can conclude that experimentally detected adsorbed species of solvated uranyl, classified as outer-sphere complexes, should involve more than a single layer of water molecules between uranyl and the surface. To check this, two types of outer-sphere models of uranyl adsorbed at the solvated Al(o) surface were studied [43]. The first model of the outer-sphere complex exhibits a direct contact of the first solvation shell with the surface (Fig. 9a). The second model deposits the solvated uranyl ion above the monolayer of adsorbed water (Fig. 9b). The first model includes explicit solvation but it shows qualitatively the same structural parameters as the outer-sphere complex without surface solvation, namely a split first coordination shell of uranyl with a shorter contact to the water facing the surface (see Fig. 9a). Geometry parameters of the optimized second model do not show any appreciable splitting of the $\text{U}-\text{O}_w$ bond lengths: all five $\text{U}-\text{O}_w$ bonds are in the range of 250–265 pm [43]. These model calculations confirm the assumption that more than one water layer should be present between an adsorbed uranyl ion and the surface to reproduce the experimentally suggested structural characteristics of outer-sphere species.

Adsorption of complexes on the basal Al(o) (001) surface of kaolinite

Apart from the solvated uranyl ion, other uranyl species like hydroxide and carbonate complexes are present in solution at environmental conditions. The most common mononuclear uranyl compounds at acidic to neutral pH are uranyl monohydroxide, $[\text{UO}_2\text{OH}]^+$, and the uranyl-carbonato complex, $[\text{UO}_2\text{CO}_3]^0$ [120]. We studied the adsorption of these species on the AlOO and AlOOH sites of the bare Al(o) basal (001) surface of kaolinite. These sites are charged, $-2 e$ and $-1 e$, while the adsorbates are either neutral or positively charged, $+1 e$. To achieve an overall neutral unit cell a proton was attached to one of the O atoms on the opposite Si(o) side of the slab models. The correction for such a neutralization was estimated as deprotonation energy of the cluster $[\text{Si}(\text{OH})_3\text{-OH-Si}(\text{OH})_3]^+$.

Various positions of the moieties OH^- and CO_3^{2-} on the surface were modeled. Fig. 10 shows schematically the adsorption complexes for both types of sites studied. All three

Table 14. Calculated structural parameters^a (in pm) for the most stable adsorption complexes of UO_2OH^+ and UO_2CO_3 at the AIOO and AIOOH sites of the Al(o) (001) kaolinite surface. Data for adsorbed UO_2^{2+} on the corresponding sites are given for comparison.

Site	Adsorbate	Model ^b	U-O _t	U-O _{surf}	U-OH/O _C	U-O _W	U-O _{eq}	U-Al
AIOO	$\text{UO}_2^{2+ \text{c}}$		187	213/219		265	245	311
	UO_2OH^+	1	187	221/230	224	267	242	315
	UO_2CO_3	5	187	234/235	225/240	263	240	319
AIOOH	$\text{UO}_2^{2+ \text{c}}$		186	213/264		260	251	332
	UO_2OH^+	1'	185	218/270	220	258	245	338
	UO_2CO_3	5'	186	228/268	223/239	255	243	338

(a) U-O_t – uranyl bond, U-O_{surf} – U bonds to the surface O, U-O_W – uranyl bonds to aqua ligands, U-O_{eq} – average equatorial uranyl-ligand bond, U-Al – distance to surface Al center. (b) For the designations of the models see Fig. 10. (c) Ref. 106.

adsorption complexes of $[\text{UO}_2\text{OH}]^+$ at the AIOO site (models 1, 2, and 3) are very close in energy. Model 1 is the most favorable; model 2 is only 3 kJ mol⁻¹ and model 3 by 9 kJ mol⁻¹ less stable. For adsorption of $[\text{UO}_2\text{OH}]^+$ on the singly deprotonated AIOOH site, models 1 and 3 are energetically degenerate, while model 2 is 33 kJ mol⁻¹ less stable. This is tentatively rationalized by the position of the OH ligand close to the O⁻ center of the AIOOH adsorption site in model 2 which might cause repulsion. For $[\text{UO}_2\text{CO}_3]^0$, adsorbed at both AIOO and AIOOH sites, model 5 is 7–9 kJ mol⁻¹ more favorable than model 4.

Structural parameters of the most favorable adsorption complexes at each site are collected in Table 14. Data for the uranyl ion adsorbed on the corresponding sites are given for comparison. First of all, note that the terminal U-O_t bonds are very similar for all adsorbates at a given adsorption site. U-O_t for the uranyl complexes adsorbed on the AIOO site is 187 pm, while on the AIOOH site it is slightly shorter (185–186 pm) due to weaker interaction with the partially protonated site. Due to the lower charge of the $[\text{UO}_2\text{OH}]^+$ adsorbate the bonds to the surface are weaker compared to UO_2^{2+} and consequently longer by ~10 pm (Table 14). As a result the U-Al distance increases slightly too, from 311 to 315 pm at the AIOO site and from 332 to 338 at the AIOOH site. Due to bond competition the U-OH bond for the adsorbed uranyl monohydroxide, 220–224 pm, is longer than for the solvated $[\text{UO}_2\text{OH}]^+$ species (214 pm, see also Section 4.1.1). Also, the average U-O_{eq} value for adsorbed $[\text{UO}_2\text{OH}]^+$ is slightly shorter, by 3–6 pm, than for UO_2^{2+} .

The neutral adsorbate $[\text{UO}_2\text{CO}_3]^0$ exhibits bonds to the surface of 234–235 pm for the AIOO site and 228–268 pm for the AIOOH site. In general, the U-O_{surf} bonds elongate with the decreasing charge of the adsorbate: UO_2^{2+} , $[\text{UO}_2\text{OH}]^+$, $[\text{UO}_2\text{CO}_3]^0$. The U-Al distances follow the same trend. Interestingly, the average value U-O_{eq} shortens to 240 and 243 pm for the $[\text{UO}_2\text{CO}_3]^0$ complex adsorbed on the AIOO and AIOOH sites, respectively. Thus, with decreasing charge of the adsorbate, the U-O_{eq} values shorten slightly: 245 pm for

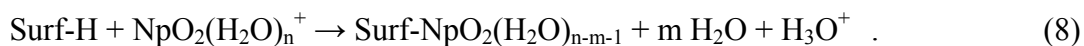
UO_2^{2+} , 242 pm for $[\text{UO}_2\text{OH}]^+$, and 240 pm for $[\text{UO}_2\text{CO}_3]^0$ adsorbed at the AlOO site. For the AlOOH site, the corresponding values are 251, 245, and 243 pm.

In general, adsorption complexes on singly deprotonated AlOOH sites are quasi monodentate species (Table 14). They all exhibit one rather short contact to the surface, 213–228 pm, and one rather long U- O_{surf} bond of 264–270 pm. Bonds to the neutral AlOH surface groups are the longer ones of these distances; these values are even slightly longer than the average U- O_{W} distances to the aqua ligands (Table 14).

Adsorption of neptunyl(V) on basal surfaces

The adsorption of neptunyl NpO_2^+ on the basal surface of kaolinite was examined in similar manner as uranyl. In view of the reduced charge of the complex, a weaker interaction with the surface was expected. The study focused on the basal Al(o) (001) surface, considering bidentate, monodentate, and outer-sphere adsorption complexes (Fig. 11). All complexes were modeled in a (2×1) surface unit cell to save computational effort. Experimentally, the coordination number of neptunyl is known to vary from 4 to 5 [29,213]. We modeled both four- and five-coordinated NpO_2^+ . The corresponding adsorption energies were calculated with reference to $\text{NpO}_2(\text{H}_2\text{O})_4^+$ and $\text{NpO}_2(\text{H}_2\text{O})_5^+$, respectively. Thus, the change of coordination number of neptunyl is not included in the estimated energies.

The structure parameters of the adsorption complexes on singly deprotonated adsorption sites of Al(o) kaolinite are collected in Table 15. The corresponding adsorption energies, also presented in Table 15, are estimated according to the formal equation



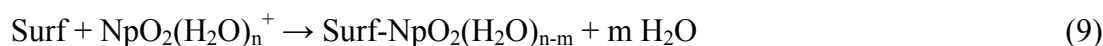
In Eq. (8) the coordination number n of the neptunyl ion, $n = 4$ or 5 , implies $m = 1$ for bidentate adsorption and $m = 0$ for monodentate adsorption. Several adsorption complexes were explored for certain types of sites, reflecting not equivalent surface O centers for the adsorption. Results for inner-sphere adsorption of five-coordinated neptunyl on singly deprotonated sites suggest that mono- and bidentate complexes may coexist. Energetically they differ by 20 kJ mol^{-1} only, in favor of bidentate coordination. All bidentate adsorption complexes on AlOOH adsorption sites exhibit similar geometry parameters and adsorption energies. The structure parameters of the monodentate five-coordinated neptunyl complex at the AlO site are very similar to those for bidentate complexes on AlOOH sites, except for the Np-Al distance. For monodentate coordination, the Np-Al distance is considerably longer. Similar results were determined for the adsorption complexes with CN = 4. Furthermore, the estimated adsorption energies of four- and five-coordinated neptunyl are very close. The only differentiating characteristic of the adsorption complexes with CN = 4 and CN = 5 is the average equatorial distance Np- O_{eq} , ~ 250 pm and ~ 258 pm, respectively (Table 15).

Table 15. Calculated structural parameters (in pm) and adsorption energies (in kJ mol⁻¹) of adsorption complexes of neptunyl on the Al(o) basal (001) surface of kaolinite. Data are given for singly deprotonated (q = -1 e) and neutral sites (q = 0 e). For the designations of the sites, see Fig. 11.

Site, q = -1	Np-O _t	Np-O _{surf}	Np-O _w	Np-O _{eq}	Np-Al	ΔE
CN = 5						
[NpO ₂ (H ₂ O) ₅] ⁺	181			257		
AlOOH	187	220/279	249/269/275	258	335	125
	186	219/274	259/265/267	257	334	145
AlO	185	229	258/258/270/273	258	373	144
CN = 4						
[NpO ₂ (H ₂ O) ₄] ⁺	180			250		
AlOOH	186	220/272	247/259	250	335	129
	185	224/275	248/257	251	334	150
AlO	185	225	248/255/258	248	373	128
Site, q = 0						
CN = 5						
AlOHOH	186	263/267	257/262/263	262	361	-119
	187	247/275	257/259/264	260	362	-119
outer	183		259/261/262/ 265/275	264		-104
CN = 4						
AlOHOH	186	254/259	254/254	255	355	-76
outer	184		246/248/259/259	253		-160
Exp. ^b						
pH 8-10	185-187			245-250		

(a) Np-O_t – neptunyl bond, Np-O_{surf} – Np bonds to the surface O, Np-O_w – neptunyl bonds to aqua ligands, Np-O_{eq} – average equatorial neptunyl-ligand bond, Np-Al – distance to surface Al center. (b) Coordination number of terminal O fixed at 2, coordination number of equatorial O fixed at 4, Ref. 214.

Table 15 also collects structural data and adsorption energies for neptunyl inner-sphere adsorption at neutral AlOHOH sites as well as outer-sphere complexes. The adsorption energies on the neutral surface were estimated according to



In Eq. (9) the coordination numbers n of the neptunyl ion, n = 4 or 5, result in m = 2 for bidentate adsorption and m = 0 for the outer-sphere complexes. Bidentate adsorption of neptunyl on neutral sites AlOHOH shows a clear preference for coordination number 5. In general, adsorption complexes of NpO₂⁺ on neutral sites of the Al(o) kaolinite surface are characterized by longer bonds to surface AlOH groups, and, in consequence, longer Np-Al and Np-O_{eq} distances compared to deprotonated sites. Unfortunately, inherent limitations of

the model prevent a comparison of adsorption energies at sites of different charge. A detailed discussion can be found in Refs. 105 and 106.

In contrast to uranyl on kaolinite, the solvated neptunyl ion adsorbed as outer-sphere complex does not exhibit any “splitting” of the Np-O bonds in the first coordination shell. The Np-O bonds vary from 259 to 275 pm for CN = 5 and from 246 to 259 pm for CN = 4 without any clear separation into two groups. Energetically, outer-sphere complexes with CN = 4 are significantly more favorable than complexes with CN = 5. Outer-sphere complexes were also calculated to be energetically more favorable than inner-sphere bidentate complexes at neutral AlOH₂OH sites.

Table 15 also provides EXAFS results of the project partner Universität Mainz for the adsorption of neptunyl on kaolinite [214]. These data were determined for neptunyl adsorption on kaolinite in Ar atmosphere at pH 8, 9, and 10. Coordination numbers for the resolved Np-O bonds were fixed to 2 and 4 for terminal and equatorial oxygen atoms, respectively [214]. The experimentally resolved Np-O_t bonds 185–187 pm, agree very well with the results calculated for the inner-sphere adsorption complexes. The EXAFS values of Np-O_{eq} vary from 245 to 250 pm, again agreeing very well with results calculated for inner-sphere adsorption complexes with CN = 4. The optimized results for adsorption complexes with CN = 5 exhibit ~10 pm longer Np-O_{eq} distances, compared to experiment. The Np-Al/Si shell was not modeled in this EXAFS analysis because of the low signal-to-noise level of the data [214]. Thus, comparison of our results with the experimental data shows the best agreement for the inner-sphere adsorption of four-coordinated neptunyl. However, such perfect agreement with experiment may be fortuitous as the present models do not include surface solvation. Recall also that structural parameters optimized with a GGA exchange-correlation functional likely are overestimated. Furthermore, the smaller (2×1) surface unit cell, compared to the (2×2) unit cell used when modeling uranyl adsorption, represents a larger surface coverage. To probe effects of the lower coverage on neptunyl adsorption, several adsorption complexes were also optimized using the larger (2×2) surface unit cell. Structure parameters hardly changed (less than 2 pm), compared to the analogous complexes modeled in the smaller unit cell. At lower coverage, the adsorption complexes in general were stabilized by ~5 kJ mol⁻¹. Thus, the size of the unit cell does not play a decisive role for the calculations presented in this study. Surface solvation shows only slight effects on inner-sphere bidentate adsorption, just as calculated for uranyl on the basal Al(o) kaolinite surface. Again, surface solvation can be omitted when striving for qualitatively correct models of actinyl adsorption complexes on basal crystal planes of kaolinite.

Adsorption of uranyl(VI) on edge surfaces

The two terminations of the (010) edge surface of kaolinite selected for adsorption studies exhibit two types of adsorption sites, (i) aluminol sites, AlOO, AlOOH, AlOH₂OH, and (ii) mixed sites where both aluminol and silanol surface groups are involved, AlO(H)-SiO(H).

Table 16. Calculated structural parameters^a (in pm) of more stable adsorption complexes of uranyl on various solvated surfaces of kaolinite.

		U-O _t	U-O _{surf}	U-OH	U-O _w
Al(o) (001)	AlOO	187	220/222		247/253/271
	AlO-AlO	188	222/223/258		252/259
S0 (010)	AlOHOH	185	236/254	223/229	275
S1 (010)	AlOH-SiO-AlOH	185	244/245/219		239/256

(a) U-O_t – uranyl bond, U-O_{surf} – U bonds to the surface O, U-OH – uranyl bonds to OH ligands resulting from water deprotonation, U-O_w – uranyl bonds to aqua ligands.

All these sites were examined for the adsorption of uranyl, first without addressing surface solvation. Only bidentate adsorption complexes were studied because monodentate complexes exhibit U-Al/Si distances that are significantly longer than those resolved in EXAFS experiments of uranyl adsorption on kaolinite [197,211,212].

During optimization most of these models of adsorption complexes changed chemically as aqua complexes of the adsorbed uranyl deprotonated [202], resulting in uranyl monohydroxide as adsorbate. A proton of the first coordination shell of uranyl moved to the surface. Various uranyl complexes adsorbed at sites of the same charge ($q = -2 e$ or $-1 e$) were calculated close in energy. Most of the complexes modeled exhibit similar characteristic structure parameters, with U-O_{eq} = 237–243 pm and U-Al = 316–333 pm (LDA results [202]). These calculated data are in a good agreement with available experimentally determined values of U-O_{eq}, 236–240(±4) pm [197]. Experimentally determined U-Al/Si distances of 310 pm and 330 pm were derived by fitting a broad peak of the EXAFS spectrum between ~300 pm and 335 pm [197]. As we did not find two U-Al distances in this range for any complex, one can expect a broad distribution of such distances which, in turn, may indicate a variety of adsorption complexes, coexisting at certain environmental conditions.

To explore surface solvation effects, uranyl adsorption complexes were modeled on both terminations of the solvated (010) edge surface of kaolinite [107]. In addition to the sites studied already for bare surfaces, aluminol and mixed sites, also bridging sites were examined for uranyl adsorption where surface groups of neighboring kaolinite layers are simultaneously involved [107]. For both terminations of the (010) surface of kaolinite, aluminol and bridging sites were calculated to be energetically more favorable than mixed adsorption sites [107]. For some adsorption complexes, an aqua ligand of the first solvation shell of uranyl deprotonates, yielding uranyl monohydroxide as adsorbate, but this happened less frequently than on the bare edge surfaces (see above), most probably in consequence of additional stabilization due to solvation. Structurally, as for the bare edge surfaces, many adsorption complexes exhibit similar parameters (Table 16) [107]. This confirms the

Table 17. Optimized bulk parameters^a of the primitive triclinic unit cell of selected 2:1 clay minerals. Distances in pm, angles in degrees.

Clay	<i>a</i>	<i>b</i>	<i>c</i>	α	β	γ
Pyro	522	907	985	91	100	90
Beidellite	523	907	1014	92	100	90
Beidellite, 8 H ₂ O	522	908	1328	93	101	90

(a) Energy cut-off 500 eV, (3×3×3) grid of k-points.

assumption that there should be several adsorption complexes in equilibrium on the surface [107].

In addition to U-Al/Si distances, EXAFS often is able to resolve two values of U-O_{eq}, ~230 and ~248 pm [211]. The shorter distance is interpreted as contacts to surface O atoms while the longer distance is tentatively assigned to the average distance to aqua ligands of the first solvation shell of uranyl [211]. Our computational study showed that there can be rather long distances to the surface as well as short U-O contacts to hydroxide ligands of uranium, formed by hydrolysis of adsorbed uranyl. Table 16 presents some examples of adsorption complexes that were calculated to be energetically preferred and exhibit long U-O contacts to the surface and short U-OH bonds. Comparison of various adsorption complexes reveals the trend that bonds to deprotonated surface O centers are short while contacts to surface OH groups are long. As some of the U-O_{surf} distances are of similar length as U-OH bonds, one cannot hope for an easy experimental discrimination. Rather, the interpretation of experimental data may be more complicated than commonly assumed.

4.2.3 Adsorption on 2:1 clay minerals

Common 2:1 clay minerals feature structural substitutions that result in charged layers, hence will require a more sophisticated modeling approach. Therefore, pyrophyllite with its neutral layers was chosen as starting point for modeling such 2:1 clay minerals. The chemical composition of pyrophyllite is Al₄Si₈O₂₀(OH)₄ [201]. Its basal surfaces offer only saturated oxygen centers; therefore, without charged substitutions, these basal surfaces can be assumed to be of minor importance for adsorbing ions such as uranyl. Thus, only adsorption on edge surfaces of pyrophyllite was studied [210]. Subsequently, as first approximation of more complex 2:1 clay minerals, a model of the charged clay mineral beidellite was constructed by exchanging one Al³⁺ ion per (2×1) unit cell for a Si⁴⁺ ion and adding one Na⁺ counterion to the interlayer region. This model was applied to examine computationally the adsorption of uranyl on the basal and edge surfaces of beidellite.

Structure of 2:1 clay minerals: pyrophyllite and beidellite

The triclinic unit cell of pyrophyllite bulk was used when optimizing the bulk structure (Table 17). Two models of beidellite were optimized. First, a bare Na⁺ counterion was used

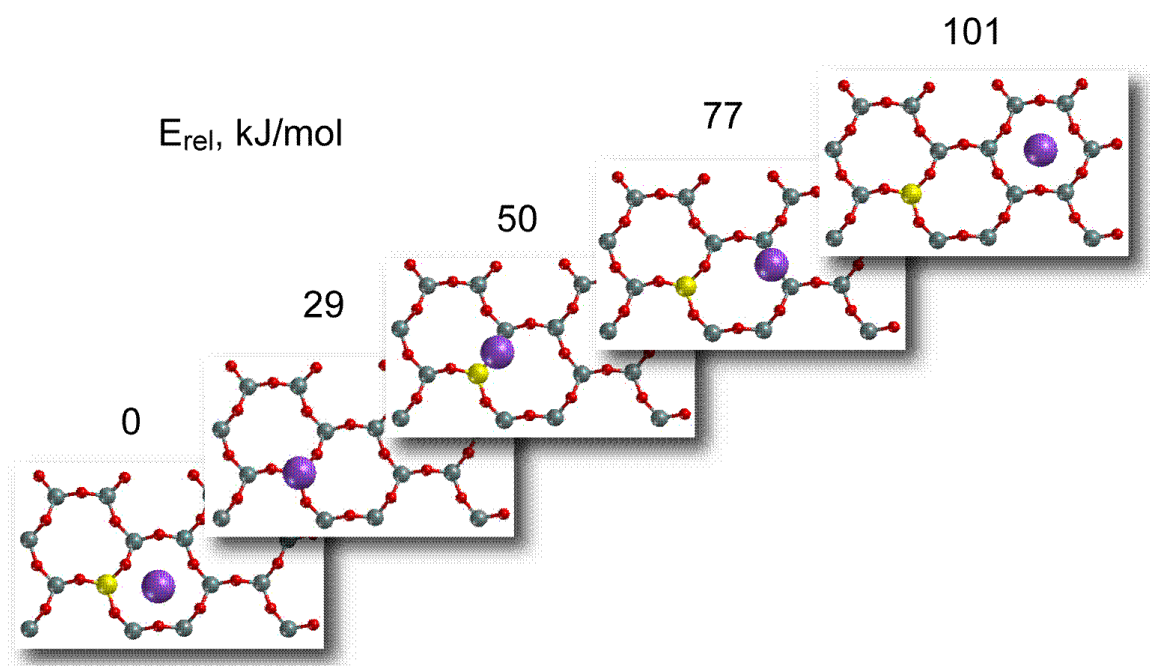


Figure 12. Relative positions of the counterion Na^+ (purple) with respect to the charged substitution on the surface (yellow) and the corresponding relative total energies in kJ mol^{-1} .

in the interlayer region; second, eight water molecules were added to approximate the solvation of the counter ion (Table 17).

The optimized bulk parameters obviously do not change much when one introduces a charged defect. Mainly, vector c is elongated. Pyrophyllite exhibits no counterions between the layers, thus vector c of its unit cell is shortest. A model of beidellite contains bare Na^+ as interlayer counterions and exhibits a vector c that is ~ 30 pm longer. Approximating solvation (swelling) by 8 water molecules per (2×1) unit cell of beidellite results in a vector c of 1328 pm which is considerably longer than that of pyrophyllite bulk (Table 17). As the other optimized bulk parameters do not change significantly, we used pyrophyllite bulk parameters in subsequent calculations when no explicit counter ion is present. This choice of the bulk parameters allows a direct comparison of neutral pyrophyllite and charged beidellite models. The basal surfaces of the 2:1 clay minerals studied were modeled by a monolayer. Thus, the interlayer spacing, reflecting mainly the length of vector c , is not important for such modeling.

The basal (001) surface of beidellite was described by a (2×2) unit cell of pyrophyllite with two substitutions of Si^{4+} by Al^{3+} in the upper Si(t) sheet to model the charge of $0.5 e$ per primitive unit cell (of pyrophyllite). The counterions Na^+ were placed at various positions relative to the charged substitution (Fig. 12). The most favorable position for Na^+ was determined in the $[(\text{Al},\text{Si}_5)\text{O}_6]$ cavity next to the substitution (Fig. 12). Na^+ was modeled as inner-sphere complex solvated by three aqua ligands and as outer-sphere complex $\text{Na}(\text{H}_2\text{O})_5^+$ adsorbed on the beidellite surface. The outer-sphere complex was

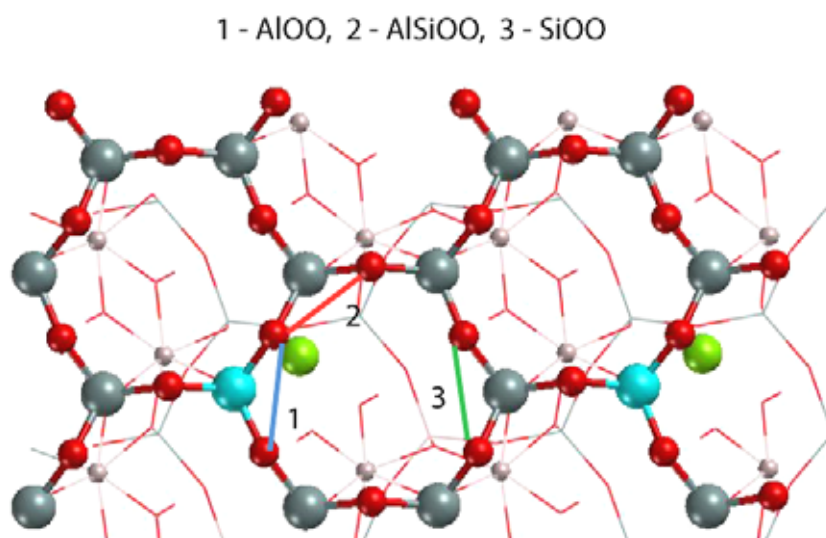


Figure 13. Possible bidentate adsorption sites for the uranyl ion on (001) beidellite surface. Substitution sites (Al^{3+}) in blue, counterions Na^+ in green.

calculated 6 kJ mol^{-1} more favorable than the inner-sphere complex. Thus, a model of one layer pyrophyllite with two substitutions per (2×2) unit cell and two solvated counterions $\text{Na}(\text{H}_2\text{O})_5^+$ adsorbed on the surface was used in the following for the (001) basal surface of beidellite.

Adsorption of uranyl(VI) on basal surfaces of beidellite

One of the adsorption mechanisms on 2:1 surface of clay minerals is ion exchange [195,215] where the positively charged counterions are exchanged by the adsorbate, uranyl in the present case. This type of adsorption was found to be prevailing for uranyl on montmorillonite at low pH values [195,215]. Experimentalists suggest that uranyl adsorbs as outer-sphere complex at low pH as only U-O_t and U-O_{eq} distances similar to those of the free uranyl ion were resolved in EXAFS experiments [195,215].

We studied inner-sphere bidentate and monodentate as well as outer-sphere adsorption complexes of uranyl on the basal (001) surface of our beidellite model. The adsorption sites on beidellite are shown in Fig. 13: SiOO (site 3), AlOO (site 1) at the substitution, and AlSiOO (site 2) which includes an O center connecting Si and Al atoms. A monodentate adsorption complex was modeled at the AlSiO center next to the substitution. We constructed two models for outer-sphere complexes, one above the substitution (model A) and one above the surface in between two substitutions (model B). Optimized structural parameters together with the relative energies are given in Table 18. Relative energies were calculated as formal reaction energies:

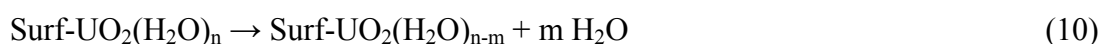
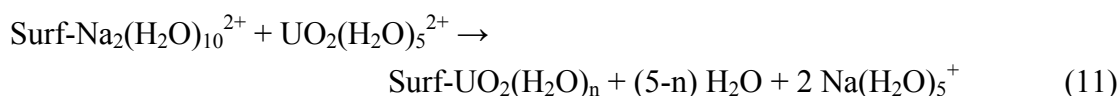


Table 18. Structural parameters^a (in pm), relative energies E_{rel} estimated according to Eq. (10), and complex formation energies E_{form} estimated by Eq. (11) (in kJ mol⁻¹) for various adsorption complexes of uranyl on the bare basal surface of beidellite.

	Site	U-O _t	U-O _{Si}	U-O _{Al}	U-O _{eq}	U-Al	U-Si	E_{rel}	E_{form}
bi	1	179		245/252	249	311		50	199
	2	179	275	234	251	376	324	22	171
	3	178	255/268		251		328	50	199
mono		178		243	248	353	346	-20	129
	CN		U-OH						
outer ^b A	4	180	216		242			0	149
	B	5	180	217	248			3	152
(4×2) ^c A	5	180	218		248				
Exp. ^d	5	179	218		241				

(a) U-O_t – uranyl bond, U-O_{Si} – U bonds to the surface O bound to Si centers, U-O_{Al} – uranyl bonds to surface O bound to Al cations, U-O_{eq} – average equatorial uranyl-ligand bond, U-Al – distance to surface Al center, U-Si – distance to surface Si center. (b) Model A: above the substitution, model B: between two substitutions. (c) Test case for a larger (4×2) unit cell with two substitutions. (d) EXAFS experiment at pH = 4.1, Ref. 195.

with an outer-sphere complex as reference. Formation energies of complexes (Table 18) were estimated as energies required for exchanging two solvated Na⁺ counterions by one adsorbed uranyl ion:



In Eqs. (10) and (11), $n = 3$ for bidentate, $n = 4$ for monodentate, and $n = 5$ for outer-sphere complexes.

Bidentate coordinated species are energetically least favorable among all studied adsorption complexes on the (001) model beidellite surface (Table 18). They are 20-50 kJ mol⁻¹ less stable than outer-sphere complexes. The monodentate species is calculated most stable, by 20 kJ mol⁻¹ more stable than the outer-sphere species. Thus, it is unlikely that bidentate adsorption complexes of uranyl are favored on the (001) surface of beidellite. Also from experiment there is no hint on inner-sphere adsorption at the basal surfaces of 2:1 clay minerals. The favorable monodentate adsorption complex exhibits an uranyl bond U-O_t of 178 pm (Table 18) which has the same length as in the solvated uranyl ion. It also shows no splitting of the equatorial U-O bond lengths. The bond to the surface U-O_{surf} is 243 pm and the average U-O_{eq} is 248 pm, which is longer than the U-O_{eq} value for solvated UO₂²⁺, 242 pm. Thus, the main structural parameters of the monodentate complex are similar to those of the solvated uranyl ion and thus may not easily be discriminated in EXAFS experiments. However, the complex also exhibits U-Al and U-Si distances of ~350 pm, distinguishing it from outer-sphere complexes. Yet, these relatively long contacts are hard to resolve in EXAFS experiments. We added one extra water molecule to the second solvation shell of

the adsorbed bidentate complex at site 2 to create a model with the same number of water molecules in the unit cell as for the monodentate complex. Direct comparison of the total energies of this model with the monodentate complex shows a slight preference for the latter one, by 8 kJ mol⁻¹ only. Thus, taking into account the relatively small energy differences between preferred bidentate, monodentate, and outer-sphere species, these complexes may well coexist on basal surfaces of beidellite.

Outer-sphere complexes adsorbed on the (001) surface of beidellite tend to hydrolyze, yielding adsorbed uranyl monohydroxide. A proton from one of the aqua ligands of the first solvation shell of uranyl attaches to a surface O center. To check whether this is the result of the high charge of the beidellite layer (-0.5 *e* per primitive unit cell) we optimized the outer-sphere complex adsorbed in a (4×2) unit cell with two substitutions only, exhibiting a lower charge of -0.25 *e* per primitive unit cell of the slab. The results remained qualitatively similar. On the bare (001) surface of beidellite, outer-sphere complexes of uranyl monohydroxide with CN = 4 (model A) or CN = 5 (model B) were calculated, with a slight preference, 3 kJ mol⁻¹, for the first one. The outer-sphere complex A positioned above the substitution, initially created as five-fold coordinated, shows one rather large U-O_w bond of 293 pm and thus is classified as four-coordinate.

Surface solvation effects were approximately included in our models by adding about a water monolayer on the (001) surface of beidellite. For outer-sphere complexes we obtained again four- and five-coordinate species which hydrolyzed, but also a stable non-hydrolyzed species. Energy differences between these species were 10 kJ mol⁻¹ at most. Thus, all these species may be present on the (001) surface of beidellite. As for uranyl on kaolinite (Section 4.2.2) we also modeled an outer-sphere complex, separated by two shells of water molecules from the surface. Also for this species we observed hydrolysis and calculated geometry parameters similar to the outer-sphere complexes in direct contact with the surface. Interestingly, this more distantly adsorbed outer sphere species is ~60 kJ mol⁻¹ less stable than the outer-sphere species close to the surface. This result is no surprise as moving an uranyl outer-sphere complex away from the surface of a negatively charged mineral corresponds to a separation of charge.

Adsorption of uranyl(VI) on edge surfaces of pyrophyllite

The basal (001) surface is prevalent for crystallites of 2:1 clay minerals like pyrophyllite or beidellite. In addition, there are edge surfaces which exhibit unsaturated O centers that deprotonate at near neutral pH, creating negatively charged adsorption sites for actinide ions. They are assumed to be responsible for adsorption on 2:1 clay minerals at elevated pH values of solution [194,195,198,215]. There are several EXAFS experiments on uranyl adsorption on montmorillonite which show inner-sphere adsorption on edge surfaces at pH 5–8 [194,195,198,215]. We studied uranyl adsorption on (010) and (110) surfaces of pyrophyllite [210] and the (010) surface of beidellite (see below).

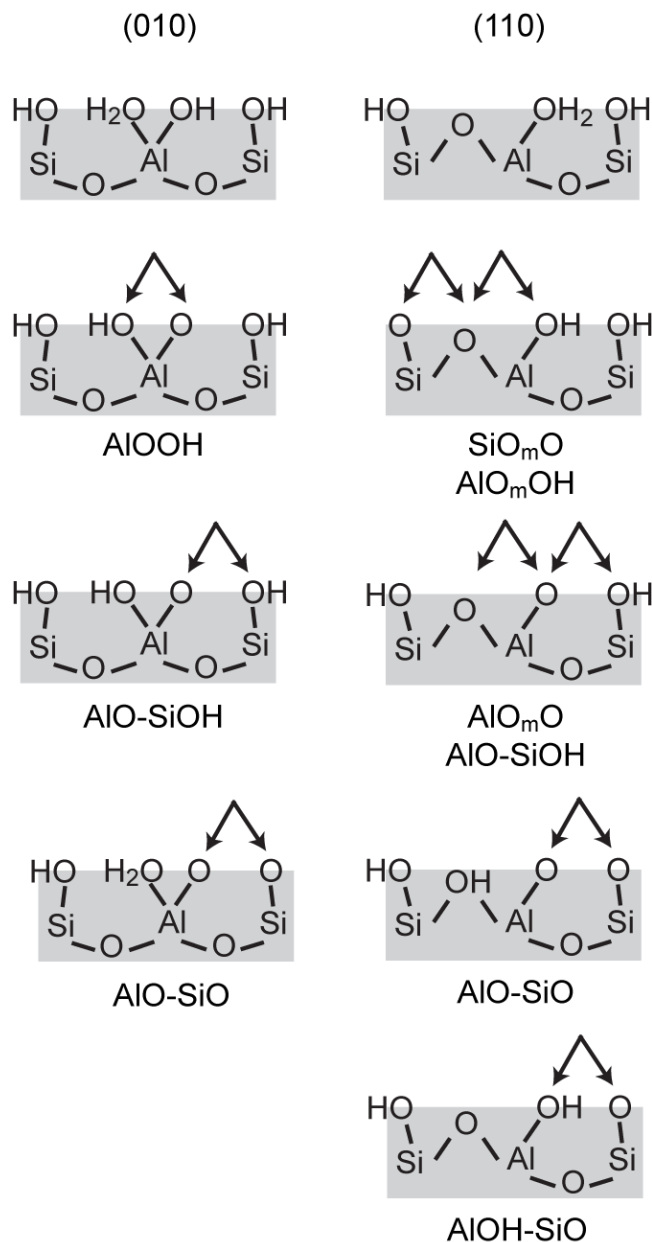


Figure 14. Adsorption sites on the (010) and (110) edge surfaces of pyrophyllite.

The structures of the (010) and (110) surfaces were created by cutting the pyrophyllite bulk along the weakest bonds and preserving the coordination numbers of Al and Si [210]. We examined only inner-sphere bidentate adsorption complexes on doubly deprotonated sites ($q = -2 e$) on the solvated edge surfaces of pyrophyllite [210] (Fig. 14). The (010) surface of pyrophyllite exhibits aluminol AlOOH sites and mixed AIO-SiO(H) sites. The (110) surface shows a larger variety of sites: aluminol sites AlO_mO(H), silanol sites SiOO, and mixed sites AIO(H)-SiO(H) (Fig. 14). The aluminol sites on the (110) surface differ from the aluminol sites of the (010) surface as the former include mixed O_m centers bound to Si and Al ions, while the latter are formed by O centers bound to Al only.

The adsorption complexes on mixed sites of pyrophyllite edge surfaces converged to 4-coordinated uranyl. The complexes on aluminol and silanol sites kept coordination

Table 19. Calculated structural parameters^a (in pm) and adsorption energies (in kJ mol⁻¹) of more favorable adsorption complexes of uranyl on solvated (010) and (110) surfaces of pyrophyllite. Experimental data for montmorillonite are given for comparison.

Site	U-O _t	U-O _{surf}	U-O _w	U-O _{eq}	U-Al/Si	ΔE _{form}
[UO ₂ (H ₂ O) ₂₀] ²⁺	183			240		
(110)						
AlO _m O	185	211/239	245/247/253	240	328	137
AlO _m OH	182	233/243	229 ^b /243/252	240	345	156
SiO _m O	181	231/240	246/247/262	245	302	198
AlOH-SiO	183	211/230	244/256	235	389/359	225
(010)						
AlO-SiO	185	211/225	243/245	231	362/340	149
AlOOH-SiOH ^c	185	208/252/261	245/257	245	327/349	210
Exp.						
UO ₂ ²⁺ solv. ^d	176			241 (5)		
pH 5 ^e	177			237 (5.7)	344	
pH 6.6 ^f	179	229 (2.1)	247 (2.1)	238 (4.2)	331	
pH 7 ^g	180	232 (2.8)	248 (2.1)	239 (4.9)	342	

(a) U-O_t – uranyl bond, U-O_{surf} – U bonds to the surface O, U-O_w – uranyl bonds to aqua ligands, U-O_{eq} – average equatorial uranyl-ligand bond, U-Al/Si – distance to surface Al/Si centers. (b) Bond length to OH ligand formed due to uranyl hydrolysis on the surface. (c) Tridentate coordination. (d) Data for solvated uranyl ion, Ref. 29. (e) Ref. 194. (f) Ref. 198. (g) Ref. 215. Experimental coordination numbers are given in parentheses.

number 5. This result can be rationalized by the rather large O_s-U-O_s angle, ~100°, of these sites, restricting the space for aqua ligands of uranyl [210]. In contrast to kaolinite, the adsorption on pyrophyllite leads less often to hydrolysis of adsorbed uranyl. Only one complex on the AlO_mOH site hydrolyzed (Table 19) [210].

Table 19 shows optimized structural parameters together with the complex formation energies for more favorable adsorption complexes on both surfaces [210]. Adsorption complexes on aluminol sites are most favorable on the (110) surface of pyrophyllite. Interestingly, uranyl adsorption on the (010) surface is favored at mixed AlO-SiO sites. We compared the trends for U-O_t and U-O_{eq} bond lengths for the solvated uranyl ion and the adsorbed uranyl ion, both observed in EXAFS [29,194,195,198,215] for montmorillonite and calculated with our models of pyrophyllite [210]. As proper reference, we optimized solvated uranyl with 20 water molecules, 5 of which modeled the first solvation shell, and another 15 were placed in the second solvation shell, as also the surface complexes included water molecules of the second shell. The U-O_t bond converged to 183 pm, and U-O_{eq} to 240 pm (Table 19). Adsorbed uranyl exhibits slightly elongated U-O_t values and shorter or similar U-O_{eq} values compared to a solvated uranyl ion at preferred sites. Similar trends are observed in experiment (Table 19). The calculated U-Al/Si distances of preferred

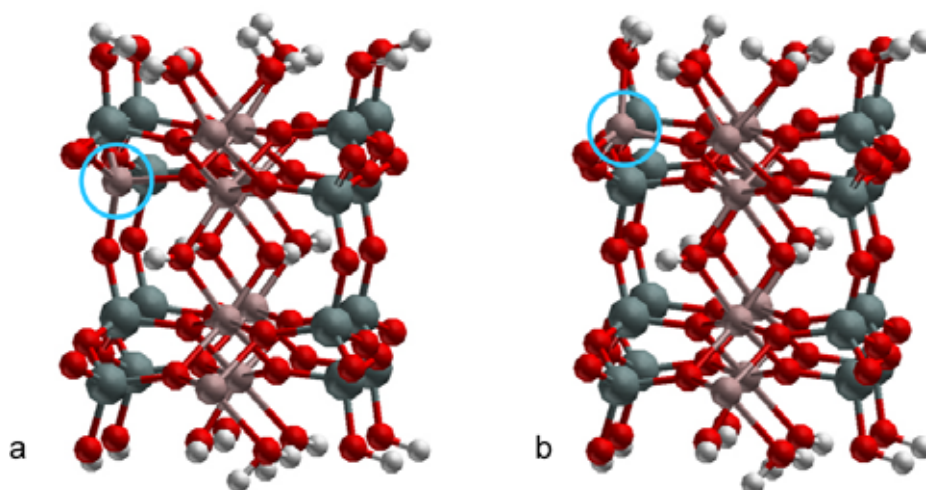


Figure 15. Structures of model beidellite (010) surfaces: (a) Defect Si^{4+} below the surface (modell A); (b) defect on the surface (model B).

complexes, 328–345 pm, fall in the range of the measured values, 331–344 pm [194,195,198,215].

The calculations showed that uranyl preferably adsorbs as five-coordinated complex on aluminol sites of the (110) surface of pyrophyllite, and as four-coordinated complex on mixed sites of the (010) surface [210]. This is at variance with the earlier assumption that uranyl adsorbs on Al (or Fe) octahedral sites [194,198]. It also shows that the adsorbed species on different edge facets may be characterized by different coordination numbers of uranyl. This is indirectly supported by fluorescence spectroscopy [216] as complexes with different CN of uranyl produce discernible spectra. We found several adsorption complexes on pyrophyllite that are close in energy and yield a distribution of key structural parameter similar to the corresponding EXAFS data. The most notable discrepancy between our computational results and EXAFS data is the coordination number of uranyl. While EXAFS determined CN mainly between 5 to 6 together with shorter U-O_{eq} values compared to solvated uranyl (CN = 5), we calculated for CN = 5 a tendency to elongated U-O_{eq} distances and for CN = 4 to shorter values than for solvated uranyl.

Adsorption of uranyl(VI) on edge surfaces of beidellite

(010) edge surfaces of a model 2:1 clay mineral with beidellitic substitution are constructed starting with the monoclinic structure of pyrophyllite as also other charged clay minerals show a monoclinic unit cell. Substitutions $\text{Si}^{4+} \rightarrow \text{Al}^{3+}$ are introduced below the surface layer (model A) or in the surface layer (model B) (Fig. 15). The charge of the substitutional defect is compensated by a proton attached to an aluminol group on the surface. In nature also short-range charge compensation is expected which either may be due to an adsorbed alkali ion or, at acidic conditions, due to a proton. Uranyl adsorption on these surfaces was examined at exemplary twofold deprotonated sites to achieve an overall neutral system. On pyrophyllite these are the most favored mixed site AlO-SiO and the AlOOH site (Table 21).

Table 20. Calculated structural parameters^a (in pm) and complex formation energies (in kJ mol⁻¹) of adsorption complexes of uranyl on (010) edge surfaces of pyrophyllite and model beidellite.

Site	U-O _t	U-O _{surf}	U-O _w	U-O _{eq}	U-Al/Si	ΔE _{form}
[UO ₂ (H ₂ O) ₂₀] ²⁺	183			240		
Pyrophyllite						
AlOOH	187	203/240	243/250/270	241	325	137
AlO-SiO	185	205/228	253/255	235	387/350	93
Beidellite^b						
A AlOHOH	184	222/236	241/245/257	240	345	155
AlO-SiOH	186	199/262	246/265/271	249	386/390	84
B AlOHOH	185	229/243	222 ^c /244/250	238	348	115
AlO-AlOH	187	201/244	248/265/274	246	386/390	23

(a) U-O_t – uranyl bond, U-O_{surf} – U bonds to the surface O, U-O_w – uranyl bonds to aqua ligands, U-O_{eq} – average equatorial uranyl-ligand bond, U-Al/Si – distance to surface Al/Si centers. (b) Modell A: Substitution below the surface; Modell B: Substitution on the surface (c) Bond length to OH ligand.

On the beidellitic model A, these sites change to AlO-SiOH and AlOHOH due to the proton compensating the defect charge. In view of the substitution at the surface the mixed site in model B corresponds to AlO-AlOH.

On the (010) edge surfaces of both models of beidellite uranyl adsorption at the mixed site AlO-SiOH and the corresponding site AlO-AlOH is more stable than at the aluminol sites, as already calculated for the (010) surface of pyrophyllite (Table 19). For the subsurface substitution in model A, uranyl is adsorbed slightly more strongly, by ~10 kJ mol⁻¹, at the favorite mixed site AlO-SiOH compared to pyrophyllite while substitution on the surface stabilized this surface complex by 70 kJ mol⁻¹. At the aluminol site a slight destabilization has to be noted for model A while the complex formation energies decreases by ~20 kJ mol for model B. Thus, a marked effect on the stability of the surface complex is only calculated when the substitutional defect lies close to the surface (Table 20).

Structure parameters seem to reflect more the effect of the extra charge compensating proton than that of the substitution. On pyrophyllite at the AlOOH site, a short contact of 203 pm to AlO and a longer one to AlOH of 240 pm is calculated. Thus, AlOHOH sites of the model beidellite show two longer contacts to oxygen atoms of the OH groups of 222-243 pm (Table 20). These bonds to the surface are longer on average; concomitantly, also the U-Al distance increases from 325 pm on pyrophyllite to 345 pm and 348 pm on the two model beidellite surfaces. For the mixed site AlO-SiO a shorter bond to the AlO group of 205 pm and a longer one of 228 pm to the SiO group is calculated for pyrophyllite (Table 20). For the corresponding sites AlO-SiOH and AlO-AlOH on the model beidellite again short bonds of ~200 pm to the AlO group are determined, while the bonds to the protonated groups

SiOH and AlOH are considerably elongated, to 262 pm and 244 pm, respectively. Again, the U-Al and U-Si distances follow these changes of the bonds to surface oxygen atoms. The distance U-Al remains essentially unchanged on going from pyrophyllite to model beidellite while U-Si elongates by 40 pm (Table 20).

Interesting results are calculated for the commonly measured parameter $U-O_{eq}$. For pyrophyllite a typical value of 240 pm is obtained for the AlOOH site and a smaller one, 235 pm, for the mixed site as a result of the reduced coordination, 4, of uranyl (Table 20). For the model beidellite the complexes at the AlOHOH site again show $U-O_{eq}$ values typical for coordination number 5 while the mixed sites yield larger values of 246 pm and 249 pm.

4.3 Methodic topics

Modeling solvation effects is a key aspect when addressing the aqueous chemistry of actinides by computational methods. Quantifying solvation effects not only determines the accuracy of the results, but to a considerable extent also the computational effort. In the studies of solvated complexes reported above, the COSMO variant of the polarizable continuum model (PCM) approach [65,217] was applied throughout to account for long-range solvation effects. In PCM methods, the reaction field of the bulk solvent is represented typically via a charge density on the surface of a cavity around the solute. That cavity is constructed of sections of atom-centered spheres. The surface of this cavity is partitioned into spherical triangles (tessellation); to each such triangle a (point) charge is assigned as an element of the surface charge density. In the course of geometry optimizations, the cavity surface changes and spherical triangles, together with their assigned point charges, may not only move, but also appear or disappear discontinuously. Our experience showed, especially when carrying out geometry optimizations, that the well established GEPOL algorithm [218,219], used until now to construct the cavity, leads to discontinuous changes of the positions of the point charges on the cavity surface which implies small, yet noticeable discontinuities of the potential energy surface, hampering the optimization procedure. To achieve a smooth potential energy surface as function of the solute geometry, a weighting of the point charges by their distance to neighboring spheres has been implemented, following the recently developed “fixed point charge with variable area” algorithm (FIXPVA) [220]. This algorithm is numerically much more stable and furnishes more accurate components due to solvation of the forces acting on the atoms of the solute. Ultimately, one observes a more stable and more efficient optimization procedure. As the FIXPVA procedure tends to underestimate the solvent excluded surface around a solute [220], implying an underestimation of solvation energies, it seemed appropriate to adjust the scaling factor of the atomic radii used to construct the cavity. In this way slightly improved values of the solvation energies were obtained from a numerically more stable optimization procedure (Table 21). For a test set of 7 cations and 8 anions, the deviation

Table 21. Solvation free energies calculated with the GEPOL and the FIXPVA tessellation schemes. Experimental values are shown for comparison. Energies in kJ mol^{-1} .

	GEPOL	FIXPVA	Exp.
H_2O	28	31	26^{a}
$[\text{H}_3\text{O}]^+$	378	377	427^{b}
OH^-	378	400	430^{c}
CH_3COOH	22	25	25^{a}
$[\text{CH}_3\text{COO}]^-$	274	286	365^{c}
UO_2^{2+}	1249	1345	$1347^{\text{d}}, 1682^{\text{e}}$

(a) Ref. 222, (b) Ref. 223, (c) Ref. 223, (d) Ref. 224, (e) Ref. 225

from experimental solvation energies was reduced by $\sim 30\%$, while essentially no change was observed for neutral species.

As an alternative to the rather accurate periodic plane-wave and PAW approach (software VASP, see Section 2) used in this project, the potential of an efficient Γ -point periodic plane-wave approach together with norm-conserving pseudopotentials as implemented in the software NWChem [226] was explored. Results of density functional GGA calculations for the uranyl(VI) aqua complex, kaolinite bulk as well as uranyl adsorbed at the AlOO site of the (001) Al(o) surface of kaolinite agreed well with the corresponding VASP calculations. As a trend, the uranyl bond was underestimated by ~ 3 pm in all calculations, in agreement with other computational studies [89] while ligand bonds were reproduced more accurately. No gain in computational efficiency was observed for NWChem compared to VASP for small test systems. Yet, we noted a more favorable scaling with increasing numbers of processors which makes this software interesting for large systems and dynamical simulations.

To examine and partially correct self-interaction artifacts of DF LDA and GGA approaches in calculations of actinide complexes, we implemented the DFT+U method in our software ParaGauss [227] and parameterized it for uranium [136]. In this empirical approach a Hubbard like repulsion term is added to the interaction of f-electrons, favoring localized f-orbitals. U parameters of 1-2 eV have been determined to be reasonable for uranium by comparison of calculated to experimental ionization potentials of UO and UO_2 . Self-interaction artifacts have been characterized for uranyl(VI) [136] and its monohydroxide [135] (Section 4.1.1). Our results demonstrate that these artifacts are more pronounced in the gas phase than in solution and that the DFT+U approach removes these artifacts to a considerable extent.

5 Summary

A detailed mechanistic understanding of actinide chemistry under environmental conditions is an important prerequisite for modeling and predicting speciation, distribution, and migration of actinides in the environment. These issues are of key importance in safety

considerations of long-term storage of highly radioactive waste in underground repositories. In this project quantum chemical computational were used to study the chemistry of actinides in solution and at clay mineral surfaces to complement pertinent experimental work. Quantum chemical studies, together with spectroscopic experiments, offer the unique opportunity to gain insight at the atomic level and thus are useful for identifying species and developing mechanistic models of actinide chemistry under pertinent conditions. Two relevant aspects of actinide environmental chemistry have been treated in this project: complexation in aqueous solution by inorganic and organic ligands and the interaction of actinide ions and complexes with surfaces of clay minerals.

Complexes of actinyl ions with small organic ligands have been examined as models of actinyl complexation by functional groups of humic substances with the goal to characterize how groups beyond carboxyl functions contribute to the ability of humic substances to form complexes with metal ions. In agreement with experimental studies we showed that sulfonate, amine, and pyridine groups are not important for actinyl complexation in comparison to the prevailing carboxyl groups. A study of ternary hydroxoacetate complexes of uranyl(VI) revealed that these complexes should be less stable than binary acetate complexes, in contrast to the interpretation of measured values of pertinent complexation constants. Thus, complexation with carboxyl functional groups at neutral to basic conditions in competition with hydrolysis raises still some questions. For the exemplary case of uranyl complexation with an acetate ligand we demonstrated that the weak increase in the complexation constant with increasing temperature has to be ascribed to a bidentate isomer and that the equilibrium between mono- and bidentate isomers of uranyl acetate is influenced by temperature. This result also showed that a fundamental understanding of actinide complexation needs to take into account the equilibrium between various isomers of a complex of given composition, a topic studied only rarely until now. Preliminary examination of the reaction mechanism of neptunyl(V) with acetate supports this view. By model calculations on Am(III) aqua and monoacetate complexes we contributed to the understanding of this rarely treated element. Finally we examined the first hydrolysis products of U(VI), U(IV), and Np(IV), providing structural and energetic parameters for these experimentally not easily accessible species.

Quantum chemical modeling of actinide adsorption at mineral surfaces was pioneered by our group and detailed studies of actinyl adsorption on clay minerals surfaces have been carried out in this project. Our results for basal and edge surfaces of kaolinite confirm the interpretation of pertinent EXAFS experiments regarding bidentate adsorption complexes of uranyl(VI). However, detailed comparison of geometries and energies revealed that monodentate coordination to the surface can not be excluded. Also, we were unable to identify clearly preferred sites for adsorption, thus various adsorption complexes may coexist.

Besides adsorbed uranyl, we also obtained uranyl hydroxide as adsorbate in our model calculations.

Comparison of structural parameters to available experimental data showed that the current interpretation of measured U-O distances to ligands and to the surface should be extended. Shorter U-O bonds have been ascribed to bonds to the surface while longer ones were ascribed to aqua ligands. We calculated also rather short bonds of U to hydroxide ligands and relatively long ones, comparable to bonds to aqua ligands, to protonated surface groups. Similar results as for kaolinite were obtained for adsorbed uranyl on edge surfaces of pyrophyllite and a model beidellite. While aluminol sites are preferred for kaolinite and the (110) edge surface of pyrophyllite, we determined a mixed aluminol-silanol site to be favorable on the (010) edge surface of pyrophyllite. Thus, preferred adsorption sites seem to depend on the exposed surface. Examination of the basal surface of beidellitic substituted pyrophyllite provided another example of a surface of a clay mineral where several adsorption complexes may coexist, as we calculated rather small differences in adsorption energies for inner- and outer-sphere complexes of uranyl.

All these examples demonstrated that actinide-clay adsorption systems are rather complex at the atomic level, featuring a variety of surface species which are not easily discriminated. Further computational as well as spectroscopic studies are necessary to develop a mechanistic model at environmental conditions to construct a basis for the interpretation of experimental results. Especially infrared spectroscopy and resonant anomalous X-ray reflectivity techniques will be helpful in this regard, besides quantum chemical studies, to complement available microscopic information.

6 Publications Resulting from this Project

- 1) R. Ramakrishnan, A. V. Matveev, S. Krüger, N. Rösch; Self-Interaction Artifacts on Structural Features of Uranyl Monohydroxide from Kohn-Sham Calculations. *Theor. Chem. Acc.* 130, 361-369 (2011).
- 2) O. Zakhariyeva, A. Kremleva, S. Krüger, N. Rösch; Uranyl Complexation by Monodentate Nitrogen Donor Ligands. A Relativistic Density Functional Study, *Int. J. Quantum Chem.* 211, 2045-2053 (2011).
- 3) A. Kremleva, S. Krüger, N. Rösch; Uranyl Adsorption at (010) Edge Surfaces of Kaolinite. A Density Functional Study, *Geochim. Cosmochim. Acta* 75, 706-718 (2011).
- 4) R. Ramakrishnan, A. V. Matveev, N. Rösch; Effects of the Self-Interaction Error in Kohn-Sham Calculations: A DFT+U Case Study on Penta-Aqua Uranyl(VI), *Comp. Theor. Chem.* 963, 337-343 (2011).
- 5) R. Ramakrishnan, The DFT+U Method in the Framework of the Parallel Density Functional Code ParaGauss, Dissertation, Technische Universität München, 2011.
- 6) A. Kremleva, S. Krüger, N. Rösch; Quantum Chemical Modeling of Uranyl Adsorption on Mineral Surfaces, *Radiochim. Acta* 98, 635-646 (2010).

- 7) B. Martorell, A. Kremleva, S. Krüger, N. Rösch; Density Functional Model Study of Uranyl Adsorption on the Solvated (001) Surface of Kaolinite, *J. Phys. Chem. C* 114, 13287–13294 (2010).
- 8) F. Schlosser, L. V. Moskaleva, A. Kremleva, S. Krüger, N. Rösch; Comparative Density Functional Study of the Complexes $[\text{UO}_2(\text{CO}_3)_3]^{4-}$ and $[(\text{UO}_2)_3(\text{CO}_3)_6]^{6-}$ in Aqueous Solution, *Dalton Trans.* 5705-5712 (2010).
- 9) R. S. Ray, S. Krüger, N. Rösch; Ternary Uranyl Hydroxo Complexes: A Computational Study of Structure, Energetics, and Stability Constants, *Inorg. Chim. Acta* 363, 263-269 (2010).
- 10) R. S. Ray, S. Krüger, N. Rösch; Uranyl Monocarboxylates of Aromatic Acids: A Density Functional Model Study of Uranyl Humate Complexation, *Dalton Trans.* 3590–3598 (2009).
- 11) A. Kremleva, S. Krüger, N. Rösch; Role of Aliphatic and Phenolic Hydroxyl Groups in Uranyl Complexation by Humic Substances, *Inorg. Chim. Acta* 362, 2542–2550 (2009).
- 12) A. Kremleva, Environmental Chemistry of Uranyl: A Relativistic Density Functional Study on Complexation with Humic Substances and Sorption at Kaolinite, Dissertation, Technische Universität München, 2009.
- 13) R. S. Ray, A Relativistic Density Functional Study of Uranyl Hydrolysis and Complexation by Carboxylic Acids in Aqueous Solution, Dissertation, Technische Universität München, 2009.
- 14) Y. Zhang, A Density Functional Study of Uranyl Complexation by Sulfur Containing Humic Acids in Aqueous Solution, Master Thesis, Technische Universität München, 2009.
- 15) A. Kremleva, S. Krüger, N. Rösch; Density Functional Model Studies of Uranyl Adsorption on (001) Surfaces of Kaolinite, *Langmuir* 24, 9515-9524 (2008).
- 16) N. Rösch, S. Krüger; Plane Wave Density Functional Model Studies of Chemistry at Surfaces, in: High Performance Computing in Science and Engineering, Transactions of the Third Joint HLRB and KONWIHR Result and Status Workshop, Garching 2007, S. Wagner, M. Steinmetz, A. Bode, M. Brehm (eds.), Springer: Berlin, 2008, pp. 173-186.
- 17) C. Chiu, Density Functional Studies on Uranyl Complexation by Amino Acids, Bachelor Thesis, Technische Universität München, 2008.

Further publications on results of this project and follow-up studies are in preparation.

7 References

- [1] J. J. Katz, G. T. Seaborg, L.R. Morss (Eds.), *The Chemistry of the Actinide Elements*, 2. ed., Chapman and Hall, New York, 1986.
- [2] L. R. Morss, N. M. Edelstein, J. Fuger (Eds.), *Actinide and Transactinide Elements*, 3. ed., Springer, Dordrecht, 2006.
- [3] Z. Szabo, T. Toraishi, V. Vallet, I. Grenthe, *Coord. Chem. Rev.* 250 (2006) 784.
- [4] Ref. 2, vol. 4, chap. 22.
- [5] D. L. Clark, D. E. Hobart, M. P. Neu, *Chem. Rev.* 95 (1995) 25.

- [6] K. H. Lieser, *Radiochim. Acta* 70/71 (1995) 355.
- [7] R. J. Silva, H. Nitsche, *Radiochim. Acta* 70/71 (1995) 377.
- [8] Ref. 2, vol. 4, chap. 23.
- [9] F. J. Stevenson, *Humus Chemistry*, 2. ed., Wiley, New York, 1994.
- [10] K. L. Nash, J. M. Cleveland, T. F. Rees, *J. Environ. Radioact.* 7 (1988) 131.
- [11] G. R. Choppin, *Radiochim. Acta* 44/45 (1988) 23.
- [12] M. A. Denecke, S. Pompe, T. Reich, H. Moll, M. Bubner, K. H. Heise, R. Nicolai, H. Nitsche, *Radiochim. Acta* 79 (1997) 151.
- [13] S. Sachs, K. Schmeide, T. Reich, V. Brendler, K. H. Heise, G. Bernhard, *Radiochim. Acta* 93 (2005) 17.
- [14] K. Schmeide, T. Reich, S. Sachs, V. Brendler, K. H. Heise, G. Bernhard, *Radiochim. Acta* 93 (2005) 187.
- [15] M. A. Denecke, T. Reich, S. Pompe, M. Bubner, K. H. Heise, H. Nitsche, P. G. Allen, J. J. Bucher, N. M. Edelstein, D. K. Shuh, *J. Phys. IV* 7 C2 (1997) 637.
- [16] S. Pompe, K. Schmeide, M. Bubner, G. Geipel, K. H. Heise, G. Bernhard, H. Nitsche, *Radiochim. Acta* 88 (2000) 553.
- [17] K. Schmeide, S. Sachs, M. Bubner, T. Reich, K. H. Heise, G. Bernhard, *Inorg. Chim. Acta* 351 (2003) 133.
- [18] S. Sachs, G. Bernhard, *Radiochim. Acta* 93 (2005) 141.
- [19] S. Pompe, M. Bubner, M. A. Denecke, T. Reich, A. Brachmann, G. Geipel, R. Nicolai, K. H. Heise, H. Nitsche, *Radiochim. Acta* 74 (1996) 135.
- [20] M. A. Denecke, *Coord. Chem. Rev.* 250 (2006) 730.
- [21] R. Steudtner, K. Müller, K. Schmeide, S. Sachs, G. Bernhard, *Dalton Trans.* 40 (2011) 11920.
- [22] R. N. Collins, T. Saito, N. Aoyagi, T. E. Payne, T. Kimura, T. D. Waite, *J. Env. Qual.* 40 (2011) 731.
- [23] S. Pompe, A. Brachmann, M. Bubner, G. Geipel, K. H. Heise, G. Bernhard, H. Nitsche, *Radiochim. Acta* 82 (1998) 89.
- [24] V. Vallet, Z. Szabó, I. Grenthe, *Dalton Trans.* (2004) 3799.
- [25] V. Vallet, P. Macak, U. Wahlgren, I. Grenthe, *Theor. Chem. Acc.* 115 (2006) 145.
- [26] Ref. 2, vol. 3, chap. 17.
- [27] H. Moll, G. Geipel, T. Reich, G. Bernhard, T. Fanghänel, I. Grenthe, *Radiochim. Acta* 91 (2003) 11.
- [28] J. Jiang, L. Rao, P. Di Bernardo, P. L. Zanonato, A. Bismondo, *J. Chem. Soc., Dalton Trans.* 8(2002) 1832.
- [29] P. G. Allen, J. J. Bucher, D. K. Shuh, N. M. Edelstein, T. Reich, *Inorg. Chem.* 36 (1997) 4676.
- [30] T. Schäfer, R. Michel, F. Claret, *Journal of Physics: Conf. Series* 186 (2009) 012095.
- [31] T. Schäfer, R. Michel, F. Claret, T. Beetz, R. Wirick, C. Jacobsen, *J. Electron Spec. Rel. Phenomena* 170 (2009) 49.
- [32] P. Benes, K. Kratzer, S. Vlckova, E. Sebestova, *Radiochim. Acta* 82 (1998) 367.
- [33] A. Krepelova, S. Sachs, G. Bernhard, *Radiochim. Acta* 94 (2006) 825.
- [34] R. Kautenburger, H. P. Beck, *ChemSusChem* 1 (2008) 295.

- [35] C. Joseph, K. Schmeide, S. Sachs, V. Brendler, G. Geipel, G. Bernhard, *Chem. Geol.* 284 (2011) 240.
- [36] M. H. Lee, E. C. Jung, K. Song, Y. H. Han, H. S. Shin, *J. Radioanal. Nuc. Chem.* 287 (2011) 639.
- [37] E. A. Jenne (Ed.), *Adsorption of Metals by Geomedia: Variables, Mechanisms and Model Applications*, Academic Press, United Kingdom, 1998.
- [38] M. Barnett, D. Kent (Eds.), *Adsorption of Metals by Geomedia II: Variables, Mechanisms, and Model Applications*, Elsevier, USA, 2008.
- [39] H. Geckeis, T. Rabung, *J. Cont. Hydrol.* 102 (2008) 187.
- [40] K. Choi, J. W. Park, *Geoscience J.* 9 (2005) 53.
- [41] S. S. Lee, P. Fenter, C. Park, N. C. Sturchio, K. L. Nagy, *Langmuir* 26 (2010) 16647.
- [42] P. Fenter, S. S. Lee, C. Park, L. Soderholm, R. E. Wilson, O. Schwindt, *Geochim. Cosmochim. Acta* 74 (2010) 6984.
- [43] A. Kremleva, S. Krüger, N. Rösch, *Radiochim. Acta* 98 (2010) 635.
- [44] G. Kresse, J. Furthmüller, *Phys. Rev. B* 54 (1996) 11169.
- [45] G. Kresse, J. Hafner, *Phys. Rev. B* 49 (1994) 14251.
- [46] G. Kresse, J. Hafner, *Phys. Rev. B* 47 (1993) 558.
- [47] G. Kresse, J. Hafner, *Phys. Rev. B* 48 (1993) 13115.
- [48] G. Kresse, J. Furthmüller, *Comput. Mater. Sci.* 6 (1996) 15.
- [49] G. Kresse, D. Joubert, *Phys. Rev. B* 59 (1999) 1758.
- [50] A. H. MacDonald, S. H. Vosko, *J. Phys. C* 12 (1979) 2977.
- [51] W. Koch, M. C. Holthausen, *A Chemist's Guide to Density Functional Theory*, 2. ed. Wiley-VCH, Weinheim, 2000.
- [52] T. Ziegler, *Chem. Rev.* 91 (1991) 651.
- [53] J. P. Perdew, A. Zunger, *Phys. Rev. B* 23 (1981) 5048.
- [54] J. P. Perdew, Y. Wang, *Phys. Rev. B* 45 (1992) 13244.
- [55] L. V. Moskaleva, V. A. Nasluzov, N. Rösch, *Langmuir* 22 (2006) 2141.
- [56] F. Schlosser, S. Krüger, N. Rösch, *Inorg. Chem.* 45 (2006) 1480.
- [57] A. Kremleva, S. Krüger, N. Rösch, *Inorg. Chim. Acta* 362 (2009) 2542.
- [58] R. S. Ray, S. Krüger, N. Rösch, *Dalton Trans.* (2009) 3590.
- [59] N. Rösch, S. Krüger, M. Mayer, V. A. Nasluzov, *The Douglas-Kroll-Hess Approach to Relativistic Density Functional Theory: Methodological Aspects and Applications to Metal Complexes and Clusters*, in: *Recent Developments and Applications of Modern Density Functional Theory*, J. M. Seminario (Eds.), *Theoretical and Computational Chemistry Series*, vol. 4, Elsevier, Amsterdam, 1996, p. 497.
- [60] N. Rösch, A. V. Matveev, V. A. Nasluzov, K. M. Neyman, L. Moskaleva, S. Krüger, *Quantum Chemistry with the Douglas-Kroll-Hess Approach to Relativistic Density Functional Theory: Efficient Methods for Molecules and Materials*, in: *Relativistic Electronic Structure Theory-Applications*, P. Schwerdtfeger (Ed.) *Theoretical and Computational Chemistry Series*, Elsevier, Amsterdam, 2004, p. 656.
- [61] T. Belling, T. Grauschopf, S. Krüger, F. Nörtemann, M. Staufer, M. Mayer, V. A. Nasluzov, U. Birkenheuer, A. Hu, A. V. Matveev, A. M. Shor, M. Fuchs-Rohr, K. Neyman, D. I. Ganyushin, T. Kerdcharoen, A. Woiterski, A. Gordienko, S. Majumder, N. Rösch, *ParaGauss, Version 3.0*, Technische Universität München, 2004.

- [62] S. H. Vosko, L. Wilk, M. Nusair, *Can. J. Chem.* 58 (1980) 1200.
- [63] A. D. Becke, *Phys. Rev. A* 38 (1988) 3098.
- [64] J. P. Perdew, *Phys. Rev. B* 33 (1986) 8822.
- [65] M. S. K. Fuchs, A. M. Shor, N. Rösch, *Int. J. Quantum Chem.* 86 (2002) 487.
- [66] G. Schreckenbach, G. A. Shamov, *Accounts Chem. Res.* 43 (2010) 19.
- [67] V. Vallet, I. Grenthe, *Comptes Rendus Chimie* 10 (2007) 905.
- [68] F. Ruiperez, C. Danilo, F. Real, J. P. Flament, V. Vallet, U. Wahlgren, *J. Phys. Chem. A* 113 (2009) 1420.
- [69] B. A. Hess (Ed.), *Relativistic Effects in Heavy Element Physics and Chemistry*, Wiley, Chichester, 2003, chap. 3.
- [70] X. Cao, M. Dolg, *Coord. Chem. Rev.* 250 (2006) 900.
- [71] S. O. Odoh, G. Schreckenbach, *J. Phys. Chem. A* 114 (2010) 1957.
- [72] E. van Lenthe, E. J. Baerends, J. G. Snijders, *J. Chem. Phys.* 99 (1993) 4597.
- [73] G. A. Shamov, G. Schreckenbach, *J. Phys. Chem. A* 109 (2005) 10961.
- [74] J. Su, L. Zhang, W. H. E. Schwarz, J. Li, *Inorg. Chem.* 50 (2011) 2082.
- [75] D. Paez-Hernandez, J. A. Murillo-Lopez, R. Arratia-Perez, *J. Phys. Chem. A* 105 (2011) 8997.
- [76] L. V. Moskaleva, S. Krüger, A. Spörl, N. Rösch, *Inorg. Chem.* 43 (2004) 4080.
- [77] M. Garcia-Hernandez, C. Lauterbach, S. Krüger, A. Matveev, N. Rösch, *J. Comp. Chem.* 23 (2002) 834.
- [78] C. Clavaguéra-Sarrio, V. Vallet, D. Maynau, C. J. Marsden, *J. Chem. Phys.* 121 (2004) 5312.
- [79] E. Fromager, V. Vallet, B. Schimmelpfennig, P. Macak, T. Privalov, U. Wahlgren, *J. Phys. Chem. A* 109 (2005) 4957.
- [80] J. Tomasi, B. Mennucci, R. Cammi, *Chem. Rev.* 105 (2005) 2999.
- [81] C. J. Cramer, D. G. Truhlar, *Acc. Chem. Res.* 41 (2008) 760.
- [82] M. Bühl, G. Wipff, *Chem. Phys. Chem.* 12 (2011) 3095.
- [83] Z. Cao, K. Balasubramanian, *J. Chem. Phys.* 123 (2005) 114309.
- [84] K. E. Gutowski, D. A. Dixon, *J. Phys. Chem. A* 110 (2006) 8840.
- [85] B. Siboulet, C. J. Marsden, P. Vitorge, *Chem. Phys.* 326 (2006) 289.
- [86] P. Wahlin, B. Schimmelpfennig, U. Wahlgren, I. Grenthe, V. Vallet, *Theor. Chem. Acc.* 124 (2009) 377.
- [87] V. Vallet, U. Wahlgren, B. Schimmelpfennig, H. Moll, Y. Szabó, I. Grenthe, *Inorg. Chem.* 40 (2001) 3516.
- [88] R. Car, M. Parrinello, *Phys. Rev. Lett.* 55 (1985) 2471.
- [89] P. Nichols, E. J. Bylaska, G. K. Schenter, W. de Jong, *J. Chem. Phys.* 128 (2008) 124507.
- [90] R. Atta-Fynn, E. J. Bylaska, G. K. Schenter, W. A. de Jong, *J. Phys. Chem. A* 115 (2011) 4665.
- [91] V. A. Cocalia, K. E. Gutowski, R. D. Rogers, *Coord. Chem. Rev.* 250 (2006) 755.
- [92] I. Infante, B. van Stralen, L. Vischer, *J. Comp. Chem.* 27 (2006) 1156.
- [93] Y. Hagiwara, M. Tateno, *J. Phys. Cond. Mat.* 22 (2010) 413101.

- [94] S. Difley, L.-P. Wang, S. Yeganeh, S. R. Yost, T. Van Voorhis, *Acc. Chem Res.* 43 (2010) 995
- [95] A. Genest, A. Woiterski, S. Krüger, A. Shor, N. Rösch, *J. Chem. Theory Comput.* 2 (2006) 47.
- [96] A. Shor, S. Krüger, N. Rösch, unpublished results.
- [97] I. Infante, L. Vischer, *J. Comp. Chem.* 25 (2004) 386.
- [98] R. Spezia, B. Siboulet, S. Abadie, R. Vuilleumier, P. Vitorge, *J. Phys. Chem. B* 115 (2011) 3560.
- [99] S. Tsushima, *J. Phys. Chem. B* 112 (2008) 7080.
- [100] A. Ikeda-Ohno, S. Tsushima, K. Takao, A. Rossberg, H. Funke, A. C. Scheinost, G. Bernhard, T. Yaita, C. Hennig, *Inorg. Chem.* 48 (2009) 11779.
- [101] S. O. Odoh, G. Schreckenbach, *J. Phys. Chem. A* 115 (2011) 14110.
- [102] X. Tan, M. Fang, X. Wang, *Molecules* 15 (2010) 8431.
- [103] L. V. Moskaleva, V. A. Nasluzov, N. Rösch, *Langmuir* 22 (2006) 2141.
- [104] H. Perron, C. Domain, J. Roques, R. Drot, E. Simoni, H. Catalette, *Inorg. Chem.* 45 (2006) 6568.
- [105] A. Kremleva, S. Krüger, N. Rösch, *Langmuir* 24 (2008) 9515.
- [106] B. Martorell, A. Kremleva, S. Krüger, N. Rösch, *J. Phys. Chem. C* 114 (2010) 13287.
- [107] A. Kremleva, S. Krüger, N. Rösch, *Geochim. Cosmochim. Acta* 75 (2011) 706.
- [108] E. Veilly, J. Roques, M.-C. Jodin-Caumon, B. Humbert, R. Drot, E. Simoni, *J. Chem. Phys.* 129 (2008) 244704.
- [109] J. Roques, E. Veilly, E. Simoni, *Int. J. Mol. Sci.* 10 (2009) 2633.
- [110] D. M. Sherman, C- L. Peacock, C. G. Hubbard, *Geochim. Cosmochim. Acta* 72 (2008) 298.
- [111] T. Hattori, T. Saito, K. Ispida, A. C. Scheinost, T. Tsuneda, S. Nagasaki, S. Tanaka, *Geochim. Cosmochim. Acta* 73 (2009) 5975.
- [112] R. Polly, B. Schimmelpfennig, R. Rabung, M. Flörsheimer, R. Klenze, H. Geckeis, , *Radiochim. Acta* 98 (2010) 627.
- [113] V. A. Glezakou, W. A. de Jong, *J. Phys. Chem. A* 115 (2011) 1257
- [114] L. C. Shuller, J. Poling, R. C. Ewing, U. Becker, *Geochim. Cosmochim. Acta* 72 (2008) A864.
- [115] C. Benzi, A. Kremleva, S. Krüger, N. Rösch, in preparation.
- [116] S. V. Churakov, *Geochim. Cosmochim. Acta* 71 (2007) 1130.
- [117] M. Flörsheimer, K. Kruse, R. Polly, A. Abdelmonem, B. Schimmelpfennig, R. Klenze, T. Fanghänel, *Langmuir* 24 (2008) 13434.
- [118] D. Tunega, M. H. Gerzabek, H. Lischka, *J. Phys. Chem. B* 108 (2004) 5930.
- [119] R. S. Ray, S. Krüger, N. Rösch, in preparation.
- [120] Ref. 2, vol. 1, chap. 5.10.2.
- [121] I. Grenthe, J. Fuger, R. J. M. Konigs, R. J. Lemire, A. B. Muller, C. Nguyen-Trung, H. Wanner, *Chemical Thermodynamics of Uranium*, vol. 1., Elsevier Science, North-Holland, Amsterdam, 1992.
- [122] V. Eliet, G. Bidoglio, N. Omenetto, L. Parma, I. Grenthe, *J. Chem. Soc., Faraday Trans.* 91 (1995) 2275.

- [123] P. L. Brown, *Radiochim. Acta* 90 (2002) 589.
- [124] F. Quiles, C. Nguyen-Trung, C. Carteret, B. Humbert, *Inorg. Chem.* 50 (2011) 2811.
- [125] P. J. Hay, R. L. Martin, G. Schreckenbach, *Phys. Chem. A.* 104 (2000) 6259.
- [126] M. Druchok, T. Bryk, M. Holovko, *J. Mol. Liq.* 120 (2005) 11.
- [127] M. Bühl, H. Kabrede, *ChemPhysChem.* 7 (2006) 2290.
- [128] K. I. M. Ingram, L. J. L. Haller, N. Kaltsoyannis, *Dalton Trans.* (2006) 2403.
- [129] Y. Oda, A. Aoshima *J. Nucl. Sci. Techno.* 39 (2002) 647.
- [130] S. Tsushima, T. Yang, A. Suzuki, *Chem. Phys. Lett.* 334 (2001) 365.
- [131] C. Nguyen-Trung, D. A. Palmer, G. M. Begun, C. Peiffert, R. E. Mesmer, *J. Soln. Chem.* 29 (2000) 101.
- [132] F. Quiles, A. Burneau, *Vibr. Spectros.* 18 (1998) 61.
- [133] C. F. Baes Jr., R. E. Mesmer, *The Hydrolysis of Cations*, J. Wiley & Sons, New York, 1976; pp. 174-182.
- [134] V. Eliet, G. Bidoglio, N. Omenetto, L. Parma, I. Grenthe, *J. Chem. Soc., Faraday Trans.* 91 (1995) 2275.
- [135] R. Ramakrishnan, A. V. Matveev, S. Krüger, N. Rösch, *Theor. Chem. Acc.* 130 (2011) 361.
- [136] R. Ramakrishnan, A. V. Matveev, N. Rösch, *Comp. Theor. Chem.* 963 (2011) 337.
- [137] Z. Szabo, H. Moll, I. Grenthe, *J. Chem Soc. Dalton Trans.* 18 (2000) 3158.
- [138] P. Zeh, K. R. Czerwinski, J. I. Kim, *Radiochim. Acta* 76 (1997) 37.
- [139] I. Pashalidis, G. Buckau, *J. Radioanal. Nucl. Chem.* 273 (2007) 315.
- [140] S. Sachs, V. Brendler, G. Geipel, *Radiochim. Acta* 95 (2007) 103.
- [141] P. Panak, R. Klenze, J. I. Kim, *Radiochim. Acta* 74 (1996) 141.
- [142] M. Morgenstern, R. Klenze, J. I. Kim, *Radiochim. Acta* 56 (1992) 79.
- [143] R. S. Ray, S. Krüger, N. Rösch, *Inorg. Chim. Acta* 363 (2010) 263.
- [144] E. H. Bailey, J. F. W. Mosselmans, P. F. Schofield, *Geochim. Cosmochim. Acta*, 68 (2004) 1711.
- [145] A. Kremleva, Y. Zhang, A. M. Shor, S. Krüger, C. Joseph, B. Radizky, K. Schmeide, S. Sachs, G. Bernhard, N. Rösch, submitted.
- [146] S. Sachs, T. Reich, G. Bernhard, *Radiochim. Acta* 98 (2010) 467.
- [147] C. Joseph, B. Raditzky, K. Schmeide, G. Geipel, G. Bernhard, in: *Uranium Mining and Hydroteology*, B. J. Merkel, A. Hasche-Berger (Eds.) Springer, Berlin, 2008, p. 539.
- [148] S. Krüger, F. Schlosser, R. S. Ray, N. Rösch, in *Lecture Series on Computer and Computational Sciences*, vol. 7, T. Simonis, G. Maroulis (Eds.) Koninklijke Brill NV, Leiden, 2006, p. 904.
- [149] F. Crea, A. De Robertis, S. Sammartano, *Ann. Chim.* 93 (2003) 1027.
- [150] R. Portanova, P. Di Bernardo, A. Cassol, E. Tondello, L. Magon, *Inorg. Chim. Acta* 8 (1974) 233.
- [151] A. Kirishima, Y. Onishi, N. Sato, O. Tochiyama, *J. Chem. Thermodynam.* 39 (2007) 1432.
- [152] Ref. 2, vol. 4, chap. 23.6.
- [153] H. Dong, H. Du, S. R. Wickramasinghe, X. Qian, *J. Phys. Chem. B*, 113 (2009) 14094.

- [154] J. J. Berard, G. Schreckenbach, P. L. Arnold, D. Patel, J. B. Love, *Inorg. Chem.* 47 (2008) 11583.
- [155] P. L. Arnold, D. Patel, A. Pécharman, C. Wilson, J. B. Love, *Dalton Trans.* 39 (2010) 3501.
- [156] O. Zakhariyeva, A. Kremleva, S. Krüger, N. Rösch, *Int. J. Quantum Chem.* 211 (2011) 2045.
- [157] C. Chiu, *Density Functional Studies on Uranyl Complexation by Amino Acids*, Bachelor Thesis, Technische Universität München, 2008.
- [158] L. Rao, *Chem. Soc. Rev.* 36 (2007) 881.
- [159] C. F. Baes, Jr., N. J. Meyer, *Inorg. Chem.* 1 (1962) 780.
- [160] J. A. Hearne, A. G. White, *J. Chem. Soc.* (1957) 2168.
- [161] P. Zanonato, P. Di Bernardo, A. Bismondo, G. Liu, X. Chen, L. Rao, *J. Am. Chem. Soc.* 126 (2004) 5515.
- [162] L. Rao, A. Garnov, J. Jiang, P. Di Bernardo, P. Zanonato, A. Bismondo, *Inorg. Chem.* 42 (2003) 3685.
- [163] L. Rao, J. Jiang, P. Zanonato, A. Bismondo, A. Garnov, *Radiochim. Acta* 90 (2002) 581.
- [164] P. Di Bernardo, P. Zanonato, A. Bismondo, H. Jiang, A. Garnov, J. Jiang, L. Rao, *Eur. J. Inorg. Chem.* 22 (2006) 4533.
- [165] T. G. Srinivasan, P. Zanonato, P. Di Bernardo, A. Bismondo, L. Rao, *J. Alloys Compd.* 408 (2006) 1252.
- [166] L. Rao, P. Zanonato, P. Di Bernardo, *J. Nucl. Radiochem. Sci.* 6 (2005) 31.
- [167] B. B. Owen, R. C. Miller, C. E. Milner, H. L. Cogan, *J. Phys. Chem.* 65 (1961) 2065.
- [168] D. J. Bradley, K. S. Pitzer, *J. Phys. Chem.* 83 (1979) 1599.
- [169] R. A. Pierotti, *Chem. Rev.* 76 (1976) 717.
- [170] M. Cossi, B. Mennucci, R. Cammi, *J. Comput. Chem.* 17 (1996) 57.
- [171] M. Cossi, V. Barone, R. Cammi, J. Tomasi, *Chem. Phys. Lett.* 255 (1996) 327.
- [172] M. Tissandier, K. Cowen, W. Feng, E. Gundlach, M. Cohen, A. Earhart, J. Coe, *J. Phys. Chem. A* 102 (1998) 7787.
- [173] S. Skanthakumar, M. R. Antonio, L. Soderholm, *Inorg. Chem.* 47 (2008) 4591.
- [174] A. Ikeda-Ohno, C. Hennig, A. Rossberg, H. Funke, A. C. Scheinost, G. Bernhard, T. Yaita, *Inorg. Chem.* 47 (2008) 8294.
- [175] J.-M. Combes, C. J. Chisholm-Brause, G. E. Brown Jr., G. A. Parks, S. D. Conradson, P. G. Eller, I. R. Triay, D. E. Hobart, A. Meijer, *Environ. Sci. Technol.* 26 (1992) 376.
- [176] K. Takao, S. Takao, A. C. Scheinost, G. Bernhard, C. Hennig, *Inorg. Chem.* 48 (2009) 8803.
- [177] S. Tsushima, T. Yang, *Chem. Phys. Lett.* 401 (2005) 68.
- [178] B. Brendebach, N. L. Banik, C. M. Marquardt, J. Rothe, M. A. Denecke, H. Geckeis, *Radiochim. Acta* 97 (2009) 701.
- [179] A. Ikeda-Ohno, C. Hennig, S. Tsushima, A. C. Scheinost, G. Bernhard, T. Yaita, *Inorg. Chem.* 48 (2009) 7201.
- [180] C. Hennig, J. Tutschku, A. Rossberg, G. Bernhard, A. C. Scheinost, *Inorg. Chem.* 44 (2005) 6655.

- [181] H. Moll, M. A. Denecke, F. Jalilehvand, M. Sandström, I. Grenthe, *Inorg. Chem.* 38 (1999) 1795.
- [182] S. Pocev, G. Johannson, *Acta Chem. Scand.* 27 (1973) 2146.
- [183] M. R. Antonio, L. Soderholm, C. W. Williams, J. P. Blaudeau, B. E. Bursten, *Radiochim. Acta* 89 (2001) 17.
- [184] P. G. Allen, J. J. Bucher, D. K. Shuh, N. M. Edelstein, I. Craig, *Inorg. Chem.* 39 (2000) 595.
- [185] T. Stumpf, C. Hennig, A. Bauer, M. A. Denecke, T. Fanghänel, *Radiochim. Acta* 92 (2004) 139.
- [186] S. Stumpf, T. Stumpf, K. Dardenne, C. Hennig, H. Foerstendorf, R. Klenze, T. Fanghänel, *Environ. Sci. Technol.* 40 (2006) 3522.
- [187] Ref. 2, vol. 2, chap. 8.8.2c
- [188] B. M. Thompson, P. A. Longmire, D. G. Brookings, *Applied Geochem.* 1 (1986) 335.
- [189] Kristallin-I, Safety Assessment Report, Nagra Technical Reports NTB 93-22E, Nationale Genossenschaft für die Lagerung radioaktiver Abfälle, Wettingen Switzerland, 1994.
- [190] A. Křepelová, S. Sachs, G. Bernhard, *Radiochim. Acta* 94 (2006) 825.
- [191] C. J. Chisholm-Brause, J. M. Berg, K. M. Little, R. A. Matzner, D. E. Morris, J. *Colloid Interface Sci.* 277 (2004) 366.
- [192] Z. M. Wang, J. M. Zachara, P. L. Gassman, C. X. Liu, O. Qafoku, W. Yantasee, J. G. Catalan, *Geochim. Cosmochim. Acta* 6 (2005) 1391.
- [193] A. Křepelová, V. Brendler, S. Sachs, N. Baumann, G. Bernhard, *Environ. Sci. Technol.* 41 (2007) 6142.
- [194] C. Hennig, T. Reich, R. Dähn, A. M. Scheidegger, *Radiochim. Acta* 90 (2002) 653.
- [195] E. R. Sylwester, E. A. Hudson, P. G. Allen, *Geochim. Cosmochim. Acta* 64 (2000) 2431.
- [196] A. Dent, J. D. F. Ramsay, S. W. Swanton, *J. Colloid Interface Sci.* 150 (1992) 45.
- [197] A. Křepelová, T. Reich, S. Sachs, J. Drebert, G. Bernhard, *J. Colloid Interface Sci.* 319 (2008) 40.
- [198] M. Schlegel, M. Descostes, *Environ. Sci. Technol.* 43 (2009) 8593.
- [199] T. Hattori, T. Saito, K. Ishida, A. C. Scheinost, T. Tsuneda, S. Nagasaki, S. Tanaka, *Geochim. Cosmochim. Acta* 73 (2009) 5975.
- [200] R. A. Young, A. W. Hewat, *Clays Clay Miner.* 36 (1988) 225.
- [201] J. H. Lee, S. Guggenheim, *Am. Miner.* 66 (1981) 350.
- [202] A. Kremleva, *Environmental Chemistry of Uranyl: A Relativistic Density Functional Study on Complexation by Humic Substances and Sorption on Kaolinite*, Doctoral Thesis, Technische Universität München, 2009.
- [203] B. R. Bickmore, K. M. Rosso, K. L. Nagy, R. T. Cygan, C. J. Tadanier, *Clays Clay Miner.* 51 (2003) 359.
- [204] P. Hartman, W. G. Perdok, *Acta Crystallogr.* 8 (1955) 49.
- [205] P. Hartman, W. G. Perdok, *Acta Crystallogr.* 8 (1955) 521.
- [206] P. Hartman, W. G. Perdok, *Acta Crystallogr.* 8 (1955) 525.
- [207] I. D. Brown, D. Altermatt, *Acta Cryst. B* 41 (1985) 244.

- [208] S. V. Churakov, *J. Phys. Chem. B* 110 (2006) 4135.
- [209] S. V. Churakov, *Geochim. Cosmochim. Acta* 73 (2006) 1130.
- [210] A. Kremleva, B. Martorell, S. Krüger, N. Rösch, *Phys. Chem. Chem. Phys.*, DOI:10.1039/C2CP23886A.
- [211] H. Thompson, G. Parks, J. Brown, in: *Adsorption of Metals by Geomedia*, E. Jenne (Ed.) Academic Press, San Diego, 1998, p. 350.
- [212] T. Reich, R. Reich, S. Amayri, J. Drebert, N. L. Banik, R. A. Buda, J. V. Kratz, N. Trautmann, *AIP Conf. Proc.* 882 (2007) 179.
- [213] T. Reich, G. Bernhard, G. Geipel, H. Funke, C. Hennig, A. Rossberg, W. Matz, N. Schell, H. Nitsche, *Radiochim. Acta* 88 (2000) 633.
- [214] C. M. Marquardt (Ed.), *Migration of actinides in the system clay, humic substances, aquifer*, FZKA Rep. 7407, 2008.
- [215] J. Catalano, G. E. Brown Jr., *Geochim. Cosmochim. Acta* 69 (2005) 2995.
- [216] A. Kowal-Fouchard, R. Drot, E. Simoni, J. J. Erhardt, *Environ. Sci. Technol.* 38 (2004) 1399.
- [217] A. Klamt, G. Schüürmann, *J. Chem. Soc., Perkin Trans. 2* (1993) 799.
- [218] J. L. Pascual-Ahuir, E. Silla, *J. Comput. Chem.*, 12 (1990) 1047.
- [219] J. L. Pascual-Ahuir, E. Silla, I. Tunon, *J. Comput. Chem.* 15 (1994) 1128.
- [220] P. Su, H. Li, *J. Chem. Phys.* 130 (2009) 074109.
- [221] A Ben-Naim, Y. Marcus, *J. Chem. Phys.* 81 (1984) 2016.
- [222] R. S. Pearson, *J. Am. Chem. Soc.* 108 (1986) 6109.
- [223] Y. Marcus, *J. Chem. Soc. Faraday Trans.* 87 (1991) 2995.
- [224] R. Denning, in *Gmelin Handbook of Inorganic Chemistry*, Springer-Verlag, Berlin, 1983, U Suppl. Vol. A6, p. 46.
- [225] H. H. Cornehl, C. Heinemann, J. Marcalo, A. P. de Matos, H. Schwarz, *Angew. Chem. Int. Ed. Engl.* 35 (1996) 891.
- [226] M. Valiev, E. J. Bylaska, N. Govind, K. Kowalski, T. P. Straatsma, H.J.J. van Dam, D. Wang, J. Nieplocha, E. Apra, T. L. Windus, W. A. de Jong, *Comput. Phys. Commun.* 181 (2010) 1477.
- [227] R. Ramakrishnan, A. V. Matveev, N. Rösch, *Chem. Phys. Lett.* 468 (2009) 158.

Joint project:

Migration of Actinides in Natural Clay Formations

**Migration of Lanthanides and Uranium in Natural Clay Formations -
From Mineral Suspensions to Compact Clays**

BMWi Project No.: 02E10196

Final report¹

2011

Ralf Kautenburger, Christina Möser, Horst P. Beck

Universität des Saarlandes

Institut für Anorganische und Analytische Chemie und Radiochemie

Campus Dudweiler, Am Markt Zeile 5, 66125 Saarbrücken

¹ Das diesem Bericht zugrunde liegende Vorhaben wurde mit Mitteln des Bundesministeriums für Wirtschaft und Technologie (BMWi) unter dem Förderkennzeichen 02E10196 gefördert. Die Verantwortung für den Inhalt dieser Veröffentlichung liegt bei den Autoren.

TABLE OF CONTENTS

1. INTRODUCTION	7
2. EXPERIMENTAL	9
2.1. Materials	9
2.1.1. Chemicals and Standards.....	9
2.1.2. Samples	9
2.1.3. Iodination of the HA	9
2.1.4. Modification of the AHA.....	10
2.1.5. Opalinus Clay and porewater	11
2.2. Instrumentation	12
2.2.1. Capillary Electrophoresis	12
2.2.2. ICP-MS.....	14
2.2.2.1. ICP-MS Measurements	14
2.2.3. CE-ICP-MS	16
2.3. Methods	17
2.3.1. OPA Leaching Experiments	17
2.3.2. Batch Experiments.....	17
2.3.2.1. Sorption Experiments	18
2.3.2.2. Desorption Experiments	19
2.3.3. Miniaturised Column Experiments	19
3. RESULTS AND DISCUSSION	21
3.1. Characterisation of the Used Opalinus clay	21
3.2. Element Leaching of the Used Opalinus clay	23
3.3. Analysis of the binary system AHA-Clay	31
3.3.1. Sorption-Isotherms of AHA onto Opalinus Clay.....	31
3.3.2. pH-edges of AHA onto Opalinus clay in PW/SP	33
3.4. Analysis of the binary system Metal-AHA	35
3.4.1. Metal-NOM-speciation with CE-ICP-MS	35
3.4.2. Influence of lanthanide concentration.....	38
3.4.3. Effect of competing cations.....	39
3.4.4. Speciation of uranium-humate-complexes.....	41
3.4.5. Influence of synthetic porewater on the speciation of europium-humates	43
3.4.6. Influence of phenolic and carboxylic functional AHA-groups.....	46
3.4.6.1. Influence of different pH-values on the complexation.....	46
3.4.6.2. Influence of AHA-functional groups on Eu complexation	49

3.5. Analysis of the Binary System Metal – Clay	52
3.5.1. Sorption experiments	52
3.5.1.1. Influence of temperature on sorption experiments with europium.....	52
3.5.1.2. Calculation of thermodynamic values via Van't Hoff Plot.....	55
3.5.2. Desorption experiments influenced by temperature.....	56
3.5.2.1. Influence of the pH-value on the desorption.....	56
3.5.2.2. Influence of the competing cations from the porewater on the desorption	58
3.5.2.3. Influence of the temperature on the desorption	59
3.5.3. The influence of temperature on pH-edges.....	60
3.5.3.1. Influence of pH and temperature on the sorption of Eu	61
3.5.3.2. Influence of pH and temperature on the sorption of U	62
3.6. Analysis of the ternary system Metal – Clay – NOM	64
3.6.1. Sorption experiments	64
3.6.2. Desorption experiments.....	67
3.6.3. Speciation of Eu-humate complexes in presence of Opalinus clay.....	68
3.6.4. Miniaturised column migration experiments	71
3.6.4.1. Optimisation of the miniaturised clay column experiments.....	71
3.6.4.2. Influence of Eu(III) on the retention of salicylate	72
3.6.4.3. Influence of temperature on the retention of Eu and lactate in OPA	73
3.6.4.4. Post mortem analysis of the compacted clay columns	74
4. CONCLUSIONS AND OUTLOOK.....	76
5. PUBLICATIONS RESULTING FROM THE PROJECT	78
6. REFERENCES.....	80

LIST OF SYMBOLS

A	Electrode surface
AHA	Aldrich humic acid
AHA-PB	Aldrich humic acid with blocked groups
β	Conditional stability constant ($\log \beta$)
c	Concentration
CE	Capillary Electrophoresis
CEC	Cation exchange capacity
CE-ICP-MS	Capillary Electrophoresis- Inductively Coupled Plasma-Mass Spectrometry
HPLC	High Performance Liquid Chromatography
HPLC-DAD	High Performance Liquid Chromatography with Diode Array Detection
MICN	Metal ion charge neutralisation model
D	Diffusion coefficient
DP	Differential-Pulse
Eq.	Equation
Eu	Europium (III)
Fig.	Figure
g	Standard acceleration due to Earth's gravity (9.81m/s^2)
Gd	Gadolinium (III)
HA	Humic acid
I	Ionic strength
ID	Inner diameter
ICP	Inductively Coupled Plasma
ICP-MS	Inductively Coupled Plasma-Mass Spectrometry
IHA	Iodinated humic acid
K	Stability constant ($\log K$)
K'	Electrochemical constant
K_c	Equilibrium constant

kPa	kilo Pascal
L	Loading in % (compared to the maximum complexation)
LC	Loading Capacity
log β	Conditional complex stability constant
M	Molar
Me ^{z+}	Metal ion
MQ	MilliQ(-water)
n	Number of electrons
NOM	Natural Organic Matter
OPA	Opalinus clay
PEC	Proton Exchange Capacity
ppb	Parts per Billion
ppm	Parts per Million
ppt	Parts per Trillion
PW	Synthetic porewater
Q-ICP-MS	Inductively Coupled Plasma-Quadrupol-Mass Spectrometry
s	Rate of potential scan
SP	NaClO ₄
Tab.	Table
TOC	Total Organic Carbon
U	Atomic units
U	Uranium (VI), Uranyl cation
UF	Ultrafiltration
V	Volt

ABSTRACT

The development of a disposal in deep geological formations for radioactive waste is a very important task for the future. The safety assessment for more than a hundred thousand years needs a full understanding of all processes of interaction between the radioactive waste and the surrounding formations. This work contributes to this understanding. The interaction between lanthanides (homologues of the actinides americium, curium and berkelium) / uranium and the host rock Opalinus clay under the influence of organic substances (NOM) has been analysed and discussed. The complex system was split into three binary basic systems with the following interactions

- Interactions between lanthanides / uranium and NOM
- Interactions between lanthanides / uranium and-Opalinus clay
- Interactions between NOM and Opalinus clay

All binary systems will be influenced by geological parameters like pH, ion strength and competing cations. The sorption / desorption of the lanthanides onto/from the Opalinus clay is analysed via inductively coupled plasma mass spectrometry. For the investigation of the complexation behaviour of metals with NOM we used capillary electrophoresis coupled with inductively coupled plasma mass spectrometry.

Under these conditions the chosen model organic humic acid affected the sorption of the lanthanides onto Opalinus clay favourably. The smaller organic compounds, which dominate in the composition of the clay organics, remobilised the metals after sorption onto clay the sorption can thereby be inhibited by NOM. Due to the reduced metal sorption onto Opalinus clay by NOM a migration through the clay may be possible.

ZUSAMMENFASSUNG

Die Entwicklung von Endlagerstätten von radioaktiven Abfällen in tiefen geologischen Formationen, ist eine wichtige Aufgabe für die Zukunft. Um eine Sicherheit für mehrere hundert Tausend Jahre zu gewährleisten, müssen die Prozesse der Wechselwirkung zwischen den eingelagerten Stoffen und der umgebenden Formation verstanden und eingeschätzt werden. Diese Arbeit leistet ihren Beitrag zu diesem Verständnis, in dem sie Wechselwirkungen zwischen den Lanthanoiden Europium, Gadolinium und Terbium (Homologe zu den Actiniden Americium, Curium und Berkelium) sowie Uran zum Wirtsgestein Opalinuston unter dem Einfluss von Organik darstellt und interpretiert. Die Wechselwirkungen des sehr komplexen Systems aus Aquifer, Opalinuston und Metall-Ionen wird in drei binäre Systeme unterteilt.

- Wechselwirkungen zwischen Lanthanoiden / Uran und Organik
- Wechselwirkungen zwischen Lanthanoiden / Uran und Ton
- Wechselwirkungen zwischen Organik und Ton

Durch geochemische Parameter (pH, Ionenstärke, Konkurrenzreaktionen) können diese stark beeinflusst werden. Die Untersuchung der Lanthanoide und ihrer Sorption / Desorption am Ton erfolgt mit Hilfe der Massenspektrometrie mit induktiv gekoppeltem Plasma.

Wechselwirkungen zwischen den Lanthanoiden und der Organik werden über eine Kopplung aus Kapillarelektrophorese und ICP-MS untersucht. Unter den gewählten Bedingungen fördert die Modellorganik Huminsäure die Sorption und damit den Rückhalt der Metalle, während die kleineren organischen Verbindungen im Opalinuston zu einer Mobilisierung der Lanthanoide führen. Da die Organik im Opalinuston durch kleine organische Verbindungen dominiert wird, werden die Metall-Ionen hier schlechter vom Ton zurück gehalten und können sich so ausbreiten.

1. Introduction

The deep geological disposal of the high level radioactive wastes is assumed to be a way of providing adequate protection for humans and the environment. For the safe isolation of radioactive waste, low permeability and high sorption capacity of the geological barrier is very important. Clay minerals play a major role in different concepts for the disposal of high-level nuclear waste (HLW) in deep geological formations [1-3]. These clay formations are one part of the natural barrier of a repository protecting the environment from the possible impact of radionuclide contamination [4-6]. The long-lived actinides uranium, neptunium, plutonium, americium and curium determine the radio-toxicity of the waste for a long time period and are of special interest for long-term safety considerations [7,8]. Work with these actinides needs special safety precautions. Therefore, in addition to uranium homologues of such actinides like europium (homologue of americium) were used in our study.

The mobility of radionuclides in the geosphere can be affected by a wide variety of chemical reactions; some of them involve humic substances. Humic material is a large and heterogeneous group of macromolecules of different molecular weight and charge density, with complex and difficultly identifiable structure [9]. The mechanism of complexation with metal ions is not well understood, especially with respect to the role of phenolic OH-groups. Additionally, the influence of metal ion and humic acid concentrations on the humate complexation, the role of metal ions on aggregation of humic molecules, and the kinetics of involved reactions are unsolved problems so far [10,11]. The experiments performed within this project should help to solve these difficult problems.

One aim of the project was to study the complexation behaviour of metal ions with natural organic matter (NOM) like humic acid (HA) or lactate/propionate and formate and to evaluate the complexation constants of corresponding chemical reactions. Such complex stability constants are required for geochemical modelling of metal-ion behaviour in the environment after assembling them in a thermodynamic database [12]. Among the different complexation models to describe the metal ion complexation by humic substances the metal ion charge neutralisation (MICN) model [13] was used within this project.

Typically used methods for the determination of complexation constants combine different chemical separation techniques, e.g. extraction methods, ion exchange, ultrafiltration or precipitation, with sensitive detection methods such as nuclear spectroscopy, soft X-ray spectromicroscopy (NEXAFS) or mass spectrometry [14-17]. Some of these methods have the adverse effect that the quantification of the different metal species is not possible or, that kinetically unstable complexes may be modified during chemical separation. Scientific insights that the chemical, biological or toxic behavior of elements changes with their form in

solution what is known as elemental speciation, and is henceforward widely used in many applications such as environmental chemistry, occupational health, nutrition and medicine [18]. For quantitative elemental speciation analysis some separation techniques like high performance liquid chromatography (HPLC), ion- (IC) or gas chromatography (GC) have been used in combination with element-selective detectors like inductively coupled plasma (ICP), optical emission (OES) and mass spectrometry (MS) or atomic absorption spectroscopy (AAS) [19,20].

Within the present study capillary electrophoresis (CE) was hyphenated with a homemade interface to inductively coupled plasma-mass spectrometry (ICP-MS) and this established and optimised CE-ICP-MS is used as a potential powerful alternative to existing speciation methods at low metal ion concentrations [21-27]. With this hyphenation it was possible to investigate the complexation behaviour between metal ions and HA and analyse its influence on the migration of the lanthanide europium and the actinide uranium in standardised laboratory experiments. However, one problem is that HA is not detectable by Quadrupol-ICP-MS (Q-ICP-MS). To make it observable in the ICP-MS, we used a simple chemical procedure to halogenate the aromatic hydrocarbon-rings in the HA with iodine as "ICP-MS" marker [28,29].

With these analytical techniques we investigated the complexation behaviour of humic acid (purified Aldrich humic acid, AHA) in standardised laboratory experiments and its influence on the migration (sorption and desorption experiments) of the lanthanides europium, gadolinium and terbium (homologues of the actinides americium, curium and berkelium) and the actinide uranium. As analytical method we used batch experiments to get a basic understanding for the complex systems. First we started with the different binary systems and finally investigated the ternary system consisting of these heavy metals, NOM and Opalinus clay (OPA) under varying experimental conditions close to nature [30,31]. In such a way the influence of geochemical parameters like pH-value, ionic strength or different competing metal cations on the metal mobility in the absence (binary system) or presence of NOM (ternary system) could be investigated. In addition to the speciation and batch studies we developed miniaturized column experiments with compacted clay as a compromise between unnatural batch studies and time-consuming diffusion experiments to analyze the influence of different geochemical parameters on the metal mobility in compacted Opalinus clay.

2. Experimental

2.1. Materials

2.1.1. Chemicals and Standards

The humic acid (AHA) used in the experiments is commercially available from Aldrich (St. Louis, USA; AHA sodium salt), and was purified as described in the literature [32]. All other chemicals (see also Table 1) were of p.a. quality or better (suprapure) and were obtained from Merck (Darmstadt, Germany). Milli-Q deionised water (18.2 M Ω) was used to prepare all solutions. The CE electrolyte buffer was a solution of 100 mM acetic acid and 10 mM Na-acetate. The single element standards of Cs, Eu and Ho were obtained from Merck. For adjusting the pH-value perchlorate acid (70 %, p.a.) and NaOH (p.a.) from Merck (Darmstadt, Germany) were applied. Argon 4.6 (99.996 %, Messer Griesheim, Germany) was used as plasma gas. All standard dilutions and samples were prepared with 10 mM NaClO₄ (SP) ionic strength. Before use all solutions for CE analysis were filtered (0.45 μ m syringe filter, Minisart, Sartorius, Germany).

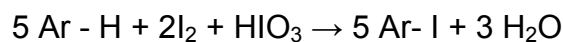
2.1.2. Samples

For the complexation studies we used a concentration of 0.5 mg·L⁻¹ Eu ($3.29 \cdot 10^{-3}$ mmol·L⁻¹), 25 mg·L⁻¹ AHA and 10 mM NaClO₄ in a final volume of 10 ml Milli-Q deionised water, respectively. The pH-values were adjusted with 1 M NaOH and 1 M HClO₄ to pH 3, 5, 7 and 10. The samples were mixed in a rotator (Stuart SB 3, Bibby Sterlin LTD., UK) for 72 h at 25°C before CE-injection. A contact time of at least 48 h was necessary to reach the complex formation equilibrium between HA and the metals. The sample preparation was the same for iodinated AHA (see section 2.1.3) and the modified AHA with blocked phenolic OH-groups (described in section 2.1.4).

2.1.3. Iodination of the HA

For an identification of the peaks in the electropherograms it was necessary to know where the complexed metal humate species migrates. Since AHA is not detectable in the Q-ICP-MS the AHA needs a structural modification. With the aid of a simple chemical reaction the cyclic or polycyclic aromatic hydrocarbon-rings in the HA was halogenated with iodine which acts

as an “ICP-MS marker”. The details of the reaction procedure and the different cleaning steps have been reported earlier [28]



The yield of the iodinated AHA was determined by TOC measurements (Total Organic Carbon; liquiTOC, Elementar Analysensysteme GmbH, Germany). The yields of iodinated HA were more than 80 % after the halogenation and clean up steps. The iodinated AHA was used in some preceding complexation experiments under identical conditions for later identification of uncomplexed and AHA complexed Eu-species.

2.1.4. Modification of the AHA

The modification of AHA was performed by the Helmholtz-Center Dresden-Rossendorf. To block the phenolic OH-groups of AHA all of them were methylated with diazomethane in a first step. In the second modification step the methyl esters of carboxyl groups were saponificated with sodium hydroxide (Figure 1). As result 84 % of the phenolic OH-groups and additionally 40 % of the carboxyl groups were blocked [33,34].

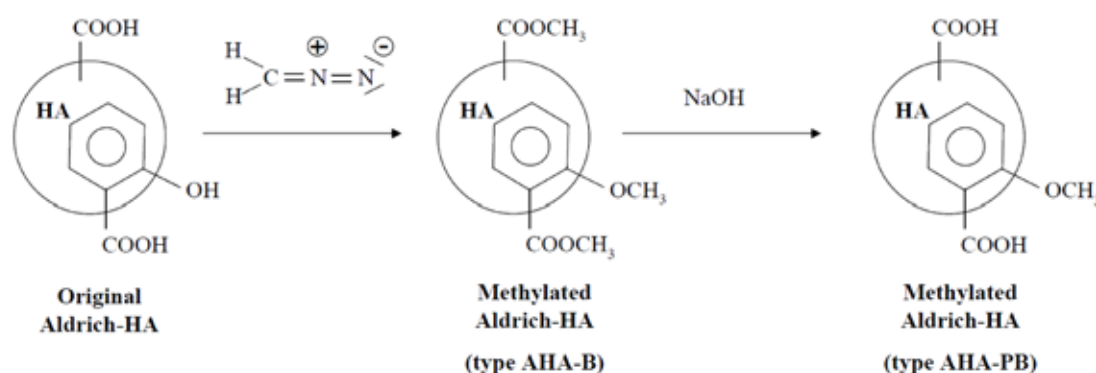


Figure 1: Modification of the Aldrich-HA (AHA) by methylation of the phenolic OH- (and COOH-) groups with diazomethane/NaOH

To determine the influence of the phenolic hydroxyl- and carboxyl-groups on the complexation behavior of AHA the identical speciation experiments were performed with Aldrich HA (AHA) and the modified Aldrich HA (AHA–PB), respectively.

2.1.5. Opalinus Clay and Porewater

The clay mineral used in this study was Opalinus clay (OPA which was obtained from a drill core (BHE-24/1) from the Mont Terri rock laboratory (Switzerland). The core sample was stored in containers with 0.5 bar Ar overpressure. The aerobe homogenate of the clay was obtained by milling the clay to a fine-grained powder with a particle size smaller than 500 μm . The ungrounded Opalinus clay represents a well characterised clay [35] with a cation exchange capacity (CEC) ranging from 9 to 12 meq / 100 g, the porosity of the sample was 10.8 % [36].

The milled clay used in our study was characterised by XRD phase analysis (Siemens D5000, OED) followed by data interpretation with the TOPAS software (version 2.1, Bruker AXS, Delft, The Netherlands). CertiPUR[®] (Merck, Darmstadt, Germany) ICP-elemental solutions ($1000 \text{ mg}\cdot\text{L}^{-1}$) of Sc and Ho were diluted 1 : 100 in Milli-Q water and used as spike and internal standard solution for all clay leaching experiments. For a comparison with the effect of Milli-Q water (Milli-Q-System, Millipore, Schwalbach, Germany) as leaching solution a synthetic porewater (PW) prepared according to Pearson [37] and Van Loon et al. [38] was also used for such leaching experiments (see Table 1).

Table 1: Chemical composition and properties of the used PW (pH 7.6) according Pearson [37]

Compound	M [g·mol ⁻¹]	Conc. [g·L ⁻¹]	C _{Metal} [mg·L ⁻¹]
NaCl	58.44	12.38	4873
Na ₂ SO ₄	142.04	2.00	647
NaHCO ₃	84.01	0.04	11
KCl	74.55	0.12	63
MgCl ₂ ·6H ₂ O	203.30	3.457	413
CaCl ₂ ·2H ₂ O	147.02	3.793	1034
SrCl ₂ ·6H ₂ O	266.62	0.136	45

2.2. Instrumentation

2.2.1. Capillary Electrophoresis

Electrophoresis is the migration of charged molecules or ions in a solution under the influence of an electric field. In the case of Capillary Electrophoresis (CE) the sample migrates in thin fused-silica capillaries (50-100 cm in length) with inner diameters ranging from 25 to 100 μm filled with an appropriate CE electrolyte. The influence of the electrical field on an ion causes a constant migration rate for every ion within the CE buffer. Cations with different electrophoretic mobility (different charge, radius or molar mass) are separated from each other and from neutral or anionic molecules or atoms as shown in Figure 2.

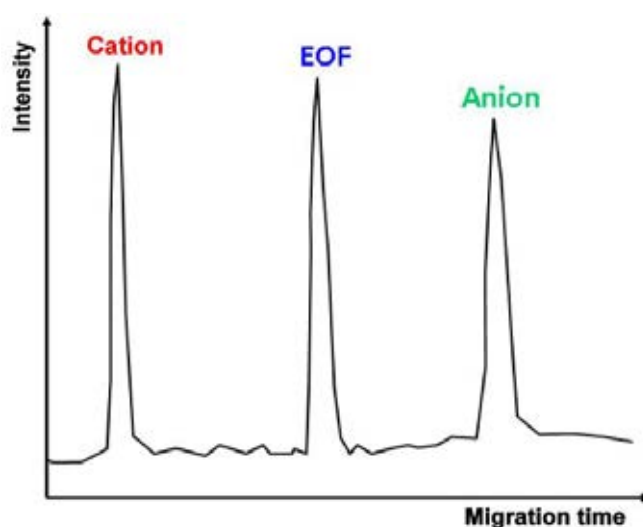


Figure 2: Principal migration of differently charged ions in capillary electrophoresis

Electro-osmotic flow (EOF) is the result of electroneutrality constraints, which cause the formation of a charge double layer at the walls of the CE capillary. The walls of a fused silica capillary contain silanol groups which ionise in contact with a high pH electrolyte solution. This dissociation produces a negatively charged wall. A layer of counter ions (e.g. metal ions) is then formed at the wall to preserve electroneutrality. When an electric field is applied these counter ions and their associated solvating water molecules migrate towards the cathode. This movement of ions and their associated water molecules results in a flow of solution towards the detector which is called electroosmotic flow (EOF). At low pH the silanol groups are not ionised and therefore the flow rate is much reduced or even zero at very low pH values. The influence of the electric field on an ion causes a constant migration rate v for every ion within the solution in the range of about 25–110 $\mu\text{m}\cdot\text{sec}^{-1}$.

The interaction between frictional force (Stokes) and electrical ones is given by the relation

$$v = \frac{z \cdot E \cdot F}{6 \cdot \pi \cdot \eta \cdot r \cdot N_A}$$

v	Electrophoretic migration velocity
z	Net charge of the analyte
N_A	Avogadro constant
r	Stokes radius
E	Electrical field
F	Faraday constant
η	Viscosity of the medium

The principal build-up of a CE is shown in Figure 3. The capillary fits into two buffer vials and the high voltage is applied through the capillary. A detector and the data acquisition are placed at one end of the capillary.

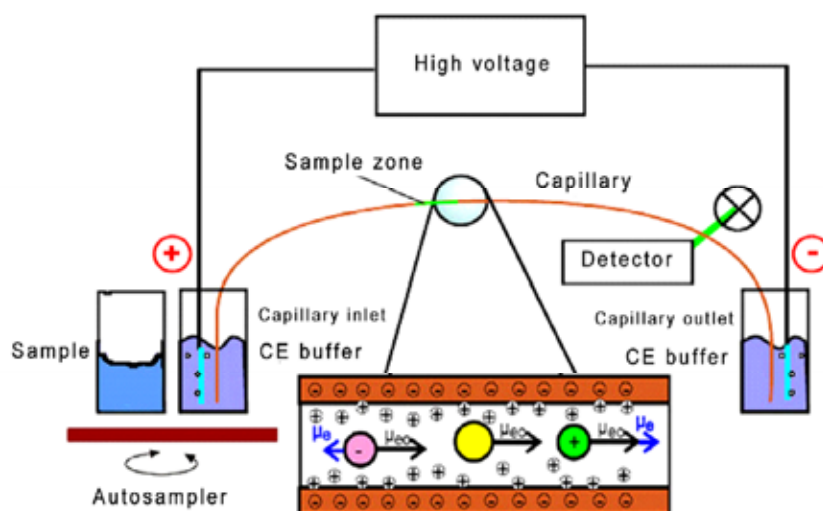


Figure 3: Principal build-up of a capillary-electrophoresis system

The idea of using capillary electrophoresis for the determination for complex stability constants for metals is not really new (especially in protein chemistry), but the direct separation of metal ions from their complexes is rarely used and - so far - even less in the case of humic acid complexes. The CE experiments were carried out with a Beckmann

P/ACE MDQ (Beckmann Instruments, USA). CZE separations were carried out in an uncoated fused silica 80 cm capillary (Polymicro Technologies, USA) and 75 μm of inner diameter.

The samples were injected hydrodynamically at 200 kPa sec (10 kPa for 20 sec) which corresponds to a sample volume of 220 nL. To precondition the capillary before each run, the capillary was rinsed with HCl (4.5 M) for 30 sec at 140 kPa, with NaOH (0.5 M) for 30 sec at 140 kPa, with Milli-Q deionised water for 20 sec at 140 kPa, and additionally with CE electrolyte buffer for 30 sec at 140 kPa. To prevent buffer depletion and to reduce background levels of lanthanides and uranium, the buffer was changed completely every 10th run. The separations were performed under optimised conditions at 30 kV and 20 kPa at 25°C.

2.2.2. ICP-MS

2.2.2.1. ICP-MS Measurements

A VG Elemental PlasmaQuad 3 (Thermo Fisher Scientific, Waltham, USA) quadrupole-based ICP-MS followed in November 2009 by an Agilent 7500cx ICP-MS (Santa Clara, USA) with collision cell (see Figure 4) was used for the isotope measurements.

Detailed analytical conditions are given in Table 2. We used ^{165}Ho as internal standard in all experiments to correct for instrumental instability. All measured isotope counts are therefore corrected by the ^{165}Ho abundance. All samples are measured by ICP-MS in triplicate (RSD values are in the range of 0.3 and 3.9 %).

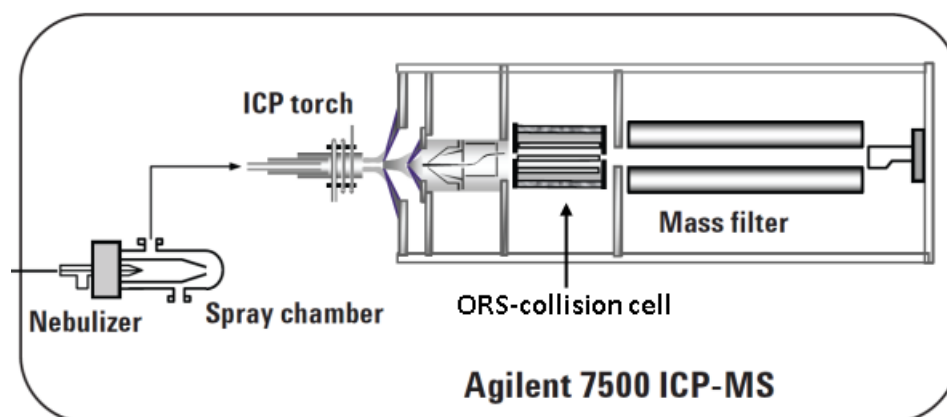


Figure 4: Diagram of the Agilent 7500cx ICP-MS with ORS-collision cell

Table 2: Operating parameters of the CE System and the ICP-MS

CE	Beckman Coulter P/ACE® MDQ
Capillary	fused silica (Polymicro Technologies)
Capillary dimensions / Temperature	74 µm ID, 362 mm o.d., 80 cm length / 25°C
CE electrolyte buffer	100 mM acetic acid, 10 mM Na-acetate, pH 3.7
Internal Standard (IS) CE buffer	200 ppb Cs
DC-voltage / current	+ 30 kV / 16–18 µA
Interface	homemade
Spray-chamber	Cinnabar cyclonic, chilled at 4°C, 20 mL volume
Nebuliser	MicroMist 50 µl, Typ AR35-1-FM005E, 2.8 bar
Make-up fluid	2 % HNO ₃ , 24 nmol·L ⁻¹ (4 ppb) Ho (IS), 112 µL·min ⁻¹
ICP-MS I	VG Elemental Plasma Quad 3
RF-power	1400 W
Cooling / Auxiliary gas flow rate	12.5 / 1.25 L·min ⁻¹
Dwell times	200 ms (Eu, Gd, I), 50 ms (Cs, Ho) 10 ms (Br)
ICP-MS II	Agilent 7500cx
RF-power	1600 W
Cooling / auxiliary gas	15.0 / 0.9 L·min ⁻¹
Dwell times / Repetition	300 ms per mass / 3 times
Samples	
Eu-, Gd-, U-ICP-standards	CertiPUR® (Merck), diluted in 10 mM HClO ₄
Analysed isotopes	⁸¹ Br, ¹²⁷ I, ¹³³ Cs, ¹⁵³ Eu, ¹⁵⁸ Gd, ¹⁶⁵ Ho, ²³⁸ U
Humic acid (AHA)	Purified AHA (Aldrich H1,675-2), modified AHA (AHA-PB, Batch M173)
Iodinated AHA	Homemade as described under Experimental
Ion strength in AHA samples:	10 mM NaClO ₄
pH-values	3, 5, 7, 10

2.2.3. CE-ICP-MS

Capillary electrophoresis (CE, Beckman Coulter P/ACE MDQ) was hyphenated by a homemade interface to inductively coupled plasma mass spectrometry (ICP-MS, VG Elemental PlasmaQuad 3 or Agilent 7500cx) to obtain a high sensitivity for the determination of the rare earth element species of europium and gadolinium with AHA [28]. To couple CE to ICP-MS a fused-silica CE-capillary was fitted into a MicroMist 50 μl nebulizer with a Cinnabar cyclonic spray chamber (chilled to 4°C) in the external homemade interface.



Figure 5: Hyphenation of CE and ICP-MS by the homemade interface

A make-up fluid including 4 ppb Ho as an internal standard was combined with the flow from the capillary within the interface to obtain a fluid throughput high enough to maintain a continuous nebulisation. Detailed analytical conditions are given in Table 2.

In the optimised CE-ICP-MS-system we used a DC-voltage of 30 kV, and additionally a pressure of 3 psi was applied as the best separation conditions for the non AHA complexed and AHA complexed metal ions. The comparison of the complexation of Eu and Gd with non-iodinated and iodinated AHA revealed no detectable differences [28].

The CE-ICP-MS method developed was checked by analysing different standard solutions. The detection limits (125 ppt for ^{153}Eu and 250 ppt for ^{158}Gd) and correlation coefficients of the calibration curves for Eu (> 0.995) and Gd (> 0.999) were very good. After calibrating the system for the measured isotopes, standard solutions containing 0.7–98.7 μmol Eu and 25 ppm iodinated AHA (pH 5) and 0.64–95.4 μM Gd and 25 ppm iodinated AHA (pH 5) were injected as a sample and the recoveries of Eu and Gd were determined.

2.3. Methods

All experiments using the batch technique (leaching, sorption, desorption experiments) in this study were performed under ambient atmosphere ($p\text{CO}_2 = 10^{-3.5}$ bar) and room temperature ($23 \pm 2^\circ\text{C}$). The experiments were performed in centrifuge tubes (VWR PP-SuperClear 15 ml, VWR International GmbH, Darmstadt, Germany) which have low metal adsorption properties.

2.3.1. OPA Leaching Experiments

In all experiments with Opalinus clay, an equivalent amount of $100 \text{ g}\cdot\text{L}^{-1}$ (1.0 g of clay was extracted with 10 ml of leaching solution, respectively) was weighted into the dried tubes. After a 120 h extraction time with the corresponding solvent on a tube rotator (Stuart SB3 Tube Rotator, Bibby Sterilin Ltd, UK), the tubes were centrifuged at 10000 rpm ($12800 \times g$) for 10 minutes. Samples were taken from the supernatant solutions. Diluted and acidified samples (the pH-value of the supernatant was adjusted to $\text{pH} < 1$ with HNO_3 suprapure) were prepared to determine the element content in the solution by ICP-MS.

2.3.2. Batch Experiments

Figure 6 shows the procedure of the batch experiments schematically. The experiments were performed in centrifuge tubes (SuperClear 15 ml, VWR International GmbH, Darmstadt, Germany) which have low metal sorption properties (step 1).

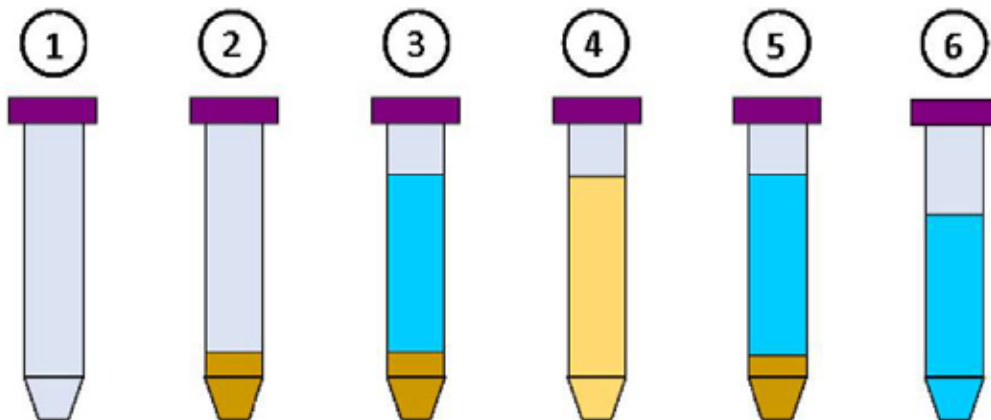


Figure 6: Schematic procedure of the batch experiments (description in the text)

The determined wall sorption for Eu and Gd is less than 5 % (for metal concentrations $> 100 \text{ ng}\cdot\text{L}^{-1}$) in the analysed pH-range. In all experiments with clay, an equivalent amount of $4 \text{ g}\cdot\text{L}^{-1}$ OPA was used (each experiment was made by weighing 40 mg OPA into a tube filled up with the adequate solution to a final volume of 10 ml (step 2). After 72 h preconditioning the clay (40 mg) with 9 ml of the corresponding background solution (10 mM NaClO_4 to buffer the ionic strength or PW), the remaining components were added (appropriate volumes of the $1 \text{ mg}\cdot\text{L}^{-1}$ or $100 \text{ mg}\cdot\text{L}^{-1}$ metal standard stock solutions or additionally, in the ternary system, NOM concentrations between 5 and $25 \text{ mg}\cdot\text{L}^{-1}$) and the pH was adjusted by addition of dilute HClO_4 or NaOH (suprapure, Merck, Darmstadt, Germany) (step 3). The samples were mixed for at least 72 h end over end in a tube rotator (Stuart SB3 Tube Rotator, Bibby Sterilin Ltd, UK) with all components present to reach a stable equilibrium (step 4). Afterwards the tubes were centrifuged at 12800 g (10000 rpm) for 10 minutes (step 5). Samples were taken from the supernatant solutions. Diluted and acidified solutions (pH-value was adjusted to $\text{pH}<1$ with HNO_3 suprapure) were prepared to determine the metal content in the solution by ICP-MS (step 6).

As the total metal concentration (before clay contact) is known and the non-adsorbed metal is measured it is possible to calculate the amount of adsorbed metal. All batch experiments containing clay were performed in this way. Filtering (e.g. ultrafiltration) as well as centrifugation of the samples were not performed due to some drawbacks (for example low metal recovery rates due to filter adsorption and disturbed sorption/desorption equilibrium) which was found out in a previous study [28].

2.3.2.1. Sorption Experiments

The sorption experiments were performed with U(VI) in the appropriate solution or all three lanthanides (Eu, Gd and Tb) together in one solution to compare directly the results of the three lanthanides under identical conditions. In doing so possible differences in sorption or desorption behaviour between the lanthanides can better be observed. In all cases an ion strength of 10 mM when using NaClO_4 (SP) or 0.42 M in the case of PW was present in the solutions.

Sorption isotherms were determined by increasing the metal concentration from $1 \text{ }\mu\text{g}\cdot\text{L}^{-1}$ (equivalent to $4.20 \text{ nmol}\cdot\text{L}^{-1}$ U(VI), $6.58 \text{ nmol}\cdot\text{L}^{-1}$ Eu, $6.36 \text{ nmol}\cdot\text{L}^{-1}$ Gd and $6.29 \text{ nmol}\cdot\text{L}^{-1}$ Tb, respectively) to $10 \text{ mg}\cdot\text{L}^{-1}$ (equivalent to $42.0 \text{ nmol}\cdot\text{L}^{-1}$ U(VI), $65.8 \text{ }\mu\text{mol}\cdot\text{L}^{-1}$ Eu, $63.6 \text{ }\mu\text{mol}\cdot\text{L}^{-1}$ Gd, and $62.9 \text{ nmol}\cdot\text{L}^{-1}$ Tb, respectively) at pH 5 ($\text{pH } 5.0\pm 0.04$) for SP or pH 7.6 ($\text{pH } 7.6\pm 0.05$) for PW. The pH-edges were determined at pH-values ranging from 2 to 12 ($\text{pH}\pm 0.05$) with a metal concentration of $300 \text{ }\mu\text{g}\cdot\text{L}^{-1}$. The correct pH-value was adjusted by use of ultra-pure

solutions (10 or 100 mM) of HClO_4 and NaOH . Sorption experiments of the metals under investigation onto OPA in the presence of the competing cations were performed with $300 \mu\text{g}\cdot\text{L}^{-1}$ of metal in one batch and increasing concentrations of Ca and Mg ranging from $100 \mu\text{g}\cdot\text{L}^{-1}$ to $30 \text{mg}\cdot\text{L}^{-1}$ at the given pH-value.

The equilibration between OPA ($4 \text{g}\cdot\text{L}^{-1}$) and 10 mM SP results in a pH-value of 5 (4.7-5.2), and that between OPA and PW in a pH-value of 7.6 (7.2-7.8). Other pH-values can induce clay decomposition (e.g. Ca, Mg or Al release) or metal precipitation (e.g. as carbonates or hydroxides). Therefore pH 5 for SP and 7.6 for PW is used in most experiments (except pH-edges) and also by all project partners to compare our results.

2.3.2.2. Desorption Experiments

The performed desorption experiments are based on the corresponding sorption experiments and simulate metal mobilisation in the course of repeated equilibrations with fresh metal-free solution. In these test series samples (centrifuged OPA with sorbed metals at the given experimental conditions without supernatant solution which was discarded) from the corresponding sorption experiments were used. The carryover volume in the desorption experiments was less than $200 \mu\text{L}$ (coming up to 2 % of a total volume of 10 mL). Assuming that a fictive desorption step leads to 50 % desorption of metal ions (we have never measured such a high desorption in one equilibrium step), the maximal error would be less than 4 %, and this bias is comparable for all desorption steps and not relevant. The solution (10 mL at the specific experimental condition) for all desorption experiments had an ionic strength of 10 mM SP or 0.42 M PW and was added to the clay samples. For pH- and competing cation test series the appropriate metal solutions (Ca, Mg or Al) were added and the pH of the desorption solutions adjusted. The samples were shaken for 72 h respectively to attain desorption equilibrium (in further experiments no significant kinetic effects were observed after 48 hours). This procedure was repeated three times for every equilibrium step. After each desorption step the tubes with the samples were centrifuged at 12800 g for 10 minutes. A subsample of 3.33 mL was taken from the supernatant solution, diluted to a final volume of 10 mL and acidified with HNO_3 (suprapure, Merck, Darmstadt, Germany) to pH 1. The desorbed metals in the samples were analysed by ICP-MS.

2.3.3. Miniaturised Column Experiments

An Agilent 1100/1200 LC system (Agilent, Waldbronn, Germany) was used for the miniaturised column experiments. The LC system consist of a capillary LC pump which can

deliver constant flow rates between 0.01 and 20.0 μL in the capillary flow mode between 15 and 400 bar. The samples are injected by an autosampler with a volume between 0.1 and 100 μL , larger volumes can be added continuously as a second eluent solution. The column (20 mm x 3.5 mm ID) can be filled with 100 % OPA as stationary phase (sorbent) or using a variable mixture with purified sea sand (total weight of 250-290 mg). The temperature of the OPA-column can be controlled exactly between 15 and 80°C in a column compartment. After the sample separation in this clay column the different sample species can be detected via a diode array detector or additionally by hyphenation with ICP-MS to detect the UV/Vis-inactive species. As mobile phase (eluent) different combinations of solutions can be mixed by a quaternary capillary LC pump. In our experiments usually 10 mM of sodium perchlorate is used as mobile phase at pH 5. As mobility (retention time) reference iodide was used as inert tracer to check the repeatability of each experiment by adding 0.1 mM NaI into all samples to correct the differences of the retention time in different experiments as well as in the different clay columns used.

3. Results and Discussion

3.1. Characterisation of the Used Opalinus Clay

The XRD phase analysis (Siemens D5000, OED) of the used Opalinus clay (OPA) followed by data interpretation with the TOPAS software (version 2.1, Bruker AXS, Delft, The Netherlands) is shown in Figure 7.

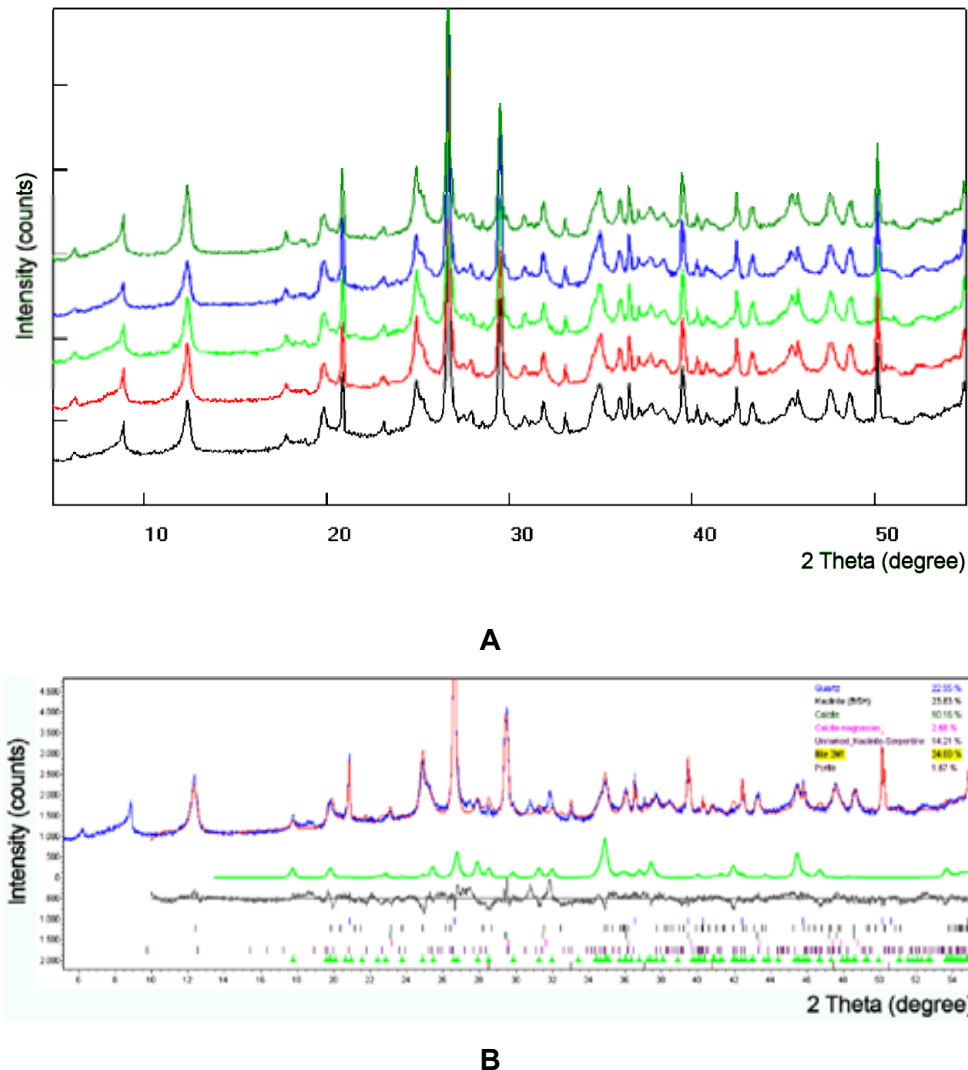


Figure 7: Powder XRD main analysis of five clay samples (A) and Rietveld refinement (TOPAS 2.1, Bruker AXS) of the OPA (B).

The results of the XRD analysis are given in Table 3. Kaolinite, illite, silica and calcite could be determined as main phases with amounts in the range of 13.1 – 26.5 %, while only 1.5 % pyrite is present. Chlorite and Feldspar could not be verified. These results

are in a good agreement with data from a XRD phase analysis from similar Opalinus clay [39].

Table 3: XRD main phase analysis of Opalinus clay (n=5) from Mont Terri [35] in comparison to the used OPA sample. Analysis and data interpretation with the TOPAS 2.1. software package; nd = not determined

Mineral	Mean \pm SD [wt%] [35]	Mean \pm SD [wt%] This work
Kaolinite	17.0 \pm 6.0	22.5 \pm 1.3
Kaolinite-Serpentine	nd	13.8 \pm 2.7
Illite	32.0 \pm 6.0	26.5 \pm 1.3
Chlorite	5.0 \pm 2.0	< 5.0
Silica	20.0 \pm 5.0	21.9 \pm 1.1
Calcite	16.0 \pm 1.0	13.1 \pm 0.7
Dolomite/Ankerite	1.0 \pm 0.4	nd
Siderite	4.0 \pm 2.4	nd
Feldspar	3.0 \pm 1.3	< 4.0
Pyrite	1.1 \pm 1.0	1.5 \pm 0.2
Organic carbon	0.6 \pm 0.3	nd

3.2. Element Leaching of the Used Opalinus Clay

Competing ions released from the repository clay formations by infiltration of percolating water or groundwater can influence the migration behaviour of radionuclides originated from a leakage in a waste disposal. Additionally, most sorption or desorption laboratory experiments in this field with metal ions like heavy metals [30,40], radionuclides [41-45] or lanthanides [31,46] and clay minerals are performed with batch techniques. This means that a certain amount of the clay sample (e.g. 1-10 g·L⁻¹) is homogenised and added to a big volume (e.g. 10-100 mL) of water or clay porewater. This unnatural contact of clay with water can lead to a high leaching of metal ions as well as other species originated from the clay and this may influence the sorption/desorption experiments with the chosen metal ions due to their competing properties or it can increase the background concentration of the metals under investigation.

In this working package we analysed the elemental composition of aqueous leachate from Opalinus clay samples by the use of the batch techniques. As leaching solutions MilliQ-water and synthetic porewater (PW) [37,38] were used to study the influence of different ion strengths on the extraction efficiency. After the leaching experiments free elemental ions in the supernatant solution were analysed by inductively coupled plasma mass spectrometry (ICP-MS).

The analysis of OPA leaching samples was performed in full scan mode (7-238 u) in the ICP-MS as shown in Figure 8. The sample “Blank (MilliQ)” was prepared by the same way as the leaching experiments with MilliQ water denoted by “Clay-extract (MilliQ)” however without clay and served as blank for these experiments. In the same way PW acts as blank (without clay) for the leaching experiments in addition to the OPA extraction by the identical PW. Each leaching experiment was performed three times and also measured with ICP-MS in triplicate.

Due to the high concentrations of metal ions like sodium, calcium and magnesium (in sum 7.0 g·L⁻¹), as well as chloride and sulphate in the used PW (as shown in Table 1), very high intensities of these elements are present in the blank samples. These elements act as competing ions and can lead to a different element extraction profile in comparison to the extraction of the clay by MilliQ water. Additionally, these extracted elements could have a strong influence on the results of sorption or desorption experiments-with metal ions onto mineral surfaces [43].

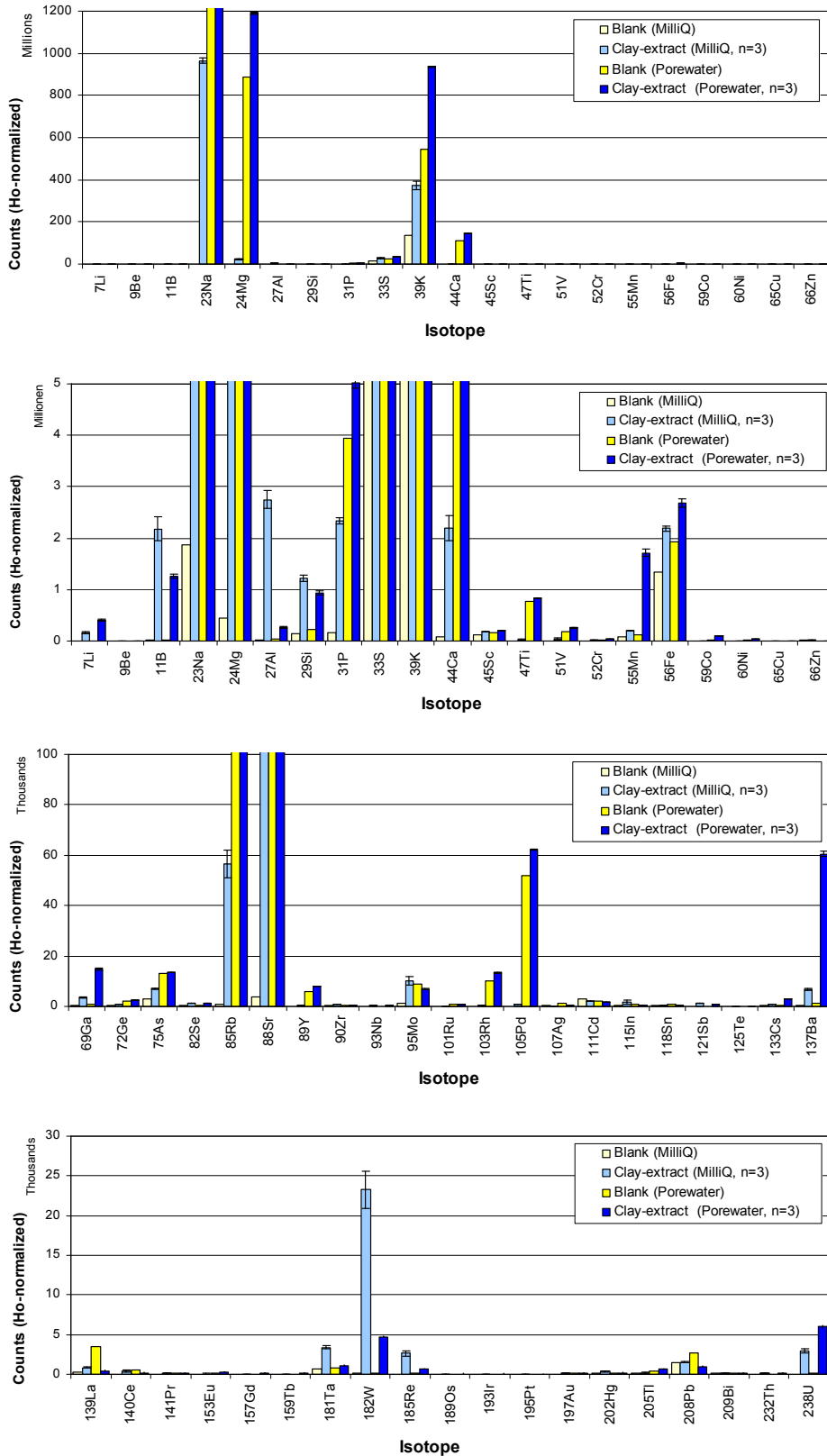


Figure 8: Ho-standardised ICP-MS scans ($1 \mu\text{g}\cdot\text{L}^{-1} \text{}^{165}\text{Ho} = 10000 \text{ counts}$) from ${}^7\text{Li}$ to ${}^{238}\text{U}$ of the two different leaching experiments (MilliQ and PW) and the corresponding blank experiments.

As result for both leaching solutions (MilliQ and PW) the following main elements are seen to be extracted from the Opalinus clay (in the order of the isotopic mass, mainly extracted elements in bold): **Li, B, Na, Mg, Al, Si, P**, (S), **K, Ca**, (Ti), (V), Cr, **Mn**, (Fe), Co, (Ni), Ga, (Rb), **Sr**, (Mo), Cs, **Ba**, Ta, W, Re, U.

For some elements the determined background concentrations in the blank samples are in the same order of magnitude or even higher in comparison to the concentrations found in the leaching experiments in the presence of clay (as shown in Figure 8) due to possible contamination during the sample preparation (e.g. contamination of the PW chemicals, see Table 5) or due to isobaric interferences (see Table 4) in the ICP-MS detection step. This is observed in the case of MilliQ treatment for the isotopic masses ^{33}S , ^{39}K , ^{55}Mn , ^{56}Fe , ^{60}Ni , ^{65}Cu , ^{66}Zn , ^{107}Ag , ^{111}Cd , ^{118}Sn and ^{208}Pb .

For the leaching experiments with PW the isotopic masses of ^{33}S , ^{47}Ti , ^{51}V , ^{52}Cr , ^{56}Fe , ^{65}Cu , ^{66}Zn , ^{72}Ge , ^{75}As , ^{89}Y , ^{90}Zr , ^{95}Mo , ^{103}Rh , ^{105}Pd , ^{107}Ag , ^{111}Cd , ^{115}In , ^{118}Sn , ^{139}La , ^{140}Ce , ^{141}Pr and ^{208}Pb can be detected with high intensities in the PW blank samples.

Table 4: Isobaric interferences for the Q(quadrupol)-ICP-MS detection by the use of high ionic strength of porewater (PW) ions

Analytes	Interferents
^{32}S	$^{16}\text{O}_2^+$
^{33}S	$^{16}\text{O}_2^1\text{H}^+$, $^{16}\text{O}^{17}\text{O}^+$
^{47}Ti	$^{40}\text{Ar}^7\text{Li}^+$, $^{12}\text{C}^{35}\text{Cl}^+$ (Cl from PW)
^{51}V	$^{12}\text{C}^{39}\text{K}^+$, $^{40}\text{Ar}^{11}\text{B}^+$, $^{16}\text{O}^{35}\text{Cl}^+$, $^{14}\text{N}^{37}\text{Cl}^+$ (Cl from PW)
^{55}Mn	$^{39}\text{K}^{16}\text{O}^+$ (K from PW)
^{56}Fe	$^{40}\text{Ar}^{16}\text{O}^+$, $^{40}\text{Ca}^{16}\text{O}^+$ (Ca from PW)
^{75}As	$^{40}\text{Ar}^{35}\text{Cl}^+$ (Cl from PW)
^{85}Rb	$^{40}\text{Ar}^{45}\text{Sc}^+$ (Sc is added as I.S.)
^{89}Y	$^{44}\text{Ca}^{45}\text{Sc}^+$ (Ca from PW, Sc is added as I.S.)
^{95}Mo	$^{40}\text{Ar}^{39}\text{K}^{16}\text{O}^+$ (K from PW)
^{103}Rh	$^{40}\text{Ar}_2^{23}\text{Na}^+$ (Na from PW), contamination from chemicals
^{105}Pd	$^{40}\text{Ar}_2^{25}\text{Mg}^+$ (Na from PW), contamination from chemicals
^{107}Ag	$^{95}\text{Mo}^{12}\text{C}^+$, contamination from chemicals
^{111}Cd	$^{95}\text{Mo}^{16}\text{O}^+$, $^{39}\text{K}_2^{16}\text{O}_2^1\text{H}^+$ (K from PW), contamination from chemicals
^{139}La	contamination from PW chemicals
^{208}Pb	contamination from PW chemicals

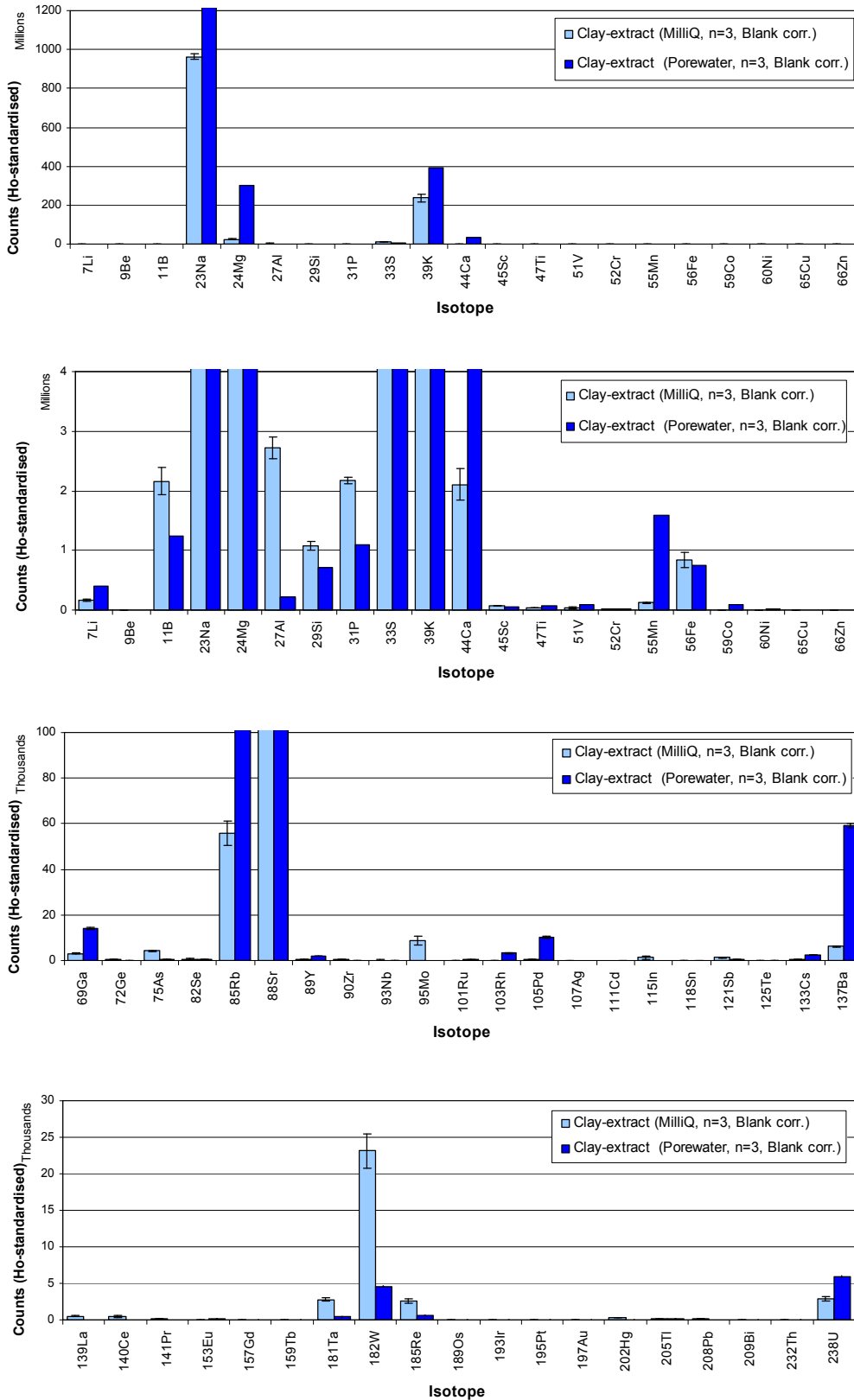


Figure 9: Ho-standardised ICP-MS scans ($1 \mu\text{g}\cdot\text{L}^{-1} \text{}^{165}\text{Ho} = 10000$ counts) from ${}^7\text{Li}$ to ${}^{238}\text{U}$ of the two different leaching experiments (MilliQ and PW). All shown isotope counts of the leaching samples are subtracted by the isotope counts of the corresponding blank sample.

To compare the characteristics and extraction efficiency of MilliQ-water and PW better ICP-MS scans of the leaching sample are corrected by the corresponding blank experiment (yellow coloured bars in Figure 8). This isotope intensity correction is necessary because the used PW contains high concentrations of metal ions like sodium, calcium and magnesium as well as chloride and sulphate. The corrected leaching results are shown in Figure 9. Due to the correction a direct comparison of the leaching efficiency for both used solutions (MilliQ and PW) is possible.

The differences in the leaching efficiency of the different solutions can clearly be seen. In both cases (MilliQ and PW) high amounts of Li, B, Na, Mg, Al, Si, P, S, K, Ca, Mn, Fe, Rb and Sr (over 50000 counts in all samples) can be extracted from the Opalinus clay. For the leaching experiments at low ionic strength (MilliQ) the elements B, Al, Si, P, Mo, Ta, W and Re are particularly extracted. These elements can be typically found as anionic species in solution for example as borates, aluminates, silicates phosphates, molybdates, tantalates, tungstates and rhenates. The last four elements are also typical compounds of hard metals like cermets. Therefore these metal ions are likely not to have originated from the OPA but rather from the borehole driller. By the use of synthetic porewater (PW) as leaching solution the elements Li, Na, Mg, K, Ca, Mn, Ga, Rb, Rh, Pd, Ba and U are mainly extracted. In comparison to the MilliQ extracted anionic species these elements are typically found as cationic compounds.

To estimate the extracted element concentrations all measured isotopes are corrected by their isotope frequency (adapted to 100 %) and the counts (cps) are compared by the internal standard Holmium where $1 \mu\text{g}\cdot\text{L}^{-1}$ reveals 10000 cps as seen in Figure 10 and Figure 11. These values can be expressed as mass concentrations (e.g. $\mu\text{g kg}^{-1}$ OPA) of the elements extracted from the clay by multiplication with the factor 10 due to the used OPA concentration of $100 \text{g}\cdot\text{L}^{-1}$ in the leaching experiments as shown in Table 5. These estimations are not absolutely accurate especially for the lighter elements but the bias is equal for the different extracted clay samples so that a relative comparison of the extraction efficiency for the different samples is possible. This bias can be estimated by evaluating the recovery of the sample spike Scandium, which is handled in the same way as the extracted elements. The recovery of Sc lies in the range of $81.2\pm 0.5 \%$ (MilliQ) and $69.5\pm 1.2 \%$ (PW).

After the background correction the mass concentrations in Table 5 show that a relevant amount of leached metal ions can be found in solution, especially the main elements contained in the clay mineral but also certain amounts of other metals which can bias the results of the batch experiments which have been carried out.

Batch experiments are often used to analyse the sorption/ desorption behaviour of metal ions like radionuclides or heavy metals onto/from clay minerals. Due to clay dissolution the unnatural contact of the clay with water or other aqueous solutions leads to a high extraction of different elements from the clay and this may influence the results of experiments.

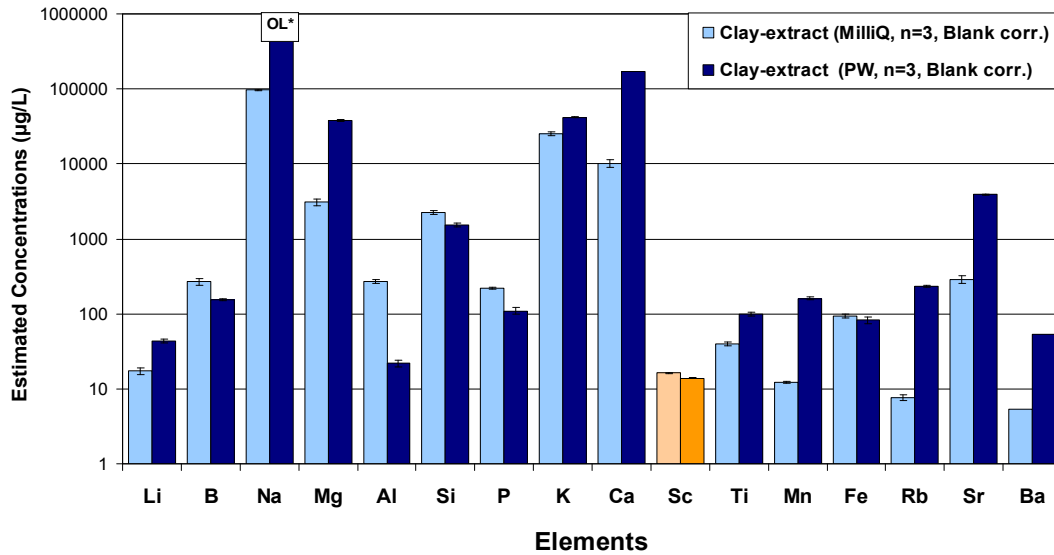


Figure 10: Mainly extracted elements ($>10 \mu\text{g L}^{-1}$, concentration is shown on logarithmic scale), Sc as internal standard

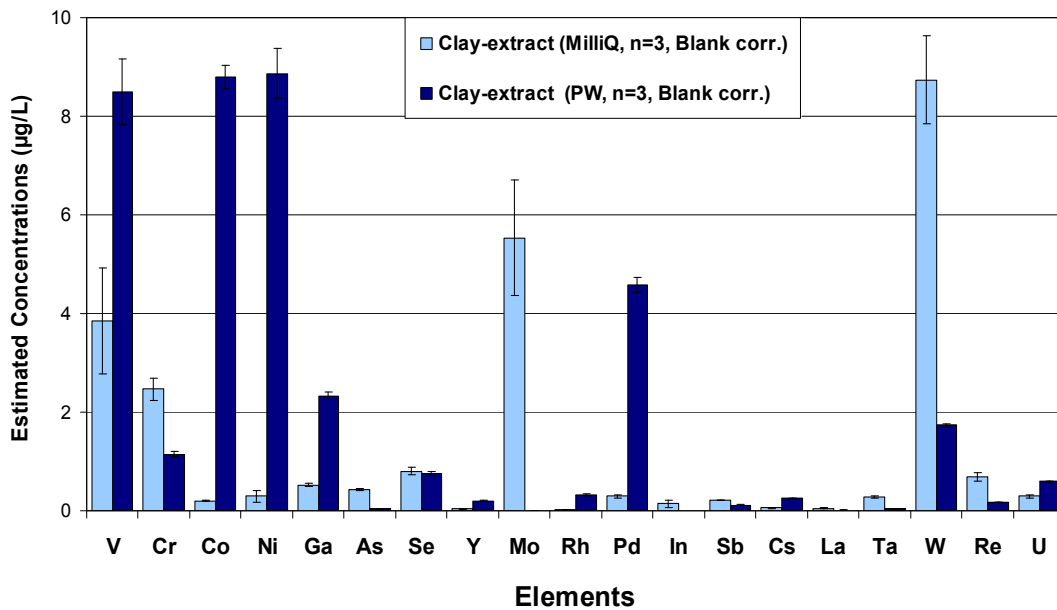


Figure 11: Minor extracted elements ($<10 \mu\text{g L}^{-1}$), Sc as internal standard

Table 5: Estimated element main ($\text{mg}\cdot\text{kg}^{-1}$ OPA) and trace concentrations ($\mu\text{g}\cdot\text{kg}^{-1}$ OPA) extracted with MilliQ and PW from OPA (concentration are corrected by the corresponding blank, shown are only elements with $c \geq 0.1 \mu\text{g}\cdot\text{kg}^{-1}$)

Element main concentrations ($\text{mg}\cdot\text{kg}^{-1}$ OPA)				
Element	MilliQ	SD a	PW	SD
B	2.7	0.3	1.6	0.1
Na	963.1	14.3	OL b	-
Mg	31.1	3.2	381.7	7.6
Al	2.7	0.2	0.2	0.0
Si	22.8	1.4	15.2	0.9
P	2.2	0.1	1.1	0.1
K	253.0	12.8	419.3	3.9
Ca	100.4	11.7	1702.1	15.1
Ti	0.4	0.0	1.0	0.0
Fe	0.9	0.1	0.8	0.1
Rb	0.1	0.0	2.3	0.1
Sr	2.9	0.3	38.9	0.5
Element trace concentrations ($\mu\text{g}\cdot\text{kg}^{-1}$ OPA)				
Li	174.0	18.3	437.6	26.8
Sc	162.3	0.7	138.9	1.6
V	38.4	10.8	84.9	6.7
Cr	24.7	2.3	11.5	0.6
Mn	0.1	0.0	1.6	0.1
Co	2.0	0.1	88.0	2.3
Ni	3.0	1.2	88.6	5.0
Ga	5.2	0.4	23.2	0.8
As	4.3	0.2	0.4	0.0
Se	8.1	0.7	7.5	0.5
Y	0.3	0.1	2.0	0.1
Mo	55.3	11.7	0.1	0.0
Rh	0.2	0.0	3.3	0.2
Pd	2.9	0.3	45.8	1.5
In	1.4	0.7	ND d	-
Sb	2.2	0.1	1.1	0.1
Cs	0.5	0.1	2.5	0.1
Ba	54.2	3.6	527.2	8.5
La	0.5	0.0	0.1	0.1
Ce	0.4	0.2	ND	-
Ta	2.8	0.2	0.4	0.1
W	87.4	8.9	17.4	0.3
Re	6.9	0.8	1.7	0.1
U	2.9	0.3	5.9	0.1

^a SD = Standard deviation (n=3), ^b OL = over detection limit: $> 2000 \text{ mg}\cdot\text{kg}^{-1}$, ^c ⁴⁵Sc: sample spike, ^d ND = not detectable.

The leached elements can act as competing cations for metal speciation with complexing ligands [47] as well as competitors for the metal sorption/desorption onto the clay, particularly for mono or bivalent metal ions [31,48]. On the other hand, the batch experiments can result in wrong interpretations of the measurements due to the high background concentration of the metal ions under investigation due to the dissolution of these elements from the clay.

In summary our results show that the leaching of Opalinus clay with solutions with low ion strength leads to a dissolution of mainly anionic element species whereas the presence of high ionic strength like porewater shows a release of mainly cationic metal ions from the clay. For our experiments the leached concentrations of REE (rare earth elements), especially for Eu, Gd and Tb which are of main interest in this study can be considered as irrelevant. However, for batch experiments concerning the sorption/desorption behaviour of metal ions such as of Al, Fe, V, Cr, Co, Ni, Sr, Ba, or U (beside the present PW ions) the concentrations of extracted metal ions (as shown in Table 5) depending on the used leaching solution have to be taken into account.

3.3. Analysis of the Binary System AHA-Clay

3.3.1. Sorption-Isotherms of AHA onto Opalinus Clay

For the determination of the AHA sorption isotherms onto Opalinus clay (OPA) we have used AHA concentrations between 1 and 500 ppm and $4 \text{ g}\cdot\text{L}^{-1}$ Opalinus clay at a pH-value of 7.6. After the equilibration and reaction step the solutions were centrifuged at 10000 g for 10 min and the AHA concentration in the supernatant was analysed by UV-Vis spectroscopy and TOC (Total organic carbon measurements).

The comparison of the AHA sorption onto OPA in NP and PW is shown in Figure 12.

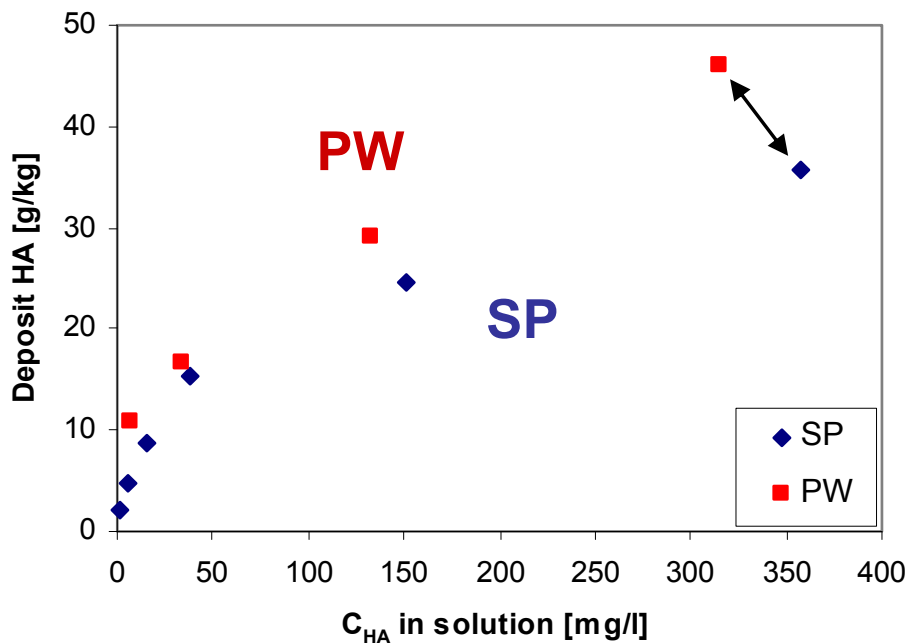


Figure 12: Correlation between deposited AHA and AHA in solution (UV-Vis at 450 nm, C_{AHA} : 1- 500 $\text{mg}\cdot\text{L}^{-1}$, m_{clay} : 4 $\text{g}\cdot\text{L}^{-1}$, pH 7.6)

As result the AHA shows a higher sorption (deposition) onto OPA in PW in comparison to SP due to the PW cations (e.g. Ca^{2+} , Mg^{2+}) present. These metals neutralise the deprotonated AHA as well as the negatively charged clay surface followed by coagulation and precipitation of the metal humates onto the clay surface (hydrophobic interactions between AHA and clay in PW).

To describe the experimentally found sorption isotherms, all experimental data obtained at pH 7.6 were analysed with the Freundlich model [49]. The Freundlich model is an empirical relationship describing the linear sorption of solutes from a liquid to a solid surface. All data

from the experiments could be described by a Freundlich-type isotherm. The equation of a Freundlich isotherm at equilibrium is expressed as follows:

$$q = K_F C^n$$

where q is the adsorbed quantity of AHA onto a unit mass of adsorbent ($\text{mol}\cdot\text{kg}^{-1}$) expressed as C_{sorb} and C is the AHA concentration in solution at equilibrium C_{eq} ($\text{mg}\cdot\text{L}^{-1}$). K_F and n are empirical constants, K_F is the Freundlich constant and n represents the degree of linearity. Figure 13 shows an attempt to describe the situation by a Freundlich isotherm as a linear correlation expressed by the equation:

$$\log C_{\text{sorb}} = n \log C_{\text{eq}} + \log K_F$$

- q adsorbed quantity of AHA onto unit mass of clay ($\text{g}\cdot\text{kg}^{-1}$)
- C_{eq} AHA concentration in solution at equilibrium ($\text{mg}\cdot\text{L}^{-1}$)
- K_F Freundlich-coefficient
- n degree of linearity

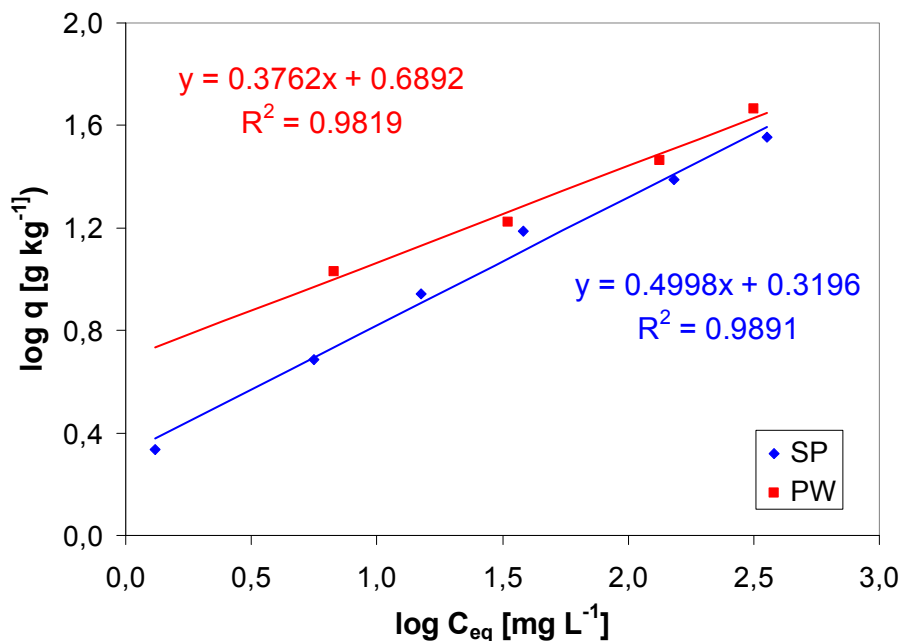


Figure 13: Freundlich sorption isotherm of AHA onto OPA, at $m/V = 4\text{g}\cdot\text{L}^{-1}$, $I = 0.01\text{ M}$ SP and 0.42 M PW, $\text{pH } 7.6\pm 0.02$.

The constants K_F and n , are determined to be 4.89 (2.09) and 0.376 (0.500), for PW and SP (in brackets) respectively, where the relative coefficient R^2 is 0.982 (0.989). It is clearly seen that such a linear relation is significant for the AHA-sorption onto OPA. In summary, for the AHA concentrations and conditions (PW and SP) used for the experiments in the system AHA/OPA the sorption can be correctly fitted by the Freundlich sorption model.

3.3.2. pH-edges of AHA onto Opalinus Clay in PW/SP

To analyse the influence of the pH-value as well as the presence of OPA on the mobility of the AHA we have measured the amount of deposited AHA in dependence of the pH-value in the range of pH 2-12 in the presence or absence of OPA in SP as seen in Figure 14.

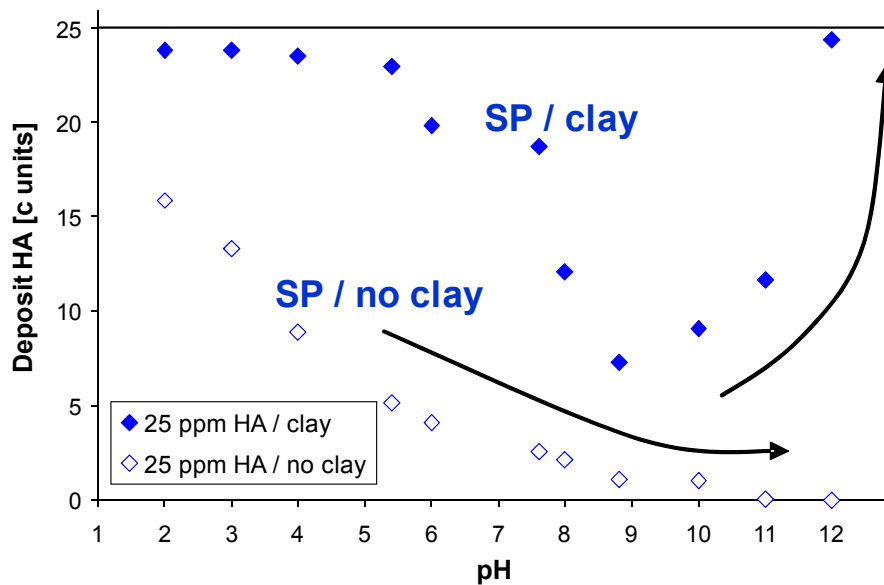


Figure 14: Influence of OPA on the AHA deposition/precipitation (UV-Vis at 450 nm, C_{Ln} : $900 \mu\text{g}\cdot\text{L}^{-1}$, C_{AHA} : $25 \text{ mg}\cdot\text{L}^{-1}$, m_{clay} : $0/4 \text{ g}\cdot\text{L}^{-1}$, pH 2-12) (ionic strength: 0.01 M NaClO_4)

In the absence of OPA we get an increase of dissolved (negatively charged) AHA from $9 \text{ mg}\cdot\text{L}^{-1}$ (at pH 2) to nearly 100 % ($25 \text{ mg}\cdot\text{L}^{-1}$ AHA at pH 11-12). In the presence of clay we get a nearly quantitative deposit of AHA in the pH range between 2 and 4 due to neutralisation of the negatively charged humic acid and of the former cation sites on the clay surfaces by protons followed by an increase of dissolved AHA between pH 5 to 9 due to deprotonation of the humic acid. At a pH-value greater than 9 we can see again a higher

deposit of AHA as neutral Me-AHA due to a higher concentration of metal ions released from the OPA due to the clay decomposition at alkaline pH regions.

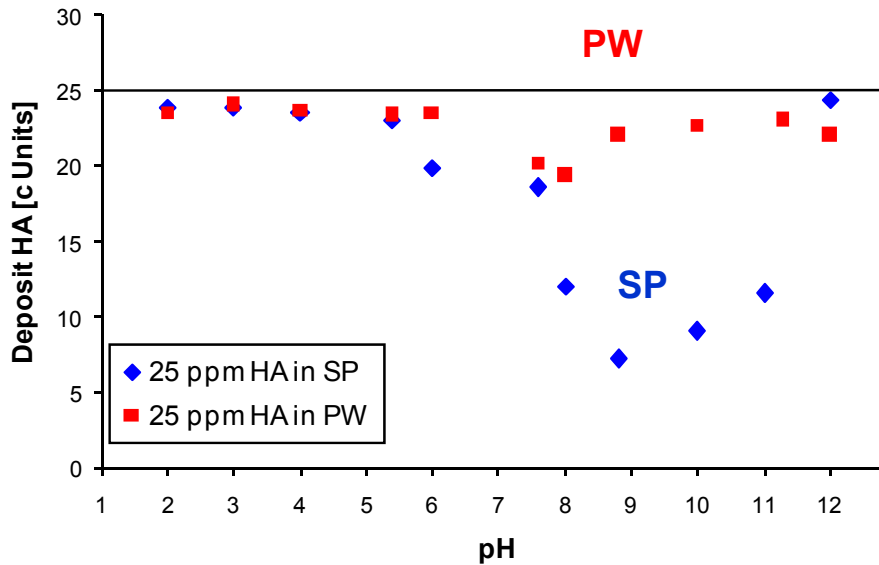


Figure 15: Comparison of AHA deposition onto OPA in PW and SP (UV-Vis at 450 nm, C_{Ln} : $900 \mu\text{g}\cdot\text{L}^{-1}$, C_{AHA} : $25 \text{ mg}\cdot\text{L}^{-1}$, m_{clay} : $0/4 \text{ g}\cdot\text{L}^{-1}$, pH 2-12)

In Figure 15 the influence of different ionic strengths (SP and PW) onto AHA deposition in the presence of OPA is shown. The high concentration of porewater cations neutralises the negatively charged AHA over the whole pH-range from 2 to 12 followed by a high deposition (> 80 % over all analysed pH values) of the neutral Me-AHA complexes. In summary, in the natural geological system consisting of Opalinus clay and porewater only a relatively small amount of dissolved humic acid is present as potentially mobile species.

3.4. Analysis of the Binary System Metal-AHA

3.4.1. Metal-NOM-Speciation with CE-ICP-MS

Natural organic matter (NOM) like humic acids can play an important role in the immobilisation or mobilisation of toxic metal ions due to complexation and colloid formation. Therefore, we investigated the complexation behaviour of humic acid and its influence on the migration or retardation of two selected lanthanides (europium and gadolinium as homologues of the actinides americium and curium). As speciation technique, capillary electrophoresis coupled with inductively coupled plasma mass spectrometry (CE-ICP-MS) has been used for the study of Eu and Gd interaction with (purified Aldrich) humic acid (AHA) [29]. In this working package we report on the influence of the lanthanide (Ln) concentration and of competing cations on the complexation behaviour in the binary system consisting of the lanthanides Eu, Gd and humic acid. As competing cations we used the alkaline earth metals calcium and magnesium and aluminium as trivalent metal ion.

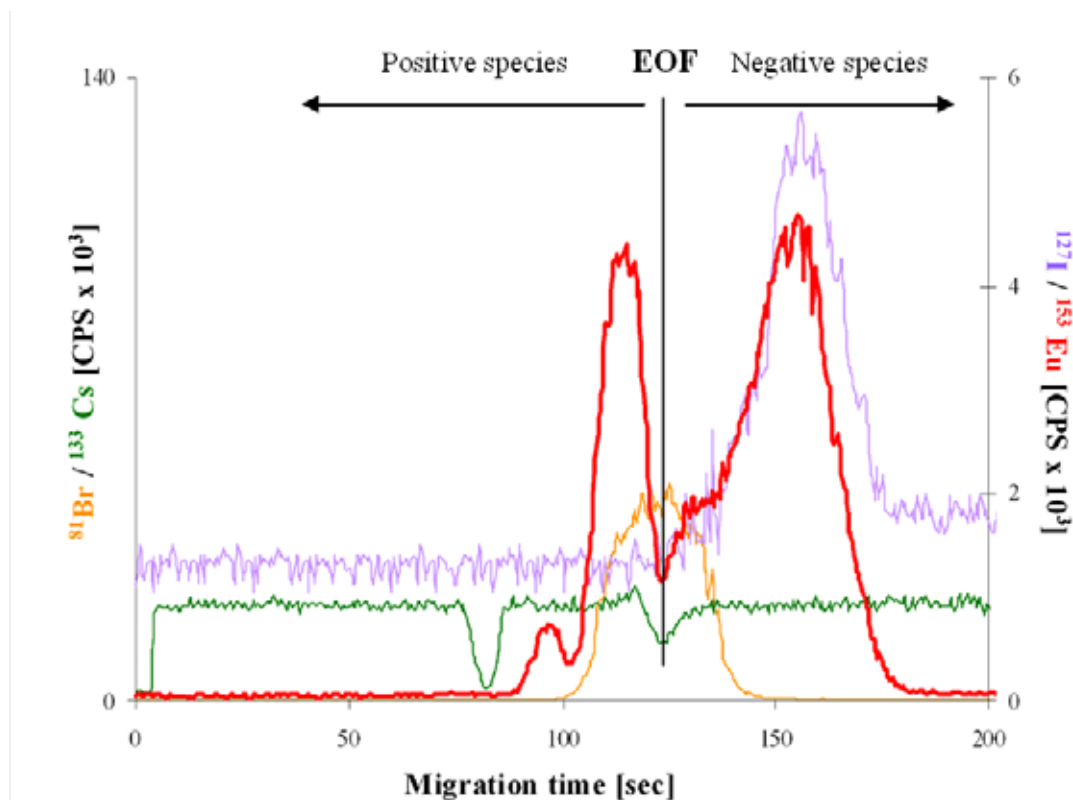


Figure 16: CE-ICP-MS electropherogram which shows Eu species (^{153}Eu) complexed or uncomplexed with iodinated AHA (^{127}I), 1-bromopropane (^{81}Br) as EOF marker and Cs (^{133}Cs) as CE electrolyte flow marker; sample: $3.29 \mu\text{mol}\cdot\text{L}^{-1}$ Eu, $25 \text{mg}\cdot\text{L}^{-1}$ AHA, 10mM NaClO_4 and pH 5

To investigate the complexation behaviour of NOM like AHA for trivalent metal ions we used the CE-ICP-MS techniques to analyse this binary system consisting of Ln and AHA. Details about the optimisation of the method and the separation system are described in the material and methods section.

Figure 16 shows a typical electropherogram with three Eu species complexed or uncomplexed by AHA after the optimisation of CE-ICP-MS method.

With the speciation method used both the free metal and metal humate can be detected in one analysis step. Furthermore, with the CE-ICP-MS method it is possible to investigate the heterogeneity in AHA-complexation of metal ions by evaluating the stability of different metal-humate-species during the CE-separation.

The speciation reveals strong and weak binding sites in the AHA for our choice of lanthanides, and thus also for the homologous actinides Am and Cm. The more labile lanthanide humates (LnAHA) partially “collapse” during the CE-separation due to the applied separation voltage of 30 kV and the interactions of the sample with the acetate in the electrolyte buffer. This leads to an interesting observation, especially on changing experimental conditions. Therefore, the influence of different Ln concentrations and the presence of competing cations were investigated and the first results are communicated here.

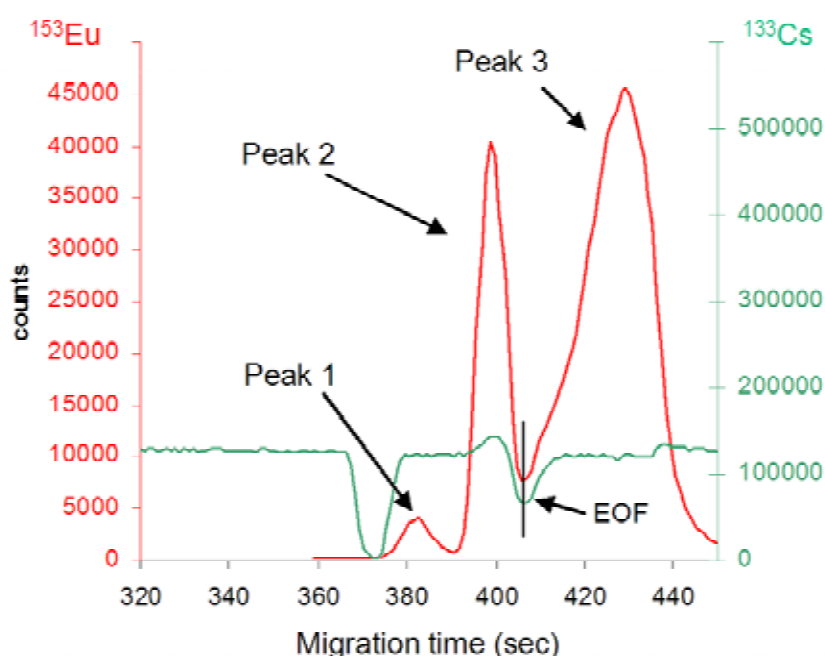


Figure 17: Typical electropherogram (after different washing and preconditioning steps in the time range not shown, the CE-separation starts at 300 sec) of uncomplexed and AHA-complexed Eu and Cs ($200 \mu\text{g}\cdot\text{L}^{-1}$) as CE flow marker analysed by CE-ICP-MS, pH 5, $c(\text{Eu})$: $500 \mu\text{g}\cdot\text{L}^{-1}$, $c(\text{AHA})$: $25 \text{mg}\cdot\text{L}^{-1}$, U: 30 kV, CE-electrolyte: 100 mM AHAc/10 mM NaAc

To investigate the complexation behaviour of NOM like AHA for trivalent metal ions we used the CE-ICP-MS techniques to analyse this binary system consisting of Ln and AHA. Details about the optimisation of the method and the separation system are described in the material and methods section. With the speciation method used both the free metal and metal humate can be detected in one analysis step. Furthermore, with the CE-ICP-MS method it is possible to investigate the heterogeneity in AHA-complexation of metal ions by evaluating the stability of different metal-humate-species during the CE-separation.

The speciation reveals strong and weak binding sites in the AHA for our choice of lanthanides, and thus also for the homologous actinides Am and Cm. The more labile lanthanide humates (LnAHA) partially “collapse” during the CE-separation due to the applied separation voltage of 30 kV and the interactions of the sample with the acetate in the electrolyte buffer. This leads to an interesting observation, especially on changing experimental conditions. Therefore, the influence of different Ln concentrations and the presence of competing cations were investigated and the first results are communicated here.

As reference for the subsequent complexation experiments, Figure 17 shows a typical electropherogram with three Eu species complexed or uncomplexed by AHA after the CE-ICP-MS run. The first signal (peak 1) represents the uncomplexed metal before CE-separation. This “free” $\text{Eu}_{(\text{aq})}^{3+}$ ion was complexed by the acetate (Ac) in the electrolyte buffer during the CE-separation and migrates as EuAc^{2+} towards the CE-cathode. The second signal observed (peak 2) represents metal complexed on weak binding sites of AHA before the CE-separation step. However, the high voltage power of the CE-system enhances the dissociation of Eu^{3+} out of the AHA-complex during CE-separation. The samples were prepared and injected in an acetate free solution (10 mM NaClO_4 is used for the experiments). During the CE separation Eu^{3+} is “extracted” out of the AHA-complex through the applied DC-voltage. For a short time this $\text{Eu}_{(\text{aq})}^{3+}$ migrates inside the sample zone (10 mM NaClO_4) faster than the EuAc^{2+} (peak 1) until it moves out of the sample zone into the surrounding CE-buffer zone which contains acetate at higher concentrations. As a result, the $\text{Eu}_{(\text{aq})}^{3+}$ is also complexed by the acetate and migrates as second peak towards the cathode. The last signal (peak 3) represents metal complexed at strong binding sites before CE-separation. During the CE-run the Eu-AHA-complex normally migrates as negatively charged complex towards the anode ($\mu_e > \mu_{eo}$) but due to the applied pressure of 3 psi versus cathode the complex is forced to migrate towards the cathode.

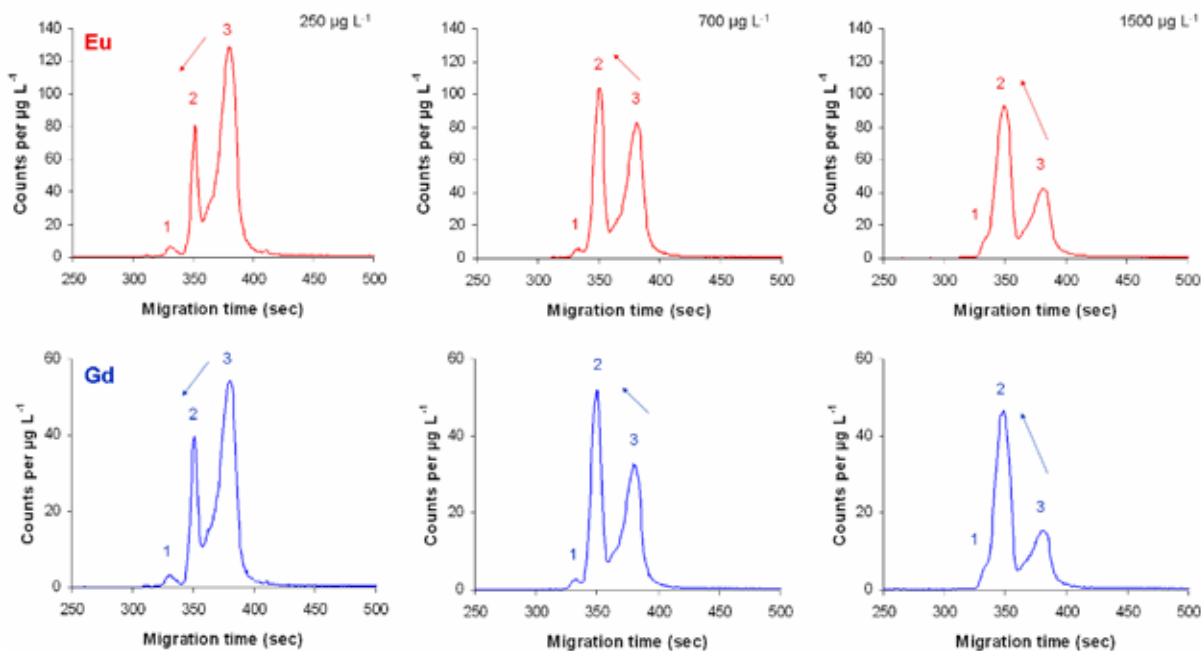


Figure 18: CE-electropherograms of uncomplexed Ln (peak 1) or AHA-complexed Ln (peak 2 and 3) with different concentrations of Ln: $250 \mu\text{g}\cdot\text{L}^{-1}$, $700 \mu\text{g}\cdot\text{L}^{-1}$ and $1.5 \text{ mg}\cdot\text{L}^{-1}$, pH 5, ionic strength (I) of the samples: 10 mM NaClO_4 , $c(\text{AHA}): 25 \text{ mg}\cdot\text{L}^{-1}$. (See text for description)

3.4.2. Influence of Lanthanide Concentration

Different concentrations of Ln can cause different behaviour in AHA-complexation as shown in Figure 18. CE-ICP-MS runs were taken at Eu- and Gd-concentrations between 50 and $3000 \mu\text{g}\cdot\text{L}^{-1}$ (0.32 - $19.7 \mu\text{mol}\cdot\text{L}^{-1}$) at pH 5. By quantification of the Ln-signals in the CE-electropherograms conditional stability constants for EuAHA and GdAHA could be calculated [50,51]. In contrast to other methods - where only one species (the uncomplexed metal species) is measured and the other (complexed species) is then calculated by difference - both the uncomplexed metal ion species and the metal-ligand complexes are measured simultaneously in one detection step by these CE-ICP-MS measurements [29].

In the concentration range up to $250 \mu\text{g}\cdot\text{L}^{-1}$ (shown on the left-hand side of the figure) the larger part of both lanthanides is not complexed by AHA, and this is represented by the two rear signals. For these low metal ion concentrations mainly stronger binding sites of the AHA, such as carboxyl groups, are occupied by Ln. Thus, only a little part of the metal is extracted from the AHA-complex during the CE-separation and the second signal is relatively small. At higher Ln concentrations (e.g. 300 - $1500 \mu\text{g}\cdot\text{L}^{-1}$) more and more weak binding sites of the AHA (e.g. hydroxyl or thiol groups) are occupied. During the CE-separation higher amounts of this weakly AHA-complexed Ln dissociate from the AHA-complex (resulting in a

significantly higher second signal, as shown in the middle and on the right-hand side of the figure) until a nearly constant amount of the LnAHA-complex (shown as peak 3 in the figure representing the amount of Ln complexed by strong binding sites) “survived” the applied high voltage of the CE-separation. At metal concentrations above $1500 \mu\text{g}\cdot\text{L}^{-1}$ a precipitation of the LnAHA-complex can be observed. Consequently, one can give a measure of the stability of the AHA-complexes by the qualitative analysis of the second signal in our CE-separations.

3.4.3. Effect of Competing Cations

Another important aspect of geochemical parameters is the influence of naturally occurring metals on the AHA complexation of heavy metals. There are several competitive metals in the environment, e.g. alkaline and alkaline earth metals, aluminium, iron, or manganese. Magnesium, calcium, and aluminium are chosen in this study due to the relatively high amount in which they can be present in nature. The influence of alkaline metals on the complexation behaviour of europium and gadolinium with AHA is very weak because of the low charge and big size of alkaline ions. Ca and Mg are usually found in groundwater and at higher concentrations the effect on the AHA complexation is more distinct than for sodium and potassium because of their bivalency. Furthermore, Al may be present in larger concentrations because of clay decomposition.

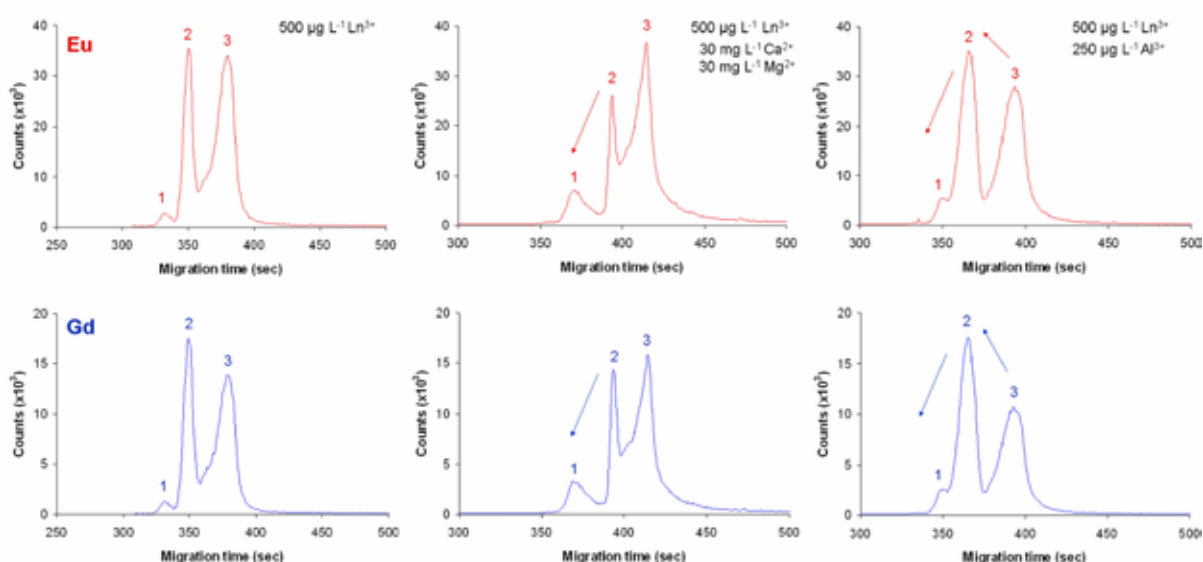


Figure 19: CE-electropherograms of uncomplexed Ln (peak 1) or AHA-complexed Ln (peak 2 and 3) by the presence of different competing ion concentrations, $c(\text{Ln}^{3+})$: $500 \mu\text{g}\cdot\text{L}^{-1}$, pH 5, (I): 10 mM NaClO_4 , $c(\text{AHA})$: $25 \mu\text{g}\cdot\text{L}^{-1}$.

Comparing the electropherograms shown in Figure 19 without the influence of competing cations (on the left-hand side) and the ones with a “competition” of $30 \text{ mg}\cdot\text{L}^{-1}$ Ca and Mg (in the middle), a significant increase of the first signal (uncomplexed Ln) can be observed. Ln are replaced by alkaline earth metals particularly in the weak binding sites of AHA. The second peak decreases for the benefit of the non AHA-complexed metal represented by the first signal. In contrast the amount of Ln complexed by strong AHA-binding sites (represented by the third signal) is nearly constant. This is due to the higher stability of the Ln^{3+} -humate complexes in comparison to Ca^{2+} - and Mg^{2+} -humate complexes.

For $250 \mu\text{g}\cdot\text{L}^{-1}$ Al^{3+} present (on the right-hand side of Figure 19) the ratios are different. The first and the second peak increase at the cost of the third one. This means that Al^{3+} is able to displace Ln^{3+} from stronger binding sites to the weak binding sites of the AHA and even to metal ion species not complexed by AHA. However, the vast amount of the displaced Ln^{3+} is found in the second peak, which shows that the metal is still AHA-complexed before the CE separation. These differences between the competitive effects of the alkaline earth metals and aluminium are illustrated in Figure 20. The largest amount of Ca (the Ca signal shows a high background noise because it must be measured as ^{44}Ca due to high isobaric and polyatomic interferences for the other Ca isotopes) and Mg is found to be an uncomplexed metal species (comparable to signal 1 of Eu) and no signal of these elements can be observed in the migration area of AHA-complexed lanthanide ions (peak 3). In contrast to these findings the predominant fraction of Al can be found in accordance to the third Eu signal which represents metal ions complexed by strong binding sites of the AHA.

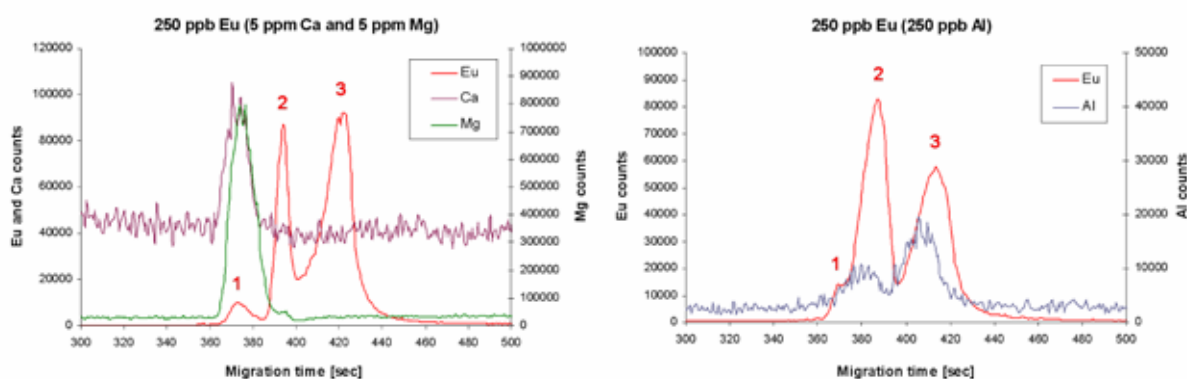


Figure 20: CE-electropherograms of uncomplexed Eu (peak 1) or AHA-complexed Eu (peak 2 and 3) in the presence of Ca and Mg as competing cations (on the left-hand side) in comparison to Al as competing ion (on the right-hand side); pH 5, (I): 10 mM NaClO_4 , $c(\text{AHA}): 25 \text{ mg}\cdot\text{L}^{-1}$

By other analysis methods, such as ultrafiltration, the changes in complexation behaviour could possibly not have been detected because these methods only distinguish between complexed and uncomplexed metal, no matter how stable the complexes really are in presence of competing ions [52-54]. Unfortunately, in the samples with Al the big second peak inhibits a reliable quantification of the uncomplexed Ln (for example peak 1 in Figure 20 on the right-hand side). The replacement of Eu and Gd from the AHA complexes is proportional to the alkaline earth concentration (not shown here). However, even at a 200fold excess concentration of Ca and Mg the amount of AHA-complexed Ln is still over 75 % due to their higher affinity to the stronger binding sites of the AHA. Relatively high alkaline earth metal concentrations are needed to make the effect significant in this system. In contrast to these findings, aluminium as a small trivalent cation represents a strong competitor to Eu and Gd (and therefore also for trivalent actinides) in AHA-complexation. Only $250 \mu\text{g}\cdot\text{L}^{-1}$ Al are sufficient to displace a large amount of Ln from stronger binding complexation sites of the AHA.

Thus, it is preferable to work at natural conditions when performing sorption and complexation studies involving clay minerals in standardised laboratory experiments. In nature the presence of strong competing metal ions, e.g. Al, due to weathering of clays can cause a (re)mobilisation of AHA-complexed heavy metal pollutants such as actinides into the aquifer.

In summary, the results of our studies clearly indicate the need for knowledge about the exact geological conditions at a potential nuclear waste disposal site. Many parameters can influence toxic metal migration such as metal concentration, pH-value and presence of competing cations, NOM like humic substances being the most important factors which can lead to a migration of the toxic heavy metal pollutants through the geological barrier.

3.4.4. Speciation of Uranium-Humate-Complexes

Until now only trivalent cations were dealt with. We then estimated the complexation behaviour of humic acid towards divalent cations like the uranyl cation. Using the same conditions as before, the separation of the different uranyl species in CE-ICP-MS was unsatisfactory. However, on reducing the hydrodynamic pressure from 3 psi to 2 psi a good separation was already obtained. Only small differences between the experiments with Eu and U were seen at first sight. The separation of the uranyl species (Figure 21) can be seen by the same identification of the peaks. The first peak represents the AHA-uncomplexed uranyl species. This fraction appears later than the first peak of the europium species. During the separation the uranyl cation is complexed by acetate and migrates as $\text{UO}_2(\text{Ac})^+$. The

single charged uranyl acetate migrates more slowly than the double charged europium acetate. The second and third peak shows the AHA complexed uranyl fraction. Similar to the europium speciation the uranyl is partially complexed on weak binding sites of the AHA. Especially, the second peak drifts behind the EOF although the uranyl species itself is not anionic. It's an effect of the size and charge of the uranyl cation. When extracted from the weak binding AHA sites, the uranyl cation migrates very slowly to the cathode due to its lower charge and larger size, especially on comparing with the europium cation.

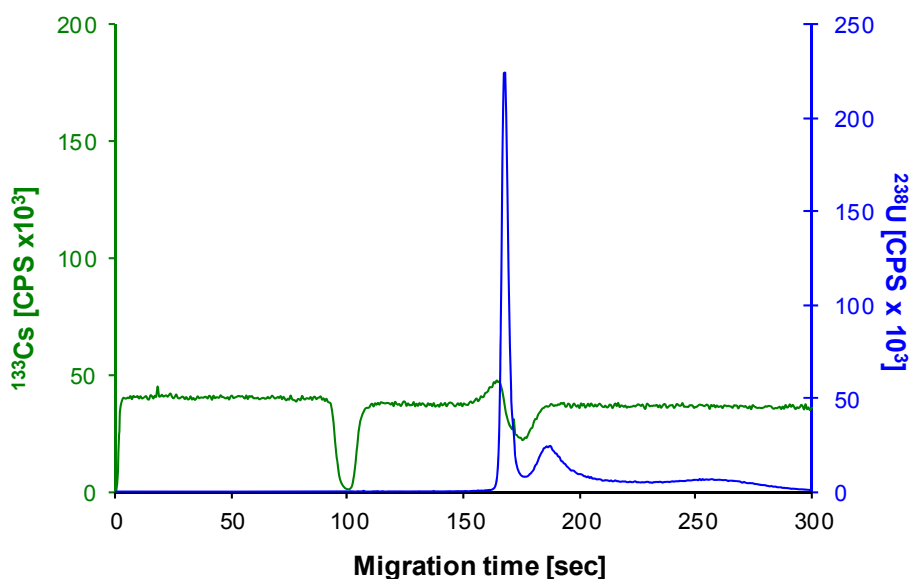


Figure 21: Electropherogram of uncomplexed and AHA-complexed ^{238}U and ^{133}Cs ($200\ \mu\text{g}\cdot\text{L}^{-1}$) as CE flow marker analysed by CE-ICP-MS, pH 5, $c(\text{U})$: $500\ \mu\text{g}\cdot\text{L}^{-1}$, $c(\text{AHA})$: $25\ \text{mg}\cdot\text{L}^{-1}$, U: 30 kV, CE-electrolyte: 100 mM HAc/10 mM NaAc

The great difference between the speciation of Eu and U is to be seen in the distribution of the cations in the different species. The humic acid complexed $95.0\pm 0.8\%$ of the europium cations, and we find $55.4\pm 1.3\%$ on strong binding sites ($n=3$). The molecular structure and the size of the uranyl cation are evidently the cause for a weaker complexation by AHA. Due to the linear constitution of the uranyl cation the bis-chelate effect of the carboxyl and hydroxyl groups from the humic acid is inhibited. Therefore, only $25.9\pm 0.5\%$ of the uranyl was complexed at the strong binding sites and $54.9\pm 1.6\%$ remain as AHA uncomplexed uranyl species.

3.4.5. Influence of PW on the Speciation of Europium-Humates

Previous studies on the influence of competing cations on the speciation of lanthanides were made with a maximum concentration of $30 \text{ mg}\cdot\text{L}^{-1}$ of divalent cations. This concentration is very low in comparison with the cation concentration in porewater. Therefore we started a series of dilution of porewater to determine the influence of increasing porewater concentration on the complexation of Eu with AHA. The sample preparation is similar to the experiments with sodium perchlorate. The dilutions and the concentration of the cations are shown in Table 6.

Table 6: Serial dilution of porewater (PW) with sodium perchlorate (SP) used to determine the influence of porewater concentration on the complexation of Eu with AHA.

Dilution PW:SP	PW [mL]	SP [mL]	Me ⁺ [mg·L ⁻¹]	Me ²⁺ [mg·L ⁻¹]
0:1	0	10	2.3	0
1:1024	0.01	9.99	5.5	1.5
1:512	0.02	9.98	10.9	2.9
1:256	0.04	9.96	21.9	5.9
1:128	0.08	9.92	43.8	11.7
1:64	0.16	9.84	87.5	23.4
1:32	0.31	9.69	175	46.9
1:16	0.63	9.37	350	93.8
1:8	1.25	8.75	700	187.5
1:4	2.5	7.5	1400	375
1:2	5	5	2800	750
1:0	10	0	5600	1500

The four electropherograms with the lowest porewater cation concentration are visible in Figure 22. In these electropherograms only Eu and Cs are shown. We observe a small decrease of peak 2 and an increase of the “free” species. The sodium cations in solution displace the Eu cations from weak binding sites of humic acid. The free europium cations are then complexed by acetate and migrate as peak 1.

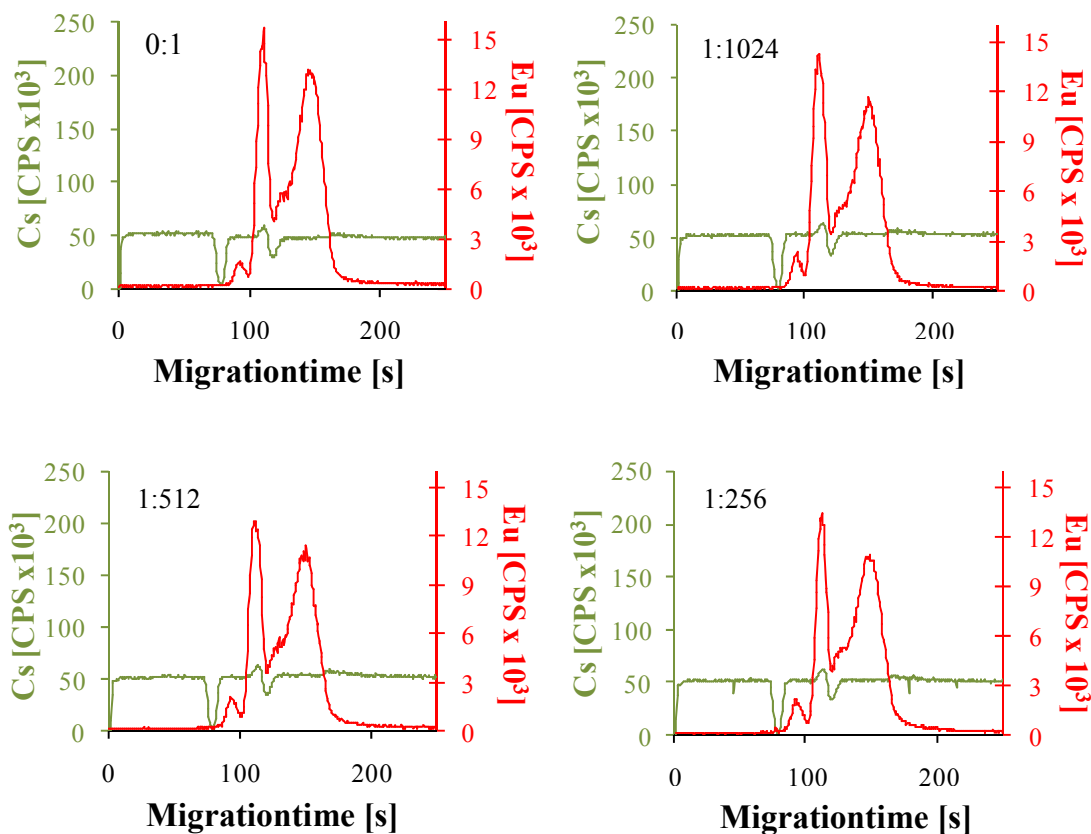


Figure 22: Electropherogram of 500 mg·L⁻¹ Eu and 25 mg·L⁻¹ humic acid influenced by porewater concentration (porewater – sodium perchlorate ratio from 0:1 to 1:256) at pH 5 (^{133}Cs green, ^{153}Eu red)

In Figure 23 the electropherograms with higher porewater concentration are shown. With increasing porewater concentration the Eu-peak 1 increases too. At low concentrations of porewater the divalent porewater cation calcium migrates with the same speed as Eu (peak 1). At the given buffer concentrations the calcium forms no acetate complex because its complex stability is much lower in comparison with the complex stability of Eu. Only when an excess of Ca cations is available does calcium displace the europium cations out of the acetate complex. Before peak 1 a new europium peak is formed. The “free” Eu^{3+} aquo-species migrates faster than the Eu-acetate species. With a higher porewater concentration peak 3 decreases very strongly and with pure porewater peak 3 is no longer to be seen. This can be explained by the precipitation of the humic acid at high cation concentrations. Additionally, peak 3 and peak 2 relocate themselves to one new peak which migrates faster than peak 2. Due to the high cation concentration the Eu-AHA-complex additionally takes up other metal cations. The whole cluster-complex migrates as positive species. Even in great excess divalent cations cannot displace europium out of the strong binding sites of humic acid.

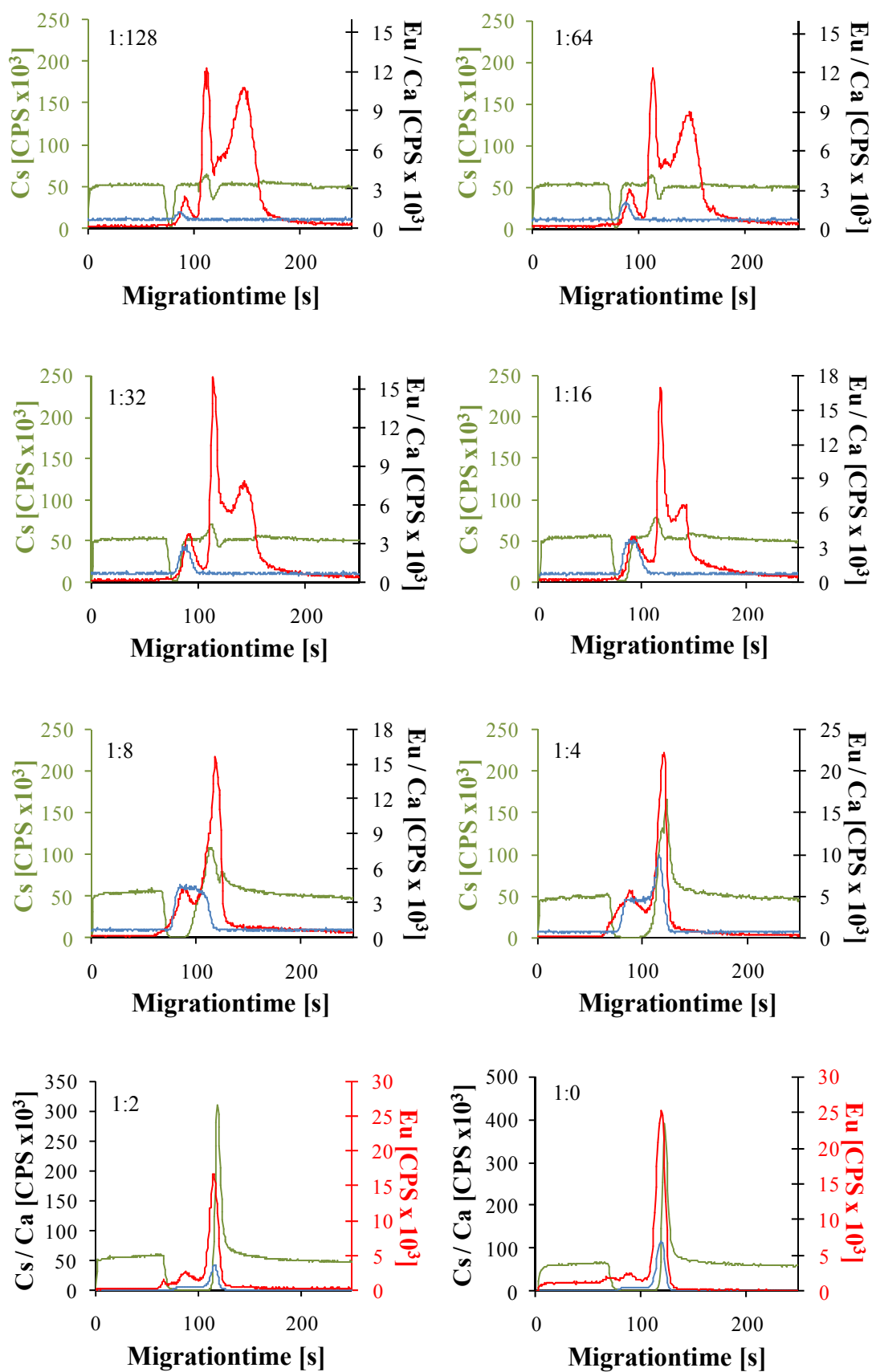


Figure 23: Electropherogram of $500 \text{ mg}\cdot\text{L}^{-1}$ Eu and $25 \text{ mg}\cdot\text{L}^{-1}$ humic acid influenced by porewater concentration (porewater – sodium perchlorate ratio from 1:128 to 1:0) at pH 5 (^{43}Ca blau, ^{133}Cs green, ^{153}Eu red)

3.4.6. Influence of Phenolic and Carboxylic Functional AHA-Groups

The migration or sorption of these actinides or lanthanides in the geosphere can be affected by a wide variety of chemical reactions; some of them involve natural organic substances (NOM) [31]. The humic material is a large and heterogeneous group of macromolecules of different molecular weight (500–250000 Dalton) and charge density, with complex and difficultly identifiable structure [5]. The structures of humic material consist of aromatic and aliphatic units and various functional groups [9,55,56]. Humic acid can play an important role in the immobilisation or mobilisation of metal ions due to complexation and colloid formation. The mechanism of such a complexation with metal ions is not well understood, above all with respect to the role of phenolic OH-groups. Hence it was discussed whether phenolic hydroxyl and carboxylic groups establish bis-chelate complexes with the metal ions [57-61]. Obviously both groups make a contribution to the strong binding of the cations by NOM like fulvic or humic acid.

One objective of this work was to clarify the influence of the different functional groups of humic acid. For this reason the speciation experiments were accomplished first with purified AHA and then also with a modified AHA with blocked phenolic hydroxyl and carboxylic groups (AHA-PB courtesy of the Helmholtz-Center Dresden Rossendorf). 84 % of the phenolic OH-groups were blocked by methylation, and partially, 40 % of the COOH-groups, too [33]. Details of the results are given in Table 7

3.4.6.1. Influence of Different pH-Values on the Complexation

The influence of the pH-value on the solubility of the AHA is very strong. It was therefore expected that the influence on the complexation of Eu would be strong, too. To investigate this influence more clearly experiments with $0.5 \text{ mg}\cdot\text{L}^{-1}$ Eu ($3.29\cdot 10^{-3} \text{ mmol}\cdot\text{L}^{-1}$) and $25 \text{ mg}\cdot\text{L}^{-1}$ AHA were performed at four different pH-values. In addition to pH 5 and 7 a pH-value in the acidic (pH 3) and in the alkaline region (pH 10) was chosen. In Figure 24 the electropherograms at pH 3, 5, 7 and 10 are shown. However, the observed influence on the Eu speciation with AHA is quite small. The largest differences can be seen in the acidic region at pH 3. The Eu-recovery (see Table 7) for this sample (62.9 %) is very low compared to the other complexation experiments (98.7-100.1 %) with Eu and AHA, and yet peak 1 is the largest in comparison to the other pH-values used. A high amount of the AHA coagulates and precipitates due to protonation and neutralisation because of the high proton excess at pH 3. The remaining AHA concentration in the solution is too low to complex a large amount of the Eu^{3+} -cations present. Therefore, a higher amount of Eu (6 %) migrates as $\text{Eu}(\text{Ac})^{2+}$ (species 1) in comparison to the situation at the other used pH-values (1-2 %) as seen in Table 7.

Table 7: CE-ICP-MS results for the Eu speciation in the presence of AHA in comparison to AHA-PB

pH	Species	t_{Mig} (min)	Counts (AHA)	% (AHA)	t_{Mig} (min)	Counts (AHA-PB)	% (AHA-PB)
3	1	1.57	5723	6	1.62	124725	85
	2	1.77	41782	42	1.85	7882	5
	3	2.43	52170	52	2.25	14520	10
	Total		99675	100		147127	100
	Rec (%) ¹		62.9			92.8	
3	Log β^*			6.04			4.01
5	1	1.52	2088	1	1.57	6663	6
	2	1.83	54168	35	1.82	92180	82
	3	2.43	100432	64	2.27	13718	12
	Total		156688	100		112561	100
	Rec (%)		98.9			71.0	
5	Log β^*			6.70			6.02
7	1	1.57	3401	2	1.57	4745	3
	2	1.88	58586	37	1.77	117265	80
	3	2.47	96657	61	2.32	24602	17
	Total		158644	100		146612	100
	Rec (%)		100.1			92.5	
7	Log β^*			6.49			6.30
10	1	1.55	2796	2	1.60	13117	13
	2	1.88	43426	28	1.92	75799	76
	3	2.45	110304	70	2.25	11227	11
	Total		156526	100		100143	100
	Rec (%)		98.7			63.2	
10	Log β^*			6.57			5.64

¹Eu-recovery in comparison to Eu standard samples without humic acid (0.5 mg·L⁻¹ Eu); t_{Mig} : Migration time of the Eu species, Counts: Determined Eu intensities (counts·sec⁻¹ · sec) for the separated species, %: Percentage of the three Eu species in each sample ($\Sigma = 100$ %), Log β^* : Conditional complex stability constant

The recovery of all three Eu species in sum at pH 3 is lower than 63 % due to the fact that the precipitated AHA contains a relatively high amount of complexed Eu. The differences between the remaining pH-values (pH 5, 7 and 10) are comparatively small. The recovery for these three pH-values is nearly about 100 %. Small differences can be explained by the presence of carbonates and hydroxides at higher pH-values that have an influence on the solubility of the europium ions and diminish these cations in solution due to precipitation as Eu-carbonates and hydroxides. Averaging over a pH-range from 3 to 10 for the complexation of Eu^{3+} and AHA a mean conditional complex stability constant $\log \beta^*$ of 6.45 ± 0.29 was determined which was in very good agreement with other studies [29,61,62].

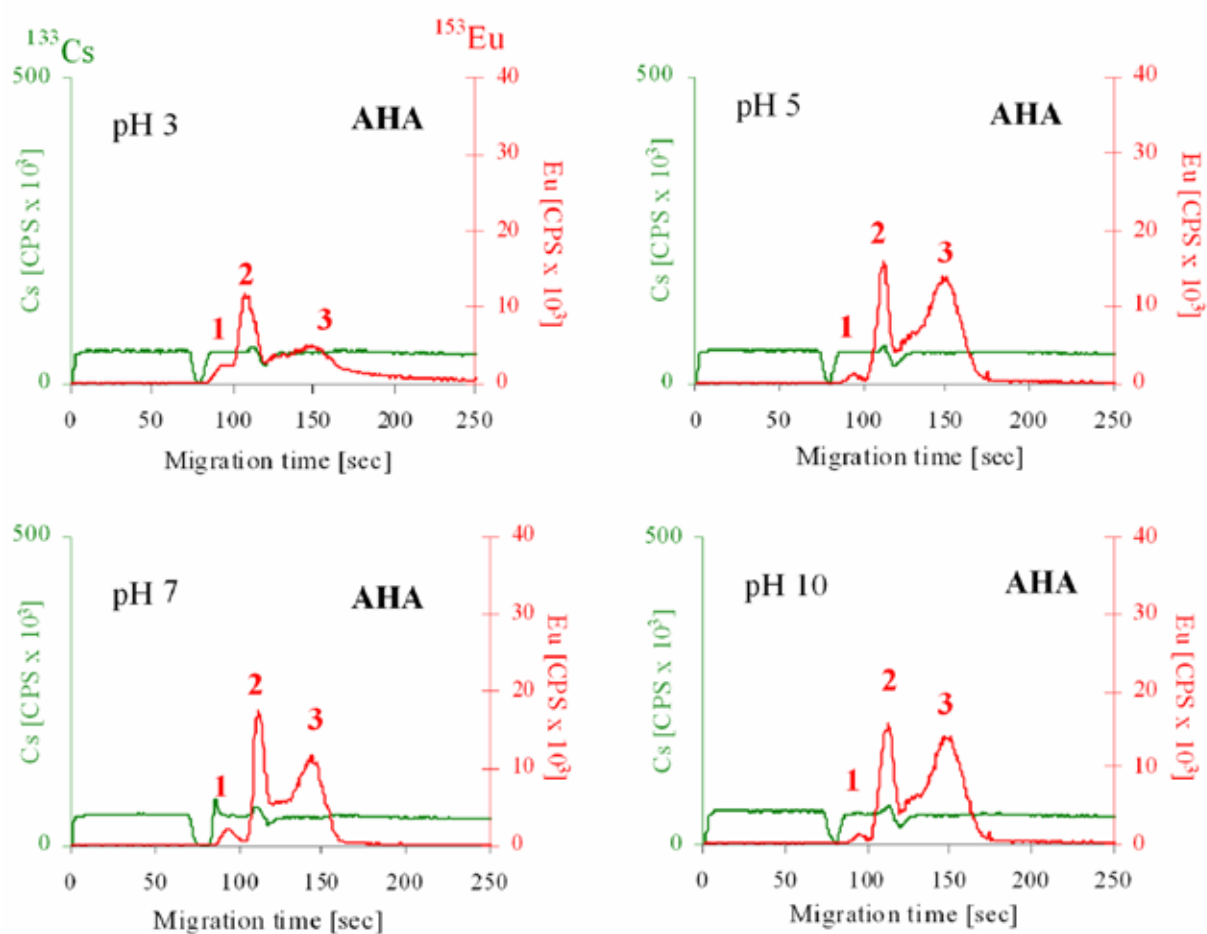


Figure 24: CE-ICP-MS electropherograms of Eu species complexed or uncomplexed with original Aldrich AHA at different pH-values and Cs as CE flow marker; samples: $3.29 \mu\text{mol}\cdot\text{L}^{-1}$ Eu, $25 \text{ mg}\cdot\text{L}^{-1}$ AHA, 10 mM SP and pH 3, 5, 7 and 10

3.4.6.2. Influence of AHA-Functional Groups on Eu Complexation

To get more insight into the interaction of Eu with humic acids we have investigated the influence of the main complexation sites (phenolic OH- and carboxylic-groups) on the complexation behavior. Therefore, a modified AHA with blocked functional groups was used. The combined attack of both carboxyl and hydroxyl groups should be responsible for the stronger negatively charged metal humate complexes due to the formation of stable chelate-configurations [10].

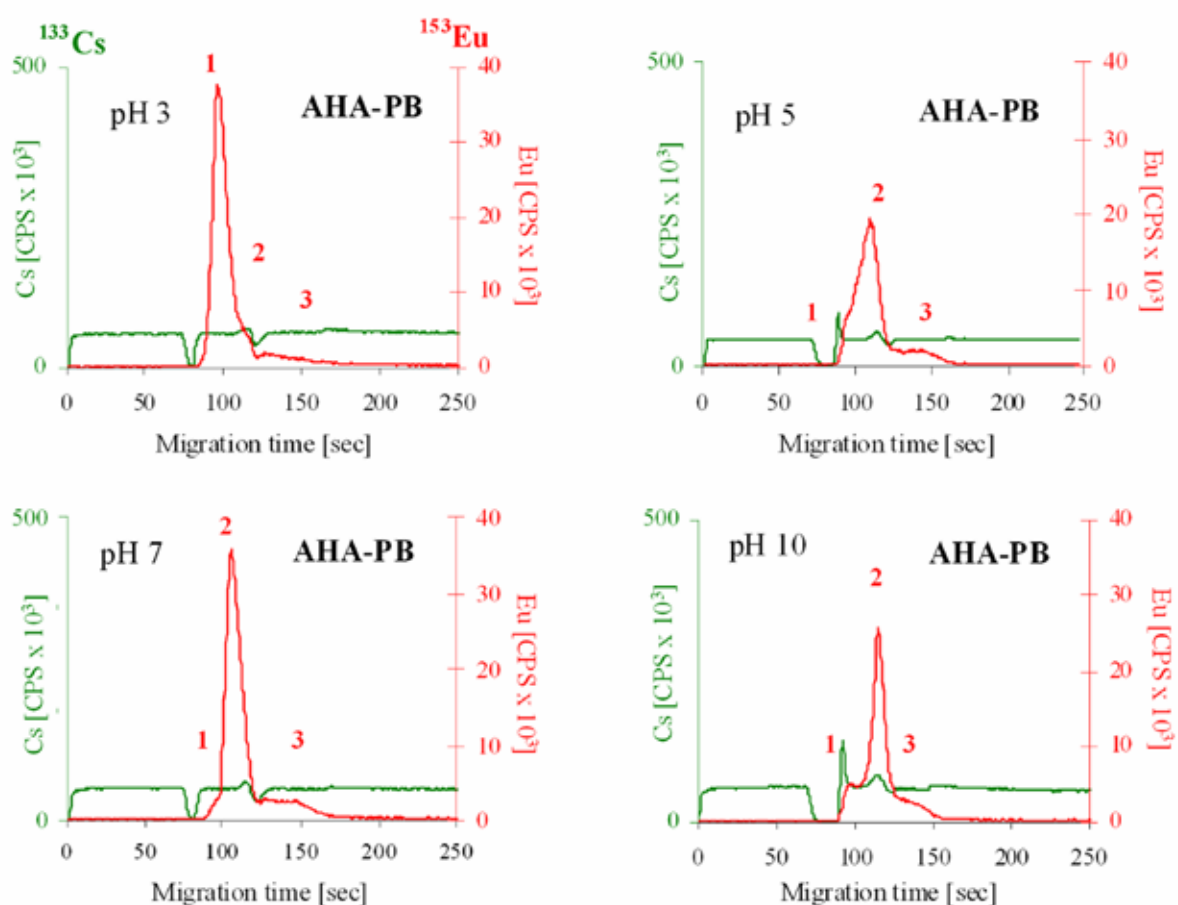


Figure 25: CE-ICP-MS electropherograms with Eu species complexed or uncomplexed with modified Aldrich HA at different pH-values and Cs as CE flow marker; sample: $3.29 \mu\text{mol}\cdot\text{L}^{-1}$ Eu, $25 \text{ mg}\cdot\text{L}^{-1}$ AHA-PB, 10 mM SP and pH 3, 5, 7, 10

Figure 25 shows results obtained with the “original” Aldrich AHA and the modified AHA-PB with blocked groups at pH 3, 5, 7 and 10 in comparison. One observation is common for all pH-values. The amount of AHA-PB complexed Eu that is bound at the strong binding sites (peak 3 in the electropherograms) has decreased significantly as shown in Table 7.

The percentage of this species (peak 3) is in the range of 10 % (pH 3) and 17 % (pH 7) in comparison to 52 % (pH 3) – 70 % (pH 5) for the interaction of Eu and unmodified AHA. This confirms the hypothesis that OH- and COOH-groups in the humic acid are both responsible for the strong bonding of metal ions like Eu. When the phenolic OH-groups are not present or only in a low concentration the COOH- groups form only weak bonds to Eu ions. This is demonstrated by the increase of peak 2 (weakly bound Eu) especially at pH-values between 5 and 10.

The Eu recovery at different pH-values is a representative value for the metal solubility in the aquifer. This solubility of Eu (found here as recovery of all Eu species in one CE run) shows strong differences in experiments with AHA or AHA-PB. In the acidic solution (pH 3) the Eu recovery increases strongly from 62.9 % (in the presence of AHA) to 92.8 % with AHA-PB present as shown in Table 7. In contrast the Eu recovery at the other pH-values decreases by the interaction of Eu with AHA-PB in comparison to AHA. The Eu-recovery decreases from nearly 100 % (98.7-100.1 %) with AHA to values between only 63.2 % (pH 10) and 92.5 % (pH 7) with AHA-PB. This may be explained by the decrease of hydrophilic groups of the AHA-PB due to the blocked functional groups which leads to a reduced water solubility of AHA-PB. A coagulation of AHA-PB is already seen at lower metal concentrations compared with AHA. At pH 3 this effect causes a higher recovery of Eu.

The high proton excess in the solution is sufficient for neutralisation of the AHA-PB followed by precipitation of the protonated form. Therefore there is not enough AHA-PB in solution to form negatively charged Eu-humate species. As consequence a high amount of Eu cations migrates as uncomplexed species (peak 1) resulting in comparably lower $\log \beta^*$ -values between 4.01 (pH 3) and 6.30 (pH 7) than determined for AHA.

A decreased total recovery of all Eu species in the samples was seen particularly at pH-values of 5, 7 and 10. With the same concentration of Eu cations the solubility of AHA-PB substantially decreases due to their lower CEC (cation exchange capacity) of $3.2 \pm 0.4 \text{ meq g}^{-1}$ [33] in comparison to $5.0 \pm 0.1 \text{ meq g}^{-1}$ for AHA [29]. Therefore, a lower amount of Eu cations is needed to neutralise the negatively charged AHA-PB in the solution followed by a precipitation of the uncharged Eu-AHA-PB complex. Due to the blocked phenolic OH- and COOH-groups of the AHA-PB the amount of the uncomplexed Eu-species (peak 1) increases at all pH-values compared to the experiments with AHA. The decrease of the OH- and COOH-groups leads to a lower complexation capacity for metal cations like Eu.

These results suggest the existence of different humic acid bounded Eu-species depending on the amount of functional groups. In addition it shows that not only COOH-groups of NOM like humic acids are important for the strong complexation of metal cations. The interaction of both functional groups is necessary for a strong Eu complexation forming negatively charged

and hence water soluble species. Therefore, particularly NOM with a high amount of phenolic OH- and COOH-groups can be responsible for a high metal mobility in the aquifer.

In summary, humic acid can highly influence the mobility of metal cations in the aquifer in the near and far field of a repository in deep geological formations. The AHA which is used in standardised laboratory experiments as model humic acid for natural occurring humic substances has a high complexation ability for lanthanides and thus for the homologous actinides. Especially highly charged metal ions like Eu^{3+} are strongly complexed by the humic acid and a high amount of negatively charged Eu-humate complexes are formed, which can increase the Eu mobility in the geological barrier of a potential waste disposal. The consequences of this metal complexation on the mobilisation or immobilisation of metal cations in clay formations for a future repository are not enough investigated. For a general statement more studies, e.g. complexation studies with natural occurring NOM, e.g. humic acids from a potential disposal site, are necessary. However, our experiments with modified humic acid show that both carboxyl- and hydroxyl- groups are very important for metal complexation, and these findings have to be taken into account in the context of a risk assessment of a future repository for high level radioactive waste.

3.5. Analysis of the Binary System Metal – Clay

An important mechanism for retarding radionuclide migration in the environment is sorption onto clay minerals present along the groundwater flow path. However, sorption and desorption processes are complicated by their dependence on various parameters.

In this working package we investigated the sorption and desorption behaviour of the trivalent lanthanides Eu, Gd, Tb as homologues of the actinides Am, Cm and Bk which are in addition to Pu and Np in large amounts in nuclear waste and nuclear materials inventories stored in various sites around the world and additionally of U(VI) as one of the major compartments of the nuclear waste. Standardised laboratory batch experiments are performed in the binary system consisting of these heavy metals (Eu, Gd and Tb) and the natural Opalinus clay under conditions close to nature. The Batch technique is “state of the art” to compare results from different studies. However, the best way would be a combination of batch and column experiments, and this will be the next step to report in our research project. The K_d -values of the metals have been determined for interaction with such clay, and some thermodynamic values for the reactions like enthalpy and entropy were estimated. Additionally, the influence of the concentration, pH-value, temperature and of different competing metal ions (calcium and magnesium) on the metal sorption onto Opalinus clay and desorption from the clay was investigated.

3.5.1. Sorption Experiments

The experiments started in sodium perchlorate (SP) solution with an ionic strength of 10 mM and in synthetic porewater (PW, $I=0.42$ M). The solid/liquid ratio between clay and solution was $4 \text{ g}\cdot\text{L}^{-1}$. After preconditioning for 72 h we added lanthanide concentrations from $10 \text{ }\mu\text{g}\cdot\text{L}^{-1}$ to $500 \text{ mg}\cdot\text{L}^{-1}$. The pH-values were adjusted to pH 5 and 7.6. The equilibrium time was 72 h. At both pH-values the sorption in sodium perchlorate solution is higher than in porewater due to the competing cations in the porewater which displace the lanthanides from the Opalinus clay. The sorption is higher at pH 7.6 in comparison to pH 5. Additionally to the sorption, a precipitation of the lanthanides as carbonate in the solution is observable.

3.5.1.1. Influence of Temperature on Sorption Experiments with Europium

To check the influence of higher temperature on the sorption of lanthanides onto Opalinus clay, we repeated the sorption experiments at 60°C with a lanthanide concentration of $900 \text{ }\mu\text{g}\cdot\text{L}^{-1}$ ($5.8 \cdot 10^{-6} \text{ mol}\cdot\text{L}^{-1}$). The other conditions are similar to the experiments at 25°C . In Figure 26 the differences between 25 and 60°C are clear visible.

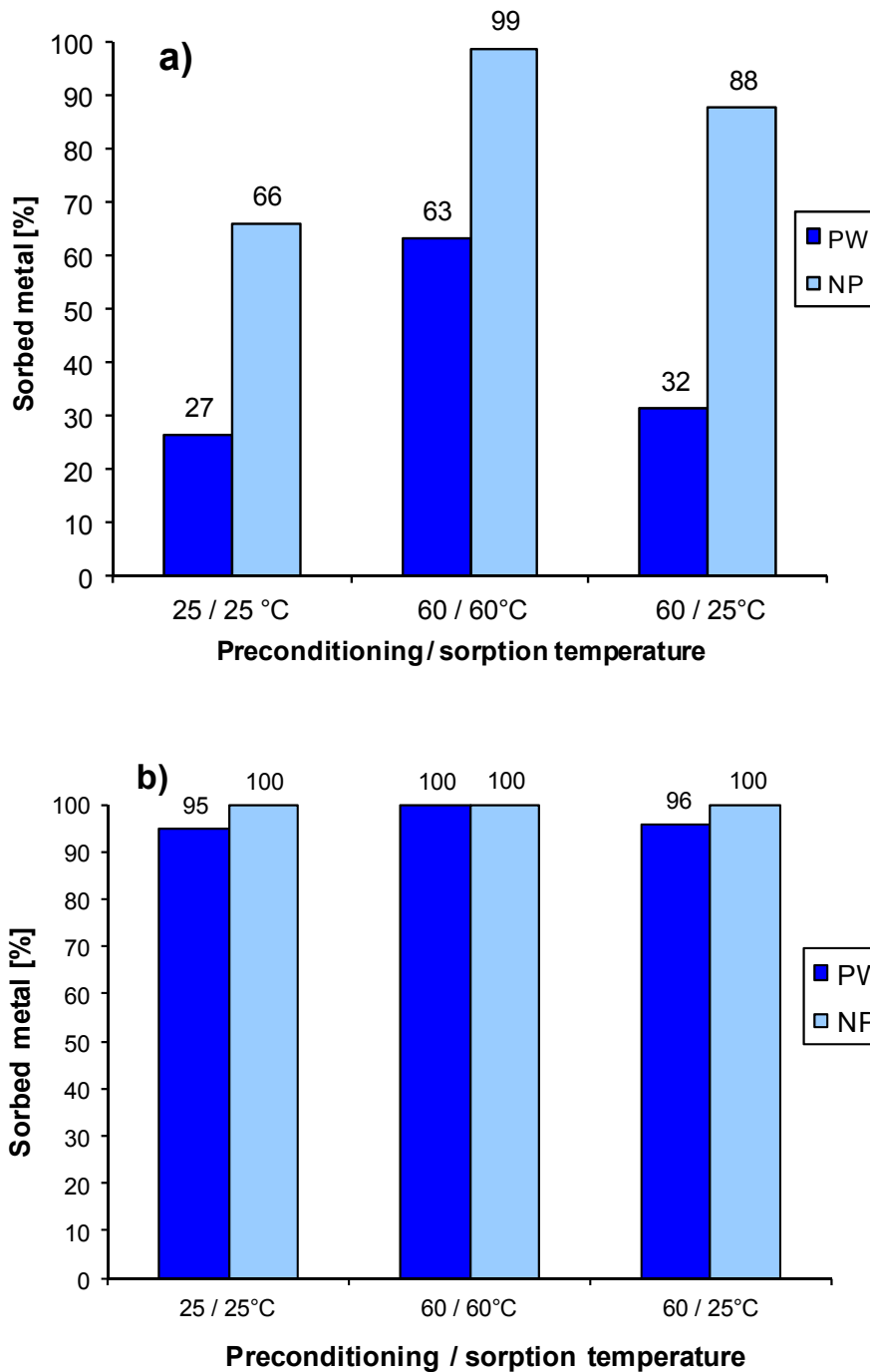


Figure 26: Influence of temperature on the sorption of europium ($C_{Eu} = 5.8 \cdot 10^{-6} \text{ mol L}^{-1}$) onto Opalinus clay; a) Sorption in sodium perchlorate (SP, $I=10 \text{ mM}$) and synthetic porewater (PW, $I=0.42 \text{ M}$) at pH 5 and 25/60°C; b) Sorption in SP and PW at pH 7.6 and 25/60°C

At pH 5 and 60°C (Figure 26a)) a higher sorption is observed in comparison to 25°C. In PW the sorption increases by more than 100 % from 27 to 63 %. In NP the sorption increases from 66 to 99 %. This observation could be an effect of the structural modification of the clay

or a temperature effect of the sorption (endothermic reaction). To give some answers it was analysed whether the increased sorption process at higher temperature is reversible. We therefore preconditioned the samples at 60°C, and let the sorption process take place at room temperature. In we can see that the sorption is slightly higher than at 25°C. This shows a partially reversibility of the sorption process. At higher temperature the clay surface is evidently etched by the solution and new binding sites develop where the lanthanides sorbed too. Figure 26b) demonstrates that at pH 7.6 the differences between the temperatures are not so distinct as at pH 5. With higher temperature the sorption increases only by 5 % in PW. In sodium perchlorate nearly 100 % of the lanthanides are sorbed at all temperatures. In this case differences between 25 and 60°C treatment could not be observed.

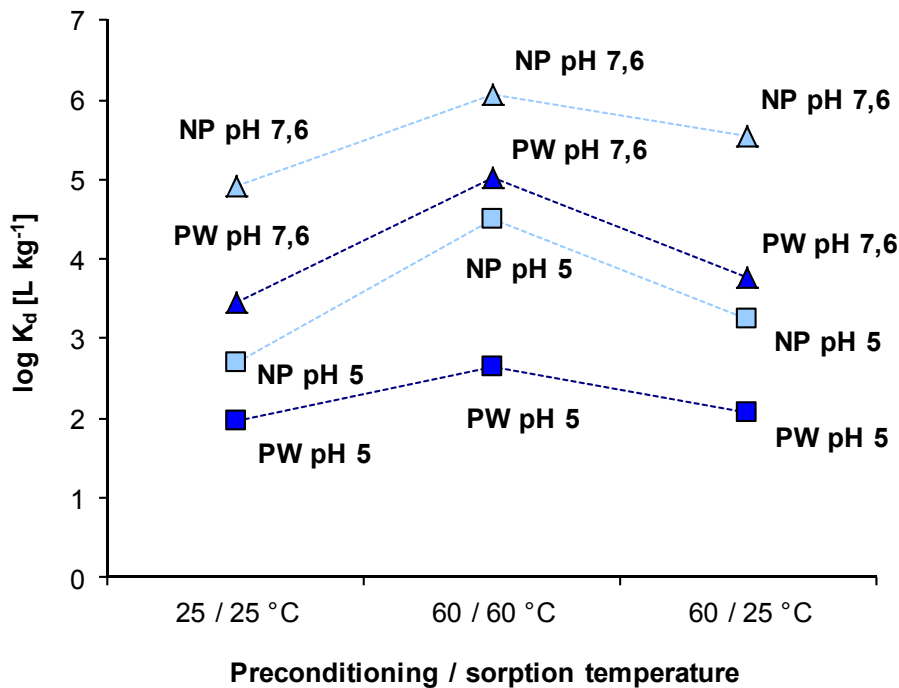


Figure 27: K_d -values of the europium sorption at pH 5/7.6 and 25/60°C in porewater and sodium perchlorate

The sorption differences at pH 7.6 between 25 and 60°C can well be described by the K_d values calculated from the results of the experiments (Figure 27). The increasing sorption at higher temperature in NP and at pH 7.6 is visible. In NP and PW the K_d -values increase from pH 5 to pH 7.6 just like from 25 to 60°C. This results show the same trend like the experiments of Tertre et al. for europium and Montmorillonite [63,64]. The log K_d -values of Tertre et al. increase from 4.6 (25°C) to 5.4 (80°C) in 0.025 M sodium perchlorate and from 3.6 (25°C) to 5.1 (80°C) in porewater with an ionic strength of 0.5 M. These results are in

good agreement with the log K_d -values of our results which increase from 4.9 to 6.1 in NP and from 3.5 to 5.0 in PW.

3.5.1.2. Calculation of Thermodynamic Values via Van't Hoff Plot

To specify the sorption as a thermodynamic process it is necessary to discuss enthalpy and entropy values, and these can well be determined from a Van't Hoff Plot. In order to calculate such thermodynamic parameters we repeated some sorption experiments at three different temperatures. We used 25, 40 and 60°C for the sorption of uranium and europium. In Figure 28 the Van't Hoff Plots of the sorption of europium and uranium in porewater at pH 7.6 are depicted. With the linear relation of the values and the following equation

$$\ln K_d = -\frac{\Delta H}{RT} + \frac{\Delta S}{R}$$

the slope m of the graph is $-\frac{\Delta H}{R}$ and the intercept b is $\frac{\Delta S}{R}$.

For europium we calculated an enthalpy of $71.0 \pm 2 \text{ kJ} \cdot \text{mol}^{-1}$ and entropy of $258.9 \pm 4.7 \text{ J} \cdot \text{K}^{-1} \cdot \text{mol}^{-1}$. The values for uranium are in a similar range with $\Delta H = 92.9 \pm 3 \text{ kJ} \cdot \text{mol}^{-1}$ and $\Delta S = 272.5 \pm 8.4 \text{ J} \cdot \text{K}^{-1} \cdot \text{mol}^{-1}$.

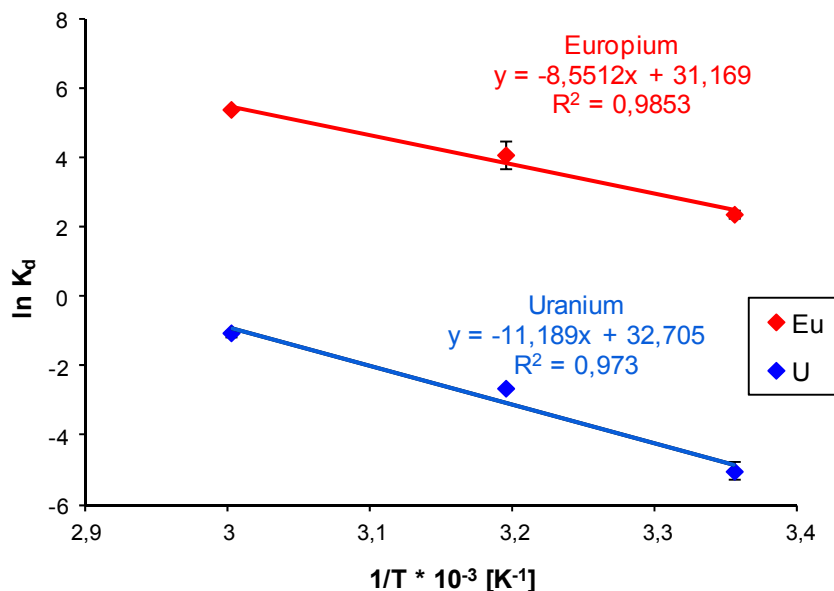


Figure 28: Linear fit of the Van't Hoff Plot of the sorption of europium and uranium onto Opalinus clay in synthetic porewater at a pH value of 7.6 (298, 313 and 333 K)

3.5.2. Desorption Experiments Influenced by Temperature

The remobilisation process is important too to estimate the retention of some metal cations like europium and uranium on the Opalinus clay.

For the desorption experiments in the first step a specified concentration of uranium ($4.2 \cdot 10^{-7} \text{ mol} \cdot \text{L}^{-1}$) or europium ($1.9 \cdot 10^{-6} \text{ mol} \cdot \text{L}^{-1}$) was sorbed onto the Opalinus clay. With the next three desorption steps we checked the remobilisation of the metal ions from the clay. Sodium perchlorate solution or porewater was added to the clay remaining after centrifugation. The equilibrium time was 72 h remobilised metal concentration in the supernatant was analysed by ICP-MS. For the evaluation the mobilised metal concentration of every step was subtracted from the initially sorbed metal concentration. Besides pH and competing cations the temperature was an important parameter too.

3.5.2.1. Influence of the pH-Value on the Eu Desorption

For the desorption experiments acidic (pH 3; 5), neutral (pH 7.6) and alkaline (pH 10; 12) pH-values were used. In Figure 29 desorption of europium in sodium perchlorate solution is described.

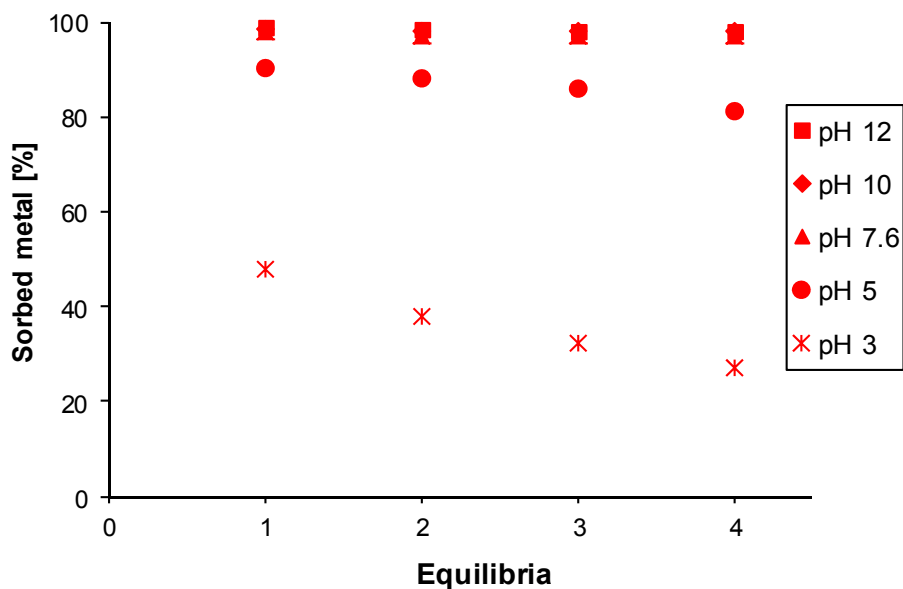


Figure 29: Influence of pH-values (pH 12/10/7.6/5/3) on the sorption and desorption of europium in SP ($c_{\text{Eu}} = 300 \mu\text{g} \cdot \text{L}^{-1}$, S / L ratio = $4 \text{ g} \cdot \text{L}^{-1}$, I = 10 mM)

At pH 12, 10 and 7.6 no decrease of sorption is to be seen. In this pH-range the europium had precipitated also as carbonate and hydroxide during the sorption steps. Due to the high concentration of carbonate- and hydroxide-ions in the solution the precipitated europium-

carbonates and hydroxides are stable. At pH 5 the sorption had been lower than at the higher pH-values and a desorption is now observable too. After the three desorption steps still 80 % of the originally added europium concentration are sorbed. The influence of the protons and the competing cations from clay dissolution is not so strong. At pH 3 only 40 % of the added europium concentration is sorbed onto the clay. Protons and competing cations inhibit a sorption. Additionally, they displace the europium from the clay in the desorption steps, 50 % of the sorbed europium was remobilised.

The results with uranium (Figure 30) show significant differences compared to those with europium. In the alkaline pH-range (pH 12, 10) no quantitative sorption is observable. At pH 12 only 90 % and at pH 10 only 75 % of the inserted uranium concentration was sorbed. Additionally a strong desorption was visible. This effect could be explained by a sorption and not by a precipitation as with europium. At pH 7.6 only 30 % of the uranium is sorbed due to a strong aquatic uranyl-calcium-carbonato-complex ($\text{Ca}_2\text{UO}_2(\text{CO}_3)_3$). The sorbed uranyl is bond on the strong binding sites of the Opalinus clay. Because of that no desorption is observable.

At pH 5 100 % of the uranium is sorbed and only a small part of uranium is remobilised after three desorption steps. No complex formation and no replacement by competing cations can be seen in contrast to the results at pH 3. The sorption is evidently suppressed due to the sterical hindrance of the uranyl cation and additionally by the competition with protons and cations from clay dissolution.

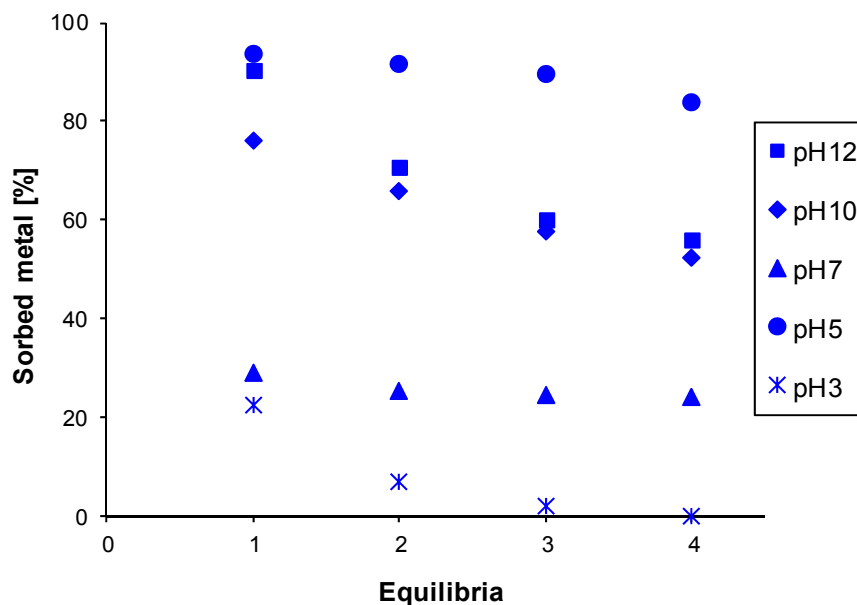


Figure 30: Influence of pH-values (pH 12/10/7.6/5/3) on the sorption and desorption of uranium in SP ($c_U = 100 \mu\text{g}\cdot\text{L}^{-1}$, S / L ratio = $4 \text{ g}\cdot\text{L}^{-1}$, I = 10 mM)

3.5.2.2. Influence of the Competing Cations from PW on the Eu Desorption

The influence of porewater is of great interest because it reflects conditions close to nature. The competing cations strongly affect the sorption and desorption results. In Figure 31 desorption experiments of europium at different pH-values are shown. In the alkaline range (pH 12/10) similar results to NP are observable but at pH 7.6 significant differences are visible. The competing cations in the porewater prevent the sorption onto the Opalinus clay. Additionally, they displace the sorbed cations from the clay. At pH 7.6 the europium cations are partially sorbed and partially precipitated by carbonate. The competing cations remobilised only the sorbed cations. Therefore, only 10 % remobilisation. In the acidic range (pH 5 / 3) the sorption onto the clay is very low. The hindrance of the sorption by protons is intensified by the competing cations of the porewater. Additionally the competing cations remobilised the few sorbed europium cations quantitatively from the clay.

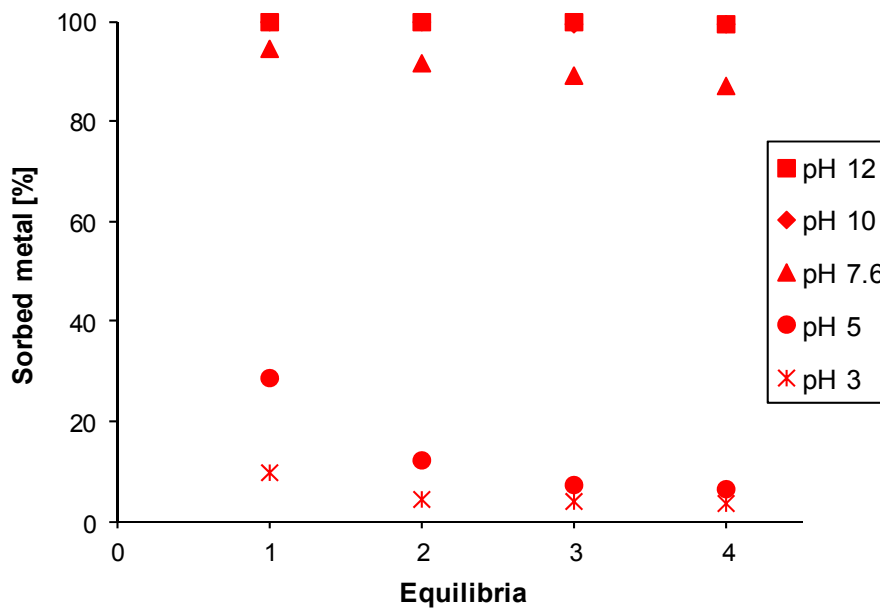


Figure 31: Influence of pH-values (pH 12/10/7.6/5/3) on the sorption and desorption of europium in PW ($c_{Eu} = 300 \mu\text{g}\cdot\text{L}^{-1}$, S / L ratio = $4 \text{ g}\cdot\text{L}^{-1}$, I = 0.4 M)

Similar to the results with Eu the competing cations from PW influence the sorption and desorption of uranyl very strongly (Figure 32). In the alkaline pH-range (pH 12/10) a high sorption and only a very low remobilisation is observable. The negative charged uranyl-carbonato- and hydroxo-species became neutralised and are precipitated by the competing cations of the porewater. At pH 7.6 only 10 % of the inserted uranium is sorbed. The calcium of the porewater enhances the formation of the calcium-uranyl-carbonato-complex, which doesn't sorb onto the Opalinus clay. A desorption of the uranyl is not observed. At pH 5 the

sorption is high but lower than in NP because of the competing cations of the porewater. Additionally a strong desorption is observable. The high amount of competing cations leads to a displacement of the uranyl from the clay.

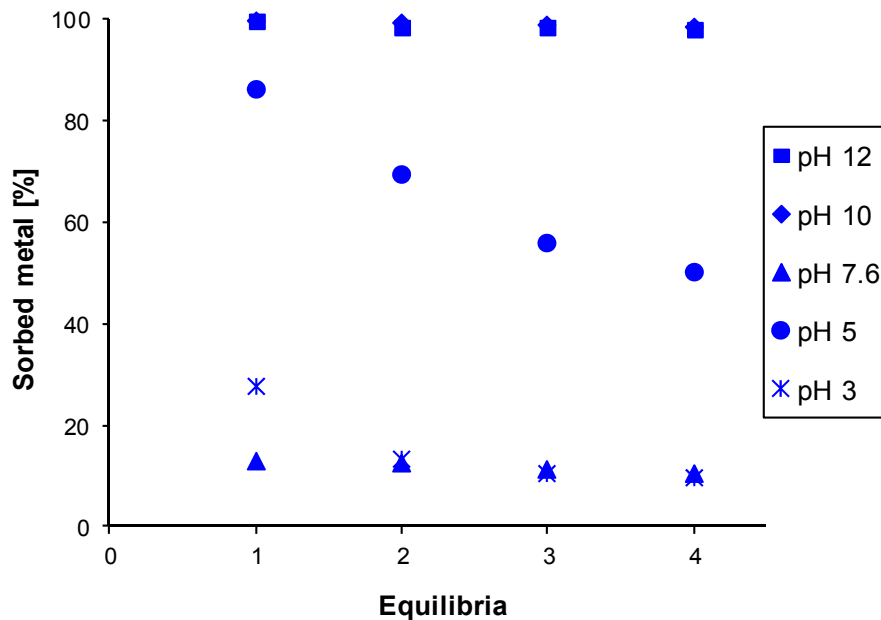


Figure 32: Influence of pH-values (pH 12/10/7.6/5/3) on the sorption and desorption of uranium in PW ($c_U = 100 \mu\text{g}\cdot\text{L}^{-1}$, S / L ratio = $4 \text{ g}\cdot\text{L}^{-1}$, $I = 0.4 \text{ M}$)

3.5.2.3. Influence of the Temperature on the Eu Desorption

In this chapter we discuss the influence of temperature on the sorption and desorption of europium. We analysed the sorption and desorption at 25 and 60°C. Additionally, we analysed the sorption at high temperature (60°C) followed by desorption at low temperature (25°C). Such conditions may occur in a repository.

In Figure 33 the results of the sorption and desorption experiments of europium in porewater at different temperatures and pH-values are described. The results in the alkaline range (pH 12/10) are the same at different temperatures. At pH 12 and 10 a quantitative sorption and no remobilisation of the europium is observable. At pH 7.6 clear differences between different sorption and desorption temperatures are noticed. The sorption increases with the temperature and the remobilisation decreases with increasing temperature. At 60°C the sorption is nearly 100 % but only a remobilisation of 3 to 5 % is seen at this temperature. Especially interesting is the sorption at 60°C and the following desorption at 25°C. A sorption at higher temperatures has an effect on the remobilisation of the sorbed metals at lower temperatures, too.

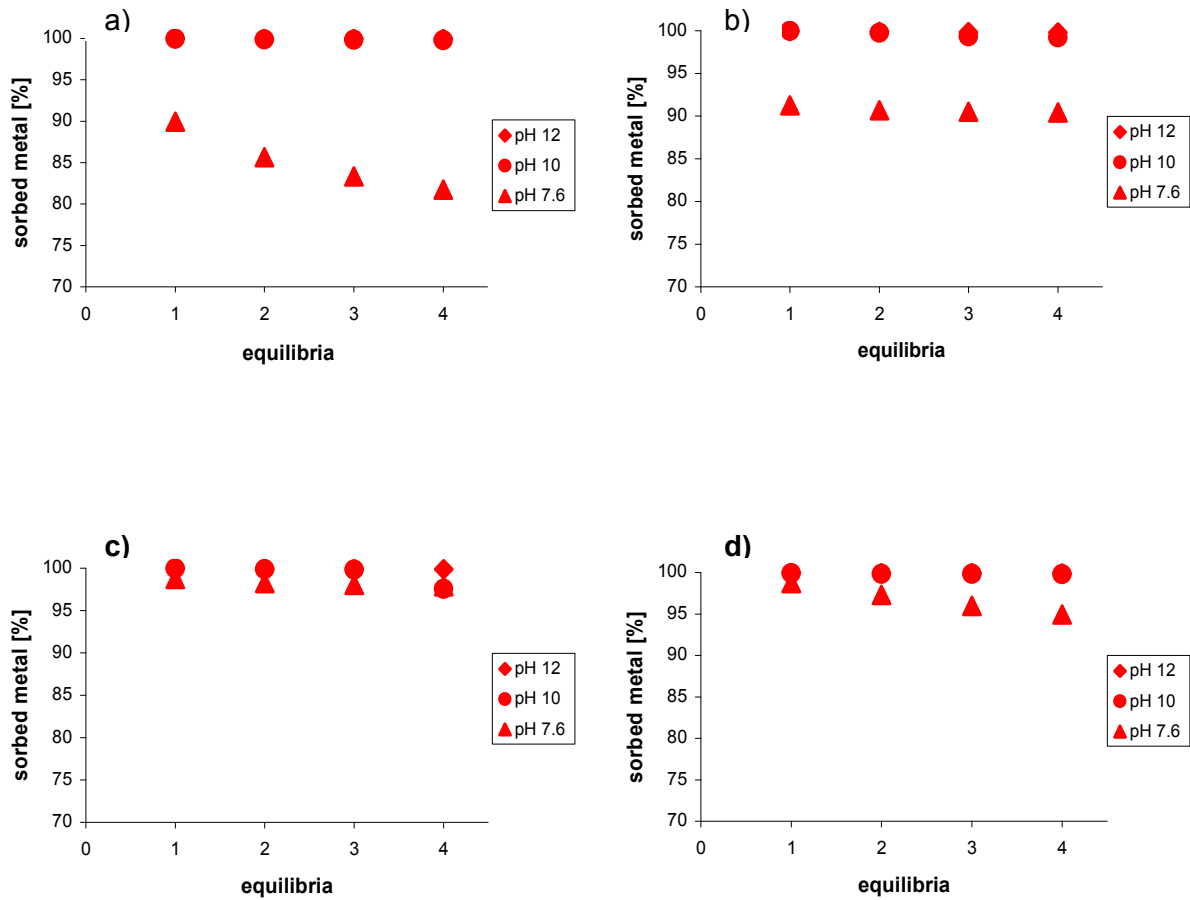


Figure 33: Sorption and desorption of europium on Opalinus clay in porewater influenced by temperature (25/60°C) and pH (pH 12/10/7.6) a) Sorption and desorption at 25°C, b) Sorption at 25°C and desorption at 60°C, c) Sorption and desorption at 60°C, d) Sorption at 60°C and desorption at 25°C

3.5.3. The Influence of Temperature on pH-Edges

The previous results show the strong influence of the pH value on the sorption. Additionally, the influence of the temperature was to be seen too. For this reason both influences must be compared. To analyse the effects on the pH-edges of europium we used $300 \mu\text{g}\cdot\text{L}^{-1}$ of europium standard ($1.9\cdot 10^{-6} \text{ mol L}^{-1}$) and for the experiments with uranium we used a concentration of $100 \mu\text{g L}^{-1}$ ($4.2\cdot 10^{-7} \text{ mol L}^{-1}$). The equilibration time was 72 h. In addition to the pH influence we checked the influence of competing cations. For all experiments on pH-edges we used sodium perchlorate and synthetic porewater.

3.5.3.1. Influence of pH and Temperature on the Sorption of Eu

In 10 mM sodium perchlorate solution the sorption decreases at pH-values lower than 6 (Figure 34 a)). The protons and the cations from clay dissolution compete with the europium cations and interfere in their sorption. In addition to protons and cations from clay dissolution the porewater cations also compete with the europium cations. The sorption in PW already decreases at pH-values lower than 8 and then even faster than in the SP case. The pH-edge is between pH 6 and 4, and is steep. At very low pH-values (< pH 4) no sorption is observable.

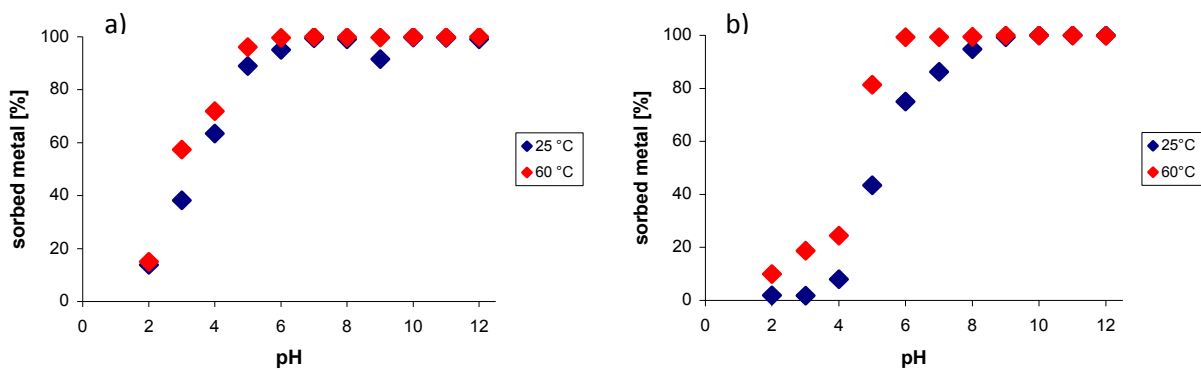


Figure 34: pH-edges of europium at two different temperatures (25/60°C); a) in sodium perchlorate SP, b) in synthetic porewater PW

In sodium perchlorate solution and in porewater higher temperatures favour a higher sorption. There are some explanations for this effect. Sorption could be an endothermic reaction. With increasing temperature the sorption would increase too, or the surface area of the clay changed by the heat treatment and would increase, and together with this effect some mineral cations could dissociate and open exchange sites for other metal cations. In the end more europium cations could adsorb onto the clay surface.

Table 8: K_d -values of europium ($1.9 \cdot 10^{-6} \text{ mol L}^{-1}$) in porewater (PW) and sodium perchlorate (SP) at pH 7.6 and 25/60°C

Eu(III)	K_d -value PW [L·kg ⁻¹]	K_d -value SP [L·kg ⁻¹]
25°C	1568.7 ± 120.2	44410.1 ± 1356.8
60°C	37021.6 ± 598.6	519720.6 ± 5684.9

The K_d -values of europium in NP and PW are shown in Table 8. There is complete sorption of Eu at pH 7.6 (see Figure 34). In this pH-range there are no differences between NP and PW. The K_d -values reflect well the decreasing sorption with competing cations from porewater and the increasing sorption at higher temperatures.

3.5.3.2. Influence of pH and Temperature on the Sorption of U(VI)

As with the desorption experiments the pH edges of europium and uranium are very different. The sorption of europium is maximal between pH 6 and 12. For uranium there is a first maximum between pH 4 and 6 and a second one between pH 9 and 11 as seen in Figure 35. In the neutral range the sorption has a minimum due to the formation of a neutral metal aquo-carbonato-complex ($\text{Ca}_2\text{UO}_2(\text{CO}_3)_3$) which does not adsorb onto the Opalinus clay. Besides the difference between europium and uranium themselves some differences between porewater and sodium perchlorate are obvious. In SP the formation of the metal aquo-carbonato-complex depends on how much calcite is dissolved. In PW a higher amount of complex is formed due to the excess of calcium ions in porewater. The sorption at pH 7.6 in porewater is clearly lower than in SP. In sodium perchlorate the sorption decreases again in the range above pH 10. The uranium forms negatively charged complexes with carbonate and hydroxide which stay in solution. These complexes are neutralised and precipitate in porewater due to the high concentration of competing cations.

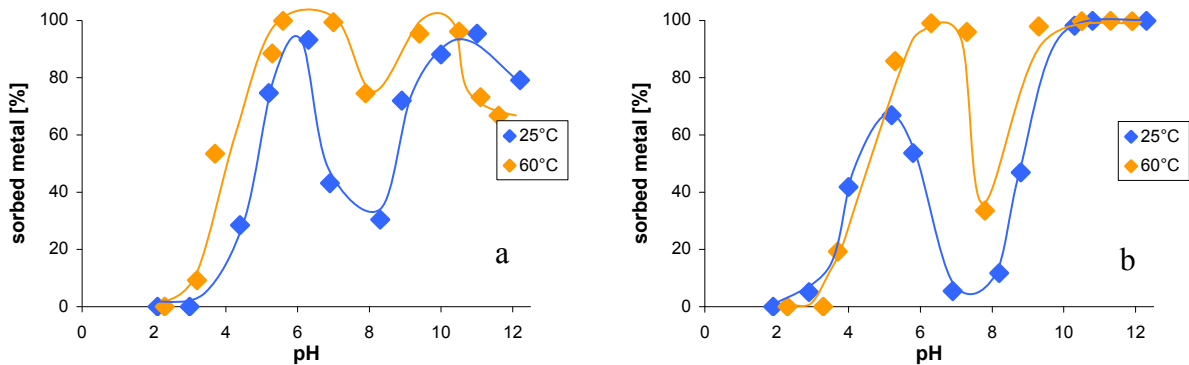


Figure 35: pH-edges of uranium at two different temperatures (25/60°C); a) in sodium perchlorate SP, b) in synthetic porewater PW

With increasing temperature the sorption increases over a wide pH-range. For this higher sorption some explanations are possible. The increasing sorption could be an effect of a structure change of the clay surface or it is an effect of the uranium speciation. For example the metal aquo complex may be less stable at high temperatures.

Table 9: K_d -values of uranium ($4.2 \cdot 10^{-7}$ mol L⁻¹) in porewater (PW) and sodium perchlorate (SP) at pH 7.6 and 25/60°C

U(VI)	K_d -value PW [L·kg ⁻¹]	K_d -value SP [L·kg ⁻¹]
25°C	23.9 ± 13.5	149.3 ± 56.6
60°C	126.3 ± 37.8	730.6 ± 4.0

The K_d -values (Table 9) at pH 7.6 show the same trend as seen in the graphics. The sorption and the K_d -values increase at higher temperatures. The values of uranium in comparison to those of europium are very low but they are in the same range as values of other project partners.

3.6. Analysis of the ternary system Metal – Clay – NOM

In the previous chapters we described, that the sorption of the lanthanides and of uranium is strongly dependent on temperature, competing cations and the pH-value. In the neutral and alkaline pH-range the influence of carbonate is an important factor. In this chapter the influence of natural organic matter on the sorption and desorption of metal ions onto clay will be treated. The illustration in Figure 36 shows the interaction of Opalinus clay, metal ions and organic compounds. The knowledge of these interactions is very important for the safety assessment of a repository. The complexation of the metal ions with organic matter could be a risk for the disposal of radioactive waste, if the complexed metal ions does not adsorb onto the clay. The influence of some model organic substances like humic acid and the smaller organic lactate was analysed with batch experiments.

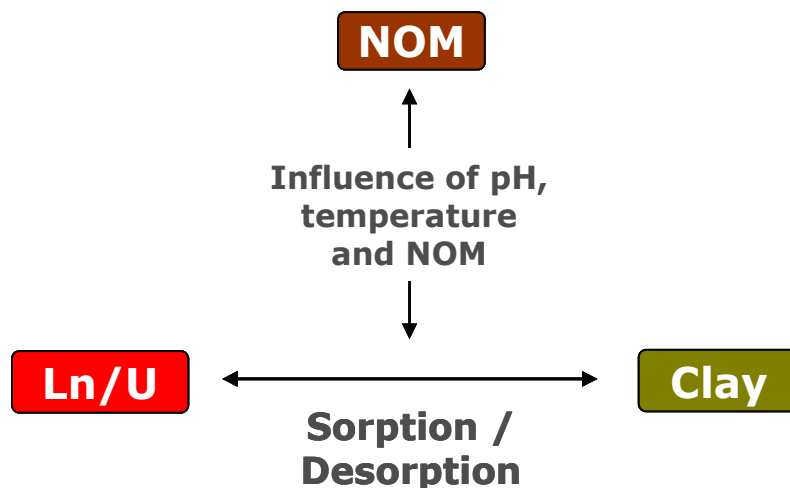


Figure 36: Simplified diagram of the influence of NOM on the interaction of metal ions and clay

3.6.1. Sorption Experiments

In the previous chapter we saw the strong influence of pH and competing cations on the migration behaviour of the analysed metal ions. In the following experiments we used only one pH (pH 7.6) and only synthetic porewater as solution. With both parameters conditions close to nature were chosen. For the sorption experiments we used concentrations of 0.5 and 5 mg·L⁻¹ for Eu(III) (3.3·10⁻⁶ mol L⁻¹/3.3·10⁻⁵ mol L⁻¹) as well as 0.5 and 2.5 mg·L⁻¹ (2.1·10⁻⁶ mol L⁻¹/1.05·10⁻⁵ mol L⁻¹) for U(VI).

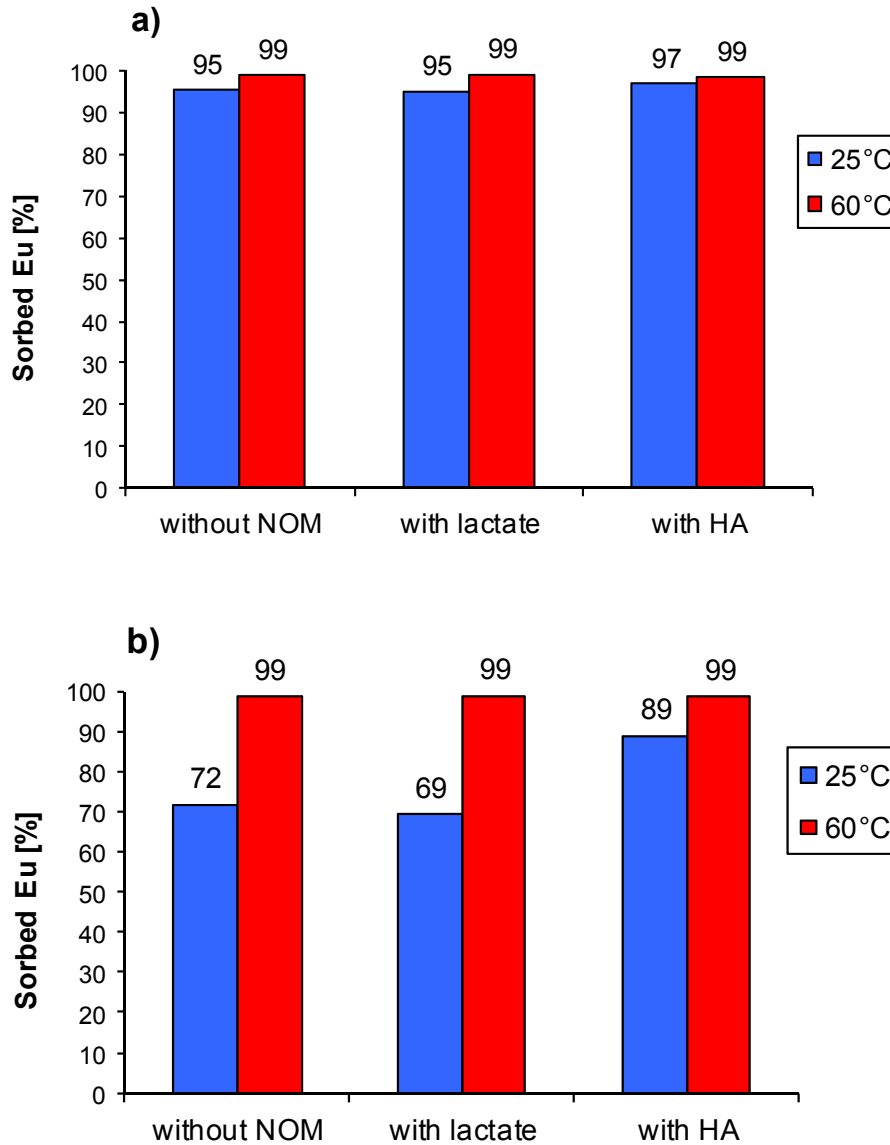


Figure 37: Sorption of europium onto Opalinus clay in porewater ($I = 0.42 \text{ M}$, $\text{pH} = 7.6$) at different temperatures (25 and 60°C) and without / with organic (lactate, HA); a) $C_{\text{Eu}} = 0.5 \text{ mg}\cdot\text{L}^{-1}$; b) $C_{\text{Eu}} = 5 \text{ mg}\cdot\text{L}^{-1}$

In Figure 37 the sorption of europium at different concentrations (0.5 and $5 \text{ mg}\cdot\text{L}^{-1}$), at different temperatures (25 and 60°C) and with different organic compounds (lactate, HA) is shown. With $0.5 \text{ mg}\cdot\text{L}^{-1}$ of Eu no differences between the organic compounds are observable. With increasing temperature the sorption increases insignificantly. At higher europium concentration ($5 \text{ mg}\cdot\text{L}^{-1}$) some differences are obvious. The percental sorption at 25°C is lower than with $0.5 \text{ mg}\cdot\text{L}^{-1}$ europium. The greater part of the binding sites of the clay is occupied, further sorption is not possible. The humic acid in the ternary system contributes to an increase in sorption. In sodium perchlorate solution negatively charged europium humate complexes would be formed. In porewater the porewater cations neutralise the

humates and the europium-humate compounds precipitate. The mobilisation of the europium decreases in comparison to the results in the binary system or in comparison to the results with lactate. At 60°C no differences between the organic compounds are visible. The sorption in the binary and ternary systems is quantitative, the presence of HA does not contribute to an increase of sorption.

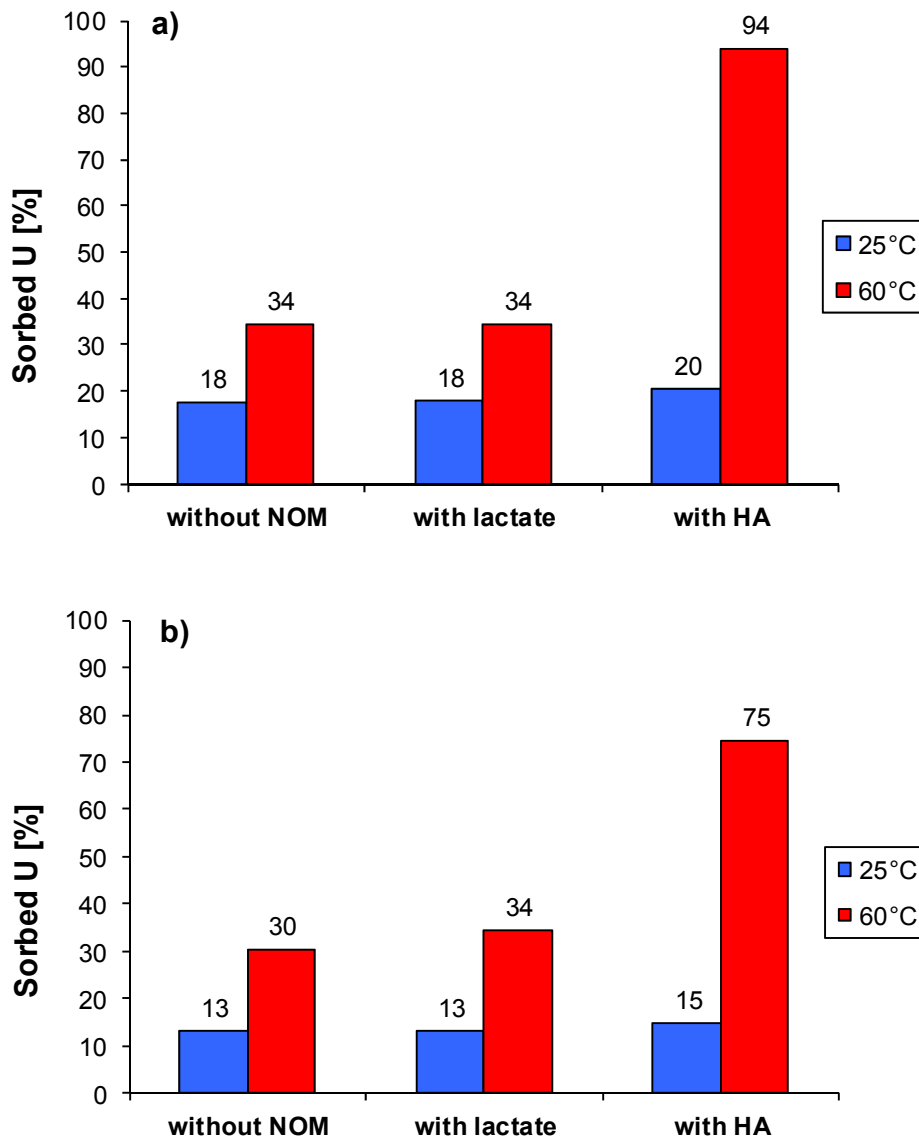


Figure 38: Sorption of uranium onto Opalinus clay in porewater ($I = 0.42 \text{ M}$, $\text{pH} = 7.6$) at different temperatures (25 and 60°C) and without / with organic (lactate, HA); a) $C_U = 0.5 \text{ mg L}^{-1}$; b) $C_U = 2.5 \text{ mg L}^{-1}$

The results with uranium are very different compared with the results with europium. Figure 38 shows the results of sorption experiments with uranium at 25 and 60°C and with different organic compounds present. At 25°C the mobilisation of the uranyl cations is very high.

Europium is adsorbed to over 70 %, uranium only to 10 to 20 %. This effect was explained with the formation of the neutral calcium-uranyl-carbonate complex, which does not adsorb onto the Opalinus clay. Under such conditions uranium stays mobile in solution. No differences were seen between the binary and ternary system and the different organic compounds. The formation of the aquo-complex is dominant.

At higher temperature (60°C) the sorption of the uranyl cations increases similar to the results with europium. Especially the sorption increases strongly in the presence of humic acid in comparison to the sorption in the presence of lactate or without organic compounds. With humic acid and for uranium concentrations of 0.5 mg·L⁻¹ the sorption increases from 34 % to 94 %, with 2.5 mg·L⁻¹ of uranium the sorption increases from 30 % (absence of organics) to 34 % (presence of lactate) and 75 % in the presence of humic acid. The speciation of the uranyl in porewater has evidently changed with increasing temperature. The neutral aquatic complex may not be stable at higher temperatures. The humic acid complexed the uranyl cation and precipitates due to the high concentration of the porewater cations.

3.6.2. Desorption Experiments

The desorption experiments in the binary system show no remobilisation of sorbed metal ions from Opalinus clay under aquifer relevant conditions (porewater, pH 7.6). The clay contains a significant concentration of organics which influences the remobilisation of the metals. In this chapter we describe the influence of these organic compounds like lactate and humic acid on the mobilisation of metal ions and compare the remobilisation of lactate and HA. In the experiments we first equilibrated the clay with 300 µg·L⁻¹ (1.9·10⁻⁶ mol L⁻¹) of europium. In the following three desorption steps we newly equilibrated the clay with fresh porewater at pH 7.6.

We have focussed our experiments on aquifer relevant conditions like porewater and pH 7.6. In Figure 39 the results of the europium desorption at different temperatures (25 and 60°C) in the ternary and binary systems are compared. In the binary system at 25°C 10 % of the sorbed europium were remobilised after 3 desorption steps. The competing cations in the porewater displace the sorbed lanthanides partially from clay. The added lactate shows only insignificant influence on the remobilisation of europium. The complexation strength is much lower than the binding strength to the clay. In contrast with humic acid a reduced remobilisation of the europium is visible (-7 %). The porewater cations displace the europium from clay but the HA complexes the free lanthanides and precipitates as neutralised europium humates.

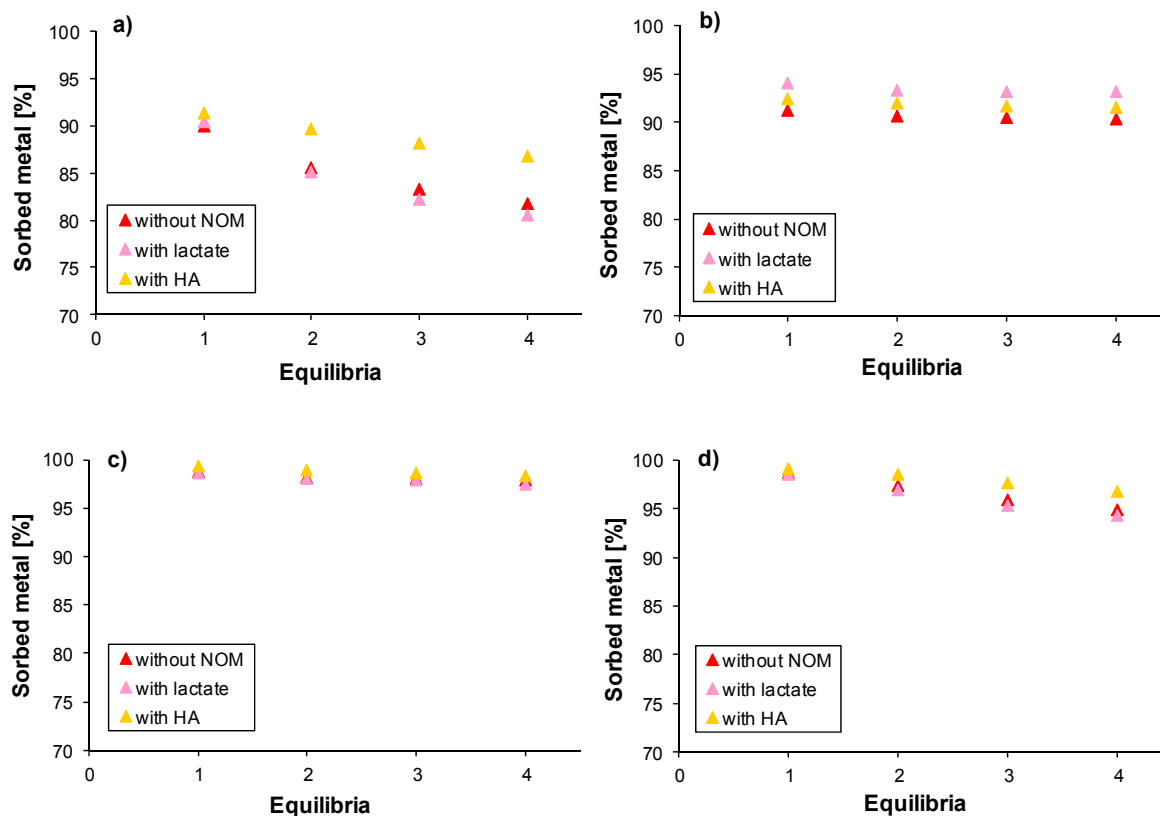


Figure 39: Sorption and desorption of europium on Opalinus clay in porewater influenced by temperature (25/60°C) at pH 7.6 with lactate (pink), humic acid (yellow) and without organic (red); a) Sorption and desorption at 25°C, b) Sorption at 25°C and desorption at 60°C, c) Sorption and desorption at 60°C, d) Sorption at 60°C and desorption at 25°C

After a sorption and desorption at 60°C no differences between the binary and ternary systems are visible. This observation is similar to the sorption experiments themselves where no influence of organic material was visible at higher temperatures. After a sorption at 60°C followed by desorption at 25°C the differences are visible but the influence of the organic compounds is very low.

3.6.3. Speciation of Eu-Humate Complexes in Presence of Opalinus Clay

The influence of NOM on the sorption of europium onto Opalinus clay was analysed in chapter 3.6.1. This chapter shows only the sorption behaviour of the clay but the different europium humate species are unknown. The speciation technique which is described in chapter 3.4 allows the estimation of different europium humate species. For the determination of the different species in the ternary system with europium, OPA and NOM

the hyphenation of CE and ICP-MS was used, too. The sample preparation was similar to the sorption experiments in the ternary systems. The conditions for separation in the CE-ICP-MS hyphenation were similar to the speciation experiments without clay.

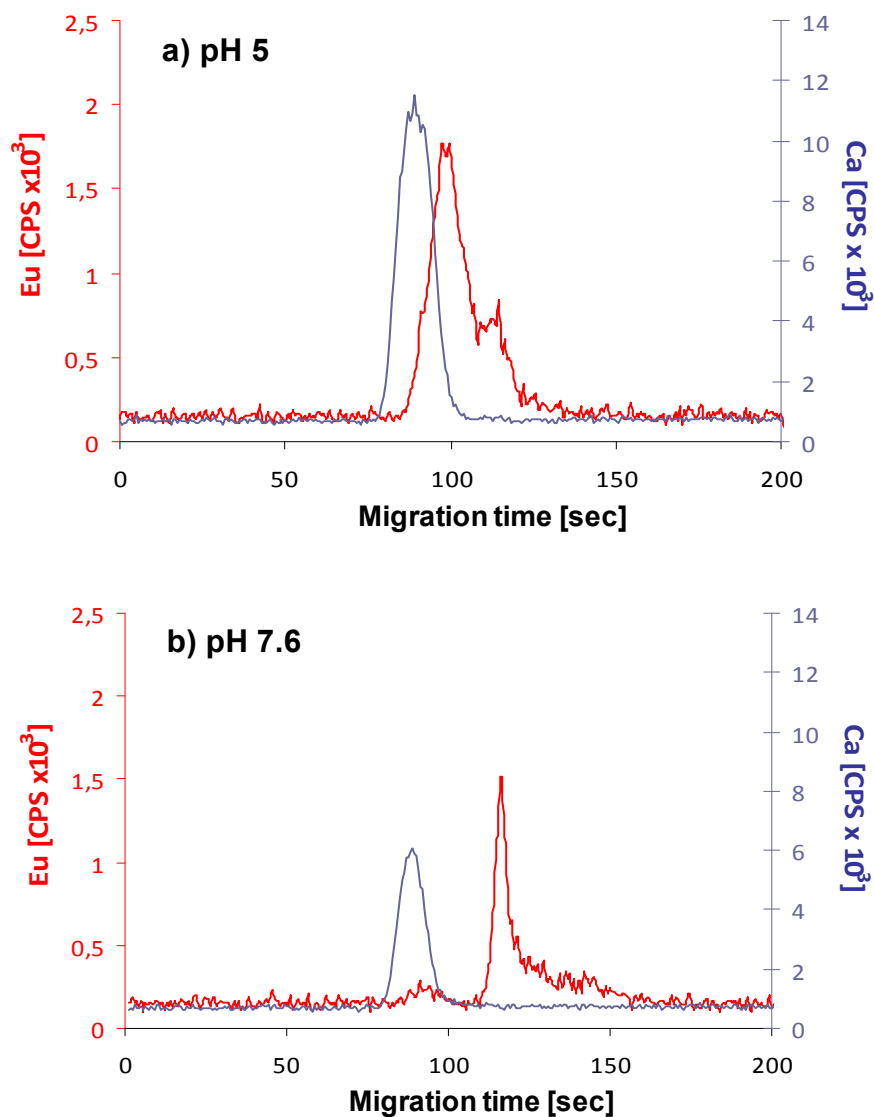


Figure 40: Comparison of the electropherograms of solutions in equilibrium in the ternary system with Eu ($500 \mu\text{g}\cdot\text{L}^{-1}$), humic acid ($25 \text{mg}\cdot\text{L}^{-1}$) and OPA ($4 \text{g}\cdot\text{L}^{-1}$) in SP (^{153}Eu signal red, ^{44}Ca signal blue); a) at pH 5; b) at pH 7.6

In Figure 40 the electropherograms of the europium humate speciation in presence of OPA are presented. In comparison with the experiments without clay less than 10 % of europium was recovered. This observation was explained with the high sorption of europium onto the clay. Great differences are seen between the experiments at pH 5 and 7.6. At pH 5 two europium peaks are visible. The first peak is the free europium which is complexed by

acetate during the separation. The second peak represents the weakly bound europium. During the separation and due to the applied voltage the europium dissociates out of the humate complex and migrates as acetate to the cathode later than the free europium. The existence of strong bonding sites for Europium cannot be verified in this case. When adjusting the pH some minerals, like calcite, dissolved. The released cations neutralise the europium humate species, the europium humate precipitates and is not detectable.

In comparison to pH 5 the electropherogram has changed at pH 7.6. The first peak is very small, vanishing nearly completely. The second peak is there but the recovery of the whole europium species is only 3 %. Additionally to the humic acid other anions like carbonates and hydroxides are available for an interaction at the chosen pH-value. Free europium ions are not existent in the solution. The concentration of the calcium ions in solution decreases from pH 5 to 7.6. At pH 7.6 only little acid is needed to adjust pH and only a small amount of calcite dissolves.

3.6.4. Miniaturised Column Migration Experiments

In this chapter we describe the new experimental setup of the miniaturised clay column experiments (for the setup see also chapter 1.2.6) and give first preliminary migration results of europium in Opalinus clay and on the influence of different organic ligands and different temperatures. These new migration experiments in the compacted clay base on a timescale of only few minutes or hours by the use of the optimised column setup and can be used as a linker between the unnatural batch techniques and the time consuming diffusion experiments.

3.6.4.1. Optimisation of the Miniaturised Clay Column Experiments

In a first step, we have tested different mixtures of OPA with sea sand, because column fillings with 100 % OPA allow only very small eluent flow rates through the clay column due to the clay swelling (by the contact with the aqueous eluent) which needs high pressures over 150 bar. The optimisation of the separation conditions were carried out by the use of iodide (I⁻) as “inert tracer” and salicylate (SAL) as one model for an organic complexing ligand.

Good analytical separation conditions (retention time, eluent flow rate and pressure) can be realised with 10 mM sodium perchlorate at pH 5 as eluent and a clay column consisting of a mixture of 85 % OPA and 15 % seasand (wt./wt.) as shown in Figure 41.

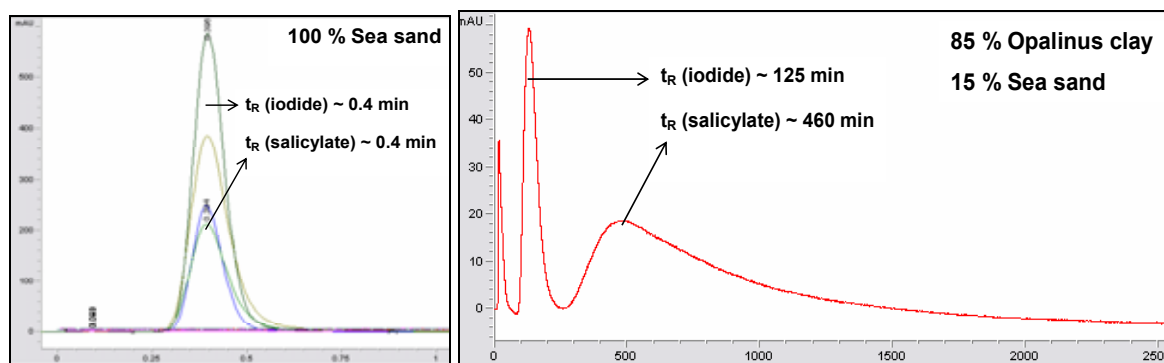


Figure 41: Optimised separation (on the right hand side) of 0.1 mM iodide and 0.1 mM SAL in a 20x3.5 mm (L x ID) OPA/seasand (85/15 wt.%) column (1 $\mu\text{L}\cdot\text{min}^{-1}$ at 15 bar) in comparison to the result in a 100 % seasand column (on the left hand side)

In a next optimisation step we have analysed the potential influence of different metal ion (europium) concentrations on the breakthrough (retention time) of SAL from the clay column.

3.6.4.2. Influence of Eu(III) on the Retention of Salicylate

To determine the potential influence of high valent metal ions like Eu on the mobility of SAL as a model substance for organic complexing ligands we have carried out clay column experiments with different Eu concentrations. Therefore we have injected samples with 0.5 mM NaI, 0.5 mM SAL and different concentrations of Eu (0-60 μM) under otherwise identical migration conditions.

At increasing Eu concentrations one can observe a constant retention time of the inert tracer iodide ($t_R = 145.1 \pm 1.1$ min) and in contrast an increase of the SAL retention time from 398.4 min in the absence of Eu to 420.6 min (30 μM Eu) and 472.5 min in the presence of 60 μM Eu(III) as seen in Figure 42. This increase of the SAL retention time at increasing concentrations of Eu can be caused by the formation of Eu-salicylate-complexes which leads to a retardation of the SAL mobility in the clay column due to a lower negative charge of these Eu-SAL species in contrast to uncomplexed salicylate

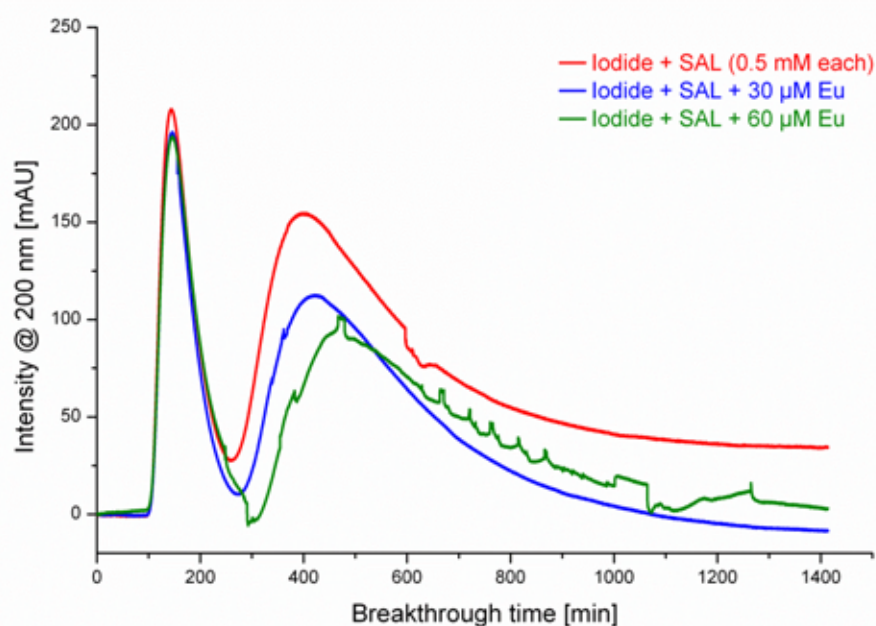


Figure 42: Separation of iodide (inert tracer) and salicylate (model organic ligand) at different concentrations of Eu^{3+} on a 20×3.5 mm (L \times ID) OPA/seasand (85/15 %) column (flow: $1.0 \mu\text{L} \cdot \text{min}^{-1}$ at 16 bar)

As a further outcome of these migration results in the new miniaturised column design one can also measure kinetic effects of the complexation behavior. Small and mobile organic substances, like salicylate or lactate, form no “innersphere” metal-NOM-complexes in contrast to high molecular organic substances, like humic acid, and this shows no influence on the HA retention time in clay columns caused by the presence of different metal concentrations [65].

Another parameter which can affect the metal mobility in clay formations are increasing temperatures caused by the heat dissipation from the radioactive decay of the disposed high level nuclear waste. With the miniaturised column experiment a simulation of different clay temperatures during the migration experiments is very simple because the OPA column can exactly be thermostatted in a PC-controlled column compartment.

3.6.4.3. Influence of Temperature on the Retention of Eu and Lactate in OPA

In this working package we have carried out several miniaturised clay column experiments to analyse the influence of higher temperatures (60°C) on the mobility of lactate in the presence and absence of europium. Therefore we have injected a total sample volume of 2 µL on a 20x3.5 mm column (60/40 OPA/seasand) consisting of NaI (0.01 mM) and lactate (1.0 mM) in the absence or presence of 200 µM Eu(III). As eluent we used 10 mM SP (flow rate: 2.4 µL·min⁻¹) at pH 5. These experiments were performed at least in triplicate under identical conditions at 25°C and 60°C, respectively.

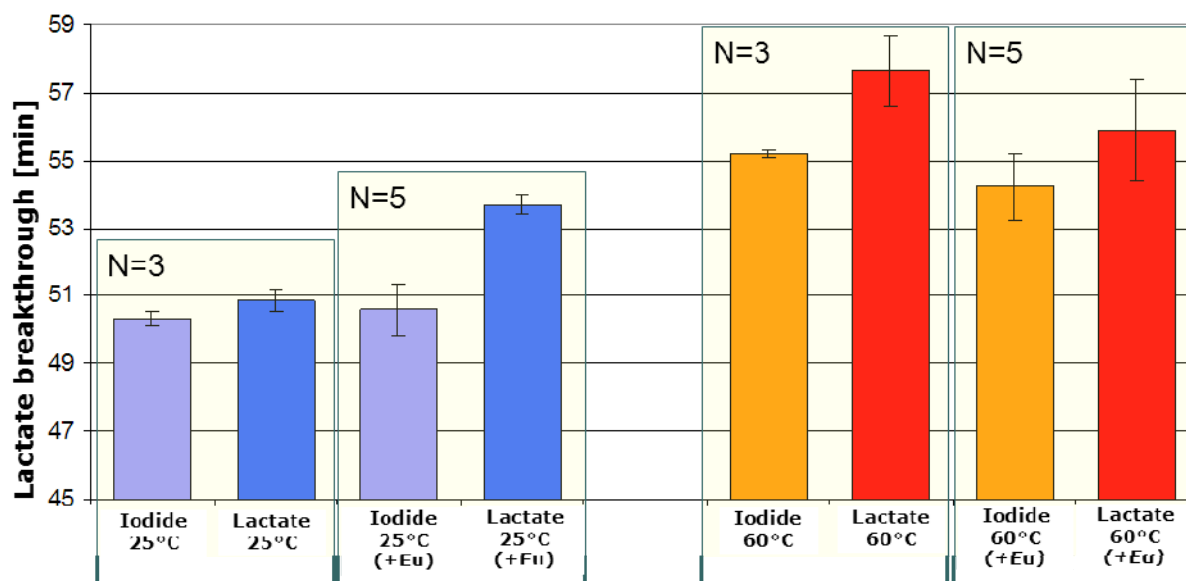


Figure 43: Influence of Eu (200 µM) and temperature (25/60°C) on the mobility of lactate (1 mM) in compacted OPA; column dimension: 20x3.5 mm LxID, filled with 60 wt.% / 40 wt.% clay/seasand); injection of 2 µL (including 10 µM NaI), N = 3-5 repetitions, flow rate: 2.4 µl·min⁻¹ in 10 mM SP at pH 5

At 25°C the breakthrough times of the inert tracer iodide (50.3±0.2 min, n=3) and the clay-organic compound lactate (50.9±0.3 min, n=3) are in the same order of magnitude as shown in Figure 43. However, in the presence of 200 µM Eu in the injected sample a significant

increase (+5.5 %) of the lactate breakthrough time (53.7 ± 0.3 min, $n=5$) in contrast to the breakthrough time (+0.6 %) of the inert tracer iodide (50.6 ± 0.8 min, $n=5$) can be seen.

In all experiments performed at 60°C , an increase of the retention time in comparison to 25°C can be observed for the inert tracer iodide as well as for lactate due to an increased sorption onto OPA at higher temperatures. This is also observed in sorption batch experiments with OPA. As a further result, the breakthrough time of iodide increases to 55.2 ± 0.1 min (+9.7 %, $n=3$) and the lactate retention time on the clay column increases by about 13.4 % to 57.7 ± 1.0 min ($n=3$).

In contrast to the results at 25°C , no significant influence of Eu(III) on the breakthrough of lactate as well as iodide from the compacted clay column can be measured at 60°C , even a trend to shorter breakthrough times in the presence of Eu can be observed. This finding suggests a temperature-dependent interaction or speciation of europium with lactate and Opalinus clay.

3.6.4.4. Post Mortem Analysis of the Compacted Clay Columns

To analyse the migration of europium (which is not online detectable in the diode array detector) in the OPA column we carried out long time breakthrough experiments with europium in the presence or absence of lactate as complexing ligand. Shortly after the experiments were finished we carried out a post mortem analysis of the compacted clay column which can be recovered as an intact bloc due to the innovative setup of the miniaturised clay column experiment.

For the space-resolved europium analysis in the OPA column, in a first experiment we injected $1 \mu\text{L}$ of 16.5 mM Eu ($\sim 2.5 \mu\text{g}$) in the presence of 165 mM lactate ($\sim 14.7 \mu\text{g}$) on a $20 \times 3.5 \text{ mm}$ (LxID) clay/seasand column (60 wt.% OPA / 40 wt.% seasand, $m \sim 280 \text{ mg}$). In the second experiment we injected the same sample solution without lactate as complexing ligand on a second column with identical dimensions and composition. After sample injection we eluted the columns with a total of $3600 \mu\text{L}$ 10 mM SP ($1.5 \mu\text{L} \cdot \text{min}^{-1}$ at 32 bar for 40 h) at pH 5, respectively. After the elution we recovered the clay column bloc, which was dried and cut into four nearly equal pieces as shown in Figure 44.



Figure 44: Scheme for the post mortem analysis of Eu(III) in the eluate and in four clay pieces from a recovered OPA-column bloc after a long time migration experiment

The Eu^{3+} was extracted from each column fraction by grinding the clay with a concentrated solution of Al^{3+} ($1 \text{ g}\cdot\text{L}^{-1}$) as competing cation for 48 h followed by phase separation via centrifugation at 10000 rpm for 30 min. The supernatant was acidified (pH 1) and the Eu amount in all fractions was analysed by ICP-MS.

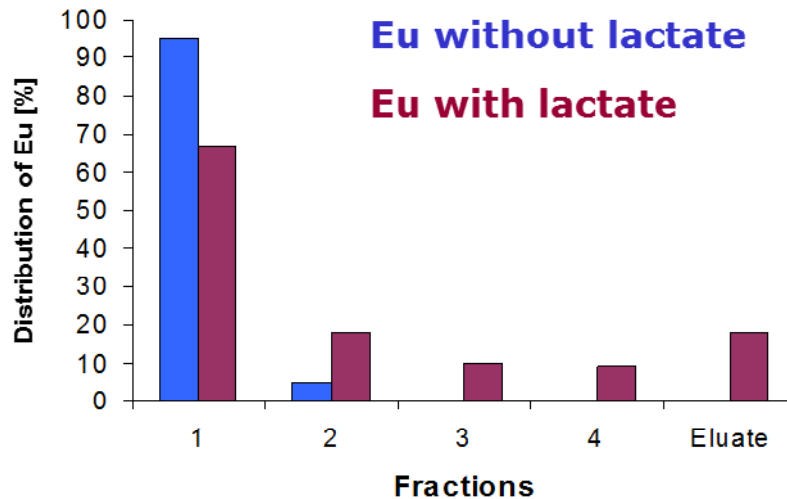


Figure 45: Comparison of the Eu amount in all analysed fractions after the long-time migration experiments with Eu in the presence/absence of lactate

The extraction of the injected $\text{Eu}(\text{III})$ with competing $\text{Al}(\text{III})$ revealed a recovery of ca. 48 % Eu ($\sim 1.2 \mu\text{g}$) in both experiments. Sorbed Eu can be recovered in the first experiment without lactate mainly (96 % of the recovered Eu) in the first fraction of the OPA column and only a small amount (4 %) was found in the second fraction as shown in Figure 45. No Eu can be detected in the third and fourth fraction as well as in the eluate. In contrast to this finding Eu can be detected in all fractions of the clay column of the second experiment where Eu was injected in the presence of lactate. For a risk assessment of a future disposal this result suggests that lactate can influence (increase) the migration of trivalent metal ions like Eu in a negative way due to the formation of negatively charged Me-lactate species, which do not adsorb strongly in Opalinus clay formations.

4. Conclusions and Outlook

For the experiments in the complex system consisting of OPA, metal ions and NOM ICP-MS was used as a highly specific and sensitive method for elemental trace analysis. For the speciation of metal ions (europium, gadolinium, terbium and uranium) with NOM (lactate or AHA), capillary electrophoresis, being a method with high separation performance, was hyphenated with ICP-MS. The complexation of metal ions like Eu^{3+} and UO_2^{2+} with humic acid and lactate was analysed by this valuable hyphenation technique.

Three different metal species were observed in the presence of AHA for all analysed metals. The first peak in the chromatogram represents the free metal which migrates as acetate (from the CE-buffer) complexed metal to the cathode. The second peak gives the metal complexed by weak binding sites of the humic acid. During the separation and due to the applied voltage the metal dissociates out of the complex and migrates later as acetate complexed metal to the cathode too. The third peak represents metal complexed by AHA strong binding sites. This metal-humate complex is stable during the separation and migrates as negatively charged metal humate to the cathode due to the applied pressure. The identification of the different species was verified by iodination of the AHA and the use of the ^{127}I -signal as AHA-ICP-MS-marker.

The verification of the different AHA binding sites was performed by exchanging AHA with a modified AHA (provided by the Helmholtz-Center Dresden-Rossendorf) with blocked phenolic hydroxyl groups. By such methods the calculation of conditional complexation stability constants is possible. Additionally, the influence of competing cations like Ca^{2+} , Mg^{2+} and Al^{3+} on the complexation of metal ions with HA could be analysed by CE-ICP-MS.

In addition to these speciation measurements batch experiments are helpful for a basic understanding of the complex system consisting of OPA, metal ions and NOM. The experiments simulate a potential water infiltration into the waste disposal. The sorption of the metal ions depends strongly on the pH-value, the presence of competing cations, temperature and organic matter. At a pH-value of pH 7.6, which is relevant for a disposal in OPA formations, the sorption of europium is much higher than the sorption of uranyl due to the formation of an uncharged aqueous calcium-uranyl-carbonato-complex ($\text{Ca}_2\text{UO}_2(\text{CO}_3)_3$) which does not sorb onto the Opalinus clay. The effect of higher temperature can be described as helpful in the storage of nuclear waste. In our laboratory experiments with higher temperatures up to 60°C the sorption of the analysed metals onto OPA increases strongly.

The batch experiments are certainly far away from natural conditions but in contrast to diffusion experiments they are not so time-consuming and nevertheless give valuable information. The diffusion experiments are performed under conditions close to nature but they require years. The miniaturised column experiments with compacted clay developed in this project are a compromise between batch studies and diffusion experiments. One measurement takes only some hours or a few days but the conditions are closer to nature than batch experiments. The setup of this miniaturised column experiments is quite complex and control of decisive parameters is difficult but the development of this method is promising. The preliminary results obtained by the use of mini-column experiments show effects comparable to batch experiments under similar conditions with respect to the influence of temperature and NOM as complexing ligand.

In the future the main work will be focused on the analysis of the influence of higher salinity on the sorption/ desorption behavior as well as the speciation of metal ions in the presence or absence of complexing ligands. In the porewater of clay formations in Northern Germany salinities of more than 3 M are possible. In sorption and desorption experiments with europium and uranium onto OPA the influence of salinity will be analysed. Difficulties are expected with the pH correction and the analysis of metal content with ICP-MS. Therefore, the analysed metals will have to be extracted out of the brine before the ICP-MS measurement due to the high salt content in the samples. The complexation of metal ions with organic (lactate, HA) and inorganic (borate) complexing ligands and the influence of high salinity on the metal speciation will be analysed by NMR and a hyphenation of CE or LC and ICP-MS.

5. Publications Resulting from the Project

- MÖSER, C., KAUTENBURGER, R. & H.P. BECK (2012): Complexation of Europium and Uranium by Humic Acids Analysed by Capillary Electrophoresis - Inductively Coupled Plasma Mass Spectrometry, *Electrophoresis* 33, 1482-1487.
- KAUTENBURGER, R. (2012): Geochemische Analytik: Endlager für radioaktiven Müll gesucht. *Analytica PRO* 2012, 59-60.
- KAUTENBURGER, R. (2011): Batch is bad? Leaching of Opalinus clay samples and ICP-MS determination of extracted elements. *Journal of Analytical Atomic Spectrometry* 26, 2089-2092.
- MÖSER, C. (2011): Untersuchungen zum Einfluss geochemischer Parameter auf die Sorption und Desorption von Lanthaniden in Opalinuston im Rahmen der Auswahl eines potentiellen Endlagers. Dissertation, Naturwissenschaftlich-Technische Fakultät III, Universität des Saarlandes, Saarbrücken.
- KAUTENBURGER, R. (2011): Untersuchungen zur Metall-Mobilität in nativen Tonformationen - Speziation von Europium, Gadolinium und Uran mit natürlich vorkommender Organik (NOM). Chemiedozententagung, Mainz, 114.
- KAUTENBURGER, R., MÖSER, C. & H.P. BECK (2011): Metal Migration in Natural Clay Formations - Speciation of Europium, Gadolinium and Uranium with NOM. *European Winter Conference on Plasma Spectrochemistry 2011*, Zaragoza, 135.
- KAUTENBURGER, R., MÖSER, C. & H.P. BECK (2011): Metal mobility in clay formations – From batch experiments with mineral suspensions to column setup with compacted clay. *Mineralogical Magazine* 75, 1157.
- MÖSER, C., KAUTENBURGER, R. & H.P. BECK (2011): Migration of Europium and Uranium in Opalinus Clay Influenced by pH and Temperature. *Mineralogical Magazine* 75, 1504.
- KAUTENBURGER, R., MÖSER, C. & H.P. BECK (2010): Influence of Lanthanide Concentration and the Presence of Competing Metal Ions on Europium and Gadolinium Speciation with Humic Acid Analyzed by CE-ICP-MS. In: *Advances in NOM and Humic Substances Research 2008-2010* (Eds: J.A. González-Pérez, F.J. González-Vila & G. Almendros). *Proceedings IHSS 15* (Vol. 1), 251-254.
- MÖSER, C., KAUTENBURGER, R. & H.P. BECK (2010): CE-ICP-MS as Speciation Technique to Analyze the Complexation Behavior of Europium, Gadolinium and Terbium with Humic Acid. In: *Advances in NOM and Humic Substances Research 2008-2010* (Eds: J.A. González-Pérez, F.J. González-Vila & G. Almendros). *Proceedings IHSS-15* (Vol. 3), 139-142.
- KAUTENBURGER, R. (2010): Endstation Tonstein? *Nachrichten aus der Chemie* 58 (Vol. 7/8), 751-756.
- KAUTENBURGER, R. & H.P. BECK (2010): Influence of geochemical parameters on the sorption and desorption behaviour of europium and gadolinium onto kaolinite. *Journal of Environmental Monitoring* 12, 1295-1301.
- MÖSER, C. & R. KAUTENBURGER (2010): CE-ICP-MS speciation of uranium and lanthanides to analyze the complexation behavior with natural organic matter (NOM). *Analytica* 2010, München.
- KAUTENBURGER, R. (2009): Influence of metal concentration and the presence of competing cations on lanthanide speciation with humic acid analysed by CE-ICP-MS. *Journal of Analytical Atomic Spectrometry* 24, 934-938.

- KAUTENBURGER, R. (2009): Untersuchung des Einflusses geochemischer Parameter auf das Komplexierungsverhalten von Europium und Gadolinium mit Huminsäure mittels CE-ICP-MS. GDCh-Jahrestagung der Fachgruppe Umweltchemie und Ökotoxikologie, Trier, 74.
- KAUTENBURGER, R. (2009): Influence of metal concentration and the presence of competing cations on europium and gadolinium speciation with humic acid analysed by CE-ICP-MS. 12th Workshop on Progress in Analytical Methodologies for Trace Metal Speciation" (TraceSpec 2009), Mainz, 62.
- MÖSER, C., KAUTENBURGER, R. & H.P. BECK (2009): CE-ICP-MS as speciation technique to analyze the complexation behavior of Europium, Gadolinium and Terbium with organic ligands. 12th Workshop on Progress in Analytical Methodologies for Trace Metal Speciation" (TraceSpec 2009), Mainz, 79.
- KAUTENBURGER, R. (2009): Untersuchungen zum Einfluss geochemischer Parameter auf das Komplexbildungsverhalten von Schwermetallen mit Huminsäure mittels CE-ICP-MS. Chemiedozentenagung, Göttingen, 120.
- KAUTENBURGER, R. (2009): Untersuchung des Einflusses geochemischer Parameter auf das Komplexierungsverhalten von Lanthaniden und Huminsäure mittels CE-ICP-MS. ANAKON 2009, Berlin, 71.
- KAUTENBURGER, R. (2009): Speciation of Heavy Metal Pollutants and Humic Acids analyzed by CE-ICP-MS. European Winter Conference on Plasma Spectrochemistry 2009, Graz, 70.
- MÖSER, C. & R. KAUTENBURGER (2009): Sorption and desorption experiments of europium, gadolinium and terbium onto Opalinus clay. European Winter Conference on Plasma Spectrochemistry 2009, Graz, 121.
- KAUTENBURGER, R. & H.P. BECK (2008): Waste disposal in clay formations: Influence of humic acid on the migration of heavy metal pollutants. ChemSusChem 1, 295-297.
- KAUTENBURGER, R. (2008): Influence of geochemical parameters on the complexation behavior of heavy metal pollutants with humic acid analyzed by CE-ICP-MS. 27th International Symposium on Chromatography, Münster, 80.
- KAUTENBURGER, R. (2008): Speziationsanalytik mit CE-ICP-MS: Untersuchung des Komplexierungsverhaltens von Lanthaniden und Huminsäure. 21. ICP-MS-Anwendertreffen, Dresden, 23.
- KAUTENBURGER, R. (2008): Speciation of Lanthanides and Humic Acid by CE-ICP-MS. Chemiedozentenagung, Kaiserslautern, 110.
- KAUTENBURGER, R. & H.P. BECK (2007): Complexation studies with lanthanides and humic acids analysed by ultrafiltration and capillary electrophoresis - inductively coupled plasma mass spectrometry. Journal of Chromatography A 1159, 75-80.
- KAUTENBURGER, R. (2007): CE-ICP-MS as speciation technique to analyze the complexation behavior of lanthanides with humic acid. 11th Workshop on Progress in Analytical Methodologies for Trace Metal Speciation" (TraceSpec 2007), Münster.
- KAUTENBURGER, R. (2007): Speciation analysis of lanthanides and humic acid by coupling CE with ICP-MS. Trends in Sample Preparation" (TRISP07), Castle Seggau.
- NOWOTKA, K. (2007): Untersuchungen zur Migration von Europium und Gadolinium in Kaolinit als Modellmineral für eine Endlagerstätte. Dissertation, Naturwissenschaftlich-Technische Fakultät III, Universität des Saarlandes, Saarbrücken.
- KAUTENBURGER, R., NOWOTKA, K. & H.P. BECK (2007): Sorption and desorption experiments of europium and gadolinium on kaolinite. 11th International Conference on Chemistry and Migration Behaviour of Actinides and Fission Products in the Geosphere (Migration '07), München, 98.

6. References

- 1 L.O. Ericsson, *Eng. Geol.*, 1999, **52**, 305-317.
- 2 M.H. Bradbury and B. Baeyens, Far field sorption data bases for performance assessment of a high-level radioactive waste repository in an undisturbed Opalinus clay host rock, PSI Bericht Nr. 03-08, Nagra NTB 02-19, Villigen, 2003.
- 3 W. Hummel and J. Schneider, *Chimia*, 2005, **59**, 909-915.
- 4 F.T. Madsen, *Clay Miner.*, 1998, **33**, 109-129.
- 5 C. McCombie and P. Smith, Multibarrier systems in geological disposal programmes, Proceedings - 10th International Conference on Environmental Remediation and Radioactive Waste Management, ICEM'05, 1634-1639, Glasgow, 2005.
- 6 S. Altmann, *J. Contam. Hydrol.*, 2008, **102**, 174-179.
- 7 J.J. Katz, G.T. Seaborg and L.R. Morss, *The Chemistry of the Actinide Elements*; Chapman & Hall; New York, 1986.
- 8 A.B., Kersting, D.W., Efurud, D.L., Finnegan, D.J., Rokop, D.K., Smith and J.L. Thompson, *Nature*, 1999, **397**, 56-59.
- 9 F.J. Stevenson, *Humus Chemistry*, Wiley, New York, 1994.
- 10 F. Schlosser, S. Krüger and N. Rösch, *Inorg. Chem.*, 2006, **45**, 1480-1490.
- 11 M.B. Hay and S.C.B. Myneni, *Geochim. Cosmochim. Acta.* 2007, **71**, 3518-3532.
- 12 C.M. Marquardt, *Migration of actinides in the system clay, humic substances, Aquifer*, Wissenschaftliche Berichte, FZKA 7407, FZ Karlsruhe, 2008.
- 13 J.I. Kim, K. R. Czerwinski, *Radiochim. Acta*, 1996, **73**, 5-10.
- 14 M. Plaschke, J. Rothe, M. Denecke and T. Fanghänel, *J. Electron. Spectrosc.*, 2004, **135**, 53-62.
- 15 H.J. Kim, K. Baek, B.K Kim and J.W. Yang, *J. Hazard. Mater.*, 2005, **122**, 31-36.
- 16 K. Wrobel, B.B. Sadi, K. Wrobel, J.R. Castillo and J.A. Caruso, *Anal. Chem.* 2003, **75**, 761-767.
- 17 S. Röllin and U.B. Eklund, *J. Chromatogr. A* 2000, **884**, 131-141.
- 19 R.M. Harrison and S. Rapsomanikis, *Environmental Analysis Using Chromatography Interfaced with Atomic Spectroscopy*, John Wiley & Sons, New York 1989.
- 20 R. Cornelis, J. Caruso, H. Crews and K. Heumann, *Handbook of Elemental Speciation II - Species in the Environment, Food, Medicine and Occupational Health*, John Wiley & Sons, Ltd, Chichester, UK 2005.
- 21 J.W. Olesik, J.A. Kinzer and S.V. Olesik, *Anal. Chem.* 1995, **67**, 1-12.
- 22 B. Michalke, *J. Anal. Atom. Spectrom.* 1999, **14**, 1297-1302.
- 23 A. Prange and D. Schaumlöffel, *Fres. J. Anal. Chem.* 1999, **364**, 452-456.
- 24 D. Schaumlöffel, A. Prange, G. Marx, K.G. Heumann and P. Bratter, *Anal. Bioanal. Chem.* 2002, **372**, 155-163.
- 25 B. Kuczewski, C.M. Marquardt, A. Seibert, H. Geckeis, J.V. Kratz and N. Trautmann, *Anal. Chem.* 2003, **75**, 6769-6774.
- 26 D. Pröfrock, P. Leonhard, W. Ruck and A. Prange, *Anal. Bioanal. Chem.* 2005, **381**, 194-204.

- 27 A.R. Timerbaev, *Electrophoresis* 2009, **31**, 192–204.
- 28 R. Kautenburger, K. Nowotka and H.P. Beck, *Anal. Bioanal. Chem.* 2006, **384**, 1416-1422.
- 29 R. Kautenburger and H.P. Beck, *J. Chromatogr. A*, 2007, **1159**, 75-80.
- 30 R. Kautenburger and H.P. Beck, *ChemSusChem* 2008, **1**, 295-297.
- 31 R. Kautenburger and H.P. Beck, *J Environ Monit.* 2010, **12**, 1295-1301.
- 32 J.I. Kim, G. Buckau, G.H. Li, H. Duschner and N. Psarros, *Fresenius J. Anal. Chem.* 1990, **338**, 245-252.
- 33 S. Sachs, M. Bubner, K. Schmeide, G.R. Choppin, K.H. Heise and G. Bernhard, *Talanta* 2002, **57**, 999-1009.
- 34 K. Schmeide, S. Sachs, M. Bubner, T. Reich, K.H. Heise and G. Bernhard, *Inorg. Chim. Acta.* 2003, **351**, 133-140.
- 35 NAGRA, *Projekt Opalinuston Synthese der geowissenschaftlichen Untersuchungsergebnisse Entsorgungsnachweis für abgebrannte Brennelemente, verglaste hochaktive sowie langlebige mittelaktive Abfälle*, Technischer Bericht NTB 02-03, NAGRA, Wettingen, 2002.
- 36 M. Lauber, B. Baeyens and M.H. Bradbury, *Sorption of Cs, Sr, Ni, Eu, Th, Sn and Se on Mont Terri Opalinus Clay: physico-chemical characterisation and sorption measurements*, PSI Bericht Nr. 00-10 Villigen, and Nagra NTB 00-11, Wettingen, 2000.
- 37 F.J. Pearson, *Opalinus Clay experimental water: A1 Type, Version 980318*, PSI Internal report TM-44-98-07, Paul Scherrer Institut, Villigen, 1998.
- 38 L.R. Van Loon, J.M. Soler and M.H. Bradbury, *J. Contam. Hydrol.*, 2003, **61**, 73-83.
- 39 L.R. Van Loon and A. Jakob, *Transport Porous Med.*, 2005, **61**, 193-214.
- 40 Š. Palágyi and H. Vodičková, *J. Radioanal. Nucl. Chem.*, 2009, **280**, 3-14.
- 41 K. Schmeide and G. Bernhard, *Appl. Geochem.*, 2010, **25**, 1238-1247.
- 42 N.L. Banik, R.A. Buda, S. Bürger, J.V. Kratz and N. Trautmann, *Radiochim. Acta*, 2007, **95**, 569-575.
- 43 W. Um, R.J. Serne, C.F. Brown and G.V. Last, *J. Contam. Hydrol.*, 2007, **93**, 255-269.
- 44 M.H. Lee, E.C. Jung, K. Song, Y.H. Han and H.S. Shin, *J. Radioanal. Nucl. Chem.* 2011, **287**, 639-645.
- 45 Y. Zhang, H. Zhao, Q. Fan, X. Zheng, P. Li, S. Liu and W. Wu, *J. Radioanal. Nucl. Chem.*, 2011, **288**, 395–404.
- 46 H. Lippold, N. Müller and H. Kupsch, *Appl. Geochem.*, 2005, **20**, 1209-1217.
- 47 R. Kautenburger, *J. Anal. At. Spectrom.*, 2009, **24**, 934-938.
- 48 L. Liao and H.M. Selim, *Soil Sci.*, 2009, **174**, 549-555.
- 49 P.W. Atkins, *Physical Chemistry*, Oxford University press, 1978.
- 50 C. Huang and D. Beauchemin, *J. Anal. At. Spectrom.*, 2006, **21**, 317-320.
- 51 L. Xing, *J. Anal. At. Spectrom.*, 2009, **24**, 336-339.
- 52 E. Bolea, M.P. Gorriz, M. Bouby, F. Laborda, J.R. Castillo, H. Geckeis, *J. Chromatogr. A*, 2006, **1129**, 236-246.

- 53 O. Pourret, M. Davranche, G. Gruau, A. Dia, *J. Colloid Interface Sci.*, 2007, **305**, 25-31.
- 54 R.A. Buda, N.L. Banik, J.V. Kratz, N. Trautmann, *Radiochim. Acta*, 2008, **96**, 657-665.
- 55 O. Pourret, M. Davranche, G. Gruau and A. Dia, *Colloid Interface Sci.* 2007, **305**, 25-31.
- 56 X.L. Tan, X.K. Wang, H. Geckeis and T. Rabung, *Environ. Sci. Technol.* 2008, **42**, 6532–6537.
- 57 C. Joseph, K. Schmeide, S. Sachs, V. Brendler, G. Geipel and G. Bernhard, *Chem. Geol.* 2011, **284**, 240-250.
- 58 J. Noémie, M.F. Benedetti and P.E. Reiller, *Environ. Sci. Technol.* 2011, **45**, 3224-3230.
- 59 I. Christl, A. Metzger, I. Heidmann and R. Kretzschmar, *Environ. Sci. Technol.* 2005, **39**, 5319-5326.
- 60 M.U. Kumke, S. Eidner and T. Kruger, *Environ. Sci. Technol.* 2005, **39**, 9528–9533.
- 61 A. Courdouan, I. Christl, T. Rabung, P. Wersin and R. Kretzschmar, *Environ. Sci. Technol.* 2008, **42**, 5985-5991.
- 62 J.E. Sonke and V.J.M. Salters, *Geochim. Cosmochim. Acta* 2006, **70**, 1495-1506.
- 63 E. Tertre, G. Berger, S. Castet, M. Loubet and E. Giffaut, *Geochim. Cosmochim. Acta* 2005, **69**, 4937-4948.
- 64 E. Tertre, G. Berger, E. Simoni, S. Castet, E. Giffaut, M. Loubet and H. Catalette, *Geochim. Cosmochim. Acta* 2006, **70**, 4563-4578.
- 65 N.D. Bryan, J. Barlow, P. Warwick, S. Stephens, J.J.W., Higgs and D. Griffin, *J. Environ. Monit.* 2005, **7**, 196-202.

Final Report of the BMWi Joint Research Project: Actinide Migration in Natural Clay Rock

December 2011

Sub-Project: Influence of Clay Organic Substances on the retardation of Actinide Ions in the Clay Barrier

N. Banik, E. Hartmann, C.M. Marquardt, P. Panak, Th. Schäfer, A. Skerencak

Das diesem Bericht zugrunde liegende Vorhaben wurde mit Mitteln des Bundesministeriums für Wirtschaft und Technologie unter dem Förderkennzeichen 02E10206 gefördert. Die Verantwortung für den Inhalt dieser Veröffentlichung liegt bei den Autoren.

KIT – Universität des Landes Baden-Württemberg und
nationales Forschungszentrum in der Helmholtz-Gemeinschaft

Zusammenfassung

Die Arbeiten innerhalb dieses Projektverbundes beschäftigten sich mit dem Migrationsverhalten von Actiniden in der natürlichen Tonbarriere. Hierzu wurden natürliche Tongesteinsproben - Opalinuston aus dem Mont Terri (Schweiz) und Callovo-Oxfordian-Ton aus Bure (Frankreich) - im Hinblick auf die für die Migration von Actiniden relevanten Eigenschaften charakterisiert. Die Sorptionseigenschaften von Opalinuston und CO_x-Ton gegenüber Europium (Eu(III)), Curium (Cm(III)), Neptunium(V) und Plutonium(V) wurden in zahlreichen Experimenten untersucht. Hierbei konnte für Eu(III) und Cm(III) gezeigt werden, dass die Tonminerale in den natürlichen Tongesteinen hauptsächlich verantwortlich sind für die Sorption der Metallkationen. Mittels eines einfachen Modells, das eine Sorption nur an den Tonmineralien berücksichtigt und die Tonminerale Illit und Montmorillonit und den Calcit in einem für das jeweilige Tongestein speziellen Verhältnis beinhaltet, konnten die experimentellen Ergebnisse gut beschrieben werden. Hierzu wurde das Oberflächenkomplexierungsmodell von [Bradbury und Baeyens, 2002, 2005a,b] angewendet.

Eine Unterscheidung nicht-sorbierter Aquoionen von „outer-sphere“ sorbierten Kationen und eine Quantifizierung der „Outer-sphere“-Komplexbildung war mit Hilfe fluoreszenzspektroskopischer Methoden – Time-resolved laser fluorescence spectroscopy (TRLFS) - bislang nicht möglich, da diese auf Veränderungen im Ligandenfeld des fluoreszierenden Kations basieren. Beide Spezies behalten jedoch ihre vollständige erste Hydrathülle. Für die Identifikation der „Outer-sphere“-Komplexbildung des Cm(III) wurde der quenchende Effekt des Eisens in der Kristallstruktur der Tone zur Hilfe genommen. Die in unterschiedlichen Tonsuspensionen (I = 0,01 mol/l, pH = 4) gemessenen Cm(III)-Fluoreszenzemissionslebensdauern korrelieren mit dem entsprechenden Eisen-gehalt des verwendeten Tones und sind signifikant kürzer (H₂O: $\geq 27 \mu\text{s}$; D₂O: $\geq 85 \mu\text{s}$) als die des Aquoions (65 - 68 μs bzw. 1250 μs). „Outer-sphere“ sorbiertes Cm³⁺ wurde in H₂O und D₂O mit Hilfe der TRLFS quantifiziert, indem das charakteristische Abklingverhalten der Fluoreszenzemission – hier vor allem der kurzlebige Anteil - analysiert wurden. Modellrechnungen zur Cm(III)-Outer-sphere-Komplexbildung an Tonen mit unterschiedlichen Kationenaustauschkapazitäten (KAK) ergeben eine sehr gute Übereinstimmung mit den experimentell ermittelten Werten. Dabei muss für die Sorption an Illit die Konkurrenz um Sorptionsplätze durch andere Kationen (insbesondere Al³⁺ und Ca²⁺/Mg²⁺) berücksichtigt werden. Diese werden durch teilweise Auflösung des Tons bei niedrigem pH aus der Kristallstruktur freigesetzt. Bei Montmorillonit hingegen muss die partielle Auflösung aufgrund ihrer ca. 4-fach höheren KAK nicht berücksichtigt werden.

Im Gegensatz zu den dreiwertigen Eu und Cm sind Np und Pu redoxsensitiv. Deshalb lag der Fokus der Untersuchungen in den Np- und Pu-Sorptionsexperimenten auf der Redoxspeziation beider Elementen. Hierzu wurden XANES, EXAFS, XPS für die Speziation auf der Tonmineraloberfläche sowie UV/Vis/NIR-Absorptions-Spektroskopie, Kapillarelektrophorese (CE) und Flüssig-flüssig-Extraktion für die Speziation in der wässrigen Phase eingesetzt. Die CE gekoppelt an eine ICP-MS ist für zukünftige Aufgaben, speziell für die Redoxspeziation bei sehr geringen Konzentrationen, eine vielversprechende Methoden. Deshalb wurden in einer Zusammenarbeit mit der Universität

Köln weitere Entwicklungsarbeiten unternommen um diese Methode zukünftig einsetzen zu können.

Bei dem redoxsensitiven Actinid Np zeigte sich, dass Np(V) bei geringen Konzentrationen von 3×10^{-7} M teilweise zu Np(IV) reduziert wird. Der relativ kleine K_d -Wert von 33 ± 9 L/kg bestätigt, dass Np(V) noch vorhanden sein muss. Eine Reduktion konnte in den Versuchen zur spektroskopischen Bestimmung des Oxidationszustands auf der Tonoberfläche bei höherer Konzentration nicht festgestellt werden. Auf der Tongesteinsoberfläche befindet sich auch nach 4 Monaten Reaktionszeit Np(V). Ein signifikanter Unterschied zwischen OPA und COx konnte in den Versuchen nicht festgestellt werden. Die Reduktion zu Np(IV) läuft kinetisch sehr langsam ab. Im Gleichgewichtszustand sollte allerdings gemäß thermodynamischen Rechnungen basierend auf den gemessenen Eh-Werten fast ausschließlich vierwertiges Np zu finden sein. Eine Modellierung der Ergebnisse mit dem Oberflächenkomplexierungsmodell von [Bradbury und Bayens, 2002, 2005a,b] sind für COx in guter Übereinstimmung, für OPA gibt es noch deutliche Abweichungen, die im Moment nicht erklärt werden können.

Fünfwertiges Plutonium (Pu(V)) war im Tongesteinssystem nicht stabil und wurde zu Pu(IV) innerhalb der ersten Wochen reduziert. Auf der Oberfläche des Tongesteins wurde vierwertiges Pu nachgewiesen. Das Ergebnis steht im Einklang mit thermodynamischen Rechnungen basierend auf den gemessenen Eh-Werten. Erwartungsgemäß wird auch ein höherer K_d -Wert gemessen von bis zu 500 L/kg. Allerdings ist der K_d -Wert abhängig vom gewählten Feststoff-zu-Lösungsmittel-Verhältnis ($K_d = 43 - 517$ L/kg). Es stellt sich die Frage im Falle von Experimenten mit Pu-Konzentrationen nahe der Löslichkeit, ob ein K_d -Wert für vierwertiges Pu eine vernünftige Größe ist, da das vierwertige Pu löslichkeitskontrolliert in Lösung vorliegt. Das bedeutet, dass es sich hier nicht um eine Sorption, sondern vornehmlich um eine Oberflächenausfällung handelt, die in einem dem Sorptionsmodell berücksichtigt werden muss. Erste EXAFS-Auswertungen geben in der Tat Hinweise auf eine Oberflächenausfällung. Sorptionsexperimente bei niedrigeren Pu-Konzentrationen ergeben deutlich höhere K_d -Werte als für Np, die innerhalb eines Jahres um eine Größenordnung angestiegen sind ($\log K_d(12 \text{ d}) = \sim 4.0$ (L/kg); $\log K_d(1 \text{ y}) = \sim 5.3$ (L/kg)). Die bisherigen Resultate zeigen deutlich, dass die Pu-Sorption unbedingt an reinen Tonmineralien untersucht werden muss, um das komplexe Verhalten im natürlichen System erklären zu können.

Der Einfluss von natürlichem organischem Material (NOM) auf die Sorption von Actiniden an Ton wurde in weiteren Experimenten untersucht. Das natürliche organische Material (NOM) ist zwar in natürlichen Tongesteinen oft nur in geringen Mengen enthalten, kann jedoch aufgrund seiner sorptionsrelevanten Eigenschaften (große spezifische Oberfläche, hohe Kationenaustauschkapazität KAK, niedriger pKs Wert) und wegen der relativ hohen $\log \beta$ -Werte für die Komplexbildung mit Actiniden deren Sorption erheblich beeinflussen. Unter bestimmten Bedingungen können lösliche huminartige Säuren in natürlichen Tongesteinen mobilisiert werden. Dies ist z. B. der Fall beim Auftreten von Hoch-pH-Lösungen, wie sie bei der Zementkorrosion in einem Endlager entstehen können. Hierzu wurden Experimente mit synthetischen Mischungen aus Montmorillonit und Huminsäure (HS) durchgeführt. In Gegenwart von HS (10 mg/l) nimmt die Eu(III)-Sorption an Montmorillonit im pH-Bereich 7 bis 9 ab, während sie in HS-freier Tonsuspension unverändert hoch

bleibt. Unter den in dieser Arbeit verwendeten experimentellen Bedingungen wurden aus dem natürlichen Tongestein jedoch keine signifikanten HS-Konzentrationen mobilisiert. Rechnungen zeigen, dass die verfügbaren Daten zur Ln(III)/An(III)-Komplexierung mit HS für das NICA-Donnan-Modell die Humatkomplexierung insbesondere im hohen pH-Bereich deutlich überschätzen.

Die Ergebnisse der vorliegenden Arbeit zeigen, dass bei einer Endlagerung in Ton mit einer Rückhaltung von dreiwertigen Actiniden vornehmlich an den Tonmineralen zu rechnen und die Sorption an anderen Mineralphasen vernachlässigbar ist. Außerdem hat die Komplexierung von An(III) mit Carbonat, das überwiegend aus dem Calcit der natürlichen Tongesteine stammt, einen großen Einfluss auf deren Sorption. Die Komplexbildung mit anderen anorganischen sowie organischen Liganden scheint hingegen bei der Endlagerung in Tongesteinen kaum eine Rolle zu spielen. Auch konnte dargestellt werden, dass die TRLFS als spektroskopische Methode zur Charakterisierung und Quantifizierung von Sorptionsprozessen, wie der Cm(III)/Ton-Outer-sphere-Komplexbildung hervorragend geeignet ist. Im Falle der redoxsensitiven Actiniden Np und Pu sind die erhaltenen Resultate für eine Beschreibung ihrer Rückhaltung im natürlichen Tongestein noch nicht zufriedenstellend. Die Ergebnisse verdeutlichen auch, dass eine aussagekräftige und allgemeingültige Beschreibung der Wechselwirkung zwischen Actiniden und der Lösung/Mineral-Grenzfläche nur auf der Grundlage eines molekularen Prozessverständnisses erfolgen kann.

Die Diffusion von Pu und HTO in OPA wurde mittels der "Through-diffusion"-Methode studiert. Die erhaltenen Diffusionskoeffizienten stimmen gut überein mit Werten anderer "Through-diffusion"-Experimenten. Allerdings zeigten sich auch experimentelle Schwierigkeiten: 20-40% des Pu wurde an den Oberflächen der Diffusionszelle sorbiert. Das nicht-sorbierte und in Lösung verbleibende Pu liegt in der fünfwertigen Oxidationsstufe vor und kann als mobiler Pu-Anteil bezeichnet werden. Das vierwertige Pu befindet sich auf oder im Tonkern, zeigt aber keinen bevorzugten Transportpfad, sondern findet sich an wenigen Stellen konzentriert wieder. Warum das Pu gerade an diesen Stellen konzentriert wird, konnte nicht geklärt werden; eine Korrelation zwischen Pu und z.B. Fe(II) im Ton konnte nicht gefunden werden. Allerdings zeigte sich, dass eine verlässliche Post-Mortem-Analyse schwieriger ist als gedacht. Deswegen wurde auf weitere Post-Mortem-Analysen verzichtet, um zunächst eine verlässliche Technik zu entwickeln. Diese konnten in dieser Projektphase noch nicht verwirklicht werden. In einem sogenannten "Out-of-diffusion"-Experiment konnte gezeigt werden, dass das Pu nicht in die wässrige Phase desorbiert wird und quasi irreversibel im Tongestein sorbiert bleibt. Damit kann Tongestein für Plutonium unter reduzierenden Bedingungen als sehr gute Rückhaltebarriere angesehen werden.

Um das Verhalten von Actiniden in natürlichen Tongesteinen besser verstehen zu können, vor allem auf der geologischen Zeitskala, wurde als natürliches Analogon eine Uran-Ablagerung in einer argillaceous-reichen Formation (Lodève Basin, Frankreich) betrachtet. Die Speziation von Uran hinsichtlich der Wechselwirkung mit der vorhandenen Tonorganik und den vorherrschenden Tonmineralien (Chlorit, Illit) war der Fokus dieser Untersuchung, um Rückschlüsse auf einen Rückhaltemechanismus zu erhalten. μ -XANES und μ -EXAFS-Resultate zeigen, dass Uran in der vierwertigen

Oxidationsstufe im Sediment vorliegt. U(IV) bildet dabei nano-kristalline UO_2 -ähnliche Phasen. Aus den Elementkorrelationen mittels verschiedener Techniken (μ -XRF, STXM and μ -FTIR) kann man die folgenden vorläufige Hypothese einer Uran-Immobilisierung entwickeln. Es existiert keine Korrelation zwischen Fe und U und damit kann man Fe-Mineralien als Reduktionsort von U(VI) zu U(IV) weitgehend ausschließen. Uran ist korreliert mit Kalium, das als ein Indikatorelement für Illit gilt. Weiterhin sind die Tonmineralien vom Illit-Typ mit organischen Komponenten des Tons assoziiert. Daraus könnte man schließen, dass U(VI) in der wässrigen Phase durch Tonorganik in schwerlösliches U(IV) reduziert wird und durch Oberflächenausfällung oder Sorption an der Tonoberfläche immobilisiert wird. Allerdings muss diese Schlussfolgerung noch bewiesen werden, da noch einige offene Fragen gegen diese Hypothese noch nicht beantwortet sind.

Ein weiteres Arbeitspaket war die Grundlagenuntersuchungen zur Wechselwirkung von Actiniden mit Tonorganik und Huminstoffen. Eine mengenmäßig relevante organische Komponente im Ton ist das Kerogen, was durch Grundwasser mit hohem pH-Wert extrahiert werden kann. Zur Komplexierung von Cm(III) durch Kerogen, welches aus natürlichem Tongestein extrahiert wurde, wurden erste Experimente durchgeführt. Die Resultate zeigen eine eindeutige Wechselwirkung des Cm(III) mit dem Kerogen-Extrakt mittels TRLFS. Allerdings konnte nicht geklärt werden, ob diese Komplexierung von dem Kerogen selbst oder durch anorganische Verunreinigungen im Kerogenextrakt wie Pyrit hervorgerufen wird. Da es unmöglich war ein reines Kerogen zu extrahieren ohne die organische Struktur zu zerstören, wurde auf ein ausgedehntes experimentelles Programm zu diesem Zeitpunkt verzichtet. Die Bestimmung einer Komplexierungskonstante hätte keine Aussagekraft und würde nur zu falschen Schlüssen führen.

Eine zweite Studie beschäftigte sich mit der Fulvat-Komplexierung von vierwertigem Np. Bekanntlich hydrolysiert Np(IV) sehr leicht und bildet Hydroxokomplexe und Kolloide. Ausgedehnte XAFS und XPS-Analysen sollten klären, ob man mit gemischten ternären Komplexen rechnen muss oder ob es sich um einfache binäre Komplexe handelt. Die Untersuchungen zeigten aber, dass man mittels XAFS- und XPS-Ergebnissen nicht eindeutig zwischen den ternären und den binären Komplexen unterscheiden kann. Auch gibt es keine eindeutigen Korrelationen zwischen den Ergebnissen der spektroskopischen Methoden und dem pH-Werten, der Reaktionsdauer und der Art der Präparation von Np(IV)-Fulvat-Komplexen. In einigen Versuchen wurden zwei Np-O-Abstände gefunden ($\sim 2.22 \text{ \AA}$ und $\sim 2.42 \text{ \AA}$), in anderen Versuchen erhielt man nur einen Np-O-Abstand der zusätzlich noch zwischen 2.30 und 2.38 \AA variierte. Allerdings kann man aus den Ergebnissen deutlich folgern, dass das Np eine Bindung zu einer Carboxylgruppe (monodentat oder bidentat) bildet und dass man keine Oligomere oder Kolloide findet. Geht man von einem reinen NpFA(IV)-Komplex aus, erhält man unter Berücksichtigung der sogenannten Beladungskapazität oder dem Deprotonierungsgrad der Fulvinsäure bei pH 1 und 1.5 eine Komplexierungskonstante für eine Ionenstärke von 0.1 M NaCl von $\log \beta = 7.0$ bzw. 7.6 . Die pH-Abhängigkeit lässt sich aber durch das gegenwärtige Komplexierungs-Modell nicht kompensieren, reiht sich aber gut in die Literaturwerte für Huminstoff-Komplexe der vierwertigen Actiniden als Funktion des pH-Wertes ein.

Die Nachbildung eines natürlichen Tonsystems aus reinen Komponenten fokuzierte in diesem Projekt auf die Polymerisation von niedermolekularen organischen Molekülen in der Gegenwart von reinem Quellton unter klar definierten Bedingungen. Dieser Ansatz der Kerogen-Synthese aus Komponenten bestehend aus C, O, H und N-Atomen hat den Vorteil, dass man anorganische Verunreinigungen vermeidet – diese konnten aus den natürlichen Extrakten niemals vollständig entfernt werden – und wichtige Erkenntnisse gewinnt über den Reaktionsweg, mögliche katalytische Effekte der Tonphasen sowie den Einfluss der Zusammensetzung austauschbarer Kationen. Mittels einer Maillard-Reaktion von D-Glukose, Glycin oder Katechol in Gegenwart von Na-/Ca-reichen Bentonit (Ibeco) wurde über eine Reaktionszeit von einem Monat bei 80 °C und verschiedenen Trocknungs- und Befeuchtungszyklen ein braunes polymeres Organik-Ton-System hergestellt. Die Komponenten wurden mit verschiedenen analytischen Methoden (Pyrolyse-Gaschromatographie-Massenspektrometrie (Py-GC/MS), μ FT-IR, XRD, TEM, STXM, NEXAFS) untersucht. Die Pyrolyseschritte wurden aufgrund der Analysenergebnisse schrittweise verändert um das organische Endprodukt hinsichtlich des H/C- und O/C-Verhältnis dem Kerogen aus Bure bzw. Tournemire anzupassen. Die letzten erhaltenen Produkte stimmten im O/C-Verhältnis gut überein, waren aber im H/C-Verhältnis zu niedrig und ähnelten eher Holzkohle/Ruß-Komponenten. In einem neuen Ansatz muss die Pyrolyse deshalb weiter angepasst werden, sodass ein CO_x-ähnliches Kerogen synthetisiert werden kann. Damit hätte man dann die Möglichkeit die Wechselwirkung eines reinen Kerogens mit Actiniden zu untersuchen.

Eine Literaturstudie wurde durchgeführt, um einen Überblick über die Komplexierung von Actiniden in verschiedenen Oxidationsstufen mit kleinen organischen Liganden zu erhalten, die im natürlichen Tonsystem gefunden wurden. Durch die Verfügbarkeit von zahlreichen Studien und eine breite Palette von Daten, wurden nur ausgewählte Ligand-Systeme mit systematischen Variationen ihrer monomolekularen Struktur diskutiert, um einen grundlegenden Einblick in die Komplexierungs-Mechanismen zu bekommen. Der Vergleich der gegebenen Stabilitätskonstanten zeigte, dass die Komplexbildung durch eine Reihe von Faktoren beeinflusst wird, wie die Alkalität des Liganden und seiner molekularen Struktur. Im Falle der aliphatischen Carbonsäure-Liganden erhöhen funktionelle Gruppen in α -, β - oder γ -Position zur bindenden COOH-Gruppe die Stabilität der Komplexe deutlich. Dieser Effekt wird einem zusätzlich bindenden Beitrag der zusätzlichen funktionellen Gruppe zugeschrieben, was teilweise eine chelatbildende Wirkung hervorruft. Die verfügbaren thermodynamischen Daten sind jedoch mit verschiedenen Methoden bestimmt worden. Die vorliegende Übersicht zeigt eine deutliche Diskrepanz zwischen Daten aus indirekten Methoden (z.B. Potentiometrie und Extraktion mit Lösungsmitteln) und von spektroskopischer Techniken. Diese Diskrepanz geht weit über die experimentellen Unsicherheiten der zwei verschiedenen Arten von Methoden hinaus. Der Unterschied ist vielmehr auf allgemeine Problem zurückzuführen. Denn die indirekten Methoden könnten das chemische Gleichgewicht während der Messung stören und falsche Ergebnisse liefern. Darüber hinaus können indirekte Methoden nicht zwischen Innersphere- und Outersphere-Komplexe unterscheiden. Damit könnten Veränderungen der Aktivitätskoeffizienten als Änderungen der log β -Werte falsch interpretiert werden. Daher ist die Anwendung der spektroskopischen Methoden (z. B. TRLFS und UV/Vis) für die präzise Bestimmung von thermodyna-

mischen Daten von großer Bedeutung, um die verfügbaren Literatur-Daten zu validieren und um eine zuverlässige thermodynamische Datenbank für Actiniden unter natürlichen Bedingungen zu schaffen.

Für zukünftige Arbeiten auf dem Gebiet der Endlagersicherheit sind Untersuchungen bei erhöhten Temperaturen zwingend notwendig. Ein wichtiges Arbeitswerkzeug ist die pH-Messung, die normalerweise potentiometrisch mittels einer Glaselektrode gemessen wird. Diese ist aber nur bei Temperaturen bis 50 °C zuverlässig. Deswegen wurden erste Anstrengungen unternommen, den pH-Wert spektroskopisch mittels Indikatorfarbstoffe zu messen. Hierzu wurde eine Messzelle eingesetzt, die über Lichtleiter an ein Spektrometer gekoppelt wird und mit der bei Temperaturen bis 200 °C und Drücken bis 30 bar gearbeitet werden kann. Im ersten Schritt wurden die Säurekonstanten der Farbstoffe Bromocresol-Blau und –Grün als Funktion der Temperatur ermittelt für den Temperaturbereich 25 – 90 °C. Anschließend wurden beide Farbstoffe als pH-Indikatoren für die pH-Messung von Propionat- und Lactatlösungen verwendet, um die Temperaturabhängigkeit der Säurekonstanten zu ermitteln. Die erhaltenen Ergebnisse für die Propionsäure stimmen sehr gut mit Literaturwerten überein zwischen 25°C und 90°C. Für Lactat wurde die Temperaturabhängigkeit der Säurekonstante für den gleichen Temperaturenbereich neu bestimmt, da sie in der Literatur nicht verfügbar ist. Diese Arbeit zeigt, dass die Methode zur spektroskopischen Messung des pH-Wertes gut geeignet ist und in zukünftigen Experimenten bei höheren Temperaturen und Drücken eingesetzt werden kann.

Summary

The work within this project network dealt with the migration behaviour of actinides in the natural clay rock barrier. To this end, samples of natural clay rock (Opalinus clay and COx) were characterised with respect to properties that are relevant for the migration of actinides. The sorption properties of Opalinus clay and COx with respect to europium (Eu (III)), curium (Cm (III)), neptunium (Np(V)) and plutonium (Pu(V)) were studied in numerous experiments. Here, we could show for Eu (III), Cm (III) that the clay minerals in natural clay rocks are mainly responsible for the sorption of metal cations. The experimental sorption data could well be described by using a simple model that considers only the sorption on the clay minerals illite, montmorillonit representing all other clay minerals and calcite as the carbonate buffering compound. For this purpose the surface complexation model of [Bradbury and Bayens, 2002, 2005a, b] has been applied.

Using time-resolved laser fluorescence spectroscopy (TRLFS), it was possible to identify outer-sphere sorbed trivalent lanthanides and actinides onto different montmorillonites and illite. Furthermore, the quantification of Cm(III)/clay outer-sphere sorption in D₂O at different ionic strengths was shown. The results were confirmed by ion exchange model calculations.

In contrast to the trivalent Eu and Cm with their fixed oxidation state, the Np and Pu are redox-sensitive metal cations. Therefore, in sorption experiments the redox speciation of Np and Pu plays an important role. For this purpose, XANES, EXAFS, XPS were used for the speciation of actinides on the clay mineral surface and UV/Vis/NIR absorption spectroscopy, capillary electrophoresis (CE) and liquid-liquid extraction were performed to determine the redox speciation in the aqueous phase. If CE is coupled to an ICP-MS, this method is a promising method for future tasks, especially for the redox speciation at very low concentrations. Therefore further development work has been undertaken in collaboration with the University of Cologne to be able to use these methods in sorption experiments and other relevant solutions up to actinide concentrations of 10⁻⁹ mol/L and lower.

For the redox-sensitive actinide Np it was found that Np(V) is partially reduced in the OPA/pore water system to Np(IV) at a low metal concentration of 10⁻⁷ M. The relatively small K_d value of 33 ± 9 L/kg confirms that Np(V) must be still in the system. XAFS characterisation that had to be performed at higher metal concentrations of 10⁻⁴ M showed that no reduction occurs, even after 4 months reaction time. A significant difference between OPA and COx could not be found in case of Np. The reduction of Np (IV) is kinetically slow. However, the Np(IV) should be the stable oxidation state in an equilibrium stage according to thermodynamic equilibrium calculations based on the measured Eh values in solution.

Pentavalent plutonium (Pu(V)) was not stable from the beginning and was reduced to Pu (IV) within the first few weeks. On the surface of the clay tetravalent Pu was detected by XPS and XANES even at high metal concentration of 10⁻⁴M. The result is consistent with thermodynamic calculations

based on the measured Eh values. As expected, a higher K_d value is measured up to 500 L/kg. However, the K_d value varies with the solid-to-solvent ratio from $K_d = 43$ to 517 L/kg. For experiments, where the Pu concentrations were near the solubility limit, the question arises whether a K_d value is a reasonable parameter to describe the sorption of tetravalent Pu. In these solutions the tetravalent dissolved Pu concentration is solubility controlled, meaning that not only sorption takes place, but mainly a surface precipitation has to be considered. Sorption experiments at lower Pu concentrations of 10^{-9} M yields in significantly higher K_d values, which increase within a year by an order of magnitude ($\log K_d$ (12 days) = ~ 4.0 (L/kg), $\log K_d$ (1 year) = ~ 5.3 (L/kg)). An explanation for this behaviour cannot be given, but clearly shows that the Pu sorption has to be investigated on pure clay minerals to be able to explain, which component is responsible for each single reaction – sorption and reduction – and to elucidate the complex behaviour in the natural system.

One further important mobilisation aspect was studied in this project: the influence of natural organic matter (NOM) on sorption of actinides on clay. Although, natural argillaceous rocks normally contain only small amounts of NOM, however, due to its sorption-related properties (high specific surface, high cation exchange capacity CEC, low pK value) and the relatively high complexation constants $\log \beta$ for the complex formation with actinides, NOM can have a significant impact on the sorption. For this purpose, experiments were performed with synthetic mixtures of montmorillonite and humic acid (HA). In the presence of HA (10 mg / l) the Eu (III) sorption on montmorillonite decreased in the pH range 7 to 9, while in HA-free clay suspension the sorption remains unchanged strong. Under the experimental conditions used in this work HS was not released from the natural clay in significant concentrations. Model calculations of the HA impact with the NICA-Donnan model show that the experimental data for Ln(III)/An(III) could qualitatively reproduced but the model significantly overestimate the complexation with HA, particularly in the high pH range.

The diffusion of Pu and HTO in OPA was studied by means of a "through-diffusion" method. The obtained diffusion coefficients agree well with values from other "through-diffusion" experiments. However, experimental difficulties occurred: 20-40% of Pu was sorbed on the surfaces of the diffusion cell. The non-sorbed and in the solution remaining Pu is present in the pentavalent oxidation state and can be regarded as mobile Pu content. The tetravalent Pu at or in the clay core shows no preferable transport path, and is concentrated in a few spots. Why the Pu is concentrated at these points could not be clarified; no correlation could be found between Pu and Fe(II) on the clay. However, it appears that a reliable post-mortem analysis is harder than expected. Therefore, we abdicated further post-mortem analysis, until we will developed a reliable technique. These couldn't unfortunately be implemented in this phase of the project. Out-of-diffusion experiments showed that the Pu is not desorbed into the aqueous phase and remains virtually irreversible sorbed in the clay. Thus, clay rock can be considered as very good retention barrier for plutonium under reducing conditions.

To better understand the behavior of actinides in natural argillaceous rocks, especially on the geological time scale, a uranium deposit in an Argillaceous -rich formation (Lodève Basin, France) was regarded as a natural analogue. The speciation of uranium with respect to the interaction with the existing and prevailing clay organic components as well as the clay minerals (chlorite, illite) was the focus of this investigation to draw conclusions on a retention mechanism. μ -XANES and μ -EXAFS results show that the uranium in the sediment exist in the tetravalent oxidation state. This U(IV) forms nano-crystalline UO₂-like phases. From the element correlations using various techniques (μ -XRF, STXM and μ -FTIR), one can develop the following but preliminary hypothesis of an uranium immobilization. There is no correlation between Fe and U, and thus Fe-minerals can be excluded as sites the U (VI) can be reduced to U (IV). But uranium is correlated with potassium, an indicator element for Illite, from clay minerals. Simultaneously, the illite-type minerals are associated with organic components of the clay. This may suggest that U (VI) in the aqueous phase is reduced to sparingly insoluble U (IV) by clay organic compounds and subsequently immobilized by sorption or surface precipitation. However, this conclusion must be proven, because open issues against this hypothesis are still not answered (see Section 4.2.1).

A further work package was the basic research of the interaction of actinides with humic substances and clay organic components (COC). One polymeric organic component in the clay is kerogen, which can be extracted from the clay by groundwater with high pH produced in presence of concrete surfaces. Complexation experiments of kerogen extracted from natural clay and Cm (III) were performed. The results from TRLS clearly show a complexation of Cm (III) by the kerogen extract. However, it could not be clarified whether this complexation is caused by the kerogen itself or by inorganic contaminants in the extract such as pyrite. Since it was impossible to extract a pure kerogen without altering the organic structure, because the calculation of a complexation constant would have no meaning and would only lead to false conclusions, we decided to abdicate on an extensive experimental program at this time.

A second study of actinide interactions with organic components focused on the complexation of tetravalent Np with fulvic acid (FA). As is generally known the tetravalent Np(IV) hydrolyses already at low pH values forming hydroxo complexes and colloids. Extended XAFS and XPS analysis should clarify whether they have to deal with mixed ternary complexes, or whether it is a simple binary complex. The investigations of the Np(IV) fulvate complexation between pH 1 and 3 showed, however, that by means of XAFS and XPS no clear distinction can be made between the ternary and the binary complex. There was no clear correlation between the results of the spectroscopic methods and the pH values, the reaction time, and the nature of the preparation of the Np(IV) fulvate. In some experiments, two Np-O distances were found ($\sim 2:22$ Å and $\sim 2:42$ Å), in other experiments only one Np-O distance varying between $2:30$ and $2:38$ Å. In any case we can clearly conclude from the results that Np is bound to a carboxyl group (monodentate or bidentate) and that oligomers or colloids forming nanoparticles can be excluded. To estimate a complexation constant at pH 1 and 1.5 – conditions with minimised hydrolysis - we started from a pure NpFA(IV) complex, taking into account the so-called loading capacity or the deprotonation of the fulvic acid. The

conditional complexation constant for an ionic strength of 0.1 M NaCl was estimated to $\log\beta = 7.0$ or 7.6 at pH 1 and 1.5, respectively. The pH dependence cannot be explained by the present model, but the conditional complexation constant qualitatively matches with literature values of humic complexes of tetravalent actinides as a function of pH.

The replica of a natural clay system with pure components focused in this project on the polymerisation of low molecular weight organic molecules in the presence of pure swelling clay under clearly defined conditions. This approach to synthesise a pure kerogen consisting of only C, O, H and N atoms has the advantage that it avoids inorganic impurities - these could be from natural extracts never completely removed - and gaining important knowledge about the pathway, possible catalytic effects of the tonal phase and the influence of the composition of exchangeable cations. By means of a Maillard reaction of D-glucose, glycine or catechol in the presence of Na-/Ca-rich bentonite (IBECO) a brown polymeric organic-clay system has been produced after a one month reaction at 80 ° C and several drying and humidification cycles. The components were investigated using various analytical methods (pyrolysis-gas chromatography-mass spectrometry (Py-GC/MS), μ FT-IR, XRD, TEM, STXM, NEXAFS). The pyrolysis was changed gradually due to the outcome of the analysis to adapt the final kerogen product in terms of organic H/C- and O/C ratio of kerogen from the Bure or Tournemire site. Our final kerogen product agreed well in the O/C ratio, but was too low regarding the H/C ratio and hence, resembles more a charcoal or soot product. In a new approach the pyrolysis must be further adapted to yield a kerogen that is very similar to a natural Kerogen from clay rock.

A literature study has been performed in order to get an overview about the complexation of actinides in different oxidation states with small organic ligands. Due to the availability of numerous studies and a broad set of data, only chosen ligand systems with systematic variations of their molecular structure are discussed to give a basic insight into the complexation mechanism. The comparison of the given stability constants showed, that the complex formation is influenced by a number of factors, like the alkalinity of the ligand and its molecular structure. In the case of aliphatic carboxylic acid ligands, functional groups in α - β - or γ -position to the coordinating COOH group increase the stability constants of the complexes distinctively. This effect is attributed to an additional contribution of the additional functional group, resulting in a partial chelating effect. However, the available thermodynamic data is determined by various methods. The present overview shows a distinct discrepancy between literature data from indirect methods (e.g. potentiometry and solvent extraction) and spectroscopic techniques, which is far beyond experimental uncertainties of these two different types of methods. The difference is rather attributed to the general problem, that indirect methods disturb the chemical equilibrium during the measurement, which might provide biased results. Furthermore, indirect methods are unable to distinguish between inner- and outer-sphere complexes and thus changes in activity coefficients may be misinterpreted for changes in $\log\beta$ values. Hence, application of spectroscopic methods (e.g. TRLFS and UV/Vis) for the precise determination of thermodynamic data is of major importance to validate the available literature data and to establish a reliable thermodynamic database for actinides under natural conditions.

The last work package dealt with the aspect of experiments at elevated temperatures. For future work in the field of repository safety, studies at elevated temperatures are necessary. An important working tool is the measurement of pH that is normally measured potentiometrically using a glass electrode, but which is reliable only at temperatures up to 50 ° C. Therefore, initial efforts have been made to measure the pH value spectroscopically using dyes. For this purpose, a measuring cell was developed, which is coupled via fiber optics to a spectrometer and which can work at temperatures up to 200 ° C and pressures up to 30 bar. In the first step, the acid constants (pK_s) of the dyes Bromocresol Green and Blue were determined as a function of temperature in the temperature range 25-90 ° C. Subsequently, both dyes were used as pH indicator for determining the acidity constants of propionate and lactate as a function of temperature. The results obtained for the propionic acid agree very well with literature values between 25° C and 90° C and confirms the reliability of the method. The new acidity constants of Lactate, which doesn't exist above 25° C in the literature, were determined in the same temperature range. This work showed that the method of spectroscopic measurement of pH is suitable and can be used in future experiments at elevated temperatures and pressures.

Contents

1	INTRODUCTION.....	1
2	CHARACTERISATION OF RELEVANT CLAY ROCK SAMPLES.....	3
2.1	ROCK SAMPLE CATALOGUE.....	3
2.2	MINERAL COMPOSITION AND PHYSICOCHEMICAL CHARACTERISTICS OF CLAY ROCK.....	5
2.3	NATURAL TRACE ELEMENT DISTRIBUTION.....	8
2.4	NATURAL ORGANIC MATTER/ KEROGEN INVENTORY	10
3	STUDIES OF THE SORPTION OF ACTINIDES ON CLAY ROCK	12
3.1	SORPTION OF TRIVALENT ACTINIDES AND LANTHANIDES (Eu(III), Cm(III)) ON OPA AND COX.....	12
3.1.1	<i>Experimental</i>	12
3.1.2	<i>Results and discussions</i>	22
3.2	EU(III)/CM(III) SORPTION ON CLAY / CALCITE MIXTURE.....	28
3.3	CONCLUSIONS FROM THE SORPTION STUDIES WITH TRIVALENT ACTINIDES.....	31
3.4	SORPTION OF PENTAVALENT NEPTUNIUM AND PLUTONIUM ON OPA AND COX	33
3.4.1	<i>Materials and Methods</i>	33
3.4.2	<i>Results and discussions</i>	36
3.5	INFLUENCE OF HUMIC ACID ON THE AN(III) SORPTION.....	44
3.6	OUTERSPHERE COMPLEXATION OF TRIVALENT ACTINIDES.....	48
3.6.1	<i>Identification of the An(III)/clay outer-sphere complexation</i>	50
3.6.2	<i>Quantification of the An(III)/clay outer-sphere complex</i>	58
4	STUDIES OF THE DIFFUSION OF ACTINIDES AND ANALOGA.....	69
4.1	DIFFUSION OF PU IN OPA CLAY ROCK	69
4.1.1	<i>Experimental set-up</i>	69
4.1.2	<i>Results</i>	73
4.1.3	<i>Conclusions</i>	78
4.2	ANALOGUE STUDY ON THE URANIUM SPECIATION IN ARGILLITES FROM THE LODÉVE BASIN (FRANCE).....	79
4.2.1	<i>Conclusions</i>	86
5	SPECIATION OF ACTINIDES IN THE CLAY SYSTEM.....	88
5.1	SPECIATION IN SOLUTION.....	88
5.1.1	<i>UV-Vis/NIR spectroscopy of Np(V)</i>	88
5.1.2	<i>Eh Measurements</i>	89
5.1.3	<i>CE-ICP-MS</i>	89
5.2	SPECIATION OF NEPTUNIUM AND PLUTONIUM ON CLAY SOLID PHASES.....	91
5.2.1	<i>XANES</i>	91
5.2.2	<i>EXAFS</i>	94

5.2.3	XPS	97
5.3	REDOX SPECIATION OF PLUTONIUM AND NEPTUNIUM IN CLAY/ POREWATER SYSTEM	100
5.4	BASIC DEVELOPMENTS ON THE CAPILLARY ELECTROPHORESIS COUPLED TO ICP-MS	102
5.4.1	<i>Development of an optimised sample introduction into the ICP-MS for the use with the CE-ICP-MS</i>	102
5.4.2	<i>Method development of a CE-DAD-ICP-MS for the simultaneous detection of humic substances (DAD) and metal ions (ICP-MS)</i>	103
5.4.3	<i>Development of separation parameters for the speciation of uranium with CE-ICP-MS.....</i>	104
5.4.4	<i>Modelling of the CE-separations for selected problematic separations.....</i>	105
6	BASIC INVESTIGATIONS OF THE ACTINIDE COMPLEXATION WITH CLAY ORGANIC COMPONENTS AND HUMIC SUBSTANCES	107
6.1	INTERACTION OF Cm(III) WITH KEROGEN EXTRACTED FROM CLAY ROCK	107
6.2	BASIC INVESTIGATIONS OF THE Np(IV) FULVATE COMPLEXATION	109
6.2.1	<i>Materials and Methods</i>	109
6.2.2	<i>Results and discussion</i>	112
7	REPRODUCTION OF A NATURAL CLAY SYSTEM FROM PURE COMPONENTS	124
8	THE ROLE OF LOW-MOLECULAR ORGANIC COMPONENTS IN THE DIFFUSION OF RADIONUCLIDES IN OPA – A LITERATURE STUDY.....	129
8.1	COMPLEXATION OF TRIVALENT ACTINIDES WITH ORGANIC LIGANDS	129
8.2	COMPLEXATION OF TETRAVALENT ACTINIDES WITH ORGANIC LIGANDS.....	131
8.3	COMPLEXATION OF PENTAVALENT ACTINIDES WITH ORGANIC LIGANDS.....	133
8.4	COMPLEXATION OF HEXAVALENT ACTINIDES WITH ORGANIC LIGANDS	134
8.5	SUMMARY	135
9	MEASUREMENT OF PH VALUES AT ELEVATED TEMPERATURES	136
9.1	THEORY	136
9.2	TECHNICAL EQUIPMENT	138
9.3	MEASUREMENT OF THE PH	138
10	REFERENCES PUBLISHED FROM PROJECT RESULTS WITH INE CONTRIBUTION	145
11	REFERENCES.....	146
12	LIST OF FIGURES	159
13	LIST OF TABLES	170

1 Introduction

For the long-term safety assessment of a nuclear repository, the knowledge is crucial of the interaction and transport of long-lived radionuclides in the technical, geotechnical and geological barriers. The actinides play a very important role. Their migration in the potential host formation – foreseen for a repository - and their transportation behaviour after releasing into the aquifer have to be known to compare the suitability of possible potential host rocks (salt, clay, granite) to provide the required proof of safety. This is necessary in order to ultimately be able to elect a host formation for a repository. The aim of this joint project is to elucidate the geochemical behavior of actinides, especially under reducing conditions in the natural clay under the influence of organics (humic substances, organic clay components) and thereby collect the necessary data to apply them for the safety case of a host formation.

The influence of the chemical environment on the mobilization or immobilization of the actinides, including the kinetics of these processes is at the forefront of considerations. Against the background for the disposal of actinides in clay, in contrast to other host formations such as salt, diffusion processes are important. The parameter dependence of the different processes has to be elucidated. The transport behaviour of actinides depends again on the composition and the corresponding physical properties of the clay rocks, but also on various parameters of the aquatic-specific system, such as pH, Eh, ionic strength, CO₂ content, concentration and charge of the actinides, competing ions, the presence of complexing ligand and the concentration of colloids. Here, just the organic ingredients can play an important role, which has to be examined based on earlier studies of kaolinite as a model clay mineral. In the aquifer system, the propagation behavior of actinides is determined strongly by humic substances due their complexing, redox and colloidal properties, Therefore, they can have a significant influence on the retention or transport of actinides in the repository. Clay organic compounds like Kerogen might play also a strong role regarding migration processes.

In this work natural clay rock samples were characterised in terms of the migration of actinides relevant properties. To obtain a sufficient understanding of the process of actinide-clay interactions like sorption and redox reactions, the spatial distribution of the clay matrix and the bonding state of dissolved and sorbed actinides were investigated. This has been started in basic investigations of the sorption process on the clay rock, as well as on single pure clay minerals. Then diffusion experiments have been performed to get information of the transport properties of actinides as well as for the diffusion mechanism. In addition the complexation of actinides with humic substances and clay organic components like Kerogen has been probed in required basic studies. To understand the origin and properties of humic substances and clay organic compounds the natural clay rock system was attempted to reconstruct the natural system with pure clay and organic components. Such "synthetic systems" also allow specific studies of the influence of natural clay organic compounds on the actinide migration in a host rock.

2 Characterisation of relevant clay rock samples

2.1 Rock sample catalogue

The Opalinus clay samples from the Mont Terri site have been delivered from the Bundesanstalt für Geowissenschaften und Rohstoffe (BGR). The samples – drilling cores - were delivered in September and November 2006, and each drilling core was wrapped in air-tight aluminium foil bags filled with nitrogen. The samples from the Benken site came from borehole BEZ E24/2. The samples from the Bure site were taken from the borehole EST104 No. 490 at an approximate depth of 490 m from the topographic surface. All clay samples were stored in a metal container filled with argon gas to avoid further oxidation of redox sensitive clay components. On time to time from this clay material powder samples for sorption experiments and smaller cores for diffusion experiments were prepared.

Table 2-1: Samples from the Mont Terri site delivered by BGR and used for the project.

No.	Borehole	Charge	Depth (m)	Comments
1	BHE 24	01	3.30 – 3.56	
2	BHE 24	02	3.56 – 3.89	
3	BHE 24	13	6.81 – 7.05	
4	BHE 25	1	2.98 – 3.16	Foil defect
5	BHE 25	10	6.27 – 6.45	
6	BHE 25	11	6.45 – 6.61	
7	BHE 25	12	6.61 – 6.81	Foil defect
8	BLT 11	01		2 small discs
9	BLT 12	01	1.58 – 2.00	Core broken
10	BLT 12	02		2 small discs
11	BLT 12	02	2.03 – 2.28	Vented
12	BLT 13	01	1.69 – 2.09	
13	BLT 13	02	2.09 – 2.49	
14	BLT 13	03	3.45 – 3.76	
15	BLT 14	01	0 – 0.25	
16	BLT 14	01	0.25 – 0.50	
17	BLT 14		0.50 – 0.90	
18	BLT 14		0.90 – 1.57	
19	BLT 14		1.57 – 2.12	
20	BLT 14		2.12 – 2.52	
21	BLT 14		2.52 – 2.97	

To minimise heterogeneity of the samples and to make the experiments of different project partners comparable, the powder and core samples prepared at KIT-INE were delivered to

each interested project partner. The name and the depth of the delivered samples from BGR are scheduled in Table 2-1. Furthermore, OPA clay from the municipality Benken, Switzerland, and Callovo-Oxfordian Clay from the Bure site, France, were used for the experiments: No. 22 and 23 in Table 2-1.

Table 2-2: OPA, COx, natural and synthetic clay minerals, and other materials used for sorption studies

Clay	Name	Location
OPA	BEZ E24 / 02 BEZ E24 / 03	Benken, Züricher Weinland (Switzerland), 113 m depth
COx	EST 104 / 490 EST 25691 PAC1001Dif1749	Bure, Meuse/Haute-Marne (France), 490 m depth
Natural Smectite, Montmorillonit Wyoming-Bentonite	SWy-1/SWy-2	Crook County, Wyoming (USA)
Natural Smectite, Montmorillonit Bentonite from Milos		Island Milos (Greece)
Texas-Montmorillonit		Gonzales County, Texas (USA)
Synthetic smectite	Beidellite	Prepared by KIT-INE
Synthetic smectite	Ca/Na-montmorillonite	Université de Haute Alsace, Mulhouse (France)
Illit du Puy	IdP-2	Le Puy en Valey, Massif Central (France)
γ -alumina	Aluminiumoxid C	Degussa
Calcite		Creel (Mexico)

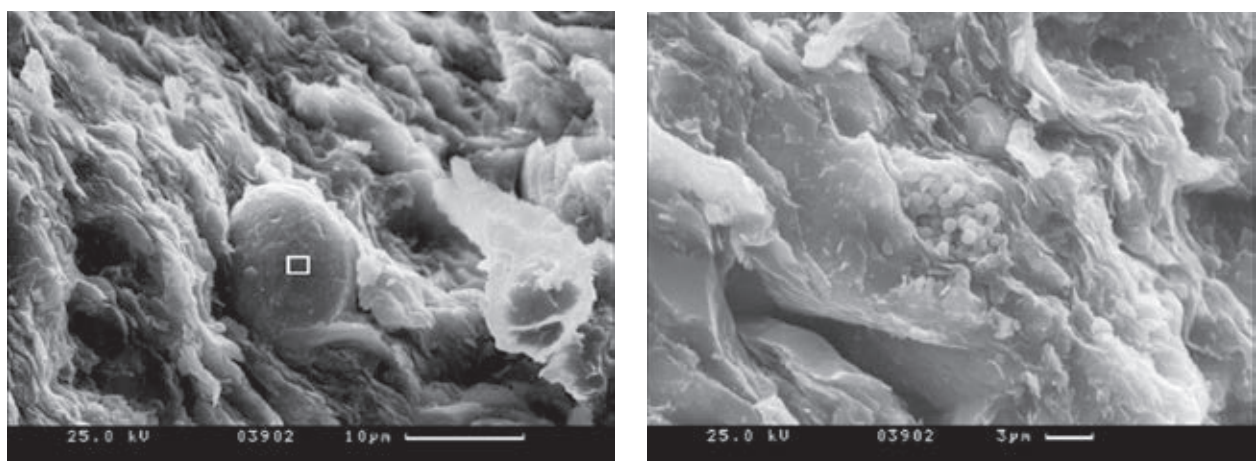


Figure 2-1: REM images of OPA clay. In the image on the left a round calcite crystal is surrounded by flaky clay minerals. In the right image a pyrite conglomerate can be seen reformed by diagenesis.

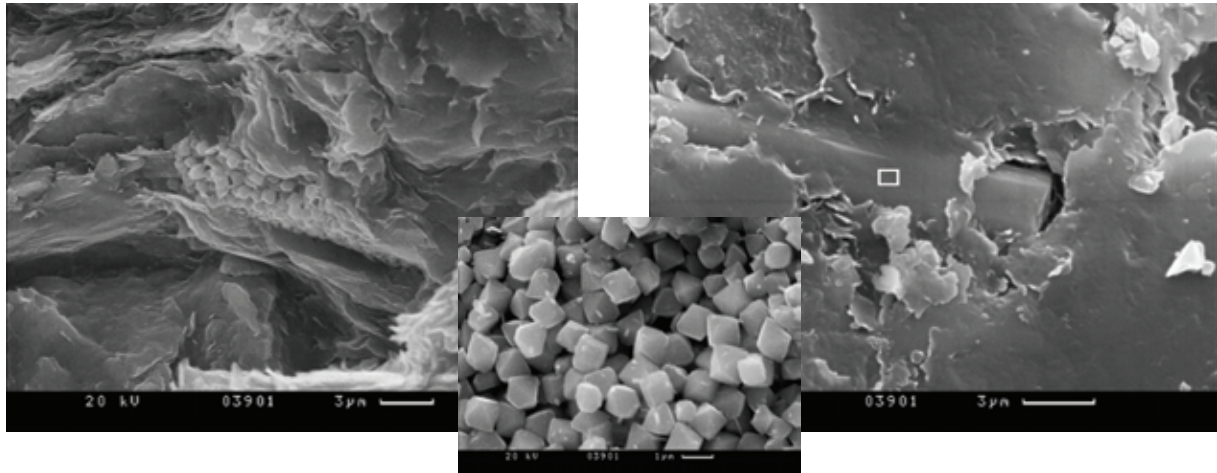


Figure 2-2: REM images of COx clay. In the left image a pyrite conglomerate surrounded by flaky clay minerals (small image: magnification of the cubical pyrite crystals), in the right image rutile crystals with their characteristic columnar habitus.

2.2 Mineral composition and physicochemical characteristics of clay rock

The OPA clay and the COx clay have been thoroughly characterised by Nagra and ANDRA using many samples. The average composition of both clay rocks are summarised in Table Table 2-3.

We assume that small variations of the mineralogy and physico-chemical properties from the average composition - Table 2-1 - have no significant influence on the conclusions from the experiments. Nevertheless, some own characterisations have been performed. Furthermore, the minerals zircon ($ZrSiO_4$), Hematite (Fe_2O_3), Sphalerite (ZnS), Rutile (TiO_2) and Apatite ($Ca_5[(PO_4)_3(OH, F, Cl)]$) were detected accessory minerals by raster electron microscopy (REM) for OPA. For COx anhydrite/gypsum, pyrite, zircon, rutile and coelestine have been found by REM as accessory minerals. The main mineral components from Table 2-1 were confirmed by x-ray diffractometry [Hartmann,2010]. The clay mineral fraction of OPA is composed mainly by kaolinite, Illite and Illite/Smectite mixed layers. In contrast to OPA, the COx contains only very small amounts of kaolinite and chlorite and the main clay minerals are Illit/Smectite mixed layers, Illite and Smectite. The amount of calcite with 17.3 wt.% is twice the amount in the OPA (8-10 wt.%).

Fe(II) has been detected by XPS with contents of 1.42 to 1.49 ± 0.3 atom-% for OPA and 1.23 wt.% for COx. Unfortunately, the location of the Fe(II) could not be achieved, maybe due to very small and finely dispersed particles. According to [Nagra, 2002], the Fe(II) of OPA is found in the minerals siderite ($FeCO_3$), ankerite ($CaFe(CO_3)_2$) and pyrite (FeS).

Table 2-3: Average mineralogical composition and physicochemical characteristics of OPA clay from Benken/Schweiz [Nagra,2002] and Callovo-Oxfordian clay COx from Bure/France (clay particle size fraction (< 2 µm) and organic carbon: [Claret et al., 2002].

Minerals	OPA ^b (wt.-%)	COx ^c (wt.-%)	SWy-2 ^d (wt.%)
Calcite	16,0 ± 10,0	20,0 ± 4,0	< 0.5
Dolomite/Ankerite	1,0 ± 0,4	4,0 ± 2,0	<0.5
Siderite/Fe-Minerals	4,0 ± 2,4	1,9 ± 0,8	3.85-4.3 ^e
Quartz	20,0 ± 5,0	22,0 – 35,0	1
Albite	1,0 ± 0,3	1,0 ± 0,1	<1
Orthoclase	2,0 ± 1,0	2,0 ± 0,1	<1
Pyrite	1,1 ± 1,0	0,7 ± 0,2	
Illite	18,0 ± 6,0	8,0 ± 1,0	1
Smectite	<	6,0 ± 1,0	97-100
Illite/Smectite mixed layers	14,0 ± 4,0	28,0 ± 2,0	
Kaolinite	17,0 ± 6,0	≤ 1,0	<1
Chlorite	5,0 ± 2,0	0,4 ± 0,1	<1
Organic carbon	0,6 ± 0,3	1,31 ± 0,3	≤ 0.15
Total CEC meq kg ⁻¹	106 ± 7	140 ^f ; 171-176 ^j , 250-400 ^g	760 ^h – 910 ⁱ
Total surfaces EGME m ² g ⁻¹	94 ± 13	n.s.	n.s.
BET external surfaces m ² g ⁻¹	28 ± 9; 32 ^j , 39 ^j	32 ^j ; 35 ± 1.5, 36.7 ^j	32-43 ^j
pH porewater	7.25	7.3 ^k	

<: below the detection limit; a: Opalinus Clay and Murchisonae layers; b: [Nagra, 2002]; c: clay fraction and organic carbon: [Claret et al. 2002]; residual mineral content: [Gaucher et al., 2004] and [Griffaut, 1999] (cited in [Motellier et al., 2003]); d: [Bradbury&Baeyens, 1995], [Rabung et al., 2005], stated for conditioned SWy-1; e: stated for total Fe as Fe2O3; f: [Bouchet et al., 1997], stated for sample at depth about 490m; g: [Claret et al., 2004]; h: [Rabung et al., 2005], stated for conditioned SWy-1; i: [Michot et al., 2004]; j: own measurements; k: [Jacquot, 2002] (cited in [Montes et al., 2005]); n.s. not specified.

The pH of clay pore water amounts to 7.25 for OPA [Nagra, 2002] and 7.30 for COx [Hartmann et al., 2008]. The Eh value was estimated to -185 to -156 mV [Jacquot, 2002; Luck-scheiter et al., 2004].

Further details of the characterization of the natural clay material included cation exchange capacity (CEC) determination by the Cobalt hexamine (Cohex)- method and XRF analysis,

which is summarized in the following tables. The specific surface area determined by N₂-BET is 36.7 m²/g for the Callovo- Oxfordian argillite (sample PAC1001Dif1749) and 39.0 m²/g for Opalinus Clay (sample OPA/BHE-24-2). Concerning the CEC of the OPA sample summing up the exchangeable cations would lead to a considerable higher CEC of 17.1-17.6 meq/100g which can originate from an excess of Na due to the high concentration of NaCl in Mont-Terri OPA. Therefore the Cohex quantification determined by UV/VIS is documented here.

Table 2-4: X-Ray fluorescence analysis (XRF) of the Callovo- Oxfordian sample (PAC1001Dif1749) and the Opalinus Clay sample (OPA/BHE-24-2).

Element (wt. %)	PAC1001Dif1749	OPA/BHE-24-2
SiO ₂	42.78	48.38
CaO	24.58	10.71
Al ₂ O ₃	14.87	22.05
Fe ₂ O ₃	7.185	8.499
K ₂ O	3.804	3.832
SO ₃	2.93	1.95
MgO	2.09	2.25
TiO ₂	1.07	1.22
P ₂ O ₅	0.21	0.352
Na ₂ O	0.212	0.465
SrO	0.0683	0.0475
MnO	0.039	0.0722
ZrO ₂	0.0301	0.0252
BaO	0.0268	0.0324
V ₂ O ₅	0.023	0.021
Cr ₂ O ₃	0.022	0.017
Rb ₂ O	0.0189	0.0186
ZnO	0.015	0.02
NiO	0.011	0.015
Y ₂ O ₃	0.0046	0.0047
CoO	n.d.	0.011
Ga ₂ O ₃	n.d.	0.004

n.d.: not detected

Table 2-5: Cation exchange capacity (CEC) as determined by the Cohex method for the Callovo- Oxfordian (COx) sample (PAC1001Dif1749) and the Opalinus Clay (OPA) sample (OPA/BHE-24-2).

	Na [meq/100g]	K [meq/100g]	Ca [meq/100g]	Sr [meq/100g]	Mg [meq/100g]	CEC (meq/100g)
COx	2.20-2.33	1.05-1.06	5.64-5.77	0.22-0.23	3.39- 3.48	11.95-12.09
OPA	6.49-6.65	1.23-1.24	5.72-5.86	0.11	3.58-3.77	12.91-12.96

2.3 Natural Trace element distribution

Other activities aimed on the role of mineral and organic reservoirs in trace metals solubility and mobility controls in clay rocks, namely Callovo-Oxfordian claystone. Two cases are explored in detail in collaborative work with BRGM to look on the natural distribution of nickel and iodine, which can determine the mobility of the radioisotopes in the formation.

In the case of nickel in deep details together with some insights from cobalt, zinc and lead behaviors were gathered and a manuscript has been submitted (Grangeon et al., 2011, in review). Most Ni-enriched phases, identified from a combination of physical and chemical methods are pyrite (~400 µg/g Ni), sphalerite (~300 µg/g Ni), chlorite (~300 µg/g), organic matter (~300 µg/g), muscovite (100- 200 µg/g) and carbonate (mainly calcite and minor dolomite, ~10 µg/g). Despite their high abundance in the formation (up to ~80% in the top of the formation), carbonates are a quantitatively minor nickel reservoir whereas most of Ni is beard by pyrite and chlorite, that are minor mineral phases. From in-situ survey of pore water composition within the formation, pyrite is shown to be a major source of solute Ni in oxidised conditions. From both laboratory kinetics experiments and in-situ pore water composition measurements, carbonate minerals appear as the main buffers of solute nickel concentration with Ni solubility range at ~0.2-1 µmol/L. Cobalt and nickel have similar distribution, whereas lead and zinc have partly different reservoirs (e.g. sphalerite, ZnS).

In the case of iodine a multidisciplinary approach was used to define iodine immobilization mechanisms by biocarbonates in the Callovo-Oxfordian formation (Lerouge et al., 2010). For this purpose, different techniques of observation (optical microscope, scanning electron microscope (SEM), cathodoluminescence (CL)) and of analyses (infrared spectrometry (IR), electron microprobe (EPMA), spatially resolved synchrotron-based X-ray fluorescence (µ-XRF) and X-ray diffraction (µ-XRD)) were performed on two entire and centimeter-sized carbonate shells. Combined (SEM, CL, IR and µ-XRD) data indicates that the biostructure of the Rhynchonella shell is relatively well-preserved but bio-aragonite slowly transforms into calcite, whereas the bivalve shell is entirely re-crystallized into diagenetic calcite and celestite. EPMA and µ-XRF data show bioaccumulation of iodine in carbonate shells, confirming previous work on present-day mollusks. EPMA analyses give evidence of iodine content up to 1200 ppm in the preserved Rhynchonella shell and up to 2000 ppm in recrystallized bivalve shell. µ-XRF elemental mapping shows that iodine is more homogeneously distributed in biocalcite of the Rhynchonella shell than in re-crystallized calcite of the bivalve shell, suggesting

a loss of iodine during re-crystallization processes, but not a total exclusion of iodine from the carbonate structure. Combined EPMA data and μ -XRF elemental maps do not give evidence of any correlation between the iodine location and the distribution of other elements.

The implication of these results for radio-iodine is that under undisturbed far-field conditions mt natural iodine would not be accessible for isotopic exchange with radio-iodine, reducing the effective K_d to negligible values.

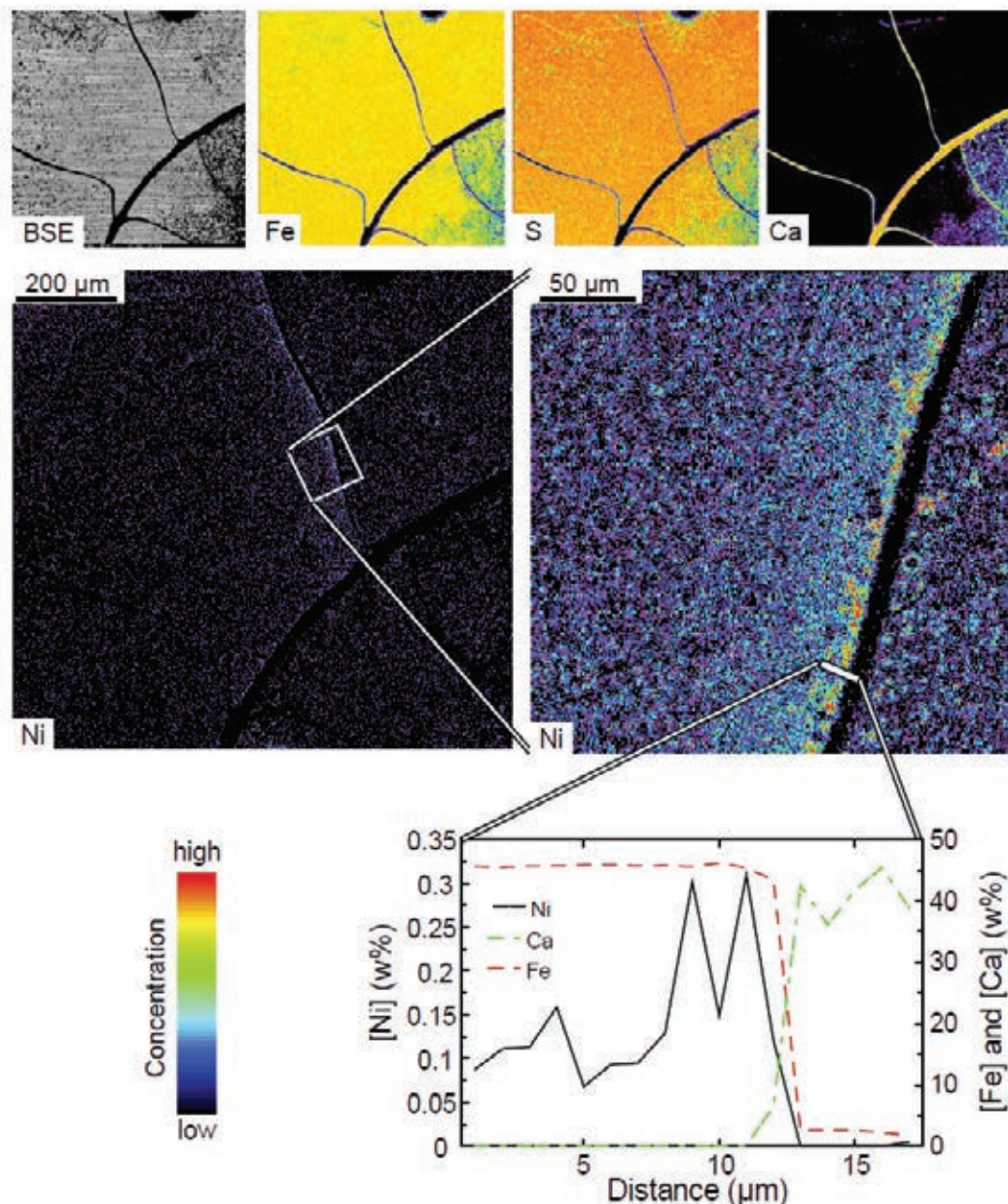


Figure 2-3: Top line, from left to right: back-scattered electron map of part of an ammonite (septa appear as dark lines and camerae as greyish zones), and corresponding Fe, S, and Ca chemical maps (microprobe experiments). Middle left: Ni chemical map. Same location, but increased in size. Enlarged view of the white square at middle right (different experiment). Bottom: Ni (solid line), Ca (dot-dashed line) and Fe (dashed line) quantitative analyses of the line materialized in white on the middle right figure. Figure taken from [Grangeon et al., 2011, in review].

2.4 Natural organic matter/ kerogen inventory

In the beginning of the project, work focused on the detailed characterization of the natural organic matter (NOM) present in the Callovo-Oxfordian clay formation and the Opalinus clay. Beside looking in detail on the nano- to microscale distribution of NOM (Schäfer and Denecke, 2010; Schäfer et al., 2009a; Schäfer et al., 2009b) another activity focused on the extraction of different hydrophilic and hydrophobic compounds from the natural claystone samples for later planned actinide complexation studies (Grasset et al., 2010).

Key findings of these activities, which are already published in peer reviewed journals were: Synchrotron based (C-, K-, Ca-, O- and Fe-edge XANES) scanning transmission X-ray microscopy (STXM) and FT-IR microspectroscopy was used to identify under high spatial resolution the distribution of clay-organic matter with different functionality using principal component and cluster analysis. The results show that in this old (Jurassic) geological formation, small parts of the organic inventory (1–5%) keeps the structure/functionality and can be mobilized as hydrophilic humic substance type material (HA and FA). HA and FA were extracted following the standard International Humic Substance Society (IHSS) isolation procedure. Target spectra analysis shows best correlation for isolated humic acids with organics found in smectite-rich regions, whereas the extractable FA has better spectral similarities with the illite mixed layer minerals (MLM) regions.

The major fraction (>95%) of the organic matter (OM) is associated with minerals. In order to understand the importance of OM on the chemistry of this formation, we have developed a protocol allowing extraction/fractionation of organic compounds in the rocks. The protocol is based on classical methods currently used for the isolation of humic substances from soils and for the separation of kerogen in ancient sediments using sequential extraction with solvents and water at different pH values. This allows us to remove a large part of the minerals and to suspend almost all (>90%) of the OM (associated with residual recalcitrant minerals) in water. The OM can then be analyzed via spectroscopic methods, such as mass spectrometry (MS), Fourier transform infra-red spectroscopy (FTIR), or C (1s) near-edge X-ray absorption fine structure (NEXAFS) spectroscopy. The molecular composition of the solvent-soluble, directly-extractable part shows the OM to be thermally immature. The solvent-soluble fractions obtained after acid and alkaline treatments are mostly polar in nature and have a high degree of aliphaticity. C(1s) NEXAFS analysis of water soluble organic fractions indicates a progressive increase in aliphaticity and a decrease in carboxylic/carbonyl groups with consecutive extraction steps.

Another activity within the project focused on the isolation of kerogen from the Opalinus Clay whole rock based on a protocol established in the petroleum community [Vandenbroucke&Largeau, 2007]. The motivation of kerogen isolation was to investigate in a further step the complexation behavior of this kerogen with respect to radionuclides (i.e. trivalent actinides; Cm) in batch sorption and spectroscopic studies. This procedure consists of

several acid attacks under anoxic atmosphere at 60-70°C. Then, the removal of pyrite is realized by an additional chemical leaching procedure [Acholla&Orr, 1993]. As mentioned before, the organic content of these formations is low in comparison to potential petroleum reservoir rocks and this fact induces difficulties to extract pure organic products without residuals of inorganic phases (i.e. silicates, pyrite) present [Deniau et al., 2008]. In petroleum research, the presence of residual inorganic materials in the isolated fraction can be neglected as the chemical methods applied afterwards are not sensitive to these impurities (i.e. Rock Eval parameters). However, in order to elucidate the potential radionuclide complexation by kerogen, which is expected to have low amounts of complexation groups, these impurities have to be minimized. We succeeded to reduce the amount of inorganic mineral phases co-extracted with the kerogen-type material. SEM-EDX measurements (see Figure below) show that the inorganic phases as shown by the quantitative analysis are still present and sum up to a total amount of 18.3 wt% (Al, Si, Fe, S). Comparing these results to literature data [Deniau et al., 2008] who found between 19.6-37.7 wt% S and 14.3-30.1 wt% Fe in isolated kerogen samples (no Si and Al quantification documented), this clearly documents the improvements made in this study.

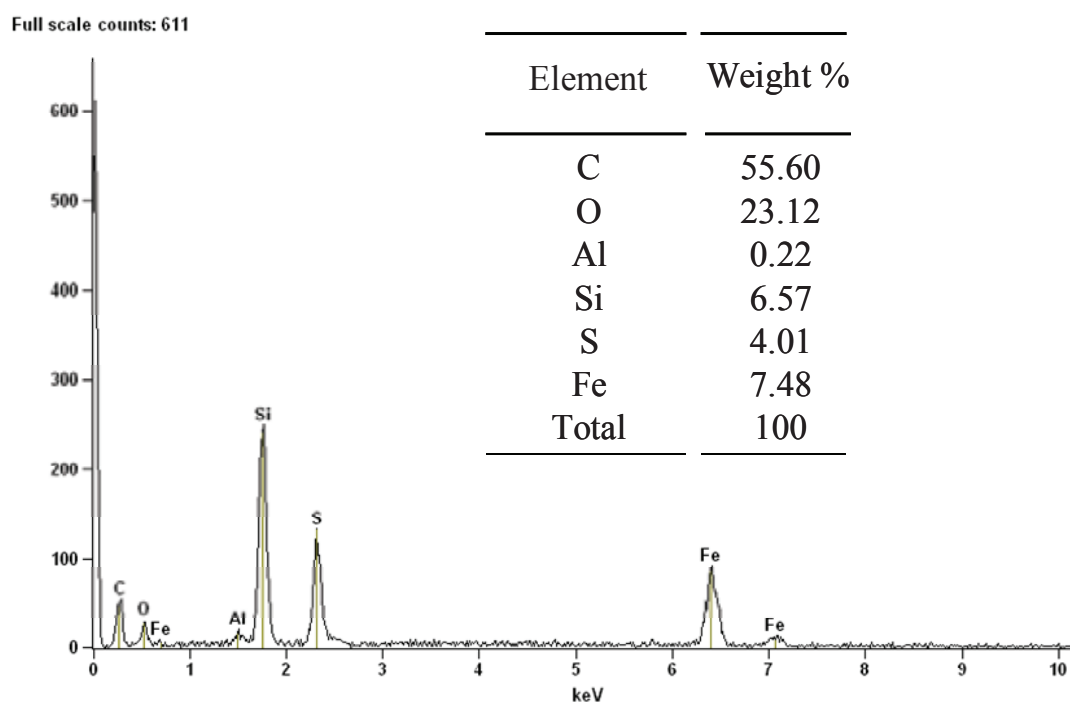


Figure 2-4: SEM measurements and quantitative results on extracted products from Opalinus Clay

3 Studies of the sorption of actinides on clay rock

The identification of the relevant mineral phases in natural clay rock responsible for the sorption can be achieved by comparing data obtained from experiments with heterogeneous composed sediments and from experiments with pure mineral phases. In this project the purified Na-rich montmorillonite SWy-2 was used as a surrogate for clay minerals occurring in clay rock. Additionally, the influence of calcite as potential sorbent and humic acid as potential complexing compound on the sorption of radionuclides in the pure clay system was studied. Comparison of results from these batch experiments in the pure system, TRLFS studies and from model calculations one can identify the main clay mineral phases in natural clay rock responsible for the sorption of radionuclides. The assignability of available geochemical data on radionuclide speciation in heterogeneous natural systems can also be assessed from these results.

3.1 Sorption of trivalent actinides and lanthanides (Eu(III), Cm(III)) on OPA and COx.

3.1.1 Experimental

The sorption of Curium, Europium and hexavalent Uranium was studied in batch experiments and by spectroscopic methods like time-resolved laser fluorescence spectroscopy (TRLFS), EXAFS, and XPS. The europium was introduced as a surrogate metal ion for the trivalent actinides.

Batch experiments

In Table 3-1 the experimental conditions of all performed batch experiments is summarised. The pH dependence of the sorption on a heterogeneously composed natural clay rock experiments was studied in the experiment No. 1 to 14. The question about the relevance of outer-sphere complexation on clay minerals has been probed with the variation of the ionic strength and the samples were characterised by TRLFS. Sodiumperchlorate that shows non-complexing properties towards the trivalent and hexavalent cations was used as electrolyte in the solution. For experiment 14 – sorption on Ca-Montmorillonit - Calciumperchlorat was used to avoid ionic exchange as competition reaction between Na^+ and Ca^{2+} .

For the batch experiment a solid to liquid ratio (S/L) of 2 g/L was chosen. At this S/L the cations are mainly bound to the “strong sorption sites” of the clay. Only at lower S/L the cations start to sorb on the “weak sorption sites”. In the experiments 15 to 18 only 0.3 g clay per 1 L NaCl was mixed to get the same conditions as in the TRLFS experiments.

OPA / COx clay samples were crushed and dissolved in the electrolyte solutions. The clay-suspensions were homogenised by stirring over several hours. The metal cations were added to 10 to 20 ml of the suspension in polyethylene (HDPE, Zinsser Analytics, Frankfurt/M.). As metal cations Eu(III) (Europium plasma standard solution, suprapure[®], 1000 µg/L Eu, 5 % HNO₃) and U(VI) (UO₂²⁺, Alfa Uranium ICP standard solution, 1000 µg/L U, 5 % HNO₃) were chosen. The used metal concentration was 1-2x10⁻⁷ mol/L. These concentrations are low enough to avoid precipitation of hydrolysis products of the metal cations. The sorption on the vial surfaces are small compared to the sorption on the clay material.

The pH value has been adjusted with 0.01 and 0.1 M NaOH or HCl (Merck, Darmstadt, Germany) in a range between 2.7 and 11.9 intervals of 0.5 (pH-meter Schott CG810, pH electrode Orion 8103 Ross[®], semi-micro combination). An alteration of the S/L was not expected because only very small amounts of acid or base were necessary to fix the pH value. Due to the high amount of carbonate in the natural clay rock of OPA and COx and the waiving of buffers a small shift of the pH was not avoidable. After adding the metal cations, the samples were slowly mixed in rotation machine for five to seven days. Then aliquots were taken for the analysis of the samples by ICP-AES and ICP-MS. Details of the experiments can also be found in [Hartmann, 2010; Hartmann et al. 2008].

The distribution ratio (R_d, L/kg) was taken for the representation of sorption data.

$$R_d = \frac{c_{initial} - c_{final}}{c_{final}} \cdot \frac{V}{m} \quad (3-1)$$

where C_{initial} (mol/L) is the initial nuclide activity/concentration, C_{final} (mol/L) the final (equilibrium) nuclide activity/ concentration, V (L) the liquid volume, and m (kg) the mass of the solid phase

Time-resolved laser fluorescence spectroscopy (TRLFS)

The set-up of the laser system is described elsewhere [Hartmann, 2010]. For the experiments a Nd:YAG pumped dye-laser (Continuum ND 6000, Powerlite 9030, 10 Hz) was used. As dye to get the appropriated wavelength for the excitation of the Cm(III) Exalite 398 was used. The excitation of the Cm(III) was performed at 396.6 nm and corresponds to the maximum in the Cm³⁺(aq) absorption and excitation spectra.

Table 3-1: Overview of experimental conditions of all batch experiments performed for the sorption experiments of Cm(III) and U(VI) (at 298 K). The Cm(III) / clay mineral-Outersphere complexation were investigated in experiment 15 to 18

	Solid matter	Condi- tions	Electro- lyte	Ionic strengths [mol/l]	S:L [g/l]	pH-value	Eu(III)- Conc. [mol/l]	U(VI)- Conc. [mol/l]
1	OPA	aerobic	NaClO ₄	0.1	2	2.7 – 11.1	1·10 ⁻⁷	-
2	COx	aerobic	NaClO ₄	0.1	2	3.8 – 11.3	1·10 ⁻⁷	-
3	SWy-2	aerobic	NaClO ₄	0.1	2	3.1 – 11.0	1·10 ⁻⁷	-
4	OPA	aerobic	NaClO ₄	0.1	2	3.3 – 10.8	-	1·10 ⁻⁷
5	COx	aerobic	NaClO ₄	0.1	2	5.8 – 10.8	-	1·10 ⁻⁷
6	SWy-2	aerobic	NaClO ₄	0.1	2	2.9 – 10.7	-	1·10 ⁻⁷
7	SWy-2 + 10 ppm HS	aerobic	NaClO ₄	0.1	2	3.9 – 11.5	1·10 ⁻⁷	-
8	SWy-2 + 10 ppm HS	aerobic	NaClO ₄	0.1	2	4.1 – 11.6	-	1·10 ⁻⁷
9	SWy-2 (80 Gew.%) + 10 ppm HS + CaCO ₃ (20 Gew.%)	aerobic	NaClO ₄	0.1	2	2.7 – 11.7	1·10 ⁻⁷	-
10	SWy-2 (80 Gew.%) + 10 ppm HS + CaCO ₃ (20 Gew.%)	aerobic	NaClO ₄	0.1	2	5.3 – 11.0	-	1·10 ⁻⁷
11	SWy-2 (80 Gew.%) + CaCO ₃ (20 Gew.%)	aerobic	NaClO ₄	0.1	2	3.1 – 11.9	1·10 ⁻⁷	-
12	SWy-2 (80 Gew.%) + CaCO ₃ (20 Gew.%)	aerobic	NaClO ₄	0.1	2	3.9 – 11.8	-	1·10 ⁻⁷
13	Beidellit	aerobic	NaClO ₄	0.1	2	2.7 – 7.0	1·10 ⁻⁷	-
14	synth. Ca-Montmo- rillonit	aerobic	Ca(ClO ₄) ₂	0.066	2	4.0 – 9.3	1·10 ⁻⁷	-
15	SWy-2	aerobic	NaCl	0.01 – 0.17	0.3	~4.0	2·10 ⁻⁷	-
16	IdP-2	aerobic	NaCl	0.01 – 0.17	0.3	~4.0	2·10 ⁻⁷	-
17	synth. Ca-Montmo- rillonit	aerobic	NaCl	0.01 – 0.17	0.3	~4.0	2·10 ⁻⁷	-
18	synth. Na-Montmo- rillonit	aerobic	NaCl	0.01 – 0.17	0.3	~4.0	2·10 ⁻⁷	-

All TRLFS measurements performed in the frame of this project are summarised in Table 3-2. The sorption of Cm(III) and Eu(III) was probed on the natural clay rock OPA and COx, the synthetic beidellite and mixture of SWy-2 and calcite in the ratio 80:20 wt.% (experiments No. 1 to 9). For that 0.3 g/L solid material in 0.1 M aqueous sodium perchlorate solution were used. This S/L was the best ratio where the loss of light due to scattered light was acceptable for the measurement. The final concentration of the trivalent cation was $1-2 \times 10^{-7}$ M. After mixing all components the samples were left under shaking for at least two days to reach equilibrium.

In experiment 10 to 25 (Table 3-2) the outersphere sorption of Cm(III) was investigated with the natural montmorillonites SWy-1, Milos and STx-1, a synthetic montmorillonite in the Na form, the Illit IdP-2 and the γ -alumina. The S/L was 0.3 g/L each and the ionic strength was varied between 0.01 and 0.20 M NaCl in H₂O and D₂O. The Cm(III) concentrations amounts 2×10^{-7} M. After two days the pH or the pD value was checked. The fluorescence emission lifetime in H₂O was measured in 5 μ s intervals at 1 ms exposure time, in D₂O in 50 μ s intervals at 10 ms exposure time. For the quantification of the outer-sphere sorption the ionic strength was increased from 0.01 M with 3 M NaCl in H₂O and D₂O, respectively.

Concerning the uranyl sorption on clay the important question of the existence of the Ca₂UO₂(CO₃)₃ complex was investigated in experiment No. 26 to 29 at conditions described in Table 3-2. Table 2-1 The uranyl concentration was 2×10^{-5} M and the S/L 2 g/L in 0.1 M NaClO₄.

Table 3-2: Summary of the experimental conditions of the performed TRLFS measurements (1 to 29 at 298 K).

	Solid matter	H ₂ O/ D ₂ O	Electrolyte	Ionic strength [mol/l]	S:L [g/l]	pH value	[Cm(III)]- [mol/l]	[Eu(III)] [mol/l]	[U(VI)] [mol/l]
1	COx	H ₂ O	NaClO ₄	0,1	0,3	7,45	1·10 ⁻⁷	-	-
2	OPA	H ₂ O	NaClO ₄	0,1	0,3	7,16	1·10 ⁻⁷	-	-
3	COx (Tonfraktion)	H ₂ O	NaClO ₄	0,1	0,3	4,95 7,41 9,96	1·10 ⁻⁷	-	-
4	COx	H ₂ O	NaClO ₄	0,1	0,3	8,77 8,89	-	2·10 ⁻⁷	-
5	OPA	H ₂ O	NaClO ₄	0,1	0,3	7,04 7,62	-	2·10 ⁻⁷	-
6	COx (Tonfraktion)	H ₂ O	NaClO ₄	0,1	0,3	3,87 3,93	-	2·10 ⁻⁷	-
7	Beidellit	H ₂ O	NaClO ₄	0,1	0,3	3,15 – 8,79	1·10 ⁻⁷	-	-
8	Beidellit	H ₂ O	NaClO ₄	0,1	0,3	4,19 – 10,34	2·10 ⁻⁷	-	-
9	SWy-2/Calcit	H ₂ O	NaClO ₄	0,1	0,3	4,43 – 12,02	2·10 ⁻⁷	-	-
10	SWy-1	H ₂ O	NaCl	0,01 – 0,20	0,3	~4,0	2·10 ⁻⁷	-	-
11	Milos	H ₂ O	NaCl	0,01	0,3	~4,0	2·10 ⁻⁷	-	-
12	STx	H ₂ O	NaCl	0,01	0,3	~4,0	2·10 ⁻⁷	-	-
13	γ-Al ₂ O ₃	H ₂ O	NaCl	0,01	0,3	~4,0	2·10 ⁻⁷	-	-
14	SWy-1	D ₂ O	NaCl	0,01 – 0,07	0,3	~4,0	2·10 ⁻⁷	-	-
15	Milos	D ₂ O	NaCl	0,01	0,3	~4,0	2·10 ⁻⁷	-	-
16	STx	D ₂ O	NaCl	0,01	0,3	~4,0	2·10 ⁻⁷	-	-
17	synth. Na-Montmorillonit	D ₂ O	NaCl	0,01	0,3	~4,0	2·10 ⁻⁷	-	-
18	γ-Al ₂ O ₃	D ₂ O	NaCl	0,01	0,3	~4,0	2·10 ⁻⁷	-	-
19	SWy-1	D ₂ O	NaCl	0,01 – 0,11	0,3	~4,0	2·10 ⁻⁷	-	-
20	Milos	D ₂ O	NaCl	0,01 – 0,12	0,3	~4,0	2·10 ⁻⁷	-	-
21	STx	D ₂ O	NaCl	0,01 – 0,11	0,3	~4,0	2·10 ⁻⁷	-	-
22	synth. Na-Montmorillonit	D ₂ O	NaCl	0,01 – 0,18	0,3	~4,0	2·10 ⁻⁷	-	-
23	SWy-1	H ₂ O	NaCl	0,001 – 0,18	0,3	~4,0	2·10 ⁻⁷	-	-
24	Milos	H ₂ O	NaCl	0,001 – 0,16	0,3	~4,0	2·10 ⁻⁷	-	-
25	IdP-2	H ₂ O	NaCl	0,01 – 0,20	0,3	~4,0	2·10 ⁻⁷	-	-
26	SWy-2/Calcit	H ₂ O	NaClO ₄	0,1	2	7,43	-	-	2·10 ⁻⁵
27	SWy-2 mit NaHCO ₃	H ₂ O	NaClO ₄	0,1	2	7,62	-	-	2·10 ⁻⁵
28	(kein Feststoff)	H ₂ O	NaClO ₄	0,1	2	3,65	-	-	2·10 ⁻⁵
29	COx	H ₂ O	NaClO ₄	0,1	2	7,80	-	-	2·10 ⁻⁵

Measurement of the pD value

For the pD measurement a special gadget was made at KIT-INE. It consists of two micro half-cells: on glass electrode and one Ag/AgCl electrode as reference electrode (Kurt-Schwabe-Institut für Mess- und Sensortechnik e.V., Meinsberg; Figure 3-1) was put into a quartz cuvette with screw top. The electrodes were calibrated with solutions of known D^+ concentrations and constant ionic strength of 0.1 M NaCl/DCl [Freyer et al. 2009] and $-\log[D^+]$ of 2, 3, and 11. From plotting the potential of the electrodes against the $-\log[D^+]$, a straight line was gotten proving that the measurement was correct (Figure 3-2). The pD value was evaluated from the linear relationship by linear regression.

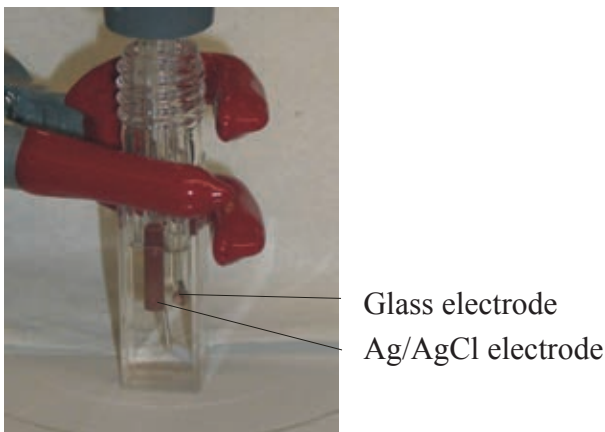


Figure 3-1: Gadget for pD measurement in a special quartz cuvette for TRLFS.

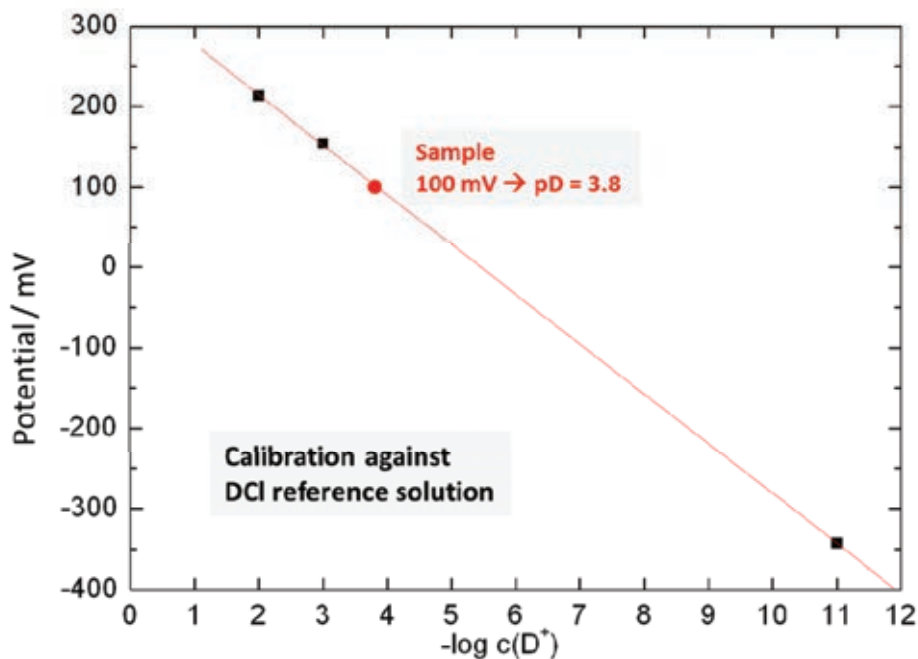


Figure 3-2: Calibration of the pD value with DCl reference solutions of known D^+ concentration.

Modelling

The calculation of the species distribution has been performed with the program ECOSAT 4.8 (*Equilibrium Calculation Of Speciation And Transport* [Keizer and van Riemsdijk 1999]). For the modelling of the metal ion sorption on clay simplifications and estimates were required due to the huge number of potential interaction in reality and the large number of unreliable surface complexation formation constants found in literature; especially for the sorption on calcite and the formation of ternary surface complexes. It is assumed that the sorption of Eu(III) mainly takes place on the clay minerals. The solid content of the clay was fixed to the real concentration of clay minerals in the OPA (54 wt.%) and COx (42 wt.%), and for calcite (OPA: 6 wt.%; COx: 17.3 wt.%).

Only for the clay minerals smectite and illite site capacities for sorption, protolysis constants, selectivity constants for the ion exchange reaction and surface complexation formation constants exist in the literature. Therefore, the sorption of the other clay minerals of kaolinite, chlorite, illite-smectite mixed layers were equated with smectite and illite. Hence, the content of these clay minerals very added one half each to the content of smectite and illite. All parameter for the surface complexation and ion exchange reaction are summarised in Table 3-3. For the modelling of the Eu(III) sorption on synthetic Montmorillonite in the Ca form the surface complexation constants were depicted from [Bradbury et al. 2005].

For the calculations, carbonate concentrations were assumed to be in equilibrium with calcite in a closed system with no gas phase. For the natural clay rock experiments, we checked this assumption by analysing the inorganic carbon concentration (DIC) exemplary in some samples. Calculated and measured values were in fair agreement.

Competitive complexation reaction of other ligands like OH⁻, CO₃²⁻, and humic acid were considered in the modelling, whereas all other water constituents were neglected, because they are very weak complexing ligands or they be available at only very low concentrations. The stability constants of all regarded aqueous species are summarised in Table 3-4 for Eu(III). The formation constants of relevant solid compounds are given in Table 3-5. According to the modelling solid phases have not formed at Eu(III) concentrations used in the experiment. The adsorption model 2PNE SC/CE (*two site protolysis non electrostatic surface complexation and cation exchange*) from [Bradbury & Bayens, 1997, 1999, 2002, 2005b; Bradbury et al., 2005] was applied. Ion exchange reactions were treated by applying the Gaines–Thomas convention [Gaines&Thomas 1953].

The effect of humic acid on the sorption of Eu(III) on natural clay rock and SWy-2/Calcite mixture was modelled with the NICA-Donnan model and the parameter set of [Milne et al. 2003] (see Table 3-6). This model is implemented in the ECOSAT code and describes the complexation of metal cations with humic acid (HA). It takes into account the heterogeneity

of the functional groups that are responsible for proton and cation binding as well as the macro-molecular properties due to its molecular size. It is a combination between the Donnan model, which describes the non-specific electrostatic interactions between the surrounding solution and the negative charge of the polyelectrolyte – humic and fulvic acids – and the NICA model (Non Ideal Competitive Adsorption) that handles the specific cation binding. In the Donnan model the humic substances are considered as behaving like a gel and possess a homogeneous charge and potential distribution over the whole humic particle.

However, the sorption of HA on clay is not considered by this model. For the total sorption of Eu(III) the experimentally determined amount of HA was taken. It was assumed that sorption behaviour of the latter is equal to the sorption behaviour of Eu(III)-humate complexes. This amount of sorbed metal humate species and the modelled amount of sorbed species in the inorganic system was summed up to yield the modelled total sorption of Eu(III).

Table 3-3: Parameters for calculations of Eu(III)/U(VI) sorption onto the different solids. In all cases the Davies Equation was used for activity corrections [Davies, 1962].

			COx		OPA			
Background electrolyte			0.1 mol/l NaClO ₄ (Ionic strength was appointed as variable value)					
Initial Eu(III)-/U(VI) concentration			1·10 ⁻⁷ mol/l					
Solid to liquid ratio (S/L)			2 g/l					
Solid	Mineral phase		42 wt.% clay minerals (20 wt.% montmorillonite, 22 wt.% illite,)		54 wt.% clay minerals (18 wt.% montmorillonite, 36 wt.% illite)			
			17,3 wt.% calcite (based on Ca ²⁺ -analysis in solution)		6,0 wt.% calcite (based on Ca ²⁺ -analysis in solution)			
			Na-montmorillonite		Na-illite		Ca-montmor.	
			Eu(III)	U(VI)	Eu(III)	U(VI)	Eu(III)	
Cation exchange capacity ^a			8.7·10 ⁻¹ eq/kg		2.25·10 ⁻¹ eq/kg			
Site capacity ^a	Typ of surface sites:	≡X ^S OH	2.0·10 ⁻³ mol/kg		2.0·10 ⁻³ mol/kg		Look at Na-montmorillonite.	
		≡X ^{W1} OH	4.0·10 ⁻² mol/kg		4.5·10 ⁻² mol/kg			
		≡X ^{W2} OH	4.0·10 ⁻² mol/kg		4.5·10 ⁻² mol/kg			
Protolysis constants [log K] ^a		≡X ^S OH + H ⁺ ⇌ ≡X ^S OH ₂ ⁺	4.5		5.5			
		≡X ^S OH ⇌ ≡X ^S O ⁻ + H ⁺	-7.9		-6.2			
		≡X ^{W1} OH + H ⁺ ⇌ ≡X ^{W1} OH ₂ ⁺	4.5		5.5			
		≡X ^{W1} OH ⇌ ≡X ^{W1} O ⁻ + H ⁺	-7.9		-6.2			
		≡X ^{W2} OH + H ⁺ ⇌ ≡X ^{W2} OH ₂ ⁺	6.0		9.0			
		≡X ^{W2} OH ⇌ ≡X ^{W2} O ⁻ + H ⁺	-10.5		-10.5			
Cation exchange reaction K _c (I = 1)		3Na-mont + Eu ³⁺ ⇌ Eu-mont + 3Na ⁺	30 ^b	-	-	-	-	-
		3Na-illit + Eu ³⁺ ⇌ Eu-illit + 3Na ⁺	-	-	76 ^a	-	-	-
		2Na-mont + UO ₂ ²⁺ ⇌ UO ₂ -mont + 2Na ⁺	-	1.4 ^c	-	-	-	-
		2Na-illit + UO ₂ ²⁺ ⇌ UO ₂ -illit + 2Na ⁺	-	-	-	4,5 ^d	-	-
		2Na-Ton + Ca ²⁺ ⇌ Ca-Ton + 2Na ⁺	4.1 ^b	4.1 ^b	11 ^d	11 ^d	-	-
		3Ca-Ton + Eu ³⁺ ⇌ Eu-Ton + 3Ca ²⁺	-	-	-	-	-	13 ^a
Surface complexation constants for „strong“ and „weak sites“ [log K _{SC}] ^{a, c, d}		≡X ^S OH + Eu ³⁺ ⇌ ≡X ^S OEu ²⁺ + H ⁺	1.6	-	3.1	-	-	0.6
		≡X ^S OH + Eu ³⁺ + H ₂ O ⇌ ≡X ^S OEuOH ⁺ + 2H ⁺	-6.4	-	-4.4	-	-	-6.2
		≡X ^S OH + Eu ³⁺ + 2H ₂ O ⇌ ≡X ^S OEu(OH) ₂ + 3H ⁺	-15.7	-	-12.7	-	-	-14.2
		≡X ^{W1} OH + Eu ³⁺ ⇌ ≡X ^{W1} OEu ²⁺ + H ⁺	-0.5	-	0.3	-	-	-1.4
		≡X ^{W1} OH + Eu ³⁺ + H ₂ O ⇌ ≡X ^{W1} OEuOH ⁺ + 2H ⁺	-	-	-6.2	-	-	-
		≡X ^S OH + Eu ³⁺ + CO ₃ ²⁻ ⇌ ≡X ^S OEuCO ₃ ⁰ + H ⁺	8.3	-	-	-	-	-
		dto. + H ₂ O ⇌ ≡X ^S OEuOHCO ₃ ⁻ + 2H ⁺	-0.25	-	-	-	-	-
		≡X ^S OH + UO ₂ ²⁺ ⇌ ≡X ^S OUO ₂ ⁺ + H ⁺	-	3.1	-	2.6	-	-
		≡X ^S OH + UO ₂ ²⁺ + H ₂ O ⇌ ≡X ^S OUO ₂ OH + 2H ⁺	-	-3.4	-	-3.6	-	-
		≡X ^S OH + UO ₂ ²⁺ + 2H ₂ O ⇌ ≡X ^S OUO ₂ (OH) ₂ + 3H ⁺	-	-11.0	-	-10.3	-	-
		≡X ^S OH + UO ₂ ²⁺ + 3H ₂ O ⇌ ≡X ^S OUO ₂ (OH) ₃ ²⁻ + 4H ⁺	-	-20.5	-	-17.5	-	-
		≡X ^{W1} OH + UO ₂ ²⁺ ⇌ ≡X ^{W1} OUO ₂ ⁺ + H ⁺	-	0.7	-	0.1	-	-
		≡X ^{W1} OH + UO ₂ ²⁺ + H ₂ O ⇌ ≡X ^{W1} OUO ₂ OH + 2H ⁺	-	-5.7	-	-5.3	-	-
Carbonate			equilibrium with calcite, closed system (no gas phase)					

X: smectite and illit respectively ^S: strong sites, ^{W1/W2}: weak sites, a: [Bradbury at al., 2005], b: [Bradbury&Baeyens, 2002], c: [Bradbury&Baeyens, 2005a], d: [Bradbury&Baeyens, 2005b]

Table 3-4: Formation constants for aqueous Eu(III) species that were considered in the model calculation (β^0 constants were corrected to I = 0). Formation constants of Am(III) species from [Guillaumont et al., 2003] were taken as analogue values for Eu(III).

Eu(III) species and reaction of formation	$\log \beta^0$	Reference
$\text{Eu}^{3+} + \text{H}_2\text{O}(\text{l}) \Leftrightarrow \text{EuOH}^{2+} + \text{H}^+$	-7,200	b
$\text{Eu}^{3+} + 2\text{H}_2\text{O}(\text{l}) \Leftrightarrow \text{Eu}(\text{OH})_2^+ + 2\text{H}^+$	-15,100	(Bradbury et al., 2005)
$\text{Eu}^{3+} + 3\text{H}_2\text{O}(\text{l}) \Leftrightarrow \text{Eu}(\text{OH})_3 + 3\text{H}^+$	-26,200	b
$\text{Eu}^{3+} + \text{CO}_3^{2-} \Leftrightarrow \text{EuCO}_3^+$	8,000	a
$\text{Eu}^{3+} + 2\text{CO}_3^{2-} \Leftrightarrow \text{Eu}(\text{CO}_3)_2^-$	12,900	a
$\text{Eu}^{3+} + 3\text{CO}_3^{2-} \Leftrightarrow \text{Eu}(\text{CO}_3)_3^{3-}$	15,000	a
$\text{Eu}^{3+} + \text{HCO}_3^- \Leftrightarrow \text{EuHCO}_3^{2+}$	3,100	a
$\text{H}^+ + \text{CO}_3^{2-} \Leftrightarrow \text{HCO}_3^-$	10,329	a
$2\text{H}^+ + \text{CO}_3^{2-} \Leftrightarrow \text{H}_2\text{CO}_3$	16,683	a

l: pure liquid; a: [Guillaumont et al., 2003]; b: [Bradbury et al., 2005]

Table 3-5: Formation constants of Eu(III)-, U(VI)- and other minerals considered in the model calculation. Formation constants of Am(III) species from [Guillaumont et al., 2003] were taken as analogue values for Eu(III).

Mineral and reaction of formation	$\log \beta^0$	Reference
$\text{Ca}^{2+} + \text{CO}_3^{2-} \Leftrightarrow \text{CaCO}_3$	8,410	a
$\text{Ca}^{2+} + 2\text{H}_2\text{O} \Leftrightarrow \text{Ca}(\text{OH})_2 + 2\text{H}^+$	5,200	a
$\text{Eu}^{3+} + 3\text{H}_2\text{O}(\text{l}) \Leftrightarrow \text{Eu}(\text{OH})_3(\text{am}) + 3\text{H}^+$	-16,900	b
$\text{Eu}^{3+} + \text{CO}_3^{2-} + \text{OH}^- \Leftrightarrow \text{EuCO}_3\text{OH}(\text{am, hyd})$	20,200	b
$\text{Eu}^{3+} + 2\text{CO}_3^{2-} + 5\text{H}_2\text{O}(\text{l}) + \text{Na}^+ \Leftrightarrow \text{NaEu}(\text{CO}_3)_2 \cdot 5\text{H}_2\text{O}(\text{cr})$	21,000	b
$\text{UO}_2^{2+} + \text{CO}_3^{2-} \Leftrightarrow \text{UO}_2\text{CO}_3(\text{cr})$	14,760	b

am: amorphous, hyd: hydrated, cr: crystalline; a: [Lindsay, 1979]; b: [Guillaumont et al., 2003];

Table 3-6: Parameter for modelling of Eu(III) and U(VI) binding on humic acid (Milne et al., 2001; Milne et al., 2003). $Q_{\max 1/2}$: number of sites with low and high affinity, $p_1/2$: heterogeneity parameter $\beta_1/2$: formation constants of Eu(III) and U(VI) humate complexes, $n_1/2$: non-ideality parameter.

NICA-Donnan-parameter	$Q_{\max 1}$ [mol/kg]	p_1	$Q_{\max 2}$ [mol/kg]	p_2
HS (suspension)	3,15	0,62	2,55	0,41
	$\log \beta_1$	n_1	$\log \beta_2$	n_2
HS _{a/b} -Eu	1,92	0,57	3,43	0,36
HS _{a/b} -UO ₂	2,45	0,45	4,81	0,32

3.1.2 Results and discussions

In Figure 3-3 the sorption of Eu(III) on OPA, COx, and SWy-2 is shown as sorption edge in $\log R_d$ (a) and % sorbed Eu(III)(b) in the pH range between 3 and 11. The Eu(III) sorption increases with the pH below values smaller than 7. From pH 7 and higher the curve flattens to a plateau with $\log R_d$ values of 4 to 5 for OPA and around 5 for COx. This corresponds to a sorption of Eu(III) higher than 95 %. In contrast to OPA and COx, the Eu(III) sorption on SWy-2 furthermore increases with pH to reach a $\log R_d$ of about 6 at pH 10.5. Similar shapes of the sorption edges have also been found for trivalent lanthanide/actinide interaction with pure clay mineral phases [Rabung et al., 2005; Bradbury & Baeyens, 2002]. It was interpreted as cation exchange on pH independent permanently charged surface sites of the clay minerals at lower pH (< 4) and inner-sphere surface complexation reactions at amphoteric surface hydroxyl groups situated at clay platelet edges at higher pH. Experiments carried out under aerobic conditions and in an Ar atmosphere (exclusion of oxygen) did not yield significantly different data. The influence on metal ion sorption of oxidized Fe(III) oxide/hydroxides, possibly generated under aerobic conditions due to pyrite oxidation, is therefore expected to be of minor relevance. Bradbury and Baeyens studied the Eu(III) sorption onto OPA [Bradbury & Baeyens, 2003a] for porewater conditions and without pH variation. Their results are in good agreement with our findings; they are also plotted in Figure 3-3 at pH 6.3 and 7.8. No data for Eu(III) sorption (or its analogues) onto COx were found in the literature.

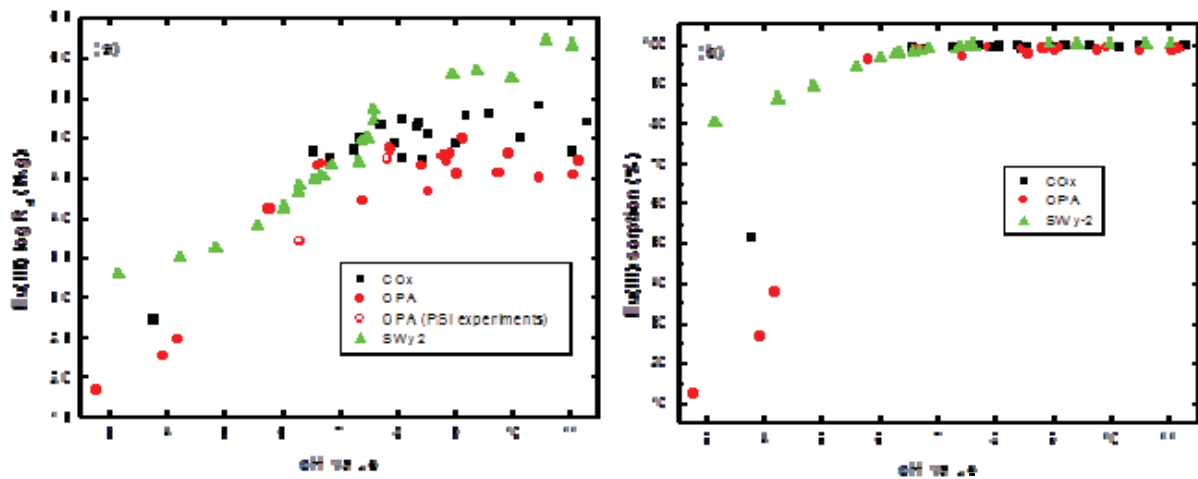


Figure 3-3: Eu(III) sorption on OPA, COx und SWy-2 in dependence of pH illustrated in $\log R_d$ (a) and % (b). Experimental conditions: [Eu(III)] = $1 \cdot 10^{-7}$ mol/l, solid to liquid ratio (S/L) = 2 g/l, I = 0,1 mol/l NaClO₄.

The different developing of the sorption at pH < 7 of the three clay materials qualitatively corresponds to their different cation exchange capacity; OPA and COx (106-121 and 350-400 meq/kg) show lower sorption than SWy-2 (870 meq/kg). Additionally, the clay mineral fraction determining the sorption amounts for SWy-2 2 g/L, but it is only 1.08 and 0.84 g/L for OPA and COx respectively due to their heterogeneous mineral content.

The calculated speciation of Eu(III) in the presence of COx and OPA is plotted in Figure 3-4. In the calculations, the natural clay rocks are simulated by a mixture consisting of illite, montmorillonite, and calcite. Due to the fact that no literature data are available for the other minerals– mainly kaolinite, chlorite – their amounts were added to the amount of illite and montmorillonite, to half each. This results in 36 wt.% Illite, 18 wt.% montmorillonite, and 6 wt. calcite. The originally exact mineral ratios are specified in Table 2-3. The total calcite content was taken from the analysis Ca^{2+} of a sample with pH of 2.8 where the total calcite should be dissolved. It is assumed that the Ca^{2+} content in solution matches the calcium of the totally dissolved calcite. An sorption of Eu(III) on the calcite was not considered in the modelling. Calculations take into account sorption to clay minerals and complexation in solution by hydroxide and carbonate ions. Dissolution and precipitation of calcite along the considered pH range is considered and this controls the dissolved carbonate concentration. At pH values < 6 , Eu(III) speciation is dominated by the free Eu(III) aquo ion and ion-exchange-bound Eu(III). The difference between model calculations and experimental data shows in terms of the calculated Eu(III) sorption a significant sorption reduction at 7–9.5. This is due to formation of aqueous $\text{Eu}(\text{CO}_3)_+$ and $\text{Eu}(\text{CO}_3)_2-$ complexes which are not considered as sorbing species in the model, but they are the dominant species in solution.

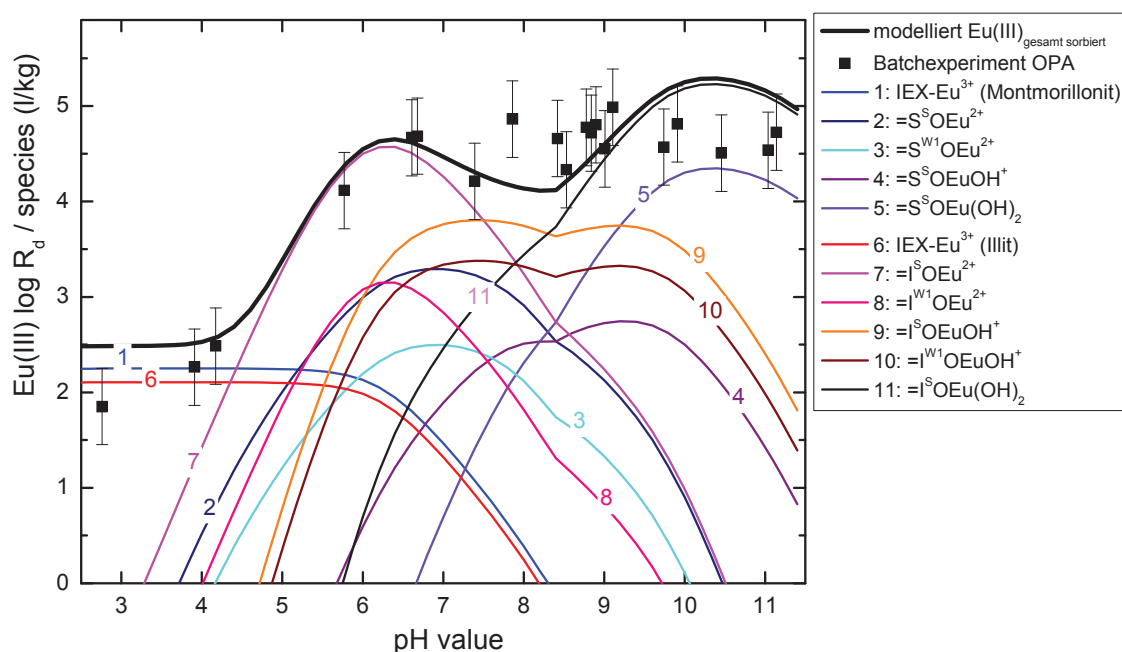


Figure 3-4: Eu(III) sorption on OPA and modelling as a function of pH. Experimental conditions: $[\text{Eu(III)}] = 1 \cdot 10^{-7} \text{ mol/l}$, $\text{S/L} = 2 \text{ g/l}$, $\text{I} = 0,1 \text{ mol/l NaClO}_4$. (IEX = Ionexchange, I = Illite, S = Smectite, S = strong sites, W1 = weak sites).

In Figure 3-5 the modelling of the COx sorption data is shown. The clay mineral fraction of COx – in total 42 wt.%, mainly composed of illite/smectite mixed layers, illite, smectite, and a little kaolinite, chlorite – was simulated in the model with 22 wt.% illite, 20 wt.% mont-

morillonite, and 17.3 wt.% calcite. The total Eu(III) sorption is modelled quite well. However, there is a significant underestimation of the total Eu(III) sorption in the calculation between pH 6.5 and 9. The largest difference between modelled and experimental values is about $\Delta(\log R_d) \sim 1.5$ L/kg at about pH 7.5. The sorption data are well described by the used model in the pH range higher than 9.

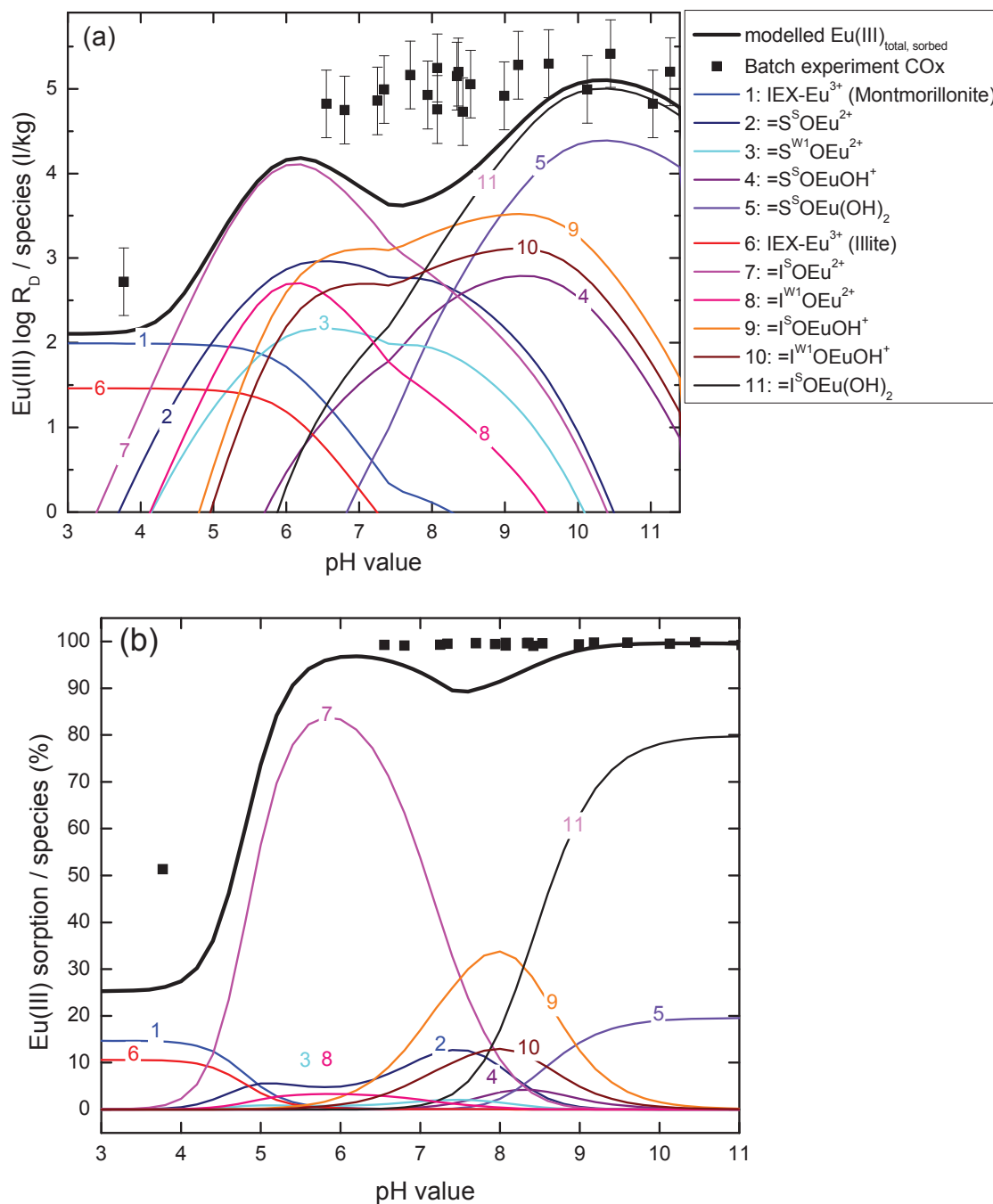


Figure 3-5: Eu(III) sorption on COx and numerical modelling in as a function of pH shown as $\log R_d$ (a) and % (b). Experimental conditions: $[\text{Eu(III)}] = 1 \cdot 10^{-7}$ mol/l, S/L = 2 g/l, I = 0,1 mol/l NaClO_4 . (IEX = ion exchange, I = illite, S = smectite, S = *strong sites*, W1 = *weak sites*).

In Figure 3-6 the amount of the Eu(III) species sorbed on illite and montmorillonite was summed up and separately illustrated for OPA and COx. In the lower pH range (<4.3) where the sorption is governed by pH independent cation exchange (outer-sphere complexation), the montmorillonite dominates the sorption. The montmorillonite possess a four times higher cation exchange capacity than illite (870 as opposed to 225 meq/kg). At higher pH values (pH < 4.3) the inner-sphere complexation is the dominating mechanism and the sorption on illite predominates. Here, the Eu(III) surface complexes $\equiv\text{I}^{\text{S}}\text{O}^{\text{S}}\text{Eu}^{2+}$, $\equiv\text{I}^{\text{S}}\text{O}^{\text{S}}\text{EuOH}^+$, and $\equiv\text{I}^{\text{S}}\text{O}^{\text{S}}\text{Eu}(\text{OH})_2$ mainly contribute to the Illite sorption. This is also expressed in the surface complexation constants of Illite-Eu(III) complexes ($\log K_{\text{SC}} = 3.1 / -4.4 / -12.7$) that are manifold higher than the corresponding montmorillonite-Eu(III) complexes ($\log K_{\text{SC}} = 1.6 / -6.4 / -15.7$). The sorption occurs on the strong sites rather than on the weak sites, even the amount of the latter one is higher in the clay rock. However, the strong sites forms more stable complexes that are occupied first by trace amounts of metal ions (1×10^{-7} M).

The calculation of the species distribution of Eu(III) in solution as a function of pH with thermodynamic data from Table 3-3, Table 3-4 and Table 3-5 shows that Eu^{3+} is the main species at pH values below 5, occurring as free Eu^{3+} in solution and as outer-sphere complex. The complex EuHCO_3^{2+} plays no role. In the pH range 6 to 9 the complexes EuCO_3^+ and $\text{Eu}(\text{CO}_3)^-$ are stable and they occur in relevant concentrations causing a decrease of the modelled amount of europium sorbed to clay. The divergence in calculated and experimental data could point to the possible existence of ternary clay/Eu(III)/carbonate surface complexes, which are not considered as sorbing species in the model. Stumpf et al. reported the existence of ternary Eu(III) complexes in smectite and kaolinite suspensions under atmospheric conditions at $\text{pH} \leq 6.65$ using TRLFS [Stumpf et al., 2002]. Marques et al. have studied the possible formation of clay / Eu(III) carbonate surface complexes on Na-rich Montmorillonite by batch experiments and modelling [Marques et al., 2008]. Their experiments could be described very well by comprising the sorption of Eu(III) carbonate and Eu(III) hydroxo carbonate complexes on strong sites forming $\equiv\text{S}^{\text{S}}\text{O}^{\text{S}}\text{EuCO}_3$ and $\equiv\text{S}^{\text{S}}\text{O}^{\text{S}}\text{EuOHCO}_3^-$ surface complexes. The surface complexation constants $\log K_{\text{SC}}$ have been estimated to



With these data a new modelling of the COx experiments was performed with surface species on montmorillonite and illite. This is illustrated in Figure 3-7. The modelling curve does now match much better with the experimental data. Unfortunately, data for the ternary surface complexes on illite are not available from literature, but the existence of them is already proved in experiments [Marques, 2010]. According to the modelling the species $\equiv\text{S}^{\text{S}}\text{O}^{\text{S}}\text{EuCO}_3$ occurs in significant amounts between pH 6 and 10 and predominates at pH ~ 7.9 the surface

species. The surface species $\equiv\text{S}^{\text{S}}\text{O}^{\ominus}\text{EuOHCO}_3$ can be neglected in contrast. Nevertheless, other reasons for the divergence of modelling curve and experimental data cannot be excluded, like the influence of other mineral phases in natural clay rock on Eu(III) sorption.

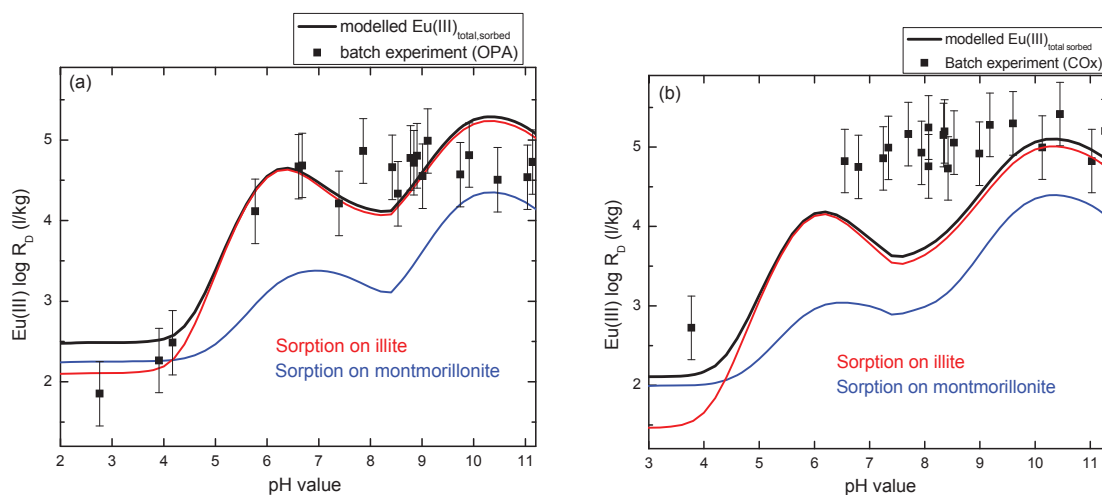


Figure 3-6: Eu(III) sorption on OPA (a) and COx (b) together with numerical modelling of the total Eu(III) sorption as well as sorption on illite and montmorillonite as function of pH. Experimental conditions: $[\text{Eu(III)}] = 1 \cdot 10^{-7}$ mol/l, $S/L = 2$ g/l, $I = 0,1$ mol/l NaClO_4 .

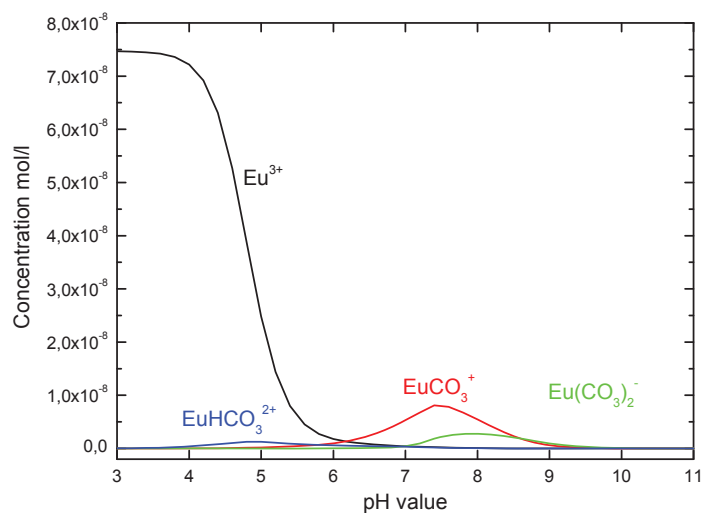


Figure 3-7: Numerical modelled aqueous Eu(III) speciation in COx suspension. Conditions: $[\text{Eu(III)}] = 1 \cdot 10^{-7}$ mol/l, $S/L = 2$ g/l, thereof 17.3 % calcite, $I = 0.1$ mol/l NaClO_4 .

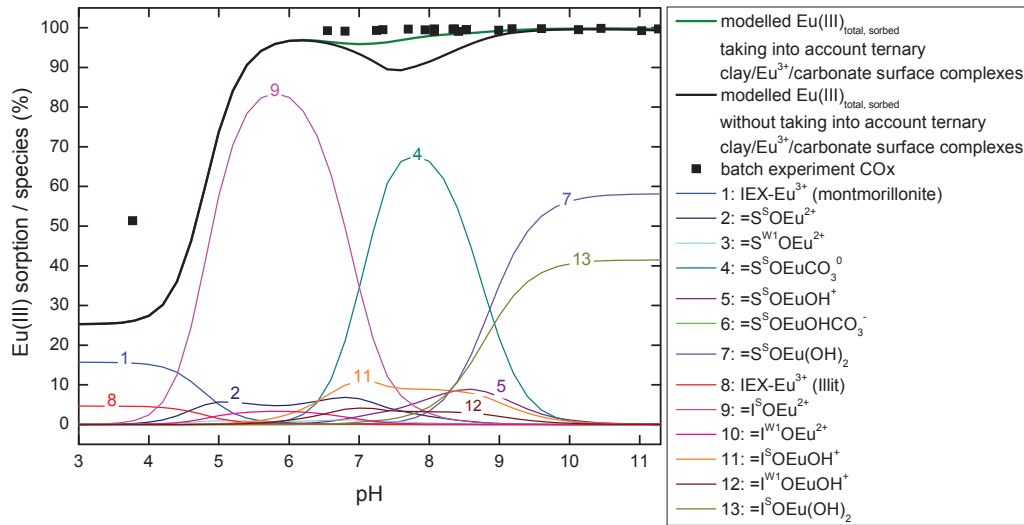


Figure 3-8: Eu(III) sorption on COx and modelling as a function of pH by regarding (dark green line) and disregarding (black line) ternary Clay/Eu³⁺/carbonate surface complexes shown in %. Experimental conditions: [Eu(III)] = 1·10⁻⁷ mol/l, S/L = 2 g/l, thereof 17.3 % calcite, I = 0.1 mol/l NaClO₄. (IEX = Ion exchange, I = illite, S = smectite, S = strong sites, W1 = weak sites).

Based on the high calcite or carbonate content of natural clay rocks – OPA contains 6 to 10 wt.% and COx 20 wt.% - the dissolved carbonate concentration is controlled by the solubility of calcite at pH > 8.5. The solubility of calcite (CaCO₃(cr)) is exceeded until pH ~7.5 and higher and limits the CO₃²⁻ concentration in solution to < 5x10⁻⁴ mol/L at pH ~ 9 (s. Figure 3-9). The OH⁻ concentration increases with the pH and at pH > 9 the Eu(III) dihydroxide surface species of Illite and Smectite preponderate.

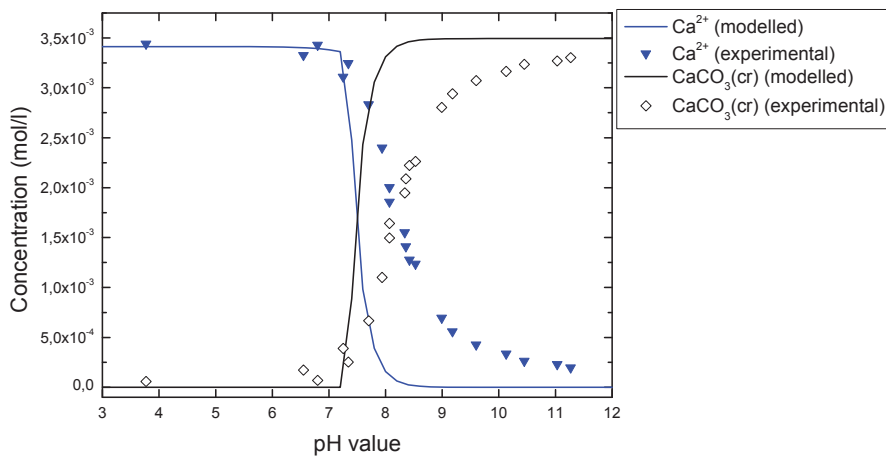


Figure 3-9: Experimentally determined Ca²⁺ concentration in the solution of the Eu(III) sorption experiments on COx and OPA as well as the modelled Ca²⁺ and CaCO₃(cr) concentration as a function of pH. The experimental CaCO₃(cr) data were extrapolated from the measured Ca²⁺ values.

3.2 Eu(III)/Cm(III) sorption on clay / calcite mixture

As already mentioned before, the OPA and COx clay consist of not only illite and montmorillonite but also of other mineral phases. One of these mineral phases at higher concentrations in the clay rock is calcite. To elucidate the role of calcite on the sorption of Eu(III) / Cm(III) some experiments have been performed with a mixture of Na-rich montmorillonite (SWy-2) and calcite in percentage of 80 : 20 wt.%. This approximately corresponds to a content of calcite in COx. The sorption of Eu(III) on this clay / calcite mixture is shown in Figure 3-10. The Eu(III) is almost totally sorbed at pH < 7, which is similar to the sorption on natural clay rock without calcite addition. The modelling result coincides quite well with the experimental data, but it underestimates again the Eu(III) sorption at pH values between 6.5 and 9. The used model specifies dissolved carbonate complexes of Eu^{3+} responsible for the inhibited sorption.

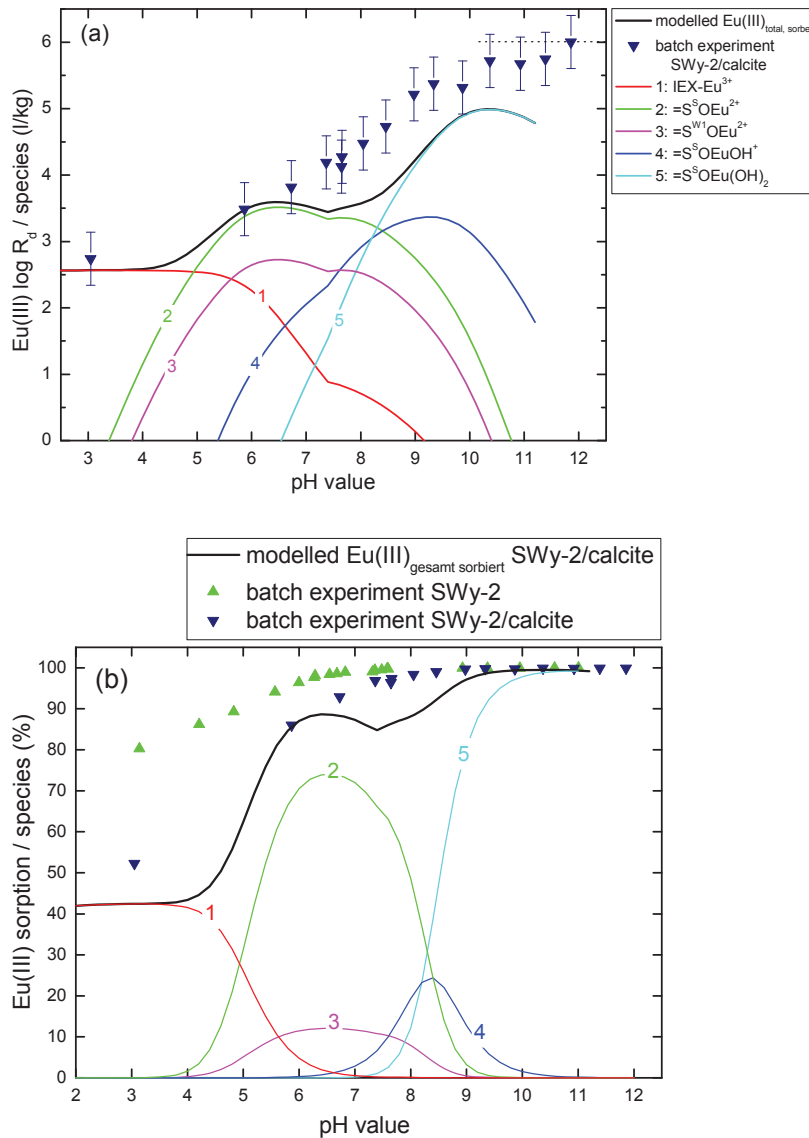


Figure 3-10: Eu(III)sorption on mixture of Na-rich montmorillonite (SWy-2) with calcite (80 : 20 wt.%) shown as (a) $\log R_d$ and (b) in Experimental conditions: $[\text{Eu(III)}] = 1 \cdot 10^{-7} \text{ mol/l}$, $S/L = 2 \text{ g/l}$, $I = 0,1 \text{ mol/l NaClO}_4$. (IEX = ion exchange, S = smectite, S = **strong sites**, W1 = **weak sites**). The dotted line corresponds to the upper limit $\log R_d$ due to the detection limit of the ICP-MS for Eu(III) analysis.

The lower sorption on SWy-2 / calcite compared to pure SWy-2 at pH < 6.5 comes from the lower content of the clay mineral and hence, a lower cation exchange capacity. Furthermore, the calcite is dissolved at lower pH and hence, the Ca²⁺ ions can compete with the Eu(III) for sorption sites. Because no other compounds than montmorillonite and calcite are present in the system and that the course of the sorption is similar to that of CO_x, one can conclude that other mineral phases as components of the natural clay rock have no significant contribution to the Eu(III) sorption. The model calculations by considering the ternary clay / Eu³⁺ / carbonate surface complexes moreover exhibit that the data of the batch experiments can be described much better in the near neutral pH range (s. Figure 3-11). The ≡S^SOEuCO₃ surface complex emerges at pH ~5.5 and predominates from pH 6.5 to 8.5 over the surface species ≡S^SOEuOH⁺ that normally prevails in the absence of carbonate. At high pH values the surface complex ≡S^SOEu(OH)₂ is the dominating species. The Eu(III) hydroxocarbonate complex is not relevant in this system over the whole pH range.

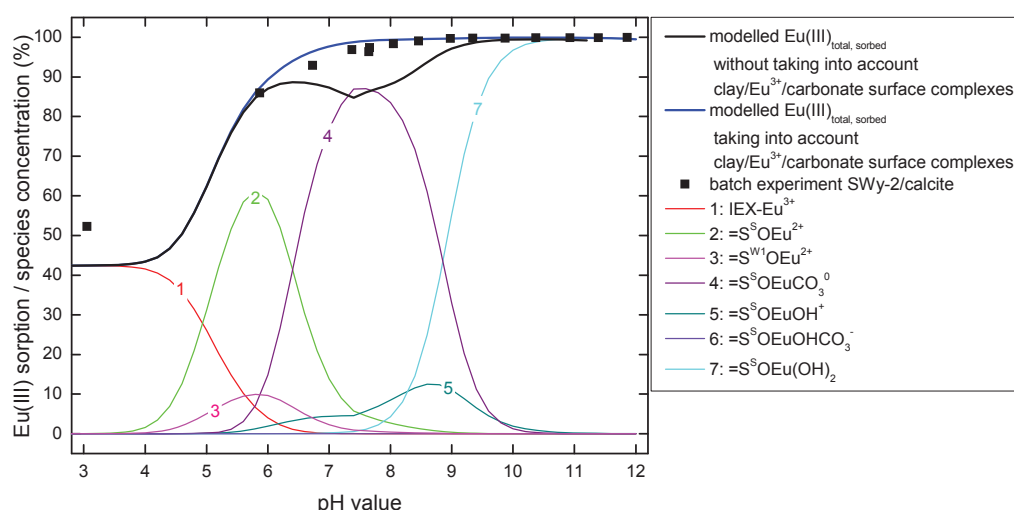


Figure 3-11: Eu(III)sorption on mixture of Na-rich montmorillonite (SWy-2) with calcite (80 : 20 wt.%) and modelling as a function of the pH value regarding (blue line) and disregarding (black line) ternary clay/Eu³⁺/carbonate surface complexes shown in %. Experimental conditions: [Eu(III)] = 1·10⁻⁷ mol/l, S/L = 2 g/l, I = 0,1 mol/l NaClO₄. (IEX = ion exchange, S = smectite, S = **strong sites**, W1 = **weak sites**).

TRLFS studies of Cm(III) sorbed on clay / calcite mixture

To elucidate the sorption of trivalent actinides on a molecular level, TRLFS measurements were performed parallel to the batch experiments. Unfortunately, the Cm(III) and Eu(III) fluorescence emission spectra in OPA and CO_x suspension could not be evaluated, because either they were extreme noisy or they had very broad undifferentiated peaks. For that, spectroscopic studies have been made with Cm(III) in Na-SWy-2 / calcite suspension. The spectra of the Cm(III) in such suspensions show the typical red shift with increasing pH value (s. Figure 3-12).

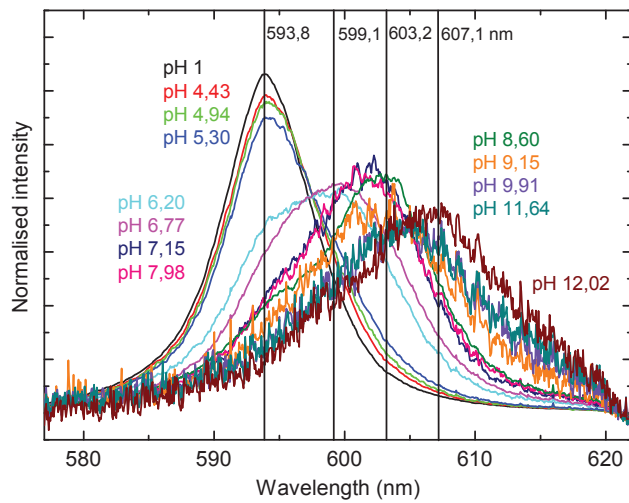


Figure 3-12: Cm(III) fluorescence emission spectra in suspension of Na-rich montmorillonite (SWy-2) and calcite mixtures (80 : 20 wt.-%) as a function of pH normalised to identical peak area. Experimental conditions: [Cm(III)] = $2 \cdot 10^{-7}$ mol/l, S/L = 0,3 g/l, I = 0,1 mol/l NaClO₄.

The spectra are identical with the pure spectra of the Cm(III) aquo ion with a peak maximum at 593.8 nm below pH values of 4. At this conditions only free Cm³⁺ or outer-sphere sorbed Cm(III) aquo ions occur. The peak maximum shifts towards higher wavelengths with increasing pH from 4 to 12. The same shift was observed in experiments of Cm(III) and smectites with peak maxima at 559.1, 603.2, 607.1 nm [Rabung et al., 2005] and 598.8 and 603.3 nm [Stumpf et al., 2001]. This could be a indication that Cm(III) sorption mainly takes place on the clay and that the calcite does not or only partially contribute to the sorption. The same hint is obtained from the fluorescence life-time of these peaks. However, the intensities of the signals are very low due to stray light effects and quench effects of the solid particles. These effects impede the evaluation of the fluorescence life-time. Nevertheless, the life-times were shorter than 200 μ s in all measurements and this is similar to the life-times of species inner-spherically bound on the clay as surface complexes. The results from the measurement of Cm(III) sorption in the clay / calcite system significantly differ from measurements in the pure calcite system [Marques, 2006; Stumpf & Fanghänel, 2002]. In these experiments two peaks were found with peak maxima at 607.5 and 618.0 nm with life-times of 314 ± 6 μ s and 1302 ± 75 μ s, indicating that two sorption species occur. The shorter lifetime represents a inner-sphere surface complex of Cm(III), whereas the longer life-time is due to a emplacement of Cm(III) into the calcite crystal.

In Figure 3-13 the spectra of Cm(III) in the SWy-2/calcite suspension and pure calcite suspension (from [Stumpf & Fanghänel, 2002]) are faced at two different contact times (48 h, and 8 as well as 6 months). The spectra clearly show that the peak of the embedded Cm(III) species increases with time whereas the contribution of the inner-sphere surface complex is reduced. In the SWy-2/calcite suspension such a peak with maximum around 618 nm and a

very long fluorescence life-time was never observed even after very long contact times. From these results we conclude that the Cm(III) is mainly sorbed by the clay only. This is additionally proved by the higher fluorescence intensities in SWy-2/calcite suspension in contrast to the pure calcite suspension.

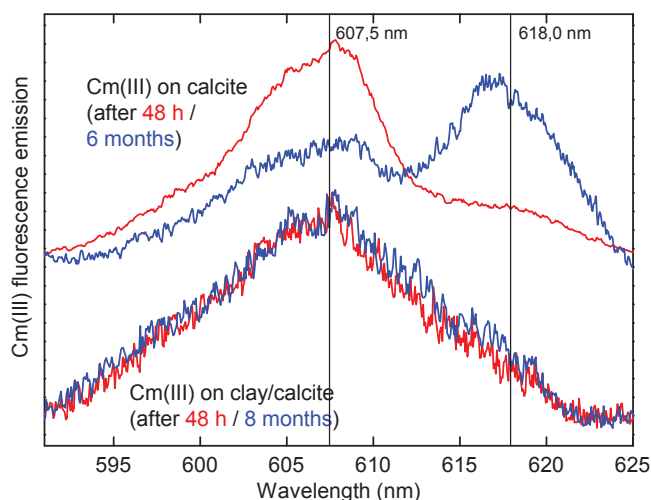


Figure 3-13: Cm(III) fluorescence emission spectra of $[Cm^{3+}] = 8.9 \cdot 10^{-8}$ mol/l in aqueous calcite suspension (pH ~ 8 , S/L = 1 g/l, I = 0.1 mol/l NaClO₄ according to (Stumpf and Fanghänel, 2002)) and of $[Cm^{3+}] = 2 \cdot 10^{-7}$ mol/l in clay / calcite suspension (pH 12.02, S/L = 0.3 g/l, I = 0.1 mol/l NaClO₄; along the lines of the Cm(III) sorption complex 3 in (Rabung et al., 2005)) after contact times of 48 h and several months.

3.3 Conclusions from the sorption studies with trivalent actinides

All results from numerical modelling of the batch experiments as well as the spectroscopic measurements indicate that the sorption of Cm(III) and Eu(III) on the heterogeneous composed clay rocks OPA and COx is caused by the clay minerals alone. Other mineral phases in the OPA and COx like calcite or quartz are obviously not relevant under the conditions of the experiments. This is also the consequence of the low specific surface of the latter mineral-phases. SWy-2 has a specific surface of 43 m²/g, whereas the calcite in the clay/calcite mixture possessed specific surface of only 0.77 m²/g. This results in a very low number of bindings sites that corresponds to only 2.7 % of all binding sites available in the same mass of montmorillonite.

The distribution of surface species of Cm(III) and SWy-2/calcite based on the evaluation of TRLFS results are shown in Figure 3-14. There is a good agreement to the numerical modelling of the surface complexes considering ternary clay/Eu(III)/carbonate surface complexes exhibited in Figure 3-11. Cm(III) species 1 corresponds to the sum of $\equiv S^S OEu^{2+}$ and $\equiv S^{W1} OEu^{2+}$. Spezies 2 is equal to the sum of $\equiv S^S OEuOH^+$ and $\equiv S^S OEuCO_3$, which could not differentiated in the spectra due to bad quality of the spectra.

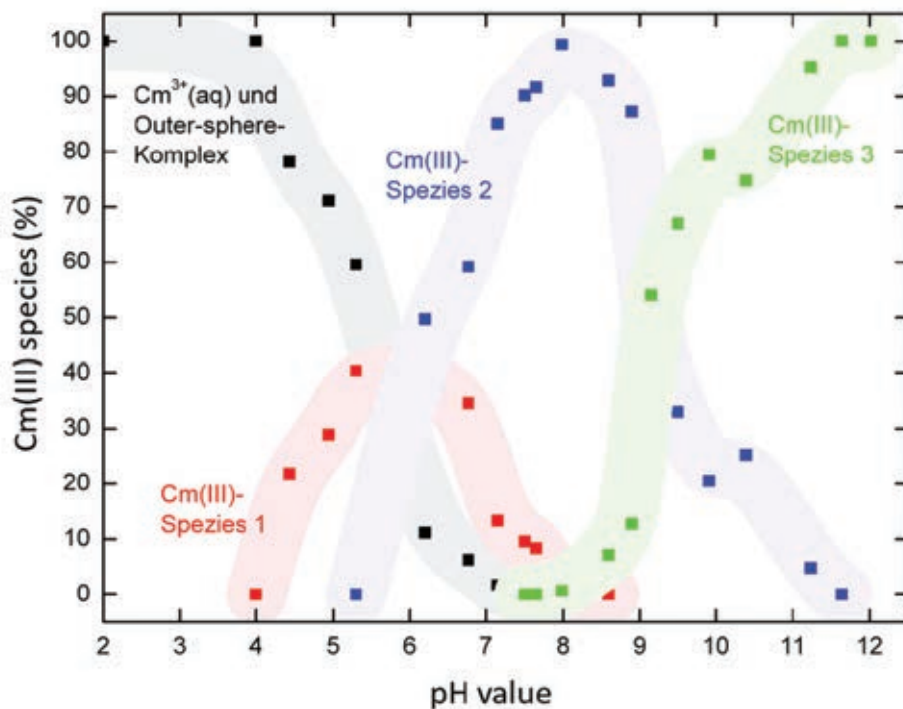


Figure 3-14: Distribution of surface species of Cm(III) on a mixture of Na-rich montmorillonite (SWy-2) and calcite (80 : 20 wt.-%). Experimental conditions: [Cm(III)] = $2 \cdot 10^{-7}$ mol/l, S/L = 0.3 g/l, I = 0.1 mol/l NaClO₄. (More details in Hartmann 2010).

The results of the batch experiments, numerical modelling and TRLFS studies show

- the dominance of clay minerals for the retention of trivalent lanthanides and actinides in natural clay rock,
- the transferability of available mechanistic sorption data to the description of Ln(III)/An(III) speciation in heterogeneous natural systems, and
- the relevance of ternary carbonate surface complexes for the retention of trivalent lanthanides/actinides. A reliable prediction in the frame of safety assessment of repositories by geochemical modelling has to regard such species.

3.4 Sorption of pentavalent neptunium and plutonium on OPA and COx

As mentioned in the former chapters, numerous studies have been performed clearly demonstrating that transport in these argillaceous rocks is controlled by molecular diffusion. However, only few studies have been performed on the sorption and redox behaviour of neptunium (Np), and plutonium (Pu) in natural clay rocks like OPA and COx. A few batch and diffusion experiments of Np(V) on OPA [Wu et al., 2009], Pu(IV) on COx [Latrille et al., 2006] has been performed. Furthermore, Wu et al. studied Np sorption in OPA clay rocks with a low solid to liquid ratio (S/L) and performed only short kinetic experiments.

The aim of this study is to characterize the retention of Np, Pu on the two selected clay rocks OPA and COx taking into consideration the redox processes. Since the distribution coefficients (K_d) for the sorption of actinide on the host rock of a nuclear waste repository are important parameters for diffusion and transport modelling. The K_d values for the sorption of actinides on OPA/COx are determined directly by batch experiments on crushed material. The objective at the end of the project is to compare this K_d value with the value derived from the in-diffusion experiments.

3.4.1 Materials and Methods

Actinides

For all sorption experiments, stock solutions of plutonium and neptunium in the pentavalent oxidation state are used. The pentavalent oxidation state of Pu(V) and Np(V) were obtained by potentiostatic electrolysis and its purity was verified by UV-Vis spectroscopy [Cohen, 1961]. The actinides concentration is determined by liquid scintillation counting (LSC).

Opalinus Clay (OPA)

For the batch type sorption studies Opalinus Clay mineral (OPA) is crushed, sieved (< 500 μm) and freeze dried under atmospheric conditions. The anaerobic OPA crushed powder is prepared under Ar atmosphere (inert glove box) from the OPA bore core BHE-24-2 (Mont Terri) [Wu et al., 2009; Van Loon et al., 2005]. The cation exchange capacity determined by the COHEX method is 12.93 ± 0.04 meq/100g.

Callovo Oxfordian Clay (COx)

The Callovo Oxfordian argillites come from boreholes (EST 25691) located on the site of the underground laboratory operated by Andra at Bure (Meuse/Haute Marne, France). A complete description of the core sample drilling and conditioning procedures is available elsewhere

[Gaucher et al., 2004]. The sample is grounded and sieved at $<500 \mu\text{m}$ in the absence of oxygen, under Ar atmosphere, in order to prevent any oxidation of redox sensitive materials such as, for example, pyrite, organic matter, adsorbed Fe(II) and iodide. The cation exchange capacity determined by the COHEX method is $12.02 \pm 0.10 \text{ meq}/100\text{g}$.

Batch experiments

All sorption experiments are conducted according to batch procedures described below at initial actinides concentrations in the range of $3.0 \times 10^{-4} - 1.0 \times 10^{-8} \text{ M}$. The batch experiments are carried out in Zinsser vials (20 mL, material: HDPE) over a period up to about 1 year at room temperature. The solid to liquid ratio (S/L) of 10, 20, 50, 200 g/L of clay rocks are chosen for the experiments, preconditioned with pore water in 0.1 M NaCl by shaking continuously the suspension for 10-15 days to achieve equilibrium pH of 7.2 for COx and 7.6 for OPA. After mixing Pu(V), Np(V) solutions with the preconditioned clay rocks suspension, the pH values were readjusted by adding 0.1 M HCl or 0.1 M NaOH. For characterisation of the suspension the solid and liquid phases were separated by ultrafiltration using 10 kD filters (5000 rpm for 1 h). The supernatants were analysed in order to determine the content of free actinides in the liquid phase by liquid scintillation counting (LSC). The sorbed amount of Np and Pu (dried clay rocks, solid phase) was also measured for some samples by XAFS and XPS. For all sorption experiments, about 10 % adsorption of RN on the Zinsser vials walls depending on S/L ratio of the clay rocks and radionuclide has been taken into consideration for evaluating the K_d values.

UV-Vis absorption spectroscopy (UV-Vis)

The oxidation states of Np(V), Pu(V) in the stock and sample solutions are confirmed by UV-Vis spectroscopy with a high-resolution UV-Vis/NIR spectrometer Cary 5 (Varian). The samples are measured in 1 cm inert-gas quartz cuvettes (Hellma) with tight screw tops, or in polystyrene semi-micro cuvettes (Brandt). UV-Vis/NIR spectra are taken from 800 nm to 1200 nm for Np, 400 nm to 900 nm for Pu.

X-ray photoelectron spectroscopy (XPS)

Clay suspensions and wet pastes were prepared for XPS analysis by drying small portions on an indium foil in an anoxic glove box. The samples were moved into the XP spectrometer (PHI model 5600ci) without air contact by means of a vacuum transfer vessel. Monochromatic Al K_{α} x-rays were used for excitation in conjunction with an electron flood gun for sample surface neutralization. Atomic concentrations were calculated from the areas of elemental lines of survey spectra. Narrow scans of elemental lines were recorded for determination of chemical shifts and spectral features.

X-ray absorption fine structure spectroscopy (XAFS)

For the XAFS measurements, filtrate solutions and suspension with clay were filled into 400 μL capped PE vials and mounted in a special air tight sample holder, which is connected to an Ar supply line at the experimental station to keep the samples under oxygen-free conditions during XAFS measurements. The measurements were performed at the INE beam line using a new inert gas sample cell design [Brendebach et al, 2009] for redox sensitive radionuclides. The spectra were calibrated against the first derivative X-ray absorption near edge structure (XANES) spectrum of a Zr foil, defining the energy of the first inflection point as $E(\text{Zr } 1s) = 17998.0 \text{ eV}$. All Pu L3, Np L3 XAFS spectra are measured in standard fluorescence yield detection mode.

Capillary electrophoresis coupled with ICP-MS (CE-ICP-MS)

A commercial Beckman Coulter P/ACE MDQ capillary electrophoresis system (Fullerton, U.S.A.) was coupled to an inductively coupled plasma sector field mass spectrometer (Element XR, Thermo Fisher Scientific, Bremen, and Germany). Conventional fused silica capillaries (Beckman Coulter, Fullerton, U.S.A.) with an internal diameter of 50 μm and lengths of 74 cm were used for the separations. A commercial parallel path micro-nebulizer (Mira Mist CE, Burgener, Canada) with a borosilicate spray chamber (Mini glass chamber, Burgener, Canada) interfaces both apparatuses. To generate an aerosol a makeup liquid (2 % HNO_3 , 10 % ethanol, 1 ppb Rh as internal standard) was introduced by a syringe pump at a nominal flow rate of 8 $\mu\text{L min}^{-1}$. For the measurement, separated supernatant solutions from clay suspension were taken in 1 mL glass vials under inert atmosphere. However the fast injection of the sample into the CE has been performed under air atmosphere. Therefore, the effect of air cannot be excluded from the experiments. Separations were performed at -20 kV and at a constant pressure of 0.8 psi (to avoid clogging) and they were completed within 15-18 min.

Liquid-liquid extraction

The oxidation state of Np and Pu at low concentration after the separation by centrifugation using 10 KD ultrafilter under anaerobic conditions and supernatant solution was analyzed by liquid-liquid extraction using 1-phenyl-3-methyl-4-benzoylpyrazolone-5 (PMBP) [Nitsche et al., 1994] and 2-thenoyltrifluoroacetone (TTA) (Merck, Germany) as extracting agents. A 0.6 mL portion of the supernatant filtrate solution was taken together with 0.2 mL 2 M HCl and 0.8 mL 0.025 M PMBP (in Xylene) and 0.5 M TTA (in Toluene) solutions and then vigorously shaken for 10 min. The phases were separated by centrifugation for 10 min (5000 rpm) and aliquots of each phase were taken for radiometric analysis.

Sorption modelling

Model calculations are performed using the computer program ECOSAT 4.8 (acronym for Equilibrium Calculation of Speciation and Transport [Keizer and van Riemsdijk, 1999]). Bradbury and Baeyens developed a 2-site Protolysis Non Electrostatic Surface Complexation

and Cation Exchange (2SPNE SC/CE) model for the description of surface complexation and cation exchange reactions [Bradbury&Bayens, 2005, 2009]. For the calculations, carbonate concentrations were assumed to be in equilibrium with calcite in a closed system with no gas phase.

3.4.2 Results and discussions

The fraction of actinides sorbed and the distribution coefficient were calculated by using the following equations:

$$Sorption = 1 - \frac{[An]_{eq}}{[An]_0} \times 100 \quad (\%) \quad (1)$$

$$K_d = \frac{x}{m} \times \frac{1}{[An]_{eq}} \quad (\text{mL/g}) \quad (2),$$

where $[An]_{eq}$ and $[An]_0$ (mol/L) are the equilibrium and initial concentrations of actinides in solution, respectively; x (mol) is the amount of sorbate; m (g) is the mass of sorbent.

The batch experiments are conducted as a function of the solid-to-liquid ratio in the range of 10–200 g/L at 0.1 M NaCl under 1% CO₂ in a glove box (<1 ppm O₂).

Sorption of neptunium on clay rocks

The sorption of Np(V) increased proportionally to the solid-to-liquid ratio (see in Figure 3-15). The highest sorption is 87±6 % at 200 g/L. This increase in the sorption is directly correlated to an increase of the surface site concentration. The results agree favorably well with previous studies [Wu et al., 2009; Amayri et al., 2011; Fröhlich et al., 2011]. For a total Np(V) concentration of 3.0×10⁻⁷ M, the K_d values 36± 15 L/kg at pH 7.6 for OPA and 27± 8 L/kg at pH 7.2 for COx is obtained, which are more or less independent of the solid-to-liquid ratios from 10–200 g/L (see in Table 3-7 and Table 3-8). However, the amount of sorbed Np at S/L = 10 is significant smaller after 6 weeks interaction time compared to 4 months interaction time. This can be a hint that a limited number of various sites on the clay surface occurs that a) differently bound Np(V) on the surface and mirror different kinetic modes, or b) a fast kinetic of the Np(V) sorption is superimposed by a slow kinetic of a reduction reaction from Np(V) to Np(IV). This limit of sites is compensated not before 50 g/L of clay, as always, the mechanism looks like.

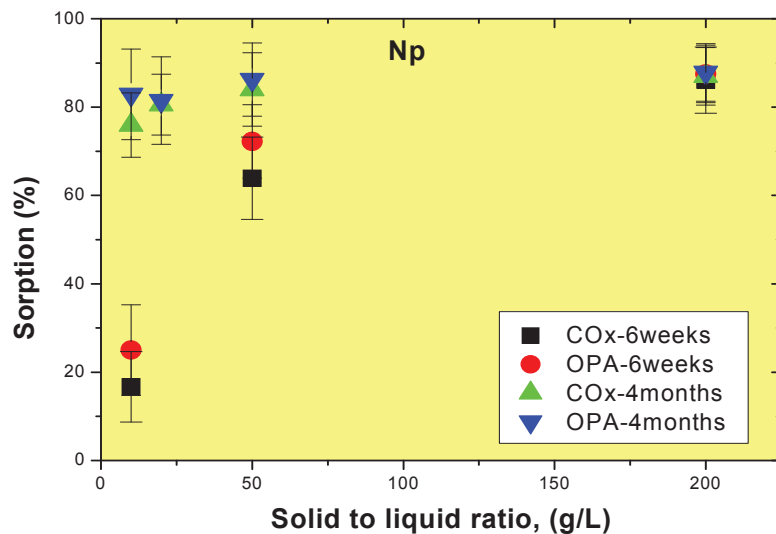


Figure 3-15: Sorption of neptunium on OPA/COx in pore water as a function of solid to liquid ratio (S/L), I = 0.1 M NaCl, [Np(V)] = 3×10^{-7} M, contact time= 6 weeks and 4 months.

Table 3-7: K_d values and percentage sorption of Np and Pu on OPA (pH 7.6) in Pore water at 3×10^{-7} M.

Solid to liquid ratio, [g/L]	K _d [L/kg] & sorption [%] of Np	K _d [L/kg] & sorption [%] of Pu
10	33.0/25±3	517/84±3
20	52.0/36±6	303/86±6
50	30.0/70±7	146/88±5
200	32.0/87±5	42.6/89±6

Table 3-8: K_d values and percentage sorption of Np and Pu on COx (pH 7.2) in pore water at 3×10^{-7} M.

Solid to liquid ratio, [g/L]	K _d [L/kg] & sorption [%] of Np	K _d [L/kg] & sorption [%] of Pu
10	20.0/17±4	242/71±6
20	35.0/33±5	367/88±3
50	32.0/64±8	166/89±4
200	30.0/86±4	68.0/93±5

The sorption of Np onto clay rocks (COx, OPA) has also been investigated as a function of metal concentration in the concentration range between $3 \cdot 10^{-8}$ mol/L and $3 \cdot 10^{-7}$ mol/L. As can be seen in Figure 3-16 for Np(V), there is almost constant K_d values in this concentration

range. The lowest sorption of Np is about 17 % at S/L ratio of 10; where as 87 %, the highest Np sorption has been found at S/L ratio of 200 g/L after 6 weeks contact time. There is a linear dependency between the total sorption and the liquid to surface area ratio (S/L range from 10-200 g/L) under these conditions showing the effect of available sorption sites.

Table 3-7 and Table 3-8 show the K_d values and the percentage of Np sorbed on COx and OPA in pore water at different S/L and at reaction time of 6 weeks. The influence of the contact time on the sorption of Pu/Np has been investigated for the solutions with the different concentrations, under inert atmosphere. A strong influence has been found between the sorption rates between 1 week and 4 months after the contact of clay rocks with both actinides (10 to 40 % of higher sorption after 4 months depending on the actinides).

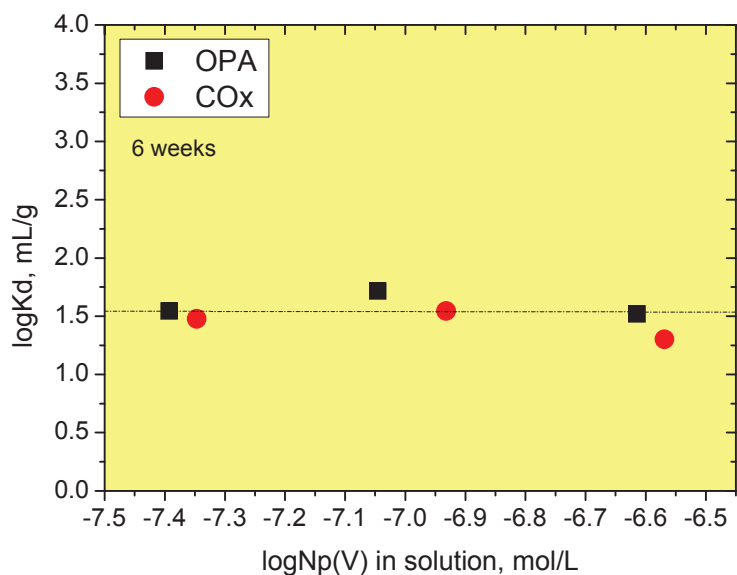


Figure 3-16: Distribution coefficient (K_d) for the sorption of Np on OPA/COx in pore water as a function of neptunium concentration, $I=0.1$ M NaCl, $[Np(V)] = 3 \times 10^{-7}$ mol/L, contact time= 6 weeks.

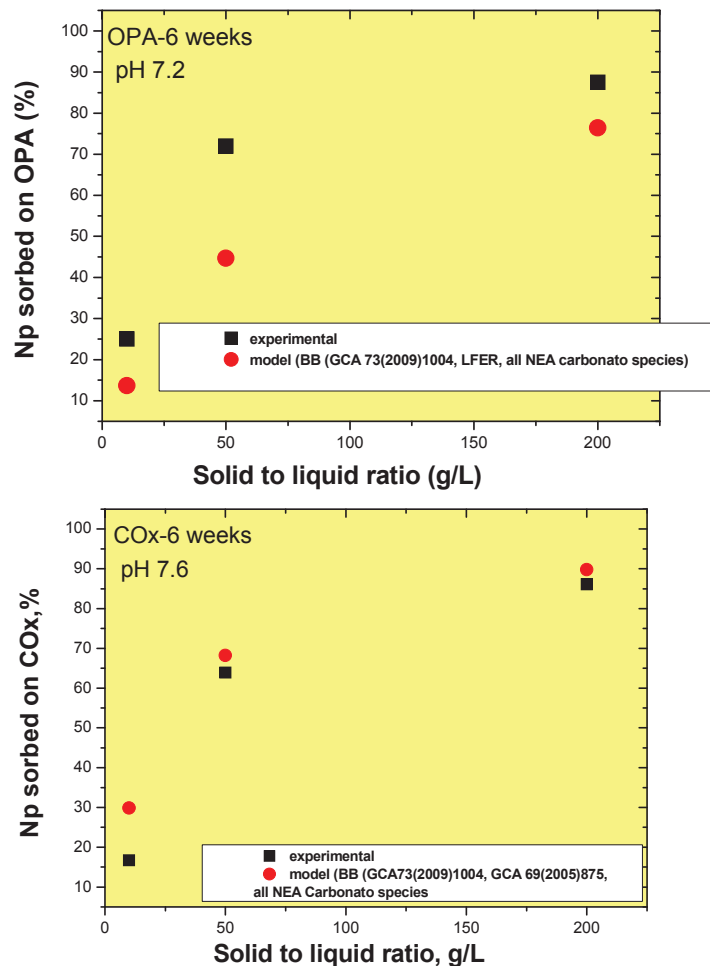
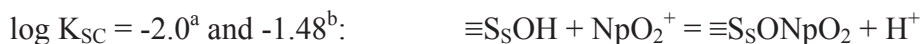


Figure 3-17: Comparison of experimental and modelling sorption studies of Np on OPA (top) and COx (bottom) clay minerals as a function of solid to liquid ratio (S/L), pH 7.6 and 7.2, $I=0.1$ M NaCl, $[Np(V)] = 3 \times 10^{-7}$ mol/L, contact time= 6 weeks.

Sorption modelling

The experimental data of Np sorption on clay has been model by the 2 site protolysis non-electrostatic surface complexation and cation exchange (2SPNE SC/CE) sorption model from [Bradbury&Baeyens, 2009]. For the species in aqueous solution – mainly hydrolysis and carbonate species - the NEA data have been taken. As solid phase the clay mineral illite has been taken. The following constants for the surface complexation of strong sites on the illite have been chosen to be



a: value directly depicted from [Bradbury&Baeyens, 2009]; b: calculated by linear free relationship (LFER) for illite in [Bradbury&Baeyens, 2009]

The sorption model calculations for Np with clay rocks OPA/COx are comparable with batch experimental data in pore water system (Figure 3-17). For the OPA the deviation is higher than for the COx. The deviation might be explained by the uncertainty in the redox behaviour of Np(V) on the surface. In the modelling 100% Np(V) is assumed, but after 6 weeks some Np(IV) has already been formed. On the other hand, if we regard the Np(IV)/Np(V) couple and pure sorption, the results are underestimated; if we include surface precipitation, the experimental data are overestimated. However, the results are due to the high uncertainties not so bad, but the modelling needs further detailed treatment.

Sorption of plutonium on clay rocks

The interaction of pentavalent plutonium with COx and OPA clay has been studied and shows that more than 85 % of the plutonium is retained on both clay mineral surfaces after 6 weeks contact time (see Figure 3-18). From spectroscopic characterisations we know that the Pu(V) is quickly reduced to Pu(IV). About 80-90% of the Pu is retained on OPA at S/L ratios from 20 to 200. However, the amount of sorbed Pu on COx at S/L ratio of 10 is with 72% lower than for OPA. At higher S/L ratios the sorbed amount of 88-93% on COx is similar to the values of OPA for a 6 weeks contact time.

A strong sorption of Pu(IV) on Callovo oxfordian was also observed by [Latrille et al., 2006] and their K_d values are comparable with our results (see Table 3-10), although their values are a little larger. The interactions between the Pu and mineral surfaces are complex because of its redox behavior. The sorption behaviour of PuO_2^+ is significantly influenced by redox conditions occurring in solution and on the mineral surfaces. PuO_2^+ can easily be reduced in contact with mineral surfaces and sorbed on mineral surfaces as in the form of Pu(IV) [Keeney-Kennicutt & Morse, 1984, 1985]. If it is really a sorption is unclear, because the Pu(IV) concentration is controlled by its solubility in solution at concentrations used for the experiments. A surface precipitation of Pu(IV) as a hydroxide or hydrated oxide cannot be excluded in our experiment, because the total concentration of Pu slightly exceeds the solubility of Pu(IV). It has to be emphasised, that the K_d concept might be not valid for tetravalent Pu experiments and should better be described by regarding its solubility. Although the K_d concept might not be valid for Pu(IV), here, anyhow the K_d values are given in this work to render results comparable with literature values. The experiment in [Latrille et al., 2006] has been performed below the solubility limit and the authors have proved that no surface precipitation occurred. So their K_d values are valid in the sense of the K_d concept. This might be the reason for their slightly higher sorption data compared to our values.

Table 3-9: logKd values for plutonium on Callovo–Oxfordian clay rock

Experimental conditions	logKd [mL/g]	logKd [mL/g]
	This work	[Latrille et al, 2006]
[²⁴² Pu(V)] = 3x10 ⁻⁷ mol/L, S/L=10-200 g/L, pore water, pH 7.2. Reaction period: 42 days	1.85-2.45	
[²³⁸ Pu(IV)] = 3x10 ⁻¹⁰ mol/L and 3x10 ⁻¹¹ mol/L, S/L=20 g/L, Reference water, pH 7.0-7.8, Reaction period: 72 days		2.50-3.50

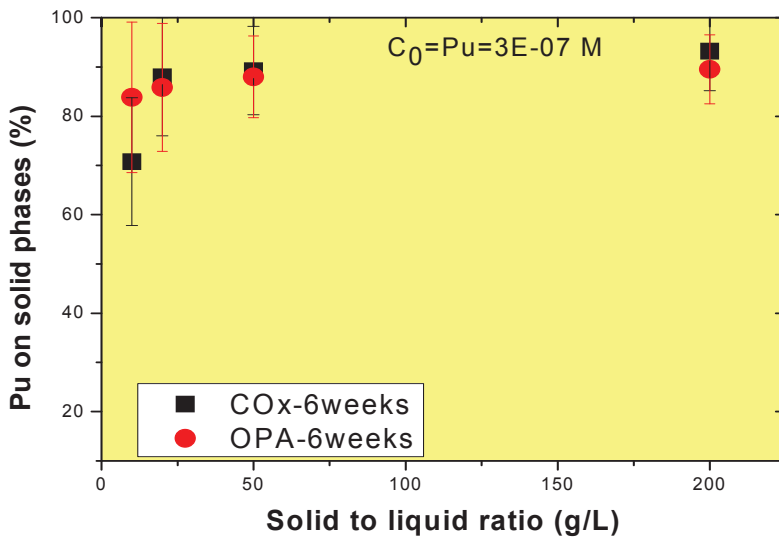


Figure 3-18: Interaction of plutonium with OPA and COx in pore water as a function of solid to liquid ratio (S/L), I= 0.1 M NaCl, [Pu(V)] = 3E-07 M, contact time= 6 weeks

To check if the Pu sorption experiments are influenced by the solubility of Pu(IV) we performed a one at Pu concentrations of about 5x10⁻⁹ M ²³⁸Pu. The Pu sorption pH edge was measured at 20°C in OPA porewater. All experiments were performed in a glove box under argon atmosphere. The pH was adjusted by adding analytical grade KOH or HCl. The experiments were performed in high density polyethylene (HDPE) 20 ml Zinsser bottles (Zinsser Analytics, FrankfurtLM.) with a solid/solution ratio of 2 g/L. At the end of the experiment the solid was separated from solution by centrifugation (10 min at 16000 rpm). 5 ml of the supernatant were acidified (2% HN03) and analyzed for Pu by LSC. Concentrations of Al, Si, Mg and K were measured on a Plasma 400 ICP-AES (Perkin-Elmer).

We monitored the concentration of Pu in solution in batch experiments in pH range from 4.75 to 10.23 over one year. Above pH 6 a “steady state concentration” was reached after 12 hours.

As a function of time no further evolution of the Pu concentration was observed. In seven batches we observed a significant drop of the Pu concentration already after one hour of reaction. The post-mortem XRD analysis of these clays with help of Rietfeld refinement method revealed in these samples an unusual high amount of pyrite (~ 40 %) compared to the other samples (~ 1 %). In the “normal samples” the Eh decreased from the initial value of ~ 350 mV to values of around ~ 200 - 150 mV after 12 hours and in the samples rich in pyrite down to a value of ~ 70 mV after one hour. Starting from pH 4.75 the Pu concentration in solution decreases with increasing pH and reaches a sorption maximum at pH 7.2 (Figure 3-19). At pH values > 7.2 the Pu concentration in solution increases again. According to the results of the batch sorption data a strong Pu sorption under the experimental conditions of the diffusion experiments is expected. Some samples were kept in the glove box and resampled after one year. The Pu concentrations for the samples at pH > 7.2 after one year were close to the detection limit of Pu in our system (detection limit in our experimental set-up 1×10^{-11} mol/L). The pH showed only slight changes and the Eh remained within the error of the measurement (± 50 mV).

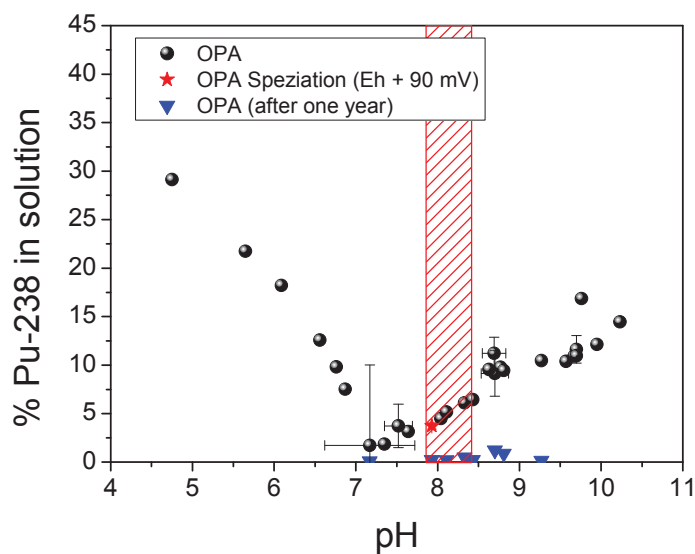


Figure 3-19: Sorption experiments of Pu-238 on Opalinus Clay. The filled pattern indicates the pH region of the diffusion experiments.

We measured the evolution of the Pu speciation as a function reaction time in the OPA supernatant porewater and on the solids at pH ~ 8. In the supernatant solution the Pu is to 87 % Pu(V/VI) and 13 % Pu(IV). To determine the oxidation state of the Pu sorbed on the clay sample we washed clay with concentrated HNO₃. The Pu removed from the clay after 24 hours consists of Pu(IV) 80 % and Pu(V/VI) 20 %. After one year all the Pu was sorbed on the clay and the oxidation state was found to be IV.

Figure 3-20 illustrates the changes of the logK_d values with the contact time in comparison to literature values from [Latrille et al., 2006], [Lujaniene et al., 2007], and [Zuo et al., 2010].

The figure demonstrates again that the K_d value for the Pu(IV) increases of about one order of magnitude during a reaction time of one year. The initial Pu concentrations of all experiments shown in the graph were below the solubility and precipitation of Pu is not expected: this work $[Pu] = 5 \times 10^{-9}$ M; [Latrille et al., 2006] $[Pu] = 3 \times 10^{-10}$ M; [Lujanienė et al., 2007] $[Pu] = 1 \times 10^{-9}$ M; [Zuo et al., 2010] $[Pu] = 1 \times 10^{-11}$ M. However, the $\log K_d$ values varies over two order of magnitudes demonstrating that the sorption experiments of Pu cannot easily be interpreted. The experiments demonstrate the need of experiments with pure clay minerals to elucidate first the question, which component of the natural clay is responsible for the sorption. If this question was clarified, then reliable K_d values, or better surface complexation constants for the surface complexation model, can be determined in the pure system and then compared with the natural system.

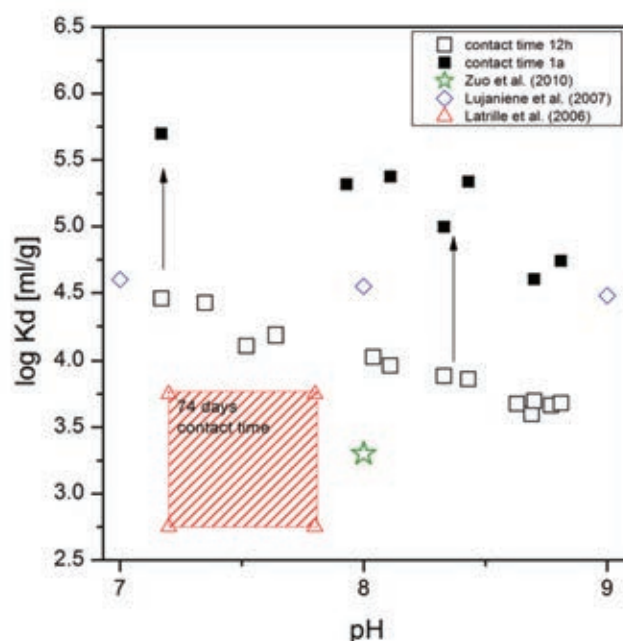


Figure 3-20: Batch sorption data of Pu(IV) sorption on Opalinus clay after 12h contact time and one year contact time showing the increase in K_d values observed. For comparison data on the Callovo-Oxfordian argillite after 74 days contact time [Latrille et al., 2006], on Triassic clay from Šaltiškiai and Chinese shale rock are inserted.

Desorption

Desorption experiments are carried out at pH values 7.2 and 7.6 under the same experimental conditions used in the sorption experiments. The Np and Pu sorbed onto both clay rocks is desorbed in fresh pore water and buffered at the appropriate pH value and shaken continuously. Almost no desorption from both clay rocks is found after contact time of 1 month.

This indicates that the Np, supposable Np(IV), and Pu(IV) ions are strongly bound onto clay rocks and shows chemisorption rather than physisorption. Therefore, the sorption is might be irreversible process. Further, it can be concluded that the inner sphere complexes of Np/Pu on both clay rocks have been expected.

3.5 Influence of humic acid on the An(III) sorption

It could be shown in some studies that organic compounds can be extracted from pore water or ground water with high pH values [Claret et al., 2002, 2003]. Such high pH values can be generated by contact of ground water with concrete, which is part of the repository's constructions. In this organic fraction compounds occur which can resemble fulvic and humic acids. Because it is well known that humic acids in solution complex the trivalent actinides very strong, an influence on the sorption, and hence, a mobilisation can not be excluded. Organic compounds fixed in the clay rock play no role concerning the sorption process. To investigate the influence of organic compounds in solution on the Eu(III) sorption on clay rock, batch experiments were performed with Eu(III) and Na-montmorillonit SWy-2 and Aldrich humic acid (AHA), as well as in the system SWy-2 / AHA / Calcite. The results of these studies are compared with results of the Eu(III) sorption investigations without humic acid. In the binary system of mineral phases and humic acid or ternary system mineral phase / humic acid / metal ion the humic acid sorption on the mineral phase depends among other parameters on the pH value of the solution [Křepelová, 2007]. Figure 3-21 shows the experimental results of the sorption of AHA on clay from various batch sorption experiments. concentration of AHA in solution was determined by measurement of the organic carbon and by UV-Vis spectroscopy. The amount of AHA on the clay decreases with increasing pH value for both systems. This behaviour was also observed in sorption studies with kaolinite [Křepelová, 2007]. This behaviour is based on electrostatic effects, because with increasing pH value the negative surface charge of the clay as well as the negative charge of AHA increases too. Therefore, the AHA is repelled by the clay surface and the sorption decreases. Nevertheless, part of the AHA is sorbed despite the negative charge and hence, other sorption mechanism must occur.

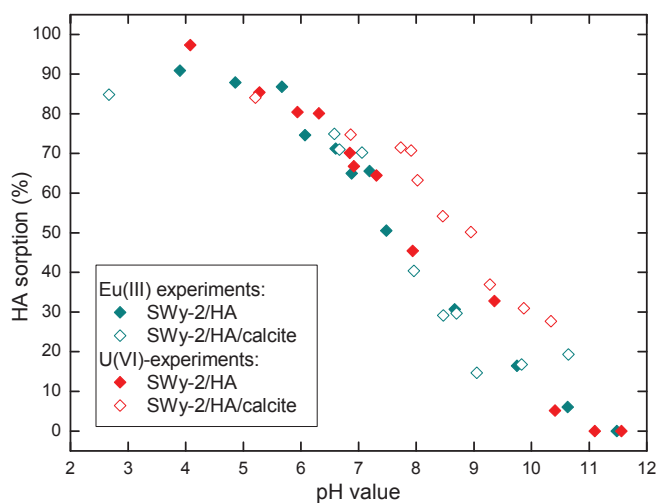
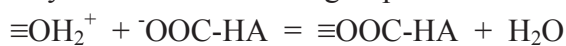
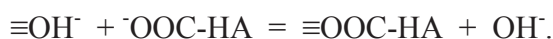


Figure 3-21: Sorption of AHA on SWy-2 as a function of pH in the sorption experiments of Eu(III) and U(VI) (not shown in this report) with AHA (2 g/l SWy-2, 10 mg/l AHA) and with AHA and calcite (1,6 g/l SWy-2, 0,4 g/l calcite, 10 mg/l AHA). [Eu(III)] bzw. [U(VI)] = 1×10^{-7} mol/L, I = 0,1 mol/L NaClO₄.

This could be (i) surface complexation, (ii) ion exchange between OH_2^+ or OH^- groups of the clay surface and anionic groups of the AHA according to the following reaction:



or



Also formation of bridges by metal cations (Al^{3+} , Ca^{2+} , Mg^{2+} , Fe^{2+}) between the negative charge of the clay and the AHA are possible [Schmeide et al., 2000].

The sorption of Eu(III) in presence of HA on Na-montmorillonite is shown in Figure 3-22. Additionally, the sorption of Eu(III) on the pure SWy-2 and SWy-2/calcite mixture including the corresponding numerical modelling are illustrated. In presence of AHA the sorption of Eu(III) is smaller in comparison to the pure SWy-2 at $\text{pH} > 6$, reaches a minimum with about 70 % at $\text{pH} \sim 8.7$ and finally increases at higher pH values. The sorption on clay/AHA reaches a maximum of 92 % at high pH values that is somewhat lower than on clay/AHA/calcite. At $\text{pH} < 6$ the Eu(III) sorption is higher on clay/HS than on the pure clay mineral.

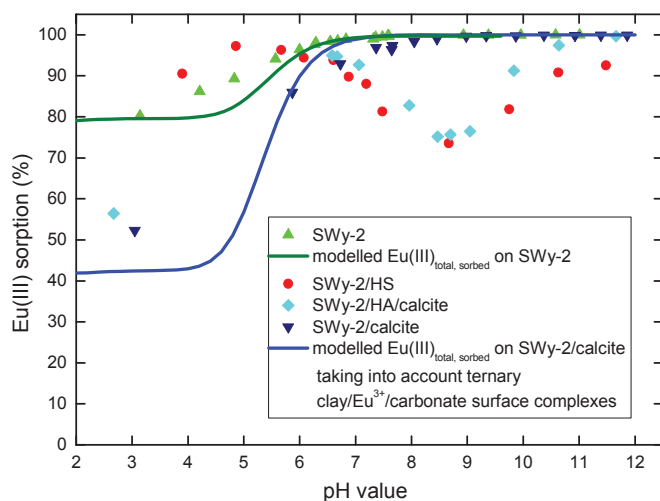


Figure 3-22: Eu(III) sorption on Na-rich montmorillonit (SWy-2) without and with Aldrich humic acid (AHA, 10 mg/l) and/or calcite (Clay : calcite = 80 : 20 wt-%) and numerical modelling of the sorption on SWy-2 (dark green) and SWy-2/calcite by considering ternary clay/Eu³⁺ carbonate surface complexes (blue) in %. [Eu(III)] = 1×10^{-7} mol/L, S/L = 2 g/L, I = 0,1 mol/L NaClO₄.

The sorption of Eu(III) is strongly influenced even in small amounts of AHA. [Rabung, 1997] has experimentally proved in the system Eu(III)/hematite/HA that the humic acid (HA) bound on the mineral is the species that governs the sorption properties of the material. The HA is mainly sorbed on the strong sites of the hematite surface [Rabung, 1997; Rabung et al., 1998].

Photo electron spectroscopy (XPS) of Uranyl on kaolinite exhibits that the HA is not sorbed on the mineral as a homogeneous layer, but occurs between the single kaolinite particles [Křepelová, 2007]. Therefore, on the surface of the mineral in the system metal ion/clay/HA many binding sites are still available for the sorption of the metal cation that are not occupied by the HA. Because the sorbed HA provides itself binding sites for the metal ion by forming humate complexes on the surface, the sorption of Eu(III) at lower pH values is higher than in the humic acid-free system.

The decreasing sorption of Eu(III) in presence of AHA in the pH range between 6 and 9 is attributed by the pH-dependent Desorption of AHA from the mineral surface (s. Figure 3-21). Here, the formation of Eu(III) humate complexes competes between HA_{surface} and HA_{solution} . [Fairhurst&Warwick, 1998]. According to Sakuragi et al. (2005), the interaction between the HA and the metal ions is not altered, regardless of sorbing the metal ion on HA in solution or HA sorbed on the mineral surface.

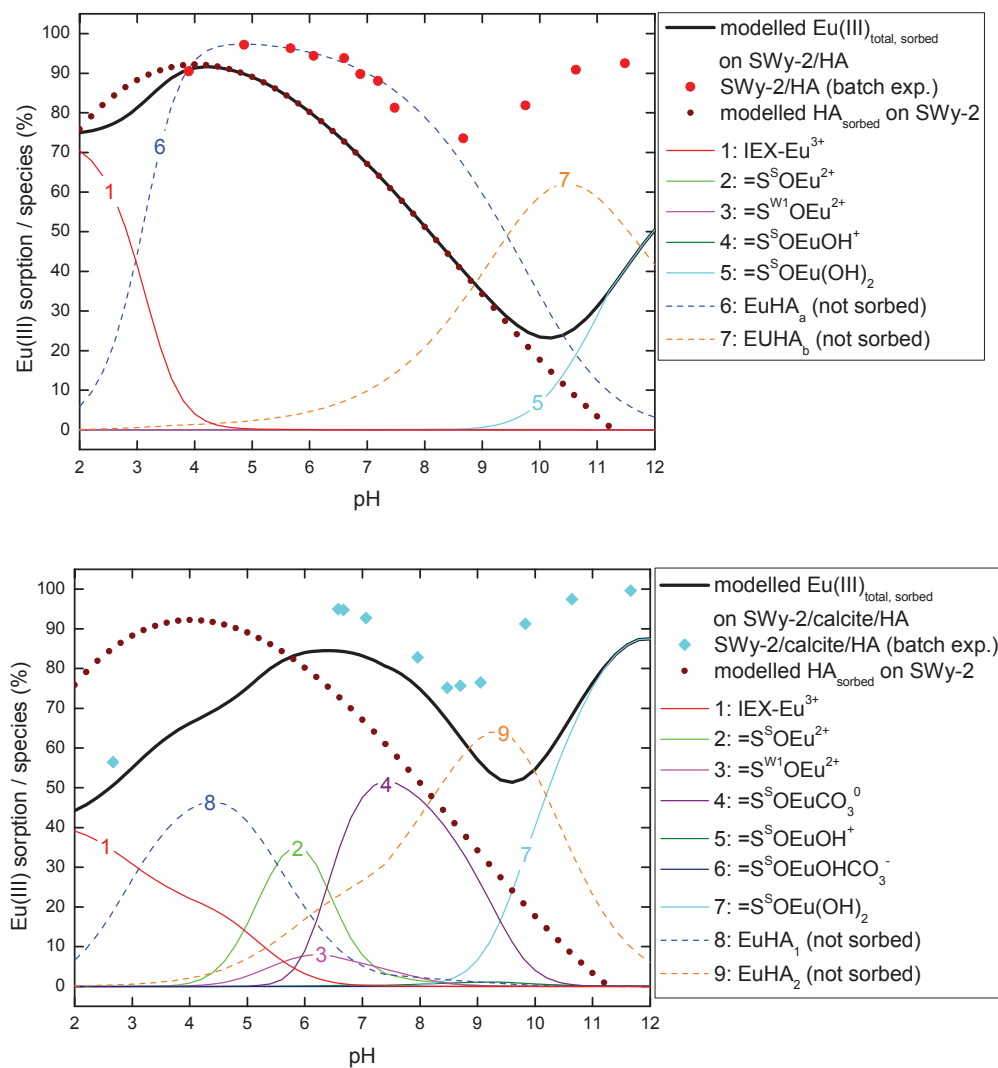


Figure 3-23: Eu(III) sorption on Na-rich Montmorillonite (SWy-2) with humic acid (10 mg/l) and (b) on Na-rich Montmorillonite (SWy-2) with humic acid (10 mg/l) and calcite (clay : calcite = 80 : 20 wt.%) as well as modelling as a function of pH value and taking into account ternary clay/ Eu^{3+} /carbonate surface complexes plotted in

%. The graph includes the experimental data of the HA sorption on SWy-2. Species 1 bis 5 (a) and 7 (b) are Eu(III) surface complexes; species 8 and 9 are the Eu(III) humate complexes in solution. Experimental conditions: [Eu(III)] = $1 \cdot 10^{-7}$ mol/l, S/L = 2 g/l, I = 0,1 mol/l NaClO₄. (IEX = Ion exchange; (= CAC), S = Smectite, S = *strong sites*, W1 = *weak sites*).

The Eu(III) sorption in the SWy-2/HA system without (a) and in presence of calcite (b) and the HA sorption on SWy-2 as well as numerical modelling based on the NICA-Donnan model are presented in Figure 3-23. It must be emphasised that the sorption of the HA is not regarded by the model. Therefore, the experimentally derived HA sorption on clay (Figure 3-21) is equilibrated to the sorption of Eu(III) humate complexes on clay in both systems, clay/HA and clay/HA/calcite. The total Eu(III) sorption results from the sum of calculated sorption of inorganic Eu(III) species on clay and the experimentally derived sorption of Eu(III) humate complexes.

In both systems the Eu(III) fraction sorbed by ion exchange dominates at $\text{pH} < 4$. The numerical modelling exhibits that a sorbed Eu(III) humate complex governs the sorption between $4 < \text{pH} < 8.5$ and suppresses other complexation reactions. In the clay/HA/calcite system significant fractions of surface complexes on clay (outer-sphere species, $\equiv\text{S}^{\text{S/W1}}\text{O}^-\text{Eu}^{2+}$, $\equiv\text{S}^{\text{S}}\text{O}^-\text{EuCO}_3$, and $\equiv\text{S}^{\text{S}}\text{O}^-\text{Eu}(\text{OH})_2$) occur beside the Eu(III) humate surface species and other solution species.

The minimum of the pH course can be modelled in principle, but it is shifted to higher pH values of around 10. The sorption is under-estimated by the modelling over the total pH range, especially at pH 8.5 and higher (in the clay/HA system up to 60 %, in the clay/HA/calcite system up to 40 %). At higher pH values the increasing sorption is caused by the species $\equiv\text{S}^{\text{S}}\text{O}^-\text{Eu}(\text{OH})_2$, which is also undervalued. Anyhow, the difference between sorption of Eu(III) in presence of HA and in the free-HA system is rather small (at pH 12 ~8% lower, Figure 3-22). One can assume that the present HA affects the sorption of Eu(III) only weakly at higher pH values. The numerical modelling overestimates the fraction of the EuHA_b complex in solution (Figure 3-23).

From other studies concerning the modelling of humate complexation by the NICA-Donnan model with parameters from Milne et al, (2001, 2003) it is known that the humate complexes are significantly overestimated [Geckeis, 2010]. This is obvious in numerical modelling of Cm(III)/Am(III) in Gorleben groundwater, where only the humate complexes are predicted at higher pH values. Instead of that, in experimental characterisation of these groundwaters the carbonate complexes are the dominating species. Anyway, the humate complexes can reduce the retention of trivalent actinide in the clay system. The available set of parameters in the NICA-Donnan model have to be revised for Ln(III) and An(III) cations.

However, the relevance of humic acid-type organic compounds occurring in porewater have to be checked, especially the question whether actinide organic complexes can be a mobile species by diffusing through the clay matrix.

3.6 Outersphere complexation of trivalent actinides

The permanent negative charge of most of the clay mineral, resulting from isomorphic substitution of higher charged to lower charged cations in the crystal lattice, is compensated by cations from the surrounding solution, which are absorbed predominantly by electrostatic attraction to the basal planes of clay minerals and they form so-called outer-sphere complexes. In the outer-sphere complexation of the cation the hydration sphere remains fully intact. Electrostatically bound cations can exchange with other cations in the supernatant solution. This happens through reactions that occur rapidly, stoichiometrically and reversibly (Bolt et al., 1976; Grim, 1953; van Olphen, 1963). In general, the sorption as a result of such cation exchange reactions is independent of the pH-value, except when, for example, competing cations are released by dissolution of the clay minerals due to changes in the pH. The cation exchange processes dominate the interactions between cations and clay minerals at low pH values (<5) and low ionic strengths.

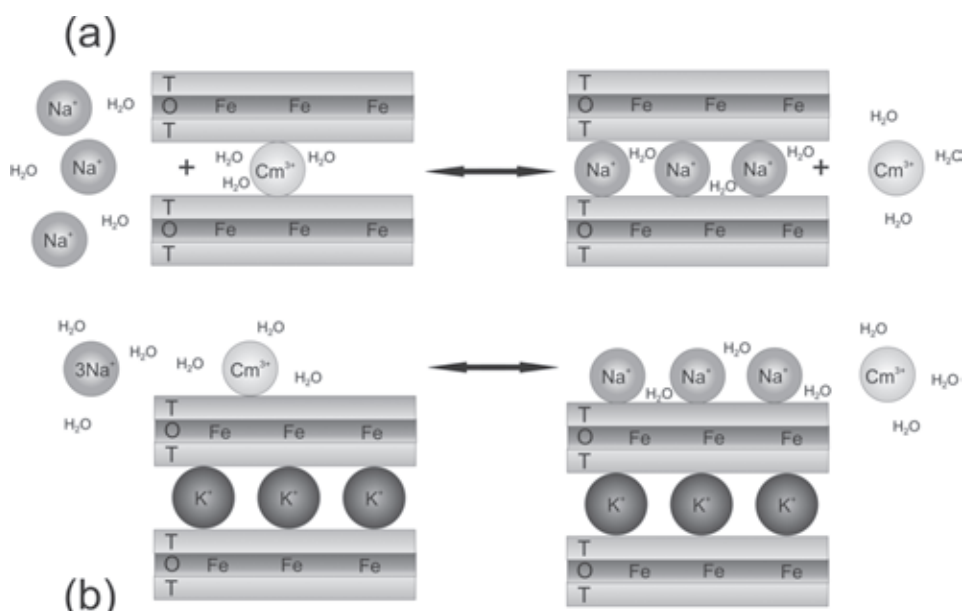


Figure 3-24: Displacement of outer-sphere sorbed Cm^{3+} by three Na^+ (a: montmorillonite, b: illite) at increasing ionic strengths resulting in increased Cm^{3+} ion concentrations in solution.

At low ionic strengths (NaCl) the cation with the higher charge (Cm^{3+}) is preferentially sorbed on the clay. The curium is released into the solution with increasing ionic strength due to ion exchange reaction between Cm^{3+} and three Na^+ ions at the outersphere sorption sites. (Figure 3-24). The cation exchange reaction takes place in case of montmorillonite not only on the surface, but also in the clay interlayer space (Figure 3-24(a)), whereas in case of illite only the cation exchange on the surface is possible due to the irreversibly bound K^+ ions in the interlayer space (Figure 3-24(b)).

Cm^{3+} and Sm^{3+} , chosen for the TRLFS- and EXAFS investigations, keep as outer-sphere complex nine water molecules in the first hydration shell. Consequently, the peak maximum in TRLFS spectra does not change for a $\text{Cm}^{3+}/\text{Sm}^{3+}$ outer-sphere complexes and the lifetime

remains constant compared to the uncomplexed aquo ion. So far, therefore, a distinction was not possible between aquo ions and outer-sphere sorbed cations by using spectroscopic methods and the outer-sphere complex formation couldn't be quantified, since these were based only on changes in the ligand field of the fluorescent cation.

The TRLFS studies presented below show the Cm (III) outer-sphere complex formation in various clay suspensions at pH \sim 4. Here, the quenching effect of iron on the Cm (III) fluorescence emission was taken to help. Iron, which was built by displacement of an Al³⁺ in the crystal structure of clay minerals, causes, in addition to H₂O, an additional diminution of Cm(III) fluorescence emission by dynamic quenching, when it comes to a collision between fluorophore and quencher and the excited molecule makes an energy exchange with the quencher transferring back into its the ground state. The higher the Fe content in the crystal lattice of clay minerals, the shorter the average distance and therefore the shorter is the lifetime of the fluorescence emission of sorbed Cm (III) species. Cm (III) ions bound as outer-sphere complex can be distinguished from non-sorbed aquo ion based on their shorter fluorescence lifetime, because the distances of aquo ions are too large for an interaction with the iron. The lifetimes should correlate with the corresponding iron content of the clays used.

Table 3-10: Physico-chemical properties of γ -Alumina (Al₂O₃), purified Na-montmorillonites (SWy-1, Milos und STx-1) and the synthetic Na-montmorillonit (NaMont_s) as well as Na-illite (IdP-2).

	Al ₂ O ₃	Na-Mont _s	Na-STx-1	Na-Milos	Na-SWy-1	IdP-2
Fe³⁺ [Gew.-%]	0	0,002	0,62	1,3	2,97	5,32
CEC [meq/kg]	0	630	912	937	881	225
N₂-BET [m ² /g]	119	98	84	28	35	138

CEC: cationic exchange capacity

In Table 3-10 the different Fe-contents of the sorbents and clays used in the experiments are listed. Since the cation exchange capacity and specific surface area for the outer-sphere complex formation play an important role, these are also listed. The origin, properties and preparation of materials and clays and other details are described in [Hartmann, 2010; Hartmann et al., 2008a].

The quantification of the outer-sphere complex formation are carried out by means of the TRLFS. This was done by gradually increasing the ionic strength (NaCl) and thereby increasing the exchange of outer-sphere sorbed Cm³⁺ by Na⁺.

The TRLFS measurements were performed for clays with high Fe contents in H₂O and D₂O. For clays with low Fe contents the Cm (III) outer-sphere complex formation was quantified only in D₂O. In H₂O the fluorescence emission lifetime of the Cm(III) is about at 65-68 microseconds due to quenching effect of the water molecules in the first coordination sphere,

if not even more quenching effects, such as by iron, manganese or organic ligands are present. Unlike for H₂O, the quenching effect of D₂O molecules on the Cm (III) fluorescence emission lifetime is low. The lifetime of the Curium in D₂O is $\sim 1250 \pm 180$ microseconds [Wimmer, 1992; Kimura&Choppin, 1994]. The difference between the fluorescence emission lifetime of the non-sorbed aquo ions and the outer-sphere sorbed Cm³⁺ quenched by the Fe is much greater and the difference between the quenching rates is much more pronounced than in H₂O. Consequently, TRLFS measurements in D₂O are more sensitive and they can also provide information about the outer-sphere sorbed fraction of Cm (III) ions sorbed on clays with very low Fe contents.

3.6.1 Identification of the An(III)/clay outer-sphere complexation

In Figure 76 (a) and (b) all measured fluorescence emission spectra are represented of Cm (III) in clay suspensions and Al₂O₃ in 0.01 mol / l NaCl at pH ~ 4 in H₂O and D₂O. The spectra are identical with the spectrum of the Cm-Aquoions concerning the peak position and width and they show a peak maximum at 593.8 nm. Under the given conditions the Cm³⁺ ion retains its hydration shell and is either completely dissolved as Cm (III) aquo ion or occurs as an outer-sphere complex [Edelstein et al., 2006].

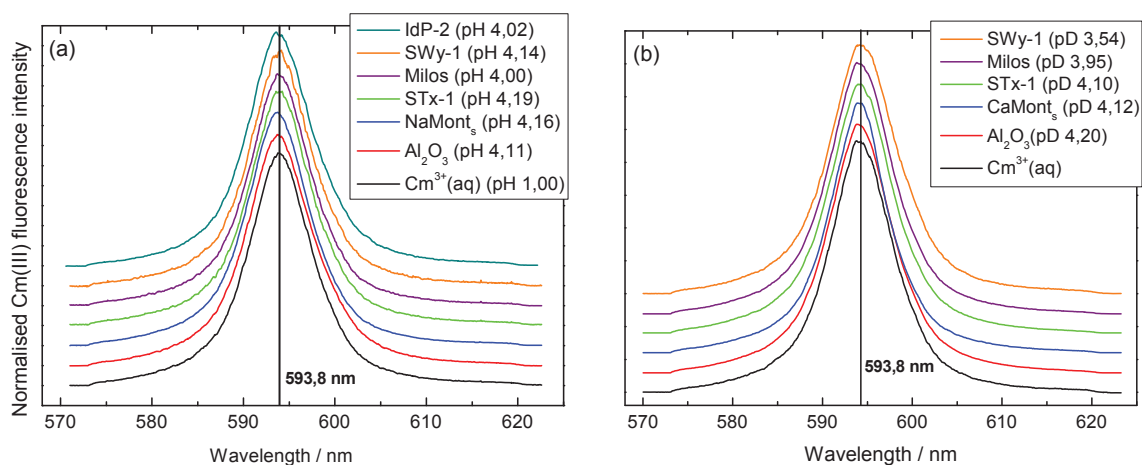


Figure 3-25: Cm(III) fluorescence emission spectra of various clay and Al₂O₃ suspensions (a) in H₂O ($2 \cdot 10^{-7}$ mol/L Cm(III), 0.3 g/L, 0.01 mol/L NaCl) at pH 4 to 4.19. The spectra for Cm³⁺(aq) was measured in HClO₄ at pH 1. (b) in D₂O ($2 \cdot 10^{-7}$ mol/l Cm(III), 0.3 g/l, 0.01 mol/l NaCl) at pD 3.54 bis 4.2. The spectra for Cm³⁺(aq) was measured in 0.01 mol/l NaCl in D₂O at pD 3.75.

In Figure 3-26, the Cm (III) fluorescence emission lifetimes in H₂O are shown, which were measured in all montmorillonite suspensions and in Al₂O₃. γ -alumina has been studied as a reference mineral with no permanent charge and without iron in the crystal structure. The

lifetimes vary for the different clay suspensions and correlate with the corresponding Fe content of the clay used (Figure 80 (a)).

The shortest life time was determined to be $\tau = 32 \pm 2$ microseconds for Cm (III) in SWy-1 suspension with the highest Fe content of 2.97 wt -% (and 4.25 wt -% Fe_2O_3) of all montmorillonites, which therefore corresponds to the most quenched fluorescence emission. For Cm (III) sorbed to Milos (1.30 wt -% Fe) and STx-1 (0.62 wt -% Fe) $\tau = 49 \pm 3$ microseconds or $\tau = 57 \pm 3$ microseconds were determined accordingly to their different Fe levels. For comparison, the Cm (III) aquo ion in HClO_4 measured at pH 1 showed a lifetime of $\tau = 68 \pm 4$ microseconds. This value agree very well with values in the literature between $\tau = 65$ and 68 microseconds [Fanghänel et al., 1995; Beitz&Hessler, 1981; Beitz et al., 1988].

The measured lifetime of Cm (III) in γ -alumina suspension of $\tau = 65 \pm 4$ ms coincides with that in the Cm (III) aquo ion in HClO_4 . In suspension of the synthetic montmorillonite NaMont_s, which has a very low Fe content of only 0.002 wt%, the outer-sphere complexation is indicated by a low quenched fluorescence emission lifetime of $\tau = 62 \pm 4$.

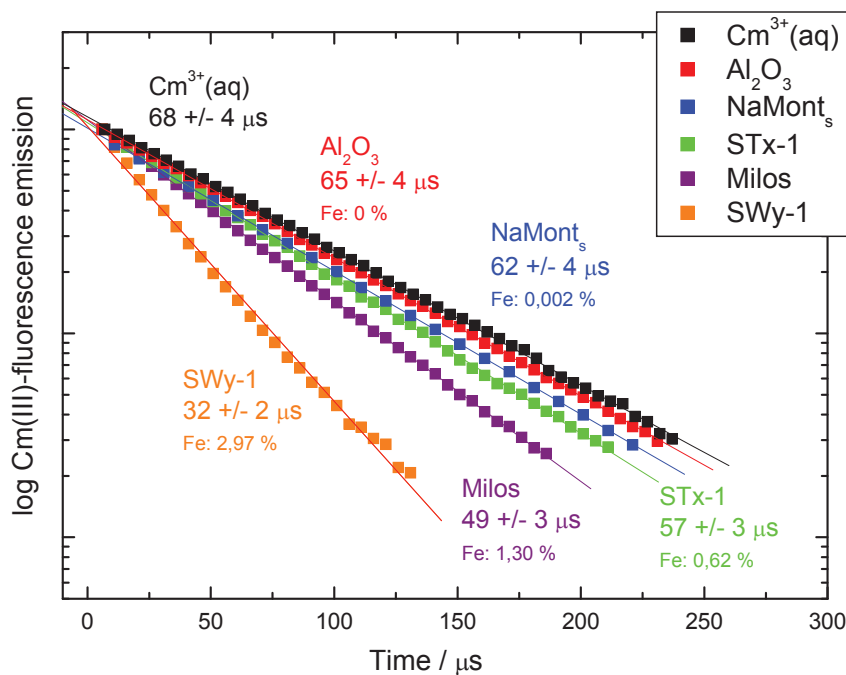


Figure 3-26: Cm(III) fluorescence emission lifetimes of various clay and Al_2O_3 suspensions in H_2O ($2 \cdot 10^{-7}$ mol/L Cm(III), 0.3 g/L, 0.01 mol/L NaCl) at pH 4 to 4.19. The lifetime for $\text{Cm}^{3+}(\text{aq})$ was measured in HClO_4 at pH 1. The lifetime of the montmorillonites show a mono-exponential decay.

In the literature, no information could be found for fluorescence emission lifetimes measured by TRLFS of Cm(III) sorbed as outer-sphere complex on clays with different iron concentrations. However, studies exist with trivalent europium sorbed on montmorillonites with different Fe contents at low pH values [Takahashi et al., 2006; Kowal-Fouchard et al., 2004; Tertre et al., 2006]. The Cm(III) fluorescence emission lifetimes for the measured montmorillonite suspensions in H_2O all show a mono-exponential curve (Figure 3-27),

because at low ionic strengths (<0.01 mol / l) and at pH ~ 4 , the Cm(III) ions on the montmorillonite are present predominantly as outer-sphere complex ($> 95\%$). The small proportion of non-sorbed Cm(III) aquo ion in H₂O is not evident from the decay curves. By comparison, in γ -alumina suspension only Cm(III) aquo ions occur due to the lack of layer charges that makes any outer-sphere complexes difficult. As expected, the measured fluorescence emission lifetime is also mono-exponential similar to that of the Cm³⁺(aq) in HClO₄ at pH 1.

The life times belonging to the the Cm-fluorescence emission spectra in D₂O from Figure 3-25(b) are shown in Figure 3-27. They show a bi-exponential pattern except for the γ -alumina. The long lifetime of 1250 ± 180 microseconds is due to the excitation of non-sorbed Cm(III) aquo ion. The short life time varies for the different clays and is correlated with the respective iron content of the clay minerals (Figure 3-29(b)).

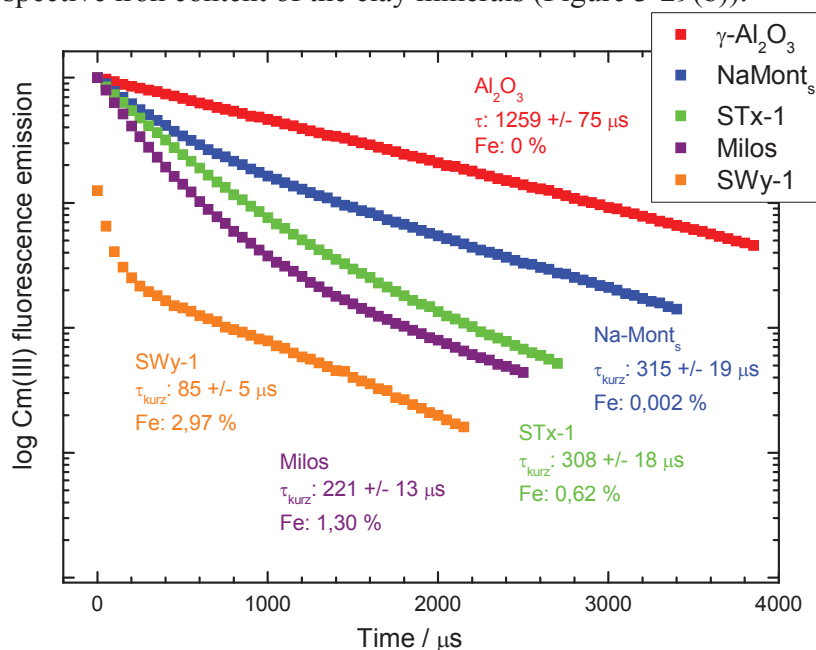


Figure 3-27: Cm(III) fluorescence emission spectra of various clay and Al₂O₃ suspensions in D₂O ($2 \cdot 10^{-7}$ mol/l Cm(III), 0.3 g/l, 0.01 mol/l NaCl) at pD 3.54 bis 4.2. The lifetime for Cm³⁺(aq) was measured in 0.01 mol/l NaCl in D₂O at pD 3.75.

The short lifetime is assigned to the Cm(III) outer-sphere complex that is quenched due to the low Fe-Cm distance. It amounts in the SWy-1-clay suspension 85 ± 5 microseconds and increases according to the decreasing iron content from Milos (221 ± 13 microseconds), STx-1 (308 ± 18 microseconds), to the synthetic Na-rich montmorillonite with the lowest Fe concentration (463 ± 28 microseconds). In the suspension with γ -alumina, which contains no iron and which forms no outer-sphere complexes due to lack of permanent charge, only one lifetime of 1259 ± 75 microseconds was measured. This is consistent with those reported in the literature values for the Cm(III) aquo ion in D₂O [Wimmer, 1992; Kimura&Choppin, 1994]. All lifetimes in the clay suspensions show a bi-exponential decay. Therefore one can assume a slow exchange between non-sorbed Cm(III) aquo ion and an outer-sphere complex

in comparison to the fluorescence lifetime of the excited state, which is much more long-lived in D₂O than in H₂O.

The long lifetime of the Cm (III) aquo ion in STx-1 suspension with ~ 661 microseconds is much shorter than 1250 ± 180 microseconds. This becomes apparent in Figure 3-27 where the decay curve at the end is much steeper than the decay curve of all other clays that are parallel to the branch measured in Al₂O₃ suspension. Possibly the STx-1 suspension was slightly contaminated with H₂O or protons during the preparation, so that the lifespan shortens. The quenching rates ($1/\tau$) itself is only slightly affected. The much larger τ_0/τ_1 ratio in D₂O increases the sensitivity of the spectroscopic quantification of outer-sphere bound curium.

A bi-exponential decay of emission was observed in the H₂O suspension of Na-illite-rich IdP-2, which has the highest Fe content (5.32 wt -%) of all examined clays (Figure 3-28).

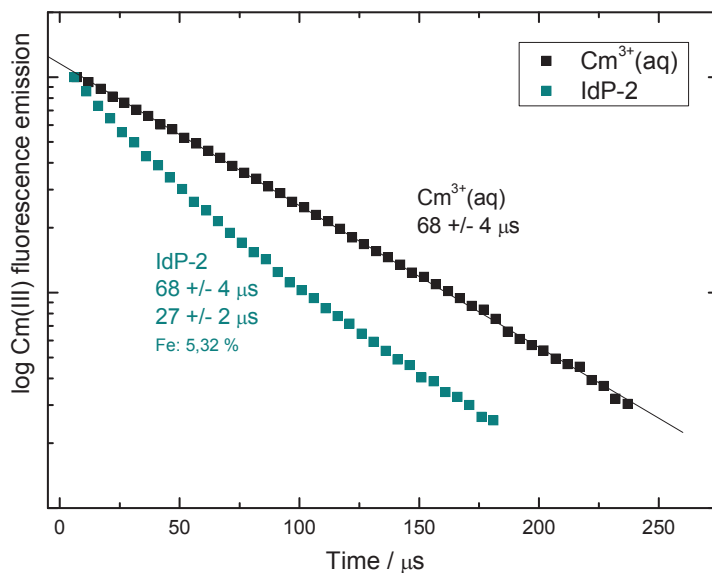


Figure 3-28: Bi-exponential decay of the fluorescence emission lifetime of Cm(III) in IdP-2 suspension in H₂O ($2 \cdot 10^{-7}$ mol/l Cm(III), 0.3 g/l, 0.01 mol/l NaCl) at pH 4.02. For comparison the mono-exponential decay of the Cm³⁺(aq) lifetime in HClO₄ at pH 1 was shown.

Illite has only a low cation exchange capacity (CEC) of 225 mEq / kg, while the montmorillonite exhibit a three-to fourfold higher CEC (Table 25). The permanent negative layer charge is compensated mainly by illite with K⁺ ions in the interlayer, which in general are not interchangeable [Bradbury&Baeyens, 2005b]. Only the cations on the external surfaces are interchangeable. Therefore, the CEC of illite is strikingly lower than that of montmorillonite, although the extent of isomorphous substitution is higher [Van Olphen, 1963]. For this reason, non-sorbed aquo ions in higher concentration occur simultaneously together with outer-sphere sorbed Cm(III) cations at low ionic strengths. The long life time of 68 ± 4 microseconds corresponds to the Cm(III) aquo ions and the short one of 27 ± 2 microseconds to the outer-sphere complex.

The fluorescence emission lifetime of Cm(III) sorbed as outer-sphere complex of illite, which is shorter than for montmorillonite, thus correlates again in good agreement with the iron concentration (Figure 80 (a)), which is the highest compared to the montmorillonite.

The efficiency of quenching depends on the distance between Cm(III) as fluorophore and Fe(III) as a quencher. Thereby the efficiency E decreases with increasing distance r according to Equation 3-1.

$$\text{Equation 3-1} \quad E = \frac{R_0^6}{R_0^6 + r^6}$$

R_0 corresponds to the Förster radius [Stryer, 1978], the distance between quencher Fe (III) and the fluorophore Cm (III) with a quenching efficiency of 50%. This means that half of all excited Cm(III) atoms relax via dynamic quenching processes into the ground state. At this radius, the measured fluorescence emission lifetime is reduced by half. The influence of dissolved Fe(III) on the quench behavior of the Cm(III) fluorescence emission was studied bei [Stumpf et al., 2004] with TRLFS in H₂O.

A Förster radius of 4.5 Å was calculated by the correlation between the Cm(III) fluorescence emission lifetimes and the concentration of Fe(III) [Stumpf, 2004], while the graphical analysis yielded a distance of 9 Å. The average distance between Fe and Cm in SWy-1 should therefore be between 4.5 and 9 Å, since the measured lifetime is reduced by about one half, while the average distance should be greater for the montmorillonite and correspondingly lower for the illite.

The different distribution of the Fe atoms embedded into the octahedral layers of the clays studied here seems to have no influence on the measurement results. According to [Vantelon et al., 2003] the individual Fe atoms are distributed homogeneously and isolated from each other in the Wyoming montmorillonite SWy-1. The octahedral layer of STx-1, however, has a heterogeneous distribution with local accumulations of iron, while the clay of Milos shall represent an intermediate stage between the two. The Fe content of each individual clay, however, correlates well with the measured lifetimes. A possible reduction in efficiency by iron accumulation as obtained for the STx-1, could not be observed.

The exchange between Cm(III) aquo ions and outer-sphere complex on illite must be very slow compared to the lifetime of the excited state of curium of about $6.8 \cdot 10^{-5}$, since the fluorescence emission lifetime shows a bi-exponential decay. The slow exchange between aquo ion and outer-sphere complex is underlined by the TRLFS measurements in D₂O. Here, the measured Cm(III) fluorescence emission lifetime for all the clay suspensions showed a bi-exponential pattern. In contrast, we assume that a fast exchange takes place among the outer-sphere sorbed Cm(III) ions, because the fluorescence lifetimes was mono-exponential for Cm in different montmorillonite suspensions with >95% outer-sphere complexation.

The spatial arrangement of the outer-sphere complexes in the area of the hexagonal cavities determined by EXAFS (Section 5.3) reveals that they must take up different distances from

the clay mineral surface to Fe incorporated into the crystal structure. These different distances would be expressed in case of a slow exchange between the outer-sphere sorbed Cm(III) ions present in multi-exponential decay curves. Since the course is clearly mono-exponential, the exchange must be relatively fast compared to the excited state. The measured lifetime is an averaged value, which is composed of various quenching effects of various Cm-Fe distances.

In Figure 80 the ratio of long and short Cm(III) fluorescence lifetimes in H₂O and D₂O are plotted as a function of the iron content of the clays as a Stern-Volmer graph. The strength of the quenching (reduced lifetime) correlates strongly with the Fe content of the clays. Thereby, the data obtained in D₂O cannot be described by a simple linear function. This is due to the fact that the distance *r* between Cm and Fe as a quencher acts with the sixth power in the quenching efficiency *E* (Equation 58).

If the data points in Figure 80 are interpolated, the curve does not achieved $\tau_0/\tau_1 = 1$ at an iron content of 0 wt.-%. Here, an intercept of ~1.05 and ~3 is obtained for H₂O and D₂O, respectively. This observation could be interpreted as evidence for a further quenching mechanism (see Section 5.1.1 and 4.3.1).

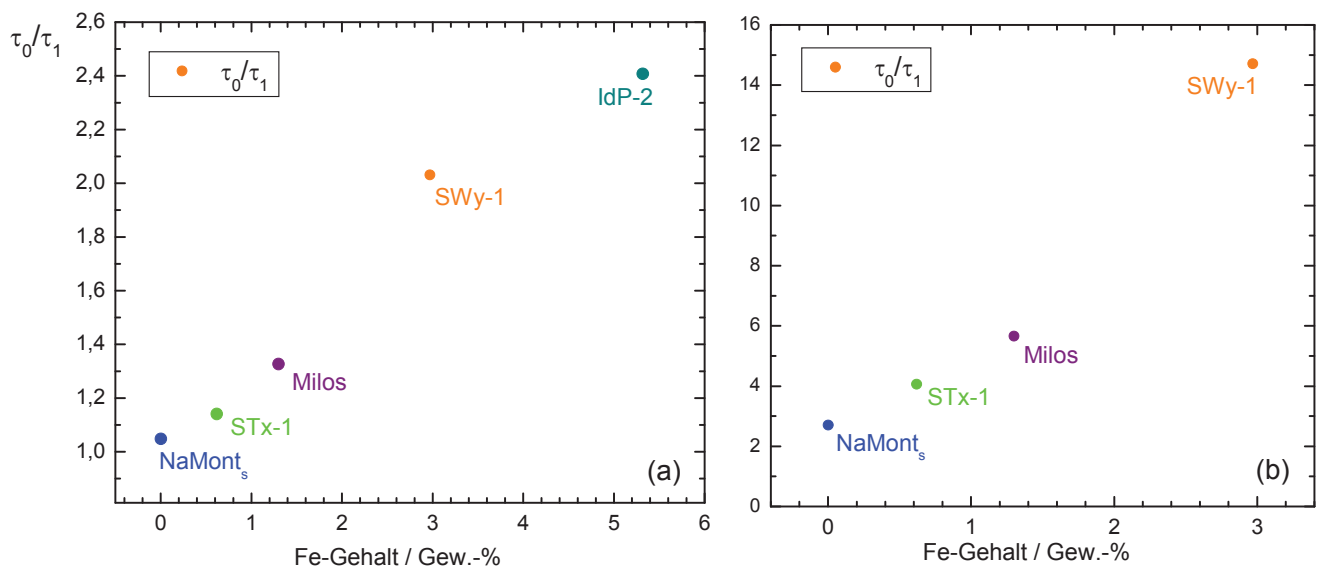


Figure 3-29: Plot of the Cm(III) fluorescence emission lifetime as a function of Fe content of the various used clays as Stern-Volmer-Plot (jeweils $2 \cdot 10^{-7}$ mol/l Cm(III), 0.3 g/l, 0.01 mol/l NaCl). Measurements (a) in various montmorillonite and illite suspensions in H₂O (pH values see Figure 3-25(a) and (b) in D₂O (pH values see Figure 3-25(b)).

Comparison of the quenching rates in H₂O und D₂O

To compare the results of the TRLFS measurements in H₂O with those from the D₂O system the quenching rates of both systems were faced. The quenching rate K_{obs} is calculated from the reciprocal of the Cm(III) fluorescence emission lifetime τ (Equation 3-2). In H₂O τ is 68

microseconds in accordance with [Fanghänel et al., 1995] and hence, the quenching rate of Cm(III) in pure H₂O is calculated to 14.7 ms⁻¹.

$$\text{Equation 3-2} \quad K_{obs} = \frac{1}{\tau [ms]}$$

Quenching rates from measurements of Cm(III) clay suspensions in H₂O are the sum of quenching rates $K_{Cm_{Fe}}$ of the energy transfer to iron incorporated in the crystal structure of the clay minerals and the rate of H₂O $K_{Cm_{H_2O}}$ (Equation 3-3) and can be calculated using Equation 3-4. They correspond to the reciprocal value of the measured short lifetime in the H₂O system.

$$\text{Equation 3-3} \quad K_{H_2O} = K_{Cm_{Fe}} + K_{Cm_{H_2O}}$$

$$\text{Equation 3-4} \quad K_{H_2O} = K_{Cm_{Fe}} + \frac{1}{0,068ms} = \frac{1}{\tau_{kurz_{H_2O}}}$$

In the D₂O system, the quenching rate is analogous to that in H₂O.

$$\text{Equation 3-5} \quad K_{D_2O} = K_{Cm_{Fe}} + K_{Cm_{D_2O}}$$

$$\text{Equation 3-6} \quad K_{D_2O} = \frac{1}{\tau_{kurz_{D_2O}}} + 0$$

K_{D_2O} corresponds to the quenching rate of iron and thus to the reciprocal value of the measured short lifetime in D₂O, as the quenching effect of D₂O ($K_{Cm_{D_2O}} = \frac{1}{1,3ms} = 0,7 \text{ ms}^{-1}$) is negligible and can be set to zero for simplification (Equation 3-6). In Table 3-11, the quenching rates are listed for the H₂O impact, estimated from the available literature values, as well as the influence of iron, which correspond to the reciprocal value of the short lifetimes measured in D₂O.

Table 3-11. Quenching rates by energy transfer to iron that corresponds to the reciprocal value of the short lifetime in D₂O and the H₂O influence for comparison of quenching rates in the D₂O- and H₂O system.

Clay	Quenching rate Fe (in D ₂ O)	Quenching rate H ₂ O	Quenching rate H ₂ O + Fe		Fe wt.-%
	$K_{Cm_{Fe}} = \frac{1}{\tau_{kurz_{D_2O}} [ms]}$	$K_{Cm_{H_2O}} = \frac{1}{0,068ms}$	$K_{Cm_{Fe}} + K_{Cm_{H_2O}}$ [ms ⁻¹]	$K_{H_2O} = \frac{1}{\tau_{kurz_{H_2O}} [ms]}$	
SWy-1	14,5	14,7	29,2	31,3	2,97
Milos	5,3	14,7	20,0	20,4	1,3
STx-1	3,9	14,7	18,6	17,5	0,62
Na-Mont _s	3,6	14,7	18,3	16,1	0,002

The quenching rates of Cm(III) fluorescence emission by H₂O and Fe determined by different ways agree very well, so that the measurement results in H₂O and D₂O system are well comparable. The TRLFS is thus suitable as a spectroscopic method for the characterization and quantification of Cm(III) / clay outer-sphere complex formation. The difference in the quenching rates is the highest for the synthetic Na-montmorillonite with 2.2 ms⁻¹. It is also striking that the quenching rates of STx-1 and Na-Monts in D₂O with 3.9 and 3.6 ms⁻¹ differ very little, although the Fe content varies by more than two orders of magnitude.

Perhaps this could be seen as an indication of additional quenching mechanisms, such as crystal lattice defects acting as energy acceptors that can occur more frequently in synthetic clay minerals due to low time for crystallisation compared to natural clays. Using the higher sensitivity of TRLFS this effect could become noticeable in D₂O especially for Na-Mont_s as the clay with the lowest Fe content, even it is of little relevance for outer-sphere complexes compared to the energy transfer to iron.

The investigations to the An(III) / clay outer-sphere sorption presented here show that iron seemingly has the highest quenching efficiency on the fluorescence emission compared to other quenching metals such as Cu²⁺, Pb²⁺, Cd²⁺, Co²⁺, Ni²⁺, Mn²⁺, Cr³⁺ and others (Section 2.4.2.3). The quenching effect of other metals is apparently negligible in the outer-sphere complex formation and the Fe content, which correlates well with the quenched fluorescence emission lifetimes and intensities can be used to quantify the outer-sphere sorbed actinide ions. The results shown in the present study, however, point to the presence of other quenchers, such as an energy transfer to crystal defects which are caused for example by the incorporation of iron and other elements in the octahedral or as well tetrahedral layer of clay minerals. This certainly appears to have only little or no relevance in the outer-sphere sorption compared to structurally bound iron. Other elements like Mg²⁺, Mn²⁺, Ti²⁺ or the Fe²⁺ have often larger ionic radii than Fe³⁺ and generate much larger deformations. Even the substitution of Si⁴⁺ by Al³⁺ or even the much less frequent exchange of Fe³⁺ and Ti⁴⁺ in the tetrahedral layer cause extensive defects, since the exchanged elements are significantly larger than Si⁴⁺. A correlation between the levels of these elements and the measured fluorescence lifetimes and intensities could not be established so far.

Table 3-12. Ionic radii of cations that might occur in tetrahedral or octahedral layers of clay minerals.

Elements	Al ³⁺	Fe ³⁺	Mg ²⁺	Mn ²⁺	Ti ²⁺	Fe ²⁺	Si ⁴⁺	Ti ⁴⁺
Ionic radius [Å]	0.57	0.67	0.78	0.91	0.80	0.82	0.26	0.61

In the inner-sphere complex formation the fluorescence emission intensities are quenched to below 10% irrespective of iron content or the content of other elements. This quenching of fluorescence emission could be caused by crystal defects.

3.6.2 Quantification of the An(III)/clay outer-sphere complex

The Cm(III) clay outer-sphere complex formation was quantified by using the fluorescence emission decay of Cm (III) as a function of ionic strength in different clays suspensions in H₂O and D₂O. For a quantification of the outer-sphere complex formation in H₂O the montmorillonites were selected with the highest concentrations of Fe (SWy-1 and Milos). Due to the high Fe content and the resulting quenching effect the difference between the fluorescence emission lifetime of the Cm(III) aquo ion and the outer-sphere sorbed Cm(III) ion for the SWY-1 is the largest from all montmorillonite systems. In addition, the quantification of the outer-sphere complex formation was also performed with the Na-rich illite IdP-2 with an almost twice as high Fe content, but with much lower CEC than the SWy-1. Firstly, TRLFS measurements in D₂O should check, whether the measurements confirm the results in H₂O. On the other hand, the proportion of outer-sphere sorbed Cm (III) to NaMont_s that has only a small percentage of structurally bound Fe (0.002 wt -%), should be quantified with the help of the higher sensitivity of TRLFS in D₂O. This was not possible in H₂O due to the small difference between the lifetime of the aquo ions (65 microseconds) and the very low quenched outer-sphere complex (62 microseconds). In Figure 3-30 (a) the different Cm(III) fluorescence emission spectra for the SWY-1 suspension in H₂O is presented at varying ionic strengths.

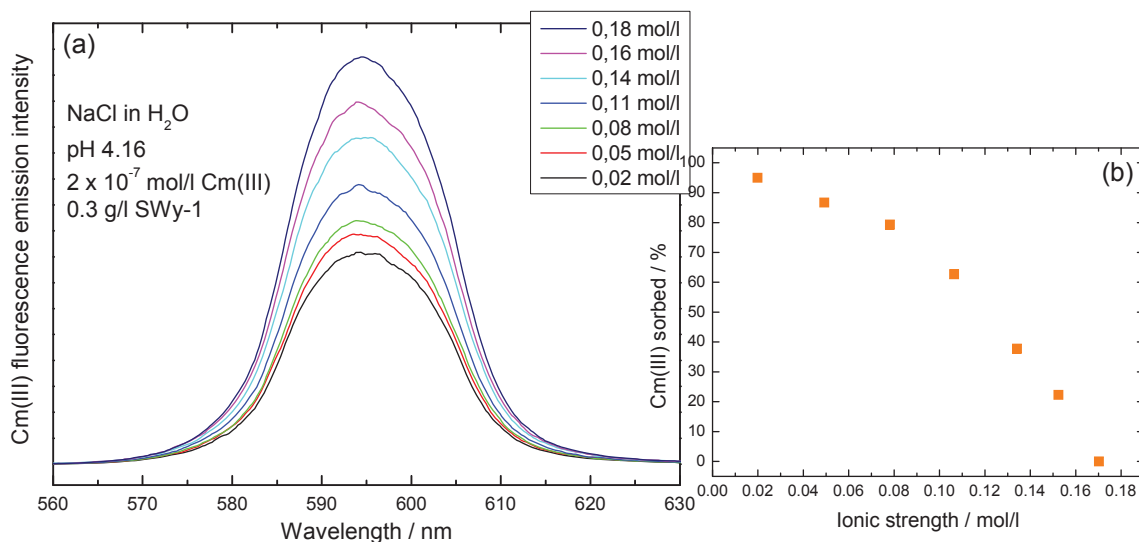


Figure 3-30: (a) Intensities of fluorescence emission of $2 \cdot 10^{-7}$ mol/l Cm(III) in aqueous SWy-1 suspensions (0.3 g/l) at pH 4.16 and different ionic strengths. The fluorescence emission spectra were taken from lifetime measurements (1 μ s delay, grating 300 lines/mm). In (b) the amounts of SWY-1 sorbed Cm(III) are shown calculated from differences in fluorescence emission intensities of emission spectra recorded at different ionic strengths.

The spectra shown are from the lifetime measurements after 1 ms time delay with a 300 lines per mm grating. By using this grating higher intensities can be achieved for the necessary

long measurement periods. The spectra are much broader than usual for fluorescence emission measurements with a grating of 1200 lines/mm, resulting in a higher resolution. With increasing ionic strength and increasing proportion of Cm (III) aquo ion in the solution and thus also a greater distance between Cm and Fe, the quenching effect of iron decreases, and hence, the fluorescence emission intensities increase. The ionic strength-dependent outer-sphere complex formation can therefore clearly be quantified by measuring the Cm(III) fluorescence emission intensities.

The amounts of Cm(III) sorbed on SWy-1 calculated from the differences of the fluorescence emission intensities in the emission spectra recorded at different ionic strengths (each at 1 ms delay) are shown in Figure 3-30 (b).

For the calculation of the sorbed amounts we assumed that approximately 95% of the curium is absorbed at an ionic strength of 0.02 mol/l. This corresponds to the amount that was quantified using the lifetimes in SWy-1 suspension (Figure 3-31). The concentration of the Cm(III) outer-sphere species quantified by fluorescence emission intensities decreases with increasing ionic strength. The decrease in fluorescence intensity with decreasing lifetime coincides with the classical Stern-Volmer theory. The validity of the relationship is illustrated by means of the fluorescence emission intensities in Figure 3-30 (a). The intensity of F_1 of the outer-sphere sorbed Cm(III) on SWy-1 is half of F_0 , which also corresponds to the ratio of lifetimes ($65 \mu\text{s}/32 \mu\text{s} = \tau_0/\tau_1$). From this result one can conclude that the assumption of an active dynamic quenching process is correct. F_0 was measured at a concentration of NaClO_4 of 0.2 mol/l where the Cm(III) is exclusively present as dissolved aquo ion. In Figure 3-31, the Cm(III) fluorescence emission lifetimes for the SWy-1 suspension that corresponds to the fluorescence emission spectra in Figure 3-30 (a) are shown at varying ionic strength. The decreasing quenching effect of Fe(III) on the fluorescence emission due to the exchange reaction of Cm^{3+} by Na^+ with increasing ionic strength is documented by the increasing fluorescence lifetimes. At an ionic strength of 0.01 mol/l a lifetime quenched by H_2O and Fe(III) of only 32 microseconds was measured in the SWy-1 suspension, while the lifetime is $\tau = 65$ microseconds at 0.20 mol/l. This time period corresponds to the fluorescence emission lifetime of the non-sorbed Cm (III) aquo ion.

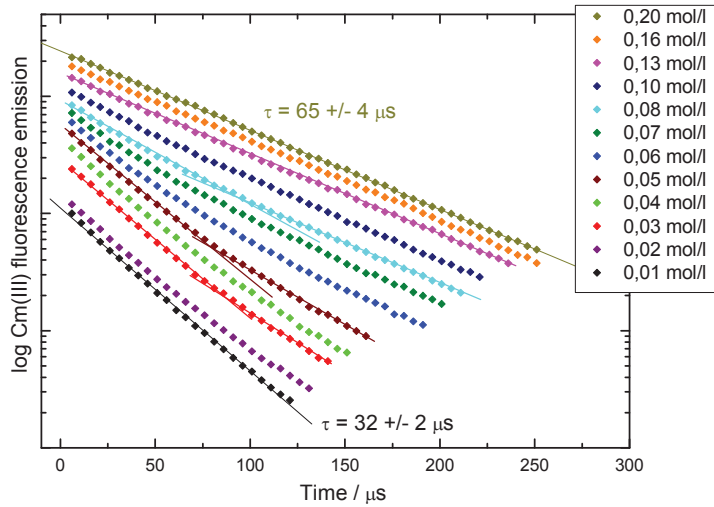


Figure 3-31: Cm (III) lifetimes in aqueous SWy-1 suspension ($2 \cdot 10^{-7}$ mol/L Cm (III), 0.3 g/l) at pH 4.16 and various ionic strengths (plotted arbitrarily for clarity). The time dependence of the fluorescence emission shows a mono-exponential decay at low and high ionic strength and a bi-exponential decay at intermediate ionic strengths.

Using the measured fluorescence emission intensities or lifetimes the outer-sphere complex formation between Cm (III) and SWy-1 could be quantified by considering the different fluorescence yields for the outer-sphere sorbed species and the aquo ion in the bulk solution. The fractions (F_0 and F_1) for aquo ion and outer-sphere complex can be obtained by bi-exponential fitting of the fluorescence decay measured at different ionic strengths. The lifetimes were fixed at 65 microseconds (Cm^{3+} aquo ion) and 32 microseconds (outer-sphere sorbed Cm^{3+}). For the outer-sphere complex the quenched lifetime determined at an ionic strength of 0.01 mol/l was used. The decrease in fluorescence with time follows a bi-exponential rate law:

Equation 3-7
$$F(x) = F_0 \cdot e^{-\frac{x}{\tau_0}} + F_1 \cdot e^{-\frac{x}{\tau_1}}$$

$F(x)$: Total fluorescence emission intensity at time x

τ_0 und τ_1 : Fluorescence emission lifetimes of Cm(III) aquo ions or outer-sphere complex

F_0 und F_1 : Total fluorescence emission intensity at time $x = 0$ of Cm(III) aquo ions or outer-sphere complex

The following applies:

Equation 3-8
$$F_0 + F_1 = 100 \%$$

However, the quantum yield generally decreases slightly with decreasing fluorescence emission lifetime, ie Equation 3-8 only conditionally applies. The lower quantum yield for the quenched lifetime of the outer-sphere complex was considered mathematically by calculating the real outer-sphere fraction from the resulting percentage for the outer-sphere complex multiplied by τ_0/τ_1 and from the sum of the result and the percentage of the real aquo ion. The R_d values were converted into [% sorbed] according to Equation 3-9. The experiments were carried out at a solution to solid ratio of 0.3 g / liter.

$$\text{Equation 3-9} \quad \%_{\text{sorbed}} = 100 \cdot \left(\frac{R_d}{R_d + \frac{V}{m}} \right)$$

V: volume of bulk solution [l]; m: mass of the clay [kg]

In Figure 3-32 the fractions of the Cm(III) outer-sphere sorbed to SWy-1 determined by using the fluorescence emission lifetimes are shown as a function of the ionic strength. At low ionic strengths (<0.01 mol/l) more than 98% of Cm (III) are sorbed as outer-sphere complex on the SWy-1 surface. With increasing ionic strength the fraction of sorbed Cm^{3+} decreases. At an ionic strength of about 0.19 mol/l more than 99% of the Cm ions are in solution and the Cm(III) outer-sphere complexation on the clay mineral is less than 1%.

Also, the outer-sphere complex formation of Cm^{3+} on the Na-rich montmorillonite Milos was quantified by TRLFS (Figure 3-32) by utilising the ionic strength effect. The lifetimes were fixed each at 65 microseconds (Cm^{3+} aquo ion) and 49 microseconds (outer-sphere sorbed Cm^{3+}). The quenched lifetime of Cm (III) outer-sphere complex was determined at an ionic strength of 0.01 mol/l (Figure 3-26). At ionic strengths <0.01 mol/l over 97% of the Cm (III) is sorbed as outer-sphere complex. The sorption again decreases with increasing ionic strengths. Furthermore, the fraction of the outer-sphere complex of Cm (III) on illite IdP-2 is displayed in Figure 3-32 as a function of the ionic strength. To quantify the outer-sphere complex formation, each lifetimes were fixed at 65 microseconds (Cm^{3+} aquo ion) and 27 microseconds (outer-sphere sorbed Cm^{3+}). The quenched lifetime of Cm (III) outer-sphere complex of 27 microseconds was determined again at an ionic strength of 0.01 mol/l (Figure 3-28), in which only ~ 85% of the Cm (III) is sorbed on illite. With increasing ionic strength the Cm^{3+} is released more easily into the solution than in montmorillonites. The reasons for the decreased sorption on illite at low ionic strengths compared to the montmorillonite are explained in more detail in [Section 5.2.1](#).

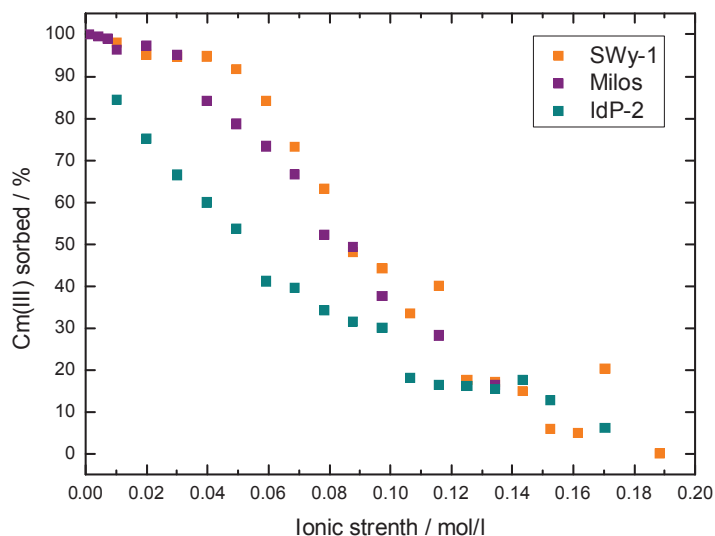


Figure 3-32: Cm(III) outer-sphere complexation in H₂O on SWy-1 at pH 4.16, Milos at pH 3.97 and IdP-2 at pH 4.02 as a function of ionic strength ($2 \cdot 10^{-7}$ mol/l Cm(III), 0.3 g/l).

In Figure 3-33, the Cm (III) fluorescence emission lifetimes for Na-Mont_s in D₂O are shown at varying ionic strength. By bi-exponential curve fitting of the fluorescence decay the fraction of sorption of Cm³⁺ + via outer-sphere complex formation can be quantified analog to the experiment in H₂O. The each long life was fixed at 1250 microseconds (Cm³⁺ aquo ion). For the outer-sphere complex, the short lifetime at an ionic strength of 0.01 mol/l was taken. These are shown in Figure 3-27.

Even slight contamination in solution, which can not be excluded from the the sample preparation, can cause quenching. But their effect on quenching rates ($1/\tau$) can be neglected. The values for τ_{long} are not the same for all experiments and are usually somewhat lower than the theoretical value for the aquo complex in D₂O. It is therefore assumed that traces of H₂O as a contaminant are present in the D₂O solution.

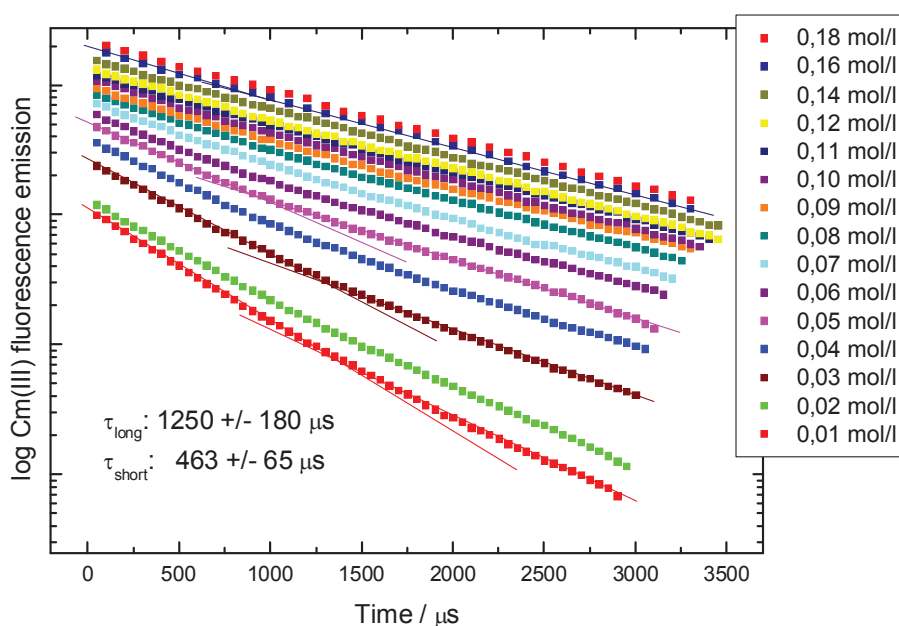


Figure 3-33: Cm(III) life time in clay suspensions of synthetic Na-montmorillonite NaMont_s in D₂O (2·10⁻⁷ mol/l Cm(III), 0.3 g/l) at pD 4.12 and various ionic strengths (plotted arbitrarily for clarity). The fluorescence emission shows a bi-exponential decay (τ_{long} = Cm(III) aquo ion, τ_{short} = Cm(III) outer-sphere complex).

In Figure 3-34 the results of the quantification of the outer-sphere complexation of Cm (III) on various clays in D₂O are plotted. The sorption curves are in good agreement within the error limits and are consistent with the calculated values of the outer-sphere complex formation in H₂O (Figure 3-32).

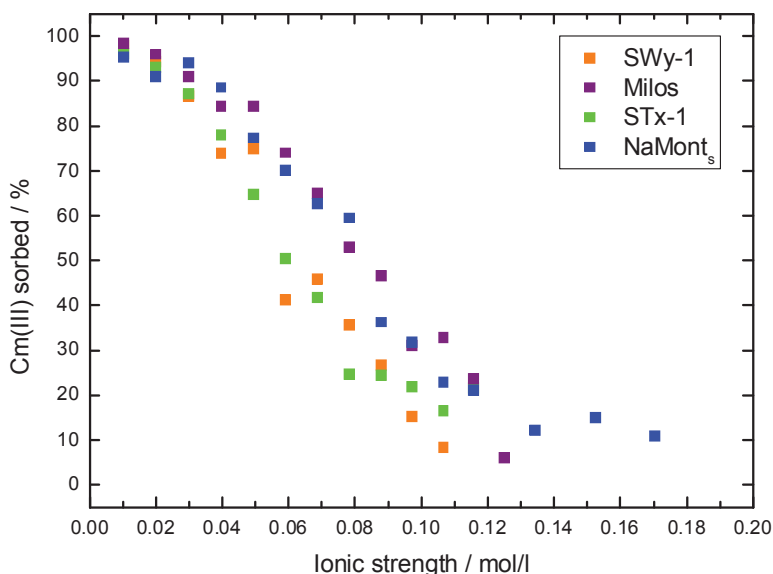


Figure 3-34: Cm(III) outer-sphere complexation in D₂O on SWy-1 at pD 3.99, Milos at pD 3.76 and NaMont_s at pD 4.12 as a function of ionic strength (2·10⁻⁷ mol/l Cm(III), 0.3 g/l)

Modelling of the Cm (III) / clay outer-sphere complex formation

The experimental quantification of the outer-sphere complex formation between Cm (III) and clay were additionally described by model calculations. Cation exchange reactions, forming outer-sphere complexes on clay minerals can be expressed with a selectivity coefficient. This is obtained by applying the mass action Act. The model calculations of the cation exchange experimentally investigated by TRLFS were performed for Na⁺-background concentrations between 0.01 and 0.2 mol/l. A selectivity coefficient of 30 ($I = 0$) was applied for the Cm-Na exchange reactions. This value was deduced from Eu-Na exchange experiments on montmorillonite (SWy-1) [Bradbury&Baeyens, 2005a]. For the model calculations 881 meq / kg and 937 meq / kg for SWy-1 and Milos, respectively, were applied as CEC (Table 25). All other parameters used in the calculations, such as protolysis, types and capacities of sorption sites are listed in Chapter 3.3 (Table 19). In Figure 3-35 the experimental and modeled data of the sorption of Cm³⁺ by outer-sphere complex formation on Na-rich montmorillonite and SWy-1 in H₂O, are shown as a function of ionic strength. The modeled results are in good

agreement with experimental data within the uncertainties of the analytical methods and the values for the selectivity coefficients and within the experimental error.

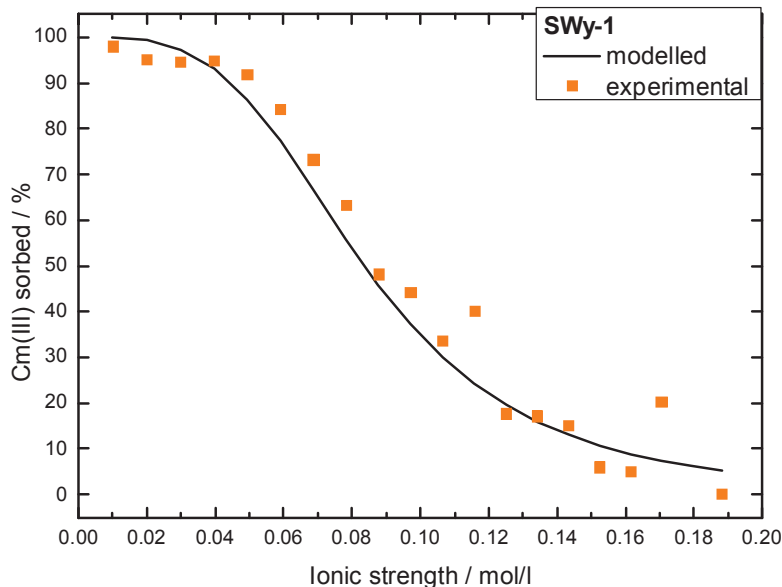


Figure 3-35: Comparison of modelled and experimental results for Cm (III) outer-sphere complex formation on SWy-1 in H₂O by TRLFS at pH 4.16 (experiment A) or pH 4.07 (experiment B) as a function of ion strength ($2 \cdot 10^{-7}$ mol/l Cm(III), 0,3 g/l).

The experimental and the modelled data of the outer-sphere complex formation of Cm³⁺ on the Na-rich montmorillonite Milos in H₂O are shown in Figure 3-36. Milos-montmorillonite has a higher cation exchange capacity (937 meq / kg) than SWy-1 (881 meq / kg). Hence, the Cm(III) sorption decreases less rapidly for Milos than for the SWy-1 at ionic strengths > 0.01 mol/l. The experimentally determined values agree very well with those from the model calculation.

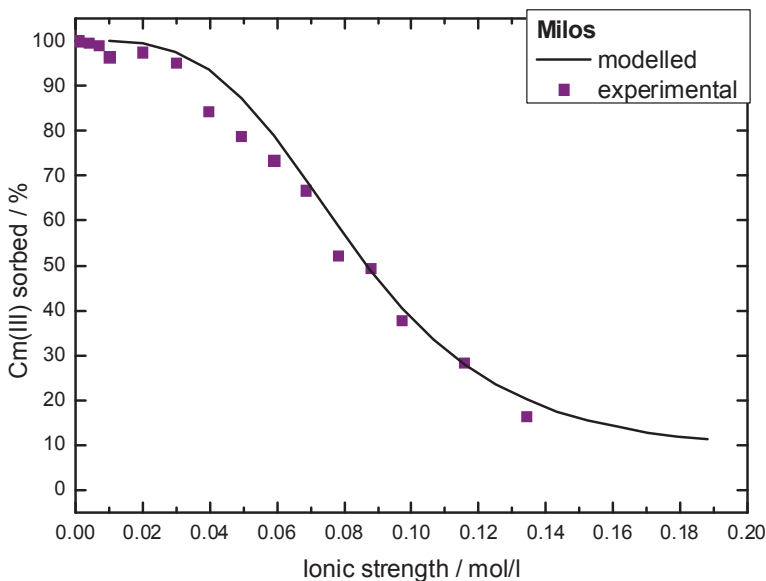


Figure 3-36 Comparison of modelled and experimental results for Cm (III) outer-sphere complex formation on Milos montmorillonite in H₂O at pH 3.97 as a function of ion strength ($2 \cdot 10^{-7}$ mol/l Cm(III), 0,3 g/l).

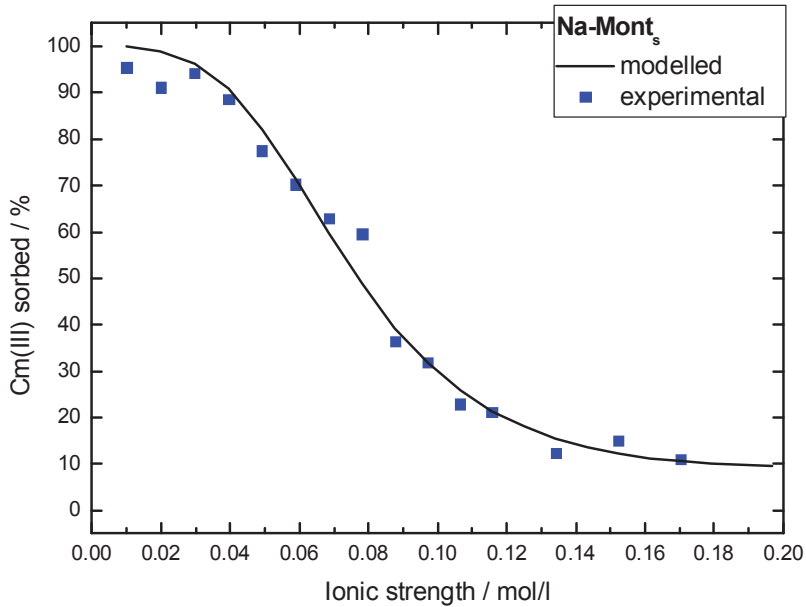


Figure 3-37 Comparison of modelled and experimental results for Cm (III) outer-sphere complex formation on synthetischem Na-montmorillonite NaMont_s in D₂O at pD 4.12 as a function of ion strength ($2 \cdot 10^{-7}$ mol/l Cm(III), 0,3 g/l). Assumptions for modelling see in the text.

In Figure 3-37 the modelled and experimental results of Cm(III) sorbed on synthetic Na-montmorillonite (CEC = 630 meq / kg) in D₂O are shown. Again, experimental and modelled data match very well. A quantification of the outer-sphere complexation can only be carried out in D₂O because of the higher sensitivity TRLFS in this medium. The much higher sensitivity makes on one hand sorption studies of clays with very low Fe content possible. On the other hand broad applications are offered to investigate spectroscopically sorption processes with other minerals containing iron at trace concentrations.

The experimental results of outer-sphere sorption experiments with Milos and STx-1 – both clays with very similar CEC – are shown in Figure 3-38. It is obvious that the calculated values deviate significantly from the experimental results for the STx-1, whereas the values match for Milos. The reason of the discrepancy might be due to a contamination of the STx – D₂O suspension with small amounts of H₂O (see also Figure 3-27). The long lifetime, which is used to quantify the Cm (III) outer-sphere sorption, is quenched to ~ 661 microseconds.

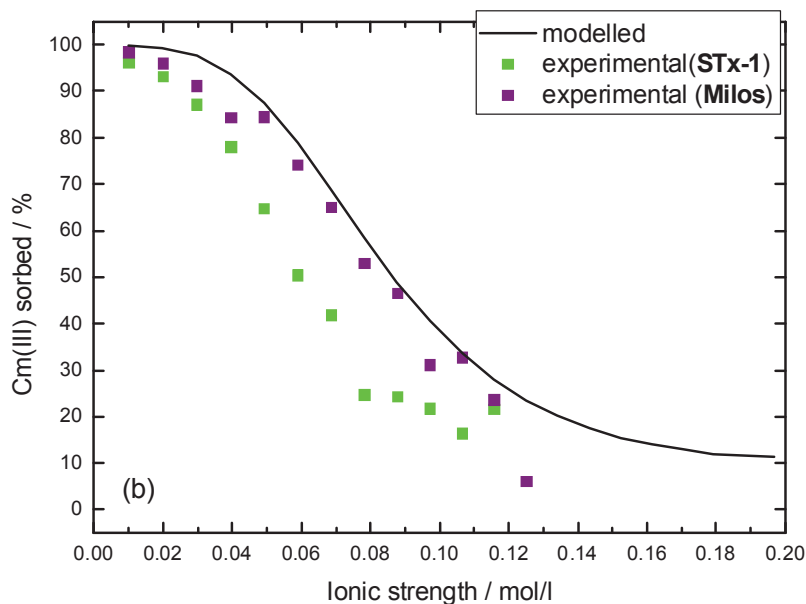


Figure 3-38: Comparison of modelled and experimental results for Cm (III) outer-sphere complex formation on Milos and STx-1 at pD 3.76 and pD 4.01 in D₂O as a function of ion strength ($2 \cdot 10^{-7}$ mol/l Cm(III), 0,3 g/l). Assumptions for modelling see in the text.

In Figure 3-39, the TRLFS results for Cm (III) sorption on IdP-2 in H₂O are compared with the modeled values. It was used by a selectivity coefficient of ${}_{Na}^{Cm}K_c = 76$, which was deduced from studies of the sorption of Eu (III) on illite du Puy (IdP-1 and IdP-2 [Bradbury & Baeyens, 2005b]). The modelled curve overestimates significantly the Cm(III) sorption (black curve in Figure 3-39) at low ionic strengths. Again, a partial dissolution of the clay at pH \sim 4 is assumed. During the reaction period particular aluminum and divalent cations such as Ca²⁺ and Mg²⁺ were released in relevant concentrations from the crystal structure of clay minerals into the solution (s. Table 3-13). These cations and Cm³⁺ compete for the available binding sites on the clay primarily at low ionic strengths. With increasing ionic strengths the competing cations are exchanged by Na⁺ from solution. Die Al³⁺ concentration is censoriously compared to Ca²⁺ or Mg²⁺ due to its higher charge and tendency for sorption. [Bradbury & Baeyens, 2005b] have measured the cation concentration as a function of ionic strength in their sorption experiments with Illit du Puy and found about 10^{-5} mol/l for Al³⁺, and about 10^{-4} mol/l for Ca²⁺/Mg²⁺. The model calculation in Figure 3-39 was performed by regarding the competing of these cations in solution of our own Eu(III) batch experiments at various ionic strengths. For the modelling the highest concentration found in the experiment were taken: Al³⁺ = $6,09 \cdot 10^{-5}$ mol/l, Ca²⁺/Mg²⁺ = $2,49 \cdot 10^{-5}$ mol/l. Other cations like Ti⁴⁺ and Mn²⁺ had much lower concentration that are relevant and they were neglected. The applied selectivity coefficient of ${}_{Na}^{Al}K_c = 10$ and ${}_{Na}^{Me^{2+}}K_c = 11$ (Me²⁺ = Ca²⁺, Mg²⁺) were depicted from [Bradbury & Baeyens, 2005b].

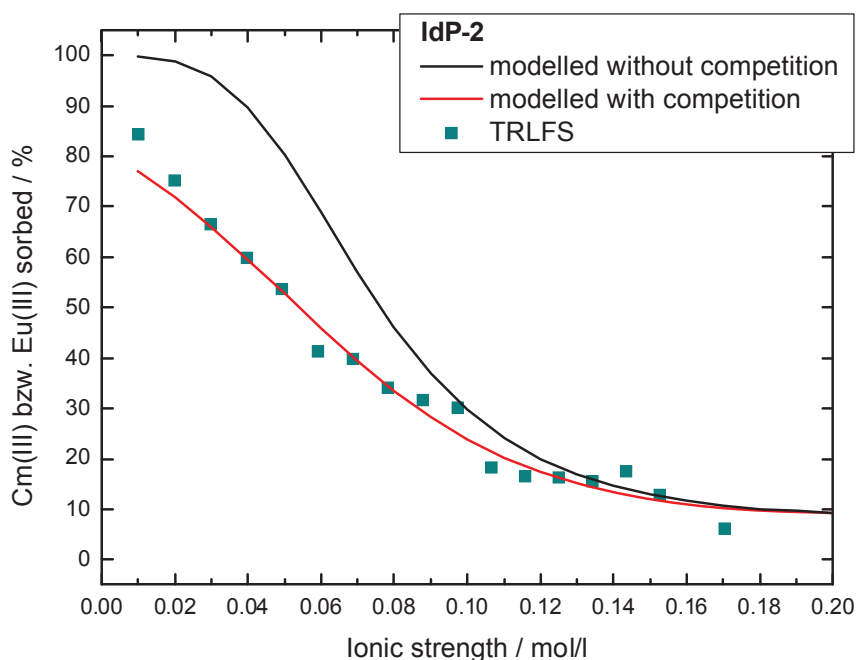


Figure 3-39: Comparison of modelled (with and without considering other competing cations) and experimental results for Cm (III) outer-sphere complex formation on IdP-2 in H₂O by TRLFS at pH 4.02 as a function of ion strength ($2 \cdot 10^{-7}$ mol/l Cm(III), 0,3 g/l). Competing cations: $6.09 \cdot 10^{-5}$ mol/l, Al³⁺ and $2.49 \cdot 10^{-5}$ mol/l Ca²⁺/Mg²⁺.

The modelled curve by regarding the competing cations agrees now very well with the experimental data measured by TRLFS. Additional calculation showed that at ionic strengths $> 0,1$ mol/l less than 10% of the total Al³⁺ in solution is sorbed on the clay. The percentage of Al³⁺ sorption increases very strongly with decreasing of the ionic strength below 0.1 M ionic strength. Therefore, the competing effect has only small or no effect on the Cm³⁺ sorption at ionic strengths above 0.1 M.

IdP-2 possesses a significant lower CEC as montmorillonite. Therefore, competing effects due to ions released from the clay at tracer concentrations plays a minor role for montmorillonite.

Table 3-13: Concentrations of cations Al³⁺, Ca²⁺ and Mg²⁺ in aqueous clay suspension due to partial dissolution of the respective clay at pH ~4. Black: elements of batch experiments; blue: elements of the TRLFS experiments.

Clay suspension Sample		Al ³⁺ [mol/l]			Ca ²⁺ [mol/l]			Mg ²⁺ [mol/l]		
		lowest	Ø	largest	lowest	Ø	largest	lowest	Ø	largest
IdP-2	Batch	1.76E-05	3.57 E-05	6.09E-05	8.40E-06	8.81 E-06	1.27E-05	3.94E-06	7.48E-06	1.22E-05
	TRLFS		2.93E-06			1.73E-05			2.96E-06	
SWy-1	Batch	1.47E-05	3.81E-05	1.04E-04	1.14E-05	1.23E-05	1.39E-05	2.70E-06	9.56E-06	1.73E-05
	TRLFS		<5.56E-07			1.45E-05			3.00E-06	
STx-1	TRLFS		<5.56E-07			2.01E-05			2.57E-06	
	TRLFS		2.94E-06			2.32E-05			1.78E-05	
Na-Mont ₂	Batch	1,34E-05	3,44E-05	6,81E-05	1,44E-05	2,24E-05	3,50E-05	1,20E-05	1,74E-05	3,06E-05

Batch experiment on Eu(III)/clay outer-sphere complexation

In Figure 3-40 the results of batch experiments with Eu(III) and IdP-2, SWy-1 and the synthetic Na-montmorillonite are compared with each of the modeled values. Here too, experiment and calculation agree quite well within the uncertainties. Deviations are particularly recognizable at higher ionic strengths. An explanation for this behaviour can not be given at the moment.

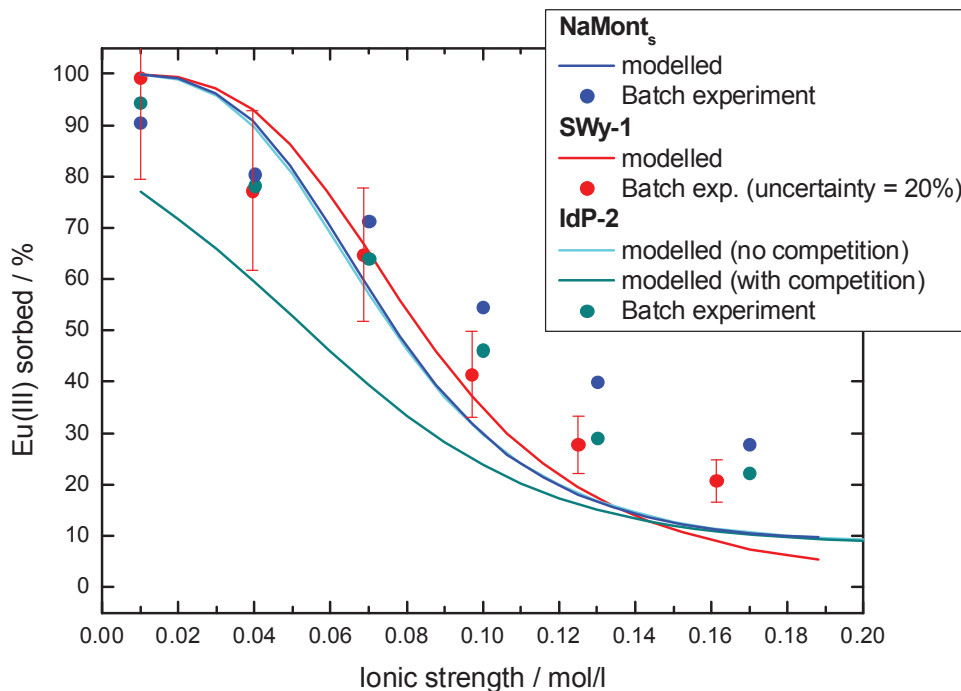


Figure 3-40: Comparison of modelled and experimental results of batch experiments on Eu(III) outer-sphere complex formation on NaMont_s, SWy-1 and IdP-2 in H₂O at pH 3.88 to 4.02 as a function of ionic strength ($2 \cdot 10^{-7}$ mol/l Eu(III), 0.3 g/l). The uncertainty of the method is estimated to be 20 %.

4 Studies of the diffusion of actinides and analogs

Owing to its small hydraulic conductivity (10^{-14} - 10^{-13}), it is expected that transport of solutes will be dominated by diffusion. The objective of this work is to understand actinide diffusion in clay mineral-rich geological formations in order to provide support for improved representation of these processes in performance assessment and to enhance safety case credibility. This study addresses the diffusion of tritiated water (HTO) and ^{238}Pu . The samples were collected in the Mont Terri underground laboratory where the OPA is situated -200 to -300 m below the surface. Therefore a sample cell -autoclave system (SCAS) was required for carrying out actinide diffusion experiments in clay stones under their natural, confining pressure. In our experiments we used ^{238}Pu Plutonium. ^{238}Pu is a radioactive isotope of plutonium with a half-life of 87.7 years and is an alpha emitter. Because of its alpha activity ($6.3 \cdot 10^{11}$ Bq/g), it can be measured by α -spectrometry down to very low concentrations (detection limit in our experimental set-up $1 \cdot 10^{-11}$ mol/L). This is important because of the low solubility of Pu in natural waters (Coppin, 2003).

4.1 Diffusion of Pu in OPA clay rock

4.1.1 Experimental set-up

The design of the INE diffusioll cell/autoclave system (SCAS)

To counteract the swelling of clay in contact with groundwater, to avoid disaggregation and to simulate the confining stress within the geological formation, a specifically adapted experimental set-up was developed. The heart of the diffusion cell is a thin-walled stainless steel cell (Figure 4-1) which holds the clay sample (0 20 mm, length 10 mm). All parts of the diffusion cell which are in contact with solution are coated with PEEK. The thickness of the wall of the stainless steel is 2/10 mm. After the positioning of the sample, two PEEK distribution plates are placed on each side of the sample and the autoclave is sealed with screws. This cell is then placed in an autoclave. This autoclave has a volume of 300 ml and is filled with 250 ml of water. With help of a stainless steel pump we pressurized the autoclave with pressures between 0-100 kbars.

Due to the construction of the cell, the confining pressure acts isotropically onto the clay sample. The tubing for tracers and sampling are constructed in such a way that they are kept under ambient pressure and tracer injection and sampling can be performed in closed circulation loops

The solutions are circularly pumped from 100 mL PE storage containers in split cycles with a 2-channel peristaltic pump (IPC, Ismatec, 1dex, USA). The Opalinus Clay samples were re-

saturated by circulating these solutions in contact with the respective end of the sample for 5 weeks. This time was found to be sufficient to reach re-saturation (Van Loon et al., 2003). Subsequently, the solutions were replaced by fresh ones and the solution in one container was spiked with the desired tracer.

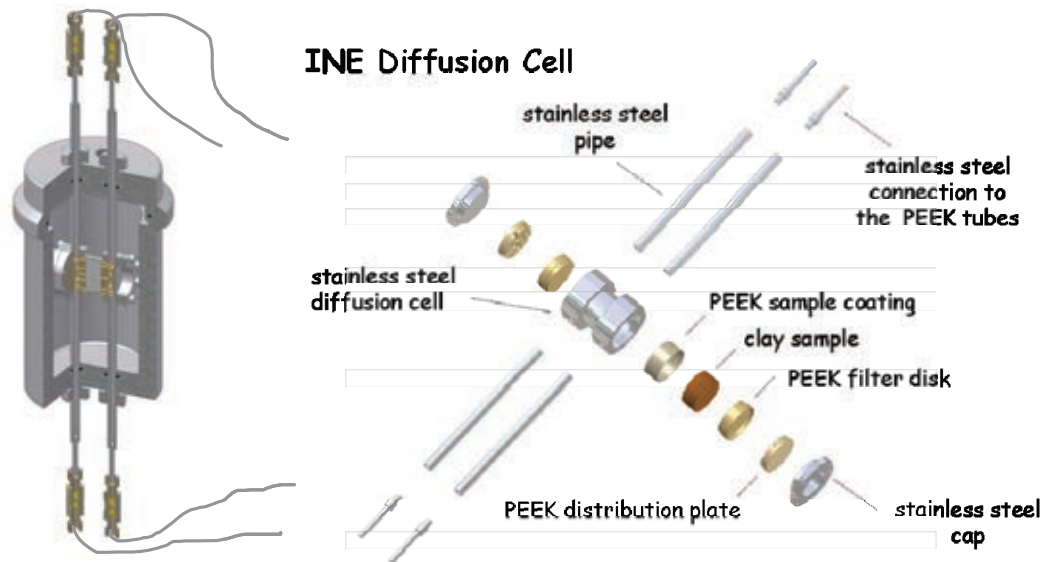


Figure 4-1: Schematic presentation of the INE diffusion cell/autoclave system (SeAS). On the left side the autoclave with the core holder and the feeding system (two pipes connected via tubes with the peristaltic pumps) is shown. On the right side the diffusion cell is illustrated.

Sample preparation and characterisation

The Opalinus (OPA) clay stone sample used for our experiments was provided by NAGRA from the Mont Terri underground research laboratory (URL). All preparation steps were performed under anaerobic conditions in a glovebox. The bore core (BEZ A24/3) with a diameter of 100 mm was sliced into 2-cm-thick pieces using a diamond saw (no lubricating fluid was used). Each slice was cut in two parts. A 20 mm diameter core was drilled out of the inner part of each slice to avoid the use of artificially oxidized clay rock material. All samples were drilled perpendicular to the bedding plane.

The residue of the core was ground in a glove box and the mineralogy of the samples was determined using X-ray diffraction. Quantitative analysis was performed using the Rietveld method (TOPAS, Bruker AXS). The mineralogical composition is comparable to the one published in (NAGRA, 2002). The porosity of the sample measured by mercury porosimetry was 10 %. The total organic matter (TOC) in the starting material was measured to be 0.5-1.3 wt % using a LECO-125 CIS analyser. The chemical composition of the sample was determined by XRF.

After completion of the diffusion experiments the samples were pushed out of the diffusion cell and embedded in epoxy-resin (Struers, Fellbach, Germany) to avoid drying out of the

sample. These samples were cut perpendicular to the bedding in two pieces using a diamond saw in the glove box (no lubricating fluid was used) after the epoxy-resin had hardened. The intersection was cleaned with Tesafilm (Beiersdorf, Hamburg) to remove remaining sawdust.

One half of the sample was used for autoradiography. As detector the phosphor storage screen technology was used (Cyclone, Storage Phosphor System, Packard Instrument Company, USA). The measurement period was between 1 h and 7 days. Radiation is stored in reusable phosphor screens of BaFBrEu²⁺ crystals as defect energy. For reading out, the screens are scanned with a red laser and the emission of blue light stored in crystal defects is detected. The main advantages compared to film techniques are the higher sensitivity and the enhanced linear dynamic range. The lateral resolution is 600 dpi equal to about 40 μm . The α -activity of the Pu in the diffusion sample was determined against a 500 ppm NIST standard of natural ²³⁸U.

In the other half of the sample, the diffusive Pu profile in the rock was determined using the high-resolution abrasive peeling method [Van Loon and Eikenberg, 2005]. Therefore, the sample was mounted on a sample holder and 46 grinding steps using a P220 abrasive paper and 32 grinding steps using a P80 abrasive paper were performed. The grinding paper was manufactured by Struers (Fellbach, Germany). The grinded samples were acidified (HN03, HF and HCl) and shaken for 24 hours. Parts of the grinded samples were used to determine the mineralogy by X-ray diffraction. Therefore a few mg were diluted in ethanol and placed on a silicon wafer (cut in the 711 direction) sealed airtight with a XX dome.

Artificial porewater

The recipe for the artificial pore water used in the diffusion experiments is given in [Van Loon et al., 2003]. Analytical grade chemicals were used to prepare the artificial pore water. The pH was adjusted to the desired values using NaOH and HCl. All the solutions were prepared with deionized water Milli-Q Reagent Water System from Millipore with a resistivity of $> 18 \text{ M}\Omega \text{ cm}^{-1}$. The solution pH was measured using an Orion 525A with a Ross electrode calibrated using 4 standard buffers (pH 3, 5, 7 and 9, Merck). Redox potentials were measured with a Orion 525A using a METROHM InLab®Redox Ag redox electrode. Commercial redox-buffers (220mv and 640 mV, Schott instruments) are used for calibration. The measured potential was converted into Eh versus standard hydrogen electrode (SHE) by correction for the potential of the Ag/AgCl reference electrode. The evolution of the Eh was in one experiment continuously in-line measured using an IONODE SI30 gel redox-electrode. The initial and final pH and Eh of the OPA porewater is given in Table 4-1.

Table 4-1: Experimental details of the Pu diffusion experiments. D_e is the effective diffusion coefficient.

Run number	Run time (days)	D_e HTO OPA (\perp) to bedding ($m^2 s^{-1}$)	Initial/final ^{238}Pu conc. (nmol/L)	Initial pH / Eh (V)	Final pH/Eh (V)
HTO test	100	1.53×10^{-11} $6.6 \pm 0.5 \times 10^{-12}$	-	7.8 / 0.360	7.9 / 0.370
OPA1-SCAS1	150*	1.55×10^{-11}	7.64 / 0.028	7.8 / 0.360	8.4 / 0.030
OPA1-SCAS2	280	1.60×10^{-11}	5.63 / 0.287	8.4 / 0.400	8.5 / 0.390
OPA2-SCAS3	93	1.45×10^{-11}	5.38 / 0.312	7.9 / 0.380	8.2 / 0.370

* 120 days in and 30 days out diffusion

Activity measurements

The activity of the Pu and HTO in solution was measured by liquid scintillation counting (LSC). For Pu 100 III of the sample was acidified with 20 III of 65 % HNO_3 . Then 20 III was placed in a 20-ml polyethylene (PE) counting vial and 10-ml scintillation cocktail was added (Ultima Gold XR, Canberra-Packard). For HTO 20 III of the sample was placed in a 20-ml polyethylene (PE) counting vial and 10-ml scintillation cocktail was added (Ultima Gold XR, Canberra-Packard). The samples were vigorously shaken and placed in a liquid scintillation counter (Quantulus, WALLAC).

The counting efficiency for each tracer was measured using artificial pore water with known amounts of activities. Background measurements were performed in a similar way using artificial pore water without radiotracers. The detection limit of the LSC for Pu in the OPA porewater is about 2×10^{-11} mol/L.

HTO and Pu diffusion in OPA

To test our experimental set-up (e. g. excluding boundary flow effects) and to compare our diffusion cell with other diffusion cells used in literature we performed HTO experiments according to [Van Loon et al., 2003].

The ^{238}Pu diffusion experiments were performed at four different run times and different initial pH values (see Table 4-1). All 3 samples were made out of a drill core from Mont Terri provided by NAGRA.

Pu oxidation states in solution

The Pu oxidation states (Figure 4-2) as a function of time in the Opalinus porewater were determined by PMBP-extraction [Nitsche et al., 1994]. In the stock Pu solution we used in our experiments 15 % Pu(IV) and 85 % Pu(VI) were initially determined in solution.

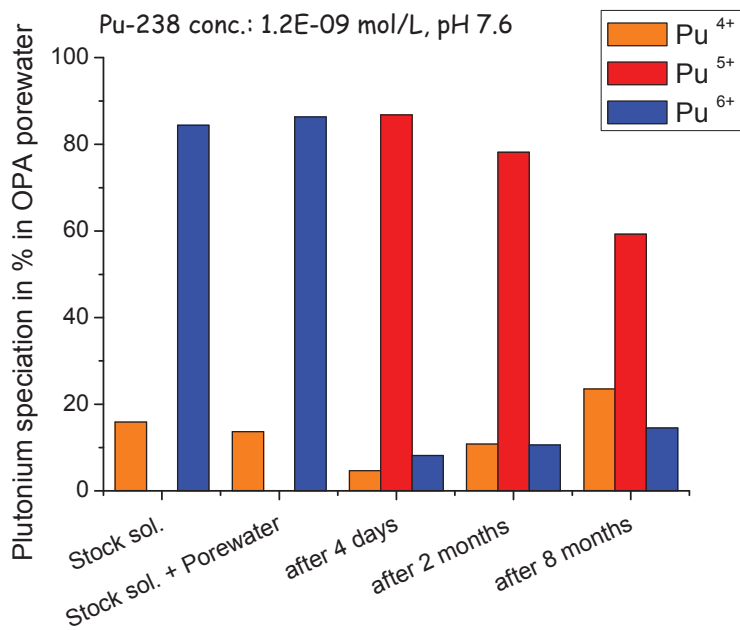


Figure 4-2: Evolution of the Pu speciation in the OPA porewater. The sorbed Pu(IV) from the container walls was added to the Pu(IV) in solution

4.1.2 Results

HTO diffusion in OPA

With four different OPA samples we measured the effective diffusion coefficient (D_e) perpendicular to the bedding for HTO. We used HTO to verify if our diffusion cells show any preferential pathways. All values are given in Table 1. The average D_e was found to be $1.53 \cdot 10^{-11}$ m²/s. All obtained results are within a variation range of 10 % of the average value. In one experiment (HTO Test) we cut the diffusion core at the end of the HTO experiment into a half to verify by autoradiography if the HTO diffusion was homogeneous within the core (Figure 4-3). The HTO distribution in the OPA is homogenous. No preferential pathway or any enrichment of the HTO within the sample was detected.

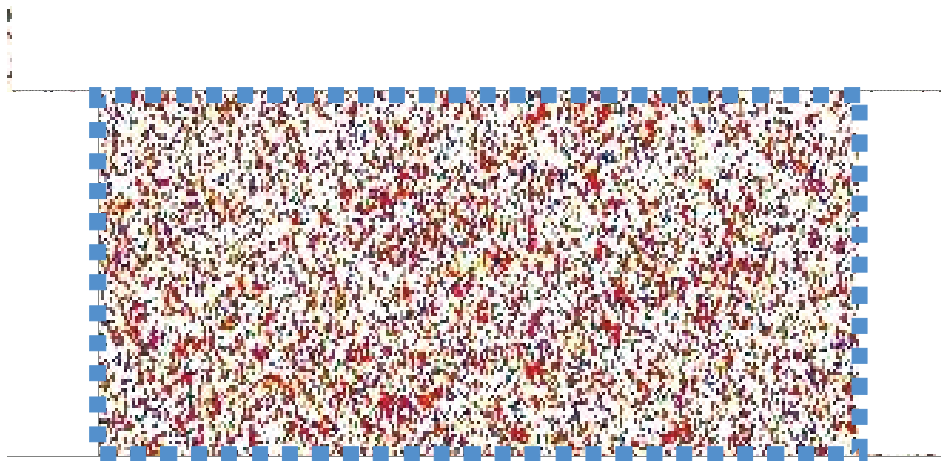


Figure 4-3: HTO diffusion in the OPA visualized by autoradiography. The blue rectangle represents the OPA core. Red indicates high HTO activity. The cooler the color gets the lower the HTO concentration. It can be seen that the HTO is distributed homogeneously within the OPA core.

Evolution of the Pu oxidation states in the OPA porewater

The Pu oxidation states (Figure 4-2) as a function of time in the Opalinus porewater, in which was no reducing component, were determined by PMBP-extraction [Nitsche et al., 1994] for a period of one year. In the Opalinus porewater the pH was adjusted in the beginning to pH 8.2 and the Eh was ~ 380 mV. No change in pH and Eh was observed during the experiment. Whereas in the stock solution 85 % Pu(VI) and 15 % Pu(IV) were observed, the Pu oxidation state changed predominantly to Pu(V/VI) (72 %) after 4 days equilibration time in the OPA porewater. The evolution of the Pu-238 concentration in solution indicates with increasing run time a continuous but steady decrease of the Pu concentration. After one year, only 26 % of the initial Pu was found in solution. After washing the container with HNO₃ at the end of the experiment the Pu were found to be sorbed on the container walls. This Pu was found to be nearly 100 % Pu(IV). Adding the sorbed Pu from the container walls to the Pu in solution (Figure 4-2) the Pu oxidation states changed to 83 % Pu(IV) and 17 % of Pu(V/VI) in the OPA. In the experiments with clay minerals present no sorption on the container wall was detected.

Results of the Pu diffusion in OPA

Three different diffusion experiments are presented, two behave equally and one is different (Figure 4-4). For OPA1-SCAS1 we observed a first strong and fast decrease in the Pu reaching a "steady state" concentration of $2.7 \cdot 10^{-11}$ mol/L after seven days. During the experimental run time of 150 days the pH shifted from 7.83 to 8.43 and the Eh dropped from 430 to 30 mV. In the two other experiments the pH and the Eh of the OPA porewater remained unchanged throughout the experiment. The Pu concentrations dropped in OPA1-SCAS2 by one order of magnitude of $\sim 6 \cdot 10^{-10}$ mol/L after 16 days. In the OPA2-SCAS3 experiments the decrease in

the Pu solution concentration appeared faster. After 70 days the Pu concentrations for both systems converged and reached a "steady state" concentration of $\sim 3 \cdot 10^{-10}$ mol/L.

At the end of the experiment OPA2-SCAS3 (93 days) the Pu oxidation state in the solution was determined. Like in the OPA porewater in contact with the Opalinus clay, we found as the dominant oxidation state Pu(V/VI) whereas on the OPA Pu(IV) was dominant.

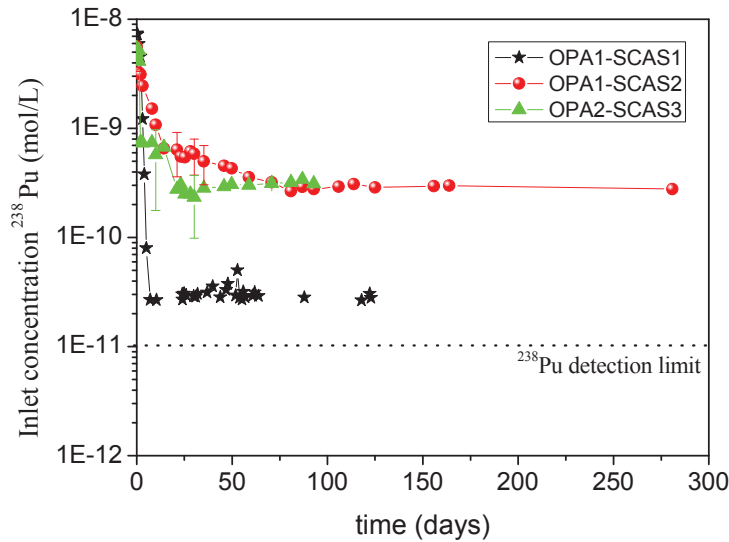


Figure 4-4: Evolution of the solution ^{238}Pu concentration in the diffusion experiment as a function of time

On the blank concentration side of the all 3 experiments the first α -activity was measured after 30 days experimental duration. A selective Pu extraction indicated that the detected α -activity was not due to through-diffusion of ^{238}Pu , but came from ^{228}Th released to the solution from the Opalinus clay sample.

At the end of the experiments the autoclave system and connected tubings were washed for two hours with 65 % HNO_3 to check sorption to the experimental set-up. This test showed that around 20-40 % of the initial ^{238}Pu concentration was sorbed on the container walls and the tubings of the diffusion experiment.

Out diffusion experiments

After 120 days of experimental run time we replaced the Pu spiked OPA porewater of the OPA1-SCAS1 experiment against fresh OPA porewater. No Pu out diffusion was observed during 30 days. Similar out diffusion experiment over 40 days have been performed after the in diffusion of Pu into Bure clay with the same result that no Pu was released from the clay into the solution. The in and out diffusion is illustrated in Figure 4-5.

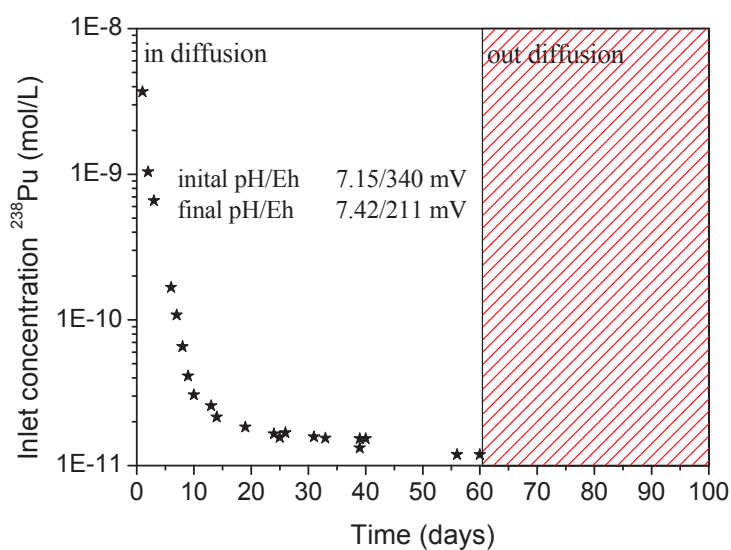


Figure 4-5: In and out diffusion experiment with ²³⁸Pu in a Bure clay (PAC 1002/K70; 13.47 – 13.61 m depth). The initial concentration of Pu in the porewater was 7.8×10^{-9} mol/L.

Analysis of the cores

Traces of saw dust contaminated the embedding medium (epoxy-resin), therefore the interface between embedding medium and the clay sample was difficult to determine by autoradiography in the first samples (Figure 4-6). By putting a silver foil to create a sharp contrast on the sample we solved the problem (Sample OPA1-SCAS1). All 3 cores show clearly that no preferential pathways for the migration of Pu exist.

It is evident that the Pu diffusion within the OPA is not homogenous. The Pu is always concentrated in distinct areas which are distributed differently within the core. In Figure 4-6 the Pu concentration is indicated by colours. Red means areas of Pu concentration and the lighter the colour, the lower the concentration. The highest punctual concentration of Pu measured was 200 ppm in the crosscut through the clay core of OPA2-SCAS3 we found 2 distinct areas on the left side where the Pu is concentrated. SEM-EDAX analysis showed no specific elemental concentration or any specific mineral phase in this area. By measuring the activity of the Pu sorbed on clay particles sticking on the distribution plate we were able to show that the solution really covered the whole sample. The measured profiles are subsequently different for the two sides of the sample. Whereas profile 1 shows the diffusion of the Pu of - 5 mm at the end of the experiment (93 days) the diffusion in profile 2 is much more restricted (- 1 mm). A similar observation was made for OPA2-SCAS2. In OPA1-SCAS1 we found some pyrite in the areas of high Pu concentration but also Pu enrichments in areas with no specific elemental concentration. In this core the Pu activity was concentrated at the surface of the core.

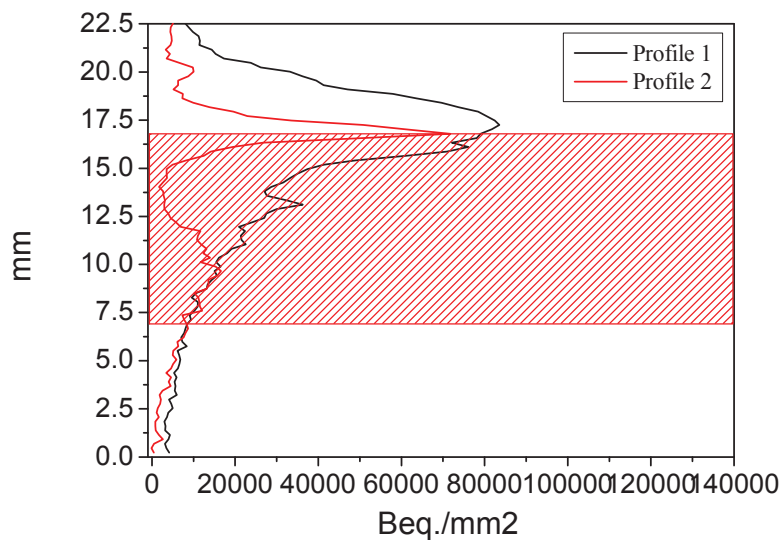
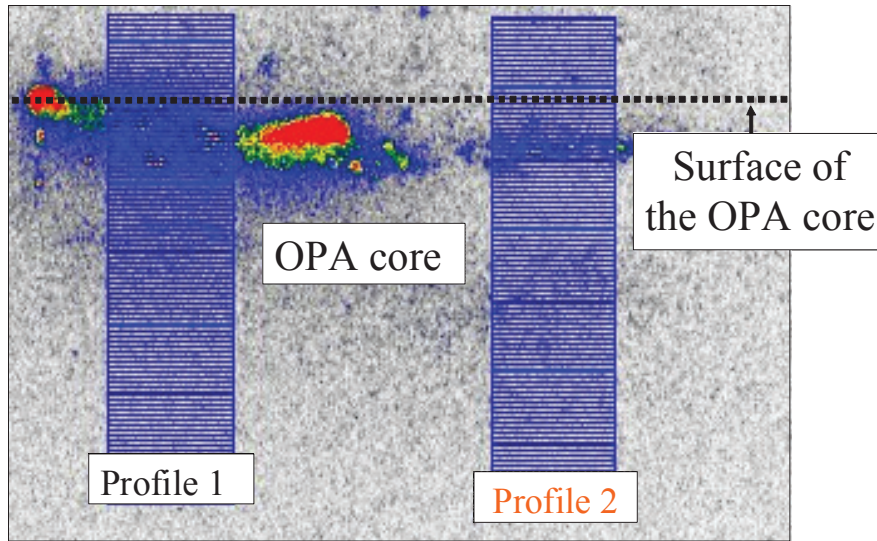


Figure 4-6: Two different diffusion profiles measured for OPA2-SCAS3 with autoradiography. The filled pattern indicates the clay sample. The dotted line indicates the background radiation from the Opalinus clay. The different colors represent different concentrations. Red indicates the highest and the grey color the lowest concentration.

HTO diffusion in OPA

The effective diffusion coefficient perpendicular to the bedding was found to be $1.53 \times 10^{-11} \text{ m}^2/\text{s}$. This value is in good agreement with the data of [Van Loon et al., 2003]. The results from the autoradiography demonstrated that the HTO diffusion within the core is homogeneous. No preferential pathways exist for the diffusion of HTO and so Pu.

Pu in the OPA pore water

To investigate the stability of Pu in the OPA porewater the Pu concentration, oxidation state distribution, pH and redox potentials were monitored as a function of time. At first the Pu(VI)

is partly reduced in the OPA porewater to Pu(V). Because of the initial low Pu concentration no change in the Eh can be observed. In the sample the Pu(VI) is nearly completely reduced to Pu(V) and further to Pu(IV). This observation is in agreement with the observation made by [Neck et al., 2007]. Because of the reduction of the Pu(V) to Pu(IV) we might exceed the equilibrium concentration and consequently precipitate colloidal Pu(IV) which sorbs on the container walls. With a concentration of 1×10^{-10} mol/L we are at the solubility limit of Pu(IV) in the given system [(Neck et al., 2007)].

Pu concentrations in the diffusion and sorption experiments

Two trends for the Pu concentration can be observed in the diffusion experiments. In OPA1-SCAS1 the Eh dropped from 430 to 30 mV during the experiment. After only seven days Pu concentration reached a steady state of $\sim 3 \times 10^{-11}$ mol/L. In the other two experiments the Eh remained unchanged and the Pu concentration decreased slowly and finally remains one order of magnitude higher than in the OPA1-SCAS1. A post mortem Rietfeld refinement method of the upper layer of the OPA1-SCAS1 diffusion core, where we observed a drop in Eh, indicates a high amount of pyrite (-45%) in the uppermost layer of the core. A similar observation was made for the sorption experiments. In some samples, enriched from the beginning in pyrite, Pu was nearly completely sorbed within one hour of contact time accompanied by a decrease in Eh. At least two different possibilities exist concerning the fate of the initial Pu(VI) in solution.

- The Pu(V/VI) was reduced in solution with electrons from the OPA porewater to Pu(IV) [Neck et al., 2007]. The resulting Pu(IV), possibly present in colloidal form, is sorbed on the surface of the minerals at preferential sites or precipitates after exceeding the solubility limit as PuO₂(hyd, am). The Pu activity in this case was concentrated on certain spots on the surface of the diffusion core.
- The other possibility is that Pu(VI) was first sorbed and finally reduced on the mineral surfaces as it was described for pyrite by [Eglizaud et al., 2006] or [Wersin et al., 1994] for U(VI).

Because of the very low concentrations used in the experiments we have no direct possibility to verify the different possibilities so far and further experiments are needed.

4.1.3 Conclusions

Diffusion of Pu and HTO in the OPA was studied by the through-diffusion method. The diffusion coefficients for HTO from our experiments were in excellent agreement with those determined in through-diffusion experiments in other laboratories. The experiments show that (i) about 20-40 % of Pu is sorbed on components of the experimental set-up, (ii) there is considerable impact of the samples natural alpha-emitting inventory, (iii) the mobile Pu inventory is dominated by Pu(V), (iii) there is no preferential transport pathway for Pu in the clay sample and that Pu is concentrated within the clay core at certain sites. The Pu sorbed on the

samples was reduced to Pu(IV). Further experiments are needed to determine the reducing and subsequent sorbing phase. Traces of oxygen in the system will lead to the formation of iron oxides/hydroxide which will sorb the Pu directly out of solution.

Trustworthy determination of the diffusion behaviour of actinide ions in clay requires carefully designed experimental set-ups and development and application of a series of analytical techniques. Careful cross-checking is required in order to verify that the samples are not subject to undue disturbances, especially those resulting in preferential artificial transport pathways. Furthermore, delineation of natural activity inventory from the studied ions and identification of inventory lost in the equipment is a precondition for adequate interpretation of the experimental results.

Trustworthy interpretation of transport experiments also requires batch sorption data and 3D distribution of along the diffusion samples. The present work shows that all these objectives have been demonstrated for an in-house built diffusion experiment system and development and application of the required associated analytical techniques. These ongoing investigations will provide the necessary basis for credible description of sorbing radionuclide mobility in clay for the nuclear waste disposal safety case.

4.2 Analogue study on the uranium speciation in argillites from the Lodève Basin (France)

Another objective was the comparison of natural organic matter clay association found in potential host rock formations (COx and OPA) with those found in uranium deposits of comparable mineralogy (i.e. argillite). Argillaceous clay-rich formations with organic matter and radionuclide (uranium) present in the Lodève Basin (France) was considered as potential analogue based on the geological history of the basin and the presence of the three main components, i.e. radionuclides (U), clays and natural organic matter, subject of our project (Marignac and Cuney, 1999; Schlepp et al., 2001). Main objective was a better understanding of the association between clay minerals (chlorite and illite), uranium and organic matter found in this sedimentary basin under the form of coal; a key question with regard to the understanding of U immobilization in nature considering geological time-scale.

Results of spatially resolved X-ray fluorescence and X-ray absorption fine structure investigations with a micrometer-scale resolution (μ -XRF and μ -XAFS, comprised of the near ionization threshold energy region, XANES, and the extended energy region, EXAFS) on two uranium-rich clay samples originating from Autunian shales in the Permian Lodève Basin (France), provided by CREGU (Centre de Recherche sur la Géologie des Matières Premières Minerals et Energétiques) are reported here. This argillaceous formation is a natural U deposit (or mineralization) associated with organic matter (bitumen) (Marignac and Cuney, 1999; Mathis et al., 1990). The goal of this study is to determine the U oxidation state in the sample and to ascertain if any correlation between the U distribution and that of other elements present in the organic-rich fine-grained pelites exists, which might give us insight into the

mechanism of U immobilization through either adsorption/co-precipitation with iron hydroxides and/or clay minerals.

Autoradiographic images and photographs of the samples are shown in Figure 4-7. Uranium-rich areas of the sample or hot spots are visible as dark spots in the autoradiographic images. Quantification of the hot spots shows that they contain ~ 2 mg $^{238}\text{U}/\text{g}$ material (sample marked P31) and ~ 25 mg $^{238}\text{U}/\text{g}$ material (sample P15).

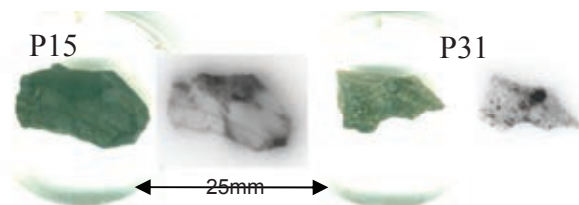


Figure 4-7: Photographs of the samples studied embedded in acrylic (designated P15 and P31) and their corresponding radiographic images.

μ -XRF and μ -XANES measurements are recorded at Beamline L at the Hamburger Synchrotron Labor (HASYLAB). A confocal irradiation-detection geometry is used, providing added depth information and allowing probing sample volumes below the surface, thereby avoiding any surface oxidation artifacts caused by cutting and polishing the clay sample. Elemental distribution maps are obtained by means of scanning μ -XRF and plotting recorded relative fluorescence intensities for each pixel and scaling them with a linear color code, with dark pixels corresponding to high count rates. By scanning arbitrary sample areas (xy scans) at different depths (z) using the confocal setup, stacks of tomographic cross sections can be easily recorded (Denecke et al., 2005a; Janssens et al., 2004). Polycapillary half lenses are used for both focusing and collimating optics. The focal spot diameter is approximately $16 \mu\text{m}$. μ -XRF measurements are recorded using a band pass of wavelengths with an average weighted energy of 17.6 keV delivered by a Mo/Si multilayer pair (AXO Dresden GmbH, Germany) and a Si drift detector (Vortex, SII NanoTechnology USA Inc., Northridge, CA). U L3 μ -XANES are recorded using monochromatic X-rays at selected sample volumes of high U concentration identified in the μ -XRF maps at Beamline L. Both XANES and EXAFS are measured at positions of high U concentration identified by line scans of windowed U L α counts registered with a high purity Ge detector (Canberra) at the INE-Beamline at the \AA ngströmquelle Karlsruhe, ANKA (Denecke et al., 2005b). The measured beamspot at the INE-Beamline is $300 \mu\text{m}$. Si(111) and Ge(422) crystals are used in the double crystal monochromator at HASYLAB and ANKA, respectively, and the energy is calibrated relative to the first inflection point in the K XANES of a Y foil (defined as 17.038 keV).

The measured distributions for K, Ca, Ti, Fe, Zr, and U in the area with the highest radioactivity at the top of sample designated P15 are shown in Figure 4-8 and Figure 4-9.

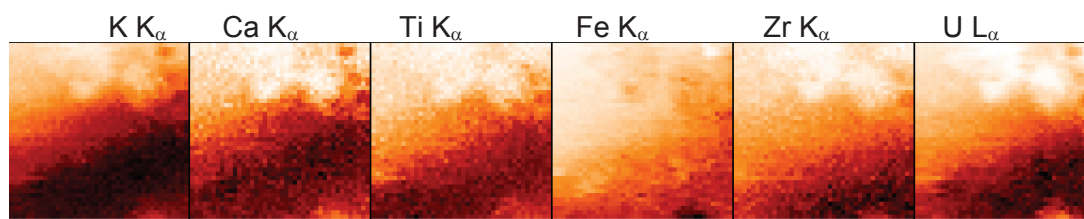


Figure 4-8: Distribution maps for the elements indicated in a 800 x 760 μm^2 section ($20 \times 20 \mu\text{m}^2$ step size), recorded near the surface of sample P15.

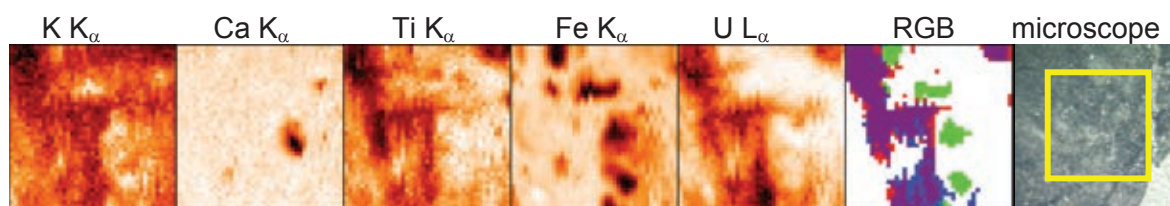


Figure 4-9: Distribution maps for K, Ca, Ti, Fe, and U in a 400 $\mu\text{m} \times 400 \mu\text{m}$ section ($10 \times 10 \mu\text{m}$ step size, 1s counting time), recorded under the surface of the sample 31 area marked in the microscope image at far right. RGB overlay image for regions of highest Ti, Fe, and U concentrations is shown.

These distributions demonstrate three general observations from this sample: 1) distinct patterns of element distributions are observed, despite the sample's general heterogeneous optical appearance 2) the U distribution is often correlated with the distributions of lighter weight elements K, Ca, and Ti (especially notable in the round features in the upper right corner of the maps) and 3) the U distribution is generally inversely correlated to areas of high Fe content.

In order to determine the valence state of the U in the pelites, U L3 μ -XANES (Figure 4-10 and Figure 4-11) and μ -EXAFS (Figure 4-12) are recorded at volumes and areas with high U L α intensity. The energy position of the most prominent absorption peak in the XANES (the white line, WL) measured for different sample regions at two different beamlines (INE-Beamline Figure 4-10 and Beamline L and Figure 4-11) all lie within less than 1 eV of that for the U(IV) reference. The XANES features themselves also provide further evidence that the U hot spots contain U(IV). No evidence for the presence of any U(VI), which would be indicated by a decreased WL intensity and multiple scattering feature around 10 eV above the WL (Denecke, 2006), was found. We conclude that U is likely present in the sample in the tetravalent state.

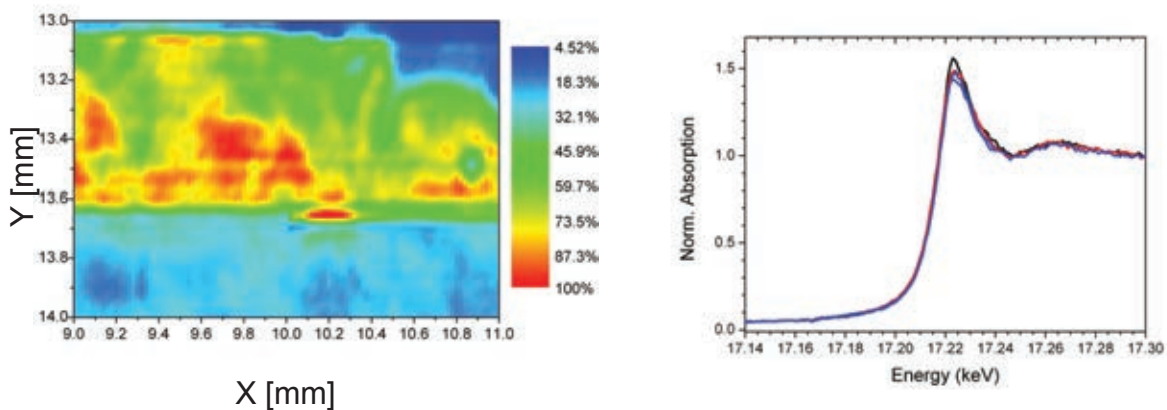


Figure 4-10: Left: U distribution for a 2000 x 1000 μm^2 section (30 x 30 μm^2 step size) recorded at the INE-Beamline at the surface of sample 15. The normalized U L α intensity scale bar is indicated. Right: U L3 μ -XANES recorded at four independent areas with high U L α intensity.

This interpretation is corroborated by the U L3 EXAFS spectrum (Figure 4-12). No short U-O distance expected for the U(VI) uranyl moiety is found in the EXAFS spectrum (Denecke, 2006). The data is well fitted beginning with a structural model similar to uraninite, UO_2 (Rundle et al., 1948). Best fit results are obtained with 4-5 O atoms at 2.29 \AA with $\sigma^2 = 0.013 \text{\AA}^2$ and 2-3 U atoms at 3.78 \AA with $\sigma^2 = 0.008 \text{\AA}^2$. The distances are 2-3% smaller than expected for UO_2 and the intensities lead to a much smaller coordination number than expected ($N(\text{O})=8$; $N(\text{U})=12$). This may indicate that the UO_2 -like phase is present as a nanoparticulate material with large surface area having relaxed (shortened) distances at the surface.

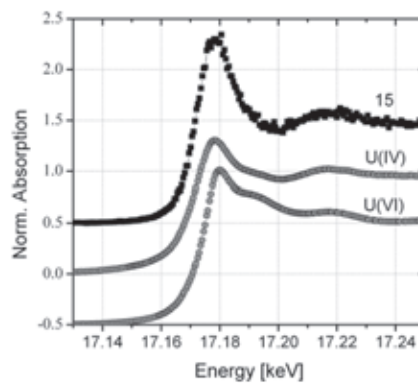


Figure 4-11: U L3 μ -XANES recorded at U hot spots of sample 15 at Beamline L (symbols) and compared to two U(IV) and U(VI) reference spectra (bottom)

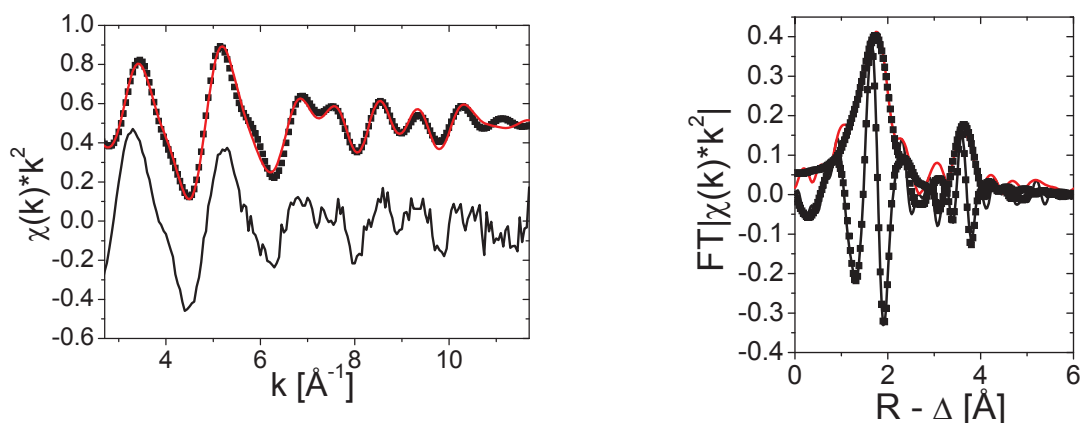


Figure 4-12: U L3 k^2 -weighted EXAFS ($\chi(k)$; left bottom), Fourier-filtered data and best fit results (left top) and corresponding k^2 -weighted Fourier transform (FT) data (right) plotted with best fit results. Experimental data = lines. Fit curves = symbols.

STXM results

The STXM data of sample 15 and results of PCA and cluster analysis are depicted in Figure 4-13. We observe a homogeneous distribution of organic carbon, with the exception of one strip (grey area, upper right in Figure 4-13), where no absorption at the carbon K-edge is detected. The yellow and red areas found in cluster analysis differ in their optical density (OD) and K content. The red areas exhibit a significantly higher OD below the carbon K-edge (OD ~ 0.8 ; see Figure 4-14) and significant absorption bands at potassium $L_{2,3}$ -edge energies. This indicates that this organic material is associated with clay minerals possibly of illite-type. The relatively large edge jump ($\Delta OD \sim 0.4$) of these regions shows that a rather large amount of organic material is associated with these clay minerals. The yellow areas indicated in the Figure 4-12 are additional organic material, which is not directly associated to these mineral phases. The low OD (< 0.1) below the carbon edge found for this material might indicate that it is of almost pure organic nature. The average cluster C(1s)-edge spectra extracted from both regions (Figure 4-13) are not very different, except for the yellow areas appearing to have a higher aromatic content (absorption at 285 eV) and the illite-clay associated organics show higher absorption in the 287 eV region that suggest a higher aliphatic character or metal complexation (Plaschke et al., 2005).

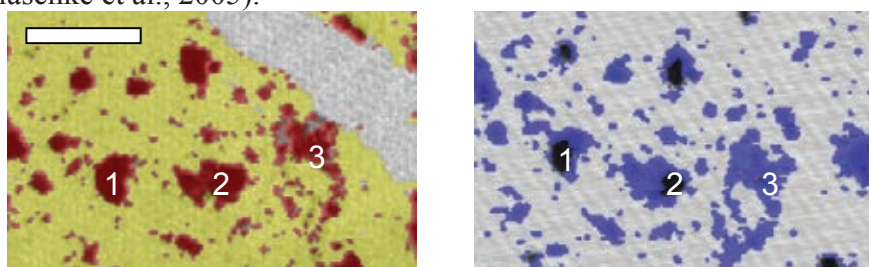


Figure 4-13: STXM PCA and cluster analysis of sample 15. (left) Distribution of organic functionality with two distinguishable clusters found using PCA and cluster analysis. (right) distribution of iron absorption. The scale bar is $10\mu\text{m}$. As the Fe L-edge region is slightly rotated counter-clockwise numbers are inserted for orientation.

Three distinct regions in the iron L-edge image of sample 15 are identified. The grey cluster shows no OD; the cluster marked with black color does not show any iron L_{2,3}-edge features but a generally high OD (see Figure 4-14); the blue region is characterized by absorption features at the Fe L-edge. The areas are nearly coincident with areas exhibiting potassium absorption peaks and highest organic absorption. Spectral feature changes within particles in the blue cluster region (not shown separately) appear to indicate that the core part of these particles either exhibit no iron content or a higher absorption in the Fe(II) energy region, whereas in the rim region of these particles have a higher Fe(III) content.

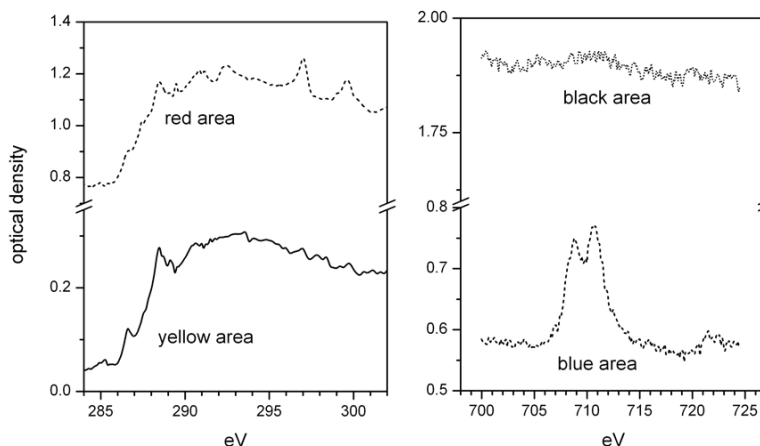


Figure 4-14: (left) Average C(1s) XANES of sample 15 of the yellow and red areas indicated in Figure 8 and (right) average Fe L-edge spectra marked in blue and black.

In the fault breccia sample 31 STXM results, PCA and cluster analysis reveal two distinct regions of organic matter. The fracture network infill region (Figure 11) is characterized by organic material with a high content of oxygen containing functional groups (i.e. carboxyl-type groups absorbing around 288.6eV) and a clear π^* peak near 290.2eV, indicative of carbonate. The second region of generally higher OD is associated with clear absorption bands at 297 and 300eV, indicative of the potassium L-edges. This organic material is apparently associated with K-containing minerals. Interestingly, both carbon spectra show no C_{arom} absorption (~285eV), but the mineral associated organics have a significant higher aliphatic content (~287.4eV absorption). Some but not all K-rich regions coincide with Fe regions in Figure 4-15. The iron L₃-edge shows there is a high content of Fe(II) phases, which is visualized in the comparison with a hematite reference spectrum in Figure 4-16.

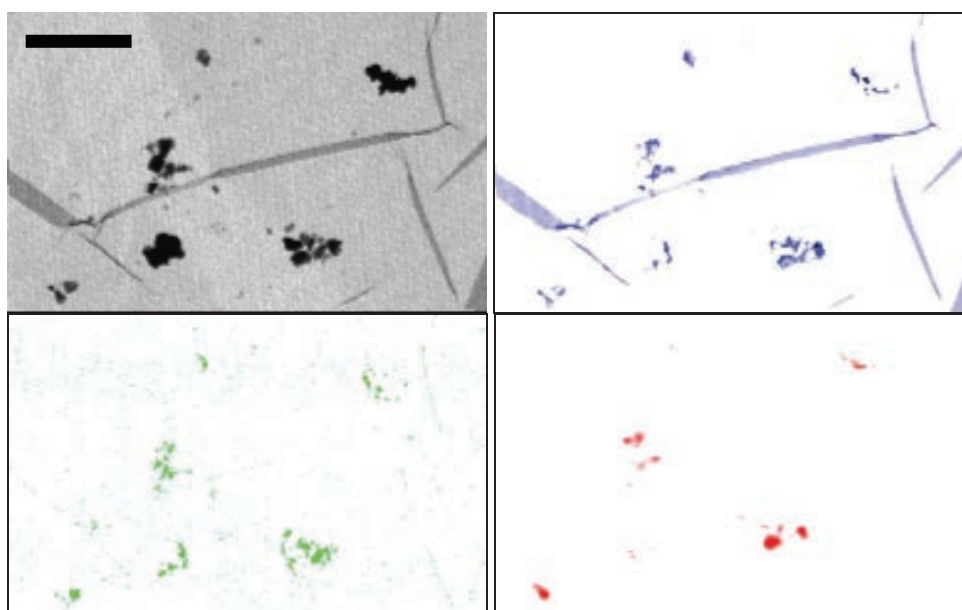


Figure 4-15: (upper row from left to right) STXM absorption image at 290eV and carbon distribution map; (lower row from left to right) potassium and iron distribution maps taken from XANES ratio images (sample 31). High color intensity indicates high content of selected element. The scale bar represents 10 μ m.

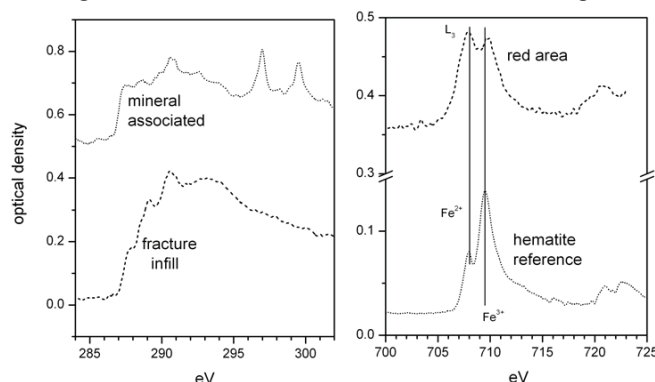


Figure 4-16: (left) Average C(1s) XANES of sample 31 fracture infill and the mineral associated organics. The mineral associated organics are clearly linked to potassium containing phases as indicated by the L-edges at 297 and 300eV. (right) Average Fe L-edge spectra from areas marked in red in Figure 11.

μ -FTIR results

Spectral maps imaging the spatial distribution of functional groups in the sample including aliphatics (ν_{CHali} ; 3000-2800 cm^{-1}), aromatics ($\nu_{C=C}$; 1750-1500 cm^{-1}), alcohols (ν_{OH} ; 3600-3100 cm^{-1}) or OH vibrations of clay minerals ('OH' 3720-3680 cm^{-1}) are extracted from scanning μ -FTIR data. An example of the maps is illustrated in Figure 4-17. Inspection of the functional group distributions reveals a correlation between the clay mineral vibration bands ('OH') and the organic matter functionalities (ν_{CHali} , $\nu_{C=C}$, ν_{OH}). This observation confirms the potassium (i.e. illite-type clay mineral) – organic matter correlation observed in the STXM investigations.

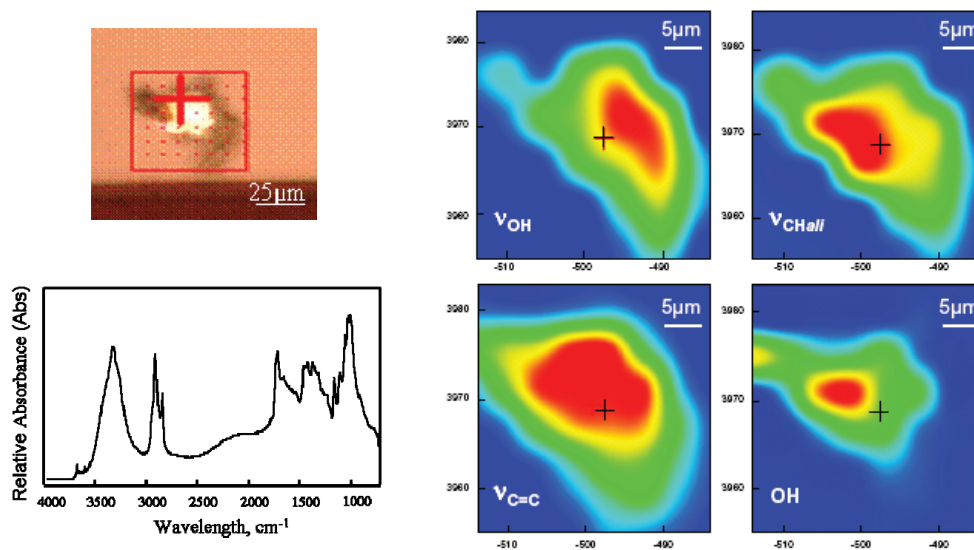


Figure 4-17: (upper left) Visible light microscope (VLM) image of the microtome sample 15 studied and (lower left) μ -FTIR spectrum of the spot marked by the cross line in the VLM image. (right) Maps of organic functional group distributions extracted from μ -FTIR data: alcohols (\square OH; 3600-3100 cm^{-1}), aliphatics (\square CHali; 3000-2800 cm^{-1}) and aromatics (\square C=C; 1750-1500 cm^{-1}), as well as OH vibrations of clay minerals ('OH' 3720-3680 cm^{-1}).

4.2.1 Conclusions

In summary, application of various spatially resolved spectroscopic methods have been successful in characterizing the uranium speciation in sediment samples from the Lodève Basin and in evaluating if organic matter or Fe^{2+} , Mn^{2+} , S^{2-} mineral phases were responsible for uranium immobilization/enrichment in the sediment. μ -XANES and μ -EXAFS results show that uranium in both sediment samples studies is found in the tetravalent state, most probably in the form of nano-crystalline UO_2 -like phase. The correlations between elements obtained by means of different techniques (μ -XRF, STXM and μ -FTIR) allow us to conclude the following. The uranium distribution in sample 15, originating from the contact zone adjacent to the fault zone, is positively correlated to the distribution of lighter weight elements (Ca, K, Ti). We deduce a correlation between clay minerals of illite-type and organic matter in the sample based on the observation that potassium (as indicator element) is found associated with both organic carbon and Fe and the observed spatial coincidence between μ -FTIR clay OH vibrations and various vibrations of organic functional groups.

Sample 31, originating from the breccia facies within the Lodève Basin fault zone, also exhibits a positive correlation between uranium and the elements K, Ti and a negative or anti-correlation between the distribution of uranium and those of Ca and iron. In sample volumes of highest potassium content, no Fe $\text{K}\alpha$ signal is observed. Two distinguishable clusters of organic material in sample 31 are identified. The first type is associated with fracture infill and lacks K and Fe signatures, but displays a detectable carbonate peak in its C(1s) XANES. The second cluster type of organic material is associated with discrete mineral aggregates, exhibiting a spatial coincidence between carbon absorption and Fe and K absorption. Because

an anti-correlation between uranium and Ca/Fe exists and because carbonates (likely Ca-containing) are associated with organics in the fracture infill we conclude that the fracture infill in this sample is not associated with uranium.

From these observations we attempt to put forward a tentative hypothesis for the mechanism of uranium immobilization. Due to the lack of the correlation between uranium and Fe, we exclude Fe-minerals as dominant reductant during immobilization of U(VI) to U(IV). Combining the knowledge that uranium is found associated with potassium and that clay minerals of illite-type are associated with organic matter we conclude that organic material associated with clay minerals might have played a role as reductant thereby reducing incoming groundwater dissolved U(VI) to less soluble U(IV). This hypothesis remains speculative; numerous unanswered questions remain. For example, what role did the clay play? Did it act as a catalyst (Giaquinta et al., 1997) or was it merely an anchor for the organic material? In addition, how do we explain the apparent discrepancy between the spatial relationship between potassium and iron distributions observed in the μ -XRF maps with that from STXM results? To help refine our understanding of the redox partner involved in the reduction of U(VI) in this sediments combined μ -XRD/ μ -XRF studies are planned.

We note a critical aspect of the comparison of μ -XRF and STXM results made in this study: the sample region actually analyzed. Disregarding the depth resolution used in the confocal setup (providing volume information), the estimated area probed with μ -XRF is 608,000 μm^2 for sample 15 and 160,000 μm^2 for sample 31. The STXM measurements are limited to an area of 1,600 μm^2 for both samples. The STXM area investigated in this study represents only 1‰ (sample 31) and 2.6‰ of the μ -XRF region probed. Expressed in another way, STXM results stem from an area equivalent to only 16 data points of all the data points plotted in the Figures 4 and 7 combined. This points to the imminent difficulty of nano-focused techniques, namely to which extent selected sample regions studied are representative of the macro-scale system of interest. With this in mind, the correlations made in this study are surprisingly consistent with one another.

5 Speciation of actinides in the clay system

The redox speciation of Np(V), Pu(V) in OPA and COx suspensions were investigated by X-ray absorption fine structure (EXAFS), UV-Vis/NIR absorption, and liquid-liquid extraction. The redox speciation of plutonium and neptunium on the solid clay was performed by EXAFS and x-ray photoelectron spectroscopy (XPS). Because of the strong sorption of some radionuclides, the concentrations in solutions are very low and reach the detection limit of radiometric measurements combined with the extraction methods. As a speciation method at such low concentrations and below, capillary electrophoresis (CE) coupled to ICP-MS was introduced and tested on the neptunium samples.

5.1 Speciation in solution

5.1.1 UV-Vis/NIR spectroscopy of Np(V)

One of the key questions is in what redox state each radionuclide occurs during the sorption process. For that the solution of each sample was measured by UV-Vis absorption spectroscopy.

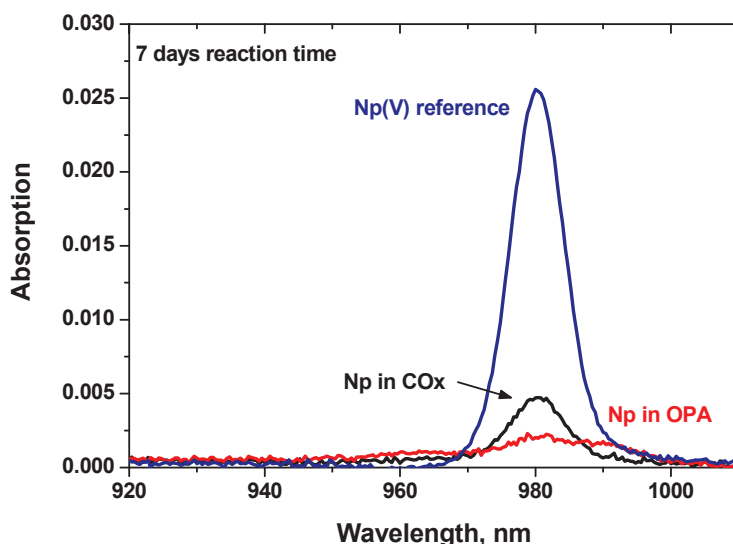


Figure 5-1: Absorption spectra of Np in supernatant solution after ultrafiltration from suspension solution of clay rocks, contact time = 1 week, S/L = 50, NaCl = 0.1 M.

In the following sections we only focus on the neptunium, because it shows a characteristic absorption band for the aquo NpO_2^+ ion at 981 nm with extinction coefficient high enough for the characterisation of Np in concentrations down to 10^{-6} mol/L. This cannot be achieved for Pu(IV,V). Figure 5-1 represents the UV-Vis spectra of the Np(V) reference solution and the supernatant solution of Np in OPA and COx clay minerals. Due to the similarity of spectral

features for both the Np samples and the Np(V) reference spectra, we conclude that the neptunium remaining in solution occurs in the pentavalent oxidation state. The amount of Np in solution calculated from the absorption coefficient is similar to the result from the radiometric measurement with in the range of about 13% uncertainties.

5.1.2 Eh Measurements

The sorption of Pu, Np increases with time supposing that they are slowly reduced to the tetravalent oxidation state. This can be confirmed by a steadily decrease of the Eh to values between -100 mV (Pu), and + 50 mV (Np) after 4 months without reaching a constant value. Looking in detail on the Pu/Np redox speciation diagram under the Eh/pH conditions for (OPA) pore water shows that the reduction to tetravalent Pu/Np is thermodynamically feasible (see Figure 5-9 and Figure 5-10).

5.1.3 CE-ICP-MS

Online-coupled capillary electrophoresis (CE) with inductively coupled plasma mass spectrometry (ICP-MS) has been successfully applied for the speciation of actinide ions at such low concentration [Kuczewski et al., 2003]. Therefore, CE-ICP-MS has been chosen as a speciation method for the characterization of Np species at low concentrations. Due to the speciation limitation of the absorption spectroscopy and the radiometric measurement we have performed Np speciation by CE-ICP-MS.

A commercial Beckman Coulter P/ACE MDQ capillary electrophoresis system (Fullerton, U.S.A.) equipped with an inductively coupled plasma sector field mass spectrometer Sector-field-ICP-MS (Element XR, Thermo Fisher Scientific, Bremen, and Germany). Conventional fused silica capillaries (Beckman Coulter, Fullerton, U.S.A.) with an internal diameter of 50 μm and lengths of 74 cm are used for the separations. A commercial parallel path micronebulizer (Mira Mist CE, Burgener, Canada) that operates with a makeup liquid (2 % HNO_3 , 10 % ethanol, 1 ppb Rh as internal standard) interfaces both apparatuses. The makeup liquid is introduced to a syringe pump at a nominal flow rate of 8 $\mu\text{L min}^{-1}$. The nebulizer is connected to a borosilicate spray chamber (Mini glass chamber, Burgener, Canada).

For the measurement, separated supernatant solutions from clay suspension are taken in 1 mL glass vials under inert atmosphere. However the measurement has been performed under air atmosphere. The concentrations of Np in clay sample are between 1.0×10^{-7} and 1.0×10^{-9} M. Before each separation, the capillary is washed with BGE during 10 min at 20 psi. Separations are completed within 15-18 min. Sample injections are hydrodynamically carried out at 5 psi during 6 s. Separations are performed at -20 kV and at a constant pressure of 0.8 psi (to avoid clogging).

The first test should show how significant the impact of air on the Np(IV) is by using our commercial injection system. For that we injected a reference solution of 100% Np(IV) at concentration of 3×10^{-7} M in 0.01 M HClO₄ into the capillary and made a separation at a potential of 20 kV in an acetic acid buffer system. Figure 5-2 shows, that the Np(IV) was partly oxidized (~ 30 %) to Np(V), but that it should be possible to qualitatively detect Np(IV). Several mixtures of Np(V) and Np(IV) with different ratios are tested, to ensure the reliability of this separation and the migration time for our system.

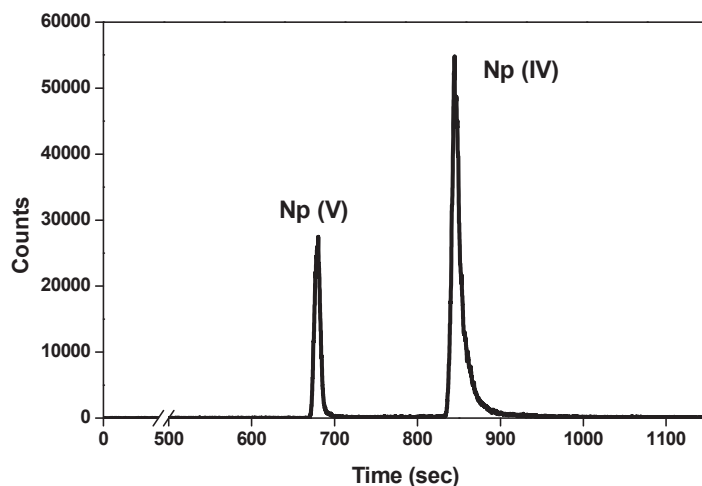


Figure 5-2: Electropherogram of an 30% Np(V) / 70% Np(IV) reference solution characterized by CE-ICP-MS, [Np]= 3×10^{-7} M, 0.01 M HClO₄, separation in 1 M acetate buffer system, at a potential of 20 kV.

For the speciation of Np in clay solutions, filtrate (10 kD) supernatant solution was taken in small vials under Ar atmosphere and then injected under air into the CE. Figure 5-3 demonstrates that only Np(V) was found in supernatant solution with a concentration of about 2×10^{-8} M and this confirms the spectroscopic result at higher concentrations.

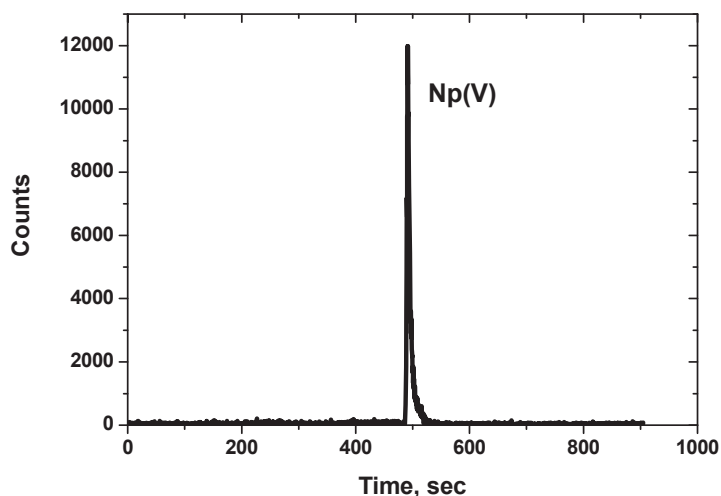


Figure 5-3: Electropherogram of Np-COx clay filtrate (aliquot) solution, [Np]_{initial} = 2×10^{-8} M, 0.1 M NaCl, S/L = 20, contact time=7 months, CE separation with 1 M acetate buffer system at 30 kV.

5.2 Speciation of neptunium and plutonium on clay solid phases

XANES and XPS are two well appropriate methods to characterise oxidation states of metal ions on the surfaces. Both methods has successfully been used for determining Pu oxidation states in humate and fulvate complexes [Marquardt et al., 2004]. Both methods were used to characterise the Np and Pu on the clay surface as well as in solution.

5.2.1 XANES

For the XAFS measurements, filtrate solutions and suspension solids of radionuclides-clay rocks are filled into 400 μ l capped PE vials and mounted in a special air tight sample holder, which is connected to an Ar supply line at the experimental station to keep the samples under <inert, near oxygen-free conditions during XAFS measurements. The measurements are performed at the INE-Beamline using this new inert gas sample cell design [Brendebach et al., 2009] for redox sensitive radionuclides. The spectra are calibrated against the first derivative X-ray absorption near edge structure (XANES) spectrum of a Zr foil, defining the energy of the first inflection point as $E(\text{Zr } 1s) = 17998.0 \text{ eV}$. All Pu L3, Np L3 XAFS spectra are measured in standard fluorescence yield detection mode.

The results of the XANES of Np, Pu are shown in Table 5-1. In all samples the Np was detected as Np(V) (NpO_2^+ , 'neptunyl') with the characteristic XANES features (low white line intensity, multiple scattering shoulder $\sim 10 \text{ eV}$ above white line). Note that the energy positions of Np(IV) and Np(V) almost coincide. This anomaly is explained for actinyl cations by charge transfer from the double-bond axial oxygen anions to the metal cation. The XANES spectrum of the Np(V) reference sample (Np(V)ref), neptunium sorbed on OPA (Np-OPA) and COx (Np-COx) are shown in Figure 5-4.

As expected, the white line maxima of the XANES of Pu in the OPA and COx samples are clearly located at the white line position of the Pu(IV) at 18067.8 eV (see Table 5-1). The XANES spectrum of Np(V)ref, Np-OPA, Np-COx are shown in Figure 5-5. The XANES spectra exhibit no multiple scattering resonance as expected for Pu(V) and Pu(VI) 'plutonyl' moieties and a strong white line intensity - the energy positions are in accordance with the Pu(IV) aquo ion. Hence, we can conclude that plutonium on the clay is in the tetravalent oxidation state and that the initial Pu(V) has to be reduced to Pu(IV) for all sorption samples.

Table 5-1: Energy positions of the XANES first inflection point and white line maximum positions for reference species and sorption samples. All values are given in eV (estimated calibration error $\Delta E \pm 0.5-1$ eV).

Sample description (contact time 1 week)	first inflection point	white line maximum
Pu(IV)ref, solution	18062.4	18067.6
Pu(V)ref, solution	18059.8	18064.3
Pu-OPA, solid	18062.1	18067.9
Pu-COx, solid	18063.0	18067.8
Np(IV)ref, solution	17609.6	17614.7
Np(V)ref, solution	17609.0	17614.0
Np-OPA, solid	17608.4	17613.0
Np-COx, solid	17607.7	17612.5

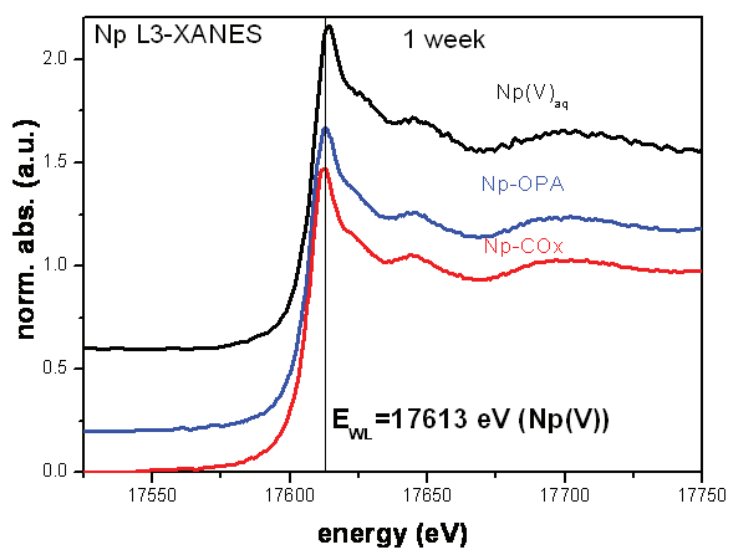


Figure 5-4: Np L3-XANES spectra of Np speciation in clay rocks (OPA, COx), [Np] = 3E-04 M, 0.1 M NaCl, S/L = 50, kinetic = 1 week, sample= filtrate suspension.

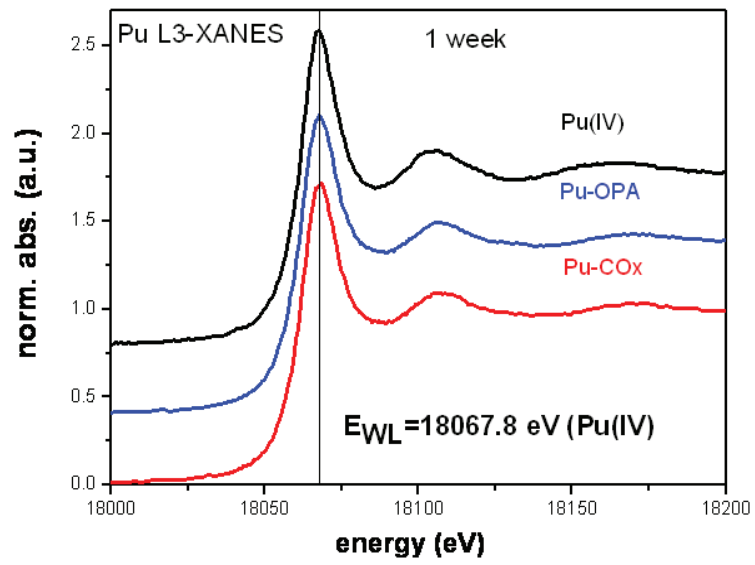


Figure 5-5: Pu L3-XANES spectra of Pu speciation in clay rocks (OPA, COx), [Pu] = 3E-04 M, 0.1 M NaCl, S/L = 50, kinetic = 1 week, sample= filtrate suspension.

Table 5-2: Energy positions of the Np L3-XANES first inflection point and white line maximum positions for references and samples from campaign August 2011. All values are given in eV (estimated calibration error $\Delta E \pm 0.5$ eV).

Sample description (4 and 8 months)	contact time (months)	first inflection point	white line maximum
Np(V)ref, aq [1]		17609.0	17614.0
Np(V)-OPA (august 2011)	8	17608.6	17612.0
Np(V)-OPA (Nov 2011)	4	17608.9	17613.3
Np(V)-OPA-Fe (august 2011)	8	17609.2	17612.7
Np(V)-OPA-Fe (Nov 2011)	4	17608.3	17613.3
Np(V)-COX (august 2011)	8	Nd	nd
Np(V)-COX (Nov 2011)	4	17608.6	17613.2
Np(V)-COX-Fe (august 2011)	8	17609.9	17613.2
Np(V)-COX-HQ (august 2011)	8	17609.7	17613.9
<i>Np(IV)ref, aq [1]</i>	-	<i>17609.6</i>	<i>17614.7</i>
<i>Np(VI)ref, aq [2]</i>	-	<i>17611.7</i>	<i>17616.0</i>

5.2.2 EXAFS

The XAFS technique is particularly useful speciation method and applied for the understanding the speciation of actinides on mineral surfaces. Atomic distances between the adsorbed actinide ions and sorbent atoms can be obtained by XAFS analysis and the interface reaction mechanisms can be inferred from the sorbate-sorbent polyhedral linkage. XAFS has proven to be valuable in discerning sorption mechanisms such as inner-sphere surface complexation, outer-sphere surface complexation, coprecipitation/structural incorporation and redox reactions.

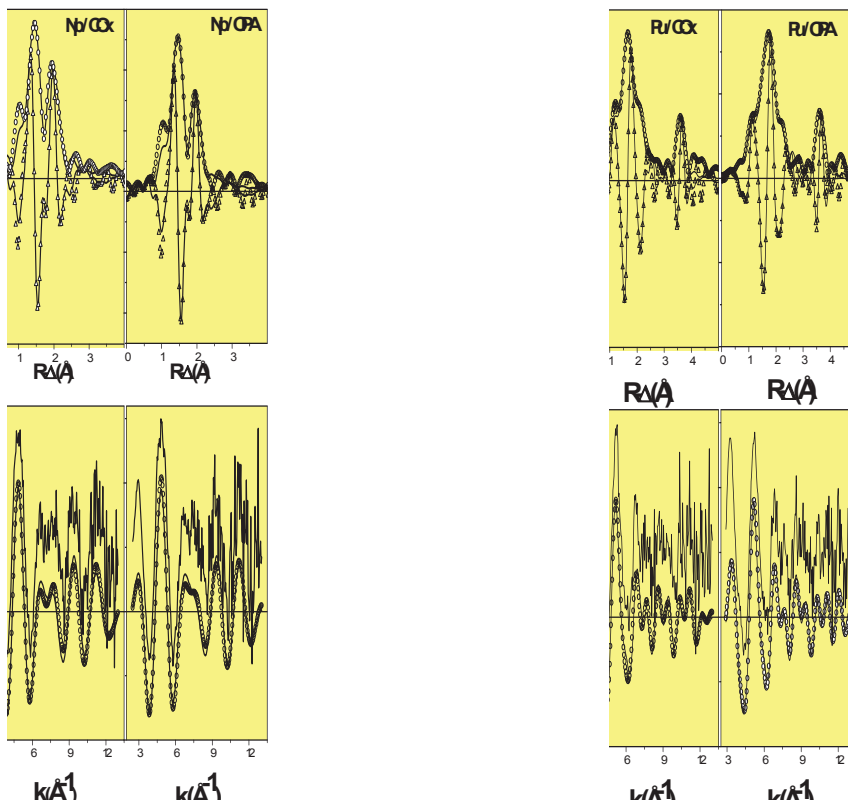


Figure 5-6: Pu/Np LIII-edge k^3 -weighted EXAFS spectra and corresponding Fourier transforms (upper: Pu/Cox and Pu/OPA sample, lower: Np/Cox and Np/OPA sample), contact time: 1 week.

The Np LIII and Pu LIII EXAFS spectra and their corresponding FT's for Np(V)/Pu(V) sorbed on COx and OPA with 1 week contact time are shown in Figure 5-6. In all FT spectra one peak dominates, which can be attributed to an average Np/Pu–O coordination shell composed of oxygen atoms from both water molecules and oxygen atoms binding the metal ion to the clay mineral surface. The EXAFS parameters obtained by fitting the spectra of Np sorbed onto the clay surfaces are also listed in Table 5-3. Figure 5-6 shows the LIII-edge k^3 -weighted EXAFS spectra and corresponding FT's of Np(V) sorbed onto COx and OPA clay mineral surface at pH 7.2 and 7.6. (Solid line – experiment; dotted line – theoretical fit results from fits to $\chi(k)$). No indication of Np–Np bond distance in the spectra, which leads to no formation of Np precipitation on clay surfaces.

There are also no further distant FT peaks, which might be attributed to an Np–Al or Np–Si distance (Al and Si cannot be distinguished by EXAFS). Observation of an Np–Al/Si peak would be direct evidence for the sorbate-substrate interaction. With no evidence for an Np–Al/Si distance we are not able to distinguish between an outer-sphere and an inner-sphere complex nor can we identify monodentate or bidentate binding to the surface in the case of inner-sphere complexation of the Np(V) species onto the clay mineral. However, a monodentate ligated silanol or aluminol group would be expected to have a relatively long Np–Si/Al distance. The length of an Np(V)–OH bond is expected to be shorter than the Np(V)–O distances associated with those of coordinated water molecules and the oxygen atoms of surface

binding sites. By comparison to a reported hydroxyl An–O bond length for Np(V) and scaling to ionic radii, we expect R(Np–O) for a hydroxo ligand to be about 2.45 Å.

Table 5-3: Metric parameter from R-space fits to Np L3 edge. EXAFS fit parameters: EXAFS fit parameters: O1 axial oxygen backscatterer, O2 equatorial oxygen backscatterer, (f) indicates fixed parameter, S02 fixed at 1.0

<i>Sample</i>	<i>k-range</i> (Å^{-1}) <i>fit-range</i> (Å)	<i>Shell</i>	<i>N</i>	<i>R</i> (Å)	ΔE_0 (<i>eV</i>)	σ^2 (Å^2)	<i>r-factor</i>
Np (V)aq ^a		O1	2.5	1.82			
		O2	4.8±1	2.45			
Np (IV) aq ^b		O2	9±1	2.37			
Np / COX	2.5-13.0	O1	2.0	1.86(1)	3.55	0.0011	0.028
	0-2.39	O2	3.1	2.49(2)	9.29	0.0022	
Np / OPA	2.5-13.05	O1	2.0 ^f	1.87(1)	4.77	0.0001	0.025
	0-2.39	O2	2.9	2.47(2)	6.83	0.0027	
Np / OPA magnetite	2.55-13.0	O1	2.0 ^f	1.86(1)	2.14	0.0004	0.011
	0-2.39	O2	3.3	2.48(2)	7.91	0.0036	

a: [Heberlin et al. 2008]; b: [Antonio et al., 2001]

Therefore, we suggest that the apparent decrease in N for Np(V) in the samples might be an indication to the formation of a ternary OH–/Np/clay surface species. In this species, the Np coordination sphere is expected to be highly asymmetric and diminish of its EXAFS amplitude is expected.

The structure parameters of the NpO_2^+ aquo ion are analyzed using EXAFS (Np–Oax distance 1.82 Å; coordination number 2.5; Np–Oex distance 2.45 Å; coordination number 4–5). EXAFS data shows differences in the Np(V)–Oax bond distance of 1.86 ± 0.01 Å for the sorbed Np on both clay rocks, and 1.82 ± 0.01 Å for the Np(V)aq ion. Batch experiments and the EXAFS results leads to the conclusion that in Np(V) is bound to equatorial about three oxygen neighbors at 2.47~2.49 Å and its remaining first coordination sphere is completed with water molecules. The coordination number of sorbed Np(V) an apparent decrease, which may be indicate the formation of ternary OH–/Np/clay mineral surface species.

Table 5-4: Metric parameter from R-space fits to Pu L3 edge. EXAFS fit parameters: O1 1st oxygen backscatterer (bridging and terminal hydroxyl groups), O2 2nd oxygen backscatterer (terminal water), (g) indicates global parameter for both oxygen shells, S02 fixed at 1.0

Sample (1 week)	k-range (\AA^{-1}) fit-range (\AA)	shell	N	R (\AA)	ΔE_0 (eV)	σ^2 (\AA^2)	r-factor
Pu(IV)aq ^a		Oex	8-9	2.39			
Pu(V)aq ^b		Oax	2	1.82	4.92	0.0003	0.002
(HClO ₄ pH 1.6)		Oeq	4.5	2.47	-3.99	0.0049	
Pu(VI)aq(1 M HClO ₄) [conradson 2001]		Oax	2	1.75			
		Oeq	5-6	2.41			
Pu / COX	2.85-13.0	O1	4.0	2.24(1)	-2.47 ^g	0.0020	
	0-3.90	O2	3.2	2.41(1)	-2.47 ^g	0.0016	0.026
		Pu	4.4	3.73(2)	-7.20	0.0074	
Pu / OPA	2.90-13.0	O1	4.1	2.26(1)	-1.61 ^g	0.0022 ^g	
	0-3.96	O2	2.8	2.41(1)	-1.61 ^g	0.0022 ^g	
		Pu	3.7	3.75(2)	-6.83	0.0059	

a: [Conradson et al., 2004]; b: [Rothe et al., 2011]

To obtain molecular-level information on the interaction of Pu with OPA and COx clay rocks, Pu L3-edge EXAFS spectra of the plutonium treated with both clay rocks are shown in Figure 5-6 together with the corresponding Fourier transforms (FT's) representing radial distribution functions of the atoms surrounding the Pu atom. In Table 5-4 shows the Pu-L₃ EXAFS structural parameters which are obtained. The average Pu-O1 (hydroxide) distance for sample Pu-OPA, Pu-COx are in the range of 2.22 – 2.26 \AA , indicating that the Pu in all samples is sorbed at the clay surfaces as Pu(IV). A Pu-Pu interaction at ~ 3.75 \AA with two Pu atoms is observed in all spectra, indicating the presence of polynuclear Pu(IV) species or Pu(IV) colloids at the clay surfaces. Finally it can be concluded that either a Pu surface precipitation occurs or an inner-sphere sorption of the polynuclear Pu(IV) species might be expected on both surfaces.

5.2.3 XPS

To investigate the redox state of sorbed radionuclides on the clay particles, surface sensitive XPS (x-ray photoelectron spectroscopy) is applied. Besides photoelectron spectroscopy of the radionuclides, analyses of the chemical states of iron and sulphur of the clay suspension indicate which of these elements may be available for reduction of the radionuclides to a less soluble state.

Actinide clay suspensions and wet pastes are prepared for XPS analysis by drying small portions on an indium foil in an anoxic glove box. The samples are conveyed into the XP spectrometer, PHI model 5600ci, without air contact by means of a vacuum transfer vessel. Monochromatic Al K_{α} x-rays are used for excitation in conjunction with an electron flood gun for sample surface neutralization. Atomic concentrations are calculated from the areas of elemental lines of survey spectra. Narrow scans of elemental lines are recorded for determination of chemical shifts and spectral features.

Actinides (Pu, Np) are doped into the clay suspensions at low concentrations, thus only the actinide 4f main lines are detected with low intensity. Fortunately, no complete spectral superpositions with elemental lines from the constituents of the clays are present. Only Pu $4f_{5/2}$ is superposed by the intense Ca 2s elemental line, while Pu $4f_{7/2}$ is not superposed. Np $4f_{7/2}$, $4f_{5/2}$, elemental lines can thoroughly be detected if present. However, Tc was not detected at the clay surfaces after a contact time of 7 days in suspension.

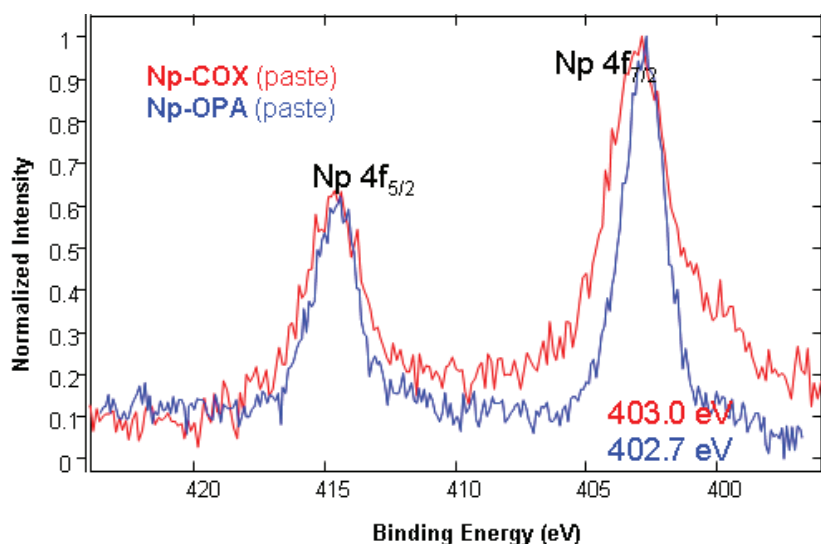


Figure 5-7: Np $4f_{7/2}$ spectrum, Al K_{α} mono x-ray excitation, charges referenced C1s (CxHy): 284.8 eV. Wet Paste: Opalinus and COx clay, Np(V) 4×10^{-4} M, 7 days contact time.

In case of Np-OPA, the Np $4f_{7/2}$ elemental line has a binding energy of 402.9 eV (Figure 5-7). However, Np(V) and Np(IV) have similar binding energies of the 4f elemental lines and conclusions concerning the valence state of Np are solely derived from the positions of 4f satellites if present. A satellite at about 6.5 eV higher binding energy is not detected indicating absence of Np(IV)oxide or Np(IV) eigencolloids. However, a distinction between sorbed Np(V) and ideal Np(IV) sorption of single, non-interacting Np atoms cannot be performed.

The Pu 4f_{7/2} elemental line at Pu-OPA samples has a binding energy of 426.0 eV typical for the tetravalent state (Figure 5-8). In addition, a satellite at about 6.5 eV higher binding energy is detected indicating a Pu(IV) oxide hydrate, presumably due to Pu eigencolloids.

The S2p spectra indicate solely the presence of sulfate and no sulfur in a reduced state like sulfide. The Fe 2p_{3/2} spectra has two components assigned to Fe(III) and Fe(II). No satellite typical for the Fe³⁺ ion was observed. No clear conclusions could be drawn about the bonding of the iron. The spectra are similar to reference spectra of Fe₃O₄ and iron silicates (iron bound in the clays).

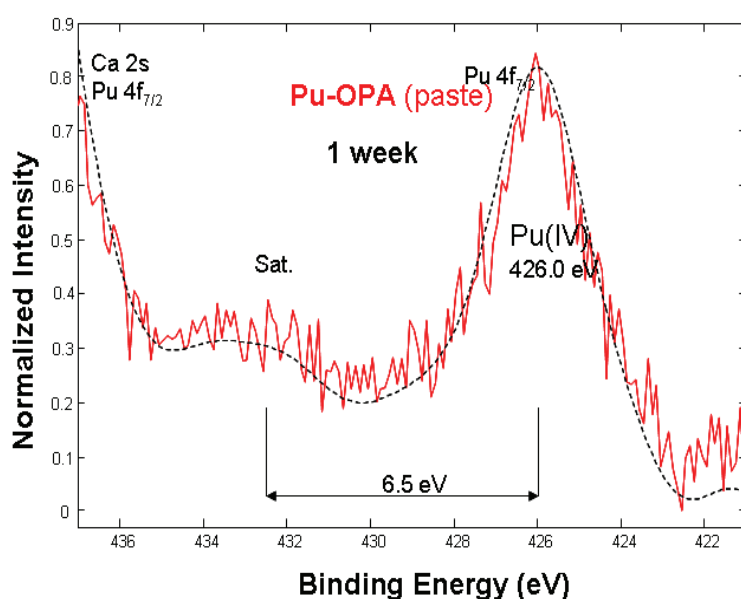


Figure 5-8: Pu 4f_{7/2} spectrum, Al K α mono x-ray excitation, charges referenced C1s (C_xH_y): 284.8 eV. Wet Paste: Opalinus clay + Pu(V) 3x10⁻⁴ M, 7d contact time.

The relative portion of Fe(II) in the CO_x sample is less than in the OPA clay. The absolute Fe concentrations within OPA and CO_x clays are comparable. A change of the Fe 2p spectra upon Np and Pu interaction is not detected as may be expected by redox-reaction which is explained by the low metal concentration.

CO_x and OPA clays both contain Fe(II) which may be available for redox reaction with added radionuclides while sulphur is oxidized to sulfate and thus is not involved in redox reactions.

5.3 Redox speciation of plutonium and neptunium in clay/ porewater system

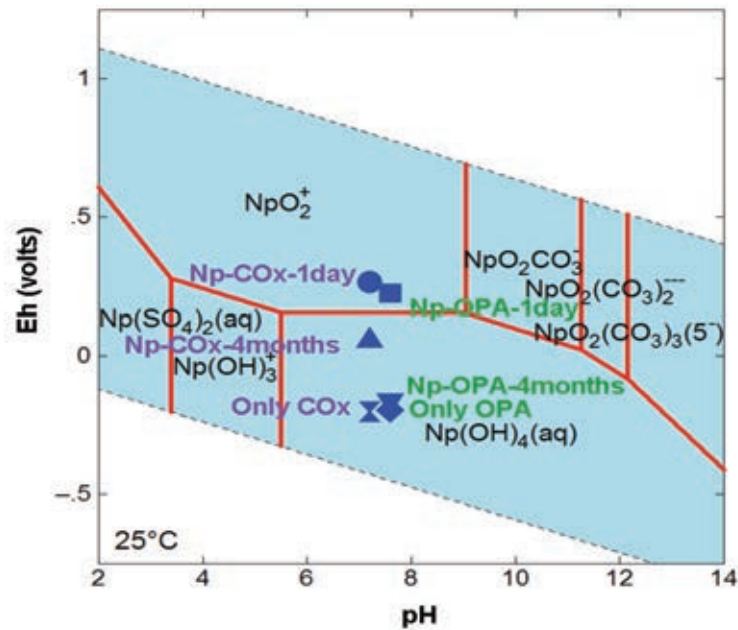


Figure 5-9: Eh-pH Diagram of neptunium OPA/COx system in pore water and speciation calculation are performed using Geochemist Workbench, thermochemical database, $[Np]_{total} = 1 \times 10^{-8} \text{ M}$, $I = 0.1 \text{ NaCl}$, $T = 25 \text{ }^{\circ}\text{C}$

Neptunium and plutonium geochemical behaviour are considerably significantly governed by their redox chemistry. Np can exist in solution as +3, +4, +5, +6, and +7 oxidation states, but only Np(IV) and Np(V) are most stable in natural environments. Neptunium's geochemical behaviour is highly influenced by its redox speciation. As seen in the Eh-pH diagram below (Figure 5-9), Np is commonly found as mobile Np(V), in the form of the dioxocation, NpO_2^+ under neutral, oxidizing conditions, and as at higher pH range the most predominant species are $Np^{(V)}O_2(CO_3)^-$ and $Np^{(V)}O_2(CO_3)_2^{--}$. However, in reducing conditions, only $Np^{(IV)}(OH)_4$ becomes the dominant species. This Np(IV) species is the least immobile because its low solubility and a strong sorption capacity to mineral surfaces [Silva et al., 1995]. Furthermore, the Np redox speciation with clay rocks system in pore water is complicated and not yet well studied. The opalinus clay and Callovo-oxfordian clay rocks are mixture of different clay minerals (like illite, Monmorilitite, kaolinite, calcite, smectite etc.) and containing trace amount redox active elements (e.g., Fe^{2+}/Fe^{3+} , sulphur, Al^{3+} etc) which might significantly influenced for the redox speciation in solution. On the contrary to redox sensitive cation, anions like sulphate plays also a role in pore water for the Np redox speciation. In Figure 5-9 the Eh-pH diagram for Np redox speciation in pore water modelled with with Geochemical Workbench is shown. Solid phases of Np are suppressed by the calculation and only dissolved

species are shown. As comparison the experimental pH and Eh values measured for the Np in clay rock suspensions - mixture of synthetic pore water and clay rocks - at varying contact time are plotted in the same graph. The measured Eh values slowly decrease with contact time between the pore water and the clay rock indicating that reaching redox equilibrium is a slow process. Obviously, the equilibrium state was not reached in our experiments, also caused by oxygen intrusion into the glove box during the experiment. However, the Eh values are located in the stability field of the tetravalent neptunium after 4 month. Hence, the Np(V) can be reduced to Np(IV). The reduction mechanism – whether the reduction takes place in solution or on the clay surface - is unclear so far.

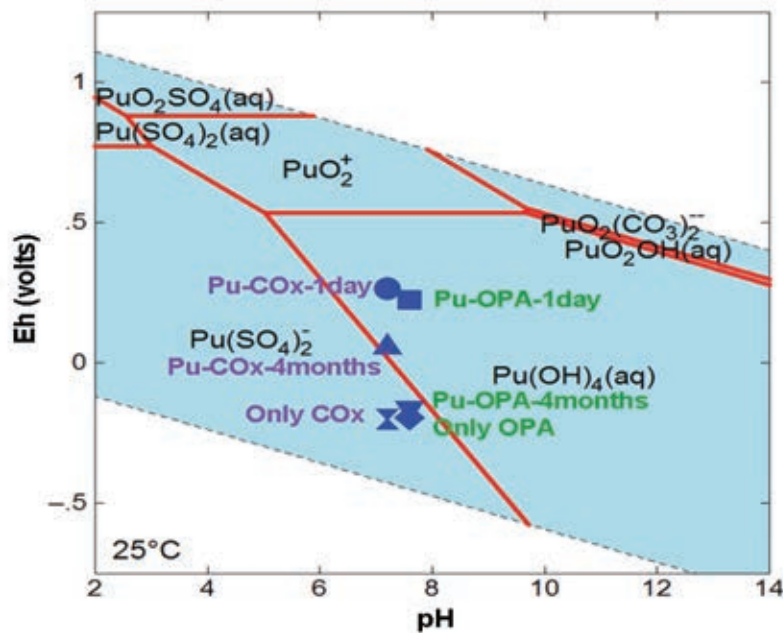


Figure 5-10: Eh-pH Diagram of plutonium OPA/COx system in pore water and speciation calculation are performed using Geochemist Workbench, thermochemical database, [Pu]_{total} = 1 x 10⁻⁸ M, I= 0.1 NaCl, T= 25 0C

Plutonium redox speciation and its geochemical behaviour is also strongly governed by the redox conditions. In aqueous solutions, Pu can coexist in the trivalent, tetravalent, pentavalent, and hexavalent oxidation state, each shows distinct chemical behaviour. The Eh-pH diagram for Pu redox speciation in pore water is shown in Figure 5-10. Solid phases of Pu are suppressed by the calculation and only dissolved species are shown. Again for comparison reasons, the experimental pH and Eh values measured for the Pu in clay rock suspensions at varying contact time are plotted in the same graph. As in the Np experiments the Eh values slowly decrease with contact time between pore water and clay rock. In contrast to Np, already at the beginning the experimental Eh values are located in the stability field of the tetravalent Pu. At neutral and basic pH values the Pu^(IV)(OH)₄ is the relevant Pu species. The sorption of Pu on the clay rock was also much faster than for Np indicating a faster reduction of Pu(V) to Pu(IV). From the very low solubility limit of Pu(OH)₄(am) in solution – this is con-

firmed by the very low Pu concentrations at the detection limit of the liquid scintillation counting - we assume that the Pu precipitates on the surface of the clay.

5.4 Basic developments on the capillary electrophoresis coupled to ICP-MS

For the speciation of actinides in solution spectrometric methods are limited to only relative high metal concentrations and they fail at tracer concentrations below 10^{-6} mol/L. For that capillary electrophoresis combined with ICP-MS (CE-ICP-MS) is a very sensitive analytic system that can have speciation limits down to 10^{-9} mol/L and lower, depending on the metal ion and composition of the solution. The CE-ICP-MS is a rather young method applied for metal speciation and therefore, development of the system, apparatus and separation system, are needed to improve reliability of the method as well as its applicability on complex composed solutions. In this work package basic developments have been made that are outlined in the following chapters. The work has been done in a collaboration with the University of Cologne (Dr. B. Kuczweski, Abteilung Nuklearchemie).

5.4.1 Development of an optimised sample introduction into the ICP-MS for the use with the CE-ICP-MS

Conventional nebulisers which are used for the CE-ICP-MS coupling like the GE Micromist offer transfer rates of 10-25%. It should be possible to increase this transfer rate due to the low sample uptake of 100 μ L/min by heating the spray chamber and the transfer line. Figure 5-11 shows the experimental setup.

From 50°C on the transfer rate is nearly 100% of the sample uptake. To prevent the condensation in the ICP-MS torch higher temperatures are required. However with higher aerosol temperature the rate of undesired oxides and double charged ions increases significantly. Therefore the optimum temperature of the spray chamber is between 50 and 55°C. Unresolved is the heating of the transfer line. This development was superseded with a new nebuliser provided by Burgener. This parallel path nebuliser offers the transfer of a dry aerosol with a sample uptake of 2-10 μ l/min which is controlled by a syringe pump.

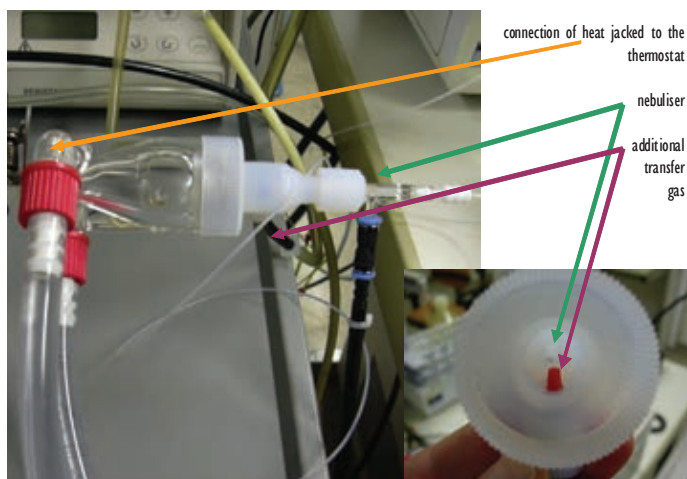


Figure 5-11: Experimental setup for the optimisation of the sample transfer of CE-ICP-MS.

5.4.2 Method development of a CE-DAD-ICP-MS for the simultaneous detection of humic substances (DAD) and metal ions (ICP-MS)

In cooperation with Johannes Gutenberg Universität Mainz the CE-ICP-MS detection unit was extended with a diode array detector. Figure 5-12 shows the scheme of the coupling. Holmium and Aldrich humic acid (AHA) were used to test the principle. Humic acid was marked with iodine to determine the humic acid as well in the ICP-MS as with the DAD. Figure 5-13 illustrates the successful and simultaneous detection of Ho and AHA in form of an electropherogram. The left graph shows the data from the diode array where one can see the UV/VIS Spectra of humic acid and free iodine which is released from the humic acid. The right graph shows the merged data from the DAD at two wavelengths with the ICP-MS data at the masses of iodine and holmium. The first peak at 135 s ICP-MS / 112.5 s DAD can be identified as iodine by the DAD-spectrum. The second one at 185 s ICP-MS / 145 s DAD can be assigned as holmium humate complex. At 240 s ICP-MS / 185 s DAD the electroosmotic flow EOF was determined. The Ho signal with the maximum at 280 s ICP-MS is free Ho that was not complexed and therefore separated fast. The Ho between 240 s und 280 s is partly released from the complex. Strong and weak binding sites for metal ions at the humic acid are the reason for this phenomenon. The weak binding sites release the Ho during the separation continuously. This cause a continuous signal of Ho between the signal of free Ho and the Ho-humate complex.

In principle the methods works well and substances with a strong UV/VIS sorption can be identified easily. Only the limit of detection of the DAD (20 pbb for humic acid) should be improved by better optical focussing into the capillary.

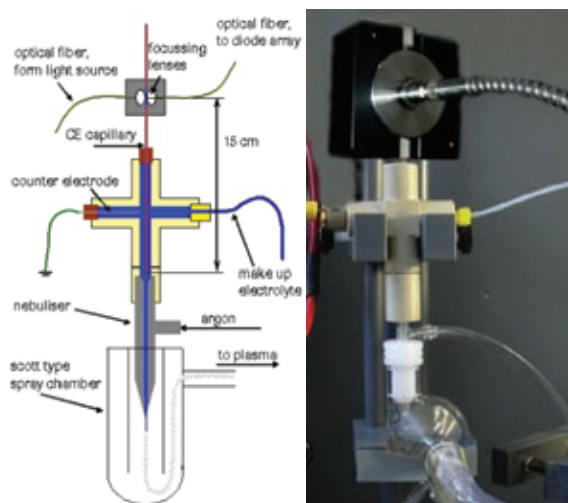


Figure 5-12: Sketch and photo of the CE-DAD-ICP-MS.

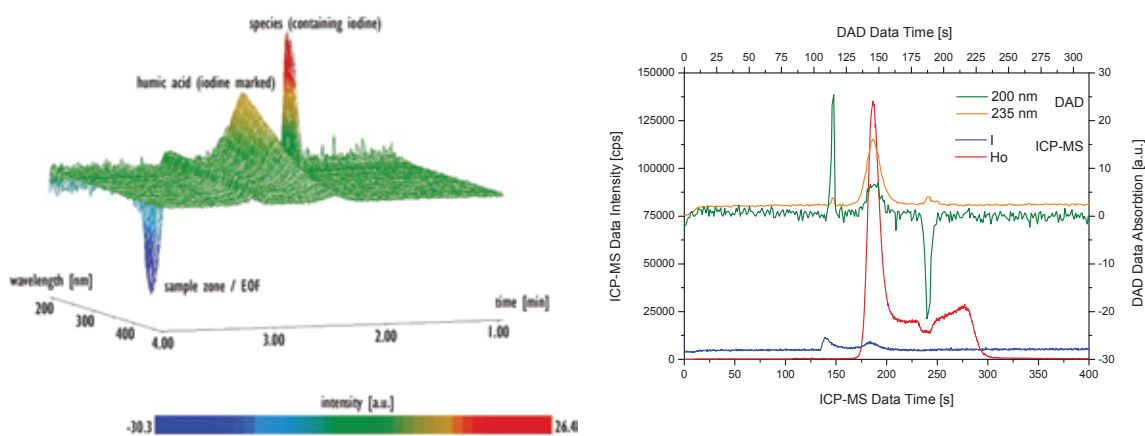


Figure 5-13: Separation of free Ho, free humic acid and Ho humate complexes by the CE-DAD-ICP-MS coupling (250 mg/L humic acid, 0,75 mg/L Ho, electrolyte 1 M AcOH, -25 kV, 250 mbar, FS capillary length 80(63) cm, 50 μ m ID).

5.4.3 Development of separation parameters for the speciation of uranium with CE-ICP-MS

The separation of plutonium and neptunium species by CE-ICP-MS is a well established method with a acetate buffer electrolyte system, but uranium could not be separated with same conditions. It was necessary to apply a stronger complexing agent than acetic acid. EDTA proved to be the best additive. Table 1 gives the separation conditions. The solution of the two oxidation states was prepared by electrolysis. The content was measured by UV/VIS spectroscopy (as reference) and with the CE-DAD-ICP-MS. The solution was not stored under special conditions, therefore a fast oxidation was expected, but the complexing agents stabilise the oxidation states well. 10 and 80 minutes after the preparation and mixing with the

electrolyte the uranium speciation measurement gives within the errors the expected values. Figure 4 shows an electropherogram of Cs (as marker), U(VI) and U(IV).

Table 5-5: Separation conditions for uranium species with CE-ICP-MS.

Electrolyte	100 mM AcOH; 10 mM Na ₂ EDTA
Sample	in 8 M HCl electrolysed solution, mixed 1:1 with electrolyte after end of electrolysis
Voltage	+ 25 kV
Pressure	150 mbar
Capillary	fused silica, length: 65 cm, diameter: 363 μm / 50 μm

Table 5-6: Validation of the uranium species separation.

	U(IV)	U(VI)
expected (UV/VIS)	83 %	17 %
measured 10 min	81 %	19 %
measured 80 min	80 %	20 %

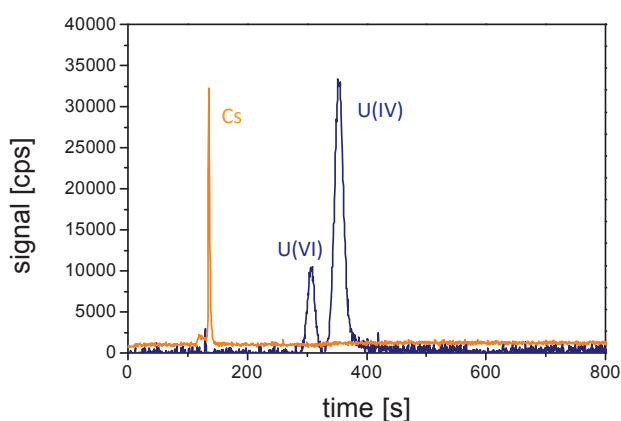


Figure 5-14: Separation of uranium species by CE-ICP-MS. (separation conditions see **Table 5-5**).

5.4.4 Modelling of the CE-separations for selected problematic separations

By support of the Charles University in Prague the model calculations of the used electrophoretic separation have been done. The software Simul allows understanding the processes, pro-

ceeding during the separation. For example the peak form differs strongly from the medium, in which the sample is injected. If plutonium standard solutions are injected into the capillary in diluted nitric acid, the peaks are broad and have a low intensity. After dilution with the electrolyte (1 M acetic acid) 1:1 the signals are small and have a higher intensity. Due to this effect the limit of detection increases in spite of dilution. By the use of Simul it was possible to give an explanation of this phenomenon. A strong change in the electric conductivity causes that the Pu ions can leave the injection zone just slowly and cannot form sharp peaks. It was found by the theoretic calculation, that a dilution of the sample 1:1 with the electrophoretic buffer is a suitable remedy. The calculated electropherograms are shown in Figure 5-15.

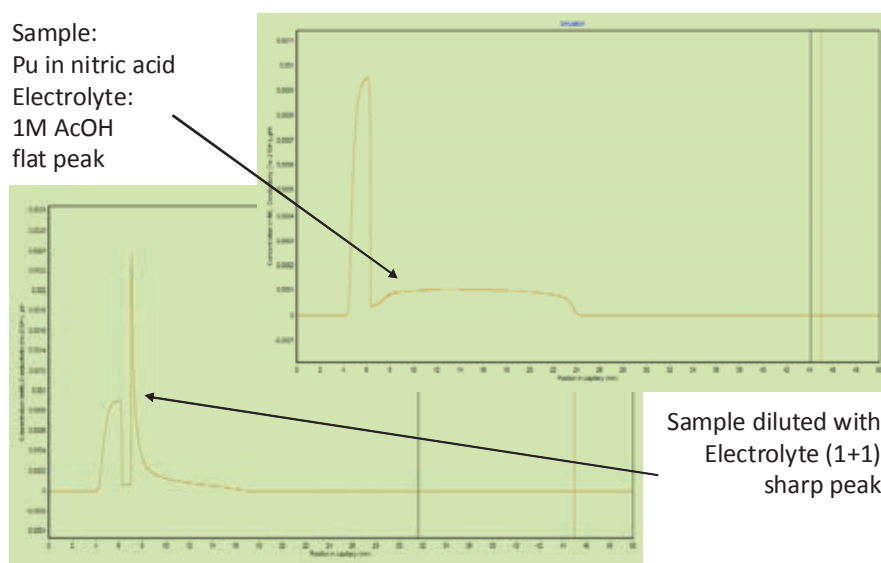


Figure 5-15: Simulation of concentration and conductivity vs. position in capillary. Right graph: Pu in nitric acid electrolyte: 1 M AcOH, left graph Pu in nitric acid 1:1 diluted with electrolyte. In each graph left signal: injection zone, right signal: resulting peak in electropherogram.

6 Basic investigations of the actinide complexation with clay organic components and humic substances

6.1 Interaction of Cm(III) with Kerogen extracted from clay rock

Kerogen is a polymeric organic material in sedimentary rocks, which can be extracted by aqueous solutions at certain conditions, e.g. high pH values (s. also Chapter 2.4). The role of Kerogen regarding the mobilisation of radionuclides in clay systems is unclear so far. For that, we started experiments to study the complexation of the trivalent actinide Cm(III) with Kerogen extracted from the OPA clay. However, we have to admit that the remaining amount of inorganic phases in the kerogen are a major problem for complexation studies and the complexation behaviour observed so far is unfortunately driven by these impurities. The impurities are mainly $\text{Fe}^{2+/3+}$ and reduced/oxidised sulphur containing mineral residues (s. Figure 6-1 and Table 6-1). The content of Fe and S amount to be about 4 and 7 wt%, respectively. It should be mentioned that Kerogen from COx and OPA is very similar concerning the spectroscopic characteristics of the Fe L-edge & S K-edge.

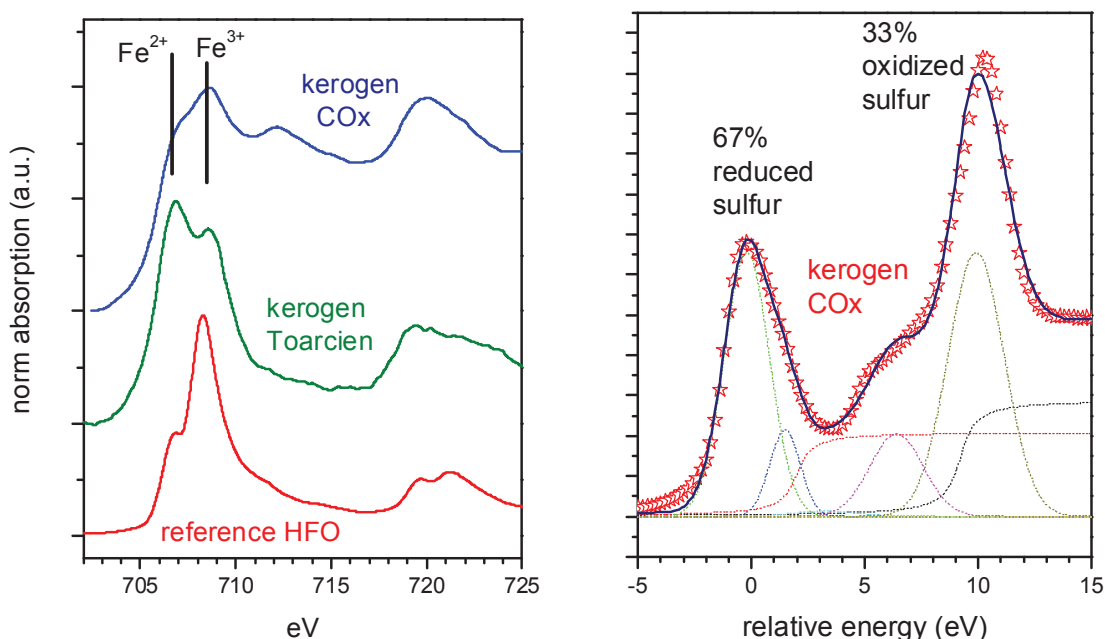


Figure 6-1: Characterisation of kerogen extracted from natural clay rock.

Table 6-1: Elemental composition of kerogen extracted from OPA. More than 78 wt.% are organic matter, but a high content of inorganic iron and sulfur compounds remain in the fraction.

Element	Weight %
C	55.60
O	23.12
Al	0.22
Si	6.57
S	4.01
Fe	7.48
Total	100

TRLFS spectra of Cm(III) in Kerogen solutions show a second peak indicating a interaction of Cm(III) with compounds in the Kerogen extract (s. Figure 6-2). Comparable drawbacks have been seen and are documented in investigations from Belgian groups where isolated kerogen from the Boom clay formation has been used. Due to this fact it was abdicated performing further Kerogen complexation experiments until the impurities can be removed without altering the structur of the Kerogen.

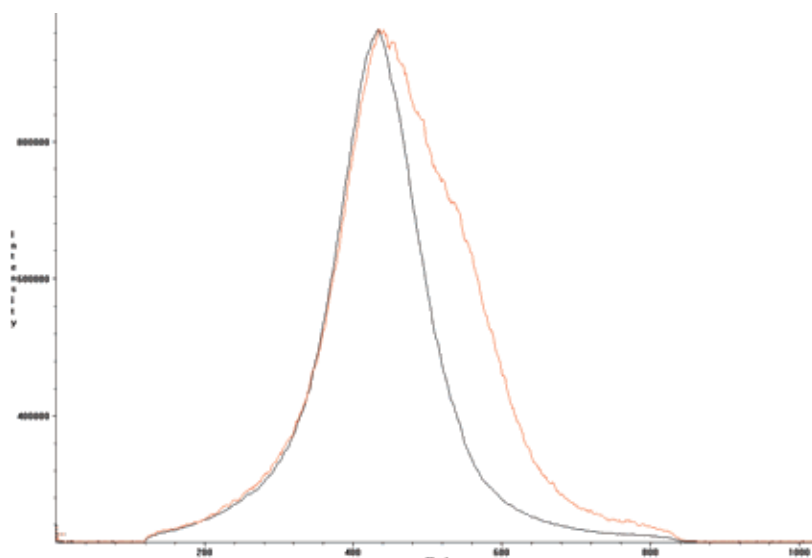


Figure 6-2: TRLFS of Cm(III) interaction with kerogen extracted from OPA.

The supposable importance of clay organic matter was shown in experiments from [Courdouan et al., 2008] with support from KIT-INE. They found a significant Cm complexation by DOM for OPA pore water, and a little complexation by DOM detected in the OPA and COx extracts under exclusion of CO₂. However, carbonates largely controlled Eu speciation under in situ conditions (pore water) of europium in OPA and COx pore water. For OPA the carbonate species EuCO₃⁺ was calculated to be 54% and the second most important species the Eu-DOM complexes were calculated to be 29% of total dissolved Eu in the pore water. Despite the fact that carbonates are dominating the DOM in the OPA pore water may enhance

the Eu solubility by 5×10^{-8} M, representing about 1/3 of total dissolvable Eu. Which organic compound of the DOM in the pore water is responsible for this enhancement is unclear so far.

6.2 Basic investigations of the Np(IV) fulvate complexation

Humic substances (HS), a mixture of organic macromolecules, are ubiquitous distributed in the ecosphere. It can be not excluded that humic or fulvic-like organic compounds are contained in organic clay material. Therefore, in the context of disposal of radionuclides in clay rock formation as well as in other geological formation data are needed about the interaction of actinides and these organic compounds. Under reducing conditions that occur in deep geological formations neptunium is stable in the tetravalent oxidation state.

Experimental data related to the interaction of tetravalent actinides are limited and mainly focused on Th(IV) which is less hydrolysable tetravalent ion and for which the complexation starts at a reasonable pH values. But data for the complexation of Np(IV) with humic substances are very scarce. The mechanism of tetravalent actinide complexation with humic or fulvic acids (HA or FA) is not well clarified, because of manifold experimental difficulties such as interfering eigen-colloid formation, strong sorption behaviour and redox reactions. Reiller et al., 2008, emphasized in their review that more sound experimental data on the complexation of tetravalent actinides by humic or fulvic acids are needed. Therefore, we have initiated studies on the Np(IV) fulvate complexation with the goal to elucidate the complexation mechanism by minimizing eigen-colloid generation of Np(IV).

Furthermore most of Np(IV) complexation studies with HS have been performed at low pH 1 and 1.5 by UV-VIS/NIR absorption spectroscopy [Marquardt et al., 2000, Pirlet, 2003], XANES and EXAFS [Denecke et al., 2002, 2005; Schmeide et al., 2005]. However, the understanding of Np(IV) speciation in containing humic substances is not satisfactory due to their formation of colloids, the various Np(IV) hydrolysis species and their mixed hydroxo fulvate complex species.

In this work we started a further approach by preparing tetravalent Np(IV) fulvate by three distinct methods, characterised the Np(IV) fulvates by UV-Vis, XANES, EXAFS, and XPS and faced all results to get more insight into the mechanism of the complexation.

6.2.1 Materials and Methods

Neptunium-237

The neptunium solution was evaporated to dryness and dissolved in 8 M HCl. The solution was purified via anion exchange (BIO RAD[®] AG 1-X8). After a washing step with several millilitres of 8 M HCl, plutonium contaminations were removed with a fresh solution of 150

mg NH₄I in 5 mL 8 M HCl. Subsequently, neptunium was eluted from the ion exchanger with 4 M HCl/ 0.05 M HF and evaporated to dryness in a PTFE beaker. To obtain a solution containing only Np(V), the solution was fumed two times with 1 M HClO₄ and the residue was dissolved in deionized water. This stock solution could be stored at a pH value of 3 for several days. Neptunium (IV) was prepared using a zinc-amalgam treatment and potentiometric electrolysis.

Gorleben fulvic acid

The natural humic acid and fulvic acid from ground water of the deep borehole Gohy-573 in the Gorleben site (lower Saxony, Germany) were isolated, purified and characterized according to [Wolf et al., 2004]. Elemental composition (C, H, N, O and S) of Gohy-573 HA and FA are shown in Table 6-2. Preparations of Gohy-573 HA and FA solution were carried out according to the procedure described above. The Proton Exchange Capacity (PEC) value of Gohy-573 FA was determined to 6.82×10^{-3} eq/g.

Table 6-2: Elemental composition of the new prepared Gohy-573 FA and HA. Summarized are the mean values of triplicate analysis, carried out by Analytische Laboratorien, Lindlar, Germany, together with the standard deviation. For comparison, also the elemental compositions of the former charges are shown (Gohy-573 FA (one analysis) and the mean value for Gohy-573 HA I and II (see, Buckau 1991)). The data are normalized to a total CHNOS content of 100 %.

Humic substance GoHy-573	C (wt.%)	H (wt.%)	O (wt.%)	N (wt.%)	S (wt.%)
FA	54.1 ± 0.1	4.23 ± 0.08	38.94 ± 0.04	1.38 ± 0.02	1.32 ± 0.01
HA	59.3 ± 0.1	4.57 ± 0.02	32.1 ± 0.1	2.01 ± 0.06	2.02 ± 0.09
FA (old batch)	57.18*	4.85	35.38	1.14	1.44
HA (old batch)	56.79	4.64	35.76	1.73	1.73**

* new calculated value; ** only the value of separate pre-batch (HA I) is given.

Different preparation paths for Np(IV)-FA complexation experiments

To minimise Np(IV) colloids formation, three different preparation paths for Np(IV) fulvate complexation have been performed. 1) Np(IV) is formed in strong acidic solution (pH<1) by electrolytic reduction of Np(V). Afterwards aliquots of the solution were mixed with fulvic acid solution to form the Np(IV) fulvate complex (preparation I). 2) Trivalent Np is mixed with fulvic acid solutions and slowly oxidised by oxygen impurities in the glove box atmosphere to form the corresponding Np(IV) fulvate complex (preparation II). Because of the slow oxidation process and the strong interaction of Np(IV) with the fulvic acid, the uncomplexed Np(IV) concentration might be kept below its solubility limit. Thus, this method will avoid colloid formation of tetravalent neptunium even at higher metal concentrations. 3) A pentavalent Np fulvate complex is prepared at pH 9. Then the Np(V) is reduced by dithionate forming the Np(IV) fulvate complex (preparation III) Then, the Np(V)FA was reduced to tetravalent

neptunium complex (Np(IV)FA) with Na-dithionite resulting in a pH of about 3, 4.5, and 5. It is assumed that the Np(IV) occurs in HA as unhydrolysed Np^{4+} ion directly after the reduction reaction, but slowly becomes hydrolysed and forms colloidal species with time.

All solutions were characterised by UV-Vis spectroscopy, x-ray photoelectron spectroscopy (XPS), and XAFS. The Np(IV) concentration was in the range of 10^{-5} to 10^{-4} M, the fulvic acid concentration was 30 - 1000 mg/L the pH of the solutions was varied between 1 and 4.5 and the ionic strength was 0.1 M NaCl. All experiments were performed in a glove box with argon atmosphere.

UV-Vis/NIR absorption spectroscopy (UV-Vis/NIR)

The oxidation states of Np(IV) in the stock and sample solutions are confirmed by UV-Vis/NIR spectroscopy with a high-resolution UV-Vis/NIR spectrometer Cary 5 (Varian). The samples are measured in 1 cm inert-gas quartz cuvettes (Hellma) with tight screw tops, or in polystyrene semi-micro cuvettes (Brandt). UV-Vis/NIR spectra are taken from 400 nm to 1100 nm. The spectra are analysed using Grams/A1 (7.02 version) software. All complexation experiments are conducted according to titration procedures with initial Np concentration in the range of $5.0 \cdot 10^{-5}$ - $2.0 \cdot 10^{-4}$ M. Multiple titration's with different concentrations of fulvic acid and Np has been performed. In each titration, appropriate aliquots of the titrant (fulvic acid) are added to the Np and mixed thoroughly with stirrer (for 1-2 min) before the spectrum has been collected.

XAFS Measurements

XAS investigations were performed at the INE-Beamline for actinide research [Rothe et al., 2006] at ANKA, Karlsruhe, Germany. A double crystal monochromator (DCM) is used, equipped with a pair of Ge(422) crystals ($2d = 2.310 \text{ \AA}$), and higher harmonic radiation suppressed by detuning the parallel alignment of the DCM crystals to 70% of photon flux peak intensity at the beginning of each scan. The incident photon flux, measured with an Ar filled ionization chamber, is held constant using a MOSTAB feedback system. The spectra presented are measured in fluorescence yield detection geometry using a five pixel Canberra LEGe detector; 8 to 10 scans are averaged to reduce the noise level. Spectra are calibrated against the first inflection point in the XANES spectrum of a Zr foil for Np L_3 -edge measurements. The energy of the inflection point is defined as the first derivative maximum set to $E(\text{Zr}1s) = 17998 \text{ eV}$ and $E(\text{Y}1s) = 17038 \text{ eV}$. XAS spectra are measured with a step width of 5 eV before the edge, 0.7 eV steps in a region of -30 eV to 30 eV relative to the edge position, and equidistant steps in wave number k of 0.03 \AA^{-1} thereafter. XANES spectra are isolated from XAS scans following subtraction of the pre-edge background absorption and normalization of the edge jump to unity. The energy position of the XANES spectrum serves as a cross-check of the redox stability of the samples after repeated EXAFS scans. EXAFS data analysis is based on standard data reduction and least squares fit techniques using the ATHENA [Ravel and Newville, 2005] and the UWXAFS [Stern et al., 1995] program packages, respec-

tively. Metric parameters (coordination numbers N , distance to neighbor atoms r , and EXAFS Debye-Waller factors σ^2) are determined using backscattering amplitude and phase shift functions for single scattering paths obtained from FEFF7 [Rehr et al., 1992]. The energy scale is transferred into wave numbers by setting the maximum of the most pronounced feature in the spectra, the so-called white line, to $k = 0 \text{ \AA}^{-1}$. A k range of $2.5 - 9.5 \text{ \AA}^{-1}$ is Fourier-transformed using a Hanning window with 0.1 \AA sills, and fits are performed in R space from $1.5 - 2.5 \text{ \AA}$ for each sample. The amplitude reduction factor S_0^2 is held constant at 1.0 [Brendebach et al., 2009].

X-ray photoelectron spectroscopy (XPS)

The XPS spectrometer used is a PHI model 5600 (7×10^{-8} Pa base pressure) with a multi channel detector. XPS spectra were acquired by use of monochromatic Al $K\alpha$ (1486.6 eV) X-ray excitation, spot size around 1 mm^2 . A neutralizer, i.e., a source of low energy electrons, is applied to compensate surface charging. The binding energy scale of the spectrometer was calibrated by making use of the well-known binding energies of Cu $2p_{3/2}$, Ag $3d_{5/2}$ and Au $4f_{7/2}$ lines of sputter cleaned pure metal foils [Schild&Marquardt, 2000]. High-resolution scans of elemental lines were recorded at 11.75 eV pass energy of the hemispherical capacitor analyzer which yields a full-width-at-half-maximum. The elemental lines of samples are charge referenced to the C 1s line of adventitious hydrocarbon or to the C 1s line assigned to hydrocarbon bonding in the case of organic compounds at a binding energy (BE) of 284.8 eV. Curve fitting was performed using nonlinear least-squares optimization of Gaussian-Lorentzian sum functions [Schild&Marquardt, 2000].

6.2.2 Results and discussion

a) Characterisation of Np(IV)-fulvate by UV/Vis/NIR spectroscopy

Fig. 1 shows the absorption spectrum in the wavelength range between 920 and 1020 nm of Np(IV) fulvate solution prepared at pH 1, 1.5 and 3 and fulvic acid concentrations between 100 and 1000 mg/L and with different preparation approaches. Three absorption bands at 960, 968 and around 978 nm dominates the spectra depending on the pH value and the fulvic acid concentrations. At pH 1 and low fulvic acid concentrations (100 mg/L) mainly the peak of Np(IV)free at 960 nm is observed. With pH increase the peaks at 968 and 978 nm evolve, corresponding to two Np(IV) fulvate species. They are denoted in the following as Np(V)-FA^(I) and Np(IV)FA^(II).

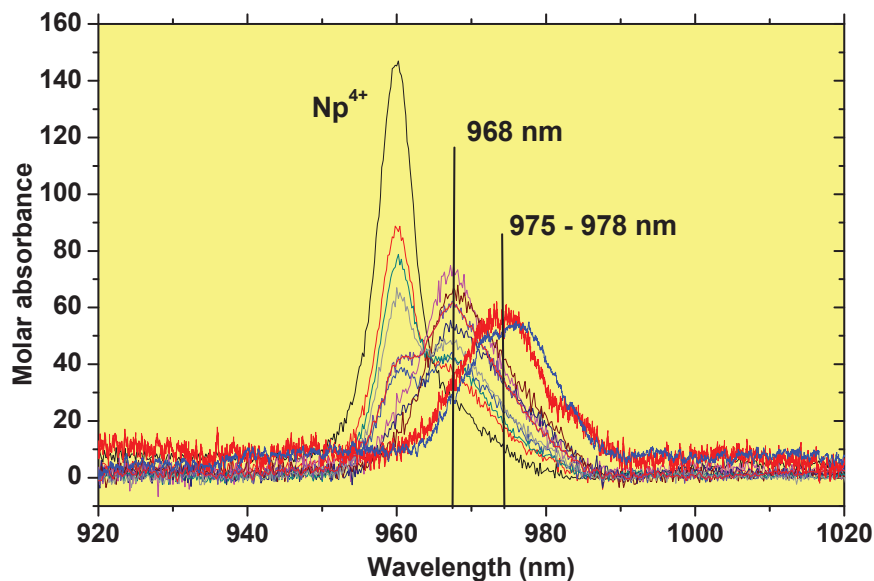


Figure 6-3: UV/Vis absorption spectra of Np(IV)-FA complexation between pH 1 and 3 and $[Np(IV)] = 5E-05$ M, $[FA] = 100-1000$ mg/L

At pH 1 and 1000 mg/L FA, mainly the absorption band at 968 nm was observed after 20 h of equilibration time and after 40 h a small new peak at 968 and 978 nm arises. By decreasing the FA concentration to 600 mg/L, 3 peaks were observed at 960 nm for the uncomplexed Np(IV) and at 968 and 978 nm for the fulvate species.

At pH 3 and 1000 mg/L FA, the peak at 978 nm besides a small one at 968 nm dominates the spectrum. No free Np(IV) was detected at 960 nm. By increasing the Np(IV) concentration, a new band near 984 nm appeared. However, only one isobestic point is found by plotting the spectra in the molar absorption scale indicating that only two species are directly correlated, the $Np(IV)_{free}$ and the $Np(IV)FA^{(I)}$. The evolution and the nature of the $Np(IV)FA^{(II)}$ species is so far unclear. Earlier studies by [Pirlet, 2003] showed also a dominating absorption band at 978 nm, by starting with the pentavalent Np(V) fulvate complex and reduction with dithionite (preparation III) but at higher pH values of about 7 than we have done (pH 3 - 5). We conclude from the pH independence of the peak maximum of the absorption band at 978 nm in the range between pH 3 and 7 that mainly one Np(IV) fulvate species prevails.

The FA concentration effect the Np(IV) fulvate complexation by varying the FA concentration from zero to 500 mg/L at constant Np(IV) concentration and pH value of 1 is illustrated in Figure 6-4. Again, one isobestic point can be found in the molar absorption scale indicating two species, the $Np(IV)_{free}$ and the $Np(IV)FA^{(I)}$. With increasing fulvate concentration the absorption at wavelengths larger than 980 nm steadily increases without evolving a new separated absorption band. In a first approach the relative weak absorption at longer wavelengths are neglected and the spectra are evaluated by only two species, $Np(IV)_{free}$ and $Np(IV)FA^{(I)}$.

The deconvolution is performed by the Program GRAMS (Galactic Co.), assuming the absorption peak area contrived by a mixed Gaussian-Lorentzian function. As shown in Figure 6-5, after subtracting the two deconvoluted peak areas from the total composite absorption area, the residual part appears statistically zero in the investigated 920 nm to 1020 nm. For the absorption peaks of Np(IV) free ion and its fulvate complex with maxima at 960 and 968 nm absorption coefficients are calculated to be $150 \pm 10 \text{ L. mol}^{-1} \cdot \text{cm}^{-1}$ and $65 \pm 15 \text{ L. mol}^{-1} \cdot \text{cm}^{-1}$ respectively.

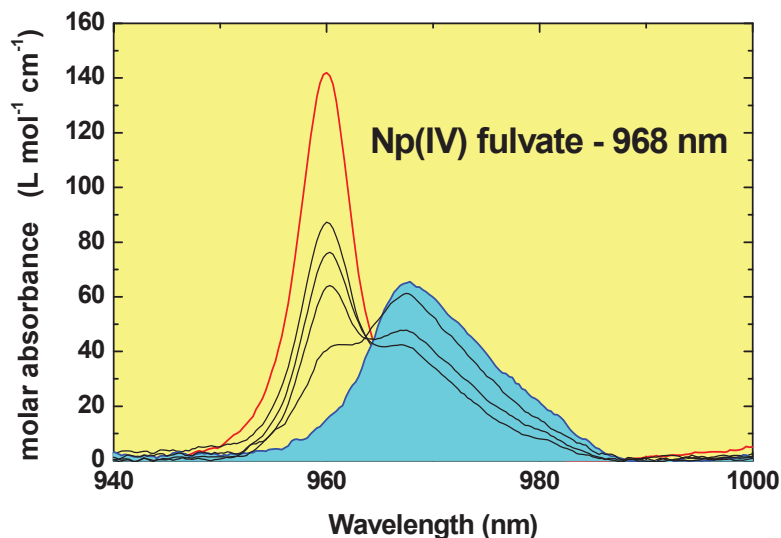


Figure 6-4: UV-Vis absorption spectra of Np(IV)-fulvate complex at 968 nm with varying FA concentration and constant Np(IV) concentration. $[\text{Np(IV)}] = 3\text{E-}05 \text{ M}$, $[\text{FA}] = 0\text{-}500 \text{ mg/L}$.

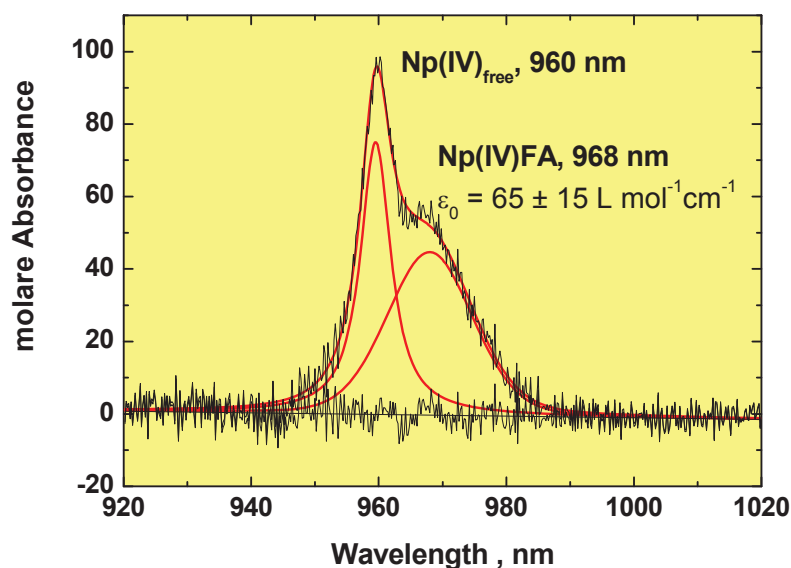


Figure 6-5: Illustration of the deconvolution spectra of the total absorption spectrum in to two single absorption bands for the free Np(IV) and Np(IV)FA(I). The peak maximums are found at 960 and 968 nm.

b) Np(IV)-fulvate by XAFS spectroscopy

XAFS measurements are performed repeatedly on various Np(IV) fulvate complexes to demonstrate that our specially designed sample cell is suitable to keep redox sensitive samples stable in an inert gas atmosphere long enough to measure good quality XAFS data.

XANES results

XANES spectra of Np(IV)FA complexes in H/NaCl solutions prepared by different approaches (method I to III, Page 110) are shown in Figure 6-6. The XANES spectrum of Np(IV)-FA shows the characteristic near-edge features of tetravalent Np compounds [Allen et al, 1997; Denecke et al, 2002, 2005; Schmeide et al, 2005; Brendebach et al, 2009]. All spectra are very similar irrespective of the preparation and the final pH value of 1.0 or 3.0. For all samples, the white line maximum are found at 17614.7 ± 0.1 eV and the errors are estimated to lie in the order of one monochromator step of 0.7 eV. The absolute values might differ from those published in previous studies [Brendebach et al, 2009; Denecke et al, 2002, 2005; Schmeide et al, 2005], which is most likely caused by different energy calibrations of the X-ray monochromator or different monochromator crystals used in these experiments. However, the edge energy of the Np(IV) and Np(V) samples, determined as the inflection point of the edge, is nearly identical. Thus, the edge shift should be less suitable to distinguish between the tetra- and pentavalent oxidation states of actinides due to the combination of structural and electronic changes. Although the intensity of the white line in the XANES of Np(IV) samples is only slightly greater than that for the Np(V) sample [Brendebach et al, 2009], together with evaluation of the EXAFS, we conclude that we can reliably distinguish between Np(IV) and Np(V) [Denecke et al., 2005].

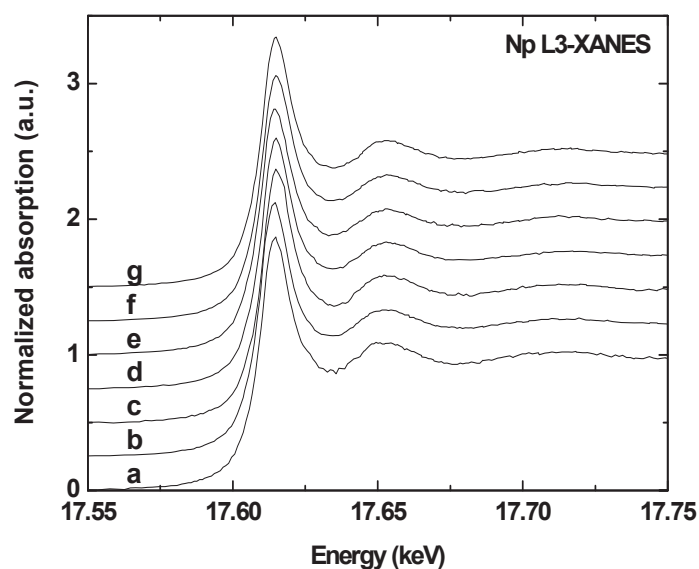


Figure 6-6: XANES of Np(IV) fulvate samples prepared in various ways (a, b: preparation (II); c, d: preparation (I); e, f, g: preparation (III)). Spectra b, d, g: pH 1.0; Spectra a, c, f: pH 3.0; Spectra e: pH 4.5. A detail about the preparation is given in the text on page 110.

EXAFS results

EXAFS measurements are performed to retrieve structural information of the first hydration shell surrounding the actinide ions. The Np LIII k³-weighted EXAFS spectra and the corresponding Fourier transforms are shown in Figure 6-7 for representative Np(IV)FA samples at pH 1, 3, and 4.5. The EXAFS spectra are very similar in the range up to 6 Å⁻¹, but show some difference at higher values. However, the scattering in the spectra in this k range makes evaluation somewhat difficult. The Fourier transform (FT) data in all cases show one dominant peak at approximately 1.9 Å (not phase shift corrected) that results from scattering on oxygen atoms of the coordinated water molecules.

Table 6-3 summarizes the structural parameters obtained from fits of the data according to the EXAFS equation. For five samples only one oxygen shell is observed with a variation in the distance between 2.24 and 2.38 Å. The Np(IV) atom is surrounded by about 6-8 oxygen atoms. There is no correlation among the preparation method and the distance as well as the coordination number of the oxygen atoms. Two samples are different from the other ones; they show two oxygen shells, one at a distance of 2.20-2.24 and one at 2.40 and 2.44 Å. This observation is in line with earlier results from [Denecke et al., 2002, 2005]. They found distances of 2.24 – 2.27 and 2.41 – 2.44. However, the coordination number of 2 and 3 for each shell is rather low compared to [Denecke et al, 2005] with 3 – 4 and 5 – 7.

The O shells of Np-O at distances of 2.20-2.24 Å is ascribed to a bonding between Np and hydroxyl ions, the longer Np-O distances at 2.40-2.44 Å is the average distance between coordinating water molecules and carboxyl groups. However, some samples showed only one average Np-O distance of 2.24 – 2.38 Å, which cannot be explained with respect to the preparation method at the moment. For the interpretation it is important that no Np-Np interaction with distances around 3.8 Å could be found in any sample. This observation is corroborated by the fact that we have not seen any dampening of the white line like it would be caused by polynuclear species. It can be concluded that the carboxylic groups of the fulvic acids are predominantly responsible for binding Np(IV) ions under the experimental conditions applied.

Table 6-3: Results from the fit EXAFS structural parameters of Np(IV) complexes with fulvic acid

Preparation of Np(IV)FA	fit range (Å)	N1 oxygen N2 oxygen	R1 (Å) R2 (Å)	σ ₂ (Å ²)	ΔE ₀ (eV)	r-factor
a) pH 3 (preparation II)	1.23-2.36	6.2	2.36	0.0096	0.92	0.0021
b) pH 1 (preparation II)	1.29-2.30	8.6	2.24	0.0096	-5.98	0.0005
c) pH 3 (preparation I)	1.20-2.30	7.5	2.28	0.0097	-3.32	0.0004

d) pH 1 (preparation I)	1.17-2.36	7.4	2.32	0.0151	-1.03	0.0052
e) pH 4.5 (preparation III)	0.98-2.36	2.3 3.1	2.20 2.40	0.0073*	-2.29*	0.0012
f) pH 3) (preparation III)	1.07-2.42	2.4 2.7	2.23 2.44	0.0069*	0.26*	0.0037
g) pH 1 (preparation III)	1.23-2.36	6.7	2.38	0.0107	1.87	0.0013

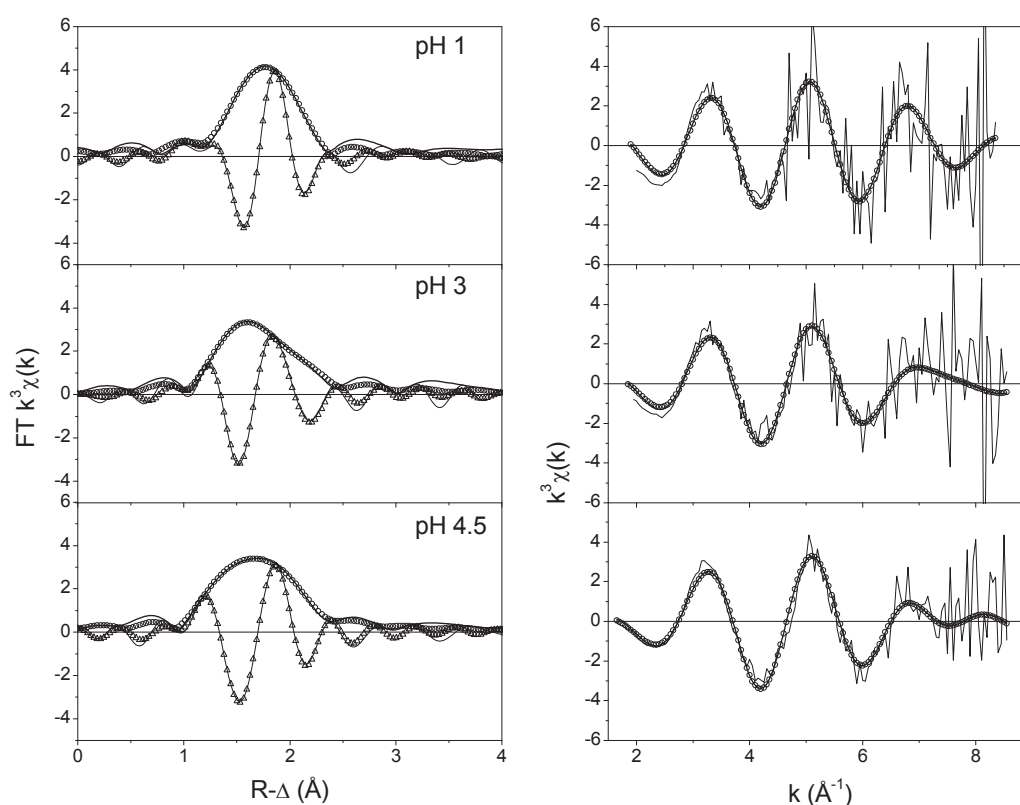
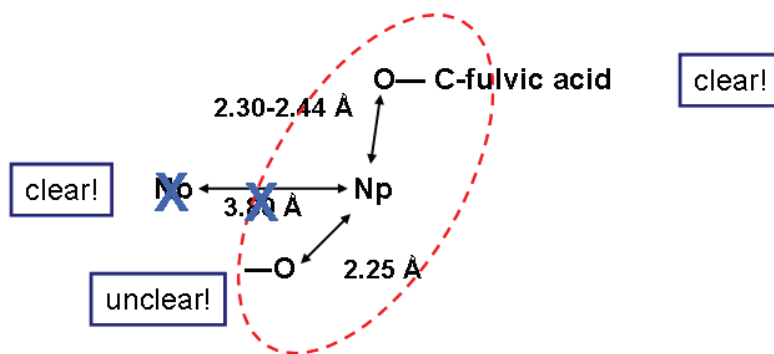


Figure 6-7: Np LIII- k^3 -weighted EXAFS spectra of Np(IV)-FA complex and corresponding Fourier transforms (upper: pH 1, middle: pH 3, lower: pH 4; preparation (III))

With our results from the XANES and EXAFS and results from other organic compounds characterised by [Bonin et al, 2009; Jeason et al, 2009, 2010] we can now suggest the following picture about the Np(IV) fulvate complexation that is illustrated in Figure 6-8.



Jeanson et al. 2009 and 2010

Complex of Np(IV) with
Nitrilotriacetic acid (NTA)
and metalloproteine
Transferrin (Tf)

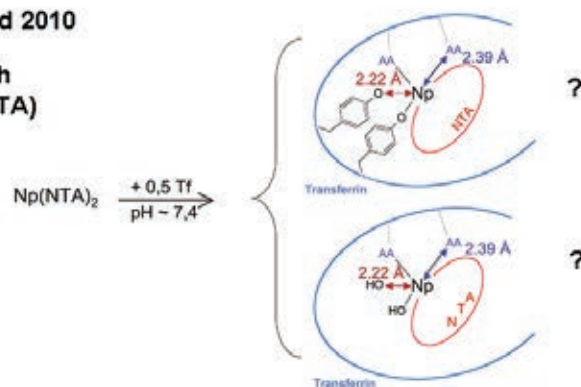


Figure depicted from Jeanson et al. 2009

Does the heterogenous FA act similar as ligand?

Figure 6-8: Schematic representation of the Np(IV)-FA complex coordination structure according to EXAFS data. Explanation is found in the text!

[Jeanson et al., 2010] made some experiments with Np(IV) and two organic compounds Nitrilotriacetic acid (NTA) and Transferrin (Tf). They observed in the EXAFS two O shells, one at 2.22 – 2.23 Å and the other at 2.39 Å, for the system Np(IV) / NTA / Tf at pH > 7. Even they had a long range contribution between 3 to 4 Å for the ternary system and the binary Np(IV)/NTA system, the short range contribution lacks for the binary system! Attempts to fit the spectra with Np-Np contributions lead to a significant improvement of some spectra, but not to the global R factor of the fit. UV/Vis/NIR and microfiltration demonstrates that hydrolysed products remain negligible. Therefore they conclude that the short distance around 2.22 Å must be the result of the ternary complex! The long range distance is explained by a combination of triple scattering paths of NTA, multiple scattering contributions by Tf and only minor contribution from hydrolysed Np(IV). Two possible structures may be considered: (i) two tyrosine residues from Tf (2.22 Å), two Tf-sites and two NTA-sites (both between 2.34 and 2.39 Å); (ii) two OH instead of the tyrosine residues, two Tf-sites and two NTA-sites. If we consider FA as a heterogeneous compound with a high variation of binding sites, ternary complexes like the Np(IV)/NTA/Tf can be assumed: Np(IV)/FA(site1)/FA(site2) with tyro-

sine like sites or hydroxide groups. However, both assumption has to be proofed in future experiments. It is clear that the distance at 2.30 – 2.38 Å corresponds to monodentate bound carboxylate, and that we have no polynuclear species in solution. However, the distance at 2.40 – 2.44 Å could also be a bidentate carboxylate complex. The nature of the short distance at around 2.22 Å is unclear so far.

We also performed a separate experiments to observe the kinetic effect of Np(IV)-FA complexation with varying contact time. The samples are prepared at pH 1 and 3 with 200 mg/L FA according to the complexation preparation II (see on Page 110). The contact time was 14 days and 3 months.

Table 6-4: Results from the fit EXAFS structural parameters of Np(IV) –FA with varying contact times

Sample	N	R (Å)	σ^2 (Å ²)	ΔE_0 (eV)	r-factor
200 mg/l FA, pH1, 14 days	9.5(1.2)	2.33(1)	0.018(2)	3.1(1.1)	0.0048
200 mg/l FA, pH3, 14 days	7.5(2.6)	2.32(2)	0.012(6)	-0.4(3.0)	0.0152
200 mg/l FA, pH1, 3 months	8.6(2.6)	2.34(3)	0.016(6)	3.7(2.6)	0.0015
200 mg/l FA, pH3, 3 months	8.6(1.3)	2.32(1)	0.018(3)	-0.3(1.3)	0.0026

Table 6-4 shows the fitted EXAFS structural parameters of Np(IV) –FA at both contact times (14 days and 3 months). The Np–O bond distance ($R = 232 \pm 0.02$ Å) are determined for all Np(IV)-fulvate samples and the Np(IV) atom is surrounded by about 8-9 oxygen atoms. Despite the long contact time of three months no Np-Np bonds were found from the EXAFS. This experiment shows that no pH effect of the Np(IV)-FA complex and no aging of complex are obtained. However, either these changes in the complex with time cannot be measured by EXAFS or the changes are very small or do not exist in the experimental pH range.

c) Np(IV)-fulvate by XPS spectroscopy

The same samples prepared for the XAFS investigations were characterised by XPS. A typical XPS spectrum of Np(IV) fulvate, as illustrated in Figure 6-9, contains two Np 4f main lines, Np 4f_{5/2} at 415.5 eV and Np 4f_{7/2} at 403.5 eV, and two weak lines at 422.0 eV and 408.0 eV, which are shake-up lines (satellites) of the main lines. The spectra of each sample are very similar. The small differences in binding energies (6.8 eV) of the Np 4 f_{7/2} lines and in the satellite spacing's of the Np(IV)-fulvates are presumably caused by different pH during preparation. From the resemblance of the spectra we conclude that only one main Np(IV)-FA species occurs at pH 3 irrespective of the preparation method.

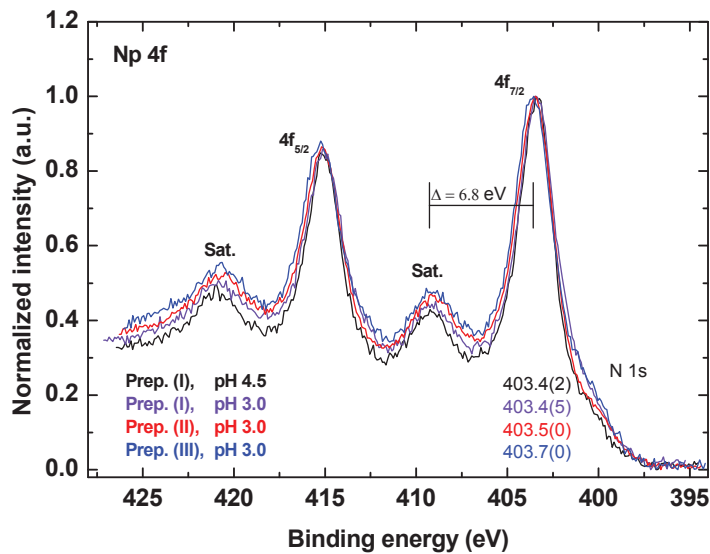


Figure 6-9: XPS spectra of Np(IV) fulvate samples prepared in various ways. Description of the preparation (I), (II), and (III) is given in the text. Np(IV) fulvate was measured as wet paste (precipitate + residual solution).

The peak separation between the main lines and shake-up satellites is indicated by (Δ). (Narrow scans of Np 4f spectra, Al K α mono; X-ray excitation, charge reference: C 1s (C_xH_y) 284.8 eV) For the kinetic experiments with 14 days and 3 months contact time, the samples reacted 3 months show higher peak intensities, and hence, higher Np concentration than the 14 days Np-FA sample at pH 1-3 (Figure 6-10). An influence of pH (1, 3, and 4.5) on the XPS spectra of the Np-FA complexes has not been found after a reaction time of 3 months. However, the same conclusion can be made as for the XAFS measurements, either these changes in the complex with time cannot be measured by XPS or the changes are very small or do not exist in the experimental pH range.

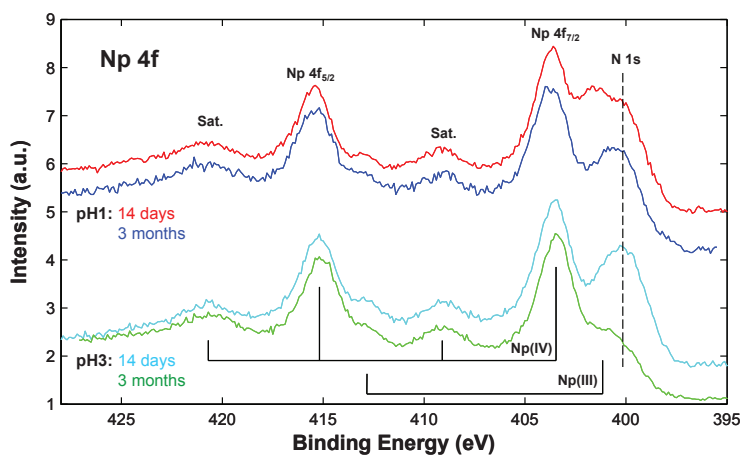


Figure 6-10: Np 4f lines and their satellites of Np(IV)-fulvates and XPS measurement performed after a reaction time of 14 days (red color line) and after 3 months of reaction (blue color line) at pH 1 and a reaction time of 14

days (olive color line) and after 3 months of reaction (green color line) at pH 3, acquired using monochromatic Al K α X-rays.

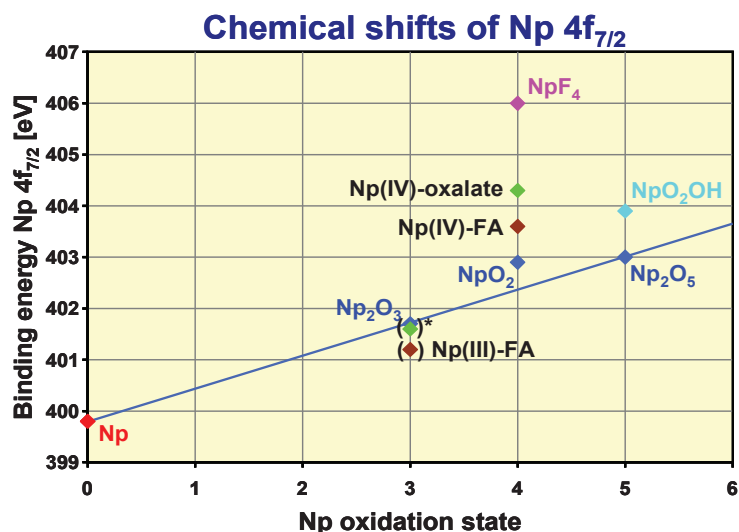


Figure 6-11: The chemical shifts of Np 4f_{7/2} spectra for the Np(III), Np(IV) and Np(V) complexes.

To get an indication how the Np 4f_{7/2} line is altered by the chemical surrounding area of the Np atom, several Np compounds were measured by XPS. Figure 6-11 presents the binding energy (BE) of Np 4f_{7/2} spectra of Np⁴⁺-fulvate, Np⁴⁺-oxalate, Np(IV) hydroxide (amp), Np³⁺-oxide, Np(III)-FA, NpO₂⁺-hydroxide, NpO₂⁺-oxide complexes. The electron density at the neptunium site is expected to be higher (decreased BE of Np 4f_{7/2} line) in the case of Np–O/OH and Np–O–C bonding than in the case of neptunium ions bound to carboxylic groups (increased BE of Np 4f_{7/2}). So, if bonds other than to carboxylates are present at Np(IV)-fulvates, caused by hydrolyzed neptunium species, larger differences in BE between the 4f_{7/2} line and the satellite are expected ($\Delta BE > 6.8$ eV, s. in Figure 6-9). Similar results are also obtained for Th(IV)-humates [Schild et al., 2000]. Np 4f_{7/2} chemical shift of Np(IV)-HS is comparable with the data of Pu(IV)-HS and Th(IV)-HS.

2) Complexation constant

As mentioned above the XAFS and XPS cannot give a definite picture of the fulvate complexation and hereby the question whether a pure NpFA(IV) or a mixed ternary complex remains unsolved. To minimise the effects of mixed complexes on the thermodynamic complexation constant, only data showing only two well separated peaks in the absorption spectra have been chosen for the evaluation. In the pH range 1 – 1.5, mainly one Np(IV) fulvate complex between Np⁴⁺ and the carboxylic groups of the FA (FA-COOH) is assumed forming the NpFA(IV) complex. Unfortunately, the hydrolysed species of the Np(IV), Np(OH)³⁺, Np(OH)₂²⁺, Np(OH)₃⁺, and Np(OH)₄(aq) cannot be differentiated by absorption

spectroscopy. The total uncomplexed tetravalent Np(IV), including all hydrolysed species, can be measured. Hence, we have to calculate the amount of Np^{4+} and this has been done by the side reaction coefficient α . α is defined by the following reaction, deduced from the law of mass action of all hydrolysed species:

$$\left. \begin{aligned} [\text{An}]_{\text{total}} &= [\text{An}^{4+}]_f \left(1 + \sum_{n=1}^4 \frac{\beta_n}{[\text{H}^+]} \right) \\ [\text{An}]_{\text{total}} &= [\text{An}^{4+}]_f \left(1 + \sum_{n=1}^4 \beta_n [\text{OH}^-]^n \right) \end{aligned} \right\}$$

$$[\text{An}]_{\text{total}} = [\text{An}^{4+}]_f \alpha_{\text{An(IV)}}$$

Another problem that is needed for the estimation of the complexation constant is the deprotonation of the FA at such low pH values. The degree of deprotonation α_H can be measured by direct acid-base titration not lower than around pH 3.5. Therefore, an linear interpolation to pH 1 was made from the plot α_H as a function of pH value. This α_H has to be regarded as a rough estimate, only. By this way for pH 1 and 1.5 a degree of deprotonation of 1% and 8%, respectively, were obtained. Another way to correct the pH-dependence of FA is the introduction of the loading capacity LC of FA for the maximum Np concentration that can be bound at a certain pH value, here, pH 1 and 1.5. In Figure 6-12 the deduction of LC from experimental data is illustrated. The fitting of the lines yield in LC for pH 1 and 1.5 of $(7 \pm 1)\%$ and $(17 \pm 1)\%$, respectively.

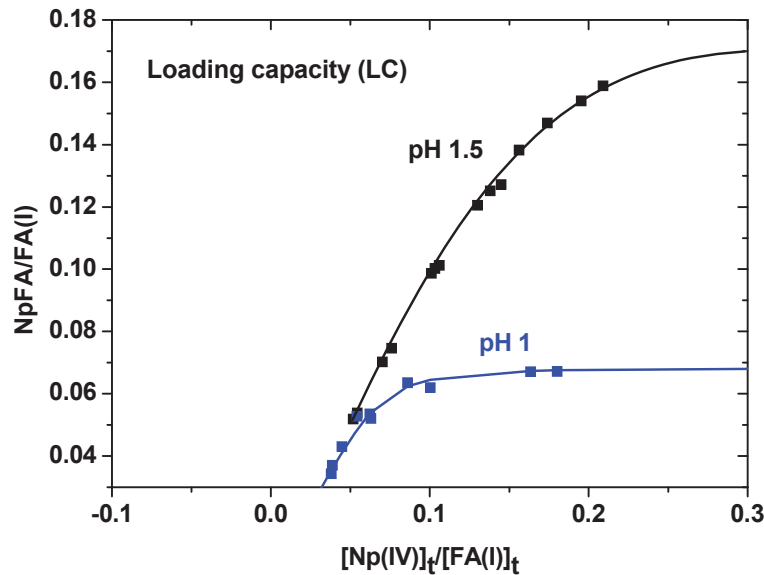


Figure 6-12: Determination of the loading capacity (LC) of fulvic acid for Np(IV) complexation at pH 1.0 and 1.5 from the experimental data according to the following expression:

$$\frac{[\text{Np-bound}]}{[\text{FA(I)}]_k} = 0.5 \cdot \left\{ \left(A \cdot \frac{[\text{Np(IV)}]_i}{[\text{FA(I)}]_t} + \text{LC}^* \right) - \left(\left(A \cdot \frac{[\text{Np(IV)}]_i}{[\text{FA(I)}]_k} + \text{LC}^* \right)^2 - 4 \cdot \text{LC}^* \cdot \frac{[\text{Np(IV)}]_k}{[\text{FA(I)}]_k} \right)^{0.5} \right\}$$

With all the needed parameter a complexation constant $\log\beta$ of the NpFA(IV) complex formation was calculated, which is summarised in Table 6-5. Although the α_H and the LC are different, the $\log\beta$ s at the same pH value are very similar. The effect of the deprotonation parameters is not significant and estimate values can be used as a first approach for the determination of the complexation constant. However, the complexation constant $\log\beta$ is not pH independent for the tetravalent neptunium.

pH	α_H (%)	LC (%)	$\log\beta(\alpha_H)$	$\log\beta(\text{LC})$
1.0	1	7 ± 1	7.0 ± 0.5	6.9 ± 0.2
1.5	8	17 ± 1	7.5 ± 0.4	7.7 ± 0.2

Table 6-5: Complexation constant of the NpFA(IV) complex at pH 1 and 1.5 and ionic strength of 0.1 M NaCl including the parameter degree of deprotonation α_H and the loading capacity LC.

If we compare the complexation constant with values deduced in the same way from experimental data of U(IV), Th(IV), Np(IV), and Pu(IV) humate complexation from [Reiller et al., 2008], the pH dependence of $\log\beta$ is confirmed. Figure 6-13 illustrates that the present complexation constants fits well in a qualitative line that expresses the $\log\beta$ as a function of pH.

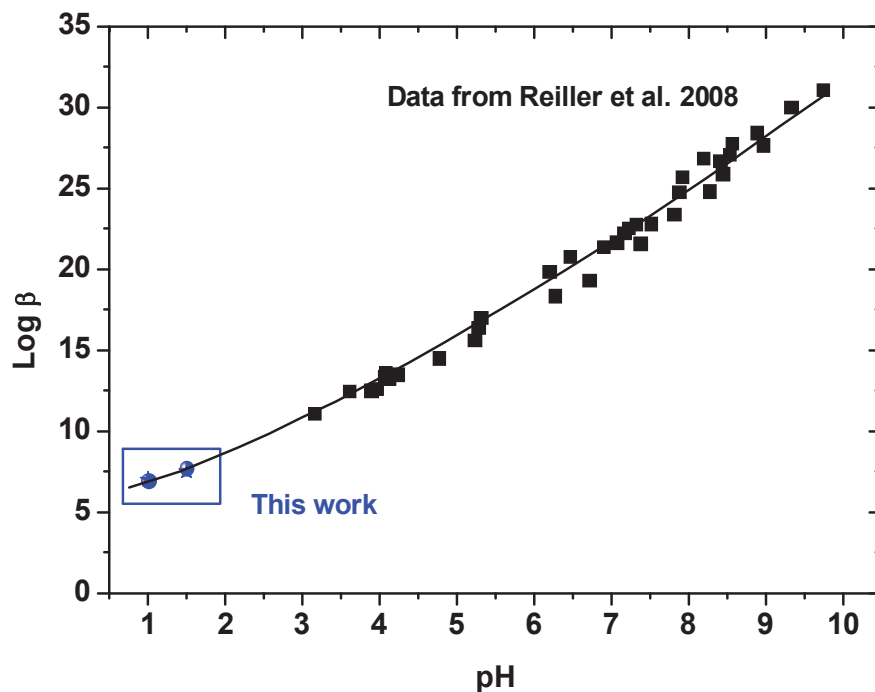


Figure 6-13: Complexation constant ($\text{Log}\beta$) for the tetravalent actinide (Th(IV), U(IV), Np(IV), and Pu(IV)) and humic substances with varying pH values.

7 Reproduction of a natural clay system from pure components

The reproduction of the natural clay system from pure components focused since the beginning of the project on the polymerization of low molecular weight compounds as natural organic matter building block under well-defined conditions and presence of swelling clay. The approach to synthesis kerogen from low molecular weight compounds containing solely the elements C, O, H and N has the advantage to avoid the problems of inorganic impurities inherent in the kerogen even after isolation and furthermore is a route to gain knowledge on the reaction pathway, possible catalytic effects of mineral phases (i.e. smectite) and influence of exchangeable cation composition. Until now several model humic substances have been synthesized (Arfaoli et al., 1997; Bosetto et al., 2002; Bosetto et al., 1997; Jung et al., 2005; Pompe et al., 2000) and most of them have been obtained via the Maillard reaction (Jokic et al., 2004; Maillard, 1912a; Maillard, 1912b) which consist in an amino-acids reduction step (melanoidin, glycine, melanoidin) via sugars and is considered to be an important pathway in natural humification processes.

In our case, condensations of low molecular weight compounds have been realized by taking as initial components: (1) 0.05 mol·L⁻¹ and 0.5 mol·L⁻¹ of D-glucose (C₆H₁₂O₆) and glycine (C₂H₅NO₂), or (2) 0.05 mol·L⁻¹ and 0.5 mol·L⁻¹ of catechol (C₆H₆O₂). Each solution was kept in contact with the <2µm purified fraction of Na- or Ca-exchanged bentonite (Ibeco) during 1 months in an oven at 80°C under wetting/drying cycles. Elevated temperature and wetting/drying cycles have been shown to activate the formation of the dark brown polymer condensate (Benzing-Purdie et al., 1985; Bosetto et al., 2002; Bosetto et al., 1997). In order to study the potential smectite catalysis of the reaction and the influence of the exchangeable cations (Na, Ca) a characterization of the organic matter polymerized by several analytical techniques have been evaluated. An evaluation of the molecular composition of solid products has been conducted by the use of pyrolysis-gas chromatography-mass spectrometric (py-GC/MS; (Gadel and Bruchet, 1987)).

An exemplary GC/MS chromatogram is shown in Figure 7-1. In the case of the D-glucose- glycine and Ca-smectite, compounds generated in the solid fractions are mainly cyclic organic compounds like alkyl-benzene or alkyl-phenol but also contains N-functions (pyridine, pyrrole, indole). Polymerization of catechol with Ca-smectite leads to the formation of aliphatic compounds (alkanes, and unsaturated alkenes) and few aromatics like alkyl-benzene.

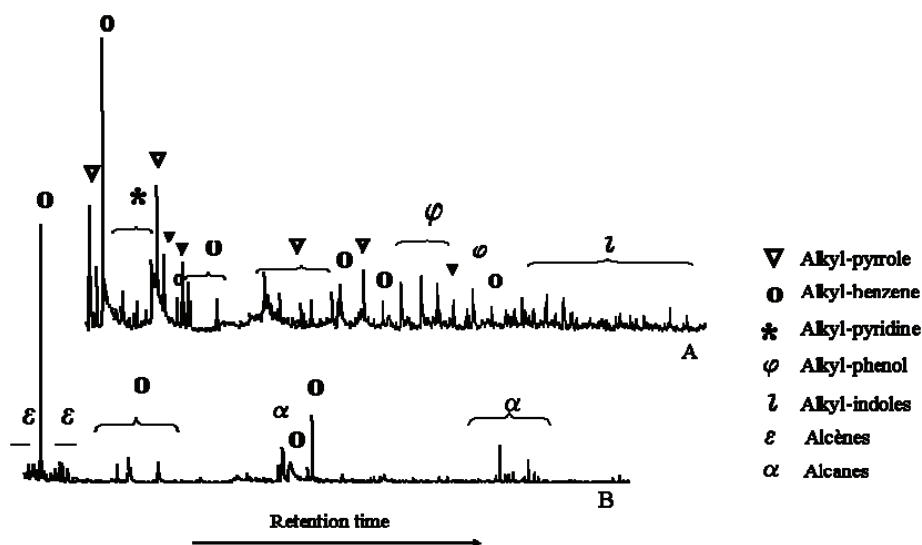


Figure 7-1: Py-GC-MS chromatograms obtained on the polymerisation products after 1 month at 80°C under wet/drying cycles. (A) Ca-smectite (smectite), Glucose (0.05mol.L-1) + Glycine (0.05mol.L-1) ; (B) Ca-smectite (Ibeco), catchol (0.05mol.L-1)

Unfortunately, the py-GC/MS experimental set-up used in GREGU (Nancy) is optimized for pure organic samples and the polymerized organic matter (OM) clay associates used in this study produced only weak signals. Precise analysis on the molecular composition of the clay mineral associated OM where therefore not possible by py-GC/MS.

However, the functionality of the OM was successfully determined by mean of μ FT-IR analyses in collaboration with GREGU (Nancy, France) (Bosetto et al., 1997) and thus it will be possible to clearly identify a potential catalytic effect of clay minerals on organic matter polymerization. This data is planned to be published soon.

The reactivity of the clay fraction and potential changes in swelling properties have been investigated by XRD and TEM measurements in collaboration with the French Museum on Natural History and GREGU (Nancy). The investigations conducted on all initial samples and interstage products showed polymerized organic material in the smectite interlayers in the case of “Glucose + glycine” samples. The polymerization process and delaminating of the smectite layers (see Figure 7-2) was hereby a function of the initial organic matter to clay mineral fraction ratio. On the contrary, polymerization of catechol doesn’t affect the swelling properties of the Ibeco smectite and no organic matter in the interlayer could be found at all OM/clay ratios investigated. These findings give possible insides in the contradicting results found in the literature on the availability of clay mineral interlayer space for organic matter preservation.

A

B

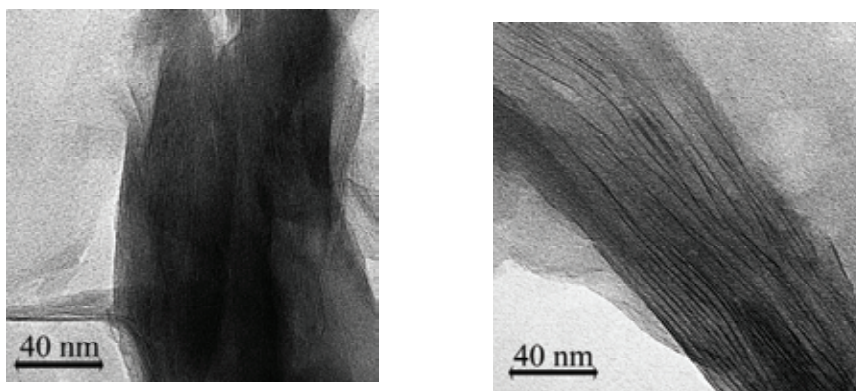


Figure 7-2: TEM images obtained on the polymerisation products after 1 month at 80°C under wet/drying cycles. (A) Ca-smectite (<2µm smectite of Ibeco bentonite), (B) Ca-smectite (<2µm of Ibeco bentonite), glucose + glycine (0.05mol.L⁻¹)

The reactivity of the clay fraction and potential changes in swelling properties has to be considered as well. In addition, synchrotron based C1s-STXM measurements (NSLS, beamline X1A, Brookhaven National Laboratory, USA) have been realized on polymerized samples. The results (see as an example Figure 7-3 and Figure 7-4) show that the organic material synthesized still contains a higher amount of oxygen containing functional groups (phenol-type groups ~286.6eV; carboxyl-type groups ~288.4eV) and cannot be directly compared to smectite associated organic material found in the Callovo-Oxfordian formation (Schäfer et al., 2005b).

Looking in detail on the via Maillard reaction clay associated organic matter in comparison to the synthetic humic substances M42 from HZDR and the isolated fulvic acid GoHy711 revealed very comparable C1s- NEXAFS spectra (Schäfer et al., 2005a; Vilas et al., 2010).

In order to overcome the problem of humic substance synthesis a series of confined pyrolysis test was conducted on the “GG -Ca-smectite” polymerized products with the aim of reaching a kerogen-type material, taking into account the O/C and H/C atomic ratios published for the Toarcian and Callovo-Oxfordian formations of the Paris Basin (Deniau et al., 2008; Vandembroucke and Largeau, 2007). Time-temperature parameters of pyrolysis were chosen to be 160°, 180°, 200° and 250°C during 24 hours in agreement with previous works published on Callovo-Oxfordian formation, see schematic figure below (Elie and Landais, 1997).

Elemental composition of the pyrolysis products are plotted in a conventional Van Krevelen diagram in the Figure 7-5 where characteristics of Toarcian and Callovo-Oxfordian kerogen are added as references. As it is visible on the Figure 7-5, the O/C values obtained are comparable with kerogen values from the Boom Clay formation (Belgium), whereas the H/C ratios fall within the range expected for black carbon (BC) or soot. Therefore, the experimental parameters of confined pyrolysis have to be adjusted and Rock Eval analysis will be performed to confirm the elemental compositions.

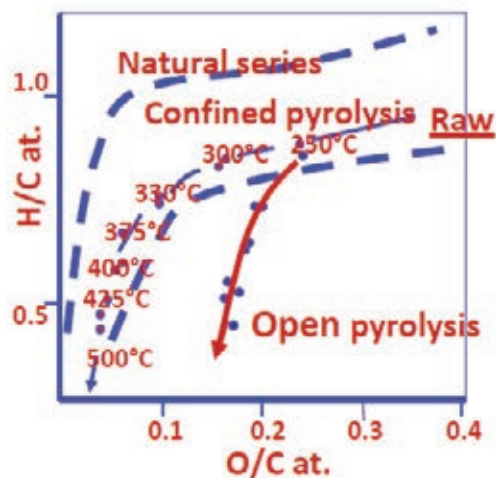


Figure 7-3: Schematic Van Krevelen diagram of the O/C vs. H/C trend observed in the natural system in comparison to the one obtained by different temperature adjustments in confined and open pyrolysis (Elie and Landais, 1997).

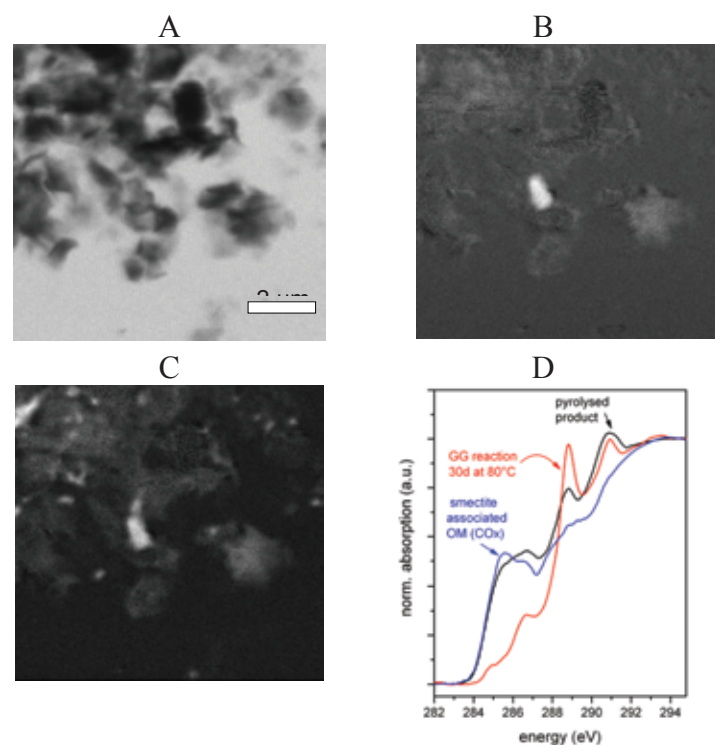


Figure 7-4: Carbon edge STXM investigations of Ca-exchanged bentonite reacted with glucose+glycine (GG) for 30 days at 70°C including wetting/drying cycles and treated with confined pyrolysis at 250°C for 24 hours. A: Absorption image at 280 eV below the carbon edge; B: Ratio image (light grey values indicate high concentration) showing the distribution of C=C functionality; C: Ratio image showing the distribution of carboxyl-type groups; D: Comparison of spectra obtained for the smectite associated natural organic matter (OM) in the Callovo-Oxfordian formation, the reaction products of GG polymerization and the polymerized samples after pyrolysis.

Taking the C1s STXM measurements of the pyrolysed products (see Figure 7-4) the polymerized organic material found shows a higher amount of oxygen containing functional groups (especially in the range of carboxyl-type groups; ~288.4 eV) confirming the elemental analysis results presented above. Interestingly, the absorption in the aromatics region (~285.2 eV) is quite comparable to the smectite associated organics found in the Callovo-Oxfordian formation and represents therefore a better analogue. However, the pyrolyzed products fall within the van Krevelen diagram more within the of char/soot or black carbon (BC) and are with respect to their H/C atomic ratio depleted, which shows that the pyrolysis parameters have to be adjusted for the Maillard reaction derived humic substances to reach the kerogen maturity of the COx organic matter.

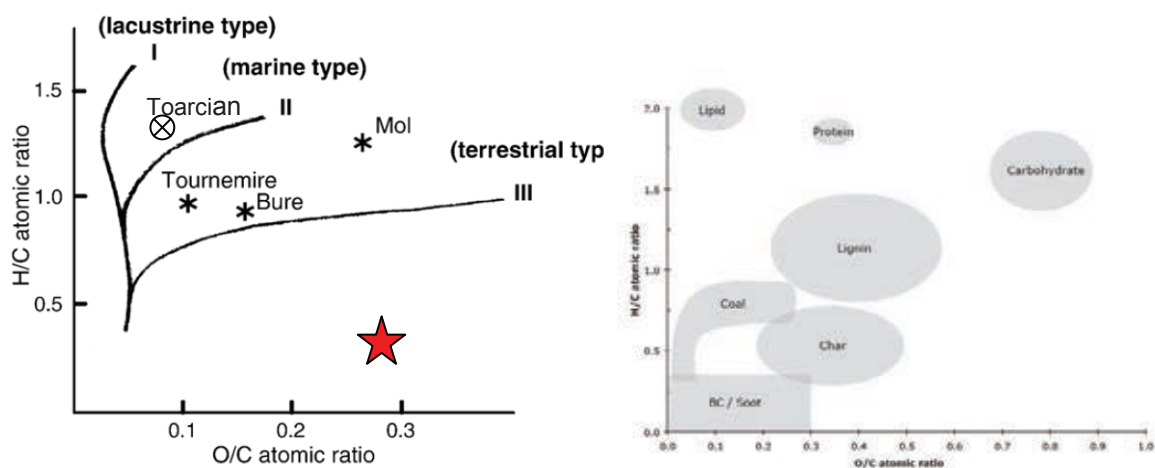


Figure 7-5: Van Krevelen diagram for natural kerogen samples (Deniau et al., 2008), additional inserted is the Toarcien kerogen (Vandenbroucke and Largeau, 2007; Vandenbroucke and Largeau, 2007). The O/C and H/C atomic ratios of the series of “D-glucose, glycine and Ca Ibecco bentonite after confined pyrolysis at 160, 180, 200 and 250°C are represented by the red star. For comparison, a figure of showing different organic materials is added (Preston and Schmidt, 2006).

8 The role of low-molecular organic components in the diffusion of radionuclides in OPA – a literature study

Rock material from the opalinus clay formation contains approximately one weight percent of organic carbon [Courdouan et al., 2007]. This organic matter is partly dissolved in the pore water of the clay material. Its composition is highly heterogeneous, showing large and complex molecules like humic and fulvic acids as well as small organic acids (e.g. formate (up to 2 μM), acetate (up to 203 μM), propionate (up to 27 μM) and lactate (up to 9 μM)). These different organic molecules are potential ligands for radionuclides which may leach into the pore water of the clay formation.

Natural clay formations show a very low hydraulic conductivity. Thus, the main transport mechanism, which will determine the migration or retention of radionuclides in clay rocks is the diffusion process [Nagra, 2002; Andra, 2005]. In order to model the long term migration of radionuclides in a nuclear waste repository in clay formations, a distinct understanding of their diffusion is mandatory. The question arises, whether the above mentioned organic complexing agents will influence this process. Thus, a detailed knowledge of the ternary systems radionuclide-organics-clay is needed. However, the modeling of such complex ternary systems is a very difficult task. Therefore, a distinct understanding of the binary systems clay-organics, clay-radionuclide and radionuclide-organics is required first.

The aim of the present work is to give a basic overview of the binary system actinide-organic ligand. Studies with ligands like acetate, propionate or lactate are of direct relevance for the natural system. Furthermore, systematic studies with more uncommon ligands like oxalic and phthalic acid are important for gaining a deeper insight into the mechanism of the complexation of actinides with organic ligands. Also, these ligands serve as model ligands for binding sites of more complex ligands like humic or fulvic acids.

In the past, numerous studies on the complexation of different actinides with organic ligands were performed, using a broad series of experimental techniques (mainly indirect methods like potentiometry or solvent extraction). Due to the large quantity of available data, several important ligand systems are selected within the scope of this work. In the following, the literature data on the respective actinide complexes is discussed with respect to their oxidation states.

8.1 Complexation of trivalent actinides with organic ligands

Experimental data on the interaction of trivalent actinides with small organic ligands is scarce. More common are studies with trivalent lanthanides. Due to the similarity of their chemical properties, selected literature data on Eu(III) and Nd(III) is also discussed within the present work. The thermodynamic $\log \beta_n^0$ values for the complexation of Ln(III) and An(III) with different organic ligands are summarised in Table 8-1. The molecular structures of these ligands in their acid form are displayed in Figure 8-1.

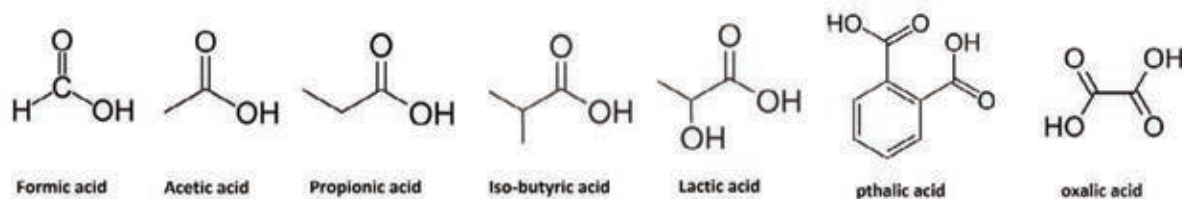


Figure 8-1: Molecular structures of formic-, acetic-, propionic-, iso-butyric-, lactic-, phthalic-, and oxalic acid

The formic-, acetic- and propionic acid differ only by the length of their aliphatic alkyl chain. The carbon chain of iso-butyric- and lactic acid is the same as for propionic acid, with an additional methyl or hydroxyl group in α -position, respectively. The alkyl chain length of oxalic acid is similar to acetic acid, but the molecule shows two carboxylic acid functional groups. Phthalic acid is a derivative of benzoic acid with an additional COOH group in ortho position.

Table 8-1: $\log \beta_n$ values for the formation of Ln(III) and An(III) acetate/propionate/iso-butyrate and lactate complexes.

Complex	pK_a ligand	$\log \beta^0_1$	$\log \beta^0_2$	Ionic strength	method	Ref
Eu(formate) $_n^{3-n}$	3.70	1.83	2.84	0	Pot.	a
Eu(acetate) $_n^{3-n}$	4.76	2.20 \pm 0.50	-	0.1 M (NaClO ₄)	TRLFS	b
		2.80 \pm 0.30	5.90 \pm 0.60	10 ⁻³ M	ESI-MS	b
		2.00	3.80	0.1 (NaClO ₄)	Spec.	c
		2.49 \pm 0.08	-	0	Solv.Ex.	d
Am(acetate) $_n^{3-n}$	4.76	-	-	0	Solv.Ex.	d
Eu(propionate) $_n^{3-n}$	4.88	2.70	4.65	0	Pot.	a
Cm(propionate) $_n^{3-}$		3.34 \pm 0.04	4.51 \pm 0.26	0	TRLFS	e
Cm(phthalate) $_n^{3-n}$	2.95 and 5.41	3.62 \pm 0.02	-	0.1 (NaClO ₄)	TRLFS	f
Eu(iso-butyrate) $_n^{3-}$	4.85	2.32	4.13	0	Pot.	a
Eu(lactate) $_n^{3-n}$	3.87	3.27	5.81	0	Pot.	a
		2.99 \pm 0.17	5.09 \pm 0.23	1.05 m (NaClO ₄)	Spec.	g
Nd(lactate) $_n^{3-n}$	3.87	2.58 \pm 0.05	4.60 \pm 0.06	1.05 m (NaClO ₄)	Spec.	g
		2.60 \pm 0.01	4.66 \pm 0.02	1.00 M (NaTf)	Pot.	h
Am(oxalate) $_n^{3-n}$	1.23 and 4.19	5.20	9.20	0.0	Solv.Ex.	i

a: [Wood, 1993]; b: [Plancque et al., 2005]; c: [FAR64]; d: [Moore et al., 1999]; e: [Höhne, 2010]; f: Panak et al., 1995]; g: [Tian et al., 2010]; h: [Zalupski et al., 2010]; i: [Choppin&Chen, 1996]

The stability constants of the Eu(III)-formate, -acetate and -propionate complexes increase according to the increasing pK_a of the ligands. The slightly smaller value of $\log \beta_n^0(\text{Eu}(\text{isobutyrate})_n^{3-n})$ by approximately 0.35 orders of magnitude can be attributed to a steric hindrance of the complex formation by the α -methyl group. Contrary, the $\log \beta_n^0(\text{Eu}(\text{lactate})_n^{3-n})$ values are by more than one order of magnitude higher, compared to $\log \beta_n^0(\text{Eu}(\text{formate})_n^{3-n})$, although the acidity of lactic acid is similar to formic acid. Furthermore, the $\log \beta_n^0(\text{Am}(\text{oxalate})_n^{3-n})$ value is by 2.5 logarithmic units higher compared to the $\text{Am}(\text{acetate})^{2+}$ complex. These increased stability constants are explained by an additional stabilisation of the complex due to the functional group in α -position.

However, the discussed data was mainly determined by potentiometric measurements or solvent extraction. These are indirect techniques, which disturb the chemical equilibrium during the measurement. In contrary, spectroscopic methods are capable to determine the solution speciation directly at equilibrium conditions. This might be the reason for the distinctive discrepancy in thermodynamic data determined by different methods. For example, the value of $\log \beta_n^0(\text{Eu}(\text{propionate})_n^{3-n})$ (potentiometric data) is by 0.6 orders of magnitude smaller than $\log \beta_n^0(\text{Cm}(\text{propionate})_n^{3-n})$, which was determined by TRLFS. A similar discrepancy is observed for the $\log \beta_n^0(\text{Eu}(\text{lactate})_n^{3-n})$ values determined by Wood (potentiometric data) and Tian et al (spectroscopic data). To compare these data, the conditional values given by Tian et al. are extrapolated to $I_m = 0$ with the SIT approach, as recommended in the NEA-TDB [Guillaumont et al. 2003]. The so calculated $\log \beta_n^0(\text{Eu}(\text{lactate})_n^{2+}) = 4.04 \pm 0.20$ and $\log \beta_n^0(\text{Eu}(\text{lactate})_n^{2+}) = 6.65 \pm 0.25$ values are distinctively larger than the respective potentiometric data. A comparable effect is also observed for the stability constants of Ln(III)/An(III) complexes with inorganic ligands. For example, large differences of the $\log \beta_n^0(\text{Cm}(\text{SO}_4)_n^{3-2n})$ values determined by indirect methods and spectroscopic techniques are found, which are beyond experimental uncertainty of the two different experimental methods. [Guillaumont et al. 2003] These findings point toward a general difference of the data demined by indirect methods and spectroscopy.

8.2 Complexation of tetravalent actinides with organic ligands

In case of the tetravalent actinides a few data on the complexation of Th(IV) with different organic ligands are available in the literature. Rao et al studied the complexation of Th(IV) with acetic acid by means of potentiometry and microcalorimetry [Rao et al., 2004]. The authors identified complexes with up to five acetate ligands and determined the respective $\log \beta_n$ values at an ionic strength of $I_m = 1.05$ (NaClO_4). The stepwise stability constants $\log K'_n$ decrease with increasing n . This effect is expected as the complex is more and more negatively charged as ligands are introduced into the first coordination sphere. Furthermore, data on the complexation of Th(IV) with different dicarboxylic acids are available in the literature. In the following, the literature data on the Th(IV) complexes with malonate, succinate, glutarate and oxydiacetate is summarized (Table 8-2). For a better comparison, exclusively condi-

tional stability constants valid for an ionic strength of $I_m \sim 1.0$ (NaClO₄) and determined by potentiometric methods are discussed. The structure of the respective ligand molecules in their acid form are shown in Figure 8-2.

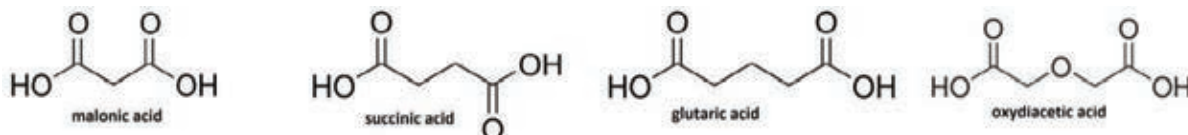


Figure 8-2: Molecular structures of malonic-, succinic-, glutaric- and oxydiacetic acid

The malonic-, succinic- and glutaric acids differ only by the length of the carbon-chain between the two terminal carboxylic acid groups. The oxydiacetic acid has the same chain length as the glutaric acid, but shows an additional ether function in β -position to both COOH groups.

The complexation of Th(IV) with dicarboxylic ligands is distinctively stronger compared to ligands with only one COOH functional group. The complexation of Th(IV) with malonic acid was studied by [DiBernardo et al., 1977], [Srinivasan et al., 2006] and [Rawat et al., 2011]. The formation of up to 1:3 complexes is confirmed by all authors and the respective conditional $\log \beta'_n$ values are determined. The given stability constants are by several orders of magnitude larger than the respective values for the acetate complexes. The increased complexation strength of dicarboxylic acids results from the chelating effect of the second COO⁻-group, similar to functionalized monocarboxylic acids. Obviously, the length of the aliphatic chain has a distinct impact on the size of the chelate ring.

Table 8-2: $\log \beta'_n$ for the complexation of Th(IV) with acetate, malonate, succinate, glutarate and oxydiacetate

ligand	pK_a ligand	$\log \beta'_1$	$\log \beta'_2$	$\log \beta'_3$	I_m (NaClO ₄)	method	Reference
acetate	4.76	3.81 ± 0.02	6.79 ± 0.02	8.71 ± 0.13	1.05	Pot.	a
malonate	2.85	7.25 ± 0.07	12.78 ± 0.17	16.74 ± 00.30	1.00	Pot.	b
	and	7.47	12.79	16.28	1.00	Pot.	c
	5.69	7.47 ± 0.04	12.84 ± 0.04	16.54 ± 0.06	1.05	Pot.	d
succinate	4.21	6.4 ± 0.2	8.8 ± 0.4	-	1.00	Pot.	b
	and 5.64						
glutarate	4.33	6.2 ± 0.1	-	-	1.00	Pot.	b
	and 5.57						
oxydiacetate	2.96 and 4.43	8.15 ± 0.08	14.82 ± 0.21	18.16 ± 0.33	1.00	Pot.	e

a: [Rao et al., 2004]; b: [Rawat et al., 2011]; c: [DiBernardo et al., 1977]; d: [Srinivasan et al., 2006]; e: [[DiBernardo et al., 1983]

The $\log \beta'_n$ for the Th(oxydiacetate)²⁺ complex is by one order of magnitude larger than the corresponding stability constant for the Th(IV) complex with the other dicarboxylic acids. This is due to the formation of a chelate complex with an additional contribution of the ether oxygen atom.

8.3 Complexation of pentavalent actinides with organic ligands

A broad variety of literature data on the complexation of Np(V) with small organic ligands is available. Within the scope of the present overview, the data for the Np(V)-acetate, -oxalate and -lactate systems are discussed. The conditional stability constants for the formation of the 1:1 complexes of Np(V) with the respective ligands are summarized in Table 8-3. Unfortunately, the data are given for different ionic strengths and ionic media in some cases. Thus the comparison of the single $\log \beta'$ values is difficult. No data on the formation of higher Np(V) complexes with the ligands is available in the literature.

Table 8-3: $\log \beta'_1$ for the complexation of Np(V) with acetate, oxalate, lactate and α -hydroxy-isobutyrate

ligand	pK _a ligand	$\log \beta'_1$	I_m (NaCl)	Method	Reference
acetate	4.76	1.13	1.0	Solv.Ex.	a
		0.99 ± 0.10	1.0 (NaClO ₄)	Solv.Ex.	b
		1.70 ± 0.04	5.0	Spect.	c
		1.93 ± 0.01	0.3 (NH ₄ ClO ₄)	Spect.	d
oxalate	1.23	3.35 ± 0.06	1.0 (NaClO ₄)	Solv.Ex.	b
	and	3.55	<0.1	Solv.Ex.	e
	4.19	3.04 ± 0.08	5.0	Spect.	c
lactate	3.87	1.11	2.0	Solv.Ex.	e
		1.48 ± 0.05	2.0	Solv.Ex.	a
		0.76 ± 0.03	5.0	Spect.	c

a: [Moore et al., 1999]; b: [Pokrovsky&Choppin, 1997]; c: [Borkovsky et al., 1996]; d: [Takai et al., 2009]; e:[Inoue&Tochiyama, 1983]

The value of $\log \beta'_{1,25^\circ\text{C}}(\text{NpO}_2(\text{acetate}))$ is by almost 3 logarithmic units smaller than the corresponding value for the Th(IV)-acetate complex. The introduction of an additional carboxylate group results in an increase of the stability constant by several orders of magnitude [Moore et al., 1999; Pokrovsky&Choppin, 1997]. This increase in the stability constant is in good agreement with the increase observed for Am(III)-complexes.[Choppin&Chen, 1996; Moore et al., 1999] Due to the large discrepancies of the data presented in Table 8-3, an increase of $\log \beta'_1$ in presence of an α -hydroxyl-group is not observable.

The available data shows rather large scattering of the values. For example the $\log \beta'_1$ (NpO₂Lac) ($I_m = 2.0$) determined by [Inoue&Tochiyama, 1983] and [Moore et al., 1999] by solvent extraction differ by almost 0.4 orders of magnitude. Additionally, a distinct difference between data determined by indirect methods and spectroscopy is observed. For this comparison, the available conditional stability constants for the NpO₂Ac complex are extrapolated to

$I_m = 0$, using the SIT approach [Guillaumont et al., 2003]. The so calculated spectroscopic values ($\log \beta^0_1$ (NpO₂Ac) = 1.92 ± 0.05 [Borkovsky et al., 1996]; $\log \beta^0_1$ (NpO₂Ac) = 1.94 ± 0.03 [Takai et al., 2009]) are by almost one order of magnitude higher than the respective data from indirect methods ($\log \beta^0_1$ (NpO₂Ac) = 1.16 ± 0.05 [Moore et al., 1999]; $\log \beta^0_1$ (NpO₂Ac) = 1.02 ± 0.12 [Pokrovsky&Choppin, 1997]). These findings are in very good agreement with the data discussed for trivalent actinides.

8.4 Complexation of hexavalent actinides with organic ligands

Numerous studies have been conducted on the complexation of UO₂²⁺ with organic ligands. In the following, only the data on U(VI)-acetate, -malonate, -oxalate, -oxydiacetate and -thiodiacetate complexes are summarised (see Table 8-4). The structures of the ligands are given in Figure 8-1 and Figure 8-2. The thiodiacetate ligand has a similar structure to oxydiacetic acid, but with a thioether bridge between the two terminal carboxylic acid groups.

The conditional stability constants of the U(VI)-acetate complexes are similar to Ln(III)/An(III) complexes [Choppin&Rizkalla, 1994]. The $\log \beta'_n$ values for the U(VI)-oxalate complexes are by several orders of magnitude higher than the corresponding $\log \beta'_n$ for the U(VI)-acetate complexes, whereas the $\log \beta'_n(\text{UO}_2(\text{malonate})_n^{2-2n})$ is by 0.7 logarithmic units lower compared to $\log \beta'_n(\text{UO}_2(\text{oxalate})_n^{2-2n})$, despite the higher pK_a values of malonate.

Table 8-4: $\log \beta'_1$ for the complexation of U(VI) with acetate, oxalate, malonate, oxydiacetate and thio-diacetate (T = 25°C)

ligand	pK _a ligand	$\log \beta'_1$	$\log \beta'_2$	$\log \beta'_3$	I_m	method	Reference
acetate	4.76	2.58 ± 0.03	4.37 ± 0.14	6.86 ± 0.04	1.0 (Na-ClO ₄)	Pot.	a
		1.68 ± 0.02	3.18 ± 0.03	-	5.0 (NaCl)		b
oxalate	1.23	7.44 ± 0.07	12.07 ± 0.10	13.40 ± 0.25	0	Spect.	c
	and 4.19	6.06 ± 0.01	10.76 ± 0.02	13.27 ± 0.22	1.0 (Na-ClO ₄)	Spect.	c
malonate	2.85 and 5.85	5.36 ± 0.01	9.39 ± 0.01	11.22 ± 0.06	1.0 (Na-ClO ₄)	Pot.	d
oxy- diacetate	2.96 and 4.43	5.01 ± 0.04	7.64 ± 0.11	-	1.0 (Na-ClO ₄)	Pot.	e
thio- diacetate		2.89 ± 0.03	-	-	1.0 (Na-ClO ₄)	Pot.	f

a: [Jiang et al., 2002]; b: [Borkovsky et al., 1996]; c: [DiBernado et al., 2009]; d: [Rao et al., 2002]; e: [Rao et al., 2003]; f: [DiBernado et al., 2006]

Introduction of an ether bridge between the two carboxylic acid groups results in even further decrease of the $\log \beta'_n$ values. This finding is in contradiction to the analogous Th(IV)-

oxydiacetate system. There, the ether functionality supports the complexation. A reasonable explanation may be a steric hindrance of the complexation due to the two oxygen atoms of the UO_2^{2+} entity. Also, the $\log \beta'_n$ value for the U(VI)-thioacetate complex is by about 2 orders of magnitude lower than the respective value for the oxydiacetate complex. This is expected, since sulfur shows weaker complexation properties towards actinides.

8.5 Summary

The present work gives a short overview of the complexation of actinides in different oxidation states with small organic ligands. Due to the availability of numerous studies and a broad set of data, only chosen ligand systems with systematic variations of their molecular structure are discussed to give a basic insight into the complexation mechanism. The comparison of the given stability constants showed, that the complex formation is influenced by a number of factors, like the alkalinity of the ligand and its molecular structure. In the case of aliphatic carboxylic acid ligands, functional groups in α -, β - or γ -position to the coordinating COOH group increase the stability constants of the complexes distinctively. This effect is attributed to an additional contribution of the additional functional group, resulting in a partial chelating effect.

However, the available thermodynamic data is determined by various methods. The present overview shows a distinct discrepancy between literature data from indirect methods (e.g. potentiometry and solvent extraction) and spectroscopic techniques, which is far beyond experimental uncertainties of these two different types of methods. The difference is rather attributed to the general problem, that indirect methods disturb the chemical equilibrium during the measurement, which might provide biased results. Furthermore, indirect methods are unable to distinguish between inner- and outer-sphere complexes and thus changes in activity coefficients may be misinterpreted for changes in $\log \beta$ values.

Hence, application of spectroscopic methods (e.g. TRLS and UV/Vis) for the precise determination of thermodynamic data is of major importance to validate the available literature data and to establish a reliable thermodynamic database for actinides under natural conditions.

9 Measurement of pH values at elevated temperatures

Many chemical reactions in aqueous solutions (e.g. complexation, dissolution/precipitation or adsorption) are a function of the proton activity. Thus, the pH can be considered as a master variable in an aquatic system, and its precise measurement is one of the key issues in a detailed understanding and description of an aqueous system [Pankow,1991] At ambient temperatures, the pH is usually monitored with good accuracy by potentiometric measurement, using a hydrogen ion sensitive glass electrode. However, this approach is accompanied by various experimental difficulties, such as electrode drift, susceptibility to electromagnetic interferences and problems with reference electrodes. Also, glass electrodes are limited mainly to solutions with low salt concentrations, since the liquid junction potential is depending on the ionic strength (Dickson, 1993). Furthermore, due to uncertainties in the liquid junction potential and lack of reference electrode stability at high temperatures and pressures, the IUPAC has recommended to use potentiometric methods only in a temperature range of 5 to 50°C [Buck et al., 2002]. An alternative to potentiometric methods is the spectroscopic measurement of the pH. This approach is a well established experimental technique at ambient temperatures. Also, it can be applied for pH measurements of solutions at high temperatures and pressures [Raghuraman et al., 2006; Millero et al., 2009; Vogel, 1961; Bates, 1964; Seok et al., 1995].

9.1 Theory

Spectroscopic pH measurement techniques use UV/Vis absorption spectroscopy of pH sensitive dyes. These dyes are weak acids, with their dissociation equilibrium defined as follows (the charge of the dye depends on the respective molecule and is omitted here).



The acid (HDye) and base form (Dye) of the dye show different absorption bands. The absorption spectrum of a dye in a solution with the pH in the range of the $pK'_a(\text{dye})$ is a linear combination of these single component spectra with respect to the molar fractions of the acid and base form of the dye. By fitting the measured spectrum with the individual absorption spectra of the respective species, the speciation of the dye can be obtained directly from the integral of the respective absorption bands (peak deconvolution). The pH is then calculated by

using the Henderson-Hasselbalch equation

$$pH = pK'_a(T) + \log\left(\frac{\chi(Dye)}{\chi(HDye)}\right) + \log\left(\frac{Y_{Dye}}{Y_{HDye}}\right)$$

$$pH = pK'_a(T) + \log\left(\frac{\chi(Dye)}{\chi(HDye)}\right) + \log\left(\frac{Y_{Dye}}{Y_{HDye}}\right) \quad \text{Equation 9-2,}$$

where K_a^0 is the temperature dependent thermodynamic equilibrium constant of Equation 9-1. $\chi(\text{Dye})$ and $\chi(\text{HDye})$ are the molar fractions of the acid and base form of the dye and γ_{Dye} and γ_{HDye} are the respective activity coefficients. For solutions with an ionic strength of $I_m \leq 0.2$ mol/kg H₂O, the activity coefficients are calculated with the Davies-equation Equation 9-3 [Pankow, 1991]:

$$\log \gamma_i = -A \cdot z_i^2 \cdot \left(\frac{\sqrt{I_m}}{1 + B a_i \cdot \sqrt{I_m}} \right) - 0.2 \cdot I_m \quad \text{Equation 9-3}$$

The individual absorption spectra of the acid and base form are obtained from reference solutions at a pH value which is at least one order of magnitude higher or lower than the $\text{p}K'_a$ of the dye. Under such conditions complete protonation or deprotonation of the dye can be assumed. Also, in order to determine the pH of a unknown solution, the dissociation constant of the respective dye must be known. The $\text{p}K'_a$ of an indicator dye can be determined at room- as well as at increased temperatures by calibration versus reference solutions with known pH(T). Such reference solutions are for example commercially available buffer solutions. An overview of the reference solutions used within the present work is given in Table 9-1.

Table 9-1 Composition of the used reference solutions and their pH(T) from 25 to 90°C

	Buffer pH 2	Buffer pH 4	Buffer pH 11
	c(C ₆ H ₈ O ₇) = 0.030 m c(HCl) = 0.069 m c(NaOH) = 0.061 m	c(C ₆ H ₈ O ₇) = 0.056 m c(HCl) = 0.044 m c(NaOH) = 0.11 m	c(H ₃ BO ₄) = 0.094 m c(KCl) = 0.048 m c(NaOH) = 0.091 m
T [°C]	pH	pH	pH
25	2.00	4.00	11.00
30	2.00	4.01	10.81
40	2.00	4.01	10.64
50	2.00	4.01	10.48
60	2.00	4.00	10.45
70	2.01	4.00	10.19
80	2.01	4.00	10.06
90	2.01	4.00	9.93

The major drawback of the spectroscopic pH measurement the limited available pH window of $\text{p}K'_a(\text{Dye}) \pm 1$, since at higher or lower pH the dye is completely protonated or deprotonated and no information can be derived from peak deconvolution.

9.2 Technical equipment

The experiments were performed in a custom build high temperature cell for spectroscopic measurements [Skerencak et al., 2009] The region which is exposed to high temperatures (hot region) is made of Ti with 0.2 wt% Pd, which has a very high resistance towards corrosion. The cold region of the cell consists of PEEK (polyetheretherketone). The overall sample volume is about 2 ml. The temperature range for spectroscopic studies is 25 to 200°C. The pressure of the cell can be increased with an external pressure pump up to 13 - 15 bar ($p_{\max} = 30$ bar). Four optical quartz windows are embedded into the central body (diameter = 8 mm, thickness = 2 mm). The cell is coupled with optical waveguides (quartz) to a UV/Vis spectrometer (Cary 50, Varian Inc.). A first test with the optical indicator dye acridin showed a very good agreement of the measured absorption spectra with literature data in the temperature range from 20 to 150°C. Also, the change of the spectra was fully reversible with decreasing temperature. Above 150°C an irreversible decrease of the absorption intensity was observed leading to a complete bleaching of the solution. A possible explanation for this is a catalytic decomposition of the dye molecule of the titanium cell walls.

9.3 Measurement of the pH

In the following, the results on the application of two different indicator dyes are described.

Indicator dye bromocresol green

Bromocresol green is an optical indicator dye of the triphenylmethane family, with a $pK'_a, 25^\circ\text{C}$ value of about 4.90 ($I_m = 0.05$ m). Thus it can be applied to monitor the pH in the region of 4 to 6. The dye molecule in its acid and base form is displayed in Figure 9-1.

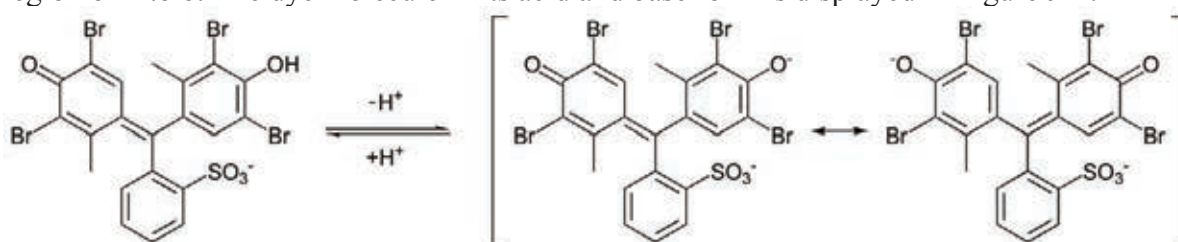


Figure 9-1: Bromocresol green in its acid (left) and base (right) form

To determine the temperature dependency of the pK'_a of bromocresol green, the dye is calibrated against the reference solutions given in Table 9-1 Composition of the used reference solutions and their pH(T) from 25 to 90°C. The absorption spectra of bromocresol green in the buffer solutions at $T = 25^\circ\text{C}$ are displayed in Figure 9-2a. At $\text{pH} = 2$ the dye exist in its acid form, showing an absorption band at 440 nm. At $\text{pH} = 11$ an absorption band at 620 nm is observed, which is attributed to the base form of the dye molecule. These assignments are in excellent agreement with the literature [Lee et al., 2001]. At $\text{pH} = 4$ the proton activity is in

a region corresponding to $pK_{a,25^\circ\text{C}}^0 \pm 1$ of bromocresol green. Hence, the acid and the base form of the dye coexist in solution and both bands are observed in the absorption spectrum.

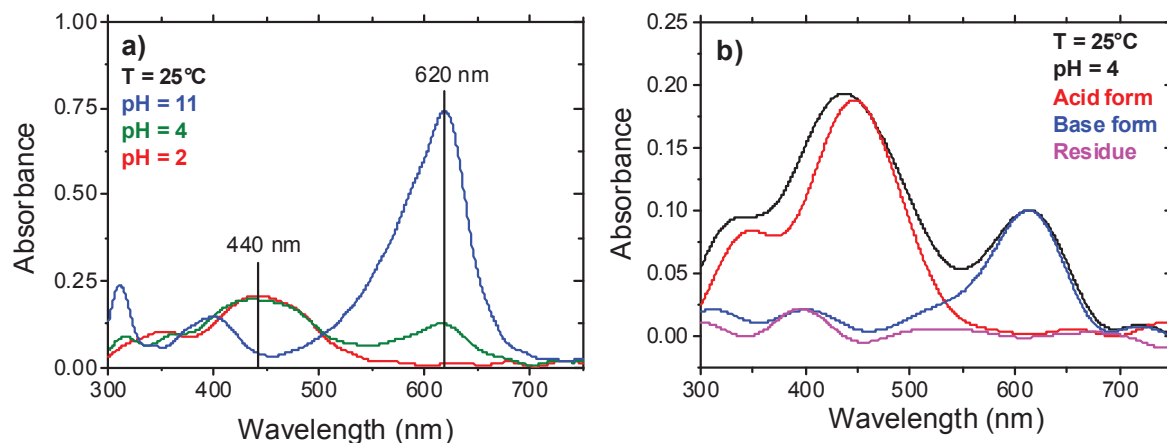


Figure 9-2: Absorption Spectra of bromocresol green at pH = 2, 4 and 11 (T = 25°C) b) exemplary peak deconvolution at T = 25°C

The measured spectrum is fitted with the previously determined absorption bands of the individual species. An exemplary peak deconvolution of an absorption spectrum of bromocresol green at pH = 4 (T = 25°C) is displayed in Figure 9-2b. Thus, the respective molar fractions are determined as function of the temperature and the $pK_a^*(T)$ is calculated according to Equation 9-2. The so determined $pK_a^*(T)$ values are displayed in Figure 9-3a. The thermodynamic $pK_a^0(T)$ values (valid for $I_m = 0$) are related to the conditional $pK_a^*(T)$ by the following equation

$$pK_a^0 = pK_a^* - \log\left(\frac{Y_{H^+} \cdot Y_{Dye}}{Y_{HDye}}\right) \quad \text{Equation 9-4}$$

The so calculated temperature dependent thermodynamic stability constants of bromocresol green are shown in Figure 9-3b.

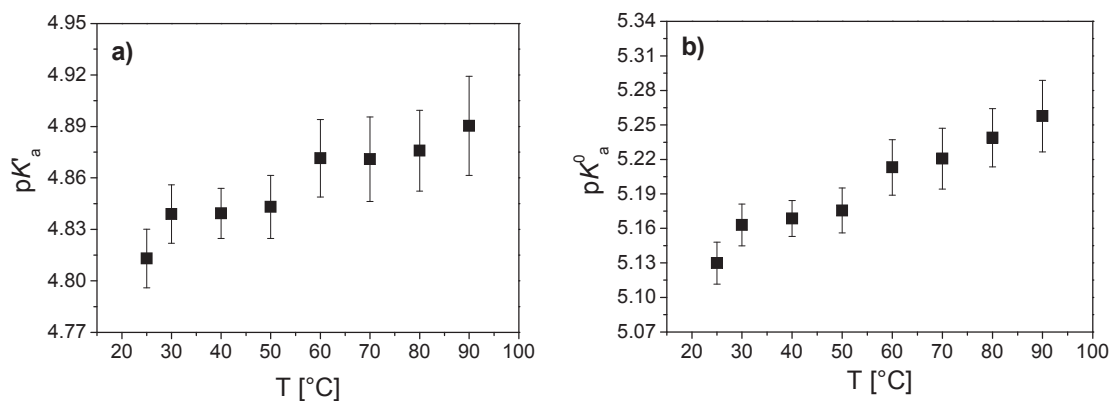


Figure 9-3: a) conditional $pK'_a(T)$ values of bromocresol green (valid for $I_m = 0.2$ m) b) respective thermodynamic $pK^0_a(T)$ values (valid for $I_m = 0$ m)

At $T = 25^\circ\text{C}$, the pK^0_a value determined in this work is in good agreement with literature data ($pK^0_{a,25^\circ\text{C,Lit}} = 4.98$) [Meloun et al., 1977]. With increasing temperature the pK^0_a increases by about 0.15 orders of magnitude, yielding a pK^0_a of 5.26 ± 0.04 at 90°C . A comparison of the temperature effect with literature data is not possible, since no data are available on the temperature dependency of the pK^0_a of bromocresol green.

Bromocresol green is applied to measure the $\text{pH}(T)$ of solutions containing propionate ions. The results are used to calculate the temperature dependency of the pK^0_a of propionic acid. Since the $pK^0_a(T)$ of propionic acid is known from the literature, this system can be used for validating the here applied experimental setup. Four sample solutions are prepared with a $\text{pH}_{25^\circ\text{C}}$ of about 4.8, corresponding to the pK^0_a propionate (see Table 9-2).

Table 9-2: Samples for the spectroscopic pH measurement with bromocresol green

No.	$[\text{NaProp}]_{\text{total}}$	$[\text{HClO}_4]_{\text{total}}$	$[\text{NaClO}_4]_{\text{total}}$	I_m
P1	0.005	0.0025	0.193	0.2
P2	0.01	0.005	0.185	0.2
P3	0.025	0.012	0.163	0.2
P4	0.05	0.025	0.125	0.2

Using the previously determined single component spectra, the dye speciation of the four samples is determined by peak deconvolution. The pH of the four samples is then calculated as function of the temperature with the $pK'_a(T)$ values of bromocresol green using Equation 9-3. The so determined $\text{pH}(T)$ values are displayed in Figure 9-4a. The results are consistent for all four samples, yielding an average value of $\text{pH}_{25^\circ\text{C}} = 4.73 \pm 0.05$ which increases by about 0.25 orders of magnitude in the studied temperature range. The temperature dependent pK^0_a of propionic acid is calculated according to Equation 9-5,

$$pK^0_a = -\log\left(\frac{([\text{H}^+]_{\text{eq}})^2 - [\text{H}^+]_{\text{eq}} \cdot [\text{H}^+]_{\text{total}} + [\text{H}^+]_{\text{eq}} \cdot [\text{Prop}^-]_{\text{total}}}{[\text{H}^+]_{\text{total}} - [\text{H}^+]_{\text{eq}}}}{\gamma_{\text{H}^+} \cdot \gamma_{\text{Prop}^-}}\right)$$

Equation 9-5

where $[\text{H}^+]_{\text{eq}}$ is the proton concentration in solution, $[\text{H}^+]_{\text{total}}$ is the total proton concentration, $[\text{Prop}^-]_{\text{total}}$ is the total sodium propionate concentration and γ_{H^+} and γ_{Prop^-} are the respective activity coefficients. Hereby, the protons originating from the dissociation of water are neglected, since their concentration is by two orders of magnitude lower than the concentration of the protons in solution. The $[\text{H}^+]$ concentration at equilibrium is related to the pH by the following equation.

$$[\text{H}^+]_{\text{eq}} = 10^{-\text{pH}} \cdot (\gamma_{\text{H}^+})^{-1}$$

Equation 9-6

The $pK_a^0(T)$ values of propionate are shown in Figure 9-4b.

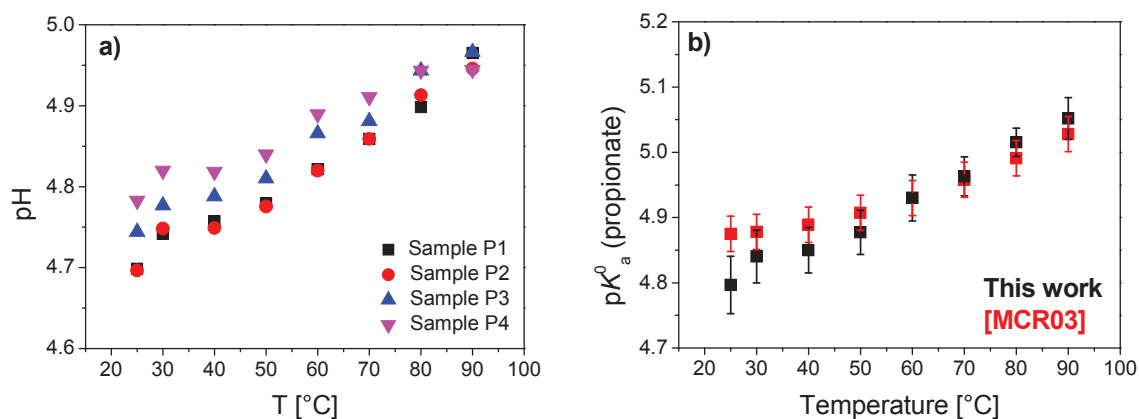


Figure 9-4: a) $pH(T)$ values of four sample solutions (see **Table 9-2**), b) $pK_a(T)$ values of propionate

The $pK_a^0(T)$ values of propionic acid determined in the present work are in good agreement with literature data [McRae et al., 2003]. This shows that our newly designed experimental setup is very well suitable for pH measurements at increased temperature.

X.3.1 Indicator dye bromophenol blue

Similar to bromocresol green, bromophenol blue is an indicator dye of the triphenylmethane family. The dye has a $pK_{a,25^\circ C}^0$ of 4.171, making it suitable for pH-measurements in a region of 3 to 5 [Manohar & Atkinson, 1993]. The acid and base form of bromophenol blue is displayed in Figure 9-5.

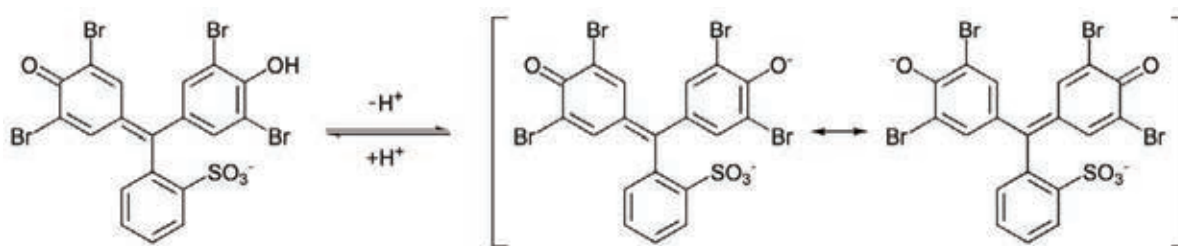


Figure 9-5: Bromophenol blue in its acid (left) and base (right) form

The temperature dependency of the pK_a^0 of bromophenol blue is determined by calibration versus the reference solutions given in Table 9-1. The respective absorption spectra at $pH_{25^\circ C} = 2, 4$ and 11 and $T = 25^\circ C$ are shown in Figure 9-6a. The absorption spectra at $pH_{25^\circ C} = 2$ and 11 display maxima at 440 nm and 591 nm , attributed to the acid and base form of the dye, respectively. The assignment of the absorption bands is confirmed by comparison with literature data [Abdel-Fattah, 1997]. At $pH_{25^\circ C} = 4$ both species are present in solution, and the measured absorption spectrum is a linear combination of the respective absorption bands. The

molar fractions of the acid and base form of the dye in the buffer solution at $\text{pH}_{25^\circ\text{C}} = 4$ are determined as function of the temperature by peak deconvolution. An exemplary fit of the spectrum at $\text{pH}_{25^\circ\text{C}} = 4$ and $T = 25^\circ\text{C}$ is shown in Figure 9-6b.

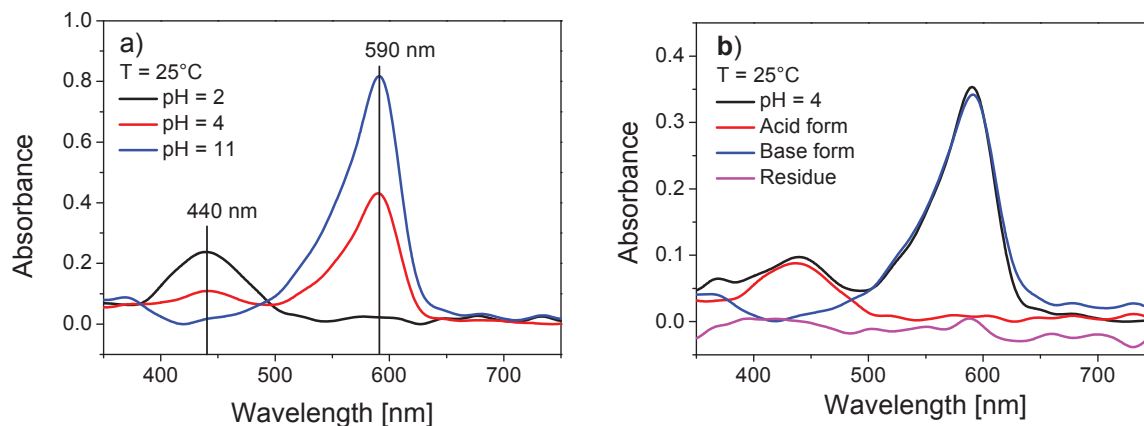


Figure 9-6: a) Absorption Spectra of bromophenol blue at $\text{pH}_{25^\circ\text{C}} = 2, 4$ and 11 ($T = 25^\circ\text{C}$) b) peak deconvolution of the spectrum at $\text{pH}_{25^\circ\text{C}} = 4$ and $T = 25^\circ\text{C}$

The conditional $\text{p}K'_a(T)$ values are determined using the dye speciation and Equation 9-2 (Figure 9-7a). By calculating the respective activity coefficients with the Davies equation (Equation 9-3) the thermodynamic $\text{p}K^0_a(T)$ values of bromophenol blue are obtained (Figure 9-7b).

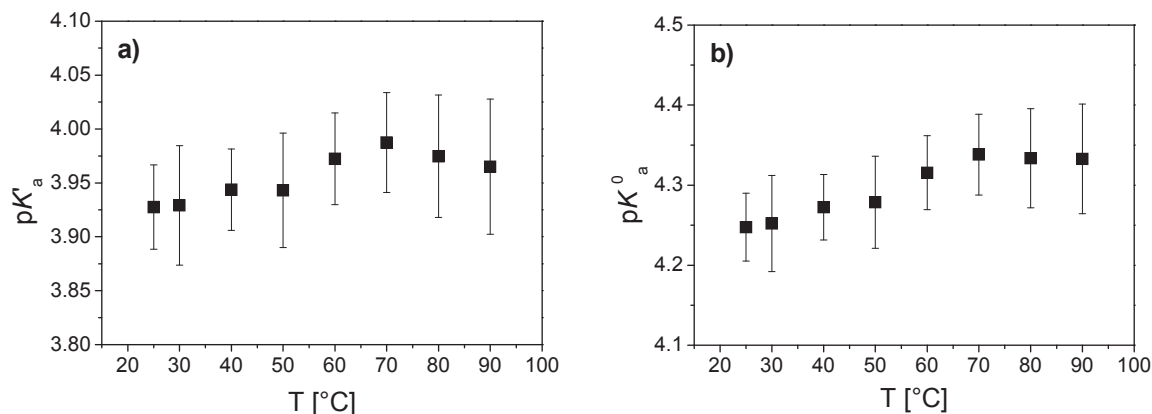


Figure 9-7: a) conditional $\text{p}K'_a(T)$ of bromophenol blue (valid for $I_m = 0.2$ m) b) thermodynamic $\text{p}K^0_a(T)$ of bromophenol blue (valid for $I_m = 0$ m)

The $\text{p}K^0_a$ of bromophenol blue determined in this work is in good agreement with literature data at $T = 25^\circ\text{C}$ [Manohar et al., 1993] No literature data is available on the temperature dependence of $\text{p}K^0_a$.

Due to its $\text{p}K_a$ value, Bromophenol blue can be used to measure the pH of solutions in the range from 3 to 5. Thus, the $\text{pH}(T)$ of three samples is measured containing defined concen-

trations of lactate (see Table 9-3). The $\text{pH}_{25^\circ\text{C}}$ of these samples is adjusted to approximately 3.7, corresponding to the $\text{p}K_a^0$ of lactic acid [Larsson & Adell, 1931].

Table 9-3: Samples for the spectroscopic pH measurement using bromophenol blue

Sample	$[\text{NaLac}]_{\text{total}}$	$[\text{HClO}_4]_{\text{total}}$	$[\text{NaClO}_4]_{\text{total}}$	I_m
L1	1.0×10^{-3} m	7.5×10^{-4} m	1.98×10^{-1} m	0.2
L2	1.0×10^{-2} m	5.0×10^{-3} m	1.85×10^{-1} m	0.2
L3	2.5×10^{-2} m	1.2×10^{-2} m	1.63×10^{-1} m	0.2

The molar fractions of the acid and base form of bromophenol blue in the respective samples are determined by peak deconvolution using the previously recorded single component absorption spectra. The pH is then calculated according to Equation 9-2 (Figure 9-8a). The $\text{pH}(T)$ values of the three samples are consistent, yielding an averaged $\text{pH}_{25^\circ\text{C}}$ of 3.71, which increases by about 0.1 orders of magnitude in the temperature range from 25 to 90°C .

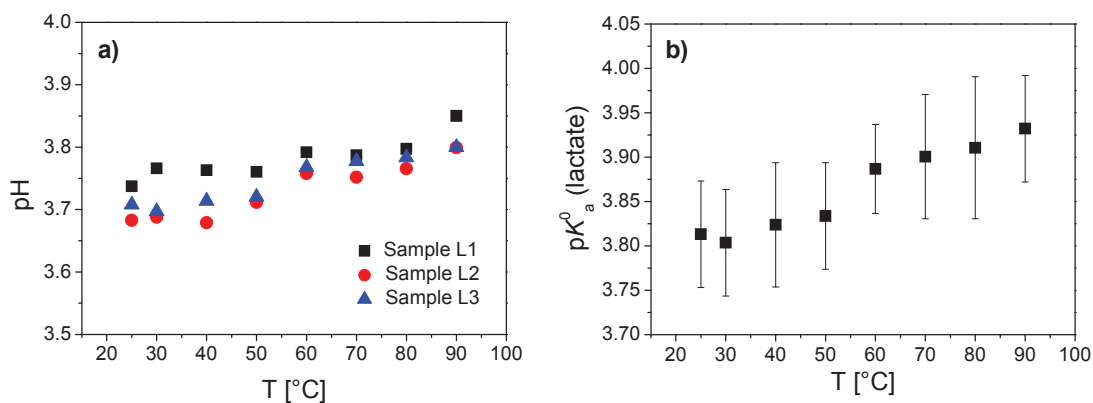


Figure 9-8: a) $\text{pH}(T)$ values of three sample solutions (see Table 9-3) b) $\text{p}K_a(T)$ values of lactate

The resulting $\text{p}K_a^0(T)$ values of lactic acid are shown in Figure 9-8b. At $T = 25^\circ\text{C}$, the results are in good agreement with literature data [Larsson & Adell, 1931]. With increasing temperature, the $\text{p}K_a^0$ increases by about 0.15 orders of magnitude. No literature data on the temperature dependency of the $\text{p}K_a^0$ of lactic acid is available.

The results show a very good applicability of the developed high temperature cell for spectroscopic pH measurements at increased temperatures and pressure. The experimental setup was tested by applying the optical indicator dyes bromocresol green and bromophenol blue to

measure the pH of solutions containing propionate and lactate ions in the temperature range from 25 to 90°C. Thus, the temperature dependency of propionic and lactic acid was determined. These results are of major importance for the thermodynamic description of the complexation of actinide ions with small organic ligands at room as well as at increased temperatures.

10 References published from project results with INE contribution

Peer reviewed:

- Grangeon, S. et al., (2011). in review. On nickel occurrence and distribution in a clay-rich formation: Implications for trace elements solubility control. *Geochimica Et Cosmochimica Acta*.
- Grasset, L. et al., (2010). Sequential extraction and spectroscopic characterisation of organic matter from the Callovo-Oxfordian formation. *Organic Geochemistry*, 41(3): 221-233.
- Hartmann, E., Geckeis, H., Rabung, T., Lutzenkirchen, J., and Fanghanel, T., (2008). Sorption of radionuclides onto natural clay rocks. *Radiochimica Acta* 96, 699-707.
- Hartmann, E., Baeyens, B., Bradbury, M. H., Geckeis, H., and Stumpf, T., (2008). A Spectroscopic Characterization and Quantification of M(III)/Clay Mineral Outer-Sphere Complexes. *Environmental Science & Technology* 42, 7601-7606.
- Hartmann, E., Brendebach, B., Polly, R., Geckeis, H., and Stumpf, T., (2010). Characterization and quantification of Sm(III) and Cm(III)/clay mineral outer-sphere species by TRLFS in D2O and EXAFS studies. *Journal of Colloid and Interface Science* 353, 562-568.
- Lerouge, C. et al., (2010). Comparative EPMA and μ -XRF methods for mapping micro-scale distribution of iodine in biocarbonates of the Callovian- Oxfordian clayey formation at Bure, Eastern part of the Paris Basin. *Physics and Chemistry of the Earth, Parts A/B/C*, 35(6-8): 271-277.
- Schäfer, T. and Denecke, M.A., (2010). Nuclear waste repository research at the micro- to nanoscale. In: M.A. Denecke and C.T. Walker (Editors), *X-Ray Optics and Microanalysis, Proceedings. AIP Conference Proceedings. Amer. Inst. Physics, Melville*, pp. 181-187.
- Schäfer, T., Michel, P. and Claret, F., (2009a). The application of STXM and μ FT-IR to characterize sedimentary organic matter in the Opalinus clay. *Journal of Physics: Conference Series*, 186: 012095.
- Schäfer, T. et al., (2009b). Radiation sensitivity of natural organic matter: Clay mineral association effects in the Callovo-Oxfordian argillite. *Journal of Electron Spectroscopy and Related Phenomena* 170: 49-56.
- Vilas, V.V. et al., (2010). Synthesis and Characterization of the Hybrid Clay-Based Material Montmorillonite–Melanoidin: A Potential Soil Model. *Soil Sci. Soc. Am. J.*, 74(6): 2239-2245.

11 References

- Abdel-Fattah, A.A., El-Kelany, M., Abdel-Rehim, F., El Miligy, A.A., (1997). *UV-sensitive indicators based on bromophenol blue and chloral hydratedyed poly (vinyl butyral)*, Journal of Photochemistry and Photobiology A: Chemistry, **110**, 291-297.
- Acholla, F.V. and Orr, W.L., (1993). Pyrite Removal from Kerogen without Altering Organic-Matter - the Chromous Chloride Method. *Energy & Fuels*, 7(3), 406-410.
- Allen, P. G., Bucher, J. J., Shuh, D. K., Edelstein, N.M., Reich, T., (1997). Investigation of aquo and chloro complexes of UO_2^{2+} , NpO_2^+ , Np^{4+} , and Pu^{3+} by X-ray absorption fine structure spectroscopy. *Inorg. Chem.* **36**, 4676.
- Altmann, R. S., Buffle, J., (1988). *Geochim. Cosmochim. Acta* 52, 1505.
- Amayri, S., Jermolajev, A., Reich, T., (2011). *Radiochim. Acta* **99**, 349–357.
- Andra Dossier 2005 – Référentiel du site de Meus/Haute Marne, (2005). C.R.P.ADS.04.0022; Andra: Paris, France.
- Ankudinov, A.L., Ravel, B., Rehr, J.J., Conradson, S.D., (1998). Real-space multiple-scattering calculation and interpretation of x-ray-absorption near-edge structure. *Physical Review B* 58(12), 7565-7576.
- Antonio, M. R., Soderholm, L., Williams, C. W., Blaudeau, J.-P., Bursten, B. E., (2001). Neptunium redox speciation. *Radiochim. Acta* 89, 17.
- Arfaioli, P., Ristori, G.G., Bosetto, M. and Fusi, P., (1997). Humic-like compounds formed from L-tryptophan and D-glucose in the presence of Cu(II). *Chemosphere*, 35(3), 575-584.
- Artinger, R., Marquardt, C. M., Kim, J. I., Seibert, A., Trautmann, N., Kratz, J. V., (2000). *Radiochim. Acta* 88, 609.
- Banik, N. L., Buda, R. A., Bürger, S., Kratz, J. V., Trautmann, N., (2007). *Journal of Alloys and Compounds*, 444, 522-525.
- Bates, R., (1964). *Determination of pH: Theory and Practice*. John Wiley & Sons, New York.
- Beitz, J.V., Hessler, J.P., (1981). Oxidation state specific detection of transuranic ions in solution. *Nuclear Technology* 51, 169-177.
- Beitz, J.V., Bowers, D.L., Doxtader, M.M., Maroni, V.A., Reed, D.T., (1988). Detection and speciation of trans-uranium elements in synthetic groundwater via pulsed-laser excitation. *Radiochimica Acta* 1988, 44-45, 87-93.
- Benzing-Purdie, L.M., Ripmeester, J.A. and Ratcliffe, C.I., (1985). Effects of temperature on Maillard Reaction Products. *J. Agric. Food Chem.*, 33, 31-33.
- Bolt, G.H., Bruggenwert, M.G., Kamphorst, A., (1976). Adsorption of cations by soils. In: *Soil chemistry A. Basic element*. Hrsg. G.H. Bolt, M.G. Bruggenwert, Elsevier, Amsterdam, p. 54-90.
- Bonin, L., Guillaumont, D., Jeanson, A., Auwer, C. D., Grigoriev, M., Berthet, J. C., Hennig, C., Scheinost, C., Moisy, P., (2009). Thermodynamics and Structure of Actinide(IV) Complexes with Nitritotriacetic Acid, *Inorg. Chem.* 48, 3943-3953.
- Borkowski, M., Lis, S., Choppin, G.R., (1996). Complexation study of NpO_2^+ and UO_2^{2+} Ions with several organic ligands an aqueous solutions of high ionic strength, *Radiochim. Acta*, 74, 117-121.
- Bosetto, M., Arfaioli, P. and Pantani, O.L., (2002). Study of the Maillard reaction products formed by glycine and D-glucose on different mineral substrates. *Clay Minerals*, 37, 195-204.

- Bosetto, M., Arfaioli, P., Pantani, O.L. and Ristori, G.G., (1997). Study of the humic-like compounds formed from L-tyrosine on homoionic clays. *Clay Minerals*, 32(3), 341-349.
- Bouchet, A., Rassineux, F., (1997). Echantillons d'argiles du forage EST104: Etude mineralogique approfondie. Rapport final DR-P- 0ERM-98-007A, ANDRA Agence nationale pour la gestion des déchets radioactifs, Chatenay-Malabry, p. 107.
- Bradbury, M.H. and Baeyens, B., (2009). Sorption modelling on illite. Part II: Actinide sorption and linear free energy relationships, *Geochim. Cosmochim. Acta* 73, 1004–1013
- Bradbury, M.H., Baeyens, B., (2005a). Modelling the sorption of Mn(II), Co(II), Ni(II), Zn(II), Cd(II), Eu(III), Am(III), Sn(IV), Th(IV), Np(V) and U(VI) on montmorillonite: Linear free energy relationships and estimates of surface binding constants for some selected heavy metals and actinides. *Geochim. Cosmochim. Acta* 69(4), 875-892.
- Bradbury, M.H., Baeyens, B., (2005b). Experimental and modelling investigations on Na-illite: Acid-base behaviour and the sorption of strontium, nickel, europium and uranyl. Paul Scherrer Institut, PSI-Bericht 05-02, Villigen.
- Bradbury, M.H., Baeyens, B.A. (2003). Comparison of Apparent Diffusion Coefficients Measured in Compacted Kunigel V1 Bentonite with Those Calculated from Batch Sorption Measurements and De (HTO) Data: A Case Study for Cs(I), Ni(II), Sm(III), Am(III), Zr(IV) and Np(V). PSI Bericht Nr. 03-02, Villigen, Switzerland.
- Bradbury, M.H., Baeyens, B., (2003a). Far field sorption data bases for performance assessment of a high-level radioactive waste repository in an undisturbed Opalinus Clay host rock. Paul Scherrer Institut, PSI-Bericht 03-08, Villigen, 128 p.
- Bradbury, M.H., Baeyens, B., (2002). Sorption of Eu on Na- and Ca-montmorillonites: Experimental investigations and modelling with cation exchange and surface complexation, *Geochim. Cosmochim. Acta*, 66(13), 2325-2334.
- Bradbury, M.H., Baeyens, B., (1999). Modelling the sorption of Zn and Ni on Ca-montmorillonite. *Geochim. Cosmochim. Acta* 63(3-4), 325-336.
- Bradbury, M.H., Baeyens, B., (1997). A mechanistic description of Ni and Zn sorption on Na-montmorillonite. Part 2, Modelling. *Journal of Contaminant Hydrology* 27(3-4), 223-248.
- Bradbury, M. H., Baeyens, B., (1995). A Quantitative Mechanistic Description of Ni, Zn and Ca Sorption on Na-Montmorillonite. Part III, Modelling. Technical Report NTB 95-06, NAGRA Nationale Genossenschaft für die Lagerung radioaktiver Abfälle, Wetingen/Schweiz, p. 75.
- Bradbury, M.H., Baeyens, B., Geckeis, H., Rabung, T., (2005). Sorption of Eu(III)/Cm(III) on Ca-montmorillonite and Na-illite. Part 2: Surface complexation modelling. *Geochim. Cosmochim. Acta* 69(23), 5403-5412.
- Brendebach, B., Banik, N. L., Marquardt, Christian M., Rothe, J., Denecke, M., Geckeis, H., (2009). *Radiochimica Acta* 97,12, 701-708.
- Buck, R.P., Rondini, S., Covington, A.K., Baucke, F.G.K., Brett, C.M.A., Camoes, M.F., Milton, M.J.T., Mussini, T., Naumann, R., Pratt, K.W., Spitzer, P., Wilson, G.S., (2002). *Measurement of pH, Definition, Standards and Procedures*, *Pure & Appl. Chem.*, **74(11)**, 2169-2200,
- Bulemela, E., Trevani, L., Tremaine, P.R., (2005). *Ionization Constants of Aqueous Glycolic Acid at Temperatures up to 250°C Using Hydrothermal pH Indicators and UV-Visible Spectroscopy*, *Journal of Solution Chemistry*, **34**, 769-788,.
- Choppin, G.R., (2003). Actinide speciation in the environment, *Radiochim. Acta* 91, 645-649.
- Choppin, G.R., Chen, J.F., (1996). Complexation of Am(III) by oxalate in NaClO₄ media, *Radiochim Acta*, 74, 105-110.

- Choppin, G.R., Rizkalla, E.N., (1994). Solution chemistry of actinides and Lanthanides, in Handbook on the physics and chemistry of rare earths, K.A.a.E. Gschneider, L., Editor, Elsevier Science B. V. p. 559-590.
- Claret, F., Sakharov, B. A., Drits, V. A., Velde, B., Meunier, A., Griffault, L., Lanson, B., (2004). Clay minerals in the Meuse-Haute marne underground laboratory (France): Possible influence of organic matter on clay mineral evolution. *Clays Clay Minerals* **52**(5), 515.
- Claret, F., Schäfer, T., Bauer, A., Buckau, G., (2003). Generation of humic and fulvic acid from Callovo-Oxfordian clay under high alkaline conditions, *Science of the Total Environment* **317**(1-3), 189-200.
- Claret, F., Bauer, A., Schäfer, T., Griffault, L., Lanson, B., (2002). Experimental investigation of the interaction of clays with high-pH solutions: A case study from the Callovo-Oxfordian formation, Meuse-HauteMarne underground laboratory (France). *Clays Clay Mineral* **50**(5), 633
- Cohen, D. (1961). Electrochemical studies of plutonium ions in perchloric acid solutions, *Journal of Inorganic Nuclear Chemistry*, **18**, 207.
- Conradson, S.D., et al., (2003). Higher order speciation effects on plutonium L-3 X-ray absorption near edge spectra *Inorganic Chemistry*, Vol. 43, No. 1, 116-131.
- Courdouan, A., Christl, I., Rabung, Th., Wersin, P., Kretzschmar, R., (2008). Proton and Trivalent Metal Cation Binding by Dissolved Organic Matter in the Opalinus Clay and the Callovo-Oxfordian Formation. *Environ. Sci. Technol.* **42**, 5985-5991.
- Courdouan, A., Christl, I., Meylan, S., Wersin, P., Kretzschmar, R., (2007). Characterization of dissolved organic matter in anoxic rock extracts and in situ pore water of the opalinus clay, *Appl. Geochem.*, **22**, 2926-2939.
- Davies, C.W., (1962). Ion association., London, Butterworths, 190 p.
- Deniau, I., Devol-Brown, I., Derenne, S., Behar, F. and Largeau, C., (2008), Comparison of the bulk geochemical features and thermal reactivity of kerogens from Mol (Boom Clay), Bure (Callovo-Oxfordian argillite) and Tournemire (Toarcian shales) underground research laboratories. *Science of The Total Environment*, **389**(2-3), 475-485.
- Denecke, M.A., (2006). Actinide speciation using X-ray absorption fine structure spectroscopy. *Coordination Chemistry Reviews*, **250**(7-8), 730-754.
- Denecke, M. A., Dardenne. K., Marquardt, C.M. (2005). Np(IV)/Np(V) valence determinations from Np L3 edge XANES/EXAFS, *Talanta* **65**,1008-1014.
- Denecke, M.A., Janssens, K., Proost, K., Rothe, J. and Noseck, U., (2005a). Confocal micrometer-scale X-ray fluorescence and X-ray absorption fine structure studies of uranium speciation in a tertiary sediment from a waste disposal natural analogue site. *Environmental Science & Technology*, **39**(7), 2049-2058.
- Denecke, M.A., Rothe, J., Dardenne, K., Blank, H. and Hormes, J., (2005b). The INE-Beamline for Actinide Research at ANKA. *Physica Scripta T115*, 1001-1003.
- Denecke, M. A., Marquardt, C. M., Rothe, J., Dardenne, K., Jensen, M. P., (2002). XAFS study of actinide coordination structure in Np(IV)-fulvates. *J. Nucl. Sci. Technol.*, Suppl. **3**, 410.
- Deniau, I., Devol-Brown, I., Derenne, S., Behar, F. and Largeau, C., (2008). Comparison of the bulk geochemical features and thermal reactivity of kerogens from Mol (Boom Clay), Bure (Callovo-Oxfordian argillite) and Tournemire (Toarcian shales) underground research laboratories. *Science of The Total Environment*, **389**(2-3), 475-485.
- DiBernardo, P., Zanonato, P., Tian, G., Tolazzi, M., Rao, L., (2009). Thermodynamics of the complexation of uranium(VI) with oxalate in aqueous solution at 10-70°C, *Dalton Trans.*, 4450-4457.

- DiBernardo, P., Zanonatp, P., Bismondo, A., Jiang, H., Garnov, A.Yu., Jiang, J., Rao, L., (2006). Complexation of Uranium(VI) with Thiodiacetic Acid in Solution at 10–85 °C, *Eur. J. Inorg. Chem.*, 4533.
- DiBernardo, P., Cassol, A., Tomat, G., Bismondo, A., Magon, L., (1983). Thermodynamics of the complex formation between Thorium(IV) and some Polydentate Ligands in aqueous Solution, *J. Chem Soc. Dalton Trans.*, 733-735.
- DiBernardo, P., DiNapoli, V., Cassol, A., Magon, L., (1977). *J. Inorg. Nucl. Chem.*, 39, 1659.
- Dickson, A.G., (1993). The *measurements of sea water pH*, *Marine Chemistry*, 44, 131-142.
- Edelstein, N.M., Klenze, R., Fanghänel, T., Hubert, S., (2006). Optical properties of Cm(III) in crystals and solutions and their application to Cm(III) speciation. *Coordination Chemistry Reviews* 2006, 250(7-8), 948-973.
- Eglizaud, N., Miserque, F., Simoni, E., Schlegel, M., Descostes, M., (2006). Uranium(VI) interaction with pyrite (FeS₂): chemical and spectroscopic studies, *Radiochim. Acta* 94, 651-656.
- Elie, M. and Landais, P., (1997). Identification et comportement thermique des matières organiques du Callovo-Oxfordien. Journées Scientifiques ANDRA-CNRS, 27 et 28 Octobre 1997, Bar-le-Duc, 35-58.
- Fairhurst, A.J., Warwick, P., (1998). The influence of humic acid on europium-mineral interactions. *Colloids and Surfaces a-Physicochemical and Engineering Aspects*, 145(1-3), 229-234.
- Fanghänel, T., Kim, J.I., Klenze, R., Kato, Y., (1995). Formation of Cm(III) chloride complexes in CaCl₂ solutions. *Journal of Alloys and Compounds* 225(1-2), 308-311.
- Fox, P.M., Davis, J.A., Zachara, J.M., (2006). The effect of calcium on aqueous uranium(VI) speciation and adsorption to ferrihydrite and quartz. *Geochimica Et Cosmochimica Acta* 70(6), 1379-1387.
- Freyer, M., Walther, C., Stumpf, T., Buckau, G., Fanghänel, T., (2009). Formation of Cm humate complexes in aqueous solution at pHc 3 to 5.5: The role of fast interchange. *Radiochimica Acta* 97, 547-558.
- Fröhlich, D.R., Amayri, S., Drebert, J., Reich, J., (2011). *Radiochimica Acta* Vol. 99, No. 2, pp. 71-77.
- Gadel, F. and Bruchet, A., (1987). Application of pyrolysis-gas chromatography-mass spectrometry to the characterization of humic substances resulting from decay of aquatic plants in sediments and water. *Water Research*, 21, 1195-1206.
- Gaines, G.L.J., Thomas, H.C., (1953). Adsorption studies on clay minerals. II. A formulation of the thermodynamics of exchange adsorption. *The Journal of Chemical Physics* 21(4), 714-718.
- Gaucher, E., Robelin, C., Matray, J. M., Negral, G., Gros, Y., Heitz, J. F., Vinsot, A., Rebours, H., Cassagnabere, A., Bouchet, A., (2004). ANDRA underground research laboratory: interpretation of the mineralogical and geochemical data acquired in the Callovian-Oxfordian formation by investigative drilling. *Phys. Chem. Earth* 29(1), 55-77.
- Geckeis, H., (2010). Modellrechnungen zur Speziation von Cm(III) bzw. Am(III) in Gorlebengrundwasser auf der Grundlage des NICA-Donnan-Modells, Institut für Nukleare Entsorgung, KIT, Karlsruhe, Persönliche Mitteilung.
- Giaquinta, D.M., Soderholm, L., Yuchs, S.E. and Wasserman, S.R., (1997). The speciation of uranium in a smectite clay: evidence for catalysed uranyl reduction. *Radiochimica Acta*, 76, 113- 121.
- Grangeon, S. et al., (2011), in review. On nickel occurrence and distribution in a clay-rich formation: Implications for trace elements solubility control. *Geochimica Et Cosmochimica Acta*.
- Grasset, L. et al., (2010). Sequential extraction and spectroscopic characterisation of organic matter from the Callovo-Oxfordian formation. *Organic Geochemistry*, 41(3), 221-233.

- Griffault, L., (1999). Référentiel géologique du site de l'Est, Technical Report A RP ADS 99-005, ANDRA Agence nationale pour la gestion des déchets radioactifs, Chatenay-Malabry.
- Grim, R.E., (1953). Clay mineralogy. New York, McGraw-Hill, p. 587
- Guillaumont, R., Fanghanel, T., Fuger, J., Grenthe, I., Neck, V., Palmer, D.A., Rand, M.H., (2003). Update on the chemical thermodynamics of uranium, neptunium, plutonium, americium and technetium. 1. Aufl. Chemical Thermodynamics, Hrsg. F.J. Mompean, M. Illemassene, C. Domenech-Orti, K. Ben-Said. Vol. 5., Amsterdam, Boston, Heidelberg, ELSEVIER, 918 p.
- Hartmann, E., (2010). Sorption von Ln(III)/An(III) und U(VI) an Tonmineralien und natürlichen Tongesteinen, PhD thesis, Fakultät für Bauingenieur-, Geo- und Umweltwissenschaften des Karlsruher Instituts für Technologie (KIT), Karlsruhe.
- Hartmann, E., Geckeis, H., Rabung, T., Lutzenkirchen, J., Fanghanel, T., (2008). Sorption of radionuclides onto natural clay rocks. *Radiochimica Acta* 96, 699-707.
- Hartmann, E., Baeyens, B., Bradbury, M., Geckeis, H., Stumpf, T., (2008a). A Spectroscopic Characterization and Quantification of M(III)/Clay Mineral Outer-Sphere Complexes, *Environ. Sci. Technol.* 42, 7601–7606.
- Heberling, F., Denecke, M.A., Bosbach, D., (2008). Neptunium(V) coprecipitation with calcite. *Environ. Sci. Technol.* 42, 471-476.
- Höhne, S.,(2010). Spektroskopische und thermodynamische Untersuchungen des Komplexbildungsverhaltens von Cm(III) mit Propionat bei erhöhten Temperaturen, Bachelor-Arbeit, Universität Heidelberg.
- Huh, Y., Lee, J.-G., McPhail, D.C., Kim, K., (1993). *Measurements of pH at elevated temperatures using the optical indicator acridine*, *J. Sol. Chem.*, 22, 651-661.
- Inoue, Y., Tochiyama, O., (1983). *Polyhedron*, 2, 627.
- Jacquot, E., (2002). Composition des eaux interstitielles des argilites du Callovo-Oxfordien non perturbées. Rapport ANDRA No. D NT ASTR 02-041, ANDRA Agence nationale pour la gestion des déchets radioactifs, Châtenay-Malabry, p. 13.
- Janssens, K., Proost, K. and Falkenberg, G., (2004). Confocal microscopic X-ray fluorescence at the HASYLAB microfocus beamline: characteristics and possibilities. *Spectrochimica Acta Part B-Atomic Spectroscopy*, 59(10-11), 1637-1645.
- Janos, P., (2003). *Journal of Chromatography A* 983, 01.
- Jeanson, A., Dahou, S., Guillaumont, D., Moisy, P., Auwer, C. D., Scheinost, C., Hennig, C., Vidaud, C., Subra, G., Solari, P. L., (2009). A comparative study of actinide complexation in three ligand systems with increasing complexity, *Journal of Physics: Conference Series* 190 012185.
- Jeanson, A., Ferrand, M., Funke, Harald., Hennig, C., Moisy, P., Solari, P. L., Vidaud, C., Den Auwer, C., (2010). The Role of Transferrin in Actinide(IV) Uptake: Comparison with ACHTUNG TRENUNG Iron(III), *Chem. Eur. J.* 16, 1378 – 1387.
- Jiang, J., Rao, L., DiBernardo, P., Zanonato, P., Bismondo, A., (2002). *J. Chem. Soc., Dalton Trans.*, 9, 1832.
- Jokic, A., Wang, M.C., Liu, C., Frenkel, A.I. and Huang, P.M., (2004). Integration of the polyphenol and Maillard reactions into a unified abiotic pathway for humification in nature: the role of \square -MnO₂. *Org. Geochem.*, 35, 747-762.
- Jung, A.-V. et al., (2005). Synthesis of amino-phenolic humic-like substances and comparison with natural aquatic humic acids: A multi-analytical techniques approach. *Org. Geochem.*, 36, 1252-1271.

- Kaszuba, J. P., Runde, W. H. (1999). The aqueous geochemistry of neptunium: Dynamic control of soluble concentrations with applications to nuclear waste disposal. *Environ. Sci. Technol.*, 33, 4427–4433.
- Keeney-Kennicutt, W. L., Morse, J. W., (1984). *Marine Chem.* 15, 133.
- Keeney-Kennicutt, W. L., Morse, J. W., (1985). *Geochim. Cosmochim. Acta* 49, 2577.
- Keizer, M.G., van Riemsdijk, W.H., (1999). ECOSAT Equilibrium Calculation Of Speciation And Transport 4.8 (user manual), Universität Wageningen, 76 p.
- Kim, J. I., Czerwinski, K. R., (1996) *Radiochimica Acta* 73, 5.
- Kim, J. I., Buckau, G., Li, G. H., Duschner, H., Psarros, N., (1990). *Fres. J. Anal. Chem.*, 338, 245–252.
- Kimura, T., Choppin, G.R., (1994). [349]
- Kinniburgh, D. G., van Riemsdijk, W. H., Koopal, L. K., Borkovec, M., Benedetti, M. F., Avena, M. J., (1999). *Colloids Surf. A* 151, 147.
- Kowal-Fouchard, A., Drot, R., Simoni, E., Marmier, N., Fromage, F., Ehrhardt, J.J., (2004). Structural identification of europium(III) adsorption complexes on montmorillonite. *New Journal of Chemistry* 28(7), 864-869.
- Krause M. O., Haire R. G., Keski-Rahkonen O. and Peterson J. R. (1988). Photoelectron spectrometry of the actinides from Ac to Es. *J. Electron Spectrosc. Relat. Phenom.* 47, 215–226.
- Křepelová, A. (2007). Influence of humic acid on the sorption of uranium(VI) and americium(III) onto kaolinite, Dissertation, Fakultät Mathematik und Naturwissenschaften, Technische Universität, Dresden.
- Kuczewski, B., Marquardt, C. M., Seibert, A., Geckeis, H., Kratz, J. V., and Trautmann, N., (2003). Separation of Plutonium and Neptunium Species by Capillary Electrophoresis-ICP-MS and Application to Natural Ground Water Samples. *Anal.Chem.* 75, 6769-6774.
- Larsson, E., Adell, B., (1931). *Z. Phys. Chem.* 157, 342-362.
- Latrille, C., Ly, J. and Herbette, M., (2006). Retention of Sn(IV) and Pu(IV) onto four argillites from the Callovo-Oxfordian level at Bure (France) from eight equilibrated sedimentary waters. *Radiochimica Acta*, 94(8), 421-427.
- Lee, T.S., Gin, J., Nampoore, V.P.N., Vallabhan, C.P.G., Unnikrishnan, N.V., Radhakrishnan, P., (2001). *A sensitive fibre optic pH sensor using multiple sol-gel coatings*, *J. Opt. A: Pure Appl. Opt.*, 3, 355-359.
- Lerouge, C. et al., (2010). Comparative EPMA and μ -XRF methods for mapping micro-scale distribution of iodine in biocarbonates of the Callovian-Oxfordian clayey formation at Bure, Eastern part of the Paris Basin. *Physics and Chemistry of the Earth, Parts A/B/C*, 35(6-8), 271-277.
- Lujanienė, G., Motiejunas, S., and Sapolaite, J., (2007). Sorption of Cs, Pu and Am on clay minerals. *Journal of Radioanalytical and Nuclear Chemistry* 274, 345-353.
- Luckscheiter, B., Kienzler, B., Bosbach, D., (2004). Literaturstudie zum Korrosionsverhalten von HAW-Gläsern in Ton: Tongestein und Versatzmaterial, Institut für Nukleare Entsorgung, FZKA 7068, Karlsruhe.
- Maillard, L.C., (1912a). Action des acides aminés sur les sucres ; formation des mélamoidines par voies méthodique. *Comptes Rendus de l'Académie des Sciences*, Séance du 8 janvier 1912, 66-68.
- Maillard, L.C., (1912b). Formation d'humus et de combustibles minéraux sans intervention de l'oxygène atmosphérique, des microorganismes, des hautes températures, ou des fortes pressions. *Comptes Rendus de l'Académie des Sciences*, Séance du 23 décembre 1912, 1554-1556.

- Manohar, S., Atkinson, G., (1993). *The effect of high pressure on the ion pair equilibrium constant of alkali metal fluorides: A spectrophotometric study*, J. Sol. Chem., **22**, 859-872.
- Marignac, C. and Cuney, M., (1999). Ore deposits of the French Massif Central: insight into the metallogenesis of the Variscan collision belt. *Mineralium Deposita*, 34(5-6), 472-504.
- Marquardt, C. M., Seibert, A., Artinger, R., Denecke, M. A., Kuczewski, B., Schild, D., Fanghänel, Th., (2004). The redox behaviour of plutonium in humic rich groundwater. *Radiochimica Acta* 92, 617-623.
- Marquardt, C.M., Kim, J. I., Pirlet, V., (2001). Complexation of tetravalent neptunium with fulvic acid, Book of Abstracts, Actinide-2001 Conference, Hayama, Japan, p. 140.
- Marquardt, C. M., Pirlet, V., Kim, J. I., (2000). Initial studies on the complexation of tetravalent neptunium with fulvic acid, in Scientific Report, FZKA 6524, Karlsruhe, 45-70.
- Marques Fernandes, M., (2010). Ternäre Eu(III)/Carbonat-Oberflächenkomplexe an Illit. LES Labor für Endlagersicherheit, PSI, Villigen, private communication, 2010.
- Marques Fernandes, M., Baeyens, B., Bradbury, M., (2008). The influence of carbonate complexation on lan-thanide/actinide sorption on montmorillonite. *Radiochimica Acta* 96, 691-697.
- Marques Fernandes, M., (2006). Spektroskopische Untersuchungen (TRLFS und XAFS) zur Wechselwirkung von dreiwertigen Lanthaniden und Actiniden mit der Mineralphase Calcit. Dissertation, Naturwissenschaftlich-Mathematische Gesamtfakultät, Ruprecht-Karls-Universität Heidelberg, 174 p.
- Mathis, V., Robert, J.-P. and Saint, M., (1990). *J Chron. Rech. Min.*, 499(31-40).
- Mavrik Zavarin, S. K. Roberts, N. Hakem, A. M. Sawvel, and A. B. Kersting, (2005). Eu(III), Sm(III), Np(V), Pu(V), and Pu(IV) sorption to calcite. *Radiochim. Acta*, Vol. 93, Issue 2, pp. 93-102.
- McRae, B.R., Patterson, B.A., Origlin-Luster, M.L., Sorenson, E.C., Woolley, E.M., (2003). *Thermodynamics of proton dissociation from aqueous 1-propanoic and 1-butanoic acids at temperatures 278.15 ≤ (T/K) ≤ 393.15 and pressure p=0.35 MPa: apparent molar volumes and apparent molar heat capacities of aqueous solutions of the acids and their sodium salts*, J. Chem Thermodynamics, 35, 301-329.
- Meloun, M., Kotrly, S., Collect., (1977). *Czech. Chem. Commun.*, **42**, 2115.
- Michot, L. J., Bihannic, I., Porsch, K., Maddi, S., Baravian, C., Mougel, J., Levitz, P., (2004). Phase diagrams of Wyoming Na-montmorillonite clay. Influence of particle anisotropy. *Langmuir* **20**(25), 10829-10837.
- Millero, F.J., DiTrollo, B., Suarez, A.F., Lando, G.,(2009). *Spectroscopic measurements of the pH in NaCl brines*, *Geochim. et. Cosmochim. Acta*, **73**, 3109-3114.
- Milne, C.J., Kinniburgh, D.G., van Riemsdijk, W.H., Tipping, E., (2003). Generic NICA-Donnan model parameters for metal-ion binding by humic substances, *Environ. Sci. Technol.*, **37**, 958-971.
- Milne, C.J., Kinniburgh, D.G., Tipping, E., (2001). Generic NICA-Donnan model parameters for proton binding by humic substances, *Environ. Sci. Technol.*, **35**(10), 2049-2059.
- Montes-H, G., Fritz, B., Clement, A., Michau, N., (2005). Modelling of geochemical reactions and experimental cation exchange in MX80 bentonite. *J. Env. Management* **77**(1), 35.
- Moore, R.C., Borkowski, M., Bronikowski, M.G., Chen, J., Pokrovsky, O.S., Xia, Y., Choppin, G.R., (1999). Thermodynamic modeling of actinide complexation with acetate and lactate at high ionic strength, *J. Sol. Chem.*, **28**(5), 521-531.
- Morse, J.W., Choppin, G.R., (1986). Laboratory studies of plutonium in marine systems, *Mar. Chem.* **20**, 73– 89.

- Motellier, S., Ly, J., Gorgeon, L., Charles, Y., Hainos, D., Meier, P., Page, J., (2003). Modelling of the ion-exchange properties and indirect determination of the interstitial water composition of an argillaceous rock. Application to the Callovo-Oxfordian low-water-content formation. *Appl. Geochem.* **18**(10), 1517.
- Nagra, (2002a). Projekt Opalinuston – Synthese der geowissenschaftlichen Untersuchungsergebnisse, Entsorgungsnachweis für abgebrannte Brennelemente, verglaste hochaktive sowie langlebige mittelaktive Abfälle. Technischer Bericht NTB 02-03, NAGRA Nationale Genossenschaft für die Lagerung radioaktiver Abfälle, Wettingen/Schweiz, p. 659.
- Nagra, (2002b). Nagra Project Opalinus Clay – safety report: Demonstration of disposal feasibility for spent fuel, vitrified-high level waste and long-lived intermediate level waste (Entsorgungsnachweis); NTB 02-05; Nagra: Wettingen, Switzerland.
- Neck, V., Altmaier, M., Seibert, A., Yun, J. I., Marquardt, C. M., Fanghanel, T., (2007). Solubility and redox reactions of Pu(IV) in hydrous oxide: evidence for the formation of PuO_{2+x}(s, hyd.). *Radiochim. Acta* **95**, 193-207.
- Newville, M., Livins, P., Yacoby, Y., Stern, E.A., Rehr, J.J., (1993). Near-edge x-ray-absorption fine-structure of Pb - A comparison of theory and experiment. *Physical Review B* **47**(21), 14126-14131.
- Nitsche, H., Roberts, K., Xi, R., Prussin, T., Becraft, K., Mahamid, I. A., Silber, H. B., Carpenter, S. A., Gatti, R. C. (1994). Long term plutonium solubility and speciation studies in a synthetic brine. *Radiochim. Acta*, **66**, 3-7.
- Panak, P., KlENZE, R., Kim, J.I., Wimmer, H., (1995). A study of intramolecular energy transfer in Cm(III) complexes with aromatic ligands by time-resolved laser fluorescence spectroscopy, *J. Alloys Comp.*, **225**, 261-266.
- Pankow, J.F., (1991). *Aquatic Chemistry Concepts*, Lewis Publisher, Inc.
- Pirlet, V., (2003). The investigation of the neptunium complexes formed upon interaction of high-level waste glass and Boom Clay medium, PhD thesis, Faculté des Sciences, Université de Liege, Liege.
- Plancque, G., Maurice, Y., Moulin, V., Toulhoat, P., Moulin, C., (2005). On the use of spectroscopic techniques for interaction studies, part I: complexation between europium and small organic ligands, *Applied Spectroscopy*, **59**, 432-441.
- Plaschke, M., Rothe, J., Altmaier, M., Denecke, M.A. and Fanghanel, T., (2005). Near edge X-ray absorption fine structure (NEXAFS) of model compounds for the humic acid/actinide ion interaction. *Journal of Electron Spectroscopy and Related Phenomena*, **148**(3), 151-157.
- Pokrovsky, O.S., Choppin, G.R., (1997). Neptunium(V) complexation by acetate, oxalate and citrate in NaClO₄ media at 25°C, *Radiochim. Acta*, **79**, 167-171.
- Pompe, S. et al., (2000). Investigation of humic acid complexation behavior with uranyl ions using modified synthetic and natural humic acids. *Radiochim. Acta*, **88**, 553-558.
- Powell, J.E., Karraker, R.H., Kolat, R.S., Farrell, J.L., (1964). Rare earth research II, proceedings of the third conference on rare earth research, R.S. Vorres, New York.
- Preston, C.M. and Schmidt, M.V.I., (2006). Black (pyrogenic) carbon: a synthesis of current knowledge and uncertainties with special consideration of boreal regions. *Biogeosciences*, **3**(397-420).
- Rabung, T., (1997). Einfluß von Huminstoffen auf die Europium(III)-Sorptions an Hämatit. Dissertation, Ma-thematisch-Naturwissenschaftliche Fakultät, Universität des Saarlandes, Saarbrücken.

- Rabung, T., Pierret, M. C., Bauer, A., Geckeis, H., Bradbury, M. H., Baeyens, B., (2005). Sorption of Eu(III)/Cm(III) on Ca-montmorillonite and Na-illite. Part 1: Batch sorption and time-resolved laser fluorescence spectroscopy experiments. *Geochim. Cosmochim. Acta* **69**(23), 5393-5402.
- Rabung, T., Geckeis, H., Kim, J.I., Beck, H.P., (1998). The influence of anionic ligands on the sorption behaviour of Eu(III) on natural hematite. *Radiochimica Acta* **82**, 243-248.
- Raghuraman, B., Gustavson, G., Mullins, O.C., Rabbito, P., (2006). *Spectroscopic pH measurement for High Temperatures, Pressures and Ionic Strengths*, *AIChE Journal*, **52**, No.9, 3257-3265.
- Rao, L., (2007). Thermodynamics of actinide complexation in solution at elevated temperatures: application of variable-temperature titration calorimetry, *Chem. Soc. Rev.*, **36**, 881-892.
- Rao, L., Zhang, Z., Zanonato, P., DiBernardo, P., Bismondo, A., Clark, S.B., (2004). Complexation of thorium(IV) with acetate at variable temperatures, *Dalton Trans.*, 2867-2872,
- Rao, L., Garnov, A.Yu., Jiang, J., DiBernardo, P., Zanonato, P., Bismondo, A., (2003). *Inorg. Chem.*, **42**, 3685.
- Rao, L., Jiang, J., Zanonato, P., DiBernardo, P., Bismondo, A., Yu, A., (2002). *Radiochim. Acta*, **90**, 581.
- Ravel, B., Newville, M., (2005). ATHENA, ARTEMIS, HEPHAESTUS: data analysis for X-ray absorption spectroscopy using IFEFFIT. *J. Synchrotron Rad.* **12**, 537.
- Rawat, N., Sharma, R.S., Nishad, A., Tomar, B.S., Manchanda, V.K., Thermodynamic study of Th(IV) complexes with dicarboxylates by potentiometry and calorimetry, *Radiochim. Acta*, **99**, 341-347, (2011).
- Rehr, J. J., Albers, R. C., Zabinsky, S. I., (1992). High-order multiple-scattering calculations of x-ray-absorption fine structure. *Phys. Rev. Lett.* **69**, 3397.
- Reiller, P.E., Evans N.D.M., Szabo G., (2008). Complexation parameters for the actinides(IV)-humic acid system: a search for consistency and application to laboratory and field observations *Radiochim. Acta*, **96**, 345-358.
- Rothe, J., Steppert, M., Walther, C., INE-Beamline, Karlsruhe Institute of Technology, unpublished data (2011)
- Rothe, J., Denecke, M. A., Dardenne, K., Fanghänel, Th., (2006). *Radiochim. Acta* **94**, 691.
- Rundle, R.E., Baenziger, N.C., Wilson, A.S. and McDonald, R.A., (1948). The structures of carbides, nitrides, and oxides of uranium. *Journal of the American Chemical Society*, **70**, 99-105.
- Sakuragi, T., Sato, S., Kozaki, T., Mitsugashira, T., Hara, P., Suzuki, Y., (2004). Am(III) and Eu(III) uptake on hematite in the presence of humic acid. *Radiochim. Acta*, **92**(9-11), 697-702.
- Sasaki, T., Takaoka, Y., Kobayashi, T., Fujii, T., Takagi, I., Moriyama, H., Hydrolysis constants and complexation of Th(IV) with carboxylates, *Radiochim. Acta*, **96**
- Schäfer, T. and Denecke, M.A., (2010). Nuclear waste repository research at the micro- to nanoscale. In: M.A. Denecke and C.T. Walker (Editors), *X-Ray Optics and Microanalysis*, Proceedings. AIP Conference Proceedings. Amer. Inst. Physics, Melville, pp. 181-187.
- Schäfer, T., Michel, P. and Claret, F., (2009a). The application of STXM and μ FT-IR to characterize sedimentary organic matter in the Opalinus clay. *Journal of Physics: Conference Series*, **186**, 012095.
- Schäfer, T. et al., (2009b). Radiation sensitivity of natural organic matter: Clay mineral association effects in the Callovo-Oxfordian argillite. *Journal of Electron Spectroscopy and Related Phenomena* **170**, 49-56.

- Schäfer, T. et al., (2005a). Origin and mobility of fulvic acids in the Gorleben aquifer system: implications from isotopic data and carbon/sulfur XANES. *Organic Geochemistry*, 36(4), 567-582.
- Schäfer, T. et al., (2005b). Source identification and characterization of humic and fulvic acids from Oxfordian argillite and Opalinus Clay. In: E.A. Ghabbour and J. Davies (Editors), *Humic Substances: Molecular Details and Applications in Land and Water Conservation*. Taylor & Francis, New York, pp. Chapter 4.
- Schild, D., Marquardt, C. M., (2000). *Radiochim. Acta* 88, 587–591.
- Schlepp, L., Landais, P., Elie, M. and Faure, P., (2001). Influence of paleoenvironment and radiolytic alteration on the geochemistry of organic matter from Autunian shales of the Lodeve uranium deposit, France. *Bulletin De La Societe Geologique De France*, 172(1), 99-109.
- Schmeide, K., Pompe, S., Bubner, M., Heise, K.H., Bernhard, G., Nitsche, H. (2000). Uranium(VI) sorption onto phyllite and selected minerals in the presence of humic acid. *Radiochim. Acta* 88 (9-11), 723-728.
- Schmeide, K., Reich, T., Sachs, S., Brendler, V., Heise, K. H., Bernhard, G., (2005). Neptunium(IV) complexation by humic substances studied by X-ray absorption fine structure spectroscopy, *Radiochim. Acta* 93, 187–196.
- Seok, Y.J., Yang, K.S., Kang, S.O., (1995). *A simple spectrophotometric determination of dissociation constants of organic compounds*, *Analytica Chimica Acta*, 306, 351-356.
- Silva, R. J., Nitsche, H., (1995). Actinide Environmental Chemistry, *Radiochim. Acta* 70–71, 377.
- Skerencak, A., Panak, P.J., Hauser, W., Neck, V., Klenze, R., Lindqvist-Reis, P., Fanghänel, Th., (2009). *TRLFS study on the complexation of Cm(III) with nitrate in the temperature range from 5 to 200°C*, *Radiochim. Acta*, 97, 385-393.
- Srinivasan, T.G., Zanonato, P., DiBernardo, P., Bismondo, A., Rao, L., (2006). Complexation of thorium(IV) with malonate at variable temperatures, *J. Alloys Comp.*, 408-412, 1252-1259.
- Stern, E. A., Newville, M., Ravel, B., Yacoby, Y., Haskel, D., (1995). The UWXAFS analysis package: philosophy and details. *Physica B* 208&209, 117.
- Stryer, L., (1978). Fluorescence energy transfer as a spectroscopic ruler. *Ann. Rev. Biochem.* 47, 819-846.
- Stumpf, S., (2004). *Spektroskopische Untersuchungen zu Sorptionsmechanismen von dreiwertigen Actiniden an Feldspäten, Quarz und Ferrihydrit*. Dissertation, Naturwissenschaftlich-Mathematische Gesamtfakultät, Ruprecht-Karls-Universität, Heidelberg.
- Stumpf, T., Fanghänel, T., (2002). A time-resolved laser fluorescence spectroscopy (TRLFS) study of the inter-action of trivalent actinides (Cm(III)) with calcite. *Journal of Colloid and Interface Science* 249(1), 119-122.
- Stumpf, T., Bauer, A., Coppin, F., Fanghänel, T., Kim, J.I., (2002). Inner-sphere, outer-sphere and ternary surface complexes: a TRLFS study of the sorption process of Eu(III) onto smectite and kaolinite. *Radiochim. Acta* 90(6), 345-349.
- Stumpf, T., Bauer, A., Coppin, F., Kim, J.I., (2001). Time-resolved laser fluorescence spectroscopy study of the sorption of Cm(III) onto smectite and kaolinite. *Environmental Science & Technology* 35(18), 3691-3694.
- Takahashi, Y., Murata, M., Kimura, T., (2006). Interaction of Eu(III) ion and non-porous silica: Irreversible sorption of Eu(III) on silica and hydrolysis of silica promoted by Eu(III). *Journal of Alloys and Com-pounds* 408, 1246-1251.
- Takai, K., Takao, S., Scheinost, A.C., Bernhard, G., Henning, C., (2009). Complex formation and molecular structure of neptunyl(VI) and -(V) acetates, *Inorg. Chem.*, 48, 8803-8810.

- Tian, G., Martin, L.R., Rao, L., (2010). Complexation of lactate with neodymium(III) and europium(III) at variable temperatures: studies by potentiometry, microcalorimetry, optical absorption and luminescence spectroscopy, *Inorg. Chem.*, 49, 10598-10605.
- Tipping, E., (1998). Humic ion-binding model VI: An improved description of the interactions of protons and metal ions with humic substances, *Aquat. Geochem.* 4(1), 3-48.
- Tertre, E., Berger, G., Simoni, E., Castet, S., Giffaut, E., Loubet, M., Catalette, H., (2006). Europium retention onto clay minerals from 25 to 150°C: Experimental measurements, spectroscopic features and sorption modelling. *Geochimica Et Cosmochimica Acta* 70(18), 4563-4578
- Vandenbroucke, M. and Largeau, C., (2007). Kerogen origin, evolution and structure. *Organic Geochemistry*, 38(5), 719-833.
- Van Loon, L. R., Eikenberg, J., (2005). A high resolution abrasive method for determining diffusion profiles of sorbing radionuclides in dense argillaceous rocks, *Appl. Rad. Isotops*, 11-21.
- Van Loon, L. R., Soler, J. M., Bradbury, M. H., (2003). Diffusion of HTO, Cl-36(-) and I-125 in opalinus clay samples from Mont Terri - effect of confining pressure, *J. Contam. Hydrol.* 61,73-83.
- Van Loon, L. R., Baeyens, B., Bradbury, M. H. (2005). Diffusion and retention of sodium and strontium in Opalinus clay: Comparison of sorption data from diffusion and batch sorption measurements, and geochemical calculations. *Appl. Geochem.*, 20, 2351–2363.
- Van Olphen, H., (1963), *An introduction to clay colloid chemistry*. New York: Interscience Publishers.
- Vantelon, D., Montarges-Pelletier, E., Michot, L.J., Briois, V., Pelletier, M., Thomas, F., (2003). Iron distribution in the octahedral sheet of dioctahedral smectites. An Fe K-edge X-ray spectroscopy study. *Phys. Chem. Minerals* 30, 44-53.
- Vilas, V.V. et al., (2010). Synthesis and Characterization of the Hybrid Clay-Based Material Montmorillonite–Melanoidin: A Potential Soil Model. *Soil Sci. Soc. Am. J.*, 74(6), 2239-2245.
- Vogel, A.I., *Text-Book of Quantitative Inorganic Analysis*, 3rd ed. John Wiley & Sons, (1961).
- Wersin, P., Hochella, M. F., Persson, P., Redden, G., Leckie, J. O., Harris, D. W., (1994). Interaction between aqueous uranium(VI) and sulfide minerals: spectroscopic evidence for sorption and reduction, *Geochim. Cosmochim. Acta* 58, 2829-2843
- Wimmer, H., (1992). Laser-induzierte optische Spektroskopie zur Speziation von f-Elementen in natürlichen aquatischen Systemen. Untersuchung der Übertragbarkeit von Labordaten auf natürliche Verhältnisse. Dissertation, Institut für Radiochemie, Technische Universität München.
- Wolf, M., Buckau, G., Geyer, S., (2004). Isolation and characterization of new batches of Gohy-573 humic and fulvic acids, internal report, Forschungszentrum Karlsruhe.
- Wood, S.A., (1993). The aqueous geochemistry of the rare-earth elements: Critical stability constants for complexes with simple carboxylic acids at 25°C and 1 bar and their application to nuclear waste management, *Engineering Geology*, 34, 229 - 259..
- Wu, T., Amayri, S., Drebert, J., Van Loon, L. R., Reich, T. (2009). Neptunium(V) sorption and diffusion in Opalinus clay. *Environ. Sci. Technol.* 43, 6567–6571.
- Zalupski, P.R., Nash, K.L., Martin, L.R., (2010). Thermodynamic features of the complexation of neodymium(III) and americium(III) by lactate in trifluoromethanesulfonate media, *J. Sol. Chem.* 39, 1213-1229.
- Zeh, P., Kim, J. I., Marquardt, C. M., Artinger, R., (1999). The Reduction of Np(V) in Groundwater Rich in Humic Substances, *Radiochim. Acta* 87, 23-28.
- Zuo, R., Teng, Y., Wang, J., and Hu, Q., (2010). Factors influencing plutonium sorption in shale media. *Radiochim. Acta* 98, 27-34.

12 List of Figures

Figure 2-1: REM images of OPA clay. In the image on the left a round calcite crystal is surrounded by flaky clay minerals. In the right image a pyrite conglomerate can be seen reformed by diagenesis.....	4
Figure 2-2: REM images of COx clay. In the left image a pyrite conglomerate surrounded by flaky clay minerals (small image: magnification of the cubical pyrite crystals), in the right image rutile crystals with their characteristic columnar habitus.	5
Figure 2-3: Top line, from left to right: back-scattered electron map of part of an ammonite (septa appear as dark lines and camerae as greyish zones), and corresponding Fe, S, and Ca chemical maps (microprobe experiments). Middle left: Ni chemical map. Same location, but increased in size. Enlarged view of the white square at middle right (different experiment). Bottom: Ni (solid line), Ca (dot-dashed line) and Fe (dashed line) quantitative analyses of the line materialized in white on the middle right figure. Figure taken from (Grangeon et al., 2011, in review).....	9
Figure 2-4: SEM measurements and quantitative results on extracted products from Opalinus Clay	11
Figure 3-1: Gadget for pD measurement in a special quartz cuvette for TRLFS.	17
Figure 3-2: Calibration of the pD value with DCI reference solutions of known D+ concentration.	17
Figure 3-3: Eu(III) sorption on OPA, COx und SWy-2 in dependence of pH illustrated in log R_d (a) and % (b). Experimental conditions: [Eu(III)] = $1 \cdot 10^{-7}$ mol/l, solid to liquid ratio (S/L) = 2 g/l, I = 0,1 mol/l NaClO ₄	22
Figure 3-4: Eu(III) sorption on OPA and modelling as a function of pH. Experimental conditions: [Eu(III)] = $1 \cdot 10^{-7}$ mol/l, S/L = 2 g/l, I = 0,1 mol/l NaClO ₄ . (IEX = Ionexchange, I = Illite, S = Smectite, S = strong sites, W1 = weak sites).....	23
Figure 3-5: Eu(III) sorption on COx and numerical modelling in as a function of pH shown as log R_d (a) and in % (b). Experimental conditions: [Eu(III)] = $1 \cdot 10^{-7}$ mol/l, S/L = 2 g/l, I = 0,1 mol/l NaClO ₄ . (IEX = ion exchange, I = illite, S = smectite, S = strong sites , W1 = weak sites).	24
Figure 3-6: Eu(III) sorption on OPA (a) and COX (b) together with numerical modelling of the total Eu(III) sorption as well as sorption on illite and montmorillonite as function of pH. Experimental conditions: [Eu(III)] = $1 \cdot 10^{-7}$ mol/l, S/L = 2 g/l, I = 0,1 mol/l NaClO ₄	26
Figure 3-7: Numerical modelled aqueous Eu(III) speciation in COx suspension. Conditions: [Eu(III)] = $1 \cdot 10^{-7}$ mol/l, S/L = 2 g/l, thereof 17.3 % calcite, I = 0.1 mol/l NaClO ₄	26

Figure 3-8: Eu(III) sorption on COx and modelling as a function of pH by regarding (dark green line) and disregarding (black line) ternary Clay/Eu³⁺/carbonate surface complexes shown in %. Experimental conditions: [Eu(III)] = 1·10⁻⁷ mol/l, S/L = 2 g/l, thereof 17.3 % calcite, I = 0.1 mol/l NaClO₄. (IEX = Ion exchange, I = illite, S = smectite, S = strong sites, W1 = weak sites)..... 27

Figure 3-9: Experimentally determined Ca²⁺ concentration in the solution of the Eu(III) sorption experiments on COx and OPA as well as the modelled Ca²⁺ and CaCO₃(cr) concentration as a function of pH. The experimental CaCO₃(cr) data were extrapolated from the measured Ca²⁺ values..... 27

Figure 3-10: Eu(III)sorption on mixture of Na-rich montmorillonite (SWy-2) with calcite (80 : 20 wt.%) shown as (a) log *R_d* and (b) in Experimental conditions: [Eu(III)] = 1·10⁻⁷ mol/l, S/L = 2 g/l, I = 0,1 mol/l NaClO₄. (IEX = ion exchange, S = smectite, S = **strong sites**, W1 = **weak sites**). The dotted line corresponds to the upper limit log *R_d* due to the detection limit of the ICP-MS for Eu(III) analysis. 28

Figure 3-11: Eu(III)sorption on mixture of Na-rich montmorillonite (SWy-2) with calcite (80 : 20 wt.%) and modelling as a function of the pH value regarding (blue line) and disregarding (black line) ternary clay/Eu³⁺/carbonate surface complexes shown in %. Experimental conditions: [Eu(III)] = 1·10⁻⁷ mol/l, S/L = 2 g/l, I = 0,1 mol/l NaClO₄. (IEX = ion exchange, S = smectite, S = **strong sites**, W1 = **weak sites**)..... 29

Figure 3-12: Cm(III) fluorescence emission spectra in suspension of Na-rich montmorillonite (SWy-2) and calcite mixtures (80 : 20 wt.-%) as a function of pH normalised to identical peak area. Experimental conditions: [Cm(III)] = 2·10⁻⁷ mol/l, S/L = 0,3 g/l, I = 0,1 mol/l NaClO₄. 30

Figure 3-13: Cm(III) fluorescence emission spectra of [Cm³⁺] = 8.9·10⁻⁸ mol/l in aqueous calcite suspension (pH ~8, S/L = 1 g/l, I = 0.1 mol/l NaClO₄ according to (Stumpf and Fanghänel, 2002)) and of [Cm³⁺] = 2·10⁻⁷ mol/l in clay / calcite suspension (pH 12.02, S/L = 0.3 g/l, I = 0.1 mol/l NaClO₄; along the lines of the Cm(III) sorption complex 3 in (Rabung et al., 2005)) after contact times of 48 h and several months..... 31

Figure 3-14: Distribution of surface species of Cm(III) on a mixture of Na-rich montmorillonite (SWy-2) and calcite (80 : 20 wt.-%). Experimental conditions: [Cm(III)] = 2·10⁻⁷ mol/l, S/L = 0.3 g/l, I = 0.1 mol/l NaClO₄. (More details in Hartmann 2010)..... 32

Figure 3-15: Sorption of neptunium on OPA/COx in pore water as a function of solid to liquid ratio (S/L), I = 0.1 M NaCl, [Np(V)] = 3x10⁻⁷ M, contact time= 6 weeks and 4 months..... 37

Figure 3-16: Distribution coefficient (K_d) for the sorption of Np on OPA/COx in pore water as a function of neptunium concentration, I= 0.1 M NaCl, [Np(V)] = 3x10⁻⁷ mol/L, contact time= 6 weeks..... 38

Figure 3-17: Comparison of experimental and modelling sorption studies of Np on OPA (top) and COx (bottom) clay minerals as a function of solid to liquid ratio (S/L), pH 7.6 and 7,2, I= 0.1 M NaCl, [Np(V)] = 3×10^{-7} mol/L, contact time= 6 weeks.....	39
Figure 3-18: Interaction of plutonium with OPA and COx in pore water as a function of solid to liquid ratio (S/L), I= 0.1 M NaCl, [Pu(V)] = 3×10^{-7} M, contact time= 6 weeks	41
Figure 3-19: Sorption experiments of Pu-238 on Opalinus Clay. The filled pattern indicates the pH region of the diffusion experiments.....	42
Figure 3-20: Batch sorption data of Pu(IV) sorption on Opalinus clay after 12h contact time and one year contact time showing the increase in Kd values observed. For comparison data on the Callovo-Oxfordian argillite after 74 days contact time [Latrille et al., 2006], on Triassic clay from Šaltiškiiai and Chinese shale rock are inserted.	43
Figure 3-21: Sorption of AHA on SWy-2 as a function of pH in the sorption experiments of Eu(III) and U(VI) (not shown in this report) with AHA (2 g/l SWy-2, 10 mg/l AHA) and with AHA and calcite (1,6 g/l SWy-2, 0,4 g/l calcite, 10 mg/l AHA). [Eu(III)] bzw. [U(VI)] = 1×10^{-7} mol/L, I = 0,1 mol/L NaClO ₄	45
Figure 3-22: Eu(III) sorption on Na-rich montmorillonit (SWy-2) without and with Aldrich humic acid (AHA, 10 mg/l) and/or calcite (Clay : calcite = 80 : 20 wt-%) and numerical modelling of the sorption on SWy-2 (dark green) and SWy-2/calcite by considering ternary clay/Eu ³⁺ carbonate surface complexes (blue) in %. [Eu(III)] = 1×10^{-7} mol/L, S/L = 2 g/L, I = 0,1 mol/L NaClO ₄	45
Figure 3-23: Eu(III)-Sorption an Na-reichem Montmorillonit (SWy-2) mit Huminsäure (10 mg/l) und (b) an Na-reichem Montmorillonit (SWy-2) mit Huminsäure (10 mg/l) und Calcit (Ton : Calcit = 80 : 20 Gew.-%) sowie Modellrechnungen in Abhängigkeit vom pH-Wert mit Berücksichtigung ternärer Ton/Eu ³⁺ /Carbonat-Oberflächenkomplexe dargestellt in %. Außerdem ist jeweils der Fit der experimentell ermittelten HS-Sorption an SWy-2 abgebildet. Spezies 1 bis 5 (a) bzw. 7 (b) sind Eu(III)-Oberflächenkomplexe, während die Konzentration der beiden Eu(III)-Humatkomplexe in Lösung dargestellt ist. Experimentelle Bedingungen: [Eu(III)] = $1 \cdot 10^{-7}$ mol/l, Feststoff zu Lösungsverhältnis = 2 g/l, I = 0,1 mol/l NaClO ₄ . (IEX = Ionenaustausch (= KAK), S = Smectit, S = strong sites , W1 = weak sites). Annahmen für Modellrechnungen siehe Kapitel 3.3.	46
Figure 3-24: Displacement of outer-sphere sorbed Cm ³⁺ by three Na ⁺ (a: montmorillonite, b: illite) at increasing ionic strengths resulting in increased Cm ³⁺ ion concentrations in solution.	48
Figure 3-25: Cm(III) fluorescence emission spectra of various clay and Al ₂ O ₃ suspensions (a) in H ₂ O ($2 \cdot 10^{-7}$ mol/L Cm(III), 0.3 g/L, 0.01 mol/L NaCl) at pH 4 to 4.19. The spectra for Cm ³⁺ (aq) was measured in HClO ₄ at pH 1. (b) in D ₂ O ($2 \cdot 10^{-7}$ mol/l Cm(III), 0.3 g/l, 0.01 mol/l NaCl) at pD 3.54 bis 4.2. The spectra for Cm ³⁺ (aq) was measured in 0.01 mol/l NaCl in D ₂ O at pD 3.75.	50

Figure 3-26: Cm(III) fluorescence emission lifetimes of various clay and Al ₂ O ₃ suspensions in H ₂ O (2·10 ⁻⁷ mol/L Cm(III), 0.3 g/L, 0.01 mol/L NaCl) at pH 4 to 4.19. The lifetime for Cm ³⁺ (aq) was measured in HClO ₄ at pH 1. The lifetime of the montmorillonites show a mono-exponential decay.	51
Figure 3-27: Cm(III) fluorescence emission spectra of various clay and Al ₂ O ₃ suspensions in D ₂ O (2·10 ⁻⁷ mol/l Cm(III), 0.3 g/l, 0.01 mol/l NaCl) at pD 3.54 bis 4.2. The lifetime for Cm ³⁺ (aq) was measured in 0.01 mol/l NaCl in D ₂ O at pD 3.75.	52
Figure 3-28: Bi-exponentiell decay of the fluorescence emission lifetime of Cm(III) in IdP-2 suspension in H ₂ O (2·10 ⁻⁷ mol/l Cm(III), 0.3 g/l, 0.01 mol/l NaCl) at pH 4.02. For comparison the mono-exponential decay of the Cm ³⁺ (aq) lifetime in HClO ₄ at pH 1 was shown.	53
Figure 3-29: Plot of the Cm(III) fluorescence emission lifetime as a function of Fe content of the various used clays as Stern-Volmer-Plot (jeweils 2·10 ⁻⁷ mol/l Cm(III), 0.3 g/l, 0.01 mol/l NaCl). Measurements (a) in various montmorillonite and illite suspensions in H ₂ O (pH values see Figure 3-25(a) and (b) in D ₂ O (pH values see Figure 3-25(b)).....	55
Figure 3-30: (a) Intensities of fluorescence emission of 2·10 ⁻⁷ mol/l Cm(III) in aqueous SWy-1 suspensions (0.3 g/l) at pH 4.16 and different ionic strengths. The fluorescence emission spectra were taken from lifetime measurements (1 μs delay, grating 300 lines/mm). In (b) the amounts of SWY-1 sorbed Cm(III) are shown calculated from differences in fluorescence emission intensities of emission spectra recorded at different ionic strengths.	58
Figure 3-31: Cm (III) lifetimes in aqueous SWy-1 suspension (2·10 ⁻⁷ mol/L Cm (III), 0.3 g/l) at pH 4.16 and various ionic strengths (plotted arbitrarily for clarity). The time dependence of the fluorescence emission shows a mono-exponential decay at low and high ionic strength and a bi-exponential decay at intermediate ionic strengths.	60
Figure 3-32: Cm(III) outer-sphere complexation in H ₂ O on SWy-1 at pH 4.16, Milos at pH 3.97 and IdP-2 at pH 4.02 as a function of ionic strength (2·10 ⁻⁷ mol/l Cm(III), 0.3 g/l).....	62
Figure 3-33: Cm(III) life time in clay suspensions of synthetic Na-montmorillonite NaMont _s in D ₂ O (2·10 ⁻⁷ mol/l Cm(III), 0.3 g/l) at pD 4.12 and various ionic strengths (plotted arbitrarily for clarity). The fluorescence emission shows a bi-exponential decay (τ _{long} = Cm(III) aquo ion , τ _{short} = Cm(III) outer-sphere complex).....	63
Figure 3-34: Cm(III) outer-sphere complexation in D ₂ O on SWy-1 at pD 3.99, Milos at pD 3.76 and NaMont _s at pD 4.12 as a function of ionic strength (2·10 ⁻⁷ mol/l Cm(III), 0.3 g/l) ..	63
Figure 3-35: Comparison of modelled and experimental results for Cm (III) outer-sphere complex formation on SWy-1 in H ₂ O by TRFLS at pH 4.16 (experiment A) or pH 4.07 (experiment B) as a function of ion strength (2·10 ⁻⁷ mol/l Cm(III), 0,3 g/l).....	64
Figure 3-36 Comparison of modelled and experimental results for Cm (III) outer-sphere complex formation on Milos montmorillonite in H ₂ O at pH 3.97 as a function of ion strength (2·10 ⁻⁷ mol/l Cm(III), 0,3 g/l).....	65

Figure 3-37 Comparison of modelled and experimental results for Cm (III) outer-sphere complex formation on synthetischem Na-montmorillonite NaMont _s in D ₂ O at pD 4.12 as a function of ion strength ($2 \cdot 10^{-7}$ mol/l Cm(III), 0,3 g/l). Assumptions for modelling see in the text.....	65
Figure 3-38: Comparison of modelled and experimental results for Cm (III) outer-sphere complex formation on Milos and STx-1 at pD 3.76 and pD 4.01 in D ₂ O as a function of ion strength ($2 \cdot 10^{-7}$ mol/l Cm(III), 0,3 g/l). Assumptions for modelling see in the text.	66
Figure 3-39: Comparison of modelled (with and without considering other competing cations) and experimental results for Cm (III) outer-sphere complex formation on IdP-2 in H ₂ O by TRLFS at pH 4.02 as a function of ion strength ($2 \cdot 10^{-7}$ mol/l Cm(III), 0,3 g/l). Competing cations: $6.09 \cdot 10^{-5}$ mol/l, Al ³⁺ and $2.49 \cdot 10^{-5}$ mol/l Ca ²⁺ /Mg ²⁺	67
Figure 3-40: Comparison of modelled and experimental results of batch experiments on Eu(III) outer-sphere complex formation on NaMont _s , SWy-1 and IdP-2 in H ₂ O at pH 3.88 to 4.02 as a function of ionic strength ($2 \cdot 10^{-7}$ mol/l Eu(III), 0.3 g/l). The uncertainty of the method is estimated to be 20 %.....	68
Figure 4-1: Schematic presentation of the INE diffusion cell/autoclave system (SeAS). On the left side the autoclave with the core holder an the feeding system (two pipes connected via tubes with the peristaltic pumps) is shown. On the right side the diffusion cell is illustrated.	70
Figure 4-2: Evolution of the Pu speciation in the OPA porewater. The sorbed Pu(IV) from the container walls was added to the Pu(IV) in solution.....	73
Figure 4-3: HTO diffusion in the OPA visualized by autoradiography. The blue rectangle represents the OPA core. Red indicates high HTO activity. The cooler the color gets the lower the HTO concentration. It can be seen that the HTO is distributed homogeneously within the OPA core.....	74
Figure 4-4: Evolution of the solution ²³⁸ Pu concentration in the diffusion experiment as a function of time.....	75
Figure 4-5: In and out diffusion experiment with ²³⁸ Pu in a Bure clay (PAC 1002/K70; 13.47 – 13.61 m depth). The initial concentration of Pu in the porewater was $7.8 \cdot 10^{-9}$ mol/L.	76
Figure 4-6: Two different diffusion profiles measured for OPA2-SCAS3 with autoradiography. The filled pattern indicates the clay sample. The dotted line indicates the background radiation from the Opalinus clay. The different colors represent different concentrations. Red indicates the highest and the grey color the lowest concentration.	77
Figure 4-7: Photographs of the samples studied embedded in acrylic (designated P15 and P31) and their corresponding radiographic images.	80
Figure 4-8: Distribution maps for the elements indicated in a 800 x 760 μm ² section (20 × 20 μm ² step size), recorded near the surface of sample P15.	81

Figure 4-9: Distribution maps for K, Ca, Ti, Fe, and U in a 400 μm x 400 μm section (10 x 10 μm step size, 1s counting time), recorded under the surface of the sample 31 area marked in the microscope image at far right. RGB overlay image for regions of highest Ti, Fe, and U concentrations is shown.	81
Figure 4-10: Left: U distribution for a 2000 x 1000 μm^2 section (30 x 30 μm^2 step size) recorded at the INE-Beamline at the surface of sample 15. The normalized U $L\alpha$ intensity scale bar is indicated. Right: U $L3$ μ -XANES recorded at four independent areas with high U $L\alpha$ intensity.	82
Figure 4-11: U $L3$ μ -XANES recorded at U hot spots of sample 15 at Beamline L (symbols) and compared to two U(IV) and U(VI) reference spectra (bottom).....	82
Figure 4-12: U $L3$ k^2 -weighted EXAFS ($\chi(k)$; left bottom), Fourier-filtered data and best fit results (left top) and corresponding k^2 -weighted Fourier transform (FT) data (right) plotted with best fit results. Experimental data = lines. Fit curves = symbols.....	83
Figure 4-13: STXM PCA and cluster analysis of sample 15. (left) Distribution of organic functionality with two distinguishable clusters found using PCA and cluster analysis. (right) distribution of iron absorption. The scale bar is 10 μm . As the Fe L-edge region is slightly rotated counter-clockwise numbers are inserted for orientation.	83
Figure 4-14: (left) Average C(1s) XANES of sample 15 of the yellow and red areas indicated in Figure 8 and (right) average Fe L-edge spectra marked in blue and black.....	84
Figure 4-15: (upper row from left to right) STXM absorption image at 290eV and carbon distribution map; (lower row from left to right) potassium and iron distribution maps taken from XANES ratio images (sample 31). High color intensity indicates high content of selected element. The scale bar represents 10 μm	85
Figure 4-16: (left) Average C(1s) XANES of sample 31 fracture infill and the mineral associated organics. The mineral associated organics are clearly linked to potassium containing phases as indicated by the L-edges at 297 and 300eV. (right) Average Fe L-edge spectra from areas marked in red in Figure 11.....	85
Figure 4-17: (upper left) Visible light microscope (VLM) image of the microtome sample 15 studied and (lower left) μ -FTIR spectrum of the spot marked by the cross line in the VLM image. (right) Maps of organic functional group distributions extracted from μ -FTIR data: alcohols (\square OH; 3600-3100 cm^{-1}), aliphatics (\square CHali; 3000-2800 cm^{-1}) and aromatics (\square C=C; 1750-1500 cm^{-1}), as well as OH vibrations of clay minerals ('OH' 3720-3680 cm^{-1}).	86
Figure 5-1: Absorption spectra of Np in supernatant solution after ultrafiltration from suspension solution of clay rocks, contact time = 1 week, S/L = 50, NaCl = 0.1 M.	88

Figure 5-2: Electropherogram of an 30% Np(V) / 70% Np(IV) reference solution characterized by CE-ICP-MS, [Np]= 3×10^{-7} M, 0.01 M HClO ₄ , separation in 1 M acetate buffer system, at a potential of 20 kV.	90
Figure 5-3: Electropherogram of Np-COx clay filtrate (aliquot) solution, [Np] _{initial} = 2×10^{-8} M, 0.1 M NaCl, S/L = 20, contact time=7 months, CE separation with 1 M acetate buffer system at 30 kV.	90
Figure 5-4: Np L3-XANES spectra of Np speciation in clay rocks (OPA, COx), [Np] = 3×10^{-4} M, 0.1 M NaCl, S/L = 50 , kinetic = 1 week, sample= filtrate suspension.	92
Figure 5-5: Pu L3-XANES spectra of Pu speciation in clay rocks (OPA, COx), [Pu] = 3×10^{-4} M, 0.1 M NaCl, S/L = 50, kinetic = 1 week, sample= filtrate suspension.	93
Figure 5-6: Pu/Np LIII-edge k ³ -weighted of EXAFS spectra and corresponding Fourier transforms (upper: Pu/Cox and Pu/OPA sample, lower: Np/Cox and Np/OPA sample), contact time: 1 week.	95
Figure 5-7: Np 4f _{7/2} spectrum, Al K α mono x-ray excitation, charges referenced C1s (CxHy): 284.8 eV. Wet Paste: Opalinus and COx clay, Np(V) 4×10^{-4} M, 7 days contact time.	98
Figure 5-8: Pu 4f _{7/2} spectrum, Al K α mono x-ray excitation, charges referenced C1s (CxHy): 284.8 eV. Wet Paste: Opalinus clay + Pu(V) 3×10^{-4} M, 7d contact time.	99
Figure 5-9: Eh-pH Diagram of neptunium OPA/COx system in pore water and speciation calculation are performed using Geochemist Workbench, thermochemical database, [Np] _{total} = 1×10^{-8} M, I= 0.1 NaCl, T= 25 0C	100
Figure 5-10: Eh-pH Diagram of plutonim OPA/COx system in pore water and speciation calculation are performed using Geochemist Workbench, thermochemical database, [Pu] _{total} = 1×10^{-8} M, I= 0.1 NaCl, T= 25 0C	101
Figure 5-11: Experimental setup for the optimisation of the sample transfer of CE-ICP-MS.	103
Figure 5-12: Sketch and photo of the CE-DAD-ICP-MS.	104
Figure 5-13: Separation of free Ho, free humic acid and Ho humate complexes by the CE-DAD-ICP-MS coupling (250 mg/L humic acid, 0,75 mg/L Ho, electrolyte 1 M AcOH, -25 kV, 250 mbar, FS capillary length 80(63) cm, 50 μ m ID).	104
Figure 5-14: Separation of uranium species by CE-ICP-MS. (separation conditions see Table 5-5).	105
Figure 5-15: Simulation of concentration and conductivity vs. position in capillary. Right graph: Pu in nitric acid electrolyte: 1 M AcOH, left graph Pu in nitric acid 1:1 diluted with electrolyte. In each graph left signal: injection zone, right signal: resulting peak in electropherogram.	106

Figure 6-1: Characterisation of kerogen extracted from natural clay rock.	107
Figure 6-2: TRLFS of Cm(III) interaction with kerogen extracted from OPA.....	108
Figure 6-3: UV/Vis absorption spectra of Np(IV)-FA complexation between pH 1 and 3 and [Np(IV)] = 5E-05 M, [FA]= 100-1000 mg/L.....	113
Figure 6-4: UV-Vis absorption spectra of Np(IV)-fulvate complex at 968 nm with varying FA concentration and constant Np(IV) concentration. [Np(IV)] = 3E-05 M, [FA]= 0-500 mg/L.	114
Figure 6-5: Illustration of the deconvolution spectra of the total absorption spectrum in to two single absorption bands for the free Np(IV) and Np(IV)FA(I). The peak maximums are found at 960 and 968 nm.	114
Figure 6-6: XANES of Np(IV) fulvate samples prepared in various ways (a, b: preparation (II); c, d: preparation (I); e, f, g: preparation (III). Spectra b, d, g: pH 1.0; Spectra a, c, f: pH 3.0; Spectra e: pH 4.5. A detail about the preparation is given in the text on page 110.	116
Figure 6-7: Np LIII- k3-weighted EXAFS spectra of Np(IV)-FA complex and corresponding Fourier transforms (upper: pH 1, middle: pH 3, lower: pH 4; preparation (III)).....	117
Figure 6-8: Schematic representation of the Np(IV)-FA complex coordination structure according to EXAFS data. Explanation is found in the text!	118
Figure 6-9: XPS spectra of Np(IV) fulvate samples prepared in various ways. Description of the preparation (I), (II), and (III) is given in the text. Np(IV) fulvate was measured as wet paste (precipitate + residual solution).	120
Figure 6-10: Np 4f lines and their satellites of Np(IV)-fulvates and XPS measurement performed after a reaction time of 1 days (red color line) and after 3 months of reaction (blue color line) at pH 1 and a reaction time of 14 days (olive color line) and after 3 months of reaction (green color line) at pH 3, acquired using monochromatic Al K α X-rays.	120
Figure 6-11: The chemical shifts of Np 4f _{7/2} spectra for the Np(III), Np(IV) and Np(V) complexes.....	121
Figure 6-12: Determination of the loading capacity (LC) of fulvic acid for Np(IV) complexation at pH 1.0 and 1.5 from the experimental data according to the following expression:.....	122
Figure 6-13: Complexation constant (Log β) for the tetravalent actinide (Th(IV), U(IV), Np(IV), and Pu(IV)) and humic substances with varying pH values.....	123
Figure 7-1: Py-GC-MS chromatograms obtained on the polymerisation products after 1 month at 80°C under wet/drying cycles.(A) Ca-smectite (smectite), Glucose (0.05mol.L-1) + Glycine (0.05mol.L-1) ; (B) Ca-smectite (Ibeco), catchol (0.05mol.L-1).....	125

Figure 7-2: TEM images obtained on the polymerisation products after 1 month at 80°C under wet/drying cycles. (A) Ca-smectite (<2µm smectite of Ibeco bentonite), (B) Ca-smectite (<2µm of Ibeco bentonite), glucose + glycine (0.05mol.L-1).....	126
Figure 7-3: Schematic Van Krevelen diagram of the O/C vs. H/C trend observed in the natural system in comparison to the one obtained by different temperature adjustments in confined and open pyrolysis (Elie and Landais, 1997).	127
Figure 7-4: Carbon edge STXM investigations of Ca-exchanged bentonite reacted with glucose+glycine (GG) for 30 days at 70°C including wetting/drying cycles and treated with confined pyrolysis at 250°C for 24 hours. A: Absorption image at 280 eV below the carbon edge; B: Ratio image (light grey values indicate high concentration) showing the distribution of C=C functionality; C: Ratio image showing the distribution of carboxyl-type groups; D: Comparison of spectra obtained for the smectite associated natural organic matter (OM) in the Callovo-Oxfordian formation, the reaction products of GG polymerization and the polymerized samples after pyrolysis.	127
Figure 7-5: Van Krevelen diagram for natural kerogen samples (Deniau et al., 2008), additional inserted is the Toarcien kerogen (Vandenbroucke and Largeau, 2007/Vandenbroucke and Largeau, 2007). The O/C and H/C atomic ratios of the series of “D-glucose, glycine and Ca Ibeco bentonite after confined pyrolysis at 160, 180, 200 and 250°C are represented by the red star. For comparison, a figure of showing different organic materials is added (Preston and Schmidt, 2006).	128
Figure 8-1: Molecular structures of formic-, acetic-, propionic-, iso-butyric-, lactic-, phthalic-, and oxalic acid.....	130
Figure 8-2: Molecular structures of malonic-, succinic-, glutaric- and oxydiacetic acid.....	132
Figure 9-1: Bromocresol green in its acid (left) and base (right) form	138
Figure 9-2: Absorption Spectra of bromocresol green at pH = 2, 4 and 11 (T = 25°C) b) exemplary peak deconvolution at T = 25°C.....	139
Figure 9-3: a) conditional pK'a(T) values of bromocresol green (valid for Im = 0.2 m) b) respective thermodynamic pK0a(T) values (valid for Im = 0 m)	140
Figure 9-4: a) pH(T) values of four sample solutions (see Table 9-2), b) pK0a(T) values of propionate.....	141
Figure 9-5: Bromophenol blue in its acid (left) and base (right) form.....	141
Figure 9-6: a) Absorption Spectra of bromophenol blue at pH _{25°C} = 2, 4 and 11 (T = 25°C) b) peak deconvolution of the spectrum at pH _{25°C} = 4 and T = 25°C	142
Figure 9-7: a) conditional pK'a(T) of bromophenol blue (valid for Im = 0.2 m) b) thermodynamic pK0a(T) of bromophenol blue (valid for Im = 0 m)	142

Figure 9-8: a) pH(T) values of three sample solutions (see **Table 9-3**) b) pK0a(T) values of lactate 143

13 List of Tables

Table 2-1: Samples from the Mont Terri site delivered by BGR and used for the project.	3
Table 2-2: OPA, COx, natural and synthetic clay minerals, and other materials used for sorption studies.....	4
Table 2-3: Average mineralogical composition and physicochemical characteristics of OPA clay from Benken/Schweiz [Nagra2002] and Callovo-Oxfordian clay COx from Bure/France (clay particle size fraction (< 2 μm) and organic carbon: [Claret et al., 2002].....	6
Table 2-4: X-Ray fluorescence analysis (XRF) of the Callovo- Oxfordian sample (PAC1001Dif1749) and the Opalinus Clay sample (OPA/BHE-24-2).....	7
Table 2-5: Cation exchange capacity (CEC) as determined by the Cohex method for the Callovo- Oxfordian (COx) sample (PAC1001Dif1749) and the Opalinus Clay (OPA) sample (OPA/BHE-24-2).	8
Table 3-1: Overview of experimental conditions of all batch experiments performed for the sorption experiments of Cm(III) and U(VI) (at 298 K). The Cm(III) / clay mineral- Outersphere complexation were investigated in experiment 15 to 18	14
Table 3-2: Summary of the experimental conditions of the performed TRLFS measurements (1 to 29 at 298 K).	16
Table 3-3: Parameters for calculations of Eu(III)/U(VI) sorption onto the different solids. In all cases the Davies Equation was used for activity corrections [Davies, 1962].	20
Table 3-4: Formation constants for aqueous Eu(III) species that were considered in the model calculation (β^0 constants were corrected to $I = 0$). Formation constants of Am(III) species from [Guillaumont et al., 2003] were taken as analogue values for Eu(III).	21
Table 3-5: Formation constants of Eu(III)-, U(VI)- and other minerals considered in the model calculation. Formation constants of Am(III) species from [Guillaumont et al., 2003] were taken as analogue values for Eu(III).	21
Table 3-6: Parameter for modelling of Eu(III) and U(VI) binding on humic acid (Milne et al., 2001; Milne et al., 2003). $Q_{max1/2}$: number of sites with low and high affinity, $p1/2$: heterogeneity parameter $\beta1/2$: formation constants of Eu(III) and U(VI) humate complexes, $n1/2$: non-ideality parameter.	21
Table 3-7: K_d values and percentage sorption of Np and Pu on OPA (pH 7.6) in Pore water at 3×10^{-7} M.	37
Table 3-8: K_d values and percentage sorption of Np and Pu on COx (pH 7.2) in pore water at 3×10^{-7} M.	37
Table 3-9: $\log K_d$ values for plutonium on Callovo–Oxfordian clay rock	41

Table 3-10: Physico-chemical properties of γ -Alumina (Al_2O_3), purified Na-montmorillonites (SWy-1, Milos und STx-1) and the synthetic Na-montmorillonit (NaMont _s) as well as Na-illite (IdP-2).	49
Table 3-11. Quenching rates by energy transfer to iron that corresponds to the reciprocal value of the short lifetime in D_2O and the H_2O influence for comparison of quenching rates in the D_2O - and H_2O system.	56
Table 3-12. Ionic radii of cations that might occur in tetrahedral or octahedral layers of clay minerals.	57
Table 3-13: Concentrations of cations Al^{3+} , Ca^{2+} und Mg^{2+} in aqueous clay suspension due to partial dissolution of the respective clay at pH ~4. Black: elements of batch experiments; blue: elements of the TRLFS experiments.	67
Table 4-1: Experimental details of the Pu diffusion experiments. D_e is the effective diffusion coefficient.	72
Table 5-1: Energy positions of the XANES first inflection point and white line maximum positions for reference species and sorption samples. All values are given in eV (estimated calibration error $\Delta E \pm 0.5$ -1 eV).	92
Table 5-2: Energy positions of the Np L3-XANES first inflection point and white line maximum positions for references and samples from campaign August 2011. All values are given in eV (estimated calibration error $\Delta E \pm 0.5$ eV).	94
Table 5-3: Metric parameter from R-space fits to Np L3 edge. EXAFS fit parameters: EXAFS fit parameters: O1 axial oxygen backscatterer, O2 equatorial oxygen backscatterer, (f) indicates fixed parameter, S02 fixed at 1.0	96
Table 5-4: Metric parameter from R-space fits to Pu L3 edge. EXAFS fit parameters: O1 1st oxygen backscatterer (bridging and terminal hydroxyl groups), O2 2nd oxygen backscatterer (terminal water), (g) indicates global parameter for both oxygen shells, S02 fixed at 1.0	97
Table 5-5: Separation conditions for uranium species with CE-ICP-MS.	105
Table 5-6: Validation of the uranium species separation.	105
Table 6-1: Elemental composition of kerogen extracted from OPA. More than 78 wt.% are organic matter, but a high content of inorganic iron and sulfur compounds remain in the fraction.	108
Table 6-2: Elemental composition of the new prepared Gohy-573 FA and HA. Summarized are the mean values of triplicate analysis, carried out by Analytische Laboratorien, Lindlar, Germany, together with the standard deviation. For comparison, also the elemental compositions of the former charges are shown (Gohy-573 FA (one analysis) and the mean value for Gohy-573 HA I and II (see, Buckau 1991)). The data are normalized to a total CHNOS content of 100 %.	110

Table 6-3: Results from the fit EXAFS structural parameters of Np(IV) complexes with fulvic acid	116
Table 6-4: Results from the fit EXAFS structural parameters of Np(IV) –FA with varying contact times.....	119
Table 6-5: Complexation constant of the NpFA(IV) complex at pH 1 and 1.5 and ionic strength of 0.1 M NaCl including the parameter degree of deprotonation α_H and the loading capacity LC.	123
Table 8-1: $\log \beta_n$ values for the formation of Ln(III) and An(III) acetate/propionate/isobutyrate and lactate complexes.	130
Table 8-2: $\log \beta'_n$ for the complexation of Th(IV) with acetate, malonate, succinate, glutarate and oxydiacetate	132
Table 8-3: $\log \beta'_1$ for the complexation of Np(V) with acetate, oxalate, lactate and α -hydroxy-isobutyrate	133
Table 8-4: $\log \beta'_1$ for the complexation of U(VI) with acetate, oxalate, malonate, oxydiacetate and thio-diacetate (T = 25°C)	134
Table 9-1 Composition of the used reference solutions and their pH(T) from 25 to 90°C....	137
Table 9-2: Samples for the spectroscopic pH measurement with bromocresol green	140
Table 9-3: Samples for the spectroscopic pH measurement using bromophenol blue	143

Final Report

Project¹:

“Interaction and transport of actinides in natural clay systems in the presence of humic substances and clay organic matter”

Subproject²:

“Spectroscopic investigations for an improved process understanding in binary and ternary Systems of humic substances – clay – lanthanides: thermodynamic and kinetic parameters”

K. Brennenstuhl, S. Eidner, K. Jahn, M.U. Kumke[#], S. Kuke, B. Marmodée, P.A. Primus, and S. Zilm-Gramkow

University of Potsdam, Institute of Chemistry, Physical Chemistry

Karl-Liebknecht-Str. 24-25, 14476 Potsdam-Golm

[#]kumke@uni-potsdam.de

¹Deutscher Titel: Wechselwirkung und Transport von Actiniden im natürlichen Tongestein unter Berücksichtigung von Huminstoffen und Tonorganika

²Deutscher Titel: Spektroskopische Untersuchungen zum erweiterten Prozessverständnis in binären und ternären Huminstoff - Tongestein – Lanthanoid Systemen: Thermodynamische und kinetische Kenngrößen

Das diesem Bericht zugrunde liegende Vorhaben wurde mit Mitteln des Bundesministeriums für Wirtschaft und Technologie und dem Förderkennzeichen 02E10216 gefördert. Die Verantwortung für den Inhalt dieser Veröffentlichung liegt bei den Autoren.

Das Forschungsvorhaben war ein Teilprojekt im Forschungsverbund „Wechselwirkung und Transport von Actiniden im natürlichen Tongestein unter Berücksichtigung von Huminstoffen und Tonorganika“ und erfolgte in Kooperation mit folgenden Institutionen:

Forschungszentrum Dresden-Rossendorf, Institut für Radiochemie (FZD-IRC)

Forschungszentrum Karlsruhe, Institut für Nukleare Entsorgung (FZK-INE)

Institut für Interdisziplinäre Isotopenforschung Leipzig (IIF)

Johannes Gutenberg-Universität Mainz, Institut für Kernchemie (UM-IKC)

Universität des Saarlandes, Institut für Anorganische und Analytische Chemie und Radiochemie (UdS-IAARC)

Technische Universität Dresden, Sachgebiet Strahlenschutz, Professur Radiochemie (TUD)

Technische Universität München, Fachgebiet Theoretische Chemie (TUM-TC)

Abstract

Within the project “*Spectroscopic investigations for an improved process understanding in binary and ternary Systems of humic substances – clay – lanthanides: thermodynamic and kinetic parameters*” an in-depth analysis of europium- and terbium-related luminescence was performed using steady-state and time-resolved spectroscopy. With respect to system complexity the full scale from well-defined organic model ligands to highly complex and heterogeneous matrices like natural organic matter (e.g., humic substance) was investigated. Binary as well as ternary systems containing clay minerals were investigated in the temperature range $5\text{ K} < T < 333\text{ K}$ and up to ionic strength $I > 4$.

In high-resolution luminescence experiments at ultra-low temperature STARK level resolved spectra were recorded, which were evaluated with respect to the complex geometry, the binding conditions (e.g., first vs. second coordination sphere influences, mono- vs. bidentate binding), number of water molecules or bond covalency. From the spectra the crystal field strength parameters were extracted. Moreover, due to the outstanding spectral resolution of those measurements it was possible to characterize the equilibrium between eight- and nine-fold coordinated aquo species of Eu(III). This equilibrium was further utilized to monitor even weak influence of counter ions as well as the overall ionic strength of the medium. From species-selective excitation and emission spectra inner- and outer-sphere binding were monitored and shifts in the equilibrium between the two aquo species were measured.

Time-resolved luminescence experiments revealed the importance of ligand-specific quenching contributions to the overall photophysics. Although by organic ligands the influence of OH-related quenching should be reduced with increasing number of organic ligands in the first coordination sphere of the lanthanide (Ln(III)) ion, for a certain group of organic ligands a further reduction in the luminescence decay time was observed. It could be shown that the activation energy connected to this quenching process is very similar for this group of ligands. A prominent member in this group, which showed a particular distinct ligand-specific quenching, is salicylic acid (2HB). Transient absorptions spectroscopy was used to further investigate the molecular processes involved. It was shown that in complexes with Eu(III) the triplet state of 2HB is fully quenched, the same is true for the solvated electron, which is seen for 2HB solutions under moderate laser irradiation. Instead a novel transient absorption signal was found, which was attributed to metal-to-ligand charge transfer transition. This MLCT transient absorption was only seen for metal ions, which were capable of accepting an electron (such as copper). In contrast, Tb(III) did quench the triplet state absorption of 2HB but no novel transient absorptions was observed.

Finally, the interlanthanide resonance energy transfer was used to investigate distances between Ln(III) ions when bound to (natural) polymers as well as to clay mineral surfaces. Using Eu(III) (or Tb(III)) as energy donor and Nd(III) as an acceptor, interionic distance up to 1.2 nm could be addressed, which is – so far – not accessible with other spatial-resolution techniques.

1. Introduction

For the risk assessment of nuclear waste repositories a sound understanding of the fundamental processes defining the fate of radionuclides in the natural environment on a molecular level is indispensable. In this context also novel analytical techniques are required and existing technologies are needed to be further improved to reach the next level in process understanding.

For long term safety handling the speciation of radionuclides in possible underground repositories is of utmost importance for their mobility in case of leakage from the primary technical safety compartment. Depending on the layout of the underground repository the presence of possible reaction partners (molecules in solutions, mineral surfaces, and the combination of both) can significantly affect the speciation and subsequently the mobility as well as bioavailability of the radionuclides. In the near but especially in the far field of the repository humic substances (HS) are key players with respect to speciation of metal ions in general (and of radionuclides in particular). HS are a major component in the aqueous and soil environment. Since these macromolecules are degradation products of plant and animal tissue, the structure of HS depends on the point of their origin. Hence, the exact structure of HS is not known. For the further development in understanding the binding interactions between HS and metal ions a sound approach is the usage of suitable model compounds. Here, small organic compounds containing the major binding motifs of HS are frequently used as proxies for HS. Ligands such as phthalic acid or salicylic acid are often considered as basic units of HS with respect to metal binding. Such small organic compounds are further important because they are major components of the clay-organic matrix and are therefore key players in clay systems with respect to complexation of metal ions.

Lanthanide ions such as terbium (Tb(III)) and europium (Eu(III)) are frequently used as natural analogs for actinides (An) in environmental studies. In addition to a comparable chemical reactivity to An(III), Tb(III) and Eu(III) show an intrinsic luminescence in aqueous solutions. Spectral and time-resolved luminescence data can be used in speciation analysis. The luminescence characteristics of the two ions are dependent on their coordination environment. Especially, Eu(III) is a luminescence probe with outstanding luminescence properties. Spectroscopic parameters such as the decay time τ , the asymmetry ratio r and the spectral position of the ${}^5D_0 \rightarrow {}^7F_0$ -transition can be used for a speciation analysis and consequently.

The interaction between molecules and/or ions happens on distances on a nanometer scale. The measurement of these short distances is a challenging task. A number of methods are available to resolve distances on this distance scale. Very often X-ray based methods are applied. But some of these methods can also be applied to solid state (like X-ray crystal structure analysis) or require special facilities (like synchrotron sources). A different approach is to use visible light as tool. Using light at wavelengths in the visible region eases instrumentation. Light can be absorbed by certain ions and molecules. After the absorption process, the ions are in an excited state. The transition back into the ground state requires losing energy. This can be achieved by radiative or non-radiative processes. One non-

radiative process is the transfer of energy from the excited molecule/ion to a second molecule/ion in the ground state. The efficiency of this energy transfer depends on the distance between the molecules/ions involved.

In the research project molecular processes of lanthanide ions (as natural analogues for actinides, Ln(III)) in binary and ternary systems consisting of organic ligands (covering the full spectrum from small, simple organic ligands via model polymers to complex humic substances) and mineral surfaces were investigated using luminescence spectroscopy as sophisticated analytical tool. Especially time-resolved laser spectroscopy and measurements at ultra-low temperature ($T \sim 5$ K) were applied to elucidate the speciation of Ln(III) and to shed light on the intra- and intermolecular interaction processes on a molecular level. Based on an in depth analysis of the set of different spectroscopic parameters (e.g., ligand field strength parameter, asymmetry ratio, luminescence decay time, interlanthanide energy transfer efficiency) conclusions on the speciation of the Ln(III) ion under specific medium conditions are drawn. Especially, the ionic strength and the influence of the temperature were considered in this context.

2. Experimental details

2.1 General experimental details

As model compounds for binding sites in HS, different (hydroxy)benzoic acids and aliphatic acids were investigated. The relative positions of the hydroxyl- and/or carboxyl group were systematically varied, in order to study the effect of complex formation and of the ligand structure on the luminescence spectra of Eu(III). All reagents were of analytical grade. Cyclohexanecarboxylic acid was obtained from SAFC supply solutions, 2-Hydroxycyclohexanecarboxylic acid was obtained from ABCR GmbH & Co. KG and 2-hydroxybenzoic acid was purchased from VEB Jenapharm. Other chemicals were ordered from Sigma-Aldrich with the highest purity available. As background electrolyte 0.1 M sodium perchlorate solution was applied. All solutions were stored in the dark at room temperature.

From speciation analysis based on stability constants taken from literature it was calculated that only a very minor concentration of the “free” $\text{Eu}_{\text{aq}}^{\text{III}}$ ion is present at a the highest Ln:ligand ratio.

To avoid formation of hydroxyl and carbonate complexes the pH was adjusted to five with sodium hydroxide and hydrochloric acid. Each solution was equilibrated for approximately 10 days prior to the luminescence measurements. In-between measurements, the samples were stored in the dark at room temperature.

2.2 Influence of ionic strength and counter ions

Aqueous Eu(III) samples were prepared from $\text{EuCl}_3 \cdot 6\text{H}_2\text{O}$. Further samples without any chloride ions were made by dissolving Eu_2O_3 in the appropriate amount of 70% HClO_4 ; the

final perchlorate ion concentration was 0.1 M. All samples were prepared in deionized water and contained 0.2 M Eu(III). Two sets of samples with $pH = 2$ and $pH = 5$ were prepared using HCl, $HClO_4$ or NaOH as required. Samples in D_2O were prepared in a glove box using dry $EuCl_3$ and $NaClO_4$. The pD of the solution was also adjusted to 5, using DCl, $DClO_4$ and NaOD. All chemicals were purchased from Aldrich with the highest purity available and used as received.

2.3 Luminescence measurements

(i) *Luminescence measurements at ambient and higher temperature*: Time-resolved laser luminescence spectroscopy measurements were performed using a pulsed Nd-YAG Laser (Spectra Physics) combined with an optical parametric oscillator (*GWU Lasertechnik*). The luminescence emission was detected with an iCCD-camera coupled to a spectrograph (*Andor Technology*). For the Eu(III) complexes the emission spectra were recorded in the spectral range of $575 \text{ nm} < \lambda_{em} < 635 \text{ nm}$, the emission spectra of the Tb(III) complexes were recorded in the range of $475 \text{ nm} < \lambda_{em} < 675 \text{ nm}$. For the measurements at room temperature ($T = 290 \text{ K}$) the excitation wavelength was 394 nm to excite directly the Eu(III) ion according to the electronic ${}^7F_0 \rightarrow {}^5L_6$ -transition. For the investigation of Tb(III) complexes a wavelength of 377 nm was chosen according to the ${}^7F_6 \rightarrow {}^5G_5$ -transition. In the time-gated detection scheme, the initial delay time after the laser flash (δt) was varied between $0.4 \mu\text{s} < \delta t < 30.4 \mu\text{s}$ (depending on the temperature) in order to minimize interference originating from the luminescence of the ${}^5D_1 \rightarrow {}^7F_0$ transition. The time dependence of the Eu(III) and Tb(III) luminescence was analysed using a box car technique. A Eu(III) luminescence spectrum was measured at different δt using an integration time of 50 μs . For a typical emission spectrum at a particular δt , 100 laser pulses were accumulated. To record a full luminescence decay, between 120 and 130 luminescence spectra were measured at increasing δt . The Tb(III) luminescence spectra were recorded in the same way.

In addition, emission spectra and decay times between $278 \text{ K} < T < 338 \text{ K}$ were also recorded using a Fluoromax 4 spectrofluorometer (*HoribaJobinYvon*) in the phosphorescence mode. Here, a pulsed Xe lamp was applied for excitation. Spectra as well as decay measurements were performed in a box car mode (*vide supra*). In order to maintain the desired temperature, a thermostat system was used (*LAUDA, Proline RP 845 C*).

(ii) *Fluorescence line narrowing (FLN) spectroscopy*: For FLN spectroscopy, sample solutions were transferred to quartz tubes (40 mm length x 4 mm o.d. x 2 mm i.d.; volume ca. 100 μL), and sealed with rubber septums. Samples were cooled to $\sim 5 \text{ K}$ in a lab-built sample holder, mounted on a closed-cycle helium refrigerator (SRDK-205 cryostat; Janis Research Company, Wilmington, MA, USA). The samples were excited using a dye laser (LPD 3002; Lambda Physics, Göttingen, Germany) pumped by a XeCl excimer laser (LPX 110i; Lambda Physics, Göttingen, Germany). Coumarin 153 (Radiant Laser Dyes & Accessories GmbH, Wermelskirchen, Germany) was used as laser dye. The laser was operated at 20 Hz with a pulse width of 10 ns. The Eu(III) emission was collected at a 90° angle relative to the

excitation light by two 10 cm F/4 quartz lenses and focused on the entrance slit of a triple monochromator (Spex 1877; Edison, NJ, USA). For detection an intensified charged-coupled device (iCCD) camera (iStar DH720-25U-03; Andor Technologies, Belfast; Northern Ireland) was used in the gated mode. In order to obtain adequate stray light suppression, delay and gate width of the iCCD were set to 1 μs and 10 ms, respectively. The achieved spectral resolution in the emission dimension was 0.1 nm (3 cm^{-1}) in a total spectral detection window of 37 nm. Each emission spectrum was accumulated for 1 s to 5 s, comprising 20 to 100 laser pulses. The excitation wavelength was varied with a scan rate ranging from 0.001 nm/s to 0.05 nm/s, yielding a resolution in the excitation dimension between 0.03 cm^{-1} and 1.5 cm^{-1} . The decay curves were extracted from time series of emission spectra (delay 1 μs , gate width 10 ms) of 200 spectra. For each sample several decay series were recorded, at each excitation wavelength λ_{exc} corresponding to a separate species in the TLS.

2.4 Data analysis

Luminescence decays: In case the luminescence decay curves were monoexponential, they were evaluated according to Eq. (1)

$$y = y_0 + B \cdot \exp\left(-\frac{t}{\tau}\right) \quad (1)$$

y is the measured luminescence intensity at time t after the laser flash, B is the luminescence intensity at $t = 0$, τ is the luminescence decay time, and y_0 accounts for residual background signal.

From the in-depth analysis of the Eu(III) luminescence, especially when recorded at cryogenic conditions, a wealth of information can be obtained:

$^5D_0 \rightarrow ^7F_0$ transition energy: The $^5D_0 \leftarrow ^7F_0$ transition is extremely weak because of parity forbiddance. It gains intensity in cases in which the symmetry of the Eu(III) complex is lowered, for instance due to the formation of non-centrosymmetric complexes or due to vibrational motion of the ligands. For being non-degenerate the $^5D_0 \leftarrow ^7F_0$ transition is a powerful indicator for the presence of different coexisting complexes in a sample. Moreover, its energy is very sensitive to specific parameters characterizing the complex. Two partly contradicting effects determine the energy of the $^5D_0 \leftarrow ^7F_0$ transition: i) the nephelauxetic effect and ii) the splitting of the 7F_1 transition, which is dependent on the crystal field exerted by the ligands.

STARK splitting, crystal field strength parameter and jackstraws plots: The 7F_1 state is further split into three STARK levels ($^7F_{1-1}$, $^7F_{1-2}$, $^7F_{1-3}$) and the effective crystal field can be quantified by the crystal field strength parameter $N_v(B_{2q})$. For weak crystal fields the crystal field strength parameter $N_v(B_{2q})$ can be calculated based on this energy difference:

$$N_v(B_{2q}) = \sqrt{\frac{\pi(2 + \alpha^2)}{0.3}} \Delta E \quad (2)$$

with
$$\alpha = \frac{E_b - E_c}{\Delta E/2}$$

where E_b is the barycentre (mean energy) of the 7F_1 multiplet and E_c is the energy of the central level (${}^7F_{1-2}$). The reduction in inhomogeneous broadening in the FLN spectra enables a precise determination of ΔE (or $N_v(B_{2q})$). A plot of the excitation energy vs. the energy difference ΔE (or the crystal field strength parameter $N_v(B_{2q})$) results in a straight line of which the length, position and slope are characteristic for the particular species (jackstraws plot).

Point symmetry group: Under site-selective excitation conditions the number of STARK levels in the ${}^5D_0 \rightarrow {}^7F_1$ and ${}^5D_0 \rightarrow {}^7F_2$ transitions can be used to determine the point symmetry group of the coordination polyhedron.

Asymmetry ratio r : The integrated intensity of the ${}^5D_0 \rightarrow {}^7F_2$ transition is especially sensitive to the complex symmetry. The more the local complex symmetry deviates from inversion symmetry the more the parity forbiddance is relaxed. In contrast, the integrated ${}^5D_0 \rightarrow {}^7F_1$ emission is not affected and can therefore be used as an internal reference. A change of the “asymmetry ratio r ” (Equation 3) indicates an alteration of the complex symmetry. In general, an increasing deformation of the coordination polyhedron following the exchange of water molecules by other ligands results in a larger r value according to:

$$r = \frac{I({}^5D_0 \rightarrow {}^7F_2)}{I({}^5D_0 \rightarrow {}^7F_1)} \quad (3)$$

The asymmetry ratio r depends on several other parameters, such as i) the polarizability of the ligands, ii) the complex-related concentration of the ligands, and iii) the dielectric constant of the solvent. Nonetheless, for samples containing the same or very similar ligands, investigated under identical experimental conditions, r may be used as a discriminator for different species present in the sample.

Number of water molecules in the first coordination sphere: A major radiationless deactivation pathway of Eu(III) is related to the OH groups present in the first, but also (to a minor extent) in the second coordination sphere of the complex. It has been established that the number of water molecules n_{H_2O} in the first coordination sphere of Eu(III) can be determined from luminescence decay time measurements τ_{obs} . The well-known empirical equations of HORROCKS et al. and KIMURA et al. have been extended to account for additional quenching contributions from other ligands and from OH groups in the second coordination sphere with the terms 0.25 and 0.4 n_{OH} , respectively.

$$n_{H_2O} = 1.2 \left(\frac{1ms}{\tau_{obs}} - 0.58 - 0.25 - n_{OH} \cdot 0.4 \right) \quad (4)$$

This formula was derived at room temperature conditions. Since no influence of temperature on the fluorescence decay time was observed ($\tau_{Eu(H_2O)_9^{3+}} = 100 \pm 10 \mu s$ at 298.15 K and $106 \pm 10 \mu s$ at 4.7 K) it is concluded that the quenching efficiency of OH vibrations is not altered with temperature and thus Equation (4) can also be used at 4.7 K.

2.5 Energy transfer

Non-radiative energy transfer can take place according to processes proposed by Dexter and Förster. The Dexter mechanism – also known as exchange mechanism – happens on relatively short distances as electrons have to be exchanged between these two molecules/ions. This requires an overlap of the orbitals involved. According to Förster's theory a different energy transfer can happen at longer – on the Nanometer to Sub-nanometer region – distances. Here, the energy transfer is based on a dipole-dipole (Coulomb) interaction between the molecules/ions. The efficiency of the energy transfer depends on the overlap between the emission spectrum of the donor and the excitation (absorption) spectrum of the acceptor as well as the distance between donor and acceptor. The donor-acceptor distance, at which the efficiency η reaches 50 percent, is called the Förster distance R_0 . The value of R_0 is given by spectral properties of the donor-acceptor pair according to the following equation (1)

$$R_0 = \sqrt[6]{\frac{9 \ln(10) \kappa^2 \Phi_D J}{128 \pi^3 N_A n^4}} \quad (5)$$

with luminescence quantum yield Φ_D of the donor, Avogadro's number N_A , refractive index n of the surrounding medium, the overlap integral J and the orientation factor κ^2 between the transition dipole moments of the donor and the acceptor. It is given by

$$J = \frac{\int F(\lambda) \epsilon(\lambda) \lambda^4 d\lambda}{\int F(\lambda) d\lambda} \quad (6)$$

Here, $F(\lambda)$ reflects the emission spectrum of the donor, $\epsilon(\lambda)$ is the wavelength dependent extinction coefficient and λ the wavelength. The efficiency of the energy transfer decreases with the sixth power of the distance R between donor and acceptor

$$\eta = \frac{R_0^6}{R^6 + R_0^6} \quad (7)$$

As a result of a transfer of energy, the luminescence decay time of the donor is quenched. By knowing the donor's luminescence decay time in absence τ_D and presence of an acceptor τ_{DA} the efficiency of the energy transfer can be calculated

$$\eta = 1 - \frac{\tau_{DA}}{\tau_D} \quad (8)$$

With eq. (7) and (8) the distance between donor and acceptor can be connected to a measured quantity. It can easily be shown, that the luminescence decay time in presence of a suitable donor τ_{DA} depends on the donor-acceptor distance

$$\frac{1}{\tau_{DA}} = \frac{1}{\tau_D} + \frac{1}{\tau_D} \left(\frac{R_0}{R} \right)^6. \quad (9)$$

Taking eq. (9) into account, the donor's luminescence decay in presence of an acceptor is given by

$$I(t) = I_0 \exp\left(-\frac{t}{\tau_{DA}}\right) = I_0 \exp\left[-\frac{t}{\tau_D} - \frac{t}{\tau_D} \left(\frac{R_0}{R} \right)^6\right]. \quad (10)$$

So far a donor-acceptor pair with a certain distance was considered. In more complex systems, like natural occurring polymers, it is more likely to assume a distribution of possible distances. This can be achieved, if eq. (6) is extended by a distribution function like a Gaussian function $P(R)$

$$P(R) = \frac{1}{\sigma\sqrt{2\pi}} \exp\left[-\frac{1}{2} \left(\frac{R-\bar{R}}{\sigma} \right)^2\right]. \quad (11)$$

In eq. (11) σ reflects the width of the distance distribution and \bar{R} is the mean distance between donor and acceptor. Now, both parameters (σ and \bar{R}) describing the distribution of distances can be deduced from the decay of the donor luminescence in presence of suitable acceptors using the following equation.

$$I(t) = I_0 \int_{R=0}^{\infty} P(R) \exp\left[-\frac{t}{\tau_D} - \frac{t}{\tau_D} \left(\frac{R_0}{R} \right)^6\right] dR \quad (12)$$

3. Results

3.1 Structure-interaction relationship of Eu(III) and small organic ligands probed by luminescence spectroscopy at room and elevated temperature

Spectral and time-resolved luminescence data of different Eu(III)-complexes with model ligands were investigated in detail. Since the chemical structure of the model ligands is fully known, many problems arising from the uncertainty in structure of HS are circumvented. This is important for the development of a fundamental understanding of the relationship between (electronic) structure of the ligands and observed luminescence response, because spectroscopic techniques are major tools in the investigation of molecular processes in natural systems. The model compounds show only moderate binding constants and in the samples investigated often a mixture of different complexes with respect to number of model ligands coordinated to the Ln(III) ion is observed. In the present study the influence of temperature on the photophysical properties of the Ln(III) complexes was used to further evaluate the intramolecular deactivation processes and to conclude on structure-related processes in the corresponding complexes.

Luminescence measurements at room temperature

Asymmetry ratio r

An useful spectroscopic parameter which is sensitive to the Eu(III) coordination environment is the asymmetry ratio r . For the $\text{Eu(III)}_{\text{aquo}}$ ion the asymmetry ratio is $r = 0.6$. Due to complexation the symmetry of the complex is changed and the asymmetry ratio is altered as well. Figure 1a shows luminescence spectra of Eu(III) complexes with 2-hydroxyphenylacetic acid. With an increasing ligand concentration the concentration of complexes is also increased. As a consequence the symmetry of the complex is affected and consequently the intensity of the hypersensitive ${}^5\text{D}_0 \rightarrow {}^7\text{F}_2$ transition may be increased. The parameter r is a good indicator to monitor the complex formation. Moreover, from the time dependence of r the presence of different species in the samples can be deduced. Hence, the evaluation of $r(t)$ can assist the interpretation of complex luminescence decay data. Figure 1b) is an example representative for the small organic ligands investigated in the present chapter. For those ligands r is independent of time indicating that only one (or only very similar) type of complex is present in the sample and/or that no excited state reaction like dissociation of the complex is operative during the luminescence decay of the sample.

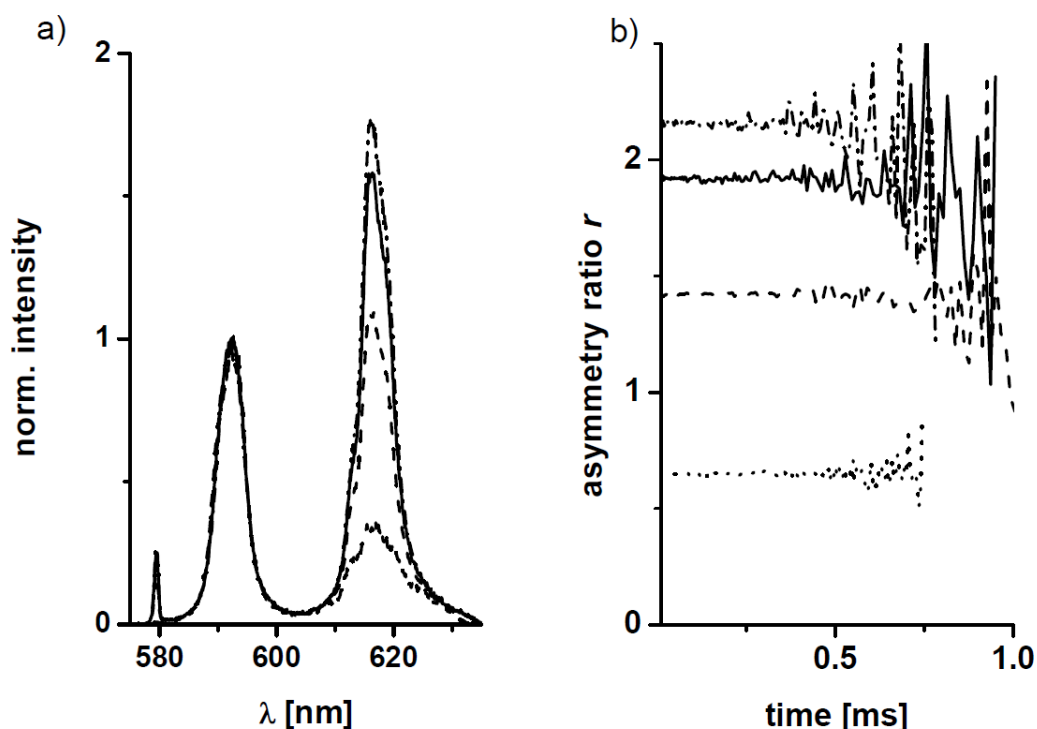


Figure 1: Luminescence spectra a) of Eu(III) complexes in 0.1 M NaClO₄ (...), with 2-hydroxyphenylacetic acid at a molar ratio of 1:1 (- - -), 1:3 (straight line) and 1:6 (line dot line) and b) the time-resolved asymmetry ratio of Eu(III)_{aq} in 0.1 M NaClO₄ and in complexes with 2-hydroxyphenylacetic acid at a molar ratio of 1:1, 1:3, and 1:6, respectively ($\lambda_{\text{ex}} = 394$ nm, $\delta t = 17.3$ μ s).

Figure 2 shows that the determined asymmetry ratio is dependent on the molar fraction of ligand. With increasing concentration of ligand the asymmetry ratio r also increases. Since the asymmetry ratio is $r > 0.6$ in the presence of any organic compound investigated, all potential ligands form complexes with Eu(III). Reasons for the different increase in r depending on the ligand could be different charge density, different symmetries of the complexes due to the specific properties of the ligand as well as mono and bidentate binding capabilities.

Decay times τ of the ⁵D₀-state of Eu(III) complexes

In water the Eu(III)_{aq} ion is surrounded by 8-9 water molecules (*vide infra*). Since the vibration state of these OH-oscillators is near the emitting state of the Eu(III) ion (⁵D₀ state), the water molecules act as quencher and the decay time is only 0.11 ms. When a ligand like glycolic acid enters the coordination sphere, quenching water molecules are displaced and the decay time of Eu(III) increases. In Figure 3 the luminescence decay curves of Eu(III) complexes with different model ligands (and at different molar fraction of ligand) are shown. Depending on the luminescence decay time of Eu(III) in the different complexes, these were (at this point) operationally divided into three groups (A, B and C).

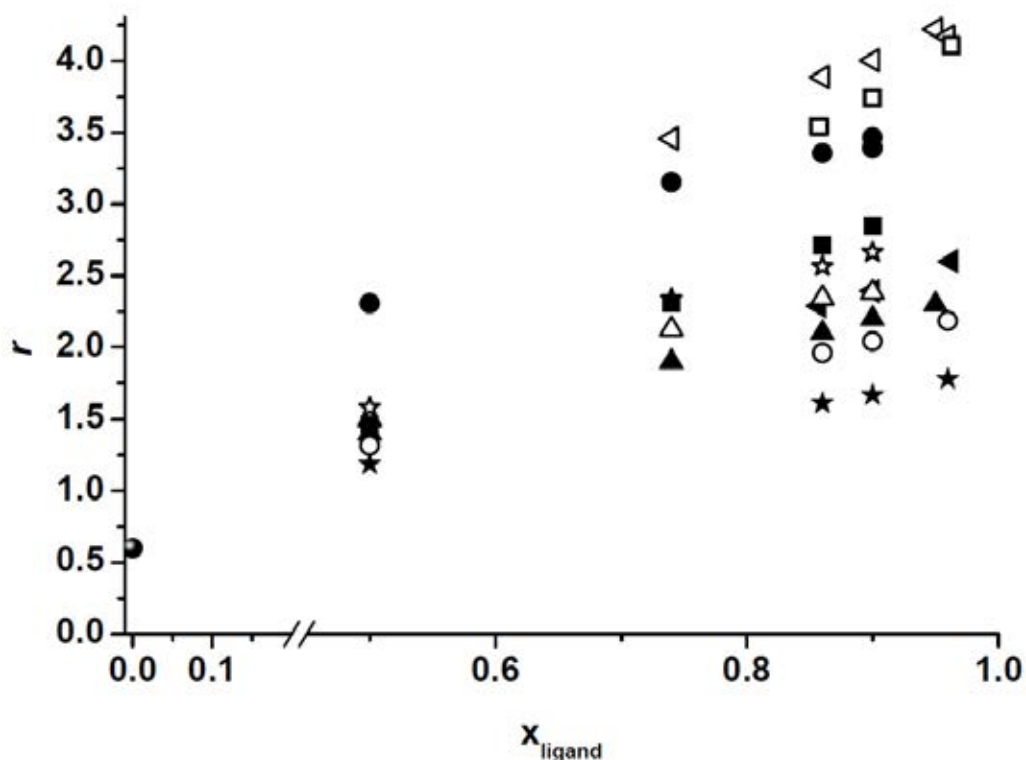


Figure 2: Asymmetry ratio r for different molar fractions of ligand: phthalic acid (.), glycolic acid (!), 2-hydroxyphenylacetic acid (7), cyclohexanecarboxylic acid (Δ), 2-methoxybenzoic acid (Ω), anthranilic acid (Ξ), 2-hydroxybenzoic acid (ξ), 2-hydroxycyclohexanecarboxylic acid (ψ), 4-hydroxybenzoic acid (∇), tropic acid (–) ($\lambda_{\text{ex}} = 394 \text{ nm}$)

Group A: The decay times of Eu(III) complexes with group A ligands are about 0.130 ms at a molar fraction of 0.5. This increase in the luminescence decay time is expected since water molecules are displaced by the coordinated ligand. With increasing molar fraction of ligand the decay time is also increasing as more complexes are formed.

Group B: Ligands like 2-methoxybenzoic acid or 4-hydroxybenzoic acid only have a small influence on the luminescence decay time τ . For complexes with a molar fraction of 0.5 a decay time of only 0.12 ms (or less) is determined. As the ligand concentration is increased only a slight increase in the decay time was observed.

Group C: Ligands attributed to this group show a non-typical behaviour of the luminescence decay time. At a molar fraction of 0.5 the decay time is only about 0.1 ms (or smaller) similar to the decay time of the $\text{Eu(III)}_{\text{aquo}}$ ion. This suggests that no complexes with Eu(III) were formed in solution. But from the asymmetry ratio of these complexes it can be concluded that the coordination sphere of the Eu(III) ion is changing with increasing ligand concentration (see Figure 2). Moreover, increasing the ligand concentration the luminescence decay time is even further decreased, which points towards a ligand-specific quenching.

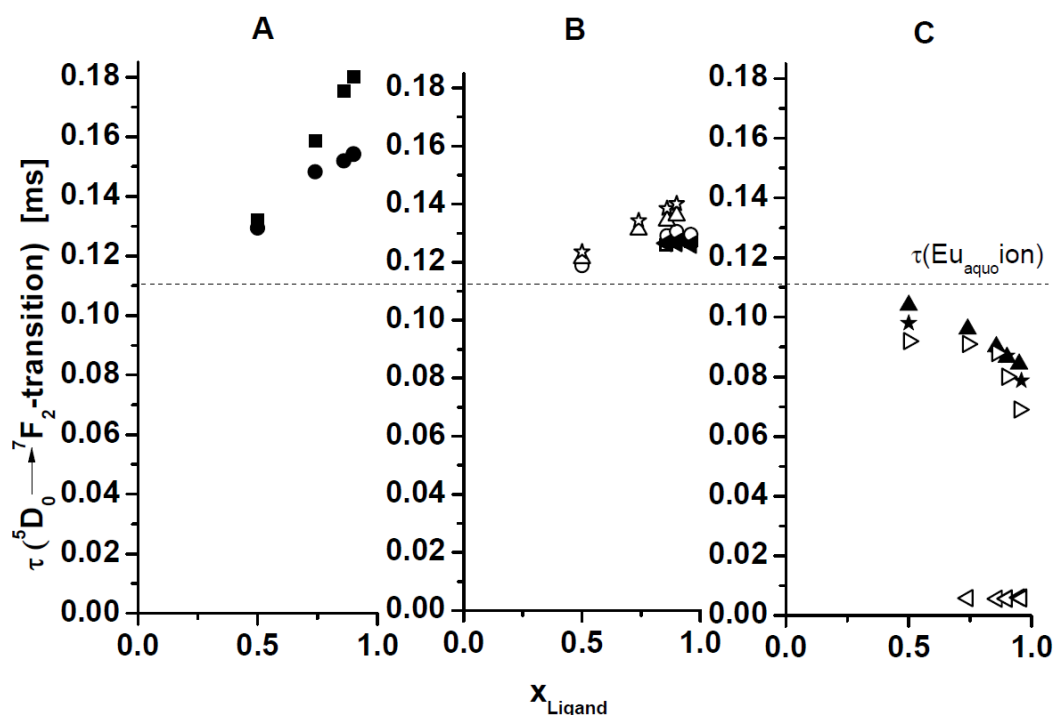


Figure 3: Decay times of the 5D_0 state dependent on the molar fraction of ligand of all investigated Eu(III) complexes with phtalic acid(,), glycolic acid(!), 2-hydroxyphenylacetic acid (7), cyclohexanecarboxylic acid (Δ), 2-methoxybenzoic acid (Ω), anthranilic acid (Ξ), 2-hydroxybenzoic acid (ξ), 2-hydroxycyclohexanecarboxylic acid(ψ), 2-mercaptobenzoic acid(χ), 4-hydroxybenzoic acid(∇), tropic acid (–) and at molar fraction of zero the $\text{Eu}_{(\text{aquo})}$ ion (sphere) is shown ($\lambda_{\text{ex}} = 394 \text{ nm}$)

Decay times τ of the 5D_4 -state of Tb(III) complexes

To further investigate the ligand-specific quenching of ligands (group C), the luminescence decay time of Tb(III) complexes was determined. The Tb(III) ion was chosen because it differs in its electronic properties compared to the Eu(III) ion: i) the emitting 5D_4 state of the Tb(III) ion has an energy of 20500 cm^{-1} , which is 3233 cm^{-1} above the emitting state of the Eu(III) ion and ii) Eu(III) can be reduced to Eu(II) at moderate oxidation potentials. In water a luminescence decay time for $\text{Tb(III)}_{\text{aquo}}$ ion of 0.4 ms is found. In Figure 4 the observed luminescence decay times for Tb(III) complexes with the different model compounds are compiled. Alike in the case of Eu(III) the ligands could again tentatively divided into three groups.

Group A: The decay time increased (e.g., for phtalic acid or glycolic acid at a molar ration of 0.5, a luminescence decay time of $0.46 \text{ ms} < \tau < 0.49 \text{ ms}$ was found). Like for the Eu(III) complexes, the decay time of Tb(III) complexes with ligands of group A is increased with increasing molar fraction of ligand.

Group B: Complexes with 2-methoxybenzoic acid, 4-hydroxybenzoic acid and tropic acid show almost no influence on the luminescence decay time of Tb(III). In that group, only a slight increase with increasing ligand concentration was observed.

Group C: The decay time of Tb(III) complexes with 2-aminobenzoic acid and 2-hydroxybenzoic acid shows an opposite trend to the Tb(III) complexes attributed to group A. Like in the case of Eu(III) complexes of group C, the luminescence decay time is decreasing with increasing ligand concentration.

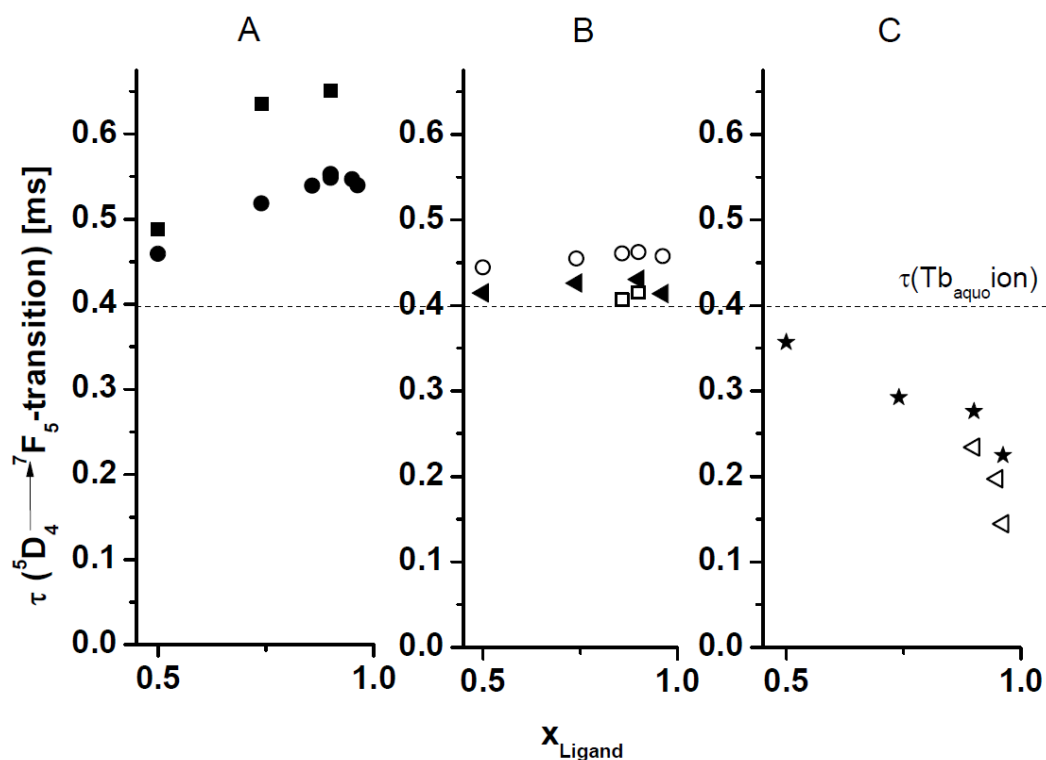


Figure 4: Decay times of the 5D_4 state dependent on the molar fraction of ligand of all investigated Tb(III) complexes with phthalic acid(,), glycolic acid(!), 2-methoxybenzoic acid (Ω), anthranilic acid (Ξ), 2-hydroxybenzoic acid (ξ), 4-hydroxybenzoic acid(∇) and tropic acid (-) ($\lambda_{\text{ex}}=377\text{nm}$)

Luminescence measurements at elevated temperatures in the range of 278 K < T < 340 K

Asymmetry ratio r

In Figure 5 the determined asymmetry ratios depending on the temperature for Eu(III) complexes with different ligands are shown. For all Eu(III) complexes investigated an increase of r with increasing temperature was observed, which could be attributed to the fact that usually the stability constants also increase with increasing temperature. The asymmetry ratio of the Eu(III) complexes with glycolic acid and 2-hydroxybenzoic acid is also increasing with increasing temperature, which is unusual because according to literature an opposite trend was expected, because complex formation with such ligands should be exothermic. The spectroscopic parameter r depends on different parameters and a possible

reason for the observed increase of r in that particular cases may be a shift of the equilibrium towards a higher stoichiometry, e.g., 1:2 complexes. When with increasing temperature more 1:2 complexes are formed, the asymmetry ratio r increases because of alterations in symmetry of the complexes.

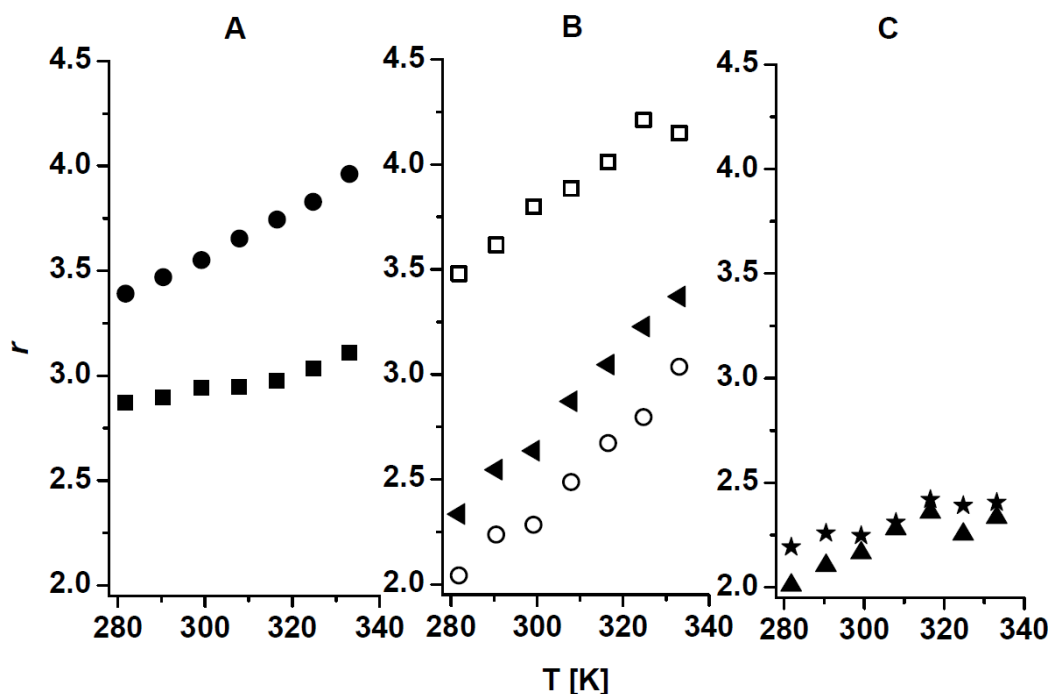


Figure 5: Determined asymmetry ratio of Eu(III) complexes with phtalic acid(.), glycolic acid(!), 2-methoxybenzoic acid (Ω), 4-hydroxybenzoic acid(∇), tropic acid (-), 2-hydroxybenzoic acid (ξ) and 2-hydroxyphenylacetic acid (B) at different temperatures

Luminescence decay times of Eu(III) complexes in the temperature range of 278 K < T < 340 K

To further elucidate the ligand-specific quenching processes luminescence measurements at elevated temperatures were performed. Figure 6 shows the measured luminescence decay times of the different Eu(III) complexes of groups A - C for the temperature range of 278 K < T < 340 K.

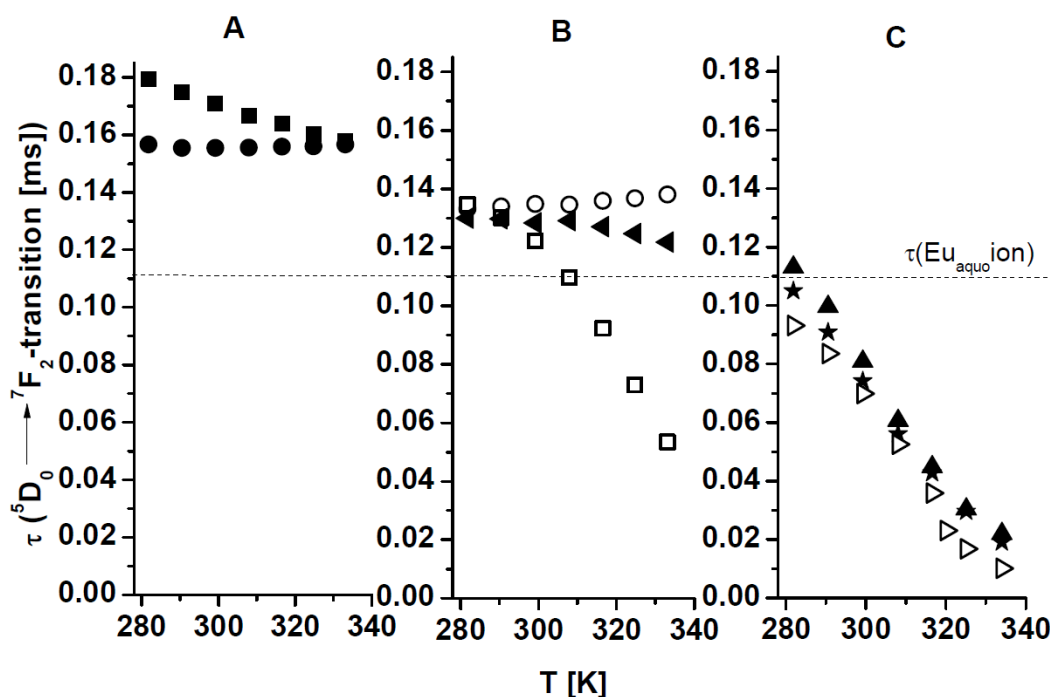


Figure 6: Decay times of Eu(III) complexes with phtalic acid(▪), glycolic acid(●), 2-methoxybenzoic acid (◻), 4-hydroxybenzoic acid(▼), tropic acid (◻), 2-hydroxybenzoic acid (★), 2-mercaptobenzoic acid (☆) and 2-hydroxyphenylacetic acid (▽) at different temperatures.

Group A: Here, complexes show slightly different trends in the temperature dependence of the luminescence decay time. The increase in the temperature seems to have no influence on the decay time of Eu(III) complexes with phtalic acid. But for the Eu(III) complex with glycolic acid a decrease in the decay time was observed. Here, a possible explanation for the decrease of the luminescence decay time may be a decrease in the complex formation with increasing temperature.

Group B: Like for group A, no clear trend is found, in the the case of complexes with 2-methoxybenzoic acid and 3-hydroxy-2-phenylpropionic acid almost no temperature dependence of the luminescence decay time was observed. On the other hand, for the Eu(III) complex with 4-hydroxybenzoic acid the decay time decreases distinctly with increasing temperature.

Group C: For that group of ligands a clear trend was found: the luminescence decay time decreased with increasing temperature and it seems that ligand-specific quenching mechanisms become more efficient.

In Figure 7 a data analysis according to Arrhenius for the group C ligands is shown. From the slopes of the lines it can readily concluded that the activation energy for the ligand-specific quenching process is not very different for the investigated compounds. In Table 1 the calculated activation energies for three compounds of group C are summarized.

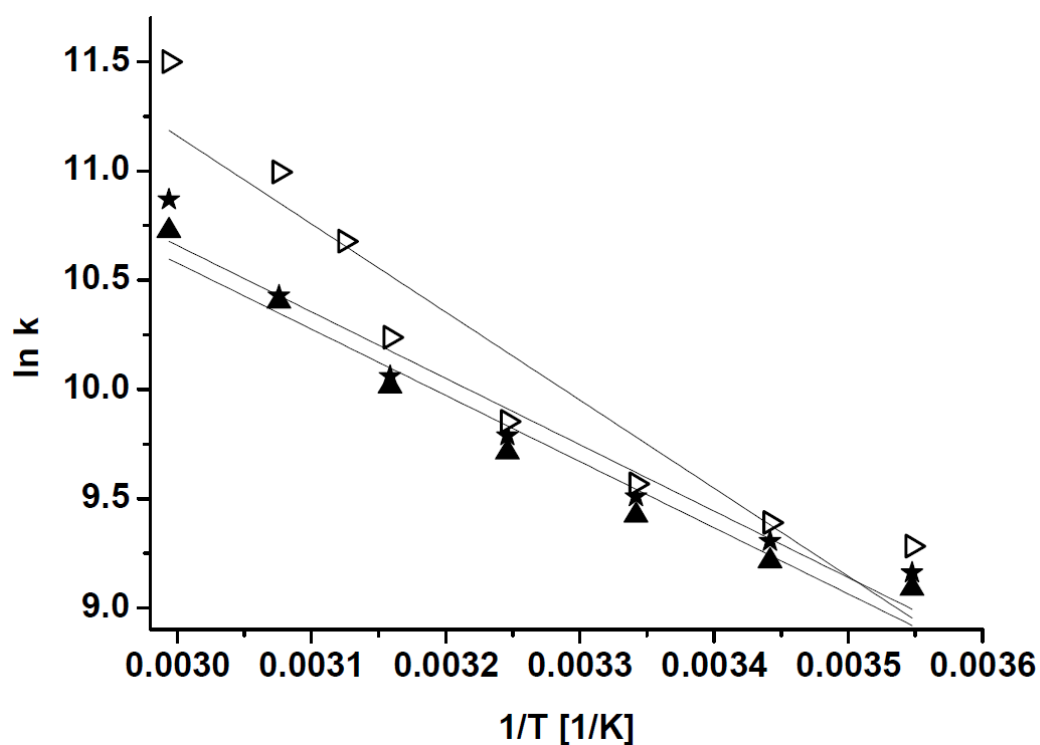


Figure 7: Evaluation of the luminescence decay times of the Eu(III) complexes of group C with 2-hydroxybenzoic acid (ξ), 2-hydroxyphenylacetic acid (\blacktriangle) and 2-mercaptobenzoic (X) acid according to Arrhenius.

The model ligands were tentatively grouped into three groups based on the spectroscopic parameters r and τ . While for groups A and B the two parameter showed slightly different pronounced trends in both parameters, the trends observed for group C were clear and in good agreement for both photophysical parameters. The observed dependence of r and τ on the ligand concentration as well as on the temperature show that the interplay between thermodynamics (complex stability, formation of higher complex stoichiometry) and ligand-specific quenching has to be understood for a proper evaluation of the luminescence data.

Table 1: Calculated activation energies E_A for Eu(III) complexes of group C

Eu(III):Ligand	E_A [cm^{-1}]
2-hydroxybenzoic acid	2100
2-hydroxyphenylacetic acid	2100
2-mercaptobenzoic acid	2800

Transient absorption spectroscopy³

Especially the ligand-specific quenching needs to be further evaluated. Often the formation of charge-transfer states is discussed as a possible source for the observed alterations in the photophysical properties of Eu(III) complexes. However, in the regular UV/Vis absorption no (or only very faint) changes are found, leaving the contribution of intra-complex charge transfer states as an explanation for the observed effects unclear.

In order to further improve the understanding of the ligand-specific quenching and to elucidate the possible contribution of a transient state, pump-and-probe experiments with 2-hydroxy benzoic acid and different Ln(III) ions were carried out. In Figure 8 the decay kinetics of the triplet state absorption of 2-hydroxy benzoic acid is shown in absence and presence of different Eu(III) concentrations. At low Eu(III) concentrations the decay of the transient absorption is quenched. Here, only a minor part of the Eu(III) is bound in a complex. A Stern-Volmer evaluation of the triplet-state related decay time showed that the corresponding quenching reaction is diffusion limited. Upon increasing the Eu(III) concentration the kinetics of the transient signal is distinctly altered. A rise of the transient signal is followed by slow decrease.

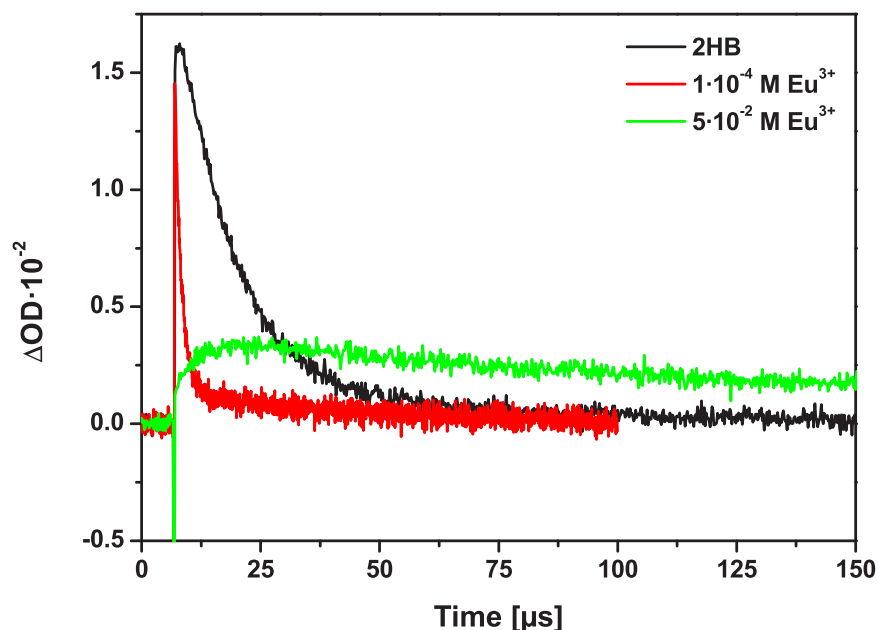


Figure 8: Transient absorption decay of 2-hydroxy benzoic acid in the absence and presence of different Eu(III) concentrations ($\lambda_{\text{ex}} = 290 \text{ nm}$, $\lambda_{\text{abs}} = 455 \text{ nm}$).

In Figure 9 the transient absorption spectra of 2-hydroxy benzoic acid in the absence and presence of La(III) and Eu(III) are depicted. A Ln(III) concentrations of $5 \cdot 10^{-2} \text{ M}$ ensure that the ligand is completely bound in a complex. In the absence of Ln(III) the spectrum shows the transient absorption of the phenoxy radical ($\lambda \sim 390 \text{ nm}$), the triplet state ($\lambda \sim 450 \text{ nm}$)

³ P. Primus, M.U. Kumke; J. Phys. Chem. A (2011), submitted for publication. "Flash photolysis study of complexes between salicylic acid and lanthanide ions in water"

and of the solvated electron ($\lambda \sim 690$ nm), respectively. The addition of La(III) does not change the spectrum and all three transient species are present. In contrast, upon addition of Eu(III) only the transient signal of the phenoxy radical is left. In addition in Figure 9 the transient spectrum of 2-hydroxy benzoic acid in the presence of Eu(III) at a time delay of 50 μ s after the laser pulse is shown.

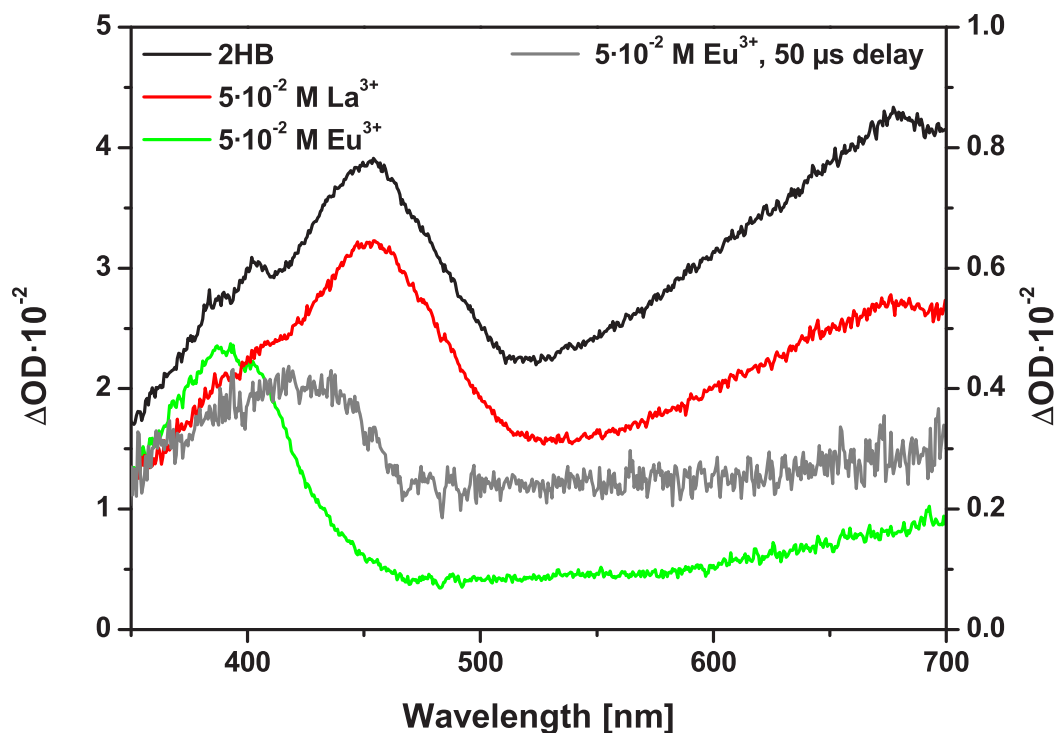


Figure 9: Transient absorption spectra of 2-hydroxy benzoic acid in the absence and presence of La(III) and Eu(III), respectively. The Ln(III) concentrations of $5 \cdot 10^{-2}$ M ensure that the ligand is completely bound in a complex.

It can be seen that a new absorption band occurs in the spectrum at $\lambda \sim 420$ nm, which was not present in the other samples investigated. The observed rise (see Figure 8) in the transient absorption kinetics and the changed decay can be attributed to the occurrence of this new species. Since such transient signals were only found in the presence of metal ions which are able to participate in a redox-related step (e.g., similar results were also found in the presence of copper), it is tempting to attribute the observed signal to a charge transfer (CT) state. This CT state is formed in complexes with ligands of group C and opens an additional deactivation pathway, which finally decreases the luminescence decay time of the corresponding Eu(III) complex. In case of Tb(III), which is not known for the formation of a +II state, different mechanisms such as energy back transfer, may be the cause for the observed effects.

3.2 Fluorescence line narrowing (FLN) spectroscopy of Eu(III) in complexes with small organic ligands^{4,5,6}

The total luminescence spectrum (TLS) measured at 4.7 K contains a wealth of information, which is especially valuable for the investigation of samples containing mixtures of Eu(III) complexes. From the width of the ${}^5D_0 \leftarrow {}^7F_0$ transition (excitation spectrum) the degree of inhomogeneity (e.g., small variations in bond lengths, bond angles or water molecules in the second coordination sphere) can be assessed, whereas non-Gaussian shaped excitation spectra point at the occurrence of several distinct "species". As a first step towards FLN analysis of Eu(III) complexes with natural ligands such as humic acids, various small organic ligands (aliphatic and aromatic carboxylic acids) were investigated as model compounds, mimicking possible binding sites in HS.

An in-depth analysis of the FLN spectra is carried out with respect to: i) the number of ${}^5D_0 \leftarrow {}^7F_0$ transitions observable in the excitation spectra, ii) the asymmetry ratio r of the ${}^5D_0 \rightarrow {}^7F_2$ and ${}^5D_0 \rightarrow {}^7F_1$ transitions, and iii) the variation of the excitation energy with the crystal field strength parameter $N_v(B_{2q})$ (referred to as jackstraws plots). Making use of the specific excitation wavelengths corresponding to the observed ${}^5D_0 \leftarrow {}^7F_0$ transitions in the TLS, species-selective luminescence decays were recorded in order to determine the number of water molecules in the first coordination sphere for a particular complex. On the basis of an integrated analysis of the excitation spectra, of the emission spectra and of the luminescence decay times, the number of different complexes coexisting in the sample, their stoichiometry and geometry (e.g., symmetry point group) were deduced.

With respect to the potential binding to Eu(III), the model ligands investigated here can be tentatively divided into two sets: *A*) ligands that may form chelates due to a hydroxyl group (or a second carboxyl group) and *B*) ligands that can bind to Eu(III) via one carboxyl group alone. TYPE A model ligands are: 2-hydroxy benzoic acid (2HB), phthalic acid (PHA), and glycolic acid (GL), while 3-hydroxy benzoic acid (3HB), 4-hydroxy benzoic acid (4HB), 4-methoxy benzoic acid (4MB), benzoic acid (BA), galic acid (GA) and 3-hydroxy propionic acid (3HP) belong to TYPE B.

⁴ B. Marmodée, J. de Klerk, F. Ariese, C. Gooijer, M.U. Kumke; *Anal. Chim. Acta* 652 (2009) 285 – 294. "High-resolution steady-state and time-resolved luminescence studies on the complexes of Eu(III) with aromatic or aliphatic carboxylic acids."

⁵ B. Marmodée, J. de Klerk, F. Ariese, C. Gooijer, M.U. Kumke; *Z. Naturforsch. A* 64a (2009) 242 – 250. „Metal binding by humic substances – characterization by high-resolution lanthanide ion probe spectroscopy (HR-LIPS).“

⁶ B. Marmodée, J. de Klerk, M.U. Kumke, F. Ariese, C. Gooijer; *J. Alloys Comp.* 451 (2008) 361 – 364. „Spectroscopic investigations of complexes between Eu(III) and aromatic carboxylic ligands.“

Total luminescence spectra

From the high-resolution TLS, the luminescence excitation and emission spectra can be derived as horizontal and vertical cross-sections, respectively (as shown for Eu(III) : 4HB in Figure 10). The position, width and shape of the excitation band as well as the splitting of the 7F_1 multiplet as a function of the excitation wavelength and subsequently the number of different species can be extracted from the TLS.

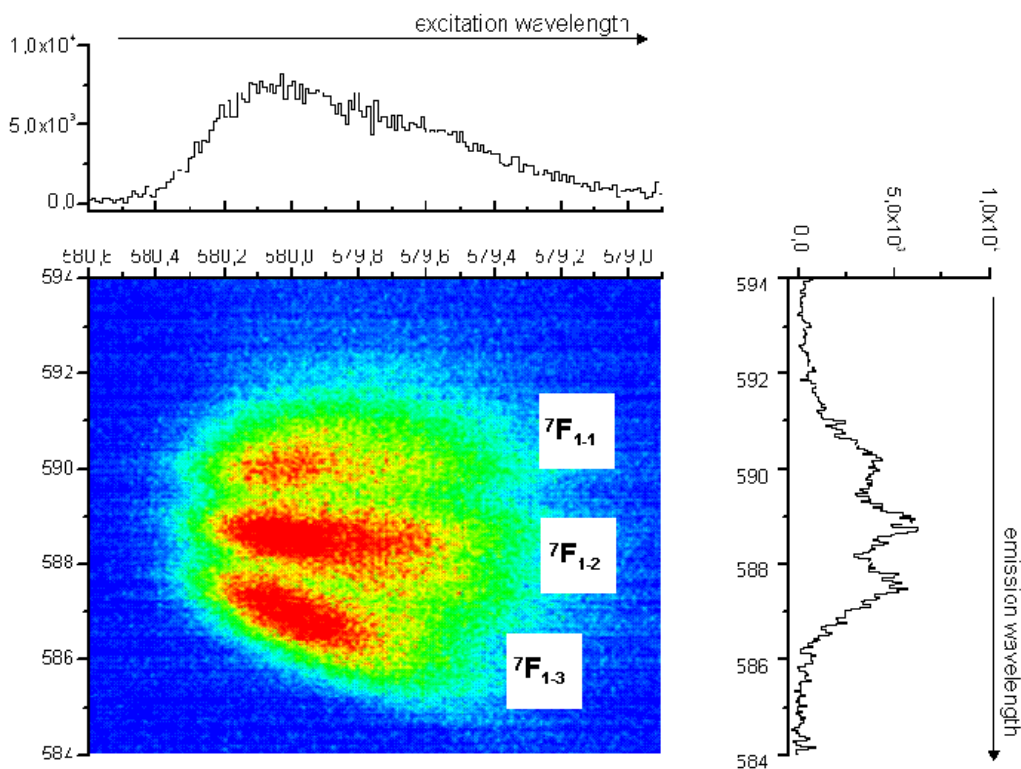


Figure 10: Contour plot of the 7F_1 multiplet of the Eu^{3+} and 4-hydroxy benzoic acid at a molar ratio of 1:9 (T = 5 K).

At a series of emission wavelengths ($614 \text{ nm} < \lambda_{\text{em}} < 620 \text{ nm}$ corresponding to $16287 \text{ cm}^{-1} > E_{\text{em}} > 16129 \text{ cm}^{-1}$), the spectral positions and the average FWHM of the ${}^5D_0 \leftarrow {}^7F_0$ transitions were obtained from the TLS (see Figure 10, for example). These spectra were also used to select the optimal excitation wavelengths for the species-selective decay time measurements (*vide infra*). For the aromatic ligands 2HB, 4HB and PHA excitation spectra (cross-sections for $\lambda_{\text{em}} = 614 \text{ nm}$, $E_{\text{em}} = 16287 \text{ cm}^{-1}$; ${}^5D_0 \rightarrow {}^7F_2$ transition) are shown in Figure 11. As reported earlier, for the crystals of the reference compound $\text{EuCl}_3 \cdot 6\text{H}_2\text{O}$ a very narrow ${}^5D_0 \leftarrow {}^7F_0$ transition was observed (FWHM of 0.2 cm^{-1}), indicating a single, well-defined Eu(III) complex. For TYPE A ligands such as salicylic acid (2HB) and phthalic acid (PHA), also relatively narrow-banded ${}^5D_0 \leftarrow {}^7F_0$ transitions were found (FWHM = 1.3 and 1.1 cm^{-1} respectively). This clearly indicates the formation of well-defined complexes, presumably with a high stability constant and a high degree of symmetry. However, for GL a broadened excitation transition was observed, probably due to the rotational freedom of the possibly chelating OH group. In contrast to 2HB and PHA for TYPE B ligands broader, non-GAUSSIAN shaped peaks already indicate a more inhomogeneous situation and often the presence of more than one species.

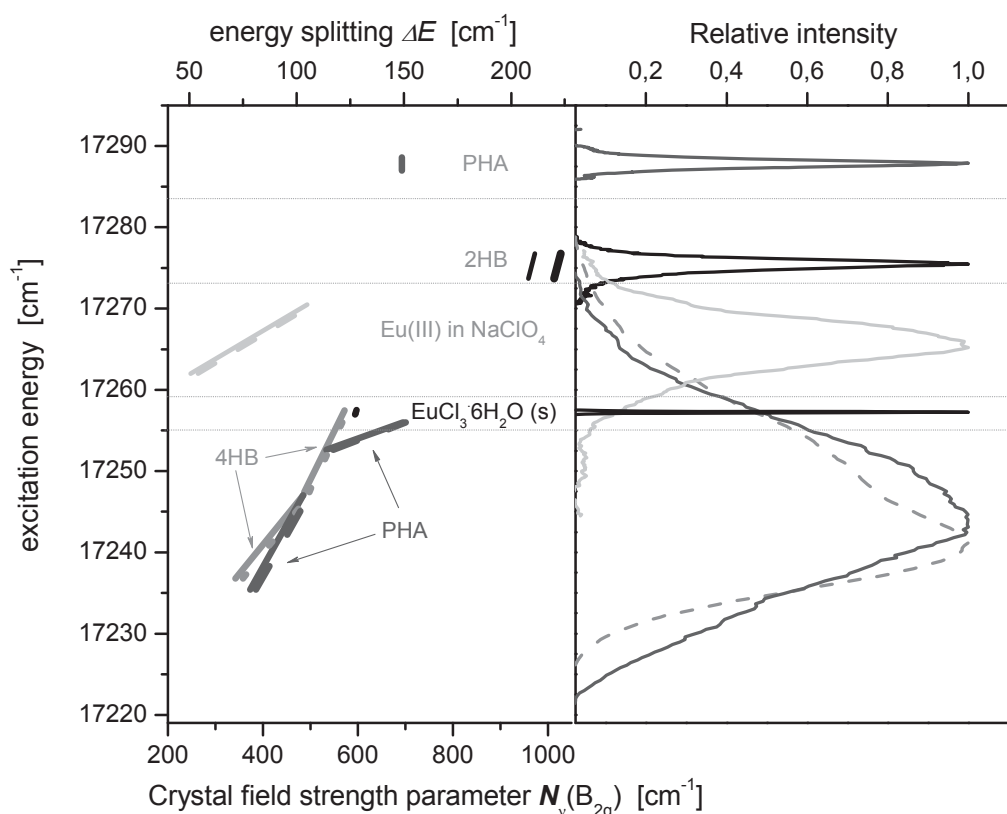


Figure 11: Smoothed excitation spectra of the Eu(III) complexes with aromatic carboxylates ($\lambda_{em} = 612 \text{ nm}$ ($E_{em} = 16340 \text{ cm}^{-1}$)) and Jackstraws plot calculated from the ${}^5D_0 \rightarrow {}^7F_1$ and the ${}^5D_0 \rightarrow {}^7F_0$ transition of the corresponding TLSs (full lines refer to $N_{\nu}(B_{2q})$, dashed lines to ΔE). 3HB and BA are omitted for clarity reasons.

Luminescence decay times

Based on the excitation spectra extracted from the TLS, species-selective excitation conditions were chosen for the cryogenic luminescence decay measurements; these decay times are summarized in Figure 12. For the interpretation of the decay time data it was assumed that the aquo ion of Eu(III) is coordinated by nine water molecules, which can be substituted by nine oxygen containing groups from ligands – which may be considered as an oversimplification because an equilibrium between eight and nine-fold coordinated water species is present (*vide infra*).

It is striking that especially for TYPE A ligands (chelate formation via carboxyl and/or a hydroxyl group) relatively short luminescence decay times were found also at $T = 5 \text{ K}$: around $420 \mu\text{s}$ for 2HB and GL (*vide supra*). Considering the decay times obtained for TYPE A ligands, and the fact that very sharp excitation peaks indicate the formation of well-defined complexes, estimating the number of water molecules n_{H_2O} in the first coordination sphere based on the standard approaches of HORROCKS *et al.* and KIMURA *et al.* should be considered with great care.

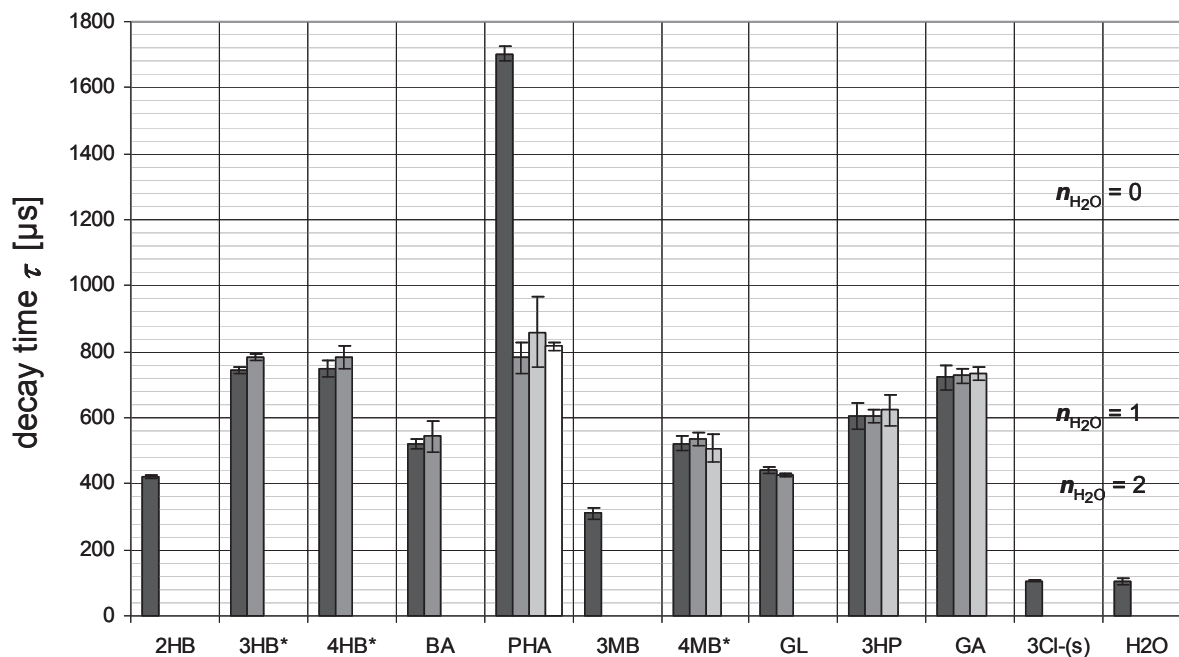


Figure 12: Decay times of the Eu(III) complexes of 2HB, 3HB, 4HB, BA, PHA, 3MB, 4MB, GL, 3HP and GA at different excitation wavelengths. The grey bars indicate the variation of decay time due to influence of individual ligand properties and the water molecules of the second coordination sphere. (*of a biexponential fit only the longer lifetime is shown).

For example, in case of 2HB the α -hydroxy group can participate in the complexation and subsequently quench the Eu(III) luminescence. Applying Equation (4), in which also quenching contributions from water molecules in the second coordination sphere and ligand-related hydroxyl groups are taken into account, at most one water molecule is left in the first coordination sphere. This interpretation is supported by the absence of quenching from ligand-related OH groups for aromatic carboxylic acids that do not possess an α -hydroxy group (3HB, 4HB: $n_{OH} = 0$). The overall steric requirements for these ligands should be at least similar to those of 2HB, e.g., a comparable number of water molecules can remain in the first coordination sphere of Eu(III). For these ligands a luminescence decay time of about 750 μs was found (see Figure 12), which based on Equation (4) corresponds to one water molecule in the first coordination sphere.

In contrast, “pure” benzoic acid (and 4MB) is free of steric constraints caused by substituents and has no additional binding possibilities. In this special case a shorter luminescence decay time of 520 μs was found, which points to one or two water molecules still present in the first coordination sphere.

For the ligands 3HB, 4HB, 4MB and PHA additional species with luminescence decay times in the range of 150 μs to 250 μs were found. Their relative intensities varied with the excitation energies and in general the fraction of these species was rather low (15 % to 30 %). Most probably we are dealing with complexes containing four to six remaining water molecules in the first coordination sphere of Eu(III), indicating complexation by less than three organic ligands.

On the other hand, in the case of one of the phthalate (PHA) complexes an extremely long luminescence decay time of $\tau = 1702 \mu\text{s}$ was found, which points to a complex without any water molecule left in the first coordination sphere. It is probably formed by the phthalate

fraction with both carboxyl groups deprotonated (no remaining OH-groups). Considering the very narrow peaks (FWHM $\sim 1 \text{ cm}^{-1}$) in excitation, it can be assumed that this species corresponds to a well-defined complex (see Figure 12). For the other phthalate species identified in the TLS somewhat shorter luminescence decay times were observed, probably due to the presence of a non-deprotonated carboxyl group in the first coordination sphere. Another possible explanation would be a bound water molecule in exchange for the carboxyl OH-group.

Compared to the other aromatic ligands investigated, the short luminescence decay time ($\tau = 310 \text{ }\mu\text{s}$) found for 3MB indicates that in this complex three water molecules are present in the first coordination sphere. A possible explanation could be the overall larger spatial requirements of the methoxy group, which limits the number of ligands and thus allows additional water molecules to be coordinated via H-bonding. This way the decay time will be shorter than in the case of BA or 4MB. This hypothesis is further supported by the spectral information, such as peak width and excitation energy, pointing to a well-defined complex and suggesting the assignment to a TYPE A ligand. This special coordination would also be possible for 3HB, for which, however, a much longer luminescence decay time was observed. Apparently, an extra 3HB ligand is bound, leaving room for only one water molecule. Here, additional information (e.g., from NMR experiments) is required to test this hypothesis.

In comparison to the aromatic carboxylates the steric requirements for aliphatic ligands are relaxed. Especially for GL chelate formation can be expected. According to the literature because of the small size of GL, even in a 1:3 complex the Eu(III) ion may still be coordinated by about three water molecules. However, in the (ice) crystal GL can act as a bridging ligand and additional water molecules can be removed from the first coordination sphere. Moreover, some of the OH groups may also be binding to the Eu(III). The observed decay time of $420 \text{ }\mu\text{s}$ could in principle be explained by four ligand hydroxyl groups and zero water molecules, or by fewer coordinating OH groups and one water molecule. The relatively broad excitation band (*vide supra*) would support the latter suggestion, in accordance with references.

The total change in entropy upon complexation consists of two fractions: the entropy increase caused by the ligand release and the entropy loss resulting from conformational rearrangement of the ligand to allow complex binding. With regard to 3HP and GA the entropy loss by ligand rearrangement overcompensates the chelate effect making chelate formation less favourable. In solution GA is bound via only one carboxyl group. In crystals the formation of a ligand bridge has been described. Under the experimental conditions applied (e.g., pH 5 and ligand in high excess), both carboxyl groups of GA should be deprotonated but a bidentate binding via only one COO^- group is favoured (one remaining water molecule), providing an explanation for the observed luminescence decay times (see Figure 12). Interestingly the luminescence decay time of 3HP is somewhat shorter than that of GA, indicating a minor influence of the ligand hydroxyl group.

Excitation energy

The effect of the geometry of the complexes (especially due to ligand-related constraints) and the covalence of the bonds to the Eu(III) ion are key factors for the energy of the $^5\text{D}_0 \leftarrow ^7\text{F}_0$ transition. Also the STARK splitting of the $^7\text{F}_1$ levels affects the energy of the $^5\text{D}_0 \leftarrow ^7\text{F}_0$ transition, which makes - due to opposed effects - predicting the shift of this transition for different ligands/complexes very difficult. Good examples are 2HB and PHA: they show the highest $^5\text{D}_0 \leftarrow ^7\text{F}_0$ transition energy among the complexes investigated, although a relatively high degree of covalence and subsequently a red-shift would be expected. However, both

ligands can form chelates and therefore there will be ligand-related geometry constraints. Apparently, the induced STARK splitting outweighs the nephelauxetic effect and an overall blueshift is observed – adding experimental evidence to the theoretically proposed influence of the 7F_1 STARK splitting. Therefore, conclusions with respect to bond covalence and/or geometry can only be drawn for very similar ligands and in combination with additional information, such as the spectral width of the ${}^5D_0 \leftarrow {}^7F_0$ transition observed under high-resolution conditions. Of course also information from accompanying techniques such as extended X-ray absorption fine structure (EXAFS) spectroscopy could help to identify geometry differences (especially bond length) in the complexes. For 3HB, 4HB, BA (and also for the minor fraction of low-energy PHA species) the excitation spectra are nearly identical (illustrated in Figure 11 for PHA and 4HB), which suggests that the geometries of those complexes are very similar (e.g., with respect to the Eu-O distances and the bond angles). The same holds true for the aliphatic ligands investigated, except for the glycolic acid, which could form chelates.

In contrast to these “inhomogeneously broadened” species (of 3HB, 4HB, BA, low-energy PHA, GA, 3HP, and 4MB, respectively), higher excitation energies are found for the 3MB complex, which is attributed to the stronger influence of the 7F_1 STARK splitting on the energy of the 7F_0 level (Figure 13, note the high ΔE and $N_v(B_{2q})$).

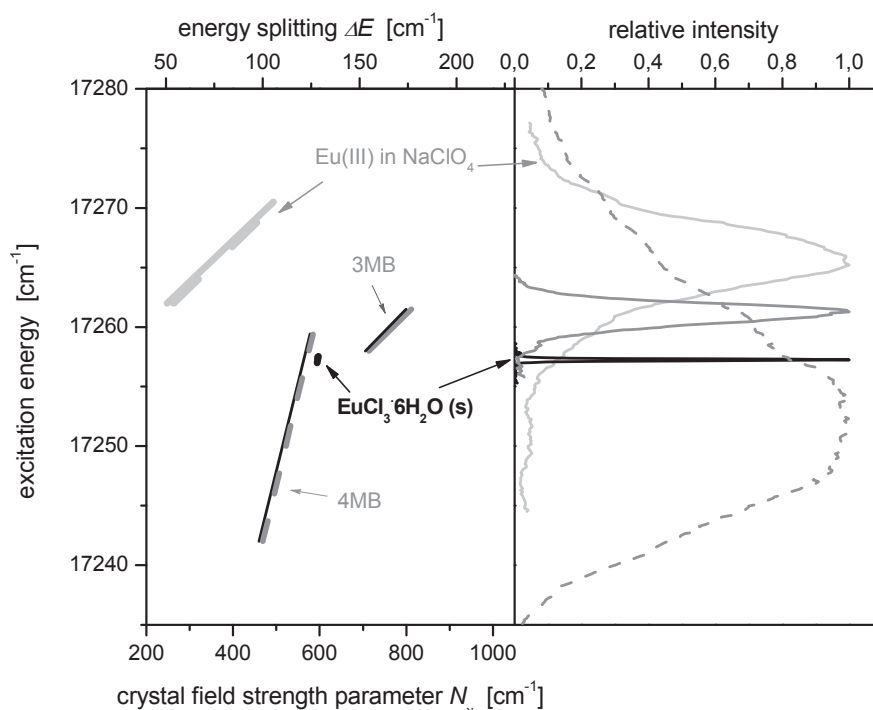


Figure 13: Smoothed excitation spectra of the Eu(III) complexes with methoxy benzoates ($\lambda_{em} = 612 \text{ nm}$ ($E_{em} = 16340 \text{ cm}^{-1}$)) and Jackstraws plot calculated from the ${}^5D_0 \rightarrow {}^7F_1$ and the ${}^5D_0 \rightarrow {}^7F_0$ transition of the related TLS (full lines refer to $N_v(B_{2q})$, dashed lines to ΔE).

Jackstraws plots, 7F_1 Stark splitting and crystal field strength parameter

The TLS of the Eu(III) complexes investigated show relatively narrow, sloping lines instead of broad, oval-shaped peaks. The same was found for the ${}^5D_0 \rightarrow {}^7F_2$ transition. This indicates that within an inhomogeneously broadened band these energies are correlated with the excitation energy ${}^5D_0 \leftarrow {}^7F_0$. A similar dependence has been reported before for the luminescence of Eu(III) in glassy matrices. Applying the data reduction procedure described before, jackstraws plots are obtained from the TLS.

Figures 11 and 13 (left frames) show that for all organic ligands investigated the observed $N_v(B_{2q})$ dependence on the excitation energy was significantly different from that of aqueous Eu(III) in NaClO₄ solution, providing an important confirmation of the actual complex formation. As a reference, also the data obtained for EuCl₃·6H₂O crystals are shown.

The energy difference ΔE is added as second abscissa. Comparing “both” diagrams it is evident that the mid STARK level has a minor influence on $N_v(B_{2q})$, because the latter includes all three 7F_1 levels, whereas ΔE is only calculated from the highest and the lowest one.

Looking at the jackstraws plots in detail, each line represents the increase in excitation energy with the crystal field strength parameter for one species of the Eu(III) ligand mixture in question. This is to be regarded as a consequence of the correlation of the 7F_1 -splitting and the excitation energy (*vide supra*). Moreover, the slopes of the lines are different. This may be attributed to the individual symmetry of the crystal field influencing the f-orbitals differently. In the procedure of data analysis and reduction it turned out that in Figures 11 and 13 different slopes can be ascribed to different species.

Moreover, comparing all different ligands it is interesting to note that the crystal field strength parameter $N_v(B_{2q})$ and the excitation energy seem to be correlated in general: the absolute excitation energy increases with increasing STARK splitting. An analogous correlation was observed by CARLOS *et al.* for $N_v(B_{2q})$ and the excitation energy, although “in principle, no evident correlation between the nephelauxetic effect and $N_v(B_{2q})$ is to be expected”.

The large ΔE (or $N_v(B_{2q})$) for Eu(III) complexes of 2HB and PHA (see Figure 11) was attributed to the formation of chelates, in which the concentration of negative charges close to the Eu(III) ion is high. As can be expected considering the formation of complexes without any coordinating water molecule for the “sharp” PHA species charge density is highest for this complex species resulting in the highest 7F_1 splitting and consequently in the largest blue shift of the excitation spectrum.

Crystal field parameters

The crystal field parameters extracted from the TLS provide an important connection to quantum mechanics. In particular, the crystal field parameters B_{20} and B_{22} are related to the crystal field strength parameter $N_v(B_{2q})$ according to Equation (17). Those two parameters are in turn involved in the quantum mechanical description of the energy states of the crystal field by the HAMILTON operator \hat{H}_{CF} (Equation (18)):

$$N_v(B_{2q}) = \sqrt{\frac{4\pi}{5}} (B_{20}^2 + 2B_{22}^2) \quad (17)$$

$$\hat{H}_{CF} = B_{20}C_0^{(2)} + B_{22}(C_{-2}^{(2)} + C_2^{(2)}) \quad (18)$$

$C_2^{(2)}$ and $C_{-2}^{(2)}$ are the one-electron tensor operators describing the crystal field. From the energy of the STARK levels ${}^7F_{1-1}$ to ${}^7F_{1-3}$ of the 7F_1 multiplet, B_{20} and B_{22} are obtained. In the

present case both parameters are negative, ranging from $-134 \text{ cm}^{-1} > B_{20} > -690 \text{ cm}^{-1}$ and $-54 \text{ cm}^{-1} > B_{22} > -304 \text{ cm}^{-1}$, respectively. The absolute values of B_{20} and B_{22} are proportional to the energy splitting of ${}^7F_{1-1}$ and the barycentre of ${}^7F_{1-2}$ and ${}^7F_{1-3}$, and to the energy splitting of ${}^7F_{1-2}$ and ${}^7F_{1-3}$, respectively. Hence, it may be concluded that ${}^7F_{1-1}$ and the barycentre of ${}^7F_{1-2}$ and ${}^7F_{1-3}$ are subject to considerable changes for a particular species itself as well as for all complexes together, whereas the energy splitting between ${}^7F_{1-2}$ and ${}^7F_{1-3}$ does not vary significantly, except for the high energy PHA species

Point symmetry group

The luminescence spectra of the ${}^5D_0 \rightarrow {}^7F_1$ and the ${}^5D_0 \rightarrow {}^7F_2$ transitions of the different species for each model ligand were evaluated with respect to the number of STARK levels visible in the spectrum. It was found that the number of observed STARK levels is dependent on the specific ligand, indicating the formation of complexes with different symmetries and/or number of ligands (species), respectively. For a particular ligand, different complex symmetries were found depending on the species at hand (e.g., a D_2 or C_{2v} symmetry for 2HB).

For the ligands investigated the highest symmetry found is D_2 , concerning the chelate PHA and 2HB species as well as the solid $\text{EuCl}_3 \cdot 6\text{H}_2\text{O}$. Here, the 7F_1 -level is split into three peaks, which means that the unit cell has orthorhombic, monoclinic or triclinic symmetry. For further refinement one has to consider the splitting of the ${}^5D_0 \rightarrow {}^7F_2$ transition, showing three lines.

Complexation is also evident from the high asymmetry ratio r for all Eu(III) ligand mixtures except for Eu(III) in water. The relatively small value for the solid $\text{EuCl}_3 \cdot 6\text{H}_2\text{O}$ confirms the high symmetry deduced from the emission spectrum (symmetry point group: D_2). In contrast, the r values for complexes with organic ligands are considerably higher due to distortions of the coordination sphere caused by the ligands. Examination of the asymmetry ratio clearly supports the presence of several species.

3.3 Direct spectroscopic evidence of eight- and nine-fold coordinated aquo Eu(III) species in H₂O and D₂O⁷

In aqueous solutions an equilibrium exists between an eight- and a nine-fold coordinated Eu(III)(aq) species.



At $T = 5$ K, any interchange reaction between potential Eu(III)(aq) species can be ruled out and a reduction of inhomogeneous spectral line-broadening is achieved. From the total luminescence spectra (TLS, excitation vs. emission wavelength) and the luminescence decay matrices (time vs. emission wavelength), fundamental species-selective spectroscopic parameters are determined: excitation wavelength λ_{exc} , decay time τ , crystal field energy splitting ΔE (crystal field strength parameter $N_{\text{v}}(\text{B}_{2\text{q}})$), crystal field parameters B_{20} and B_{22} , asymmetry ratio r , and point symmetry group. The spectroscopic findings were analyzed with respect to the presence of different Eu(III) aquo species. To check the possible influence of the counter ion to inner-sphere coordination, samples were prepared with different counter ions (Cl^- , ClO_4^-) and at different pH (2 and 5).

In Figure 14 the ${}^5\text{D}_0 \rightarrow {}^7\text{F}_1$ low-temperature TLS of Eu(III) in water at pH = 5 is shown for the excitation wavelength range of $578.8 \text{ nm} < \lambda_{\text{exc}} < 579.8 \text{ nm}$, which corresponds to the non-degenerate ${}^5\text{D}_0 \leftarrow {}^7\text{F}_0$ transition of Eu(III). Therefore, in case of a single Eu(III) aquo species one expects the excitation spectra (horizontal cross-sections, see top spectrum in Fig. 14) to show only one peak and the corresponding high resolution emission spectrum (${}^5\text{D}_0 \rightarrow {}^7\text{F}_1$ transition with $J = 1$; vertical cross-section of the TLS), should exhibit at most three STARK levels. However, two distinct peaks are visible in the excitation spectrum. Moreover, in the emission spectrum shown on the right of Fig. 1 (extracted from the TLS at $\lambda_{\text{exc}} = 579.26 \text{ nm}$), four clearly resolved peaks are observed. Closer inspection of the TLS (Fig. 14, middle) reveals even six peaks. Especially the high-energy emission bands around 590 nm are clearly different, as indicated by the two separate slanted "islands" for the two excitation wavelengths. Thus, from the excitation and emission spectra the presence of two different Eu(III) aquo species, such as $[\text{Eu}(\text{H}_2\text{O})_8]^{3+}$ and $[\text{Eu}(\text{H}_2\text{O})_9]^{3+}$, was already deduced. Very similar spectral (see Table 2) and also temporal (*vide infra*) features were found at pH 2 or in the presence of different anions, which excludes the formation of hydroxyl complexes or any inner sphere complexation of the counterions.

From the high-resolution TLS, the crystal field splitting energy ΔE of the ${}^7\text{F}_1$ multiplet and the crystal field strength parameter $N_{\text{v}}(\text{B}_{2\text{q}})$ was extracted. For ΔE ($N_{\text{v}}(\text{B}_{2\text{q}})$) values of $(142 \pm 4) \text{ cm}^{-1}$ ($(656 \pm 16) \text{ cm}^{-1}$) and $(124 \pm 4) \text{ cm}^{-1}$ ($(568 \pm 17) \text{ cm}^{-1}$) were determined for the different species (see Table 2). For $[\text{Eu}(\text{H}_2\text{O})_8]^{3+}$ it is expected that water ligands can approach the central ion more closely and subsequently a stronger crystal field is exerted on the Eu(III), which is reflected in a larger ΔE ($N_{\text{v}}(\text{B}_{2\text{q}})$). This expectation is also supported by crystal field calculations, according to which the crystal field splitting would be significantly larger for the eightfold coordinated species than for the nine-fold coordinated. Therefore, species 1 with its excitation maximum at $\lambda_{\text{exc}1} = 579.43 \text{ nm}$ is assigned to an eightfold coordinated

⁷ B. Marmodée, K. Jahn, F. Ariese, C. Gooijer, M.U. Kumke; J. Phys. Chem. A 114 (2010) 13050-13054. „Direct spectroscopic evidence of 8- and 9-fold coordinated Europium(III) species in H₂O and D₂O“

europium aquo ion. This species shows the strongest splitting of the $^5D_0 \rightarrow ^7F_1$ transition (larger $\Delta E (N_V(B_{2q}))$), as can be seen in Fig. 14 and 15.

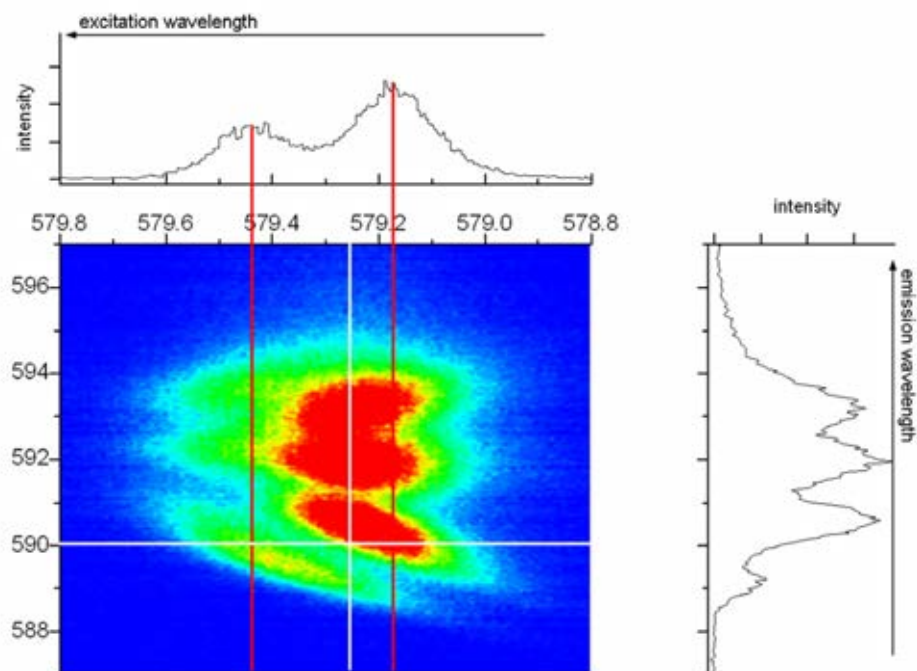


Figure 14: TLS of a 0.2 M solution of EuCl_3 in water at $\text{pH} = 5$; $T = 5$ K. The top spectrum shows the excitation cross-section at $\lambda_{\text{em}} = 590$ nm, while the graph on the right hand side shows the emission spectrum applying non-selective excitation at $\lambda_{\text{exc}} = 579.26$ nm (white lines). Red lines indicate the cross-sections at species-selective excitation wavelengths ($\lambda_{\text{exc}1} = 579.43$ nm and $\lambda_{\text{exc}2} = 579.17$ nm), of which the corresponding emission spectra are shown in Figure 15.

Furthermore, it is interesting to consider the ratio of the crystal field parameters B_{20} and B_{22} , determined from the energy splitting of the 7F_1 multiplet. B_{20} represents the energy splitting between the highest ($^7F_{1-3}$) and the lowest energy level ($^7F_{1-1}$) in relation to the barycenter, whereas B_{22} displays the energy separation of the $^7F_{1-2}$ and the $^7F_{1-3}$ level. Obviously, the $^7F_{1-1}$ level of species 1 exhibits a significantly lower energy than that of the other species, resulting in a higher absolute value of B_{20} and in turn of the ratio B_{20}/B_{22} (see Table 1). The latter was also predicted by the crystal field calculations and therefore further supports the assignment of species 1 as eightfold coordinated.

This assignment is also in good agreement with the expected relative excitation energies for eight- and nine-fold coordination. Considering the nephelauxetic effect, the excitation energy is dependent on bond covalence, which in turn is mainly determined by the distance and number of the coordinating molecules. Thus, according to MALTA et al. an increase of the overlap polarizability, mainly caused by a contraction of the Eu(III)-to-ligand distance, is accompanied by a red-shift of the excitation wavelength. Hence, the excitation wavelength of the eight-fold coordinated Eu(III) (species 1) is expected to be red-shifted compared to the nine-fold coordinated (species 2), if the contraction of the bond length outweighs the loss of one H_2O ligand. Preliminary DFT calculations indicated that within the eightfold coordinated species more charge of the Eu(III) is transferred to the ligands than in

$[\text{Eu}(\text{H}_2\text{O})_9]^{3+}$. Therefore, the bonds are slightly more covalent in species 1, which is in agreement with the species assignment based on the position of the ${}^5\text{D}_0 \rightarrow {}^7\text{F}_0$ transition.

Table 2: Data collected for the two distinct species in aqueous solution at 5 K.

			species 1	species 2
number of coordinating H_2O molecules	$n_{\text{H}_2\text{O}}$		8	9
excitation wavelength	λ_{exc}	[nm]	579.43	579.17
decay time	τ	[μs]	123 \pm 9	109 \pm 8
crystal field energy splitting	ΔE	[cm^{-1}]	142 \pm 4	124 \pm 4
crystal field strength parameter	$N_{\text{v}}(\text{B}_{2\text{q}})$	[cm^{-1}]	656 \pm 16	568 \pm 17
crystal field parameters	B_{20}	[cm^{-1}]	-392 \pm 11	-328 \pm 13
	B_{22}	[cm^{-1}]	-98 \pm 13	-103 \pm 9
ratio of crystal field parameters (calc. values)	B_{20}/B_{22}		4.0 (3.1)	3.2 (2.5)
point symmetry group			C_1, C_2 or C_s	$\text{C}_{2\text{v}}$
asymmetry ratio	r		0.56 \pm 0.07	0.35 \pm 0.04

In Figure 15 high-resolution luminescence spectra of the eight- and nine-fold coordinated species are shown. The spectra were obtained from the total luminescence spectrum for site-selective excitation at $\lambda_{\text{exc}1} = 579.43$ nm and $\lambda_{\text{exc}2} = 579.17$ nm (see Figure 14, red vertical lines).

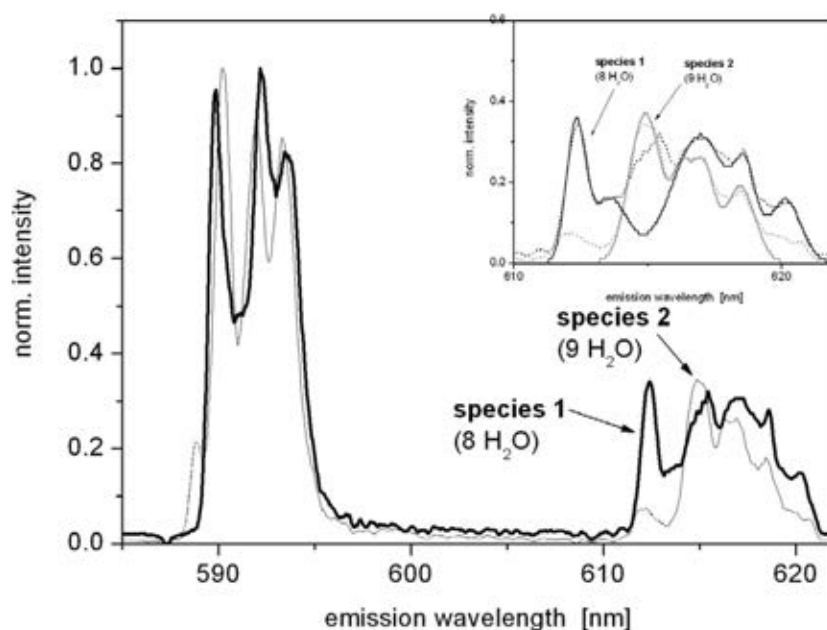


Figure 15: Normalized luminescence emission spectra (${}^5\text{D}_0 \rightarrow {}^7\text{F}_1$ and ${}^5\text{D}_0 \rightarrow {}^7\text{F}_2$ transition) of both species in H_2O , at selective excitation wavelengths indicated in Figure 14 as

vertical red lines. Black curve: species 1, $\lambda_{\text{exc1}} = 579.43$ nm; grey curve: species 2, $\lambda_{\text{exc2}} = 579.17$ nm. The dotted parts of the spectrum of species 2 (approx. at $\lambda_{\text{em}} = 589$ nm and 612 nm) are related to residual emission belonging to species 1 (see Figure 14). For clarity, the inset shows the splitting of the ${}^5\text{D}_0 \rightarrow {}^7\text{F}_2$ transition in detail; the transition was fitted with five and four GAUSS peaks for the eight- and the ninefold coordinated Eu(III) species, respectively.

From the emission spectra one can calculate the asymmetry ratio r , it is expected to be larger for the eightfold coordinated species because of larger distortion from inversion symmetry. For species 1, r_1 was calculated to be 0.56 ± 0.07 , whereas for species 2, $r_2 = 0.35 \pm 0.04$ was found (see Table 2). For species 1 literature data are available ($r = 0.56$), which are in excellent agreement with the value at hand and thus further confirm the assignment made for species 1 and 2 (see Table 2).

For eightfold-coordinated Eu(III) a square antiprismatic coordination polyhedron (ideal polyhedron: D_{4d} symmetry) and for ninefold coordinated $[\text{Eu}(\text{H}_2\text{O})_9]^{3+}$ a tricapped trigonal prismatic coordination polyhedron (ideal: D_{3h} symmetry) is expected, based on crystal data of model compounds. In the case of species 1, we found that the ${}^5\text{D}_0 \rightarrow {}^7\text{F}_1$ transition shows three STARK levels, and five were found for the ${}^5\text{D}_0 \rightarrow {}^7\text{F}_2$ transition (corresponding to the maximum STARK splitting; see Figure 15). Therefore, the lowest point symmetry groups possible (C_1 , C_2 or C_s) can be assigned to species 1. For the ninefold coordinated species 2, a C_{2v} symmetry can be determined from the STARK splitting pattern (see Figure 2): the ${}^5\text{D}_0 \rightarrow {}^7\text{F}_1$ transition shows 3 lines (the peak at 589 nm belongs to species 1 as can be seen in Fig. 1, see the cross section for 579.17 nm) and the ${}^5\text{D}_0 \rightarrow {}^7\text{F}_2$ transition shows 4 lines (see inset of Figure 15, the peak at 612 nm belongs to species 1). These findings suggest that in the frozen solutions distorted coordination polyhedra are present. Regarding the dynamic interchange between species 1 and 2 in liquid samples, with a water molecule entering/leaving the coordination polyhedron, the latter is not able to stay in an ideal symmetry at all and a lowering of the average symmetry down to C_{2v} and even lower symmetry for the liquid state can be expected. Thus, in the frozen solutions a snapshot is seen. Changing the solvent from H_2O to D_2O , independent on the counter ion, virtually the same TLS was obtained and no isotopic effect in the luminescence spectra was detectable.

In order to further support the species assignment of the spectral analysis, luminescence decays under site-selective excitation conditions were recorded in H_2O as well as in D_2O . In H_2O for $\lambda_{\text{exc1}} = 579.43$ nm and $\lambda_{\text{exc2}} = 579.17$ nm mono-exponential luminescence decays were obtained, with decay times $\tau_1 = (123 \pm 9)$ μs (species 1; 8 H_2O) and $\tau_2 = (109 \pm 8)$ μs (species 2; 9 H_2O ; see Table 2), respectively. In aqueous solutions, the major contribution in the deactivation of Eu(III) is attributed to the presence of hydroxyl groups in the first coordination sphere. Hence, due to the absence of OH-induced quenching, the luminescence decay times measured in D_2O solutions are considerably longer: (3.5 ± 0.12) ms for species 1 and (3.7 ± 0.18) ms for species 2.

Utilizing the correlation between decay time and the extent of OH coordination, equations such as Equation (7) have been derived empirically.

$$n_{\text{H}_2\text{O}} = 1.11 \cdot \left(\frac{1}{\tau_{\text{H}_2\text{O}}} - \frac{1}{\tau_{\text{D}_2\text{O}}} - 0.31 \right) \quad (19)$$

In spite of being frequently used to estimate the number of coordinated water molecules ($n_{\text{H}_2\text{O}}$) from luminescence decay time measurements, such correlations have certain

limitations, especially when comparing complexes with strongly different ligands, in different media or under different physical conditions. However, they work very well in the case of eight- and ninefold coordinated Eu(III)(aq) measured under identical experimental conditions: the decay time data of the present study are in good agreement with literature data, such as of YAMASE et al. ($\tau = 130 \pm 10 \mu\text{s}$ for $[\text{Eu}(\text{H}_2\text{O})_8]^{3+}$ determined in a solid host crystal at 4.2 K). Moreover, the findings enable an extension of the data basis for Equation (19), which so far was based on measurements of Eu(III) complexes with $n_{\text{H}_2\text{O}} \leq 6$. Combining literature data with our data set, the coefficients of Equation (19) are only slightly changed, and hence the overall validity of the equation is further supported. Thus, the time resolved approach further supports the assignments that were made based on spectral data: species 1 ($\lambda_{\text{exc}} = 579.43 \text{ nm}$; longer decay time) \rightarrow eightfold coordinated, species 2 ($\lambda_{\text{exc}} = 579.17 \text{ nm}$; shorter decay time) \rightarrow ninefold coordinated. From the spectroscopic data collected it may be further concluded that the majority of Eu(III) is coordinated by nine H_2O molecules.

Influence of chloride or sulphate anions on the speciation of europium in D_2O monitored by site-selection spectroscopy at 5 K

In the preceding chapter the “frozen” equilibrium between the eight- and ninefold Eu(III) species in H_2O at ultra-deep temperature ($\approx 4 \text{ K}$) using FLN spectroscopy was characterized in depth. The equilibrium was chosen as a sensitive intrinsic probe to monitor even small effects of the ionic strength on the solution conditions. In the present paragraph high-resolution site-selective luminescence spectroscopy was applied to monitor the influence of different inorganic ligands – namely perchlorate, chloride, and sulphate – on the equilibrium between eight- and nine-fold coordinated Eu(III) in D_2O (The deuterated solvent was chosen because the strong OH-group related quenching was eliminated and significantly higher luminescence intensities were obtained improving the signal-to-noise ratio of the measurements).

While sulphate was expected to be a relatively strong ligand, perchlorate as well as chloride are considered a weak ligands not entering the first coordination sphere of the Eu(III) ion. The influence of these anions on the luminescence characteristics was monitored up to an ionic strength of $I = 6$. Based on the spectroscopic results conclusions on the second coordination sphere depending on the counter ion are drawn.

Figure 16 shows the excitation spectra of Eu(III) in the presence of the different anions for an ionic strength.

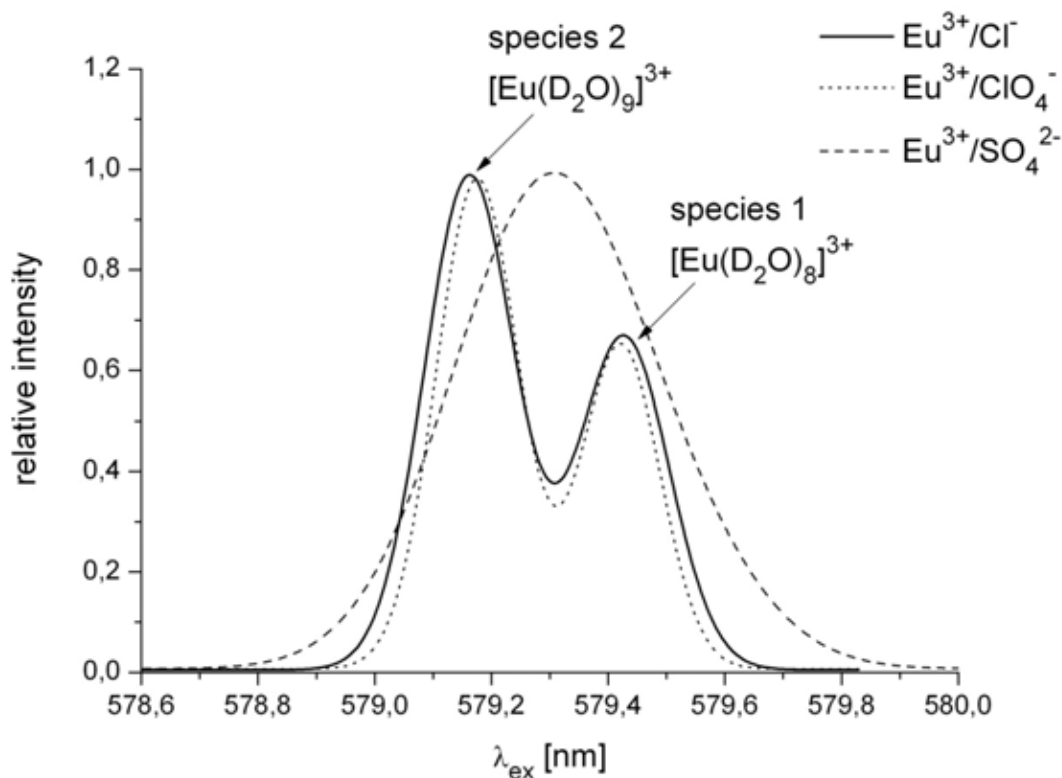


Figure 16: Excitation spectra of a 0.2 M Eu(III) solution in the presence of different counter ions for the wavelength range of $578.6 \text{ nm} < \lambda_{\text{ex}} < 580.0 \text{ nm}$, which corresponds to the ${}^5\text{D}_0 \leftarrow {}^7\text{F}_0$ transition (in D_2O , $I = 0.4$ in case of perchlorate and chloride, $I = 0.7$ in case of sulphate).

It can be seen that perchlorate and chloride yielded almost identical excitation spectra with two distinct peaks at $\lambda_{\text{ex}} = 579.17 \text{ nm}$ and $\lambda_{\text{ex}} = 579.43 \text{ nm}$ corresponding to $[\text{Eu}(\text{D}_2\text{O})_9]^{3+}$ and $[\text{Eu}(\text{D}_2\text{O})_8]^{3+}$, respectively. Considering the relative height of the two peaks, the equilibrium seems to be largely independent on the anions. The nearly unaltered excitation spectrum of Eu(III) suggests that perchlorate and chloride are weak ligands forming only outer-sphere complexes.

In contrast, in the presence of sulphate ions a distinctly altered excitation spectrum was found. The observed strong change is attributed to the formation of inner-sphere complexes, in which water molecules are removed from the first coordination sphere by the sulphate. Compared to highly crystalline samples like $\text{EuCl}_3 \cdot 6\text{H}_2\text{O}$ (solid), which show very sharp peaks, in case of sulphate an increased inhomogeneous broadening of the excitation spectrum is found. Moreover, a closer inspection of the excitation spectrum showed a slight asymmetry which is an indication that different species may be present in the sample, although according to a species analysis based on literature data only $\text{Eu}(\text{SO}_4)_2^-$ complexes are expected.

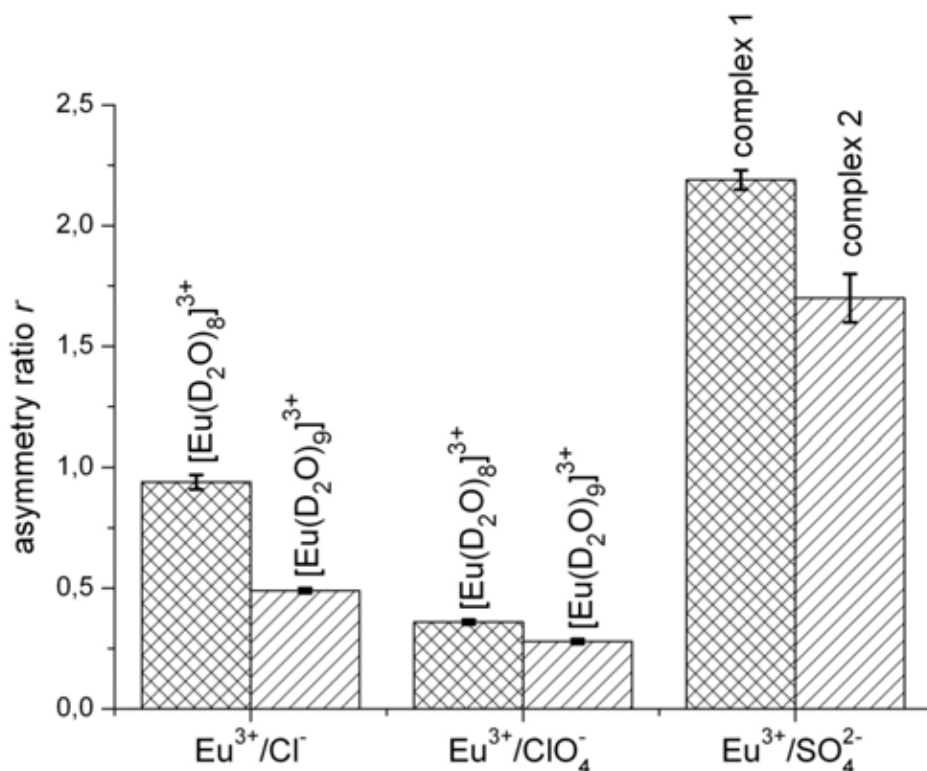


Figure 17: Asymmetry ratio r of a 0.2 M Eu(III) solution with several counter ions in D_2O ($I = 0.4 - 0.7$, $\lambda_{\text{ex1}} = 579.58 \text{ nm}$ and $\lambda_{\text{ex2}} = 579.17 \text{ nm}$)

From the emission spectra obtained under site-selective excitation the asymmetry ratio r was calculated (Figure 17). The difference in the absolute values of r between chloride and perchlorate on the one hand side and sulphate on the other side underlines that the complexation mode of these ions is different. In general, the replacement of water (or D_2O in the present study) from the first coordination sphere of europium by an (in)organic ligand leads to changes in complex geometry (symmetry), which in turn are expected to have an impact on the intensity of the hypersensitive ${}^5\text{D}_0 \rightarrow {}^7\text{F}_2$ transition (and subsequently on r). Compared to asymmetry ratio of sulphate the asymmetry ratio r of perchlorate is five times smaller. The distinct increase of r in case of sulphate is a strong indication for the formation of inner-sphere complexes. Chloride and perchlorate yielded smaller values of r pointing to outer-sphere complexes with water (or D_2O) distributed relatively symmetrically in the first coordination sphere of europium. Due to the stronger polarizability of chloride in comparison to the perchlorate, the intensity of the ${}^5\text{D}_0 \rightarrow {}^7\text{F}_2$ is expected to be higher yielding a slightly higher r (see Figure 17).

In addition also site-selectively excited luminescence-decays were recorded. In all cases mono-exponential luminescence decays were obtained. The calculated luminescence decay times are summarized in Table 3. Here, for sulphate the shortest luminescence decay times were found indicating that sulphate ions are intrinsically quenching the Eu(III)-luminescence (possibly via a S=O bond vibration). The comparison of the luminescence decay times for the eight- and nine-fold coordinated species in case of chloride or perchlorate and for “red” and “blue” excitation in case of sulphate also revealed slight but distinct differences. While for perchlorate very similar values for the luminescence decay times of the two species were found, in case of chloride and sulphate slightly different numbers were calculated. The

perchlorate data underline the very weak potential of the ion to enter the first coordination sphere of europium independent on the number of surrounding water molecules. On the other hand chloride seems to respond to the number of water molecules in the first coordination sphere of europium. Chloride ions may even quench the Eu(III) luminescence in the special case of inner-sphere complexation. Although from the spectral measurements no indication for an inner-sphere complexation of chloride was found, the slight difference in the decay times may be seen as an effect resulting from chloride located in the second coordination sphere of the eight-fold coordinated species. Here, the chloride may approach the europium ion slightly closer due a decrease in the shielding by the water molecules of the first coordination sphere.

Table 3: Luminescence-decay times of the 5D_0 -sublevel of a 0.2 M Eu(III) ($I = 0.4 - 0.7$) solution with different counter ions in D_2O ($^a \lambda_{ex} = 579.58$ nm).

	τ [ms] $\lambda_{ex} = 579.48$ nm $n_{H_2O} = 8$	τ [ms] $\lambda_{ex} = 579.17$ nm $n_{H_2O} = 9$
Eu ³⁺ /Cl ⁻	3.54 ± 0.03	3.88 ± 0.09
Eu ³⁺ /ClO ₄ ⁻	3.59 ± 0.07	3.50 ± 0.07
Eu ³⁺ /SO ₄ ²⁻	2.78 ± 0.05 ^a	2.98 ± 0.06

Variation of the ionic strength

Since sulphate showed an inner-sphere complexation already at moderate ionic strength, only chloride and perchlorate were further investigated up to an ionic strength of $I = 12$. In the experiments luminescence excitation spectra as well as site-selectively excited emission spectra (calculation of asymmetry ratio r) and luminescence decay times were collected.

Perchlorate: In Figure 18 the excitation-spectra of Eu(III) as a function of ionic strength for the range of $0.5 < I < 12$ are shown. The normalized spectra indicate that the relative amount of eight- and nine-fold coordinated europium is influence by the ionic strength (see Figure 18). The increase of the relative contribution of the nine-fold coordinated species can be seen from the ratio of the related areas (fitted with a Gaussian function) in the excitation spectrum. The shift of the equilibrium towards the nine-fold coordinated species upon increasing the ionic strength is strongest for the range of $I < 4$. A similar tendency is seen for the asymmetry ratio. The asymmetry ratio r decrease from 0.5 at low ionic strength to about 0.3 at ionic strength $I > 2$. It seems that at medium to high ionic strength the small differences between eight- and nine-fold coordinated europium are “overruled” by the presence of a large excess of perchlorate.

In Table 4 the luminescence decay times for both species determined at different ionic strength obtained for site-selective excitation conditions are compared. Although the ionic strength was varied over a large range, neither for the eight-fold nor the nine-fold coordinated europium aquo species any clear influence on τ was found, which is in good agreement with the findings of BUENZLI ET AL. This further stresses the fact that perchlorate shows – if any - only very weak specific interactions with europium.

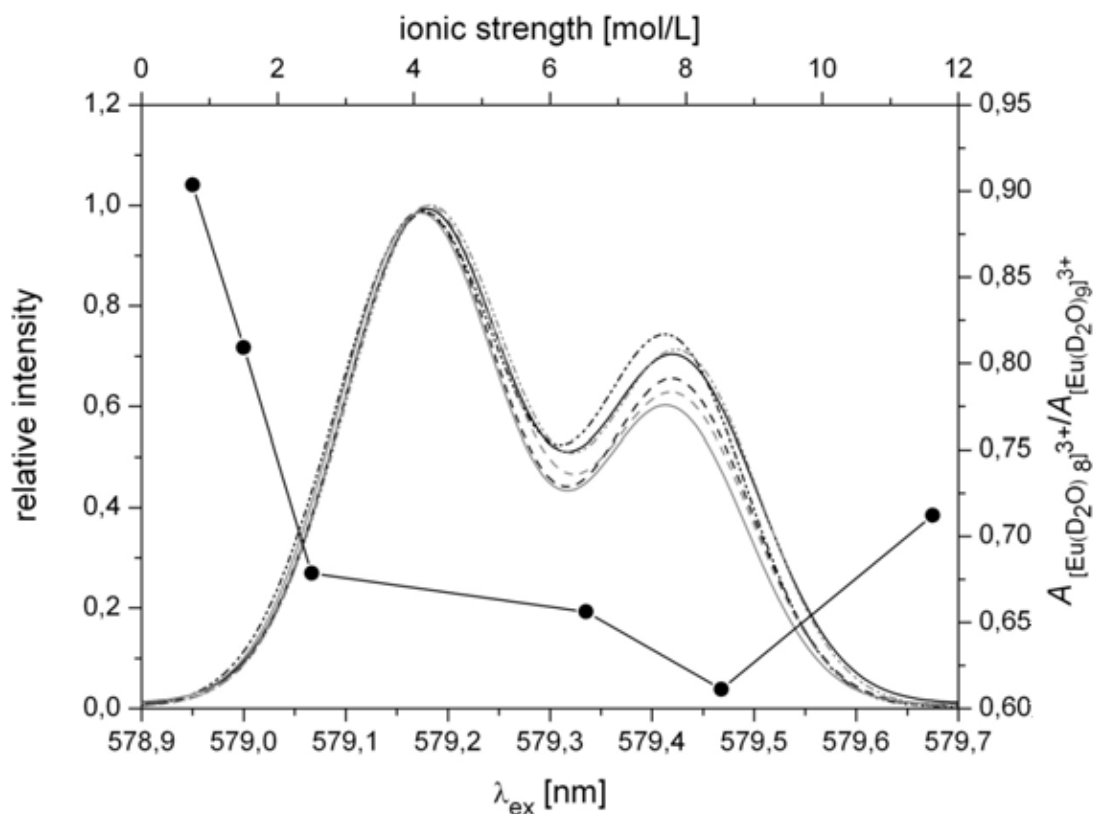


Figure 18: Normalized excitation spectra of Eu(III) solutions in D₂O in the wavelength range of 578.9 nm < λ_{ex} < 579.7 nm, which corresponds to the $^5\text{D}_0 \leftarrow ^7\text{F}_0$ transition, as a function of ionic strength (counter ion was perchlorate; T = 5 K).

Table 4: Luminescence-decays of Eu(III) in D₂O as a function of ionic strength (counter ion was perchlorate; $^a\lambda_{\text{ex}} = 579.48$ nm; $^b\lambda_{\text{ex}} = 579.17$ nm; T = 5 K).

ionic strength	$[\text{Eu}(\text{D}_2\text{O})_8]^{3+}$ τ^a [ms]	$[\text{Eu}(\text{D}_2\text{O})_9]^{3+}$ τ^b [ms]
0.75	3.60 ± 0.12	3.54 ± 0.06
1.50	3.59 ± 0.07	3.50 ± 0.07
2.50	3.43 ± 0.15	3.45 ± 0.12
6.53	3.52 ± 0.19	3.45 ± 0.09
8.52	3.51 ± 0.05	3.56 ± 0.03
11.62	3.40 ± 0.03	3.50 ± 0.07

Chloride: The overall intensity of the $^5\text{D}_0 \leftarrow ^7\text{F}_0$ transition increases with increasing ionic strength. Like for perchlorate the relative amount of eight- and nine-fold coordinated aquo species of europium changed with increasing ionic strength. In Figure 19 the ratio of the surface integrals obtained from a Gaussian fit is plotted in dependence of ionic strength. As seen for chlorated the relative contribution of $[\text{Eu}(\text{H}_2\text{O})_8]^{3+}$ drops with increasing chloride concentration (ionic strength). In contrast to perchlorate the asymmetry ratio r is increasing with increasing chloride concentration. In Figure 20 the asymmetry ratios of the eight- and nine-fold coordinated species are shown. For both species a comparable increase of r is found. While the eight- and nine-fold coordinated species show a small difference in their

related luminescence decay times, for each species no effect of the ionic strength adjusted by the chloride concentration was observed (see Table 5). This is in accordance with the findings for perchlorate, which did also not induce any alteration of the luminescence decay time.

Table 5: Luminescence-decays of 5D_0 -sublevel of Eu(III) solutions in D_2O as a function of ionic strength (counter ion chloride; $^a\lambda_{ex} = 579.48$ nm; $^b\lambda_{ex} = 579.17$ nm; $T = 5$ K).

ionic strength I	$[Eu(D_2O)_8]^{3+}$ τ^a [ms]	$[Eu(D_2O)_9]^{3+}$ τ^b [ms]
0.12	3.39 ± 0.08	3.73 ± 0.07
0.60	3.48 ± 0.04	3.79 ± 0.02
1.14	3.54 ± 0.03	3.88 ± 0.09
3.10	3.45 ± 0.04	3.80 ± 0.04
4.60	3.43 ± 0.04	3.85 ± 0.04
6.20	3.45 ± 0.06	3.80 ± 0.04

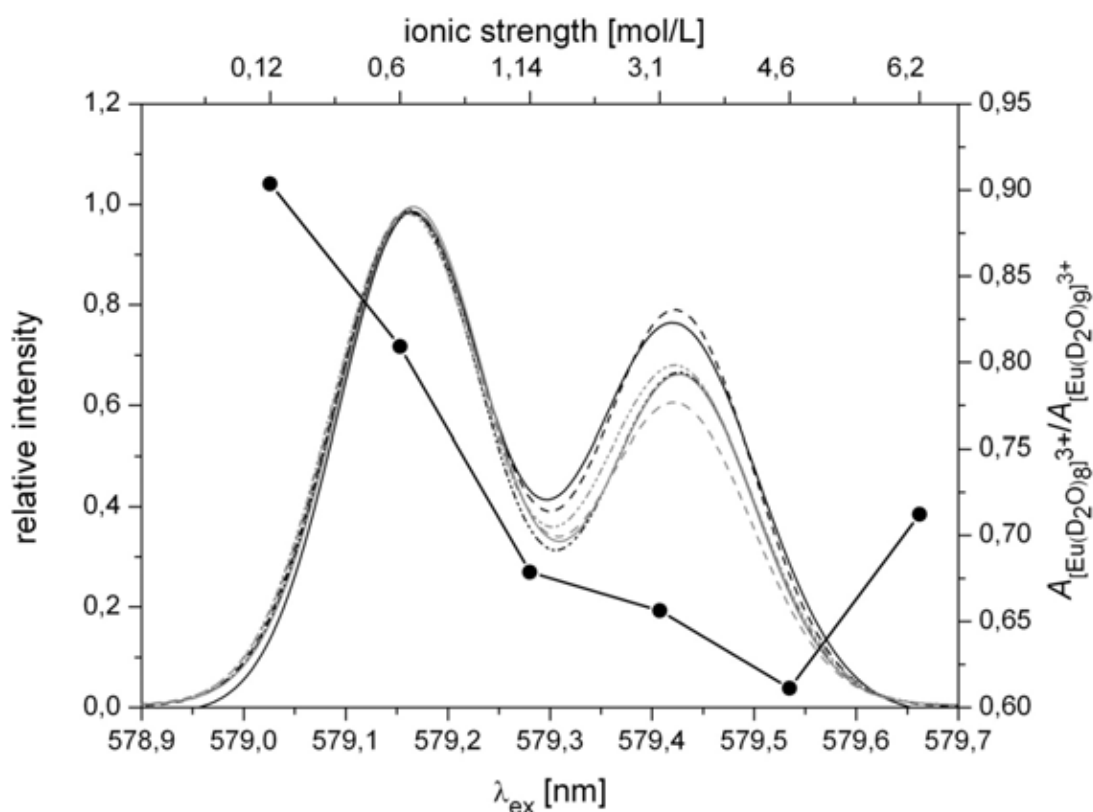


Figure 19: Normalized excitation spectra of Eu(III) solutions in D_2O in the wavelength range of $578.9 \text{ nm} < \lambda_{ex} < 579.7 \text{ nm}$, which corresponds to the $^5D_0 \leftarrow ^7F_0$ transition, as a function of ionic strength (counter ion chloride; $T = 5$ K).

The intensity increase of the $^5D_0 \leftarrow ^7F_0$ transition has been described by BREEN and HORROCKS was attributed to an inner-sphere complexation of chloride ions, which contradicts findings of STUMPF et al., who describe a luminescence quenching by chloride due to inner-sphere

complexation. From the spectral and time-resolved luminescence data presented in this study, it can be concluded that no inner-sphere complexation by chloride is observed. Especially the spectral data point to an outer-sphere complexation, since no spectral shift is observed (like in case of sulphate), only the asymmetry ratio r was found to increase (for both species). The increased intensity of the ${}^5D_0 \leftarrow {}^7F_0$ transition and the alteration of r are related to alterations of the second coordination sphere (outer-sphere binding) of the europium ion by the increased concentration of chloride ions. A distortion in the second coordination sphere will also slightly influence the inner coordination sphere and subsequently may be reflected by small changes in the transition probabilities of the different electronic transitions of the europium ion (e.g., the ${}^5D_0 \leftarrow {}^7F_0$ transition or the ${}^5D_0 \leftarrow {}^7F_2$ transition).

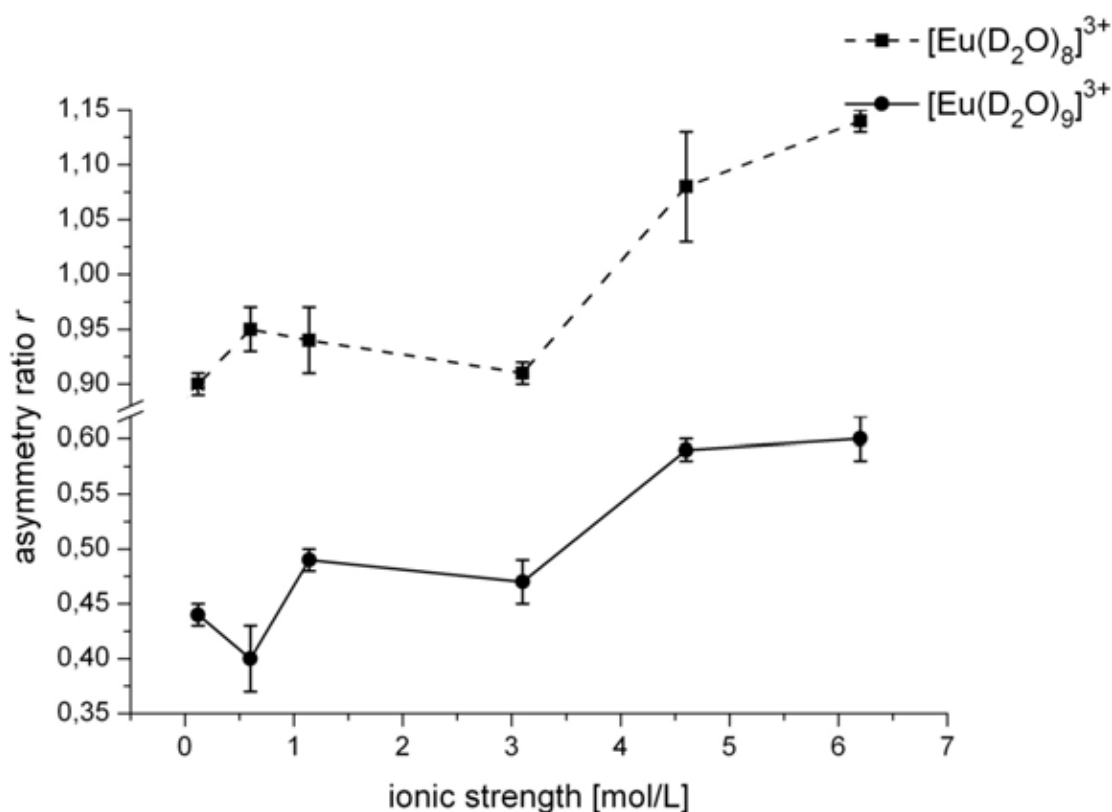


Figure 20: Asymmetry ratios of Eu(III) solutions in D_2O as a function of ionic strength (counter ion chloride; $T = 5 \text{ K}$).

3.4 Molecular ruler

Distribution of binding sites in model polymers

The distribution of binding sites in natural occurring polymers, like humic and fulvic acids, as well as on mineral surfaces is a key question for the understanding of sorption processes between metal ions and complexing agents like organic and inorganic ligands. As model

system for natural occurring polymers, poly (acrylic acid) acid (PAA⁸) was used. For a first insight on the distribution of inorganic binding sites on mineral surfaces Kaolinit KGa 2 was used. In the field of a final disposal of nuclear waste, the metal ions of main interest are actinide and lanthanide ions. As it is known that the energy transfer mechanism proposed by Förster can be applied to lanthanide ions, this study deals with the intra-lanthanide energy transfer (ILET). Here, Eu(III) and Tb(III) can be used as donors. A suitable acceptor is Nd(III). In contrast La(III) cannot act as an acceptor for ILET. Due to this fact, from measurements with La(III) one can observe effects on the donor luminescence resulting only from the presence of additional metal ions, which can compete for binding sites. The main difference in the addition of La(III) or Nd(III) to solutions containing PAA and Tb(III) is shown in Figure 21.

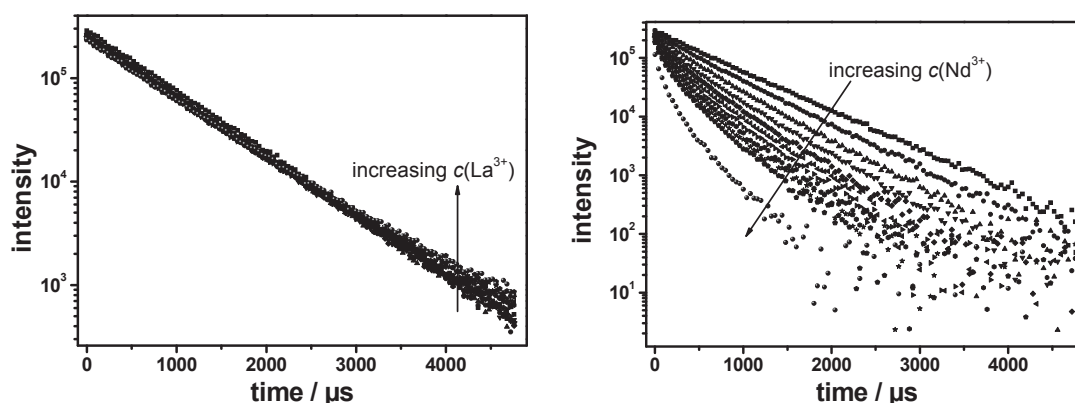


Figure 21: Influence upon addition of different lanthanide ions (left: La(III), right: Nd(III)) on the time-dependent Tb(III) luminescence in complexes with PAA 450 000. The concentration of Nd(III) and La(III) increases from 0 mmol·L⁻¹ up to 0.91 mmol·L⁻¹. $\lambda_{\text{ex}} = 377 \text{ nm}$, $\lambda_{\text{em}} = 545 \text{ nm}$, pH 5, $c_{\text{Tb(III)}} = 0.2 \text{ mmol}\cdot\text{L}^{-1}$, $c(\text{PAA}) = 5 \text{ g}\cdot\text{L}^{-1}$.

While upon addition of Nd(III) to Tb(III)-PAA complexes the Tb(III) luminescence decay becomes faster, the addition of La(III) shows nearly no effect. Only a slight increase in the Tb(III) luminescence decay time could be observed. A comparable behavior was also found for Eu(III) as donor. From the measurements with La(III) it can be deduced, that the quenching of the donor's luminescence is not only an effect of a replacement of donor ions from binding sites, but must be the result of a different process. The quenching of the luminescence is caused by an intra-lanthanide energy transfer (ILET). As mentioned above, La(III) cannot act as acceptor in an ILET. Therefore, the donor's luminescence decay time is not quenched due to the presence of La(III) ions. As shown in Equation (10) the donor's luminescence decay time in presence of an energy acceptor like Nd(III) depends on the Förster distance R_0 and the distance R between donor and acceptor. The calculation of distances from the quenching of the donor's luminescence requires the knowledge of the

⁸ PAA with two different molecular weights – 450 000 g·mol⁻¹ (PAA 450 000) and 1 800 g·mol⁻¹ (PAA 1 800) – was included.

value of R_0 . In this study, it was tried to calculate R_0 according to Equation (5). Therefore, the orientation factor was set to $\kappa^2=2/3$ and the refractive index to $n = 1.334$. The overlap integral J can be calculated according Equation (6) from the donor luminescence spectrum and the acceptor absorption spectrum. A crucial parameter is the donor quantum yield Φ_D . In case of Eu(III) the quantum yield can be calculated from the luminescence emission spectrum

$$\Phi_D^{Eu^{3+}} = \frac{\tau(Eu^{3+})}{\beta(Eu^{3+})} \frac{64\pi^4 n^2}{3h} D_{MD,1} \quad (20)$$

with $D_{MD,1} = 884 \cdot 10^{-8} D^2$, ν_1 is the energy difference between the 5D_0 and the 7F_1 energy level in Eu(III), $\tau(Eu^{3+})$ is the luminescence decay time of the Eu(III) in absence of any energy acceptors, h is Planck's constant and $\beta(Eu^{3+})$ is the proportion of the luminescence intensity of the ${}^5D_0 \rightarrow {}^7F_1$ transition to the total luminescence intensity. In case of Tb(III) the equation for the luminescence quantum yield is

$$\Phi_D^{Tb^{3+}} = \frac{\tau(Tb^{3+})}{\beta(Tb^{3+})} A_{D_4 \rightarrow F_6} \quad (21)$$

The Einstein coefficient for the spontaneous transition ${}^5D_4 \rightarrow {}^7F_6$ can be calculated according Strickler-Berg from the absorption spectrum of the Tb(III) ion. The luminescence decay time of the Tb(III) is given by $\tau(Tb^{3+})$. Here, $\beta(Tb^{3+})$ is the proportion of the luminescence intensity of the ${}^5D_4 \rightarrow {}^7F_6$ transition to the total Tb(III) luminescence intensity. At this stage, the luminescence quantum yields for both donor lanthanide ions can be calculated from spectroscopic parameters like luminescence emission and/or absorption spectrum as well as luminescence decay time. Figure 22 shows the resulting Förster distances R_0 for Eu(III) or Tb(III) as donors and Nd(III) as acceptor in complexes with PAA as function of pH.

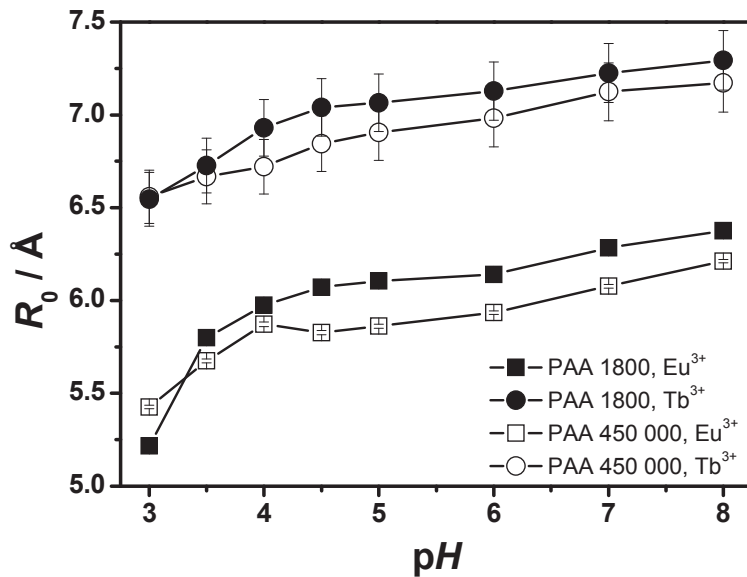


Figure 22: Förster distances R_0 as a function of pH for the donor-acceptor pair Eu(III)/Nd(III) (squares) and Tb(III)/Nd(III) (circles) in complexes with PAA 1 800 (closed symbols) or PAA 450 00 (open symbols).

For both donor-acceptor pairs – Eu(III)/Nd(III) and Tb(III)/Nd(III) – independent of the molecular weight of the PAA similar Förster distances were found. In case of Eu(III)/Nd(III) the Förster distance increases from values around $R_0 = 5.2 \text{ \AA}$ at pH 3 to $R_0 = 6.3 \text{ \AA}$ at pH 8. For the same pH range the donor-acceptor pair Tb(III)/Nd(III) gives Förster distances between 6.5 \AA and 7.3 \AA . The increase in the Förster distance results mainly from the increase of the quantum yield of the donor luminescence. Taking into account, that the transfer efficiency can only be measured with an accuracy between $1\% < \eta < 99\%$, the distance range, which can be observed with time-resolved measurements is $0.5 R_0 < R < 2R_0$.

According to Equation (9) it should be possible to deduce distances between a suitable acceptor like Nd(III) and a donor lanthanide ion like Tb(III) or Eu(III) from luminescence decay measurements in absence and presence of Nd(III). As can be seen from Figure 21, the donor luminescence decay becomes non-monoexponential upon addition of Nd(III). In the system under investigation, the lanthanide ions are complexed to binding sites (in this case carboxylic groups) on a polymer chain. As the concentration of the lanthanide ions is chosen, that no saturation of binding sites can happen, the lanthanide ions are randomly distributed on the polymer chains. Furthermore, the polymer chains themselves will have their certain conformation, which results from the number of charges arising from deprotonation of carboxylic groups as a function of pH and complexation of lanthanide ions. Therefore, the found non-monoexponential behavior of the luminescence decays of the donor lanthanides is addressed to a distribution of distances between the lanthanide ions acting as donor and acceptor. As shown in Equation (11) and (12), a Gaussian distribution can be applied to fit the measured luminescence decays. From the fitting, the mean distance between the lanthanide ions and the width of the distribution can be obtained.

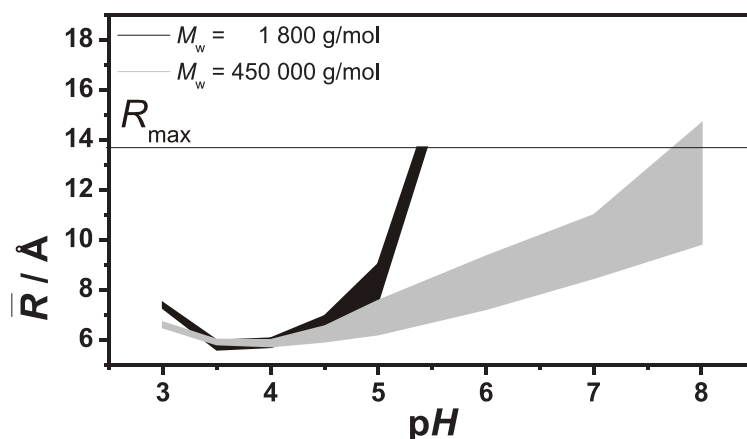


Figure 23: Distribution of distances obtained by time-resolved luminescence measurements. The black (PAA 1 800) and gray (PAA 450 000) filled domains results from averaging of the fitting of the donor's luminescence decay according Equation (8) in measurements with both donor-acceptor pairs – Eu(III)/Nd(III) and Tb(III)/Nd(III).

In Figure 23 the pH dependence of the distances between the donor lanthanide ion and acceptor lanthanide ion is shown. For both PAA the distance decreases slightly from pH 3 to a range between pH = 3.5 and pH = 4.0. At pH values above pH 4 the distance increases. Above pH = 5.5 the behavior for both PAA changes. For PAA 450 000 a virtually linear increase in the distance between donor and acceptor lanthanide ion was found, whereas for PAA 1 800 distances could only be deduced up to a pH = 5.5. At higher pH values the distance of both, donor and acceptor, lanthanide ions are too far for an efficient energy transfer.

The main difference between both PAA samples is the molecular weight and consequently the average length of the polymer chains. It is attempted to assume, that in case of PAA 450 000 donor and acceptor lanthanide ion are complexed to the same polymer chain and with increasing pH the unraveling of the polymer chain can be observed, reflected by a steady increase in the donor-acceptor distance. With increasing pH the degree of deprotonation of the carboxylic groups increases. Therefore, it is more likely for PAA 1 800 that donor and acceptor lanthanide ion are located at different polymer chains even at slightly acidic pH values. As a consequence, the mean distance between both ions is too far for an energy transfer as every polymer chain can diffuse freely through the solution.

As for both PAA the lanthanide ions are complexed by functional groups (binding sites) of the polymer chain, the distances of the lanthanide ions reflect the distribution of binding site along this polymer chain.

Distances between binding sites on mineral surfaces

The distribution of binding sites is also of interest in sorption processes. Here, mineral phases can act as inorganic complexation agents. The objective of this study is to apply the ILET – which was studied very detailed in the interaction of lanthanide ions with PAA – also to these sorption phenomena. The underlying idea is that sorption on mineral surfaces occurs at specific sites with certain distances to each other.

For this study Tb(III)/Nd(III) was chosen as donor-acceptor pair and KGa-2 as mineral phase. As a starting point, isotherms for the adsorption of Tb(III) onto KGa-2 were measured at pH 3 and pH 5. The amount of Tb(III) adsorbed to KGa-2 were calculated from the difference between the Tb(III) concentration in the solution before and after addition of 1 g of KGa-2. Before the luminescence measurements supernatant and solution was separated by centrifugation.

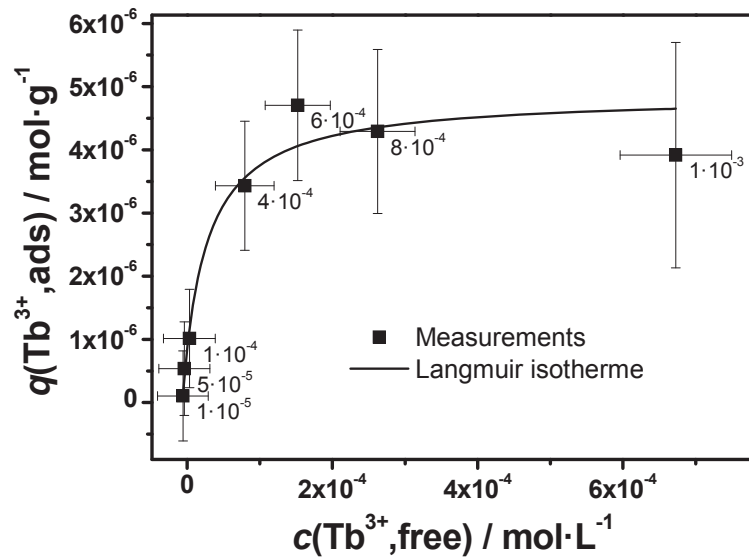


Figure 24: Adsorption isotherm of Tb(III) onto KGa-2 at room temperature and pH 3. In these measurements 1 g KGa-2 was added to 10 mL Tb(III) solution. The amount of sorbed Tb(III) was calculated from the difference of the Tb(III) concentration before and after addition of KGa-2 to this solution. The line results from the fitting of the experimental points according Equation (22).

The results of the sorption experiments are shown in Figure 24. A Langmuir isotherm was fitted to the experimental points

$$q = q_{\max} \frac{Kc}{1+Kc} \quad (22)$$

with q_{\max} the maximum number of sorption sites, K the equilibrium constant of the sorption process and c the concentration of the unsorbed Tb(III). The fitting showed a slight increase in the maximum number of binding sites from $q_{\max} = (4.9 \pm 0.5) \times 10^{-6} \text{ mol}\cdot\text{g}^{-1}$ at pH 3 to $q_{\max} = (6.4 \pm 0.6) \times 10^{-6} \text{ mol}\cdot\text{g}^{-1}$ at pH 5, which was expected as deprotonation increases with pH. The sorption constant K increases in the same pH range from $\lg(K/\text{L}\cdot\text{mol}^{-1}) = 4.5 \pm 0.2$ to $\lg(K/\text{L}\cdot\text{mol}^{-1}) = 5.1 \pm 0.3$. In the experiments with Tb(III) and Nd(III) the lanthanide ion concentration was fixed to $c(\text{Ln(III)}) = 4 \times 10^{-4} \text{ mol}\cdot\text{L}^{-1}$ to avoid saturation of the sorption sites.

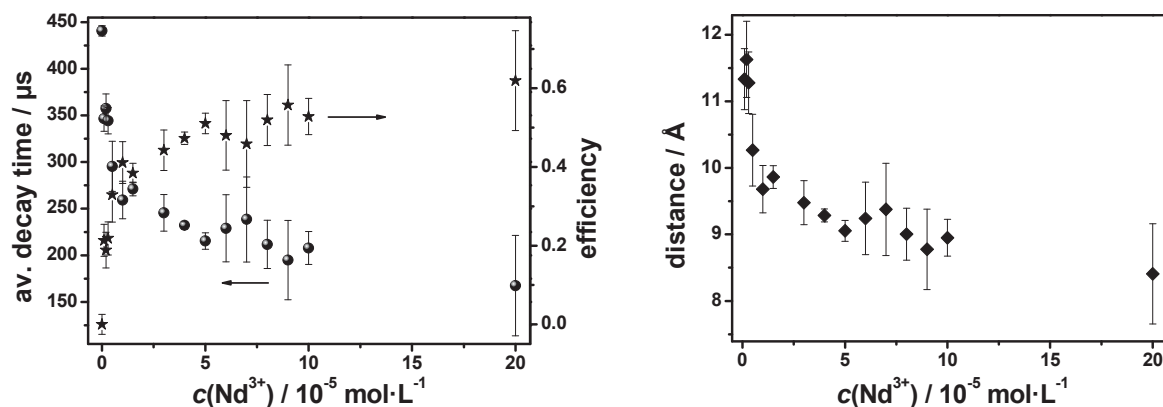


Figure 25: Left: Decrease in averaged luminescence decay time of Tb(III) (spheres) upon increasing Nd(III) concentration due to a transfer of energy. The energy transfer efficiency η (stars) was calculated according Equation (8). Right: From the efficiency of the energy transfer, the distances between Tb(III) and Nd(III) was calculated using Equation (7) and $R_0 = 9.12 \text{ \AA}$. This value was taken from the literature referenced in the text.

Figure 25 show some results of the sorption experiments, when Tb(III) and Nd(III) are present. After addition of KGa-2 and equilibrating of the suspension the solid and liquid phase were separated by centrifugation. With increasing Nd(III) concentration a decrease of the averaged luminescence decay time of Tb(III) was found. A similar decrease did not show up neither in the solution before nor in the supernatant after addition of KGa-2 (data not shown). Only adsorbed to a surface, both lanthanide ions are located close enough for an energy transfer.

As above derived, the decrease in luminescence decay time of Tb(III) can be connected to the distance between Tb(III) and Nd(III) (cf. Equation (7) and (8)). In this case the value of the Förster distance $R_0 = 9.12 \text{ \AA}$ was taken from the literature⁹. The calculations show a decrease of the donor-acceptor distance from $R = 1.2 \text{ nm}$ down to $R = 0.85 \text{ nm}$ following an increase of the Nd(III) concentration from $1 \mu\text{mol}\cdot\text{L}^{-1}$ up to $200 \mu\text{mol}\cdot\text{L}^{-1}$. As the distances derived stay virtually constant at concentration above $100 \mu\text{mol}\cdot\text{L}^{-1}$ it appeared, that 0.85 nm should be the shortest possible distance between the lanthanide ions and hence, the distance between suitable sorption sites for lanthanide ions.

⁹ from: Horrocks et al., Accounts of Chemical Research, 14, 384–392 (1981)

4. Summary

Eu(III) luminescence spectroscopy, both in the steady-state and the time-resolved mode, is an appropriate technique to study the properties of complexes between heavy metal ions and humic substances (or model compounds of such), which play a key role in the distribution of metal species in the environment. Unfortunately, room temperature luminescence spectra of Eu(III) complexes with aromatic and aliphatic carboxylic acids – model compounds of binding sites in humic substances – are too broad to fully exploit their potential analytical information content. It is shown that under cryogenic conditions fluorescence-line-narrowing (FLN) is achieved, and the highly resolved spectra provide detailed information on the complexes with different model ligands. Total luminescence spectra (TLS) were recorded, using the $^5D_0 \leftarrow ^7F_0$ transition for excitation and the $^5D_0 \rightarrow ^7F_1$ and $^5D_0 \rightarrow ^7F_2$ transitions for emission. The energy of the excitation transition depends on the ligand involved and the structure and composition of the complex. For most ligands, discontinuities in the high-resolution TLS indicated that more species, i.e. distinct complex structures coexisted in the sample. Selective excitation was performed to measure the species-associated luminescence decay times τ . The latter strongly depends on nearby OH oscillators from coordinating water molecules or ligand hydroxyl groups. Furthermore, the asymmetry ratios r were calculated and the variation of the excitation energy E_{exc} with the splitting of the 7F_1 triplet (ΔE) was determined, which yielded the crystal field strength parameter $N_v(B_{2q})$, as well as the crystal field parameters B_{20} and B_{22} .

The results extracted can uniquely complement data obtained from X-ray techniques. Moreover, limitations of other techniques due to averaging (e.g. EXAFS) can be overcome using site-selective excitation. All ligands investigated bind to the Eu(III) ion via oxygen (either neutral or charged) and there are just slight differences between the ligands with respect to the interacting groups (COO^- and/or OH). Consequently, the observed distinct differences in the high-resolution excitation and emission spectra (e.g., position of the $^7F_0 \leftarrow ^5D_0$ transition, STARK splitting) have to be attributed to heterogeneity of the sample, the number of different species as well as the stoichiometry of the complex, the corresponding geometry, and the capability of the ligand to form chelates. The latter is directly correlated with the strength and kinetic lability of the complexes formed. From the STARK splitting of the 7F_1 and 7F_2 multiplets a symmetry point group analysis was performed.

The interpretation of the data in terms of covalence of the bonds formed (nephelauxetic effect) is far from straightforward and should only be done with great care. The excitation energy is determined by several factors, each with ligand-specific contributions (covalent bonding, symmetry of the coordination polyhedron, STARK splitting), otherwise all lines in the jackstraws plots would coincide. Especially the different geometries of complexes have a significant impact on the STARK splitting. This in turn can affect the energy of the $^7F_0 \leftarrow ^5D_0$ transition, opposite to the shift caused by the nephelauxetic effect.

The overall comparison of $N_v(B_{2q})$ for aromatic carboxylates, aliphatic acids, and methoxybenzoates suggests to classify these ligands into different groups: “loose” complexes with low crystal field strength parameters (e.g. 4HB, BA, 4MB, GL, 3HP and GA), and more rigid complexes with high $N_v(B_{2q})$ values (e.g. 2HB, PHA, 3MB).

A straightforward interpretation of the cryogenic luminescence decay times with respect to the number of water molecules left in the first coordination sphere of Eu(III) is crucial. The reliability of this approach depends on whether a thorough calibration can be performed. In addition to the better spectral resolution and higher specificity of the excitation wavelength,

an important advantage of the cryogenic approach is the suppression of activated decay processes, thus providing a clearer picture of the influence of OH oscillators. Two major effects on the luminescence decay times have to be considered: i) water molecules in the second coordination sphere and ii) especially the presence of a hydroxyl group in α -position. Depending on the topology of the ligand, quenching contributions from coordinating OH groups and steric restrictions play a role and need to be considered.

The photophysical characterization of different europium aquo species is difficult at room temperature since the exchange of water molecules in the first coordination sphere is fast compared to the luminescence decay: $k \approx 1.6 \cdot 10^9 \text{ s}^{-1}$ (water exchange) vs. $9 \cdot 10^3 \text{ s}^{-1}$ (luminescence decay rate). Under the experimental ultra low temperature conditions applied an equilibrium representative for temperatures close to the freezing point of the solution was investigated, which is reasonable because after the solutions are frozen any reaction involving a major molecular movement – such as ligand exchange - should become extremely slow. Possible changes in the structure of the polycrystalline ice matrix surrounding Eu(III) i) are very weak and are not reflected in the spectral properties and ii) may be similar for the two aquo species investigated.

A clear spectroscopic evidence for the presence of two Eu(III) species in H₂O as well as in D₂O was found. These two species are assigned to eightfold coordinated (minor fraction) and ninefold coordinated (major fraction) aquo ions, based on an in-depth analysis of the high-resolution TLS and of the luminescence decays. The eightfold coordinated species 1 shows a longer decay time, has shorter Eu(III)-water distances and a less symmetrical arrangement in comparison with the ninefold coordinated species 2.

As a continuation of our spectroscopic investigations of Eu(III) under kryogenic conditions ($T \sim 5 \text{ K}$) the influence of counter ion as well as the of the ionic strength on the luminescence characteristics was evaluated. High-resolution total luminescence spectra of Eu(III) were collected in the presence of different inorganic counter ions (perchlorate, chloride, and sulphate) covering a ionic strength of the medium up to $I = 6$. For the different inorganic counter ions the effect on the equilibrium of eight- and nine-fold coordinated water was investigated determining fundamental spectroscopic parameters such luminescence decay time or crystal field parameters. Switching the solvent from H₂O to D₂O greatly eliminated the strong luminescence quenching effect of OH-oscillators and allowed to monitor less effective interactions of europium with different anions. Monitoring the equilibrium between eight- and nine-fold coordinated deuterio species at increasing concentrations of perchlorate and chloride showed distinct differences in the excitation spectra, in the site-selective emission spectra as well as in the site-selectively excited luminescence decay times. The high resolution power of ultra-low temperature luminescence measurements resolved effects of the second coordination sphere on the luminescence of europium. Perchlorate and chloride form exclusively outer-sphere complexes with Eu(III). In contrast, sulphate ions form inner-sphere complexes and significantly alter the equilibrium of eight- and nine-fold coordinated species. From the luminescence decay times obtained for “red-edge” and “blue-edge” excitation it may be concluded that more than one species is present in the sulphate ions containing system, probably due to variation in the coordination of the sulfate ligand between mono-or bidentate binding or due to a different number of coordinated D₂O molecules – but from the spectral measurements no clear distinction can be made. Perchlorate and chloride form only outer-sphere complexes with Eu(III) and influence only subsequently the first coordination sphere – at a much smaller extent. Both ions shift the

equilibrium towards $[\text{Eu}(\text{D}_2\text{O})_9]^{3+}$ when increasing the concentration of the corresponding anion. The asymmetry ratio showed different trends for the two anions with increasing ionic strength of the medium. While perchlorate showed no distinguishable effect on the eight- and nine-fold coordinated species, chloride affected the two species clearly in different ways. This can be also concluded from the differences in the luminescence decay times.

Depending on the electronic properties of the organic ligand the observed luminescence properties – especially the luminescence decay time – of the lanthanide complex are defined. For Eu(III) it could be shown that ligands with the capability to form charge transfer states in the complex are prone to a strong ligand-specific quenching. For salicylic acid (and related compounds) the temperature dependence of the ligand-specific quenching was evaluated. It was found that the determined activation energies for different ligands all lay within the same range indicating that the corresponding luminescence quenching in those complexes may be related to the same fundamental process. From transient absorption spectroscopy experiments it was concluded that the formation of an LMCT state with the Eu(III) complex is responsible for the efficient radiationless deactivation. Lanthanide ions such as Tb(III) (or La(III)) do not show comparable transient signals because the formation of a LMCT state in the complex with this class of ligands is not possible.

Energy transfer is a powerful tool to derive distances between energy donors and energy acceptors from luminescence measurements. In case of lanthanide ions, this energy transfer is referred to as ILET – intra-lanthanide energy transfer. From the experiments with PAA it can be concluded, that it is possible to derive any parameter needed for the calculation from luminescence measurements (emission and absorption). ILET can be applied to dissolved as well as sorbed species. Here, ILET was used to deduce information about the distribution of binding sites in a natural polymer analogue and on a mineral surface. In these type of calculations more sophisticated models, like distance distributions, can be included, which gives additional information – beyond mean distances – about the distribution. Furthermore, to be able to measure distances between 5 Å to 12 Å extends the observation range of distances accessible by other methods like EXAFS measurements.



JOINT PROJECT

INTERACTION AND TRANSPORT OF ACTINIDES IN NATURAL CLAY ROCK WITH CONSIDERATION OF HUMIC SUBSTANCES AND CLAY ORGANICS

Subproject

Investigations of temperature dependence of complexation and sorption of trivalent actinides (Am(III)) in the system actinid-NOM-natural clay rock-aquifer

MARGRET ACKER, ASTRID BARKLEIT, MELANIE MÜLLER,
JULIANE SCHOTT, STEFFEN TAUT, GERT BERNHARD

FINAL REPORT

Das diesem Bericht zugrunde liegende Vorhaben wurde mit Mitteln des Bundesministeriums für Wirtschaft und Technologie unter dem Förderkennzeichen **02 E 10417** gefördert.

Die Verantwortung für den Inhalt dieser Veröffentlichung liegt bei den Autoren.

VERBUNDEVORHABEN: Wechselwirkung und Transport von Actiniden im natürlichen Tongestein unter Berücksichtigung von Huminstoffen und Tonorganika

TEILPROJEKT: Untersuchungen zur Temperaturabhängigkeit der Komplexbildung und Sorption dreiwertiger Actinide (Am(III), Pu(III)) im System Actinid-NOM-natürliches Tongestein-Aquifer

Ausführende Institution: TU Dresden
Fakultät für Mathematik und Naturwissenschaften
Fachbereich Chemie und Lebensmittelchemie
Professur für Radiochemie
01062 Dresden

TU Dresden
Sachgebiet Strahlenschutz
01062 Dresden

Dresden, den 06.12.2011

Contents

1	Introduction	1
2	Am(III) and Eu(III) complexation by small organic ligands	3
2.1	Experimental	3
2.2.1	Solutions and reagents	3
2.1.2	Potentiometric titrations	3
2.1.3	Time-resolved laser-induced fluorescence spectroscopy	3
2.1.4	UV-vis spectroscopy with a Long Path Flow Cell	5
2.1.5	Data analysis and determination of complex formation constant	8
2.1.6	Fourier-transform infrared (FTIR) spectroscopy and Density functional theory (DFT) calculation	9
2.1.7	Isothermal titration calorimetry	9
2.2	Results and discussions	10
2.2.1	Potentiometric titration	10
2.2.2	Pyromellitic acid	11
2.2.3	Salicylic acid	20
2.2.4	Lactic acid	22
2.2.5	Citric, tartaric, and acetic acid	25
2.3	Conclusions and update of the thermodynamic database	28
3	Eu(III) sorption on Opalinus Clay	31
3.1	Experimental	31
3.1.1	Solutions and reagents	31
3.1.2	Batch experiments	31
3.1.3	Time-resolved laser-induced fluorescence spectroscopy	32
3.2	Results and discussion	33
3.2.1	Influence of Eu(III) concentration	33
3.2.2	Influence of pH	34
3.2.3	Influence of temperature	37
3.2.4	Influence of small organic ligands	40
3.3	Conclusions	43
4	References	44

Abstract

The main objective of this project was to study the interaction processes between An(III)/Ln(III) (represented by Am(III) and Eu(III), respectively), organic model ligands, and Opalinus Clay at elevated temperatures (until 80°C). The thermodynamic data ($\log\beta$, ΔG , ΔH and ΔS) for the complexation and sorption processes have been obtained. This broadens the thermodynamic database by data at elevated temperatures.

The complexation of Am(III)/Eu(III) with small organic ligands (pyromellitic, salicylic, lactic, acetic, citric, and tartaric acid) that serve as model ligands for natural organic material, like humic substances or clay organic was investigated by temperature dependent UV-vis and time-resolved laser-induced fluorescence spectroscopy (TRLFS).

For the first time, the UV-vis absorption spectroscopy utilizing an Long Path Flow Cell (LPFC) has been established for the speciation analysis of Am(III) at trace concentrations. A detection limit of $5 \cdot 10^{-9} \text{ mol} \cdot \text{L}^{-1}$ Am(III) was determined with a 2 m LPFC.

Several Am(III)/Eu(III)-organic ligand complexes were spectroscopically and thermodynamically characterized. General, all studied complexation reactions are endothermic and driven by entropy.

Furthermore, the interaction of Eu(III) with pyromellitic acid (1,2,4,5-benzene-tetracarboxylic acid) had been studied in detail with additional methods like isothermal titration calorimetry (ITC) and Fourier-transform infrared spectroscopy in combination with density function theory (DFT) calculations. At elevated temperature and higher concentration ($> 5 \text{ mM}$ Eu(III) and pyromellitic acid) a temperature-dependent polymerization was observed. It had been shown, that predominantly chelating coordination with two carboxylic groups in the monomeric complex and monodentate binding of a single carboxylic group in the polymeric complex of the polycarboxylate with Eu(III) occur.

The sorption of Eu(III) on Opalinus Clay was investigated in absence and presence of the small organic ligands citric and tartaric acid at different temperatures and under synthetic pore water conditions ($I = 0.4 \text{ M}$, $\text{pH} = 7.6$) by batch experiments. Time-resolved laser-induced fluorescence spectroscopy was used for analysis of the Eu(III) speciation in the binary system Eu(III)-Opalinus clay and ternary system Eu(III)-Opalinus clay-small organic ligand under pore water conditions.

The Eu(III) sorption was found to increase generally with temperature in a considerably endothermic reaction with an enthalpy of about $50 \text{ kJ} \cdot \text{mol}^{-1}$. In presence of tartrate or citrate the Eu(III) sorption decreases with increasing ligand concentration due to a complex formation of Eu(III) in solution. This complex formation was verified by TRLFS investigations. The detected Eu(III) surface species on Opalinus Clay with a luminescence lifetime of $(201 \pm 9) \mu\text{s}$ is not influenced by the presence of the studied organic ligands.

1 Introduction

To assess the long-term safety of nuclear waste repositories for high level radioactive waste a wide knowledge about the chemical and physical behaviour of radionuclides, particularly the actinides, is essential. In worst case scenarios like a water leakage into the repository a multitude of reactions of the stored radionuclides with solved or suspended components as well as interactions with the host rocks and backfill materials have to be considered quantitatively.

At present, argillaceous rock, like the Opalinus Clay formation in Switzerland, are under examination as potential host rocks for nuclear waste repositories due to their high sorption capacity for radionuclides, water impermeability and swelling properties [HOT2007, NAG2002]. In the framework of our project “Interaction and transport of actinides in natural clay rock with consideration of humic substances and clay organic” Opalinus Clay (OPA sample from bore core BHE-24/1) was chosen as model for such natural argillaceous rock. Opalinus clay consists of clay minerals like illite, chlorite, and kaolinite as well as minerals like quartz, calcite, pyrite, and siderite as main components [NAG2002]. In a repository based on argillaceous rock an initial temperature of around 100°C is expected [NAG2002] and should not be exceeded during the storage of radioactive waste [NEL2008]. The risk assessment has to consider this temperature, since the individual processes that determine the migration behaviour of radionuclides in a repository depend significantly on the temperature. Opalinus clay contains natural organic matter up to 1 %. Such natural organic matter (NOM) includes large macromolecules, like the ubiquitous humic and fulvic substances, kerogene as well as small molecules, like acetate or lactate, which are well soluble in water [HOT2007]. These compounds can interact as complexing agents with radionuclides and therefore impact the radionuclide migration. Thus, reliable thermodynamic data for the complexation behaviour of radionuclides with NOM are crucial to model and to predict the radionuclide transport in the near and far field of a nuclear waste repository.

The current thermodynamic databases are lacking fundamental data for the complexation of trivalent americium with small ligands at elevated temperatures. These small organic ligands like pyromellitate, salicylate, acetate, citrate, lactate, and tartrate can serve as model ligands for NOM. One aim of the project was to study the complexation behaviour of Am(III) and Eu(III) with these small organic ligands at higher temperature, up to 60°C. From the temperature dependent complexation constants the complexation enthalpies and entropies can be derived.

Two different spectroscopic methods were applied to study the complexation behaviour in detail. The time-resolved laser-induced fluorescence spectroscopy (TRLFS) was carried out to study the Eu(III) and for the first time also the Am(III) complexation with small molecule ligands. The UV-vis spectroscopy with an Long Path Flow Cell was applied to study the Am(III) complexation reactions at low Am(III) concentrations ($< 5 \cdot 10^{-7}$ M) which are of higher relevance for environmental conditions than the typically concentration of about $\sim 1 \cdot 10^{-4}$ M used in UV-vis measurements with a 1 cm cuvette. Additionally the isothermal microtitration calorimetry (ITC) as well as FT-IR measurements in combination with DFT calculations were used to investigate the Eu(III) complexation with pyromellitic acid in detail.

So far, investigations on the retention behaviour of OPA to radionuclides are mainly limited to ambient temperature [HAR2008, FRÖ20011, GLA2005, JOS2011, WU2009]. Only few studies deal with the impact of temperature on the radionuclide retention [BAU2005, TER2005, TER2006]. Tetre et al. [TER2006] investigated the sorption of different lanthanides on montmorillonite up to 150°C and observed that the sorption increases with

rising temperature at $\text{pH} > 6$. Bauer et al. did not observe any impact of temperature [BAU2005]. These contradictory results concerning the influence of temperature gave rise to the second aim of the present work to investigate the sorption of Eu(III) at elevated temperatures up to 60°C .

As a third aim, the impact of the small organic ligands on the Eu(III) sorption at elevated temperatures was studied. In literature was found that organic and inorganic ligands either increase or decrease the sorption of radionuclides (in dependence of pH, ionic strength, the concentration of complexing agents, the nature of complexing agents, and of the sorbent). Pathak et al. [PAT2007] found an increase of the Eu(III) sorption on silica in the presence of oxalate and phosphate due to the formation of ternary surface complexes, and a decrease of the Eu(III) sorption in the presence of acetate, carbonate, citrate, and EDTA due to a complex formation in solution in sequence of the complex formation strength of these ligands (acetate < carbonate < citrate < EDTA). In this work two small organic ligands, the citric and the tartaric acid were chosen as model ligands.

The present work discusses the Eu(III) sorption on OPA under realistic OPA pore water conditions ($\text{pH} 7.6$, $I = 0.4 \text{ M}$). The temperature influence and the impact of tartaric and citric acid on the Eu(III) sorption on OPA was investigated by batch sorption experiments up to 60°C . The temperature dependent distribution coefficients R_d were determined and the thermodynamic parameters enthalpy and entropy of the sorption were derived. In addition TRIFS investigations and experiments with ^{14}C -labeled citric acid provided an insight into the sorption mechanism and the influence of the organic ligands.

This work was part of a BMWi joint project between the Universities Mainz, Potsdam, München, Saarbrücken and the Institute of Nuclear Waste Management at the Karlsruher Institute of Technology and the Institute of Radiochemistry at the Helmholtz-Zentrum Dresden-Rossendorf.

2 Am(III) and Eu(III) complexation by small organic ligands

2.1 Experimental

2.1.1 Solutions and reagents

Eu₂O₃, EuCl₃·6H₂O, pyromellitic acid, salicylic acid, sodium salicylate, tartaric acid and sodium lactate were purchased from Aldrich or Fluka and used without further purification. Eu₂O₃ was dissolved in 0.1 M HClO₄ to obtain a 5·10⁻³ M Eu(III) stock solution. The Eu(III) concentration was verified with ICP-MS (Perkin Elmer).

The ²⁴³Am(III) stock solution was prepared by dissolving of AmO₂ powder (Oak Ridge National Laboratory) in 30% HNO₃. The Am(III) concentrations of sample solutions as well as the purity of the isotope was verified by α- and γ-spectrometry (Canberra, Ortec). Only the daughter nuclide of α-decay, Np-239 (half-life: 2.355 d), in equilibrium was determined (about 0.0001 % of Am).

In the complexation experiments, the ionic strength was adjusted with NaClO₄ (Merck, analytical grade) to 0.1 M. Necessary pH adjustments were performed with a pH meter (WTW) consisting of a pH electrode (Blue Line, Schott), filled with 3 M KCl, and a temperature sensor. The pH electrode was calibrated with buffer solutions (Merck) at the selected temperature. The adjustments were carried out with small amounts of NaOH (Merck) and HClO₄ (Merck) solutions of different concentrations with an accuracy of 0.05 pH units.

2.1.2 Potentiometric titration

Samples were prepared in an inert gas box (nitrogen) with carbonate-free deionized water. The measurements were carried out at CO₂ free condition under nitrogen atmosphere in 0.1 M NaClO₄ as an acid-base titration. 30 mL samples of 0.01 M ligand (pyromellitic acid, salicylic acid, tartaric acid, initial pH 2.0 each) were automatically titrated (736 GP Titrino / TiNet 2.50, Metrohm) with 0.1 M NaOH (carbonate-free, Titrisol, Merck) at temperatures between 10 and 60°C. Dynamic titration was used with a minimum drift of 0.5 mV/min and a delay time of at least 60 s at each point before measuring the pH with a Schott BlueLine 11 pH combination electrode with platinum diaphragm. The electrode was calibrated for each experimental run with standard buffers (pH 4.008 and 6.865, Schott). Titrations were done in triplicate between pH 2 and 7 at each temperature and analyzed using the program HYPERQUAD2006.

2.1.3 Time-resolved laser-induced fluorescence spectroscopy

Europium

Luminescence spectra were recorded using a pulsed flash lamp pumped Nd:YAG-OPO laser system from Continuum (Santa Clara, CA, U.S.A.) as described in [MOL2008]. The excitation wavelength was 394-395 nm. A constant time window of 1 ms was used for all measurements. Static and time-dependent luminescence spectra of Eu(III) were recorded at 565 – 650 nm (1200 line mm⁻¹ grating, 0.2 nm resolution, 2000 accumulations) and at 440 – 780 nm (300 line mm⁻¹ grating, 0.7 nm resolution, 200 accumulations), respectively. For time-resolved measurements, 41 spectra were recorded with 15-50 μs separation. Spectrophotometric titrations were done at least in triplicate starting with 5, 10 or 30 μM Eu(III) in 0.1 M NaClO₄ at pH 5.0 or 6.0. Subsequent additions of aliquots of a 0.01, 0.1, 0.5 or 2.5 M ligand stock solution (0.1 M NaClO₄, pH 5.0 or 6.0) covered ligand concentrations

from 10.0 μM to 1 mM (pyromellitic acid) or 0.1 M (salicylate, lactate). At least 20 spectra each were measured in the 25 to 70°C range using a stirred temperature-controlled cuvette holder (Flash 300TM, Quantum Northwest, U.S.A.) and 30 min initial equilibration time and additional 10 min after each injection of ligand at a given temperature.

Americium

For the first time Am(III) complexation with a small organic ligand was characterized with time-resolved laser-induced fluorescence spectroscopy (TRLFS) at room temperature and trace metal concentration [BAR2011a]. Only few speciation studies of Am(III) have been published until now, using the emission of the $^5\text{D}_1$ - $^7\text{F}_1$ transition at around 690 nm [BEI1994, KIM1998, KIM2001, RUN2000, STU2006, THO1993, YUS1990].

For spectrophotometric TRLFS titration 2.7 mL of 2 μM Am $^{3+}$ at pH 5.0 or 6.0 and 0.1 M NaClO₄ were titrated with aliquots (3, 10 or 15 μL) of a 0.01, 0.1 or 1 M ligand solution (pH 5.0 or 6.0, 0.1 M NaClO₄). 10-20 titration steps up to a ligand concentration of 0.1 mM (pyromellitate) or 0.1 M (lactate) were performed; every mixture was allowed to equilibrate for at least 15 min. At the beginning and after every titration step both a static and a time-resolved fluorescence spectrum was measured for pyromellitic acid at room temperature and for lactic acid in a temperature range between 25 and 65°C using a stirred temperature-controlled cuvette holder (Flash 300TM, Quantum Northwest, U.S.A.).

The TRLFS measurements were carried out with a pulsed Nd:YAG-MOPO laser system from Spectra Physics (Mountain View, USA), combined with a Spectrograph M270 and an ICCD camera system Spectrum One from Horiba-Jobin Yvon. The time difference between the trigger of the laser system and the start of the camera was adjusted by a delay generator DG 540 from Stanford Research Instruments. The laser source was set to an excitation wavelength of 503-506 nm ($^7\text{F}_0$ - $^5\text{L}_6$ transition) with pulse energies of 15 mJ. The optimum of excitation wavelength strongly depends on the absorption of the Am $^{3+}$ ion which is red-shifting upon complexation. Fig. 2-1 shows the fluorescence intensity of the Am $^{3+}(\text{aq})$ ion (left) and Am $^{3+}$ with 0.1 M lactate in dependency of the excitation wavelength. Whereas for the aquo ion 503-504 nm excitation causes the highest fluorescence intensity, for the Am-lac complex 506-507 nm excitation is the best.

Emission spectra were recorded between 625 and 773 nm, averaging five spectra with accumulating total 2500 laser pulses. The gate time of the camera was set to be 1 μs . The step width between two spectra in time-revolved mode was 2 or 5 ns, 15-20 delay steps were measured for every sample. The spectrograph and the camera system were controlled by Spectramax from Horiba-Jobin Yvon.

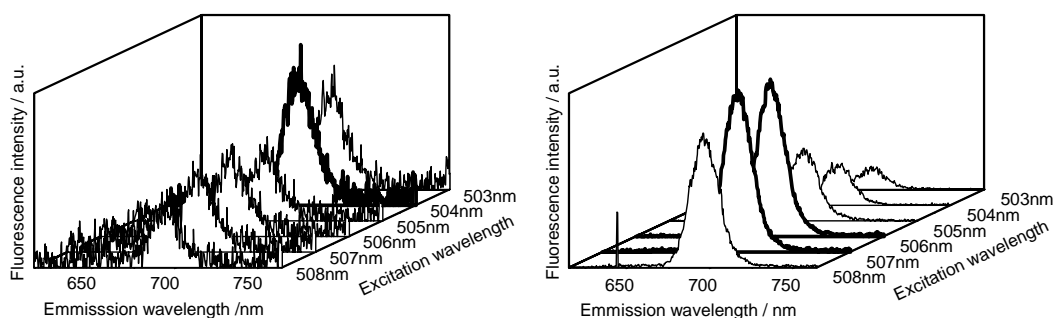


Fig. 2-1: Left: Emission spectra of 5 μM Am(III). Right: Emission spectra of 5 μM Am(III) and 0.1 M lactate in dependency of the excitation wavelength

Data analysis of the TRLFS spectra

TRLFS spectra were analyzed with Origin 7.5G to obtain the positions of peak maxima. Eu(III) spectra were normalized to the peak area of the 5D_0 - 7F_1 transition. This magnetic dipole transition is independent from the chemical environment of the metal ion.

The luminescence lifetimes were determined from the time-resolved measurements with Origin by fitting the integrated luminescence signal of the emission bands to a sum of exponential decay functions:

$$E(t) = \sum_i E_i \cdot \exp(-t/\tau_i) \quad (2-1)$$

E is the total fluorescence intensity at the time t, E_i the fluorescence intensity of the species i at the time t, and τ_i the corresponding lifetime.

With these lifetimes the number of water molecules was calculated using the following empirical equations [HOR1979, KIM1994b, and KIM1998]:

$$n(\text{H}_2\text{O}) \pm 0.5 = 1.07 \times \tau^{-1} (\text{ms}) - 0.62 \quad \text{for Eu(III)} \quad (2-2)$$

$$n(\text{H}_2\text{O}) \pm 0.5 = 2.56 \times 10^{-7} \times \tau^{-1} (\text{s}) - 1.43 \quad \text{for Am(III)} \quad (2-3)$$

2.1.4 UV-vis spectroscopy with a Long Path Flow Cell [MÜL2010]

TRLFS, see chapter 2.1.3, which is so far the most sensitive technique for measurements of actinide speciation, is limited to analytes that exhibit suitable fluorescence properties. In case of Am(III), the quantum yield of the fluorescence signal strongly depends on the solvent. In general, the nonradiative decay processes are predominant in aqueous solution [THO1993]. In sodium perchlorate medium the quantum yield of Am(III) is very low and the fluorescence emission lifetime very short (~ 23 ns, see chapter 2.2.2) in comparison to U(VI) or Cm(III), so that the detection limit of the used laser spectroscopic system described in chapter 2.1.3 is achieved. Therefore the UV-vis spectroscopy using a Long Path Flow Cell (**LPFC**, World Precision Instruments) for measurements of Am(III) speciation and non fluorescent actinides (for example Pu(III)) was established. A LPFC increases significantly the optical path of light through an analyte solution and therefore pushes detection limit towards lower concentrations according to Lambert Beer's law [WAT1997, WIL2005].

A LPFC is a capillary cell made of silica tubing coated with Teflon AF, (an amorphous copolymer of tetrafluoroethylene and 2,2-bis(trifluoromethyl)-4,5-difluoro-1,3-dioxole) [MIC2003]. This material combines the properties of amorphous plastics with those of perfluorinated polymers and exhibits a high thermal and chemical stability, a good optical transparency, a low dielectric constant and the lowest refractive index for an organic polymer [RES1997]. The light propagates through the capillary by total internal reflection at the interface between silica and Teflon AF. LPFCs are available in different lengths from 0.05 to 5 m. The inner diameter of the capillary is only 500 to 550 μm , thus a quite small sample volume is sufficient to fill the cell, which is an important fact for the work with radioactive actinides. The absorption spectroscopy utilizing a LPFC exhibits some specific features, for example the low spectral resolution of the mostly used fiber-optic spectrometer in support of a high signal to noise ratio, the great inner surface, which may cause wall adsorption and the light loss through the optical way and disturbing effects (like scattering by microparticles and gas bubbles, Schlieren formation) [INF2008].

The range for application of a 2 m LPFC is between 350 and 900 nm and with maximum transmission efficiency between 450 and 600 nm. The absorption spectra of Am(III) as well as of Eu(III) and Nd(III) exhibit prominent bands in this suitable wavelength range (Tab. 2-1). In our system the LPFC is coupled with a multichannel diode array spectrometer (MCS601, Carl Zeiss, spectral resolution < 2.3 nm) as detection system.

The determination complex stabilities at trace metal concentrations by UV-vis spectroscopy using a LPFC requires the characterization of the lower end of the measuring range of this system. The German Standard DIN 32645 [DIN08] provides two different types of decision limits for this purpose, depending on the analytical question which has to be answered. DIN 32645 [DIN08] is made for chemical analysis and describes the mathematical procedure for the evaluation of detection limit (DL) and for the limit of determination (LoD). Both are critical values of the measured variable. The detection limit is adequate to answer the question whether the analyte is present or not. The limit of determination (DoL) describes the lowest value of the analytical value at which the quantification of the analyte is achieved with a certain statistical significance. In between both limits, the presence of the analyte is proven. However, a significant quantification is not possible. All decision limits are calculated from a calibration function, i.e. from the relationship between absorption and analyte concentration according to Lambert Beer's law.

Exemplarily, Fig. 2-2 (left) depicts the Am(III) absorption spectra. Fig 2-2 (right) shows the clear linearity between the area of the absorption bands of Am(III) and the analyte concentration down to low concentrations. The detection limit (DL) and limit of determination (LoD) of Am(III), Eu(III), and Nd(III) are summarized in Tab. 2-1. The determined absorption maximum and oscillator strength are in good agreement with literature values [CAR1979, RAO1987]. Values of LD and LoD show clearly that the method is suitable for measurements in the low concentration range. However, the quality of the spectra depends on the wavelength of absorption maxima. For example, in case of Eu(III) with absorption maximum near the border of the transmission of the LPFC the baseline effects may cause a somewhat higher detection limit due to stronger noise.

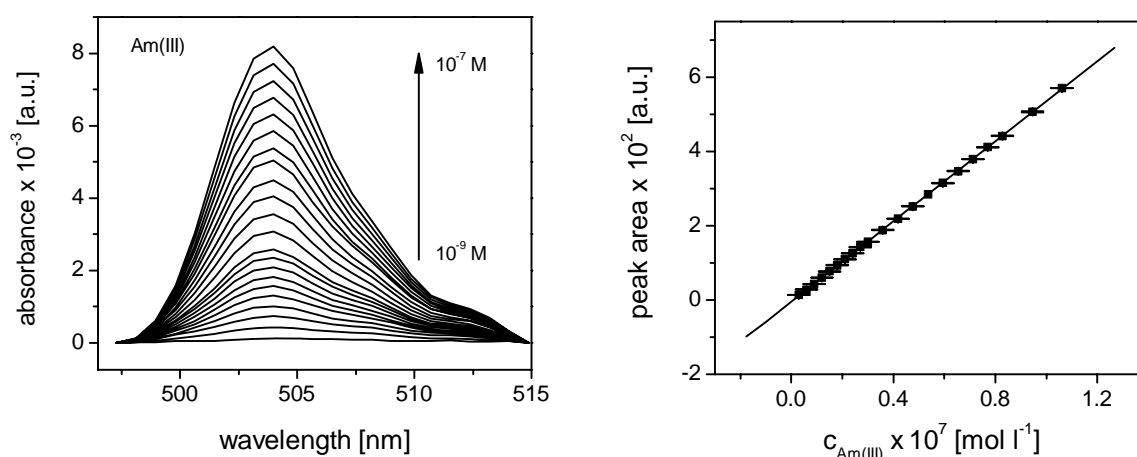


Fig. 2-2: Left: Absorption spectra of Am(III). Right: Integrated absorption signal as function of Am(III) concentration (pH = 3, 0.1 M NaClO₄)

Tab. 2-1: Absorption properties of Am(III), Eu(III) and Nd(III) [ACK2011]

	Am(III)	Eu(III)	Nd(III)
examined transition	${}^7F_0-{}^5L_6$	${}^7F_0-{}^5L_6$	${}^4I_{9/2}-{}^4G_{5/2}$
determined absorption maximum [nm]	503.9	394.0	575.0
molar extinction coefficient [$M^{-1}\cdot cm^{-1}$]	393 ± 2 [MÜL2010]	2,77 [CAR1979]	7,20 [RAO1987]
determined oscillator strengths	485	1,7 ^{a)}	9,4 ^{a)}
detection limit (DL) [$mol\cdot L^{-1}$] ^{b)}	$5\cdot 10^{-9}$	$5\cdot 10^{-6}$	$4\cdot 10^{-7}$
limit of determination (LoD) [$mol\cdot L^{-1}$] ^{b)}	$1\cdot 10^{-8}$	$2\cdot 10^{-5}$	$2\cdot 10^{-6}$

a) values in good agreement with values published in [CAR1968, RAO2010],

b) optical path length 2 m

For temperature dependent measurements all relevant components, e.g. the LPFC and the sample were arranged in an (isolated) acrylic glass box and then brought to temperature with an Air-Therm (ATX World Precision Instruments). The Air-Therm uses hot air to heat up a fixed volume to temperatures up to 60°C. Since no cooling is possible with the Air-Therm room temperature is the lowest available temperature. The temperatures in the sample and at the LPFC were determined continuously with thermocouple elements.

The spectra of all investigated Ln(III) and Am(III) ions show a slight temperature dependence. In the studied temperature range a linear decrease in the absorption intensity and the peak area with increasing temperature is observed (Fig. 2-3 left). Unavoidable temperature differences between sample vessel and LPFC, mostly around 3K, are the major source of uncertainties. They lead to the error bars shown in Fig. 2-3 (right). The linear relationship between the analyte concentration and the peak area is not affected by temperature [SCH2008].

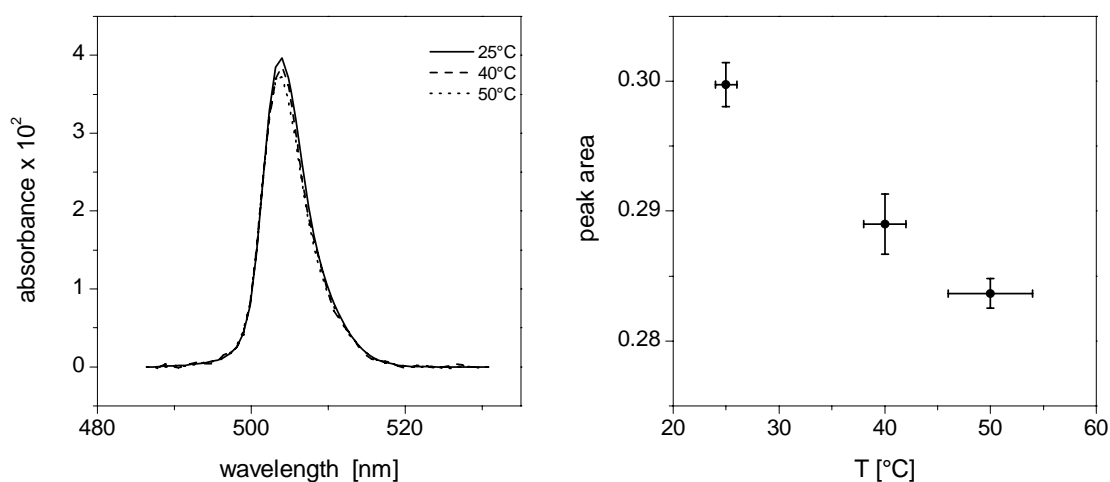


Fig. 2-3: Left: Absorption spectra of Am(III). Right: Integrated absorption signal as function of temperature (pH = 3, 0.1 M NaClO₄, c_{Am(III)} = 7·10⁻⁷ M)

The Am(III) absorption band at 503 nm is influenced by the chemical environment due to its hypersensitivity [CAR1964]. In the majority of cases a small bathochromic shift (in nm) of the absorption band is observed caused by nephelauxetic effect [BAR1996]. Information on formed complex species can be obtained from this shift. The stability constants of Am(III)-ligand complexes were determined from spectrophotometric UV-vis titration. Solutions with $5 \cdot 10^{-7}$ M Am^{3+} in 0.1 M NaClO_4 (in 5 ml) and pH values between 4.0 and 5.0 were titrated with small aliquots (2 to 10 μl) of a 0.001, 0.01 or 0.1 M ligand solution (with the same pH value). 20-40 titration steps up to a ligand concentration of $1 \cdot 10^{-3}$ M were performed at the chosen temperature.

2.1.5 Data analysis and determination of complex formation constant

For both methods, UV-vis and TRFS spectroscopy the complex stoichiometries were determined graphically using the general formula of complex formation



and the corresponding mass action law

$$K = \frac{c[\text{M}(\text{Lig})_n^{3+}]}{c[\text{M}^{3+}] \cdot c[\text{Lig}]^n} \quad (2-5)$$

followed by a slope analysis on the basis of the modified logarithmic linear form of the mass action law:

$$\log \frac{c[\text{M}(\text{Lig})_n^{3+}]}{c[\text{M}^{3+}]} = n \cdot \log c[\text{Lig}] + \log K \quad (2-6).$$

The concentrations of the uncomplexed and complexed species were calculated from the deconvoluted absorption or static luminescence spectra.

The complex stability constants were derived from the spectra using SPECFIT [BIN2005]. Input parameters for the data fitting were the total concentrations of the metal ion and the ligand, the pH, the known stability constants for the Eu(III) or Am(III) hydroxides [GUI2003, HUM2002b], and the $\text{p}K_a$ values of the ligands.

Plotting temperature-dependent complex formation constants as natural logarithm versus the reciprocal temperature, the thermodynamic data parameters enthalpy (ΔH) and entropy (ΔS) were calculated from the slope and the intercept by the Van't Hoff equation in a modified linear form:

$$\ln K = -\frac{\Delta H}{R} \cdot \frac{1}{T} + \frac{\Delta S}{R} \quad (2-7).$$

The uncertainty of all given experimental values is given as 1σ .

2.1.6 Fourier-transform infrared (FTIR) spectroscopy and Density functional theory (DFT) calculation

FTIR

FTIR spectra were recorded in aqueous phase using a Vector-22 spectrometer (BRUKER, Karlsruhe, Germany) equipped with a diamond attenuated total reflectance (ATR) unit (RESULTEC, Illerkirchberg, Germany). The ligand was measured at pH 7.0 and 100 mM pyromellitic acid. For the solution with precipitations, 20 μL 100 mM EuCl_3 solution (pH 7.0) was mixed with 20 μL of a 100 mM ligand solution (pH 7.0), resulting in a final concentration of $5 \cdot 10^{-2}$ M for Eu(III) and ligand each. The mixture precipitates rapidly and was therefore measured as a suspension. The monomeric complex was measured at pH 5.0, 1 mM Eu(III), 1 mM ligand and 0.1 M NaCl in a flow cell (volume: 200 μL) with a constant flow rate of 200 $\mu\text{L}/\text{min}$ and the absorption difference was calculated from the spectra of the complex and the pure ligand. For every single spectra 4×256 scans were co-added. Spectral resolution was 2 cm^{-1} . Water single-channel spectra were used as reference to calculate absorption spectra.

DFT

DFT calculations were performed using Gaussian 03 [FRI2004]. Geometries were optimized in the aqueous phase at the B3LYP level using the CPCM solvation model [BAR1998] with UAHF radii [BON1964]. The large core effective core potential (LC-ECP) as well as the corresponding basis set suggested by Dolg et al. was used on Eu [DOL1989]. For C, O, and H, all-electron valence triple-zeta basis set plus polarization and diffuse functions have been used [KRI1980]. The LC-ECP used in this study is specifically designed for the trivalent Eu incorporating six unpaired 4f electrons into the core potential, thereby enabling “closed-shell” calculations on Eu(III) which has the formal electronic configuration of the septet spin state. This simplification is justified because the 4f orbital is strongly contracted, shielded by valence orbitals, and does not participate in the chemical bond between Eu(III) and the ligand. The final geometries were confirmed to be the energy minimum through vibrational frequency analysis where no imaginary frequency was found to be present. The vibrational spectra were fitted with the half-width of 8 cm^{-1} at half-height using the calculated harmonic frequencies and IR intensities.

The Spin-orbit effect and multi-configurational character of the system were neglected. Both effects are expected to be important for the accurate determination of the electronic energy levels of the Eu(III) complex. Their contributions to the ground state geometry, however, are small because 4f electrons are localized on the Eu atom in the ground state and low energy excited states and do not contribute to ligand interactions. According to the recent study on Cm(III) complexes [CAO2009], which are analogous to the Eu(III) complexes, solvation energy is the most critical factor for the determination of geometries and vibrational frequencies. The first coordination sphere around Eu was saturated with water molecules fixing the coordination number to 8 or 9. The rest of the solvation shells were also considered through the use of the CPCM model.

2.1.7 Isothermal titration calorimetry

ITC measurements were done with a Microcal VP-ITC calorimeter (GE Healthcare, Buckinghamshire, UK) at different temperatures (25, 40 and 60°C). A total of 56 aliquots (5 μL of 10 mM pyromellitic acid in 0.1 M NaClO_4 , pH 5.7) were injected in 1.412 mL of 1 mM EuCl_3 (0.1 M NaClO_4 , pH 5.7) in 5 min intervals at 25°C , and in 27 min intervals at 40 and 60°C to allow the completion of slow reactions at these temperatures. The measurements

were corrected for the heat of dilution of the titrant, determined in separate runs. Measurements were analyzed with the associated software Origin 7.5.

2.2. Results and discussions

2.2.1 Potentiometric titration

In addition to the proton dissociation constants of the ligands at 25°C which are mostly literature known [POW2005] those at higher temperatures are required for the determination of Ln(III)/An(III) complex stability constants at elevated temperatures. Tab. 2-2 to 2-4 summarize the dissociation constants for pyromellitic acid, salicylic acid, and tartaric acid at elevated temperatures and the corresponding enthalpies and entropies calculated with Eq. 2-7. For ambient temperature our data are within the range of reported values. All protonation reactions are slightly endotherm (increasing pK_a values with rising temperatures). The thermodynamic data agree well with published calorimetric data at 25°C for pyromellitic acid [CHO1994, PUR1972]. Slightly negative enthalpies were published for salicylic and tartaric acid [DER1999, HAS1990a]. Possibly the different methods and temperatures (temperature dependent potentiometric titration versus calorimetry at room temperature) or the different background electrolytes (sodium perchlorate versus sodium chloride) can cause these contradictory results.

Tab. 2-2: pK_a values and thermodynamic data of pyromellitic acid (in 0.1 M NaClO₄) at varying temperature determined by potentiometric titration.

T [°C]	pK_{a1}	pK_{a2}	pK_{a3}	pK_{a4}	Ref.
25	1.92 ± 0.03	2.77 ± 0.03	4.36 ± 0.02	5.35 ± 0.02	this work
25		2.63	4.18	5.25	[CHO1994]
25	1.70	3.12	4.92	6.23	[PUR1972]
30	1.91 ± 0.02	2.86 ± 0.01	4.45 ± 0.01	5.43 ± 0.01	this work
40	2.05 ± 0.02	2.88 ± 0.01	4.48 ± 0.01	5.48 ± 0.01	this work
50	2.11 ± 0.01	2.88 ± 0.01	4.47 ± 0.01	5.51 ± 0.01	this work
60	2.13 ± 0.02	2.91 ± 0.02	4.50 ± 0.01	5.50 ± 0.02	this work
$\Delta_r H$ [kJ·mol ⁻¹]	13.2 ± 2.2	6.0 ± 2.2	6.0 ± 2.4	7.7 ± 2.3	this work
		6.8	1.3	4.5	[CHO1994] ^{a)}
	13.0	6.6	3.3	6.7	[PUR1972] ^{a)}
$\Delta_r S$ [J·K ⁻¹ ·mol ⁻¹]	81 ± 7	74 ± 7	104 ± 8	129 ± 8	this work
		73	84	116	[CHO1994] ^{a)}
	76	82	106	142	[PUR1972] ^{a)}

a) from calorimetry (25°C)

Tab. 2-3: pK_a values and thermodynamic data of salicylic acid (in 0.1 M NaClO₄) at varying temperature determined by potentiometric titration.

T [°C]	pK_a	Ref
10	2.77 ± 0.01	this work
20	2.79 ± 0.01	this work
25	2.72	[HAS1989]
25	2.82	[GON1987]
30	2.80 ± 0.01	this work
40	2.83 ± 0.01	this work
50	2.85 ± 0.01	this work
60	2.87 ± 0.02	this work
$\Delta_r H$ [kJ·mol ⁻¹]	4.1 ± 0.1	this work
	-4.0	[HAS1989] ^{a)}
$\Delta_r S$ [J·K ⁻¹ ·mol ⁻¹]	67 ± 1	this work
	39	[HAS1990b] ^{a)}

a) from calorimetry (25°C)

Tab. 2-4: pK_a values and thermodynamic data of tartaric acid (in 0.1 M NaClO₄) at varying temperature determined by potentiometric titration.

T [°C]	pK_{a1}	pK_{a2}	
10	2.739 ± 0.003	3.906 ± 0.002	
20	2.773 ± 0.002	3.939 ± 0.001	
25	2.828	3.949	[DER1999]
25	2.850	3.968	[ARE1980]
30	2.857 ± 0.002	3.976 ± 0.001	
40	2.904 ± 0.002	3.999 ± 0.002	
50	2.883 ± 0.002	4.017 ± 0.002	
$\Delta_r H$ [kJ·mol ⁻¹]	7.4 ± 1.6	5.0 ± 0.3	
	-0.5	-0.9	[DER1999] ^{a)}
$\Delta_r S$ [J·K ⁻¹ ·mol ⁻¹]	79 ± 5		
	17	92 ± 1	[DER1999] ^{a)}

a) from calorimetry (25°C)

2.2.2 Pyromellitic acid [BAR2011b]

The pyromellitic acid mimics the structural arrangement of carboxylates in polyphenols and serves as a model compound for the binding of heavy metals to humic acids. The formation of aggregates is typical of humic acids and prevails in pyromellitic acid and related compounds. It emphasizes their suitability as model compounds also with respect to this environmentally important but little investigated property [BAR2011b and references therein].

Europium – TRLFS

Fig. 2-4 (left) shows the spectrophotometric titration of Eu(III) with pyromellitic acid at 25°C. With increasing ligand concentration, a strong increase of the intensity of the emission of the hypersensitive ⁵D₀-⁷F₂ transition at 615 nm is observed. The appearance of the formally forbidden ⁵D₀-⁷F₀ transition at 579 nm indicates the deformation of the first hydration shell of

the Eu(III) ion upon complexation. Irrespective of the ligand concentration, the luminescence exhibits a mono-exponential decay despite the intrinsically different decay times for the fully hydrated and the coordinated Eu(III) ion. Due to a fast kinetic equilibration at room temperature, the observed apparent lifetime is actually a mixture of the decay rates of the excited states of both, the uncomplexed and the complexed Eu(III) species. The initial luminescence lifetime of $111 \pm 4 \mu\text{s}$ (25°C), which is typical of the Eu(III)(aq) ion, increases to a constant value of $135 \pm 3 \mu\text{s}$ (25°C , averaged) with more than 60 fold excess of ligand. A similar lifetime for the Eu(III)-pyromellitate system was measured by Wang et al. [WAN1999]. The measured luminescence lifetimes do not depend on temperature between 25 and 60°C (60°C : $109 \pm 1 \mu\text{s}$, Eu³⁺(aq), and $130 \pm 2 \mu\text{s}$, averaged, Eu(III)-pyromellitate). The number of water molecules coordinating the unbound Eu(III) ion is 9.0 ± 0.5 at 25°C and 9.2 ± 0.5 at 60°C , whereas the prolonged luminescence lifetime of the complex agrees with the presence of 7.3 ± 0.5 (25°C) to 7.5 ± 0.5 (60°C) water molecules. Thus, 1 to 2 water molecules are replaced by the carboxyl oxygens upon coordination by pyromellitate. The slope analysis according to Eq. 2-4 to 2-6 revealed a stoichiometry of the Eu(III)-pyromellitate complex close to 1:1 at all temperatures. The complex stability constants for the 1:1 complex are summarized in Tab. 2-5. The stability constant increases with temperature. The linearity of the Van't Hoff plot (Fig. 2-4, right) further shows that the enthalpy of complex formation is virtually independent of temperature ($18.5 \text{ kJ}\cdot\text{mol}^{-1}$) and agrees, together with the obtained reaction entropy of $152 \text{ J}\cdot\text{mol}^{-1}\cdot\text{K}^{-1}$, with published data [CHO1994].

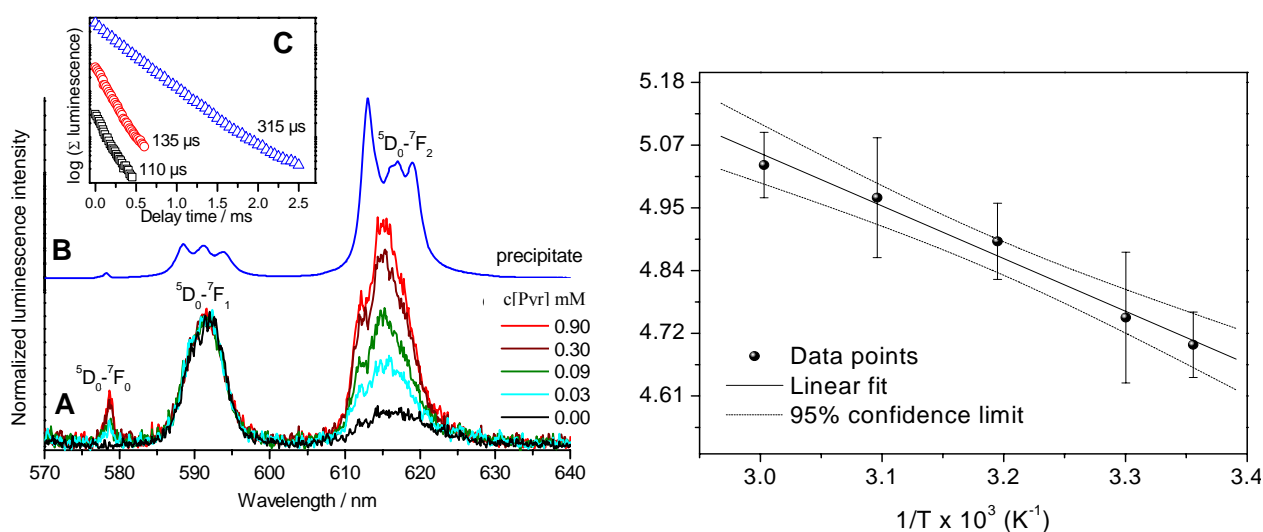


Fig. 2-4: Left : Luminescence properties of Eu(III)-pyromellitate complexes. A) Selected emission spectra of the spectrophotometric titration of $30 \mu\text{M}$ Eu(III) with pyromellitate (Pyr) (25°C , pH 5.0, 0.1 M NaClO₄). B) Luminescence of the precipitate forming at 1 mM Eu(III) and 1 mM pyromellitate (40°C , pH 5.7). C) Luminescence decay traces and corresponding lifetimes of Eu(III)aq (black), Eu(III)-pyromellitate aqueous complex at $30 \mu\text{M}$ Eu(III), 4.5 mM ligand, 25°C , pH 5.0 (red), and the Eu(III)-pyromellitate precipitate (composition like B) (blue). Right: Van't Hoff plot of the Eu(III)-pyromellitate complex formation.

Eu(III) concentrations above 0.5 mM added to equimolar amounts of pyromellitate at neutral pH value caused aggregation. At 40°C and mM concentrations of both pyromellitate and Eu³⁺ aggregates formed even at pH 5.7. Figure 2-4 (left) compares the luminescence spectra of aggregates formed at equimolar concentration (1 mM) of Eu(III) and pyromellitic acid at pH 5.7, 40°C with those of the soluble complex. The $^5\text{D}_0$ - $^7\text{F}_0$ peak (579 nm) is less pronounced in the aggregate, indicative of a more symmetrical structure than in solution. The lifetime of Eu(III) luminescence in the multimeric state increases to $205 \pm 3 \mu\text{s}$ (pH 7.0, 25°C)

and $315 \pm 5 \mu\text{s}$ (pH 5.7, 40-60°C), respectively, corresponding to 4.5 ± 0.5 and 2.8 ± 0.5 coordinating water molecules which implies the additional exchange of 2 to 4 water molecules upon aggregation of the monomeric complex.

Europium – Isothermal titration calorimetry

Isothermal calorimetric titration experiments were carried out at 25, 40 and 60°C (Fig. 2-5). All ITC traces showed endothermic binding of pyromellitate to Eu(III). The corresponding binding stoichiometries obtained from single site fits were 1.0, 1.2, and 0.9, respectively. At 25°C, the reaction enthalpy $\Delta_r H$ is $(16.5 \pm 0.1) \text{ kJ}\cdot\text{mol}^{-1}$ and the entropy $\Delta_r S$ is $(130 \pm 3) \text{ J}\cdot\text{mol}^{-1}\cdot\text{K}^{-1}$ as derived from the ITC data in Fig. 2-5 (right). These numbers are in very good agreement with literature data [CHO1994] (Tab. 2-7). The endothermic ITC response at 25 °C was complete within less than 2 min (Fig. 2-5 left, inset). With rising temperature, however, it became biphasic with a “tailing heat uptake” resulting in an apparent $\Delta_r H$ of $(34.2 \pm 0.3) \text{ kJ}\cdot\text{mol}^{-1}$ ($\Delta_r S = 210 \pm 9 \text{ J}\cdot\text{mol}^{-1}\cdot\text{K}^{-1}$), i.e. close to twice the molar enthalpy observed at 25°C (Fig. 2-5 right). This indicates that at higher temperatures an additional reaction succeeds the fast complex formation. Fig. 2-5 (right) exemplifies the biphasic behavior at 40°C by deconvoluting the ITC signal into a fast reaction with similar kinetics as measured at 25°C and a slower phase that covers the extra heat uptake observed at higher temperatures. The slow phase becomes further pronounced at 60°C (Fig. 2-5 right, inset). Instead of the classical evaluation of the ITC curve using a single binding reaction, it is thus reasonable to split the reaction heat separately in different time windows. It is indeed possible to divide the total heat uptake into the sum of the two isotherms shown in Fig. 2-5 (right) (lower panel). With increasing amount of Eu(III), the heat taken up in the early phase (i.e. within the first 30 seconds) is successively reduced in relation to that absorbed over the following time. This indicates that the complex reaction underlying the fast component saturates earlier than the ensuing reaction. Remarkably, the integrated heats of the early and late phase of the transient can be modeled with individual enthalpies of 14.6 and 16.3 kJ mol^{-1} (with reaction entropies of 138 and 160 $\text{J}\cdot\text{mol}^{-1}\cdot\text{K}^{-1}$, respectively, and a stoichiometry of 0.8-0.9). These values are very close to those of the 1:1 complex formation reaction at 25°C. Therefore, the data indicate that at temperatures above 40°C, the slow heat release that follows the formation of the 1:1 complex originates in an ensuing second Eu(III) coordinating interaction with thermodynamic parameters very similar to those of the fast initial complex formation. In agreement with the onset of visually observable precipitation at 40°C, the additional Eu(III) coordination appears to be crucial for the formation of polymeric states. Remarkably, the ITC data demonstrate that at 40°C an overall 1:1 stoichiometry also holds for the aggregated Eu pyromellitate complex.

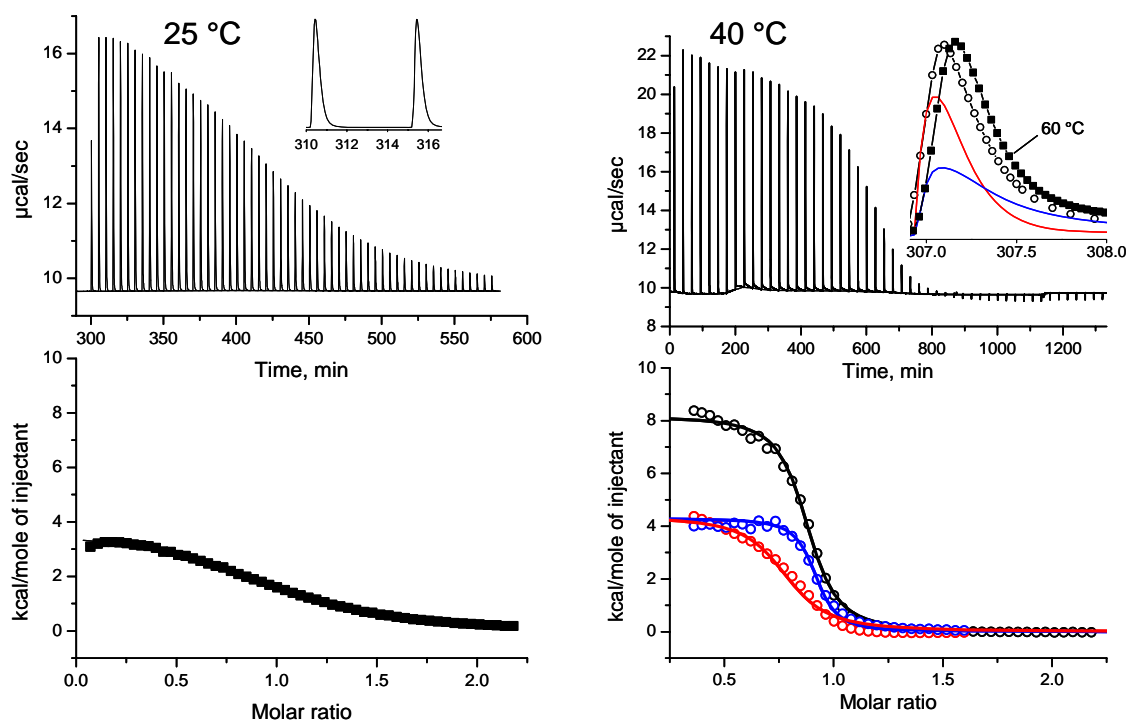


Fig. 2-5: Heat uptake during Eu(III)-pyromellitate complex formation measured by isothermal titration calorimetry at different temperatures. Explanation see text.

Europium – FTIR spectroscopy and DFT analysis

In an attempt to relate the most prominent experimentally determined vibrational features to those derived from DFT calculations for specific coordination modes, the structures of soluble (monomeric) and insoluble (polymeric) Eu(III)-pyromellitate complexes were assessed by FTIR spectroscopy at room temperature and compared with DFT calculations. It should be noted that the DFT calculations were used here to assign IR bands to the most likely predominant coordination modes and only the 1:1 complex has been calculated by DFT. The structures and IR spectra of Eu(III)-pyromellitate complexes were calculated with different coordination number (CN) of 8 and 9 and also with different coordination modes (monodentate, bidentate and chelate ring formation). The structures and relative Gibbs energies including the solvation energy are shown in Fig. 2-6. In both monodentate and bidentate complexes, the CN 8 was found to be more stable than the CN 9 by 44.6 and 33.1 $\text{kJ}\cdot\text{mol}^{-1}$, respectively, which is a clear indication of CN 8 prevalence over CN 9. For the chelate ring complex, the energy difference between CN 8 and CN 9 is only 11.6 $\text{kJ}\cdot\text{mol}^{-1}$ and thus too small to identify a unique CN. It can also be seen in Fig. 2-6 that the energy differences among the complexes with different coordination modes and CN 8 are overall small. They all lie within the energy difference of 5 $\text{kJ}\cdot\text{mol}^{-1}$ and do not allow identifying a predominant coordination mode on purely theoretical grounds. It will be shown, however, that the FTIR results in combination with TRLFS data allow proposing the structural model that is most consistent with both, DFT and spectroscopy.

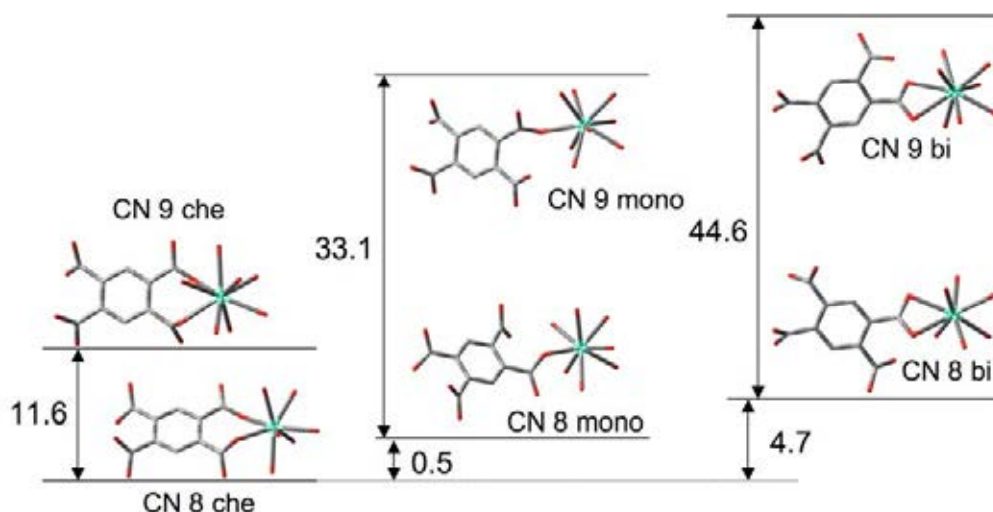


Fig. 2-6: The structures and relative Gibbs free energy [$\text{kJ}\cdot\text{mol}^{-1}$] (including of the solvation) of Eu(III)-pyromellitate complex with different coordination number (CN 8 and 9) and different coordination modes (chelate, monodentate, and bidentate). Hydrogen atoms are omitted for clarity. When comparing the energy of the complexes with different number of water, one or two water molecules were added in the second coordination shell of the complex with less number of water(s).

In DFT calculations we have calculated IR spectra of the complexes with three different coordination modes (monodentate, bidentate, and chelate) and two different CN (8 and 9) (Fig. 2-7).

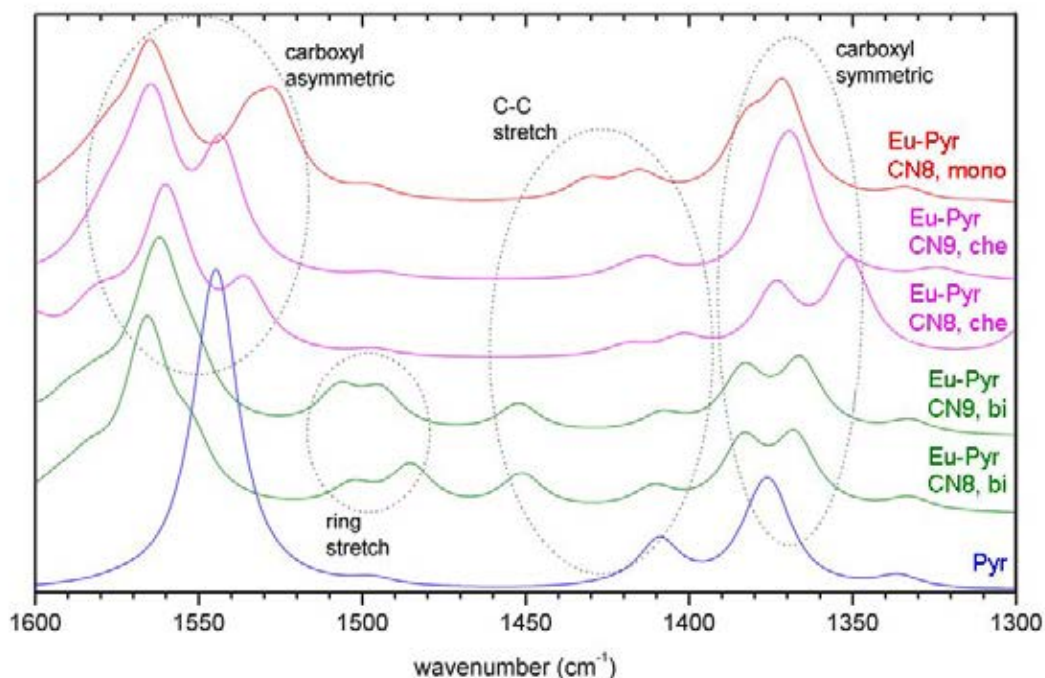


Fig. 2-7: IR spectra of pyromellitic acid and Eu(III)-pyromellitate complexes obtained by DFT calculations monodentate (mono), bidentate (bi), chelate (che)

Fig. 2-8 (left) shows the experimental and theoretical IR spectra of free pyromellitate (A) and pyromellitate complexed with Eu(III) ((B) monomer, (C) polymer).

Structural conclusions are based on the carboxylate vibrations as they are the most sensitive to the coordination mode. The comparison of the data of the free ligand (Fig. 2-8 A) shows that the relative positions and intensities of the calculated vibrational bands are in good accordance with the measured spectrum. DFT calculation (Fig. 2-7) shows that Eu(III) binding splits either the asymmetric (1550 to 1600 cm^{-1}) (monodentate or chelate) or the symmetric (1350 to 1400 cm^{-1}) (bidentate) carboxylate band of the ligand, leading to broad overlapping bands between 1520 and 1600 cm^{-1} and from 1350 to 1400 cm^{-1} , respectively. The bidentate coordination does not cause band splitting of the asymmetric COO^- stretch but strongly shifts it to lower frequency, whereas splitting is observed for the symmetric stretch. Such shifts and splittings will affect mainly the total band width in the 1500 to 1600 cm^{-1} range due to the broad absorption bands in the experimental spectra. The $\nu_{(\text{as})\text{COO}^-}$ stretches clearly cover a larger frequency range in the monomeric complex (Fig. 2-8 B) than in the free ligand (Fig. 2-8 A). The increased absorption above and below the $\nu_{(\text{as})\text{COO}^-}$ of the additionally present free carboxylate (Fig. 2-8, dotted line) indicates that splitting does indeed occur upon monomer formation. Thus, a bidentate coordination can be ruled out. Also the two energetically most preferred binding modes, the chelate and bidentate complexes with CN 8 each can be ruled out at least for the monomeric form due to the TRLFS results. These coordination modes would retain 6 water molecules in the first coordination shell of Eu^{3+} . This is contrary to TRLFS findings, where we found that 7 to 8 water molecules remain after complexation. Instead, the two DFT spectra which agree best with experiment are shown in Fig. 2-8. These are the chelate complex with CN 9 corresponding best with the monomer absorption (Fig. 2-8 B) and the monodentate complex with CN 8 corresponding best with the polymer (Fig. 2-8 C). In the latter, the splitting is even broader (as is the total band width in the experimental spectra) leading to a more distinct low frequency $\nu_{(\text{as})\text{COO}^-}$ stretch at 1530 cm^{-1} also seen experimentally. Additionally, a high frequency shoulder is produced in the $\nu_{(\text{s})\text{COO}^-}$ band both in the calculated and measured spectra. These most likely predominant coordination modes support our TRLFS data, which show that a chelating coordination requires a CN 9 and that 7 to 8 water molecules still remain in the first coordination shell of Eu^{3+} in the monomeric complex. The large experimental bandwidth indicates that multiple coordination modes exist in both the monomer and polymer (see Fig. 2-8, right).

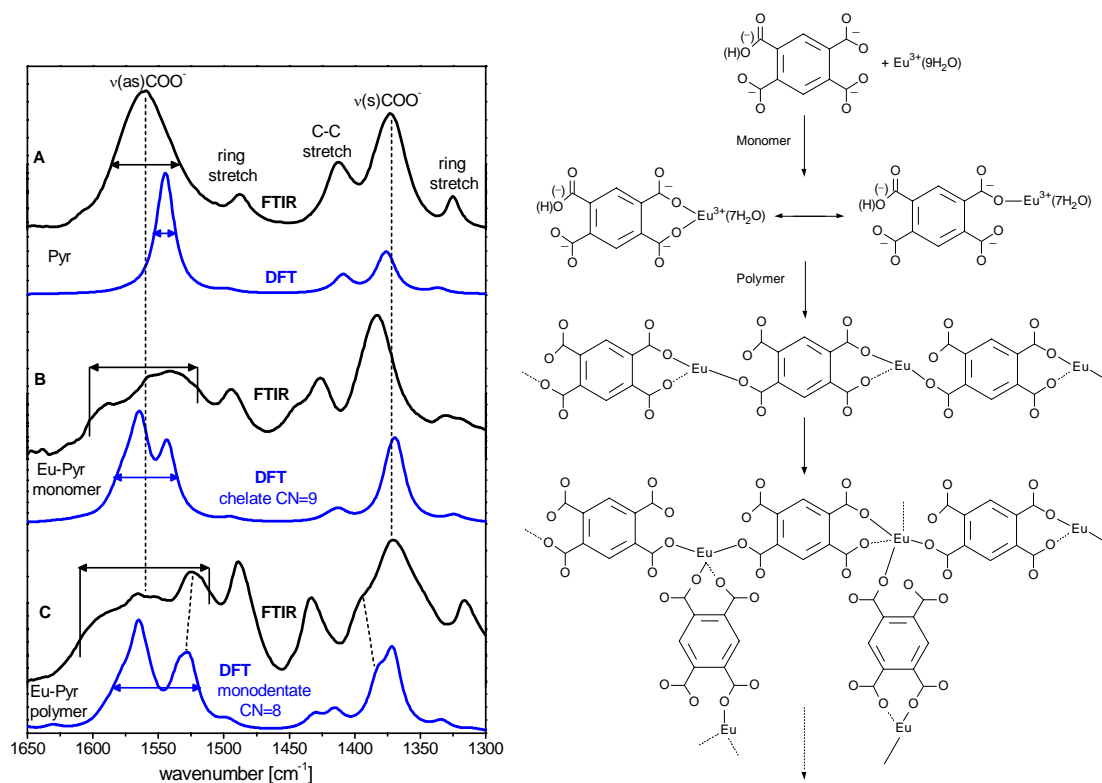


Fig. 2-8: Left: Comparison of experimental (black) and theoretical IR spectra (blue, derived from DFT calculations of pyromellitate (Pyr) and Eu(III)-pyromellitate (Eu-Pyr) complexes). **A)** Pyromellitate in 0.1 M NaClO₄ without europium. **B)** Eu(III)-pyromellitate complex under conditions of a prevalent monomeric state of 1:1 stoichiometry. **C)** Eu(III)-pyromellitate complex under polymerizing conditions with 1:1 stoichiometry. Right: Schematic description of the stepwise formation of the Eu(III)-pyromellitate polymer demonstrating possible chelating and monodentate binding modes and the prevalence of a 1:1 stoichiometry in both the monomeric and polymeric states. For clarity, values, protons and water molecules are omitted in the polymeric structures.

Americium - TRIFS

Fig. 2-9 depicts a summary of the measured fluorescence spectra of the Am(III)-pyromellitate system at fixed Am³⁺ concentration (2 μM), fixed pH (5.0), and varying ligand concentration (1 μM to 90 μM). For Am³⁺(aq) we observe the emission of the ⁵D₁-⁷F₁ transition at 691 nm. With increasing ligand concentration no shift of the peak maximum but an increase of the luminescence intensity is observed, indicating a complex formation. The intensity remains nearly equal at more than approximately 30-fold ligand excess, where the complexation seems to be completed. The intensity development at 691 nm is depicted in Fig.2-9 as an insert.

At any studied Am(III)-ligand mixture, we observe mono-exponential decay. The initial lifetime of Am³⁺(aq) of 23.2 ± 2.2 ns is in very good accordance with literature data (23 ± 2 ns [RUN2000], 24.6 ± 0.6 ns [KIM1998], 25.0 ± 0.8 ns [KIM2001]). The number of the associated hydration water molecules in the inner coordination sphere, calculated with Eq. 2-3, is 9.6 ± 0.5. With increasing ligand concentration the lifetime increases due to complex formation until an approximately constant value of 27.2 ± 1.2 ns at 30-fold ligand excess. The lifetime of the Am(III)-pyromellitate complex species corresponds to 8.0 ± 0.5 water molecules remaining in the inner coordination sphere of Am (considering the error of the lifetime), indicating the replacement of 1-2 water molecules through ligand coordination sites. A stoichiometry of the Am(III)-pyromellitate complex species of 1:1 was derived from the slope analysis by Eq.2-4 to 2-6 (slope of 1.26 ± 0.11). The stability constant of this complex, which is un-known until now, was calculated to be log β₁₁₀ = 5.42 ± 0.16 (Tab. 2-6).

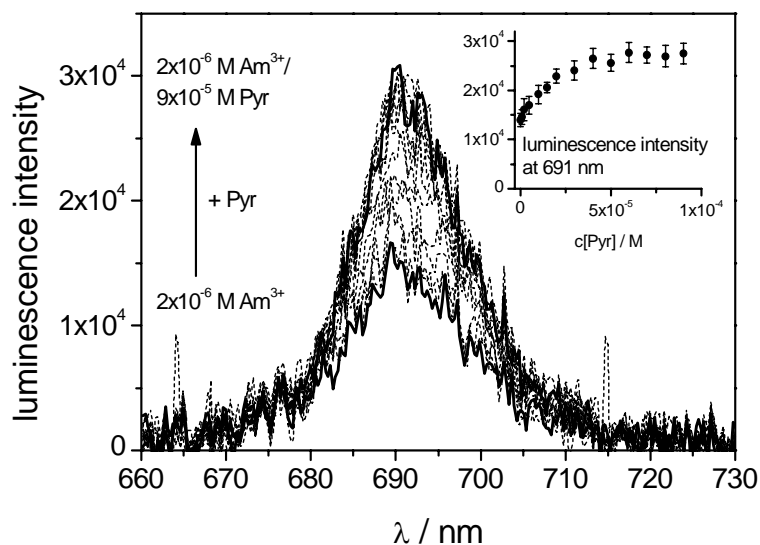


Fig. 2-9: TRLFS spectra of 2 μM Am(III) in dependence of pyromellitate concentration (pH = 5.0, I = 0.1 M NaClO_4 , T = $21 \pm 1^\circ\text{C}$). Small insert: Luminescence intensity at 691 ± 1 nm in dependence of the ligand concentration.

Americium –UV-vis

Fig. 2-10 shows the absorption spectra of Am(III) with stepwise addition of the pyromellitic acid. The ligand concentration was varied between 10^{-6} and 10^{-3} M. The spectra exhibit a slight bathochromic shift induced by ligand addition. Additionally the maximum absorption intensity changes in two different ways. It decreases first and rises again after further addition of the ligand. The shifting of absorption band clearly indicates a complex formation with the carboxylate ligand. The formation of two complex species (1:1 and 1:2 complexes) was indicated by slope analysis (Eq. 2-4 to 2-6). The 1:1 complex exhibits a slightly decreased absorption. The 1:2 complex species has an absorption maximum at 504.8 nm and slightly higher extinction coefficient.

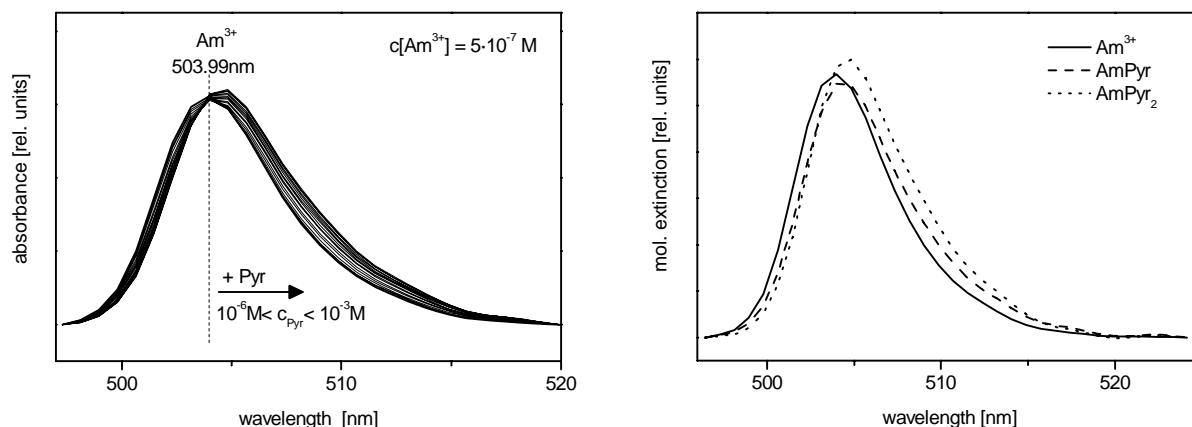


Fig. 2-10: Left: UV-vis absorption spectra of Am(III) at 25°C , pH = 5.0 and I = 0.1 M NaClO_4 in dependence of pyromellitate concentration (varied from 10^{-6} to 10^{-3}). Right: single component spectra determined with SPECFIT.

The spectrophotometric titration experiments were repeated at increased temperatures up to 55°C and no significant deviations from the presented trend were observed. The Van't Hoff plots, shown in Fig. 2-11, reveal always a linear relationship. The derived thermodynamic data are listed in Tab.2-6.

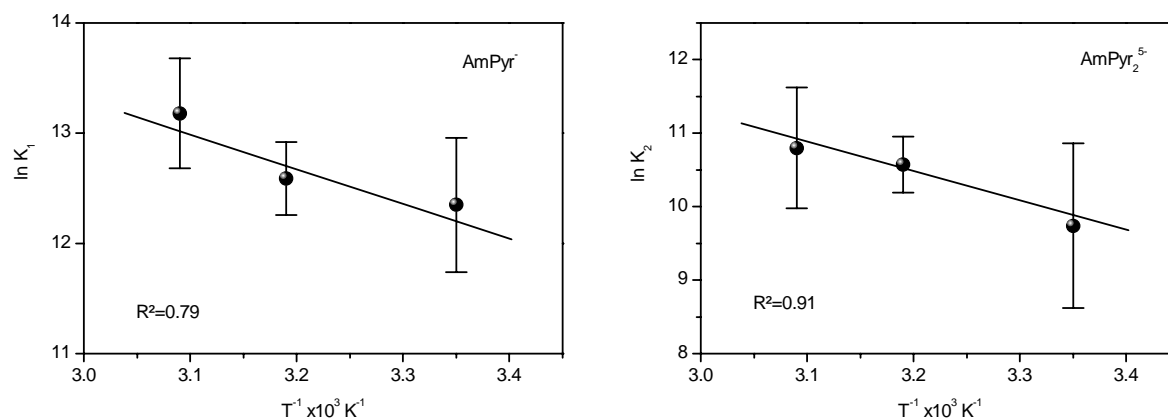


Fig. 2-11: Van't Hoff plots of the Am(III)-pyromellitate complex formation determined by UV-vis spectroscopy. Left: 1:1 complex. Right: 1:2 complex

Thermodynamic data of Eu(III) and Am(III) complexation with pyromellitic acid

In Tab. 2-5 to 2-7 the complex stability constants and derived thermodynamic data of the system Eu(III)/Am(III)-pyromellitic acid are summarized. It can be concluded that the formation of Am(III)- and Eu(III)-pyromellitate complexes are endothermic and driven by entropy. For the first time the complex stability constants of the 1:1 and 1:2 Am(III)-pyromellitate complexes were derived from spectroscopic measurements. Until now no literature data are available. However, the obtained values are in the same order of magnitude as those reported for the analogue Eu(III) (see Tab. 2-5 and 2-7) [BAR2011b] or Nd(III) complexes [ZES2011].

Tab. 2-5: Complex stability constants at varying temperature for the monomeric 1:1 Eu(III)-pyromellitate complex ($I = 0.1 \text{ M NaClO}_4$) determined by TRLFS.

T [°C]	$\log\beta_{110}$	Ref.
25	4.70 ± 0.06	this work
25	4.86 ± 0.03	[CHO1994] ^{a)}
30	4.75 ± 0.12	this work
40	4.89 ± 0.07	this work
50	4.97 ± 0.11	this work
60	5.03 ± 0.06	this work

a) from potentiometric titration

Tab. 2-6: Thermodynamic data for Am(III)-pyromellitate complexes ($I = 0.1 \text{ M NaClO}_4$) determined by UV-vis and TRLFS

T [°C]	$\log\beta_{110}$	$\log\beta_{120}$	method	Ref.
20	5.42 ± 0.16	-	TRLFS	this work [BAR2011a]
25	5.4 ± 0.3	9.74 ± 1.12	UV-vis	this work
40	5.5 ± 0.1	10.57 ± 0.38	UV-vis	this work
50	5.7 ± 0.2	10.80 ± 0.82	UV-vis	this work
<hr/>				
$\Delta_r H$ [kJ·mol ⁻¹]	26 ± 13	33 ± 10	UV-vis	this work
$\Delta_r S$ [J·K ⁻¹ ·mol ⁻¹]	189 ± 43	139 ± 33	UV-vis	this work

Tab. 2-7: Summary of the thermodynamic data for the 1:1 Eu(III)-pyromellitate complex (I = 0.1 M NaClO₄).

T [°C]	$\Delta_r H$ [kJ·mol ⁻¹]	$\Delta_r S$ [J·K ⁻¹ ·mol ⁻¹]	$\Delta_r G$ [kJ·mol ⁻¹]	method	Ref.
25-60	18.5 ± 1.5	152 ± 5	-26.8 (25 °C) ^{a)}	TRLFS	this work [BAR2011b]
25	17.0 ± 1.6	150 ± 1	-27.7	ITC	[CHO1994]
25	16.5 ± 0.1 ^{b)}	130 ± 3	-22.2	ITC	this work
40	34.2 ± 0.3 ^{b),c)}	210 ± 9	-31.5	ITC	this work
60	46.9 ± 0.2 ^{b),c)}	247 ± 9	-35.4	ITC	this work

a) calculated with the formula $\Delta_r G = \Delta_r H - T \Delta_r S$.

b) $\Delta C_p = 0.9 \text{ kJ}\cdot\text{mol}^{-1}\cdot\text{K}^{-1}$ was calculated from $\Delta H/\Delta T$.

c) apparent values (explanation in chapter Eu-Isothermal titration calorimetry)

2.2.3 Salicylic acid

Europium - TRLFS

The complexation of Eu(III) with salicylate was studied with TRLFS in the temperature range between 25°C and 60°C. The luminescence spectrum of Eu(III) shows in presence of the ligand the typical changes which indicate a complexation: The intensity of the hypersensitive ⁵D₀-⁷F₂ transition at about 615 nm increases strongly, the symmetry-forbidden ⁵D₀-⁷F₀ transition appears (see Fig. 2-12, right), and the luminescence lifetime prolongs. The luminescence lifetimes of the Eu(III) aquo ion are nearly similar within the studied temperature range (115 ± 2 μs at 25°C or 109 ± 2 μs at 55 °C). Applying Eq. 2-2, the lifetimes correspond to a number of 9 water molecules in the first spherical coordination shell of Eu(III) (8.6 ± 0.5 at 25°C and 9.2 ± 0.5 at 55°C). The luminescence lifetime is prolonged with ligand addition and reaches a constant value with more than 0.05 M salicylate of about 305 ± 5 μs. This corresponds to a number of 3 remaining water molecules in the first coordination shell of Eu(III); 6 water molecules has been substituted by coordination sites of ligand molecules. A similar lifetime (about 300-340 μs) was found by Kuke et al. [KUK2010] for a concentrated Eu(III) salicylate mixture at decreased temperatures (80-200 K); at room temperature they observed quenching contributions, possibly due to the high concentration of both metal and ligand.

Salicylate can act as unidentate or chelating ligand, either with bidentate coordination of the carboxylate group or with a monodentate coordination of the carboxylate and an additional coordination of the hydroxyl group [KUK2010, TOR2005]. A theoretical study on the molecular structure of Eu-salicylate complexes in aqueous system revealed that the 1:1 carboxylate-coordinated complex takes unidentate coordination with 8 remaining water molecules in the first coordination shell of Eu(III), but also an intra-molecular chelate ring closure with the OH group under replacement of 3 water molecules seems to be possible. A bidentate coordination of the carboxylate group was excluded due to the higher formation energy [TOR2005]. The substitution of up to 6 water molecules in the first coordination shell of Eu(III) upon complexation with salicylate suggests the formation of more than a 1:1 complex. Also complexes with 1:2 and 1:3 metal-to-ligand stoichiometry seem to be formed. The high water substitution rate implies furthermore the formation of chelate coordination with carboxylate and (protonated) hydroxyl; a unidentate coordination mode seems to be unlikely. These assumptions are underlined by a crystal structure of Eu(Sal)₃ where both the carboxylate and hydroxyl group coordinate the metal ion in a chelating manner [KUK2010].

The stoichiometry of the formed complexes was calculated with slope analysis according to Eq. 2-4 to 2-6. At 25°C, up to approximately 0.01 M salicylate a slope of 0.7 ± 0.1 suggests the dominance of the 1:1 complex EuSal²⁺, whereas with higher ligand concentration the

slope of 1.8 ± 0.2 indicates the formation of the 1:2 complex $\text{Eu}(\text{Sal})_2^+$. The average slope over the whole measured concentration range is 1.3 ± 0.2 . With higher temperatures the slope at higher ligand concentration increases slightly up to 2.0 ± 0.2 (55°C) and the average slope increases up to 1.7 ± 0.1 (60°C). Provided that the formation of the 1:1 and 1:2 complexes occur in this region a formation of a 1:3 complex $\text{Eu}(\text{Sal})_3$ seems to be reasonable.

The complex stability constants for these 3 complexes could be determined in the studied temperature range between 25°C and 60°C (Tab. 2-8). Up to date only the stability constants for the 1:1 and 1:2 complexes and only at room temperature have been determined [AOY2004, HAS1989, IRV1970]; the 1:2 complex was observed only once [HAS1989]. The literature values are somewhat higher than ours (see Tab. 2-8). This is possibly due to a small amount of undetected 1:3 complex, which might be enlarged apparently the constants of the 1:1 and 1:2 complexes. The thermodynamic data of the complexes calculated from the Van't Hoff plot depicted in Fig. 2-12 (right) are listed in Tab. 2-8.

The values indicate that the formation of the 1:1 complex is nearly temperature independent. In accordance with the literature the reaction enthalpy $\Delta_r H$ is close to zero within the error bars [HAS1990]. The formation of the 1:2 complex is slightly endothermic (similar to the literature value [HAS1990]), and the 1:3 complex is even stronger endothermic. This might be an explanation why this complex was not detected at room temperature so far. The reaction entropy is positive and increases with increasing ligand number. This is in accordance with the fact given by the luminescence lifetimes that each ligand substitutes about 2 water molecules in the first coordination shell of Eu(III).

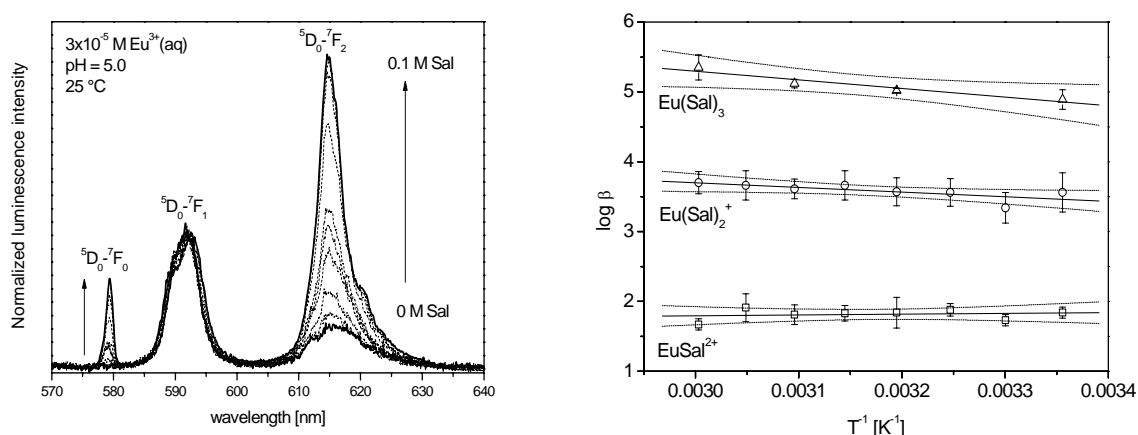


Fig. 2-12: Left: Luminescence emission spectra of the spectrophotometric titration of $3 \cdot 10^{-5}$ M Eu(III) with 0.001-0.1 M salicylate (25°C , $\text{pH} = 5.0$, $I = 0.1$ M NaClO_4). Right: Van't-Hoff plot of the Eu(III)-salicylate complex formation.

Thermodynamic data of complexation of Eu(III) and Am(III) with salicylic acid

For the first time a 1:3 Eu(III)-salicylate complex was identified and thermodynamically characterized. With increasing complex stoichiometry the complexation enthalpies and entropies increase (Tab. 2-8). This indicates, that the formation of the 1:2 and particularly the formation of the 1:3 complexes are more driven by entropy than the 1:1 complexes.

Furthermore, Tab. 2-8 contains the data of the complexation of Am(III) with salicylic acid, published by Müller et al [Mül2010]. These complexes were UV-vis-spectroscopically identified and thermodynamically characterized for the first time.

Tab. 2-8: Stability constants at varying temperatures and thermodynamic data of Eu(III)/Am(III) complexes with salicylate determined by TRLFS (I = 0.1 M NaClO₄).

Am(III)				
T [°C]	logβ ₁₁₀	logβ ₁₂₀	logβ ₁₃₀	Ref.
25	2.56 ± 0.08	3.93 ± 0.19		this work [MÜL2010] ^{a)}
Eu(III)				
T [°C]	logβ ₁₁₀	logβ ₁₂₀	logβ ₁₃₀	Ref.
25	2.02	3.84		[HAS1989]
25	2.08			[AOY2004]
25	2.59			[IRV1970]
25	1.84 ± 0.08	3.56 ± 0.28	4.89 ± 0.14	this work
30	1.73 ± 0.08	3.34 ± 0.22		this work
35	1.88 ± 0.09	3.56 ± 0.20		this work
40	1.84 ± 0.22	3.57 ± 0.15	5.02 ± 0.13	this work
45	1.83 ± 0.11	3.66 ± 0.21		this work
50	1.81 ± 0.14	3.61 ± 0.22	5.12 ± 0.16	this work
55	1.91 ± 0.14	3.66 ± 0.21		this work
60	1.67 ± 0.08	3.70 ± 0.16	5.35 ± 0.18	this work
Δ _r H [kJ·mol ⁻¹]	-2.14 ± 4.9 1.3 ^{b)}	12.7 ± 4.8 5.7 ^{b)}	23.7 ± 4.9	this work [HAS1990]
Δ _r S [J·K ⁻¹ ·mol ⁻¹]	28 ± 15	109 ± 15	172 ± 16	this work

^{a)}UV-vis with LPFC ^{b)} from calorimetry (25°C)

2.2.4 Lactic acid

Lactic acid is an alpha hydroxyl acid, which is considered as ubiquitous in environment. It can be regarded as decomposition product of larger molecules, e.g. humic acids and is an important intermediate in metabolism. Furthermore it is used in large amount in food industry. Due to its prominence it is used as model ligand for complex formation with various metal ions [TIA2010].

Europium - TRLFS

Fig. 2-13 (left) shows the luminescence spectra of Eu(III) with lactate. With increasing ligand concentration we observe the spectral changes which are typical for complex formation: strong increase of the intensity of the hypersensitive ⁵D₀-⁷F₂ transition at about 615 nm, appearance of the symmetry-forbidden ⁵D₀-⁷F₀ transition, and a prolongation of the luminescence lifetime. This general behavior remains equal within the temperature range between 25 and 70°C and between pH 5 and 6. The luminescence lifetime increases from 111 ± 2 μs for the Eu(III) aquo ion up to 225 ± 2 μs at 0.1 M lactate. This corresponds to a number of 5 remaining water molecules; 4 water molecules have been removed upon complexation with lactate. This is in good accordance to literature, where a luminescence lifetime of 197 μs for the highest lactate concentration was observed [TIA2010]. Following the interpretation of Tian et al. [TIA2010], that the hydroxyl group of lactate is involved in

the coordination of the Eu^{3+} ion and about 1.5 water molecules are exchanged through 1 lactate it is assumed that 1:1, 1:2 and 1:3 Eu(III)-lactate complexes are formed. The stability constants of these 3 complexes were determined for various temperatures (Tab. 2-9) and with Eq. 2-7 thermodynamic data were determined (Tab. 2-9 and Fig. 2-14). Whereas the formation of the 1:1 and 1:2 complexes are nearly temperature independent, the 1:3 complex formation reaction is slightly exothermic. In contrast, Tian et al. [TIA2010] observed exothermic formation reactions for all 3 complexes. Indeed, they carried out their experiments at an ionic strength of 1.0 M. This difference is possibly caused by the different ionic strengths. A possible relationship between thermodynamic data and the ionic strength will be a topic in the following project.

Americium – TRIFS

The Am(III) aquo ion shows at pH 3-6 and between 25 and 65°C a luminescence lifetime of 23.2-23.8 ns. Applying Eq. 2-3, this corresponds to approximately 9 coordinating water molecules. Complexation with lactate causes a strong increase of the luminescence intensity and a red shift of the luminescence maximum of about 5 nm (Fig. 2-13, right). The luminescence lifetime is prolonged up to 37 ns which corresponds to 5-6 remaining water molecules, indicating an exchange of about 3-4 water molecules with coordination sites of ligand molecules, similar to the Eu-lactate system, which implies the formation of 1:1, 1:2 and 1:3 complexes.

The slope analysis applying Eq. 2-4 – 2-6 shows that up to a lactate concentration of 0.01 M mainly the 1:1 complex is formed. At higher ligand concentration additionally the 1:2 and 1:3 complexes are coexistent. We were not able to separate these higher complexes. Therefore we only determined the stability constant of the 1:1 complex at various temperatures and derived the thermodynamic data of this complex (Tab. 2-9 and Fig. 2-14). The values are in very good agreement with those of the Eu(III)-lactate 1:1 complex.

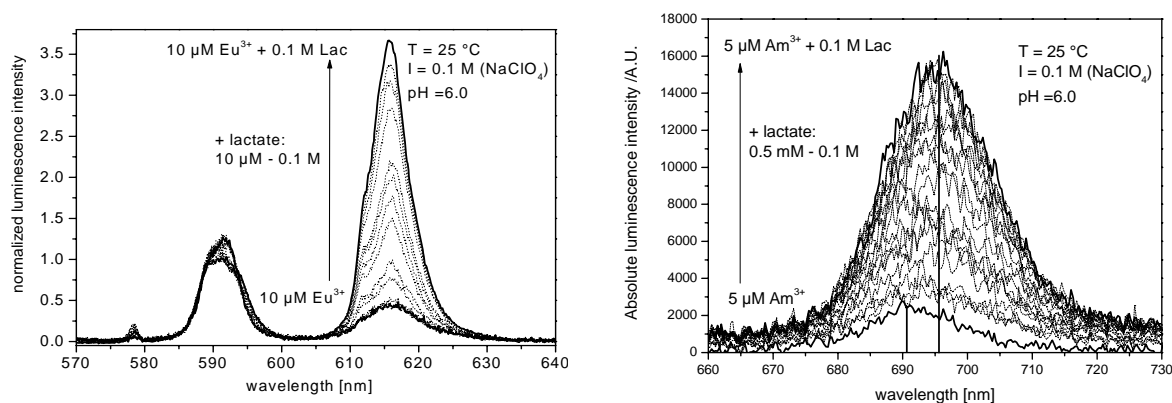


Fig. 2-13: Left: Luminescence emission spectra of the spectrophotometric titration of $1 \cdot 10^{-5}$ M Eu(III) with lactate (25°C , $\text{pH} = 6.0$, $I = 0.1\text{ M NaClO}_4$). Right: Luminescence emission spectra of the spectrophotometric titration of $5 \cdot 10^{-6}$ M Am(III) with lactate (25°C , $\text{pH} = 6.0$, $I = 0.1\text{ M NaClO}_4$).

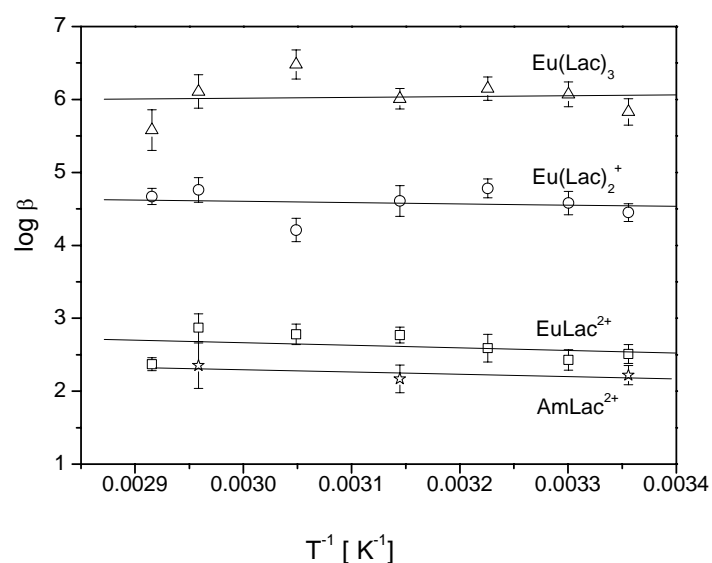


Fig. 2-14: Van't-Hoff plots of the Eu(III) and Am(III) lactate complex formation determined by TRLFS

Americium – UV-vis

Fig. 2-15 (left) shows the absorption spectra of Am(III) with increasing ligand concentration. The addition of ligand induces a slight bathochromic shift of the absorption band. Until a ligand concentration of 10^{-3} M the shift is smaller than 1 nm. This shift is a clear hint for complex formation (Fig. 2-15 right).

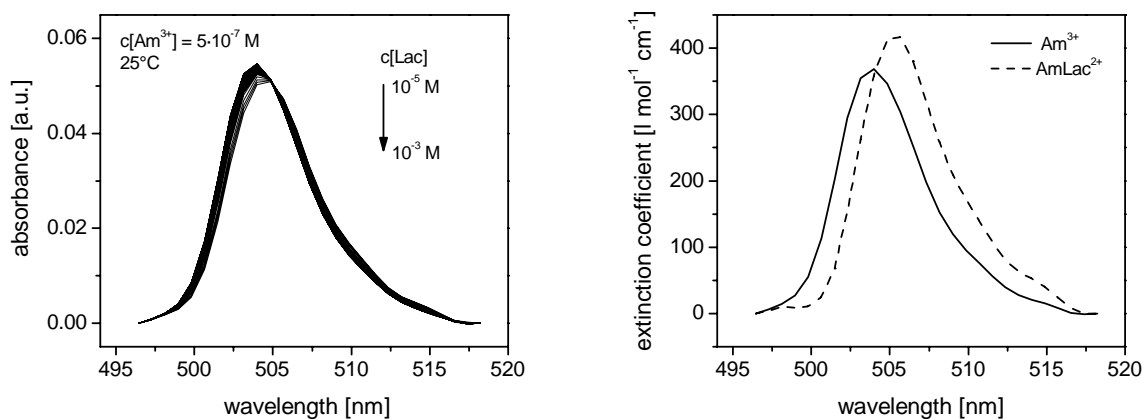


Fig. 2-15: Left: UV-vis absorption spectra of Am(III) at pH 5.0 and 0.1 M NaClO₄ with increasing ligand concentration at 25°C. The slight decrease of the Am(III) absorption is caused by dilution effects during spectrophotometric titrations. Right: single component spectra determined with SPECFIT.

The model free factor analysis provided by SPECFIT as well as the slope analysis indicate the formation of one complex species within the investigated concentration range. The complex stability constants determined from the measurements at 25°C and 50°C are listed in Tab. 2-9 and indicate an endothermic reaction. This is in agreement with the results from TRLFS as well as with the findings for the analogue Eu(III) complex.

Thermodynamic data of complexation of Eu(III) and Am(III) with lactic acid

Tab. 2-9: Stability constants at varying temperatures and thermodynamic data of Eu(III) and Am(III) complexes with lactate determined by TRLFS and UV-vis ($I = 0.1 \text{ M NaClO}_4$).

system	Am(Lac) ²⁺	Eu(Lac) ²⁺	Eu(Lac) ₂ ⁺	Eu(Lac) ₃ ⁺	Ref.
T [°C]	logβ ₁₁₀	logβ ₁₁₀	logβ ₁₂₀	logβ ₁₃₀	
25	2.22 ± 0.13 2.24 ± 0.04 ^{a)}	2.51 ± 0.13	4.45 ± 0.12	5.83 ± 0.18	this work this work ^{a)}
		2.80	4.76	6.33	[TIA2010] ^{c)} [LUN1984] ^{b),c)}
30	2.43	2.43 ± 0.14	4.58 ± 0.16	6.07 ± 0.17	this work
37		2.59 ± 0.19	4.78 ± 0.13	6.15 ± 0.16	this work
45	2.17 ± 0.19	2.77 ± 0.11	4.61 ± 0.21	6.01 ± 0.14	this work
50	2.75 ± 0.04 ^{a)}				this work ^{a)}
55		2.78 ± 0.14	4.21 ± 0.16	6.48 ± 0.20	this work
65	2.35 ± 0.31	2.87 ± 0.19	4.76 ± 0.17	6.11 ± 0.23	this work
70		2.37 ± 0.09	4.67 ± 0.11		this work
Δ _r H [kJ·mol ⁻¹]	6.0 ± 6.6 -16	6.7 ± 9.2	3.3 ± 1.3	-2.1 ± 1.6	this work [LUN1984] ^{c),d)} [TIA2010] ^{c),d)}
Δ _r S [J·K ⁻¹ ·mol ⁻¹]	62 ± 20 -6	28 ± 15	109 ± 15	172 ± 16	this work [LUN1984] ^{c),d)} [TIA2010] ^{c),d)}
		46	76	78	

^{a)} UV-vis with LPFC, not used for Vant' Hoff plot ^{b)} solvent extraction. ^{c)} $I = 1 \text{ M (NaClO}_4)$. ^{d)} calorimetry

2.2.5 Citric, tartaric, and acetic acid

The further organic compounds acetic, tartaric, and citric acids also occur in the environment and therefore are widely used as model ligands for natural organic matter. Tartaric and citric acid are hydroxyl carboxylic acids with two and three carboxyl groups, respectively. The hydroxyl groups are non-dissociated until $\text{pH} > 12$ and do not contribute to the complex formation in the considered pH range between 4 and 5. Under the studied conditions at $\text{pH} = 5$ the deprotonation of three carboxylic groups of citric acid yields to the relevant species CitH_2^- with two protons, CitH^{2-} with one proton, and the deprotonated form Cit^{3-} . Several authors suggest that the fully deprotonated species Cit^{3-} are the predominant ligands in the formed Ln(III)/Am(III) complexes [MAT2007, OHY1971, EBE1972, HUB1974, HEL2010]. In contradiction, under the given conditions the single protonated species CitH^{2-} has the highest concentration compared to the other species.

For the acetic and tartaric acid only the entirely deprotonated species are relevant in the investigated pH range.

The complexation of Am(III) with these three acids were studied by UV-vis absorption spectroscopy with LPFC only. As already found for pyromellitic acid, salicylic acid [MÜL2010], and lactic acid a small red shift of the Am(III) and Eu(III) absorption bands were found with increasing concentrations of acetic, tartaric, and citric acid.

Fig. 2-16 shows exemplarily the Am(III) absorption spectra with increasing citric acid concentration at $\text{pH} 5$ and an ionic strength of 0.1 M NaClO_4 . Two different species were

identified within the spectra. The absorption spectrum of the first species is shifted about 1 nm and the second species about 2 nm in comparison to the Am(III) aquo ion. The species are designated as 1:1 and 1:2 complex species and are assumed to be formed by the fully deprotonated Cit³⁻ species. The spectrophotometric titration was performed at different temperatures between 25 and 50°C and the corresponding stability constants were calculated using SPECFIT.

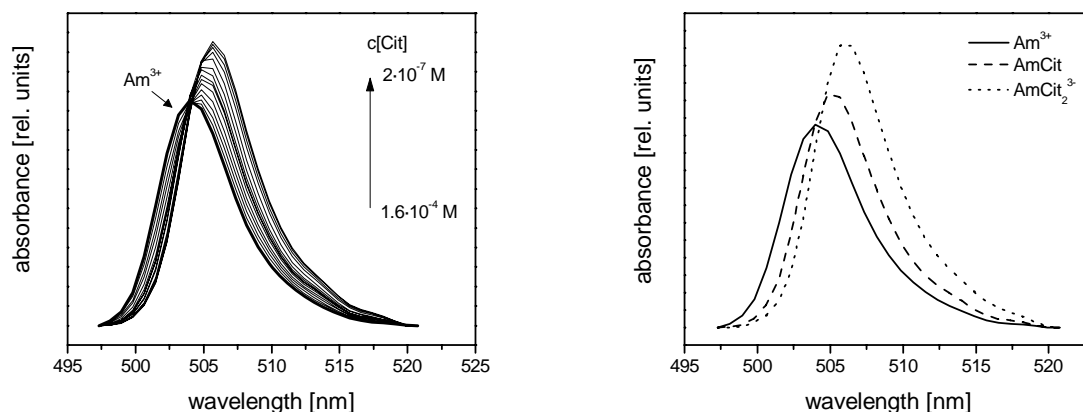


Fig. 2-16: Left: UV-vis absorption spectra of Am(III) at 25°C, pH 5.0 and I = 0.1 M NaClO₄. The Am(III) concentration is fixed at 5·10⁻⁷ M. Right: single component spectra determined with SPECFIT.

The thermodynamic parameters listed in Tab. 2-10 were calculated from the Van't Hoff plots in Fig. 2-17. The values show considerable uncertainties and the linear relationship between the two quantities is of poor quality, as indicated by the quite low R². Heller, who studied the complexation with Eu(III) under similar conditions assumed that several Eu(III) citrate complexes with different numbers of ligands and, furthermore, with ligands of different degree of protonation are formed at this pH [HEL2010]. However, it is yet unclear if the shift originated by different protonated Am(III) complex species is pronounced enough so that different complexes can be identified or even distinguished from each other. An evidence for the existence of an AmCitH species at pH 5 was obtained by spectrometric pH titration at constant Am(III) and ligand concentration (Fig 2-18).

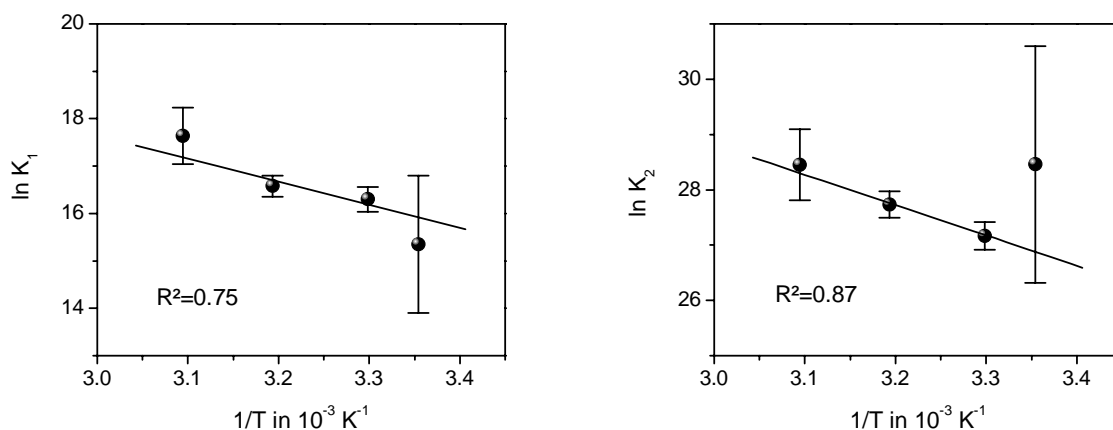


Fig. 2-17: Van't Hoff plots of the Am(III)-citrate complex formation determined by UV-vis spectroscopy. Left: 1:1 complex. Right: 1:2 complex

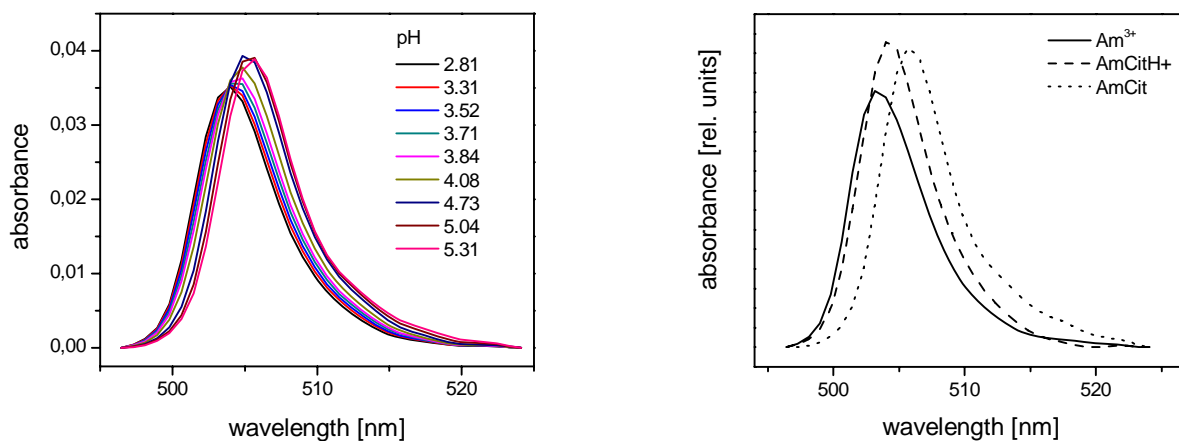


Fig. 2-18: Left: UV-vis absorption spectra of Am(III) at 25°C as function of pH and $I = 0.1 \text{ M NaClO}_4$. The Am(III) concentration is fixed at $5 \cdot 10^{-7} \text{ M}$. Right: single component spectra determined with SPECFIT.

Fig. 2-18 shows pH dependent spectra of $5 \cdot 10^{-7} \text{ M}$ Am(III) solution with 10^{-5} M citric acid at 25°C. At pH below 3 no complexation is observed. At pH 3.5 a clear red shift of the absorption band to higher wavelength and higher absorption occurs. At pH 4 a sudden, strong bathochromic shift and a significant decrease in absorption is found. This is a clear hint for the existence of a second complex species. It is unresolved yet, if this can either be attributed to a changed complex stoichiometry, i.e. a 1:2 complex, or to a 1:1 complex with a probably deprotonated ligand. Further measurements at lower ligand concentration need to be done to exclude or to verify these hypotheses. In addition, the question for the dominant species at pH 5 has to be answered.

The complexation of Am(III) with acetic and tartaric acid were studied in the same manner. The results on the found complexes, their stoichiometry, and the thermodynamic data are summarized in Tab. 2-11 for acetic acid and in Tab. 2-12 for tartaric acid.

Tab. 2-10: Stability constants at varying temperatures and thermodynamic data of Am(III) complexes with citrate determined by UV-vis ($I = 0.1 \text{ M NaClO}_4$).

T [°C]	$\log\beta_{110}$	$\log\beta_{120}$	Ref ^{c)}
25	$7.5 \pm 0.2^{\text{a)}$	$11.4 \pm 0.4^{\text{a)}$	[HEL2010]
25	6.67 ± 0.63	12.36 ± 0.93	this work
30	7.08 ± 0.11	11.80 ± 0.11	this work
40	7.20 ± 0.10	12.04 ± 0.11	this work
50	7.66 ± 0.26	12.36 ± 0.28	this work
$\Delta_r H$ [kJ mol ⁻¹]	41 ± 17	46 ± 12	this work
	$11.1 \pm 3.1^{\text{b)}$	$19 \pm 3.9^{\text{b)}$	[MAT2007]
$\Delta_r S$ [J mol ⁻¹ K ⁻¹]	268 ± 53	376 ± 39	this work
	$154 \pm 10^{\text{b)}$	$265 \pm 13^{\text{b)}$	[MAT2007]

a) for the analogue Eu(III) complex

b) $I=6.6 \text{ mol kg}^{-1}$, pH 3.6, solvent extraction

c) more references to Ln(III)/An(III) citrate complexes are given in [HEL2010] and [MOM2005]

Tab. 2-11: Stability constants at varying temperatures and thermodynamic data of Am(III) complexes with acetate determined by UV-vis ($I = 0.1 \text{ M NaClO}_4$).

T [°C]	$\log\beta_{110}$	Ref
25	2.39 ± 0.05	[RAO1987]
25	2.14 ± 0.07	this work
40	2.26 ± 0.07	this work
50	2.30 ± 0.12	this work
<hr/>		
$\Delta_r H$ [kJ mol ⁻¹]	11 ± 1	this work
	$7.1 \pm 0.03^{\text{a}}$	[ZAN2001]
<hr/>		
$\Delta_r S$ [J mol ⁻¹ K ⁻¹]	78 ± 3	this work
	$66 \pm 0.4^{\text{a}}$	[ZAN2001]

a) determined for the Nd(III) acetate complex at $I = 2.2 \text{ mol kg}^{-1} \text{ NaClO}_4$ and 25°C

Tab. 2-12: Stability constants of Am(III)/Eu(III) complexes with tartrate determined by UV-vis at 25°C ($I = 0.1 \text{ M NaClO}_4$).

ion	$\log\beta_{110}$	$\log\beta_{120}$	Ref
Eu(III)	4.17 ± 0.13	7.27 ± 0.23	this work [ACK2011]
	4.3^{a}	6.0^{a}	[KUL1986]
Am(III)	3.84 ± 0.10	6.54 ± 0.15	this work [ACK2011]
	$4.2 \pm 0.06^{\text{b}}$	$6.84 \pm 0.07^{\text{b}}$	[RAO1987]

a) 0.1 M NaNO₃, polarography

b) 0.5 M NH₄Cl, solvent extraction

2.3 Conclusions and update of the thermodynamic database

In the present study the complexation behavior of Am(III) and Eu(III) with several small organic acids were studied as function of temperature by means of UV-vis measurements in a LPFC and TRLFS. The stoichiometry of the formed complexes, their stability constants, and thermodynamic data were determined. Several new complexes were identified and thermodynamically characterized, such as the 1:3 Eu(III)-salicylate complex, the 1:1 and 1:2 Am(III)-pyromellitate complexes, and the 1:1 and 1:2 Am(III)-salicylate complexes. Already known complexes were examined by spectrometric methods for the first time, such as the Am(III) complexes with tartaric, citric, acetic, and lactic acid.

Table 2-13 summarizes the obtained complex formation constants and Gibbs free energies of complexation for the 1:1 complexes at an ionic strength of $I = 0$ (calculated by Davies equation). In any of the studied metal-ligand systems the complexation enthalpies for the 1:1 complexes were found to proceed endothermic with a positive change in the entropy during the complexation. Therefore, the complex formation is driven by entropy. Among the studied acids, citric, pyromellitic, and tartaric acid form complexes with the highest stability. Fig. 2-19 shows a sound correlation between the $\log\beta^0$ of the complexes with the number of carboxylic groups per ligand molecule. The higher the number of the COOH-groups the higher the complex stability. Pyromellitic acid with four carboxylic groups per molecule is an exemption since the complexation of a metal ion by all of the four groups is sterically hindered.

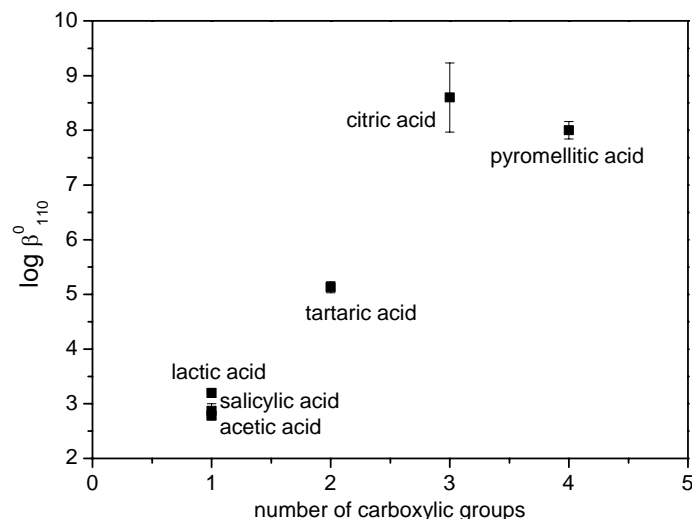


Fig. 2-19: Stability constants $\log\beta_{110}^0$ of 1:1 Am(III)-ligand complexes as function of carboxylic group number

Complexes with a stoichiometry of higher than 1:1 are typically formed at higher ligand concentrations. For salicylic and lactic acid an excess of the ligand of 0.1 M compared to a metal ion concentration in the micromolar range was necessary to form 1:3 complexes. The thermodynamic data were determined of the found complexes. However, they are considered as less relevant for migration studies.

Pyromellitic acid forms again an interesting exception. This compound exhibits a strong tendency to polymerization in presence of Eu(III). That occurs at higher Eu(III) concentrations (millimolar solutions) already at room temperature. The formed polymeric species are able to form complexes with the present metal ions.

A closer look at the Gibbs free energies of complexation at an ionic strength of $I = 0$ reveals an interesting detail (Tab. 2-13). The complexes formed between Am(III) and pyromellitic and salicylic acid are slightly more stable than the analogues complexes with Eu(III). If non-aromatic acids are used for complexation, the Eu(III) complexes exhibit a slightly higher stability than those of Am(III) with the same ligands. However, the derived enthalpies and entropies of complexation (Tab. 2-14) exhibit an uncertainty that is too high to attribute the different complex stabilities to an enthalpic or entropic contribution. A further interpretation is useful if more thermodynamic data are available. The next step will be done in the succeeding project with the study of complexation by micro-titration calorimetry.

Tab. 2-13: Stability constants and the Gibbs free energies of 1:1 Am(III)/Eu(III)-ligand complexes at $T = 25^\circ\text{C}$ and $I = 0$

ligand	$\log\beta_{110}^0$		ΔG^0 [kJ·mol ⁻¹]	
	Eu(III)	Am(III)	Eu(III)	Am(III)
pyromellitate	7.28 ± 0.06	8.00 ± 0.16	-41.5 ± 0.3	-45.6 ± 0.9
salicylate	2.48 ± 0.08	3.20 ± 0.08	-14.1 ± 0.5	-18.3 ± 0.5
lactate	3.15 ± 0.13	2.87 ± 0.13	-18.0 ± 0.7	-16.4 ± 0.7
acetate	3.46 ± 0.05 ^{a)}	2.78 ± 0.07	-19.7 ± 0.3	-15.9 ± 0.4
tartrate	5.46 ± 0.13	5.13 ± 0.10	-31.1 ± 0.7	-29.3 ± 0.6
citrate	9.43 ± 0.20 ^{b)}	8.60 ± 0.63	-53.8 ± 1.1	-49.1 ± 3.6 ^{c)}

a) calculated from value given in [ZOT200]

b) calculated from value given in [HEL2010]

c) value in very good agreement by the in [MOM2005] selected values ($\log\beta_{110}^0 = 8.55 \pm 0.2$ and $\Delta_r G^0 = -48.806 \pm 1.142$)

Tab. 2-14: Enthalpy ΔH^0 and entropy ΔS^0 of Am(III)/Eu(III) ligand 1:1 complexes at 25°C and I = 0

ligand	Eu(III)		Am(III)	
	ΔH^0 [kJ·mol ⁻¹]	ΔS^0 [J·mol ⁻¹ ·K ⁻¹]	ΔH^0 [kJ·mol ⁻¹]	ΔS^0 [J·mol ⁻¹ ·K ⁻¹]
pyromellitate	34.7 ± 1.2	256 ± 4	103.2 ± 58.9	496 ± 189
salicylate	2.0 ± 4.9	54 ± 15	--	--
lactate	10.9 ± 9.3	98 ± 29	10.4 ± 6.5	89 ± 20
acetate	--	--	16.5 ± 2.0	109 ± 6
tartrate	--	--	--	--
citrate	--	--	76.8 ± 13.3	424 ± 43

a) ΔH^0 and ΔS^0 values were recalculated from Van't Hoff plots using $\log\beta_{110}^0$ (converted by Davies equation)

3 Eu(III) sorption on Opalinus Clay [SCH2012]

3.1 Experimental

3.1.1 Solutions and reagents

An aerobic OPA sample prepared from the bore core BHE-24/1 from the underground rock laboratory Mont Terri, Switzerland, was used without any purification and other treatments. The average mineral composition of OPA is given in [NAG2002]. The physicochemical properties (N_2 -BET surface area, cation exchange capacity) of the OPA sample BHE-24/1 are summarized in [JOS2011].

To simulate the aqueous medium in the OPA rock formation the sorption experiments were carried out in synthetic OPA pore water with a pH of 7.6 and an ionic strength of 0.4 M. The composition of the synthetic OPA pore water was taken from [VAN2003]. In some batch experiments 0.4 M sodium perchlorate as background electrolyte was used to compare the results with published ones in the literature.

Synthetic OPA pore water was prepared under the composition described in [VAN2003]. Chemicals of analytical grade were used without any purification. Different stock solutions (0.01 M, 0.1 M and 1 M) of citric acid (Merck) and tartaric acid (Merck) were prepared by dissolving the according amounts of the solids in deionized water. For sorption experiments with citric acid, ^{14}C -labeled citric acid (Hartmann Analytic) were used [SCH2010b]. A carrier free ^{152}Eu solution (Amersham Lifescience) was diluted in the synthetic OPA pore water to get a stock solution with a radiotracer concentration of $5 \cdot 10^{-7}$ M. The ^{152}Eu concentration of this stock solution was verified by γ -spectroscopy (Ortec, detector GMX20P4-70). Aliquots from a $5 \cdot 10^{-3}$ M stock solution of inactive Eu(III) (chapter 2.1.1) were used for TRIFS samples with higher Eu(III) concentrations (10^{-5} M).

Necessary pH adjustments were done with NaOH or $HClO_4$ with an accuracy of 0.05 pH units like described in chapter 2.1.1.

3.1.2 Batch experiments

All sorption experiments were carried out as batch experiments under aerobic conditions ($p(CO_2) = 10^{-3.5}$ atm) in 10 mL polyethylene centrifuge tubes (Sigma Laborzentrifugen GmbH) with 7.5 mL suspensions of OPA in synthetic OPA pore water. The total Eu(III) concentration in each sample was $2 \cdot 10^{-9}$ M. Following series of samples were investigated:

- ◆ Sorption experiments with OPA suspensions at solid-to-liquid ratios from $0.33 \text{ g}\cdot\text{L}^{-1}$ to $3 \text{ g}\cdot\text{L}^{-1}$ in dependence on temperature between 15°C and 50°C and in the absence of citrate and tartrate
- ◆ Sorption experiments in the presence of citrate and tartrate in dependence on temperature between 15°C and 50°C with OPA suspensions at a solid-to-liquid ratio of $2 \text{ g}\cdot\text{L}^{-1}$. The ligand concentration was varied up to $5 \cdot 10^{-3}$ M.
- ◆ pH serie with OPA suspensions at a solid-to-liquid ratio of $2 \text{ g}\cdot\text{L}^{-1}$ and at 25°C

Comprehensive leaching experiments by Joseph et al. [JOS2011] showed that the equilibrium between the clay and the OPA pore water was reached after 7 days. During this period of time aluminate, silicate, sulfate, carbonate and calcium ions are released due to dissolution processes of some OPA components such as calcite. Thus, in our sorption experiments the OPA was preconditioned at the selected temperature for 5 to 7 days in the synthetic OPA pore water until a stable pH was reached.

After addition of aliquots of ^{152}Eu and tartrate or citrate to the samples the suspensions were equilibrated. During the conditioning of the clay and during the Eu(III) sorption the pH of the samples was readjusted to 7.6 for several times. All samples were permanently stored in a temperature adjustable shaker (HLC, KühlThermomixer) or in an heatable metal block. The Eu(III) sorption was carried out for 7 days to ensure a steady state of the sorption reaction [BAU2005]. After that the samples were centrifuged (3K30H, Sigma Laborzentrifugen GmbH) at the selected temperature and 40,000 g for 1 h. Investigations of the centrifuged clay samples with photon correlation spectroscopy showed supernatants free of particles.

The supernatants, the suspensions, and the acidified suspensions of the sorption samples were analyzed concerning the ^{152}Eu activity by gamma counting (Packard, CobraII) to determine the distribution of Eu(III) between the synthetic OPA pore water and OPA. For that two 1 mL samples of the supernatant of each sorption sample were taken for the analysis. Each sorption sample was then shaken vigorously to get a fine suspension. Two samples of 1 mL of the suspension of each sorption sample were taken for the analysis again. At the end, the remaining part of the suspension was acidified to determine the Eu(III) sorption on the tube wall. Again two samples of 1 mL were taken for the analysis. Around 5 % of the total amount of Eu(III) were found as sorbed on the tube walls.

The distribution coefficient R_d was calculated by Eq. 3-1 [LAU2000],

$$R_d = \frac{c_{in} - c_{eq}}{c_{eq}} \cdot \frac{L}{S} \quad (3-1)$$

(R_d : distribution coefficient [$\text{L}\cdot\text{kg}^{-1}$], c_{in} : added Eu(III) concentration [$\text{mol}\cdot\text{L}^{-1}$], c_{eq} : equilibrium concentration of Eu(III) [$\text{mol}\cdot\text{L}^{-1}$], $L\cdot S^{-1}$: liquid-to-solid ratio [$\text{L}\cdot\text{kg}^{-1}$]).

Another method to determine R_d values is to analyze the experimental sorption isotherms with the Freundlich model in logarithmic form (Eq. 3-2),

$$\log a = \log R + n \log c_{eq} \quad (3-2)$$

(a : loading of the clay with Eu(III) [$\text{mol}\cdot\text{kg}^{-1}$], c_{eq} : equilibrium concentration of Eu(III) [$\text{mol}\cdot\text{L}^{-1}$], R : Freundlich coefficient [$\text{L}\cdot\text{kg}^{-1}$], n : Freundlich coefficient). For $n = 1$ $\log R$ is equal to $\log R_d$ [KLI2007].

3.1.3 Time-resolved laser-induced fluorescence spectroscopy

For the TRLFS studies the total Eu(III) concentration in each sample was 10^{-5} M. Samples with and without OPA were investigated:

- ◆ synthetic OPA pore water samples (without OPA) with citrate and tartrate at 25°C . The ligand concentration was varied up to 10^{-3} M.
- ◆ Sorption samples at 25°C in the presence of citrate and tartrate with OPA suspensions at a solid-to-liquid ratio of $2 \text{ g}\cdot\text{L}^{-1}$. The ligand concentration was varied up to 10^{-3} M. The sorption samples were prepared analogue to the batch sorption experiments at 25°C (section 3.1.2).

The TRLFS measurements were performed using a Nd:YAG-OPO laser system (Continuum). Europium luminescence spectra of the supernatants and suspensions were recorded with an optical multichannel analyser consisting of a spectrograph (Oriel MS 257) and an ICCD camera (Andor iStar) with a constant excitation wavelength of 395 nm and pulse energy of 4 mJ. Static and time-resolved spectra were recorded in the wavelength range of 565-650 nm

(1200 line mm^{-1} grating, 0.2 nm resolution, 3000 accumulations) and 440-780 nm (300 line mm^{-1} grating, 0.7 nm resolution, 200 accumulations), respectively. The time-resolved luminescence spectra were recorded with delay times between 10 μs and 100 μs . The samples were transferred into a quartz cuvette, measured with the laser system at 25°C and continuously stirred during the measurements.

The spectra were analyzed with the graphing and data analysis software package Origin™ (version 7.5, OriginLab Corporation). All raw spectra were baseline corrected in the wavelength range between 570 nm and 640 nm. The spectra were normalized to the peak area of the emissions band at 592 nm and the ratios F_1/F_2 of the peak area of the fluorescence emissions band at 592 nm and 616 nm were calculated. The analysis of the time-resolved spectra were carried out like in chapter 2.1.3 described.

3.2 Results and discussion

3.2.1 Influence of Eu(III) concentration

The batch sorption experiments in synthetic pore water were carried out at Eu(III) concentrations $\sim 10^{-9}$ M, that are realistic for environmental conditions. For the spectroscopic characterisation of the Eu sorption process on OPA with TRLFS higher concentrations ($\sim 10^{-5}$ M) of Eu(III) were necessary, so the Eu(III) speciation in pore water for both concentrations has to be considered (Fig. 3-1)

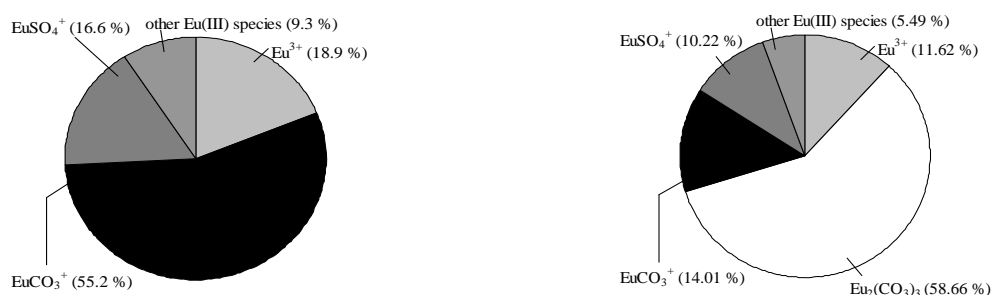


Fig. 3-1: Eu(III) speciation under synthetic pore water conditions. Left: $c_{\text{Eu(III)}} = 2 \cdot 10^{-9}$ M. Right: $c_{\text{Eu(III)}} = 1 \cdot 10^{-5}$ M. Complexation constants were taken from [HUM2001] and [RAR1985]. Speciation was calculated with the computer code EQ3/6 [WOL1992].

At low concentrations the dominated species is the EuCO_3^+ , at higher concentration the neutral species $\text{Eu}_2(\text{CO}_3)_3$ occurs. Precipitations of $\text{Eu}_2(\text{CO}_3)_3(\text{s})$ was not observed neither in synthetic pore water nor in the centrifuged clay samples as verified with photon correlation spectroscopy.

With increasing Eu(III) concentration, the Eu sorption and consequently the R_d values decrease (Fig. 3-2). This decrease may be explained on the one side by a weaker sorption mechanism of the neutral species $\text{Eu}_2(\text{CO}_3)_3$ and on the other side by high- and low affinity sorption sites. At higher concentration high affinity sorption sites are already occupied and thus low affinity sites should be embraced, which is resulting in a weaker sorption [FRÖ2011].

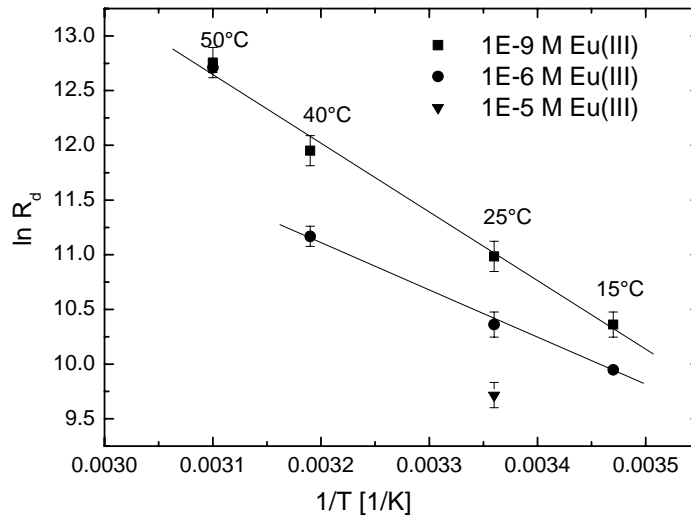


Fig. 3-2: Eu(III) sorption on Opalinus Clay as function of Eu(III) concentration and temperature (synthetic pore water)

3.2.2 Influence of pH

It is well known that the sorption of trivalent lanthanides and actinides on clay minerals depends on pH [BRA2006, BAU2005, HAR2008, RAB2005, FER2008]. Thus, the same behaviour is observed at Eu(III) sorption on OPA in pore water medium. There is a low sorption at pH values smaller than 6. A strong sorption with > 95% Eu(III) sorption occurs at pH values larger than 9. The distribution coefficient R_d increases with increasing pH (Tab. 3-1)

Tab. 3-1: Sorbed Eu(III) and R_d as function of pH, $T = 25^\circ\text{C}$ (synthetic pore water)

pH	sorbed Eu [%]	R_d
2.1	< 1	0.37 ± 0.26
3.9	5 ± 1	1.43 ± 0.05
5.1	42 ± 5	2.56 ± 0.05
6.4	70 ± 1	3.14 ± 0.05
7.6	90 ± 5	4.77 ± 0.06
9.4	96 ± 2	5.65 ± 0.05

The pH dependence is accompanied by a change in Eu(III) speciation, as shown by speciation calculations and TRLFS investigations. The different Eu species in pore water solutions interact differently with the OPA surface.

The dominating Eu species between pH 2 and 5 are the positively charged species $\text{Eu}^{3+}_{\text{aqua}}$ (~47.8%), EuSO_4^+ (~41.6%), and EuCl^{2+} (~7.7%). The non-specific electrostatic attraction between these species with the negative charged OPA surface [JOS2011b] results in an outer-sphere complex formation. The strong increase of the sorption at pH values larger than 5 goes along with a complex formation between the dominating Eu-carbonato species (EuCO_3^+) and the hydroxyl groups of the OPA surface.

Investigations of the pH dependence of Eu-(sorption) speciation with TRLFS were performed to validate this interpretation. The results are summarized in Tab. 3-2.

In synthetic pore water without clay, there are no changes in speciation of Eu(III) until pH 5. The fluorescence properties are nearly constant. The luminescence emission lifetime is in good agreement with that of the Eu(III) aquo ion in water given by $(110 \pm 5) \mu\text{s}$ corresponding to 9 water molecules [MOU1999, PLA2003].

At pH 6 the ratio F_1/F_2 of the intensities of the fluorescence emissions band at 592 nm and 616 nm was changed and at pH > 7 the fluorescence emission lifetime increases. The observed enhanced luminescence emission lifetime of $139 \pm 2 \mu\text{s}$ is caused by the formation of Eu(III)-carbonato species, like EuCO_3^{2+} , $\text{Eu}_2(\text{CO}_3)_3$ (see Fig. 3-1). In the literature the luminescence emission lifetimes of EuCO_3^{2+} and $\text{Eu}_2(\text{CO}_3)_{3(s)}$ are given by $170 \pm 10 \mu\text{s}$ and $234 \pm 10 \mu\text{s}$, respectively [KIM1994, RUN2000].

The results of the TRLFS investigations correlate with the results of the batch experiments:

Until pH 5 in the suspensions no sorbed species on the OPA can be detected with TRFLS. The analyzed Eu(III) species in the supernatants has nearly the same fluorescence spectra and properties like the species in the synthetic pore water without clay (Tab. 3-2).

At pH ≥ 6 the sorption increases strongly and a sorbed species was observed in the clay suspension and simultaneous, in the supernatant the concentration of not sorbed Eu(III) is deemed to be too low (smaller than 5% of the total Eu(III) concentration) for an analysis with TRLFS. The luminescence emission lifetime of the sorbed Eu(III) species under atmospheric synthetic OPA pore water conditions was determined to be $(190 \pm 7) \mu\text{s}$ corresponding to 5.0 ± 0.5 water molecules (Tab. 3-2, Eq. 2-2). So the sorption process of Eu(III) on OPA causes a loss of four water molecules. Thus, an inner sphere surface complex formation between a Eu(III) species, most likely the Eu(III) carbonato species EuCO_3^+ , $\text{Eu}_2(\text{CO}_3)_3$, and the minerals in OPA under pore water conditions can be postulated.

For comparison, the luminescence emission lifetimes for sorbed Eu(III) species on different minerals given in Tab. 3-3 demonstrate a good accordance between this work and previously published values. An(III)/Ln(III) carbonato surface complexes are postulated from modelling calculations [FER2008] and spectroscopic investigations [FER2010, STU2002] at pH > 7.

Tab. 3-2: Luminescence emission lifetime (τ), amounts of water molecules in the first coordination shell ($n(\text{H}_2\text{O})$) and ratio of transition bands at 592 nm and 616 nm (${}^5\text{D}_0 \rightarrow {}^7\text{F}_1$ to ${}^5\text{D}_0 \rightarrow {}^7\text{F}_2 \equiv F_1/F_2$) in (1) synthetic pore water, (2) the supernatant of the sorption sample and (3) the suspension of the sorption sample. Lifetime error: $\pm 1 \sigma$ from repeated experiments

pH	2	3	4	5	6	7.6	9
pore water							
$\tau_{(1)}$ [μs]	116 ± 2	121 ± 6	121 ± 6	109 ± 9	118 ± 2	139 ± 2	363 ± 73
$n(\text{H}_2\text{O})_{(1)}$	8.6 ± 0.5	8.2 ± 0.5	8.2 ± 0.5	9.2 ± 0.5	8.4 ± 0.5	7.1 ± 0.5	2.3 ± 0.5
F_1/F_2	1.21	1.17	1.14	1.12	1.16	0.49	0.41
<i>species</i>	Eu ³⁺ _{aq} (~ 47.8%), EuSO ₄ ⁺ (~ 41.6%), EuCl ²⁺ (~ 7.7%)					EuCO ₃ ²⁺ (14%), Eu ₂ (CO ₃) ₃ (59%)	Eu-carbonates hydroxides
supernatant							
$\tau_{(2)}$ [μs]	121 ± 4	106 ± 5	106 ± 5	117 ± 10	115 ± 6	n.d.	n.d.
$n(\text{H}_2\text{O})_{(2)}$	7.5 ± 0.5	9.5 ± 0.5	9.5 ± 0.5	8.5 ± 0.5	8.7 ± 0.5	n.d.	n.d.
F_1/F_2	1.10	1.05	0.98	0.89	0.96	n.d.	n.d.
<i>species</i>	Eu ³⁺ _{aq} (~ 47.8%), EuSO ₄ ⁺ (~ 41.6%), EuCl ²⁺ (~ 7.7%)						
suspension							
$\tau_{(3)}$ [μs]	n.d.	n.d.	n.d.	n.d.	112 ± 9	190 ± 7	849 ± 23
$n(\text{H}_2\text{O})_{(3)}$	n.d.	n.d.	n.d.	n.d.	8.9 ± 0.5	5.0 ± 0.5	0.6 ± 0.5
F_1/F_2	n.d.	n.d.	n.d.	n.d.	0.30	0.34	0.42
<i>species</i>	--	--	--		Eu(III)carbonato surface complex		

n.d. not detectable

Tab. 3-3: Luminescence emission lifetimes of sorbed Eu(III) species under atmospheric conditions

system	t [μs]	Ref.
Eu(III), OPA, pH 7.6	190 ± 7	this work
Eu(III), OPA, pH 7.6 (in presence of citric or tartaric acid)	201 ± 9	this work (averaged)
Eu(III), γ -Al ₂ O ₃ , pH 7	239	[RAB2000]
Eu(III), SiO ₂ , pH 8	215	[PAT2007]
Eu(III), smectite, pH 7.9	180	[BAU2005]
Eu(III), gibbsite, pH 6.9	220 ± 30	[TER2006]
Eu(III), smectite, pH 7.1	333 ± 20	[STU2001]

3.2.3 Influence of temperature

These batch experiments were performed under synthetic pore water conditions at pH 7.6. Similar experiments which are described in literature were done in sodium perchlorate medium. Hence for comparisons with literature values several additional batch experiments were carried out in NaClO₄ solution with the same ionic strength like the pore water. Averaged distribution coefficients R_d for the different solid-to-liquid ratios calculated at different temperatures as well as selected literature values are compared in Table 3-4.

Tab. 3-4: Log R_d values for the sorption of some radionuclides on OPA and other clay minerals. R_d [$l \cdot kg^{-1}$] Error: $\pm 1 \sigma$ from repeated experiments

T [°C]	system	log R_d calculated by		reference
		Eq. 3-1	Eq. 3-2 ($n = 1$)	
15	Eu(III), OPA, pore water, pH 7.6	4.50 ± 0.05	4.47 ± 0.01	this work
25	Eu(III), OPA, pore water, pH 7.6	4.77 ± 0.06	4.79 ± 0.01	this work
40	Eu(III), OPA, pore water, pH 7.6	5.19 ± 0.06	5.16 ± 0.02	this work
50	Eu(III), OPA, pore water, pH 7.6	5.54 ± 0.06	5.51 ± 0.01	this work
15	Eu(III), OPA, 0.4 M NaClO ₄ , pH 7.6	5.38 ± 0,10	n.e.	this work
25	Eu(III), OPA, 0.4 M NaClO ₄ , pH 7.6	5.53 ± 0,15	n.e.	this work
40	Eu(III), OPA, 0.4 M NaClO ₄ , pH 7.6	5.62 ± 0,31	n.e.	this work
50	Eu(III), OPA, 0.4 M NaClO ₄ , pH 7.6	5.82 ± 0,28	n.e.	this work
25	Eu(III), OPA, pore water, pH 7.2		4.78	[BRA2003]
25	Eu(III), OPA, 0.1 M NaClO ₄ , pH 7.6		~ 4.6	[HAR2008]
25	Am(III), OPA, pore water, pH 7.6		4.48	[BRA2003]
25	Np(V), OPA, saturated calcite solution, pH 8.2		2.15	[FRÖ2011]
25	Np(V), OPA, pore water, pH 7.6		1.34	[BAU2005]
25	U(VI), OPA, pore water, pH 7.6		1.48	[AMA2007]
25	U(VI), OPA, pore water, pH 7.6		1.35	[JOS2011]
25	Eu(III), montmorillonite, 0.5 M NaClO ₄ , pH 7.6		~ 4.8	[TER2006]
40	Eu(III), montmorillonite, 0.5 M NaClO ₄ , pH 7.6		~ 5.2	[TER2006]
25	Eu(III), kaolinite, 0.5 M NaClO ₄ , pH 7.6		~ 3.1	[TER2006]
40	Eu(III), kaolinite, 0.5 M NaClO ₄ , pH 7.6		~ 4.1	[TER2006]

n.e. not estimated

The sorption isotherms shown in Fig. 3-3 are parallel shifted to lower Eu(III) equilibrium concentrations with increasing temperature. Fitting by the Freundlich formalism (Eq. 3-2) with a fixed slope of 1 yields to R_d values which are consistent to the R_d values calculated by Eq. 3-1 (Tab. 3-4)

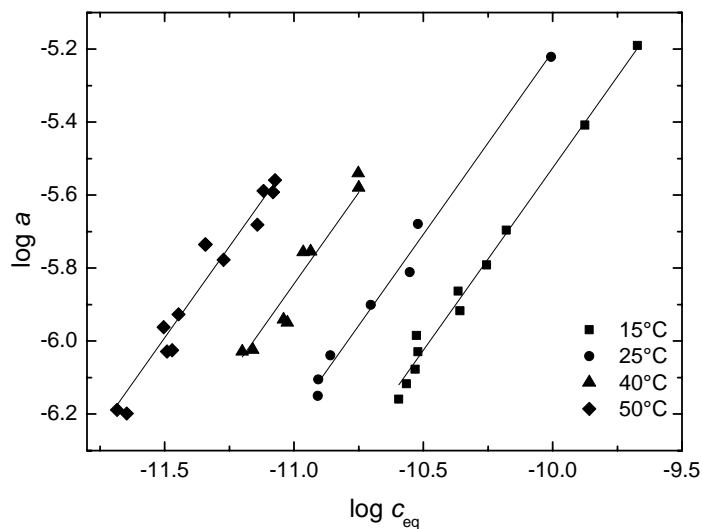


Fig. 3-3: Sorption isotherms at different temperatures for the Eu(III) sorption on OPA in synthetic pore water fitted with the Freundlich model ($n = 1$); $c_{\text{Eu(III)}} = 2 \cdot 10^{-9}$ M

The free fitting of the sorption isotherms leads independently to slopes of the isotherms of about 1.

The R_d values determined in synthetic pore water are lower than the values determined in sodium perchlorate solutions (Tab. 3-4, Fig. 3-4). A possible explanation for this fact might be a competition between the cations in the synthetic pore water and Eu(III) cations for the sorption sites of the OPA. Generally, the determined R_d values are in good agreement with the literature data for comparable conditions and analogous systems (Tab. 3-4).

The sorption of Eu(III) on OPA is an endothermic surface reaction in synthetic pore water as well as in NaClO_4 medium. From the $\ln R_d$ versus T^{-1} plot (Fig. 3-4) a sorption enthalpy ΔH_{sorb} of $(52 \pm 4) \text{ kJ} \cdot \text{mol}^{-1}$ was determined for synthetic OPA pore water and a value of $(21 \pm 13) \text{ kJ} \cdot \text{mol}^{-1}$ for 0.4 M NaClO_4 . The sorption entropies ΔS_{sorb} were calculated as $(267 \pm 12) \text{ J} \cdot \text{K}^{-1} \cdot \text{mol}^{-1}$ and $(176 \pm 44) \text{ J} \cdot \text{K}^{-1} \cdot \text{mol}^{-1}$, respectively.

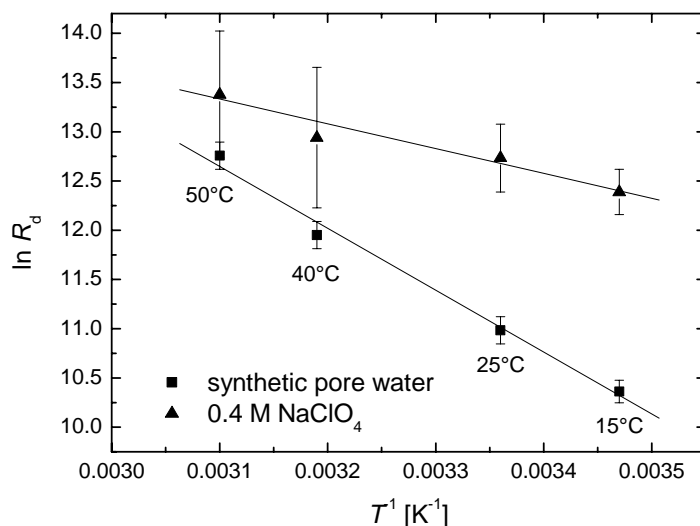


Fig. 3-4: R_d of the Eu(III) sorption on OPA as a function of the temperature. Error bar: $\pm 1\sigma$ from repeated experiments

The calculated value for ΔH_{sorb} in pore water confirms the ΔH_{sorb} value of $(47 \pm 8) \text{ kJ}\cdot\text{mol}^{-1}$, which was determined in [SCH2010]. Hence, the reproducibility of the sorption experiments is ensured. Tertre et al. [TER2005] determined a comparable ΔH_{sorb} value of $(39 \pm 15) \text{ kJ}\cdot\text{mol}^{-1}$ for the system Eu(III)/montmorillonite in 0.025 M $NaClO_4$. In our investigation the temperature dependent Eu(III) sorption in pore water medium is higher pronounced than in the sodium perchlorate medium.

The increasing sorption with rising temperature could be explained with an increase of the negative surface charge [BRA1994, TER2006b, ROZ2009]. This induces more binding sites for positively charged Eu(III) species, like $EuCO_3^+$, which is the dominant Eu(III) species under synthetic OPA pore water conditions at very low Eu(III) concentrations (see Fig. 3-1). Another possible explanation for the observed sorption behaviour could be that changes in the hydration shell of Eu(III) lead to an enforced connection to the clay surface. Such changes in the hydration shell of metal ions with rising temperature are reported for instance in [LIN2005] and [LIM2010].

High R_d values, and the pronounced temperature dependence of R_d for the Eu(III) sorption on OPA under synthetic OPA pore water conditions indicate an inner sphere surface complex formation. An outer sphere surface complex, which is a non-specific electrostatic interaction, would be characterized by small R_d values and weak temperature dependence [TER2005]. The inner sphere surface complex formation takes place between the hydroxyl groups located on the mineral surfaces [HAR2008, BAU2005, TER2005] and the Eu(III) species. The TRLFS results (see chapter 3.2.2) indicate, that the $EuCO_3^+$ species is involved in the sorption process.

3.2.4 Influence of small organic ligands

In the presence of small organic ligands like citrate or tartrate the Eu(III) sorption decreases with increasing ligand concentration at all investigated temperatures due to a complex formation between Eu(III) and the ligands in solutions (Fig. 3-5).

A significant decrease of the Eu(III) retention on OPA at a fixed temperature could be observed for a tartrate concentration above 10^{-4} M (Fig. 3-5 left) or a citrate concentration of 10^{-5} M (Fig. 3-5 right). Tab. 3-5 shows the decrease of the Eu(III) retention at the highest investigated ligand concentration ($5 \cdot 10^{-3}$ M) for different temperatures.

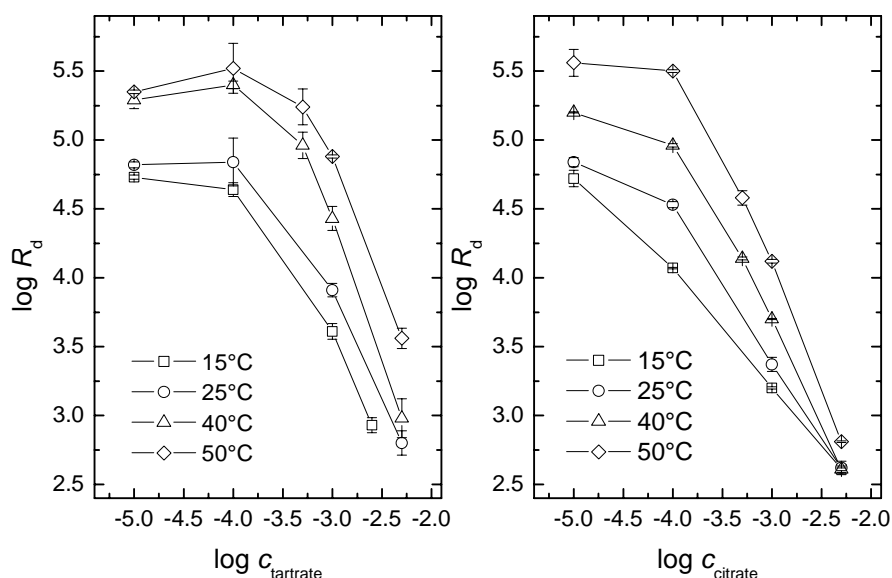


Fig. 3-5: Log R_d of the Eu(III) sorption on OPA in dependence on the ligand concentration and temperature. Left: tartrate, $c_{\text{Eu(III)}} = 2 \cdot 10^{-9}$ M, $S \cdot L^{-1} = 2 \text{ g} \cdot \text{L}^{-1}$. Right: citrate, $c_{\text{Eu(III)}} = 2 \cdot 10^{-9}$ M, $S \cdot L^{-1} = 2 \text{ g} \cdot \text{L}^{-1}$. Error bar: $\pm 1 \sigma$ from repeated experiments

Tab. 3-5 Comparison of the influence of tartrate and citrate on the Eu(III) sorption on OPA; $c_{\text{Eu(III)}} = 2 \cdot 10^{-9}$ M, $S \cdot L^{-1} = 2 \text{ g} \cdot \text{L}^{-1}$

T [°C]	Eu(III) sorption on OPA [%]		
	in the absence of the ligand	at $5 \cdot 10^{-3}$ M tartrate	at $5 \cdot 10^{-3}$ M citrate
15	95	50	44
25	95	53	44
40	95	62	43
50	95	79	56

Citrate causes a greater lowering of the Eu(III) retention than tartrate. Hence, the influence of citrate and tartrate correlates with the complex stability as the formation constants $\log \beta_{120}$ of the 1:2 complex, which is assumed to be formed at this pH value: Eu-tartrate: 7.3 ± 0.5 [ACK2011, chapter 2.2.6], Eu-citrate: 11.4 ± 0.4 [HEL2011] for $I = 0.1 \text{ M NaClO}_4$.

The temperature influence in the presence of citrate or tartrate is the same as in the absence of these ligands. With rising temperature the sorption of Eu(III) increases (Fig. 3-5). The most pronounced effect is observed at small ligand concentrations. Hence, the complex formation in solution exceeds the temperature influence on the Eu(III) sorption on OPA.

The complex formation between Eu(III) and citrate/tartrate was confirmed by TRFLFS experiments at 25°C. Starting from a citric acid concentration of $5 \cdot 10^{-5}$ M and from a tartaric acid concentration of $1 \cdot 10^{-4}$ M changes in the TRFLFS spectra (Fig. 3-6 (1a) and (1b)) and luminescence emission lifetimes (Tab. 3-7) of Eu(III) are observed for the pore water samples (without OPA). At these ligand concentrations detectable amounts of the Eu(III) tartrate or citrate complexes occur in solution. From this spectroscopic result no impact on the Eu(III) sorption until these critical ligand concentrations was assumed for the subsequent TRFLFS experiments like the following results showed.

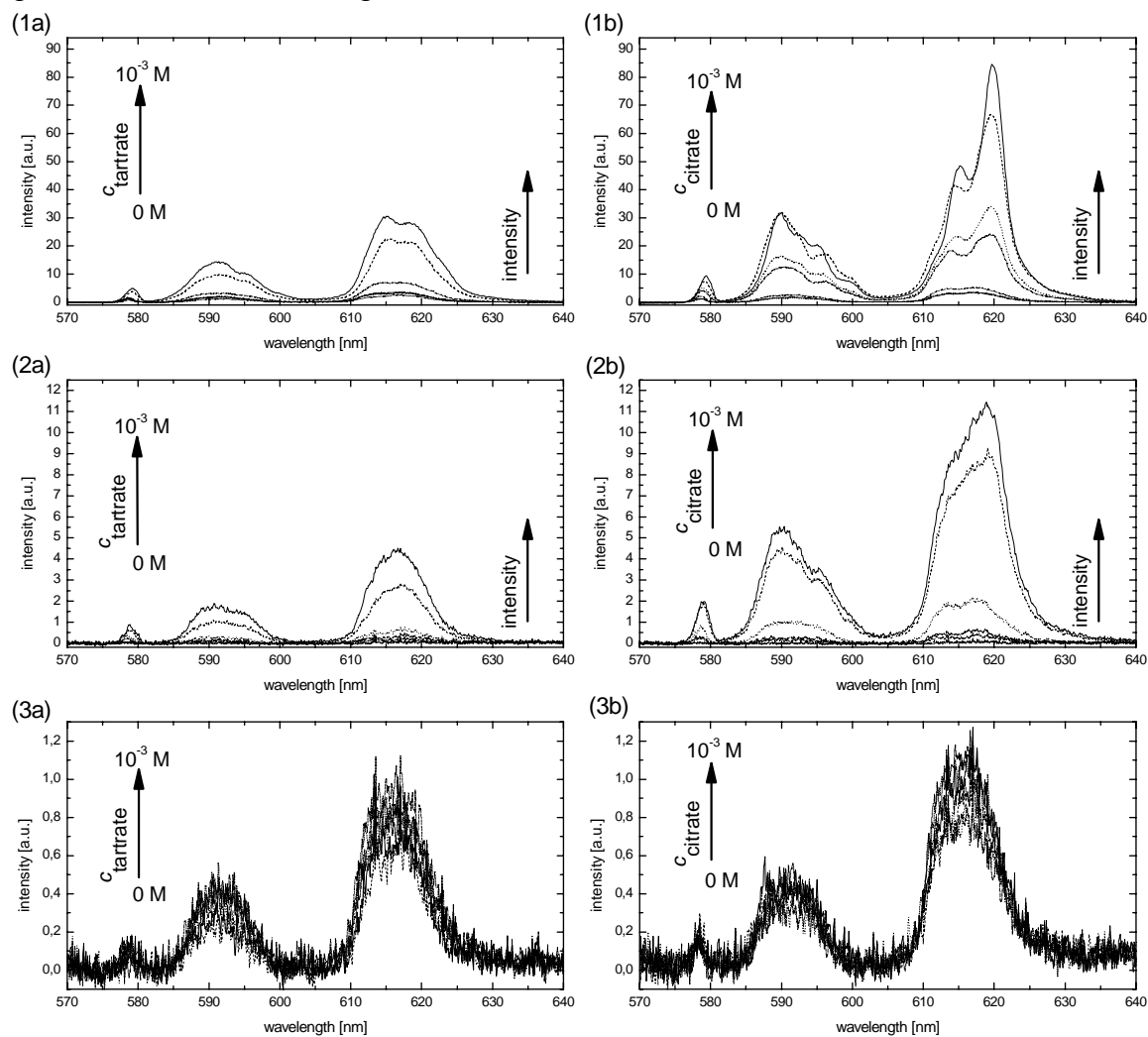


Fig. 3-6: Luminescence spectra of Eu(III) ($c_{\text{Eu(III)}} = 10^{-5}$ M) in (1) the synthetic OPA pore water, (2) the supernatant of the sorption sample and (3) the suspension of the sorption sample ($S \cdot L^{-1} = 2 \text{ g} \cdot \text{L}^{-1}$), in dependence on (a) the tartrate concentration and (b) the citrate concentration

Fig. 3-6 (3a and 3b), shows the Eu(III) luminescence spectra of the supernatants of the sorption samples in dependence on the citrate and tartrate concentration. Until a tartrate concentration of 10^{-4} M and a citrate concentration of 10^{-5} M only small amounts of Eu(III), which are assigned to unadsorbed Eu(III), were detected – but not enough to determine luminescence emission lifetimes (Tab. 3-7). From a tartrate concentration of 10^{-4} M and a citrate concentration of 10^{-5} M changes in the TRFLFS spectra and luminescence emission lifetimes could be determined again (Tab 3-7).

Combining the results of the spectroscopic investigations of the pore water samples and the supernatants with the results of the batch sorption experiments it can be concluded that the Eu(III) desorption from OPA correlates with the occurrence of significant amounts of the Eu(III) tartrate or citrate complexes in solution.

The luminescence spectra and the luminescence emission lifetimes of the suspensions differ between 0 M and 10^{-3} M tartrate and citrate marginally (Fig. 3-6, (3a) and (3b), Tab. 3-7). From this result it can be assumed that the sorbed Eu(III) species undergo no structural changes in the presence of the used ligands. That means, that tartrate and citrate are not involved in the formation of the Eu(III) surface complex, contrary to e.g. humic acids, which could form coatings on minerals or ternary complexes with metal ions [MUR1992, STE2011]. The metal ion binding to the mineral surface could then occur due to the humic acid coating in dependence on pH and ionic strength [FAI1995, WAN2004, TAK1998] or due to the sorption of the mentioned ternary complexes. Tartrate and citrate play a role in solution as complexing agents and, therefore, as desorbing agents exclusively. The reason for that is a weak outer sphere sorption of small organic ligands, like citrate, on minerals, which is described elsewhere [ANG2006, KUB1999, LAC2003]. In this work a weak ($< 15\%$ at $1 \cdot 10^{-3} \text{ mol} \cdot \text{l}^{-1}$) and nearly temperature independently ($\Delta H_{\text{sorb}} \sim -7 \pm 2 \text{ kJ} \cdot \text{mol}^{-1}$) sorption of citric acid on OPA was determined in batch sorption experiments with ^{14}C -labelled citric acid in absence of Eu(III) [SCH2010b].

The luminescence emission lifetime of the sorbed Eu(III) species averaged over all suspension spectra in the absence as well as in the presence of the organic ligands was determined with $(201 \pm 9) \mu\text{s}$ and agrees with the literature values for sorbed Eu(III) species under atmospheric conditions (Tab. 3-3). This luminescence emission lifetime corresponds to the loss of 4 water molecules in comparison to the Eu(III) aquo ion with 9 water molecules.

Tab. 3-7: Luminescence emission lifetimes (τ) and amounts of water molecules in the first coordination shell ($n(\text{H}_2\text{O})$) of Eu(III) in (1) the synthetic OPA porewater without clay, (2) the supernatant of the sorption sample and (3) the suspension of the sorption sample, in dependence on the tartrate and citrate concentration. Lifetime error: $\pm \sigma$ from repeated experiments

c_{tartrate} [mol/l]	0	$5 \cdot 10^{-6}$	$1 \cdot 10^{-5}$	$5 \cdot 10^{-5}$	$1 \cdot 10^{-4}$	$5 \cdot 10^{-4}$	$1 \cdot 10^{-3}$
$\tau_{(1)}$ [μs]	139 ± 2	146 ± 2	129 ± 1	149 ± 2	199 ± 2	381 ± 3	423 ± 3
$n(\text{H}_2\text{O})_{(1)}$	7.1 ± 0.5	6.7 ± 0.5	7.7 ± 0.5	6.6 ± 0.5	4.7 ± 0.5	2.2 ± 0.5	1.9 ± 0.5
$\tau_{(2)}$ [μs]	--	--	--	--	157 ± 6	303 ± 4	360 ± 10
$n(\text{H}_2\text{O})_{(2)}$	--	--	--	--	6.2 ± 0.5	2.9 ± 0.5	2.4 ± 0.5
$\tau_{(3)}$ [μs]	190 ± 7	205 ± 9	198 ± 7	181 ± 6	181 ± 8	204 ± 12	208 ± 11
$n(\text{H}_2\text{O})_{(3)}$	5.0 ± 0.5	4.6 ± 0.5	4.8 ± 0.5	5.3 ± 0.5	5.3 ± 0.5	4.6 ± 0.5	4.5 ± 0.5

Continue **Tab. 3-7**

C_{citrate} [mol/l]	0	$5 \cdot 10^{-6}$	$1 \cdot 10^{-5}$	$5 \cdot 10^{-5}$	$1 \cdot 10^{-4}$	$5 \cdot 10^{-4}$	$1 \cdot 10^{-3}$
$\tau_{(1)}$ [μs]	139 ± 2	131 ± 3	151 ± 3	316 ± 6	469 ± 6	556 ± 4	539 ± 4
$n(\text{H}_2\text{O})_{(1)}$	7.1 ± 0.5	7.5 ± 0.5	6.5 ± 0.5	2.8 ± 0.5	1.7 ± 0.5	1.3 ± 0.5	1.4 ± 0.5
$\tau_{(2)}$ [μs]	--	--	130 ± 7	148 ± 5	179 ± 3	345 ± 6	391 ± 4
$n(\text{H}_2\text{O})_{(2)}$	--	--	7.6 ± 0.5	6.6 ± 0.5	5.4 ± 0.5	2.5 ± 0.5	2.1 ± 0.5
$\tau_{(3)}$ [μs]	190 ± 7	206 ± 8	204 ± 8	200 ± 10	216 ± 10	227 ± 9	212 ± 7
$n(\text{H}_2\text{O})_{(3)}$	5.0 ± 0.5	4.6 ± 0.5	4.6 ± 0.5	4.7 ± 0.5	4.3 ± 0.5	4.1 ± 0.5	4.4 ± 0.5

3.3. Conclusions

The Eu(III) sorption on OPA was investigated with batch sorption experiments and TRLFS. The sorption is characterized by a very strong sorption to the clay surface in comparison to the U(VI) and Np(V) sorption in the same system (Tab. 3-4). The luminescence emission lifetimes of determined Eu(III) surface species are similar to the luminescence emission lifetimes of surface species on single mineral phases. Thus, with respect to the literature, e.g. [STU2002], and the TRLFS results of this work a ternary OPA/Eu(III)/carbonato inner sphere surface complex can be assumed. A possible surface species for the investigated Eu(III)/OPA/synthetic OPA pore water system could be $\equiv\text{X-OEuCO}_3^{\pm 0}$ [FER2008]. However another possible structure of the Eu(III) surface species might be deduced from the TRLFS results: The Eu(III) species could be coordinated bidentate to the hydroxyl surfaces and bidentate to CO_3^{2-} to the structure $(\equiv\text{X-O})_2\text{EuCO}_3^-$. Eu(III) could also be incorporated into the bulk structure of OPA. Both, the bidentate connection of Eu(III) to the mineral surface and the possible incorporation would explain the strong sorption of Eu(III) and trivalent actinides on OPA. At this point EXAFS investigations could provide specified information about the structure of this Eu(III) inner sphere surface complex.

It could be shown that the Eu(III) sorption increases with rising temperature. The sorption enthalpy was calculated with around $50 \text{ kJ} \cdot \text{mol}^{-1}$. This work makes a contribution to close the gap in the thermodynamic sorption data up to 50°C . However, more temperature related speciation and sorption data ($> 50^\circ\text{C}$) have to be measured for safety assessments and modelling of the radionuclide migration.

Small organic ligands, like citrate and tartrate influence the Eu(III) sorption on OPA. With increasing ligand concentration the Eu(III) sorption decreases. It can be concluded that the stability constant of the Eu(III) inner sphere surface complex is weaker than the complexes between Eu(III) and citrate or tartrate in solution. Therefore, these small organic ligands are able to increase the mobilization of trivalent lanthanides and, most likely, actinides. However regarding to the very low NOM content, which is found in the OPA formation of Mont Terri, Switzerland, the organic matter should influence the Ln(III)/An(III) sorption on OPA only marginally. Thus, in this OPA formation the sorption should be the dominant physiochemical process in addition to diffusion processes.

The investigations in this work proved that argillaceous rock formations, like Opalinus Clay are efficient materials to sorb trivalent lanthanides and, most likely, actinides, which makes it interesting as potential host rocks and backfill materials for nuclear waste repositories.

4 References

- [AMA2007] Amayri, S., Buda, R. A., Fröhlich, D., Heinrich, J., Klimach, T., Kratz, J. V., Reich, T., Trautmann, N., Wunderlich, T.: Sorption of Actinides (Th, U, Np, Pu, Am) on Opalinus Clay in Synthetic Porewater. Jahresberichte, Institut für Kernchemie, Universität Mainz (2007)
- [ACK2011] Acker, M., Müller, M., Barkleit, A., Taut, S.: UV-vis study of complexation of trivalent Am, Eu, and Nd by tartaric acid at low metal concentrations. HZDR-IRC Annual Report 2010, 46 Helmholtz-Zentrum Dresden-Rossendorf (2011)
- [ANG2006] Angove, M. J., Wells, J. D., Johnson, B. B.: Influence of temperature on the adsorption of mellitic acid onto kaolinite. *Langmuir* 22, 4208 (2006)
- [AOY2004] Aoyagi, N., Toraishi, T., Geipel, G., Hotokezaka, H., Nagasaki, S., Tanaka, S.: Fluorescence characteristics of complex formation of europium(III)-salicylate. *Radiochim. Acta.* 92, 589-593 (2004)
- [ARE1980] Arena, G., Cali, R., Grasso, M., Musumeci, S., Sammartano, S., Rigano, C.: Formation of proton and alkali-metal complexes with ligands of biological interest in aqueous-solution. 1. Potentiometric and calorimetric investigation of H⁺ and Na⁺ complexes with citrate, tartrate and malate. *Thermochim. Acta.* 36, 329-342 (1980)
- [BAR1995] Barbanel, Y. A.: Nephelauxetic Effect in the Optical Spectra of Americium(III). *Radiochemistry* 38, 27 (1996)
- [BAR1998] Barone, V., Cossi, M.: Quantum calculation of molecular energies and energy gradients in solution by a conductor solvent model. *J. Phys. Chem. A.* 102, 1995-2001 (1998)
- [BAR2011a] Barkleit, A., Geipel, G., Acker, M., Taut, S., Bernhard, G.: First fluorescence spectroscopic investigation of Am(III) complexation with an organic carboxylic ligand, pyromellitic acid. *Spectrochim. Acta A* 78, 549 (2011)
- [BAR2011b] Barkleit, A., Tsushima, S., Savchuk, O., Philipp, J., Heim, K., Acker, M., Taut, S., Fahmy, K.: Eu(3+)-Mediated Polymerization of Benzenetetracarboxylic Acid Studied by Spectroscopy, Temperature-Dependent Calorimetry, and Density Functional Theory. *Inorg. Chem.* 50, 5451-5459 (2011)
- [BAU2005] Bauer, A., Rabung, T., Claret, F., Schäfer, T., Buckau, G., Fanghänel, T.: Influence of temperature on sorption of europium onto smectite: The role of organic contaminants. *Applied Clay Science* 30, 1 (2005)
- [BEI1994] Beitz, J. V.: F-state luminescence of trivalent lanthanide and actinide ions in solution. *J. Alloys Compd.* 207, 41 (1994)
- [BIN2005] Binstead, R. A., Zuberbühler, A. D., Jung, B., SPECFIT Global Analysis System, Version 3.040, Spectrum Software Associates, Marlborough, MA, US 2005
- [BON1964] Bondi, A.: Van der waals volumes + radii. *J. Phys. Chem.* 68, 441 (1964)
- [BRA1994] Brady, P. V.: Alumina surface chemistry at 25, 40, and 60°C. *Geochim. Cosmochim. Acta* 58, 1213 (1994)
- [BRA2003] Bradbury, M. H., Baeyens, B.: Far-Field Sorption Data Bases for Performance Assessment of a High-Level Radioactive Waste Repository in an Undisturbed Opalinus Clay Host Rock. Technischer Bericht NTB 02-19, NAGRA Nationale Genossenschaft für die Lagerung radioaktiver Abfälle (2003).
- [BRA2006] Bradbury, M. H., Baeyens, B.: Modelling sorption data für the actinides Am(III), Np(V) and Pa(V). *Radiochimica Acta* 94, 619 (2006)
- [CAO2009] Cao, Z. J., Balasubramanian, K., Calvert, M. G., Nitsche, H.: Solvation Effects on Isomeric Preferences of Curium(III) Complexes with Multidentate phosphonopropionic Acid Ligands: CmH(2)PPA(2+) and CmHPPA(+) Complexes. *Inorg. Chem.* 48, 9700 (2009)
- [CAR1964] Carnall, W. T., Wybourne, B. G.: Electronic energy levels of the lighter actinides: U³⁺, Np³⁺, Pu³⁺, Am³⁺, and Cm³⁺. *J. of Chem. Phys.* 40, 3428 (1964)

- [CAR1968] Caranall, W. T., Fields, R. P., Ranjak, K.: Spectral Intensities of the Trivalent Lanthanides and Actinides in Solution. II. Pm^{3+} , Sm^{3+} , Eu^{3+} , Gd^{3+} , Tb^{3+} , Dy^{3+} , and Ho^{3+} , *J. of Chem. Phys.* 49, 4412 (1968)
- [CHO1994] Choppin, G. R., Rizkalla, E. N., Elansi, T. A., Dadgar, A.: Complexation Thermodynamics of Lanthanide Ions by Benzenepolycarboxylate Ligands. *J. Coord. Chem.* 31, 297 (1994)
- [DER1999] De Robertis, A., De Stefano, C., Foti, C.: Medium effects on the protonation of carboxylic acids at different temperatures. *J. Chem. Eng. Data.* 44, 262 (1999)
- [DIN2008] DIN 32645, Chemical analysis - Decision limit, detection limit and determination limit under repeatable conditions - Terms, methods, evaluation. Beuth Verlag, (2008)
- [DOL1989] Dolg, M., Stoll, H., Savin, A., Preuss, H.: Energy-adjusted pseudopotentials for the rare-earth elements. *Theor. Chim. Acta.* 75, 173 (1989)
- [EBE1972] Eberle, S. H., Moattar, F.: Die Komplexe des Am(III) mit Zitronensäure. *Inorg. Nucl. Chem. Letters* 8, 265 (1972)
- [FAI1995] Fairhurst, A. J., Warwick, P., Richardson, S.: The influence of humic acid on the adsorption of europium onto inorganic colloids as a function of pH. *Colloids Surfaces A: Physicochem. Eng. Aspects* 99, 187 (1995)
- [FER2008] Fernandes, M. M., Baeyens, B., Bradbury, M. H.: The influence of carbonate complexation on lanthanide/actinide sorption on montmorillonite, *Radiochimica Acta* 96, 691 (2008)
- [FER2010] Fernandes, M. M., Stumpf, T., Baeyens, B., Walther, C., Bradbury, M. H.: Spectroscopic Identification of Ternary Cm-Carbonate Surface Complexes. *Environ. Sci. Technol.* 44, 921 (2010).
- [FRI2004] Frisch, M. J., Trucks, G. W., Schlegel, H. B., Scuseria, G. E., Robb, M. A., Cheeseman, J. R., Montgomery, J., J. A., Vreven, T. K., K. N., Burant, J. C., Millam, J. M., Iyengar, S. S., Tomasi, J., Barone, V., Mennucci, B., Cossi, M., Scalmani, G., Rega, N., Petersson, G. A., Nakatsuji, H., Hada, M., Ehara, M., Toyota, K., Fukuda, R., Hasegawa, J., Ishida, M., Nakajima, T., Honda, Y., Kitao, O., Nakai, H., Klene, M., Li, X., Knox, J. E., Hratchian, H. P., Cross, J. B., Bakken, V., Adamo, C., Jaramillo, J., Gomperts, R., Stratmann, R. E., Yazyev, O., Austin, A. J., Cammi, R., Pomelli, C., Ochterski, J. W., Ayala, P. Y., Morokuma, K., Voth, G. A., Salvador, P., Dannenberg, J. J., Zakrzewski, V. G., Dapprich, S., Daniels, A. D., Strain, M. C., Farkas, O., Malick, D. K., Rabuck, A. D., Raghavachari, K., Foresman, J. B., Ortiz, J. V., Cui, Q., Baboul, A. G., Clifford, S., Cioslowski, J., Stefanov, B. B., Liu, G., Liashenko, A., Piskorz, P., Komaromi, I., Martin, R. L., Fox, D. J., Keith, T., Al-Laham, M. A., Peng, C. Y., Nanayakkara, A., Challacombe, M., Gill, P. M. W., Johnson, B., Chen, W., Wong, M. W., Gonzalez, C., Pople, J. A.: Gaussian 03, Revision D.01. Gaussian, Inc., Wallingford CT (2004).
- [FRÖ2011] Fröhlich, D. R., Amayri, S., Drebert, J., Reich, T.: Sorption of neptunium(V) on Opalinud Clay under aerobic/anaerobic conditions. *Radiochimica Acta* 99, 1 (2011)
- [GLA2005] Glaus, M. A., Baeyens, B., Lauber, M., Rabung, T., Van Loon, L. R.: Influence of water-extractable organic matter from Opalinus Clay on the sorption and speciation of Ni(II), Eu(III) and Th(IV). *Appl. Geochem.* 20, 443 (2005).
- [GON1987] Goncalves, M. L. S., Mota, A. M.: Complexes of vanadyl and uranyl ions with the chelating groups of humic matter. *Talanta.* 34, 839 (1987)
- [GUI2003] Guillaumont, R., Fanghänel, T., Fuger, J., Grenthe, I., Neck, V., Palmer, D. A., Rand, M. H.: Update on the Chemical Thermodynamics of Uranium, Neptunium, Plutonium, Americium and Technetium. Amsterdam: Elsevier, 2003.
- [HAR2008] Hartmann, E., Geckeis, H., Rabung, T., Lützenkirchen, J., Fanghänel, T.: Sorption of radionuclides onto natural clay rocks, *Radiochimica Acta* 96, 699 (2008)
- [HAS1989] Hasegawa, Y., Morita, Y., Hase, M., Nagata, M.: Complexation of lanthanoid(III) with substituted benzoic or phenylacetic acids and extraction of these acids. *Bull. Chem. Soc. Jpn.* 62, 1486 (1989)
- [HAS1990] Hasegawa, Y., Yamazaki, N., Usui, S., Choppin, G. R.: Effects of phenyl groups on thermodynamic parameters of lanthanoid(III) complexation with aromatic carboxylic-acids. *Bull. Chem. Soc. Jpn.* 63, 2169 (1990a)

- [HEL2010] Heller, A.: Spektroskopische Untersuchungen zur Komplexbildung von Cm(III) und Eu(III) mit organischen Modellliganden sowie ihrer chemischen Bindungsform in menschlichem Urin (in vitro). PhD thesis, Technische Universität Dresden (2011)
- [HEL2011] Heller, A., Barkleit, A., Foerstendorf, H., Bernhard, G.: Luminescence and absorption spectroscopic study on the complexation of europium(III) with citric acid. HZDR-IRC Annual Report 2010, Helmholtz-Zentrum Dresden-Rossendorf (2011)
- [HOR1979] Horrocks, W. D., Sudnick, D. R.: Lanthanide ion probes of structure in biology - laser-induced luminescence decay constants provide a direct measure of the number of metal-coordinated water-molecules. *J. Am. Chem. Soc.* 101, 334 (1979)
- [HOT2007] Hoth, P., Wirth, H., Reinhold, K., Bräuer, V., Krull, P., Feldrappe, H.: Endlagerung radioaktiver Abfälle in tiefen geologischen Formationen Deutschlands. Untersuchung und Bewertung von Tongesteinsformationen. Bundesanstalt für Geowissenschaften und Rohstoffe BGR (2007).
- [HUB1974] Hubert, S., Hussonnois, M., Brillard, L., Goby, G., Guillaumont, R.: Determination simultanee de constants de formation de complexes citrique de l'Amercium, du Curium, du Californium, de l'Einsteinium et du Fermium. *J. Inorg. Nucl. Chem.* 36, 2361 (1974)
- [HUM2002] Hummel, W., Berner, U., Curti, E., Pearson, F. J., Thoenen, T.: Nagra / PSI Chemical Thermodynamic Data Base 01/01. Technischer Bericht 02-16, NAGRA National Cooperative for the Disposal of Radioactive Waste (2002).
- [HUM2002b] Hummel, W., Berner, U., Curti, E., Pearson, F. J., Thoenen, T.: Nagra/PSI chemical thermodynamic data base 01/01. *Radiochim. Acta.* 90, 805 (2002)
- [INF2008] Infante, C. M. C.; Rocha, F. R. P.: A critical evaluation of a long pathlength cell for flow-based spectrophotometric measurements. *Microchemical Journal* 90, 19 (2008)
- [IRV1970] Irving, H., Sinha, S. P.: Formation constants of europium(III)-salicylate complexes and their extraction into isoamyl alcohol. *Anal. Chim. Acta.* 49, 449 (1970)
- [JOS2011] Joseph, C.: Sorption of uranium(VI) onto Opalinus Clay in the absence and presence of humic acid in Opalinus Clay pore water. *Chem. Geol.* 284, 240 (2011)
- [JOS2011b] Joseph, C.: personal communication, Institute of Radiochemistry, Helmholtz Zentrum Dresden-Rossendorf, November 2011
- [KIM1994] Kim, J. I., Klenze, R., Wimmer, H., Runde, W., Hauser, W.: A study of the carbonate complexation of Cm-III and Eu-III by time-resolved laser fluorescence spectroscopy. *Journal of Alloys and Compounds* 213, 333 (1994).
- [KIM1994b] Kimura, T., Choppin, G. R.: Luminescence study on determination of the hydration number of Cm(III). *J. Alloys Compd.* 213, 313 (1994)
- [KIM1998] Kimura, T., Kato, Y.: Luminescence study on determination of the inner-sphere hydration number of Am(III) and Nd(III). *J. Alloys Compd.* 271, 867 (1998)
- [KIM2001] Kimura, T., Nagaishi, R., Kato, Y., Yoshida, Z.: Luminescence study on solvation of americium(III), curium(III) and several lanthanide(III) ions in nonaqueous and binary mixed solvents. *Radiochim. Acta.* 89, 125 (2001)
- [KLI2007] Klimach, T., Amayri, S., Reich, T.: Sorption isotherms for ²⁴¹Am(III) on kaolinite. *Jahresberichte, Institut für Kernchemie, Universität Mainz* (2007)
- [KRE2007] Krepelova, A.: Influence of Humic Acid on the Sorption of Uranium(VI) and Americium(III) onto Kaolinit, PhD thesis, Technische Universität Dresden (2007)
- [KRI1980] Krishnan, R., Binkley, J. S., Seeger, R., Pople, J. A.: Self-consistent molecular-orbital methods. 20. Basis set for correlated wave-functions. *J. Chem. Phys.* 72, 650 (1980)
- [KUB1999] Kubicki, J. D., Schroeter, L. M., Itoh, M. J., Nguyen, B. N., Apitz, S. E.: Attenuated total reflectance Fourier-transform infrared spectroscopy of carboxylic acids adsorbed onto mineral surfaces. *Geochim. Cosmochim. Acta* 63, 2709 (1999)

- [KUK2010] Kuke, S., Marmodee, B., Eidner, S., Schilde, U., Kumke, M. U.: Intramolecular deactivation processes in complexes of salicylic acid or glycolic acid with Eu(III). *Spectrochim. Acta A: Mol. Biomol. Spectrosc.* 75, 1333 (2010)
- [KUL1986] Kulshrestha, R., Sengar, N., Singh, M.: Polarographic studies of mixed ligand complexes of europium(III) with α -, β - and γ -picolines & carboxylate ions. *Indian J. of Chemistry* 26A, 940 (1987)
- [LAC2003] Lackovic, K., Johnson, B. B., Angove, M. J., Wells, J. D.: Modeling the adsorption of citric acid onto Mulloorina illite and related clay minerals. *J. Colloid Interface Sci.* 267, 49 (2003)
- [LAU2000] Lauber, M., Baeyens, B., Bradbury, M. H.: Physico-Chemical Characterisation and Sorption Measurements of Cs, Sr, Ni, Eu, Th, Sn and Se on Opalinus Clay from Mont Terri. *Technischer Bericht NTB 00-11*, NAGRA Nationale Genossenschaft für die Lagerung radioaktiver Abfälle (2000)
- [LIM2010] Lim, L. H. V., Prebil, A. B., Ellmerer, A. E., Randolph, B. R., Rode, B. M.: Temperature Dependence of Structure and Dynamics of the Hydrated Ca(2+) Ion According to ab initio Quantum Mechanical Charge Field and Classical Molecular Dynamics. *Journal of Computational Chemistry* 31, 1195 (2010)
- [LIN2005] Lindqvist-Reis, P., Klenze, R., Schubert, G., Fanghanel, T.: Hydration of Cm³⁺ in aqueous solution from 20 to 200 degrees C. A time-resolved laser fluorescence spectroscopy study. *Journal of Physical Chemistry B* 109, 3077 (2005)
- [LUN1984] Lundqvist-Reis, P., Lu, J. F., Svantesson, I.: Hydrophilic complexes of the actinides. III. Lactates of Am³⁺, Eu³⁺, U⁴⁺ and UO₂²⁺. *Acta Chem. Scand. A.* 38, 501 (1984)
- [MAT2007] Mathur, J. N., Cernochova, K., Choppin, G. R.: Thermodynamics and laser luminescence spectroscopy of binary and ternary complexation of Am³⁺, Cm³⁺ and Eu³⁺ with citric acid, and citric acid + EDTA at high ionic strength. *Inorg. Chim. Acta* 360, 1785 (2007)
- [MIC2003] Michel, U., Resnick, P., Kipp, B., DeSimone, J. M.: Copolymerization of tetrafluoroethylene and 2,2-bis(trifluoromethyl)-4,5-difluoro-1,3-dioxole in supercritical carbon dioxide. *Macromolecules* 36, 7107 (2003)
- [MOL2008] Moll, H., Johnsson, A., Schäfer, M., Pedersen, K., Budzikiewicz, H., Bernhard, G.: Curium(III) complexation with pyoverdins secreted by a groundwater strain of *Pseudomonas fluorescens*. *BioMetals.* 21, 219 (2008)
- [MOM2005] Mompean F. J. (ed.): *CHEMICAL THERMODYNAMICS OF COMPOUNDS AND COMPLEXES OF U, Np, Pu, Am, Tc, Se, Ni AND Zr WITH SELECTED ORGANIC LIGANDS*, (Chemical Thermodynamics Vol. 9) Elsevier 2005
- [MOU1999] Moulin, C., Wei, J., Van Iseghem, P., Laszak, I., Plancque, G., Moulin, V.: Europium complexes investigations in natural waters by time-resolved laser-induced fluorescence. *Anal. Chim. Acta* 396, 253 (1999).
- [MÜL2010] Müller, M., Acker, M., Taut, S., Bernhard, G.: Complex formation of trivalent americium with salicylic acid at very low concentrations. *J. Radioanal. Nucl. Chem.* 286, 175 (2010)
- [MUR1992] Murphy, E. M., Zachara, J. M., Smith, S. C., Phillips, J. L.: The sorption of humic acids to mineral surfaces and their role in contaminant binding. *Sci. Tot. Environ.* 118, 413 (1992)
- [NAG2002] NAGRA: Projekt Opalinuston - Synthese der geowissenschaftlichen Untersuchungsergebnisse, Entsorgungsnachweis für abgebrannte Brennelemente, verglaste hochradioaktive sowie langlebige mittelaktive Abfälle. *Technischer Bericht NTB 02-03*, NAGRA National Cooperative for the Disposal of Radioactive Waste (2002)
- [NEL2008] Neles, J., Mohr, S., Schmidt, G.: Endlagerung wärmeentwickelnder radioaktiver Abfälle in Deutschland; Anhang Abfälle Entstehung, Mengen und Eigenschaften von wärmeentwickelnden radioaktiven Abfällen. *GRS Gesellschaft für Anlagen- und Reaktorsicherheit* (2008).
- [OHY1971] Ohyoshi, E., Ohyoshi, A.: A study of complexes with a polybasic acid - Am(III) Citrate complexes. *J. Inorg. Chem.* 33, 4265 (1971)

- [PAT2007] Pathak, P. N., Choppin, G. R.: Effect of complexing anions on europium sorption on suspended silica: a TRLFS study for ternary complex formation. *Radiochim. Acta* 95, 267 (2007)
- [PLA2003] Plancque, G., Moulin, V., Toulhoat, P. and Moulin, C.: Europium speciation by time-resolved laser-induced fluorescence. *Anal. Chim. Acta* 478, 11 (2003)
- [POW2005] Powell, K. J.: The IUPAC Stability Constants Database. (2005).
- [PUR1972] Purdie, N., Tomson, M. B., Riemann, N.: The Thermodynamics of Ionization of Polycarboxylic Acids. *J. Solution Chem.* 1, 465 (1972)
- [RAB2000] Rabung, T., Stumpf, T., Geckeis, H., Klenze, R., Kim, J. I.: Sorption of Am(III) and Eu(III) onto gamma-alumina: experiment and modelling. *Radiochim. Acta* 88, 711 (2000)
- [RAB2005] Rabung, T., Pierret, M.C., Bauer, A., Geckeis, H., Bradbury, M. H., Baeyens, B.: Sorption of Eu(III)/Cm(III) on Ca-montmorillonite and Na-illite. Part I: Batch sorption and time-resolved laser fluorescence spectroscopy experiments, *Geochimica et Cosmochimica Acta*, 69 5393 (2005)
- [RAO1987] Rao, V. K., Mahajan, G. R., Natarajan, P. R.: Hydrolysis and Carboxylate Complexation of Trivalent Americium. *Inorg. Chim. Acta* 128, 131 (1987)
- [RAO2005] Rao, L., Zanonato, P. L., Di Bernardo, P.: Interaction of Actinides with Carboxylates in Solution: Complexation of U(VI), Th(IV), and Nd(III) with Acetate at Variable Temperatures. *J. Nucl. Radiochem. Sci.* 6, 31 (2005)
- [RAO2010] Rao, L., Tian, G. Srinivasan, G. T., Zanonato, P. L., Di Bernardo, P.: Spectrophotometric and Calorimetric Studies of Np(V) Complexation with Acetate at Various Temperatures from $T = 283$ to 343 K. *J. of Solution Chemistry*, DOI 10.1007/s10953-010-9592-z (2010)
- [RAR1985] Rard, J. A.: Chemistry and thermodynamics of europium and some of its simpler inorganic compounds and aqueous species. *Chemical Review* 85, 555 (1985)
- [RES1997] Resnick, P. R., Buck, W. H. In: *Modern Fluoropolymers*. Scheirs, J., Ed. John Wiley & Sons: Chichester, 397 (1997)
- [ROZ2009] Rozalen, M., Brady, P. V., Huertas, F. J.: Surface chemistry of K-montmorillonite: Ionic strength, temperature dependence and dissolution kinetics. *J. Colloid Interface Sci.* 333, 474 (2009)
- [RUN2000] Runde, W., Van Pelt, C., Allen, P. G.: Spectroscopic characterization of trivalent f-elements (Eu, Am) solid carbonates. *Journal of Alloys and Compounds* 303, 182 (2000)
- [SCH2008] Schott, J.: Temperaturabhängige Untersuchungen zur Komplexbildung von Eu(III) mit dem Huminstoff-Modellliganden 2,5-Dihydroxybenzoesäure. Bachelor thesis (2008)
- [SCH2010] Schott, J., Acker, M., Barkleit, A., Taut, S., Bernhard, G.: Sorption of Eu(III) onto Opalinus Clay - temperature depending investigations. *FZD-IRC Annual Report 2009*, Forschungszentrum Dresden-Rossendorf (2010)
- [SCH2010b] Schott, J.: Untersuchungen zum Einfluss der Temperatur und kleiner organischer Liganden auf die Sorption von Eu(III) am Opalinuston. Master thesis, TU Dresden (2010)
- [SCH2012] Schott, J. Acker, M, Barkleit, A., Brendler, V., Taut, S., Bernhard, G.: The influence of temperature and small organic ligands on the sorption of Eu(III) on Opalinus Clay, *Radiochim. Acta* 100, 1-10 (2012)
- [STE2011] Steudtner, R., Müller, K., Schmeide, K., Sachs, S., Bernhard, G.: Binary and Ternary Uranium(VI) Humate Complexes Studied by Attenuated Total Reflection Fourier-transform Infrared Spectroscopy. *Dalton Trans.* (2011) submitted
- [STU2002] Stumpf, T., Bauer, A., Coppin, F., Fanghänel, T., Kim, J. I.: Inner-sphere, outer-sphere and ternary surface complexes: a TRLFS study of the sorption process of Eu(III) onto smectite and kaolinite. *Radiochim. Acta* 90, 345 (2002)
- [STU2006] Stumpf, T., Fernandes, M. M., Walther, C., Dardenne, K., Fanghänel, T.: Structural characterization of Am incorporated into calcite: A TRLFS and EXAFS study. *J. Colloid Interface Sci.* 302, 240 (2006)

- [TAK1998] Takahashi, Y., Minai, Y., Kimura, T., Tominaga, T.: Adsorption of europium(III) and americium(III) on kaolinite and montmorillonite in the presence of humic acid. *J. Radioanal. Nucl. Chem.* 234, 277 (1998)
- [TER2005] Tertre, E., Berger, G., Castet, S., Loubet, M., Giffaut, E.: Experimental sorption of Ni^{2+} , Cs^+ and Ln^{3+} onto a montmorillonite up to 150°C. *Geochim. Cosmochim. Acta* 69, 4937 (2005)
- [TER2006] Tertre, E., Berger, G., Simoni, E., Castet, S., Giffaut, E., Loubet, M., Catalette, H.: Europium retention onto clay minerals from 25 to 150°C: Experimental measurements, spectroscopic features and sorption modelling. *Geochim. Cosmochim. Acta* 70, 4563 (2006)
- [TER2006b] 45. Tertre, E., Castet, S., Berger, G., Loubet, M., Giffaut, E.: Surface chemistry of kaolinite and Na-montmorillonite in aqueous electrolyte solutions at 25 and 60 °C: Experimental and modeling study. *Geochim. Cosmochim. Acta* 70, 4579 (2006).
- [THO1993] Thouvenot, P., Hubert, S., Moulin, C., Decambox, P., Mauchien, P.: Americium trace determination in aqueous and solid matrices by time-resolved laser-induced fluorescence. *Radiochim. Acta.* 61, 15 (1993)
- [TIA2010] Tian, G. X., Martin, L. R., Rao, L. F.: Complexation of Lactate with Neodymium(III) and Europium(III) at Variable Temperatures: Studies by Potentiometry, Microcalorimetry, Optical Absorption, and Luminescence. *Inorg. Chem.* 49, 10598 (2010)
- [TOR2005] Toraishi, T., Nagasaki, S., Tanaka, S.: A theoretical study on molecular structure of Eu(III)-salicylate complexes in aqueous system. *Theochem-J. Mol. Struct.* 757, 87 (2005)
- [VAN2003] Van Loon, L. R., Soler, J. M., Bradbury, M. H.: Diffusion of HTO, $^{36}\text{Cl}^-$ and $^{125}\text{I}^-$ in Opalinus Clay samples from Mont Terri: Effect of confining pressure. *J. Contam. Hydrol.* 61, 73 (2003)
- [WAN1999] Wang, Z. M., van de Burgt, L. J., Choppin, G. R.: Spectroscopic study of lanthanide(III) complexes with carboxylic acids. *Inorg. Chim. Acta.* 293, 167 (1999)
- [WAN2004] Wang, X. K., Rabung, T., Geckeis, H., Panak, P. J., Klenze, R., Fanghänel, T.: Effect of humic acid on the sorption of Cm(III) onto gamma- Al_2O_3 studied by the time-resolved laser fluorescence spectroscopy. *Radiochim. Acta* 92, 691 (2004)
- [WAT1997] Waterbury, R. D., Yao, W., Byrne, R. H.: Long pathlength absorbance spectroscopy: trace analysis of Fe(II) using a 4.5 m liquid core waveguide. *Anal. Chim. Acta* 357, 99 (1997)
- [WIL2005] Wilson, R. E., Hu, Y.-J., Nitsche, H.: Detection and quantification of Pu(III, IV, V, and VI) using a 1.0-meter core waveguide. *Radiochim. Acta* 93, 203 (2005)
- [WOL1992] Wolery, T. J.: EQ3/6, A Software Package for the Geochemical Modeling of Aqueous Systems. UCRL-MA-110662 Part I. Lawrence Livermore National Laboratory (1992).
- [WU2009] Wu, T., Amayri, S., Drebert, J., Van Loon, L. R., Reich, T. : Neptunium(V) Sorption and Diffusion in Opalinus Clay. *Environ. Sci. Technol.* 43, 6567 (2009).
- [YUS1990] Yusov, A. B.: Photoluminescence of americium(III) in aqueous and organic solutions. *J. Radioanal. Nucl. Chem.* 143, 287 (1990)
- [ZAN2001] Zanonato, P. L., Di Bernardo, P., Bismondo, A., Rao, L., Choppin, G. R.: Thermodynamic studies of the complexation between Neodymium and Acetate at Elevated Temperatures. *J. Solution Chem.* 30, 1 (2001)
- [ZES2011] Zessin, J.: UV/VIS-Spektroskopische Untersuchungen zur Komplexierung von Neodym(III) mit Pyromellitsäure. Bachelor thesis, TU Dresden (2011)
- [ZOT2002] Zotov, A. V., Tagirov, B. R., Diakonov, I. I., Ragnarsdottir, K. V.: A potentiometric study of Eu^{3+} complexation with acetate ligand from 25 to 170°C at P_{sat} . *Geochim. Cosmochim. Acta* 66, 3599 (2002)

